University of Southampton

Faculty of Engineering and Physical Sciences

School of Chemistry

Doped Scandium-Based Layered Oxychalcogenides

by

Liam Paul Kemp

ORCID ID 0009-0007-7110-5888

Thesis for the degree of Doctor of Philosophy

March 2025

University of Southampton

Abstract

Faculty of Engineering and Physical Sciences

School of Chemistry

Doctor of Philosophy

Doped Scandium-Based Layered Oxychalcogenides

by

Liam Paul Kemp

Layered oxychalcogenides are a branch of Mixed Anion Layered Materials, known for their electrical properties and are studied for transparent conducting applications. Their large optical band gaps and intrinsic layering permits the transport of charge carriers which may be improved by doping.

The wide band gap layered quinternary '325' oxychalcogenide $Sr_3Sc_2O_5Cu_2S_2$ has been long acknowledged as a promising candidate material for *p*-type transparent conductivity due to an exceptional undoped hole mobility, but has received limited research attention since its initial recognition. In *Chapter 3*, the electrical enhancement of $Sr_3Sc_2O_5Cu_2S_2$ is achieved by the aliovalent doping of sodium and potassium and the introduction of strontium vacancies without compromising transparency. This is the first reported doping study of this material.

Greater potential was arguably observed by the selenide analogue, $Sr_3Sc_2O_5Cu_2Se_2$, whose undoped conductivity is greater than $Sr_3Sc_2O_5Cu_2S_2$ but at the expense of transparency. A comprehensive doping study of $Sr_3Sc_2O_5Cu_2Se_2$ was carried out containing eight unique dopants or site vacancies, of which five yielded improved performance. The most impressive enhancements of the electrical conductivity of $Sr_3Sc_2O_5Cu_2Se_2$ resulted from the doping of K^+ or Na^+ on the Sr^{2+} site, or Mg^{2+} on the Sc^{3+} site. Heavy sodium doping produced an almost five order of magnitude increase in conductivity up to 23.4 S cm^{-1} with no reduction in band gap. To the best of the author's knowledge this is the most extensive doping investigation of any single material in literature.

The '426' relatives of these materials, $Sr_4Sc_2O_6Cu_2S_2$ and $Sr_4Sc_2O_6Cu_2Se_2$, are explored within *Chapter 4* to the same aim. These are not as impressive but still show an order of magnitude improved performance by doping. A delicate thermodynamic balance encountered during the synthesis of these materials is reported whereby purity is compromised by formation of the more stable $Sr_3Sc_2O_5Cu_2S_2$ and $Sr_3Sc_2O_5Cu_2Se_2$ phases. This also harms their electrical properties through an inability to be sufficiently densified. These oxychalcogenides were produced alongside their gallium and indium counterparts, the former yielding greater conductivities but both with band gaps too small for use in commercial transparent conducting applications.

Finally, solid-state metathesis is explored in *Chapter 5* as a method for oxychalcogenide synthesis, applied to materials of this type only once before. The scandium material $Sr_3Sc_2O_5Cu_2Se_2$ described above was synthesised successfully by metathesis for the first time, including a detailed temperature dependency experiment compared to the conventional method. This process was applied to a novel combinatorial approach whereby multiple oxychalcogenides may be yielded from a 'one-pot' parallel reaction, but undesirable product site mixing limits the scalability and applicability of this method in practice.

This work furthers our understanding of scandium-based layered oxychalcogenides for *p*-type conductivity.

Table of Contents

Table of Contents **3**

Table of Tables **10**

Table of Figures **12**

Research Thesis: Declaration of Authorship **39**

Acknowledgements **40**

List of Abbreviations **42**

Chapter 1 Introduction and Literature Review **44**

1.1 Mixed Anion Layered Materials: Structures, Properties, and Phase Space **44**

1.1.1 Ternary and Quaternary MALMs 45

1.1.2 Nomenclature, Conventions, and Exceptions 47

1.1.3 Quinternary MALMs 50

1.1.3.1 The Ruddlesden-Popper Oxides 51

1.1.3.2 $A_2BO_2M_2Q_2$; the 212 structure 52

1.1.3.3 $A_3B_2O_5M_2Q_2$; the 325 structure 54

1.1.3.4 $A_4B_2O_6M_2Q_2$; the 426 structure 58

1.1.3.5 Other Quinternary Oxychalcogenide Structures 61

1.1.3.6 Structural Review Summary 63

1.2 Transparent Conductivity **64**

1.2.1 Invisible Metals 64

1.2.2 Band Theory 66

1.2.2.1 Conductors, Semiconductors, and Insulators 66

1.2.2.2 Optical Transparency 69

1.2.2.3 Semiconductor Doping 70

1.2.2.4 Indium Tin Oxide: A Case Study of Degenerate Doping 72

1.2.3 Transparent Conducting Oxides 76

1.2.3.1 *N*-type 76

1.2.3.2 *P*-type 78

1.2.3.3 MALMs as *P*-type TCOs 79

1.3 Research Motivation and Aims of this Work 82

Chapter 2 Experimental Methods 83

2.1 Solid-State Chemistry 83

2.1.1 Syntheses in Air 83

2.1.2 Syntheses under Vacuum 84

2.2 Analytical Techniques 86

2.2.1 X-ray Diffraction 86

2.2.1.1 A Short History of Diffraction 86

2.2.1.2 Diffraction of a Crystal Lattice 89

2.2.1.3 Generating X-rays 91

2.2.1.4 The Diffraction Measurement 94

2.2.1.5 Refining a Powder Diffraction Pattern 95

2.2.1.6 Sample Preparation and Instrument Settings 97

2.2.1.7 Air Sensitive X-ray Diffraction 97

2.2.2 UV-Vis Spectroscopy 99

2.2.2.1 Principles of UV-Vis 99

2.2.2.2 The Spectrophotometer 100

2.2.2.3 The Spectroscopy Measurement 101

2.2.2.4 Tauc Plots for Band Gap Estimation 104

2.2.2.5 Sample Preparation and Instrument Settings 106

2.2.3 Electrical Conductivity 107

2.2.3.1 Conductivity, Resistivity and Resistance 107

2.2.3.2 Two Probe vs Four Probe Resistivities 108

2.2.3.3 The van der Pauw Technique 110

2.2.3.4 Sample Preparation and Instrument Settings 113

2.3 The Syntheses of Binary Compounds 114

2.3.1 Strontium Oxide, SrO 115

2.3.2 Strontium Sulfide, SrS 117
2.3.3 Strontium Selenide, SrSe 118
2.3.4 Barium Selenide, BaSe 121
2.3.5 Sodium Selenide, Na_2Se 124
2.3.6 Copper Sulfide, Cu_2S 128

Chapter 3 The Synthesis and Conductivity Investigation of Doped $Sr_3Sc_2O_5Cu_2Ch_2$ '325' Oxychalcogenides 136

3.1 Introduction 136
3.1.1 The ACu_3Ch_2 impurities 138
3.2 Experimental 139
3.2.1 Precursors 139
3.2.2 Synthesis of Pristine Materials 139
3.2.3 Synthesis of Doped Materials 140
3.2.4 Rietveld Refinement of Doped Materials 141
3.2.4.1 The Modelling of Doped MALM Products as Pristines 141
3.2.4.2 The Refinement of Impurities in Doped MALMs 144
3.3 $Sr_3Sc_2O_5Cu_2S_2$ 146
3.3.1 Repeated Literature Synthesis of Pristine $Sr_3Sc_2O_5Cu_2S_2$ 146
3.3.1.1 Alternate Synthesis Attempts 149
3.3.2 Potassium Doping, $(Sr_{3-x}K_x)Sc_2O_5Cu_2S_2$ 151
3.3.3 Sodium Doping, $(Sr_{3-x}Na_x)Sc_2O_5Cu_2S_2$ 159
3.3.4 Strontium Deficiencies, $Sr_{3-x}Sc_2O_5Cu_2S_2$ 164
3.3.5 $Sr_3Sc_2O_5Cu_2S_2$ Doping Conclusions 169
3.4 $Sr_3Sc_2O_5Cu_2Se_2$ 171
3.4.1 Repeated Literature Synthesis of Pristine $Sr_3Sc_2O_5Cu_2Se_2$ 171
3.4.2 Potassium Doping, $(Sr_{3-x}K_x)Sc_2O_5Cu_2Se_2$ 173
3.4.3 Sodium Doping, $(Sr_{3-x}Na_x)Sc_2O_5Cu_2Se_2$ 182
3.4.4 Magnesium Doping, $Sr_3(Sc_{2-x}Mg_x)O_5Cu_2Se_2$ 190

3.4.5 Barium Doping, $(Sr_{3-x}Ba_x)Sc_2O_5Cu_2Se_2$ 196

3.4.6 Yttrium Doping, $Sr_3(Sc_{2-x}Y_x)O_5Cu_2Se_2$ 203

3.4.7 Lanthanum Doping, $Sr_3(Sc_{2-x}La_x)O_5Cu_2Se_2$ 208

3.4.8 Strontium Deficiencies, $Sr_{3-x}Sc_2O_5Cu_2Se_2$ 214

3.4.9 Copper Deficiencies, $Sr_3Sc_2O_5Cu_{2-x}Se_2$ 219

3.4.10 $Sr_3Sc_2O_5Cu_2Se_2$ Doping Conclusions 224

3.5 Conclusions and Future Work 227

Chapter 4 The Synthesis and Conductivity Investigation of Doped $Sr_4B_2O_6Cu_2Ch_2$ '426' Oxychalcogenides 228

4.1 Introduction 228

4.2 Experimental 229

4.2.1 Precursors 229

4.3 $Sr_4Sc_2O_6Cu_2S_2$ 230

4.3.1 Pristine Synthesis 230

4.3.2 The Annealing Impasse 232

4.3.3 Sodium Doping, $(Sr_{4-x}Na_x)Sc_2O_6Cu_2S_2$ 235

4.3.4 The Flash Anneal Technique 239

4.3.5 Flash Annealed Sodium and Potassium Doped $Sr_4Sc_2O_6Cu_2S_2$ 241

4.4 $Sr_4Sc_2O_6Cu_2Se_2$ 243

4.4.1 Pristine Synthesis 243

4.4.2 Flash Annealed Sodium and Potassium Doped $Sr_4Sc_2O_6Cu_2Se_2$ 244

4.5 Comparison to the Gallium and Indium Analogues 247

4.6 Conclusions and Future Work 252

Chapter 5 Solid-State Metathesis: A Viable Pathway to Combinatorial MALM Synthesis? 253

5.1 Introduction 253

5.1.1 Solid-State Metathesis 253

5.1.2 Parallel Synthesis: A Novel Route to Rapid Materials Discovery? 256

5.1.3 The Phase Space of Light and Heavy Layer Precursors 259
5.1.4 Potential Flaws of Metathesis in a Parallel Synthesis Application 261
5.1.4.1 X-ray Diffractogram Convolution 261
5.1.4.2 Precursor Diversity 262
5.1.4.3 The Salt By-Product Hypothesis 263
5.1.5 Research motivation 264
5.2 Experimental 265
5.2.1 Precursors 265
5.3 Precursor Syntheses 266
5.3.1 Light Layer Precursors 266
5.3.1.1 $Sr_3Co_2O_5Cl_2$ 266
5.3.1.2 $Sr_3Fe_2O_5Br_2$ 270
5.3.1.3 $Sr_4Co_2O_6Cl_2$ 271
5.3.1.4 $Sr_4Sc_2O_6Cl_2$ 272
5.3.1.5 $Sr_3Sc_2O_5Cl_2$ 273
5.3.1.6 $Sr_3Fe_2O_5Cl_2$ 274
5.3.1.7 $Sr_4Fe_2O_6Cl_2$ 275
5.3.1.8 $Sr_4Fe_2O_6Br_2$ 276
5.3.1.9 Other Attempted Light Layer Synthesis 277
5.3.2 Heavy Layer Precursors 278
5.3.2.1 $Na_2Cu_2Se_2$ 278
5.4 Metathesis Investigations 281
5.4.1 $Sr_3Sc_2O_5Cu_2Se_2$ Investigation 282
5.4.2 $Sr_3Fe_2O_5Cu_2Se_2$ Investigation 288
5.4.3 Metathesis Experiments with Remaining Light Layer Precursors 295
5.4.3.1 Cobalt MALMs 295
5.4.3.2 Iron MALMs 298
5.4.3.3 Scandium MALMs 301
5.4.3.4 Comparison 302

5.5 The Salt Hypothesis 303

5.6 Proof of Concept Parallel Synthesis Trials 310

5.6.1 Trial 1 311

5.6.2 Trial 2 314

5.6.3 Trial 3 315

5.6.4 Trial 4 317

5.7 An Evaluation of Solid-State Metathesis and Parallel Synthesis 318

Chapter 6 $Sr_3In_2O_5Cu_2Se_2$: A Novel Oxychalcogenide 321

6.1 $Sr_3In_2O_5Cu_2Se_2$ 321

6.2 $Sr_3In_2O_5Cu_2S_2$ 324

6.3 $Sr_3In_2O_5Cl_2$ 325

6.4 $Sr_4In_2O_6Cl_2$ 326

6.5 Conclusions and Future Work 327

Chapter 7 Conclusions and Outlook 328

Appendix A Refined Crystal Structure Parameters 330

A.1 $Sr_3Sc_2O_5Cu_2S_2$ 330

A.2 $Sr_3Sc_2O_5Cu_2Se_2$ 332

A.3 $Sr_4Sc_2O_6Cu_2S_2$ 334

A.4 $Sr_4Sc_2O_6Cu_2Se_2$ 336

A.5 $Sr_3Fe_2O_5Cu_2Se_2$ 338

A.6 $Sr_3In_2O_5Cu_2Se_2$ 340

A.7 $Sr_4In_2O_6Cl_2$ 342

Appendix B Structural, Compositional, Analytical and Graphical Data for Synthesised Materials 344

B.1 Materials from Chapter 3 344

B.1.1 Potassium doped 325 sulfide MALMs, $(Sr_{3-x}K_x)Sc_2O_5Cu_2S_2$ 344

B.1.2 Sodium doped 325 sulfide MALMs, $(Sr_{3-x}Na_x)Sc_2O_5Cu_2S_2$ 356

B.1.3 Strontium deficient 325 sulfide MALMs, $Sr_{3-x}Sc_2O_5Cu_2S_2$ 370

B.1.4 Potassium doped 325 selenide MALMs, $(Sr_{3-x}K_x)Sc_2O_5Cu_2Se_2$ 382

B.1.5 Sodium doped 325 selenide MALMs, $(Sr_{3-x}Na_x)Sc_2O_5Cu_2Se_2$ 401

B.1.6 Magnesium doped 325 selenide MALMs, $Sr_3(Sc_{2-x}Mg_x)O_5Cu_2Se_2$ 420

B.1.7 Barium doped 325 selenide MALMs, $(Sr_{3-x}Ba_x)Sc_2O_5Cu_2Se_2$ 428

B.1.8 Yttrium doped 325 selenide MALMs, $Sr_3(Sc_{2-x}Y_x)O_5Cu_2Se_2$ 436

B.1.9 Lanthanum doped 325 selenide MALMs, $Sr_3(Sc_{2-x}La_x)O_5Cu_2Se_2$ 445

B.1.10 Strontium deficient 325 selenide MALMs, $Sr_{3-x}Sc_2O_5Cu_2Se_2$ 454

B.1.11 Copper deficient 325 selenide MALMs, $Sr_3Sc_2O_5Cu_{2-x}Se_2$ 466

B.2 Materials from Chapter 4 478

B.2.1 Sodium doped 426 sulfide MALMs, $(Sr_{4-x}Na_x)Sc_2O_6Cu_2S_2$ 478

B.2.2 Flash Annealed $(Sr_{3.9}Na_{0.1})Sc_2O_6Cu_2S_2$ 489

B.2.3 Flash Annealed $(Sr_{3.9}K_{0.1})Sc_2O_6Cu_2S_2$ 491

B.2.4 Flash Annealed $(Sr_{3.9}Na_{0.1})Sc_2O_6Cu_2Se_2$ 493

B.2.5 Flash Annealed $(Sr_{3.9}Na_{0.1})Sc_2O_6Cu_2Se_2$ 495

B.2.6 Gallium Pristines 497

B.2.7 Indium Pristines 498

B.3 Materials from Chapter 5 499

B.3.1 Light Layer Precursors 499

B.3.2 Heavy Layer Precursors 510

B.3.3 $Sr_3Sc_2O_5Cu_2Se_2$ Metathesis Investigation 511

B.3.4 $Sr_3Fe_2O_5Cu_2Se_2$ Metathesis Investigation 521

B.3.5 Metathesis Tests with Remaining Light Layers 532

B.3.6 Salt Flux Investigation 538

B.3.7 Parallel Synthesis Attempts 544

Bibliography 548

Table of Tables

Table 1 The band gaps of a range of materials. Data sourced from literature.[122-131] .. 72

Table 2 A comparison of the common n-type TCOs 77

Table 3 A comparison of the ionic radii of 12 and 8-coordinate Sr^{2+}, and 6-coordinate Sc^{3+}, alongside those of the ions recommended by Scanlon et al to be doped onto those sites in $Sr_3Sc_2O_5Cu_2Ch_2$. 137

Table 4 The refined structural parameters and key performance metrics of pristine material $Sr_3Sc_2O_5Cu_2S_2$, compared to other publications of this material in literature.147

Table 5 The target and maximum possible dopant content within each MALM in the $(Sr_{3-x}K_x)Sc_2O_5Cu_2S_2$ series. The pristine material $Sr_3Sc_2O_5Cu_2S_2$ is included as a reference. 153

Table 6 The refined structural parameters and key performance metrics of pristine material $Sr_3Sc_2O_5Cu_2Se_2$, compared to other publications of this material in literature.172

Table 7 The target and maximum possible dopant content within the six highest doped MALMs in the $(Sr_{3-x}Na_x)Sc_2O_5Cu_2Se_2$ series. All samples before x = 0.200 show no trace of sodium-containing impurities therefore the maximum x is the target x, so these have been omitted for brevity. The pristine material $Sr_3Sc_2O_5Cu_2Se_2$ is included as a reference. 186

Table 8 The target and maximum possible dopant content within the MALMs of the $Sr_3(Sc_{2-x}La_x)O_5Cu_2Se_2$ series. The pristine material $Sr_3Sc_2O_5Cu_2S_2$ is included as a reference. 211

Table 9 A comparison of the four doped samples of $Sr_4Sc_2O_6Cu_2Ch_2$ densified by flash anneal. 246

Table 10 A comparison of the synthesis conditions and physical properties of the six synthesised pristine $Sr_4B_2O_6Cu_2Ch_2$ materials (B = Ga, Sc, or In. Ch = S or Se).251

Table 11 An illustration of the parallel synthesis technique using the building block analogy discussed previously. Three light layers represented by white, red and green blocks react with three (grey, yellow and blue block) heavy layers, to produce nine potential products. 257

Table 12 A hypothetical 3 × 2 parallel synthesis reaction between light layer precursors $Sr_2CoO_2Cl_2$, $Sr_3Fe_2O_5Br_2$, and $Ba_4In_2O_6F_2$, with heavy layer precursors $Na_2Cu_2Se_2$ and $Li_2Fe_2As_2$. Green boxes indicate known published MALM products and red boxes indicate unknown potential new MALM products. Salt by-products are omitted for brevity. 258

Table 13 Tabulated phase fractions of the five component samples in the series of experiments targeting $Sr_3Sc_2O_5Cu_2Se_2$ by metathesis. The phases are colour coded to match the accompanying bar chart, and the tick marks on all constituent diffractograms. 282

Table 14 Tabulated phase fractions of the five component samples in the series of experiments targeting $Sr_3Sc_2O_5Cu_2Se_2$ by conventional ceramic syntheses. The phases are colour coded to match the accompanying bar chart, and the tick marks on all constituent diffractograms. 286

Table of Tables

Table 15 Tabulated phase fractions of the five component samples in the series of experiments targeting $Sr_3Fe_2O_5Cu_2Se_2$ by metathesis. The phases are colour coded to match the accompanying bar chart, and the tick marks on all constituent diffractograms. 289

Table 16 Tabulated phase fractions of the five component samples in the series of experiments targeting $Sr_3Fe_2O_5Cu_2Se_2$ by conventional ceramic syntheses. The phases are colour coded to match the accompanying bar chart, and the tick marks on all constituent diffractograms. 292

Table 17 Tabulated results of the eight individual metathesis reactions. 302

Table 18 The melting points of six salts with formula AX where A = Na or K, and X = F, Cl or Br. 303

Table 19 The permutations of the combination of two salts with a cation of either sodium or potassium, and an anion of either fluorine, chlorine or bromine. Grey permutations represent pairings where either the cation or anion repeat, gold permutations represent the six unique permutations where the ions do not repeat. 304

Table 20 Tabulated qualitative results of the reactions of the six salt permutations. 309

Table 21 The targeted constituent metathesis reactions of the four parallel synthesis proof of concept trials. Based on the individual metathesis experiments previously: green boxes indicate a predicted successful outcome, red indicates a predicted unsuccessful outcome (due to target product instability) and orange indicates uncertainty. 310

Table 22 The two constituent metathesis reactions of Parallel Synthesis Trial 1. Green boxes indicate predicted successful reactions. 311

Table 23 Refined unit cell parameters of $Sr_4Fe_2O_6Cu_2Se_2$ and $Sr_4Sc_2O_6Cu_2Se_2$, alongside the mixed occupancy MALM product $Sr_4(FeSc)O_6Cu_2Se_2$ of Trial 1. Pristine data obtained from literature.[87, 89] 312

Table 24 Refined unit cell parameters of NaCl and NaBr, alongside the mixed occupancy phase $Na(Br_{0.5}Cl_{0.5})$ of Trial 1. Pristine data obtained from literature.[335, 336] 313

Table 25 The two constituent metathesis reactions of Parallel Synthesis Trial 2. Green boxes indicate predicted successful reactions. 314

Table 26 The three constituent metathesis reactions of Parallel Synthesis Trial 3. Green boxes indicate predicted successful reactions, and red unsuccessful reactions. ... 315

Table 27 Refined unit cell parameters of NaCl and NaBr, alongside the mixed occupancy phase $Na(Br_{0.033}Cl_{0.66})$ of Trial 3. Pristine data obtained from literature.[335, 336] 316

Table 28 The three constituent metathesis reactions of Parallel Synthesis Trial 4. Red boxes indicate predicted unsuccessful reactions, orange indicates uncertainty.... 317

Table 29 Structural parameters of the refined model of pristine $Sr_3In_2O_5Cu_2Se_2$ in the I4/mmm space group at room temperature, where a = 4.14553(9) Å and c = 27.1013(7) Å. 322

Table 30 Structural parameters of the refined model of pristine $Sr_4In_2O_6Cl_2$ in the P4/nmm space group at room temperature, where a = 4.12995(6) Å and c = 14.24373(19) Å. 327

Table of Figures

Figure 1 Isometric projections of Mixed Anion Layered Materials, a) LaOCuS, b) $Sr_3Sc_2O_5Cu_2S_2$, and c) $Sr_2ZnO_2Cu_2S_2$. Projections are viewed along the x-axis, and are to scale with each other. For simplicity only covalent bonding is shown. These projections and others included herein were generated using CrystalMaker ® [10] 44

Figure 2 Isometric projections of a) La_2O_2S, and b) BiOCl. Projections are viewed along the x-axis, and are to scale with each other. For simplicity only covalent bonding is shown. 46

Figure 3 Isometric projections of a) LaOCuSe, and b) $Fe_2La_2O_3Se_2$. Projections are viewed along the x-axis, and are to scale with each other. For simplicity only covalent bonding is shown. 46

Figure 4 Isometric projections of a) BaFZnAs, and b) $Sm_2Ta_2O_5N_2$. Projections are viewed primarily along the x-axis, and are not to scale with each other. For simplicity only covalent bonding is shown. 49

Figure 5 Permutations of the five distinct atomic sites of a quinternary MALM projected onto the periodic table. Elements highlighted in green, pink, red, blue and yellow are elements with at least one recorded example occupying respectively the A, B, O, M or Q sites of a MALM. Diagonally split cells indicate elements which may occupy more than one site, not necessarily in the same MALM. Unhighlighted elements have not been reported in MALMs. 50

Figure 6 Isometric projections of the crystal structures of two $A_{n+1}M_nO_{3n+1}$ Ruddlesden-Popper oxides a) Sr_2RuO_4 where n = 1, b) $Sr_3Ru_2O_7$ where n = 2, and c) the pure perovskite structure $SrRuO_3$ where n = ∞. All structures viewed primarily along the x-axis. The blue dashed lines denote the unit cell. 51

Figure 7 Isometric projections of a generic depiction of the structure of the $A_2BO_2M_2Q_2$ ('212') MALM, showing a) one unit cell, and b) a 2 × 5 × 2 expanded unit cell. Both projections are viewed primarily along the x-axis, and are not to scale with each other. The interactions of A^{2+} to O^{2-} / Q^{2-} are largely ionic, and so for clarity these bonds are not shown. The blue dashed lines denote the unit cell. 52

Figure 8 Polyhedra showing the coordination environments of a 212 MALM: a) the inter-layer A atom site with 4-coordinate anti-prism interactions with oxygen ions, and b) the B atom site with 4-coordinate square-planar interactions with oxygen ions. Projections are to scale with each other. 53

Figure 9 Isometric projections of a generic depiction of the structure of the $A_3B_2O_5M_2Q_2$ ('325') MALM, showing a) one unit cell, and b) a 2 × 5 × 2 expanded unit cell. Both projections are viewed primarily along the x-axis, and are not to scale with each other. The interactions of A^{2+} to O^{2-} / Q^{2-} are largely ionic, and so for clarity these bonds are not shown. The blue dashed lines denote the unit cell. 54

Figure 10 Polyhedra showing the coordination environments of a 325 MALM: a) the inter-layer A atom site with 8-coordinate anti-prism interactions with oxygen and chalcogen ions, b) the intra-layer A atom site with 12-coordinate cuboctahedral interactions with oxygen ions, and c) the B atom site with 5-coordinate square-based pyramidal interactions with oxygen ions. Projections are to scale with each other 55

Figure 11 The GGA+U calculated band structure of $Sr_3Sc_2O_5Cu_2S_2$. The top of the valence band is set to 0 eV. Figure adapted from Scanlon 2009, showing a direct band gap of 2.12

eV, an underestimate of the experimentally measured band gap of 3.1 eV.[46] [53-56] 57

Figure 12 Isometric projections of a generic depiction of the structure of the $A_4B_2O_6M_2Q_2$ ('426') MALM, showing a) one unit cell, b) the unit cell with origin shifted by 0.25, 0.25, 0.575 to display it in the convention used previously, c) a 1 × 1 × 2 expanded unit cell, and d) a 2 × 5 × 4 expanded unit cell. All projections are viewed primarily along the x-axis. Projections a, b, and c are to scale with each other, but not to d. The interactions of A^{2+} to O^{2-} / Q^{2-} are largely ionic, and so for clarity these bonds are not shown. The blue dashed lines denote the unit cell. 58

Figure 13 Polyhedra showing the coordination environments of a 426 MALM: a) the inter-layer A atom site with 8-coordinate anti-prism interactions with oxygen and chalcogen ions, b) the intra-layer A atom site with 9-coordinate capped square prism coordination with oxygen ions, and c) the B atom site with 5-coordinate square-based pyramidal interactions with oxygen ions. Projections are to scale with each other. 59

Figure 14 Isometric projections of the generic unit cells of a) $A_4B_3O_8M_2Q_2$, b) $A_5B_4O_{11}M_2Q_2$, c) $A_6B_5O_{14}M_2Q_2$, d) $A_4B_4O_8M_2Q_2$, e) $A_2BO_2M_{3.5}Q_3$, and f) $A_2BO_2M_{5.5}Q_4$. Projections are viewed primarily along the x-axis, and are to scale with each other. For consistency, d and e are 1 × 1 × 2 expanded unit cells. The interactions of A^{2+} to O^{2-} / Q^{2-} are largely ionic, and so for clarity these bonds are not shown. The blue dashed lines denote the unit cell. 62

Figure 15 The research progression of 212 (black), 325 (red) and 426 (blue) MALMs presented through a) the number of unique published materials over time and b) publication count over time, from their initial publications through to the end of 2024. 63

Figure 16 The electrical conductivities of five common conductive material, represented on a $\log_{10}$ scale. Data sourced from literature.[109-113] 64

Figure 17 An illustration of the solar cell trade-off between maximising surface area (grey) for solar energy conversion and maximising electron collection with metal strands (black). The leftmost case shows maximum solar conversion but minimal electron collection, the rightmost case shows minimal solar conversion but maximum electron collection. 65

Figure 18 The molecular orbital diagram of H_2. The atomic orbitals of two hydrogen atoms combine to form one bonding molecular orbital (filled) and one antibonding molecular orbital (vacant). 66

Figure 19 Molecular orbital diagram of Lithium 2s interactions. The energy levels are discrete when the number of bonded atoms is finite, and form bands when n is infinite. All 1s MOs are fully filled and non-bonding, so for conciseness are not shown. The blue and white bands are the valence and conduction bands respectively. The red dashed line is the Fermi level. 67

Figure 20 The band structures of a) a metal where the band gap is negligibly small because the bands are touching, b) a metal where there is no band gap because the bands overlap (staggered for clarity), c) a semiconductor with a small band gap, and d) an insulator with a large band gap. The blue and white bands are the valence and conduction bands respectively. 68

Figure 21 Visible light (with a maximum energy of 3.3 eV) interacting with a) an wide band gap insulator such as diamond, whose band gap is too large to absorb visible light and is transparent, and b) a semiconductor such as silicon, whose band gap is smaller than

the energy of visible light, so the light is absorbed and an electron is promoted. 69

Figure 22 The promotion of an electron from the valence band (blue) to the conduction band (white) of a semiconductor, leaving behind a positively charged hole. The red dashed line is the Fermi level. 70

Figure 23 Illustrations of a) pristine undoped intrinsic silicon, b) silicon extrinsically p-type doped with boron, and c) silicon extrinsically n-type doped phosphorous. The sizes of boron and phosphorous compared to silicon are exaggerated for effect and are not to scale. A simplified square-planar structure of silicon is used here for clarity; the true structure of silicon is diamond with four-coordinate tetragonal bonding. 71

Figure 24 The band structures of a) pristine undoped intrinsic silicon, b) silicon extrinsically p-type doped with electron deficient boron, and c) silicon extrinsically n-type doped with phosphorous. The red dashed line is the Fermi level. The partial band depopulation and population is exaggerated for effect. 72

Figure 25 Band structures illustrating the degenerate doping of indium oxide, resulting in a Fermi level raised into the conduction band. The red dashed line is the Fermi level. 73

Figure 26 An illustration of the Moss Burstein effect for an n-type degenerately doped semiconductor, where a) is the actual band gap, b) is the apparent optical band gap, and c) the Moss-Burstein shift. The red dashed line is the Fermi level. 74

Figure 27 Isometric projections of a) Cu_2O, and b) $CuAlO_2$. Projections are viewed primarily along the x-axis, and are not to scale with each other. For simplicity only covalent bonding is shown. 79

Figure 28 a) an isometric projection LaOCuCh, viewed primarily along the x-axis, and b) the trends in hole mobility (increasing) and band gap (decreasing) along the chalcogenide series of S to Se to Te. 80

Figure 29 A labelled illustration of a silica tube loaded with crucibles containing pelletised powder samples, ready to be sealed with an oxypropane flame to create a vacuum ampoule. 84

Figure 30 An illustration of Young's double slit experiment. Coherent light interacts with two slits, producing multiple lines of light on a screen behind the slits. 87

Figure 31 An illustration of the constructive and destructive interference of light waves in Young's double slit experiment: a) coherent light projected onto two small slits in a wall, b) the diffracted light waves propagating away from the slits, where the grey straight lines show the constructive interference, c) lines of light on a wall behind the slits caused by interference, and d) the approximate intensity pattern of the lines of light. 88

Figure 32 Wave diagrams to illustrate a) the constructive interference of two in-phase waves with amplitude x producing a resultant wave with amplitude $2x$, and b) the destructive interference of two out-of-phase waves with amplitude x cancelling out to an amplitude of zero and thus producing no resultant wave. 88

Figure 33 The first X-ray diffraction pattern ever published, Friedrich et al 1912.[183] 89

Table of Figures

Figure 34 An illustration of two X-ray waves interacting with parallel atomic planes of a crystal lattice, highlighting the conditions under which Bragg's Law is satisfied and diffraction occurs. 90

Figure 35 An illustration of the radiation emitted as the result of bombarding a metal target with accelerated electrons, where a) is the Bremsstrahlung 'braking energy' radiation, b) is the characteristic radiation of the metal source, and c) is the resulting total output radiation. Other characteristic peaks are omitted for simplicity. Not to scale..... 92

Figure 36 An illustration of the monochromation of the X-ray emissions of a metal source, removing the Bremsstrahlung and Kβ to target Kα radiation: a) the 'raw' radiation containing the Bremsstrahlung, Kβ and Kα radiation, and b) the resulting monochromatic Kα radiation. Other characteristic peaks are omitted for simplicity. Not to scale. 93

Figure 37 An illustration of a typical powder X-ray diffraction experiment with Bragg-Brentano geometry. 94

Figure 38 Powder X-ray diffractogram of an empty airtight sample holder. The small blue circles represent the observed diffracted intensity. The visible peaks are the by-product of the removal of the beam knife and the amorphous reflection is the by-product of the use of a glass plate to maintain correct sample height. No sample or other diffracting material is present within the holder. 98

Figure 39 An illustration of the electromagnetic spectrum containing the seven primary components from long wavelength low energy radio waves through short wavelength high energy gamma radiation. Wavelength scale is illustrative and not to scale..... 99

Figure 40 An illustration of a single-beam liquid sample spectrophotometer setup. A bulb produces a broad band of UV-Vis radiation which is filtered down to a single wavelength by a monochromator. The resulting light is passed through the sample compartment which contains a homogenous liquid sample in a cuvette. Light which is not absorbed is recorded by the detector. Not to scale. 102

Figure 41 An illustration of a solid sample spectrophotometer setup. A bulb produces a broad band of UV-Vis radiation which is filtered down to a single wavelength by a monochromator. The resulting light enters the integrating sphere and hits the sample, usually a film or powder. Reflected light is radiated equally around the highly reflective sphere, measured by the detector. The baffle blocks non-integrated reflections. Not to scale. 103

Figure 42 An example of UV-Vis spectroscopy raw diffuse reflectance data obtained from a material with target composition $Sr_3Sc_2O_5Cu_2Se_2$. The drop-off in reflectance can be observed at approximately 400 to 430 nm. 104

Figure 43 An example of a Tauc plot, created from the diffuse reflectance data depicted in Figure 42 from a material with target composition $Sr_3Sc_2O_5Cu_2Se_2$. The linear region can be extrapolated (red line) to estimate the optical band gap from the x-axis, which in this case is 2.94 eV, corresponding to 422 nm. 105

Figure 44 An illustration of the two point probe method for measuring the resistance of a material. 108

Figure 45 An illustration of the four point probe method for measuring the resistance of a material. Here 'HI' and 'LO' are standard notation for the positive and negative ports of a digital multimeter respectively. 109

Figure 46 An illustration depicting four possible valid device shapes for van der Pauw resistivity measurements. The four black circles on the edges of each shape indicate the probe positions. 111

Figure 47 An illustration of the eight permutations of probe placements in the van der Pauw resistivity technique for a given pellet material. The top row depicts the vertical permutations and the bottom row depicts the horizontal permutations. Probe placements are described by the van der Pauw notation at the centre of each pellet. 112

Figure 48 An illustration of an annealed pelletised sample with silver paint, assembled on a spring clip sample board for a van der Pauw resistivity measurement in the $R_{12,34}$ permutation. 113

Figure 49 Representations of strontium oxide: a) an isometric projection of the unit cell, and b) a photograph of a portion of the synthesised sample. 115

Figure 50 Powder X-ray diffractogram of material with target composition SrO (space group Fm-3m) after 48 hours of heating at 1000 °C. The small blue circles represent the observed diffracted intensity, the green line represents the Rietveld-refined calculated model, the red line represents the background, and the grey line represents the difference between observed and calculated intensities. The black tick marks show the reflections of the refined model of SrO; no impurity phases are observed. Duration: 2 minutes. Data points: 3457. Interval: 0.02 °. GOF: 1.14. R_{wp}: 27.420 %. 116

Figure 51 Powder X-ray diffractogram of material with target composition SrS (space group Fm-3m) after 6 hours of heating at 850 °C. The small blue circles represent the observed diffracted intensity, the green line represents the Rietveld-refined calculated model, the red line represents the background, and the grey line represents the difference between observed and calculated intensities. The black tick marks show the reflections of the refined model of SrS; no impurity phases are observed. Duration: 10 minutes. Data points: 3142. Interval: 0.022 °. GOF: 1.08. R_{wp}: 11.142 %. 117

Figure 52 Representations of strontium sulfide: a) an isometric projection of the unit cell, and b) a photograph of a portion of the synthesised sample. 118

Figure 53 Representations of strontium selenate: a) an isometric projection of the unit cell, and b) a photograph of a portion of the synthesised sample. 118

Figure 54 Powder X-ray diffractogram of material with target composition $SrSeO_4$ (space group $P2_1/n$) after ionic displacement and 2 hours of heating at 80 °C. The small blue circles represent the observed diffracted intensity, the green line represents the Rietveld-refined calculated model, the red line represents the background, and the grey line represents the difference between observed and calculated intensities. The black tick marks show the reflections of the refined model of $SrSeO_4$; no impurity phases are observed. Duration: 6 minutes. Data points: 3457. Interval: 0.02 °. GOF: 1.08. R_{wp}: 18.262 %. 119

Figure 55 Representations of strontium selenide: a) an isometric projection of the unit cell, and b) a photograph of a portion of the synthesised sample. 120

Figure 56 Powder X-ray diffractogram of material with target composition SrSe (space group Fm-3m) after 16 hours of heating at 650 °C. The small blue circles represent the observed diffracted intensity, the green line represents the Rietveld-refined calculated model, the red line represents the background, and the grey line represents the difference between observed and calculated intensities. The black tick

marks show the reflections of the refined model of SrSe; no impurity phases are observed. Duration: 80 seconds. Data points: 3456. Interval: 0.02 °. GOF: 1.15. R_{wp}: 38.988 %. 121

Figure 57 Representations of barium selenate: a) an isometric projection of the unit cell, and b) a photograph of a portion of the synthesised sample. 122

Figure 58 Powder X-ray diffractogram of material with target composition $BaSeO_4$ (space group Pnma) after ionic displacement. The small blue circles represent the observed diffracted intensity, the green line represents the Rietveld-refined calculated model, the red line represents the background, and the grey line represents the difference between observed and calculated intensities. The black tick marks show the reflections of the refined model of $BaSeO_4$; no impurity phases are observed. Duration: 1 hour. Data points: 3456. Interval: 0.02 °. GOF: 1.26. R_{wp}: 12.864 %. 122

Figure 59 Powder X-ray diffractogram of material with target composition BaSe (space group Fm-3m) after 16 hours of heating at 650 °C. The small blue circles represent the observed diffracted intensity, the green line represents the Rietveld-refined calculated model, the red line represents the background, and the grey line represents the difference between observed and calculated intensities. The black tick marks show the reflections of the refined model of BaSe; no impurity phases are observed. Duration: 2 minutes. Data points: 3457. Interval: 0.02 °. GOF: 1.11. R_{wp}: 12.395 %. 123

Figure 60 Representations of barium selenide: a) an isometric projection of the unit cell, and b) a photograph of a portion of the synthesised sample. 124

Figure 61 Representations of sodium selenide: a) an isometric projection of the unit cell, and photographs of a portion of the synthesised sample b) pre-heating and c) post-heating. 125

Figure 62 Powder X-ray diffractogram of material with target composition Na_2Se (space group Fm-3m) after 2 hours of heating at 500 °C. The small blue circles represent the observed diffracted intensity, the green line represents the Rietveld-refined calculated model, the red line represents the background, and the grey line represents the difference between observed and calculated intensities. The black tick marks show the reflections of the refined model of Na_2Se; no impurity phases are observed. Duration: 60 seconds. Data points: 3457. Interval: 0.02 °. GOF: 1.11. R_{wp}: 40.483 %. 126

Figure 63 Powder X-ray diffractograms showing the degradation of Na_2Se over time, where a) t = 0, b) t = 2 minutes, c) t = 4 minutes, and d) t = 2 years. The small blue circles represent the observed diffracted intensities, the green lines represent the Rietveld-refined calculated models, and the red lines represent the backgrounds. For simplicity and compactness, the grey difference lines are omitted. The black tick marks show the reflections of the refined model of Na_2Se, whilst the blue, red, green and orange tick marks represent refined impurity phases $Na_2Se{\cdot}5H_2O$, Na_2SeO_3, Na_2SeO_4 and Se respectively. Weight fractions for each phase are cited in the figure legends. a) Duration: 1 minute. Data points: 3457. Interval: 0.02 °. GOF: 1.11. R_{wp}: 40.483 %. b) Duration: 1 minute. Data points: 3457. Interval: 0.02 °. GOF: 1.09. R_{wp}: 37.916 %. c) Duration: 1 minute. Data points: 3457. Interval: 0.02 °. GOF: 1.15. R_{wp}: 39.818 %. d) Duration: 20 minutes. Data points: 3703. Interval: 0.02 °. GOF: 1.96. R_{wp}: 10.898 %. 127

Figure 64 The phase diagram of the Cu-S system. Adapted from a diagram in Szopa 2021,[233] which itself was produced using data from Evans 1979.[231] 128

Figure 65 Powder X-ray diffractograms of copper powder (space group Fm-3m), a) before reduction and containing a Cu_2O impurity, and b) after reduction for 16 hours at 550 °C under H_2. The small blue circles represent the observed diffracted intensities, the green lines represent the Rietveld-refined calculated models, the red lines represent the backgrounds, and the grey lines represent the differences between observed and calculated intensities. The black tick marks show the reflections of the refined model of Cu, whilst the blue tick marks represent refined impurity phase Cu_2O. Weight fractions for each phase are cited in the figure legends. The two inset plots are magnifications of the area where the largest peak of Cu_2O appears, illustrating its removal during the reduction reaction. a) Duration: 1 minute. Data points: 3457. Interval: 0.02 °. GOF: 1.04. R_{wp}: 18.028 %. b) Duration: 3 minutes. Data points: 3457. Interval: 0.02 °. GOF: 1.03. R_{wp}: 10.691 %. 130

Figure 66 Powder X-ray diffractogram of material with target composition Cu_2S (space group $P2_1/c$) after 24 hours of heating at 700 °C. The small blue circles represent the observed diffracted intensity, the green line represents the Rietveld-refined calculated model, the red line represents the background, and the grey line represents the difference between observed and calculated intensities. The black tick marks show the reflections of the refined model of Cu_2S (96.3 %); whilst the blue tick marks represent refined impurity phase Cu (3.7 %). Duration: 10 minutes. Data points: 3457. Interval: 0.02 °. GOF: 1.08. R_{wp}: 7.814 %. 131

Figure 67 The phase diagram of the sulfur system. Adapted from a diagram in Ferreria 2011.[242] The solid lines indicate phase boundaries. Black triangles represent the two triple points. All symbols other than black triangles differentiate data obtained from various references in the original work. The black dotted line represents room pressure, 100 kPa. The red dotted line represents ampoule pressure, 0.015 kPa. Note the different temperature scales. 132

Figure 68 Representations of copper sulfide: a) an isometric projection of the unit cell, and b) a photograph of a portion of the synthesised sample. 134

Figure 69 Powder X-ray diffractogram of material with target composition Cu_2S (space group $P2_1/c$) after 24 hours of heating at 700 °C. The small blue circles represent the observed diffracted intensity, the green line represents the Rietveld-refined calculated model, the red line represents the background, and the grey line represents the difference between observed and calculated intensities. The black tick marks show the reflections of the refined model of Cu_2S; no impurity phases are observed. Duration: 30 minutes. Data points: 3457. Interval: 0.02 °. GOF: 1.25. R_{wp}: 4.051 %. 135

Figure 70 An isometric projection of a 2 × 2 × 2 expanded unit cell of KCu_3S_2. The interaction of K^+ to S^{2-} is ionic, and so for clarity these bonds are not shown. Colour key: purple - K, blue - Cu, and yellow - S. 138

Figure 71 Simulated powder X-ray diffractograms of a) $Sr_3Sc_2O_5Cu_2S_2$, b) $Sr_3Sc_2O_5Cu_2S_2$ successfully doped with Ga, resulting in the composition $Sr_3(Sc_{1.8}Ga_{0.2})O_5Cu_2S_2$, and c) $Sr_3Sc_2O_5Cu_2S_2$ successfully doped with Ga, where unreacted Ga_2O_3 precursor remains as an impurity. The asterisks in plot c) represent the peak positions of impurity Ga_2O_3. The inset image is a magnified and overlaid view of two major reflections of the $Sr_3Sc_2O_5Cu_2S_2$ pattern when pristine (blue) and successfully doped (red), to highlight the observable but very minor difference in peak shape between pristine and doped samples. 143

Figure 72 Powder X-ray diffractogram of material with target composition $(Sr_{2.975}Na_{0.025})Sc_2O_5Cu_2S_2$, used as an example to illustrate the positions of the largest reflections of the three most common impurities in this investigation. The black line

represents the observed diffracted intensity. The circular, square and triangular markers represent the peak positions of SrS, $SrCO_3$ and Sc_2O_3 respectively. The inset shows the magnified region of 2θ = 30 to 34 ° to highlight the primary impurity peak for Sc_2O_3. 145

Figure 73 Powder X-ray diffractogram of material with target composition $Sr_3Sc_2O_5Cu_2S_2$ (space group I4/mmm) after 36 hours of heating at 800 °C. The small blue circles represent the observed diffracted intensity, the green line represents the Rietveld-refined calculated model, the red line represents the background, and the grey line represents the difference between observed and calculated intensities. The black tick marks show the reflections of the refined model of $Sr_3Sc_2O_5Cu_2S_2$ (96.5 %), whilst the blue, red and green tick marks represent impurity phases SrS (1.3 %), $SrCO_3$ (0.8 %) and Sc_2O_3 (1.4 %) respectively. Duration: 12.5 hours. Data points: 4444. Interval: 0.02 °. GOF: 1.92. R_{wp}: 2.490 %. 146

Figure 74 UV-Vis spectrometry data for sample with target composition $Sr_3Sc_2O_5Cu_2S_2$ after 36 hours of heating at 800 °C. Plot a) is the raw diffuse reflectance data showing the drop off in reflectance between the visible region and the ultraviolet region occurring at approximately 400 nm. Plot b) is the resulting Tauc plot obtained from the first derivative of the Diffuse Reflectance data, magnified between 2.5 and 3.5 eV to highlight the drop-off, where the intercept between the red extrapolated tangent line and the x-axis is used to estimate an optical band gap of 3.10 eV / 400 nm. 147

Figure 75 Powder X-ray diffractogram of material with target composition $Sr_3Sc_2O_5Cu_2S_2$ (space group I4/mmm) after 36 hours of heating at 800 °C. The small blue circles represent the observed diffracted intensity, the green line represents the Rietveld-refined calculated model, the red line represents the background, and the grey line represents the difference between observed and calculated intensities. The black tick marks show the reflections of the refined model of $Sr_3Sc_2O_5Cu_2S_2$ (95.5 %), whilst the blue, red and green tick marks represent impurity phases $SrCO_3$ (0.3 %), $SrSO_4$ (3.6 %) and Cu (0.6 %) respectively. Duration: 45 minutes. Data points: 3457. Interval: 0.02 °. GOF: 1.38. R_{wp}: 5.554 %..... 149

Figure 76 Powder X-ray diffractogram of material with target composition $Sr_3Sc_2O_5Cu_2S_2$ (space group I4/mmm) after 36 hours of heating at 800 °C. The small blue circles represent the observed diffracted intensity, the green line represents the Rietveld-refined calculated model, the red line represents the background, and the grey line represents the difference between observed and calculated intensities. The black tick marks show the reflections of the refined model of $Sr_3Sc_2O_5Cu_2S_2$ (92.5 %), whilst the blue, red, green and orange tick marks represent impurity phases SrS (3.4 %), $SrCO_3$ (1.7 %) Sc_2O_3 (1.4 %) and Cu (1.0 %) respectively. Duration: 45 minutes. Data points: 3457. Interval: 0.02 °. GOF: 1.12. R_{wp}: 3.655 %. 150

Figure 77 Purities of the six potassium doped MALMs in the $(Sr_{3-x}K_x)Sc_2O_5Cu_2S_2$ series. The pristine material $Sr_3Sc_2O_5Cu_2S_2$ is included as a reference at $x = 0$ mol and is represented by a star. All values are derived from the Rietveld refinements of PXRD data using GSAS-II, and reported as weight percentages. 151

Figure 78 Powder X-ray diffractograms of a) the least doped sample of the series with target composition $(Sr_{2.975}K_{0.025})Sc_2O_5Cu_2S_2$, and b) the most doped sample of the series with target composition $(Sr_{2.850}K_{0.150})Sc_2O_5Cu_2S_2$ (both space group I4/mmm) after 36 hours of heating at 800 °C. The small blue circles represent the observed diffracted intensities, the green lines represent the Rietveld-refined calculated models, the red lines represent the backgrounds, and the grey lines represent the differences between observed and calculated intensities. The black tick marks show the reflections of the refined model of $Sr_3Sc_2O_5Cu_2S_2$, whilst the blue, red, green and

orange tick marks represent refined impurity phases SrS, $SrCO_3$, Sc_2O_3 and KCu_3S_2 respectively. Weight fractions for each phase are cited in the figure legends. a) Duration: 45 minutes. Data points: 3457. Interval: 0.02 °. GOF: 1.16. R_{wp}: 5.282 %. b) Duration: 45 minutes. Data points: 3457. Interval: 0.02 °. GOF: 1.09. R_{wp}: 4.756 %. 152

Figure 79 The calculated maximum possible levels of dopant incorporation into the $(Sr_{3-x}K_x)Sc_2O_5Cu_2S_2$ MALMs. Values were derived from the wt % of the potassium-containing impurities of each sample. The pristine material $Sr_3Sc_2O_5Cu_2S_2$ is included as a reference at $x = 0$ mol and is represented by a star. The red dashed line represents 100 % dopant incorporation into the MALM, statistically no values may surpass this line. The black data points are the estimated upper bound of dopant incorporation for each sample. 154

Figure 80 A photographic comparison of the colour of the $(Sr_{3-x}K_x)Sc_2O_5Cu_2S_2$ MALM series. Dopant concentration increases from left to right. 156

Figure 81 Comparisons of a) the a unit cell parameter, b) the c unit cell parameter, c) unit cell volume, and d) the optical band gap, of the six potassium doped MALMs in the $(Sr_{3-x}K_x)Sc_2O_5Cu_2S_2$ series. The pristine material $Sr_3Sc_2O_5Cu_2S_2$ is included as a reference at $x = 0$ mol and is represented by a star. 157

Figure 82 UV-Vis spectrometry data for sample with target composition $(Sr_{2.900}K_{0.100})Sc_2O_5Cu_2S_2$ after 36 hours of heating at 800 °C. Plot a) is the raw diffuse reflectance data showing the drop off in reflectance between the visible region and the ultraviolet region occurring at 350-450 nm. Plot b) is the resulting Tauc plot obtained from the first derivative of the Diffuse Reflectance data, magnified to highlight the drop-off, where the intercept between the red extrapolated tangent line and the x-axis is used to estimate an optical band gap of 3.09 eV / 401 nm. 157

Figure 83 The electrical conductivities of the six potassium doped MALMs in the $(Sr_{3-x}K_x)Sc_2O_5Cu_2S_2$ series, represented on a $\log_{10}$ scale. The pristine material $Sr_3Sc_2O_5Cu_2S_2$ is included as a reference at $x = 0$ mol and is represented by a star. All values are derived from van der Pauw 4 probe resistivity measurements of 8mm annealed pellet samples. 158

Figure 84 Purities of the eight sodium doped MALMs in the $(Sr_{3-x}Na_x)Sc_2O_5Cu_2S_2$ series. The pristine material $Sr_3Sc_2O_5Cu_2S_2$ is included as a reference at $x = 0$ mol and is represented by a star. All values are derived from the Rietveld refinements of PXRD data using GSAS-II, and reported as weight percentages. 159

Figure 85 Powder X-ray diffractograms of a) the least doped sample of the series with target composition $(Sr_{2.975}Na_{0.025})Sc_2O_5Cu_2S_2$, and b) the most doped sample of the series with target composition $(Sr_{2.800}Na_{0.200})Sc_2O_5Cu_2S_2$ (both space group I4/mmm) after 36 hours of heating at 800 °C. The small blue circles represent the observed diffracted intensities, the green lines represent the Rietveld-refined calculated models, the red lines represent the backgrounds, and the grey lines represent the differences between observed and calculated intensities. The black tick marks show the reflections of the refined model of $Sr_3Sc_2O_5Cu_2S_2$, whilst the blue, red, green and orange tick marks represent refined impurity phases SrS, $SrCO_3$, Sc_2O_3 and $NaCu_3S_2$ respectively. Weight fractions for each phase are cited in the figure legends. a) Duration: 45 minutes. Data points: 3457. Interval: 0.02 °. GOF: 1.08. R_{wp}: 4.456 %. b) Duration: 45 minutes. Data points: 3457. Interval: 0.02 °. GOF: 1.12. R_{wp}: 4.844 %. 160

Figure 86 The weight percentages of four impurity phases present in the $(Sr_{3-x}Na_x)Sc_2O_5Cu_2S_2$ series. The pristine material $Sr_3Sc_2O_5Cu_2S_2$ is included as a reference at x = 0 mol and is represented by stars. 161

Figure 87 The calculated maximum possible levels of dopant incorporation into the $(Sr_{3-x}Na_x)Sc_2O_5Cu_2S_2$ MALMs. Values were derived from the wt % of the sodium-containing impurities of each sample. The pristine material $Sr_3Sc_2O_5Cu_2S_2$ is included as a reference at x = 0 mol and is represented by a star. The red dashed line represents 100 % dopant incorporation into the MALM, statistically no values may surpass this line. The black data points are the estimated upper bound of dopant incorporation for each sample. 162

Figure 88 The electrical conductivities of the eight sodium doped MALMs in the $(Sr_{3-x}Na_x)Sc_2O_5Cu_2S_2$ series, represented on a $\log_{10}$ scale. The pristine material $Sr_3Sc_2O_5Cu_2S_2$ is included as a reference at x = 0 mol and is represented by a star. All values are derived from van der Pauw 4 probe resistivity measurements of 8mm annealed pellet samples. 163

Figure 89 Purities of the seven strontium deficient MALMs in the $Sr_{3-x}Sc_2O_5Cu_2S_2$ series. The pristine material $Sr_3Sc_2O_5Cu_2S_2$ is included as a reference at x = 0 mol and is represented by a star. All values are derived from the Rietveld refinements of PXRD data using GSAS-II, and reported as weight percentages. 165

Figure 90 The weight percentages of four impurity phases present in the $Sr_{3-x}Sc_2O_5Cu_2S_2$ series. The pristine material $Sr_3Sc_2O_5Cu_2S_2$ is included as a reference at x = 0 mol and is represented by stars. 166

Figure 91 Powder X-ray diffractograms of a) the least deficient sample of the series with target composition $Sr_{2.95}Sc_2O_5Cu_2S_2$, and b) the most deficient sample of the series with target composition $Sr_{2.00}Sc_2O_5Cu_2S_2$ (both space group I4/mmm) after 36 hours of heating at 800 °C. The small blue circles represent the observed diffracted intensities, the green lines represent the Rietveld-refined calculated models, the red lines represent the backgrounds, and the grey lines represent the differences between observed and calculated intensities. The black tick marks show the reflections of the refined model of $Sr_3Sc_2O_5Cu_2S_2$, whilst the blue, red, green and orange tick marks represent refined impurity phases SrS, $SrCO_3$, Sc_2O_3 and $SrSO_4$ respectively. Weight fractions for each phase are cited in the figure legends. a) Duration: 45 minutes. Data points: 3457. Interval: 0.02 °. GOF: 1.10. R_{wp}: 4.416 %. b) Duration: 45 minutes. Data points: 3457. Interval: 0.02 °. GOF: 1.54. R_{wp}: 6.080 %. 167

Figure 92 The electrical conductivities of the seven strontium deficient MALMs in the $Sr_{3-x}Sc_2O_5Cu_2S_2$ series, represented on a $\log_{10}$ scale. The pristine material $Sr_3Sc_2O_5Cu_2S_2$ is included as a reference at x = 0 mol and is represented by a star. All values are derived from van der Pauw 4 probe resistivity measurements of 8mm diameter annealed pellet samples. 168

Figure 93 The electrical conductivities of the potassium doped (black), sodium doped (blue), and strontium deficient (red) $Sr_3Sc_2O_5Cu_2S_2$ series, presented on a $\log_{10}$ scale. The pristine material $Sr_3Sc_2O_5Cu_2S_2$ is included as a reference at x = 0 mol and is represented by a star. The inset shows a magnification of the low doping region. 169

Figure 94 Powder X-ray diffractogram of material with target composition $Sr_3Sc_2O_5Cu_2Se_2$ (space group I4/mmm) after 36 hours of heating at 800 °C. The small blue circles represent the observed diffracted intensity, the green line represents the Rietveld-refined calculated model, the red line represents the background, and the grey line represents the difference between observed and calculated intensities. The black tick

marks show the reflections of the refined model of $Sr_3Sc_2O_5Cu_2Se_2$ (99.1 %), whilst the blue and red tick marks represent refined impurity phases SrSe (0.5 %), and $SrCO_3$ (0.4 %) respectively. Duration: 12 hours. Data points: 8887. Interval: 0.01 °. GOF: 1.51. R_{wp}: 2.486 %. 171

Figure 95 UV-Vis spectrometry data for material with target composition $Sr_3Sc_2O_5Cu_2Se_2$ after 36 hours of heating at 800 °C. Plot a) is the raw diffuse reflectance data showing the drop off in reflectance between the visible region and the ultraviolet region occurring at 350-450 nm. Plot b) is the associated magnified Tauc plot for this region, where the intercept between the red extrapolated tangent line and the x-axis is used to estimate an optical band gap of 2.94 eV, which corresponds to 422 nm. ... 172

Figure 96 A visualisation of the ranges of doping explored in the $(Sr_{3-x}K_x)Sc_2O_5Cu_2Se_2$ series. The pristine sample was first synthesised alone, then eight samples ranging from x = 0.025 to 0.200 mol, and finally five further sample ranging from x = 0.300 to 1.000 mol. The y-axis is illustrative..... 173

Figure 97 Purities of the thirteen potassium doped MALMs in the $(Sr_{3-x}K_x)Sc_2O_5Cu_2Se_2$ series. The pristine material $Sr_3Sc_2O_5Cu_2Se_2$ is included as a reference at x = 0 mol and is represented by a star. The two data points at x = 0.750 mol and x = 0.100 mol are coloured red to indicate the presence of unknown impurities in these samples, and as a result the cited purity values are likely to be slight overestimates. All values are derived from the Rietveld refinements of PXRD data using GSAS-II, and reported as weight percentages..... 174

Figure 98 Powder X-ray diffractograms of a) the least doped sample of the series with target composition $(Sr_{2.975}K_{0.025})Sc_2O_5Cu_2Se_2$, and b) the most doped sample of the series with target composition $(Sr_{2.000}K_{1.000})Sc_2O_5Cu_2Se_2$ (both space group I4/mmm) after 36 hours of heating at 800 °C. The small blue circles represent the observed diffracted intensities, the green lines represent the Rietveld-refined calculated models, the red lines represent the backgrounds, and the grey lines represent the differences between observed and calculated intensities. The black tick marks show the reflections of the refined model of $Sr_3Sc_2O_5Cu_2Se_2$, whilst the blue, red, green, orange and pink tick marks represent refined impurity phases SrSe, $SrCO_3$, KCu_3Se_2, $SrSc_2O_4$ and $K_3Cu_8Se_6$ respectively. Weight fractions for each phase are cited in the figure legends. a) Duration: 45 minutes. Data points: 3457. Interval: 0.02 °. GOF: 1.11. R_{wp}: 6.050 %. b) Duration: 45 minutes. Data points: 3457. Interval: 0.02 °. GOF: 1.53. R_{wp}: 6.628 %. 175

Figure 99 The weight percentages of five impurity phases present in the $(Sr_{3-x}K_x)Sc_2O_5Cu_2Se_2$ series. The pristine material $Sr_3Sc_2O_5Cu_2Se_2$ is included as a reference at x = 0 mol and is represented by stars. The inset plot is a magnification of the x = 0 to 0.200 mol region where doping and impurity quantities are low. Note the change in y scaling at 20 wt %..... 176

Figure 100 A photographic comparison of the colour of the $(Sr_{3-x}K_x)Sc_2O_5Cu_2Se_2$ MALM series. Dopant concentration increases from left to right. The sample where x = 0.175 mol is absent from this photograph as it was sent to the ISIS Neutron and Muon Source for Neutron Powder Diffraction at the time of writing..... 176

Figure 101 The calculated maximum possible levels of dopant incorporation into the $(Sr_{3-x}K_x)Sc_2O_5Cu_2Se_2$ MALMs. Values were derived from the wt % of the potassium-containing impurities of each sample. The pristine material $Sr_3Sc_2O_5Cu_2Se_2$ is included as a reference at x = 0 mol and is represented by a star. The red dashed line represents 100 % dopant incorporation into the MALM, statistically no values may surpass this line. The black data points are the estimated upper bound of dopant incorporation for each sample..... 177

Figure 102 Comparisons of a) the α unit cell parameter, b) the c unit cell parameter, c) unit cell volume, and d) the optical band gap, of the thirteen potassium doped MALMs in the $(Sr_{3-x}K_x)Sc_2O_5Cu_2Se_2$ series. The pristine material $Sr_3Sc_2O_5Cu_2Se_2$ is included as a reference at x = 0 mol and is represented by a star. The x = 1.000 mol sample band gap is missing due to lack of drop-off in diffuse reflectance, see Appendix Table 29. 178

Figure 103 The electrical conductivities of the thirteen potassium doped MALMs in the $(Sr_{3-x}K_x)Sc_2O_5Cu_2Se_2$ series, represented on both a $\log_{10}$ scale (blue data; left hand y-axis) and a linear scale (red data; right hand y-axis). The pristine material $Sr_3Sc_2O_5Cu_2Se_2$ is included as a reference at x = 0 mol and is represented by a star. All values are derived from van der Pauw 4 probe resistivity measurements of 8mm annealed pellet samples. 179

Figure 104 The purities (black data; left hand y-axis), and electrical conductivities (red data; right hand y-axis), of the thirteen potassium doped MALMs in the $(Sr_{3-x}K_x)Sc_2O_5Cu_2Se_2$ series. The pristine material $Sr_3Sc_2O_5Cu_2Se_2$ is included as a reference at x = 0 mol and is represented by a star. Purity values are derived from the Rietveld refinements of PXRD data using GSAS-II, and reported as weight percentages. Conductivity values are derived from van der Pauw 4 probe resistivity measurements of 8mm annealed pellet samples. 181

Figure 105 Purities of the thirteen sodium doped MALMs in the $(Sr_{3-x}Na_x)Sc_2O_5Cu_2Se_2$ series. The pristine material $Sr_3Sc_2O_5Cu_2Se_2$ is included as a reference at x = 0 mol and is represented by a star. The two data points at x = 0.750 mol and x = 0.100 mol are coloured red to indicate the presence of unknown impurities in these samples, and as a result the cited purity values are likely to be slight overestimates. All values are derived from the Rietveld refinements of PXRD data using GSAS-II, and reported as weight percentages. 182

Figure 106 The weight percentages of five impurity phases present in the $(Sr_{3-x}Na_x)Sc_2O_5Cu_2Se_2$ series. The pristine material $Sr_3Sc_2O_5Cu_2Se_2$ is included as a reference at x = 0 mol and is represented by stars. The inset plot is a magnification of the x = 0 to 0.200 mol region where doping and impurity quantities are low. Note the y-axis scale change at 20 wt %. 183

Figure 107 Powder X-ray diffractograms of a) the least doped sample of the series with target composition $(Sr_{2.975}Na_{0.025})Sc_2O_5Cu_2Se_2$, and b) the most doped sample of the series with target composition $(Sr_{2.000}Na_{1.000})Sc_2O_5Cu_2Se_2$ (both space group I4/mmm) after 36 hours of heating at 800 °C. The small blue circles represent the observed diffracted intensities, the green lines represent the Rietveld-refined calculated models, the red lines represent the backgrounds, and the grey lines represent the differences between observed and calculated intensities. The black tick marks show the reflections of the refined model of $Sr_3Sc_2O_5Cu_2Se_2$, whilst the blue, red, green, orange and pink tick marks represent refined impurity phases SrSe, $SrCO_3$, Sc_2O_3, $NaCu_3Se_2$ and $SrSc_2O_4$ respectively. Weight fractions for each phase are cited in the figure legends. a) Duration: 45 minutes. Data points: 3457. Interval: 0.02 °. GOF: 1.07. R_{wp}: 6.269 %. b) Duration: 45 minutes. Data points: 3457. Interval: 0.02 °. GOF: 2.05. R_{wp}: 8.228 %. 184

Figure 108 The electrical conductivities of the thirteen sodium doped MALMs in the $(Sr_{3-x}Na_x)Sc_2O_5Cu_2Se_2$ series, represented on a $\log_{10}$ scale. The pristine material $Sr_3Sc_2O_5Cu_2Se_2$ is included as a reference at x = 0 mol and is represented by a star. All values are derived from van der Pauw 4 probe resistivity measurements of 8mm annealed pellet samples. 185

Figure 109 The calculated maximum possible levels of dopant incorporation into the $(Sr_{3-x}Na_x)Sc_2O_5Cu_2Se_2$ MALMs. Values were derived from the wt % of the sodium-containing impurities of each sample. The pristine material $Sr_3Sc_2O_5Cu_2Se_2$ is included as a reference at $x = 0$ mol and is represented by a star. The red dashed line represents 100 % dopant incorporation into the MALM, statistically no values may surpass this line. The black data points are the estimated upper bound of dopant incorporation for each sample. 186

Figure 110 The electrical conductivities of the first eight sodium doped MALMs in the $(Sr_{3-x}Na_x)Sc_2O_5Cu_2Se_2$ series up to 0.200 mol, represented on a $\log_{10}$ scale. The pristine material $Sr_3Sc_2O_5Cu_2Se_2$ is included as a reference at $x = 0$ mol and is represented by a star. All values are derived from van der Pauw 4 probe resistivity measurements of 8mm annealed pellet samples. 188

Figure 111 Purities of the four magnesium doped MALMs in the $Sr_3(Sc_{2-x}Mg_x)O_5Cu_2Se_2$ series. The pristine material $Sr_3Sc_2O_5Cu_2Se_2$ is included as a reference at $x = 0$ mol and is represented by a star. All values are derived from the Rietveld refinements of PXRD data using GSAS-II, and reported as weight percentages. 190

Figure 112 Powder X-ray diffractograms of a) the least doped sample of the series with target composition $Sr_3(Sc_{1.95}Mg_{0.05})O_5Cu_2Se_2$, and b) the most doped sample of the series with target composition $Sr_3(Sc_{1.80}Mg_{0.20})O_5Cu_2Se_2$ (both space group I4/mmm) after 36 hours of heating at 800 °C. The small blue circles represent the observed diffracted intensities, the green lines represent the Rietveld-refined calculated models, the red lines represent the backgrounds, and the grey lines represent the differences between observed and calculated intensities. The black tick marks show the reflections of the refined model of $Sr_3Sc_2O_5Cu_2Se_2$, whilst the blue and red tick marks represent refined impurity phases SrSe and $SrCO_3$ respectively. Weight fractions for each phase are cited in the figure legends. a) Duration: 45 minutes. Data points: 3457. Interval: 0.02 °. GOF: 1.13. R_{wp}: 4.460 %. b) Duration: 45 minutes. Data points: 3457. Interval: 0.02 °. GOF: 1.24. R_{wp}: 5.274 %. 192

Figure 113 The calculated maximum possible levels of dopant incorporation into the $Sr_3(Sc_{2-x}Mg_x)O_5Cu_2Se_2$ MALMs. Values were derived from the wt % of the magnesium-containing impurities of each sample, of which there were none. The pristine material $Sr_3Sc_2O_5Cu_2Se_2$ is included as a reference at $x = 0$ mol and is represented by a star. The red dashed line represents 100 % dopant incorporation into the MALM, statistically no values may surpass this line. The black data points are the estimated upper bound of dopant incorporation for each sample. 193

Figure 114 The electrical conductivities of the four magnesium doped MALMs in the $Sr_3(Sc_{2-x}Mg_x)O_5Cu_2Se_2$ series, represented on both a $\log_{10}$ scale (blue data; left hand y-axis) and a linear scale (red data; right hand y-axis). The pristine material $Sr_3Sc_2O_5Cu_2Se_2$ is included as a reference at $x = 0$ mol and is represented by a star. All values are derived from van der Pauw 4 probe resistivity measurements of 8mm annealed pellet samples. 194

Figure 115 Comparisons of a) the α unit cell parameter, b) the c unit cell parameter, c) unit cell volume, and d) the optical band gap, of the four magnesium doped MALMs in the $Sr_3(Sc_{2-x}Mg_x)O_5Cu_2Se_2$ series. The pristine material $Sr_3Sc_2O_5Cu_2Se_2$ is included as a reference at $x = 0$ mol and is represented by a star. 195

Figure 116 Purities of the four barium doped MALMs in the $(Sr_{3-x}Ba_x)Sc_2O_5Cu_2Se_2$ series. The pristine material $Sr_3Sc_2O_5Cu_2Se_2$ is included as a reference at $x = 0$ mol and is represented by a star. All values are derived from the Rietveld refinements of PXRD data using GSAS-II, and reported as weight percentages. 196

Figure 117 Powder X-ray diffractograms of a) the least doped sample of the series with target composition $(Sr_{2.95}Ba_{0.05})Sc_2O_5Cu_2Se_2$, and b) the most doped sample of the series with target composition $(Sr_{2.80}Ba_{0.20})Sc_2O_5Cu_2Se_2$ (both space group I4/mmm) after 36 hours of heating at 800 °C. The small blue circles represent the observed diffracted intensities, the green lines represent the Rietveld-refined calculated models, the red lines represent the backgrounds, and the grey lines represent the differences between observed and calculated intensities. The black tick marks show the reflections of the refined model of $Sr_3Sc_2O_5Cu_2Se_2$, whilst the blue and red tick marks represent refined impurity phases SrSe and $SrCO_3$ respectively. Weight fractions for each phase are cited in the figure legends. a) Duration: 45 minutes. Data points: 3457. Interval: 0.02 °. GOF: 1.04. R_{wp}: 4.430 %. b) Duration: 45 minutes. Data points: 3457. Interval: 0.02 °. GOF: 1.05. R_{wp}: 4.496 %. 197

Figure 118 The calculated maximum possible levels of dopant incorporation into the $(Sr_{3-x}Ba_x)Sc_2O_5Cu_2Se_2$ MALMs. Values were derived from the wt % of the barium-containing impurities of each sample, of which there were none. The pristine material $Sr_3Sc_2O_5Cu_2Se_2$ is included as a reference at x = 0 mol and is represented by a star. The red dashed line represents 100 % dopant incorporation into the MALM, statistically no values may surpass this line. The black data points are the estimated upper bound of dopant incorporation for each sample. 198

Figure 119 Comparisons of a) the α unit cell parameter, b) the c unit cell parameter, c) unit cell volume, and d) the optical band gap, of the four barium doped MALMs in the $(Sr_{3-x}Ba_x)Sc_2O_5Cu_2Se_2$ series. The pristine material $Sr_3Sc_2O_5Cu_2Se_2$ is included as a reference at x = 0 mol and is represented by a star. 199

Figure 120 The observed lattice parameters a + c and unit cell volumes of the $(Sr_{3-x}Ba_x)Sc_2O_5Cu_2Se_2$ series, projected against a theoretical Vegard's Law relationship (green dashed line) between pristine $Sr_3Sc_2O_5Cu_2Se_2$ and $Ba_3Sc_2O_5Cu_2Se_2$, represented by a star and a triangle respectively. 200

Figure 121 The electrical conductivities of the four barium doped MALMs in the $(Sr_{3-x}Ba_x)Sc_2O_5Cu_2Se_2$ series, represented on a $\log_{10}$ scale. The pristine material $Sr_3Sc_2O_5Cu_2Se_2$ is included as a reference at x = 0 mol and is represented by a star. All values are derived from van der Pauw 4 probe resistivity measurements of 8mm annealed pellet samples. 201

Figure 122 Purities of the four yttrium doped MALMs in the $Sr_3(Sc_{2-x}Y_x)O_5Cu_2Se_2$ series. The pristine material $Sr_3Sc_2O_5Cu_2Se_2$ is included as a reference at x = 0 mol and is represented by a star. All values are derived from the Rietveld refinements of PXRD data using GSAS-II, and reported as weight percentages. 203

Figure 123 The weight percentages of three impurity phases present in the $Sr_3(Sc_{2-x}Y_x)O_5Cu_2Se_2$ series. The pristine material $Sr_3Sc_2O_5Cu_2Se_2$ is included as a reference at x = 0 mol and is represented by stars. 204

Figure 124 Powder X-ray diffractograms of a) the least doped sample of the series with target composition $Sr_3(Sc_{1.95}Y_{0.05})O_5Cu_2Se_2$, and b) the most doped sample of the series with target composition $Sr_3(Sc_{1.80}Y_{0.20})O_5Cu_2Se_2$ (both space group I4/mmm) after 36 hours of heating at 800 °C. The small blue circles represent the observed diffracted intensities, the green lines represent the Rietveld-refined calculated models, the red lines represent the backgrounds, and the grey lines represent the differences between observed and calculated intensities. The black tick marks show the reflections of the refined model of $Sr_3Sc_2O_5Cu_2Se_2$, whilst the blue, red and green tick marks represent refined impurity phases SrSe, $SrCO_3$ and Y_2O_3 respectively. Weight fractions for each phase are cited in the figure legends. a) Duration: 45 minutes. Data

points: 3457. Interval: 0.02 °. GOF: 1.09. R_{wp}: 4.244 %. b) Duration: 45 minutes. Data points: 3457. Interval: 0.02 °. GOF: 1.21. R_{wp}: 4.777 %. 205

Figure 125 The calculated maximum possible levels of dopant incorporation into the $Sr_3(Sc_{2-x}Y_x)O_5Cu_2Se_2$ MALMs. Values were derived from the wt % of the yttrium-containing impurities of each sample. The pristine material $Sr_3Sc_2O_5Cu_2Se_2$ is included as a reference at $x = 0$ mol and is represented by a star. The red dashed line represents 100 % dopant incorporation into the MALM, statistically no values may surpass this line. The black data points are the estimated upper bound of dopant incorporation for each sample. 206

Figure 126 Comparisons of a) the α unit cell parameter, b) the c unit cell parameter, c) unit cell volume, and d) the optical band gap, of the yttrium doped 325 selenide MALMs with general formula $Sr_3(Sc_{2-x}Y_x)O_5Cu_2Se_2$. The pristine material $Sr_3Sc_2O_5Cu_2Se_2$ is included as a reference at $x = 0$ mol and is represented by a star. 207

Figure 127 The electrical conductivities of the four yttrium doped MALMs in the $Sr_3(Sc_{2-x}Y_x)O_5Cu_2Se_2$ series, represented on a $\log_{10}$ scale. The pristine material $Sr_3Sc_2O_5Cu_2Se_2$ is included as a reference at $x = 0$ mol and is represented by a star. All values are derived from van der Pauw 4 probe resistivity measurements of 8mm annealed pellet samples. 207

Figure 128 Purities of the four lanthanum doped MALMs in the $Sr_3(Sc_{2-x}La_x)O_5Cu_2Se_2$ series. The pristine material $Sr_3Sc_2O_5Cu_2Se_2$ is included as a reference at $x = 0$ mol and is represented by a star. All values are derived from the Rietveld refinements of PXRD data using GSAS-II, and reported as weight percentages. 208

Figure 129 The weight percentages of three impurity phases present in the $Sr_3(Sc_{2-x}La_x)O_5Cu_2Se_2$ series. The pristine material $Sr_3Sc_2O_5Cu_2S_2$ is included as a reference at $x = 0$ mol and is represented by stars. 209

Figure 130 Powder X-ray diffractograms of a) the least doped sample of the series with target composition $Sr_3(Sc_{1.95}La_{0.05})O_5Cu_2Se_2$, and b) the most doped sample of the series with target composition $Sr_3(Sc_{1.80}La_{0.20})O_5Cu_2Se_2$ (both space group I4/mmm) after 36 hours of heating at 800 °C. The small blue circles represent the observed diffracted intensities, the green lines represent the Rietveld-refined calculated models, the red lines represent the backgrounds, and the grey lines represent the differences between observed and calculated intensities. The black tick marks show the reflections of the refined model of $Sr_3Sc_2O_5Cu_2Se_2$, whilst the blue, red and green tick marks represent refined impurity phases SrSe, $SrCO_3$ and $La_2CuO_{3.98}$ respectively. Weight fractions for each phase are cited in the figure legends. a) Duration: 45 minutes. Data points: 3457. Interval: 0.02 °. GOF: 1.11. R_{wp}: 4.497 %. b) Duration: 45 minutes. Data points: 3457. Interval: 0.02 °. GOF: 1.49. R_{wp}: 6.606 %. 210

Figure 131 The calculated maximum possible levels of dopant incorporation into the $Sr_3(Sc_{2-x}La_x)O_5Cu_2Se_2$ MALMs. Values were derived from the wt % of the lanthanum-containing impurities of each sample. The pristine material $Sr_3Sc_2O_5Cu_2Se_2$ is included as a reference at $x = 0$ mol and is represented by a star. The red dashed line represents 100 % dopant incorporation into the MALM, statistically no values may surpass this line. The black data points are the estimated upper bound of dopant incorporation for each sample. 211

Figure 132 The electrical conductivities of the four lanthanum doped MALMs in the $Sr_3(Sc_{2-x}La_x)O_5Cu_2Se_2$ series, represented on a $\log_{10}$ scale. The pristine material $Sr_3Sc_2O_5Cu_2Se_2$ is included as a reference at $x = 0$ mol and is represented by a star. All values are derived from van der Pauw 4 probe resistivity measurements of 8mm annealed pellet samples. 212

Table of Figures

Figure 133 Comparisons of a) the α unit cell parameter, b) the c unit cell parameter, c) unit cell volume, and d) the optical band gap, of the lanthanum doped 325 selenide MALMs with general formula $Sr_3(Sc_{2-x}La_x)O_5Cu_2Se_2$. The pristine material $Sr_3Sc_2O_5Cu_2Se_2$ is included as a reference at x = 0 mol and is represented by a star. 213

Figure 134 Purities of the seven strontium deficient MALMs in the $Sr_{3-x}Sc_2O_5Cu_2Se_2$ series. The pristine material $Sr_3Sc_2O_5Cu_2Se_2$ is included as a reference at x = 0 mol and is represented by a star. The two data points at x = 0.750 mol and x = 0.100 mol are coloured red to indicate the presence of unknown impurities in these samples, and as a result the cited purity values are likely to be slight overestimates. All values are derived from the Rietveld refinements of PXRD data using GSAS-II, and reported as weight percentages. 214

Figure 135 The weight percentages of five impurity phases present in strontium deficient 325 selenide MALMs with general formula $Sr_{3-x}Sc_2O_5Cu_2Se_2$. The pristine material $Sr_3Sc_2O_5Cu_2Se_2$ is included as a reference at x = 0 mol and is represented by stars. 215

Figure 136 Powder X-ray diffractograms of a) the least deficient sample of the series with target composition $Sr_{2.95}Sc_2O_5Cu_2Se_2$, and b) the most deficient sample of the series with target composition $Sr_{2.00}Sc_2O_5Cu_2Se_2$ (both space group I4/mmm) after 36 hours of heating at 800 °C. The small blue circles represent the observed diffracted intensities, the green lines represent the Rietveld-refined calculated models, the red lines represent the backgrounds, and the grey lines represent the differences between observed and calculated intensities. The black tick marks show the reflections of the refined model of $Sr_3Sc_2O_5Cu_2Se_2$, whilst the blue, red, green, orange and pink tick marks represent refined impurity phases SrSe, $SrCO_3$, Sc_2O_3, $SrSeO_4$ and Cu_2Se respectively. Weight fractions for each phase are cited in the figure legends. a) Duration: 45 minutes. Data points: 3457. Interval: 0.02 °. GOF: 1.05. R_{wp}: 6.288 %. b) Duration: 45 minutes. Data points: 3457. Interval: 0.02 °. GOF: 2.18. R_{wp}: 8.641 %. 216

Figure 137 The electrical conductivities of the strontium deficient 325 selenide MALMs with general formula $Sr_{3-x}Sc_2O_5Cu_2Se_2$, represented on a $\log_{10}$ scale. The pristine material $Sr_3Sc_2O_5Cu_2Se_2$ is included as a reference at x = 0 mol and is represented by a star. All values are derived from van der Pauw 4 probe resistivity measurements of 8mm diameter annealed pellet samples. 217

Figure 138 A photographic comparison of the colour of the strontium deficient $Sr_{3-x}Sc_2O_5Cu_2Se_2$ series. Dopant concentration increases from left to right. 218

Figure 139 Purities of the seven copper deficient MALMs in the $Sr_3Sc_2O_5Cu_{2-x}Se_2$ series. The pristine material $Sr_3Sc_2O_5Cu_2Se_2$ is included as a reference at x = 0 mol and is represented by a star. The data points at x = 0.100 mol is coloured red to indicate the presence of unknown impurities in this sample, and as a result the cited purity value is likely to be a slight overestimate. All values are derived from the Rietveld refinements of PXRD data using GSAS-II, and reported as weight percentages. 219

Figure 140 Powder X-ray diffractograms of a) the least deficient sample of the series with target composition $Sr_3Sc_2O_5Cu_{1.95}Se_2$, and b) the most deficient sample of the series with target composition $Sr_3Sc_2O_5Cu_{1.00}Se_2$ (both space group I4/mmm) after 36 hours of heating at 800 °C. The small blue circles represent the observed diffracted intensities, the green lines represent the Rietveld-refined calculated models, the red lines represent the backgrounds, and the grey lines represent the differences between observed and calculated intensities. The black tick marks show the reflections of the refined model of $Sr_3Sc_2O_5Cu_2Se_2$, whilst the blue, red, green and orange tick marks represent refined impurity phases SrSe, $SrCO_3$, Sc_2O_3, and $SrSeO_4$ respectively.

Weight fractions for each phase are cited in the figure legends. a) Duration: 45 minutes. Data points: 3457. Interval: 0.02 °. GOF: 1.07. R_{wp}: 4.998 %. b) Duration: 45 minutes. Data points: 3457. Interval: 0.02 °. GOF: 1.92. R_{wp}: 8.116 %. 220

Figure 141 The weight percentages of five impurity phases present in the copper deficient 325 selenide MALMs with general formula $Sr_3Sc_2O_5Cu_{2-x}Se_2$. The pristine material $Sr_3Sc_2O_5Cu_2Se_2$ is included as a reference at x = 0 mol and is represented by stars. 221

Figure 142 A photographic comparison of the colour of the copper deficient 325 selenide MALMs with general formula $Sr_3Sc_2O_5Cu_{2-x}Se_2$. Deficiency increases from left to right. 221

Figure 143 Comparisons of a) the a unit cell parameter, b) the c unit cell parameter, c) unit cell volume, and d) the optical band gap, of the copper deficient 325 selenide MALMs with general formula $Sr_3Sc_2O_5Cu_{2-x}Se_2$. The pristine material $Sr_3Sc_2O_5Cu_2Se_2$ is included as a reference at x = 0 mol and is represented by a star. 222

Figure 144 The electrical conductivities of the copper deficient 325 selenide MALMs with general formula $Sr_3Sc_2O_5Cu_{2-x}Se_2$, represented on a $\log_{10}$ scale. The pristine material $Sr_3Sc_2O_5Cu_2Se_2$ is included as a reference at x = 0 mol and is represented by a star. All values are derived from van der Pauw 4 probe resistivity measurements of 8mm diameter annealed pellet samples..... 223

Figure 145 The electrical conductivities of the potassium (black), sodium (blue), magnesium (red), barium (green), yttrium (orange), and lanthanum (pink) doped, and strontium (cyan) and copper (grey) deficient $Sr_3Sc_2O_5Cu_2Se_2$ series, presented on a $\log_{10}$ scale. The pristine material $Sr_3Sc_2O_5Cu_2Se_2$ is included as a reference at x = 0 mol and is represented by a star. The horizontal dashed lines represent the electrical conductivities of three 'champion' benchmark materials: Indium Tin Oxide (black), Magnesium doped LaOCuSe (blue), and the pristine $Sr_3Sc_2O_5Cu_2S_2$ reported by Liu et al (red). 225

Figure 146 Powder X-ray diffractogram of material with target composition $Sr_4Sc_2O_6Cu_2S_2$ (space group P4/nmm) after 48 hours of heating at 500 - 600 °C. The small blue circles represent the observed diffracted intensity, the green line represents the Rietveld-refined calculated model, the red line represents the background, and the grey line represents the difference between observed and calculated intensities. The black tick marks show the reflections of the refined model of $Sr_4Sc_2O_6Cu_2S_2$ (98.0 %), whilst the blue and red tick marks represent refined impurity phases SrS (1.7 %), and Cu (0.3 %) respectively. Duration: 16 hours. Data points: 8985. Interval: 0.01 °. GOF: 1.61. R_{wp}: 2.617 %. 231

Figure 147 UV-Vis spectrometry data for material with target composition $Sr_4Sc_2O_6Cu_2S_2$ after 48 hours of heating at 500-600 °C. Plot a) is the raw diffuse reflectance data, and plot b) is the associated magnified Tauc plot for this region, where the intercept between the red extrapolated tangent line and the x-axis is used to estimate an optical band gap of 3.17 eV, which corresponds to 391 nm. 231

Figure 148 Powder X-ray diffractogram of material with target composition $Sr_4Sc_2O_6Cu_2S_2$ (space group P4/nmm) after annealing for 12 hours at 800 °C. The small blue circles represent the observed diffracted intensity, the green line represents the Rietveld-refined calculated model, the red line represents the background, and the grey line represents the difference between observed and calculated intensities. The black tick marks show the reflections of the refined model of $Sr_4Sc_2O_6Cu_2S_2$ (67.1 %), whilst the blue, red and green tick marks represent refined impurity phases $Sr_3Sc_2O_5Cu_2S_2$ (29.7

%), SrS (0.6 %) and $SrCO_3$ (2.6 %) respectively. Duration: 45 minutes. Data points: 4444. Interval: 0.02 °. GOF: 1.14. R_{wp}: 7.141 %. 233

Figure 149 The effect of increasing annealing temperature on the electrical conductivity (left y-axis, bar chart) and pellet density (right y-axis, line graph). All anneal experiments were performed for 24 hours. 234

Figure 150 Purities of the ten sodium doped MALMs in the $(Sr_{4-x}Na_x)Sc_2O_6Cu_2S_2$ series. The pristine material $Sr_3Sc_2O_5Cu_2Se_2$ is included as a reference at $x = 0$ mol and is represented by a star. The two data points at $x = 0.500$mol and $x = 0.100$ mol are coloured red to indicate the presence of unknown impurities in these samples, and as a result the cited purity values are likely to be very slight overestimates. All values are derived from the Rietveld refinements of PXRD data using GSAS-II, and reported as weight percentages. 235

Figure 151 The weight percentages of four impurity phases present in the sodium doped 426 sulfide MALMs with general formula $(Sr_{4-x}Na_x)Sc_2O_6Cu_2S_2$. The pristine material $Sr_4Sc_2O_6Cu_2S_2$ is included as a reference at $x = 0$ mol and is represented by a star. 236

Figure 152 Powder X-ray diffractograms of a) the least doped sample of the series with target composition $(Sr_{3.975}Na_{0.025})Sc_2O_6Cu_2S_2$, and b) the most doped sample of the series with target composition $(Sr_{3.000}Na_{1.000})Sc_2O_6Cu_2S_2$ (both space group P4/nmm) after 36 hours of heating at 500 - 550 °C. The small blue circles represent the observed diffracted intensities, the green lines represent the Rietveld refined calculated models, the red lines represent the backgrounds, and the grey lines represent the differences between observed and calculated intensities. The black tick marks show the reflections of the refined model of $Sr_4Sc_2O_6Cu_2S_2$, whilst the blue, red, green and orange tick marks represent refined impurity phases $Sr_3Sc_2O_5Cu_2S_2$, SrS, Cu and $NaScO_2$ respectively. Weight fractions for each phase are cited in the figure legends. a) Duration: 45 minutes. Data points: 3457. Interval: 0.02 °. GOF: 1.29. R_{wp}: 5.892 %. b) Duration: 45 minutes. Data points: 3457. Interval: 0.02 °. GOF: 1.35. R_{wp}: 6.016 %. 237

Figure 153 The calculated maximum possible levels of dopant incorporation into the $(Sr_{4-x}Na_x)Sc_2O_6Cu_2S_2$ MALMs. Values were derived from the wt % of the sodium-containing impurities of each sample. The pristine material $Sr_4Sc_2O_6Cu_2S_2$ is included as a reference at $x = 0$ mol and is represented by a star. The red dashed line represents 100 % dopant incorporation into the MALM, statistically no values may surpass this line. The black data points are the estimated upper bound of dopant incorporation for each sample. 238

Figure 154 The electrical conductivities of the ten sodium doped MALMs in the $(Sr_{4-x}Na_x)Sc_2O_5Cu_2S_2$ series, represented on a $\log_{10}$ scale. The pristine material $Sr_4Sc_2O_6Cu_2S_2$ is included as a reference at $x = 0$ mol and is represented by a star. All values are derived from van der Pauw 4 probe resistivity measurements of 8mm diameter annealed pellet samples. 239

Figure 155 Powder X-ray diffractogram of material with target composition $Sr_4Sc_2O_6Cu_2S_2$ (space group P4/nmm) after annealing for 10 - 30 minutes at 1000 °C. The small blue circles represent the observed diffracted intensity, the green line represents the Rietveld-refined calculated model, the red line represents the background, and the grey line represents the difference between observed and calculated intensities. The black tick marks show the reflections of the refined model of $Sr_4Sc_2O_6Cu_2S_2$ (93.6 %), whilst the blue, red and green tick marks represent refined impurity phases $Sr_3Sc_2O_5Cu_2S_2$ (5.1 %), SrS (0.4 %) and $SrCO_3$ (0.9 %) respectively. Duration: 3 hours. Data points: 4444. Interval: 0.02 °. GOF: 1.67. R_{wp}: 4.158 %. 240

Figure 156 Powder X-ray diffractogram of material with target composition $(Sr_{3.9}Na_{0.1})Sc_2O_6Cu_2S_2$ (space group P4/nmm) after 24 hours of heating at 550 °C. The small blue circles represent the observed diffracted intensity, the green line represents the Rietveld-refined calculated model, the red line represents the background, and the grey line represents the difference between observed and calculated intensities. The black tick marks show the reflections of the refined model of $Sr_4Sc_2O_6Cu_2S_2$ (95.4 %), whilst the blue, red and green tick marks represent refined impurity phases SrS (2.9 %), Cu (0.9 %) and $SrCO_3$ (0.7 %) respectively. Duration: 3 hours. Data points: 4444. Interval: 0.02 °. GOF: 1.22. R_{wp}: 3.523 %. 241

Figure 157 Powder X-ray diffractogram of material with target composition $(Sr_{3.9}K_{0.1})Sc_2O_6Cu_2S_2$ (space group P4/nmm) after 24 hours of heating at 550 °C. The small blue circles represent the observed diffracted intensity, the green line represents the Rietveld-refined calculated model, the red line represents the background, and the grey line represents the difference between observed and calculated intensities. The black tick marks show the reflections of the refined model of $Sr_4Sc_2O_6Cu_2S_2$ (95.2 %), whilst the blue, red and green tick marks represent refined impurity phases SrS (3.2 %), Cu (0.9 %) and $SrCO_3$ (0.8 %) respectively. Duration: 3 hours. Data points: 4444. Interval: 0.02 °. GOF: 1.39. R_{wp}: 3.631 %. 242

Figure 158 Powder X-ray diffractogram of material with target composition $Sr_4Sc_2O_6Cu_2Se_2$ (space group P4/nmm) after 48 hours of heating at 500 - 650 °C. The small blue circles represent the observed diffracted intensity, the green line represents the Rietveld-refined calculated model, the red line represents the background, and the grey line represents the difference between observed and calculated intensities. The black tick marks show the reflections of the refined model of $Sr_4Sc_2O_6Cu_2Se_2$ (98.5 %), whilst the blue and red tick marks represent refined impurity phases $Sr_3Sc_2O_5Cu_2Se_2$ (1.2 %), and SrSe (0.3 %) respectively. Duration: 16 hours. Data points: 8887. Interval: 0.01 °. GOF: 3.72. R_{wp}: 3.107 %..... 243

Figure 159 UV-Vis spectrometry data for material with target composition $Sr_4Sc_2O_6Cu_2Se_2$ after 48 hours of heating at 500 - 650 °C. Plot a) is the raw diffuse reflectance data, and plot b) is the associated magnified Tauc plot for this region, where the intercept between the red extrapolated tangent line and the x-axis is used to estimate an optical band gap of 2.95 eV, which corresponds to 420 nm. 244

Figure 160 Powder X-ray diffractogram of material with target composition $(Sr_{3.900}K_{0.100})Sc_2O_6Cu_2S_2$ (space group P4/nmm) after 24 hours of heating at 550 °C and before flash annealing. The small blue circles represent the observed diffracted intensity, the green line represents the Rietveld-refined calculated model, the red line represents the background, and the grey line represents the difference between observed and calculated intensities. The black tick marks show the reflections of the refined model of $Sr_4Sc_2O_6Cu_2S_2$ (95.2 %), whilst the blue, red and green tick marks represent refined impurity phases SrS (3.2 %), Cu (0.9 %) and $SrCO_3$ (0.8 %) respectively. Duration: 3 hours. Data points: 4444. Interval: 0.02 °. GOF: 1.39. R_{wp}: 3.631 %. 245

Figure 161 Powder X-ray diffractogram of material with target composition $(Sr_{3.900}Na_{0.100})Sc_2O_6Cu_2Se_2$ (space group P4/nmm) after 24 hours of heating at 550 °C and before flash annealing. The small blue circles represent the observed diffracted intensity, the green line represents the Rietveld-refined calculated model, the red line represents the background, and the grey line represents the difference between observed and calculated intensities. The black tick marks show the reflections of the refined model of $Sr_4Sc_2O_6Cu_2Se_2$ (95.9 %), whilst the blue and red tick marks represent refined impurity phases SrSe (3.7 %) and Cu (0.4 %) respectively. Duration: 3 hours. Data points: 4444. Interval: 0.02 °. GOF: 1.59. R_{wp}: 4.412 %. 246

Table of Figures

Figure 162 Powder X-ray diffractogram of materials with target composition a) $Sr_4Ga_2O_6Cu_2S_2$ after synthesis at 700 °C, and b) $Sr_4Ga_2O_6Cu_2Se_2$ after synthesis at 830 °C (both space group P4/nmm). The small blue circles represent the observed diffracted intensity, the green line represents the Rietveld-refined calculated model, the red line represents the background, and the grey line represents the difference between observed and calculated intensities. The black, blue, and red tick marks show the reflections of the refined models of $Sr_4Ga_2O_6Cu_2Ch_2$, $Sr_3Ga_2O_6$, and SrS respectively. Weight fractions for each phase are cited in the figure legends. a) Duration: 12 hours. Data points: 8887. Interval: 0.01 °. GOF: 2.28. R_{wp}: 3.16 %. b) Duration: 12 hours. Data points: 8887. Interval: 0.01 °. GOF: 3.72. R_{wp}: 3.30 %. 248

Figure 163 Powder X-ray diffractogram of materials with target composition a) $Sr_4In_2O_6Cu_2S_2$ after synthesis at 800 °C, and b) $Sr_4In_2O_6Cu_2Se_2$ after synthesis at 700 °C (both space group P4/nmm). The small blue circles represent the observed diffracted intensity, the green line represents the Rietveld-refined calculated model, the red line represents the background, and the grey line represents the difference between observed and calculated intensities. The black, blue, and red tick marks show the reflections of the refined models of $Sr_4In_2O_6Cu_2Ch_2$, $SrIn_2O_4$, and SrCh respectively. Weight fractions for each phase are cited in the figure legends. a) Duration: 12 hours. Data points: 8887. Interval: 0.01 °. GOF: 2.09. R_{wp}: 2.81 %. b) Duration: 12 hours. Data points: 8887. Interval: 0.01 °. GOF: 3.07. R_{wp}: 4.01 %. 249

Figure 164 A comparison of the six synthesised pristine $Sr_4B_2O_6Cu_2Ch_2$ materials (B = Ga, Sc, or In. Ch = S or Se), comparing the B ion radii against a) the unit cell a parameter, b) the unit cell c parameter, and c) the unit cell volume. Circles represent selenide materials and squares represent sulfides. Blue, red and green data points represent gallium, scandium and indium MALMs respectively. Part d) depicts a generic unit cell of the 426 structure highlighting the a and c parameters, and e) depicts the 'doubled' unit cell convention used throughout this work. 250

Figure 165 A comparative illustration of the synthesis of a material via a) the conventional ceramic method, and b) solid-state metathesis. Samples are depicted as building blocks to highlight the pre-formed ionic blocks employed in the metathetic pathway. 253

Figure 166 Isometric projections of the $A_3B_2O_5M_2Q_2$ '325' structure type MALM, showing a) one unit cell, b) a 2 × 5 × 2 expanded unit cell, c) the $[A_3B_2O_5]^{2+}$ light layer subunit, and d) the $[M_2Q_2]^{2-}$ heavy layer subunit. Projections are viewed primarily along the x-axis, and are not to scale with each other. The blue dashed lines denote the unit cell. The coloured regions represent the light (pastel blue) and heavy (pastel pink) layer subunits, which are the ionic building blocks in a metathesis synthesis. Colour key: green - A, pink - B, red - O, blue - M, and yellow - Q. 254

Figure 167 Isometric projections of the precursors and products in the synthesis of $Sr_3Fe_2O_5Cu_2Se_2$ via a metathesis pathway. Projections are viewed primarily along the x-axis, and are to scale with each other. The blue dashed lines denote the unit cell. Colour key: green - Sr, light brown - Fe, red - O, blue - Cu, yellow - Se, white - Na, and dark brown - Br. 256

Figure 168 Isometric projections of generic depictions of the possible light layer and heavy layer precursors utilised in a MALM metathetic synthesis. The light layer precursors with structure types a) 212, b) 325, c) 438 and d) 426, contain halide counter-anions. The heavy layer precursors with structure types e) PbClF, f) $BaZn_2P_2$ and g) $ThCr_2Sr_2$ contain group 1 or 2 metal counter-cations. Projections are viewed primarily along the x-axis, and are not to scale with each other. The blue dashed lines denote the unit cell. Colour key: green - A, pink - B, red - O, blue - M, yellow - Q, brown - halide counter anion, and white - metal counter cation. 260

Figure 169 A simulated Powder X-ray diffractogram of the example 3 × 2 parallel synthesis described in Table 12 on page 258. This simulation assumes the 'worst case scenario' for diffractogram convolution, where all precursors are present, as well as three reported MALMs and their associated salt by-products. All included phases are at equal weight ratios. 262

Figure 170 Powder X-ray diffractogram of material with target composition $Sr_2Co_2O_5$ (space group I4/mmm) after 36 hours of heating at 1000 °C. The small blue circles represent the observed diffracted intensity, the green line represents the Rietveld-refined calculated model, the red line represents the background, and the grey line represents the difference between observed and calculated intensities. The black and blue tick marks show the reflections of the refined models of $Sr_6Co_5O_{15}$ (98.5 %) and Co_3O_4 (1.5 %). Duration: 5 hours. Data points: 3457. Interval: 0.02 °. GOF: 2.03. R_{wp}: 1.468 %. 268

Figure 171 Powder X-ray diffractogram of material with target composition $Sr_3Co_2O_5Cl_2$ (space group I4/mmm) after 96 hours of heating at 800 to 900 °C. The small blue circles represent the observed diffracted intensity, the green line represents the Rietveld-refined calculated model, the red line represents the background, and the grey line represents the difference between observed and calculated intensities. The black tick marks show the reflections of the refined model of $Sr_3Co_2O_5Cl_2$, no impurity phases are observed. Duration: 45 minutes. Data points: 3457. Interval: 0.02 °. GOF: 1.20. R_{wp}: 2.849 %. 269

Figure 172 Powder X-ray diffractogram of material with target composition $Sr_3Fe_2O_5Br_2$ (space group I4/mmm) after 72 hours of heating at 580 to 850 °C. The small blue circles represent the observed diffracted intensity, the green line represents the Rietveld-refined calculated model, the red line represents the background, and the grey line represents the difference between observed and calculated intensities. The black tick marks show the reflections of the refined model of $Sr_3Fe_2O_5Br_2$, no impurity phases are observed. Duration: 45 minutes. Data points: 3457. Interval: 0.02 °. GOF: 1.43. R_{wp}: 5.344 %. 270

Figure 173 Powder X-ray diffractogram of material with target composition $Sr_4Co_2O_6Cl_2$ (space group I4/mmm) after 72 hours of heating at 800 to 900 °C. The small blue circles represent the observed diffracted intensity, the green line represents the Rietveld-refined calculated model, the red line represents the background, and the grey line represents the difference between observed and calculated intensities. The black tick marks show the reflections of the refined model of $Sr_4Co_2O_6Cl_2$, no impurity phases are observed. Duration: 45 minutes. Data points: 3457. Interval: 0.02 °. GOF: 1.34. R_{wp}: 3.617 %. 271

Figure 174 Powder X-ray diffractogram of material with target composition $Sr_4Sc_2O_6Cl_2$ (space group I4/mmm) after 96 hours of heating at 500 to 1050 °C. The small blue circles represent the observed diffracted intensity, the green line represents the Rietveld-refined calculated model, the red line represents the background, and the grey line represents the difference between observed and calculated intensities. The black tick marks show the reflections of the refined model of $Sr_4Sc_2O_6Cl_2$, no impurity phases are observed. Duration: 45 minutes. Data points: 3457. Interval: 0.02 °. GOF: 1.16. R_{wp}: 6.118 %. 272

Figure 175 Powder X-ray diffractogram of material with target composition $Sr_3Sc_2O_5Cl_2$ (space group I4/mmm) after 96 hours of heating at 500 to 1050 °C. The small blue circles represent the observed diffracted intensity, the green line represents the Rietveld-refined calculated model, the red line represents the background, and the grey line represents the difference between observed and calculated intensities. The black tick marks show the reflections of the refined model of $Sr_3Sc_2O_5Cl_2$, no impurity phases

are observed. Duration: 45 minutes. Data points: 3457. Interval: 0.02 °. GOF: 1.17. R_{wp}: 6.082 %. 273

Figure 176 Powder X-ray diffractogram of material with target composition $Sr_3Fe_2O_5Cl_2$ (space group I4/mmm) after 72 hours of heating at 600-850 °C. The small blue circles represent the observed diffracted intensity, the green line represents the Rietveld-refined calculated model, the red line represents the background, and the grey line represents the difference between observed and calculated intensities. The black tick marks show the reflections of the refined model of $Sr_3Fe_2O_5Cl_2$, no impurity phases are observed. Duration: 45 minutes. Data points: 3457. Interval: 0.02 °. GOF: 1.07. R_{wp}: 3.972 %. 274

Figure 177 Powder X-ray diffractogram of material with target composition $Sr_4Fe_2O_6Cl_2$ (space group I4/mmm) after 72 hours of heating at 600-850 °C. The small blue circles represent the observed diffracted intensity, the green line represents the Rietveld-refined calculated model, the red line represents the background, and the grey line represents the difference between observed and calculated intensities. The black tick marks show the reflections of the refined model of $Sr_4Fe_2O_6Cl_2$. A small unknown impurity is present in the material. Duration: 45 minutes. Data points: 3457. Interval: 0.02 °. GOF: 1.35. R_{wp}: 4.381 %. 275

Figure 178 Powder X-ray diffractogram of material with target composition $Sr_4Fe_2O_6Br_2$ (space group I4/mmm) after 72 hours of heating at 600-850 °C. The small blue circles represent the observed diffracted intensity, the green line represents the Rietveld-refined calculated model, the red line represents the background, and the grey line represents the difference between observed and calculated intensities. The black tick marks show the reflections of the refined model of $Sr_4Fe_2O_6Br_2$ (98.0 %), whilst the blue marks represent refined impurity phase $SrCO_3$ (2.0 %). Duration: 45 minutes. Data points: 3457. Interval: 0.02 °. GOF: 1.28. R_{wp}: 4.142 %. 276

Figure 179 Powder X-ray diffractogram of material with target composition $Ba_3Y_2O_5Cl_2$ (space group I4/mmm) after 96 hours of heating at 900 to 1050 °C. The small blue circles represent the observed diffracted intensity, the green line represents the Rietveld-refined calculated model, the red line represents the background, and the grey line represents the difference between observed and calculated intensities. The black tick marks show the reflections of the refined model of $Ba_3Y_2O_5Cl_2$ (80.9 %), whilst the blue and red marks represent refined impurity phases Y_2O_3 (12.4 %) and Ba_4OCl_6 (6.7 %) respectively. Duration: 45 minutes. Data points: 3457. Interval: 0.02 °. GOF: 1.55. R_{wp}: 8.979 %. 277

Figure 180 Powder X-ray diffractogram of material with target composition $Na_2Cu_2Se_2$ (space group I4/mmm) after 24 hours of heating at 800 °C. The small blue circles represent the observed diffracted intensity, the green line represents the Rietveld-refined calculated model, the red line represents the background, and the grey line represents the difference between observed and calculated intensities. The black tick marks show the reflections of the refined model of $Na_2Cu_2Se_2$, no impurity phases are observed. Data was collected with the domed air-tight holder, responsible for the background-refined peaks at 13.3 and 50.5 °. Duration: 10 minutes. Data points: 3457. Interval: 0.02 °. GOF: 1.15. R_{wp}: 5.847 %. 280

Figure 181 A comparison of the colours of the bank of metathesis precursors: a) $Sr_3Co_2O_5Cl_2$, b) $Sr_3Fe_2O_5Br_2$, c) $Sr_4Co_2O_6Cl_2$, d) $Sr_4Sc_2O_6Cl_2$, e) $Sr_3Sc_2O_5Cl_2$, f) $Sr_3Fe_2O_5Cl_2$, g) $Sr_4Fe_2O_6Cl_2$, h) $Sr_4Fe_2O_6Br_2$, and i) $Na_2Cu_2Se_2$. 280

Figure 182 A bar chart illustrating the phase fractions of $Sr_3Sc_2O_5Cu_2Se_2$ (black), $Sr_3Sc_2O_5Cl_2$ (blue), $Na_2Cu_2Se_2$ (pink), SrSe (green), $NaCu_3Se_2$ (orange) and NaCl (red) from the five

component samples in the series of experiments targeting $Sr_3Sc_2O_5Cu_2Se_2$ by metathesis..... 283

Figure 183 Powder X-ray diffractograms of materials resulting from attempted metathesis synthesis of $Sr_3Sc_2O_5Cu_2Se_2$ after 12 hours of heating at a) 500 °C and b) 800 °C. The small blue circles represent the observed diffracted intensity, the green line represents the Rietveld-refined calculated model, the red line represents the background, and the grey line represents the difference between observed and calculated intensities. The black, blue, pink, green, orange and red tick marks show the reflections of the refined models of $Sr_3Sc_2O_5Cu_2Se_2$, $Sr_3Sc_2O_5Cl_2$, $Na_2Cu_2Se_2$, SrSe, $NaCu_3Se_2$ and NaCl respectively. Weight fractions for each phase are cited in the figure legends. Data was collected with the domed air-tight holder, responsible for the background-refined peaks at 13.3 and 50.5 °. a) Duration: 45 minutes. Data points: 3457. Interval: 0.02 °. GOF: 1.28. R_{wp}: 2.945 %. b) Duration: 45 minutes. Data points: 3457. Interval: 0.02 °. GOF: 1.17. R_{wp}: 2.779 %..... 284

Figure 184 A bar chart illustrating the phase fractions of $Sr_3Sc_2O_5Cu_2Se_2$ (black), $Sr_4Sc_2O_6Cu_2Se_2$ (grey), SrSe (green), and Cu (copper) from the five component samples in the series of experiments targeting $Sr_3Sc_2O_5Cu_2Se_2$ by conventional ceramic syntheses.285

Figure 185 Powder X-ray diffractograms of materials resulting from attempted conventional synthesis of $Sr_3Sc_2O_5Cu_2Se_2$ after 12 hours of heating at a) 500 °C and b) 800 °C. The small blue circles represent the observed diffracted intensity, the green line represents the Rietveld-refined calculated model, the red line represents the background, and the grey line represents the difference between observed and calculated intensities. The black, grey, green, and copper tick marks show the reflections of the refined models of $Sr_3Sc_2O_5Cu_2Se_2$, $S_4Sc_2O_6Cu_2Se_2$, SrSe and Cu respectively. Weight fractions for each phase are cited in the figure legends. Data was collected with the domed air-tight holder, responsible for the background-refined peaks at 13.3 and 50.5 °. a) Duration: 45 minutes. Data points: 3457. Interval: 0.02 °. GOF: 1.15. R_{wp}: 2.750 %. b) Duration: 45 minutes. Data points: 3457. Interval: 0.02 °. GOF: 1.04. R_{wp}: 2.543 %. 287

Figure 186 A bar chart illustrating the phase fractions of $Sr_3Fe_2O_5Cu_2Se_2$ (black), $Sr_3Fe_2O_5Cl_2$ (blue), $Na_2Cu_2Se_2$ (pink), SrSe (green), $NaCu_3Se_2$ (orange) and NaCl (red) from the five component samples in the series of experiments targeting $Sr_3Fe_2O_5Cu_2Se_2$ by metathesis..... 288

Figure 187 Powder X-ray diffractograms of materials resulting from attempted metathesis synthesis of $Sr_3Fe_2O_5Cu_2Se_2$ after 12 hours of heating at a) 500 °C and b) 800 °C. The small blue circles represent the observed diffracted intensity, the green line represents the Rietveld-refined calculated model, the red line represents the background, and the grey line represents the difference between observed and calculated intensities. The black, blue, pink, green, orange and red tick marks show the reflections of the refined models of $Sr_3Fe_2O_5Cu_2Se_2$, $Sr_3Fe_2O_5Cl_2$, $Na_2Cu_2Se_2$, SrSe, $NaCu_3Se_2$ and NaCl respectively. Weight fractions for each phase are cited in the figure legends. Data was collected with the domed air-tight holder, responsible for the background-refined peaks at 13.3 and 50.5 °. a) Duration: 45 minutes. Data points: 3457. Interval: 0.02 °. GOF: 1.27. R_{wp}: 2.920 %. b) Duration: 45 minutes. Data points: 3457. Interval: 0.02 °. GOF: 1.13. R_{wp}: 2.557 %..... 290

Figure 188 Powder X-ray diffractogram of material resulting from attempted metathesis synthesis of $Sr_3Fe_2O_5Cu_2Se_2$ (space group I4/mmm) after 12 hours of heating at 700 °C, then washed in distilled H_2O to remove the NaCl by-product. The small blue circles represent the observed diffracted intensity, the green line represents the Rietveld-refined calculated model, the red line represents the background, and the grey line represents the difference between observed and calculated intensities. The black tick

marks show the reflections of the refined model of $Sr_3Fe_2O_5Cu_2Se_2$, no NaCl or impurity phases were observed. Duration: 16 hours. Data points: 8887. Interval: 0.01 °. GOF: 1.70. R_{wp}: 1.642 %. 291

Figure 189 A bar chart illustrating the phase fractions of $Sr_3Fe_2O_5Cu_2Se_2$ (black), $Sr_4Fe_2O_6Cu_2Se_2$ (grey), SrSe (green), and Fe_2O_3 (cyan) from the five component samples in the series of experiments targeting $Sr_3Fe_2O_5Cu_2Se_2$ by conventional ceramic syntheses.293

Figure 190 Powder X-ray diffractograms of materials resulting from attempted conventional synthesis of $Sr_3Fe_2O_5Cu_2Se_2$ after 12 hours of heating at a) 500 °C and b) 800 °C. The small blue circles represent the observed diffracted intensity, the green line represents the Rietveld-refined calculated model, the red line represents the background, and the grey line represents the difference between observed and calculated intensities. The black, grey, green, and cyan tick marks show the reflections of the refined models of $Sr_3Fe_2O_5Cu_2Se_2$, $S_4Fe_2O_6Cu_2Se_2$, SrSe and Fe_2O_3 respectively. Weight fractions for each phase are cited in the figure legends. Data was collected with the domed air-tight holder, responsible for the background-refined peaks at 13.3 and 50.5 °. a) Duration: 45 minutes. Data points: 3457. Interval: 0.02 °. GOF: 1.24. R_{wp}: 2.839 %. b) Duration: 45 minutes. Data points: 3457. Interval: 0.02 °. GOF: 1.15. R_{wp}: 2.574 %. 294

Figure 191 Powder X-ray diffractogram of material resulting from attempted metathesis synthesis of $Sr_3Co_2O_5Cu_2Se_2$ after 12 hours of heating at 600 °C. The small blue circles represent the observed diffracted intensity, the green line represents the Rietveld-refined calculated model, the red line represents the background, and the grey line represents the difference between observed and calculated intensities. The black, blue, red, and green tick marks show the reflections of the refined models of $Sr_2CoO_2Cu_2Se_2$ (71.9 %), NaCl (18.5 %), CoO (6.8 %), and SrSe (2.8 %) respectively. Data was collected with the domed air-tight holder, responsible for the background-refined peaks at 13.3 and 50.5 °. Duration: 45 minutes. Data points: 3457. Interval: 0.02 °. GOF: 1.24. R_{wp}: 2.692 %. 296

Figure 192 Powder X-ray diffractogram of material resulting from attempted metathesis synthesis of $Sr_4Co_2O_6Cu_2Se_2$ after 12 hours of heating at 600 °C. The small blue circles represent the observed diffracted intensity, the green line represents the Rietveld-refined calculated model, the red line represents the background, and the grey line represents the difference between observed and calculated intensities. The black, blue, red, and green tick marks show the reflections of the refined models of $Sr_2CoO_2Cu_2Se_2$ (64.9 %), NaCl (21.4 %), CoO (9.4 %), and SrSe (4.3 %) respectively. Data was collected with the domed air-tight holder, responsible for the background-refined peaks at 13.3 and 50.5 °. Duration: 45 minutes. Data points: 3457. Interval: 0.02 °. GOF: 1.47. R_{wp}: 3.156 %. 297

Figure 193 Powder X-ray diffractogram of material resulting from attempted metathesis synthesis of $Sr_3Fe_2O_5Cu_2Se_2$ after 12 hours of heating at 600 °C. The small blue circles represent the observed diffracted intensity, the green line represents the Rietveld-refined calculated model, the red line represents the background, and the grey line represents the difference between observed and calculated intensities. The black and blue tick marks show the reflections of the refined models of $Sr_3Fe_2O_5Cu_2Se_2$ (75.0 %) and NaBr (25.0 %) respectively. Data was collected with the domed air-tight holder, responsible for the background-refined peaks at 13.3 and 50.5 °. Duration: 45 minutes. Data points: 3457. Interval: 0.02 °. GOF: 1.06. R_{wp}: 2.369 %. ... 298

Figure 194 Powder X-ray diffractograms of materials resulting from the attempted metathesis syntheses of $Sr_4Fe_2O_6Cu_2Se_2$ with a) $Sr_4Fe_2O_6Cl_2$ and b) $Sr_4Fe_2O_6Br_2$, after 12 hours of heating at 600 °C. The small blue circles represent the observed diffracted intensity, the green lines represent the Rietveld-refined calculated model, the red lines

represent the background, and the grey lines represent the difference between observed and calculated intensities. The black, blue, red, green, orange, pink and cyan tick marks show the reflections of the refined models of $Sr_4Fe_2O_6Cu_2Se_2$, $Sr_3Fe_2O_5Cu_2Se_2$, NaCl, $NaCu_3Se_2$, SrSe, NaBr and $SrCO_3$ respectively. Weight fractions for each phase are cited in the figure legends. Data was collected with the domed air-tight holder, responsible for the background-refined peaks at 13.3 and 50.5 °. a) Duration: 45 minutes. Data points: 3457. Interval: 0.02 °. GOF: 1.13. R_{wp}: 2.597 %. b) Duration: 45 minutes. Data points: 3457. Interval: 0.02 °. GOF: 1.13. R_{wp}: 2.500 %. 300

Figure 195 Powder X-ray diffractogram of material resulting from attempted metathesis synthesis of $Sr_4Sc_2O_6Cu_2Se_2$ after 12 hours of heating at 600 °C. The small blue circles represent the observed diffracted intensity, the green line represents the Rietveld-refined calculated model, the red line represents the background, and the grey line represents the difference between observed and calculated intensities. The black, blue, and red tick marks show the reflections of the refined models of $Sr_3Sc_2O_5Cu_2Se_2$ (69.9 %), NaCl (27.9 %), and SrSe (2.2 %) respectively. Data was collected with the domed air-tight holder, responsible for the background-refined peaks at 13.3 and 50.5 °. Duration: 45 minutes. Data points: 3457. Interval: 0.02 °. GOF: 1.43. R_{wp}: 3.417 %. 301

Figure 196 The simulated powder X-ray diffractograms of KBr (orange), KCl (pink), NaBr (green), NaCl (blue), KF (red), and NaF (black). Plots are labelled, and listed in ascending order of the 2θ value of the 200 reflection. 305

Figure 197 Powder X-ray diffractograms of materials resulting from the reactions of a) NaF and KCl, b) NaF and KBr, and c) NaCl and KBr, after 12 hours of heating at 700 °C. The small blue circles represent the observed diffracted intensities, the green lines represent the Rietveld-refined calculated models, the red lines represent the backgrounds, and the grey lines represent the differences between observed and calculated intensities. Weight fractions for each phase are cited in the figure legends but should be approached qualitatively. a) Duration: 2 minutes. Data points: 3457. Interval: 0.02 °. GOF: 1.19. R_{wp}: 39.476 %. b) Duration: 2 minutes. Data points: 3457. Interval: 0.02 °. GOF: 1.33. R_{wp}: 34.434 %. c) Duration: 2 minutes. Data points: 3457. Interval: 0.02 °. GOF: 1.80. R_{wp}: 47.499 %. 306

Figure 198 Powder X-ray diffractograms of materials resulting from the reactions of a) NaCl and KF, and b) NaBr and KCl, after 12 hours of heating at 700 °C. The small blue circles represent the observed diffracted intensities, the green lines represent the Rietveld-refined calculated models, the red lines represent the backgrounds, and the grey lines represent the differences between observed and calculated intensities. Weight fractions for each phase are cited in the figure legends but should be approached qualitatively. a) Duration: 2 minutes. Data points: 3457. Interval: 0.02 °. GOF: 1.21. R_{wp}: 44.674 %. b) Duration: 2 minutes. Data points: 3457. Interval: 0.02 °. GOF: 1.66. R_{wp}: 42.694 %. 307

Figure 199 Powder X-ray diffractogram of material resulting from the reaction of NaBr and KF, after 12 hours of heating at 700 °C. The small blue circles represent the observed diffracted intensity, the green line represents the Rietveld-refined calculated model, the red line represents the background, and the grey line represents the difference between observed and calculated intensities. The black and blue tick marks show the reflections of the refined models of NaBr (0.5 %) and NaKBrF (99.5 %) respectively. Duration: 2 minutes. Data points: 3457. Interval: 0.02 °. GOF: 1.76. R_{wp}: 42.060 %. 308

Figure 200 Powder X-ray diffractogram of material resulting from attempted parallel metathetic syntheses of $Sr_3Fe_2O_5Cu_2Se_2$ and $Sr_3Sc_2O_5Cu_2Se_2$ after 12 hours of heating at 600 °C.

The small blue circles represent the observed diffracted intensity, the green line represents the Rietveld-refined calculated model, the red line represents the background, and the grey line represents the difference between observed and calculated intensities. The black, blue, red, green, orange, and pink tick marks show the reflections of the refined models of $Sr_4(FeSc)O_6Cu_2Se_2$ (58.8 %), SrSe (4.7 %), $Na(Br_{0.5}Cl_{0.5})$ (28.5 %), $NaCu_3Se_2$ (2.8 %), $SrCO_3$ (1.3 %), and Sc_2O_3 (0.4 %) respectively. Duration: 3 hours. Data points: 4444. Interval: 0.02 °. GOF: 5.28. R_{wp}: 10.021 %. 312

Figure 201 Powder X-ray diffractogram of material resulting from attempted parallel metathetic synthesis of $Sr_3Fe_2O_5Cu_2Se_2$ after 12 hours of heating at 600 °C. The small blue circles represent the observed diffracted intensity, the green line represents the Rietveld-refined calculated model, the red line represents the background, and the grey line represents the difference between observed and calculated intensities. The black and blue tick marks show the reflections of the refined models of $Sr_3Fe_2O_5Cu_2Se_2$ (80.4 %), and $Na(Br_{0.5}Cl_{0.5})$ (19.6 %) respectively. Duration: 3 hours. Data points: 4444. Interval: 0.02 °. GOF: 1.20. R_{wp}: 2.326 %. 314

Figure 202 Powder X-ray diffractogram of material resulting from attempted parallel metathetic syntheses of $Sr_3Fe_2O_5Cu_2Se_2$, $Sr_3Sc_2O_5Cu_2Se_2$ and $Sr_3Co_2O_5Cu_2Se_2$ after 12 hours of heating at 600 °C. The small blue circles represent the observed diffracted intensity, the green line represents the Rietveld-refined calculated model, the red line represents the background, and the grey line represents the difference between observed and calculated intensities. The black, blue, red, green, orange, and pink tick marks show the reflections of the refined models of $Sr_4(FeSc)O_6Cu_2Se_2$ (43.2 %), $Sr_2CoO_2Cu_2Se_2$ (14.7 %), SrSe (7.7 %), $Na(Br_{0.33}Cl_{0.66})$ (28.8 %), Sc_2O_3 (4.9 %), and CoO (0.7 %) respectively. Duration: 3 hours. Data points: 4444. Interval: 0.02 °. GOF: 4.33. R_{wp}: 7.638 %. 316

Figure 203 Powder X-ray diffractogram of material resulting from attempted parallel metathetic syntheses of $Sr_4Fe_2O_6Cu_2Se_2$, $Sr_4Sc_2O_6Cu_2Se_2$ and $Sr_4Co_2O_6Cu_2Se_2$ after 12 hours of heating at 600 °C. The small blue circles represent the observed diffracted intensity, the green line represents the Rietveld-refined calculated model, the red line represents the background, and the grey line represents the difference between observed and calculated intensities. The black, blue, red, green, orange, pink and cyan tick marks show the reflections of the refined models of $Sr_4(FeSc)O_6Cu_2Se_2$ (45.0 %), $Sr_2CoO_2Cu_2Se_2$ (13.8 %), SrSe (20.7 %), $Na(Br_{0.33}Cl_{0.66})$ (18.3 %), $NaCu_3Se_2$ (0.7 %), $SrCO_3$ (0.9 %) and CoO (0.5 %) respectively. Duration: 3 hours. Data points: 4444. Interval: 0.02 °. GOF: 3.79. R_{wp}: 6.647 %. 318

Figure 204 Powder X-ray diffractogram of material with target composition $Sr_3In_2O_5Cu_2Se_2$ (space group I4/mmm) after 36 hours of heating at 900 °C. The small blue circles represent the observed diffracted intensity, the green line represents the Rietveld-refined calculated model, the red line represents the background, and the grey line represents the difference between observed and calculated intensities. The black tick marks show the reflections of the refined model of $Sr_3In_2O_5Cu_2Se_2$ (80.2 %), whilst the blue and red tick marks represent refined impurity phases $SrIn_2O_4$ (12.0 %), and SrSe (7.8 %) respectively. Duration: 12 hours. Data points: 3457. Interval: 0.01 °. GOF: 1.52. R_{wp}: 7.227 %. 322

Figure 205 UV-Vis spectrometry data for material with target composition $Sr_3In_2O_5Cu_2Se_2$ after 48 hours of heating at 500 - 900 °C. Plot a) is the raw diffuse reflectance data, and plot b) is the associated magnified Tauc plot for this region, where the intercept between the red extrapolated tangent line and the x-axis is used to estimate an optical band gap of 2.33 eV, which corresponds to 532 nm. 323

Figure 206 Powder X-ray diffractogram of material with target composition $Sr_3In_2O_5Cu_2S_2$ after 48 hours of heating at 500 - 900 °C. The small blue circles represent the observed diffracted intensity, the green line represents the Rietveld-refined calculated model, the red line represents the background, and the grey line represents the difference between observed and calculated intensities. The black and blue tick marks show the reflections of the refined models of $SrIn_2O_4$ (72.8 %) and SrS (27.2 %) respectively. Duration: 1 hour. Data points: 3457. Interval: 0.02 °. GOF: 2.54. R_{wp}: 13.422 %. 324

Figure 207 Powder X-ray diffractogram of material with target composition $Sr_3In_2O_5Cl_2$ after 36 hours of heating at 700 - 1000 °C. The small blue circles represent the observed diffracted intensity, the green line represents the Rietveld-refined calculated model, the red line represents the background, and the grey line represents the difference between observed and calculated intensities. The black, blue, red, green and orange tick marks show the reflections of the refined models of $Sr_4In_2O_6Cl_2$ (21.2 %), $SrIn_2O_4$ (56.5 %), $SrCl_2{\cdot}6H_2O$ (8.3 %), Sr_4OCl_6 (8.0 %) and Sr(OH)Cl (6.0 %) respectively. Duration: 1 hour. Data points: 4691. Interval: 0.02 °. GOF: 1.48. R_{wp}: 10.350 %. 325

Figure 208 Powder X-ray diffractogram of material with target composition $Sr_4In_2O_6Cl_2$ (space group P4/nmm) after 72 hours of heating at 1000 °C. The small blue circles represent the observed diffracted intensity, the green line represents the Rietveld-refined calculated model, the red line represents the background, and the grey line represents the difference between observed and calculated intensities. The black tick marks show the reflections of the refined model of $Sr_4In_2O_6Cl_2$ (88.0 %), whilst the blue tick marks represent refined impurity phase $SrIn_2O_4$ (12.0 %). Duration: 13 hours. Data points: 3457. Interval: 0.02 °. GOF: 7.88. R_{wp}: 8.992 %. 326

Figure 209 UV-Vis spectrometry data for material with target composition $Sr_4In_2O_6Cl_2$ after 84 hours of heating at 750 - 1000 °C. Plot a) is the raw diffuse reflectance data, and plot b) is the associated magnified Tauc plot for this region, where the intercept between the red extrapolated tangent line and the x-axis is used to estimate an optical band gap of 4.35 eV, which corresponds to 285 nm. 327

Research Thesis: Declaration of Authorship

Print name: Liam Kemp

Title of thesis: Doped Scandium-Based Layered Oxychalcogenides

I declare that this thesis and the work presented in it are my own and has been generated by me as the result of my own original research.

I confirm that:

1. This work was done wholly or mainly while in candidature for a research degree at this University;
2. Where any part of this thesis has previously been submitted for a degree or any other qualification at this University or any other institution, this has been clearly stated;
3. Where I have consulted the published work of others, this is always clearly attributed;
4. Where I have quoted from the work of others, the source is always given. With the exception of such quotations, this thesis is entirely my own work;
5. I have acknowledged all main sources of help;
6. Where the thesis is based on work done by myself jointly with others, I have made clear exactly what was done by others and what I have contributed myself;
7. Parts of this work have been published as:

   Observation and enhancement through alkali metal doping of *p*-type conductivity in the layered oxyselenides $Sr_2ZnO_2Cu_2Se_2$ and $Ba_2Zn_{1-x}O_{2-x}Cu_2Se_2$ - *Journal of Materials Chemistry C*, 2024, **12**, 17574-17586. Z. Malik, S. Broadley, S. J. C. Herkelrath, D. W. Newbrook, L. Kemp, G. Rutt, Z. A. Gál, J. N. Blandy, J. Hadermann, D. W. Davies, R. D. Smyth, D. O. Scanlon, R. Huang, S. J. Clarke and G. Hyett.

   Transport Properties of Doped Wide Band Gap Layered Oxychalcogenide Semiconductors Sr_2GaO_3Cu*Ch*, Sr_2ScO_3Cu*Ch*, and Sr_2InO_3Cu*Ch* (*Ch* = S or Se) - *Chemistry of Materials*, 2024, **36**, 11326-11337. Z. Malik, L. Kemp, B. F. Grosso, D. W. Davies, D. O. Scanlon and G. Hyett.

   Metathesis and the building block approach to novel layered mixed anion materials - useful tool or synthetic dead-end? - Materials Horizons, 2025. L. Kemp and G. Hyett.

   Optical and electronic properties of alkali metal doped layered oxychalcogenides $Sr_3Sc_2O_5Cu_2S_2$ and $Sr_3Sc_2O_5Cu_2Se_2$ - L. Kemp, Z. Malik, G. Limburn and G. Hyett. [Publication in Progress]

Signature: ..... Date: 21 / 03 / 25

Acknowledgements

In November 2024 a personality test told me that perfectionism is my biggest professional weakness. Four and a half years, 681 samples, and the thickness of this book would all like to politely disagree. This process has been the most brilliant, fatiguing, enriching, excruciating, fulfilling, debilitating thing I have ever endured. A rare combination of something so sapping yet so gratifying, a process I wouldn't ever do again but that I will painfully miss. It would not have been possible without the help, personal or professional, of so many people, a mere handful of which are listed here.

My gratitude goes first and furthest to my PhD supervisor Geoff. To say your support and advice has been helpful over these years would be an understatement. You have never been anything less than extremely supportive, and generous with your time. From home-bound early stage experiment planning in 2020, to our ever-growing list of rainy day tangent experiments, to the weekly "*These 426s are NOT repeatable, I swear this is random*", to the painful death and rebirth of the parallel synthesis project, your patience has been a constant. There is a comfort in sitting in your office every other Monday at 10am to talk about science, that I fear I won't find elsewhere. However - you wouldn't let me call this thesis *'MALM WARS: A New Dope'* for which I am bitterly disappointed, that's some of my best work right there, but hey one disagreement in 4.5 years isn't bad right?

You arrived as a pair, you live and breathe as a pair, so it's only right to acknowledge you as a pair. George and Niamh you have been brilliant friends. Our game nights, lunch quartets, double dates and Parkruns have been the most enjoyable ways to disconnect from the academia meat grinder. It'll be a pleasure to see you married this summer. Georgey boy if I ever need a card game explained or get asked about the three royal towns of the UK in a pub quiz I'll give you a call so you can tell me for the 227th time. Niamh, I'll cherish the arsenal of nicknames, I can only apologise for how close your brilliant sense of humour is to my own.

Thank you to all members of the Hyett group past and present with whom I have had the pleasure to work alongside. Firstly, to Zahida who showed me the ropes upon my arrival and provided invaluable guidance. For the first two years of this project I was the only PhD student in the group, but I leave behind now a large, friendly, and collaborative group of people. The arrivals of PhD students Thomas, Mubasher, George and Nathan, and Postdoc Maryana, was a pleasant reprieve from the solitude of lonely COVID-era research. Thank you all. *"Your time has come Grandad",* Nathan told me as I reached the four-year mark, *"It's time to move on now".* From day one that usurper was after my job.

Acknowledgements

My thanks extend to the five undergraduate students of the six projects I've supervised during this project; Max, Nathan, Tam, Ben, and Yanjia. Thank you to our wonderful Genny, who describes her coffee as *"strong and hot, just like you"*, the flirt. Thank you to Matt for saving this thesis; the reason I didn't have to write this whole thing from start to finish in six weeks. Thank you to Mark, Andrew and Robert for feedback on the milestones of this project. Thank you to Southampton University and to the EPSRC for the opportunity to undertake this project. Thank you to Colin, Thomas, Sam and the Teaching Lab crew for over a thousand hours of conversation. Thank you to Sam and Doug at Monash for convincing me I was PhD material. Thank you to Henry and Sam for summer days on the bike and winter nights on the sim. Thank you to the Barry M. Selenide Binary Synthesis Company: *Why Buy It When You Can Hyett?* Thank you to the Saffron Box for reminding me that if I ever feel like a failure at least I'm not as bad you. Finally, thank you to everybody else on Level 2, particularly the *Mansoor's Movers* circa Autumn 2024, for the company and friendship. A special thanks to Charley: secret keeper, farm manager extraordinaire, and self-confessed "always right". You taught me a lot about what not to do around here, including advice about deadlines and timelines, which I *thoroughly* ignored but it's the thought that counts.

India, I cannot thank you enough for your help. For every late night run, for every early morning coffee, and for throwing me into an ultramarathon with three days' notice and making it almost enjoyable. We crossed paths for years and never spoke, it took a 5am email and a tub of lab-grade sand to get your attention. I will miss our evenings in the XRD room, truthfully I knew you wouldn't achieve diffraction with nanoparticles that small, I just loved hanging out with you. When you once offered me *omelette* (or, '*omlet*') as a wordle starter, I knew I didn't want your help with proofreading, but in every other conceivable way you have been wonderful. Special thanks go to the builder who failed to fireproof our lab doors, whose actions inadvertently butterfly-effected my getting to know you. I'm really grateful for your support. You're up next, and I'm here for all of it.

Finally, to Mum, Dad, Lewis, and the rest of the family. You've given me a home that I'm always welcome in and a place to escape at times when the last thing I wanted to think about was chemistry. You let me slip away to write on Christmas Day when my conscience couldn't permit a whole day off (*Section 3.4.9* if you're curious). I brought my work home with me for years, now I'll leave it there in a book with my name on it. Thank you to my boys JackJack 🐾 and TedTed 🖐 for creature comforts, you don't understand the chemistry but I've certainly complained to you about it. Thanks Nan for knowing only that I "*did science*", so telling friends and family that I invented the COVID vaccine. Close enough.

List of Abbreviations

212 ..... A MALM of type $A_2BO_2M_2Q_2$, with light layer stoichiometry 2:1:2

3-RBF ..... Three-neck Round Bottomed Flask

325 ..... A MALM of type $A_3B_2O_5M_2Q_2$, with light layer stoichiometry 3:2:5

426 ..... A MALM of type $A_4B_2O_6M_2Q_2$, with light layer stoichiometry 4:2:6

438 ..... A MALM of type $A_4B_3O_8M_2Q_2$, with light layer stoichiometry 4:3:8

5411 ..... A MALM of type $A_5B_4O_{11}M_2Q_2$, with light layer stoichiometry 5:4:11

6514 ..... A MALM of type $A_6B_5O_{14}M_2Q_2$, with light layer stoichiometry 6:5:14

ATO ..... Antimony-doped Tin Oxide

AZO ..... Aluminium-doped Zinc Oxide

CB ..... Conduction Band

CBM ..... Conduction Band Minimum

CIF ..... Crystallographic Information File

CMVB ..... Chemical Modulation of the Valence Band

DFT ..... Density Functional Theory

DUT ..... Device Under Test

EDX ..... Electron Dispersive X-ray Spectroscopy

FTO ..... Fluorine-doped Tin Oxide

GGA ..... Generalised Gradient Approximation

GOF ..... Goodness of Fit

GSAS-II ..... General Structure Analysis System II

HAM ..... Heteroanionic Material

HOMO ..... Highest Occupied Molecular Orbital

HSAB ..... Hard and Soft Acid and Base Theory

ICSD ..... International Crystal Structure Database

IPA ..... Isopropyl Alcohol

ITO ..... Indium Tin Oxide

List of Abbreviations

IUPAC..... International Union of Pure and Applied Chemistry

LED..... Light Emitting Diode

LUMO..... Lowest Unoccupied Molecular Orbital

MALM ..... Mixed Anion Layered Material

MO..... Molecular Orbital

NPD..... Neutron Powder Diffraction

PMMA..... Polymethyl Methacrylate

PXRD ..... Powder X-ray Diffraction

PTFE ..... Polytetrafluoroethylene

R-P ..... Ruddlesden-Popper

R_{wp}..... Weight Profile Residual, or 'R factor'

SEM..... Scanning Electron Microscopy

SPS ..... Spark Plasma Sintering

SSM..... Solid-State Metathesis

TC..... Transparent Conductor

TCO ..... Transparent Conducting Oxide

UV ..... Ultraviolet

UV-Vis ..... Ultraviolet-Visible

VB ..... Valence Band

VBM ..... Valence Band Maximum

XRD ..... X-ray Diffraction

Chapter 1 Introduction and Literature Review

1.1 Mixed Anion Layered Materials: Structures, Properties, and Phase Space

Mixed Anion Layered Materials (MALMs) are an emerging class of solid-state inorganic materials, whose structures contain two chemically distinct anionic sites. The interplay of anions with varying electronegativity, size, charge and coordination creates a vast phase space for materials chemists to explore. MALMs may be synthesised and tuned to fit design requirements for applications such as LEDs,[1] superconductors,[2] batteries,[3] photocatalysts,[4] and transparent displays.[5]

Within a MALM, one of the anions is almost invariably an oxide ion, referred to as the 'light' anion. In contrast, the other is denoted 'heavy' because it is larger and heavier than the oxide ion. It can therefore be any anion except O^{2-}, N^{3-} or F^{-}, such as a chalcogenide (a sulfide, selenide or telluride), a pnictide (a phosphide, arsenide, antimonide or bismuthide), or a halide. Some exceptions to this are discussed later. The 'oxy-' prefix is attached to the heavy anion to indicate the mixed anion nature, therefore a MALM may be described as an oxysulfide or oxychalcogenide, for example.

The size discrepancy results in long range ordering, which is accommodated for by the segregation of the anions into layers.[6] Site sharing between the light and heavy anions is prohibited due to their sizes, therefore each of the anions is inherently, preferentially and exclusively bound to its own site and layer, separated from the other. The layering of three example MALMs, LaCuOS,[7] $Sr_3Sc_2O_5Cu_2S_2$[8] and $Sr_2ZnO_2Cu_2S_2$,[9] is illustrated in Figure 1 below. In each example, the light anion is O^{2-} (red) and the heavy anion is S^{2-} (yellow), which are segregated by the layered structure.

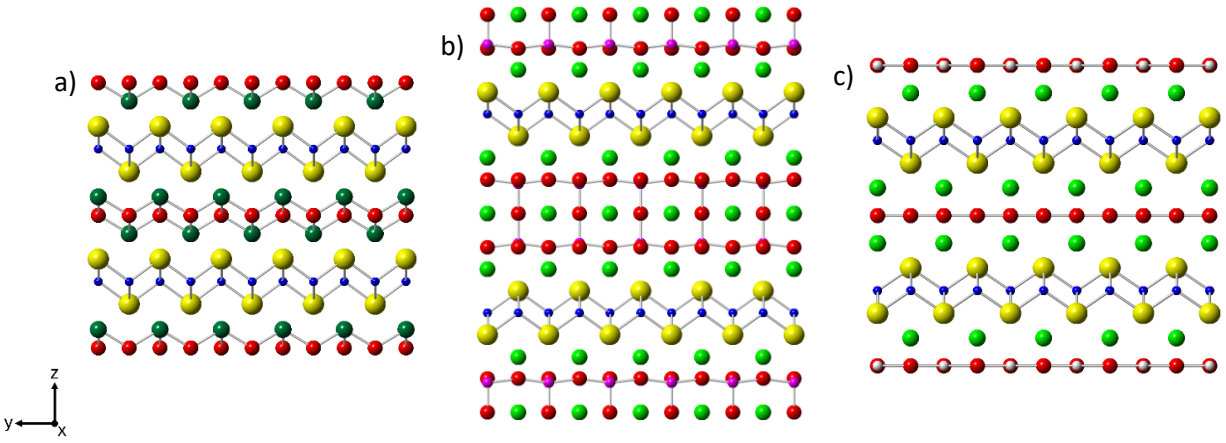

Figure 1 *Isometric projections of Mixed Anion Layered Materials, a) LaOCuS, b) $Sr_3Sc_2O_5Cu_2S_2$, and c) $Sr_2ZnO_2Cu_2S_2$. Projections are viewed along the x-axis, and are to scale with each other. For simplicity only covalent bonding is shown. These projections and others included herein were generated using CrystalMaker ® [10]*
Colour key: Teal - La, light green - Sr, pink - Sc, red - O, white - Zn, blue - Cu, and yellow - S.

The segregation may be explained using the Hard and Soft Acid and Base (HSAB) theory.[11] The O^{2-} anion is small and hard, with a strong ionic character to its bonding, whilst a heavy anion such as S^{2-} is larger, softer, and bonds with a greater covalent character. Therefore, the coordination environment of the anions will be different, to the extent that each is incompatible with the site of the other. The oxide ion resides in what is termed herein as the 'light layer', and the heavy anion in the 'heavy layer'.

The cations present are also separated by virtue of the anion segregation. Harder cations such as alkaline earth metals preferentially bond to oxygen, so reside in the light layer, often bonding heteroleptically (to more than one ion) and ionically. Softer late transition metals favour homoleptic (to one ion type) covalent interactions with the chalcogenide / pnictide anion of the heavy layer. The layers stack alternately, held together by equal and opposing charges. Inter-layer bonding is exclusively ionic, but intra-layer bonding has a greater covalent component, depending on the substituent atoms.

1.1.1 Ternary and Quaternary MALMs

The distinct layering behaviour is ubiquitous in MALMs, and occurs spontaneously. Often, the most interesting properties of these structures to researchers are a direct result of the layering. For example, MALMs exhibit high hole mobility semiconduction, for which the covalent character of the heavy layer, both through fortuitous orbital hybridisation alignment and its crystalline imperfection, is responsible, as discussed later.

Another significant benefit of layering is an expanded phase space, which contains multiple novel structure types that usually do not exist in monoanionic systems. The phase space of MALMs is vast, and is primarily composed of structures containing three, four or five atomic sites, which are termed ternary, quaternary and quinternary respectively, each with a greater phase space of explorable materials than the previous. In each, two of the sites are occupied by the light and heavy anions, and the remaining are cations.

In ternary MALMs, the light layer consists of a metal cation bonded to oxygen, separated by a layer composed solely of heavy layer ions. Figure 2 on the next page depicts the structures of La_2O_2S,[12] and BiOCl,[13] both ternary and similar in structure, adopting the *La_2O_3* [14] and *PbClF* [15] structure types respectively. The structure of La_2O_2S can be described as La_2O_3 but with sulfide occupying the octahedral oxygen sites, creating planes of sulfide ions which separate layers of $[La_2O_2]^{2+}$. In BiOCl, the -1 oxidation state of the chloride ion results in a 1 : 1 : 1 ratio of $Bi^{3+} : O^{2-} : Cl^-$, thus the heavy layer contains twice as many ions as in La_2O_2S. In each of these examples the cation is bound heteroleptically: bonding covalently to the oxide anion and ionically to the heavy layer anion.

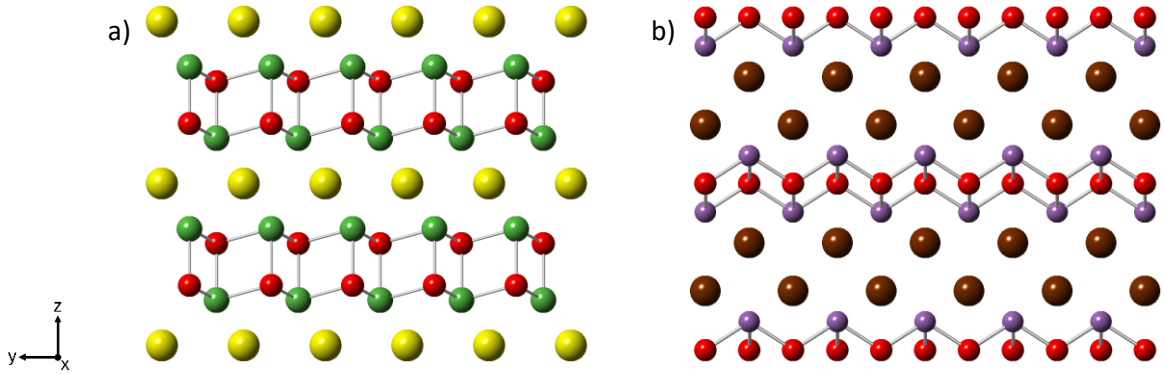

Figure 2 *Isometric projections of a) La_2O_2S, and b) BiOCl. Projections are viewed along the x-axis, and are to scale with each other. For simplicity only covalent bonding is shown. Colour key: Teal - La, red - O, yellow - S, plum - Bi, and brown - Cl.*

Whilst both of these example materials have a light layer exhibiting a tetrahedral arrangement, one may observe that the $[Bi_2O_2]^{2+}$ light layer of BiOCl closely resembles that of the $[Cu_2S_2]^{2-}$ heavy layers in the three materials of Figure 1. This is the *litharge* motif, the anti-structure of which (*anti-litharge*) will be discussed in great detail herein as the heavy layer structure central to many of the interesting properties of MALMs, and it is present in every MALM synthesised within this work. The tetrahedral network of La_2O_2S is distorted in comparison, more akin to two interlinked hexagonal $[La_2O_2]^{2+}$ layers, where La and O have triangle based pyramidal coordination environments.

Figure 3 below illustrates two examples of quaternary MALMs. The first is LaOCuSe,[7] the selenide analogue of Figure 1a. This material, which exhibits a 1 : 1 : 1 : 1 stoichiometry, crystallises in the *ZrCuSiAs*[16] structure type, which is by far the most common amongst quaternary MALMs. The $[La_2O_2]^{2+}$ light layer and $[Cu_2Se_2]^{2-}$ heavy layer form *litharge* and *anti-litharge* motifs respectively. Figure 3b is $Fe_2La_2O_3Se_2$, the holotype of the *$Fe_2La_2O_3Se_2$* structure.[17] This complex bonding in $Fe_2La_2O_3Se_2$ is more easily ascertained when re-written as $La_2O_2Fe_2OSe_2$. The light layer *litharge* $[La_2O_2]^{2+}$ motif separates layers of $[Fe_2OSe_2]^{2-}$, which is a single layer of the *perovskite* structure, another extremely common motif, explored in greater detail in the next section.

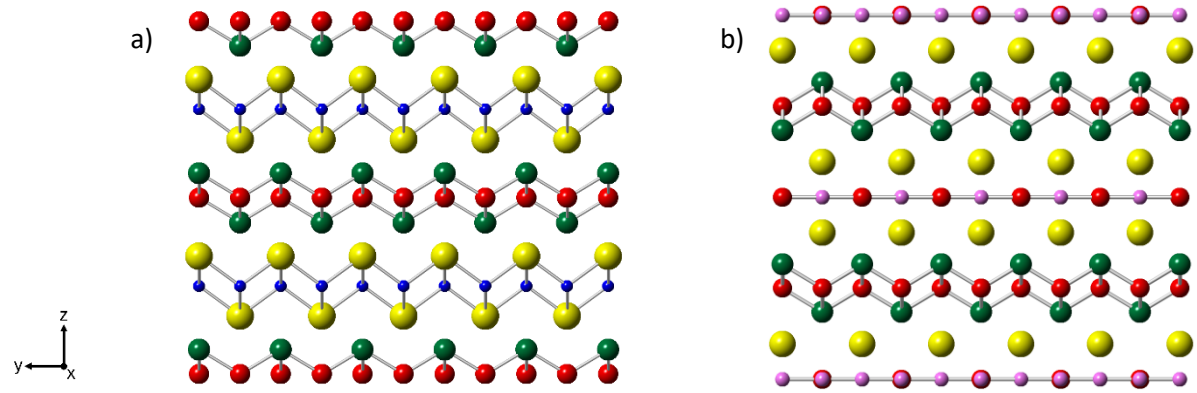

Figure 3 *Isometric projections of a) LaOCuSe, and b) $Fe_2La_2O_3Se_2$. Projections are viewed along the x-axis, and are to scale with each other. For simplicity only covalent bonding is shown. Colour key: Teal - La, red - O, blue - Cu, yellow - Se, and pink - Fe.*

In this section, some common examples of ternary and quaternary MALM structures have been discussed. While serving as an interesting introduction to the field, and establishing key concepts for future discussion, these structure types are not the focus of this work. Instead, it is quinternary MALMs, those which are composed of five elements, that are of interest. Herein all investigations, syntheses and discussions will concern quinternary MALMs, which comprise a vast phase space of largely unexplored permutations.

To illustrate the structure types of ternary and quaternary MALMs, the examples of real materials were given. It is appropriate in some instances, and useful within upcoming discussions, to describe structures using generic placeholder atoms where the site and its coordination are of more interest than whichever atom is housed within. Further to this, owing to the inherent extra complexity that a fifth ion site grants upon quinternary MALMs, certain notations are employed to emphasise structural features such as site substitution and layering. For this reason, before continuing with discussions of quinternary MALM structures, it is fitting to first establish the nomenclature used to describe them.

1.1.2 Nomenclature, Conventions, and Exceptions

The term Mixed Anion Layered Material (MALM) is often used interchangeably in literature with the term Heteroanionic Material (HAM). In practice the two may often be exchangeable, but there are differences, such as some cases later where the indistinctness and imprecision of the latter may be more appropriate. Within this work, only the term Mixed Anion Layered Material is used.

It is very rare that for a given structure type there is only one known permutation. Often, there are multiple different atoms that may occupy a given site, whilst the larger structure stays fundamentally identical. In discussions of the structure type rather than the specific atoms, it is useful to employ placeholder atoms to represent a type of ion. This is most applicable to the heavy anion. As discussed, the light anion is always oxygen, but the heavy anion may be a chalcogenide, pnictide, or halide, which may be represented as *Ch*, *Pn*, or *X* within structures, where *Q* describes the site in general regardless of occupation. For example, in the previous section both LaOCuS and LaOCuSe were discussed; collectively their structure may be expressed LaOCu*Ch*.

Other placeholder atoms used within this work include *A*, a large, hard cation such as an alkaline earth or alkali metal which bonds heteroleptically and primarily ionically in the light layer. *B* also represents a light layer cation, +1 to +4 oxidation state depending on the structure, which is small, hard, and bonds covalently with O^{2-}. Finally, *M* is a soft late transition metal which bonds homoleptically and covalently with *Q* in the heavy layer. Placeholder atoms are always italicised to avoid confusion, for example between placeholder *B* and a boron atom B. The structure of $Sr_3Sc_2O_5Cu_2S_2$ from the previous section may be described $A_3B_2O_5M_2Q_2$, which is by far the most discussed structure within this work.

In accordance with IUPAC nomenclature convention,[18] the constituent elements of inorganic materials such as MALMs should be listed in order of increasing electronegativity,[19] such as TiO_2, $MgCO_3$, and NaCl. While conventionally correct and suitable for most inorganic materials, this method is less intuitive in ascertaining the layering of a MALM. As a result, quinternary materials in this work will be described in the style $A_aB_bO_cM_2Q_2$ where $A_aB_bO_c$ is the light layer in increasing electronegativity and M_2Q_2 is the heavy layer in increasing electronegativity. This conscious deviation of convention allows facile realisation of the structure, by always grouping the light layer components followed by the heavy layer components. The structure of the previously described materials LaOCuS and $Sr_3Sc_2O_5Cu_2S_2$ can be deduced quickly, compared to the conventional electronegativity ordering of LaCuSO and $Sr_3Sc_2Cu_2S_2O_5$.

The light and heavy layers of a MALM, each with a non-zero charge (usually ±2 for quinternary), will be denoted in square brackets with charges when discussed in isolation, such as $[LaO]^+$ and $[CuS]^-$ for LaOCuS, and $[Sr_3Sc_2O_5]^{2+}$ $[Cu_2S_2]^{2-}$ for $Sr_3Sc_2O_5Cu_2S_2$. This further aids in illustrating the layered nature.

By definition, materials containing polyanions such as SO_4^{2-}, PO_4^{3-}, and CO_3^{2-} are not considered MALMs even in the cases where they contain two anions, as the oxygen ions of these units coordinate homoleptically only to the cation, such that the whole unit can be considered one large point group anion. The 'mixed anions' of MALMS refer exclusively to monoanions such as O^{2-} or Se^{2-}.

It is common for MALMs to be synthesised with mixed occupancy on certain atomic sites, such as when a non-integer *B* site oxidation state is required, or when doping to improve properties such as electrical conductivity. Where mixed occupancy occurs, brackets will be placed around the atoms sharing a given atomic site for clarity, for example: $Ba_3(ScIn)O_5Cu_2S_2$,[20] $(Ca_2Sr)Fe_2O_5Cu_2S_2$,[21] or the $(Sr_{3-x}K_x)Sc_2O_5Cu_2S_2$ doping series explored in *Chapter 3.*

As discussed, quinternary MALMs are those containing five atoms. This does not specifically equate to five distinct atomic sites. For instance, many of the quinternary materials studied herein contain two strontium and two oxygen sites for a total of seven distinct sites, but the total element count remains five thus the materials are classed as quinternary. There are various examples where a structure which is otherwise most commonly quinternary contains one element in two distinct sites, for example $Ba_2CuO_2Cu_2S_2$[22] or $Sr_2MnO_2Mn_2As_2$.[23] In the latter, the two Mn sites are distinct, the light layer *B* site houses a +2 cation whilst the heavy layer *M* site houses a +1 cation, and it may therefore be better described as $Sr_2Mn^{II}O_2Mn^{I}_2As_2$. Whilst these are structure types commonly adopted by quinternary materials, by definition these two specific examples are quaternary MALMs. This further exemplifies the importance of the above convention deviations, as '$Sr_2Mn_3As_2O_2$' is less useful for implying structural detail or the manganese site differentiation than '$Sr_2MnO_2Mn_2As_2$'.

When a structure is discussed, the holotype structure for which its structure type was named is often referenced. The holotype structures are always italicised, such as *PbClF* for the ternary MALM BiOCl, or *ZrCuSiAs* for quaternary MALM LaOCu*Ch*. Also italicised are structure motifs such as *litharge*, *rock salt* and *perovskite*. These motifs are common across many MALMs and help to describe in words an otherwise complex structure.

Finally, there are some exceptions to the 'light anion' rules established in the opening section. For the purposes of all materials synthesised in this work, and the vast majority within literature, it is sufficient to assume the light anion is always oxygen and that the heavy anion is any other than oxide, nitride or fluoride. There are however exceptions, such as a very small number of materials where the light anion is fluorine or nitrogen, such BaFZnAs (Figure 4a)[24] and ThFeAsN.[25] These exceptions are almost all examples of the quaternary 1 : 1 : 1 : 1 *ZrCuSiAs* structure.

There is also a sizeable and as yet undiscussed family of mixed anion materials where the two anions are oxide and either nitride or fluoride, materials, called oxynitrides and oxyfluorides, are in contravention of many of the nomenclature rules outlined here. For example, the 'light' and 'heavy' prefixes do not apply given that N^{3-} is lighter than O^{2-}, and F^- is negligibly heavier. The size similarity also allows for site mixing; therefore, these materials exhibit only short-range ordering and the two sites are not distinct. The lack of site segregation can sometimes negate the formation of layers, such as in $Sm_2Ta_2O_5N_2$[26] in Figure 4b, which exhibits the *$LaZrO_2N$*[27] structure type and a *pyrochlore* network of partially segregated (but not layered) N^{3-} (blue) and O^{2-} (red) ions. In cases such as this, even the term 'Mixed Anion Layered Materials' would be misleading and the more ambiguous term 'Heteroanionic Material' (HAM) would be more appropriate. An example of a layered oxynitride is Sr_2TaO_3N,[28] based on the $n = 1$ *Ruddlesden-Popper* structure described in the next section, with structure type *K_2NiF_4*.[29]

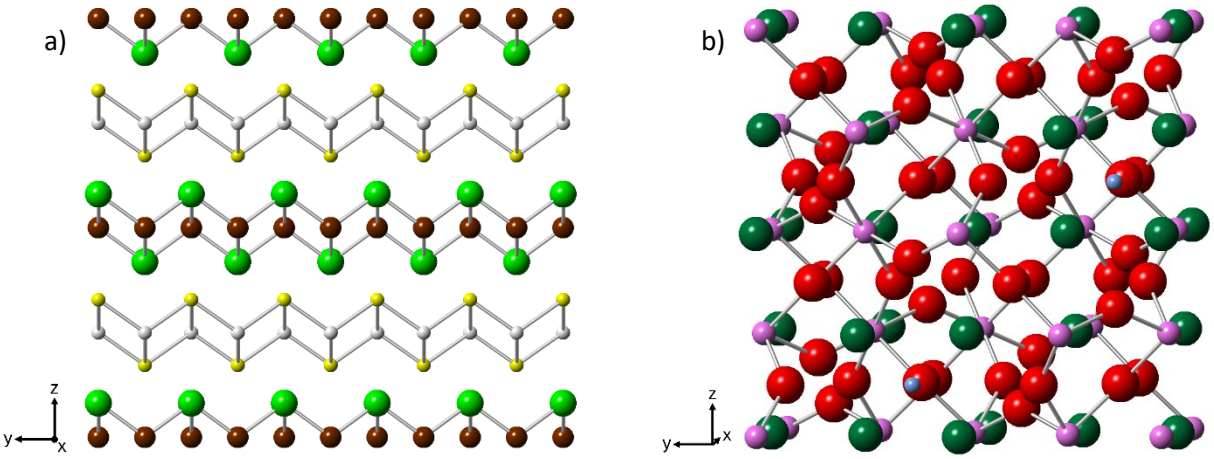

Figure 4 *Isometric projections of a) BaFZnAs, and b) $Sm_2Ta_2O_5N_2$. Projections are viewed primarily along the x-axis, and are not to scale with each other. For simplicity only covalent bonding is shown.*
Colour key: Green - Ba, brown - F, white - Zn, yellow - As, teal - Sm, pink - Ta, red - oxygen, cyan - N

1.1.3 Quinternary MALMs

With at least five distinct ion sites and a wide range of elements that may occupy a given site, the phase space of quinternary MALMs is a vast and largely unexplored landscape for solid-state materials scientists to explore new permutations, expand structural families and discover novel materials in pursuit of technologies such as a *p*-type conductors and photocatalysts.

With the aforementioned exceptions aside, herein all MALMs will contain the oxide ion in the light layer, and a chalcogenide, pnictide or halide in the heavy layer, and the term 'MALM' unless stated otherwise refers exclusively to quinternary MALMs. The light layer usually consists of an alkaline earth metal on the *A* site, a transition or post-transition metal on the *B* site, and the oxide ion. Bonding is covalent between *B* and O, whilst *A* is largely ionic and often straddles the layers. Within the heavy layer, a late transition metal *M* bonds covalently with heavy anion *Q*. The five sites can be described by the general formula $A_aB_bO_cM_2Q_2$, where $[A_aB_bO_c]^{2+}$ and $[M_2Q_2]^{2-}$ are the light and heavy layers. All quinternary MALMs share the *anti-litharge* $[M_2Q_2]^{2-}$ heavy layer motif discussed previously in LaOCu*Ch*. No evidence of polytypism is observed or reported across the various permutations of MALMs.

A comprehensive literature review of the main quinternary MALM structures was carried out to accompany this structural review. To the best of the author's knowledge this collection is the culmination and assimilation of every reported instance of these MALM structures to date. Three structures stand out as by far the most abundant in the material phase space, and as such have received the greatest research attention. These are $A_2BO_2M_2Q_2$, $A_3B_2O_5M_2Q_2$, and $A_4B_2O_6M_2Q_2$, denoted the '212', the '325' and the '426' structures respectively, referring to the stoichiometry of the three atom sites in the light layer, for example $[A_3B_2O_5]^{2+}$ in the case of the 325. Figure 5 illustrates the permutations of atoms that may occupy these generic MALM sites. The colours used in this figure align with those used in the depictions of all generic MALM structures herein.

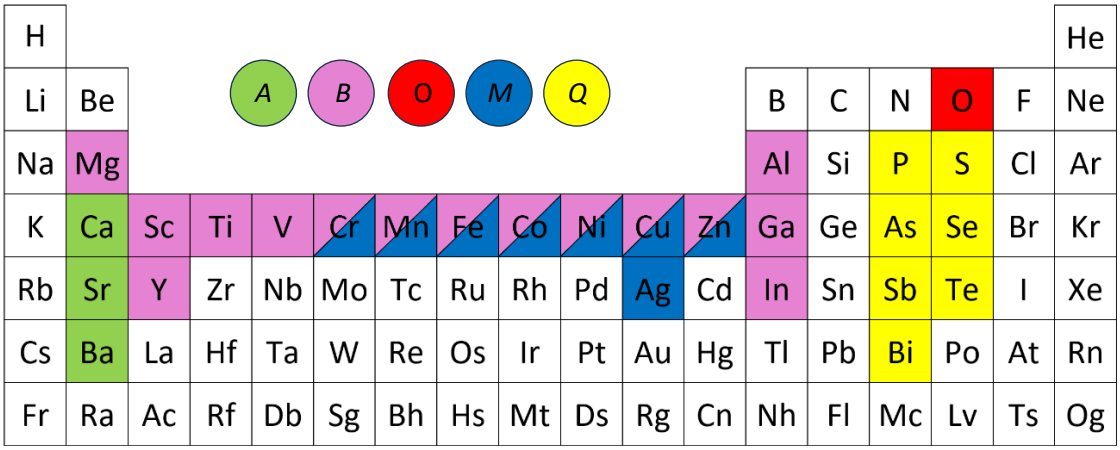

Figure 5 *Permutations of the five distinct atomic sites of a quinternary MALM projected onto the periodic table. Elements highlighted in green, pink, red, blue and yellow are elements with at least one recorded example occupying respectively the A, B, O, M or Q sites of a MALM. Diagonally split cells indicate elements which may occupy more than one site, not necessarily in the same MALM. Unhighlighted elements have not been reported in MALMs.*

1.1.3.1 The Ruddlesden-Popper Oxides

The oxide light layers of the $A_2BO_2M_2Q_2$ and $A_3B_2O_5M_2Q_2$ (212 and 325) MALMs adopt structures derived from the $A_{n+1}B_nO_{3n+1}$ *Ruddlesden-Popper* (*R-P*) configuration,[30, 31] where *A*, *B*, and O have oxidation states of +2, +4, and -2 respectively. The *R-P* structures consist of a *perovskite* slab (whose size is determined by *n*) sandwiched between *rock salt* layers. Figure 6 depicts the unit cells of Sr_2RuO_4 (*n* = 1) and $Sr_3Ru_2O_7$ (*n* = 2), alongside the *n* = ∞ configuration which is the pure *perovskite*, in this case $SrRuO_3$.[32]

The 212 and 325 MALMs adopt variants this structure (*n* = 1 and 2 respectively) with heavy layers interwoven between the *R-P* motifs at the expense of two oxide ions. This yields the general formula $[A_{n+1}B_nO_{3n-1}][M_2Q_2]$. Examples of MALMs derived from the *R-P* structure include $Sr_2NiO_2Ag_2Se_2$ (*n* = 1)[33] and $Ba_3Y_2O_5Ag_2Se_2$ (*n* = 2).[34] The light layer thickness therefore increases with *n*, extending the unit cell in the *c* direction.

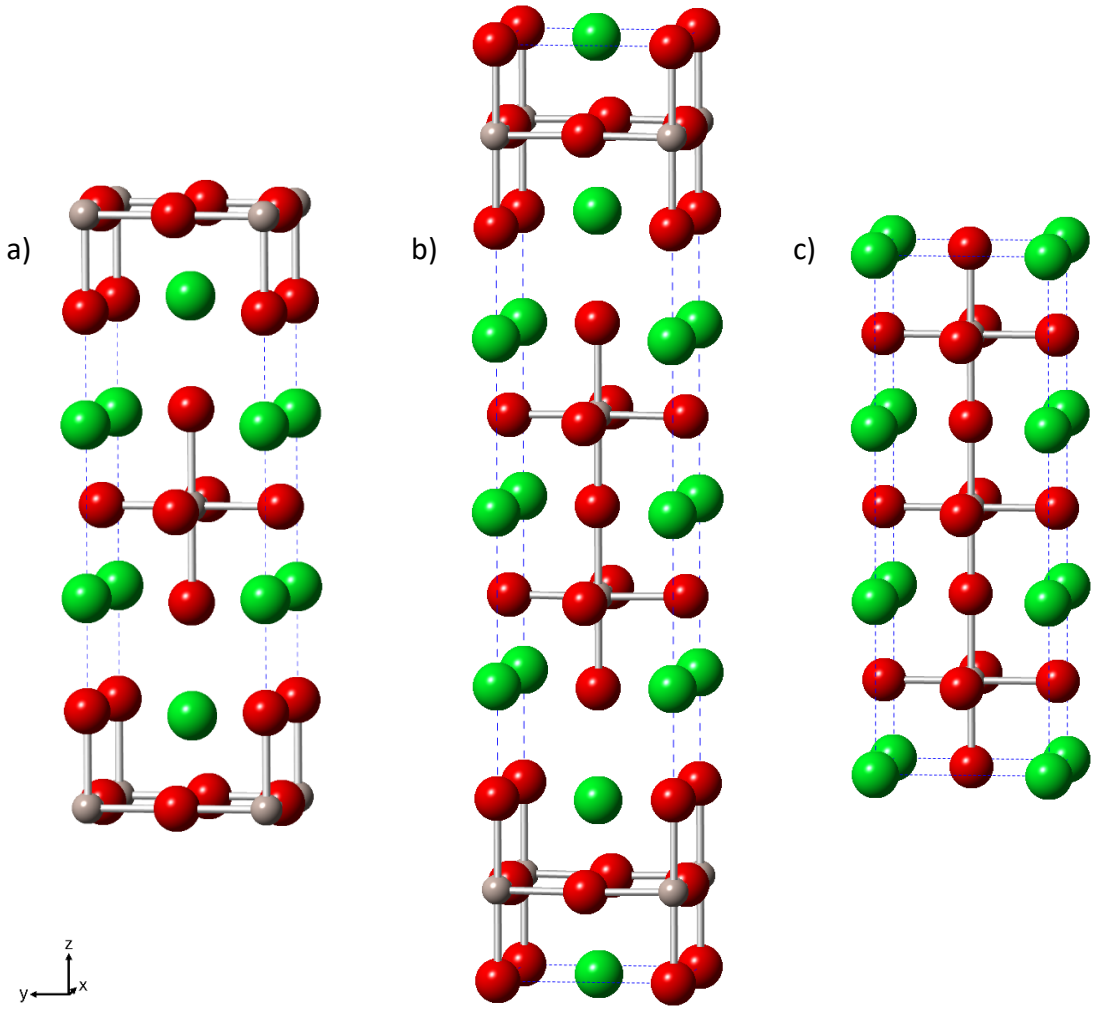

Figure 6 *Isometric projections of the crystal structures of two $A_{n+1}M_nO_{3n+1}$ Ruddlesden-Popper oxides a) Sr_2RuO_4 where n = 1, b) $Sr_3Ru_2O_7$ where n = 2, and c) the pure perovskite structure $SrRuO_3$ where n = ∞. All structures viewed primarily along the x-axis. The blue dashed lines denote the unit cell.*
Colour key: green - Sr, grey - Ru, and red - O.

1.1.3.2 $A_2BO_2M_2Q_2$; the 212 structure

The first and lowest order member of the *Ruddlesden-Popper* $A_{n+1}B_nO_{3n-1}M_2Q_2$ family is $A_2BO_2M_2Q_2$, where $n = 1$. This structure is referred to as the '212' structure owing to the stoichiometry of the atoms in the *perovskite* layer: $[A_2B_1O_2]^{2+}$. With at least 36 published reported materials possessing the 212 structure type, this is the most commonly occurring MALM structure in literature. These materials crystallise in the *I*4/*mmm* space group (#139), and exhibit the $Sr_2Mn_3Sb_2O_2$ structure type,[35] where in this exemplar material Mn occupies both the B^{2+} and M^{+} sites. The light layers of *perovskite* $[A_2B_1O_2]^{2+}$ are separated by heavy layers of *anti-litharge* $[M_2Q_2]^{2}$, which in the 212 configuration is usually a copper chalcogenide such as $[Cu_2S_2]^{2-}$ or a silver chalcogenide such as $[Ag_2Se_2]^{2-}$. In all reported $A_2BO_2M_2Q_2$ materials, *A* is barium or strontium, a large alkaline earth 2+ oxidation state cation. This is the only of the three common MALM structures where no calcium analogues are reported, as the structure favours a large *A* site cation paired with a small (usually first row) transition metal in the 2+ oxidation state, such as Co^{2+}, Ni^{2+} or Mn^{2+}.

Figure 7a shows the unit cell of $A_2BO_2M_2Q_2$, where it can be observed that each occurrence of a light or heavy layer is staggered from the previous by half a unit cell length, thus the symmetry of each layer repeats every two occurrences. For this reason, the unit cell requires two formula units of $A_2BO_2M_2Q_2$ in order to describe the smallest repeating unit.

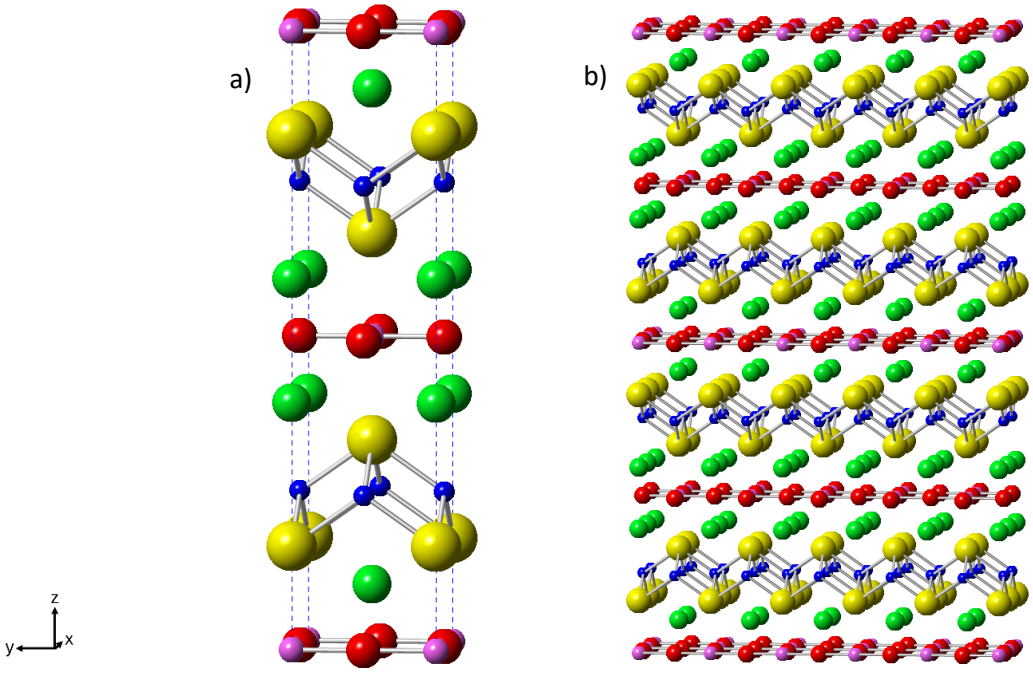

Figure 7 *Isometric projections of a generic depiction of the structure of the $A_2BO_2M_2Q_2$ ('212') MALM, showing a) one unit cell, and b) a 2 × 5 × 2 expanded unit cell. Both projections are viewed primarily along the x-axis, and are not to scale with each other. The interactions of A^{2+} to O^{2-} / Q^{2-} are largely ionic, and so for clarity these bonds are not shown. The blue dashed lines denote the unit cell.*
Colour key: green - A, pink - B, red - O, blue - M, and yellow - Q.

The *A* cation in $A_2BO_2M_2Q_2$ resides in the light layer but bridges the two, exhibiting a largely ionic 8-coordinate anti-prism interaction with the oxygen ions of the light layer and the chalcogen ions of the heavy layer, see Figure 8a. The *B* cation resides at the centre and corners of the unit cell, situated between four oxygen ions in a symmetrical square planar coordination, Figure 8b. The light layer may be considered as layers of BO_2 separated from the $[M_2Q_2]^{2-}$ layers by the alkaline earth cation.[6]

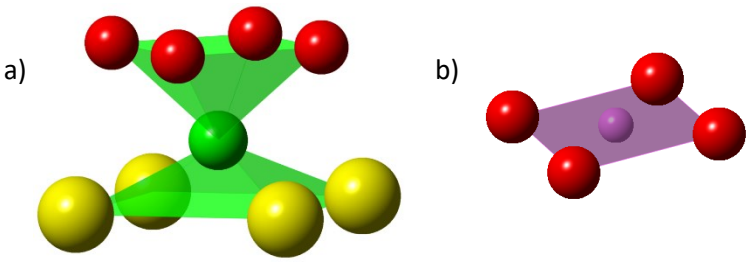

Figure 8 *Polyhedra showing the coordination environments of a 212 MALM: a) the inter-layer A atom site with 4-coordinate anti-prism interactions with oxygen ions, and b) the B atom site with 4-coordinate square-planar interactions with oxygen ions. Projections are to scale with each other.*
Colour key: green - A, pink - B, red - O, and yellow - Q.

The first $A_2BO_2M_2Q_2$ material discovered was the aforementioned $Sr_2MnO_2Mn_2Sb_2$ in 1979,[35] the holotype material for the 212 structure type, $Sr_2Mn_3Sb_2O_2$. It was published as part of a series with formula $A_2MnO_2Mn_2Q_2$ where *A* = Ba or Sr and *Q* = As or Sb. Not only were these the first reported 212 MALMs, this was the first discovered quinternary MALM structure of any kind.* It was 15 years before another material was published, $Sr_2ZnO_2Zn_2As_2$ in 1994,[36] around the time that attention for the 212 materials and MALMs in general began to increase.

The most commonly investigated property in publications of 212 materials is magnetism, beginning with Zhu in 1997 who reported the magnetic properties and structures of $Sr_2BO_2Cu_2S_2$ (*B* = Mn, Zn) and $A_2CoO_2Cu_2S_2$ (*A* = Ba, Sr).[9, 37] Magnetism is not explored within this current work due to the exclusive use of closed-shell ions (which eliminates *d-d* transitions and improves transparency), but of greater relevance is that Zhu's publications were also the first to cite the electrical conductivity values of these materials. $Sr_2MO_2Cu_2S_2$ is denoted only 'low conductivity',[9] whilst $Sr_2CoO_2Cu_2S_2$ measures an impressive 0.25 S cm^{-1}.[37]

Other properties and applications investigated in 212 material research are superconductivity, such as in $Sr_2BO_2Cu_2S_2$ (*B* = Cu, Ni),[8] thermoelectric behaviour such as in $Sr_2BO_2Cu_2Se_2$ (*B* = Co, Ni, Zn),[38] and transparent conductivity such as in $A_2ZnO_2Cu_2Se_2$ (*A* = Ba, Sr),[39] a publication to which research from this project, though not discussed within this work, contributed.

* This specific material is quaternary by definition due to the atom count of four, despite five unique atom sites. The light layer *B* manganese is in the +2 oxidation state and the heavy layer *M* manganese is +1, but this does not promote the MALM to quinternary. When these two sites of the $Sr_2Mn_3Sb_2O_2$ structure contain different atoms, the material is quinternary.

1.1.3.3 $A_3B_2O_5M_2Q_2$; the 325 structure

The $n = 2$ member of the quinternary $A_{n+1}B_nO_{3n-1}M_2Q_2$ family is $A_3B_2O_5M_2Q_2$, herein described as the '325' structure, denoted as such according to the stoichiometry of the light layer unit, $[A_3B_2O_5]^{2+}$. It is closely related to the previously described 212 configuration, exhibiting the same oxide layer fragment, now lengthened by one *perovskite* unit, see Figure 9. It may be described structurally as the 212 configuration with an additional 'slice' of *perovskite* (an $[ABO_3]$ unit), within the light layer. This larger oxide layer means that the *c* unit cell parameter is increased, whilst *a* is retained. Examples of further additions to this *perovskite* unit, configurations of $A_{n+1}B_nO_{3n-1}M_2Q_2$ where $n > 2$, are later described in *Section 1.1.3.5 - Other Quinternary Oxychalcogenide Structures*.

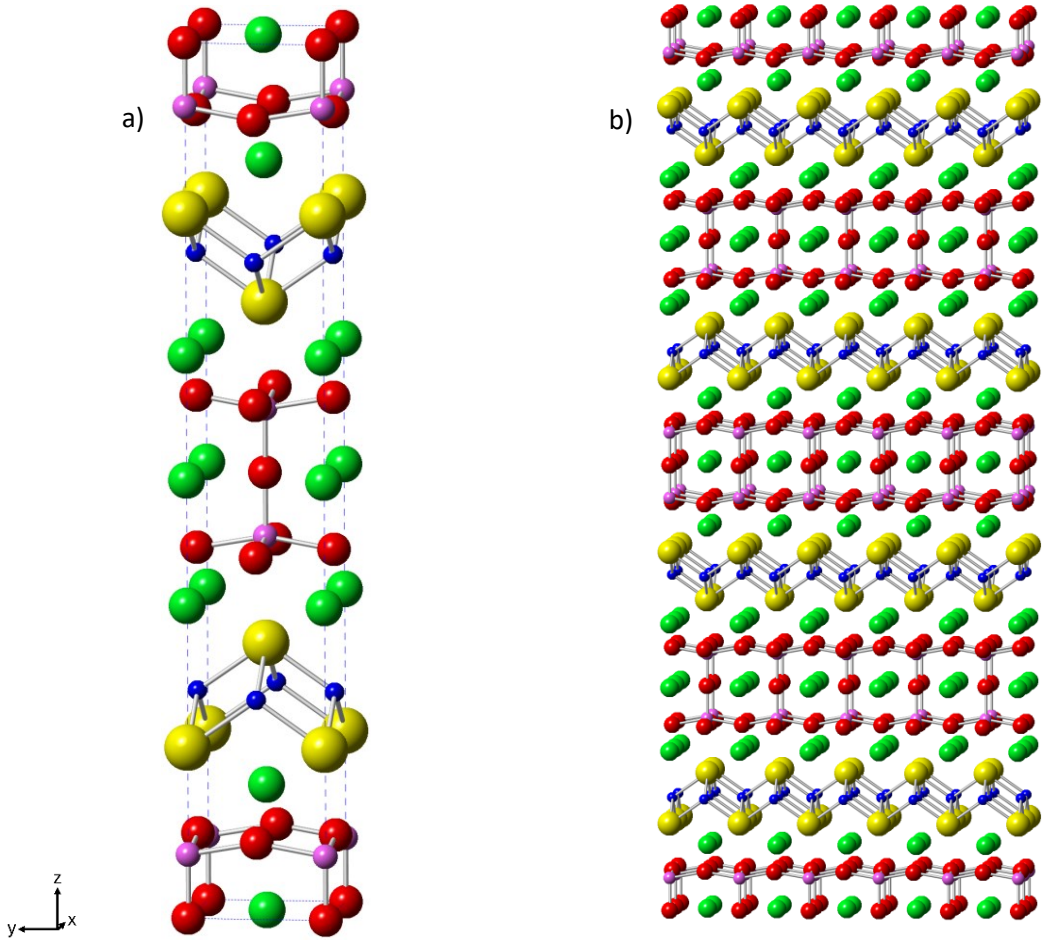

Figure 9 *Isometric projections of a generic depiction of the structure of the $A_3B_2O_5M_2Q_2$ ('325') MALM, showing a) one unit cell, and b) a 2 × 5 × 2 expanded unit cell. Both projections are viewed primarily along the x-axis, and are not to scale with each other. The interactions of A^{2+} to O^{2-} / Q^{2-} are largely ionic, and so for clarity these bonds are not shown. The blue dashed lines denote the unit cell.*
Colour key: green - A, pink - B, red - O, blue - M, and yellow - Q.

The 325 MALM configuration crystallises in the tetragonal *I*4/*mmm* space group (#139) and is represented by the *SmNi₃Ge₃* structure holotype.[40] It is not easy to elucidate a structure from the formula of *SmNi₃Ge₃*, but when illustrated by an example material such as $Sr_3Sc_2O_5Cu_2S_2$, (where the unit cell contains two formula units) the layering once again becomes apparent. The *anti-litharge* $[M_2Q_2]^{2-}$ conductive heavy layer motif is present here, usually a copper chalcogenide such as $[Cu_2S_2]^{2-}$ or an iron pnictide such as $[Fe_2As_2]^{2-}$. Alongside the square-anti-prismatic inter layer bridging *A* cation site described in the 212 configuration, this structure contains a second distinct site for the *A* cation (which is usually Ba^{2+} or Sr^{2+} in these structures) in a large central 12-coordinate environment to oxygen ions within the *perovskite* layer, see Figure 10. All 12 bonds are of equal length, resulting in a cuboctahedral bonding environment. The *B* ion site houses a 3+ oxidation state metal cation, often Sc^{3+} or Fe^{3+}, which exists in a square-based pyramidal coordination to oxygen. Adopted by at least 26 published MALMs, this is a very common MALM structure type.

MALMs with the 325 configuration are by far the most explored within this work. They comprise the entirety of *Chapter 3* which investigates their conductive enhancement through *p*-type doping. They also appear in *Chapter 4* as a competing phase to the targeted 426 materials, in *Chapter 5* as the most promising candidates for metathesis syntheses, and in *Chapter 6* as the structure of a novel MALM.

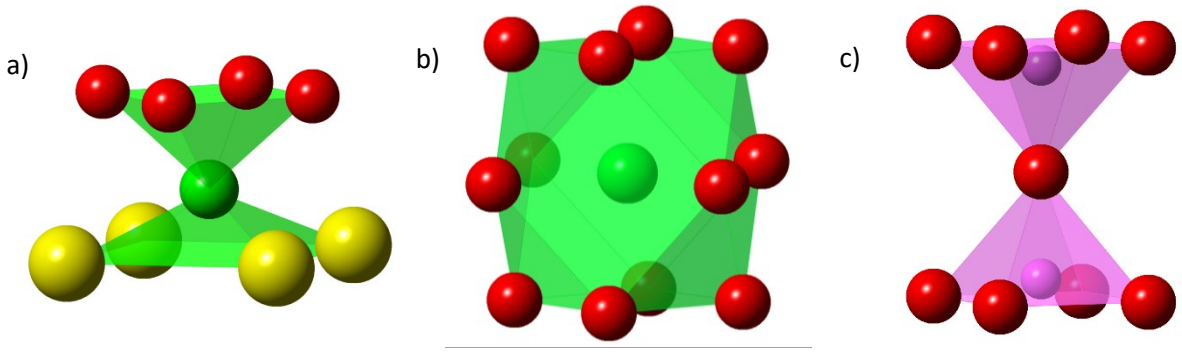

Figure 10 *Polyhedra showing the coordination environments of a 325 MALM: a) the inter-layer A atom site with 8-coordinate anti-prism interactions with oxygen and chalcogen ions, b) the intra-layer A atom site with 12-coordinate cuboctahedral interactions with oxygen ions, and c) the B atom site with 5-coordinate square-based pyramidal interactions with oxygen ions. Projections are to scale with each other*
Colour key: green - A, pink - B, red - O, and yellow - Q.

Interest in Mixed Anion Layered Materials sporting the 325 structure undoubtedly originated with the discovery of the benchmark material $Sr_3Sc_2O_5Cu_2S_2$, however it was not the first of its kind. Zhu and Hor reported the first 325 MALM, $Sr_3Fe_2O_5Cu_2S_2$, in 1997 as a follow-up to an investigation into the 212 class of MALMs.[41] It was two years after this in 1999 that $Sr_3Sc_2O_5Cu_2S_2$ was discovered and published of by Otzschi et al as a candidate superconductor.[8] Despite the potential for the expansion of the MALM phase space catalysed by the discovery of the $A_3B_2O_5M_2Q_2$ structure type, progress of research in the field slowed, and it was a further 8 years until materials of this type reappeared in literature.

In 2007, Liu et al published a detailed study of $Sr_3Sc_2O_5Cu_2S_2$,[42] this time focusing not on its prospective superconducting properties but instead on those of *p*-type conductivity and transparency, with the specific focus of transparent electronics. This new attraction towards $Sr_3Sc_2O_5Cu_2S_2$ is attributed to the geometry of its copper-sulfide layer, which exhibits the same highly-conductive $[Cu_2S_2]^{2-}$ 'heavy layer' motif as other promising *p*-type semiconductors such as $BaCu_2S_2$[43] and LaOCuS,[44] both of which demonstrate impressive conductivities and the latter boasting a wide band gap of 3.1 eV suitable for applications requiring transparency. $Sr_3Sc_2O_5Cu_2S_2$ was prepared undoped, and Hall measurements confirmed its *p*-type conductivity (reported here as 2.8 S cm^{-1}, on par with Sr-doped analogues of the aforementioned LaOCuS[45]) with a room-temperature hole mobility of 150 $cm^2\ V^{-1}\ s^{-1}$, the greatest of any *p*-type material at the time of its publishing. For an undoped material, these values are very high, to which one could hypothesise an even greater improvement upon the inclusion of dopants. The authors acknowledge that the conductivity value is higher than would be expected since the carrier concentration in undoped $Sr_3Sc_2O_5Cu_2S_2$ is relatively low (1×10^{-17} cm^{-3}), and hypothesise that strontium and/or copper vacancies within the structure may give rise to holes, thereby unintentionally doping the otherwise pristine material similar to the effect that an alkali metal dopant such as K^+ or Na^+ might have if partially incorporated into those atomic sites. Both of these possibilities: alkali metal doping and atom site vacancies, are explored within this work in *Chapter 3*.

In 2009, with still surprisingly little research interest in non-$Sr_3Sc_2O_5Cu_2S_2$ 325 MALMs, Scanlon et al published a computational study on the geometry and electronic properties of $Sr_3Sc_2O_5Cu_2S_2$ to further explore its interesting *p*-type behaviour.[46] Here, Density Functional Theory (DFT) was employed to support the values of conductivity and hole mobility reported previously, and to confirm a direct optical band gap of 3.1 eV, shown in Figure 11 on the next page.

Crucially, this publication presents recommendations for doping this MALM to enhance both its electrical conductivity by increasing charge carriers, and/or its optical transparency by isovalently engineering the unit cell parameters to manipulate the Cu-Cu distances. Until this current work, to the best of the author's knowledge, these recommendations have not been explored in the literature.

Around the same time, interest in the superconductive properties of these materials was renewed by the discovery of iron-arsenide heavy layers in 325 MALMs, following success with this motif in other materials such as $(Ba_{1-x}K_x)Fe_2As_2$[47] and $Li_2Fe_2As_2$.[48] $Sr_3Sc_2O_5Fe_2As_2$ was successfully synthesised as an iron-arsenide analogue to the cuprate $Sr_3Sc_2O_5Cu_2S_2$ system in the pursuit of room-temperature superconductivity,[49, 50] and spawned a new avenue of superconductivity-based 325 discovery with materials such as $Ca_3Al_2O_{5-y}Fe_2Pn_2$ (*Pn* = As, P)[51] and $Ba_3Sc_2O_5Ni_2As_2$.[52]

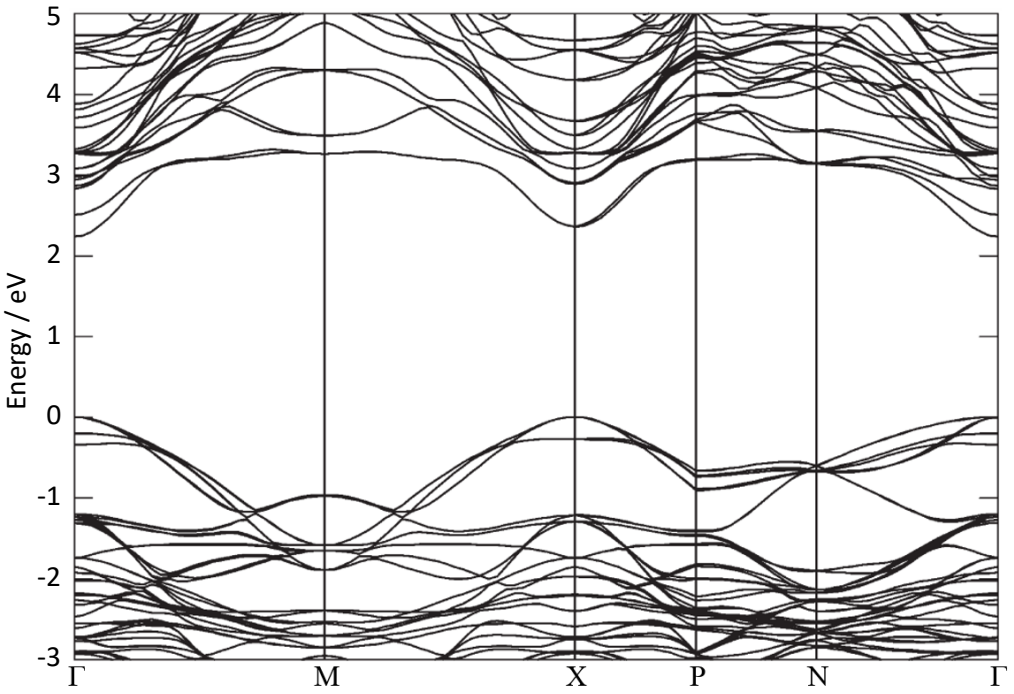

Figure 11 The GGA+U calculated band structure of $Sr_3Sc_2O_5Cu_2S_2$. The top of the valence band is set to 0 eV. Figure adapted from Scanlon 2009, showing a direct band gap of 2.12 eV, an underestimate of the experimentally measured band gap of 3.1 eV.[46 †]

Bar one brief study into its luminescence properties in 2012,[57] it was another decade of dormancy before $Sr_3Sc_2O_5Cu_2S_2$ once again received significant research attention. In 2019, Iwasa et al explored its optical properties in more detail, in comparison to selenide analogue $Sr_3Sc_2O_5Cu_2Se_2$ and novel silver selenide $Sr_3Sc_2O_5Ag_2Se_2$.[58] The next year, a series of solid-solutions between $Sr_3Sc_2O_5Cu_2S_2$ and novel wide band gap MALM $Ba_3Sc_2O_5Cu_2S_2$ was produced,[59] revealing a relationship between the two which obeyed Vegard's Law[60] and allows tuning of the optical band gap between 3.10 and 3.24 eV.

Other notable research within the field of 325 MALMs includes the synthesis of $Sr_3Fe_2O_5Cu_2Se_2$, $Sr_3Fe_2O_5Ag_2Se_2$, and $Sr_3Fe_2O_5Ag_2S_2$ via solid-state metathesis by Cario in 2005 (repeated and investigated in *Chapter 5*),[61] the computational prediction of eight novel stable 325 phases by Williamson in 2020,[62] and the compositional tuning of optical band gap by Limburn et al with the solid-solutions $Ba_3(In_{2-x}Sc_x)O_5Cu_2S_2$ and $Ba_3In_2O_5Cu_2(S_{2-y}Se_y)$, which used the electrochemical degradation of dyes to quantify the photocatalytic behaviour enhanced by a widened band gap.[20]

† DFT (Density Functional Theory) is a quantum mechanical method used to analyse the electronic structure of many-body systems like crystal lattices. It probes the overall distribution (or *density*) of electrons, rather than for each individual electron, which is more difficult.[53, 54] GGA+*U* (Generalised Gradient Approximation, with Hubbard correction *U*) is a form of DFT which measures density changes across space, where the *U* correction accounts for dense electron activity around atoms.[55] GGA+*U* is popular for its computational efficiency, but it regularly underestimates the band gap due to imperfection of the Hubbard correction method.[56] Nonetheless it provides reliable relative comparisons between structures and, in this case, confirms that the band gap of $Sr_3Sc_2O_5Cu_2S_2$ is direct.

1.1.3.4 $A_4B_2O_6M_2Q_2$; the 426 structure

At first glance the $A_4B_2O_6M_2Q_2$ structure may appear to be the n = 3 member of the $A_{n+1}B_nO_{3n-1}M_2Q_2$ family, however this is not the case, the n = 3 member is $A_4B_3O_8M_2Q_2$ discussed in the next section. $A_4B_2O_6M_2Q_2$ is actually unrelated to the $A_{n+1}B_nO_{3n-1}M_2Q_2$ series as it is not derived from the Ruddlesden-Popper structure. Instead, it is a unique structure type, more complex than those previously. This composition is herein described as the '426' structure, denoted as such according to the stoichiometry of the light layer unit, $[A_4B_2O_6]^{2+}$. Despite no relation to the previously described series, the 426 structure (Figure 12) appears very similar, possesses similar properties, and is synthesised by largely the same procedure. The 426 MALM structure appears in at least 34 published examples in literature. Whilst there are more unique examples of 212 materials, the 426 is by far the most studied due to its superconducting properties (vide infra).

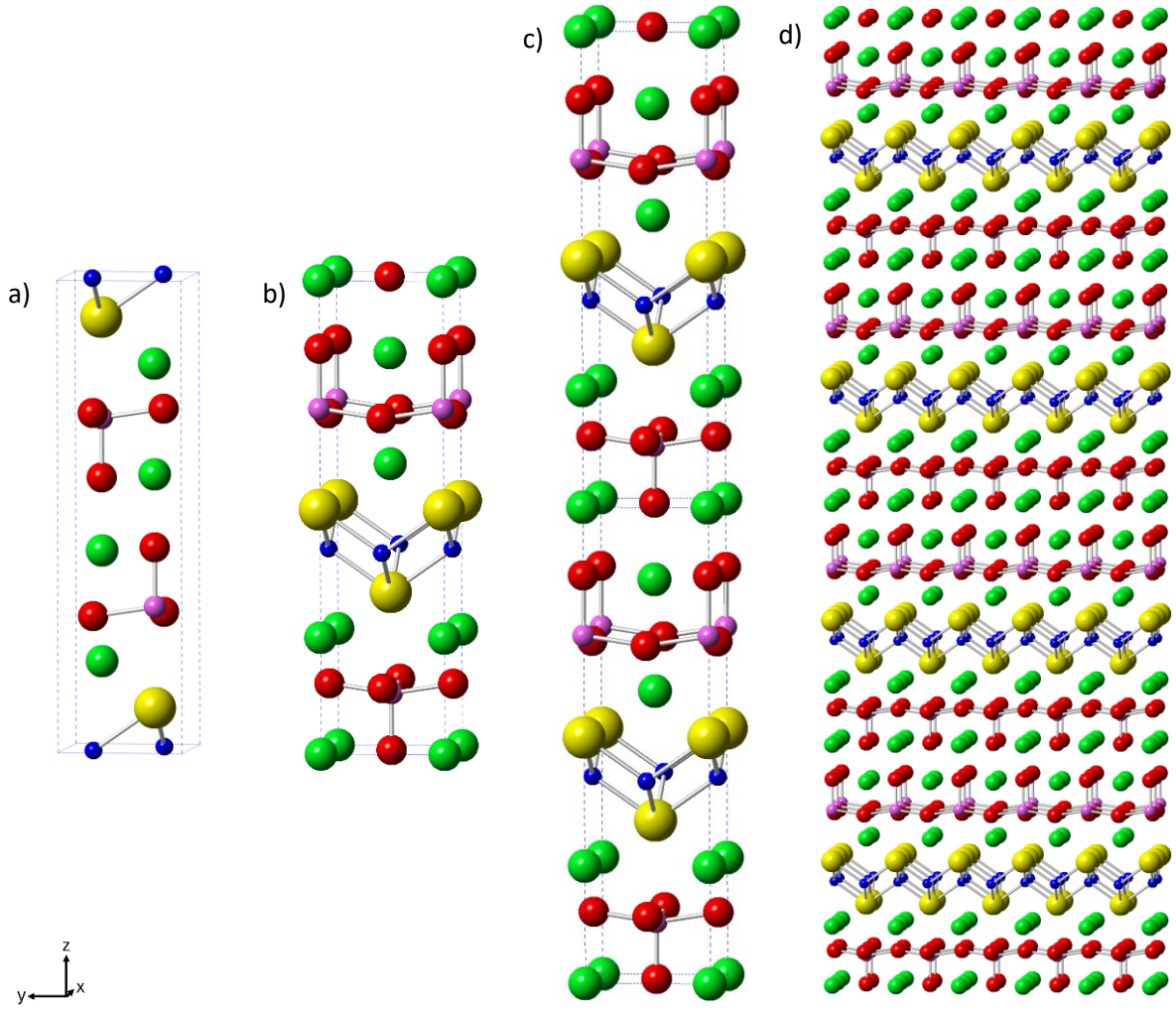

Figure 12 *Isometric projections of a generic depiction of the structure of the $A_4B_2O_6M_2Q_2$ ('426') MALM, showing a) one unit cell, b) the unit cell with origin shifted by 0.25, 0.25, 0.575 to display it in the convention used previously, c) a 1 × 1 × 2 expanded unit cell, and d) a 2 × 5 × 4 expanded unit cell. All projections are viewed primarily along the x-axis. Projections a, b, and c are to scale with each other, but not to d. The interactions of A^{2+} to O^{2-} / Q^{2-} are largely ionic, and so for clarity these bonds are not shown. The blue dashed lines denote the unit cell.*
Colour key: green - A, pink - B, red - O, blue - M, and yellow - Q.

Unlike the 212 and 325 structures, the layers in the 426 material are not staggered from each other by half of a unit cell. In other words, each layer type (best visualised by the tetrahedral chevron shape of the heavy layer in the unit cell) are in phase. This increases the symmetry and results in a smaller unit cell that contains only one formula unit. As such, the standard unit cell (Figure 12a) is not intuitive of the larger structure, but if the origin is shifted as per Figure 12b, then doubled in length in the c direction as per Figure 12c, the structure can be depicted in the same style as the previous materials and it's close similarity to these phases becomes apparent. The 426 unit cell is not centrosymmetric as the others are, exhibiting translational symmetry rather than a mirror plane.

Expressed in its empirical and most irreducible form, the 426 structure $A_4B_2O_6M_2Q_2$ is A_2BO_3MQ (or '213'). This nomenclature is widespread in literature, and in isolation it is a logical description of the structure given the unit cell contains one formula unit. However, within this work the doubled formula $A_4B_2O_6M_2Q_2$ is always used, which not only permits illustration of the formula and unit cell in a form more akin to the other MALM structures, but maintains the consistency of the $[M_2Q_2]^{2-}$ heavy layer motif. The 426 structure crystallises in the *P*4/*mnn* space group (#129) and is represented by the *$Sr_2CuGa(SO_3)$* structure type,[63] which may be rewritten as $Sr_4Ga_2O_6Cu_2S_2$ to present it comparable to other MALMs. $Sr_4Ga_2O_6Cu_2S_2$ is discussed in *Chapter 4* in comparison to the scandium analogue, and within a 2024 publication by Malik et al to which this work contributed.[64]

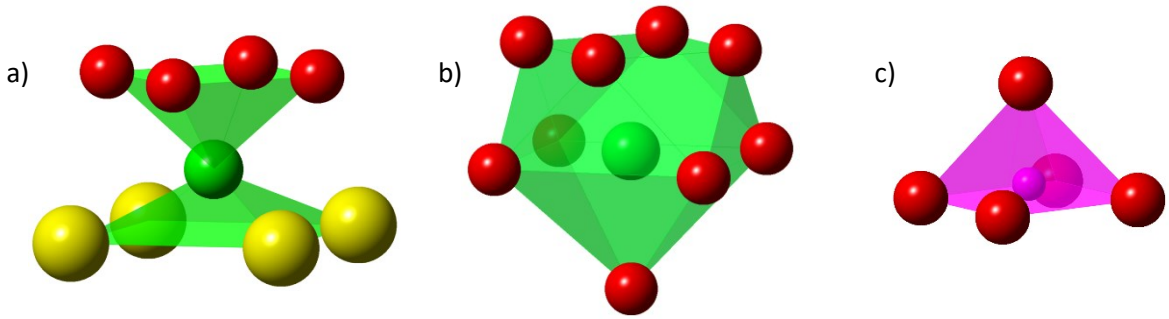

Figure 13 *Polyhedra showing the coordination environments of a 426 MALM: a) the inter-layer A atom site with 8-coordinate anti-prism interactions with oxygen and chalcogen ions, b) the intra-layer A atom site with 9-coordinate capped square prism coordination with oxygen ions, and c) the B atom site with 5-coordinate square-based pyramidal interactions with oxygen ions. Projections are to scale with each other.*
Colour key: green - A, pink - B, red - O, and yellow - Q.

The structure of the $A_4B_2O_6M_2Q_2$ oxide light layer is complex, and can be described as a rock salt $[Sr_2O_2]$ centre sandwiched by two layers of *perovskite* $[SrScO_2]^+$, Figure 12. Like the 325, there are two distinct *A* sites within the light layer of $A_4B_2O_6M_2Q_2$, an 'intra' site which exhibits nine-coordinate bonding with oxygen atoms in a capped square prism environment, and the same 'inter' site observed in the 212 and 325 which straddles the light and heavy layers, bonded to four chalcogen and four oxygen atoms in an anti-prismatic arrangement. The bonding of both *A* sites is largely ionic in nature. The *B* cation resides in a five-coordinate square-based pyramidal site similar to the 325 *B* site, Figure 13c.

Not only do the 325 and 426 structures have similar atomic sites, but they also both accommodate a +3 oxidation state *B* atom. In stoichiometric terms, the 426 structure differs from the 325 structure only by one unit of *A*O. Therefore, in practice, syntheses of the two structure types are dictated by the inclusion or exclusion or one molar quantity of the alkaline earth oxide. Equation 1 describes the synthesis of 325 material $Ba_3In_2O_5Cu_2S_2$,[20] and Equation 2 that of its 426 analogue $Ba_4In_2O_6Cu_2S_2$.[65]

Equation 1 $2\ BaO + BaS + In_2O_3 + Cu_2S \rightarrow Ba_3In_2O_5Cu_2S_2$

Equation 2 $3\ BaO + BaS + In_2O_3 + Cu_2S \rightarrow Ba_4In_2O_6Cu_2S_2$

As is often the case, research into this class of materials began slowly. The maiden report of this structure type with $Sr_4Ga_2O_6Cu_2S_2$ by Zhu and Hor in 1997 was followed closely followed by their publications of $Sr_4B_2O_6Cu_2S_2$ (*B* = Cr, In, Fe, Mn) the same year.[41, 66] There was then only one further publication in this field in the next decade, that of $Sr_4Zn_2O_6Cu_2S_2$,[67] which interestingly was the first not only to cite a 426 *p*-type electrical conductivity but also the first to show enhancement by doping with an astounding 5,500,000 fold improvement from 2.2×10^{-8} to 1.2×10^{-1} S cm^{-1} in $(Sr_{3.9}Na_{0.1})Zn_2O_6Cu_2S_2$.

A breakthrough 2009 publication by Ogino et al reported superconductivity at 17 K in $Sr_4Sc_2O_6Fe_2P_2$.[68] This ignited a boom of superconductivity research into iron 426 MALMs in the five year period from 2009 to 2013. The scandium iron phosphide that began the surge received further attention,[69-71] as did its arsenide analogue $Sr_4Sc_2O_6Fe_2As_2$.[72-74] All of these materials are iron-based, with either strontium or calcium on the *A* site and a small *B* cation. This results in a very short basal lattice parameter *a* and subsequently a narrow Se-Cu-Se angle, which (with an optimum at the ideal tetrahedral angle of 109.48 °) is believed to be responsible for the superconducting properties.[75] The chromium iron arsenide $Sr_4Cr_2O_6Fe_2As_2$[76-78] and its vanadium analogue $Sr_4V_2O_6Fe_2As_2$[79-81] (which remains the most researched of all MALMs by more than twice the nearest contender) were also identified as promising superconducting candidates by virtue of their near-ideal heavy layer geometry, the latter with a reported critical temperature of 37 K,[82] increased to 56 K under high pressure.[83, 84]

Superconductivity is by far the largest branch of 426 research, but more relevant to this work is their *p*-type conductivity, which varies widely across at least 12 orders of magnitude. Examples include $Ca_4Fe_2O_6Cu_2Ch_2$ (often investigated for magnetic behaviour)[85, 86] with conductivities of 1.25×10^{-4} (*Ch* = S) and 1.25×10^{-5} S cm^{-1} (*Ch* = Se),[87] $Sr_4Ga_2O_6Cu_2S_2$ cited at 2.2×10^{-4} S cm^{-1}, and the metallic $Sr_4Sc_2O_6Ni_2P_2$ and $Sr_4Sc_2O_6Co_2P_2$ cited at 5.88×10^2 and 2.22×10^2 S cm^{-1} respectively.[88]

MALMs with the 426 structure are featured significantly in this work. They are explored in *Chapter 4*, a study of $Sr_4Sc_2O_6Cu_2Ch_2$ (*Ch* = S, Se) to improve conductivity by *p*-type aliovalent doping with group 1 metal ions. Each has been reported only once previously,[57, 89] and the structure of the selenide is reported in this work for the first time. *Chapter 5* also features 426 MALMs, where the sparsely reported 'solid-state metathesis' method is applied to syntheses of this structure type for the first time.

1.1.3.5 Other Quinternary Oxychalcogenide Structures

The 212 ($A_2BO_2M_2Q_2$) and 325 ($A_3B_2O_5M_2Q_2$) structures described previously are the n = 1 and n = 2 members of the $A_{n+1}B_nO_{3n-1}M_2Q_2$ family of quinternary MALMs derived from the Ruddlesden-Popper *perovskite* structure. The 426 ($A_4B_2O_6M_2Q_2$) structure is not part of this series, yet all three share the same *anti-litharge* $[M_2Q_2]^{2-}$ conductive heavy layer motif, differing by one additional $[ABO_3]$ 'slice' of insulating *perovskite* layer. Whilst the 212 and 325 structures are widely researched and easily synthesisable, higher order members where $n > 2$ become increasingly unstable as the *perovskite* block widens due to tendency towards forming lower order members.

The n = 3 member of the $A_{n+1}B_nO_{3n-1}M_2Q_2$ series, one $[ABO_3]$ unit larger than the 325 structure, is $A_4B_3O_8M_2Q_2$. The mean oxidation state of the *B* metal cation is +3.$\dot{3}$, therefore conventional full occupation by a single oxidation state cation is not possible. There are three reported methods by which to account for this oxidation state, the first is the use of a cation like manganese which is stable across multiple oxidation states, such as in $Sr_4Mn_3O_8Cu_2Ch_2$ (*Ch* = S, Se),[66, 90] which more specifically is $Sr_4(Mn^{3+}{}_2Mn^{4+})O_8Cu_2Ch_2$. The second method is similar: site sharing on the *B* site with differently charged cations to balance the charges such as in $Sr_4(Sc_2Ti)O_8Fe_2As_2$[91] or $Ca_4(MgTi_2)O_8Fe_2As_2$.[84] Thirdly, introducing an oxygen deficiency can reduce the mean oxidation state of the *B* site to +3 allowing a single oxidation state cation, such as in $Ba_4Sc_3O_{7.5}Fe_2As_2$[92] and $Ba_4Sc_3O_{7.5}Ni_2As_2$.[52] 438 materials almost exclusively contain *B* or O vacancies for charge and structural balance.

Zhu and Hor, the first to publish both the 325 and 426 structures in 1997,[41, 63] were also the first to report the 438, with $Sr_4Mn_3O_8Cu_2Ch_2$ (*Ch* = S, Se) in 2000.[66] It was seven years before any further study into this structure type,[90] followed by the superconductivity research boom circa 2010 where various reports of the 438 structure emerged, whose large insulating *perovskite* layers allow precise control of the conducting heavy layer geometry, such as $Ca_4(Al_2Ti)O_8Fe_2As_2$[93] and $Ca_4(Sc_2Ti)O_8Fe_2As_2$.[94, 95]

The higher order n = 4 and 5 members are cited in only a small number of publications exclusively from the Ogino research group in Tokyo. Materials with general formulae $A_5B_4O_{11}M_2Q_2$ ('54<u>11</u>') and $A_6B_5O_{14}M_2Q_2$ ('65<u>14</u>') have been reported, but their structures not formally published as they have never been synthesised phase pure. The 54<u>11</u> structure has a mean *B* oxidation state of +3.5, therefore either contains a 1:1 ratio of +3 and +4 oxidation state cations such as $Ca_5(Sc_2Ti_2)O_{11}Fe_2As_2$[96, 97] or a 1:3 ratio of +2 and +4 such as $Ca_5(MgTi_3)O_{11}Fe_2As_2$.[98] The 65<u>14</u> mean *B* oxidation state is +3.6, achieved with a 2:3 ratio of +3 and +4 cations such as $Ca_6(Al_2Ti_3)O_{14}Fe_2As_2$[99] or $Ca_6(Sc_2Ti_3)O_{14}Fe_2As_2$.[94] Usually these ratios are not precise, and also accompany a small oxygen vacancy. All instances of 54<u>11</u> and 65<u>14</u> materials are calcium iron arsenides, and are targeted for their superconducting properties.

The inability of these structures to form as pure phases results from the tendency of the vast insulating block towards the pure *perovskite* phase $CaTiO_3$, accompanied by the driving force of the 325 phase stability, resulting in phase separation according to Equation 3 (5411) and Equation 4 (6514) below:

Equation 3 $Ca_5(Sc_2Ti_2)O_{11}Fe_2As_2 \rightarrow 2\ CaTiO_3 + Ca_3Sc_2O_5Fe_2As_2$

Equation 4 $Ca_6(Sc_2Ti_3)O_{14}Fe_2As_2 \rightarrow 3\ CaTiO_3 + Ca_3Sc_2O_5Fe_2As_2$

Other reported but extremely uncommon MALM phases include $Ba_4Mn_4O_8Cu_{1.8}S_2$, the sole report of a '448' structure to date. With a mean Mn oxidation state of +2.55 and an inherent copper deficiency, it was discovered unintentionally during syntheses of the 438 class.[100] Finally, in a deviation of the $[M_2Q_2]^{2-}$ motif observed across all previous MALMs, $Sr_2MnO_2Cu_{3.5}S_3$ and $Sr_2MnO_2Cu_{5.5}S_4$ were reported in 2006.[101, 102] These may be considered 212 materials with extended heavy layers, and were investigated for lithium insertion in battery applications.[103]

Figure 14 is a comparative visualisation of these and the other uncommon MALM structure types discussed in this section.

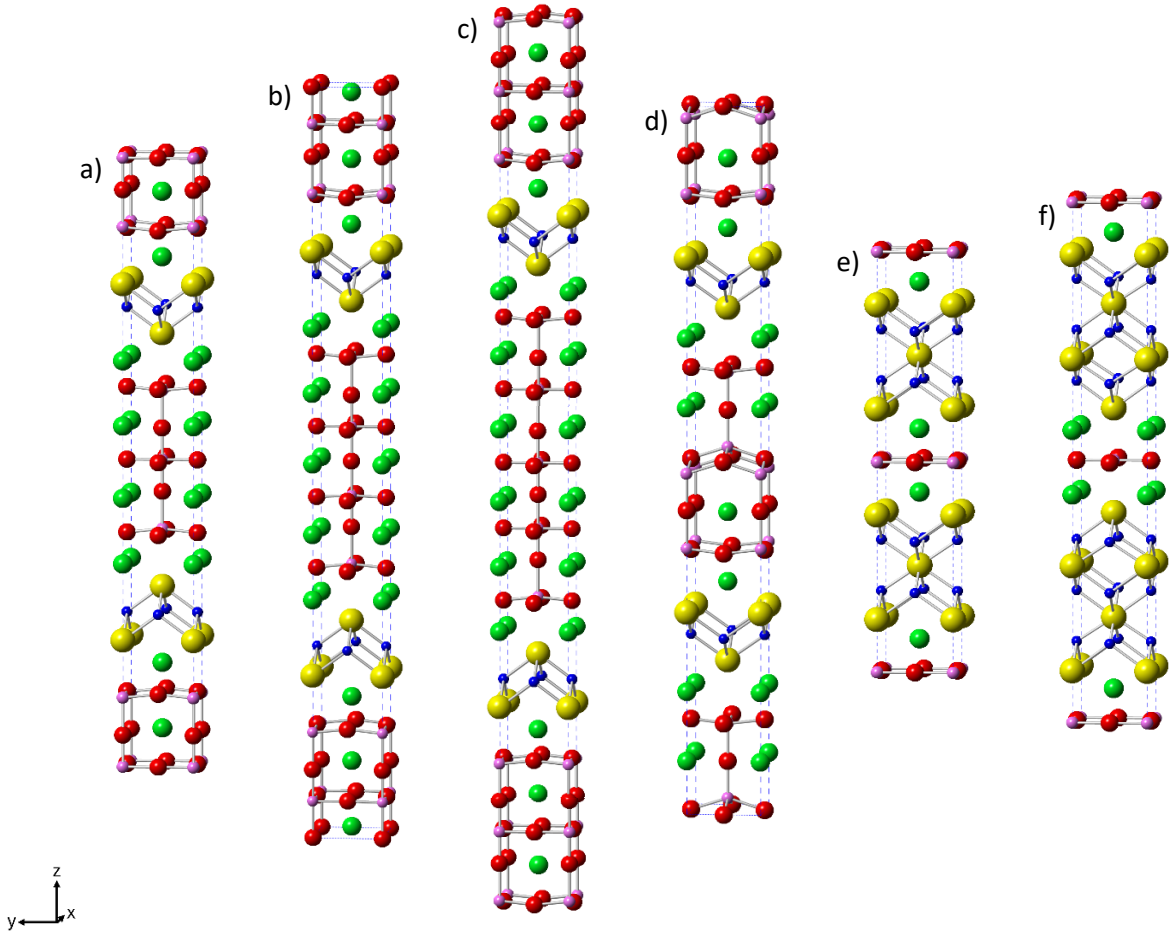

Figure 14 *Isometric projections of the generic unit cells of a) $A_4B_3O_8M_2Q_2$, b) $A_5B_4O_{11}M_2Q_2$, c) $A_6B_5O_{14}M_2Q_2$, d) $A_4B_4O_8M_2Q_2$, e) $A_2BO_2M_{3.5}Q_3$, and f) $A_2BO_2M_{5.5}Q_4$. Projections are viewed primarily along the x-axis, and are to scale with each other. For consistency, d and e are 1 × 1 × 2 expanded unit cells. The interactions of A^{2+} to O^{2-} / Q^{2-} are largely ionic, and so for clarity these bonds are not shown. The blue dashed lines denote the unit cell. Colour key: green - A, pink - B, red - O, blue - M, and yellow - Q.*

1.1.3.6 Structural Review Summary

Below, in Figure 15, the research timelines of these structure types are presented graphically. This includes, to the best of the author's knowledge, all known publications of MALMs up to the end of 2024, a collection of 111 unique publications.

Research into the 212s outdates the other structures by almost 20 years, and long remained the focus of MALM researchers as measured by both publication volume and number of unique materials. That is until the aforementioned superconductivity boom circa 2009 when interest surged, primarily for the 426 structure type. The volume of 426 publications during this time spiked significantly higher than the number of materials because much focus was directed towards fewer known candidates rather than new materials, for example $Sr_4V_2O_6Fe_2As_2$ which is by far the most researched MALM with 13 unique publications at the time of writing, more than double the nearest competitor. From the mid 2010's onwards, interest in all three structures has increased steadily and equally.

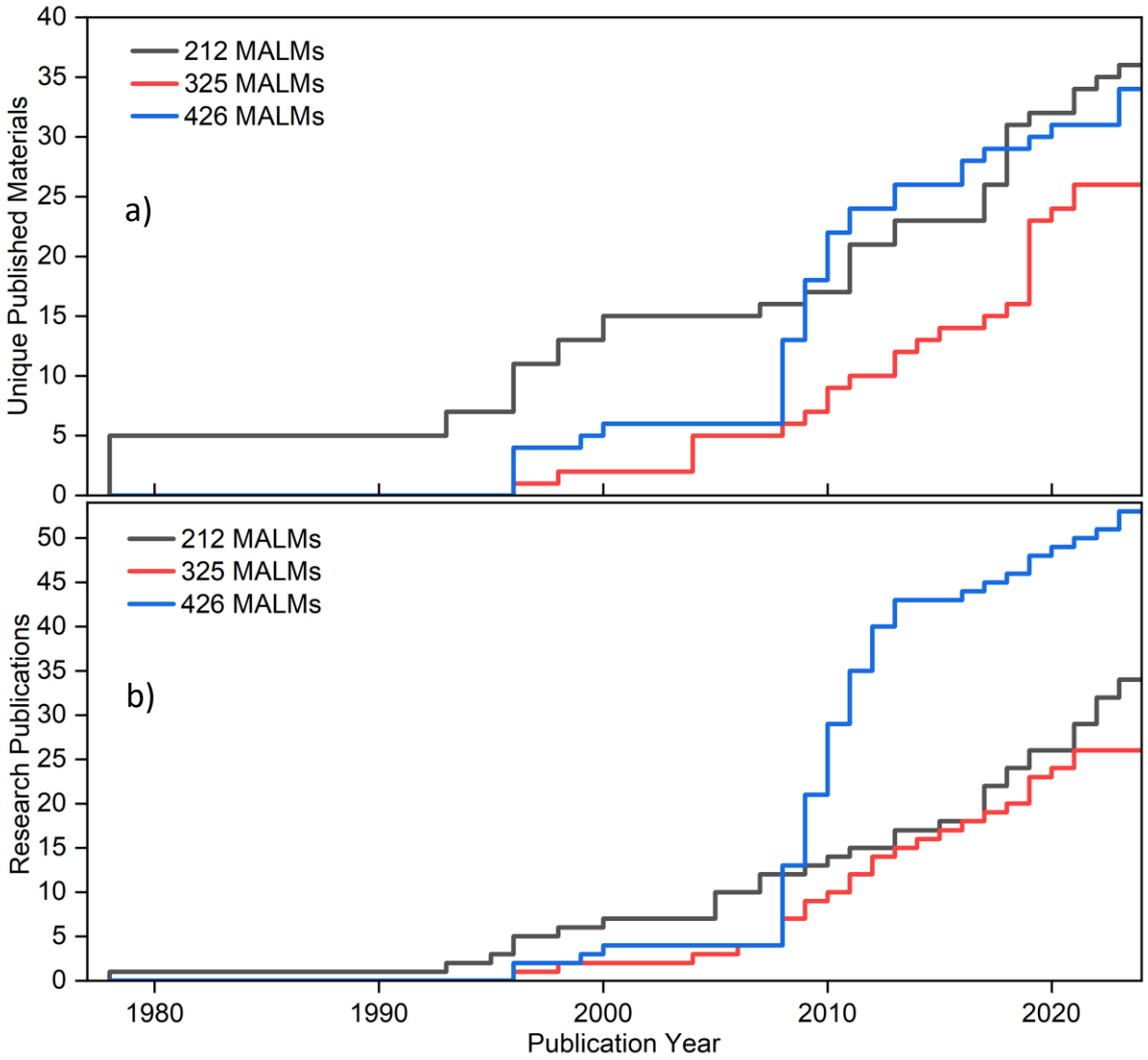

Figure 15 *The research progression of 212 (black), 325 (red) and 426 (blue) MALMs presented through a) the number of unique published materials over time and b) publication count over time, from their initial publications through to the end of 2024.*

1.2 Transparent Conductivity

1.2.1 Invisible Metals

Electrical conductivity and optical transparency are seemingly mutually exclusive properties. High performance in one metric almost always comes at the expense of the other. Metals, for example, are excellent conductors of electricity, but are opaque to light, whilst materials like glass and ceramics are transparent but insulating. Semiconductors like silicon and germanium arsenide are good conductors, but highly absorbing.[104] Metals have no band gap, therefore cannot be transparent – invisible metals are an impossibility. Materials produced in pursuit of both conductivity and transparency, called Transparent Conductors (TCs), will always be a compromise of these properties.

TCs combine electrical conductivity and optical transparency into a single material. Indium doped tin oxide (ITO) is the standout candidate with 97 % of the TC market share, demonstrating up to 90 % transparency when deposited as a film, and a conductivity of 1×10^4 S cm^{-1}.[105, 106] With a rarity on par with silver,[107] indium is not a common or mineable metal, and is produced exclusively from the refinement of zinc ores.[108] The conductivity of ITO is good, but less than that of metals (Figure 16). ITO is not a metal, but a very conductive semiconductor. The allure of true 'invisible metals' remains, for now, quixotic.

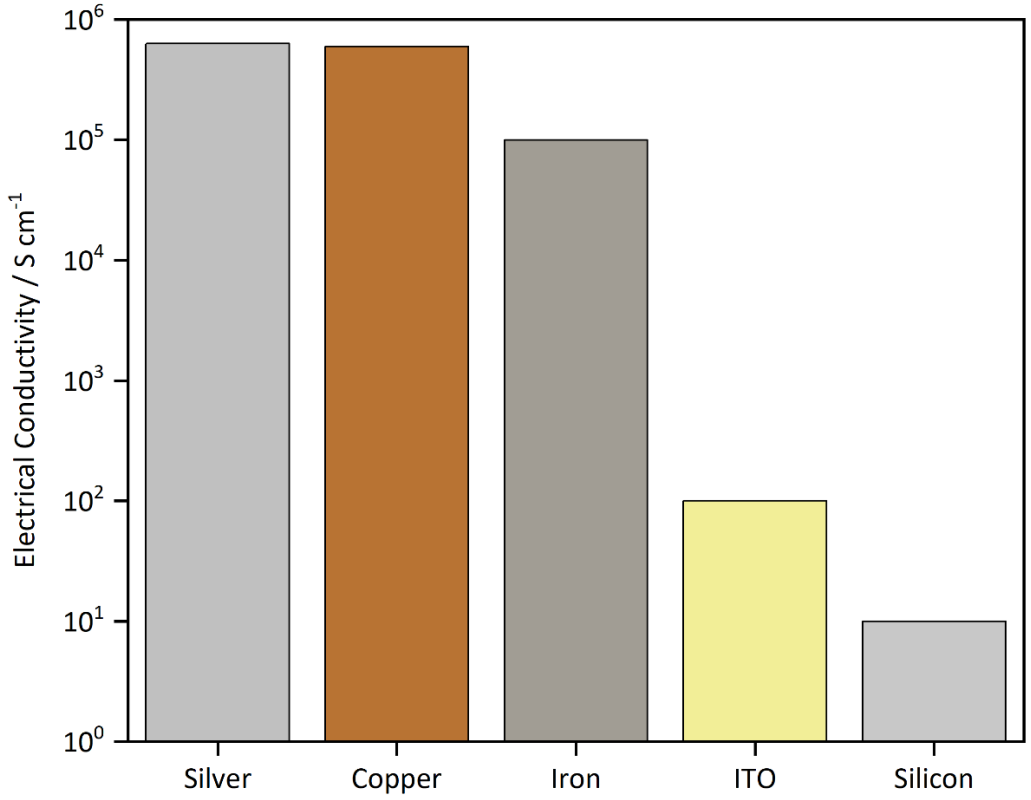

Figure 16 The electrical conductivities of five common conductive material, represented on a $\log_{10}$ scale. Data sourced from literature.[109-113]

Transparent conductors are essential for technologies of the modern world, notably flat panel displays and the touch screens of smart devices. Both of these applications require a conductive material, but one which also must be transparent to visible light. As such these technologies are dominated by ITO, which remains the obvious and most effective choice of TC. ITO is a Transparent Conducting Oxide (TCO), a class of materials under the Transparent Conductor umbrella, which contain oxygen.

An application that would be revolutionised by the invention of a sustainable, scalable TC is solar energy technology. An ideal solar cell is a semiconducting slab to absorb light and produce electrons, with a thin metal covering applied to transport the electrons away. Of course, covering the cell with metal defeats the transparency, so the current solution is thin metallic strands across the cell surface. The greater the metal coverage, the better the electron transport but the less surface is exposed to light. Cover less surface and the cell absorbs more light, but promoted electrons are more likely to be lost to heat dissipation before reaching the nearest metal strand. An illustration of this trade-off can be seen in Figure 17 below. A high-performance transparent conductor could, in theory, fully cover the cell surface for maximum solar conversion. ITO coated glass is sufficient, and some modern cell research makes use of it,[114-116] but the rarity and scalability of indium is not at all sustainable, and the inherent UV opacity of the glass reduces total transparency to 80 %.[117] With the transparency of glass but the conductivity of a metal, a true transparent conductor, an invisible metal, could revolutionise green energy production.

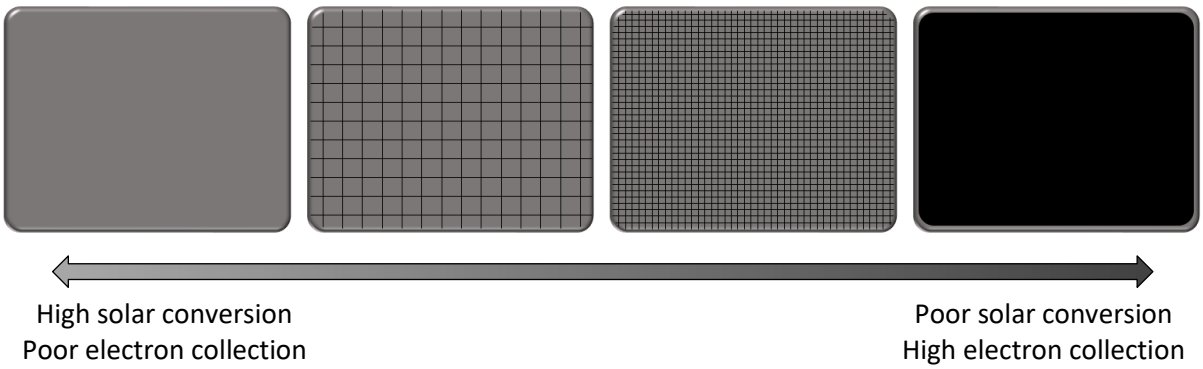

Figure 17 *An illustration of the solar cell trade-off between maximising surface area (grey) for solar energy conversion and maximising electron collection with metal strands (black). The leftmost case shows maximum solar conversion but minimal electron collection, the rightmost case shows minimal solar conversion but maximum electron collection.*

This is just one example of many technological applications motivating the research of materials chemists in the design and synthesis of novel conducting materials. To investigate and design transparent conductors, the mechanisms behind transparency and conductivity must first be understood. In this section the underlying theory, history and design considerations of transparent conductors is discussed.

1.2.2 Band Theory

1.2.2.1 Conductors, Semiconductors, and Insulators

The band theory of solids, first proposed by Felix Bloch in 1929,[118] describes the interactions and resulting energy levels of bonded atoms. Two atomic orbitals combine to form two molecular orbitals (MOs) at distinct energy levels: a lower energy bonding orbital and a higher energy antibonding orbital. Three atoms will produce three MOs, etc. The number of atoms, *n*, will always equal the number of resulting MOs. Figure 18 shows the combination of two hydrogen atoms to produce a filled bonding orbital (σ) and an unfilled antibonding orbital (σ*).

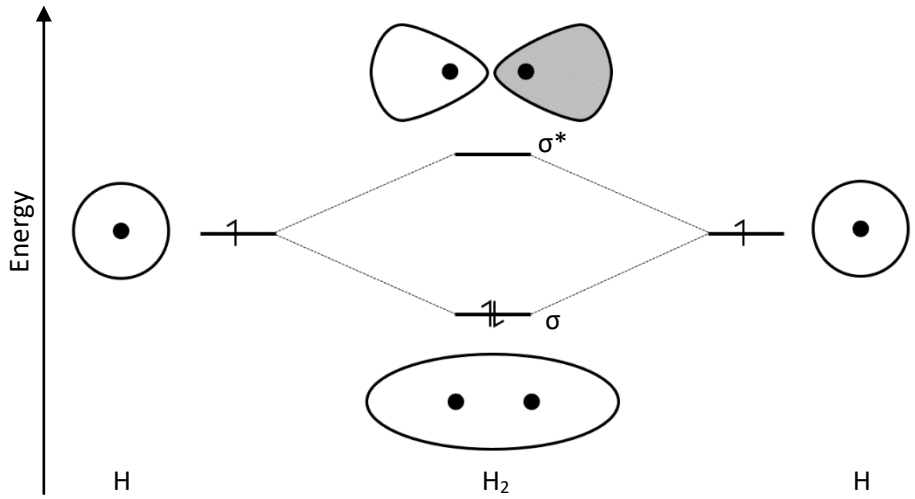

Figure 18 The molecular orbital diagram of H_2. The atomic orbitals of two hydrogen atoms combine to form one bonding molecular orbital (filled) and one antibonding molecular orbital (vacant).

In a bulk solid, considered $n = \infty$, there are an infinite number of MOs and therefore the energy gap between each is infinitesimally small. The energy levels are no longer quantised or discrete, and can be considered a band within which electrons are free to move. The transition of the molecular orbital diagram from a single atom through to an 'infinite' bulk solid is illustrated in Figure 19, where the example of elemental lithium is used. The bands on the rightmost edge of the plot show the $n = \infty$ case. For example, in one mole of lithium, ≈ 7 grams, there are 6.022×10^{23} energy levels which is far beyond the limit where energy levels may be considered or measured discrete.

Electrons in extended solid structures occupy the MOs from the lowest energy upwards according to the Aufbau Principle. Atoms are held together by filled bonding orbitals, and a bond becomes weaker upon the population of antibonding orbitals or the depopulation of bonding orbitals. In the lithium example (electronic structure $1s^2 2s^1$), each atom contributes one bonding electron from its 2*s* orbital, All bonding orbitals are filled, resulting in a large band of filled MOs called the Valence Band (VB) and a large band of unfilled antibonding MOs called the Conduction Band (CB).

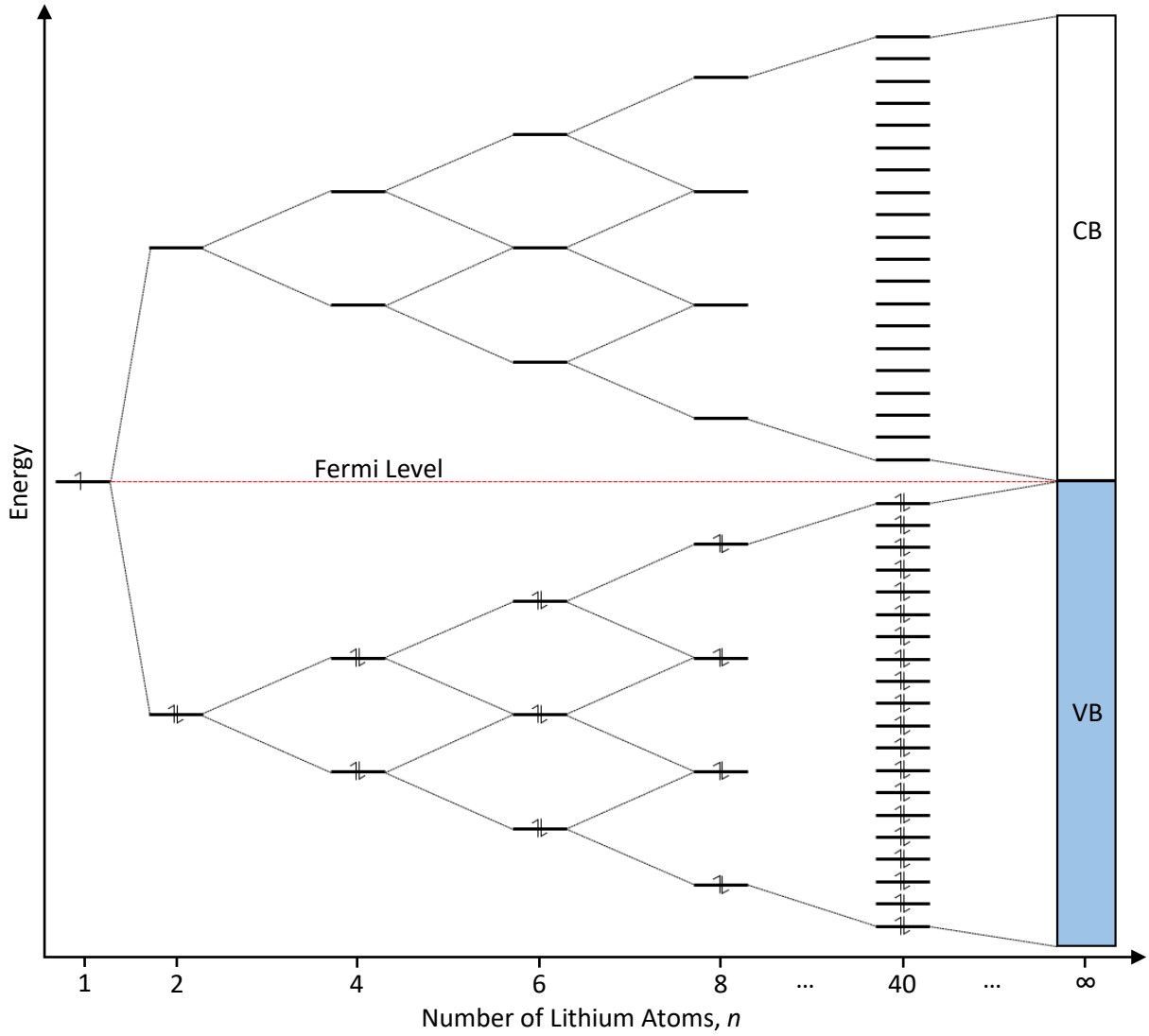

Figure 19 *Molecular orbital diagram of Lithium 2s interactions. The energy levels are discrete when the number of bonded atoms is finite, and form bands when n is infinite. All 1s MOs are fully filled and non-bonding, so for conciseness are not shown. The blue and white bands are the valence and conduction bands respectively. The red dashed line is the Fermi level.*

Between the VB and the CB is the Fermi level, represented by a red dashed line, which is the average energy of the electrons at absolute zero. At this temperature the electrons have zero thermal energy and must therefore occupy only the lowest possible states, forming a “Fermi sea” of electronic states, with the Fermi level at the very top. Figure 19 demonstrates this, where all electrons are in the lowest possible energy states. Regardless of the Fermi level position, if there is no band at a given energy, an electron cannot reside in that region.

In the lithium example above, the difference between the Highest Occupied Molecular Orbital (HOMO) and the Lowest Unoccupied Molecular Orbital (LUMO) is zero, as the bands either touch or overlap. Electrons can therefore move freely between bands with no energy barrier, an important property that allows metals to conduct electricity. These materials are called conductors, characterised by a negligible difference between the VB and the CB. The movement of an electron between these bands is so facile that this configuration is often referred to as an ‘electron gas’.

Conversely, materials which have a large difference between the valence and conduction bands are insulators. The energy difference is referred to as the band gap, at the centre of which the Fermi level lies. Electrons are bound within the valence band and cannot be promoted across the band gap due to the large energy requirement. Insulators will therefore not conduct electricity at anything other than extremely high temperatures. Examples include diamond, glass, rubber, wood, and most plastics.

Between these two extremes of conductors and insulators lie semiconductors, which have a moderate band gap between a mostly filled VB and a mostly unfilled CB. The band gap is large enough that electrons cannot cross with no energy barrier like in a metal, but small enough that thermal energy can promote some electrons from the bonding orbitals of the VB across the band gap to the antibonding orbitals of the CB. This slight CB population results in modest conduction of electricity, less than that of metals but greater than that of insulators. Semiconductors, such as silicon, germanium and tin, are defined by their small band gap and increasing conductivity with temperature, a phenomena that arises because greater thermal energy results in a greater population of the CB.

The opposite is true for conductors, whose conductivities decrease with temperature. As electrons move within a material they may collide with atoms. Collisions become more likely at higher temperatures due to increased thermal vibrations of the nuclei, slowing the electrons and increasing the resistivity. The conductivity of a material is therefore determined by the ability of electrons to cross the band gap from the VB to the CB, a property dictated by the size of the band gap.[119] Figure 20 compares and contrasts the band structures of conductors, semiconductors and insulators. Note that all conductivities within this work, be they references or observed values, are recorded at room temperature unless stated otherwise.

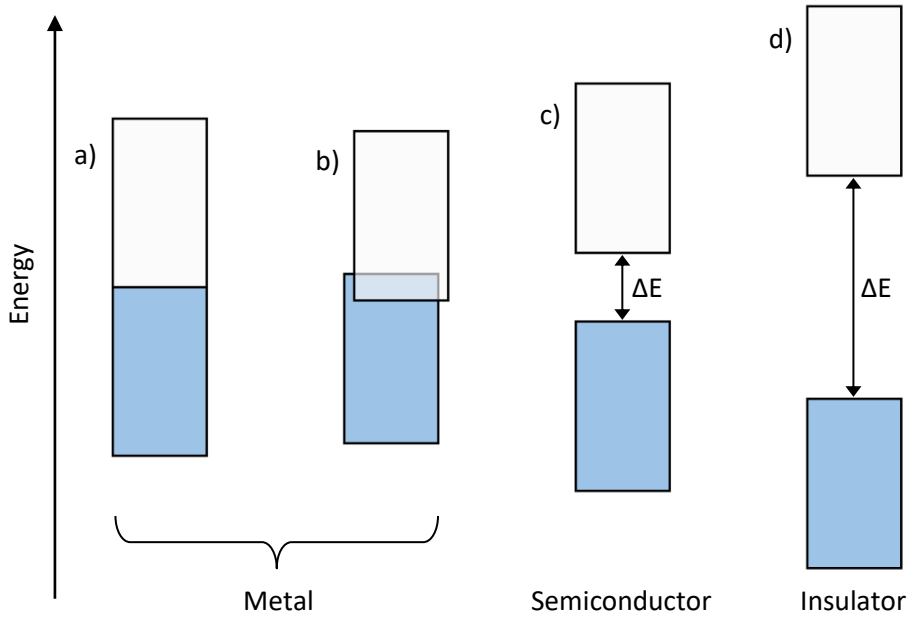

Figure 20 *The band structures of a) a metal where the band gap is negligibly small because the bands are touching, b) a metal where there is no band gap because the bands overlap (staggered for clarity), c) a semiconductor with a small band gap, and d) an insulator with a large band gap. The blue and white bands are the valence and conduction bands respectively.*

1.2.2.2 Optical Transparency

Thermal energy is not the only possible pathway by which an electron may be promoted from the valence band to the conduction band of a semiconductor; promotion may also be caused by incident light. If the energy of incident light is equal to the band gap, an electron may become excited and cross the band gap, and the photon of light is absorbed.

If the band gap of a material is greater than the energy of visible light, the light is of insufficient energy to promote an electron and the light is not absorbed. Visible light ranges from 1.6 eV (below which is infrared light) to 3.3 eV (above which is ultraviolet light). Therefore, a material with a band gap greater than 3.3 eV will be transparent, allowing all visible light to pass through such as in Figure 21a. Materials with band gaps smaller than the energy of visible light will be able to absorb some of the higher energy components of the light, appearing translucent, such as in Figure 21b.

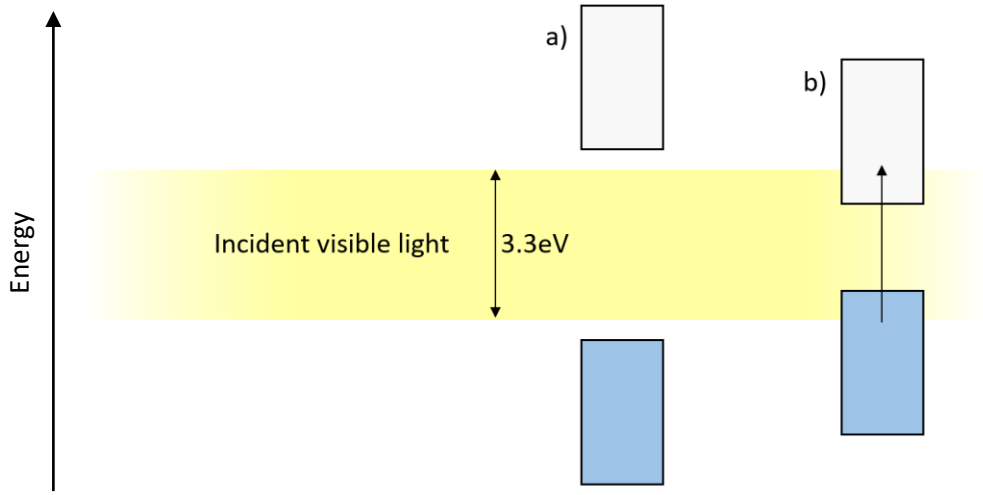

Figure 21 *Visible light (with a maximum energy of 3.3 eV) interacting with a) an wide band gap insulator such as diamond, whose band gap is too large to absorb visible light and is transparent, and b) a semiconductor such as silicon, whose band gap is smaller than the energy of visible light, so the light is absorbed and an electron is promoted.*

This explains the opacity of metals. Metals have no band gap, so the energy cost to promote an electron is negligible, and as a result a metal will absorb or reflect all incident light. Metals are always opaque, and so despite sporting the best conductivities they cannot be used as transparent conductors because they cannot be transparent. Insulators on the other hand are often transparent, such as glass, quartz or diamond, because their band gaps are so large that no visible light possesses sufficient energy to promote an electron across the band gap, yet it is this same property that renders an insulator unable to conduct an electric current.

Metals cannot be made transparent, and insulators cannot be made to conduct electricity, so generally it is semiconductors, those with intermediate properties between metals and insulators, that are the focus of research by materials scientists to design and synthesise transparent conductors.

1.2.2.3 Semiconductor Doping

As discussed previously, for a semiconducting substance to conduct electricity, an electron must be promoted from the highly populated valence band to the mostly unoccupied conduction band. This occurs naturally at a small scale due to thermal vibrations, and is enhanced by light. The promotion of an electron leaves behind a positively charged hole in the valence band. Both are charge carriers, the promoted electrons may move within the conduction band to carry charge, and electrons within the valence band can move using the unoccupied holes left behind by the promoted electrons.

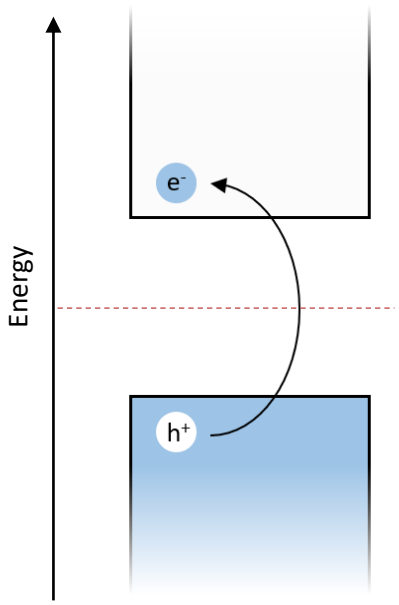

Figure 22 *The promotion of an electron from the valence band (blue) to the conduction band (white) of a semiconductor, leaving behind a positively charged hole. The red dashed line is the Fermi level.*

Compared to the free movement of electrons within the bands of a metal, the band gap of a semiconductor presents a significant energy barrier for conductivity in semiconductors. For this reason, semiconductors, whilst conductive, are still far less conductive than metals (silicon for example is almost 60,000 times less conductive than copper).[110, 112] Generally, the larger the band gap, the more insulating a material will be, leading to a mutual exclusivity of conductivity and transparency in pure materials.

Semiconductors fall into two categories based on the origin of their conductivity: intrinsic and extrinsic. All semiconducting behaviour described so far has been that of intrinsic semiconductors, which are pure materials with a small band gap, such as silicon or germanium. Thermal and light energy can promote an electron across the band gap producing a hole, facilitating the flow of charge. The Fermi level represents a balance of charge carriers, rising when electrons are the majority carrier, and lowering when holes are the majority carrier. In intrinsic semiconductors, the number of holes is always equal to the number of excited electrons, and the Fermi level sits in the middle of the band gap.

The other category of semiconducting materials are extrinsic semiconductors. In pure form, semiconductors with a wide band gap (approaching that of insulators) are often poorly conductive as a result. Excitation of electrons is difficult as the energy barrier is high. However, conductivity may be enhanced and controlled by the purposeful addition of foreign material into the substance, in a process called doping. These are 'extrinsic' semiconductors.

In a pristine semiconducting material, the number of electrons and holes are always equal. Adding an electron deficient dopant will introduce a hole to the material without an accompanying electron. This slightly depopulates the filled valence band, allowing current to easily flow within the band without an energy barrier due to the introduction of holes as a charge carrier. The depletion of electrons in the material moves the Fermi level down towards the VB. This is known as '*p*-type' doping because the majority charge carrier is *p*ositively charged holes. Adding an electron rich dopant does the opposite: an extra electron is added to the material, which cannot occupy the already filled valence band so must occupy an antibonding orbital of the conduction band. Population of the CB again allows current to flow with little resistance, this time with excess electrons as the charge carrier. The Fermi level moves up towards the slightly populated CB. This is '*n*-type' doping, due to the addition of *n*egatively charged electrons.

Doping is not exclusive to wide band gap poor semiconductors; conductive intrinsic semiconductors such as silicon may also be made extrinsic and further enhanced by doping. Figure 23 above describes the extrinsic enhancement of silicon with boron (*p*-type) and phosphorous (*n*-type), and Figure 24 on the next page describes the effect on the band structure and Fermi level. These are by far the most common dopants for the conductive enhancement of silicon.[120, 121]

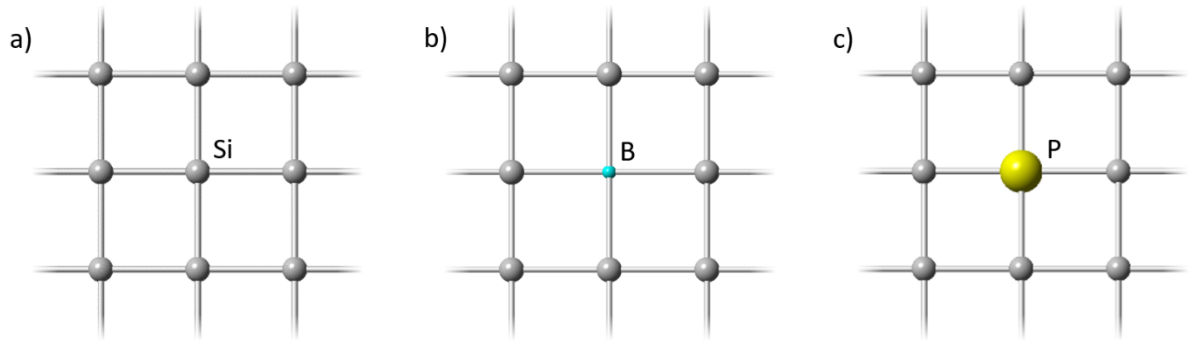

Intrinsic silicon
Undoped

Extrinsic silicon
p-type doped

Extrinsic silicon
n-type doped

Figure 23 *Illustrations of a) pristine undoped intrinsic silicon, b) silicon extrinsically p-type doped with boron, and c) silicon extrinsically n-type doped phosphorous. The sizes of boron and phosphorous compared to silicon are exaggerated for effect and are not to scale. A simplified square-planar structure of silicon is used here for clarity; the true structure of silicon is diamond with four-coordinate tetragonal bonding.*
Colour key: white - Si, cyan - B, yellow - P.

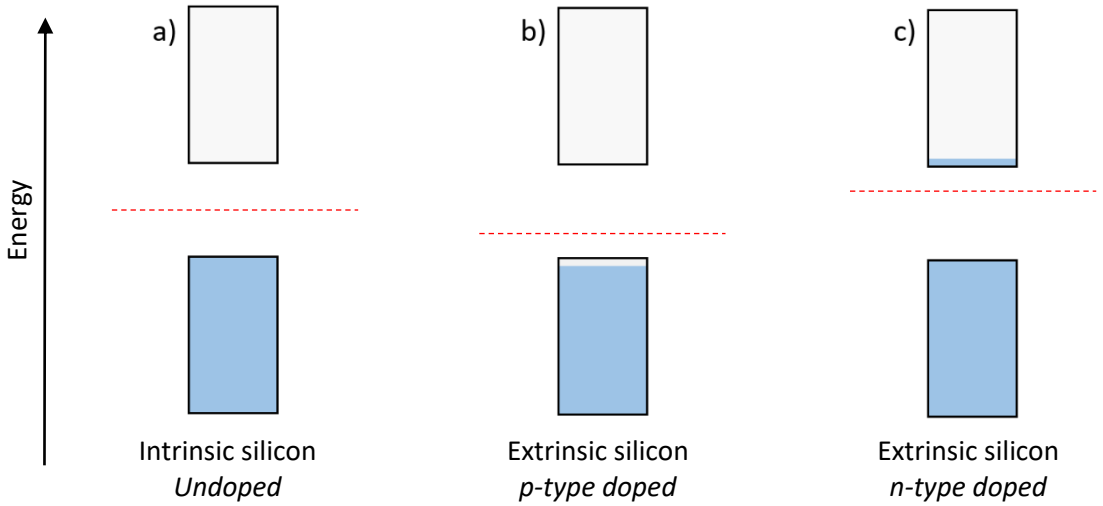

Figure 24 *The band structures of a) pristine undoped intrinsic silicon, b) silicon extrinsically p-type doped with electron deficient boron, and c) silicon extrinsically n-type doped with phosphorous. The red dashed line is the Fermi level. The partial band depopulation and population is exaggerated for effect.*

1.2.2.4 Indium Tin Oxide: A Case Study of Degenerate Doping

Extrinsic doping is responsible for Indium Tin Oxide (ITO), the best performing commercial TCO. Pristine undoped indium oxide, In_2O_3, is a wide band gap semiconductor (considered *n*-type due to inherent oxygen vacancies) with a conductivity of 10^{-2} S cm^{-1} and a large band gap of 3.75 eV. The difficulty of electrons to cross this band gap gives In_2O_3 a charge carrier concentration so low that it is almost insulating. The band gap of In_2O_3 is compared in Table 1 below to a range of other conducting, semiconducting and insulating materials.

Table 1 *The band gaps of a range of materials. Data sourced from literature.*[122-131]

Material		Band gap / eV	Material type
Copper	Cu	0	Conductor
Indium antimonide	InSb	0.18	Semiconductor
Germanium	Ge	0.80	Semiconductor
Silicon	Si	1.18	Semiconductor
Gallium arsenide	GaAs	1.42	Semiconductor
Copper oxide	Cu_2O	2.17	Semiconductor
Zinc oxide	ZnO	3.37	Semiconductor
Indium oxide	In_2O_3	3.75	Semiconductor
Carbon (diamond)	C	5.47	Insulator
Silica (α-quartz)	SiO_2	9.65	Insulator

However, this large band gap does render In_2O_3 transparent to visible light as it is greater than 3.3 eV, and as such it has been widely reported deposited as transparent thin films.[131-134] The optical properties of In_2O_3 make it a promising candidate for development of a transparent conductor, but in order to engineer such a material its poor conductivity must be improved without damaging the large band gap. The band gap cannot be manually reduced to improve electron promotion (and doing so would be detrimental to the transparency), but extensive doping will move the Fermi level. When positive and negative charge carriers are balanced such as in an intrinsic semiconductor or an insulator, the Fermi level resides at the centre of the band gap, but when the charge carriers become imbalanced the Fermi level will move higher (*n*-type) or lower (*p*-type).

Indium oxide can be doped *n*-type with its elemental neighbour tin, which has one valence electron more than indium, to produce tin doped indium oxide, also referred to an $Sn:In_2O_3$ or ITO. Each atom of tin within the structure of In_2O_3 adds an electron to the conduction band without introducing an accompanying hole in the valence band, which makes electrons the majority carrier and raises the Fermi level. As previously discussed, this will improve the conductivity. However, doping in ITO is degenerate, which means tin is added to such a large extent that the Fermi level actually moves up into the conduction band, Figure 25. Now, with no band gap to cross in order for charge to flow, ITO has a near-metallic conductivity of 10^4 S cm^{-1} and a negligible energy barrier to electron movement. Degenerate doping requires extremely heavy substitution, approximately 10 % of indium in In_2O_3 is replaced by tin to produce ITO.

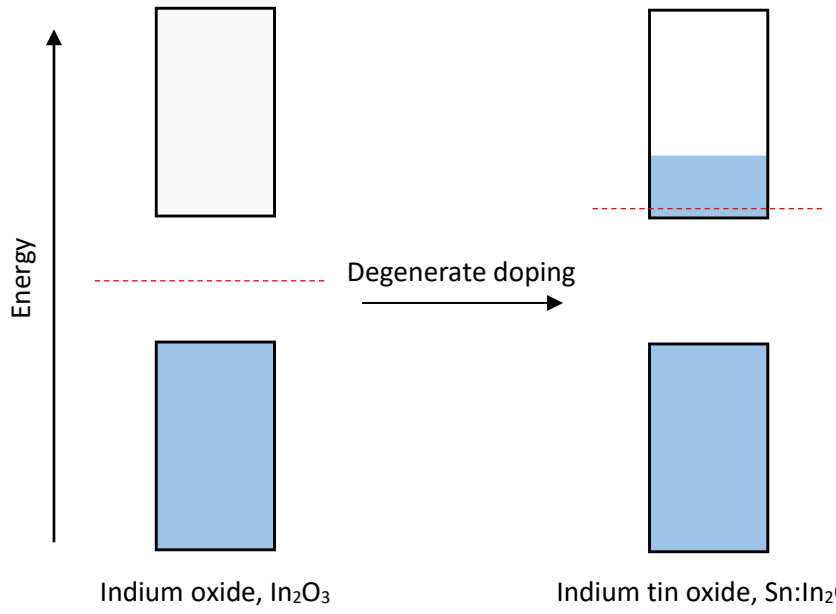

Figure 25 *Band structures illustrating the degenerate doping of indium oxide, resulting in a Fermi level raised into the conduction band. The red dashed line is the Fermi level.*

Crucially for TCO applications, the wide band gap is not only retained but slightly widened due to a Moss-Burstein shift,[135, 136] a phenomena where the band gap of degenerately doped extrinsic semiconductors appears to increase due to the Fermi level residing within a band. When electrons are excited from the valence band, they may only be excited into the unoccupied region of the conduction band above the Fermi level. Excitation of an electron into the CB region below the Fermi level is forbidden by Pauli's exclusion principle. Therefore, the observed optical band gap is the actual band gap plus the Moss-Burstein shift, see Figure 26 below. Note that the true band gap has not changed, only that which is observed by spectroscopies.[137]

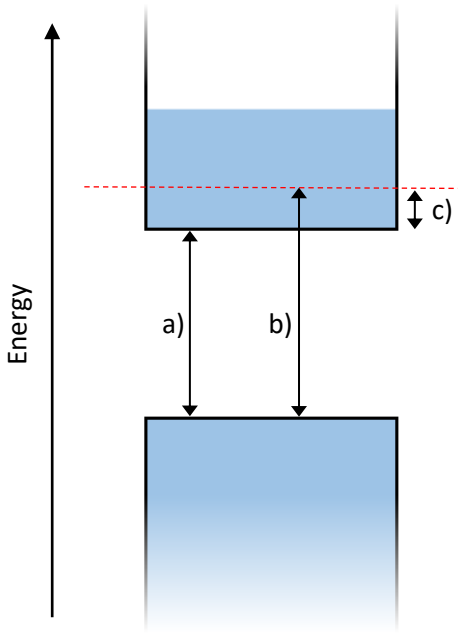

Figure 26 *An illustration of the Moss Burstein effect for an n-type degenerately doped semiconductor, where a) is the actual band gap, b) is the apparent optical band gap, and c) the Moss-Burstein shift. The red dashed line is the Fermi level.*

As shown in this section, the size of the band gap strongly correlates with conductivity in any kind of undoped material, but when doped, especially degenerately, the band gap is no longer the energy barrier inhibiting conduction. The electrical conductivity of a degenerately doped semiconductor (like a TCO) is directly related to its carrier concentration and carrier mobility according to Equation 5:

Equation 5 $\sigma = n e \mu$

[where σ is the electrical conductivity, n is the carrier concentration, e is the elementary charge, and μ is the mobility]

Carrier concentration n is the ease of generation of mobile charge carriers (electrons for n-type and holes for p-type). This is therefore intrinsically determined by the extent of doping, or defects within the material structure. The carrier mobility μ is a measure of how easily the charge carriers can move throughout a material, a complex parameter derived from features such as carrier effective mass, grain boundaries and the presence of impurities which disrupt the flow of charge through a material.

The conductivity of ITO may be rationalised by this relationship. High mobility of the electrons in the conduction band (between 40-60 $cm^2 V^{-1} s^{-1}$)[113] combined with vast charge carriers (electrons) provided by tin, combine for good conductivity but both are below that of a conductive metal such as copper or silver.

In *Section 1.2.1 - Invisible Metals*, the application of ITO to flat panel displays and touch screens was briefly discussed, made possible by its transparency to visible light. There exists another convenient application of ITO specifically due to the size of its band gap. Because the band gap of ITO is only narrowly wider than the threshold of visible light (around 4 eV accounting for the Moss-Burnstein shift), it remains transparent to all visible light whilst most UV light (> 3.3 eV) is able to excite electrons and is absorbed. On the other end of the visible light scale, infrared light (< 1.6 eV) is also able to be absorbed, exciting electrons within the conduction band itself. This means that ITO is not only transparent to visible light, it is transparent *only* to visible light, whilst opaque to all other forms. This means it also finds application in UV / IR blockers. It is this property that renders it inappropriate for widespread solar cell integration, as visible light represents only 42 - 43 % of solar radiation,[138] the rest is IR and UV which would be largely absorbed or reflected by ITO.

There are other benefits of ITO beyond its conductivity and transparency, properties which are often overlooked but must be considered during the scaling of any candidate transparent conductor. Firstly, ITO is moisture resistant.[139] Weatherproofing is an extremely important and often overlooked property, for even a theoretical true invisible metal would be limited to very few applications if it were not stable against water, temperature cycles, radiation and abrasion. ITO is waterproof, abrasion-proof, and stable at up to 1000 °C.[140] Conversely, ITO is quite unstable in acidic conditions and at high voltages.[141, 142] ITO is also very accommodating to deposition as a thin film onto glass, a process which has been reported through various means such as spin coating,[106] spray pyrolysis,[143] pulsed laser deposition,[144] and chemical vapour deposition.[145] Often a bulk material is of little practical use in solid-state chemistry, especially in the field of transparent conductors, so ease of deposition is a very important property which strengthens the appropriateness of ITO in its applications.

On the surface ITO appears to be an almost perfect material, and such a designation is not unjustified given its widespread adoption, particularly in technological applications within electronic devices as a transparent conductor.[146] Its largest downside, however, as briefly discussed in the introduction to this section, is its indium content. Indium is a rare metal, a by-product of the refinement of zinc ores, particularly Sphalerite (Zinc sulfide).[107] Demand for indium is expected to problematically surpass reasonable levels of supply within the next decade,[147] not aided by its poor recycling rate (from ITO) of less than 1 %.[148] There exists, therefore, an increasingly important need for a suitable replacement for ITO given the ever increasing demand for electronic displays and the transition towards green energy sources, of which solar is the third largest contributor at 18 % behind hydro and wind.[149]

1.2.3 Transparent Conducting Oxides

Transparent Conducting Oxides (TCOs) are a subset of Transparent Conductors with significant oxygen content. Usually these are binary metal oxides, but may be ternary where the metal cation is degenerately doped such as was described with ITO. TCOs are the primary focus of research into transparent conductors, culminating in thousands of research papers over the past century.[150] TCOs have emerged as a promising class of materials found in numerous applications owing to their high conductivity (on the scale of weak metals, 10^4 S cm^{-1}) and high transparency (above 80 %).[‡]

The general design strategy for TCOs is the degenerate doping of a metal oxide, which balances the trade-off of mobility and charge carriers. All commercial TCOs are *n*-type, including ITO, and *p*-type alternatives have proved unsatisfactory. This is because in *p*-type TCOs the mobility of electrons in the CB is high, but electrons are not the majority carriers, holes are, and hole mobility within the VB is very poor. The CB is composed of metal cation *s* orbitals with good covalent overlap resulting in good mobility, whereas the VB is composed of the *p* orbitals of oxide ions with poor overlap due to ionic bonding, hence poor mobility.[151] There is therefore a gap in the TCO market for *p*-type TCOs, the focus of the majority of recent TCO research. In this section, the design progression of Transparent Conduction Oxides is reviewed, beginning with a discussion of the other non-ITO *n*-type commercial TCOs, through to the development of *p*-type TCOs aiming to break the VB mobility stalemate.

1.2.3.1 *N*-type

N-type commercial TCOs are the degenerately doped oxides of late transition metals such as indium, tin or zinc. These have large band gaps of greater than 3.1 eV, establishing a high transparency around which the conductivity can be artificially engineered by doping. These metals are all closed-shell d^{10}, therefore have no unpaired *d*-electrons, a crucial property which eliminates the possibility of *d*-*d* transitions causing any undesirable colouring or carrier trap states.[152] Electrons are the primary charge carrier, with a facile pathway through the widely dispersed *s* orbitals of the metal ion in the CB.

The first TCO was cadmium oxide, CdO, produced by Bädeker in 1907.[153] It boasted an excellent conductivity of 8.3×10^2 S cm^{-1} but a modest 40 % transparency. Although poor by today's standards, the performance of CdO was the first step towards cracking the impossibility of an invisible metal. Bädeker is affectionately cited as the 'Father of Transparent Conductors' for his discovery.[154] Despite a high mobility of great research interest,[155] the toxicity of cadmium has relegated CdO to history.

[‡] The terms transparency and transmittance are often cited interchangeably. Transparency is a measure of how easily light passes through a material, whilst transmittance is a measure of how much light passes through. Generally, both are cited as a percentage and (especially in visible light) refer to the same thing. In this work the term transparency is used, cited between 0 to 100 %.

Antimony doped Tin Oxide (ATO) was developed as a transparent defroster for aircraft windshields during World War II, and was patented in 1947 shortly after.[156] This was the first large scale use of a TCO, in an application for which TCOs including ATO are still employed today. ATO has a reported band gap of 3.3 eV, a conductivity of 10^3 S cm^{-1} and a transparency of > 85 %.[157, 158] Its constituent elements are safer and more abundant than indium, an advantage over ITO.

Also developed for aircraft windshields in the 1940's but now primarily used within solar cells,[159] Fluorine doped Tin Oxide (FTO) has a conductivity of almost 8×10^2 S cm^{-1} and a transparency of 81 %.[160] Whilst it does not match the other TCOs discussed here in terms of performance, its cost is low due to abundant and sustainable constituent elements. It has high thermal stability and is robust against moisture and chemical damage.[161]

Lastly, Aluminium doped Zinc Oxide (AZO) is by far the least expensive and safest of these materials, containing very abundant and non-toxic metals. It has a modest conductivity reported between 10^2 and 10^3 S cm^{-1}, but an excellent transparency of over 90 %.[162, 163] It is often employed in research into flexible electronics,[164, 165] but used primarily as a cheaper yet conductively inferior replacement for ITO in transparent electronic displays.

In summary, ITO remains the benchmark *n*-type transparent conducting oxide with a conductivity 10x greater than its nearest competitor, but the environmental and sustainability concerns of indium mean that the search for a replacement is necessary. FTO and ATO present a good compromise of performance and cost, alongside improved sustainability, whilst AZO is weaker in its electronic properties yet easily the least expensive, safest, and most sustainable candidate, an ideal choice when high conductivity is not essential. Table 2 on the next page compares and contrasts these materials, which is by no means an exhaustive list but a broad overview of the common TCOs.

Table 2 A comparison of the common n-type TCOs

Material	**Conductivity / S cm^{-1}**	**Transparency / %**	**Band gap / eV**	**Primary use**	**Pros**	**Cons**
ITO	10^4	80	3.5 - 4.3	Transparent displays	Heat / moisture resistance	Indium rarity and toxicity
ATO	10^3	85	3.5 - 3.7	Smart windows	Inexpensive	Antimony toxicity
FTO	10^2	81	3.5 - 3.8	Solar cells	Heat / moisture resistance	Relative poor conductivity
AZO	10^2 - 10^3	90	3.3 - 3.5	Transparent displays	Inexpensive and non-toxic	Relative poor conductivity

1.2.3.2 *P*-type

ITO, ATO, FTO and AZO are all *n*-type degenerately doped TCOs based on wide band gap metal oxide insulators, benefitting from high conduction band mobility for electrons. *p*-type equivalents have always performed inferior due to poor mobility for holes in the valence band, which is composed of highly localised oxygen 2*p* orbitals bound ionically and with poor overlap. There is a need for *p*-type TCOs, both as an alternative to rival the excellent yet imperfect *n*-types,[166] and to perform alongside them in technologies such as *p*-*n* heterojunctions.[167, 168] This section explores the research progression of *p*-type TCOs.

Copper (I) oxide was found to be an exception to this trend. The high effective nuclear charge of Cu means that its 3*d* orbitals (closed shell) are reduced in energy such that they may hybridise with the oxygen 2*p* orbitals that form the valence band. The more delocalised 3*d* orbitals produce a greatly improved VB hole mobility of 10^2 cm^2 V^{-1} s^{-1}, but a band gap of only 2.17 eV which is too small for transparent conductivity.[127]

Inspired by the surprising mobility of Cu_2O, Hosono et al proposed the 'Chemical Modulation of the Valence Band' (CMVB) concept in 1997, a procedure to increase the mobility of the valence band by leveraging the delocalised 3*d* orbitals of Cu^+ by degenerate *p*-type doping with transition metals, in their case Al. A series of materials known as the *delafossites* were produced with general formula Cu*M*O_2 (where *M* = Al,[169] In,[170] Sc,[171] Y,[172] and Ga[173]). Of their discovery of $CuAlO_2$,[169] Hosono stated:

> *"Although the conductivity of our candidate material is significantly lower than that observed for the best n-type conducting oxides, it is sufficient for some applications, and demonstrates that the development of transparent p-type conductors is not an insurmountable goal."*

The *delafossites* have reduced hole mobilities compared to CuO and conductivities are moderate, ranging from 0.01 to 30 S cm^{-1} across the range of *M* metals. However, they possess superior wide band gaps of 3.3 to 3.9 eV, and transparencies of 40 to 80 %. The difference in band gap between these materials and Cu_2O is due to the structure of the *delafossites*, which are layered, Figure 27. They consist of $[CuO_2]^{3-}$ linear units separated by a layer of transition metal M^{3+} ions, a structure not dissimilar from those of the ternary MALMs described in *Section 1.1*, however crucially these contain only one anion so are not MALMs. The layering reduces dimensionality, which increases the band gap whilst retaining the conductivity gained from the better orbital overlap. The degenerately doped *delafossites*, exhibiting both conductivity and transparency, were the first good performing family of *p*-type TCO materials. The Hosono group successfully applied a *delafossite*-derived material, $SrCu_2O_2$,[174] in a *p*-*n* junction with ZnO.[175]

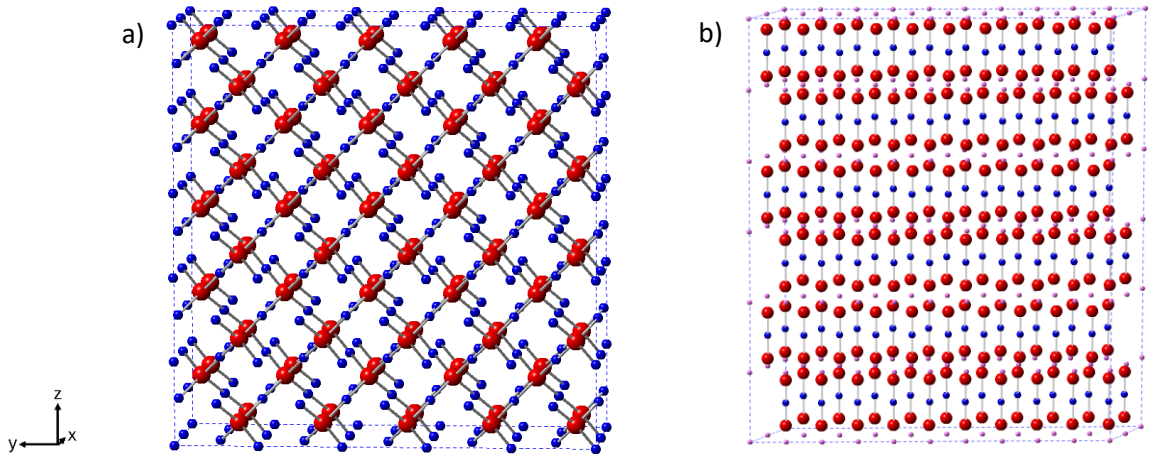

Figure 27 *Isometric projections of a) Cu_2O, and b) $CuAlO_2$. Projections are viewed primarily along the x-axis, and are not to scale with each other. For simplicity only covalent bonding is shown. Colour key: blue - Cu, red - O, and pink - Al.*

With the key design rule of hybridising the localised oxygen orbitals with delocalised low lying orbitals of the cation now established and proven, the CMVB concept was extended to the chalcogens in replacement of oxygen, detailed in the next section. Layered copper chalcogenides would in theory retain the dimensionality and band gaps of the *delafossites*, but with a larger and more diffuse *Ch* atom which would allow even more favourable interaction with the Cu $3d^{10}$ orbitals, further increasing the VB hole mobility.[151]

1.2.3.3 MALMs as *P*-type TCOs

The extension of the CMVB principle to the use of chalcogen atoms lead to the interest in layered oxychalcogenides for *p*-type conductivity, which are mixed anion, and so returns our discussion to the MALMs outlined in great detail previously. The chalcogenides were explored because stronger covalent interactions were expected between copper and the *p* orbitals of the chalcogen series from oxygen to sulfur to selenium to tellurium, a fortuitous tuneability that was not possible with the binary or ternary oxides. The first material type of interest in the pursuit of copper chalcogenides for *p*-type TCOs was that of *ZrCuSiAs*, such as LaOCuS.

LaOCuS consists of $[LaO]^+$ light layers and $[CuS]^-$ heavy layers. The interactions of the tetrahedral copper and sulfur atoms make up the top of the valence band, allowing conduction through hole transport. The $[LaO]^+$ layers confine the dimensionality of the $[CuS]^-$ *anti-litharge* layer to produce a large optical band gap of 3.1 eV. With increasing chalcogen size, the dispersion of its orbitals becomes greater and thus the overlap with copper is strengthened. This leads to better mobility, and in turn conductivity, a trend found to be linear between the $LaOCuS_{1-x}Se_x$ solid solutions.[176]

With this in mind, the use of tellurium LaOCu*Ch* for optimal hole mobility appears obvious, however it is not that simple. The trend in band gap is the opposite, decreasing down the chalcogenides due to a lowering of the *Ch* $2p^6$ antibonding orbitals that comprise the bottom of the conduction band.[6] As such, LaOCuS shows the highest band gap of 3.1 eV but the lowest electrical conductivity of 6×10^{-5} S cm^{-1},[45, 177] whereas the telluride analogue LaOCuTe has the smallest bandgap of 2.3 eV but an impressive conductivity of 1.65 S cm^{-1},[178] with the selenide analogue a modest compromise between the two.[179] This trend is illustrated by a 2024 study by He et al,[65] which reported the conductivity increase from S to Se to Te in $Sr_4In_2O_6Cu_2Ch_2$: 10^{-4}, 10^{-2}, and 10^{0} S cm^{-1}. This was accompanied by a band gap decrease from 2.25 to 1.78 to 1.20 eV.

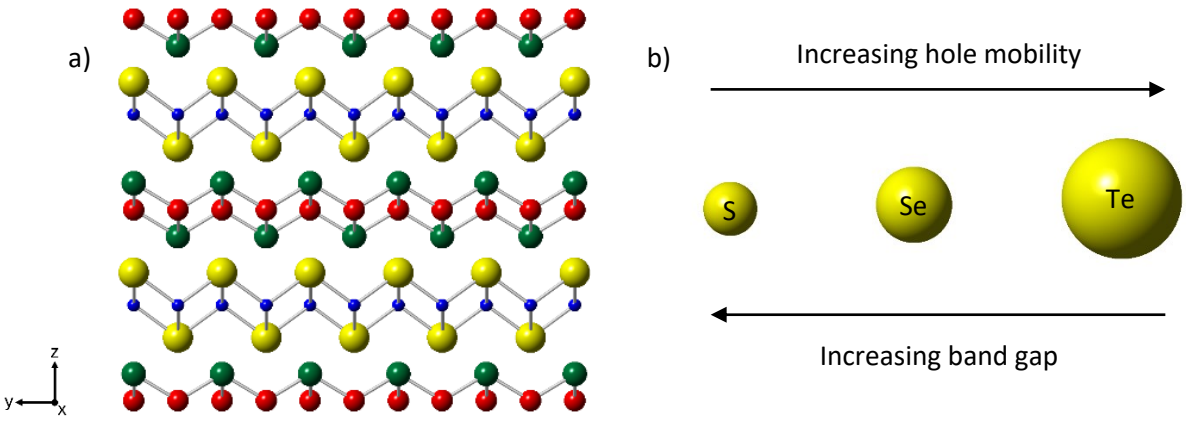

Figure 28 *a) an isometric projection LaOCuCh, viewed primarily along the x-axis, and b) the trends in hole mobility (increasing) and band gap (decreasing) along the chalcogenide series of S to Se to Te.Chalcogen atoms not to scale.*
Colour key: teal - La, red - O, blue - Cu, and yellow - Ch.

Given that poor conductivity may be improved by doping, whereas a small band gap is more 'inherent' to the material and difficult to widen, LaOCuTe is not considered to be a *p*-type TCO owing to its small band gap and poor transparency. Research into the sulfide and selenide analogues is vast, containing most notably the highest reported conductivity of any *p*-type TCO: 140 S cm^{-1} in Mg doped LaOCuSe.[179]

Another promising but far less explored *p*-type MALM TCO candidate is the 325 material $Sr_3Sc_2O_5Cu_2S_2$. The research progression of this material is discussed in detail in *Section 1.1.3.3*, from its discovery and publication by Otzschi in 1999,[8] to its recognition as a potential *p*-type TCO in 2007,[42] to the confirmation of its direct 3.1 eV band gap by DFT,[46] to a generous list of dopant recommendations with which $Sr_3Sc_2O_5Cu_2S_2$ could be doped to improve its conductivity and potentially even its band gap (by doping of the oxide block to modulate the copper sulfide geometry), by Scanlon et al in 2009.[46] These recommendations include aliovalent doping of the Sr^{2+} site for charge carrier enhancement and isovalent doping of the Sc^{3+} site for transparency improvements.

$Sr_3Sc_2O_5Cu_2S_2$ has received very little research attention since this time, appearing only in a handful of research publications,[57-59] none of which acting upon the doping recommendations laid out by Scanlon. This is surprising, given that this material was cited with an exceptional hole mobility of 150 $cm^2 V^{-1} s^{-1}$ and an equally impressive room temperature conductivity of 2.8 S cm^{-1}, the highest of any *p*-type TCO and establishing $Sr_3Sc_2O_5Cu_2S_2$ as a promising candidate for *p*-type technologies.[42] The carrier concentration (which contributes to conductivity alongside mobility) is not high, a mere 1×10^{-17} cm^{-3}, thus there exists a seemingly obvious room for improvement through doping to increase the charge carriers and improve the electrical conductivity further. Below are three quotes from literature pertaining to the unusual lack of attention given to $Sr_3Sc_2O_5Cu_2S_2$:

"It is undoubtedly of significant interest to prepare this material into thin films and dope it with monovalent cations (K^+) at Sr sites or divalent (Mg^{2+}) at Sc sites to improve the conductivity in this material."

K. Zhang et al, in their 2016 review of *p*-type TCOs.[104]

"$Sr_3Sc_2O_5Cu_2S_2$, which was originally synthesized as a candidate superconductor, could possibly represent the ideal structural motif for designing high figure of merit p-type transparent conducting materials that are so sought after by materials scientists. Further investigation of aliovalent and isovalent doping of $Sr_3Sc_2O_5Cu_2S_2$ is thus warranted."

D. Scanlon et al, in their 2009 computational analysis of $Sr_3Sc_2O_5Cu_2S_2$.[46]

"$Sr_3Sc_2O_5Cu_2S_2$ has very high undoped p-type conductivity with two cation sites for doping to further improve both transparency and conductivity, but only one experimental work has been reported for this material […] This might partly be due to the difficulty of achieving such a phase via conventional methods, but it is worthwhile to re-investigate such a material and unfold its full potential."

N. Zhang et al, in their 2019 review of copper-based TCOs.[151]

1.3 Research Motivation and Aims of this Work

In *Chapter 3* of this work, the promising *p*-type TCO candidate $Sr_3Sc_2O_5Cu_2S_2$ is explored in greater detail, including three doping studies pursuing the recommendations laid out by Scanlon. Reasons for potential irreproducibility of its benchmark conductivity value are discussed, which may suggest there is not a lack of wider interest in $Sr_3Sc_2O_5Cu_2S_2$ but rather a lack of successful conductivity replication. The selenide analogue $Sr_3Sc_2O_5Cu_2Se_2$ is also explored, which would be expected to exhibit a higher electrical conductivity but a lower band gap due to the more dispersed but lower energy $2p^6$ orbitals of selenium. $Sr_3Sc_2O_5Cu_2Se_2$ has also received little research attention besides its initial synthesis and a study of its band structure reporting an optical band gap of 2.7 eV, both by Iwasa et al.[58, 89] Its electrical conductivity has never been published, until this work. Scanlon's doping recommendations are also applied to this material but to a much greater extent than its sulfide counterpart due to more interesting conductive properties. Following the three doping studies of $Sr_3Sc_2O_5Cu_2S_2$, *Chapter 3* contains eight distinct and novel doping studies of $Sr_3Sc_2O_5Cu_2Se_2$, some yielding almost 100,000 times improvements in conductivity with no accompanying reduction in band gap.

Chapter 4 is an investigation into the 426 MALMs $Sr_4Sc_2O_6Cu_2Ch_2$ where again *Ch* = S and Se, in comparison to their gallium and indium counterparts produced by colleagues in collaboration for the 2024 publication "*Transport Properties of Doped Wide Band Gap Layered Oxychalcogenide Semiconductors Sr_2GaO_3CuCh, Sr_2ScO_3CuCh, and Sr_2InO_3CuCh (Ch = S or Se)*" by Malik et al,[64] towards which this work contributed significantly. The complex thermodynamic interplay between the 325 and 426 structures in the Sr-Sc-O-Cu-*Ch* system is explored, a phenomenon applicable only to the scandium materials due to stability of the 325 phases. These six MALMs are doped aliovalently with group 1 metal ions, yielding modest improvements to their electrical conductivities. The structure of $Sr_4Sc_2O_6Cu_2Se_2$, synthesised in this work, is reported within the publication for the first time.

Chapter 5 explores solid-state metathesis, an alternate and more convoluted synthesis method for layered materials using pre-formed 'building blocks' of the light and heavy layers, which has been applied only once in literature to MALMs.[61] The conventional method for solid-state synthesis, used elsewhere in this work, is discussed in detail in *Section 2.1.* Proof of concept of the metathesis technique was achieved by the concurrent syntheses of $Sr_3M_2O_5Cu_2Se_2$ (*M* = Sc, Fe) by conventional and metathetic reactions. Following a comprehensive literature review of all known building blocks across 450 publications, a small bank was assembled and applied to a novel metathesis-driven 'parallel synthesis' concept, an idea evaluated for appropriateness of application to novel materials synthesis.

Finally in *Chapter 6*, the novel oxychalcogenide MALM $Sr_3In_2O_5Cu_2Se_2$, discovered during this work, is reported for the first time. Attempts to synthesise its metathesis precursor $Sr_3In_2O_5Cl_2$ were unsuccessful, but lead to the accidental discovery of another novel structure, $Sr_4In_2O_6Cl_2$.

Chapter 2 Experimental Methods

2.1 Solid-State Chemistry

Diffusion of ions in the solid state is slow because no molten or solvated phase is present to allow rapid movement and contact between species. Solid reactions occur initially at the boundary between particles of precursors, and then within particles of the product phase as the reaction progresses.[180] As such, it is essential in solid-state chemistry that particle surface contact is maximised by means of thorough powder grinding and pelletising, and high temperatures are necessary to force the progress of slow diffusion. Solid-state reactions are difficult to monitor because analysis cannot take place until a sample has cooled, so multiple heating cycles are often required, where the intermediate regrind between them is vital for re-establishing the close particle contact.

This section explains the general synthetic approach applied to the majority of materials investigated within this work. Samples were synthesised by a conventional solid-state method,[181] often referred to as the ceramic method, on the scale of 0.5 to 5 grams. The general procedure for a synthesis of this type depends on the air stability of both the target material and the precursors required.

2.1.1 Syntheses in Air

In the case where both the target material and the precursors that comprise it are air stable, and the reaction itself may take place in air, the general procedure is as follows. First, the appropriate quantities of high purity powder precursors are measured to a 0.0001 g scale on a four decimal balance. These precursors are combined and ground in an agate pestle and mortar for at least 5 minutes until homogenous in colour, appearance and texture. Given most precursors for these materials are dark black or bright white powders, grinding usually results in a dull grey powder mixture. Mixtures are then transferred to a pellet die and pressed into 13 mm pellets under 10 tonnes. Pellets are placed within alumina crucibles and heated inside a box furnace in air to the desired temperature, usually between 500 and 1000 ˚C, for a duration of usually 12 to 24 hours with a pre-heating ramp rate of 2 ˚C min^{-1}. Samples are allowed to cool naturally to room temperature inside the furnace.

It is common in solid-state chemistry that one heat cycle is insufficient to drive a reaction to completion due to the inherent slow nature of solid-state diffusion. Samples will typically be reground and reheated multiple times to break down larger grains of precursor/intermediate material and maximise their surface contact, with progress assessed by X-ray Diffraction (XRD). Air stable syntheses of this type are uncommon in this work due to the frequent use of precursors which require inert storage, however in-air synthesis was routine for the production of oxyhalide precursors in *Chapter 5*.

2.1.2 Syntheses under Vacuum

For target materials which are not air stable, or contain precursors or intermediates that are not air stable, a more complicated process of total air exclusion must be executed. In these cases, the preparative process described above now takes place under an inert atmosphere, in a nitrogen glovebox (less than 10 ppm O_2 or H_2O). This applies to the majority of materials synthesised in this work, including all of those in *Chapter 3* and *Chapter 4* where end products are stable but precursors and intermediates are not.

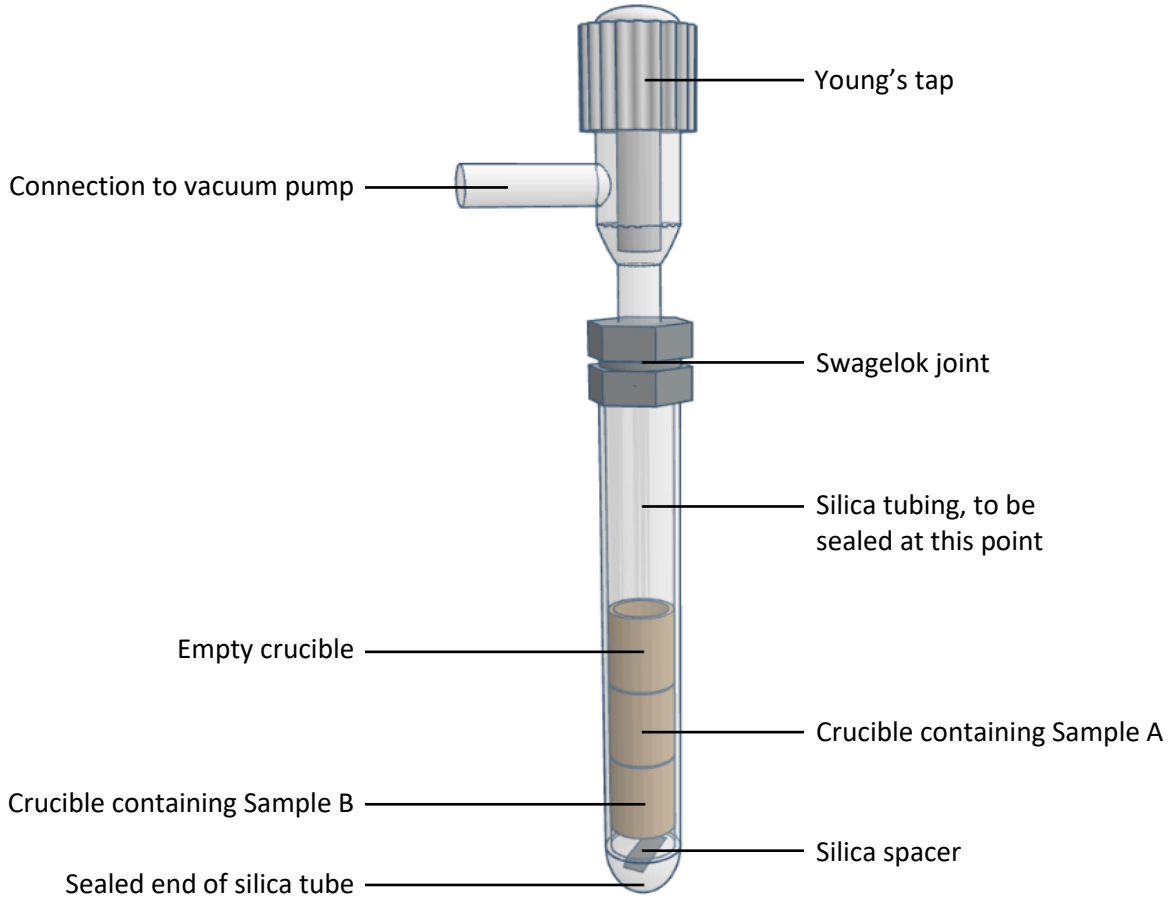

Figure 29 A labelled illustration of a silica tube loaded with crucibles containing pelletised powder samples, ready to be sealed with an oxypropane flame to create a vacuum ampoule.

After weighing, grinding, and pelletising as above, within the glovebox, the samples are placed into alumina crucibles, themselves then placed within a silica tube. The tube has been pre-sealed at one end, such that it presents like a test tube. A small piece of silica is added to the base of the tube such that the crucibles rest above it. The spacer separates the crucibles from the sealed end, to prevent any alumina thermal expansion upon heating from rupturing the weakened sealed end of the tube. An empty crucible is placed on top to cover the samples and to prevent any spillage. A Swagelok union is employed to seal the open end of the tube, fitted with a Young's tap adapter. With the tap closed, the apparatus, Figure 29, maintains an inert nitrogen atmosphere within the tube such that it can now be safely removed from the glovebox without exposure to air.

Connecting the side arm of the Young's tap adapter to a vacuum pump and slowly opening the tap exposes the tube to a dynamic vacuum. An oxypropane blowtorch is used to seal the middle of the tube, between the crucibles and the Swagelok union. The result is a silica ampoule, sealed under vacuum and containing samples which have been manipulated without exposure to air throughout this process. Ampoules are heated in a box furnace as described previously.

Once the heating cycle has completed and the ampoule cooled to room temperature within the furnace it is returned to the glovebox. The ampoule is broken to retrieve the samples within, which are reground in a pestle and mortar and analysed by XRD. In cases where the product is not stable in air, such as some binary materials in *Section 2.3 - The Syntheses of Binary Compounds*, and some precursors in *Chapter 5*, XRD may take place in a sealed sample holder to maintain an inert atmosphere. This is discussed in greater detail in the next section. The grinding and heating cycles are repeated until the XRD results are consistent, and the reaction deemed to have reached completion.

The ampoule method cannot be used for reactions that will evolve a gas, as this may pressurise and explode the silica tube during heating. Secondly, if a precursor has a melting point similar to or lower than the desired reaction temperature, a lower temperature heating cycle will be performed first to begin the reaction and convert the sensitive material to a more thermally stable state, before re-grinding, re-pelletising, and heating to the desired temperature to continue the reaction. This was the case for the synthesis of Cu_2S in *Section 2.3.6*, and in many instances of MALM doping where elemental selenium or sulfur are employed to balance reaction stoichiometry. Materials which have previously melted are difficult to extract from the crucible and to re-grind, and may also damage both the sample and the crucibles, so temperatures should be carefully selected to avoid this.

Purification of MALMs is difficult due to non-solubility and usually not attempted in practice, so eliminating the need for purification by ensuring sample purity beforehand is a preferable approach. Great care is therefore taken to ensure the accurate weighing of precursors using a four decimal balance, and that the materials used are themselves of high purity, ideally purchased from a supplier. The use of elemental precursors is avoided where possible due to uncertainties of purity due to surface oxidation (particularly of metals). In the case where the use of elemental precursors is unavoidable, such as the synthesis of Na_2Se in *Section 2.3.5*, pellets or 'shots' are used preferentially to minimise the effect of surface degradation, and all manipulations take place within a glovebox.

Unless stated otherwise, syntheses of MALMs and other precursors herein are undertaken using this general procedure, whereby any exceptions are discussed in the relevant sections.

2.2 Analytical Techniques

2.2.1 X-ray Diffraction

Powder X-ray Diffraction (PXRD)* is a rapid and powerful analytical process within materials chemistry to investigate the bulk structure of a crystalline material. PXRD employs X-rays, high frequency high energy electromagnetic radiation with a wavelength of 0.01 to 10 nm. The process takes place within a diffractometer, which consists of three main parts: a source which generates and monochromates X-rays, a sample plate to hold and often rotate a crystalline and finely dispersed powdered sample, and a detector to measure X-rays diffracted by the sample.

XRD is used heavily within this research as a rich source of quantitative and qualitative sample information. Uses include, but are not limited to: determining the presence of a target material within a sample, gauging the completeness of a reaction, assessing the purity of a product, and extracting parameters such as the dimensions of a unit cell, or the bond angles between atoms within it.

2.2.1.1 A Short History of Diffraction

Diffraction is a phenomena that occurs when waves interact with a slit or obstruction, resulting in an attenuation of the wave. All electromagnetic radiation travels in waves, as does sound, and other species such as atoms, electrons and neutrons which exhibit wave-like behaviour. Waves travel in oscillating straight lines, but may reflect, refract, or diffract when interacting with matter.

Diffraction refers to the bending or interference of waves when encountering obstacles or openings that are comparable in size to the wavelength of the wave. The concept was proposed by physicist Christiaan Huygens in 1690 in a theory of propagating wavelets within the wavefront of a wave interacting with a slit or corner, changing direction slightly. This was an attempt to explain why sound waves can bend around obstructions, such as around an open doorway, despite travelling in straight lines. He extended this theory to account for light, which he proposed must also travels in waves because it reflects from mirrors in accordance with his theory of wavelet propagation. He hypothesised that light changes direction when passing through a medium such as water or a prism due to a reduction in the speed of light within the medium. Isaac Newton disagreed on the theorised wave nature of light and favoured a particle theory, arguing that light does not bend around large objects like sound does, forming sharp shadows instead.

* X-ray Diffraction (XRD) is an umbrella term which covers a range of techniques, of which Powder X-ray Diffraction (PXRD) is just one; XRD and PXRD are not the same process. However, within this work all samples are powders, thus all XRD is PXRD and the terms are used interchangeably.

On a smaller scale, it was shown that light can bend through a small single slit. Light and sound behaved similarly, but not identically, and this experiment alone was insufficient to prove light exhibits wave-like behaviour. Newton proposed that the interactions of light with a medium must have a different, so far unknown, reasoning. Due to his prestige, Newton's hypotheses prevailed.

It wasn't until the famous 'double slit' experiment in 1801, long after the deaths of Huygens and Newton, that physicist Thomas Young confirmed Huygens's principle and provided the most convincing evidence that light does indeed travel in waves. Young's work laid the foundation for new research into the phenomena of diffraction, inspiring studies on other types of electromagnetic radiation such as X-rays.

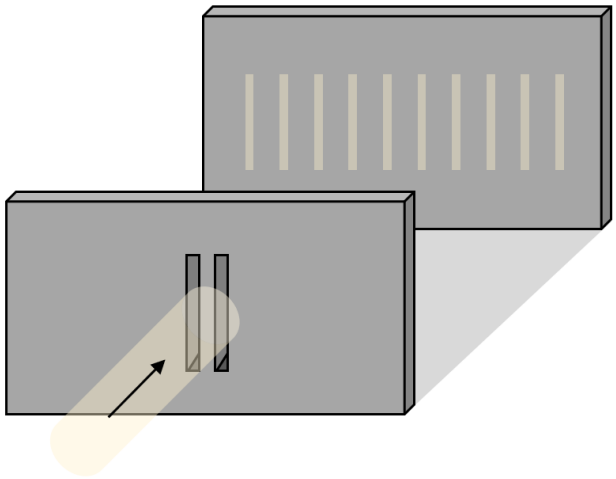

Figure 30 *An illustration of Young's double slit experiment. Coherent light interacts with two slits, producing multiple lines of light on a screen behind the slits.*

As shown in Figure 30, Young passed visible light through a single slit to produce coherent light, that which is all in-phase. Exposing this coherent light to two very narrow closely positioned slits produces two sources of coherent light behind the slits, which propagate in waves away from the slits until they reach a surface. Multiple lines of resulting light are visible, because the two coherent light sources interact with each other to produce areas of converging constructive and destructive interference, illustrated in Figure 31b. The amplitudes of waves are summative, and when phases are aligned the overlapping waves reinforce each other through combination of their amplitudes; resulting in constructive interference, illustrated in Figure 32a. Conversely, when the trough of one phase meets the crest of another, the anti-aligned waves will destructively interfere and cancel out to produce a weaker signal, Figure 32b. The greatest intensity of light is observed when constructive interference is at its maximum. If diffraction did not occur (or if light did not travel in waves) only two lines of light would be visible behind the slits. Huygen's theory, once met with scepticism, was correct, and the wave-nature of light gained widespread acceptance as a result of Young's experiments.

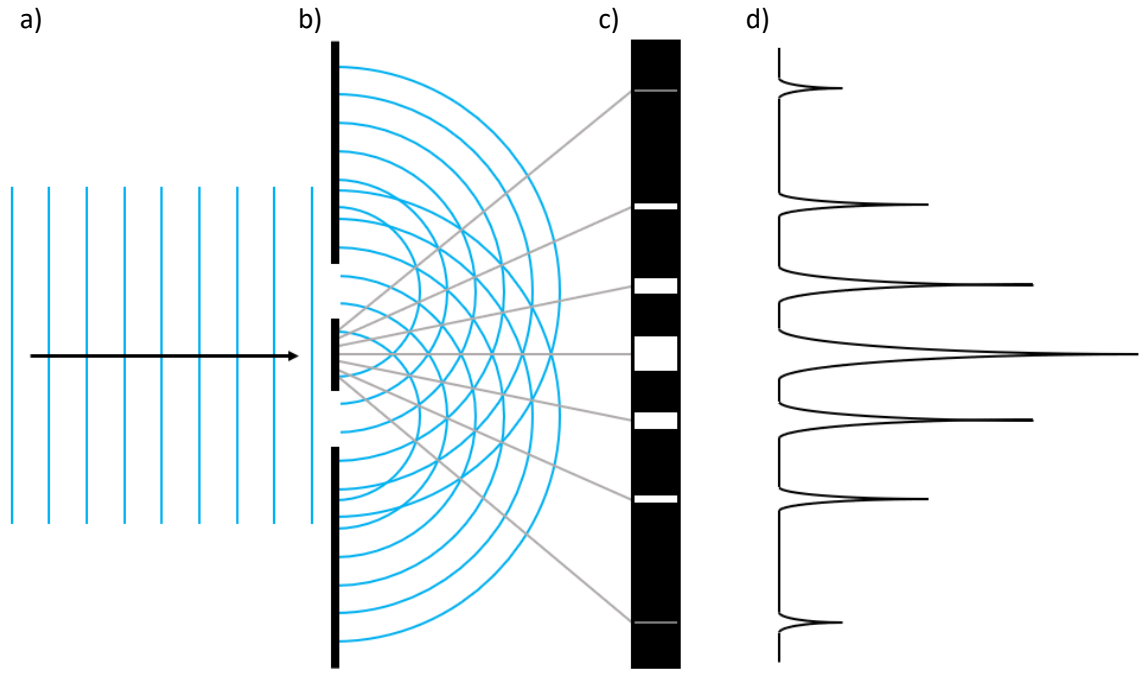

Figure 31 *An illustration of the constructive and destructive interference of light waves in Young's double slit experiment: a) coherent light projected onto two small slits in a wall, b) the diffracted light waves propagating away from the slits, where the grey straight lines show the constructive interference, c) lines of light on a wall behind the slits caused by interference, and d) the approximate intensity pattern of the lines of light.*

It is now known that the reason light and sound diffract through slits of very different sizes is due to wavelength. The wavelength of sound is so large, on the magnitude of metres, that it can diffract from a slit as large as a doorway in the same way light diffracts from a small slit on the scale of millimetres. The same logic can be extrapolated to the atomic scale: diffracting the spacing between atoms of a molecule or lattice requires electromagnetic radiation of an extremely short wavelength on the nanometre scale. The wave nature of X-rays therefore allows diffraction to be used in the study of molecular and atomic structures.

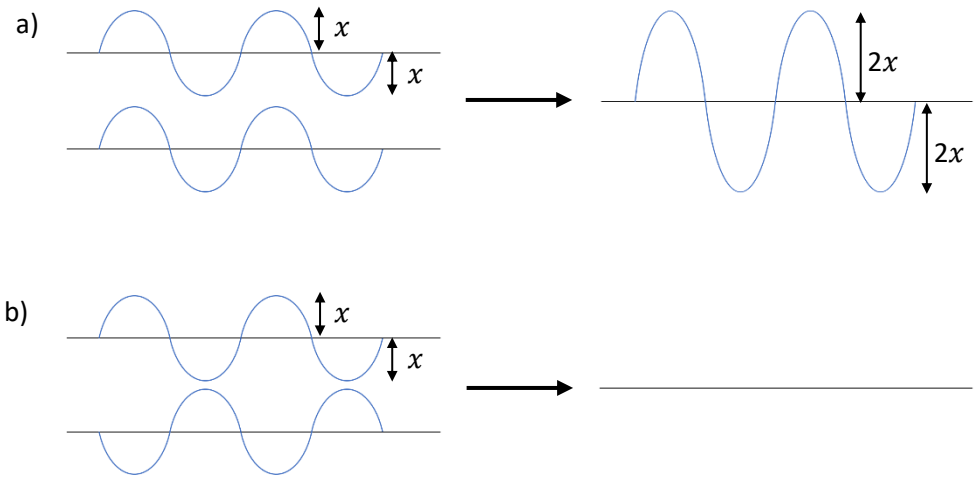

Figure 32 *Wave diagrams to illustrate a) the constructive interference of two in-phase waves with amplitude x producing a resultant wave with amplitude $2x$, and b) the destructive interference of two out-of-phase waves with amplitude x cancelling out to an amplitude of zero and thus producing no resultant wave.*

2.2.1.2 Diffraction of a Crystal Lattice

X-rays were discovered unintentionally by Wilhelm Röntgen in 1895, during an investigation of a cathode ray tube. Exposure of these rays to his wife's hand revealed a shadow of the bones and of her wedding ring. This discovery revolutionised medical imaging, providing a non-invasive view into the human body. Two decades later, Max von Laue observed that this newly-discovered electromagnetic radiation can be diffracted by solid crystalline material.[182, 183] He proposed the spacing between planes of atoms are acting as a diffraction grating, similar to the slits in Young's experiment. Exploring this hypothesis, Laue published the first recorded diffraction pattern, shown in Figure 33, during analysis of zinc sulfide on homemade equipment. This was the catalyst for a new era of analytical chemistry.

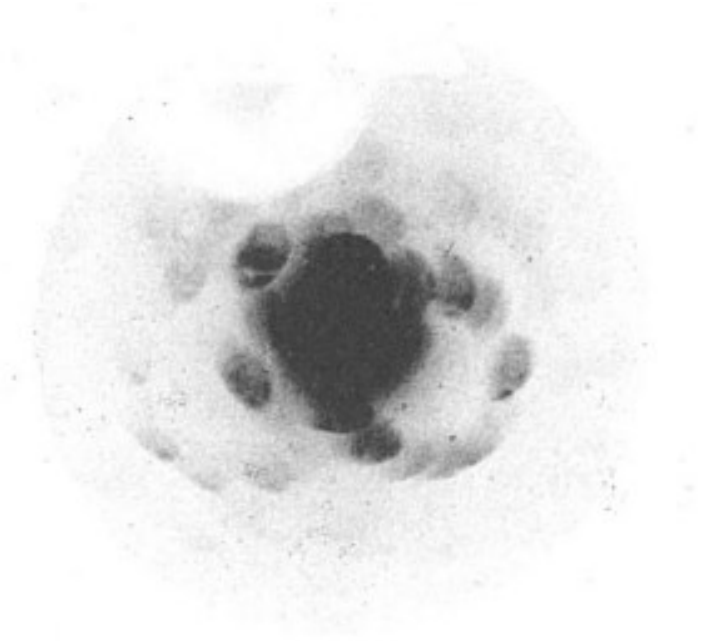

Figure 33 The first X-ray diffraction pattern ever published, Friedrich et al 1912.[183]

The father and son duo of William Henry Bragg and William Lawrence Bragg would lay the foundation for modern X-ray techniques by greatly improving upon the instrumentation involved in the process of detecting diffracted X-rays. The Braggs also simplified the complex mathematics initially proposed by Laue[184] into a more intuitive form, describing the angles at which X-rays will diffract from a lattice. They proposed Bragg's Law, a simple relationship between X-ray incident angle, wavelength and *d*-spacing to describe the conditions under which crystal diffraction will occur, which states the following:

"When the X-ray is incident onto a crystal surface, its angle of incidence, θ, will reflect with the same angle of scattering, θ. And, when the path difference, d, is equal to a whole number, n, of wavelength, λ, constructive interference will occur."

This law ensures that constructive interference only occurs at specific angles, where the path length *d* is an integer multiple of the radiation wavelength. Diffraction will occur only when this law is satisfied, thus for a given wavelength (λ) and atomic spacing (d), one can predict the diffraction angles (θ) at which a material will diffract, without any physical experiments. The law can be written mathematically, the Bragg Equation:

Equation 6 $n\lambda = 2d \sin \theta$

[where n is an integer, λ is the X-ray wavelength, d is the distance between planes of atoms, and θ is the incident/reflected angle of the X-ray beam.]

For their discoveries and contributions in the field of X-rays and diffraction, William Henry Bragg and William Lawrence Bragg (shared), Wilhelm Röntgen, and Max von Laue all received Nobel Prizes in physics.[185-187] Instrumentation has developed greatly since this time, and diffractometers are now common bench-top devices. In the most sophisticated instruments, resolution has increased to the point of identifying a singular atom by X-ray analysis.[188] Detection limits have fallen to the range of hundreds of ppm, and data acquisition can occur on the microsecond scale.[189]

Only crystalline materials will diffract X-rays. This is because X-ray diffraction relies on the combined constructive interference of a regular symmetrical repeating structure within a lattice. If this is not present (if the sample is amorphous) there will be no diffracting interaction with X-rays.

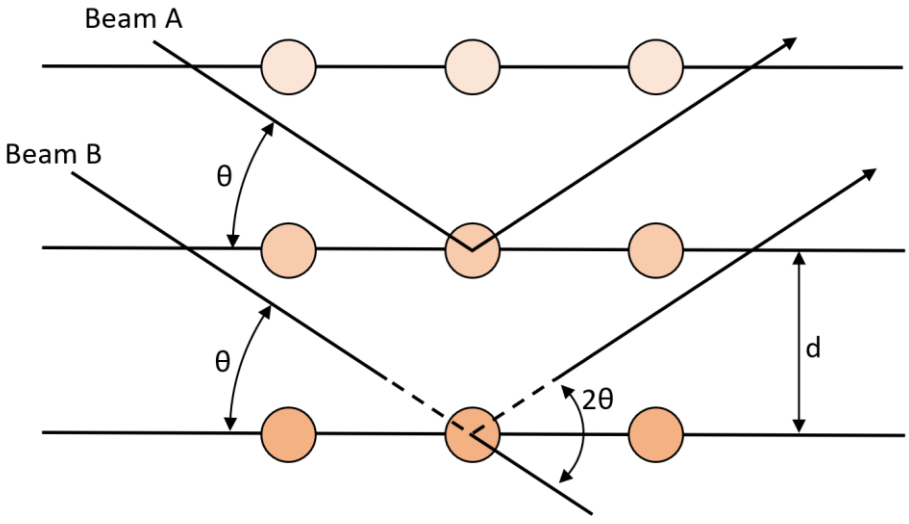

Figure 34 *An illustration of two X-ray waves interacting with parallel atomic planes of a crystal lattice, highlighting the conditions under which Bragg's Law is satisfied and diffraction occurs.*

Figure 34 depicts two parallel X-ray beams, A and B, penetrating a crystal lattice. The angle of incidence, θ, is the same for both beams as they originate from the same monochromatic source and are in-phase. The dashed lines show the extra distance that beam B, which has interacted with an atom deeper within the material than beam A, has travelled compared to beam A. When this extra distance is exactly equal to an integer number of wavelengths of radiation (denoted n), the Bragg Equation is satisfied, and the X-ray beams have been diffracted by the 'slit' between the two atom rows. Constructive interference occurs and the detector, which is scanning all angles, will measure the constructive reflected beams as a 'spot' in 3D space at the angle of diffraction. Constructive interference will occur only at the precise angles where n is an integer. The extra distance travelled by beam B, given by $2d \sin \theta$, is dependent on the distance between the planes of atoms, d, known as the d-spacing.

When translated to a diffractogram the constructive interference will be represented as a peak at the specific angles where diffraction takes place. Observing a range of 2θ angles will reveal all angles where diffraction occurs within the sample material, resulting in a series of characteristic peaks known as a diffraction pattern. Diffraction occurs on multiple atomic planes within the observed material, each responsible for a characteristic peak in the diffraction pattern.

When analysing a homogenous powdered sample, one can assume that all directions of grains are observed across the 'infinite' randomly oriented crystallites. The measurement effectively collapses into one dimension, 2θ, which can be represented as a conventional PXRD diffractogram.

2.2.1.3 Generating X-rays

The process of X-ray generation within the source of an X-ray diffractometer actually begins with the generation of electrons. A filament is heated to a temperature of 2000 °C inside a cathode ray tube. Usually, this filament is made of tungsten due to its incredibly high melting point of 3422 °C, the highest of any metal and far greater than the operating temperature within the cathode ray tube (a feature which facilitates its more common application: incandescent lightbulb filaments). Upon heating, the tungsten filament copiously emits electrons.

Accelerated by an electric field within a vacuum, the electrons are fired onto a metal target, such as copper, molybdenum, iron, or chromium. Each produces characteristic X-ray emission energies, and will be selected accordingly. The incoming electrons are of sufficient energy to dislodge a tightly bound inner shell electron from the target material, and in doing so both the incoming and dislodged electrons leave the atom (the former now of far less energy having transferred this to the latter) leaving behind a vacant hole. This is an energetically unfavourable state, and the hole is immediately filled by an outer shell electron, releasing energy in the form of a photon of X-ray radiation.

Each metal target has its own characteristic spectrum of emitted X-rays, an example shown in Figure 35. The distinct peaks are the result of outer shell electrons occupying the vacant inner shell holes produced by the accelerated electrons. The wavelength of these peaks corresponds to the electron's movement between shell, more specifically the difference between the energy level it originated from and the energy level it dropped to. The characteristic radiation is classified as K, L, or M depending on whether the hole filled was in the first shell, second shell or third shell respectively. These are then further classified by where the electron that falls into it originated; 'α' if from an adjacent shell (such as 2 → 1) , or β if from a non-adjacent shell (such as 3 → 1). The two most prominent peaks are usually the Kβ which results from a 3*p* electron filling a vacant 1*s* hole, and the Kα peak which results from a 2*p* electron filling a 1*s* hole. The Kα radiation is actually a closely spaced doublet, consisting of $K\alpha_1$ and $K\alpha_2$ in a 2 : 1 ratio, due to spin-orbit coupling in the 2*p* orbitals from which the demoting electron originated. As they are so close in energy (that distinguishing them requires very high resolution instrumentation), they are often treated one emission peak.[†]

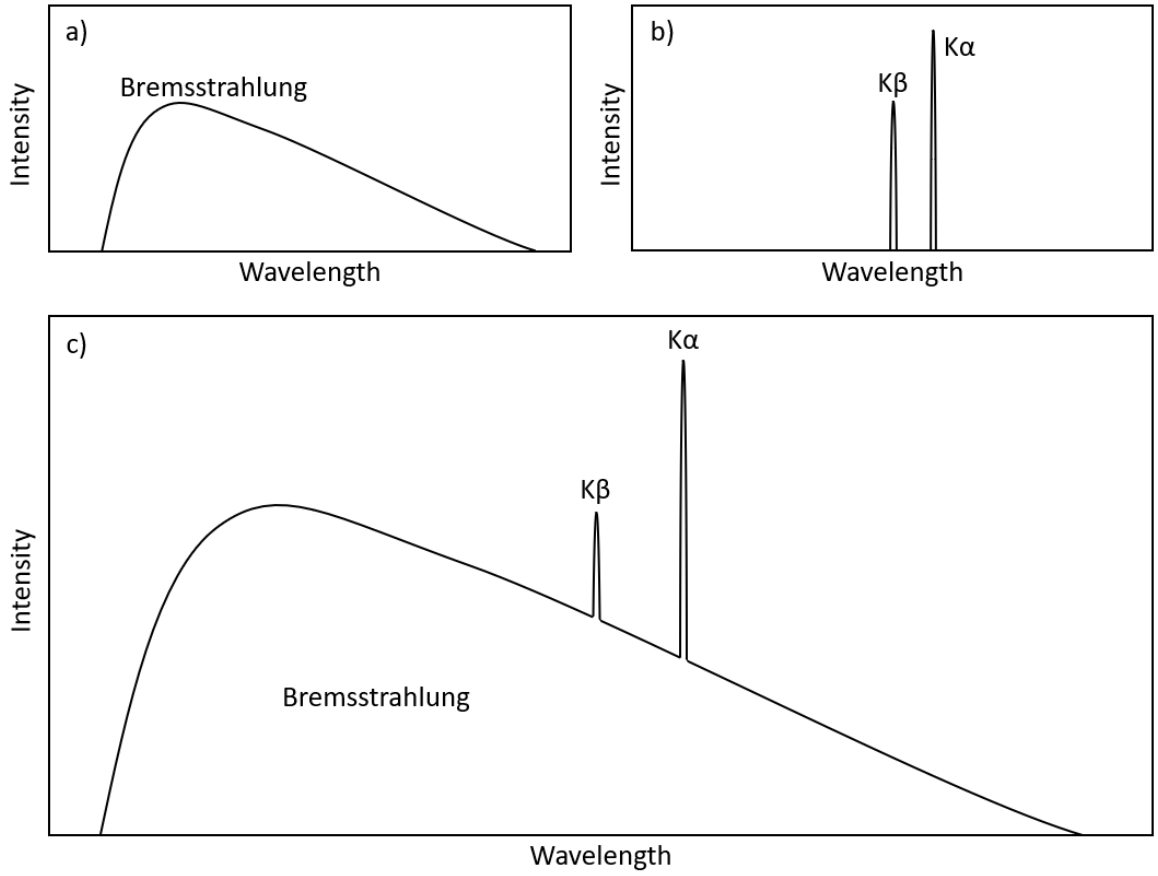

Figure 35 An illustration of the radiation emitted as the result of bombarding a metal target with accelerated electrons, where a) is the Bremsstrahlung 'braking energy' radiation, b) is the characteristic radiation of the metal source, and c) is the resulting total output radiation. Other characteristic peaks are omitted for simplicity. Not to scale.

[†] Sometimes denoted $K\overline{\alpha}$, indicating a weighted average of $K\alpha_1$ and $K\alpha_2$.

The Bremsstrahlung, German for 'braking energy', is a broad peak spanning most of the X-ray spectrum. When an accelerated electron passes close to a metal atom's nucleus but does not strike it, the electron is electrostatically attracted to the nucleus and deviates slightly from its original trajectory, as if briefly orbiting the nucleus. It continues away from the nucleus, but the energy lost from this 'braking' interaction is released as a low wavelength X-ray photon, which on a macro scale comprises the Bremsstrahlung radiation, Figure 35b. This radiation makes up 80 % of the X-ray output; but it is a by-product, serves no purpose and is filtered out as part of monochromation.

If the voltage accelerating the electrons is too low the characteristic radiation will not be present as the electrons are of insufficient energy to dislodge a core electron from the metal, but if the voltage is too large the Bremsstrahlung will overwhelm the characteristic peaks. A sweet spot therefore exists for each metal source to produce the optimum desired characteristic radiation.

The raw emitted X-rays contain a broad spectrum of wavelengths and must be filtered down to just the desired wavelength (in this example, Kα), in a process known as monochromation, Figure 36. Monochromation is essential in PXRD to ensure only a single wavelength of X-ray is utilised. X-rays of different wavelengths will diffract different values of path length *d*, thus disagree on diffraction angles and their resulting diffractograms. A single wavelength normalises the wavelength component of the Bragg Equation, maintaining consistency and predictability in diffraction experiments. A complex system of mirrors and lenses filter out the undesirable Kβ radiation and the Bremsstrahlung, leaving just Kα. This is the X-ray radiation that will be used in the diffraction experiment.

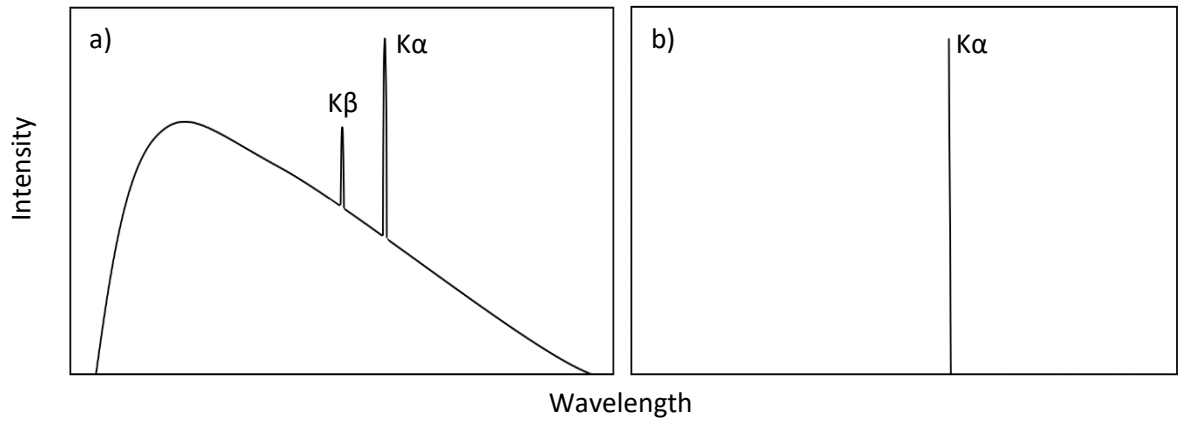

Figure 36 An illustration of the monochromation of the X-ray emissions of a metal source, removing the Bremsstrahlung and Kβ to target Kα radiation: a) the 'raw' radiation containing the Bremsstrahlung, Kβ and Kα radiation, and b) the resulting monochromatic Kα radiation. Other characteristic peaks are omitted for simplicity. Not to scale.

2.2.1.4 The Diffraction Measurement

A powdered sample is finely ground and dispersed upon a sample holder (usually made from polymethyl methacrylate, PMMA, a non-diffracting material to prevent competing interference of the holder in the pattern). The powder may also be held in place suspended upon thin double-sided tape, or a thin film of grease. Whatever their composition, both the sample holder and the tape/grease should be amorphous to prevent any competing diffraction from these external materials, which could not only disturb the pattern of the sample but often completely overwhelm it. A similar procedure is undertaken for air-sensitive samples, except that the sample holder has a domed lid transparent to X-rays to seal the sample within an inert atmosphere, and is prepared in a glovebox. This is explored in more detail in *Section 2.2.1.7 - Air Sensitive X-ray Diffraction.* In any case, care should be taken to ensure a flat, evenly distributed layer of solid sample with no loose powder atop.

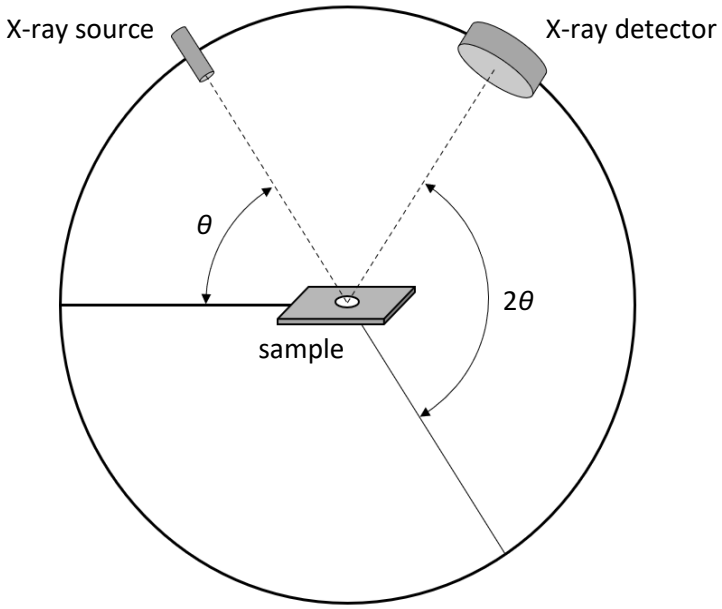

Figure 37 An illustration of a typical powder X-ray diffraction experiment with Bragg-Brentano geometry.

Inside the diffractometer, the sample holder is placed on a central support, around which the X-ray source and detector rotate to measure angles of diffraction. A powdered sample is assumed to contain an infinite number of crystallites containing randomly oriented grains, so the diffractometer needs only to measure diffraction in one dimension. Figure 37 illustrates Bragg-Brentano geometry, a common diffractometer setup.[190] In this geometry the sample is mounted at the centre of a goniometer, receiving X-rays from a stationary source at angle θ, while the detector rotates at a fixed radius to collect diffracted radiation at angles of 2θ.

When the detector, (usually a solid-state device) receives X-rays upon itself, diffraction is occurring at its exact current 2θ angle. This is translated to the computational software as an electrical current, represented to the user graphically as a plot of 2θ against diffracted X-ray intensity.

2.2.1.5 Refining a Powder Diffraction Pattern

The analysis of a powder X-ray diffractogram to ascertain its structure and composition, usually in comparison to a known pattern, is termed its 'refinement'. This employs computational software such as the General Structure Analysis System II (GSAS-II),[191] used widely in this work. If the target material is already documented in literature or its crystallographic parameters are otherwise known, a PXRD pattern can be obtained from this information. This is done by either constructing the structure manually within GSAS-II from precise tabulated unit cell data, or acquisition from a database of structures (such as the International Crystal Structure Database,[192] ICSD) as a Crystallographic Information File (CIF, a file format for storing crystallographic structures), and imported into the refinement software. If the target material is not reported in literature, a similar material may be imported as a logical first step towards solving the observed pattern,[‡] and adjusted to better fit the observed data. Powder diffractograms often contain more than one material. In this case, each individual material (or 'phase') within the observed pattern will produce its own characteristic set of reflections, and each requires its own CIF to be modelled in the refinement.

The calculated model must be manipulated in order to match that which is observed, adjusting parameters such as unit cell dimensions or atom positions. Dutch crystallographer Hugo Rietveld developed a procedure to fit a calculated pattern to an observed pattern by a least-squares process.[193] The 'Rietveld refinement' method compares datasets on a point-by-point basis, attempting to reduce the difference between the observed and calculated patterns at each data point. This method was developed for neutron powder diffraction data but popularised for X-ray powder diffraction in 1977.[194] The process is automated; the user selects one or more parameters to be refined and the software then makes changes to those values for a given number of cycles until an improvement in fit is achieved, translated visually onto the calculated diffraction pattern.

The aim of Rietveld refinement is to generate a diffraction pattern from a structural model to match the observed patten. Using refinement software, the user can modify and fit known patterns as close as possible to the observed pattern in order to determine the observed structure. How closely these models agree is called the 'goodness of fit'. Rietveld refinement employs a least squares statistical procedure whereby the program aims to minimise the sum of squared differences between the observed intensities and the calculated intensities, Equation 7. The smaller this value, the less difference exists between the calculated and observed data sets, thus the better the goodness of fit of the refined data.

[‡] Herein the term 'observed' diffraction pattern will refer to the pattern obtained from the diffractometer, and 'calculated' diffraction pattern will refer to the modelled pattern.

Equation 7 $$S = \sum(I_{observed} - I_{calculated})^2$$

[where S is the sum of the squares differences, $I_{observed}$ is the intensity of the observed X-rays, and $I_{calculated}$ is the intensity of calculated (modelled) X-rays.]

Goodness of fit can also be measured using the weighted-profile reliability factor, R_{wp}, another statistical method to gauge how closely the observed and calculated data sets match. Throughout this work R_{wp} values are reported as a representation of goodness of fit. The weighted profile reliability factor, Equation 8, is the square root of the sum of squared differences, divided by the total squared observed intensity and a weight factor. The weight factor, Equation 9, is inversely proportional to the observed intensity.

Equation 8 $$R_{wp} = \sqrt{\frac{\sum w_I (I_{observed} - I_{calculated})^2}{\sum w_I (I_{observed})^2}}$$

Equation 9 $$w_I = \frac{1}{| I_{observed} |}$$

[where R_{wp} is the weighted-profile reliability factor, and w_I is the weight factor].

These goodness of fit indicators can be adjusted by the user to sum over all data points, or to sum over certain regions where diffraction density is highest. This may be employed when the background of the observed pattern is particularly noisy, such that comparison to the flat simulated background of the calculated pattern produces an inaccurately large R_{wp}. In this situation, measuring the difference only on areas of significant density (peaks) will negate the negative effects of the noisy background and give a truer indication of fit. R_{wp} is given as a percentage where 0 % implies an identical match on every data point. In practice, an R_{wp} value of < 10 % is considered a good match and < 5 % considered excellent. All R_{wp} values given within this work are calculated over all data points.

Alongside statistical values such as R_{wp}, GSAS-II illustrates goodness of fit graphically with a difference line on the diffractogram; the difference between the calculated and observed intensities at a given 2θ angle. Any deviation from a flat line indicates a disagreement between the observed and calculated patterns and should be accounted for during the refinement process if possible. A refinement is considered complete when a good fit is achieved visually and statistically.

In PXRD diffractograms within this work, observed X-ray diffraction data is uniformly represented by small blue circular data points, modelled calculated data is plotted as a green line, the background plotted as a red line, and the goodness of fit gauging “difference” plot is represented by a grey line beneath the given plot.

2.2.1.6 Sample Preparation and Instrument Settings

All XRD patterns reported in this work are those of powdered samples. Regardless of the composition of the mixture or the state of completion of the reaction, preparation was the same for all air stable samples. The powder was finely ground to ensure a small particle size, allowing all diffraction angles of the bulk composition to be measured due to the random orientation of the homogenised particles. Once ground, the sample was dispersed onto a Bruker PMMA low-background silicon wafer sample holder, atop a very thin layer of Dow Corning dimethyl siloxane high vacuum grease.

Powder X-ray diffraction patterns were recorded using a Bruker D2 Phaser at room temperature using Bragg-Brentano optics geometry. A CuKα X-ray source (λ = 1.54056 Å) was used, a common wavelength choice for benchtop diffractometers in materials chemistry to probe the crystal scale. A beam slit of 0.6mm was applied and the beam knife set to a clearance of 3mm above the sample surface. Diffraction was typically measured over a 2θ range of 10 ° to 80 °, at increments of 0.02 °, with a measurement time of 20 to 60 minutes. For a successful or interesting product, a more detailed measurement over the course of 12 – 16 hours was obtained by increasing the collection time at each increment, and halving the increment to 0.01 °. Diffraction was recorded and diffractograms produced by Bruker DiffracSuite software, and Rietveld refinements performed using General Structure and Analysis Software II (GSAS-II).[191]

2.2.1.7 Air Sensitive X-ray Diffraction

Air sensitive materials can often still be analysed by in-air diffraction, albeit for a much shorter scan time. This was the case in *Section 2.3 - The Syntheses of Binary Compounds* where materials degraded on the scale of minutes but could be analysed quickly in air before this occurred. PXRD data was collected more than 100 times faster than those of air-stable MALMs reported elsewhere in this work. Care was taken to ensure the entire scan completes before degradation of the sample occurs.

In the cases of materials where air stability was so poor that even a short 30 second PXRD scan was not possible, or where such a scan was too noisy to allow adequate analysis, a Bruker air-tight domed specimen holder was employed to seal the material in an inert atmosphere. Within a glovebox, a small sample was deposited on a piece of thin 1 mm glass slide, on a thin layer of siloxane high vacuum grease as before. This slide exactly fills a 1 mm well in the base of the sample holder; so that sample sits flush with the surface of the holder without the need to fill the well with an ample quantity of bulk powder to reach the same effect. An X-ray transparent thin PMMA dome was then screwed onto the sample holder. The downside of using the glass plate is a small amorphous peak centred at around

2θ = 21.5 °, but this is still preferable to the (often destructive) use of multiple grams of bulk powder otherwise required to fill the sample holder.

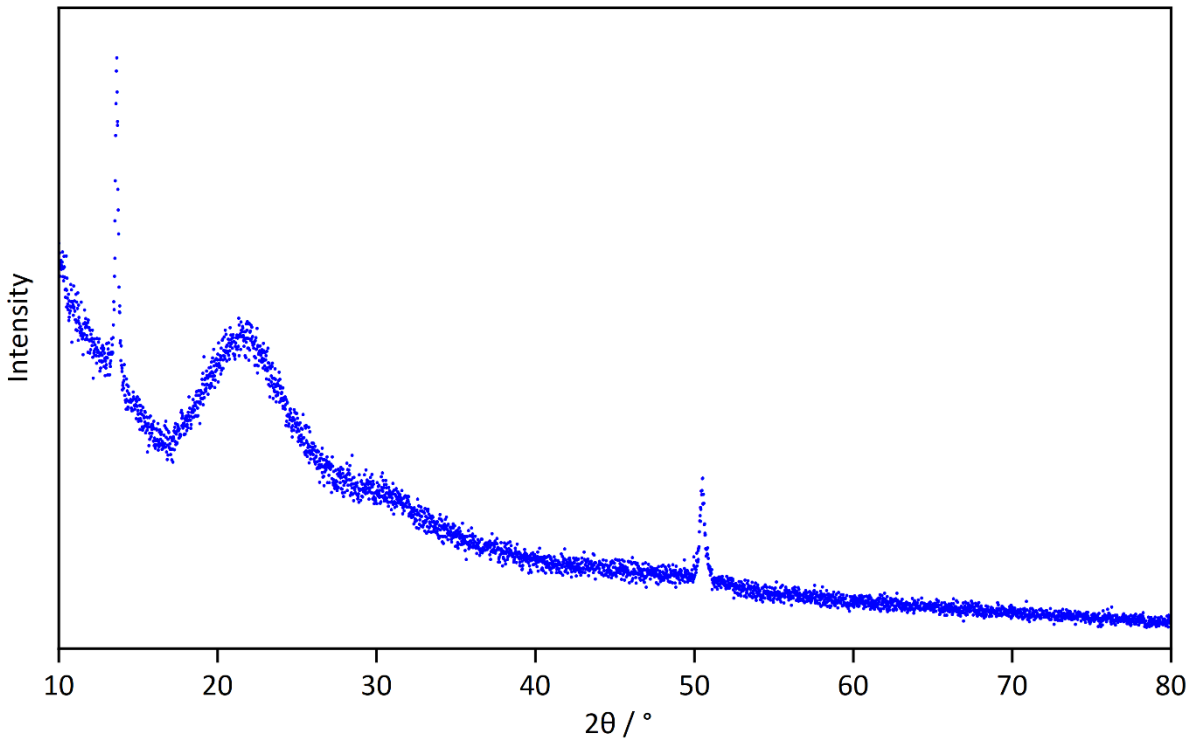

Figure 38 *Powder X-ray diffractogram of an empty airtight sample holder. The small blue circles represent the observed diffracted intensity. The visible peaks are the by-product of the removal of the beam knife and the amorphous reflection is the by-product of the use of a glass plate to maintain correct sample height. No sample or other diffracting material is present within the holder.*

Using this holder, data collection proceeded as normal, with the exception that the beam knife 3mm above the sample must be removed in order to fit the dome within the diffractometer. The purpose of the knife is to block stray radiation from reaching the detector and reduce noise at low angles. Removing the knife results in the emergence of two peaks in the background of data collected using the dome, at 2θ = 13.6 ° and 50.5 °, see Figure 38. These peaks are not avoidable using this method, but can be refined as part of the PXRD background using GSAS-II, therefore do not affect the quality of the refinement.

This method was used heavily in the metathesis syntheses of MALMs in *Chapter 5*.

2.2.2 UV-Vis Spectroscopy

Ultraviolet-Visible spectroscopy is a powerful analytical technique that uses light in the ultraviolet (UV) and visible regions to probe the electronic structures and behaviours of materials. It is a simple, inexpensive and non-destructive technique that returns data in seconds, requiring minimal sample preparation and modest data interpretation. UV-Vis spectroscopy (herein called 'UV-Vis spectroscopy' or just 'UV-Vis') is used within this work to quantitatively estimate the optical band gap of semiconductor materials. It is of particular importance during *Chapter 3*, where the wide band gaps of '325' type MALMs were monitored with UV-Vis spectroscopy to observe any changes when doping to improve conductivity.

2.2.2.1 Principles of UV-Vis

The human eye can interpret the region of electromagnetic radiation between 380 nm and 780 nm, which are interpreted as blue and red respectively. This is the visible light region, and comprises only a small portion of the whole electromagnetic spectrum, Figure 39. Above this can be found the infrared, microwave and radio regions, radiation with low energy and long wavelengths on the scale of bacteria to buildings, all invisible to the eye. Below the visible region, light has high energy and short wavelengths on the scale of large molecules down to subatomic particles. This is comprised of the ultraviolet region which extends from 380 nm to 100 nm, and below that X-rays, gamma rays and cosmic radiation, all also invisible to the eye.

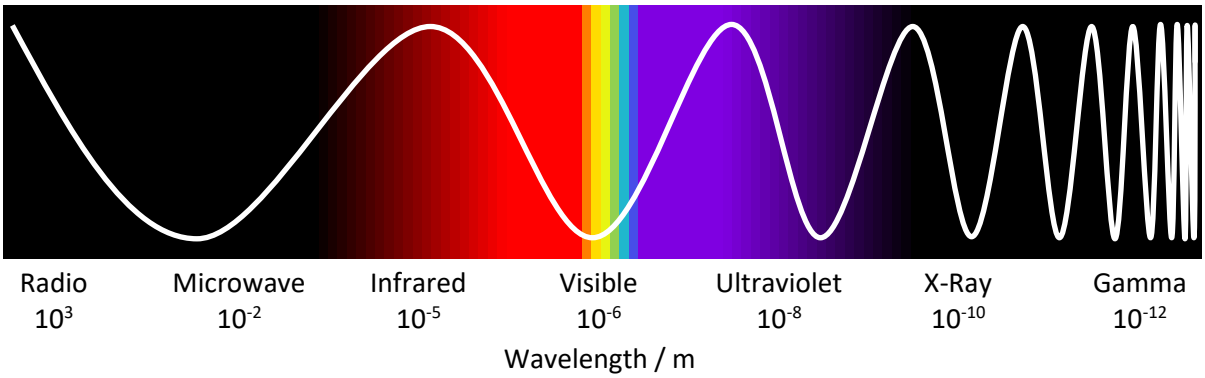

Figure 39 *An illustration of the electromagnetic spectrum containing the seven primary components from long wavelength low energy radio waves through short wavelength high energy gamma radiation. Wavelength scale is illustrative and not to scale.*

UV-Vis spectroscopy is an analytical technique that uses the ultraviolet and visible regions of the electromagnetic spectrum, typically 200 to 800 nm, to probe matters and investigate its interaction with this light. It may be utilised to, among other uses, determine the concentration of a solution, characterise the absorbance or transmittance of a material, measure the colour of a material or study chemical or biological reactions.

UV-Vis is therefore an invaluable technique within all corners of science, and solid-state materials chemistry is no exception. The energy of light in the UV-Vis region is approximately 1.5 eV to 6 eV, which is comparable to that of semiconductor band gaps; thus UV-Vis can be used as a powerful band gap estimation tool.

When light of any wavelength strikes a material, it may be reflected, diffracted, scattered, absorbed, or re-emitted in the form of fluorescence or phosphorescence. It may also induce a photochemical reaction such as a bond breaking. Because light is a form of energy, the material may absorb the energy of the incoming photon, which if sufficient may promote an electron from a low energy state to a higher energy state. In semiconductors, this electron promotion takes place from the valence band to the conduction band, the energy gap between which is denoted the optical band gap. (*Section 1.2.2)*. Incoming radiation must be of equal or greater energy than the band gap in order to promote an electron; thus photons with less energy than the band gap will not initiate an electronic transition. To light of insufficient energy, the material is considered transparent.

The greater the energy of light, E, the lower the wavelength, λ, in an inversely proportional relationship according to Equation 10.

Equation 10 $$E = \frac{h\,c}{\lambda}$$

[where E is the photon energy in Joules, h is Planck's constant (6.6261×10^{-34} J s), c is the speed of light (2.9979×10^{8} m s^{-1}), and λ is the light wavelength in m.]

In practice, E and λ are usually expressed in the more practical units of eV and nm respectively. 1 eV is equal to 1.6021×10^{-19} J, so Equation 10 may be rewritten as follows:

Equation 11 $$E\,(eV) = \frac{1239.841949}{\lambda\,(nm)}$$

2.2.2.2 The Spectrophotometer

Spectroscopy methods vary depending on the aim of the experiment, but some components are fundamental to all spectroscopic setups. A spectrophotometer (the instrument that undertakes a spectroscopy measurement) will always consist of at least 4 principal components: a bulb, a monochromator, a sample holder and a detector. Depending on the type of experiment and the quality of the instrument there may be multiple of each of these components.

All spectroscopic configurations employ a lamp. This bulb is usually mercury or deuterium and must generate a broad band of wavelengths that span the ultraviolet and visible regions of the electromagnetic spectrum. Deuterium lamps are most intense in the UV region, whereas mercury favours the visible region. spectrophotometers will commonly employ multiple bulbs and change between them over the course of an experiment to optimise intensity over all wavelengths.

The next important component is the monochromator. Spectrophotometer bulbs produce a broad light spectrum but only one wavelength is of interest at a given moment of the experiment, so the monochromation process must ensure only this wavelength is incident on the sample, and all others eliminated. It must therefore adjust continually over the course of the experiment. The process of monochromation is similar to that which was previously described for X-rays, and uses a variety of gratings, prisms and lenses to disperse the incident light and filter for one wavelength. State of the art spectrophotometers will employ multiple monochromators in series to further refine the light, reducing the possibility for stray light to enter the system.

All spectrophotometers have a sample compartment, which may be a cuvette holder if liquid or a clamp to secure solid substrates such as a contained powder or a thin film. This part depends entirely on the desired experiment and even the position within the instrument may vary.

Finally, akin to PXRD, a detector converts light into electrical signal. It should, like the bulb, operate over a broad band of UV-Vis wavelengths and produce low noise. Example detector types include the photomultiplier tube which amplifies the signal, useful for low intensity light where sample absorbance is high. Other types include silicon diode detectors which excel over a wide range of wavelengths, and indium gallium arsenide detectors which operate best in the near-infrared region.

2.2.2.3 The Spectroscopy Measurement

Liquid samples are by far the most common use case of UV-Vis spectroscopy, where absorption is the primary interaction with light, and reflections and scattering are minimal. UV-Vis is useful in determining the concentration of a liquid sample by first measuring its absorbance. The absorbance, A, is a unitless metric defined by the log of the ratio of light that interacts with the sample, I_0, versus that which passes through it, I, according to Equation 12. This value is related to the extinction coefficient, ε, a characteristic value of a material's ability to absorb light at a given wavelength, and also to the concentration of the sample, c, and the length of the sample path through which the light must travel, l, according to Equation 13, the Beer-Lambert law.

Equation 12 $A = \log (I_0 / I)$

Equation 13 $A = \varepsilon c l$

As discussed, there are various types of spectrophotometer set up, but a common example to probe liquids is shown in Figure 40 below. The illustration depicts a single beam spectrophotometer set up to measure the absorbance of a liquid sample. The user must first place a reference (usually the solvent) and record a background scan before then replacing the reference with the sample in question and scanning again. The spectrophotometer subtracts the background from the sample data to eliminate any absorption by or artifacts relating to the solvent. The reference is treated as 100 % transmission (or 0 % absorbance, again assuming negligible reflections). An alternative is the double beam setup, where the incoming beam is split to pass through a reference cuvette and a sample cuvette in parallel, performing the same calculation and giving the same end result but without the requirement to change cuvettes between measurements.

Liquid samples, handled in cuvettes, are also homogenous, allowing for straightforward measurement with little concern for non-uniformity or variations in intensity, as one would expect for example on a thin film.

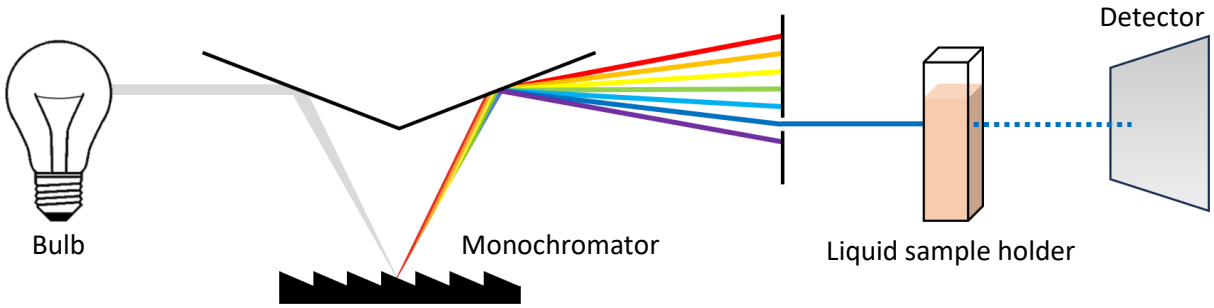

Figure 40 *An illustration of a single-beam liquid sample spectrophotometer setup. A bulb produces a broad band of UV-Vis radiation which is filtered down to a single wavelength by a monochromator. The resulting light is passed through the sample compartment which contains a homogenous liquid sample in a cuvette. Light which is not absorbed is recorded by the detector. Not to scale.*

For solid samples however, of which this work exclusively contains, the UV-Vis process is similar but has some major differences. There is, for example, no path length nor concentration applicable to a solid material interacting with light within a spectrophotometer. While some rare exceptions exist such as single crystal thin films, solid UV-Vis typically measures reflection rather than absorption. In liquids reflections are minimal and can often be assumed to be negligible, but when analysing solid samples reflections and scattering are not only a significant interaction but often the primary and cannot be ignored. Reflections and scattering are recorded in the reflectance mode of a spectrophotometer.

Reflections in solid-state UV-Vis may be specular or diffuse. The former is the reflection of light from smooth and uniform mirror-like surfaces, where all light is reflected at an angle of reflectance equal to the angle of incidence. The latter results from reflection from inhomogeneous irregular surfaces such as films or powders where light is scattered at random angles. As such, for solid samples an integrating sphere may be employed to correct for this, see Figure 41. The sphere walls are made of a highly reflective matte coating which radiates reflected light around the sphere, such that the whole sphere receives an equal, average, 'integrated' radiance upon all of its surface, measured by the detector. Between the solid sample and the detector is a baffle, a physical wall of reflective surface which prevents light reflected from the sample from reaching the detector before it has achieved at least two reflections from the sphere walls.

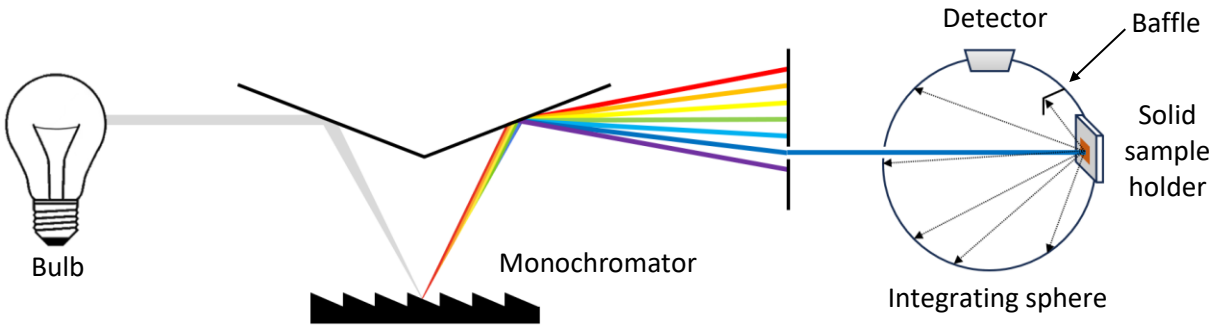

Figure 41 *An illustration of a solid sample spectrophotometer setup. A bulb produces a broad band of UV-Vis radiation which is filtered down to a single wavelength by a monochromator. The resulting light enters the integrating sphere and hits the sample, usually a film or powder. Reflected light is radiated equally around the highly reflective sphere, measured by the detector. The baffle blocks non-integrated reflections. Not to scale.*

Solid samples are not always chemically homogenous, as can be assumed for liquid samples. Reflections measured from a thin film may differ greatly at two neighbouring points on the film due to variations in uniformity and chemical composition across the surface, and experiments should be performed in triplicate to obtain an average. This work utilises powder samples, which unlike films can be described as chemically homogeneous, such as after grinding (but still cannot possess a homogenous surface such as to produce specular reflections). One can assume homogeneity of a powder sample, but only if it has been thoroughly well ground and will not degrade or decompose in air during the course of the experiment, so a single UV-Vis scan for a powder sample is usually sufficient. In the cases where UV-Vis spectroscopy is used herein, these conditions are met, therefore chemical homogeneity is assumed in all cases.

Finally, rather than a 100 % transmission reference taken either before the sample or in parallel, solid samples instead require a 100 % reflectance reference. This involves placing a diffuse relefectance standard 'mirror' in the solid sample holder which is scanned across the desired wavelength range to determine the background for the main samples in question.

2.2.2.4 Tauc Plots for Band Gap Estimation

All UV-Vis measurements within this work were performed with the intention of semiconductor band gap estimation. This is a simple procedure which can be computationally automated for ease and repeatability. Raw diffuse reflectivity data is manipulated to produce a Tauc plot, from which the band gap may be estimated using a straight line extrapolation of a linear region. The method was developed by Jan Tauc in 1967 to estimate optical band gaps of crystalline germanium samples.[195, 196]

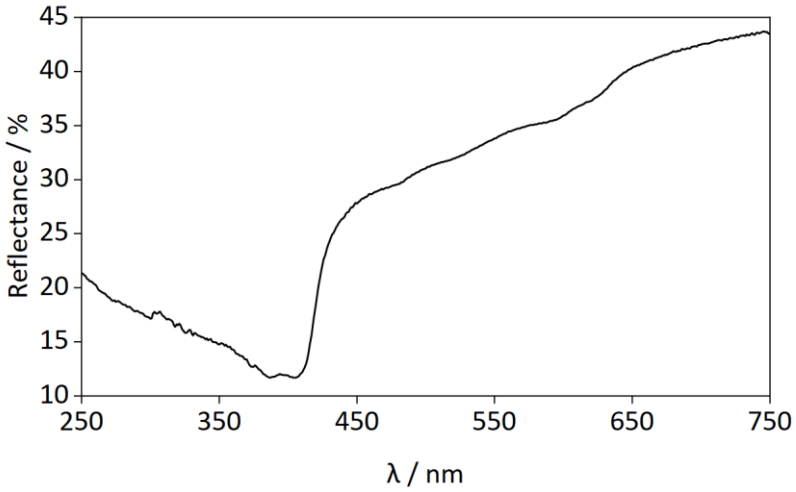

Figure 42 *An example of UV-Vis spectroscopy raw diffuse reflectance data obtained from a material with target composition $Sr_3Sc_2O_5Cu_2Se_2$. The drop-off in reflectance can be observed at approximately 400 to 430 nm.*

A diffuse reflectivity plot, of which an example is shown in Figure 42, is a measurement of the diffuse reflectivity of a solid sample over a range of wavelengths. The visible region shows moderate reflectivity (no MALMs of this type demonstrate particularly high reflectivity in any region), which drops to low reflectivity in the UV region where light is of sufficient energy to promote electrons across the band gap, thus absorption prevails. This drop-off can be analysed by means of a Tauc plot.

A Tauc plot compares photon energy, $h\nu$, to $(\alpha h\nu)^2$, where h is Planck's constant (6.6261×10^{-34} J s), ν is frequency in s^{-1}, and α is the attenuation coefficient: a metric for how easily a material may be penetrated by light,[197] with units cm^{-1}. This plot enhances the drop-off that resides between the high reflectivity and low reflectivity areas (the wavelengths with and without the sufficient energy to promote an electron across the optical band gap) producing a clear linear region. This linear region, if extrapolated to the x-axis, yields the energy difference between the valence and conduction bands (the band gap) at the value of x where $y = 0$.

The x-axis values of *hv*, in J, are derived from the relationships between *hv* with *E* (in eV), and λ (in nm) as described in Equation 14:

Equation 14 $$E = \frac{1239.841949}{\lambda} = h\nu$$

The y-axis values of $(\alpha h\nu)^2$, unitless, are more complex. The attenuation coefficient, α, can be derived from its relationship with the Kubelka-Munk[198] function of diffuse reflectance, f_R (Equation 15), and a scattering coefficient, *s*. The scattering coefficient exists to account for the non-homogeneity of powder samples. It does not however vary significantly with the energy of light, and so can be assumed constant and omitted, according to Equation 16.

Equation 15 $$f_R = \frac{(1 - R)^2}{2R}$$

Equation 16 $$\alpha = s f_R \approx f_R$$

[Where f_R is the Kubelka-Munk function of reflectance, *R* is the measured diffuse reflectance, α is the attenuation coefficient and *s* is the scattering coefficient.]

Plotting *hv* against $(\alpha h\nu)^2$ produces the Tauc plot, an example of which is shown below in Figure 43:

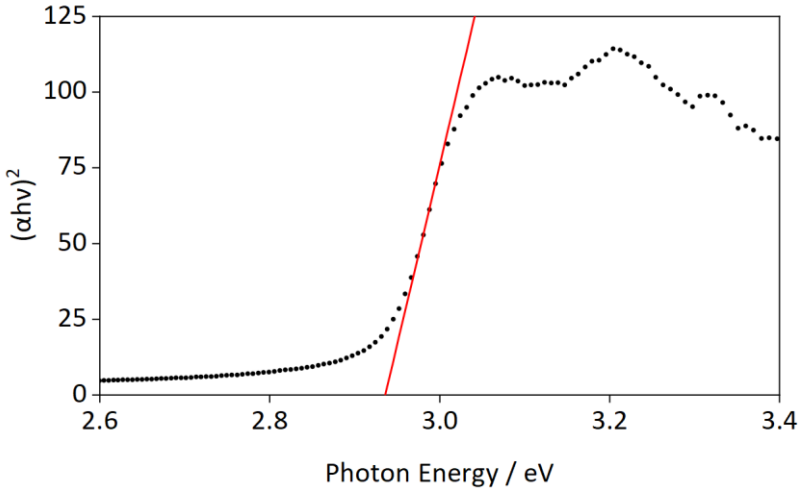

Figure 43 *An example of a Tauc plot, created from the diffuse reflectance data depicted in Figure 42 from a material with target composition $Sr_3Sc_2O_5Cu_2Se_2$. The linear region can be extrapolated (red line) to estimate the optical band gap from the x-axis, which in this case is 2.94 eV, corresponding to 422 nm.*

The first derivative of every pair of $(\alpha h\nu)^2$ data points within the linear region was taken, where the largest difference in derivatives marks the point of steepest decline. A linear line was plotted passing between these two points, creating a pseudo 'best fit' line that may be extrapolated to the x-axis to assess the band gap. In practice the band gap is calculated using the tangent gradient where $y = 0$, not read directly by eye from the x-axis, but the axis allows for visual representation of this estimation. All Tauc plots within this work are therefore always plotted such that the y-axis begins at $y = 0$.

2.2.2.5 Sample Preparation and Instrument Settings

All UV-Vis data within this work is that of solid powder samples. For all samples the preparation was identical. A sample was first thoroughly ground within a pestle and mortar, and was loaded into a homemade plastic sample holder within which it could be mounted vertically into the spectrophotometer, at the back of the integrating sphere, akin to the setup illustrated in Figure 41 on page 103. Diffuse reflectance was measured using a Perkin Elmer Lambda 750 S Spectrophotometer, equipped with deuterium and tungsten lamps and a 100 mm integrating sphere. For most samples a wavelength range of 250 to 750 nm was measured, at intervals of 1 nm. Any deviations to this procedure are explained in the relevant figure captions. A 100 % reflectance 'autozero' reference scan was recorded first using a diffuse reflective standard mirror. A guide light within the diffractometer was employed when loading each sample to ensure uniform central mounting of the powder sample within the line of the beam, both for consistency and to maximise the exposure of each sample to light (and thus maximise reflectance). Data was recorded and processed using the Perkin Elmer UVWinLab software package. Diffuse reflectance data were used to calculate the Kubelka-Munk function, which was assumed to be approximately equal to the attenuation coefficient (see Equation 16), and plotted against wavelength (converted to photon energy in eV) to produce Tauc plots from which band gaps were estimated using extrapolation of the resulting linear region, on Microsoft Excel.

2.2.3 Electrical Conductivity

Measuring the electrical properties of a device is a vital characterisation technique in solid-state materials chemistry. With this information, materials such as thin films or LEDs may be tailored for specific applications by the tuning of their electrical conductivities. To understand the electronic properties of conducting materials such as MALMs, especially in the case of doping to improve conductive performance, as explored in *Chapter 3* and *Chapter 4*, a reliable and repeatable method of measuring sample conductivity is essential.

2.2.3.1 Conductivity, Resistivity and Resistance

In practice, one cannot directly measure a materials conductivity, σ (S m^{-1}), and must instead first calculate the resistivity ρ (Ω m). Resistivity is the reciprocal of conductivity according to Equation 17:

Equation 17 $$\sigma = \frac{1}{\rho}$$

Conductivity and resistivity are intrinsic properties; those which are inherent to the material and do not vary with shape and size. Resistivity, which is also not directly measurable, is calculated from resistance R (Ω), a property which is proportional to resistivity, but which varies with the materials length L (m) and area A (m^2):

Equation 18 $$\rho = \frac{A\,R}{L}$$

Resistance is calculated using Ohm's Law, the fundamental relationship between resistance R (Ω), voltage V (V), and current I (A):

Equation 19 $$R = \frac{V}{I}$$

Combining the above, conductivity can therefore be expressed as a function of resistance, area and length (Equation 20), three simple properties which can be easily calculated in a laboratory setting.

Equation 20 $$\sigma = \frac{L}{A\,R}$$

Methods to measure a materials resistivity involve first measuring the physical dimensions of the device to quantify the relevant dimensions, then placing digital multimeter probes onto the sample, applying a constant current, and measuring the resulting voltage from which resistance can be derived.

2.2.3.2 Two Probe vs Four Probe Resistivities

There are numerous experimental approaches to calculate resistivity. Three common resistivity measurements discussed here are the two probe technique, the linear four probe technique, and the van der Pauw four probe technique.

The two probe (also called the 'two point' or 'two wire') method is the simplest but least accurate method with which to measure the resistivity of a device. Two multimeter wires are attached to the DUT (Device Under Test), a current is applied,[§] the voltage measured, and the resistance calculated.

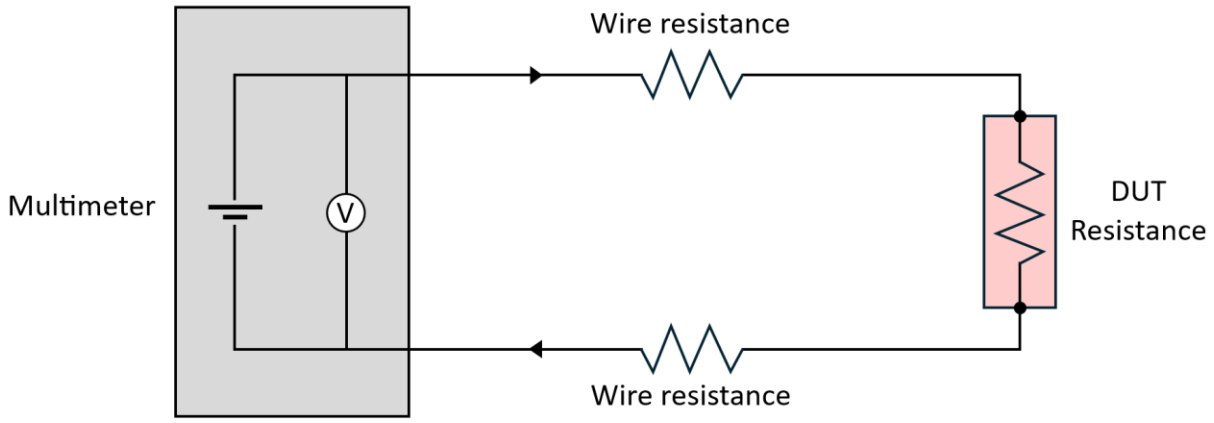

Figure 44 An illustration of the two point probe method for measuring the resistance of a material.

As illustrated above in Figure 44, the two probe setup is simple but the lack of accountability for wire resistances presents a significant flaw in the technique. The resistance measured across the DUT includes the wires through which the current flows, and it therefore is impossible with this setup to determine what proportion of the resistance is due to the wires. The test current is slowed by the wires, causing a voltage drop, and crucially therefore a difference in voltage readings between the DUT and the multimeter, resulting in error.

Typical wire resistances range from 10 mΩ to 1 Ω, therefore the two probe method is not recommended for devices with very low resistance because the measured resistance may be swamped by (or worse, primarily composed of) wire resistances. Resistances between the probes and the material surface produce a similar problem.

[§] Applying a constant current and measuring the resulting voltage is one method to measure resistance according to Ohm's law. One may also apply a constant voltage and measure the resulting current, to exactly the same effect. Herein, the only former is described, but for any determination of resistance either route is acceptable and valid, and remains the decision of the user.

To overcome the flaws of the two probe method, the linear four probe method introduces a second circuit to measure and offset the wire resistances. The original 'force' circuit of a constant current and measured voltage remains the same, but two further probes in a 'sense' circuit measure the voltage directly across the device, separate from the force circuit but in a linear fashion[199] as illustrated in Figure 45.

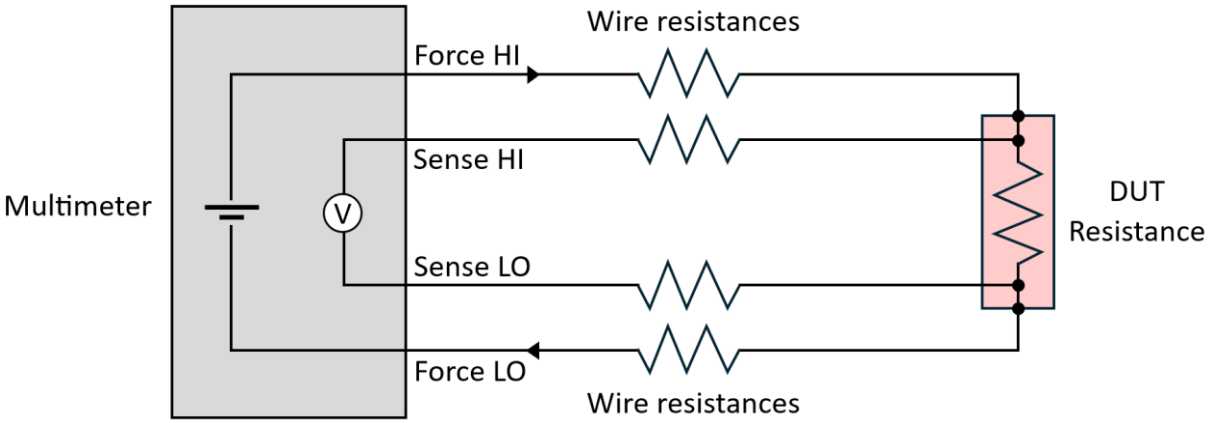

Figure 45 *An illustration of the four point probe method for measuring the resistance of a material. Here 'HI' and 'LO' are standard notation for the positive and negative ports of a digital multimeter respectively.*

Measuring the DUT voltage directly using the sense wires eliminates any voltage drop due to the resistivity of the wires because the current-providing force probes no longer measure the voltage, nor are the voltage-measuring sense probes sourcing any current. Any current flowing through the sense leads is assumed to be so small (on the scale of picoamps) as to be negligible, that said the sense circuit should be as small as possible to further reduce the effect of wire resistances. Device resistances measured using this technique should use the distance between the sense leads as the length value, not the length of the whole device as in the two probe technique.

In both the two and four probe techniques, the device is assumed to be rectangular or a bar as the force probes source a current (or voltage, depending on setup) across the whole length of the device. In practice, devices are rarely perfectly rectangular or cylindrical, so deviations in shape and size will introduce error using the above techniques. In solid-state chemistry for example, including within this work, materials are often prepared and densified as thin cylindrical pellets, whose surface nor edge comprise a 'length' parameter akin to that required for the above methods.

A third technique, the van der Pauw four probe resistivity test, is the most versatile and reliable of the three discussed methods, and the most forgiving in terms of sample dimensions. Where the linear four probe method improves upon the two probe method by eliminating wire resistances, the van der Pauw method outperforms both, by no longer requiring that the device be rectangular or cylindrical with probes placed at either end of the length of the DUT.

2.2.3.3 The van der Pauw Technique

Within this work, the conductivities of pellet samples are derived from four probe resistivity measurements using the van der Pauw technique. This method is simple, precise and versatile, permitting resistivity calculations of samples of varying size, shape and thickness, for values which can be easily converted to conductivity.

Developed by Leo J. van der Pauw in 1958,[200] the van der Pauw technique is a variant of the linear four probe technique designed for measuring the average resistivity of a two dimensional solid sample. Unlike the linear four probe technique, there is no requirement for the probes to be positioned linearly because there is no requirement for the DUT to be rectangular or a bar. For this technique to be valid, the sample must be approximately two-dimensional, significantly wider than it is thin, but may be any two dimensional solid shape with no holes.

In this method, the two force probes and two sense probes are placed around the edge of a 'flat' device, such as an annealed pellet, as close to the perimeter as possible. As before, a constant current is applied through the force wires and the resulting voltage measured through the sense wires to derive the device resistance.

There are five methodological considerations for valid application of the van der Pauw method:[201]

1. The four contacts must be placed on edge of the sample. In a system where the contact pins are 'top down' such as those described in this work, the pins must be placed as close to the edge of the material as possible.

2. The sample must have a flat surface and be of uniform thickness.

3. The sample must not have any isolated holes. It has been shown that the technique is still valid on samples with one hole maximum,[202, 203] but this is not relevant to materials within this work.

4. The sample must be homogenous and isotropic.

5. The contact area of a probe must be at least an order of magnitude smaller than the sample surface.[204]

Figure 46 highlights the versatility of the van der Pauw method with regard to shape, depicting four possible device shapes. While symmetry and regularity are preferential for minimal error, all of these shapes are valid devices on which to measure average resistivity using the van der Pauw method.

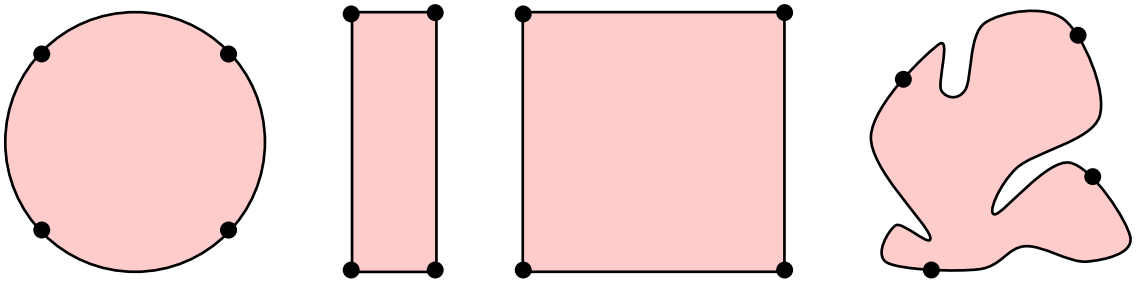

Figure 46 *An illustration depicting four possible valid device shapes for van der Pauw resistivity measurements. The four black circles on the edges of each shape indicate the probe positions.*

As suggested by the lack of requirement for device dimensions to be measured, and in some device shapes the inability to do so, the van der Pauw method measures average resistivity differently to the standard two or four probe methods, using the following formula:

Equation 21 $\rho = R_S t$

[where ρ is resistivity in Ω cm, R_S is sheet resistivity in Ω sq^{-1}, and t is thickness in m.]

Taking a resistance measurement using the van der Pauw technique does not involve passing a current across the body of the shape, but instead along its edge. A current is induced along two neighbouring probes, and voltage is measured across the other two. In van der Pauw notation, the four probe points are numbered 1 through 4, starting with the left topmost point and numbering counterclockwise. A resistance measurement can therefore be described by the following notation:

Equation 22 $$R_{12,34} = \frac{V_{34}}{I_{12}}$$

[where V_{34} is the voltage measured across points 3 and 4 (V_4 - V_3), I_{12} is the current injected at point 1 and removed at point 2, and $R_{12,34}$ is the resistance measured under these conditions.]

The above resistance measurement, $R_{12,34}$, describes probes in a vertical arrangement around the pellet. If combined with another similar experiment in a horizontal arrangement, such as $R_{23,41}$ the sheet resistivity of the sample may be derived from the van der Pauw formula[200], Equation 23:

Equation 23 $$e^{-\pi R_{12,34} / R_S} + e^{-\pi R_{23,41} / R_S} = 1$$

The sheet resistivity value may be made more accurate by expanding the number of constituent resistance measurements that comprise the van der Pauw formula. Firstly, the measurements of $R_{AB,CD}$ and $R_{CD,AB}$ are reciprocals and mathematically equivalent, thus one may calculate an average vertical resistance measurement using the reciprocal permutations $R_{12,34}$ and $R_{34,12}$, and an average horizontal resistance using $R_{23,41}$ and $R_{41,23}$.

Further to this, reversing the probe polarities for each of the four permutations above gives another four permutations, totalling four vertical and four horizontal resistances which may be averaged according to the following equations:

Equation 24 $$R_v = \frac{R_{12,34} + R_{21,43} + R_{34,12} + R_{43,21}}{4}$$

Equation 25 $$R_h = \frac{R_{23,41} + R_{32,14} + R_{41,23} + R_{14,32}}{4}$$

And the revised van der Pauw formula becomes:

Equation 26 $$e^{-\pi R_v / R_S} + e^{-\pi R_h / R_S} = e^{\left(\frac{-\pi R_{12,34} + R_{21,43} + R_{34,12} + R_{43,21}}{4 R_S}\right)} + e^{\left(\frac{-\pi R_{23,41} + R_{32,14} + R_{41,23} + R_{14,32}}{4 R_S}\right)} = 1$$

The circuit diagrams of the eight permutations of probe arrangements are depicted in Figure 47 below, which also shows the numbering of the probe positions and the accompanying '$R_{AB,CD}$' notation:

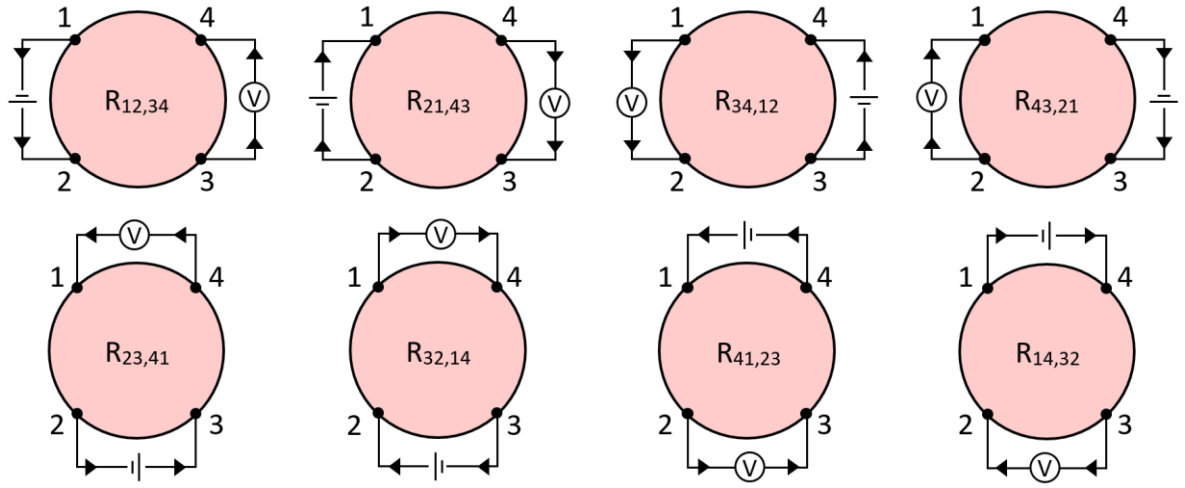

Figure 47 *An illustration of the eight permutations of probe placements in the van der Pauw resistivity technique for a given pellet material. The top row depicts the vertical permutations and the bottom row depicts the horizontal permutations. Probe placements are described by the van der Pauw notation at the centre of each pellet.*

The van der Pauw formula cannot be directly solved for sheet resistivity R_S, so is instead solved by an iterative Newton-Raphson method which uses an estimated starting value of R_S in a formula that quickly converges upon the true value.[205, 206] An initial value of R_S is selected, the mean of R_v and R_h, and the next value in the iteration, R_S^+, is defined as:

Equation 27 $$R_S^+ = R_S + R_S^2 \left(\frac{1 - s^{R_v} - s^{R_h}}{\pi \left(R_v s^{R_v} + R_h s^{R_h}\right)} \right) \qquad \text{where } s = e^{-\pi R_S}$$

[where R_S is the sheet resistivity, R_S^+ is the next value in the series, R_v is the average of the four vertical resistances, R_h is the average of the four horizontal resistances, and s is a variable defined above, to simplify the notation.]

The series usually converges upon average sheet resistivity, R_S, within 5 cycles. For completeness, 20 iterative cycles are performed. The resulting value of average sheet resistivity is converted to resistivity using the formula described previously in Equation 21 on page 111, from which the conductivity of the pellet can finally be obtained according to Equation 17 on page 107.

Equation 21 $$\rho = R_S\, t$$

Equation 17 $$\sigma = \frac{1}{\rho}$$

2.2.3.4 Sample Preparation and Instrument Settings

Electrical conductivity was calculated using annealed pelletised samples. 0.15 g of a completed powder sample was pressed into an 8mm pellet under 2 tonnes, resulting in a pellet thickness of 0.8 g to 1.1 g depending on the sample. The pellet was sealed in a silica ampoule under vacuum and heated, usually 800 °C for 12 hours, to anneal. These pellets differ from the usual 13 mm pellets pressed at 10 tonnes used for ceramic syntheses, as these pellets must be small enough to be annealed within crucibles without breaking.

Pellet thickness was measured after annealing using calipers. At this point, while not relevant to the conductivity measurement, pellet diameter and mass were also recorded to later calculate pellet density. SCP Electrolube Silver conductive paint was applied to four equally spaced points at the pellet edge and surface, such that it resembles a poker chip. This paint ensures minimal resistance between the probe-pellet contact area. The pellet was assembled onto a Sel-Tek Ecopia Spring clip sample board with four gold-coated pogo pins as per Figure 48, connected by copper wires to a Keithley DMM6500 digital multimeter set to 4-wire resistivity mode. The eight resistance measurement permutations were executed to obtain a value of pellet conductivity. For consistency, the sample and pellet were not disturbed during the experiments, only the wire connections to the multimeter.

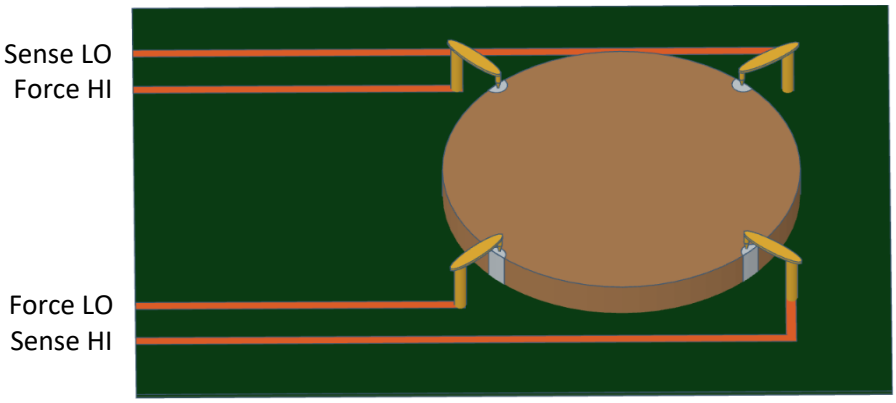

Figure 48 *An illustration of an annealed pelletised sample with silver paint, assembled on a spring clip sample board for a van der Pauw resistivity measurement in the $R_{12,34}$ permutation.*

2.3 The Syntheses of Binary Compounds

The oxides, chalcogenides and pnictides of alkali and alkaline earth metals are essential precursors in many solid-state reactions, and are employed ubiquitously throughout this project. Almost every solid-solid-state reaction herein comprises some combination of binaries, with few exceptions such as metal carbonates or elemental chalcogens. These binaries are usually purchased, in which case details of manufacturer and purity are provided in every case, but often due to price or availability these materials necessitate in-house manufacture. In other cases, the combination of a facile synthetic route and the ease of attaining high purity and yield, warrants in-house manufacture as a faster and greener alternative to purchasing.

Binaries can be synthesised in various ways, and in this section five synthetic routes are detailed for the synthesis of six unique binary materials: the decomposition of $SrCO_3$ to form SrO, the sulfurisation of $SrCO_3$ to form SrS, the syntheses of SrSe and BaSe by reduction of the selenate under H_2 gas, the synthesis of Na_2Se by direct elemental combination of sodium and selenium in anhydrous liquid ammonia, and finally the conventional solid-state synthesis of Cu_2S.

These binary materials are very air sensitive, particularly the group 1 and 2 sulfides and selenides. They will rapidly deteriorate following exposure to air, so in each case the material is synthesised and stored under an inert atmosphere, and strict care is taken to minimise exposure to air at any stage of these processes.

Owing to this air instability, PXRD is performed very fast over a short time scale. The scan length of each respective pattern is therefore a rough indicator of lifetime before impurities begin to appear. All materials described here are air-sensitive, but were found to survive this brief window of PXRD such that analysis could be performed. The high crystallinity of these binaries, resulting from small and highly symmetrical unit cells, is such that this short time scale is more than sufficient to confidently ascertain a qualitative and quantitative assessment of material purity due to intense, sharp reflections. Whilst air-sensitive PXRD equipment was available, as described in Section *2.2.1.7 - Air Sensitive X-ray Diffraction*, in theory permitting a longer and more detailed scan, the irregular background and extraneous peaks associated with this equipment deemed a short in-air PXRD the superior method in these cases. Very large R_{wp} values are observed in this section, for refinements that are clearly phase pure and exhibiting a sufficient fit. This is a result of the fast scan rate and thus large degree of noise in the background. In this section, R_{wp} is not an important or informative metric and should not otherwise detract from a good fit and high purity.

2.3.1 Strontium Oxide, SrO

The preparation of strontium oxide is one of the most widely observed in-house syntheses of a binary metal oxide precursor in solid-state chemistry literature. Despite the low cost of SrO offered by industrial manufacturers, it is very common for solid-state chemistry researchers to produce this compound in-house, for two main reasons inter alia. Firstly, strontium oxide is a significant precursor in the synthesis of every strontium-based quinternary MALM, regardless of structure type (strontium-based 212, 325 and 426 MALMs are approximately 20 %, 30 %, and 40 % strontium oxide by weight, respectively), therefore large quantities are required which validates in-house manufacturing. Secondly the synthesis is straightforward, can be easily scaled and requires simple equipment, and phase purity can be achieved with ease.

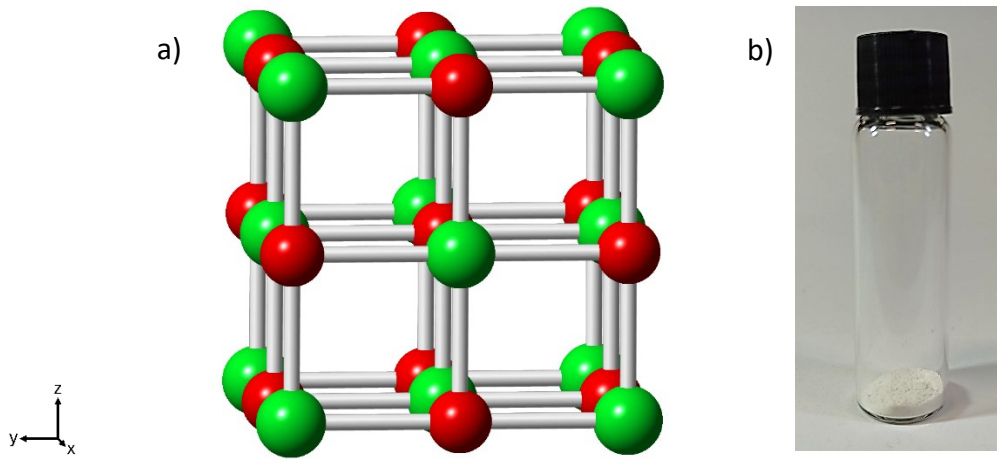

Figure 49 *Representations of strontium oxide: a) an isometric projection of the unit cell, and b) a photograph of a portion of the synthesised sample.*
Colour key: green - Sr, and red - O.

Strontium oxide was synthesised on a 10 gram scale by the calcination of $SrCO_3$ (Merck, 99.9 %) under vacuum.at 1000 °C, according to Equation 28:

Equation 28 $SrCO_3 \rightarrow SrO + CO_2$

The carbonate was finely ground before being loaded into an alumina boat crucible within a large quartz tube sealed at one end. The opening was sealed with a glass joint comprising a neck with a Young's tap adapter, which was attached to a vacuum pump to remove CO_2 formed during the decomposition. The apparatus was placed inside a tube furnace and heated to 1000 °C at 5 °C per minute, under vacuum, for 24 hours. After cooling, the material was opened and reground finely in air before the process was repeated again, totalling 48 hours at 1000 °C.

Using the Young's tap to seal the final product within the vacuum apparatus, the product was transferred to and ground within a nitrogen glovebox. The off-white powder product was extremely fine and readily moved under static charge when handled, rendering grinding and weighing difficult and inaccurate. Whilst XRD analysis at this stage revealed a phase-pure material, degradation occurred extremely quickly, an impurity of $Sr(OH)_2$ appears at 33 % by weight after just 5 minutes of air exposure, and $SrCO_3$ appears over a longer time scale.

It was hypothesised that the above anomalous behaviours were the result of a very small particle size resulting from the aggressive decomposition, thus the product was pressed into 13 mm pellet under 10 tonnes, sealed within a silica ampoule as per conventional solid-state chemistry, and heated to 900 °C to anneal the small particles. Following a final regrind, the static behaviour subsided and the material behaved as expected when handled. XRD analysed confirmed the phase purity of the material had been maintained (Figure 50) and the pre-degradation lifetime significantly increased. $Sr(OH)_2$ no longer appears as a degradation by-product when exposed to air, only $SrCO_3$, suggesting the particle size dictates the degradation product, and that smaller particles preferentially form the hydroxide.

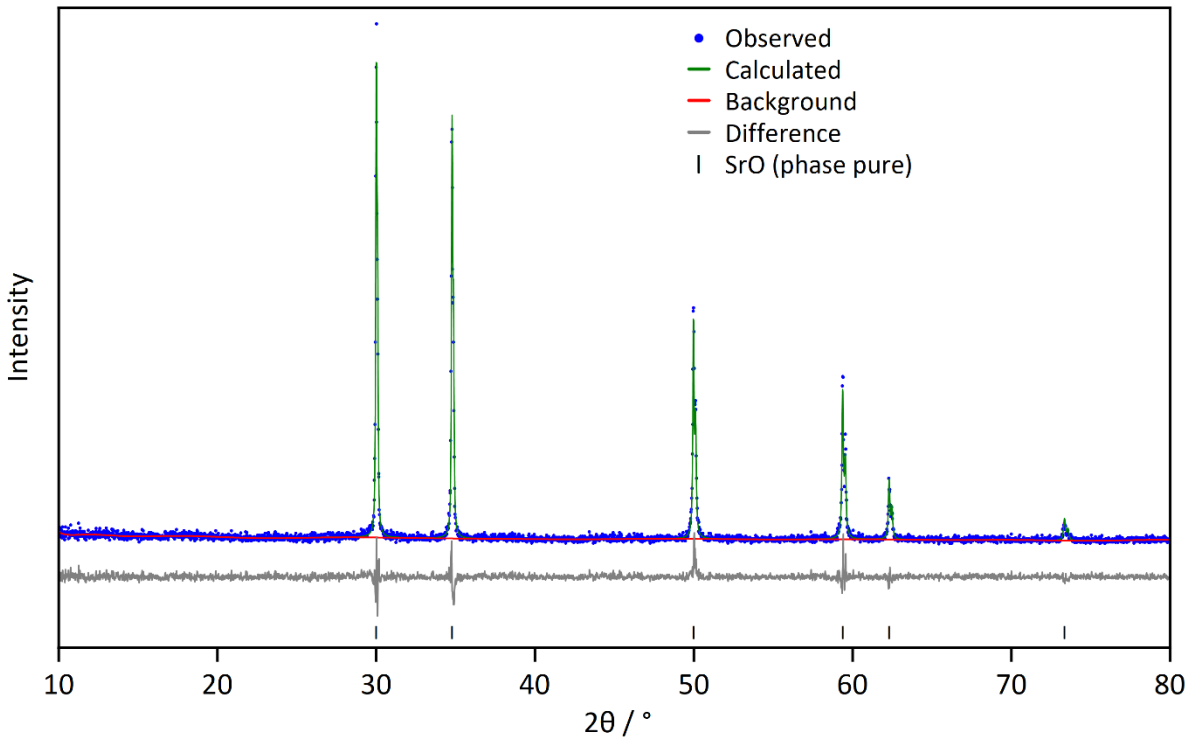

Figure 50 *Powder X-ray diffractogram of material with target composition SrO (space group Fm-3m) after 48 hours of heating at 1000 °C. The small blue circles represent the observed diffracted intensity, the green line represents the Rietveld-refined calculated model, the red line represents the background, and the grey line represents the difference between observed and calculated intensities. The black tick marks show the reflections of the refined model of SrO; no impurity phases are observed.*
Duration: 2 minutes. Data points: 3457. Interval: 0.02 °. GOF: 1.14. R_{wp}: 27.420 %.

2.3.2 Strontium Sulfide, SrS

Strontium sulfide was synthesised on a 10 gram scale by the sulfurisation of $SrCO_3$ (Merck, 99.9 %) using CS_2 (Honeywell, 99.9 %), under N_2 at 850 °C, according to Equation 29:

Equation 29 $2\ SrCO_3 + CS_2 \rightarrow 2\ SrS + 3\ CO_2$

Similar to the preparation of SrO described previously, this synthesis begins with the fine grinding of $SrCO_3$ and placement within an alumina boat crucible in a quartz tube within a tube furnace. A setup is prepared so that nitrogen can flow through a bubbler of CS_2 (currently empty), then through the reaction tube, then through a pair of downstream bubblers containing hydrogen peroxide and bleach respectively to quench any sulfurous products that are formed.

At this point, CS_2, approximately 50 mL, was added to its bubbler. Carbon disulfide is extremely toxic, and care should be taken when handling. Any glassware or PPE in contact with CS_2 was left within a fume hood overnight for the liquid to evaporate. The nitrogen flow was initiated, and the furnace raised to 850 °C at 5 °C per minute for 6 hours. It was found that a single heat was sufficient for the product, a grey powder, to form phase pure (Figure 51) without the requirement for a regrind or anneal.

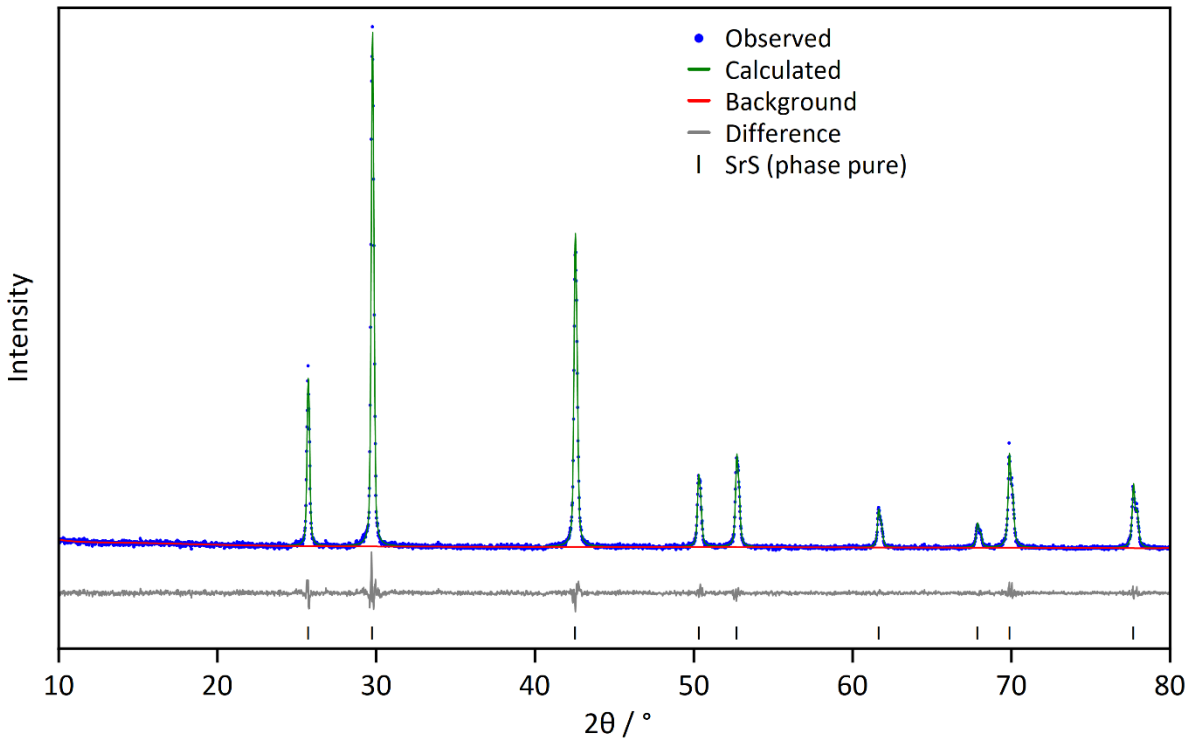

Figure 51 *Powder X-ray diffractogram of material with target composition SrS (space group Fm-3m) after 6 hours of heating at 850 °C. The small blue circles represent the observed diffracted intensity, the green line represents the Rietveld-refined calculated model, the red line represents the background, and the grey line represents the difference between observed and calculated intensities. The black tick marks show the reflections of the refined model of SrS; no impurity phases are observed.*
Duration: 10 minutes. Data points: 3142. Interval: 0.022 °. GOF: 1.08. R_{wp}: 11.142 %.

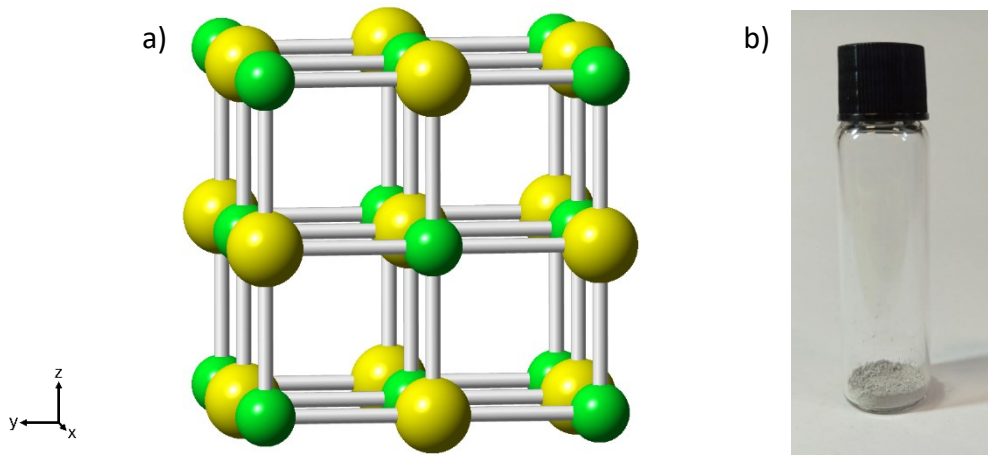

Figure 52 *Representations of strontium sulfide: a) an isometric projection of the unit cell, and b) a photograph of a portion of the synthesised sample.*
Colour key: green - Sr, and yellow - S.

2.3.3 Strontium Selenide, SrSe

There are various reported methods in literature for the synthesis of strontium selenide, SrSe, such as direct elemental combination by solid-state chemistry,[61] synthesis in liquid ammonia,[207] and the reduction of strontium selenate, $SrSeO_4$, under hydrogen.[208] The latter method was employed here.

Whilst group 1 sulfates and selenates (A_2ChO_4 where A = Na / K and Ch = S / Se) are commercially affordable and were purchased for use within this work, the high cost of commercially purchasing the group 2 analogues ($AChO_4$ where A = Ba / Sr and Ch = S / Se) necessitates in-house preparation of the $SrSeO_4$ material also. This is reported via by precipitation in water.[209] Therefore the synthesis of strontium selenide consists of two distinct experimental tasks: the synthesis of $SrSeO_4$, and the reduction of $SrSeO_4$ to SrSe.

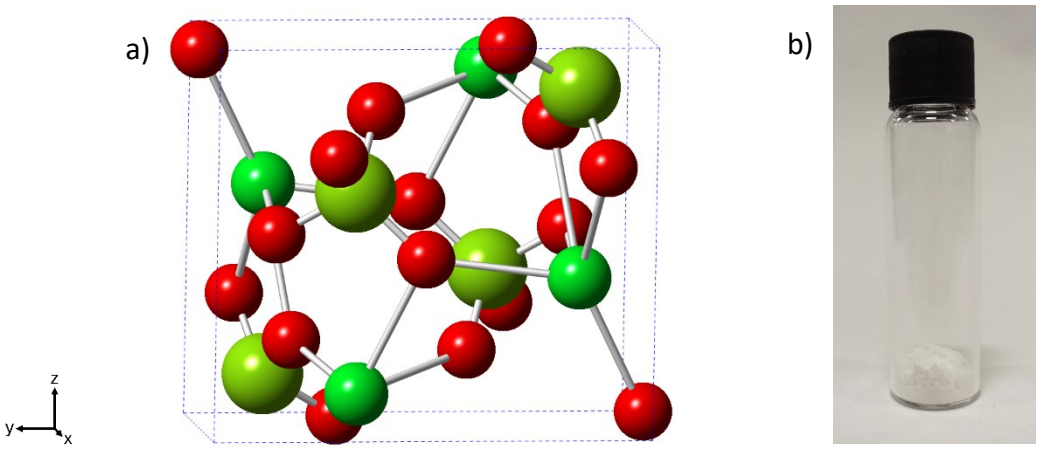

Figure 53 *Representations of strontium selenate: a) an isometric projection of the unit cell, and b) a photograph of a portion of the synthesised sample.*
Colour key: small green - Sr, larger green - Se, and red - O.

Strontium selenate was synthesised on a 23 gram scale by an aqueous-phase displacement reaction between strontium chloride (Alfa Aesar, 99.5 %), and sodium selenate (Alfa Aesar, 99.8 %). These precursors were chosen for their high solubility in water: 54.7 g and 58.5 g respectively in 100 g at 20 °C.[210] When combined in the aqueous phase the two react to form insoluble $SrSeO_4$ alongside the soluble by-product NaCl (0.115 g and 36.0 g respectively in 100 g water at 20 °C). It is the insolubility and subsequent rapid precipitation of $SrSeO_4$ that drives this displacement, according to Equation 30:

Equation 30 $$SrCl_{2\,(aq)} + Na_2SeO_{4\,(aq)} \rightarrow SrSeO_{4\,(s)} + 2\,NaCl_{\,(aq)}$$

100 mL solutions of 1 molar $SrCl_2$ and Na_2SeO_4 were prepared. In an adaptation of procedures previously outlined in literature,[209, 211] the Na_2SeO_4 was added dropwise to the rapidly stirred $SrCl_2$. Precipitation of $SrSeO_4$ was immediately observed, and after complete addition the solution was warmed to 80 °C and held for 2 hours with stirring before it was filtered and washed with room temperature distilled water. The heating step is performed due to the retrograde solubility of $SrSeO_4$,[**] so warming the mixture will favour the solid precipitate form of $SrSeO_4$ rather than the dissolved state. The washing stage was found to be essential, if omitted some NaCl inevitably remains.

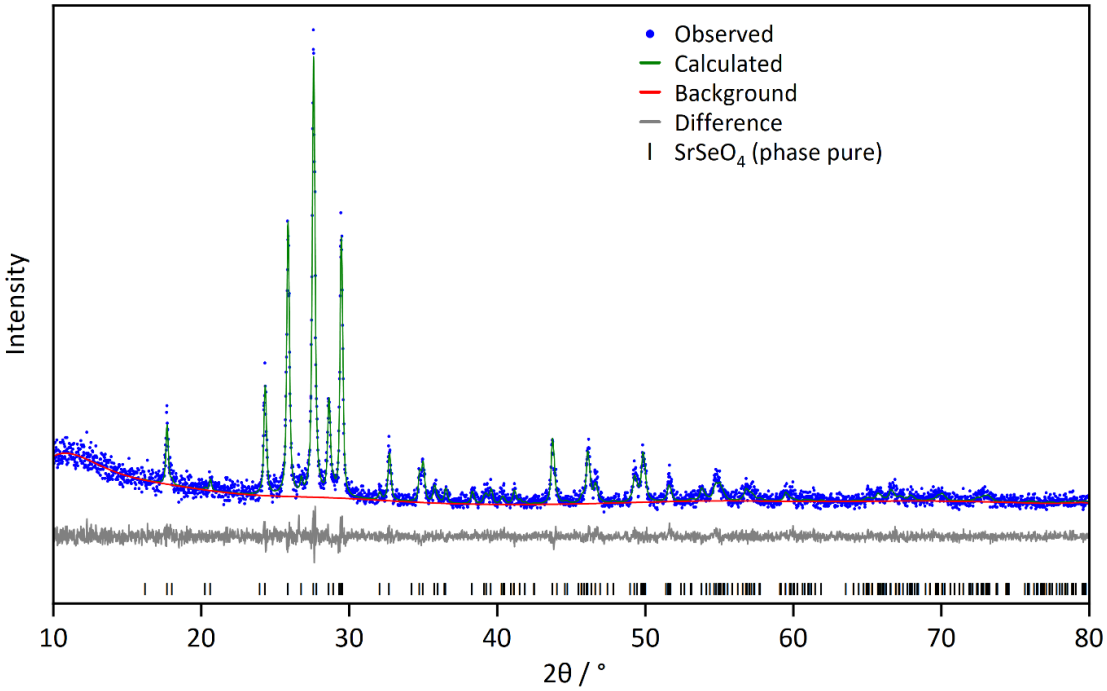

Figure 54 *Powder X-ray diffractogram of material with target composition $SrSeO_4$ (space group $P2_1/n$) after ionic displacement and 2 hours of heating at 80 °C. The small blue circles represent the observed diffracted intensity, the green line represents the Rietveld-refined calculated model, the red line represents the background, and the grey line represents the difference between observed and calculated intensities. The black tick marks show the reflections of the refined model of $SrSeO_4$; no impurity phases are observed.*
Duration: 6 minutes. Data points: 3457. Interval: 0.02 °. GOF: 1.08. R_{wp}: 18.262 %.

[**] Retrograde solubility is an unusual phenomenon whereby a solid substance is more soluble in cold solvent (in this case water) than hot solvent. Usually, dissolution is endothermic, but for some substances (such as $SrSeO_4$,[212] $CaSO_4$,[213] and Li_2SO_4[214]) dissolution is exothermic and thus hot solvents will favour the solid phase over the aqueous phase, according to Le Chatelier's principle.[215]

The washed product is an air stable white chalk-like powder; it was dried at 80 °C overnight in air and then confirmed phase pure by XRD, see Figure 54.

The formation of $SrSeO_4$ was also found to be successful using air-stable and less expensive precursors $SrCl_2{\cdot}6H_2O$ (Alfa Aesar, 99 %) and $Na_2SeO_4{\cdot}10H_2O$ (Thermo Scientific, 99.8 %), according to Equation 31. Due to the waters of crystallisation this method reasonably requires larger quantities of precursor for the same amount of end product, but avoids the use of a glovebox for preparation. The two materials are equally as soluble as their anhydrous analogues.

Equation 31 $SrCl_2{\cdot}6H_2O_{(aq)} + Na_2SeO_4{\cdot}10H_2O_{(aq)} \rightarrow SrSeO_{4\,(s)} + 2\,NaCl_{(aq)} + 16\,H_2O_{(l)}$

Next, using the $SrSeO_4$ synthesised above, SrSe was synthesised on a 5 gram scale by the reduction of $SrSeO_4$ under hydrogen, according to Equation 32:

Equation 32 $SrSeO_4 + 4\,H_2 \rightarrow SrSe + 4\,H_2O$

$SrSeO_4$ was finely ground and loaded into an alumina boat crucible in a quartz tube sealed at one end. The opening was sealed with a glass joint comprising two necks each with Young's tap adapters, one to supply hydrogen and the other to allow its escape. The apparatus was placed into a tube furnace under a steady flow of 5 % H_2/N_2, and was heated for 8 hours at 650 °C. Thermal wool was placed between the furnace-quartz interface to insulate the system and reduce energy wastage. The outlet gas was passed through a pair of bleach bubblers to oxidise any volatile selenides.

After cooling under hydrogen, the material was thoroughly reground in air, and heated again to 650 °C for another 8 hours under hydrogen. The Young's taps allow the entire apparatus to be sealed once cooled and moved into a nitrogen glovebox for grinding and analysis.

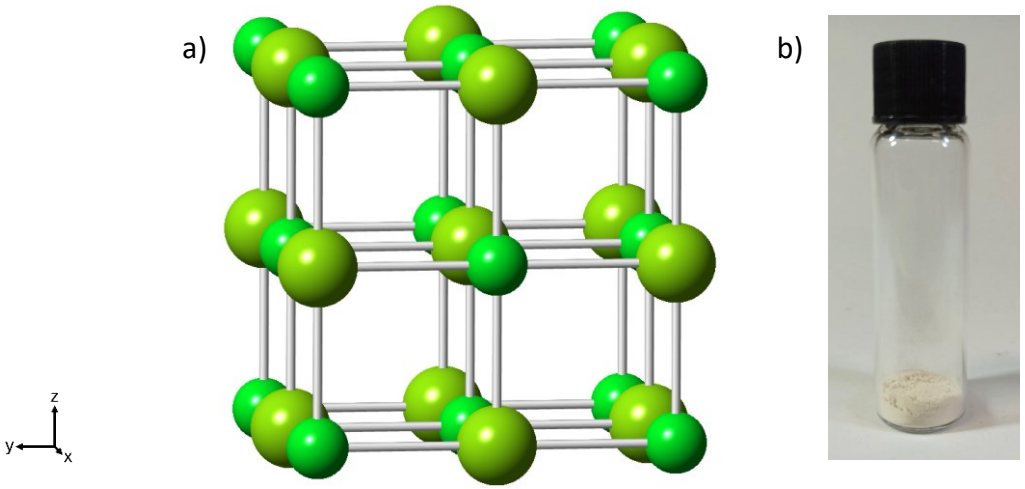

Figure 55 *Representations of strontium selenide: a) an isometric projection of the unit cell, and b) a photograph of a portion of the synthesised sample.*
Colour key: small green - Sr, and larger green - Se.

The resulting product was an air-sensitive beige powder and was confirmed pure by XRD, Figure 56. The reduction is reversible, so if exposed to air SrSe will revert back to $SrSeO_4$. Occasionally, a third heat cycle was necessary to force the reaction to completion and achieve phase purity.

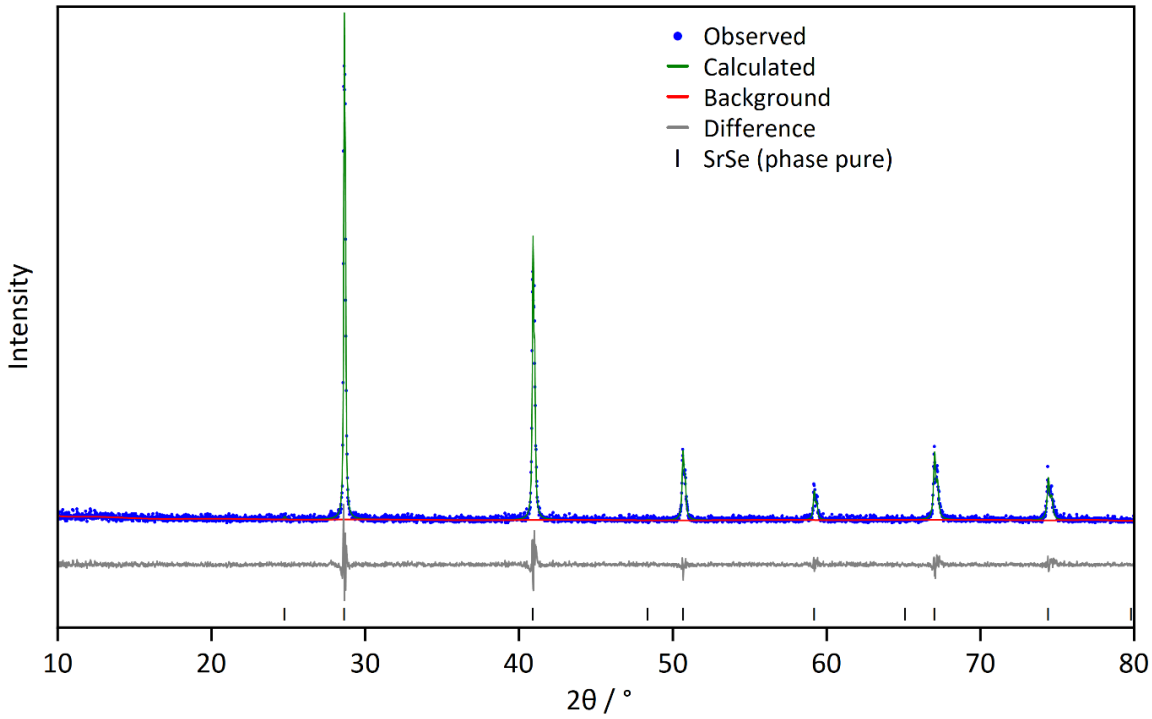

Figure 56 *Powder X-ray diffractogram of material with target composition SrSe (space group Fm-3m) after 16 hours of heating at 650 °C. The small blue circles represent the observed diffracted intensity, the green line represents the Rietveld-refined calculated model, the red line represents the background, and the grey line represents the difference between observed and calculated intensities. The black tick marks show the reflections of the refined model of SrSe; no impurity phases are observed.*
Duration: 80 seconds. Data points: 3456. Interval: 0.02 °. GOF: 1.15. R_{wp}*: 38.988 %.*

2.3.4 Barium Selenide, BaSe

The synthetic process for the production of barium selenide, BaSe, is similar to that of the previously described strontium analogue with some subtle differences. In literature BaSe is usually synthesised from the elements,[22, 216] but here the reduction method is employed again.[20, 217] As before, the selenate material was synthesised first by a precipitation reaction between barium nitrate, $Ba(NO_3)_2$, and sodium selenate, Na_2SeO_4, then used as a precursor in a reduction reaction to produce BaSe.

$BaSeO_4$ was produced on a 28 gram scale from $Ba(NO_3)_2$ (Sigma Aldrich, 99 %) and Na_2SeO_4, (Alfa Aesar , 99.8 %). The procedure was adapted from literature and akin to that of $SrSeO_4$ synthesis,[217] according to Equation 33. The reagents were again selected for their solubilities. $Ba(NO_3)_2$ and Na_2SeO_4 react to produce insoluble target product $BaSeO_4$ and by-product $NaNO_3$: 10.3 g, 58.5 g, 0.015 g and 91.2 g respectively in 100 g water at 20 °C.[210]

Equation 33 $Ba(NO_3)_{2\,(aq)} + Na_2SeO_{4\,(aq)} \rightarrow BaSeO_{4\,(s)} + 2\,NaNO_{3\,(aq)}$

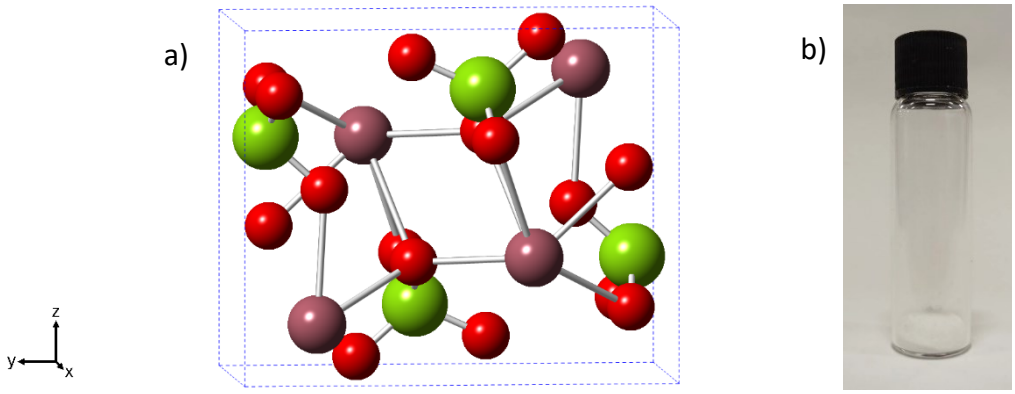

Figure 57 *Representations of barium selenate: a) an isometric projection of the unit cell, and b) a photograph of a portion of the synthesised sample.*
Colour key: plum - Ba, green - Se, and red - O.

1 molar 100 mL solutions of each were targeted, but in the case of $Ba(NO_3)_2$ the relatively low solubility meant that a 1 molar solution was not possible, thus the minimum amount of extra distilled water was added until the material had fully dissolved, aided by sonication. Unlike in the synthesis of $SrSeO_4$, the dropwise addition and heating steps are not required, so the two solutions were mixed and stirred. $BaSeO_4$ rapidly precipitated from solution, aided by an ice bath. The white precipitate was filtered, washed with ice-cold water, and dried at 80 °C overnight. The resulting product was an air-stable white powder, phase pure by XRD, Figure 58.

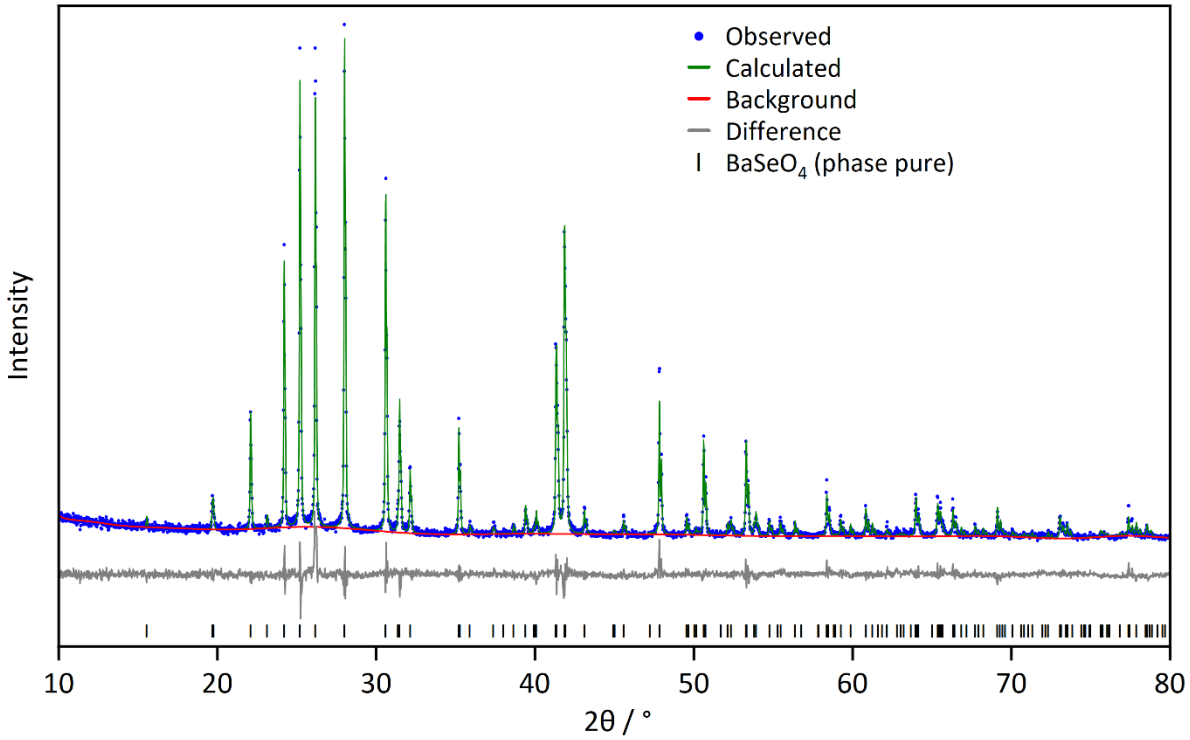

Figure 58 *Powder X-ray diffractogram of material with target composition $BaSeO_4$ (space group Pnma) after ionic displacement. The small blue circles represent the observed diffracted intensity, the green line represents the Rietveld-refined calculated model, the red line represents the background, and the grey line represents the difference between observed and calculated intensities. The black tick marks show the reflections of the refined model of $BaSeO_4$; no impurity phases are observed.*
Duration: 1 hour. Data points: 3456. Interval: 0.02 °. GOF: 1.26. R_{wp}: 12.864 %.

Barium nitrate is air stable, so similarly to the synthesis of SrSe this procedure can be altered to use only air-stable precursors, by replacing Na_2SeO_4 with $Na_2SeO_4 \cdot 10H_2O$ according to Equation 34:

Equation 34 $Ba(NO_3)_{2\,(aq)} + Na_2SeO_4 \cdot 10H_2O_{\,(aq)} \rightarrow BaSeO_{4\,(s)} + 2\,NaNO_{3\,(aq)} + 10\,H_2O_{\,(l)}$

BaSe was produced on a 5 gram scale by the reduction of $BaSeO_4$ under hydrogen, according to Equation 35:

Equation 35 $BaSeO_4 + 4\,H_2 \rightarrow BaSe + 4\,H_2O$

The procedure is identical to that previously described for SrSe: finely ground $BaSeO_4$ was added to an alumina boat crucible within a quartz apparatus in a tube furnace. The selenate was subjected to two 8 hour heating cycles at 650 °C with an intermediate regrind in air. The product is a light orange powder, phase pure by XRD (Figure 59). Like SrSe it is unstable in air and will revert back to $BaSeO_4$ upon exposure to air.

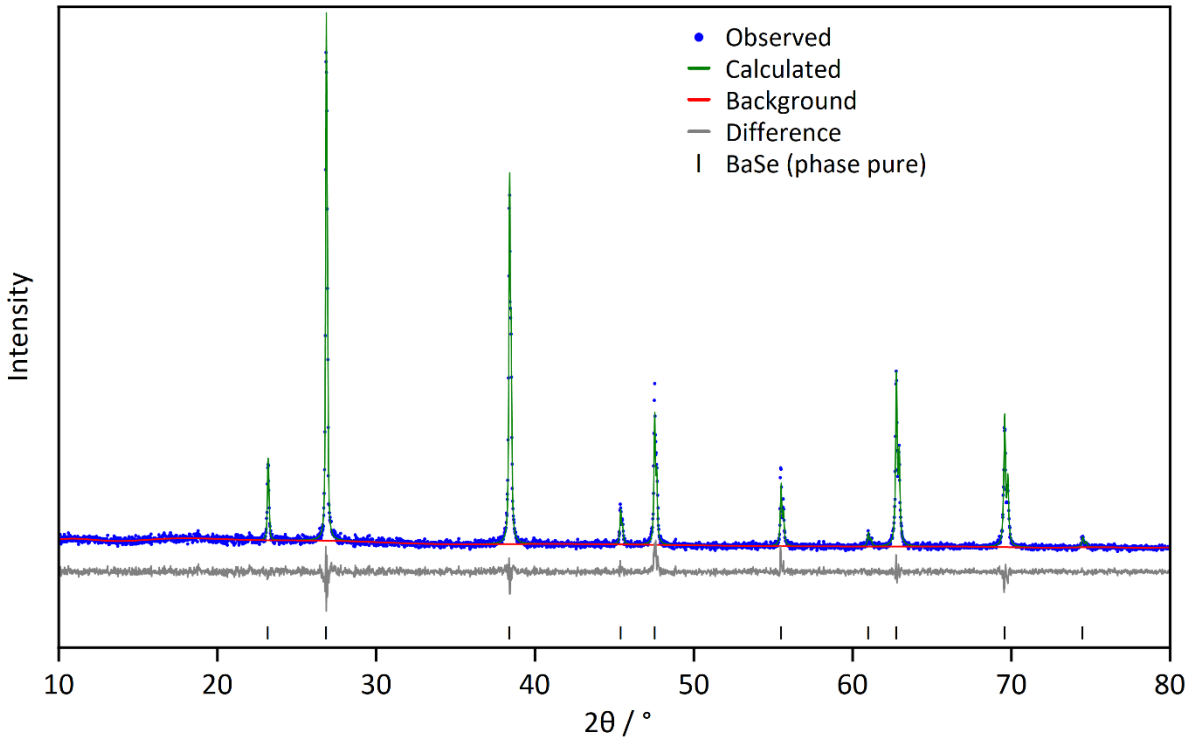

Figure 59 *Powder X-ray diffractogram of material with target composition BaSe (space group Fm-3m) after 16 hours of heating at 650 °C. The small blue circles represent the observed diffracted intensity, the green line represents the Rietveld-refined calculated model, the red line represents the background, and the grey line represents the difference between observed and calculated intensities. The black tick marks show the reflections of the refined model of BaSe; no impurity phases are observed.*
Duration: 2 minutes. Data points: 3457. Interval: 0.02 °. GOF: 1.11. R_{wp}*: 12.395 %.*

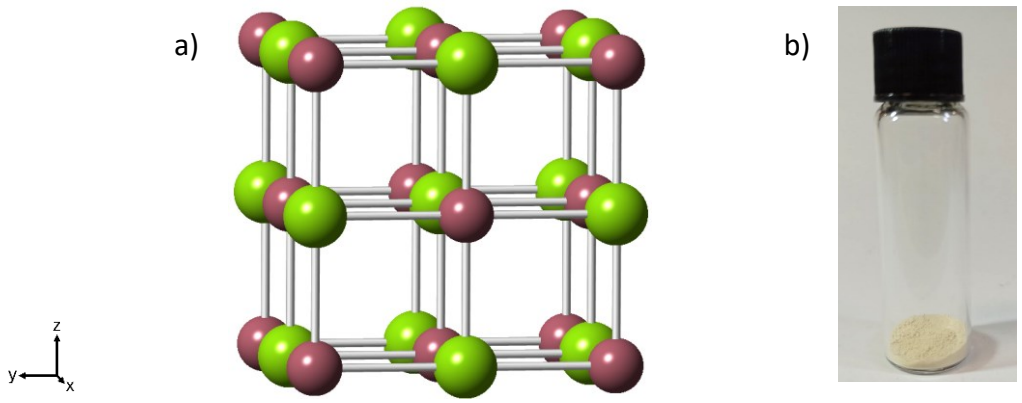

Figure 60 *Representations of barium selenide: a) an isometric projection of the unit cell, and b) a photograph of a portion of the synthesised sample.*
Colour key: plum - Ba, and green - Se.

2.3.5 Sodium Selenide, Na_2Se

The synthesis of group 1 chalcogenides such as Na_2Se is not a simple one. Routes in literature include the reduction of Se with sodium hydroxymethanesulfinate,[218] or reduction of Na_2Se_2 sodium with dithionite,[219] however the process explored in this section is a direct combination of elemental sodium and selenium in liquid ammonia, a procedure which requires total isolation from air at all times due to the instability of precursors and products to air and moisture. Since its first publication in 1939,[220] the ammonia synthesis of Na_2Se is the most common method of production and has been outlined numerous times across literature,[221-223] textbooks[216, 224] and patents.[225]

The procedure involves the condensation of purified ammonia onto a 2 : 1 ratio of Na and Se. After 2 hours of stirring the ammonia is evaporated to leave behind Na_2Se. Sodium selenide was synthesised on a 5 g scale by direct combination of the elemental sodium (Aldrich, 99.9 %) and selenium (Strem, 99.99 %) according to Equation 36:

Equation 36 $2\,Na + Se \rightarrow Na_2Se$

Inside a nitrogen-filled glovebox, a 2 : 1 molar ratio of elemental sodium and selenium was prepared, and the two precursors added to a three-neck round-bottomed flask (3-RBF). The sodium used was in the form of cubes, which even under paraffin oil and within a glovebox exhibits some surface oxidation, so must first be prepared by cutting away these tarnished surfaces to expose clean metallic sodium. A second flask was prepared to which a small piece of sodium (< 0.1 g) was added. The two flasks are herein referred to as the reaction flask and purification flask respectively. Glass stirrer bars were added to each, because regular polytetrafluoroethylene (PTFE) stirrer bars react in liquid ammonia,[226] becoming black and charred. Sealed with stoppers with Young's tap adapters, the flasks were removed from the glovebox and suspended beneath a Schlenk line.

The purification flask was suspended in a -78 ˚C bath of dry ice and isopropyl alcohol (IPA). This flask is now the 'cold point'; the position of the cold point is important to target where the condensation of liquid ammonia is desired at a given moment. A constant flow of argon was maintained across the system at all times to ensure an inert atmosphere. To prevent the risk of explosion, at no point was pressure allowed to build in any isolated location in the system; downstream exit oil bubblers were monitored for blockages at all times. A higher flow of anhydrous ammonia was then introduced (2.5 mmHg vs 1.0 mmHg), which subsequently began to condense in the purification flask, where the cold point of the system resided. The sodium piece within the flask dissolved, allowing a reaction with any moisture present, further purifying the already anhydrous ammonia to maximise purity at later stages. The stirred solution was dark blue, an example of the solvated electron effect.[227, 228]

Once approximately 200 mL ammonia had condensed in the purification flask, the ammonia gas supply was ceased, and the two 3-RBFs were connected with rubber tubing under a temporarily increased argon flow to maintain isolation from air. The dry ice bath, and thus the cold point, was moved to the reaction flask, and the purification bath was warmed in a bath of room temperature IPA to initiate the transfer of the purified ammonia by evaporation and recondensation. As recondensation began, the reaction flask was gently stirred, and the sodium and selenium within began to dissolve. In the warmed purification flask, sodium metal was left behind along with any impurities or moisture extracted from the ammonia.

Once all ammonia had transferred between flasks, the connecting tube was removed, and the isolated reaction flask was vigorously stirred for 2 more hours. It was then left overnight, under an argon flow and a slow stir, to warm to room temperature naturally as the dry ice sublimes and the IPA bath returns to room temperature. The evaporated ammonia left behind sodium selenide, dark orange in colour and resembling pencil shavings due to its recrystallisation under a dry stir. The Young's tap attachment allowed the flask to be evacuated by the vacuum of the Schlenk line, sealed, and then transferred into the glovebox.

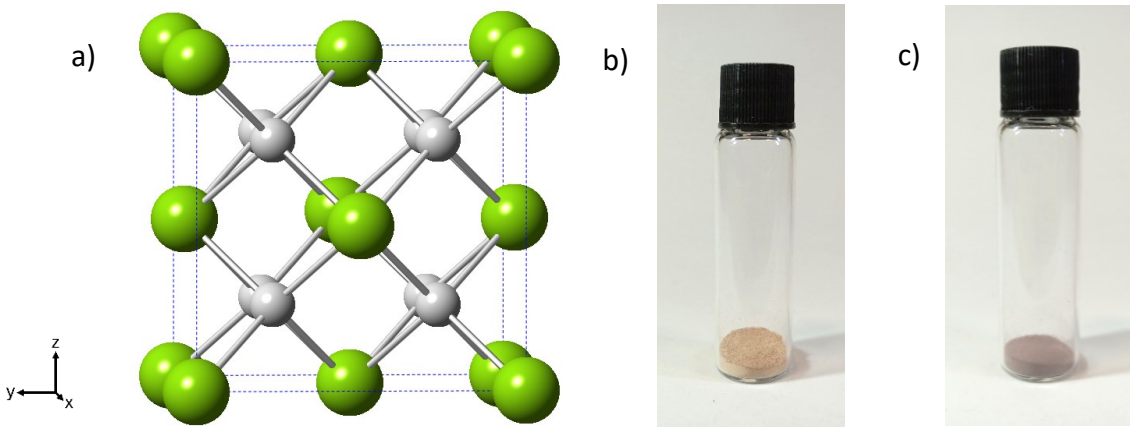

Figure 61 *Representations of sodium selenide: a) an isometric projection of the unit cell, and photographs of a portion of the synthesised sample b) pre-heating and c) post-heating. Colour key: silver - Na, and green - Se.*

The orange powder product, Figure 61b, was ground, and XRD analysis revealed it to be phase pure yet poorly crystalline. The product was sealed in an ampoule and heated to 500 °C for 2 hours, and then reground inside the glovebox. This yielded a dull purple powder product (Figure 61c). XRD revealed that the heated Na_2Se was now crystalline and phase pure (Figure 62).

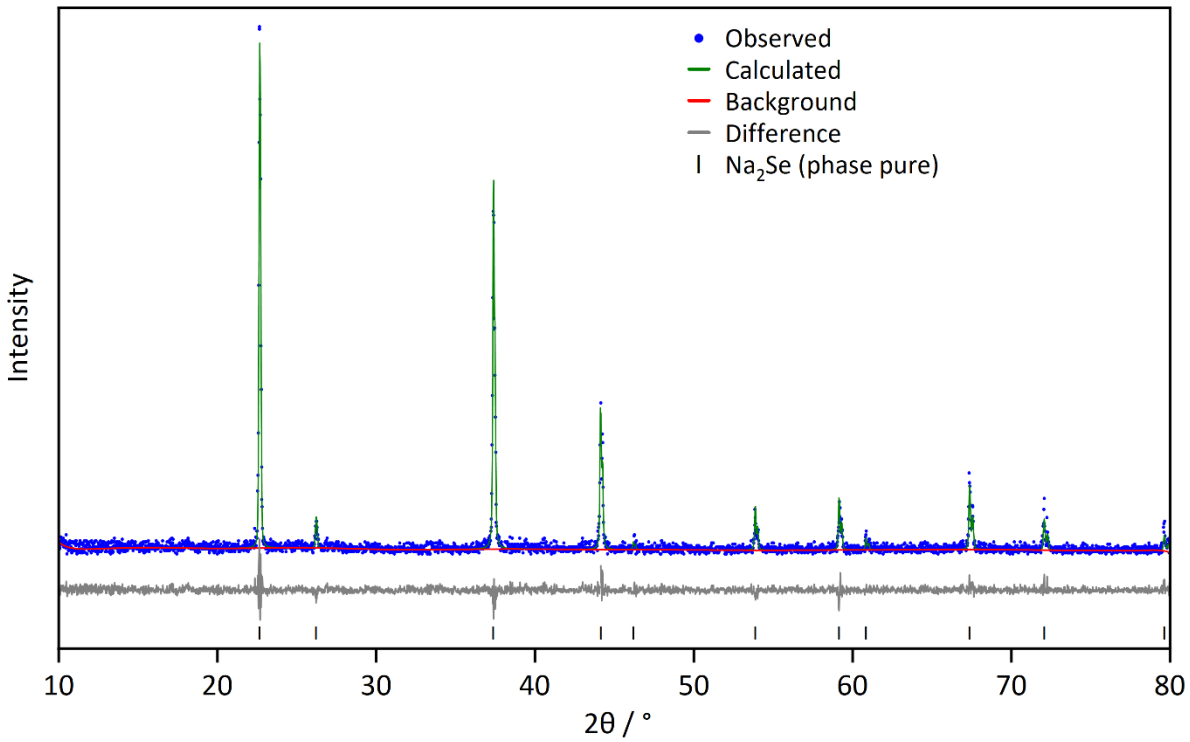

Figure 62 *Powder X-ray diffractogram of material with target composition Na_2Se (space group Fm-3m) after 2 hours of heating at 500 °C. The small blue circles represent the observed diffracted intensity, the green line represents the Rietveld-refined calculated model, the red line represents the background, and the grey line represents the difference between observed and calculated intensities. The black tick marks show the reflections of the refined model of Na_2Se; no impurity phases are observed.*
Duration: 60 seconds. Data points: 3457. Interval: 0.02 °. GOF: 1.11. R_{wp}: 40.483 %.

The same procedure outlined here can be used to synthesise sodium sulfide, sodium telluride, potassium sulfide, potassium telluride, and potassium selenide.

Na_2Se is extremely sensitive to air or moisture, turning grey within seconds of exposure and forming the pentahydrate impurity $Na_2Se{\cdot}5H_2O$ within minutes. A small sample of Na_2Se was left exposed to air and re-analysed after 2 years, after which time the material had converted almost entirely to Na_2SeO_3; see Figure 63.

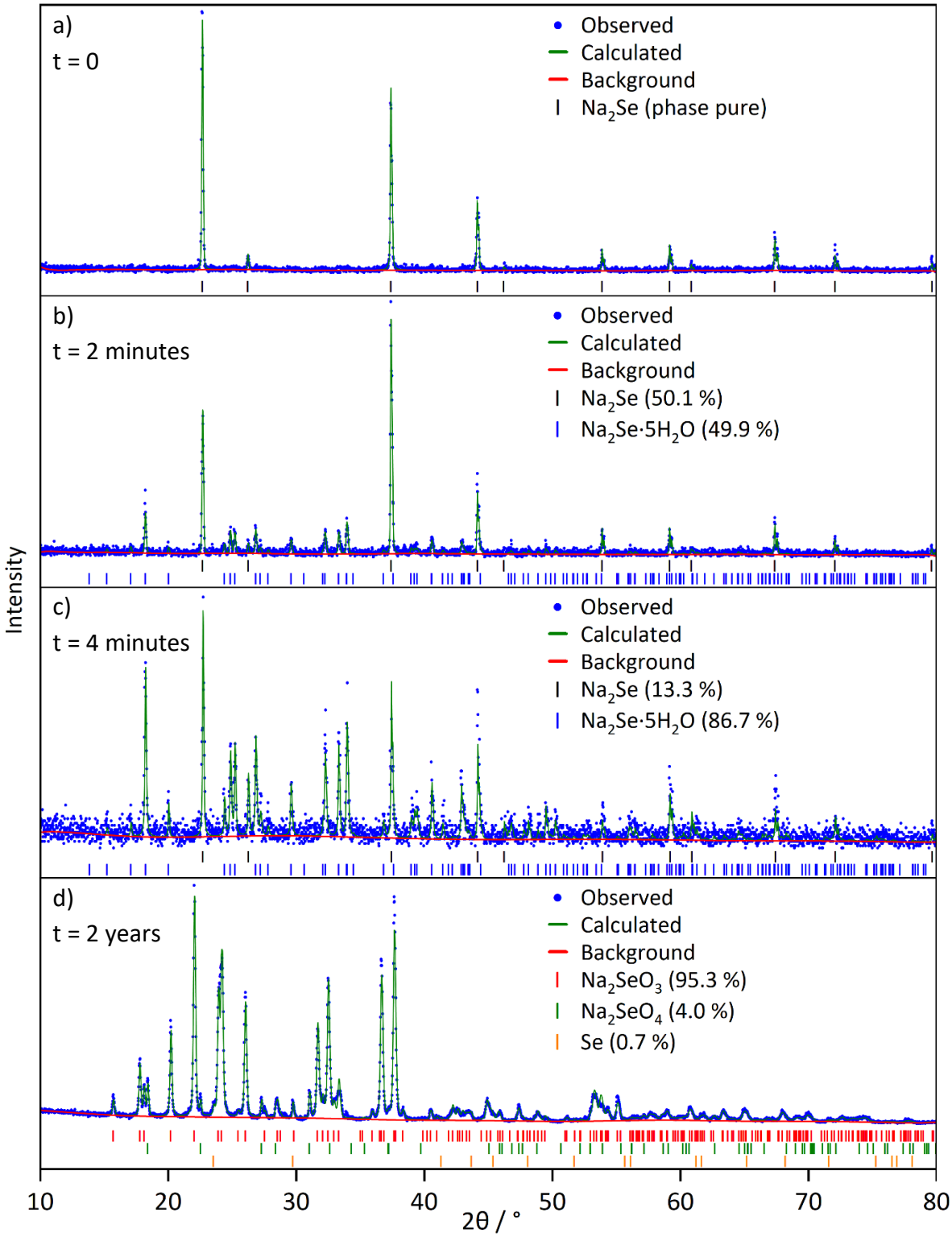

Figure 63 *Powder X-ray diffractograms showing the degradation of Na_2Se over time, where a) t = 0, b) t = 2 minutes, c) t = 4 minutes, and d) t = 2 years. The small blue circles represent the observed diffracted intensities, the green lines represent the Rietveld-refined calculated models, and the red lines represent the backgrounds. For simplicity and compactness, the grey difference lines are omitted. The black tick marks show the reflections of the refined model of Na_2Se, whilst the blue, red, green and orange tick marks represent refined impurity phases $Na_2Se·5H_2O$, Na_2SeO_3, Na_2SeO_4 and Se respectively. Weight fractions for each phase are cited in the figure legends.*
a) Duration: 1 minute. Data points: 3457. Interval: 0.02 °. GOF: 1.11. R_{wp}: 40.483 %.
b) Duration: 1 minute. Data points: 3457. Interval: 0.02 °. GOF: 1.09. R_{wp}: 37.916 %.
c) Duration: 1 minute. Data points: 3457. Interval: 0.02 °. GOF: 1.15. R_{wp}: 39.818 %.
d) Duration: 20 minutes. Data points: 3703. Interval: 0.02 °. GOF: 1.96. R_{wp}: 10.898 %.

2.3.6 Copper Sulfide, Cu_2S

Of the six binary syntheses described in this section, that of copper sulfide proved to be by far the most difficult in terms of attaining phase purity due to competing phases, the inherent complexities of elemental combination, and the volatility of sulfur. The phase space of the Cu-S system is complicated and likely incomplete, with nine known unique compositions of Cu_xS: covellite (CuS), yarrowite ($Cu_{1.12}S$), spionokopite ($Cu_{1.39}S$), geerite ($Cu_{1.60}S$), anilite ($Cu_{1.75}S$), roxbyite ($Cu_{1.78}S$), digenite ($Cu_{1.80}S$), djurleite ($Cu_{1.96}S$), low chalcocite (Cu_2S), and high chalcocite (Cu_2S).[229, 230] The relationships between the more common of these phases are illustrated in Figure 64, a phase diagram for the part of this system where x > 1.7 mol. Those not described either exist outside of the described conditions or are metastable, and are therefore not relevant to the current work.

There are two phases of Cu_xS where $x \approx 2$ at ambient conditions: the Cu_2S 'low chalcocite' structure, a common mineral form of copper, and 'djurleite', a competing phase with structure Cu_xS where x = 1.934 to 1.965,[231] though usually cited in the stoichiometry in which it was discovered, $Cu_{1.96}S$.[232]

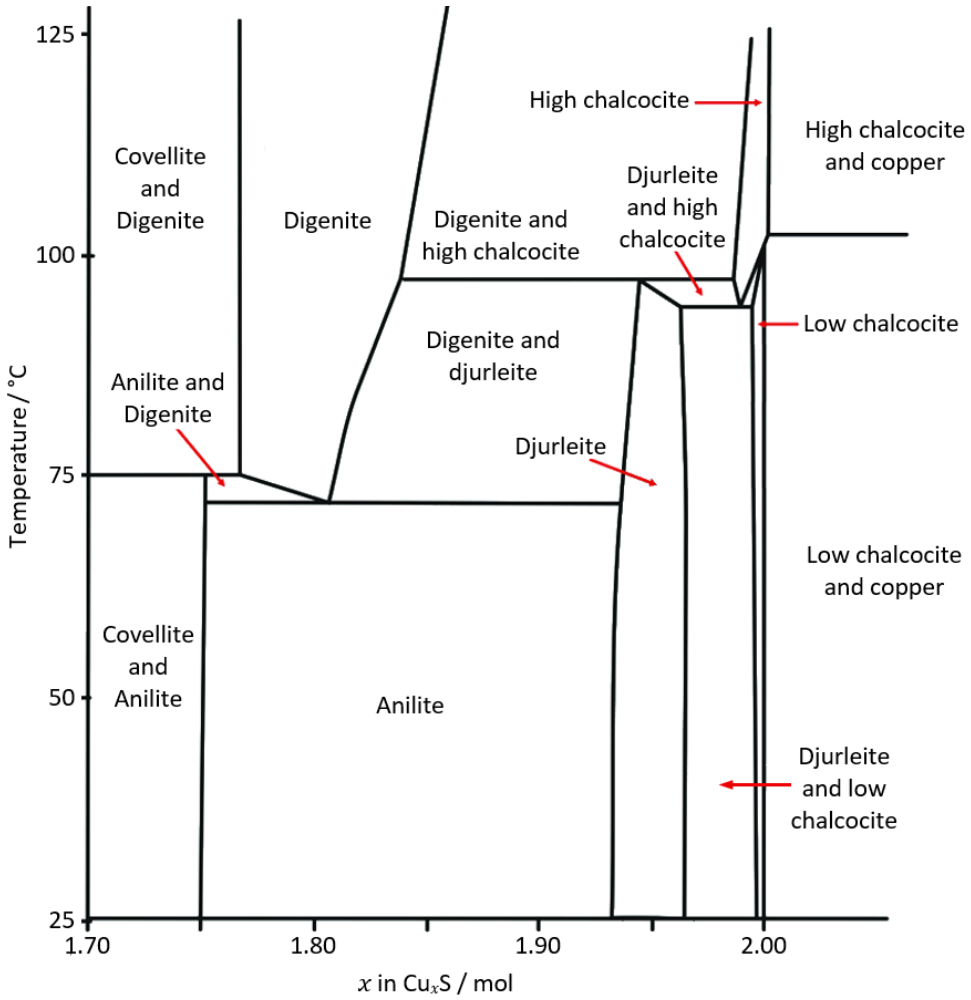

Figure 64 The phase diagram of the Cu-S system. Adapted from a diagram in Szopa 2021,[233] which itself was produced using data from Evans 1979.[231]

Low chalcocite and djurleite are closely related in structure, specifically djurleite is a disordered form of low chalcocite with some altered copper coordination environments. Both phases have large and complex unit cells, with that of low chalcocite containing 48 Cu_2S units and that of djurleite containing 8 $Cu_{31}S_{16}$ units. At 105 °C and 93 °C, low chalcocite and djurleite respectively both transition to a disordered high temperature Cu_2S phase 'high chalcocite', and a mixture of the two ambient phases is produced upon cooling.

Low chalcocite is the focus of this synthesis, not only as the most common and therefore obtainable form of Cu-S, but because its precise x = 2 stoichiometry is preferable for ease of establishing purity by PXRD. Any copper or sulfur appearing in the X-ray diffractogram of low chalcocite is an impurity diverging from the desired stoichiometry of x = 2. For use as a precursor, the actual structure is not important, however the stoichiometry, and by proxy the purity, is very important, as any deviation from phase purity at this stage will propagate into all later syntheses which utilise this precursor, and result in undesired deficiencies or excesses. It is vital, therefore, that low chalcocite Cu_2S is produced phase pure in this synthesis, with no remaining Cu, S, or competing Cu-S phases. Djurleite is neither targeted nor observed in this work because conditions and stoichiometry are such that it is avoided.

In literature, bulk Cu_2S has been produced by various routes such as the direct sulfurisation of copper powder,[234] sonication-induced electrochemical synthesis,[235] hydrothermal synthesis,[236, 237] and direct elemental combination by conventional solid-state chemistry.[90, 100, 238-240] It was decided that the solid-state chemistry route[††] was the most logical given the nature of this work and the equipment available: a reaction between Cu powder (Alfa Aesar, 99.9 %) and S (Thermo Fisher Scientific, 99.9995 %) according to Equation 37:

Equation 37 $2\,Cu + {}^{1}/_{8}\,S_8 \rightarrow Cu_2S$

The phase diagram above depicts the very narrow window within which low chalcocite Cu_2S exists, however the diagram reassuringly implies that it should be possible to isolate this phase with careful control of precursor stoichiometry to ensure a precise 2 : 1 Cu : S ratio.

First, the copper powder was treated to remove a small impurity (approximately 1.5 wt %) of Cu_2O that had arisen during long-term storage of the material within a nitrogen glovebox. Following a method adapted from literature,[241] the powder was finely ground and reduced under 5 % H_2/N_2 in a tube furnace at 550 °C, before XRD revealed successful conversion of all Cu_2O back to Cu, illustrated in Figure 65. Lower reduction temperatures of 400 °C and 450 °C were attempted and were not successful.

[††] The term 'solid-state chemistry' is used here to indicate that the methodology and conditions are akin to that of conventional solid-state chemistry. All reagents and products are solid so the term is used, though it is acknowledged that intermediates may be liquid or, undesirably, gaseous.

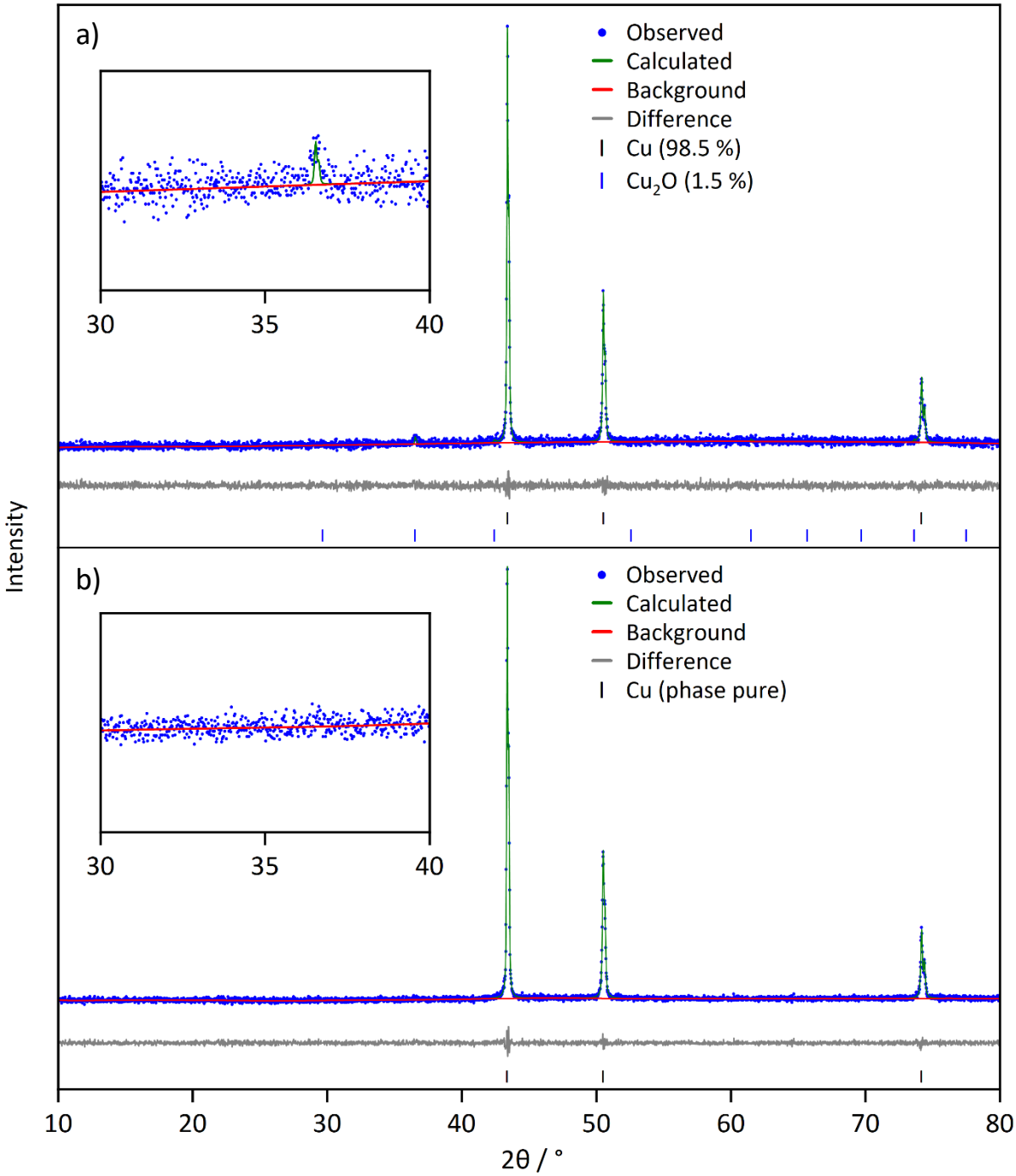

Figure 65 *Powder X-ray diffractograms of copper powder (space group Fm-3m), a) before reduction and containing a Cu_2O impurity, and b) after reduction for 16 hours at 550 °C under H_2. The small blue circles represent the observed diffracted intensities, the green lines represent the Rietveld-refined calculated models, the red lines represent the backgrounds, and the grey lines represent the differences between observed and calculated intensities. The black tick marks show the reflections of the refined model of Cu, whilst the blue tick marks represent refined impurity phase Cu_2O. Weight fractions for each phase are cited in the figure legends. The two inset plots are magnifications of the area where the largest peak of Cu_2O appears, illustrating its removal during the reduction reaction.*
a) Duration: 1 minute. Data points: 3457. Interval: 0.02 °. GOF: 1.04. R_{wp}: 18.028 %.
b) Duration: 3 minutes. Data points: 3457. Interval: 0.02 °. GOF: 1.03. R_{wp}: 10.691 %.

A 2 : 1 molar combination of copper and sulfur was ground to homogeneity, added to an alumina crucible and sealed within a silica ampoule according to the conventional solid-state chemistry procedure outlined in *Section 2.1 - Solid-State Chemistry*. In this first attempt, the sealed ampoule was heated to 400 °C for 16 hours and 700 °C for 24 hours with an intermediate regrind, aggressive conditions akin to regular solid-state chemistry. This did produce low chalcocite Cu_2S but at only 96.3 % purity with a 3.7 % Cu impurity, see Figure 66. Combined, the stoichiometry of this mixture is $Cu_{2.0299}S$, not far from that of Cu_2S, but was deemed far insufficient for that of a precursor.

It was hypothesised that the copper excess was the result of sulfur sublimation[‡‡] from the reaction mixture. This could happen either during the sealing of the ampoule which results in the sulfur being removed from the system by vacuum, or during heating where any sublimed sulfur is kept within the system and is able to be reabsorbed into the reaction mixture until the ampoule is opened.

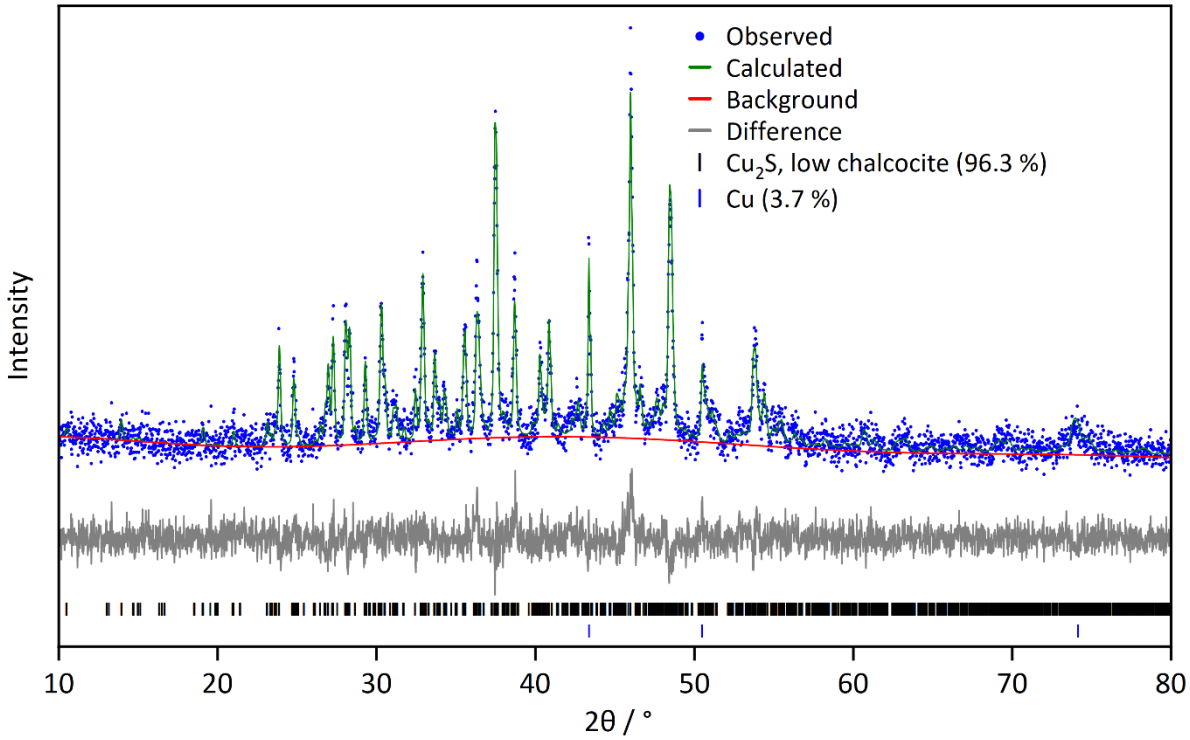

Figure 66 *Powder X-ray diffractogram of material with target composition Cu_2S (space group $P2_1/c$) after 24 hours of heating at 700 °C. The small blue circles represent the observed diffracted intensity, the green line represents the Rietveld-refined calculated model, the red line represents the background, and the grey line represents the difference between observed and calculated intensities. The black tick marks show the reflections of the refined model of Cu_2S (96.3 %); whilst the blue tick marks represent refined impurity phase Cu (3.7 %). Duration: 10 minutes. Data points: 3457. Interval: 0.02 °. GOF: 1.08. R_{wp}: 7.814 %.*

[‡‡] The term 'sublimation' is typically used to describe specifically a transition from solid to gas, whilst a liquid to gas transition is described as 'vaporisation'. In this section it is not known, nor is it important, from which phase the sulfur originates when it becomes a gas, so the term 'sublimation' is used here to describe generally the loss of sulfur as a gas from the reaction mixture, regardless of its state of matter prior.

This reaction was repeated various times more, experimenting with fewer or more heating cycles, and adjusting the temperature of the initial heat. All resulted in very similar purities to the initial run whereby Cu_2S prevails (95 to 98 wt %) and a copper impurity was present. Quenching the hot ampoule in liquid nitrogen was also attempted to investigate whether rapid cooling may crystallise a purer product. This was unsuccessful, producing Cu_2S at 95 % purity alongside copper. At no point was an excess of sulfur observed, due to the inability for copper to be lost from the system, only sulfur.

Sulfur sublimation was a persistent challenge during the attempted syntheses of Cu_2S, so the sulfur system was probed to a greater level with the goal to create conditions that favour the solid or liquid states. Ferreira and Lobo published a detailed phase diagram of the sulfur system, Figure 67, which consists of two solid forms of sulfur, rhombic and monoclinic, a liquid phase, and a gas phase.[242] Sulfur has two triple points, the first between rhombic, monoclinic and gaseous phases, the second between liquid, monoclinic and gaseous phases. The black dotted line on the diagram indicates room pressure, 100 kPa. Following this line from left to right, sulfur exists as the rhombic solid at or below room temperature, converting to monoclinic upon heating, then melting at approximately 118 °C before vaporising at approximately 445 °C. At room pressure therefore, sulfur has a low melting point but can withstand up to 445 °C as a liquid before becoming a gas. Within the ampoule, conditions are very different from this.

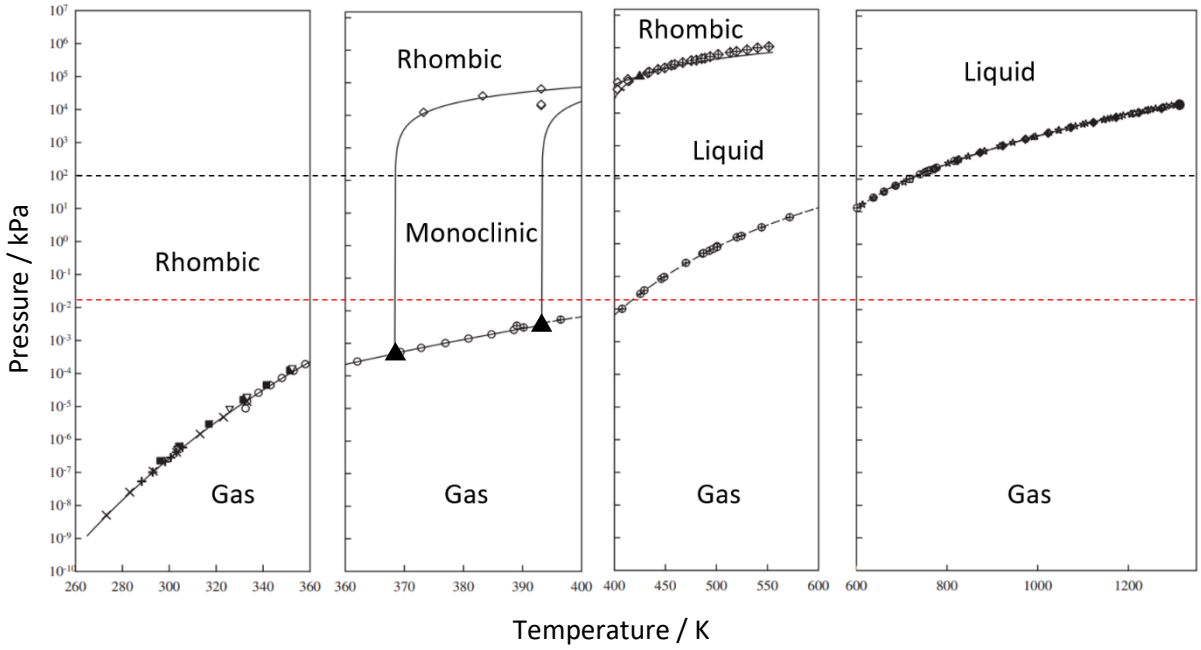

Figure 67 *The phase diagram of the sulfur system. Adapted from a diagram in Ferreria 2011.[242] The solid lines indicate phase boundaries. Black triangles represent the two triple points. All symbols other than black triangles differentiate data obtained from various references in the original work. The black dotted line represents room pressure, 100 kPa. The red dotted line represents ampoule pressure, 0.015 kPa. Note the different temperature scales.*

The red dotted line represents an estimate of the pressure inside the ampoule, 0.015 kPa. From this line one can observe that the melting transition between solid monoclinic sulfur and liquid sulfur occurs at the same temperature as at room pressure, due to the pressure-independent melting point in this region. The vaporisation point however is significantly lower, now occurring at approximately 150 °C. This is very informative, suggesting that for the majority of the heating cycle the sulfur is far above the stable temperatures for its solid or liquid phases, therefore the temperature of the initial heat (tested between 300 - 500 °C) is likely far too hot and the cause of the sulfur sublimation.

At ampoule pressure there exists only a small temperature window within which the sulfur is liquid, and this would be the ideal temperature to target for the first heating cycle: hot enough to melt the sulfur and allow rapid reaction with the solid copper powder, but not hot enough to sublime or vaporise it. Melted precursor is usually undesirable in solid-state chemistry, but here the temperature where solid sulfur exists is insufficient for conventional solid-state chemistry to occur, thus the liquid state is desired for the reaction to begin. Note that the value of 0.015 kPa is likely to be an underestimate due to slight vacuum loss when sealing, or in the eventuality of sulfur sublimation, so the liquid window may be slightly larger than anticipated.

Alongside investigation into the sulfur system, various modifications were made to the procedure in order to further minimise sulfur sublimation and improve Cu_2S purity:

1. A large silica tube was used when sealing the unreacted mixture within an ampoule, so that the sample itself could be kept at least 20 cm from the oxypropane flame. This large silica headspace not only protects the sample from sulfur sublimation during sealing, but reduces the likelihood of the ampoule exploding in the event that sublimation does still occur.

2. The part of the silica tube containing the sample was submerged in cold water during ampoule sealing to further minimise or prevent sulfur sublimation caused by heating.

3. Quenching was deemed to be unhelpful in this reaction, and after experimenting with quenching in both cold water and in liquid nitrogen, the approach was discontinued. It was theorised that a slower cooling to convert any high chalcocite or other competing Cu-S phase back into low chalcocite would be more advantageous than attempting to ‘lock in’ a metastable high temperature phase.

4. The initial grinding of precursors was reduced to a stir with a spatula, so that no sulfur would sublime under the pressure exerted by grinding in a pestle and mortar. The solid copper powder is the only other precursor that the melted sulfur needs to react with, so it was assumed that because the sulfur would absorb into the copper when liquid, an intimate mixture would not be essential. The intermediate regrind(s) were performed as normal.

Combining all of the above modifications with conditions targeting the liquid phase of sulfur, a new procedure was attempted as follows:

A 2 : 1 molar combination of Cu and S powders was mixed gently with a spatula within a nitrogen glovebox, loaded into an alumina crucible and sealed within a silica ampoule with a large headspace. The sample was submerged in cold water during sealing. The large ampoule was heated to 110 °C at 1 °C per minute for 24 hours, conservatively targeting just below the melting point of sulfur. Opening the ampoule revealed a black powder alongside some unreacted sulfur. A gentle regrind preceded a second identical heat cycle at 110 °C, after which the product was homogenous, black and crystalline, indicative of Cu_2S. At this point the sulfur cannot sublime as it is 'locked' within a stable configuration within the Cu-S system, so it is safe to thoroughly regrind and increase the temperature to drive towards phase purity. The ground sample was heated to 700 °C for 24 hours at 2 °C per minute, and upon cooling was held at 70 °C for a further 24 hours to convert any other Cu-S phases to low chalcocite Cu_2S. An outlier compared to all other conventional solid-state syntheses in this work, the majority of the reaction is occurring here at the low temperature of 110 °C, where the high temperature run exists only to purify and homogenise.

This procedure finally yielded phase pure Cu_2S, all in the low chalcocite phase, shown in Figure 69. No copper is observed which suggests sulfur sublimation was successfully averted. Compared to the other binaries produced in this section, Cu_2S is sufficiently stable for a 30 minute XRD. Tested initially on a 5 gram batch, this procedure was scaled to 20 grams and produced phase pure binary material yet again.

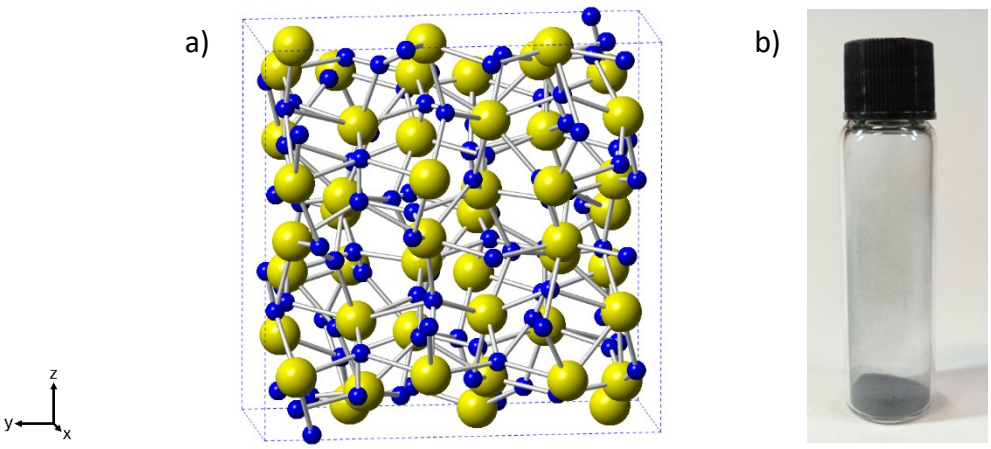

Figure 68 *Representations of copper sulfide: a) an isometric projection of the unit cell, and b) a photograph of a portion of the synthesised sample.*
Colour key: blue - Cu, and yellow - S.

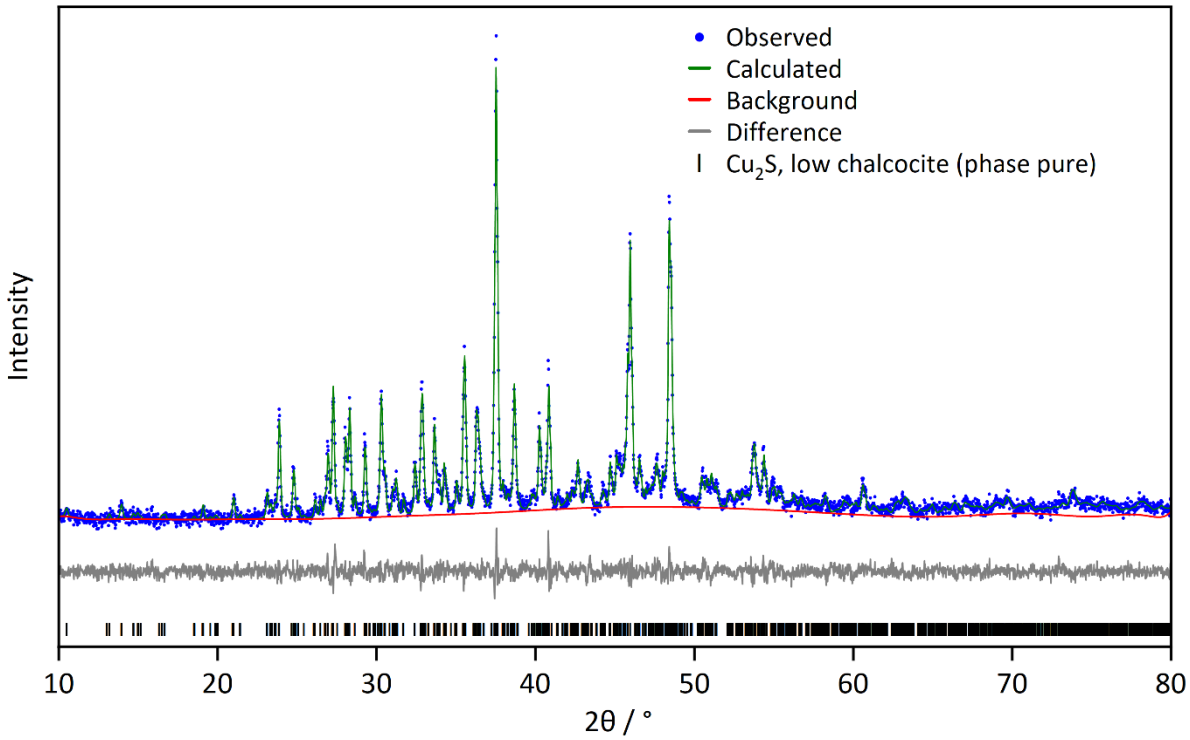

Figure 69 *Powder X-ray diffractogram of material with target composition Cu_2S (space group $P2_1/c$) after 24 hours of heating at 700 °C. The small blue circles represent the observed diffracted intensity, the green line represents the Rietveld-refined calculated model, the red line represents the background, and the grey line represents the difference between observed and calculated intensities. The black tick marks show the reflections of the refined model of Cu_2S; no impurity phases are observed.*
Duration: 30 minutes. Data points: 3457. Interval: 0.02 °. GOF: 1.25. R_{wp}: 4.051 %.

In conclusion, it was found that the preferential selection of Cu_2S in the low chalcocite phase over other Cu-S phases was not difficult, as demonstrated by the absence of other phases in any appreciable quantity as to be observed by benchtop PXRD. Instead, the volatility of sulfur powder proved a far more difficult and unexpected experimental challenge, overcome by delicate control of reaction conditions to favour a stable yet reactive 'sweetspot' in the small window where sulfur exists as a liquid at ampoule pressure.

Chapter 3 The Synthesis and Conductivity Investigation of Doped $Sr_3Sc_2O_5Cu_2Ch_2$ '325' Oxychalcogenides

3.1 Introduction

In *Chapter 1*, the quinternary oxychalcogenide MALM $Sr_3Sc_2O_5Cu_2S_2$ was discussed, which has been identified within literature as a promising candidate for transparent conductivity. Its wide band gap of 3.1 eV and exceptional hole mobility of 150 $cm^2\ V^{-1}\ s^{-1}$ affords $Sr_3Sc_2O_5Cu_2S_2$ an impressive room temperature conductivity of 2.8 S cm^{-1}, which is the highest of any *p*-type TCO.[42, 46, 58]

In 2009, a detailed report by Scanlon et al confirmed the direct band gap of $Sr_3Sc_2O_5Cu_2S_2$ and outlined a selection of recommendations by which to dope it to improve either the charge carrier concentration or the optical band gap, further enhancing its transparent conductive ability. Despite its acclaim this material has received limited follow-up research interest with no publications acting upon Scanlon's recommendations, an observation noted by reviews of the field.[104, 151]

Firstly, Scanlon notes that the band gap may be increased by doping or replacement of the Sc^{3+} ion with a larger ion such as Y^{3+} or La^{3+}. This would increase the *a* lattice parameter and thus the Cu-Cu distance, lowering the VBM and increasing the energy gap to the conduction band. This substitution is isovalent thus no charge imbalance is introduced, so high dopant levels may be achievable without inducing a structural breakdown. The isovalent replacement of Sr with Ba was recommended to the same end.

Recommendations to increase charge carriers by aliovalent *p*-type doping include Na^+ or K^+ on the Sr^{2+} site, and Ca^{2+} or Mg^{2+} on the Sc^{3+} site. The replacement of S^{2-} for Se^{2-} or Te^{2-} is, expectedly, recommended as another method to increase conductivity but at the expense of the wide band gap. If aliovalent band gap widening could be performed to allow selenide replacement of the sulfide ions whilst maintaining a wide band gap, exceptional performance in both conductivity and transparency may be realised.

In this work, Scanlon's recommendations are explored. Pristine $Sr_3Sc_2O_5Cu_2S_2$ is synthesised, and doping with group 1 metal ions Na^+ and K^+ is explored. The selenide analogue $Sr_3Sc_2O_5Cu_2Se_2$ is also produced and its performance is deemed to be superior, therefore greater attention was devoted to the doping of this material. K^+, Na^+, Mg^{2+}, Ba^{2+}, Y^{3+} and La^{3+} are all explored as dopants targeting either a band gap increase or a conductivity improvement. Further to this, atomic deficiencies are introduced on the Sr^{2+} and Cu^+ sites to simulate *p*-type doping.

Table 3 *A comparison of the ionic radii of 12 and 8-coordinate Sr^{2+}, and 6-coordinate Sc^{3+}, alongside those of the ions recommended by Scanlon et al to be doped onto those sites in $Sr_3Sc_2O_5Cu_2Ch_2$.*

a)	12-coordinate ion size / Å	8-coordinate ion size / Å
Strontium, Sr^{2+}	1.44	1.26
Potassium, K^+	1.64 *(+14 %)*	1.51 *(+20 %)*
Sodium, Na^+	1.39 *(-3.5 %)*	1.18 *(-6.5 %)*
Barium, Ba^{2+}	1.61 *(+12 %)*	1.42 *(+13 %)*

b)	6-coordinate ion size / Å
Scandium, Sc^{3+}	0.745
Magnesium, Mg^{2+}	0.72 *(-3.5 %)*
Lanthanum, La^{3+}	1.032 *(+39 %)*
Yttrium, Y^{3+}	0.90 *(+21 %)*

The radii of each of these ions is compared in Table 3, which serves as a rough indicator of the likelihood of successful doping, and degree of incorporation by the host ion. In aliovalent examples these sizes should serve exclusively as a qualitative guide, as the host and dopant ions exhibit different oxidation states, so the radius of a dopant ion may change slightly on incorporation into a differently charged site. The close size match between scandium and magnesium, for example, is an early indicator of successful incorporation, explored in *Section 3.4.4.*

To the best of the author's knowledge, this study of the $Sr_3Sc_2O_5Cu_2Ch_2$ system, particularly the selenides of which the majority of this work pertains to, is the largest doping study of a single material in literature. Improvements in the optical band gaps were underwhelming, but improvement to the conductive behaviour was very impressive, particularly that resulting from Na^+, K^+ and Mg^{2+}. The best sample yielded an improvement to the electrical conductivity of $Sr_3Sc_2O_5Cu_2Se_2$ by a factor of almost 100,000 times.

3.1.1 The ACu_3Ch_2 impurities

The main focus of this chapter is the doping of $Sr_3Sc_2O_5Cu_2Ch_2$ (*Ch* = S, Se) with K^+ and Na^+. At higher doping levels, any excess dopant not incorporated into the MALM appears as an impurity of the form ACu_3Ch_2, (*A* = K, Na)* Monitoring these impurities is important because this structure type is highly conductive due to vacancies in the copper layer, and may threaten false-positive sample conductivity. Compositionally these materials may be considered Cu_2Ch, with some substitution of Cu^+ for K^+.

These materials are black narrow band gap semiconductors which exhibit low hole mobility but high charge carrier concentrations. They crystallise in the $CsAg_3S_2$ structure type with monoclinic space group *C*2/*m*. KCu_3S_2 for example, reported by Burschka et al in 1977,[243] Figure 70, contains a copper-chalcogenide motif similar to that of MALMs and other highly conductive materials such as copper sulfide. Potassium ions are seven-fold ionic coordinated to sulfur; separating infinite $[Cu_{3-x}S_2]^-$ layers where copper occupies either a three-coordinate bent trigonal planar site or a four-coordinate distorted tetrahedral site. Approximately 3 % of Cu sites in ACu_3Ch_2 are vacant, hence they are often cited in the form $ACu_{3-x}Ch_2$.[244]

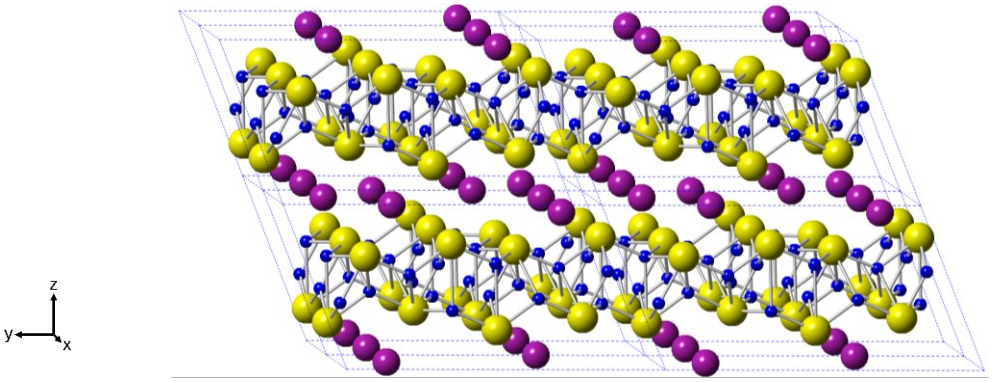

Figure 70 *An isometric projection of a 2 × 2 × 2 expanded unit cell of KCu_3S_2. The interaction of K^+ to S^{2-} is ionic, and so for clarity these bonds are not shown.*
Colour key: purple - K, blue - Cu, and yellow - S.

Jacyna-Onyszkiewicz reported KCu_3Se_2 in 2003, the only of the four permutations with comprehensive published property data. It has a narrow band gap of 1.35 eV, showing metallic behaviour at low temperatures and semiconducting at high temperatures. Its resistivity at room temperature is reported at 6.5×10^{-5} Ω cm, corresponding to an excellent conductivity of 1.5×10^3 S cm^{-1}. Zhou et al reported the sodium analogues $NaCu_3S_2$ and $NaCu_3Se_2$ in 2022.[245] The stoichiometrically similar material $K_3Cu_8Se_6$ is also observed in this work,[246] but its sulfide equivalent $K_3Cu_8S_6$ is not observed.[247] Attempts to synthesise KCu_3S_2 for in-house conductivity measurements were unsuccessful due to competing phases in the K-Cu-S phase space,[248] and was not pursued further.

* In doping studies, the dopant is often termed an 'impurity'. To avoid confusion, this work reserves the term 'impurity' exclusively for undesirable material in the end product, be that a by-product, a competing phase, or an unreacted precursor. Herein the dopant is always termed 'dopant', unless it fails to incorporate and appears as an impurity, like those of the ACu_3Ch_2 type described in this section.

3.2 Experimental

3.2.1 Precursors

Materials within this chapter were synthesised using the following precursors:

SrO (made in-house by the decomposition of $SrCO_3$, Merck, 99.9 %), Sc_2O_3 (Thermo Scientific, 99.999 %), Cu_2S (made in-house by the reaction of Cu, Alfa Aesar, 99.9 %, and S, Thermo Fisher Scientific, 99.9995 %), Cu_2Se (Thermo Fisher Scientific, 99.5 %), SrS (made in-house by the reaction of $SrCO_3$, Merck, 99.9 %, and CS_2, Honeywell, 99.9 %), SrSe (made in-house by reduction of $SrSeO_4$, also made in-house), Na_2Se (made in-house by the reaction of Na, Aldrich, 99.9 %, and Se, Strem, 99.99 %), Na_2S (Thermo Scientific, 95 %), K_2S (Strem, 95 %), K_2Se (Thermo Scientific, 95 %), S (Thermo Fisher Scientific, 99.9995 %), Se (Strem, 99.99 %), MgO (Aldrich, 99.99 %), BaO (Sigma Aldrich, 99.5 %), Y_2O_3 (Alfa Aesar, 99.999 %), and La_2O_3 (Thermo Fisher Scientific, 99.99 %).

3.2.2 Synthesis of Pristine Materials

$Sr_3Sc_2O_5Cu_2S_2$ and $Sr_3Sc_2O_5Cu_2Se_2$ were produced on a 1 gram scale by conventional solid-state chemistry as outlined in *Chapter 2*, following the route for materials unstable in air.

Intimate mixtures of the powder precursors were ground to homogeneity within a nitrogen-filled glovebox. The powder mixture was added to an alumina crucible and sealed within a silica tube under vacuum. In a typical experiment, this ampoule was heated to 800 °C in a muffle furnace at a ramp rate of 2 °C per minute, then held for 12 hours before cooling naturally to room temperature. Once cooled the materials were reground thoroughly and pressed into 13mm diameter pellets under 10 tonnes. Pellet samples were once again sealed within silica ampoules and subjected to another 800 °C heating cycle, after which they were considered complete. Specific equations for each doping study are stated at each stage.

Samples were analysed by powder X-ray diffraction and modelled by Rietveld refinement to assess composition, purity and structural features, and then by UV-Vis spectroscopy to estimate an optical band gap. Finally, a small 8mm pellet of approximately 0.15 grams of completed sample was subjected to a third heating cycle, again at 800 °C, to anneal it ahead of a 4 probe van der Pauw resistivity measurement to estimate the conductivity of the material. Precise diameter and thickness values were also obtained from the annealed pellet in order to obtain an estimation of density as a percentage of the density of the bulk crystalline sample.

3.2.3 Synthesis of Doped Materials

The synthesis of doped materials is largely the same as described in the previous section for pristine materials, with some minor differences:

As with the pristines, all doped materials were synthesised on a 1 gram scale. Initial unreacted powder mixtures of most doped materials often contain elemental sulfur or selenium in order to balance the stoichiometry of the target product. The melting points of these materials are low, 112 °C and 220 °C respectively, and even lower when under vacuum.[242, 249] In order to minimise melting or sublimation of these precursors, the sealed silica ampoule was held at 100 °C (for materials containing elemental sulfur) or 180 °C (for selenium) for 12 hours before then being raised to the usual 800 °C heat. This is done within the same ampoule not only for convenience and maintenance of purity, but to allow for any sublimed material to potentially be reabsorbed into the mixture rather than lost during regrinding. Owing to the thermodynamic stability of the strontium-scandium 325 phases, (the syntheses of which produce only minor binary impurities and no competing MALM phases), this procedure can be generalised for all doped $Sr_3Sc_2O_5Cu_2Ch_2$ samples, with no requirement for any final heating temperatures higher or lower than 800 °C.

Secondly, in materials doped with alkali metals, there is often a requirement for a very small amount of dopant material A_2Ch (*A* = Na or K, *Ch* = S or Se) and an even smaller amount of either sulfur or selenium to balance the stoichiometry. Weighing errors of measurements on this scale are more significant than those of larger quantities, so in order to minimise this, larger 2-gram batches of four binary mixtures were prepared according to the following equations:

Equation 38 $K_2S + {}^1/_8\,S_8 \rightarrow [K_2S + S]$

Equation 39 $Na_2S + {}^1/_8\,S_8 \rightarrow [Na_2S + S]$

Equation 40 $K_2Se + Se \rightarrow [K_2Se + Se]$

Equation 41 $Na_2Se + Se \rightarrow [Na_2Se + Se]$

These unreacted mixtures are used in replacement of their constituent precursors, which crucially are always required in 1:1 molar ratios. Not only does this minimise weighing error by using larger amounts of A_2Ch_2 than would be required of A_2Ch or *Ch*, but it reduces the number of required precursors in the main reaction by one, in most cases from 6 to 5. Within reaction equations each of these mixtures is herein denoted as [A_2Ch + *Ch*], for example [K_2S + S], to indicate that this reagent is a mixture and not an actual binary phase.

Specific reaction equations for each dopant, along with any deviations from this general procedure, are outlined within each respective section.

3.2.4 Rietveld Refinement of Doped Materials

Powder X-ray Diffraction (PXRD) has long proven an invaluable tool in solid-state chemistry, and unsurprisingly plays a major role in this investigation in the enhancement of 325 $Sr_3Sc_2O_5Cu_2Ch_2$ MALMs through doping. The interpretation of PXRD data through Rietveld refinement within the General Structure Analysis System II (GSAS-II) allows for quantitative assessments of sample composition and structure.

The procedure used to analyse doped materials via PXRD using GSAS-II builds upon that which is outlined in Section 2.2.1, with some minor adjustments in order to, inter alia, normalise the refinement process both within a given sample set and across different sample sets. The materials described in this chapter regularly contain multiple impurities, a behaviour typical of doped solid-state materials, however these impurities are usually small, often less than 1 % by weight and exhibiting very small reflections on an X-ray diffractogram. This can make accurately determining the phase fraction and phase properties during Rietveld refinement problematic and/or inaccurate.

As such, a method was developed to maximise regularity between refined data in this investigation, comprising two parts: the modelling of doped MALMs as if they were pristine, and the generalisation of the way impurity phases are treated across samples.

3.2.4.1 The Modelling of Doped MALM Products as Pristines

Within this study, all doped materials were modelled as pristine material during Rietveld refinements, an experimental choice that was made for a number of reasons:

Firstly, there are various obstacles faced when attempting to refine a doped MALM in GSAS-II, especially with data collected on a benchtop diffractometer. If the exact doped sample composition is known (which is, in practice, impossible) one may use restraints and mixed occupancies to artificially create a substitution of a given percentage of host atoms for doped atoms, on the desired atomic site, to simulate doping. This is suitable for cases when the guest atom is certain to have been incorporated, such as a well-explored solid-solution or a very low level of doping onto a known accommodating site similar in size. In the case, however, of new hitherto unexplored dopants where the success of incorporation is unknown, and also when attempting to dope to a level far beyond that which the host material can accommodate, manually simulating the dopant onto the site is not appropriate, and an assumption that all dopant will be incorporated onto the target site is not valid.

Secondly, the physical change to a powder diffraction pattern upon doping, especially when doping to a very small extent, is so small as to often be within the noise of the data and thus unnoticeable. With data obtained on a benchtop diffractometer and collected on the scale of 45 minutes per sample, the data quality is more than sufficient for a general refinement of the target material, especially given the high crystallinity of the materials explored herein, but the quality is far insufficient to accurately model the near-negligible difference in peak shape and height that might arise from dopant types and concentrations explored within this chapter. Modelling, for example, the successful incorporation of a very minor amount of dopant vs an undoped pristine material would result in two crystalline and high-quality yet effectively indistinguishable diffraction patterns. For this reason, modelling the MALM as pristine in lieu of modelling the dopant is a valid experimental choice and does not detract from the goodness of fit of the model, and arguably enhances the repeatability and regularity across different samples because a variable of the refinement process has been controlled.

Finally, if the site fraction of a host and guest atom were to be flagged for refinement by GSAS-II, the obtained value will have a large degree of uncertainty due to the negligible effect that the action of doping often has on peak shape, size and 2θ position. The resulting modelled dopant occupancy, even if constrained correctly, may therefore swing far above or below the true value, and relies on the experience of the user to judge the validity of a result, a task made difficult when differences between samples and even between whole data sets are so small. By eliminating this variable and modelling all doped materials as pristines, two negative possibilities are avoided: the opportunity for cherry-picked dopant incorporation values, and the opportunity for false positive goodness-of-fit values that might arise from GSAS-II incorrectly assessing a site fraction (to better fit a model to an observed pattern).

For the above experimental liberty to be employed effectively, there must exist an alternative method to infer, even if qualitatively, the amount of dopant in a doped MALM, as the lack of such a measure would be a valid rebuttal to this technique. Within this investigation, the presence and quantity of specific impurities is used as a measure of a doped sample reaching dopant saturation, or (such as in the case of Yttrium doping in *Section 3.4.6*) a measure of if any dopant was incorporated at all. While the effect of doping on the phase profile of a MALM is minimal, the presence of impurities is a very noticeable and measurable variable.

Some assumptions are made when using this method. In a diffractogram of a doped material, if no precursor or impurities contain any dopant, it can be assumed that all dopant has been incorporated into the MALM, hence its omission in any other phase. If, however, the dopant atom appears in any phase other than the MALM, it must be the case that some or all of the dopant has not been incorporated.

To illustrate this preference visually, Figure 71 depicts two simulated hypothetical outcomes from an attempt to dope 0.20 mol of gallium onto the scandium site of $Sc_3Sc_2O_5Cu_2Se_2$.[†] The blue plot labelled a) is $Sc_3Sc_2O_5Cu_2Se_2$, an undoped pristine with no dopants introduced. Two possible outcomes, one where full dopant incorporation is achieved and another where no dopant incorporation is achieved, are shown in plots b) and c) respectively. The unreacted precursor in plot c), Ga_2O_3, is clear even as a trace impurity. These reflections are marked with asterisks. The pristine and doped plots are near identical, differing only by miniscule changes in peak shape as shown in the magnified inset. This demonstrates the difficulty of refining peak shape to estimate dopant integration, supporting the experimental choice to eliminate it.

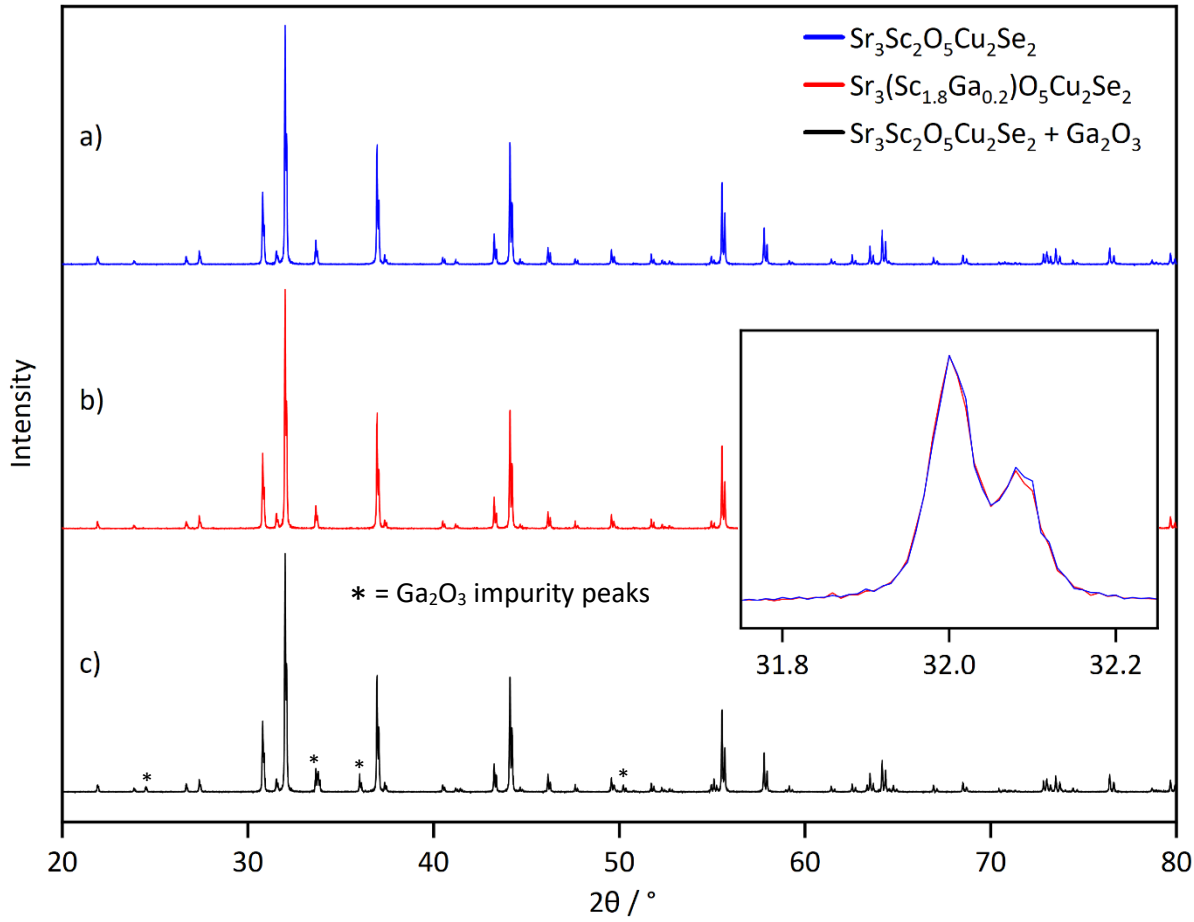

Figure 71 *Simulated powder X-ray diffractograms of a) $Sr_3Sc_2O_5Cu_2S_2$, b) $Sr_3Sc_2O_5Cu_2S_2$ successfully doped with Ga, resulting in the composition $Sr_3(Sc_{1.8}Ga_{0.2})O_5Cu_2S_2$, and c) $Sr_3Sc_2O_5Cu_2S_2$ successfully doped with Ga, where unreacted Ga_2O_3 precursor remains as an impurity. The asterisks in plot c) represent the peak positions of impurity Ga_2O_3. The inset image is a magnified and overlaid view of two major reflections of the $Sr_3Sc_2O_5Cu_2S_2$ pattern when pristine (blue) and successfully doped (red), to highlight the observable but very minor difference in peak shape between pristine and doped samples.*

[†] This example is purely illustrative, and was chosen specifically because this doping permutation is not attempted in this work. $Sc_3Ga_2O_5Cu_2Se_2$ and $Sc_3Ga_2O_5Cu_2S_2$, as pristines, have been shown not to exist due to the gallium Ga^{3+} cation being too small to occupy the M site of the 325 MALM.[59]

3.2.4.2 The Refinement of Impurities in Doped MALMs

The second component to the Rietveld refinement method used within this investigation, is the uniformity of the treatment of impurity phases.

Recognising impurity phases and introducing them to the refinement process is a facile task, as is estimating approximate relative amounts of these impurities between samples, by eye or by computer-aided refinement. Impurity and unreacted precursor phases in this chapter (herein just referred to as impurities) are prevalent but usually very small. This presents issues similar to those described previously with pristine vs doped peak profiles, in that very small phases are difficult to refine reliably or repeatably, and certain parameters such as size, strain and thermal ellipsoids may not be appropriate to refine for such a small phase for risk of receiving an incorrect value solely to falsely improve the goodness of fit. Incorrect size or thermal ellipsoid values, for example, can skew the phase fraction to also become incorrect, and must be avoided. The instrument conditions employed here produced diffractograms where noise is consistently low and the background is flat, but even then, some phases are considered too small to be refined by the usual means, hence the creation of this procedure in order to pseudo-normalise the treatment of impurity phases across data sets and prevent anomalous or erroneous refinements. The procedure is as follows:

Firstly, the CIF of the main MALM phase is imported into GSAS-II. This material, as described previously, is modelled as a pristine, but all relevant parameters such as unit cell size, uniaxial particle size, particle strain, atom positions and isotropic thermal ellipsoid size, are refined as usual to produce a model which has a good fit to the observed data. During this process the background is also refined.

At this point there exists only one phase in the diffraction pattern, therefore exhibiting a weight fraction of 100 %. This is very rarely the case when doping, so next the CIFs of any impurity phases are added into the pattern by aligning the major unrefined peaks against known patterns of expected or possible impurity phases. Impurities in this investigation are regular and predictable, and thus can usually be recognised by eye. The first to be added, if present, is Sr*Ch*, a prevalent and highly crystalline impurity with a large peak at 2θ = 29.7 ° (when *Ch* = S) and 2θ = 28.6 ° (when *Ch* = Se). $SrCO_3$ is added next, with a pair of small broad peaks at 2θ = 25.3 ° and 2θ = 26.0 °, followed by Sc_2O_3, whose primary peak at 2θ = 31.5 ° lies between the large characteristic MALM peaks in that region. Any other impurities are then added, such as $NaCu_3Ch_2$, Y_2O_3, or $SrSc_2O_4$. The peak positions of the three most common impurity phases are illustrated in Figure 72, an example diffractogram from the investigation into sodium doped $Sr_3Sc_2O_5Cu_2S_2$.

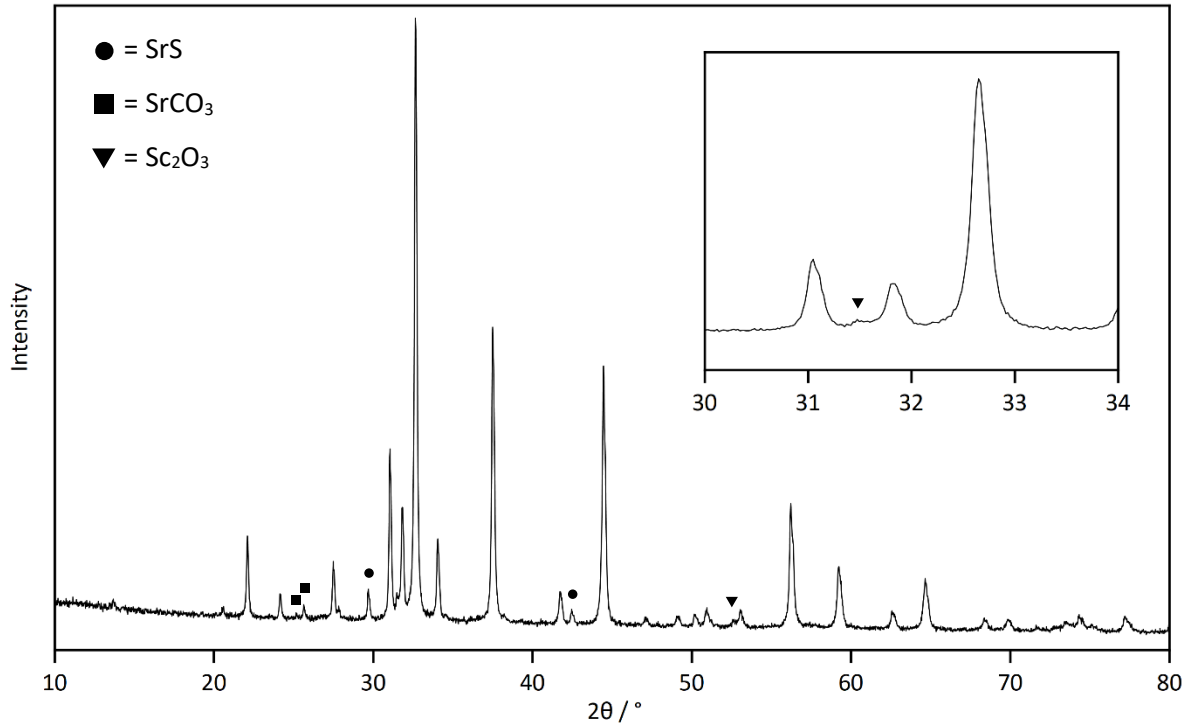

Figure 72 *Powder X-ray diffractogram of material with target composition $(Sr_{2.975}Na_{0.025})Sc_2O_5Cu_2S_2$, used as an example to illustrate the positions of the largest reflections of the three most common impurities in this investigation. The black line represents the observed diffracted intensity. The circular, square and triangular markers represent the peak positions of SrS, $SrCO_3$ and Sc_2O_3 respectively. The inset shows the magnified region of 2θ = 30 to 34 ° to highlight the primary impurity peak for Sc_2O_3.*

In the method developed for this investigation, an impurity phase is imported and first given a phase fraction of zero, and the particle size set to that which was obtained from the 12 hour sample. The phase fraction is increased manually until a good fit is achieved. The program is then allowed to refine the phase fraction and unit cell parameters, alongside a further refinement of the background. When all phases have been added, these parameters will be refined together along with the main phase, improving the fit of all phases concurrently and providing appropriate phase fractions.

The thermal parameters and strain parameters of impurity phases are never refined, as doing so rarely gives repeatable results. The default thermal parameters given in the CIF, the default 0.1 µm size and 1000 microstrain assigned to all imported phases, alongside refined values for unit cell parameters, particle size, and phase fraction, are together more than sufficient for a good fit to be achieved without further manipulation. Using the procedure outlined above, one can be confident that a phase fraction difference between an impurity in two different samples is actually due to a difference in physical quantity, and not due to a difference in the way the impurity was refined in each sample. For diffractograms as similar as those presented herein, this repeatability is very important. This process comes at a very slight cost of goodness of fit, but this is outweighed by the reassurance of consistency. Goodness of fit is, after all, only a measure of fit between observed and modelled data sets, and itself should not be used to judge the quality or purity of a sample.

3.3 $Sr_3Sc_2O_5Cu_2S_2$

3.3.1 Repeated Literature Synthesis of Pristine $Sr_3Sc_2O_5Cu_2S_2$

$Sr_3Sc_2O_5Cu_2S_2$ was synthesised on a 1 gram scale using conventional solid-state chemistry and the procedure outlined in the previous section, according to Equation 42:

Equation 42 $2\ SrO + Sc_2O_3 + Cu_2S + SrS \rightarrow Sr_3Sc_2O_5Cu_2S_2$

The ground powder material was heated for 12 hours at 800 °C, reground, pelletised, and heated again for 24 hours at 800 °C, as per methods reported in literature for this material.[8, 42, 59] The resulting product was a beige-brown powder, consistent with the reported "brownish white",[42] and had a purity of 96.5 % extracted from Rietveld refinement. The resulting PXRD pattern is shown below.

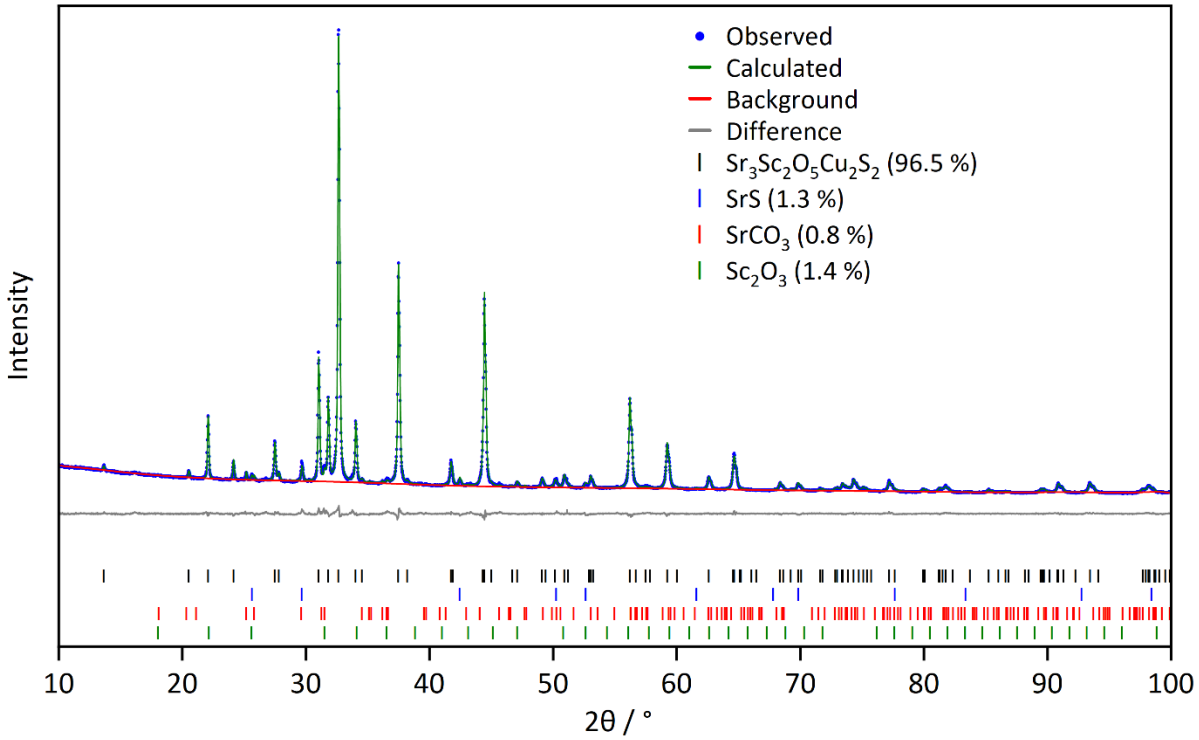

Figure 73 *Powder X-ray diffractogram of material with target composition $Sr_3Sc_2O_5Cu_2S_2$ (space group I4/mmm) after 36 hours of heating at 800 °C. The small blue circles represent the observed diffracted intensity, the green line represents the Rietveld-refined calculated model, the red line represents the background, and the grey line represents the difference between observed and calculated intensities. The black tick marks show the reflections of the refined model of $Sr_3Sc_2O_5Cu_2S_2$ (96.5 %), whilst the blue, red and green tick marks represent impurity phases SrS (1.3 %), $SrCO_3$ (0.8 %) and Sc_2O_3 (1.4 %) respectively. Duration: 12.5 hours. Data points: 4444. Interval: 0.02 °. GOF: 1.92. R_{wp}: 2.490 %.*

Table 4 *The refined structural parameters and key performance metrics of pristine material $Sr_3Sc_2O_5Cu_2S_2$, compared to other publications of this material in literature.*

Source	*a* / Å	*c* / Å	Cell volume / Å^3	R_{wp} / %	Band gap / eV	Conductivity / S cm^{-1}
This work	4.07463(4)	25.9578(3)	430.966(12)	2.49	3.10	2.28×10^{-3}
Otzschi 1999 [8]	4.0758(2)	25.985(2)	431.666(44)	9.42	*n/a*	*n/a*
Liu 2007 [42]	4.08	25.99	432.64	*n/a*	3.10	2.8
Limburn 2020 [59]	4.07	26.02	431.02	6.26	3.10	*n/a*

The refined unit cell parameters of the synthesised $Sr_3Sc_2O_5Cu_2S_2$ pristine MALM are shown in Table 4, in comparison to those published in literature. A refined structural model of this material is reported in *Appendix A.1*. The unit cell parameters *a* and *c*, found here to be approximately 4.07 Å and 25.96 Å respectively, are in close agreement with the tabulated published values. UV-Vis spectrometry data, shown below in Figure 74, revealed an estimated optical band gap of 3.10 eV which equates to 400 nm and is an exact match to both reported literature examples in Table 4.

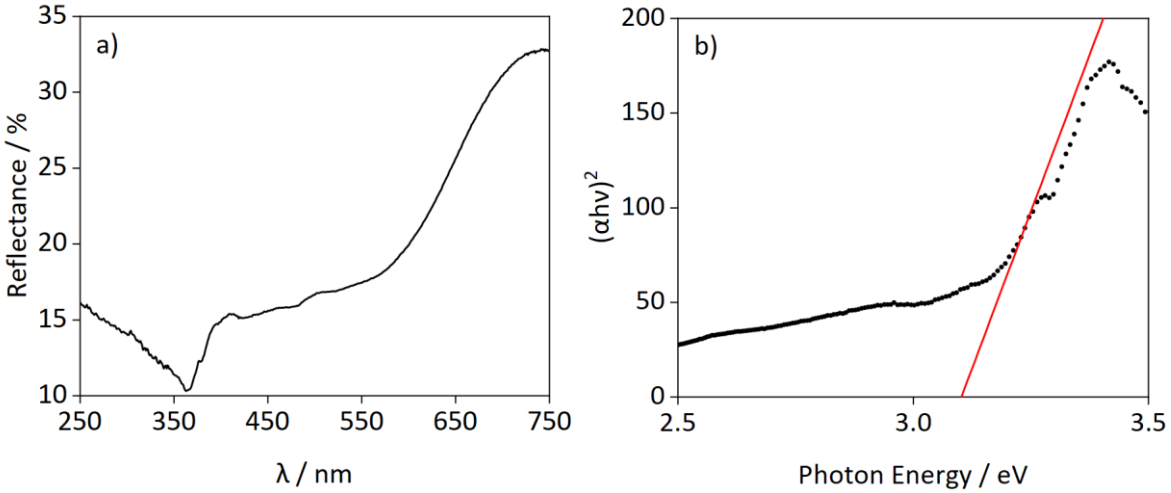

Figure 74 *UV-Vis spectrometry data for sample with target composition $Sr_3Sc_2O_5Cu_2S_2$ after 36 hours of heating at 800 °C. Plot a) is the raw diffuse reflectance data showing the drop off in reflectance between the visible region and the ultraviolet region occurring at approximately 400 nm. Plot b) is the resulting Tauc plot obtained from the first derivative of the Diffuse Reflectance data, magnified between 2.5 and 3.5 eV to highlight the drop-off, where the intercept between the red extrapolated tangent line and the x-axis is used to estimate an optical band gap of 3.10 eV / 400 nm.*

Where this synthesised material does not agree with published data, however, is in the estimation of its conductivity. Four probe van der Pauw resistivity testing yielded an estimated bulk conductivity of 2.28×10^{-3} S cm^{-1}. This value is poor, but could be improved through doping or through deposition as a thin film (due to higher density, lower porosity, and improved grain connectivity). Liu et al report a conductivity value of 2.8 S cm^{-1}, 1200 times greater than that which is observed here.[42]

The large disparity in these values is concerning. Repeated syntheses of this sample over multiple years and by various colleagues of the author support the observed value, eliminating experimental or user error. Sample purity is unlikely to be the cause of an observed conductivity difference to this extent.

There are two significant experimental differences between this work and that of Liu et al which could explain the large discrepancy in sample conductivity. The first is sample washing. Washing is uncommon in solid-state chemistry but Liu's material was washed with cyanide to remove "*an undesired Cu_xS phase*". The Cu_xS family are highly conductive,[250, 251] so it is logical to assume that its presence may erroneously increase the sample conductivity, likewise that its removal would decrease it (to the correct value).[‡] Therefore, assuming the cyanide wash had no other unsought effect on the structure or chemistry of $Sr_3Sc_2O_5Cu_2S_2$, it is unlikely that the removal of Cu_xS is responsible for the improved conductivity, and may have actually reduced it from an even greater false-positive value.

The second experimental difference, almost certainly that which is responsible for the difference in reported conductivity values, is the method of densification of pellet samples. Liu's method involves pressing a 10mm pellet under 60 MPa, while simultaneously heating to 800 °C in a Spark Plasma Sintering (SPS) furnace. The 8mm pellets annealed for conductivity measurements in this investigation were pressed at 2 tonnes and then heated in an ampoule to 800 °C in a furnace at ambient pressure. Whilst this is approximately a 5x greater pelletising force than employed by Liu,[§] compared to SPS it is expected to produce a far less dense material. SPS is a superior method of densification, employing pressure, heat and a current simultaneously to sinter a powder material into an extremely dense pellet in minutes, usually for densification but also for direct synthesis.[252] Crucially, this method enhances grain growth, in turn minimising grain boundaries which detrimentally effect electrical conductivity.[253]

The lack of such a facility likely means that all materials produced here are hampered in conductivity by the limitations of equipment available, but it is important to note that the experimental conditions were kept strictly uniform across all samples described in this chapter so as to produce a self-consistent data set. Densities (and crucially, conductivities) of materials produced within this work may be lower than their theoretical maximum, but can be reliably compared to each other through consistency of the methodology. In turn, they can less confidently be compared to materials such as that of Liu, produced under superior conditions. Liu does not cite a pellet density, but SPS has been shown to produce densities of up to 98 % relative to the bulk crystal density,[254-256] so it is expected that Liu's sample density would certainly be higher than that which is measured here, 70.7 %, a value on par with all samples in this chapter and unable to be improved under the current conditions.

[‡] A similar effect is observed in this work when doping $Sr_3Sc_2O_5Cu_2Ch_2$ with K^+ and Na^+.

[§] The pelletising force in Liu's investigation and this investigation are 4.71 kN and 19.62 kN respectively.

3.3.1.1 Alternate Synthesis Attempts

In *Section 2.3.6*, the difficult synthesis of Cu_2S from the elements was discussed. This binary precursor was previously purchased, but doubts concerning its purity warranted an in-house synthesis from Cu and S by conventional solid-state chemistry. Coinciding with this process, with temporarily no reliable source of Cu_2S, two new synthetic routes to pristine material $Sr_3Sc_2O_5Cu_2S_2$ were attempted to circumvent the use of Cu_2S as a precursor, and to hopefully increase on the high but improvable purity of $Sr_3Sc_2O_5Cu_2S_2$, 96.5 wt %.

The first involved the use of Cu and S as elements in place of Cu_2S, with all other precursors kept the same. The sample was subjected to an initial 100 °C heat cycle (as described in *Section 3.2.3* for doped materials containing elemental sulfur to avoid sublimation) then a 12 hour powder heat and a 24 hour pellet heat at 800 °C. The synthesis was attempted according to Equation 43:

Equation 43 $$2\ SrO + Sc_2O_3 + 2\ Cu + {}^1/_8\ S_8 + SrS \rightarrow Sr_3Sc_2O_5Cu_2S_2$$

$Sr_3Sc_2O_5Cu_2S_2$ formed relatively pure in this synthesis, but not to a level greater than the original synthesis and so was not pursued further.

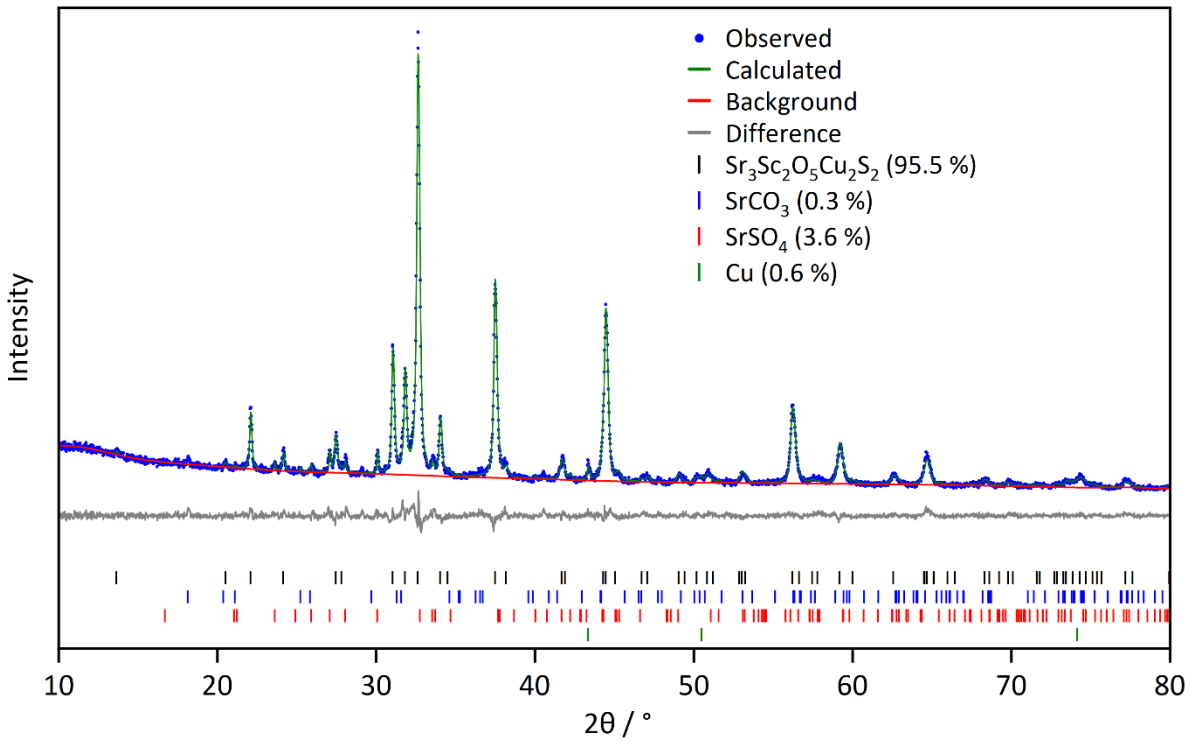

Figure 75 *Powder X-ray diffractogram of material with target composition $Sr_3Sc_2O_5Cu_2S_2$ (space group I4/mmm) after 36 hours of heating at 800 °C. The small blue circles represent the observed diffracted intensity, the green line represents the Rietveld-refined calculated model, the red line represents the background, and the grey line represents the difference between observed and calculated intensities. The black tick marks show the reflections of the refined model of $Sr_3Sc_2O_5Cu_2S_2$ (95.5 %), whilst the blue, red and green tick marks represent impurity phases $SrCO_3$ (0.3 %), $SrSO_4$ (3.6 %) and Cu (0.6 %) respectively. Duration: 45 minutes. Data points: 3457. Interval: 0.02 °. GOF: 1.38. R_{wp}: 5.554 %.*

The second alternate synthesis pathway used Cu_2O in place of Cu_2S, and in order to balance the stoichiometry employs one less molar unit or SrO than the conventional synthesis and one extra unit of SrS, according to Equation 44. This maintained the oxidation states of all component atoms, unlike the previous route using elemental Cu and S which required oxidation and reduction respectively.

Equation 44 $SrO + Sc_2O_3 + Cu_2O + 2\,SrS \rightarrow Sr_3Sc_2O_5Cu_2S_2$

The powder mixture was heated to 800 °C for 12 hours, followed by an intermediate regrind and then another 800 °C for 24 hours as a pellet. As before, this synthesis was successful, but to a lesser quality than the original synthesis, see Figure 76. The conventional synthesis attempted in *Section 4.3*, which produced the 96.5 wt % purity sample of $Sr_3Sc_2O_5Cu_2S_2$, was deemed to be the best route for high purity (and that which has been reported in purity), and was selected as the method to be taken forward as a template for the synthesis of doped samples in the upcoming investigations.

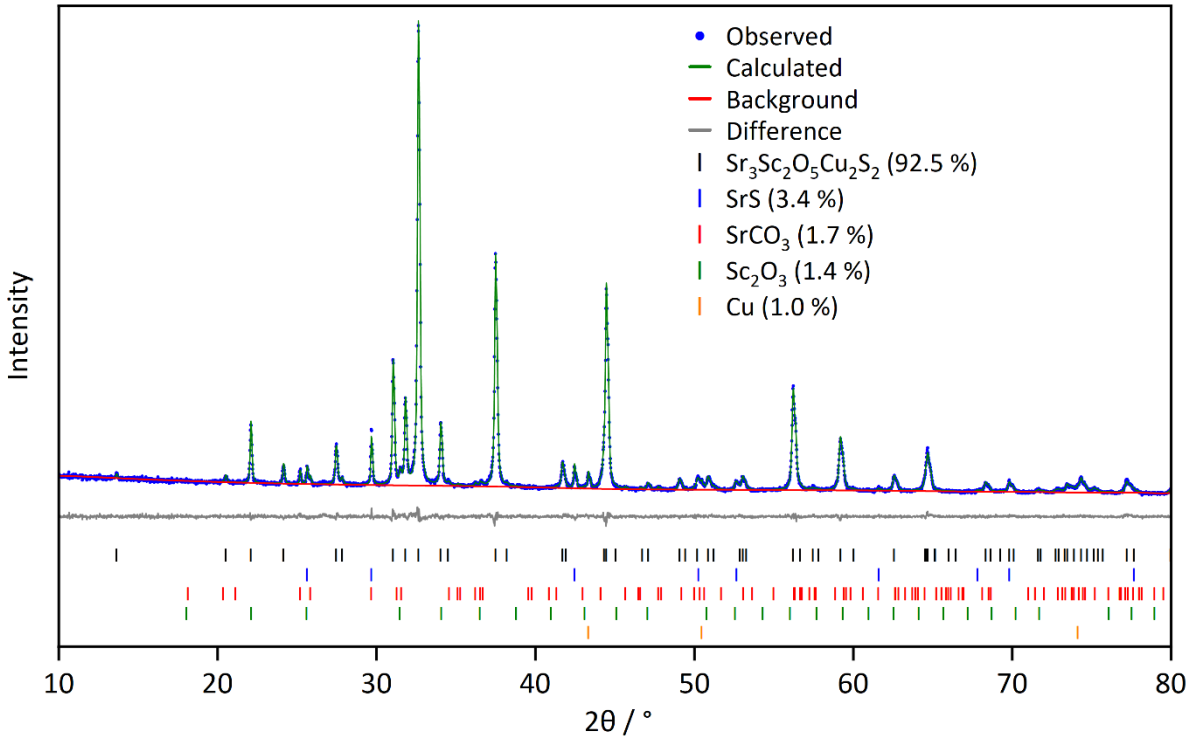

Figure 76 *Powder X-ray diffractogram of material with target composition $Sr_3Sc_2O_5Cu_2S_2$ (space group I4/mmm) after 36 hours of heating at 800 °C. The small blue circles represent the observed diffracted intensity, the green line represents the Rietveld-refined calculated model, the red line represents the background, and the grey line represents the difference between observed and calculated intensities. The black tick marks show the reflections of the refined model of $Sr_3Sc_2O_5Cu_2S_2$ (92.5 %), whilst the blue, red, green and orange tick marks represent impurity phases SrS (3.4 %), $SrCO_3$ (1.7 %) Sc_2O_3 (1.4 %) and Cu (1.0 %) respectively.*
Duration: 45 minutes. Data points: 3457. Interval: 0.02 °. GOF: 1.12. R_{wp}: 3.655 %.

3.3.2 Potassium Doping, $(Sr_{3-x}K_x)Sc_2O_5Cu_2S_2$

Potassium was introduced as an aliovalent dopant onto the strontium site of $Sr_3Sc_2O_5Cu_2S_2$ such that the target material takes the form $(Sr_{3-x}K_x)Sc_2O_5Cu_2S_2$. This was achieved by reducing SrS content and supplementing with $[K_2S + S]$ (a 1:1 molar mixture of K_2S and S), according to Equation 45 below:

Equation 45 $$2\ SrO + Sc_2O_3 + Cu_2S + 1\text{-}x\ SrS + \frac{x}{2}[K_2S + S] \rightarrow (Sr_{3-x}K_x)Sc_2O_5Cu_2S_2$$

The ground powder precursors (1 gram scale) were heated within an ampoule for 12 hours at 100 °C, then raised to 800 °C for a further 12 hours in the same ampoule. They were then reground, pelletised, and heated again for 24 hours at 800 °C. Six samples were synthesised, with a dopant level ranging from x = 0.025 mol to x = 0.150 mol at equal increments of 0.025 mol, all synthesised in one self-consistent sample set. This x range was selected with the presumption that it would encompass the entire effective doping range, including the point of dopant saturation (presumed to be the optimum in terms of conductivity) where beyond that, performance would decline. As explained later, a larger range would be more informative, inspiring large ranges in later series. The complete compositional, analytical and graphical data for each sample in this section can be found in *Appendix B.1.1*.

Purity values remained relatively high during this investigation (see Figure 77 below), with all samples refined to between 93 % and 98 % purity by weight, on par with that of the undoped pristine analogue and with only a small downward trend at higher doping amounts.

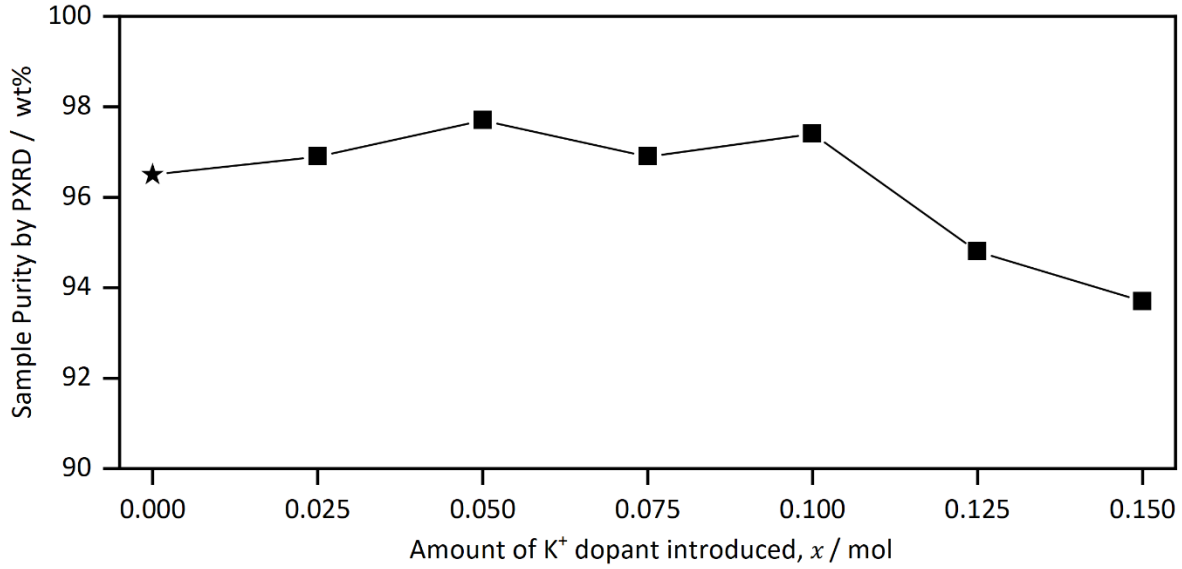

Figure 77 *Purities of the six potassium doped MALMs in the $(Sr_{3-x}K_x)Sc_2O_5Cu_2S_2$ series. The pristine material $Sr_3Sc_2O_5Cu_2S_2$ is included as a reference at x = 0 mol and is represented by a star. All values are derived from the Rietveld refinements of PXRD data using GSAS-II, and reported as weight percentages.*[**]

[**] In this plot and in all other analogous plots herein, unless stated otherwise, lines between scatter data points serve as a guide to the eye and are not to imply linear trends between data points.

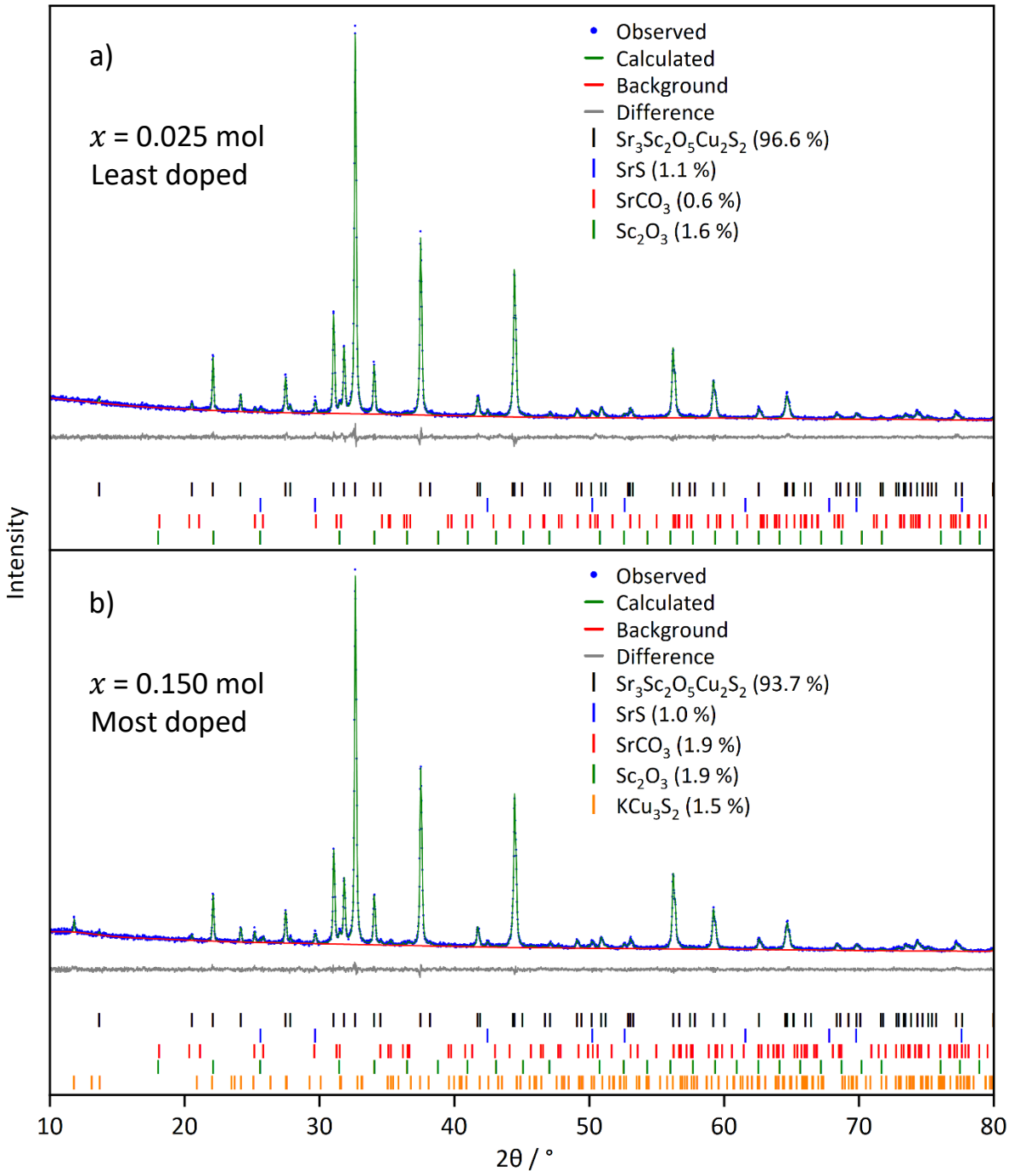

Figure 78 *Powder X-ray diffractograms of a) the least doped sample of the series with target composition $(Sr_{2.975}K_{0.025})Sc_2O_5Cu_2S_2$, and b) the most doped sample of the series with target composition $(Sr_{2.850}K_{0.150})Sc_2O_5Cu_2S_2$ (both space group I4/mmm) after 36 hours of heating at 800 °C. The small blue circles represent the observed diffracted intensities, the green lines represent the Rietveld-refined calculated models, the red lines represent the backgrounds, and the grey lines represent the differences between observed and calculated intensities. The black tick marks show the reflections of the refined model of $Sr_3Sc_2O_5Cu_2S_2$, whilst the blue, red, green and orange tick marks represent refined impurity phases SrS, $SrCO_3$, Sc_2O_3 and KCu_3S_2 respectively. Weight fractions for each phase are cited in the figure legends.*
a) Duration: 45 minutes. Data points: 3457. Interval: 0.02 °. GOF: 1.16. R_{wp}: 5.282 %.
b) Duration: 45 minutes. Data points: 3457. Interval: 0.02 °. GOF: 1.09. R_{wp}: 4.756 %.

The Rietveld-refined PXRD pattern of the least doped sample (where x = 0.025) is seen in Figure 78a, showing the minor impurity phases SrS, $SrCO_3$, and Sc_2O_3, each of which is observed in all samples in this series. What is interesting to note however, is that while these impurities are commonplace here (and MALMs in general), there is no potassium-containing impurity in the low level doped samples from x = 0.025 to x = 0.100, but KCu_3S_2 emerges as an impurity in the two samples above this. This suggests that the strontium site of $Sr_3Sc_2O_5Cu_2S_2$ permits some incorporation of potassium as a dopant, up to a level of approximately x = 0.100, beyond which any additional dopant appears as an impurity phase. The highest-doped sample (x = 0.150, the PXRD pattern of which is also shown in Figure 78b in comparison to the least doped sample), contains the greatest amount of KCu_3S_2 at 1.5 % by weight, with its largest peak at 2θ = 11.5 °. It was hypothesised that increasing the doping amount beyond the highest attempted level of x = 0.150 mol would produce increasingly impure materials, surpassing far beyond the amount of dopant that can be incorporated into the material. This was found to be the case in various later investigations on the selenide analogues, where doping is attempted to almost an order of magnitude greater extent.

For each sample in the series, the level of dopant incorporation may be estimated using the amounts and compositions of impurity materials. For the first four samples, no impurities containing potassium were observed and therefore up to 100 % of the potassium may be attributed to the MALMs. With no evidence suggesting otherwise the targeted values of x may be assumed to be equal or very close to the actual values of x. These values are likely to always be an overestimate for reasons explained below, so serve as an absolute maximum for the saturation of these four materials due to the lack of impurities accounting for dopant elsewhere.

Table 5 *The target and maximum possible dopant content within each MALM in the $(Sr_{3-x}K_x)Sc_2O_5Cu_2S_2$ series. The pristine material $Sr_3Sc_2O_5Cu_2S_2$ is included as a reference.*

Target x / mol	**Maximum K in product / %**	**Maximum x / mol**
0 (pristine)	100	0
0.025	100	0.025
0.050	100	0.050
0.075	100	0.075
0.100	100	0.100
0.125	76.449	0.096
0.150	79.014	0.119

For the x = 0.125 and 0.150 samples however, 23.5 % and 21.0 % (by weight) of supplied K manifested as KCu_3S_2 in the end products respectively. In any sample where dopant is observed within an impurity phase, be that due to the host material having reached saturation, the stability or inertness of a dopant-containing impurity/precursor, or complete dopant incompatibility with the host material, 100 % dopant incorporation is impossible and the actual x must be lower than the target x. Some amount of dopant exists outside of the MALM elsewhere in the material composition, therefore the MALM must have less than the intended value of dopant. The other 76.5 % and 79.0 % of potassium in the x = 0.125 and 0.150 samples serve as an upper limit for the amount of supplied K that could have been incorporated into the MALM, which translates to maximum x values of 0.096 and 0.119 respectively.

This data is represented in Table 5 on the previous page, and Figure 79 below. In the latter, the dashed red line represents 100 % dopant incorporation. At low dopant levels the samples lie close to this line, with no observed KCu_3S_2 and a maximum possible dopant incorporation of 100 %. Above this, the samples stray from the line with some dopant accounted for by KCu_3S_2.

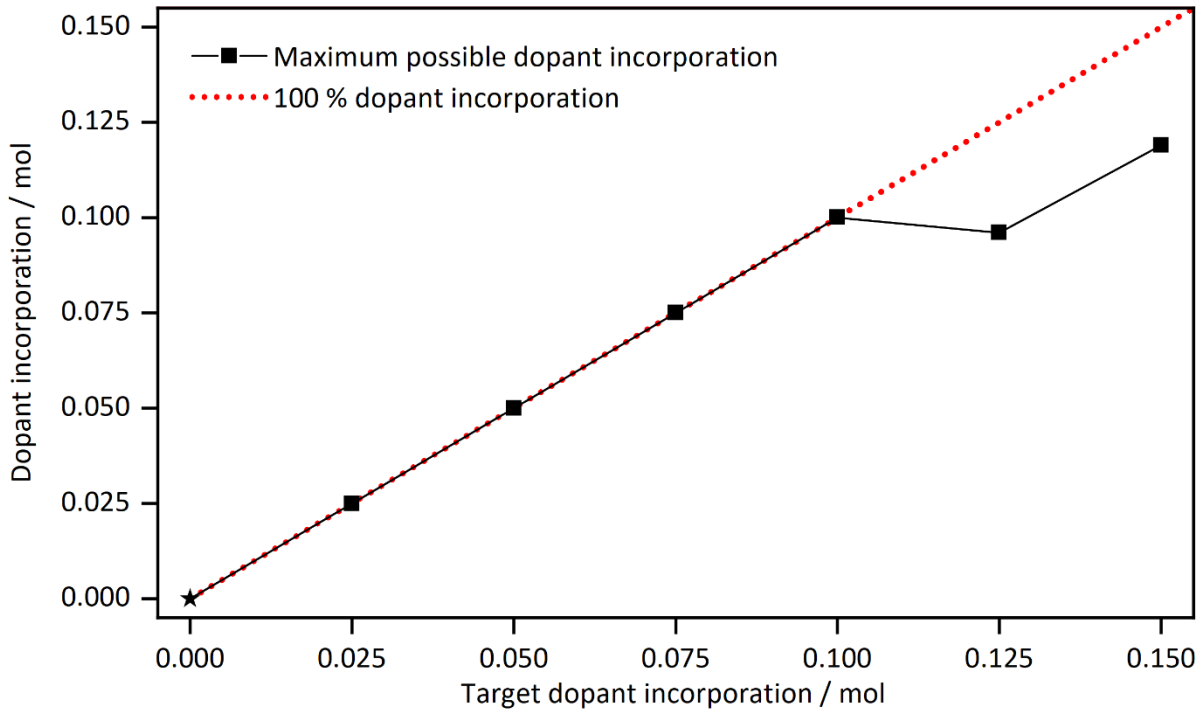

Figure 79 *The calculated maximum possible levels of dopant incorporation into the $(Sr_{3-x}K_x)Sc_2O_5Cu_2S_2$ MALMs. Values were derived from the wt % of the potassium-containing impurities of each sample. The pristine material $Sr_3Sc_2O_5Cu_2S_2$ is included as a reference at x = 0 mol and is represented by a star. The red dashed line represents 100 % dopant incorporation into the MALM, statistically no values may surpass this line. The black data points are the estimated upper bound of dopant incorporation for each sample.*

Assuming correct experimental procedures were followed and that no material may be added to or removed from the reaction mixture throughout the synthetic process, the actual dopant incorporation in the MALM can never exceed the target. In practice this means data points may never lie above the red dashed line, and that a material with a target x of, for example, 0.150 mol, may have an actual x value equal to or less than 0.150 mol. Only the pristine material may be assumed to lie exactly on this line, where no dopant is supplied and thus the target and actual values of x are both zero.

There are several reasons why the dopant incorporation values must not be treated as actual values, only upper limits. Firstly, it cannot be assumed that KCu_3S_2 is the only dopant containing phase. Other phases may be present and either too small to be observed within the detection limits of PXRD, or amorphous.

It can also not be assumed that all of the potassium not contained within KCu_3S_2 is incorporated into the MALM because other impurity phases may also be unintentionally doped. After all, this work presents ample evidence for the successful doping of group 1 metals onto the Sr^{2+} site of MALMs, so one must not rule out the possibility for Sr^{2+} site doping in phases such as SrS and $SrCO_3$ observed here or $SrSc_2O_4$ observed elsewhere in this chapter. While this is usually assumed not to be a possibility, and would have little effect due to low impurity quantities, it is not possible to rule out any doping of these phases, which would lower the actual x value.

A final argument is the error associated with modelling small phases such as KCu_3S_2 in Rietveld refinements. As shown in *Section 3.1.1 - The ACu_3Ch_2 Impurities*, the largest and often only visible peak of KCu_3S_2 is at 2θ = 11.8 °. Modelling a trace phase with only one significant peak is difficult and subject to user interpretation, even when applying the procedure outlined in *Section 3.2.4.2 - The Refinement of Impurities in Doped MALMs*, hence some error on the phase fraction is inevitable. While difficult to estimate, this small error should be considered alongside the possibility for amorphous phases or other doped impurities as small yet valid reasons why the estimated value of dopant incorporation is an upper limit and must not be considered the actual value.

Dopant incorporation plots such as Figure 79 are used frequently in this chapter as a visual indication of the propensity of these $Sr_3Sc_2O_5Cu_2Ch_2$ MALMs to doping. The range of low dopant concentrations where full incorporation is probable, and the saturation point where this behaviour ends, can be easily visualised. If the assumption that a true saturation point exists where no more dopant may be added beyond a fixed given point, these plots should plateau at that value of y, but this is scarcely observed, meaning either that some dopant incorporation continues beyond the point where full incorporation ends, or that the arguments detailed above for impurity doping, small or amorphous phases and modelling errors are contributing to false positive incorporation values and that they do in fact plateau.

The impurity levels in these samples, despite increasing across the series, were so small overall as to have no noticeable effect on sample colour, Figure 80, which is expected to darken with increasing concentrations of black impurities such as ACu_3Ch_2. In various later series, particularly those which extend to far greater doping levels and therefore experience greater impurity, pronounced colour changes are observed.

Figure 80 A photographic comparison of the colour of the $(Sr_{3-x}K_x)Sc_2O_5Cu_2S_2$ MALM series. Dopant concentration increases from left to right.

Doping at this extent appears to have very little effect on the size of the unit cell, see Figure 81, where most changes between neighbouring samples are within error, as extracted from GSAS-II. The pristine sample has smaller errors as the refinement was performed on a 12 hour PXRD scan, compared to 45 minutes for the doped samples, all of which are published in *Appendix B.1.1*. Patterns which resemble trends at this resolution (in the case of the *a* parameter, 0.0001 Å) are well within the noise of the instrument and the subjective user error of Rietveld refinement, and therefore show no change.

Unit cell size consistency across this series is to be expected. While the K^+ cation is larger than Sr^{2+} (1.64 Å vs 1.44 Å respectively on the 12-coordinate intra-layer A site, a 14 % difference, and 1.51 Å vs 1.26 Å respectively on the 8-coordinate inter-layer A site, a 20 % difference), the degree to which the parent material has been doped with potassium is relatively low, and only the samples doped with x = 0 to 0.100 mol of K^+ can be assumed to have incorporated the target amount of dopant. The ion size estimates also assume that K^+ is occupying a site for a +1 oxidation state ion, which in 325 materials such as $Sr_3Sc_2O_5Cu_2S_2$, it is not, so ion size comparisons should remain qualitative.

Potassium doping into $Sr_3Sc_2O_5Cu_2S_2$ appears fortuitously to also have very little effect on sample transparency, with all six samples exhibiting estimated optical band gaps between 3.06 and 3.15 eV, thus no significant difference to the undoped material at 3.10 eV. The diffuse reflectance data of moderately doped $(Sr_{2.900}K_{0.100})Sc_2O_5Cu_2S_2$, for example, is shown in Figure 82a, alongside the associated Tauc plot used to calculate the band gap shown in part Figure 82b. The stability of the optical band gap is a trend observed across most of the dopant permutations explored herein, with some exceptions such as magnesium and lanthanum doping of the selenide 325.

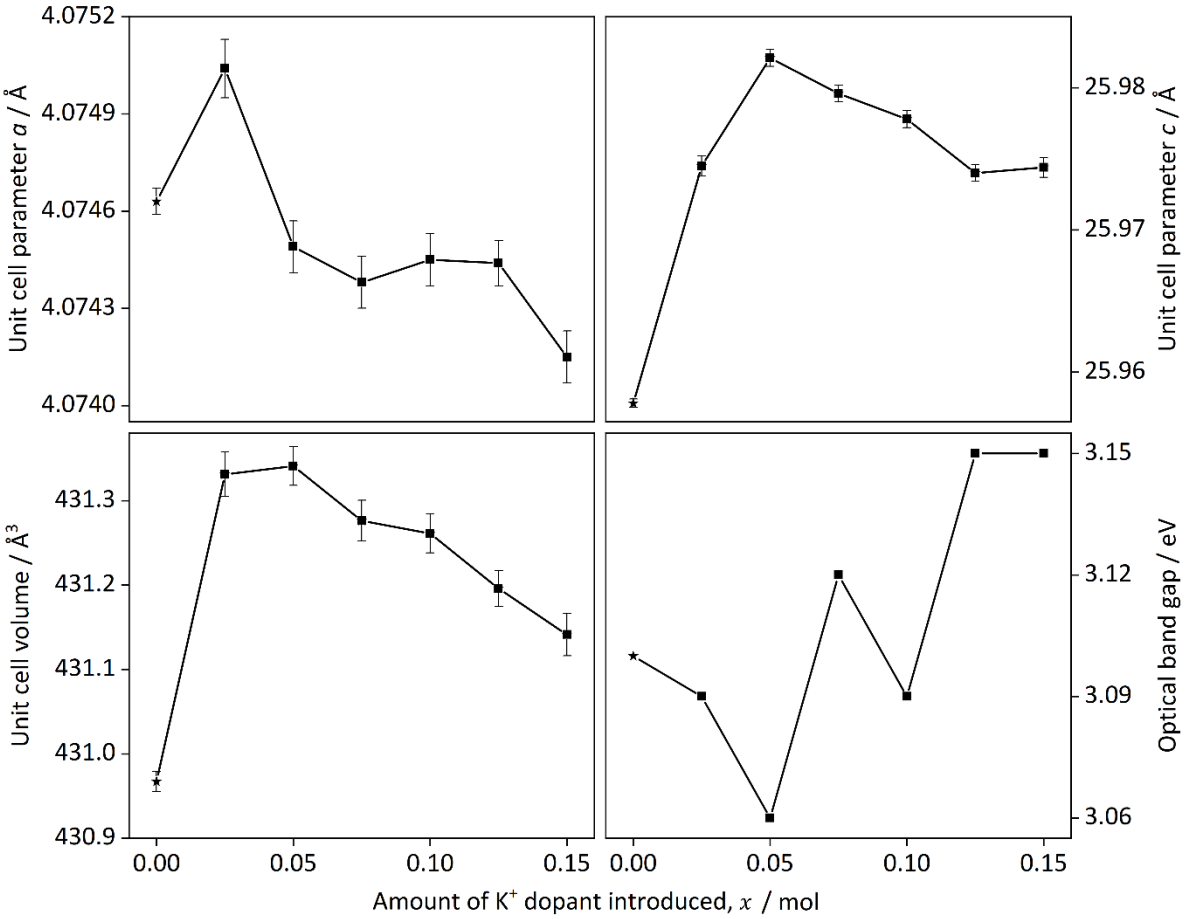

Figure 81 *Comparisons of a) the a unit cell parameter, b) the c unit cell parameter, c) unit cell volume, and d) the optical band gap, of the six potassium doped MALMs in the $(Sr_{3-x}K_x)Sc_2O_5Cu_2S_2$ series. The pristine material $Sr_3Sc_2O_5Cu_2S_2$ is included as a reference at $x = 0$ mol and is represented by a star.*

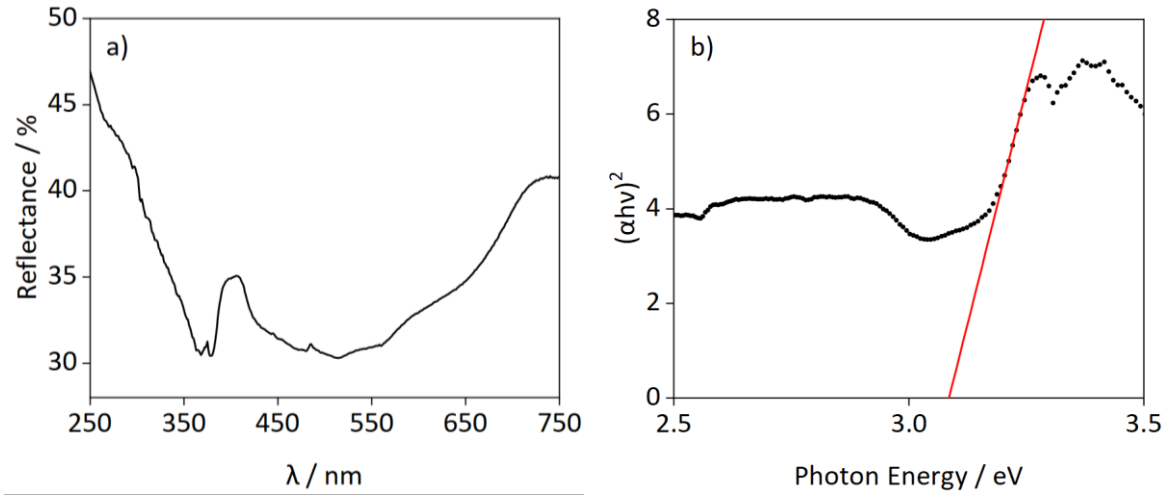

Figure 82 *UV-Vis spectrometry data for sample with target composition $(Sr_{2.900}K_{0.100})Sc_2O_5Cu_2S_2$ after 36 hours of heating at 800 °C. Plot a) is the raw diffuse reflectance data showing the drop off in reflectance between the visible region and the ultraviolet region occurring at 350-450 nm. Plot b) is the resulting Tauc plot obtained from the first derivative of the Diffuse Reflectance data, magnified to highlight the drop-off, where the intercept between the red extrapolated tangent line and the x-axis is used to estimate an optical band gap of 3.09 eV / 401 nm.*

Figure 83 depicts the conductivity values obtained from analysis of the six samples using the 4 probe van der Pauw method outlined previously, on 8 mm 0.15 g pellets that had been annealed at 800 °C for 12 hours. Undoped conductivity was found to be 2.28×10^{-3} S cm^{-1} in the pristine sample, and it was hypothesised that this value will increase following successful dopant incorporation implied by PXRD analysis. An approximately linear trend is observed in conductivity as doping is increased, demonstrating an increase of 1 order of magnitude.

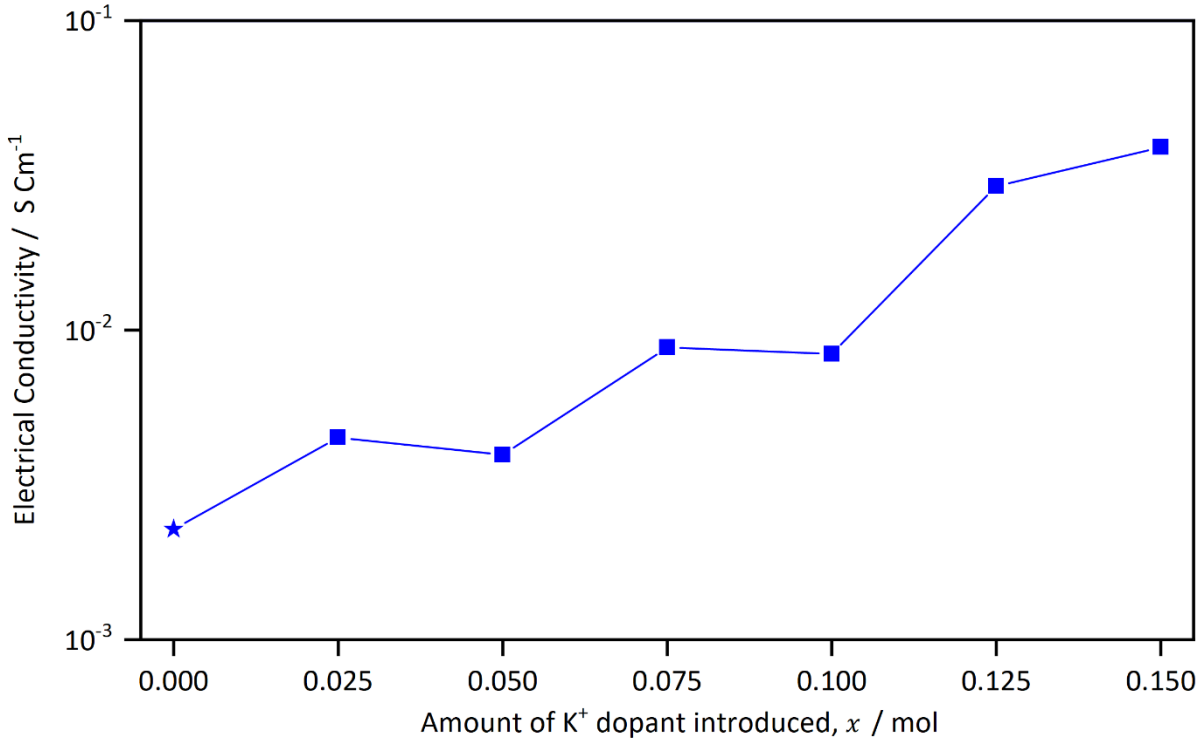

Figure 83 *The electrical conductivities of the six potassium doped MALMs in the $(Sr_{3-x}K_x)Sc_2O_5Cu_2S_2$ series, represented on a log_{10} scale. The pristine material $Sr_3Sc_2O_5Cu_2S_2$ is included as a reference at $x = 0$ mol and is represented by a star. All values are derived from van der Pauw 4 probe resistivity measurements of 8mm annealed pellet samples.*

The most doped sample unsurprisingly has the greatest conductivity, at 3.89×10^{-2} S cm^{-1}, although by this point dopant incorporation is limited and doping may have plateaued with the parent material having reached saturation, and any further addition of dopant is instead facilitating the formation of the conductive by-product KCu_3S_2. There is a negligible difference in conductivity between the samples where $x = 0.075$ and 0.100 mol, therefore the optimum level of potassium doping for $Sr_3Sc_2O_5Cu_2S_2$ would therefore be $x = 0.075$ mol; the greatest value of conductivity before conductive by-products emerge. Future research on this series should probe higher doping levels to explore the plateau or drop-off in conductivity once the *A* site is certain to have saturated.

In conclusion, regardless of the composition of the material, this study suggests that the doped series $(Sr_{3-x}K_x)Sc_2O_5Cu_2S_2$ remains tuneable in conductivity, whilst maintaining a wide band gap appropriate for visible light interaction, albeit over a small range of just one order of magnitude compared to the pristine.

3.3.3 Sodium Doping, $(Sr_{3-x}Na_x)Sc_2O_5Cu_2S_2$

Sodium was introduced as an aliovalent dopant onto the strontium site of $Sr_3Sc_2O_5Cu_2S_2$ such that the target material takes the form $(Sr_{3-x}Na_x)Sc_2O_5Cu_2S_2$. This was achieved by reducing SrS content and supplementing with $[Na_2S + S]$, according to Equation 46 below:

Equation 46 $$2\ SrO + Sc_2O_3 + Cu_2S + 1\text{-}x\ SrS + \frac{x}{2}[Na_2S + S] \rightarrow (Sr_{3-x}Na_x)Sc_2O_5Cu_2S_2$$

The ground powder precursors (1 gram scale) were heated within an ampoule for 12 hours at 100 °C, then raised to 800 °C for a further 12 hours in the same ampoule. They were then reground, pelletised, and heated again for 24 hours at 800 °C. Eight samples were synthesised, with a dopant level ranging from x = 0.025 mol to x = 0.200 mol at equal increments of 0.025 mol, all synthesised in one self-consistent sample set. The complete compositional, analytical and graphical data for each sample in this section can be found in *Appendix B.1.2*.

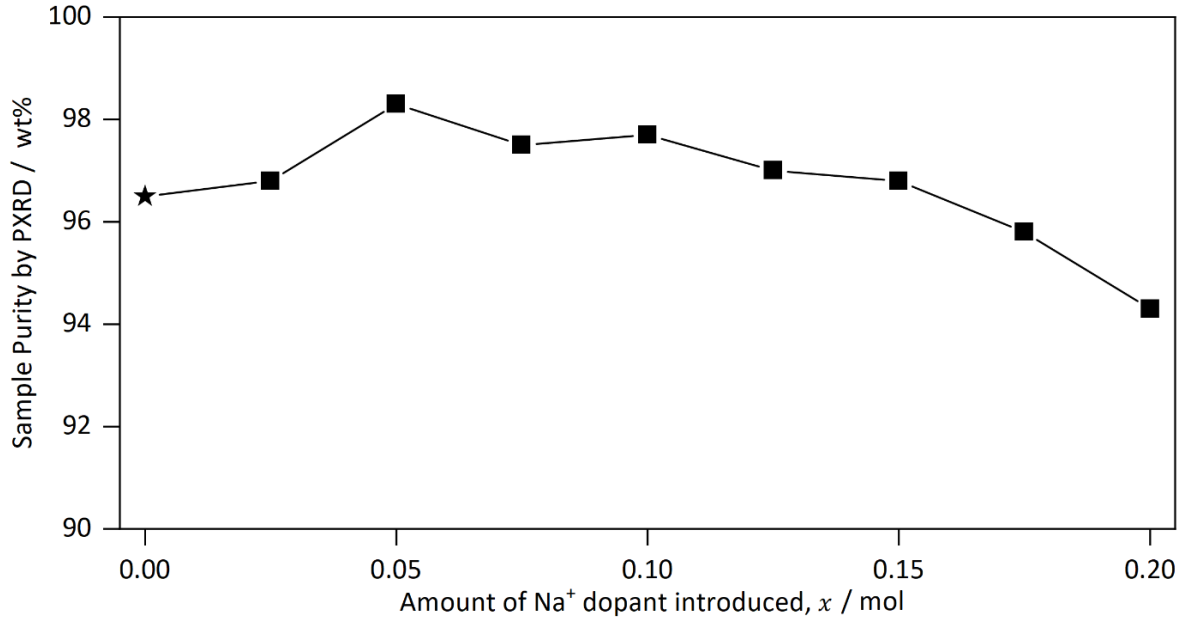

Figure 84 *Purities of the eight sodium doped MALMs in the $(Sr_{3-x}Na_x)Sc_2O_5Cu_2S_2$ series. The pristine material $Sr_3Sc_2O_5Cu_2S_2$ is included as a reference at x = 0 mol and is represented by a star. All values are derived from the Rietveld refinements of PXRD data using GSAS-II, and reported as weight percentages.*

These samples behaved very similarly to the previously described potassium doped $Sr_3Sc_2O_5Cu_2S_2$ MALMs. The sodium analogues demonstrate high purity (Figure 84), declining steadily as dopant level increases, from a maximum of 98.3 % when x = 0.050 mol. Doping is taken to a greater extent here, with two further samples extending up to x = 0.200 mol to investigate surpassing the point where the dopant can be confidently assumed to be incorporated. The Rietveld-refined powder diffractogram of this sample can be seen in comparison to the least doped sample, x = 0.025 mol, in Figure 85, where visually the patterns are extremely similar owing to the high purity maintained throughout this series.

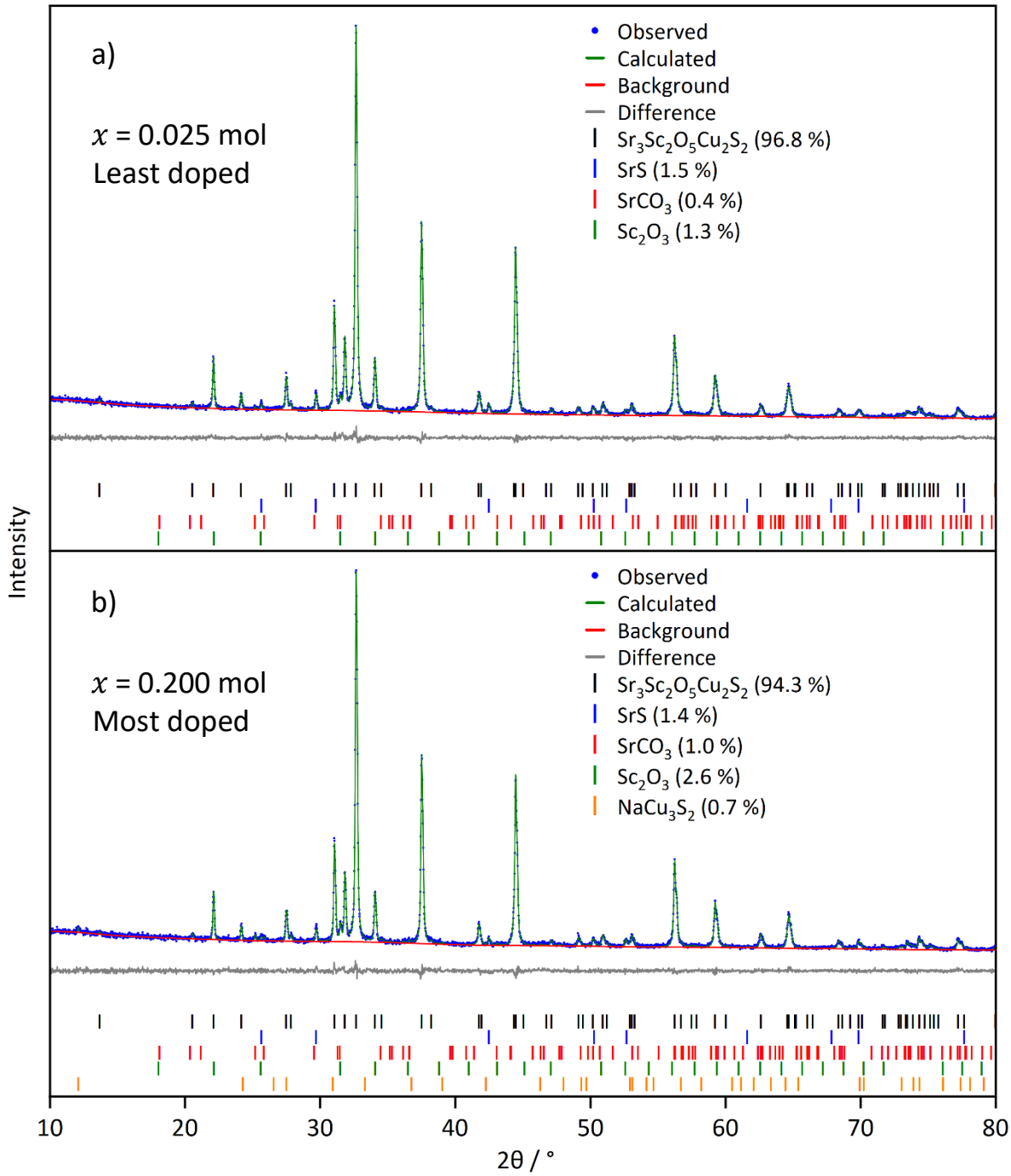

Figure 85 *Powder X-ray diffractograms of a) the least doped sample of the series with target composition $(Sr_{2.975}Na_{0.025})Sc_2O_5Cu_2S_2$, and b) the most doped sample of the series with target composition $(Sr_{2.800}Na_{0.200})Sc_2O_5Cu_2S_2$ (both space group I4/mmm) after 36 hours of heating at 800 °C. The small blue circles represent the observed diffracted intensities, the green lines represent the Rietveld-refined calculated models, the red lines represent the backgrounds, and the grey lines represent the differences between observed and calculated intensities. The black tick marks show the reflections of the refined model of $Sr_3Sc_2O_5Cu_2S_2$, whilst the blue, red, green and orange tick marks represent refined impurity phases SrS, $SrCO_3$, Sc_2O_3 and $NaCu_3S_2$ respectively. Weight fractions for each phase are cited in the figure legends.*
a) Duration: 45 minutes. Data points: 3457. Interval: 0.02 °. GOF: 1.08. R_{wp}: 4.456 %.
b) Duration: 45 minutes. Data points: 3457. Interval: 0.02 °. GOF: 1.12. R_{wp}: 4.844 %.

Akin to the potassium series, the first four samples of $(Sr_{3-x}Na_x)Sc_2O_5Cu_2S_2$ where $x = 0.025$ to 0.100 mol contain the impurities SrS, $SrCO_3$ and Sc_2O_3 at levels analogous to that of the pristine $Sr_3Sc_2O_5Cu_2S_2$ sample, but crucially no impurities containing sodium. From $x = 0.125$ mol onwards $NaCu_3S_2$ (the sodium analogue of the previously observed KCu_3S_2) is observed, the weight percentage of which increases linearly with additional sodium dopant concentration, Figure 86.

Whilst ion sizes must again be used with caution due to oxidation state differences, Na^+ ions are closer in size to Sr^{2+} than K^+ is (1.39, 1.44 and 1.64 Å respectively on a 12-coordinate site; 1.18, 1.26 and 1.51 Å on an 8-coordinate site), so higher purities and greater incorporation are expected from sodium.

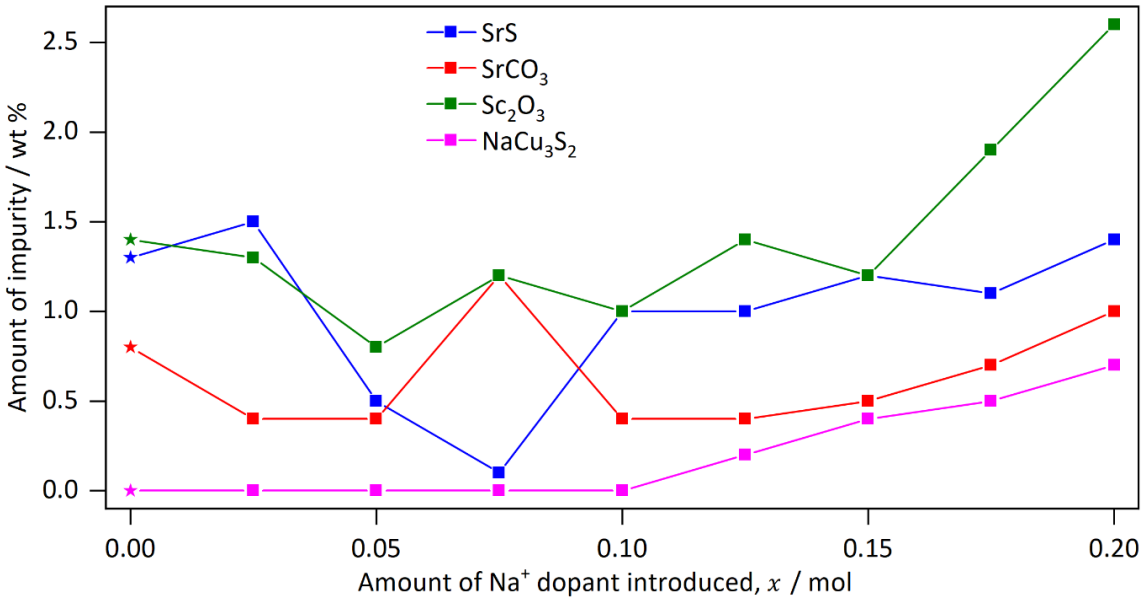

Figure 86 *The weight percentages of four impurity phases present in the $(Sr_{3-x}Na_x)Sc_2O_5Cu_2S_2$ series. The pristine material $Sr_3Sc_2O_5Cu_2S_2$ is included as a reference at $x = 0$ mol and is represented by stars.*

The emergence of this by-product is much less pronounced than the potassium analogue, with the four highest doped samples containing only 0.2, 0.4, 0.5 and 0.7 % $NaCu_3S_2$ respectively, therefore it remains a trace by-product in even the highest doped sample. These materials contain less than one third of the weight percentages of the $NaCu_3S_2$ observed in the equivalent samples of the potassium series. Small quantities of $NaCu_3S_2$ appearing in these otherwise high purity samples suggests that at the point where dopant is no longer all incorporated by the MALM, the plateau or decrease in incorporation is less severe. In turn, the dopant incorporation plot in Figure 87 shows the samples lying much closer to the theoretical 100 % maximum incorporation line. The point where deviation from the line occurs appears in the same region as it did for potassium, between $x = 0.100$ and 0.125 mol, beyond which doping appears to continue to have an effect, and full saturation may not yet have been reached. For potassium, this was deemed the saturation point, but here that may not be the case. As discussed, these values are upper limits and should not be considered actual values of x, however the estimated maximum amounts of dopant incorporation remain so close to the target that it cannot be confidently asserted that doping has ceased beyond 0.100 mol; likely just reduced.

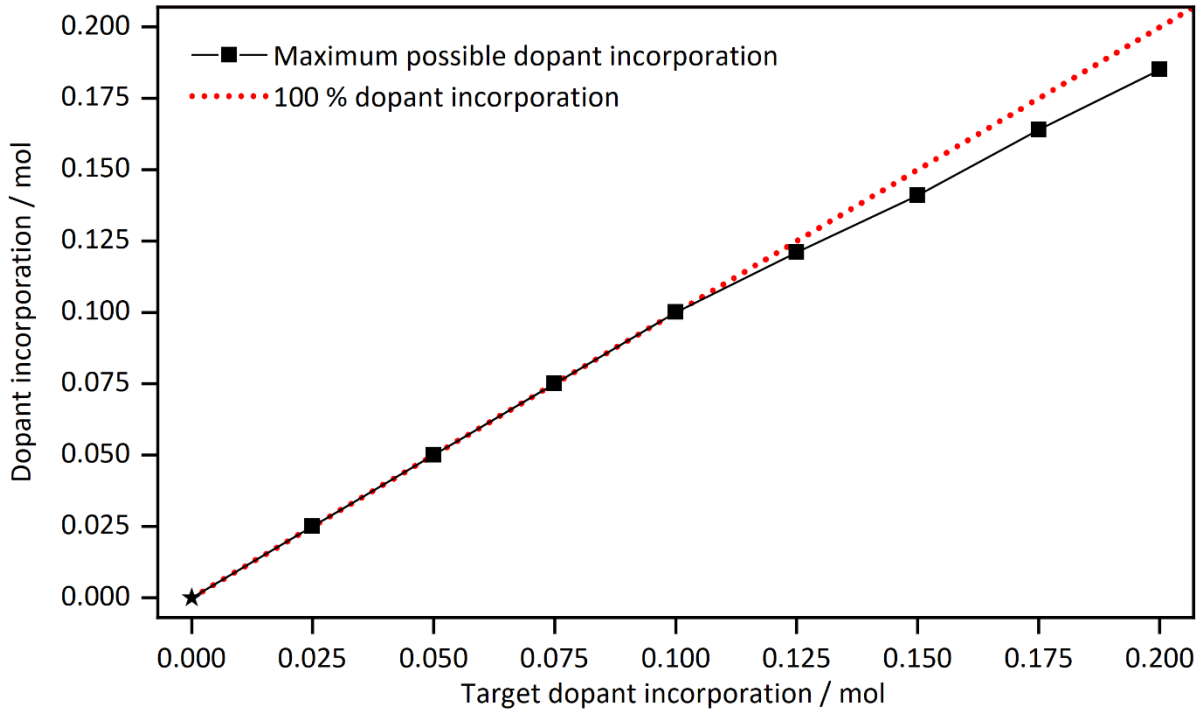

Figure 87 *The calculated maximum possible levels of dopant incorporation into the $(Sr_{3-x}Na_x)Sc_2O_5Cu_2S_2$ MALMs. Values were derived from the wt % of the sodium-containing impurities of each sample. The pristine material $Sr_3Sc_2O_5Cu_2S_2$ is included as a reference at x = 0 mol and is represented by a star. The red dashed line represents 100 % dopant incorporation into the MALM, statistically no values may surpass this line. The black data points are the estimated upper bound of dopant incorporation for each sample.*

Samples of the $(Sr_{3-x}Na_x)Sc_2O_5Cu_2S_2$ series exhibit an increase of approximately 1.5 orders of magnitude in conductivity from pristine through to x = 0.200 mol. While this increase is again relatively small, the incorporation of dopant has a positive effect on sample conductivity in every case with each showing improvement over the pristine material, as shown in Figure 88. The small amounts of $NaCu_3S_2$ do not appear to have a significant effect on sample conductivity, at least initially, but by x = 0.200 mol a further half an order of magnitude increase is observed (relative to the point where full incorporation ends at x = 0.100 mol) which may be the result of a greater presence of $NaCu_3S_2$.

There are two observations to be made here, the first is what appears to be a plateau in the already poor conductivity increase when low-level sodium doping, with the first six samples comprising not even one order of magnitude increase. The second observation is the increase over the final two samples. These two samples contain the highest amounts $NaCu_3S_2$ and therefore lie furthest from the 100 % line on the dopant incorporation plot, and will have a greater contribution of conductivity from $NaCu_3S_2$ than the previous samples, along with that of increased doping. That said, the variations in both the quantities of $NaCu_3S_2$ and the conductivity differences are so small that the results may simply be within error. More certainty can be placed upon a conductivity increase if the difference spans multiple orders of magnitude, as will be later demonstrated in the selenide version of this doping series.

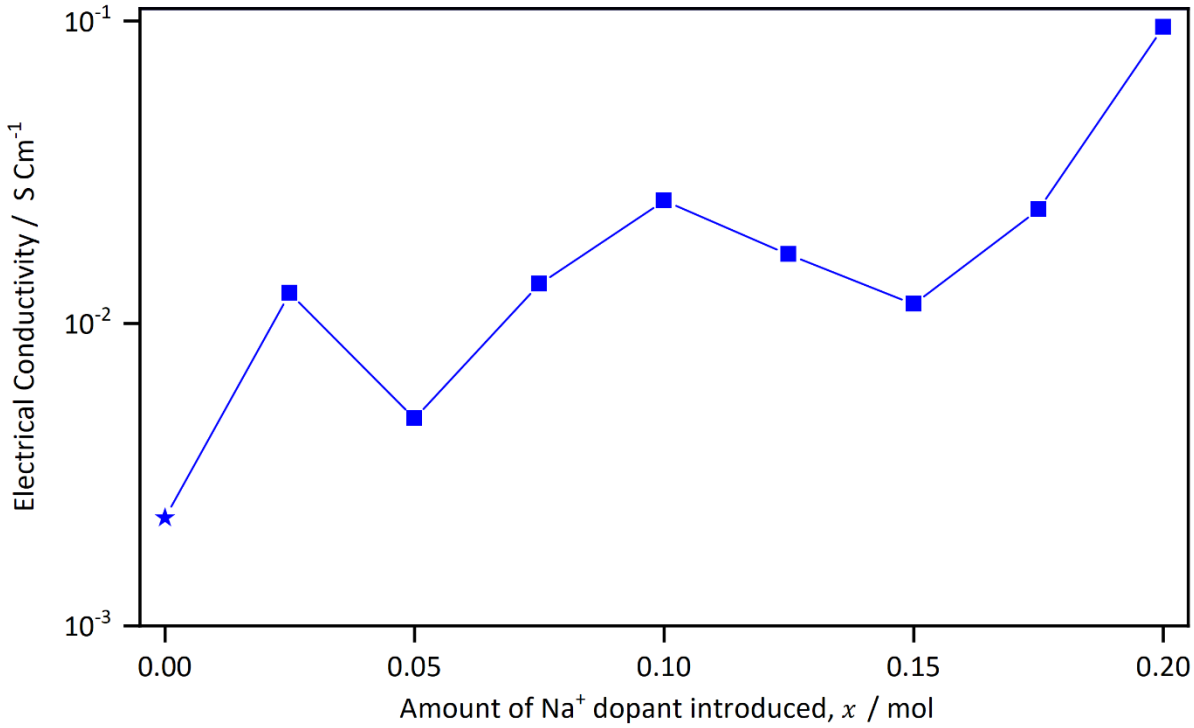

Figure 88 *The electrical conductivities of the eight sodium doped MALMs in the $(Sr_{3-x}Na_x)Sc_2O_5Cu_2S_2$ series, represented on a log_{10} scale. The pristine material $Sr_3Sc_2O_5Cu_2S_2$ is included as a reference at $x = 0$ mol and is represented by a star. All values are derived from van der Pauw 4 probe resistivity measurements of 8mm annealed pellet samples.*

The conductivity of $Sr_3Sc_2O_5Cu_2S_2$ should be considered 'less tuneable' when doped with sodium rather than potassium, as whilst a similar trend is demonstrated, greater variability in conductivity between samples is observed in this series and as such the trend should not be considered to be simply linear. The data is poor and the conductivity increase is weak. This variability is almost certainly explained by the large irregularity involved in the 4 probe resistivity testing of the 325 sulfide MALMs, discussed in the conclusions to $Sr_3Sc_2O_5Cu_2S_2$ doping, *Section 3.3.5*, and which may be mediated with more intermediate data points or modifications to the experimental method for calculating conductivity.

Selecting an optimum dopant level for this series is subjective, and doing so with certainty would require exploration of higher dopant levels to find the incorporation level where sodium addition conclusively stops. If a pure sample with a conductivity increase the result exclusively of doping alone is desired, then the optimum dopant quantity for this series is x = 0.100 mol, where sample purity is still very high at 97.7 wt %, and conductivity reaches a local maximum of 2.54×10^{-2} S cm^{-1}. This is the highest level of dopant incorporation before the emergence of the disruptive conductive impurity $NaCu_3S_2$, and so could be considered the saturation point for sodium into $Sr_3Sc_2O_5Cu_2S_2$ beyond which it is unknown if the MALM continues to accept further dopant. The unit cell parameters and optical band gaps again show negligible changes in this series (see *Appendix Figure 30*), as is to be expected at such relatively low doping levels despite the apparent better incorporation of the smaller sodium ion onto the strontium site compared to potassium.

3.3.4 Strontium Deficiencies, $Sr_{3-x}Sc_2O_5Cu_2S_2$

It has been observed in this work that pristine $Sr_3Sc_2O_5Cu_2S_2$ has modest electrical conductivity, but that doping of this material with potassium or sodium produces slight improvements in conductivity, on the order of one order of magnitude in each series before conductive by-products containing the dopant atom emerge, and any further conductivity increases may be attributable to these.

An interesting trend in both series is the continued increase in conductivity after the cessation or reduction of dopant incorporation onto the strontium site. Both potassium and sodium doping show apparent full dopant incorporation until x = 0.100 mol, after which incorporation slows but the increase in the (albeit weak) conductivity does not.

It was hypothesised that the conductive by-products are the cause of this behaviour, however it should be noted that the emergence of these ACu_3Ch_2 impurities is inherently tied with the lessening of dopant incorporation, therefore the relationship between the two observations may simply be correlated and not causal. In other words, the absence of dopant in impurity phases at or below x = 0.100 mol alongside an increase in conductivity can confidently be attributed to doping. Above this level, the further increase in conductivity may either be due to the conductive impurities (which requires the assumption that dopant incorporation stops at a given point and no more may be tolerated by the host site) or due to continued but lessened doping (which assumes the site continues to accept dopant beyond the point which has been previously deemed the 'saturation point' where full incorporation stops), or, a combination of both. Both theories are possible and would require either Hall measurements to measure sample mobility across the series, or exploration further into the series to gauge conductive behaviour at levels where further addition cannot practicably be possible.

A competing hypothesis, atomic site vacancies, may also explain the behaviour of these materials. Experimentally when doping with K or Na (as described in the general synthetic equations of the series, Equation 45 on page 151 for potassium and Equation 46 on page 159 for sodium), the addition of dopant is paired with a deficit of strontium, so that the total occupancy for a given site is maintained. In practice this means the reduction of SrS as a precursor and supplementation with A_2S and S to maintain full occupancy on the *A* site, and eliminating any competition between dopant and Sr for the site. At the level of doping where K or Na begin to appear in impurities, the unoccupied site cannot instead be occupied by strontium in the absence of K or Na because that quantity of strontium was not supplied. Therefore, the failure of dopant to occupy the target site may either lead to a lower purity of MALM (which is not the case) or to a maintained purity but with a vacancy on the strontium site which neither Sr^{2+} nor dopant occupy. A vacancy introduces a hole (a charge carrier), which would be expected to increase conductivity, whilst showing little change in *a* and *c* parameters due to a negligible stoichiometry difference from the pristine. This theory may explain the behaviour of both series, so the tolerance of $Sr_3Sc_2O_5Cu_2S_2$ to vacancies was investigated further.

A vacancy on the strontium site of $Sr_3Sc_2O_5Cu_2S_2$ was introduced to simulate the effect of a dopant, such that the target material takes the form $Sr_{3-x}Sc_2O_5Cu_2S_2$. This was achieved by reducing SrS content and supplementing with S, according to Equation 47 below:

Equation 47 $2\ SrO + Sc_2O_3 + Cu_2S + 1\text{-}x\ SrS + x\ S \rightarrow Sr_{3-x}Sc_2O_5Cu_2S_2$

The ground powder precursors (1 gram scale) were heated within an ampoule for 12 hours at 100 °C, then raised to 800 °C for a further 12 hours in the same ampoule. They were then reground, pelletised, and heated again for 24 hours at 800 °C. Seven samples were synthesised, four with a dopant level ranging from x = 0.050 mol to x = 0.200 mol at equal increments of 0.050 mol, plus x = 0.500, 0.750 and 1.000 mol, synthesised in one self-consistent sample set. The complete compositional, analytical and graphical data for each sample in this section can be found in *Appendix B.1.3.*

The data point intervals in this series were selected to extend almost an order of magnitude further than was explored in the group 1 metal dopant sections, with a near certainty of significant purity decline at the highest doping levels. In this section, the variable of dopant-containing conductive impurities is controlled, because no dopant is present, therefore any conductivity increase is the result exclusively of manipulation of the parent MALM.

It was hypothesised that a small vacancy on the strontium site would be tolerated due to the usual excellent stability of these 325 materials, compared for example to that of the 426 materials in *Chapter 4,* where a vacancy would likely not be tolerated nor measurable before degradation. It was assumed that once the small vacancy 'limit' is reached, purity will decline and impurities will dominate, rather than the MALM continuing to accommodate an ever-increasing strontium vacancy.

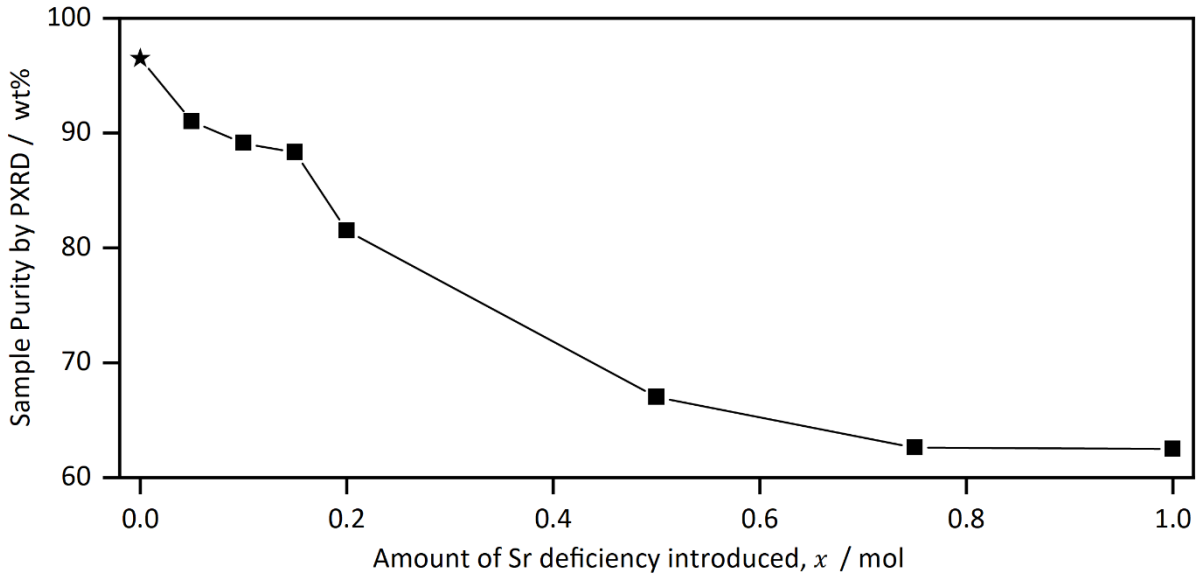

Figure 89 *Purities of the seven strontium deficient MALMs in the $Sr_{3-x}Sc_2O_5Cu_2S_2$ series. The pristine material $Sr_3Sc_2O_5Cu_2S_2$ is included as a reference at x = 0 mol and is represented by a star. All values are derived from the Rietveld refinements of PXRD data using GSAS-II, and reported as weight percentages.*

Compared to the K and Na doping studies previously where lightly doped samples exhibit very high purity, believed to be the result of high dopant incorporation at those levels, here an immediate purity decline is observed, Figure 89. By x = 0.100 mol of strontium deficiency, a level which in previous series was considered an optimum level of doping, the purity is already below 90 %, and which falls further to almost 60 % when the target deficiency is ten times greater. This data alone cannot reveal whether a small strontium deficiency is tolerated, but it does strongly imply that a large deficiency (above than x = 0.200 mol where the purity significantly drops) is not tolerated. This is expected, and the series was designed to not only contain the 'saturation point' but exceed far beyond it to gauge extreme levels.

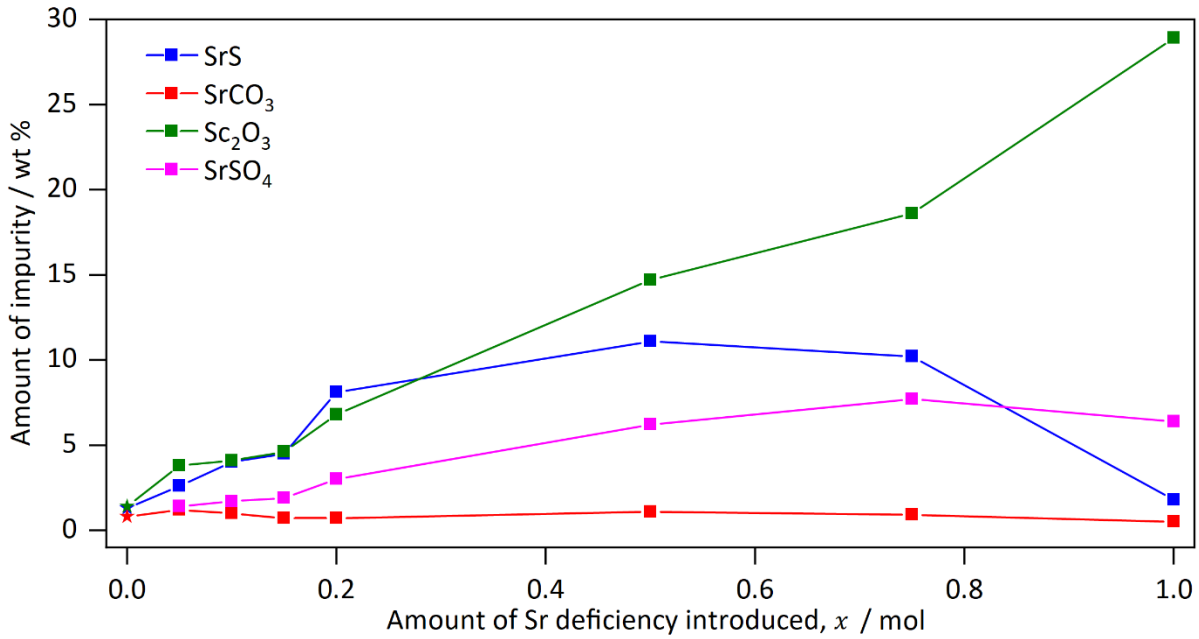

Figure 90 *The weight percentages of four impurity phases present in the $Sr_{3-x}Sc_2O_5Cu_2S_2$ series. The pristine material $Sr_3Sc_2O_5Cu_2S_2$ is included as a reference at x = 0 mol and is represented by stars.*

The usual impurities of SrS, $SrCO_3$ and Sc_2O_3 are observed, Figure 90, alongside an impurity not yet observed, $SrSO_4$. Another white wide band gap (7.6 eV)[257] semiconductor, this impurity is not expected to adversely affect sample conductivity and is observed only within this data set. Its formation here is thought to be merely a by-product of the decomposition / non-formation of $Sr_3Sc_2O_5Cu_2S_2$.

As is often the case, there are no copper impurities present. This is fortuitous because copper and many materials that comprise it are conductive, but interesting because all other atoms are present in the impurities of every sample, implying copper is somehow the limiting reagent of $Sr_3Sc_2O_5Cu_2S_2$ formation. There is little to no unidentified material in even the complex and messy PXRD pattern of the most deficient material where x = 1.000 mol, so the likelihood for unnoticed and unrefined copper impurities (therefore, conductive impurities) is low. This sample is seen in Figure 91b in comparison to the sample with the smallest deficiency, x = 0.050 mol, where purity is significantly higher.

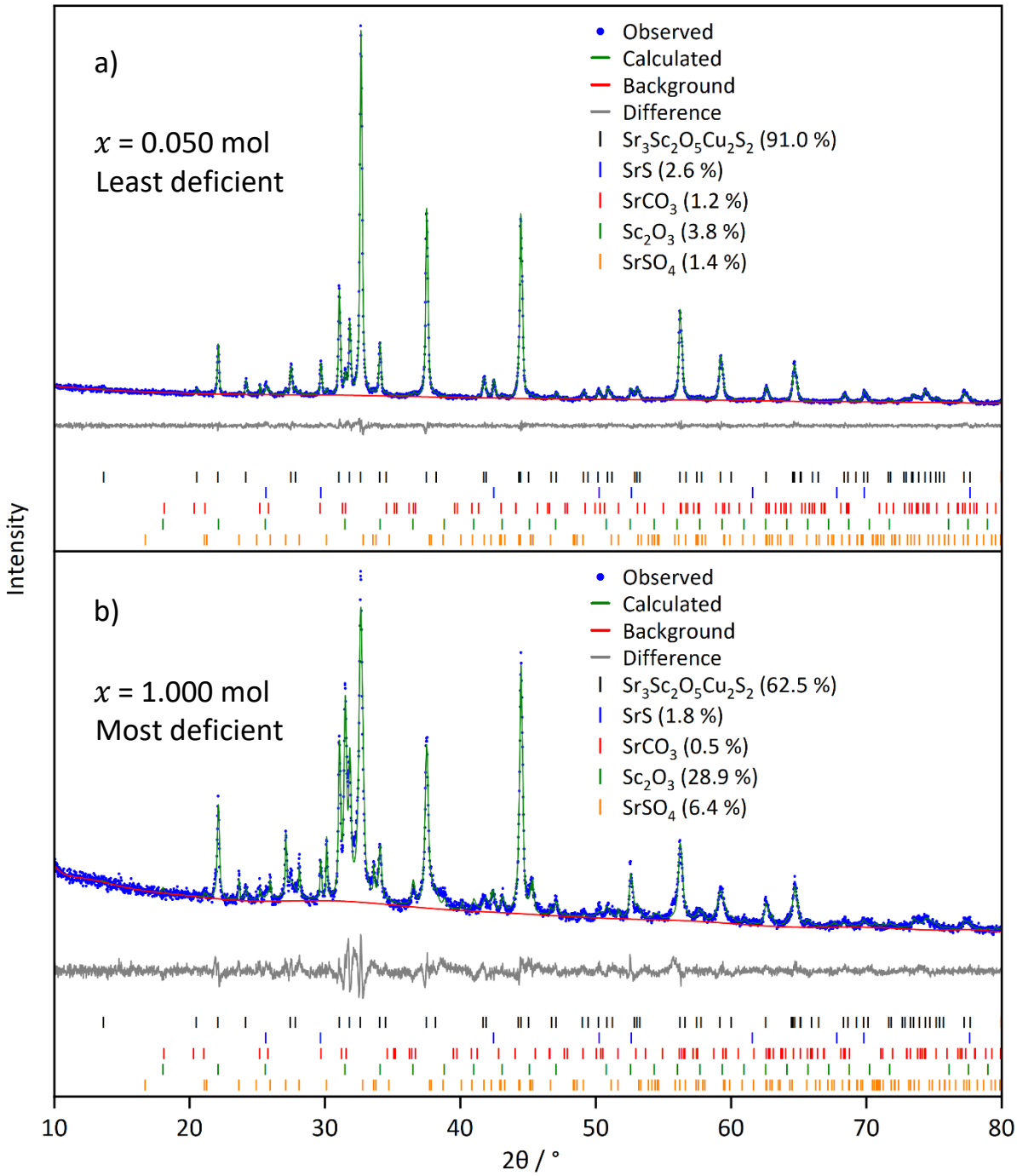

Figure 91 *Powder X-ray diffractograms of a) the least deficient sample of the series with target composition $Sr_{2.95}Sc_2O_5Cu_2S_2$, and b) the most deficient sample of the series with target composition $Sr_{2.00}Sc_2O_5Cu_2S_2$ (both space group I4/mmm) after 36 hours of heating at 800 °C. The small blue circles represent the observed diffracted intensities, the green lines represent the Rietveld-refined calculated models, the red lines represent the backgrounds, and the grey lines represent the differences between observed and calculated intensities. The black tick marks show the reflections of the refined model of $Sr_3Sc_2O_5Cu_2S_2$, whilst the blue, red, green and orange tick marks represent refined impurity phases SrS, $SrCO_3$, Sc_2O_3 and $SrSO_4$ respectively. Weight fractions for each phase are cited in the figure legends. a) Duration: 45 minutes. Data points: 3457. Interval: 0.02 °. GOF: 1.10. R_{wp}: 4.416 %. b) Duration: 45 minutes. Data points: 3457. Interval: 0.02 °. GOF: 1.54. R_{wp}: 6.080 %.*

The electrical conductivities of these samples offer a theory to explain the tolerance of $Sr_3Sc_2O_5Cu_2S_2$ to a strontium impurity. There is a steady increase in conductivity between the pristine x = 0.000 mol sample at 2.28 × 10^{-2} S cm^{-1}, and the x = 0.500 mol sample at 3.49 × 10^{-1} S cm^{-1}, encompassing approximately two orders of magnitude. Beyond this the conductivity plateaus and appears to slightly decline, though data points are distributed widely in this region, Figure 92.

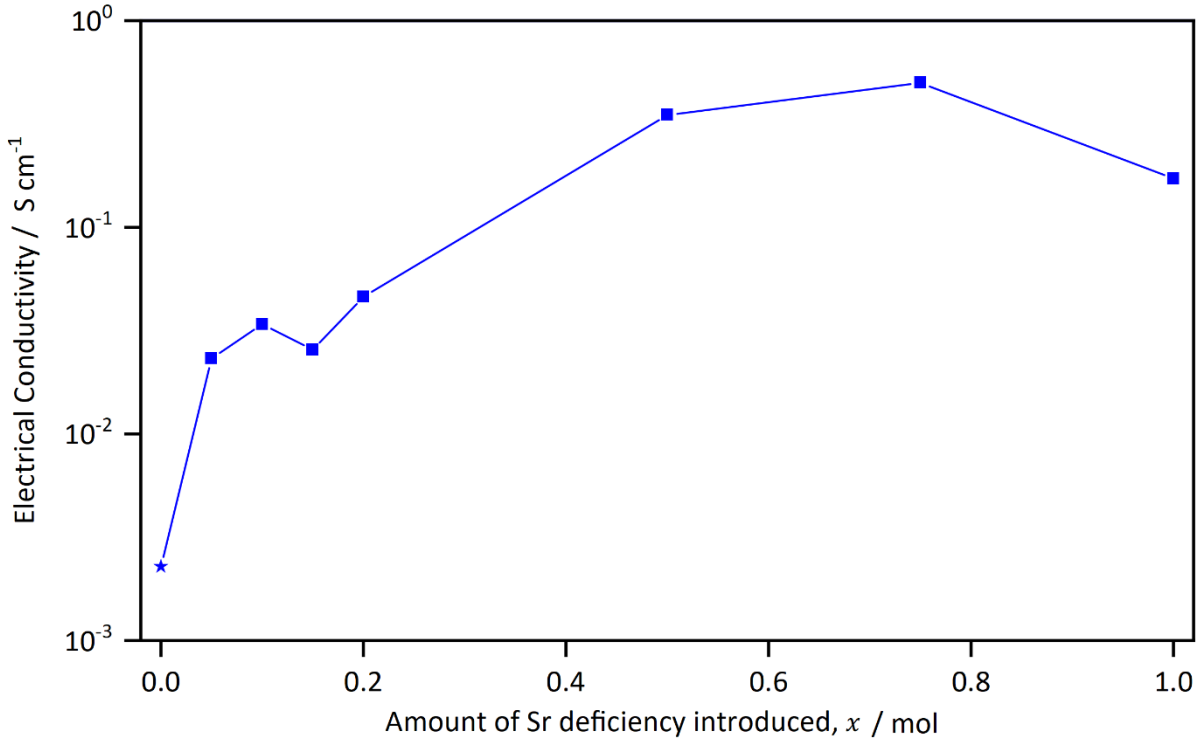

Figure 92 *The electrical conductivities of the seven strontium deficient MALMs in the $Sr_{3-x}Sc_2O_5Cu_2S_2$ series, represented on a log_{10} scale. The pristine material $Sr_3Sc_2O_5Cu_2S_2$ is included as a reference at x = 0 mol and is represented by a star. All values are derived from van der Pauw 4 probe resistivity measurements of 8mm diameter annealed pellet samples.*

As discussed previously, and unlike previous series, any conductivity increase observed here cannot be attributed to conductive by-products because there are none present, and instead are very likely to be the result of a deficiency, causing increased charge carriers. This is especially true at lower deficiency levels where the purity is sufficient to believe that the MALM does not exhibit major distortions or other site deficiencies. The highest target deficiency samples are, by design, extreme deficiencies that could not realistically be tolerated and these MALMs are unlikely to be forming as intended with all other sites filled, regardless of the actual Sr deficiency.

The combined data of this series suggests that in low deficiency region of x = 0.500 mol and below, where purity is relatively high and the conductivity exhibits its sharpest improvement, a small strontium deficiency is tolerated. Above this, further tolerance is dubious due to a cessation of conductivity improvement, and the purities become so poor that these samples are of little use.

3.3.5 $Sr_3Sc_2O_5Cu_2S_2$ Doping Conclusions

The conductivity of $Sr_3Sc_2O_5Cu_2S_2$, measured in this work, is poor. It has been shown here that potassium doping may yield a 17x increase on the 2.28×10^{-2} S cm^{-1} pristine material, Figure 93, with an optimum dopant concentration of $x = 0.075$ mol before conductive impurities appear in the samples. Sodium doping proved more effective, producing a 42x increase at its peak and with an optimum sodium concentration of $x = 0.100$ mol. These doping series do present tuneable sample conductivities; however the improvements are very small, limited by dopant saturation. Incorporation at low levels is strongly suggested, but to minimal effect, thus it appears to be the case that $Sr_3Sc_2O_5Cu_2S_2$ is simply not tolerant to high concentrations of K or Na dopants on the Sr site.

Increases in conductivity were observed beyond the point where doping into $Sr_3Sc_2O_5Cu_2S_2$ had either ceased or slowed. This was believed to be the result of the ACu_3S_2 impurities which appeared consistently in these series but at low concentrations, and may undesirably contribute to false positive sample conductivities. A competing theory of increased charge carriers due to unintentional strontium site vacancies was proposed, and this was investigated by the introduction of intentional strontium vacancies. A similar conductivity trend was observed, demonstrating an approximately 15x increase in conductivity when $x = 0.100$ mol of vacancy was targeted. Greater targeted vacancies produced better conductivities (up to 219x improvement) but were too impure, ≈ 60 %, to provide meaningful conclusions. A strontium vacancy is, in isolation, a poor method for improving sample conductivity.

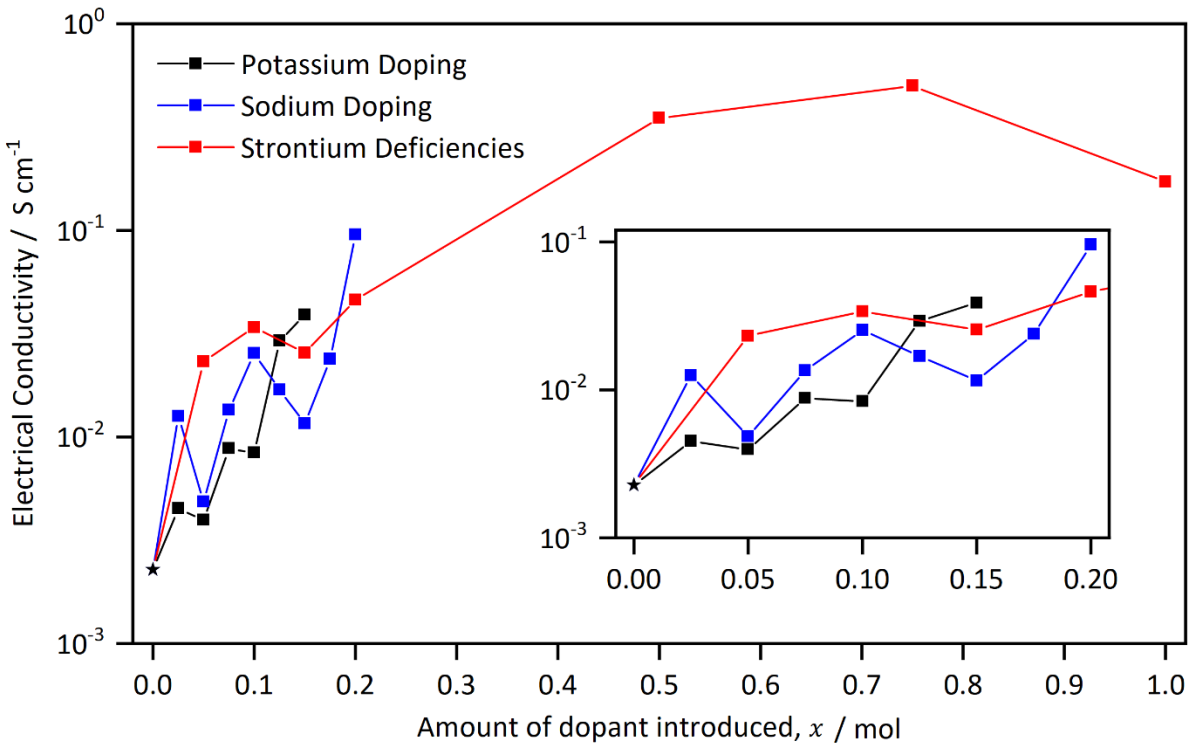

Figure 93 *The electrical conductivities of the potassium doped (black), sodium doped (blue), and strontium deficient (red) $Sr_3Sc_2O_5Cu_2S_2$ series, presented on a log_{10} scale. The pristine material $Sr_3Sc_2O_5Cu_2S_2$ is included as a reference at $x = 0$ mol and is represented by a star. The inset shows a magnification of the low doping region.*

A strontium vacancy may therefore account for the observed continuity of electrical conductivity improvement beyond the saturation points of potassium and sodium in those respective series. Specifically, the increases in conductivity at the highest doping levels of the two doping series may be explained by a small strontium vacancy which is introduced at the point where dopant no longer fully incorporates the strontium site, supported by the maintenance of sample purity beyond the saturation point. If this hypothesis is correct, extending the K and Na series to the x range of the strontium deficiency series would be expected to show a conductivity plateau akin to that of the deficiency series, once further dopant incorporation has fully ceased and the subsequent strontium vacancy is too large for the material to tolerate. For this reason, the K and Na dopant series for the selenide MALM $Sr_3Sc_2O_5Cu_2Se_2$ extend to this range to probe these extreme doping levels.

The conductivity trends observed in these series are often irregular, with sporadicity in data points, an issue introduced briefly on page 163. This is likely due to the large variation in resistance observed during van der Pauw 4 probe testing of these materials, where the measured resistance value varies in a sinusoidal-like manner, oscillating up and down across an order of magnitude, where each peak and trough are separated by approximately 30 seconds of real time. These resistance values, if measured over time, would resemble a sine wave. It is not understood why this phenomenon occurred, and it was observed for every sulfide sample yet none of the selenide samples discussed later. To obtain a conductivity value from the oscillating resistance, the centre, that with zero amplitude in the sine wave analogy, was measured. Multiple repeats of each sample were attempted and no significant changes were observed, supporting the validity of the results. Two probe testing (see *Section 2.2.3.2*) was attempted, with recognition it may be inappropriate for the low resistivities of the most doped samples. The same phenomenon materialised, the method was not pursued further, and the oscillations remain an interesting and undesirable quirk of $Sr_3Sc_2O_5Cu_2S_2$ samples. These series would benefit from increased intermediate data points to strengthen the observed trends.

The published value of 2.8 S cm^{-1} for pristine $Sr_3Sc_2O_5Cu_2S_2$ by Liu et al[42] was never realised here, even by doped samples. It is very likely therefore, as discussed in *Section 4.3*, that the exceptional reported mobility of 150 $cm^2\ V^{-1}\ s^{-1}$ is the result of the extreme densification of the annealed pellet by spark plasma sintering, a process unavailable here. Densities of each pellet were measured and are detailed in the Appendix, with each (sufficiently pure) sample measuring between 68 to 72 % of the bulk crystal density. These are consistent, which allows valid comparisons between series, but these are too low to be compared to the superior published values of samples densified by spark plasma sintering.

In conclusion, the electrical conductivity of $Sr_3Sc_2O_5Cu_2S_2$ may be improved by K^+, Na^+ or vacancy doping, but the improvements are modest. The selenide analogue explored in greater detail in the upcoming work presents a lower initial pristine conductivity with poor hole generation ability, but is significantly more receptive to doping, can be improved further, and is explored in far greater detail.

3.4 $Sr_3Sc_2O_5Cu_2Se_2$

3.4.1 Repeated Literature Synthesis of Pristine $Sr_3Sc_2O_5Cu_2Se_2$

$Sr_3Sc_2O_5Cu_2Se_2$ was synthesised on a 1-gram scale using conventional solid-state chemistry, according to Equation 48 below:

Equation 48 $2\ SrO + Sc_2O_3 + Cu_2Se + SrSe \rightarrow Sr_3Sc_2O_5Cu_2Se_2$

The ground powder material was heated for 12 hours at 800 °C, reground, pelletised, and heated again for 24 hours at 800 °C, slightly lower than the temperature of 900 °C reported in literature.[58, 89] Small quantities of SrSe and $SrCO_3$ were observed in the diffractogram (Figure 94), but the main phase purity of 99.1 wt % remains exceptionally high for a material of this type. The colour of $Sr_3Sc_2O_5Cu_2Se_2$, not discussed in the literature, was found here to be light brown.

This material was also synthesised in *Chapter 5*, by both solid-state metathesis and a conventional ceramic synthesis, achieving purities and sample parameters which agree with those presented here.

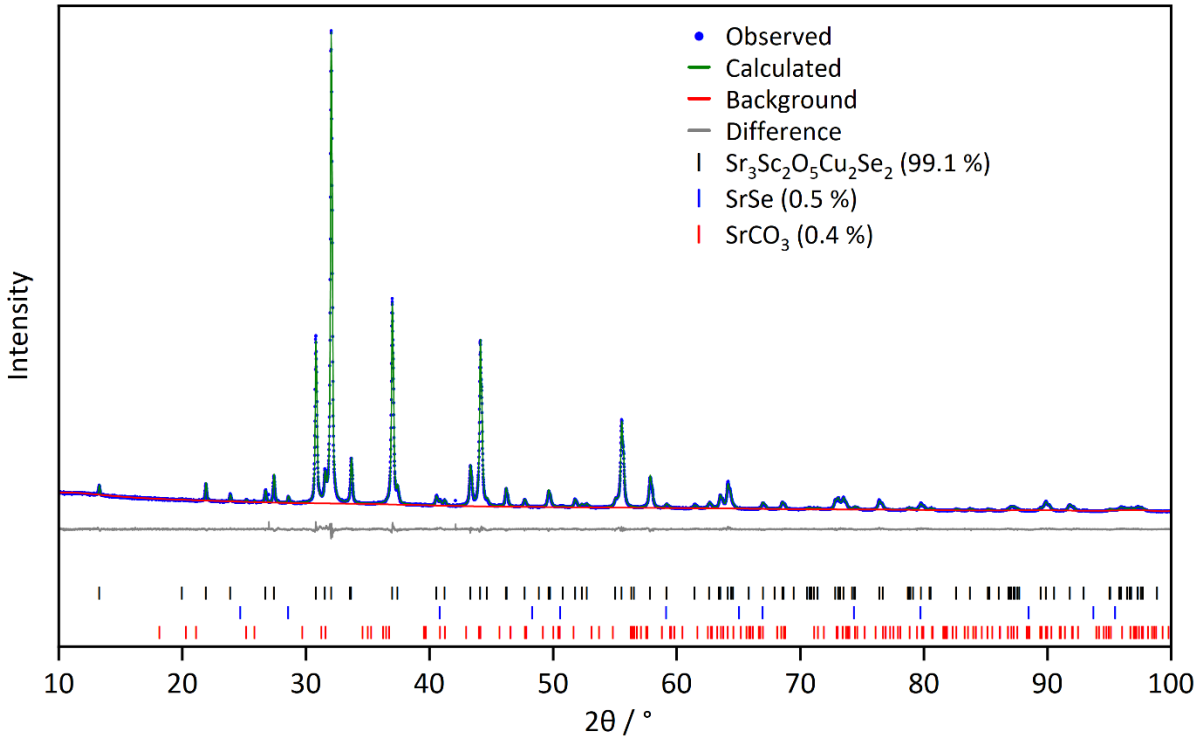

Figure 94 *Powder X-ray diffractogram of material with target composition $Sr_3Sc_2O_5Cu_2Se_2$ (space group I4/mmm) after 36 hours of heating at 800 °C. The small blue circles represent the observed diffracted intensity, the green line represents the Rietveld-refined calculated model, the red line represents the background, and the grey line represents the difference between observed and calculated intensities. The black tick marks show the reflections of the refined model of $Sr_3Sc_2O_5Cu_2Se_2$ (99.1 %), whilst the blue and red tick marks represent refined impurity phases SrSe (0.5 %), and $SrCO_3$ (0.4 %) respectively.*
Duration: 12 hours. Data points: 8887. Interval: 0.01 °. GOF: 1.51. R_{wp}: 2.486 %.

To the best of the author's knowledge, the conductivity of $Sr_3Sc_2O_5Cu_2Se_2$ has not been published in literature; as the two published reports of this material in literature by Iwasa et al retain a primary focus on the optical properties. Conductivity is therefore cited here for the first time, a value of 2.61×10^{-4} S cm^{-1} obtained by van der Pauw 4 probe resistivity measurement.

Table 6 *The refined structural parameters and key performance metrics of pristine material $Sr_3Sc_2O_5Cu_2Se_2$, compared to other publications of this material in literature.*

Source	*a* / Å	*c* / Å	Cell volume / Å^3	R_{wp} / %	Band gap / eV	Conductivity / S cm^{-1}
This work	4.10329(4)	26.68472(25)	449.290(8)	2.48	2.94	2.61×10^{-4}
Iwasa 2018 [89]	4.102	26.67	448.760	*n/a*	2.90	*n/a*
Iwasa 2019 [58]	4.10407	26.6881	449.518	3.330	2.90	*n/a*

Table 6 details the unit cell parameters *a* and *c*, which are in agreement with and lie between the tabulated literature reports by Iwasa et al. The optical band gap was found to be 2.94 eV, corresponding to a wavelength of 422 nm. The band gap, the diffuse reflectance and Tauc plots for which are presented in Figure 95 below, is slightly larger than literature values but in close agreement.

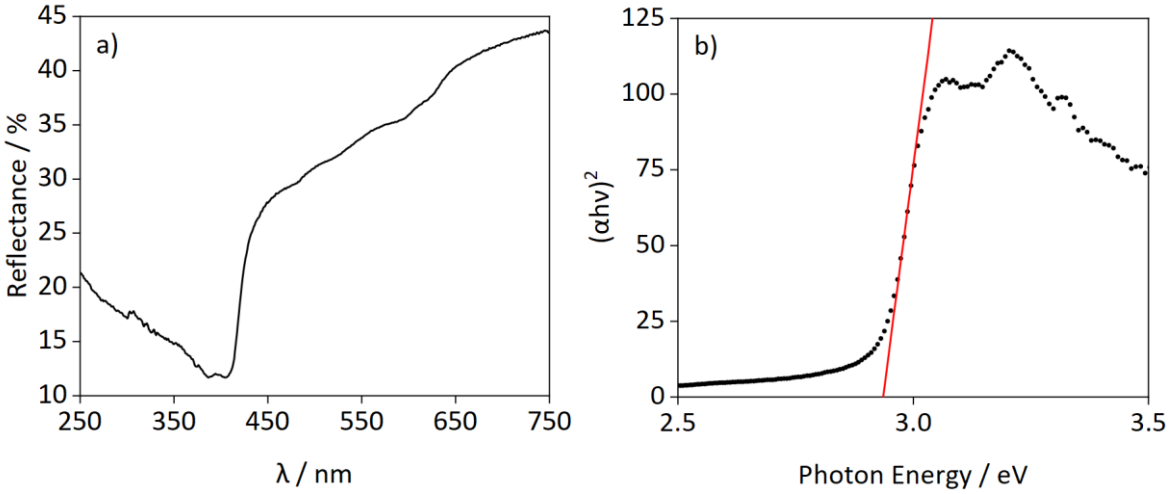

Figure 95 *UV-Vis spectrometry data for material with target composition $Sr_3Sc_2O_5Cu_2Se_2$ after 36 hours of heating at 800 °C. Plot a) is the raw diffuse reflectance data showing the drop off in reflectance between the visible region and the ultraviolet region occurring at 350-450 nm. Plot b) is the associated magnified Tauc plot for this region, where the intercept between the red extrapolated tangent line and the x-axis is used to estimate an optical band gap of 2.94 eV, which corresponds to 422 nm.*

3.4.2 Potassium Doping, $(Sr_{3-x}K_x)Sc_2O_5Cu_2Se_2$

Potassium was introduced as an aliovalent *p*-type dopant onto the strontium site of $Sr_3Sc_2O_5Cu_2Se_2$ such that the target material takes the form $(Sr_{3-x}K_x)Sc_2O_5Cu_2Se_2$. This was achieved by reducing SrSe content and supplementing with [K_2Se + Se], according to Equation 49 below:

Equation 49 $$2\ SrO + Sc_2O_3 + Cu_2Se + 1\text{-}x\ SrSe + \frac{x}{2}[K_2Se + Se] \rightarrow (Sr_{3-x}K_x)Sc_2O_5Cu_2Se_2$$

The ground powder precursors (1 gram scale) were heated within an ampoule for 12 hours at 180 °C, then raised to 800 °C for a further 12 hours in the same ampoule. They were then reground, pelletised, and heated again for 24 hours at 800 °C. Thirteen samples were synthesised in total across two separate self-consistent sample sets. First, eight samples were synthesised with a dopant level ranging from x = 0.025 mol to x = 0.200 mol at equal increments of 0.025 mol. To further explore this series following the discovery of interesting electrical properties, a further five samples were produced to explore the behaviour of these materials when very heavily doped, far beyond that which is expected to yield pure materials or full dopant saturation, illustrated in Figure 96. These five additional samples targeted x = 0.300, 0.400, 0.500, 0.750 and 1.000 mol. The complete compositional, analytical and graphical data for each sample in this section can be found in *Appendix B.1.4*.

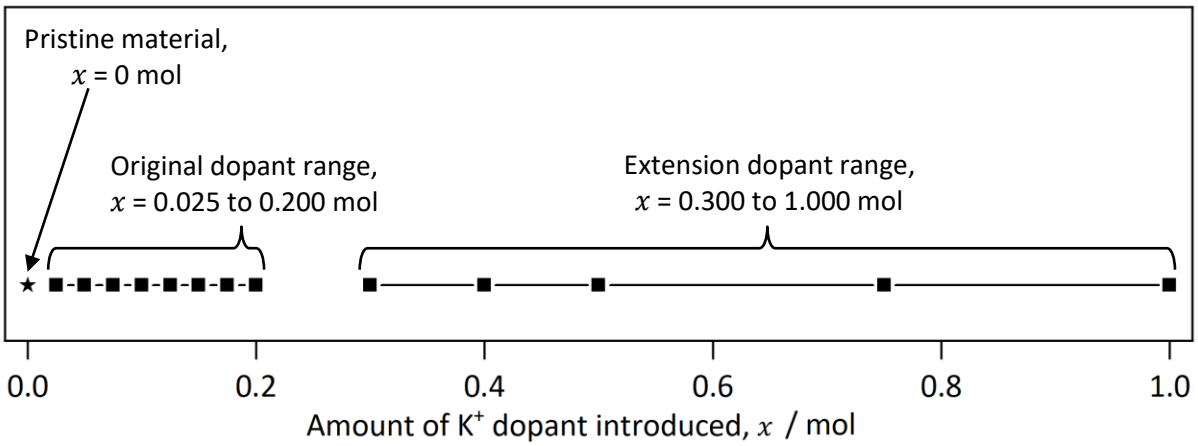

Figure 96 *A visualisation of the ranges of doping explored in the $(Sr_{3-x}K_x)Sc_2O_5Cu_2Se_2$ series. The pristine sample was first synthesised alone, then eight samples ranging from x = 0.025 to 0.200 mol, and finally five further sample ranging from x = 0.300 to 1.000 mol. The y-axis is illustrative.*

This is the greatest extent of attempted doping explored thus far, and gives insight into the behaviour of the material at low doping levels where the dopant is assumed to be readily and fully incorporated, at moderate and optimal doping levels where the material cannot accept any more dopant but maintains good purity, and then beyond that point where the supplied dopant exceeds that which can be incorporated onto the host site, and manifests as an impurity.

Unlike previously explored series, and likely as a direct result of the K^+ concentration range, potassium doped $Sr_3Sc_2O_5Cu_2Se_2$ exhibits a clear drop-off in purity, but not immediately. In Figure 97 it can be seen that purity stays high (> 96 wt %) and with the usual slight downward trend until x = 0.400 mol. From x = 0.400 mol onwards the purities decrease rapidly and almost linearly with increasing dopant. These two trends, that of high purity until x = 0.400 mol and the consistent decrease beyond it, is an early suggestion of a saturation level somewhere in the crossover point between these two purity trends, to be later supported by impurity and conductivity data.

In the cases of x = 0.750 mol and x = 1.000 mol, where doping was attempted at a level clearly beyond that which the host material can accommodate, purity was so low that some diffraction peaks were not refined, belonging to an unrecognised impurity. While this accounted for only a small amount of material (the small unrefined peaks can be observed in Figure 98b), it means the 325 phase purity is slightly lower in reality than is obtained from GSAS-II. The data points for these slightly false-positive samples are highlighted in red in the Figure 97 purity plot, though it is expected these changes would not deviate the observed trend from the linear decrease.

Impurities were ubiquitous in this series and tell an interesting story about how the concentration of dopant influences the presence and quantities of various undesirable phases, and how the presence of potassium in these impurities influences the total MALM purity even once maximum saturation is exceeded.

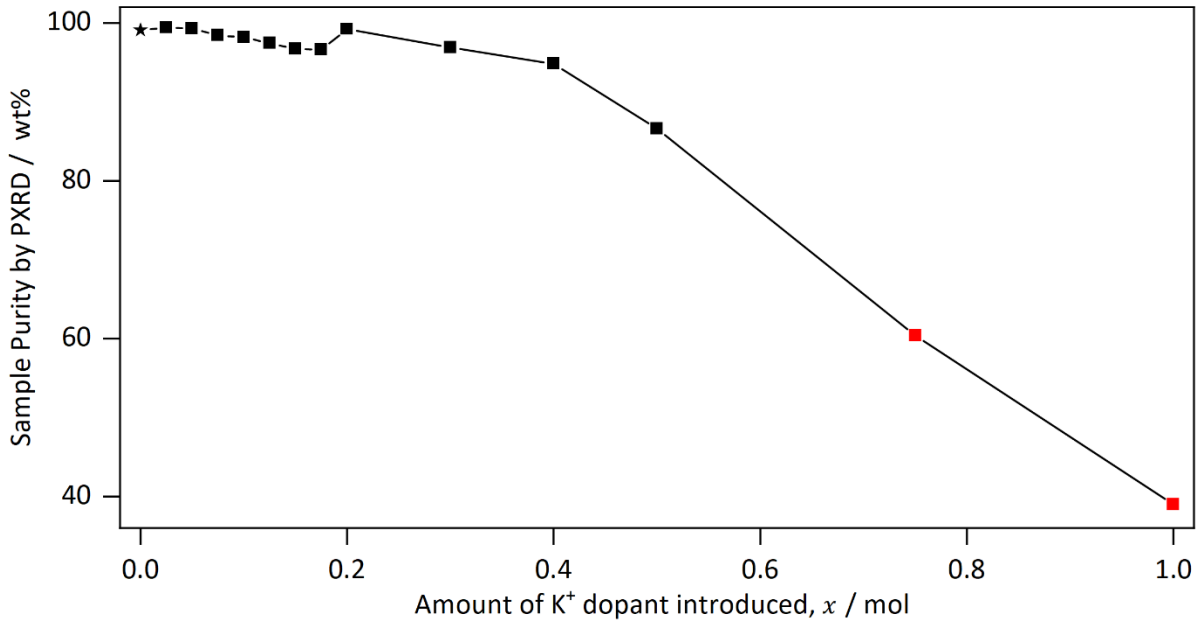

Figure 97 *Purities of the thirteen potassium doped MALMs in the $(Sr_{3-x}K_x)Sc_2O_5Cu_2Se_2$ series. The pristine material $Sr_3Sc_2O_5Cu_2Se_2$ is included as a reference at x = 0 mol and is represented by a star. The two data points at x = 0.750 mol and x = 0.100 mol are coloured red to indicate the presence of unknown impurities in these samples, and as a result the cited purity values are likely to be slight overestimates. All values are derived from the Rietveld refinements of PXRD data using GSAS-II, and reported as weight percentages.*

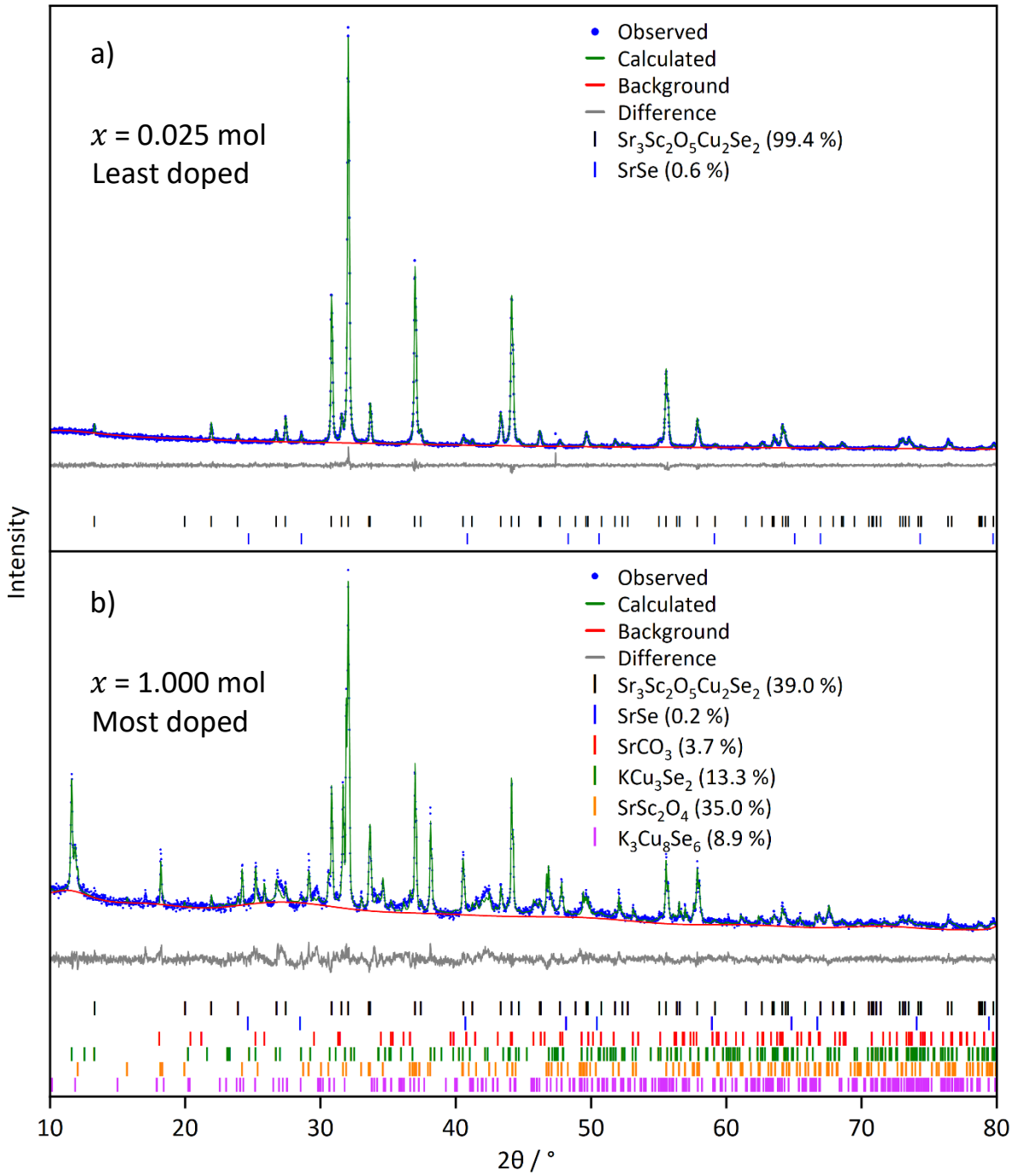

Figure 98 *Powder X-ray diffractograms of a) the least doped sample of the series with target composition $(Sr_{2.975}K_{0.025})Sc_2O_5Cu_2Se_2$, and b) the most doped sample of the series with target composition $(Sr_{2.000}K_{1.000})Sc_2O_5Cu_2Se_2$ (both space group I4/mmm) after 36 hours of heating at 800 °C. The small blue circles represent the observed diffracted intensities, the green lines represent the Rietveld-refined calculated models, the red lines represent the backgrounds, and the grey lines represent the differences between observed and calculated intensities. The black tick marks show the reflections of the refined model of $Sr_3Sc_2O_5Cu_2Se_2$, whilst the blue, red, green, orange and pink tick marks represent refined impurity phases SrSe, $SrCO_3$, KCu_3Se_2, $SrSc_2O_4$ and $K_3Cu_8Se_6$ respectively. Weight fractions for each phase are cited in the figure legends.*
a) Duration: 45 minutes. Data points: 3457. Interval: 0.02 °. GOF: 1.11. R_{wp}: 6.050 %.
b) Duration: 45 minutes. Data points: 3457. Interval: 0.02 °. GOF: 1.53. R_{wp}: 6.628 %.

KCu_3Se_2 is observed in all but the first four samples, increasing in quantity across the series until x = 1.000 mol, which has slightly less KCu_3Se_2 than the x = 0.750 mol sample. This is only because another potassium-containing phase is present in this sample, $K_3Cu_8Se_6$, so in total the x = 1.000 sample has by far the most total K impurity. This single sample is the only occurrence of $K_3Cu_8Se_6$ in this work. The two potassium phases KCu_3Se_2 and $K_3Cu_8Se_6$ are comparable stoichiometrically, where the latter could be expressed as $KCu_{2.66}Se_2$, a similar yet copper-deficient analogue.[246] Below x = 0.125 mol, no such phases are observed, so it may be assumed that all dopant has been incorporated. The emergence of impurities across the series is visible in Figure 99 and Figure 100 below.

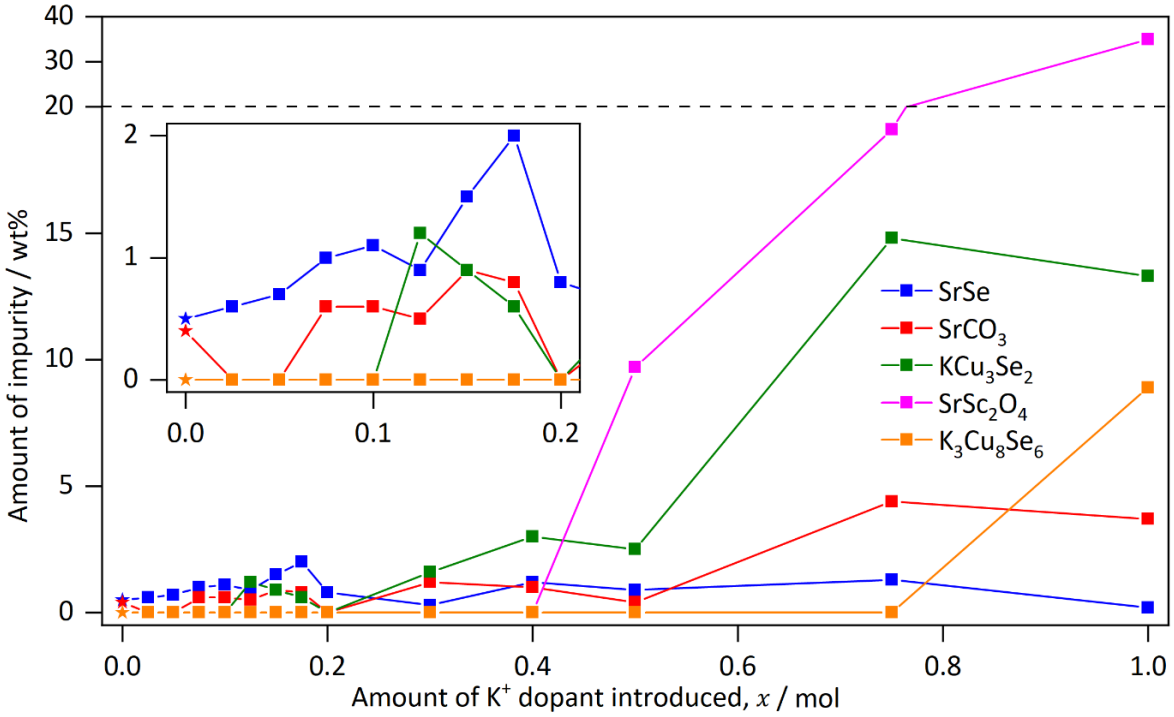

Figure 99 *The weight percentages of five impurity phases present in the $(Sr_{3-x}K_x)Sc_2O_5Cu_2Se_2$ series. The pristine material $Sr_3Sc_2O_5Cu_2Se_2$ is included as a reference at x = 0 mol and is represented by stars. The inset plot is a magnification of the x = 0 to 0.200 mol region where doping and impurity quantities are low. Note the change in y scaling at 20 wt %.*

Figure 100 *A photographic comparison of the colour of the $(Sr_{3-x}K_x)Sc_2O_5Cu_2Se_2$ MALM series. Dopant concentration increases from left to right. The sample where x = 0.175 mol is absent from this photograph as it was sent to the ISIS Neutron and Muon Source for Neutron Powder Diffraction at the time of writing.*

From x = 0.400 mol onwards, a significant and consistently increasing concentration of impurity phase $SrSc_2O_4$ is observed in these samples. In this work, this impurity appears only in the K^+ and Na^+ doped $Sr_3Sc_2O_5Cu_2Se_2$ series, and its presence suggests a level of doping so high that the large quantity of potassium is driving the formation of the $K_xCu_ySe_z$ impurities, leaving excesses of Sr, Sc and O which present as $SrSc_2O_4$. In other words, so significant is the quantity of Cu and Se drawn from the mixture into $K_xCu_ySe_z$, that MALM purity decreases drastically, with $SrSc_2O_4$ the next most stable permutation of those atoms left behind. Together $SrSc_2O_4$, KCu_3Se_2 and $K_3Cu_8Se_6$ comprise 57 % of the weight of the x = 1.000 mol sample and portrays the extent to which purity drops when doping is attempted so high.

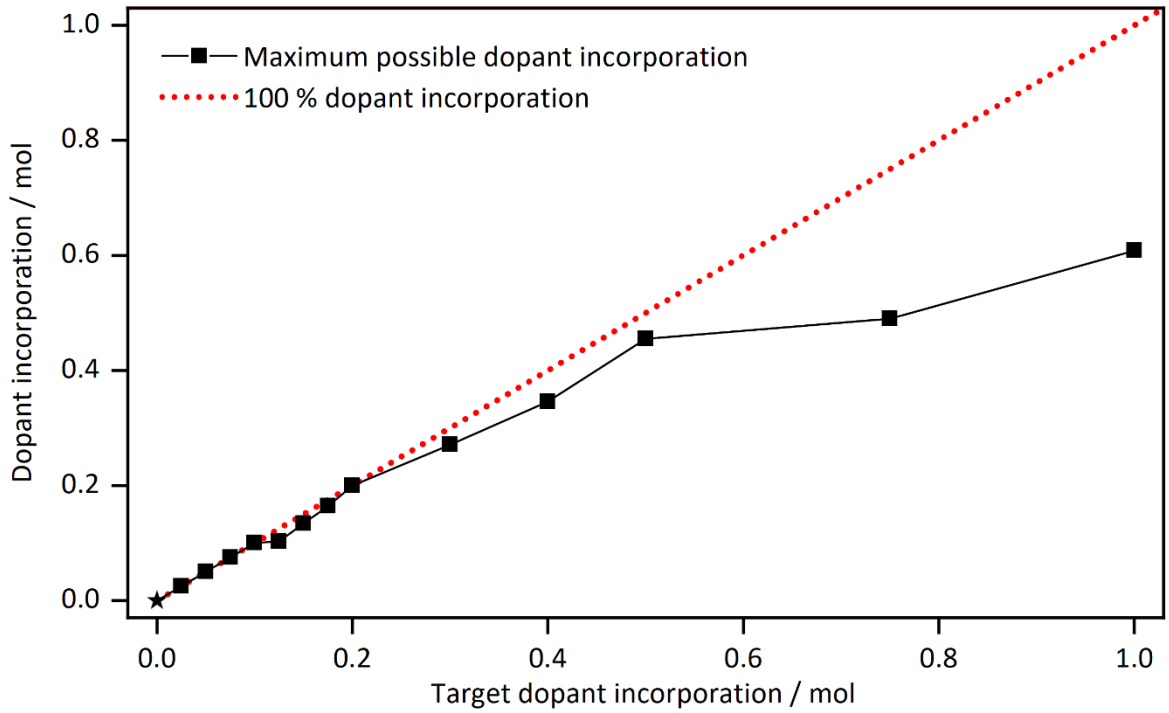

Figure 101 The calculated maximum possible levels of dopant incorporation into the $(Sr_{3-x}K_x)Sc_2O_5Cu_2Se_2$ MALMs. Values were derived from the wt % of the potassium-containing impurities of each sample. The pristine material $Sr_3Sc_2O_5Cu_2Se_2$ is included as a reference at x = 0 mol and is represented by a star. The red dashed line represents 100 % dopant incorporation into the MALM, statistically no values may surpass this line. The black data points are the estimated upper bound of dopant incorporation for each sample.

At x = 0.500, 8.9 % of supplied potassium is found in the impurity phase KCu_3Se_2, therefore a maximum of 91.1 % may be attributed to MALM doping (Figure 101). This is still an exceptionally high incorporation rate at this level of doping if true, however it should be reiterated that these values are the 'best case scenario'. The true value is almost guaranteed to be lower due to (as outlined previously in *Section 3.3.2 - Potassium Doping*) the possibilities of amorphous impurities invisible in the X-ray diffractogram, trace impurities unobservable within the resolution of the scan, unintentional and immeasurable K^+ doping of strontium-containing impurities such as SrS, $SrCO_3$ and $SrSc_2O_4$, and finally uncertainties in the Rietveld refinement of the ACu_3Ch_2 phase with just one major reflection. 91.1 % of K^+ successfully doped translates to a maximum x of 0.455 against a target of 0.500.

Beyond this point an incorporation plateau is observed, where the x = 0.750 and 1.000 samples have a maximum x of only 0.469 and 0.608 respectively, significantly lower than the target. The x values are beyond what the material can tolerate, so doping fails, purity drops, and impurity phases prevail.

At low levels of doping both the *a* and *c* parameters remain stable, Figure 102, but in highly doped samples where impurities dominate there is a very small increase in *a* and therefore in the cell volume. There are two possible reasons for this. Firstly, these data might suggest the continued incorporation of K^+ beyond the point where full incorporation ends, increasing the unit cell size because K^+ is larger than Sr^{2+} as previously discussed. It is clear that much of the K^+ is not incorporated in highly doped samples however the high concentration may be a driving force to facilitate a slight saturation increase.

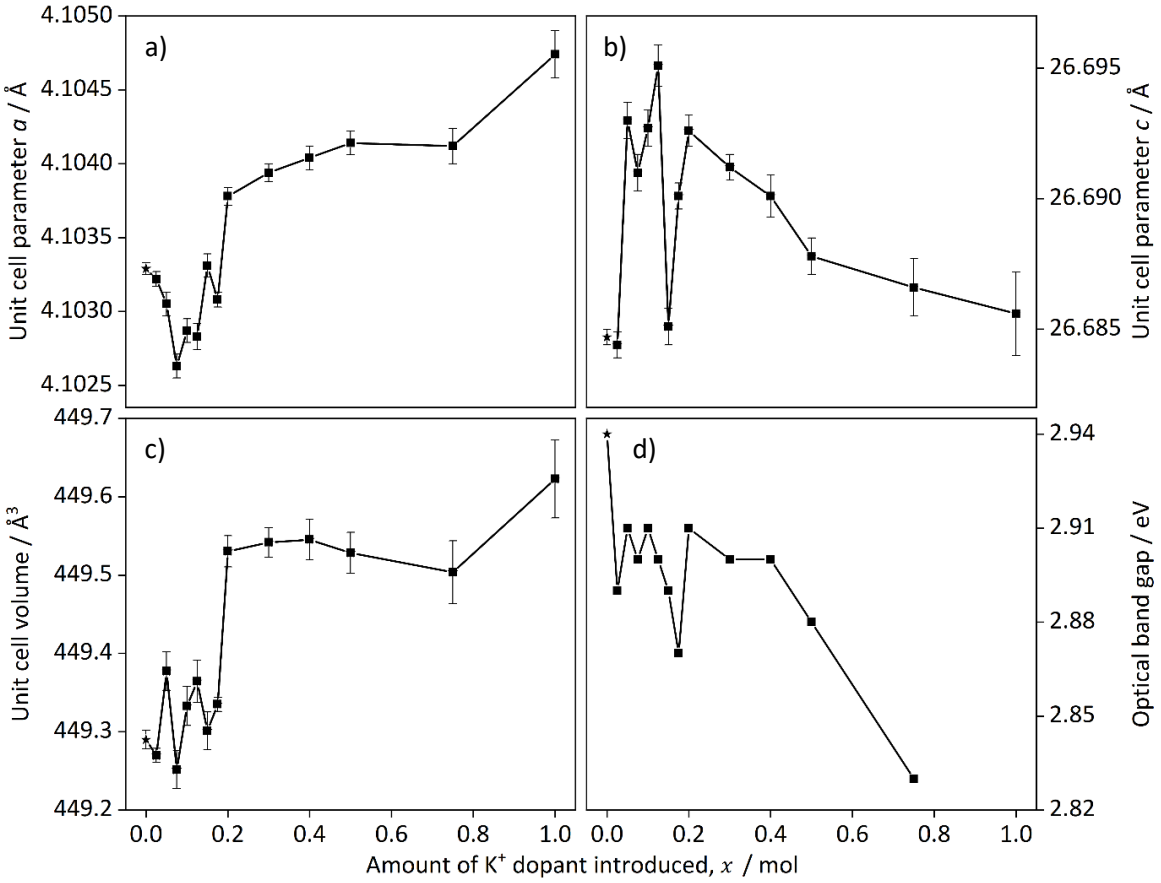

Figure 102 Comparisons of a) the α unit cell parameter, b) the c unit cell parameter, c) unit cell volume, and d) the optical band gap, of the thirteen potassium doped MALMs in the $(Sr_{3-x}K_x)Sc_2O_5Cu_2Se_2$ series. The pristine material $Sr_3Sc_2O_5Cu_2Se_2$ is included as a reference at x = 0 mol and is represented by a star. The x = 1.000 mol sample band gap is missing due to lack of drop-off in diffuse reflectance, see Appendix Table 29.

An alternative or concurrent theory to explain these trends, is that the unusual cell parameters are the result not (exclusively) of increased doping but of distorted or deficient MALMs. When extensive impurity formation occurs, the MALM is unlikely to possess the desired target stoichiometry, and site vacancies are probable. It is possible therefore that increasingly 'distorted' and non-stoichiometric MALMs resulted from such large concentrations of K^+, extracting Cu and Se from the solid solution to form the $K_xCu_ySe_z$ impurities.

Copper vacancies in the MALM due to $K_xCu_ySe_z$ formation would also explain the late downward trend in the band gaps. Figure 102d shows band gap stability initially, unaffected by K doping, before dropping on formation of the theorised distorted MALMs. Cu vacancies result in lattice distortions and slight decreases in band gap due to worsened Cu-Se hybridisation.[151] It should be noted that these trends are extremely tenuous, and could be the result of unavoidable (and regularly observed) slight differences between two self-consistent data sets.

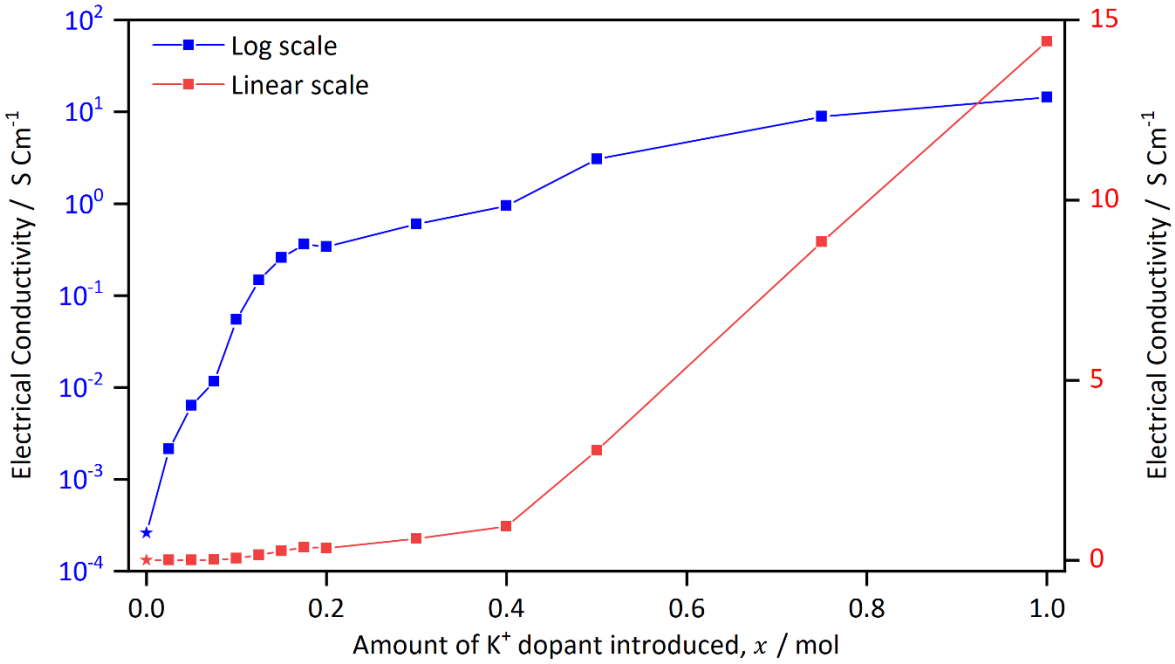

Figure 103 The electrical conductivities of the thirteen potassium doped MALMs in the $(Sr_{3-x}K_x)Sc_2O_5Cu_2Se_2$ series, represented on both a log_{10} scale (blue data; left hand y-axis) and a linear scale (red data; right hand y-axis). The pristine material $Sr_3Sc_2O_5Cu_2Se_2$ is included as a reference at $x = 0$ mol and is represented by a star. All values are derived from van der Pauw 4 probe resistivity measurements of 8mm annealed pellet samples.

It was hypothesised that the greatest conductivity would be observed in the sample whose stoichiometry was closest to that of the optimum amount of possible dopant, the saturation point of $Sr_3Sc_2O_5Cu_2Se_2$. One might therefore expect a 'bell curve'-like distribution of conductivities around the saturation point. After all, samples below the saturation point possess insufficient dopant to exhibit the enhanced conductivity demonstrated by the optimum material, and samples above the saturation point are plagued by mobility-diminishing impurities which detract from the conductive properties of a doped conductor, except for those which are themselves highly conductive and may enhance the conductivity.

Figure 103 presents an extraordinary 5.5 orders of magnitude increase in conductivity across the series. $Sr_3Sc_2O_5Cu_2Se_2$, which possessed an unimpressive conductivity of 2.61×10^{-4} S cm^{-1}, can be enhanced by *p*-type aliovalent potassium doping to 14.4 S cm^{-1} at the highest recorded point.

These data show not a bell curve or even a complete plateau but a continuous increase, which at first appears to suggest the above hypothesis is incorrect. At low levels of doping, below x = 0.200 mol, the MALMs increase steadily in conductivity compared to the pristine sample, enhancing its conductivity by three orders of magnitude. At this point, where sample purity begins to faulter, the conductivity continues to increase but now at a much steadier rate, where the conductivity difference between the x = 0.200 mol and x = 1.000 mol samples is approximately two further orders of magnitude, from 3.40×10^{-1} S cm^{-1} to 14.4 S cm^{-1}. This change in the rate of conductivity increase suggests an interesting conclusion which serves only to support the above hypothesis.

At the steepest increase in conductivity, below x = 0.200 mol, there is little to no potassium impurity present. Where these impurities prevail (impurities which are, importantly, extremely conductive), the sample conductivity increases but far steadier. Given these impurities only appear when exceeding the saturation point, this suggests that the initial sharp conductivity increase where no K^+ impurities are present is the effect of successful doping, and that the gradual conductivity increase beyond this is the effect of a linear concentration increase of the conductive impurities.

The weight percentages of the MALMs are vital evidence for this theory. Comparing these to the electrical conductivity, Figure 104, reveals a clear contrasting and almost mirrored relationship: sample purity correlates negatively with conductivity. If the increase in conductivity beyond x = 0.200 mol is a result of potassium doping, the sample purities should remain high and the excesses of potassium-containing impurities should not be observed.

The purity and conductivity data suggest an optimum dopant concentration in the range of x = 0.150 to 0.200 mol. The actual x = 0.200 mol sample, $(Sr_{2.800}K_{0.200})Sc_2O_5Cu_2Se_2$, was anomalously pure at 99.2 % as shown in Figure 97 on page 174, within the natural variation normal to solid-state doping chemistry, so the overall trend would suggest that x = 0.175 mol, $(Sr_{2.825}K_{0.175})Sc_2O_5Cu_2Se_2$, is the optimum of the investigated doping levels.

The sharp conductivity increase due to doping came at the expense of only a very slight reduction in optical band gap, with all samples in this range measuring between 2.89 and 2.91 eV, compared to the pristine band gap of 2.94 eV. A further conductivity increase of two orders of magnitude can be observed when dopant is added beyond this optimum concentration, but is suggested to be the result of conductive impurities and not the MALM sample itself. However, this series is still tuneable, as whilst the conductivity trend at high dopant levels may not be the result of doping, it is still consistent and correlates highly with both sample purity and the concentration of conductive impurity, so could be engineered to attain a specific desired value.

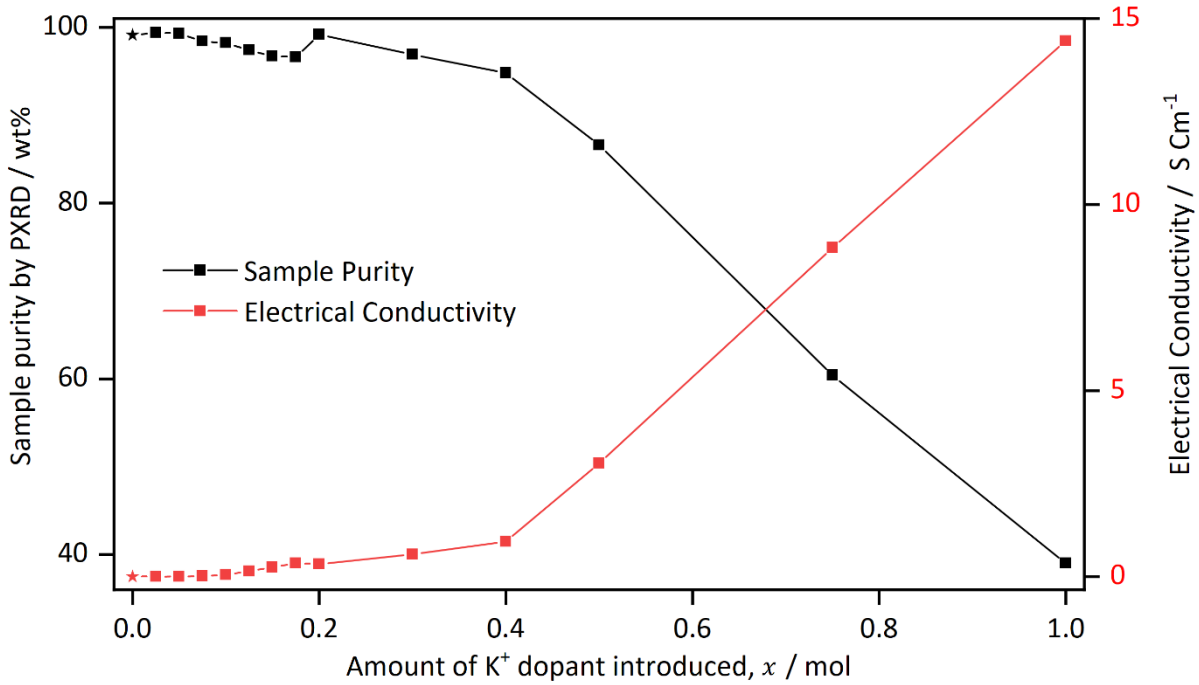

Figure 104 *The purities (black data; left hand y-axis), and electrical conductivities (red data; right hand y-axis), of the thirteen potassium doped MALMs in the $(Sr_{3-x}K_x)Sc_2O_5Cu_2Se_2$ series. The pristine material $Sr_3Sc_2O_5Cu_2Se_2$ is included as a reference at $x = 0$ mol and is represented by a star. Purity values are derived from the Rietveld refinements of PXRD data using GSAS-II, and reported as weight percentages. Conductivity values are derived from van der Pauw 4 probe resistivity measurements of 8mm annealed pellet samples.*

3.4.3 Sodium Doping, $(Sr_{3-x}Na_x)Sc_2O_5Cu_2Se_2$

Sodium was introduced as an aliovalent *p*-type dopant onto the strontium site of $Sr_3Sc_2O_5Cu_2Se_2$ such that the target material takes the form $(Sr_{3-x}Na_x)Sc_2O_5Cu_2Se_2$. This was achieved by reducing SrSe content and supplementing with [Na_2Se + Se], according to Equation 50 below:

Equation 50 $$2\ SrO + Sc_2O_3 + Cu_2Se + 1\text{-}x\ SrSe + \frac{x}{2}[Na_2Se + Se] \rightarrow (Sr_{3-x}Na_x)Sc_2O_5Cu_2Se_2$$

The ground powder precursors (1 gram scale) were heated within an ampoule for 12 hours at 180 °C, then raised to 800 °C for a further 12 hours in the same ampoule. They were then reground, pelletised, and heated again for 24 hours at 800 °C. Like the potassium doped $(Sr_{3-x}K_x)Sc_2O_5Cu_2Se_2$ series outlined previously, thirteen samples were synthesised in total across two separate self-consistent sample sets: eight with a dopant level ranging from x = 0.025 to 0.200 mol at equal increments of 0.025 mol, and a further five samples at x = 0.300, 0.400, 0.500, 0.750 and 1.000 mol to extend the total investigated doping range. The complete compositional, analytical and graphical data for each sample in this section can be found in *Appendix B.1.5*.

In *Section 3.3* - $Sr_3Sc_2O_5Cu_2S_2$ it was observed that the sodium doped sulfide MALMs exhibited very similar trends to their potassium doped equivalents, albeit with less-uniform trends and less predictable material behaviour, but higher purities. Here, a similar pattern emerged for the potassium and sodium doped selenides.

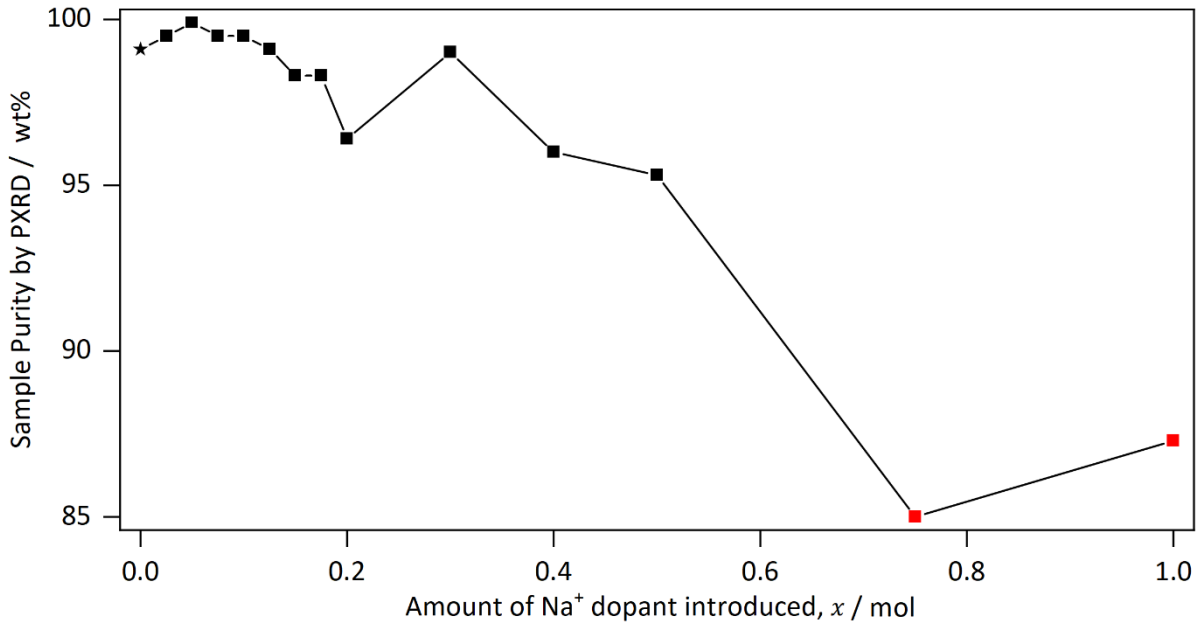

Figure 105 Purities of the thirteen sodium doped MALMs in the $(Sr_{3-x}Na_x)Sc_2O_5Cu_2Se_2$ series. The pristine material $Sr_3Sc_2O_5Cu_2Se_2$ is included as a reference at x = 0 mol and is represented by a star. The two data points at x = 0.750 mol and x = 0.100 mol are coloured red to indicate the presence of unknown impurities in these samples, and as a result the cited purity values are likely to be slight overestimates. All values are derived from the Rietveld refinements of PXRD data using GSAS-II, and reported as weight percentages.

Sample purities in this Na doped series are superior to that of the potassium analogues, see Figure 105. All samples doped to x = 0.175 mol or less have purities above 98 wt % which is exceptionally high for materials of this type, and crucially no samples within this range contain the conductive impurity $NaCu_3Se_2$. The only impurities present in this range are SrSe and $SrCO_3$, commonplace within MALMs, doped or otherwise, and insulating thus not falsely enhancing observed conductivity. The final two data points are again the result of a doping level so high that some small unknown material remained unrefined in the pattern, As before the phase appears very small, so the assumption was made that this has no effect besides a small false positive wt % value for all other phases present.

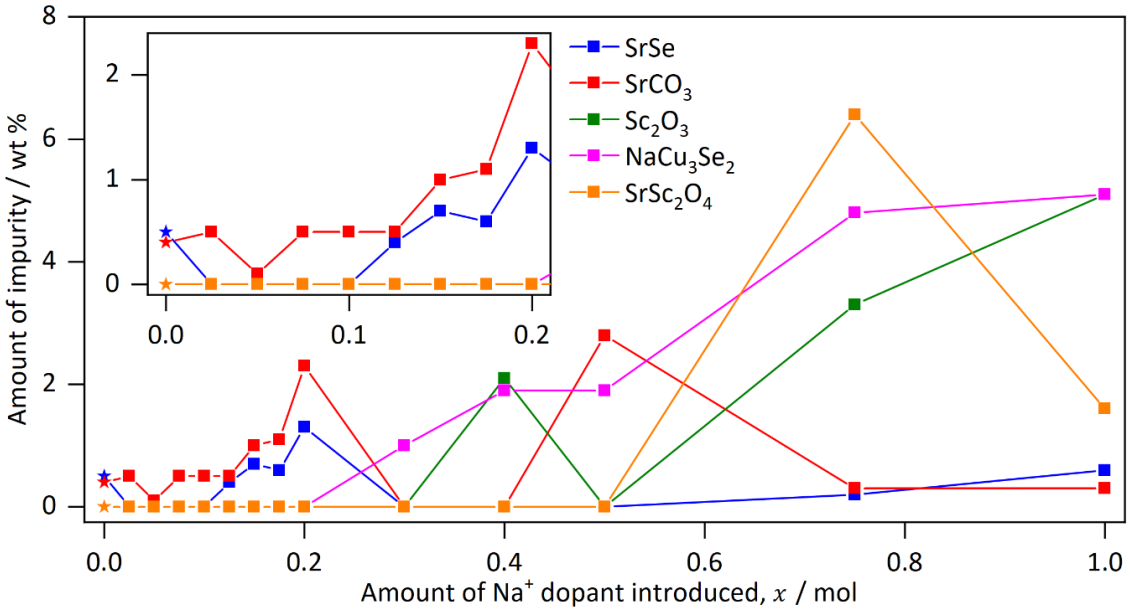

Figure 106 *The weight percentages of five impurity phases present in the $(Sr_{3-x}Na_x)Sc_2O_5Cu_2Se_2$ series. The pristine material $Sr_3Sc_2O_5Cu_2Se_2$ is included as a reference at $x = 0$ mol and is represented by stars. The inset plot is a magnification of the $x = 0$ to 0.200 mol region where doping and impurity quantities are low. Note the y-axis scale change at 20 wt %.*

It is not until the five samples of the supplementary data set that $NaCu_3Se_2$ is present, and it is observed in far smaller quantities than KCu_3Se_2 was in the previous section, see Figure 106 above. Even the most doped sample with target composition $(Sr_{2.000}Na_{1.000})Sc_2O_5Cu_2Se_2$ contains only 5.1 wt % $NaCu_3Se_2$. Impurity formation is sporadic in this series, likely due to inaccuracies of refining trace phases in Rietveld refinement. The one exception is $NaCu_3Se_2$ which increases steadily and linearly, sufficient in the x = 0.750 and 1.000 mol samples to induce formation of $SrSc_2O_4$ as seen previously. It should be noted that the apparent jump in purity between x = 0.200 and 0.300 is likely an artifact of two separate self-consistent data sets.

The comparative PXRD plot in Figure 107 shows that whilst five impurity phases and some unknown unrefined material are present in the x = 1.000 mol sample, the main 325 phase still dominates at 87.3 wt %, a purity greater than would be expected for a material doped to this extent. Compared to the potassium equivalents, sodium doped $Sr_3Sc_2O_5Cu_2Se_2$ forms purer at all doping levels and appears to incorporate more of the supplied dopant, as evidenced by $NaCu_3Se_2$, or lack thereof.

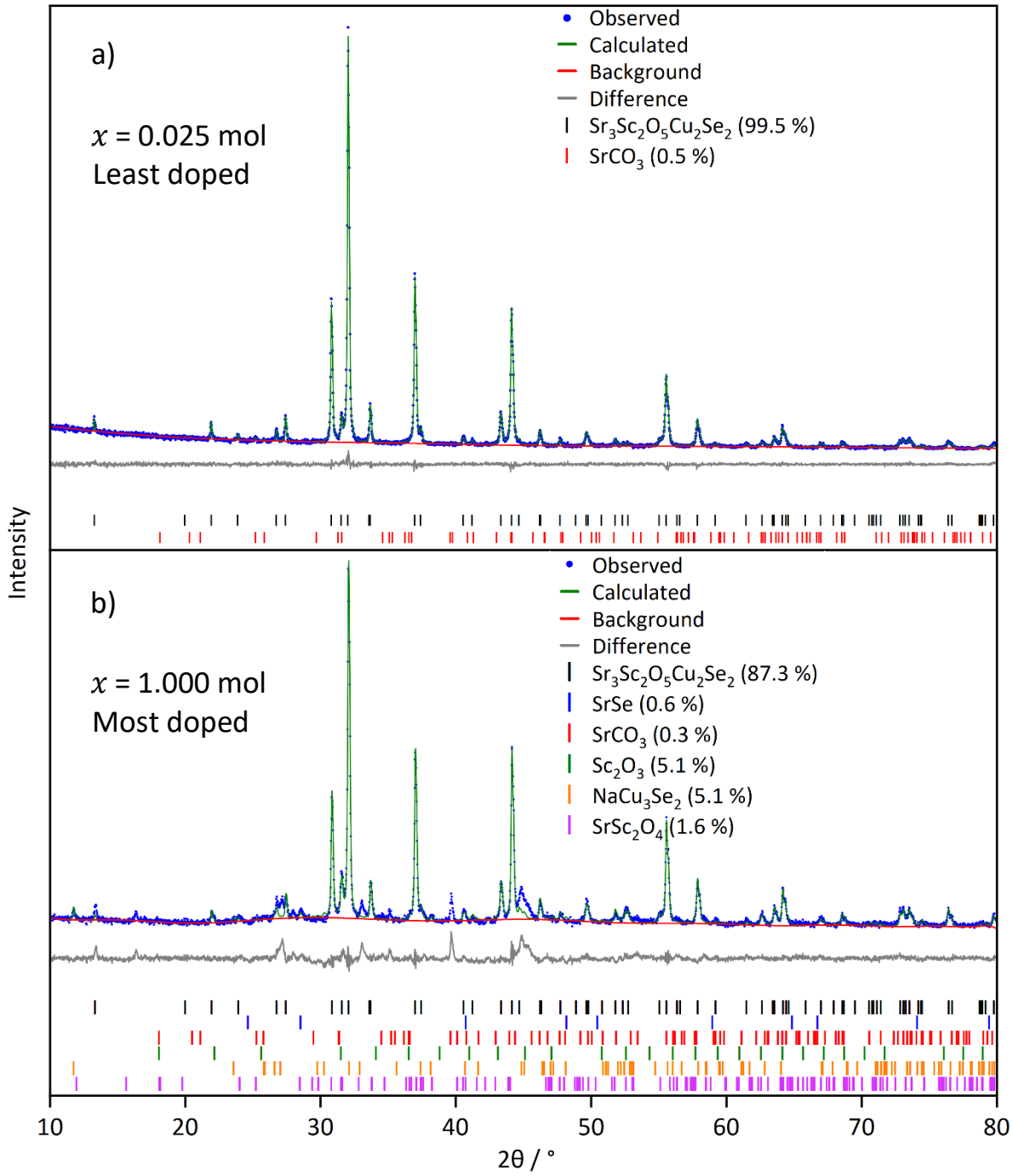

Figure 107 *Powder X-ray diffractograms of a) the least doped sample of the series with target composition $(Sr_{2.975}Na_{0.025})Sc_2O_5Cu_2Se_2$, and b) the most doped sample of the series with target composition $(Sr_{2.000}Na_{1.000})Sc_2O_5Cu_2Se_2$ (both space group I4/mmm) after 36 hours of heating at 800 °C. The small blue circles represent the observed diffracted intensities, the green lines represent the Rietveld-refined calculated models, the red lines represent the backgrounds, and the grey lines represent the differences between observed and calculated intensities. The black tick marks show the reflections of the refined model of $Sr_3Sc_2O_5Cu_2Se_2$, whilst the blue, red, green, orange and pink tick marks represent refined impurity phases SrSe, $SrCO_3$, Sc_2O_3, $NaCu_3Se_2$ and $SrSc_2O_4$ respectively. Weight fractions for each phase are cited in the figure legends.*
a) Duration: 45 minutes. Data points: 3457. Interval: 0.02 °. GOF: 1.07. R_{wp}: 6.269 %.
b) Duration: 45 minutes. Data points: 3457. Interval: 0.02 °. GOF: 2.05. R_{wp}: 8.228 %.

The conductivities of this series are again very similar to the potassium samples. There is an initial sharp rise in conductivity from 2.61 × 10^{-4} S cm^{-1} in the pristine x = 0 sample, through to 4.42 S cm^{-1} in the x = 0.200 sample. This familiar pattern represents a region of high certainty of successful doping where impurities (specifically $NaCu_3Se_2$) are low or zero, and conductivity is exponentially increasing. The peak reached here is 10x higher than it is in in the potassium series, so this initial region encompasses four orders of magnitude of predictable tuneable conductivity, a highly desirable behaviour for prospective conducting materials.

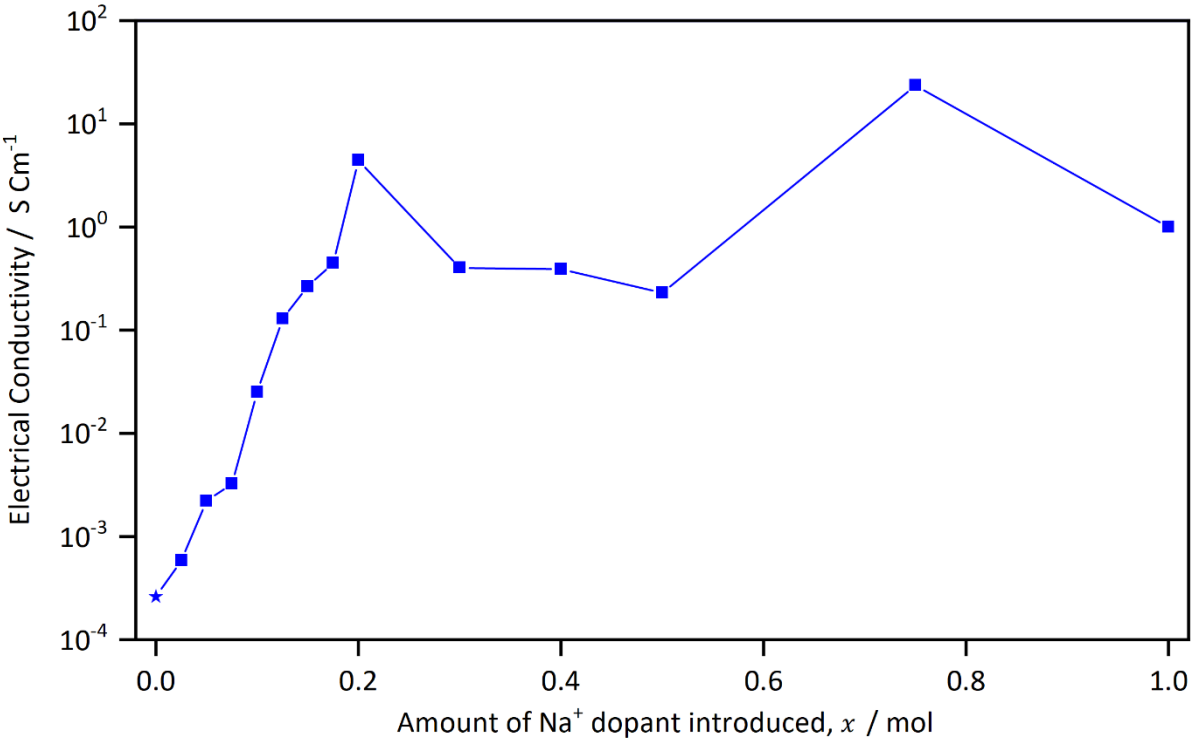

Figure 108 The electrical conductivities of the thirteen sodium doped MALMs in the $(Sr_{3-x}Na_x)Sc_2O_5Cu_2Se_2$ series, represented on a log_{10} scale. The pristine material $Sr_3Sc_2O_5Cu_2Se_2$ is included as a reference at x = 0 mol and is represented by a star. All values are derived from van der Pauw 4 probe resistivity measurements of 8mm annealed pellet samples.

Beyond this point the conductivities plateau between 0.1 and 1 S cm^{-1} where further increases in dopant concentration appear no longer to have an effect, suggesting both a saturation point and an optimum dopant concentration at x = 0.200. Conductivity then peaks again at 23.4 S cm^{-1} in the x = 0.750 mol sample, which is the highest single pellet conductivity reported in the entirety of this work and almost 100,000 times greater than the pristine sample, before dropping once more in the final sample where x = 1.000, resistivity is 1.000 Ω cm, and conductivity is 1.000 S cm^{-1}.

There is a very slight conductivity decline in the three samples where x = 0.300, 0.400 and 0.500 mol, which is uncommon in these series and provides yet more evidence of saturation having been achieved and further attempts to dope proving unsuccessful. However, the unusually conforming behaviour of these samples in the dopant incorporation graph below disagrees, providing opposing evidence that is in suggestion of further dopant incorporation being successful.

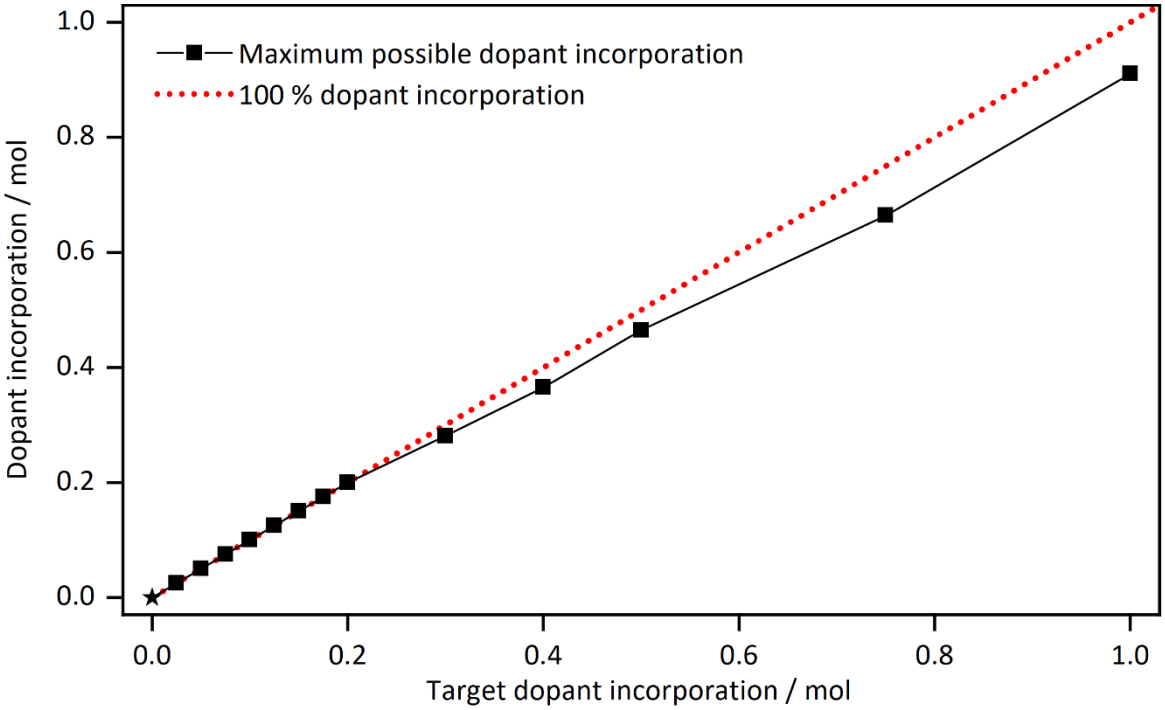

Figure 109 *The calculated maximum possible levels of dopant incorporation into the $(Sr_{3-x}Na_x)Sc_2O_5Cu_2Se_2$ MALMs. Values were derived from the wt % of the sodium-containing impurities of each sample. The pristine material $Sr_3Sc_2O_5Cu_2Se_2$ is included as a reference at x = 0 mol and is represented by a star. The red dashed line represents 100 % dopant incorporation into the MALM, statistically no values may surpass this line. The black data points are the estimated upper bound of dopant incorporation for each sample.*

Table 7 *The target and maximum possible dopant content within the six highest doped MALMs in the $(Sr_{3-x}Na_x)Sc_2O_5Cu_2Se_2$ series. All samples before x = 0.200 show no trace of sodium-containing impurities therefore the maximum x is the target x, so these have been omitted for brevity. The pristine material $Sr_3Sc_2O_5Cu_2Se_2$ is included as a reference.*

Target x / mol	**Maximum Na in product / %**	**Maximum x / mol**
0.200	100	0.200
0.300	93.734	0.281
0.400	91.154	0.365
0.500	92.989	0.465
0.750	88.471	0.664
1.000	91.035	0.910

These values are calculated from the weight percentages of conductive impurities, which in this series are sparsely observed leading to high estimations of incorporation. $NaCu_3Se_2$ appears in the final five samples only, and in very low quantities, thus the promising values of maximum x per sample in Figure 109, tabulated in Table 7. This suggests incorporation is the highest of all series discussed thus far, which contrasts the conductivity data on the previous page which implies a plateau in conductivity due to reduced dopant incorporation. One would expect continued dopant incorporation to yield a continued improvement in conductivity, especially when combined with an impurity type evidenced repeatedly to increase the sample conductivity, yet this is not the case in this series.

There are various possible explanations for this phenomena. First, the usual frequently discussed caveats of the dopant incorporation plot may be disguising a saturation point with apparent high incorporation values. While these are upper bounds and always likely to be lower than those shown, this explanation remains unlikely.

With MALM purities in this series being so high, conductive impurities so low, and estimated x values so close to the target x values, there is overwhelming evidence that the dopant incorporation plot is correct and that the conductivity values are those which challenge expectation. Consequently, a second explanation is that dopant is being incorporated successfully, fully until x = 0.200 mol, and then slightly decreasing in effectiveness on further addition, as suggested in Figure 109 and Table 7. In this explanation the emergence of impurities may be damaging the conductive behaviour of the MALMs, acting as insulating 'roadblocks' to physically inhibit the flow of charge, reducing the mobility. This hypothesis is also doubtful because if impurities inhibit flow here, they would be expected to behave similarly in previous series where this purity-conductivity disagreement is not observed.

The simplest explanation is that which requires the fewest assumptions. The most probable reasoning for this phenomenon is that dopant is incorporated as described by the incorporation plot, but crucially, its addition stops having an effect in the region of x = 0.200 to 0.300 mol. Incorporation continues beyond this point, MALM purity remains relatively high and impurities remain low, but conductivity plateaus. This is due to the balance between MALM mobility and charge carriers, where doping has greatly improved the charge carrying capacity of the material such that conductivity is now limited by the sample mobility, which cannot easily be improved. This theory is supported by the sample purities, conductivities, the $NaCu_3Se_2$ emergence and the dopant incorporation data. The high concentration values in the most extreme doping levels may be attributed as is usually the case, to the conductive by-product $NaCu_3Se_2$. Hall measurements of these samples to quantify both the inherent sample mobility, and also the change in charge carriers across the series, should be considered essential future work in this area.

Despite slight contradictions between some of the data obtained here, this series has the most impressive conductivities, purities and dopant incorporation of any thus far within this work. The low to moderately doped region of x = 0 to 0.200 mol (which appears linear on the log scale, thus is an exponential rise) serves as an excellent display of tuneable conductivity: a 17,000x improvement. This region, displayed in greater detail in Figure 110, can be solely attributed to successful doping due to the lack of any sodium in impurities up to this point, or at least that which is measurable by PXRD.

The optimum dopant value in this series is x = 0.200, the point where the predictable behaviour begins to break down, and full incorporation can no longer be assumed. As with all previous series, attempting to dope samples beyond the full incorporation point does not yield useful materials, as competing by-products, decreasing main phase purity and potentially the sample mobility may damage the intended conductive performance.

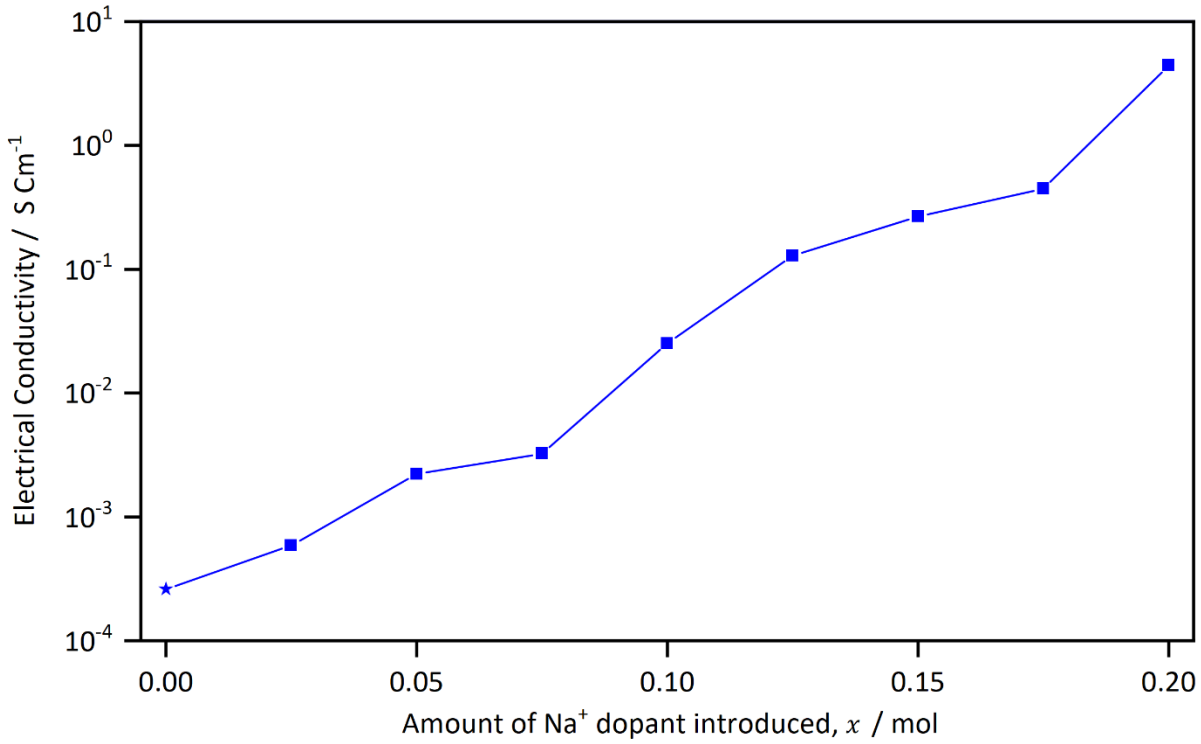

Figure 110 *The electrical conductivities of the first eight sodium doped MALMs in the $(Sr_{3-x}Na_x)Sc_2O_5Cu_2Se_2$ series up to 0.200 mol, represented on a log_{10} scale. The pristine material $Sr_3Sc_2O_5Cu_2Se_2$ is included as a reference at x = 0 mol and is represented by a star. All values are derived from van der Pauw 4 probe resistivity measurements of 8mm annealed pellet samples.*

The optical band gap, for which data can be found in *Appendix Figure 98*, was found to remain unchanged throughout this series, measuring 2.92 ± 0.02 eV.

The behaviours of $Sr_3Sc_2O_5Cu_2Se_2$ when doped with the group 1 metals K^+ and Na^+ is now understood over a wide range of dopant concentrations. The various interplays between successful doping, unincorporated dopant, mobility concerns and site vacancies combine to produce doped materials with predictable tuneable behaviour at low concentrations, and more conductive yet less predictable behaviour at higher concentrations, with no decrease in transparency. Introducing strontium vacancies would be a useful experiment to further understand of how an increase in charge carriers may behave, if possible, with no dopant to fill them. This is explored later, in *Section 3.4.8*.

Next, a series of four smaller $Sr_3Sc_2O_5Cu_2Se_2$ doping investigations were performed to probe other atomic sites and other forms of doping, each pursuing a recommendation listed by Scanlon et al in their 2009 study.[46] [††] First, magnesium was doped aliovalently onto the scandium site with the goal of introducing charge carriers, akin to the strontium site doping studies described previously. Then, barium was isovalently doped onto the strontium site targeting an increase in the basal *a* lattice parameter to improve transparency. Finally, also with the aim to improve transparency, yttrium and lanthanum were isovalently doped onto the scandium site.

Each of these four doping series are smaller in scale than the previous, favouring breadth over depth of available dopant options. The ranges explored cover the previously determined most useful and predictable region from x = 0 to x = 0.200 mol. This range should be sufficient to detect any desirable behaviours and dictate the direction of future work recommendations in the field.

[††] Scanlon published these recommendations concerning the sulfide MALM $Sr_3Sc_2O_5Cu_2S_2$, but with the recognition that selenium doping (or rather substitution) onto the sulfur site would also enhance conductivity but damage the optical transparency. Given $Sr_3Sc_2O_5Cu_2Se_2$ has greater room for improvement in transparency, and behaves more predictably with larger conductivities, these recommendations were applied instead to the selenide. $Sr_3Sc_2O_5Cu_2Se_2$ may be considered $Sr_3Sc_2O_5Cu_2S_2$ doped completely with Se, thus an assumption was made that the theoretical improvements of one may also apply to the other.

3.4.4 Magnesium Doping, $Sr_3(Sc_{2-x}Mg_x)O_5Cu_2Se_2$

Magnesium was introduced as an aliovalent *p*-type dopant onto the scandium site of $Sr_3Sc_2O_5Cu_2Se_2$ such that the target material takes the form $Sr_3(Sc_{2-x}Mg_x)O_5Cu_2Se_2$. This was achieved by reducing Sc_2O_3 content and supplementing with MgO. This leaves an oxygen deficiency due to the differences in the metal oxide stoichiometries, which is accounted for by increasing the only other oxygen-containing material, SrO. This in turn leaves excess strontium, accounted for by a reduction of SrSe, which leaves a deficiency of Se, which is accounted for by elemental selenium. This unusually complex permutation of precursors arises from the requirement for oxygen to balance the product stoichiometry. To do this, ratios of the supplied precursors are staggered to shift the deficiency from O, which cannot be added as an elemental precursor, to Se, which can, according to Equation 51 below. In all previous series, the initial deficiency was S or Se which could be supplied directly.

Equation 51

$$(2 + \tfrac{x}{2})\ SrO + (1 - \tfrac{x}{2})\ Sc_2O_3 + Cu_2Se + (1 - \tfrac{x}{2})\ SrSe + x\ MgO + \tfrac{x}{2}\ Se \rightarrow Sr_3(Sc_{2-x}Mg_x)O_5Cu_2Se_2$$

The ground powder precursors (1 gram scale) were heated within an ampoule for 12 hours at 180 °C, then raised to 800 °C for a further 12 hours in the same ampoule. They were then reground, pelletised, and heated again for 24 hours at 800 °C. Four samples were synthesised, with a dopant level ranging from x = 0.050 mol to x = 0.200 mol at equal increments of 0.050 mol, all synthesised in one self-consistent sample set. The complete compositional, analytical and graphical data for each sample in this section can be found in *Appendix B.1.6.*

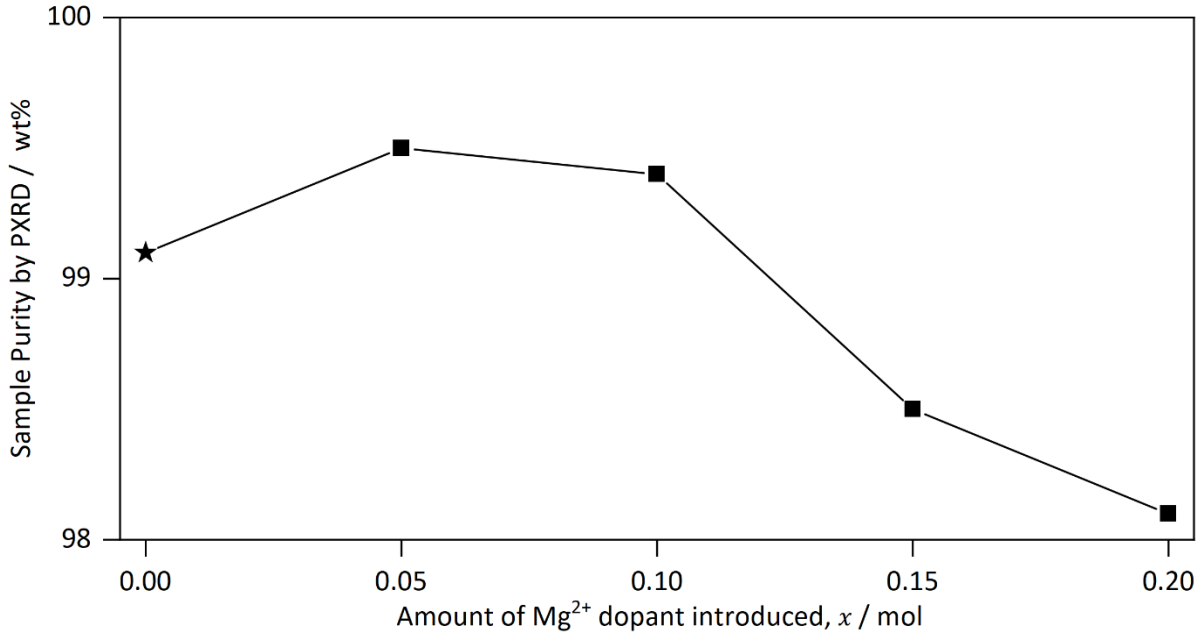

Figure 111 Purities of the four magnesium doped MALMs in the $Sr_3(Sc_{2-x}Mg_x)O_5Cu_2Se_2$ series. The pristine material $Sr_3Sc_2O_5Cu_2Se_2$ is included as a reference at x = 0 mol and is represented by a star. All values are derived from the Rietveld refinements of PXRD data using GSAS-II, and reported as weight percentages.

It is immediately obvious that magnesium doping into $Sr_3Sc_2O_5Cu_2Se_2$ is not only possible but successful. Sample purities, Figure 111, remain exceptionally high across the series, some actually higher than the pristine but within the subjective error of Rietveld refinement. The difference in purity between the least and most doped samples in this small series is approximately 1 wt %, an unusually excellent consistency. These two samples are evaluated in the comparative plot Figure 112 on the following page, showing an almost negligible difference between their diffractograms.

The only impurities appearing in these samples are SrSe in all four, and $SrCO_3$ in the two highest-doped, and the amount of each impurity increases steadily as expected throughout the series.

The manifestation and detection of magnesium as an unreacted dopant should be approached differently based on what was learned from the K and Na series. The A_2Ch binary precursors used in the four group 1 metal doping studies are extremely unstable in air, as discussed in *Section 2.3*, so the probability of unreacted K or Na manifesting as Na_2Ch or K_2Ch in the product is almost zero. Instead, the ACu_3Ch_2 impurities formed, which are conductive and damaging to overall MALM purity by catalysing the accompanying formation of $SrSc_2O_4$.

In the case of magnesium saturation however, the dopant cation Mg^{2+} is unlikely to manifest as a conductive impurity as was observed with K^+ and Na^+, because more stable forms exist such as the carbonate $MgCO_3$ or the initial oxide precursor MgO. These are air stable and insulating (wide band gap) forms of magnesium,[258, 259] phases which never appeared in the potassium or sodium series because they are less stable than the magnesium equivalents.

It should be noted that whilst these stable insulating by-products allow more confidence in the measured conductivity values, MgO is very light compared to other precursors or by-products used or found herein, so may be more difficult to detect by PXRD. Magnesium and sodium are neighbouring metals on the periodic table thus have similar masses, however in this work sodium appears alongside heavier atoms such as copper, sulfur or selenium resulting in heavier molecules which are more detectable by PXRD. Magnesium, supplied in its oxide form, may provide weaker reflections in resulting patterns, making it more difficult to identify and quantitatively measure.

Despite this precaution, there is no evidence of any unincorporated magnesium throughout this series, suggesting a strong uptake by $Sr_3Sc_2O_5Cu_2Se_2$. This is supported by ion sizes. The *B* site of a 325 MALM is 5-coordinate, an environment very uncommon for scandium and as such data for this coordination environment is not widely available. Using instead a (far more common) 6-coordinate environment as an example, Sc^{3+} and Mg^{2+} are incredibly close in size, 0.745 Å and 0.72 Å respectively, a mere 3.5 % difference. This should remain a qualitative assessment, as with all aliovalent comparisons, because this size is based on a +2 environment for magnesium which is not the case here. However, the two cations are a very good size match, supporting what appears to be facile doping of Mg^{2+} onto Sc^{3+}.

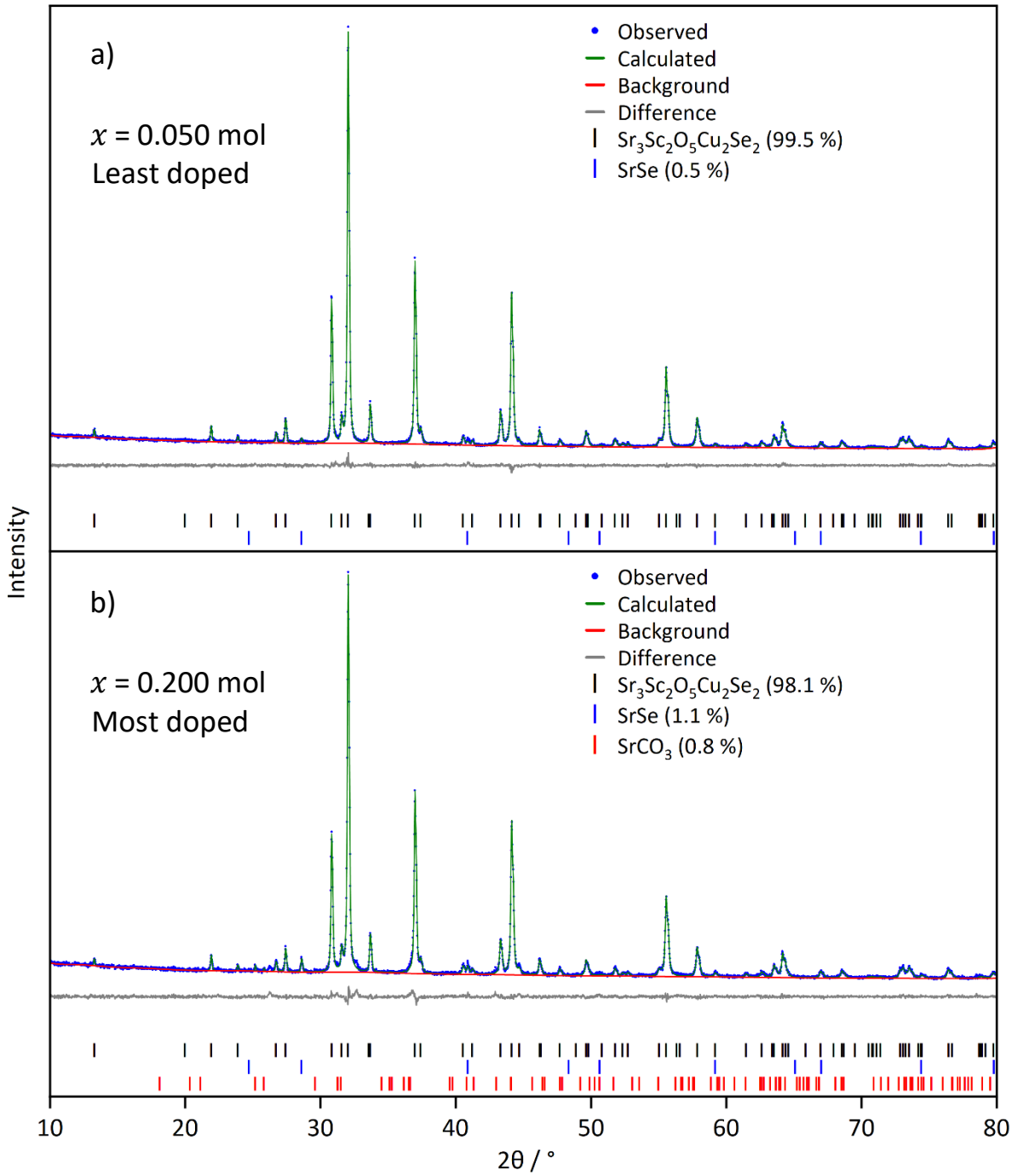

Figure 112 *Powder X-ray diffractograms of a) the least doped sample of the series with target composition $Sr_3(Sc_{1.95}Mg_{0.05})O_5Cu_2Se_2$, and b) the most doped sample of the series with target composition $Sr_3(Sc_{1.80}Mg_{0.20})O_5Cu_2Se_2$ (both space group I4/mmm) after 36 hours of heating at 800 °C. The small blue circles represent the observed diffracted intensities, the green lines represent the Rietveld-refined calculated models, the red lines represent the backgrounds, and the grey lines represent the differences between observed and calculated intensities. The black tick marks show the reflections of the refined model of $Sr_3Sc_2O_5Cu_2Se_2$, whilst the blue and red tick marks represent refined impurity phases SrSe and $SrCO_3$ respectively. Weight fractions for each phase are cited in the figure legends. a) Duration: 45 minutes. Data points: 3457. Interval: 0.02 °. GOF: 1.13. R_{wp}: 4.460 %. b) Duration: 45 minutes. Data points: 3457. Interval: 0.02 °. GOF: 1.24. R_{wp}: 5.274 %.*

The absence of any magnesium-containing impurities or precursors in these samples produces an interesting 'ideal case' of dopant incorporation where it is possible, perhaps probable, that full dopant incorporation may have taken place, see Figure 113. Whilst these values are always upper bounds and not treated as true values, this is the first case so far in this work where all dopant appears fully incorporated. The usual caveats of potential amorphous or XRD-invisible impurities still apply, more than usual in the case of lightweight Mg, but the main source of error in these calculations is usually the Rietveld refinement of the dopant-containing impurities. This error is not applicable in this series, due to the lack of Mg-containing impurities, supporting the inference of high dopant uptake.

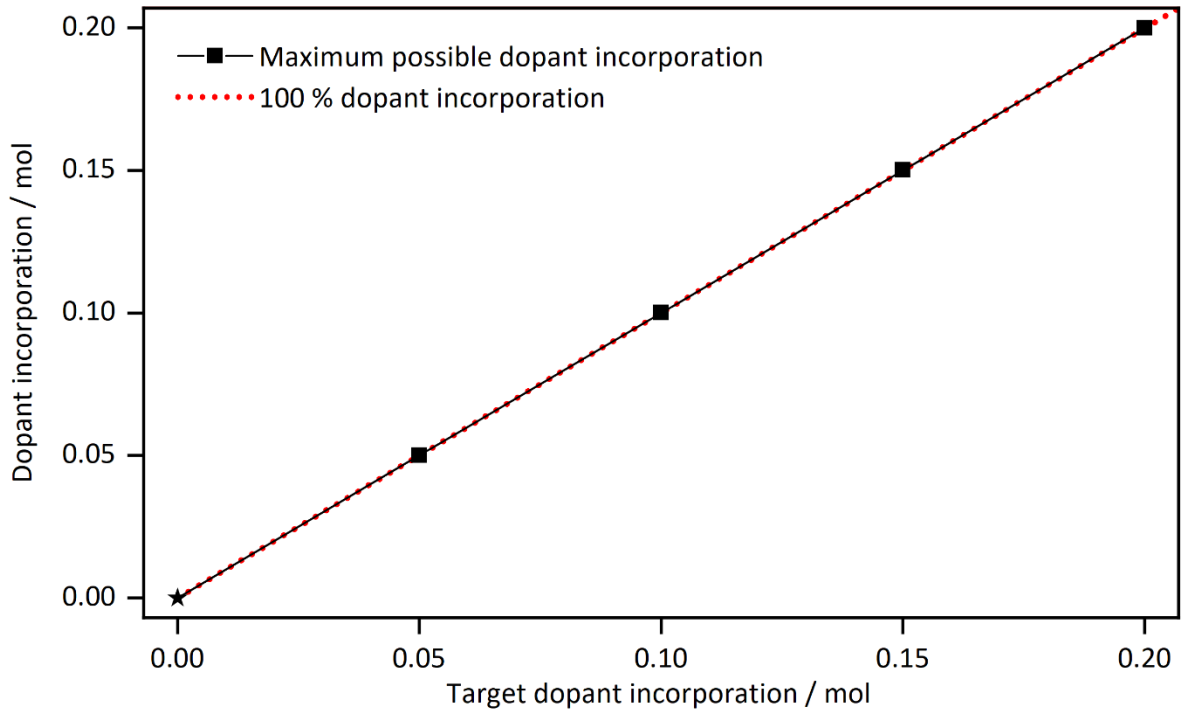

Figure 113 *The calculated maximum possible levels of dopant incorporation into the $Sr_3(Sc_{2-x}Mg_x)O_5Cu_2Se_2$ MALMs. Values were derived from the wt % of the magnesium-containing impurities of each sample, of which there were none. The pristine material $Sr_3Sc_2O_5Cu_2Se_2$ is included as a reference at x = 0 mol and is represented by a star. The red dashed line represents 100 % dopant incorporation into the MALM, statistically no values may surpass this line. The black data points are the estimated upper bound of dopant incorporation for each sample.*

It is logical to assume from both the sample compositions and dopant incorporation estimates that the saturation point of $Sr_3Sc_2O_5Cu_2Se_2$ has not been reached in this series. While this does not detract from the applicability of magnesium doping to tuning this material for applications, it would be a useful metric to quantify a useful doping limit which may be significantly above that which has been investigated here. Sodium doping in the previous section showed similar behaviour, which became less predictable above x = 0.200 mol when exceeding the window of highly incorporated doping concentrations, suggesting Mg^{2+} may behave similarly. Exploration of higher dopant concentrations would probe this limit and ascertain the impurity form that magnesium takes when no longer accommodated as a dopant.

The electrical conductivities of this series are, unsurprisingly, very impressive. The improvement displayed in Figure 114 appears to plateau on a log scale but is actually linear, therefore tuneable. On the log scale an initial sharp increase is observed, with a 400 fold improvement from 2.61×10^{-4} S cm^{-1} to 0.106 S cm^{-1} following the incorporation of just 0.05 mol of magnesium. From here the improvements continue for another half an order of magnitude, peaking at 0.572 S cm^{-1} in the x = 0.200 mol sample, a conductivity enhancement of more than 2000 times that of the pristine.

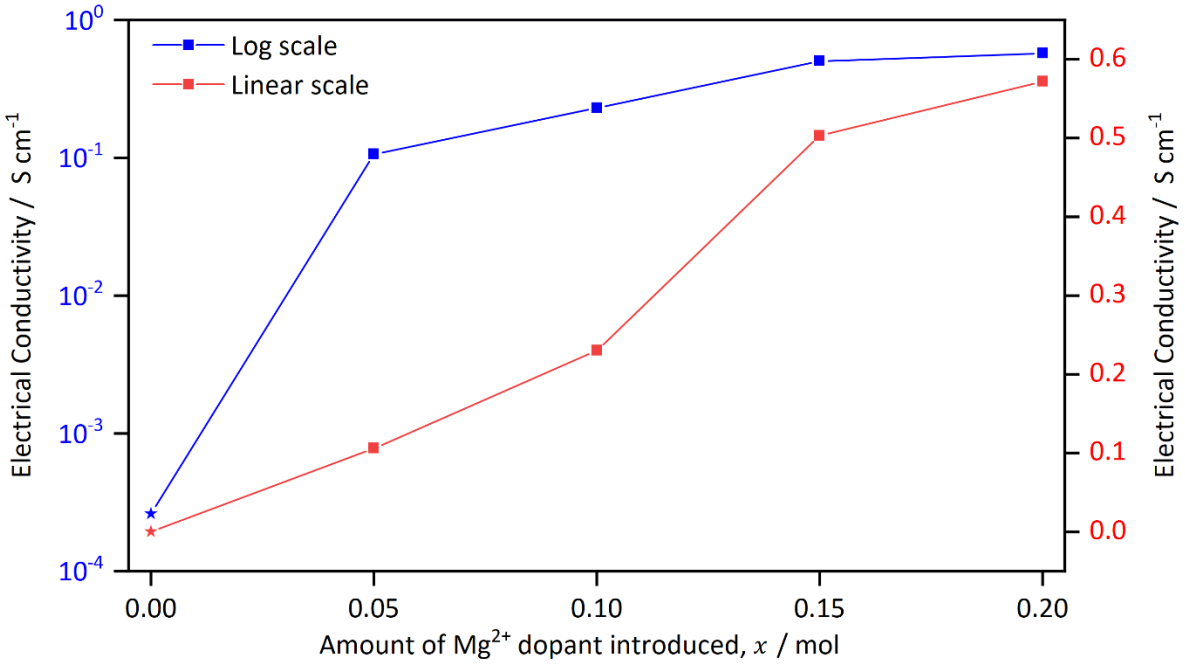

Figure 114 The electrical conductivities of the four magnesium doped MALMs in the $Sr_3(Sc_{2-x}Mg_x)O_5Cu_2Se_2$ series, represented on both a log_{10} scale (blue data; left hand y-axis) and a linear scale (red data; right hand y-axis). The pristine material $Sr_3Sc_2O_5Cu_2Se_2$ is included as a reference at x = 0 mol and is represented by a star. All values are derived from van der Pauw 4 probe resistivity measurements of 8mm annealed pellet samples.

The plateau in log conductivities is similar to that which was observed in the previous series, where sodium doped samples maintained high estimated dopant incorporation, but improvement in conductivity ceased. This magnesium series, more than the sodium case where $NaCu_3Se_2$ was observed, suggests that incorporation is still very high, so the likelihood that this plateau is the result of a saturation point around x = 0.050 is low. The optimum Mg^{2+} level is therefore x = 0.200 with the data available, but is likely even higher, so greater levels of doping should be explored.

As discussed in detail in the previous series, it is more probable that this weakening increase in conductivity is the result of the sample mobility limiting what would otherwise be an exceptionally high conductivity resulting from increased charge carriers. The magnesium is very likely incorporated successfully across the levels of doping measured, and charge carriers are therefore increasing, but conductivity is limited and mobility is a likely cause. As before, Hall measurements to quantify these metrics would be enlightening.

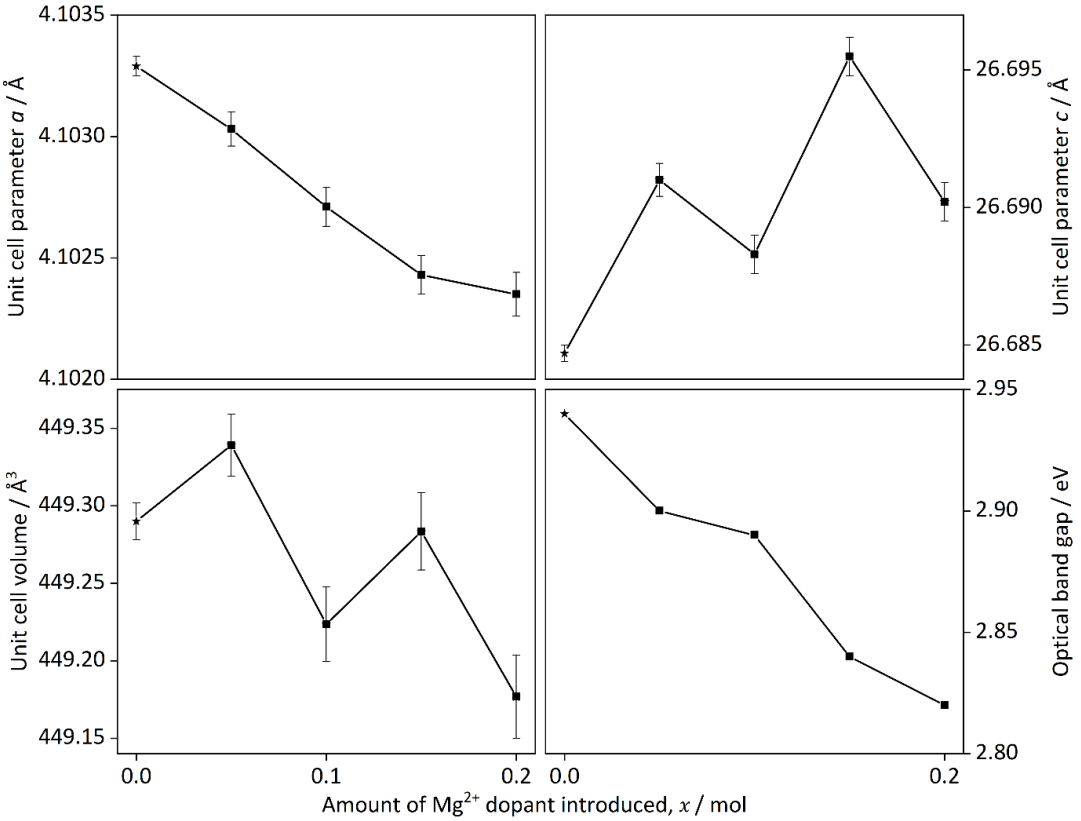

Figure 115 Comparisons of a) the α unit cell parameter, b) the c unit cell parameter, c) unit cell volume, and d) the optical band gap, of the four magnesium doped MALMs in the $Sr_3(Sc_{2-x}Mg_x)O_5Cu_2Se_2$ series. The pristine material $Sr_3Sc_2O_5Cu_2Se_2$ is included as a reference at x = 0 mol and is represented by a star.

This series is the first to show a plausible trend in optical band gap (Figure 115), a linear decrease from 2.94 eV in the pristine down to 2.82 eV in the x = 0.200 sample. This decrease is not drastic, especially as a product of an impressive conductivity improvement, but it does detract from the applicability of magnesium doping in an application such as a transparent conductor. The transparency of undoped $Sr_3Sc_2O_5Cu_2Se_2$ is already poor, and doping techniques that reduce it further are not desirable.

In accordance with the above findings, isovalent magnesium doping has been shown in literature to in increase material conductivity,[179, 260, 261] but this may come at the expense of band gap.[262] This may be due to changes in copper oxidation states to counter the substitution of Sc^{3+} for Mg^{2+}, the introduction of copper vacancies, or distortions in the lattice structure due to the size differences between Sc^{3+} and Mg^{2+}, reducing the effectiveness of Cu-Se hybridisation and narrowing the band gap. The latter is unlikely given the good size match between Sc^{3+} and Mg^{2+}.

Surprisingly, given the size match, magnesium doping produces a decrease in the *a* lattice parameter, and therefore the volume. Whilst both are very slight, it would be logical to assume that these changes would accompany a decrease in the Se-Cu-Se bond angle, which would explain the linear decrease in band gap. This is not the case: with values of 108.74, 108.88, 108.59 and 108.57 ° there is no change in this angle across the series. In reality the decrease in *a* is so small, narrowly beyond error, that it appears to have no measurable effect on Se-Cu-Se bond angle.

3.4.5 Barium Doping, $(Sr_{3-x}Ba_x)Sc_2O_5Cu_2Se_2$

Barium was introduced as an isovalent dopant onto the strontium site of $Sr_3Sc_2O_5Cu_2Se_2$ such that the target material takes the form $(Sr_{3-x}Ba_x)Sc_2O_5Cu_2Se_2$. This was achieved by reducing SrO content and supplementing with BaO, according to Equation 52 below:

Equation 52 $$2\text{-}x\ SrO + Sc_2O_3 + Cu_2Se + SrSe + x\ BaO \rightarrow (Sr_{3-x}Ba_x)Sc_2O_5Cu_2Se_2$$

The ground powder precursors (1 gram scale) were heated within an ampoule for 12 hours at 800 °C. They were then reground, pelletised, and heated again for 24 hours at 800 °C. Four samples were synthesised, with a dopant level ranging from x = 0.050 mol to x = 0.200 mol at equal increments of 0.050 mol, all synthesised in one self-consistent sample set. The complete compositional, analytical and graphical data for each sample in this section can be found in *Appendix B.1.7.*

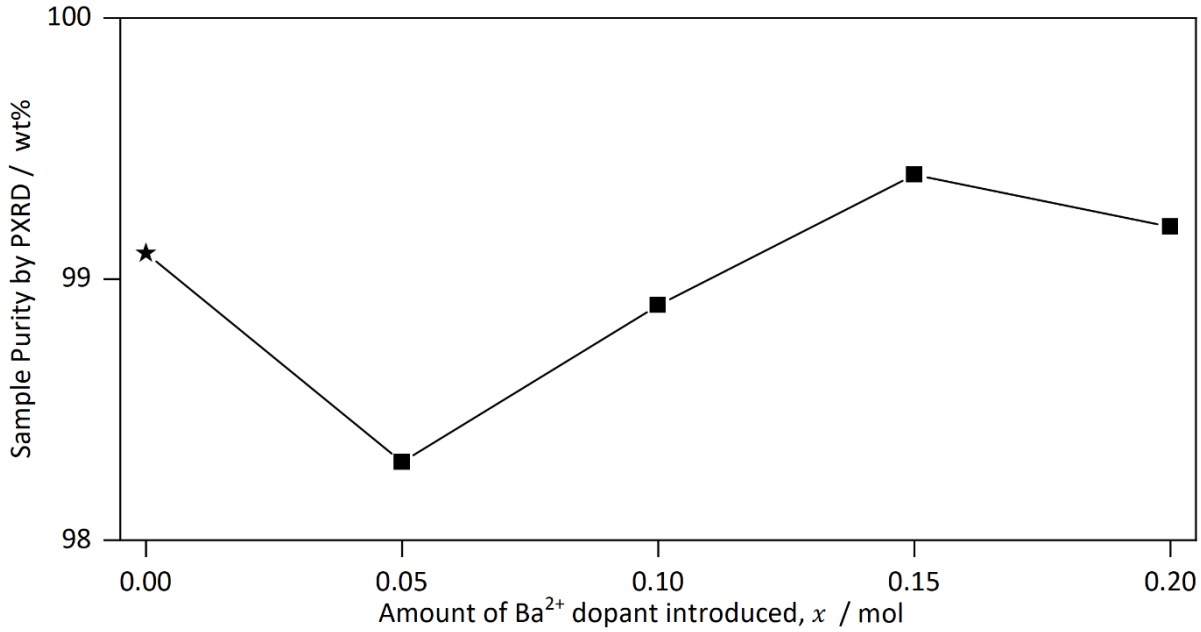

Figure 116 Purities of the four barium doped MALMs in the $(Sr_{3-x}Ba_x)Sc_2O_5Cu_2Se_2$ series. The pristine material $Sr_3Sc_2O_5Cu_2Se_2$ is included as a reference at x = 0 mol and is represented by a star. All values are derived from the Rietveld refinements of PXRD data using GSAS-II, and reported as weight percentages.

This is the first instance of isovalent doping within this work. Isovalent doping is not expected to improve conductivity as it should not improve the charge carrying capacity of the material. Given the equal oxidation states of the host and dopant ions Sr^{2+} and Ba^{2+}, there are no deficiencies or excesses in the precursors used because the oxides SrO and BaO have identical stoichiometries. As a result, Equation 52 resembles that of a pristine more than those of previous series have, because no elemental precursors are used. Purities are expected to be greater in isovalent doping because the absence of elemental selenium in the reaction mixture means there is no required changes in oxidation states to accommodate it. As expected the purities of the barium doped MALMs are extremely high (Figure 116) such that for the first and only occurrence within this work, the comparative plot Figure 117 actually depicts a very small purity improvement from x = 0.050 mol to x = 0.200 mol.

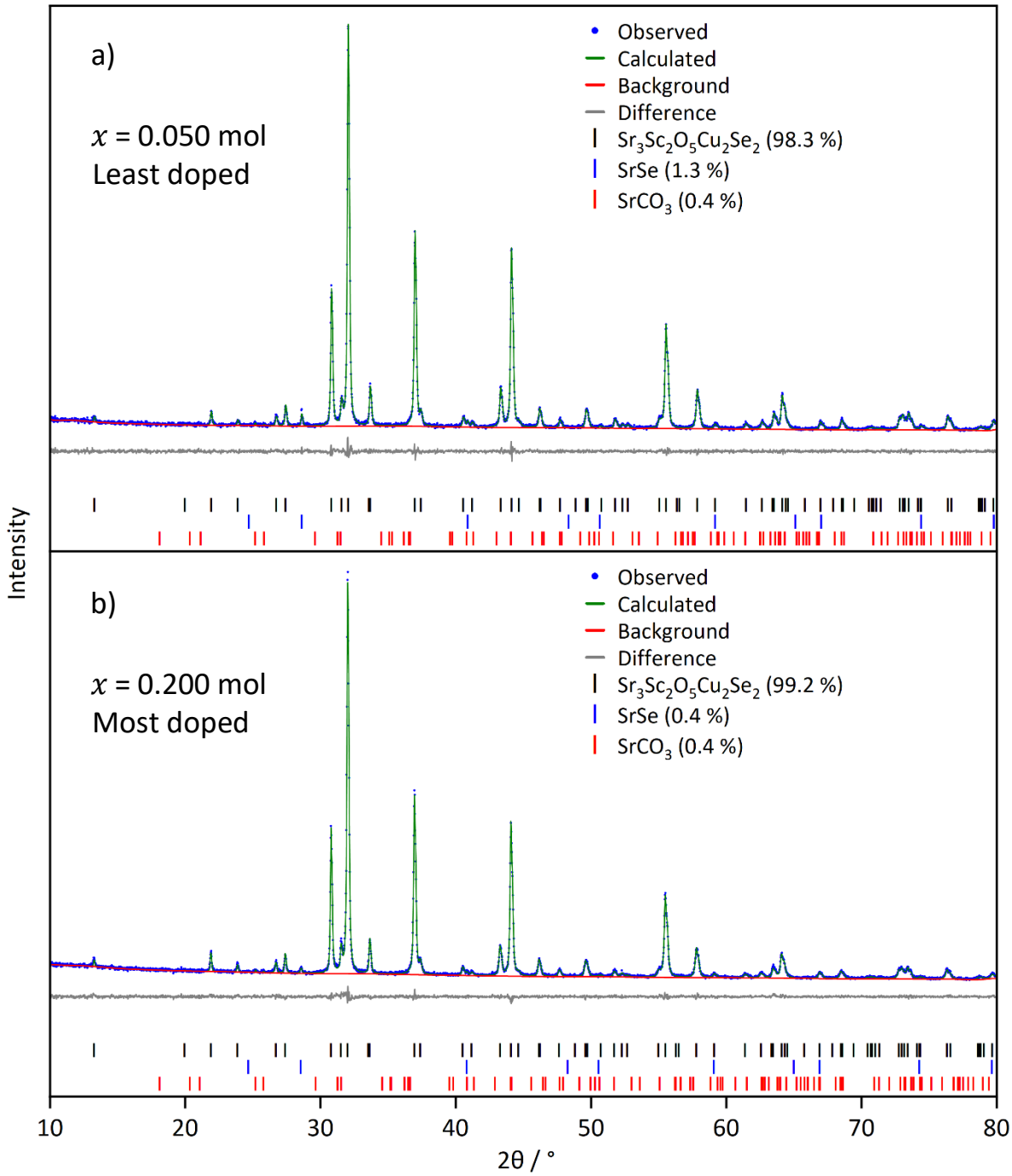

Figure 117 Powder X-ray diffractograms of a) the least doped sample of the series with target composition $(Sr_{2.95}Ba_{0.05})Sc_2O_5Cu_2Se_2$, and b) the most doped sample of the series with target composition $(Sr_{2.80}Ba_{0.20})Sc_2O_5Cu_2Se_2$ (both space group I4/mmm) after 36 hours of heating at 800 °C. The small blue circles represent the observed diffracted intensities, the green lines represent the Rietveld-refined calculated models, the red lines represent the backgrounds, and the grey lines represent the differences between observed and calculated intensities. The black tick marks show the reflections of the refined model of $Sr_3Sc_2O_5Cu_2Se_2$, whilst the blue and red tick marks represent refined impurity phases SrSe and $SrCO_3$ respectively. Weight fractions for each phase are cited in the figure legends. a) Duration: 45 minutes. Data points: 3457. Interval: 0.02 °. GOF: 1.04. R_{wp}: 4.430 %. b) Duration: 45 minutes. Data points: 3457. Interval: 0.02 °. GOF: 1.05. R_{wp}: 4.496 %.

The four samples synthesised here contained only SrSe and $SrCO_3$ as minor impurity phases, similar to the magnesium series. The dopant incorporation plot, therefore, also presents similarly, with no barium-containing precursors or impurities observable in the diffractograms. In this series exclusively, full dopant incorporation is expected because there are multiple instances in literature of the strontium and barium sites of materials of this type accommodating the other, such as $(Sr_{3-x}Ba_x)Sc_2O_5Cu_2Se_2$,[59] $(Sr_{2-x}Ba_x)CoO_2Cu_2Se_2$,[263] and $(Ba_{3-x}Sr_x)Fe_2O_5Cu_2Se_2$.[264]

Forming a dopant incorporation plot (Figure 118) identical to that of the magnesium series, barium doping appears to be successful, as predicted, at all dopant concentrations tested.

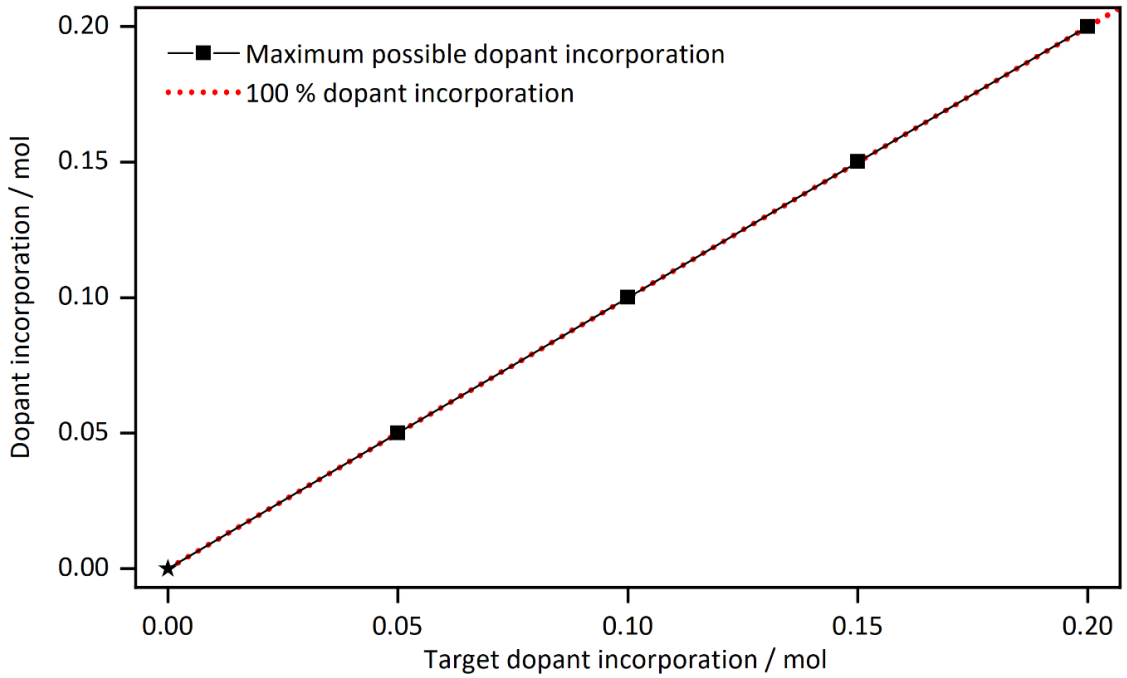

Figure 118 The calculated maximum possible levels of dopant incorporation into the $(Sr_{3-x}Ba_x)Sc_2O_5Cu_2Se_2$ MALMs. Values were derived from the wt % of the barium-containing impurities of each sample, of which there were none. The pristine material $Sr_3Sc_2O_5Cu_2Se_2$ is included as a reference at $x = 0$ mol and is represented by a star. The red dashed line represents 100 % dopant incorporation into the MALM, statistically no values may surpass this line. The black data points are the estimated upper bound of dopant incorporation for each sample.

This series presents the unusual case where the '100 % doped' $x = 3.000$ mol member of the series, exists: $Ba_3Sc_2O_5Cu_2Se_2$.[217] In the equivalent sulfide series $(Sr_{3-x}Ba_x)Sc_2O_5Cu_2S_2$, the fully-substituted end members $Sr_3Sc_2O_5Cu_2S_2$ and $Ba_3Sc_2O_5Cu_2S_2$ exist and there is a published Vegard's Law[60] relationship between the lattice parameters of these two end members.[59] Within that work, $Sr_3Sc_2O_5Cu_2S_2$ and $Ba_3Sc_2O_5Cu_2S_2$ are shown to be tuneable between optical band gaps of 3.1 and 3.24 eV respectively, thus the transparency of $Sr_3Sc_2O_5Cu_2S_2$ is improved by barium doping. An analogous relationship between the selenides has not been reported, but given that the end members are stable and $Ba_3Sc_2O_5Cu_2Se_2$ has a published optical band gap of 3.05 eV, the assumption that intermediate partially substituted materials can be synthesised is reasonable. Whilst $Ba_3Sc_2O_5Cu_2Se_2$ at 3.05 eV is a significant improvement over $Sr_3Sc_2O_5Cu_2Se_2$ at 2.94 eV, it remains outside the visible light threshold of 3.1 eV.

In this series there is no optimum dopant concentration with regard to incorporation, since barium always fully occupies the strontium site. Incorporation has been shown successfully here between x = 0 and x = 0.200 mol, but the existence of $Ba_3Sc_2O_5Cu_2Se_2$ suggests incorporation at any desired concentration between x = 0 and x = 3.000 mol is possible. With the aim of improving transparency, x = 3.000 mol would be the optimum concentration in theory since it would be extremely unlikely that any intermediate member of the solid solution exceeds its band gap of 3.05 eV.

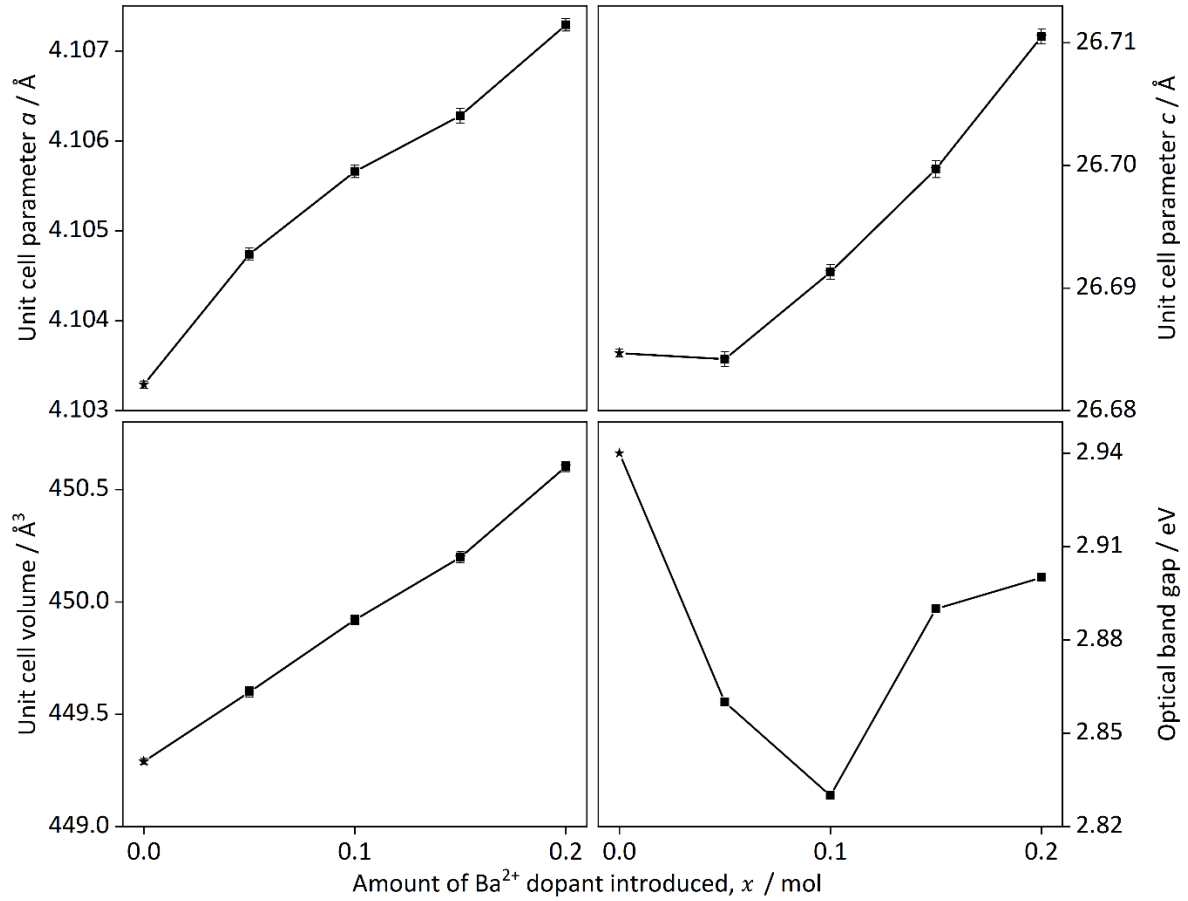

Figure 119 Comparisons of a) the α unit cell parameter, b) the c unit cell parameter, c) unit cell volume, and d) the optical band gap, of the four barium doped MALMs in the $(Sr_{3-x}Ba_x)Sc_2O_5Cu_2Se_2$ series. The pristine material $Sr_3Sc_2O_5Cu_2Se_2$ is included as a reference at x = 0 mol and is represented by a star.

As expected, Figure 119 reveals that the trends in unit cell lattice parameters *a* and *c*, and the unit cell volumes, are approximately linear. The pristine sample actually appears to be the most anomalous with a slightly smaller *a* and larger *c* than would be expected given those of the doped samples, but with a volume fitting the observed linear trend exactly.

Disappointingly however, the anticipated improvement in band gap was not observed. In each sample an optical band gap lower than the pristine was measured, with no obvious trend. Lattice parameters trended as expected but this did not translate into manipulation of the Cu-Se network (the interactions of which are predominantly responsible for the position of the valence band),[265] however this did not manifest. Partial substitution may cause lattice disorder which can decrease the band gap through formation of mid-gap states, another possible explanation.

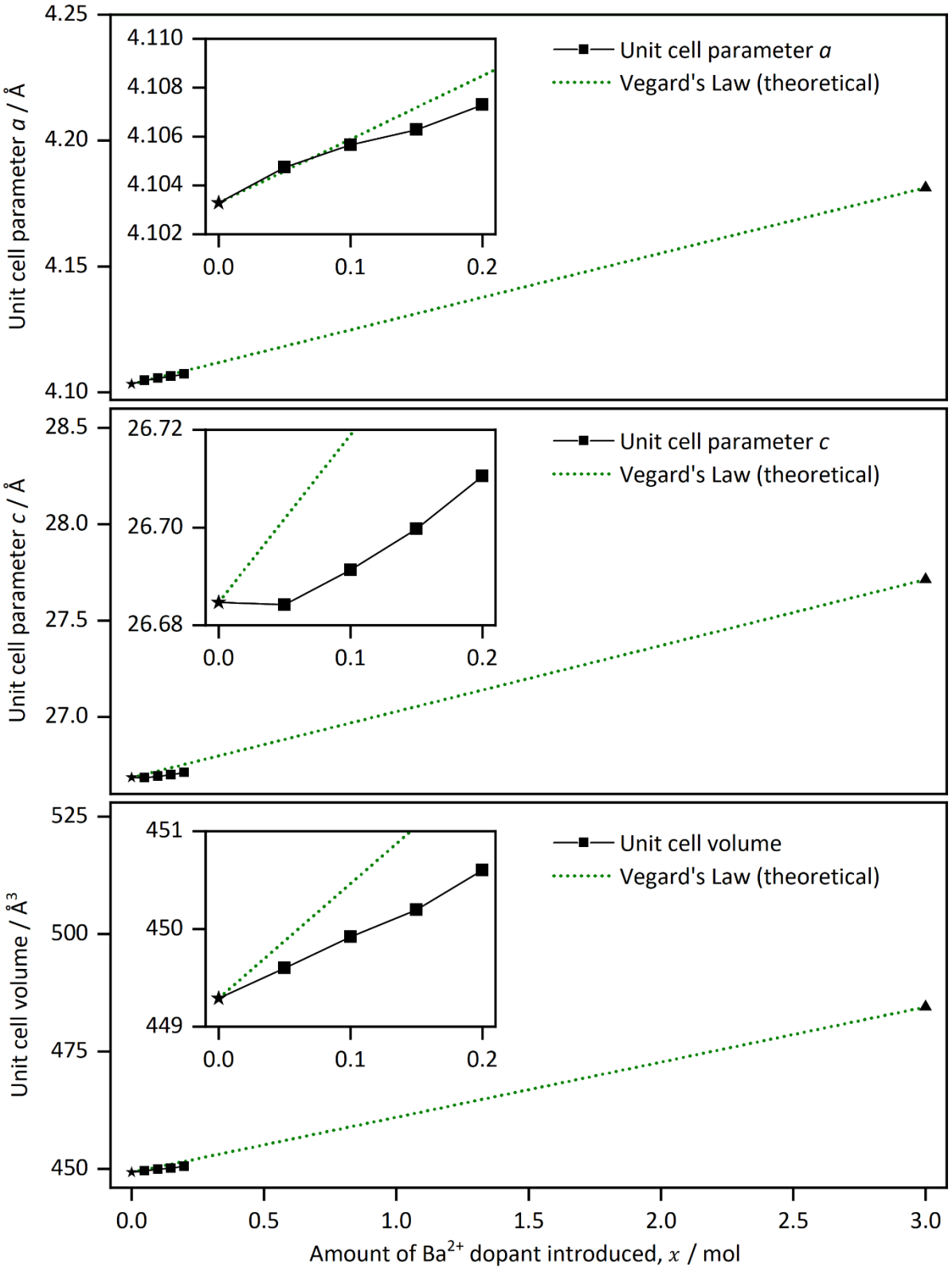

Figure 120 *The observed lattice parameters a + c and unit cell volumes of the $(Sr_{3-x}Ba_x)Sc_2O_5Cu_2Se_2$ series, projected against a theoretical Vegard's Law relationship (green dashed line) between pristine $Sr_3Sc_2O_5Cu_2Se_2$ and $Ba_3Sc_2O_5Cu_2Se_2$, represented by a star and a triangle respectively.*

Whilst band gap manipulation was the primary focus of this series, not the trends of the lattice parameters, the obedience of this series to Vegard's Law remains an interesting venture nonetheless, a relationship which, to the best of the author's knowledge, has not been described in literature. Using published lattice parameter values of end member $Ba_3Sc_2O_5Cu_2Se_2$,[217] a theoretical Vegard relationship was constructed, Figure 120. This plot suggests that the assumption of a linear Vegard relationship of these properties in the $(Sr_{3-x}Ba_x)Sc_2O_5Cu_2Se_2$ solid solution may not be valid. The *a* parameter follows the expected theoretical Vegard line closest, but all three parameters are smaller than would be predicted for the given amount of barium incorporated.

Two different explanations may explain the divergence of the cell parameters from expectation. The first is that the series simply may not exhibit a Vegard relationship: possible but unlikely. The second is that barium incorporation into these MALMs was less than was intended. These materials were exceptionally pure, and as a heavy atom any manifestation of barium as an impurity should be detectable by PXRD, yet none was observed. More intermediate samples would be required to fully elucidate this solid series. Likewise, supplementary analysis techniques such as Neutron Powder Diffraction (NPD), or Scanning Electron Microscopy (SEM) with Energy Dispersive X-ray spectroscopy elemental analysis (EDX) could measure the presence of impurities such as barium oxide or carbonate better than PXRD.

Conductivity was not the focus of this series and it was not assumed that isovalent doping of this type would cause any significant change. This assumption was correct, with negligible change compared to the pristine, Figure 121.

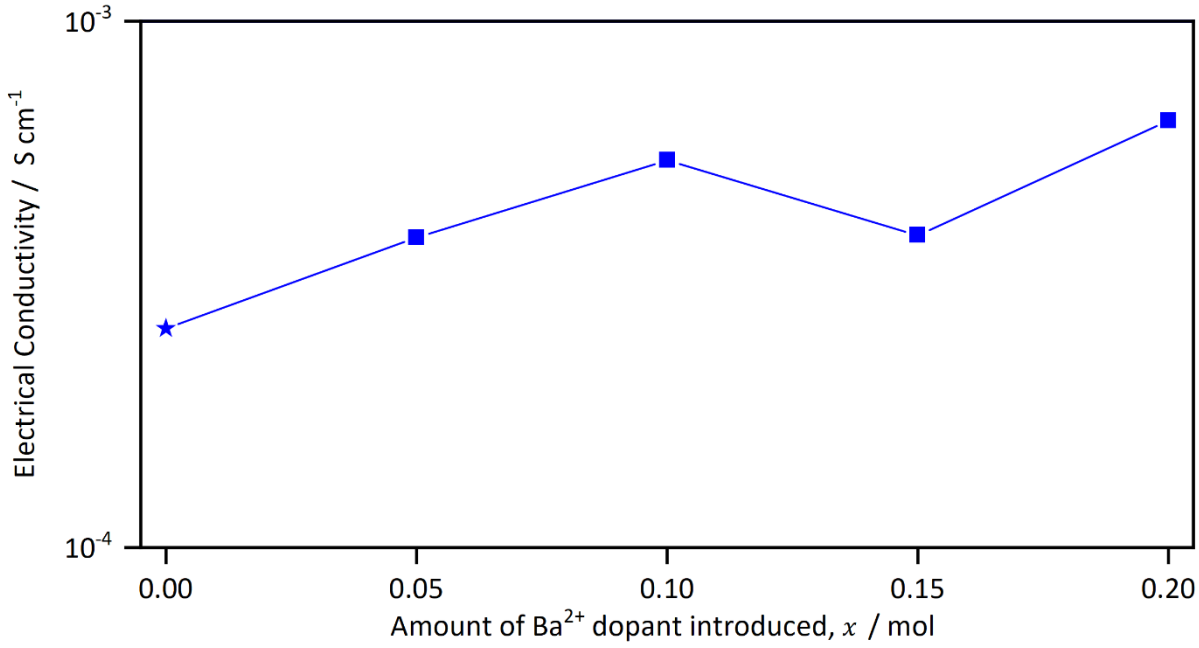

Figure 121 The electrical conductivities of the four barium doped MALMs in the $(Sr_{3-x}Ba_x)Sc_2O_5Cu_2Se_2$ series, represented on a log_{10} scale. The pristine material $Sr_3Sc_2O_5Cu_2Se_2$ is included as a reference at $x = 0$ mol and is represented by a star. All values are derived from van der Pauw 4 probe resistivity measurements of 8mm annealed pellet samples.

It should be noted that Ca^{2+} (1.34 Å) would be a more suitable size match than Ba^{2+} (1.61 Å) to isovalently replace Sr^{2+} (1.44 Å), using the 12-coordinate *A* site of the 325 structure $A_3B_2O_5M_2Q_2$ as an example. Calcium has also been reported as a dopant onto the strontium-containing *A* site in other 212, 325 and 426 MALMs such as $Sr_2CoO_2Cu_2Se_2$,[263] $Sr_3Fe_2O_5Cu_2Ch_2$ (*Ch* = S or Se),[21] and $Sr_4V_2O_6Fe_2As_2$.[266] However, the aim of this series was not to find the atom with the best fit, therefore the most readily able to dope, but that of a larger atom which causes a lengthening of the *a* lattice parameter to improve MALM transparency. Calcium, despite its similar size to strontium, appears fully occupied in very few materials of the 325 MALM structure type due to its size incompatibility with large *B* cations such as Sc^{3+}. It appears only in those where small cations such as Al^{3+} occupy the *B* site, such as $Ca_3Al_2O_5Fe_2Pn_2$ (where *Pn* = P or As), where the extremely small *a* parameters (3.715 Å and 3.742 Å respectively) are thought to be responsible for superconductivity.[51, 267, 268]

No reports of the $(Sr_{3-x}Ca_x)Sc_2O_5Cu_2Se_2$ end member $Ca_3Sc_2O_5Cu_2Se_2$ exist in literature and lattice parameter lengths render its existence extremely unlikely. Calcium doping would also have the adverse effect of a unit cell length decrease; therefore Calcium doping was not attempted in this work despite a superior size match and the potential for better dopant incorporation at small concentrations.

Excellent sample purities and apparent full dopant incorporation notwithstanding, barium doping failed to increase the optical band gap of $Sr_3Sc_2O_5Cu_2Se_2$ and the aim of this series was not achieved. Barium doping is therefore not recommended as a means to improve transparency in this case.

3.4.6 Yttrium Doping, $Sr_3(Sc_{2-x}Y_x)O_5Cu_2Se_2$

Following unsuccessful attempts to widen the optical band gap by doping barium onto the *A* site of $Sr_3Sc_2O_5Cu_2Se_2$, similar experiments isovalently doping yttrium and lanthanum onto the *B* site were carried out next. The Sc^{3+} ion in a 6-coordinate environment has a radius of 0.745 Å. The magnesium series highlighted the importance of a close size match when doping, with a radius of 0.72 Å and apparent full incorporation as a result. In this case, with the goal of lengthening the basal *a* lattice parameter to manipulate the Cu-Se network, an exact B^{3+} cation size match is undesirable. The employed cation must be slightly larger, enough to increase *a*, but not so large as to fail to be incorporated. Y^{3+} and La^{3+} have 6-coordinate ion sizes of 0.90 and 1.032 Å respectively, significantly larger than the 0.745 Å of Sc^{3+}. As isoelectronic ions, more confidence can be placed in size arguments than with Mg^{2+} whose size was compared only qualitatively due to differing oxidation states.

Yttrium was introduced as an isovalent dopant onto the scandium site of $Sr_3Sc_2O_5Cu_2Se_2$ such that the target material takes the form $Sr_3(Sc_{2-x}Y_x)O_5Cu_2Se_2$. This was achieved by reducing Sc_2O_3 content and supplementing with Y_2O_3, according to Equation 53 below:

Equation 53 $$2\ SrO + (1 - \tfrac{x}{2})\ Sc_2O_3 + Cu_2Se + SrSe + \tfrac{x}{2}\ Y_2O_3 \rightarrow Sr_3(Sc_{2-x}Y_x)O_5Cu_2Se_2$$

The ground powder precursors (1 gram scale) were heated within an ampoule for 12 hours at 800 °C. They were then reground, pelletised, and heated again for 24 hours at 800 °C. Four samples were synthesised, with a dopant level ranging from x = 0.050 mol to x = 0.200 mol at equal increments of 0.050 mol, all synthesised in one self-consistent sample set. The complete compositional, analytical and graphical data for each sample in this section can be found in *Appendix B.1.8.*

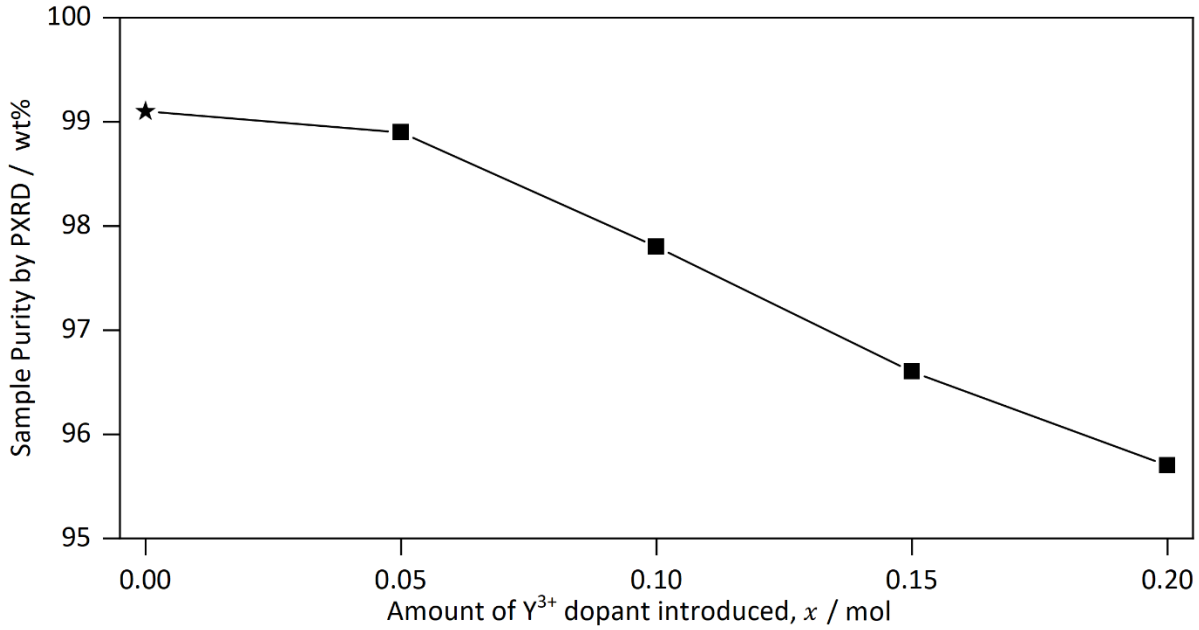

Figure 122 Purities of the four yttrium doped MALMs in the $Sr_3(Sc_{2-x}Y_x)O_5Cu_2Se_2$ series. The pristine material $Sr_3Sc_2O_5Cu_2Se_2$ is included as a reference at x = 0 mol and is represented by a star. All values are derived from the Rietveld refinements of PXRD data using GSAS-II, and reported as weight percentages.

While samples purities remained relatively high in general across this series, there is a clear negative trend with increasing dopant, Figure 122. As is standard for these materials there is a small quantity of SrSe and $SrCO_3$ across all four samples, each below 1 wt % at all times. The purity trend is the result of a linear increase of unreacted yttrium oxide precursor, shown in green in Figure 123 below. The least doped x = 0.050 mol sample contains only 0.4 % Y_2O_3 by weight, increasing across the series to 1.1 %, 1.9 %, and finally 2.7 % in the most doped x = 0.200 mol sample.

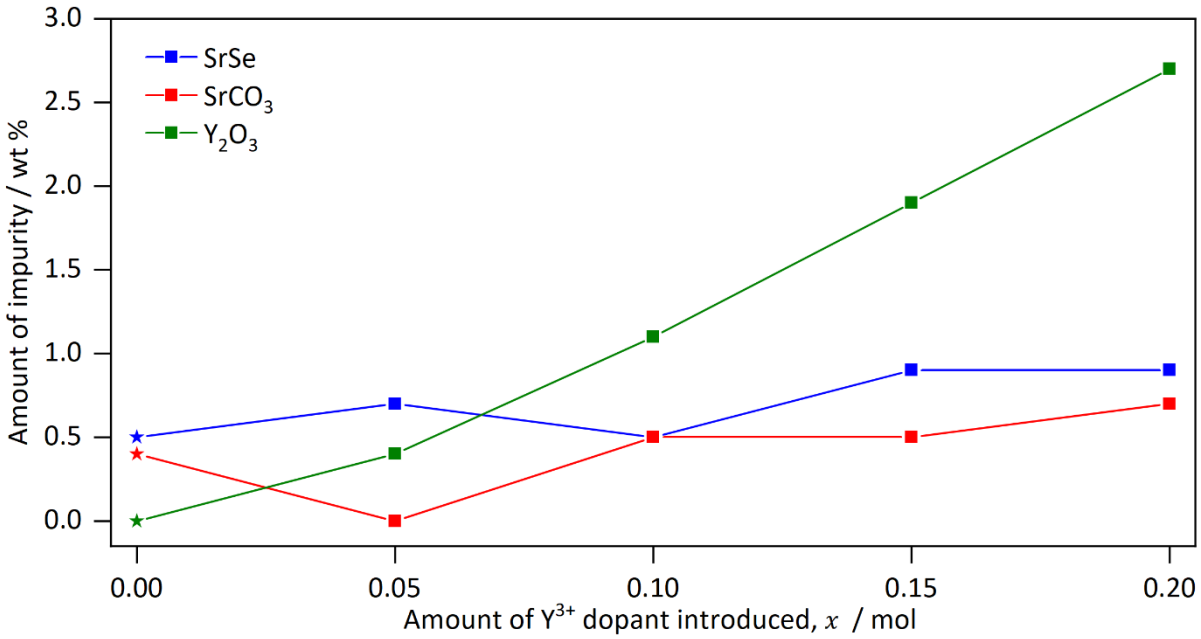

Figure 123 *The weight percentages of three impurity phases present in the $Sr_3(Sc_{2-x}Y_x)O_5Cu_2Se_2$ series. The pristine material $Sr_3Sc_2O_5Cu_2Se_2$ is included as a reference at $x = 0$ mol and is represented by stars.*

The increase in Y_2O_3 between x = 0.050 and x = 0.200 mol is remarkably linear, deviating from linearity only between the pristine x = 0 and x = 0.050. This suggests that in each sample a very small amount of Y^{3+} is incorporated into the MALM and the rest rejected. Given no Y_2O_3 was supplied in the pristine sample, this data point lies slightly off the trend because the hypothesised small degree of yttrium incorporation was not possible.

This is the first and only occurrence within this work where dopant incorporation appears almost entirely rejected by the MALM. This is also the lowest dopant concentration where dopant-containing impurities have been detected, compared to the sodium and potassium doping studies where x = 0.125 was the lowest concentration that such an impurity was observed. The largest XRD peak resulting from the unreacted Y_2O_3 precursor is at 2θ = 29.2 °, observed beside the primary peak of SrSe at 2θ = 28.6 ° in the comparative diffractogram plot, Figure 124 on the next page.

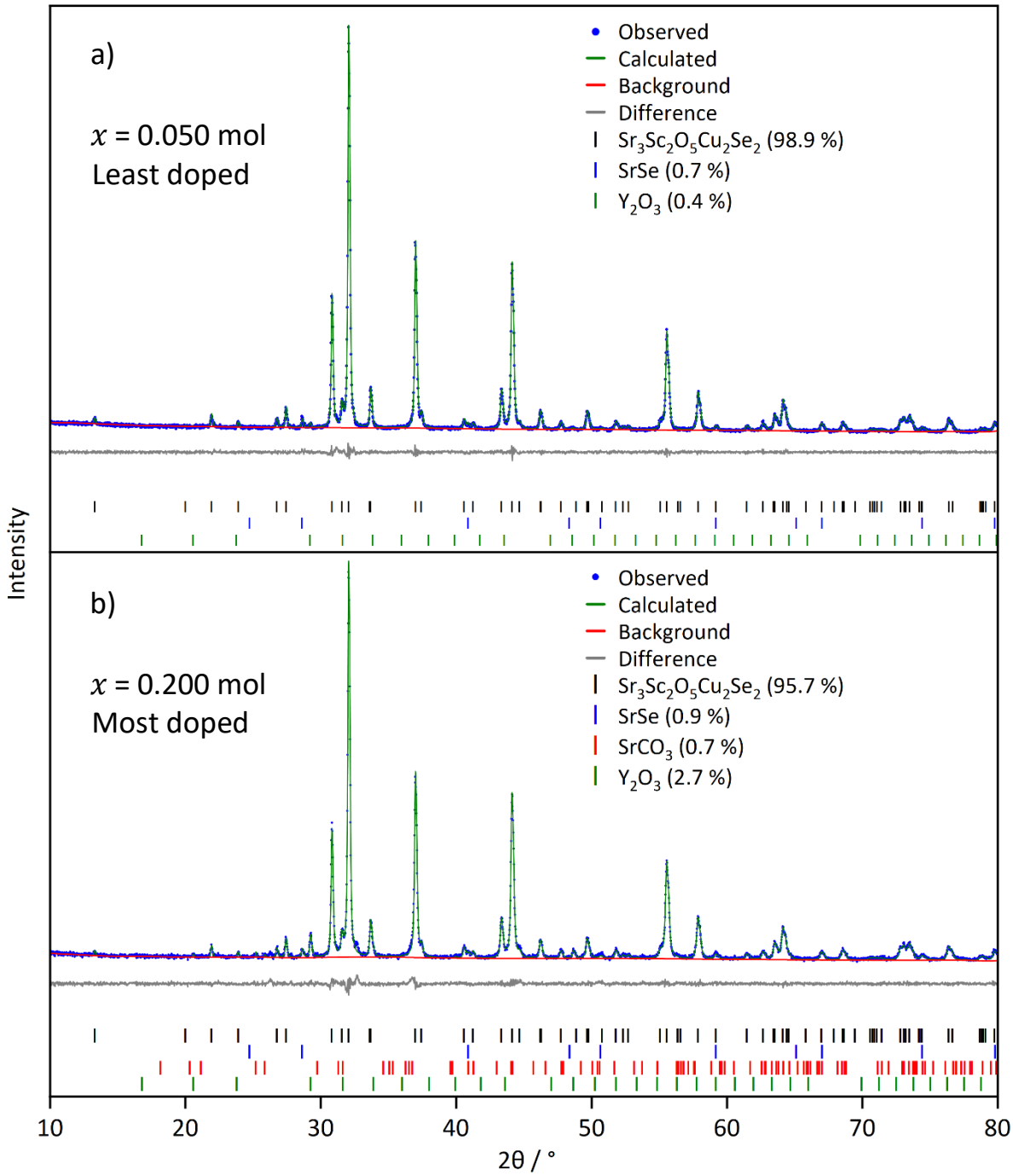

Figure 124 *Powder X-ray diffractograms of a) the least doped sample of the series with target composition $Sr_3(Sc_{1.95}Y_{0.05})O_5Cu_2Se_2$, and b) the most doped sample of the series with target composition $Sr_3(Sc_{1.80}Y_{0.20})O_5Cu_2Se_2$ (both space group I4/mmm) after 36 hours of heating at 800 °C. The small blue circles represent the observed diffracted intensities, the green lines represent the Rietveld-refined calculated models, the red lines represent the backgrounds, and the grey lines represent the differences between observed and calculated intensities. The black tick marks show the reflections of the refined model of $Sr_3Sc_2O_5Cu_2Se_2$, whilst the blue, red and green tick marks represent refined impurity phases SrSe, $SrCO_3$ and Y_2O_3 respectively. Weight fractions for each phase are cited in the figure legends.*

a) Duration: 45 minutes. Data points: 3457. Interval: 0.02 °. GOF: 1.09. R_{wp}: 4.244 %.

b) Duration: 45 minutes. Data points: 3457. Interval: 0.02 °. GOF: 1.21. R_{wp}: 4.777 %.

Expectedly, the dopant incorporation plot, Figure 125, illustrates extremely poor uptake of yttrium into $Sr_3Sc_2O_5Cu_2Se_2$. Given the observed plateau in estimated maximum incorporation, and also that each of these values is an upper bound, it is possible that no dopant at all has been successfully incorporated. More likely is the previously discussed hypothesis that a very small and equal amount of yttrium has been incorporated in each case, with a maximum (and optimum) level at a concentration between x = 0 and x = 0.050, and which cannot be increased upon.

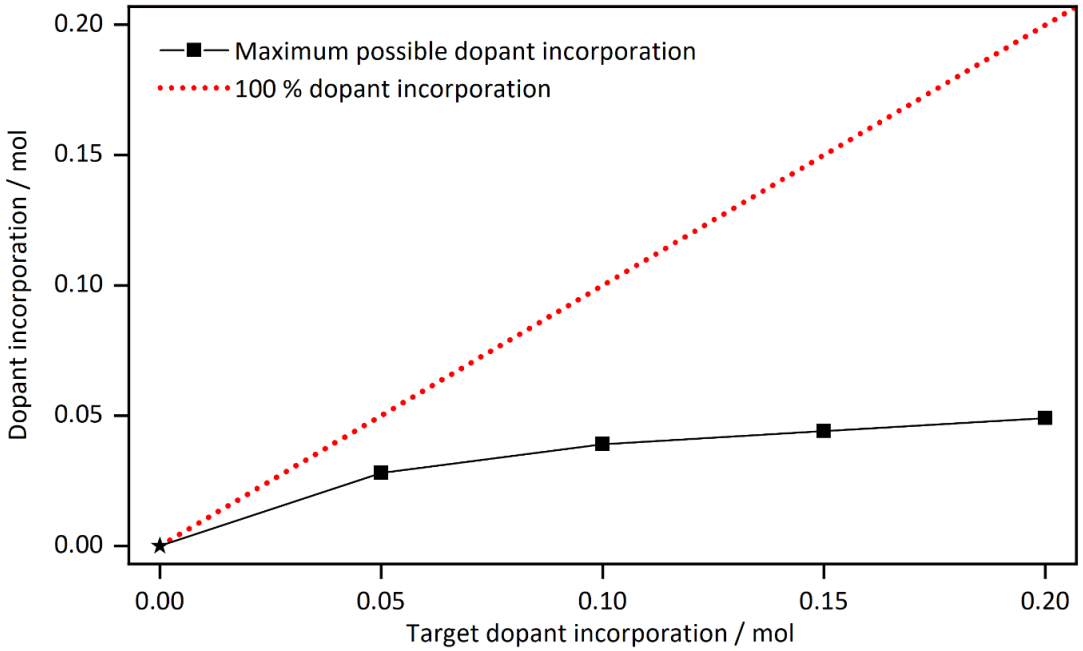

Figure 125 The calculated maximum possible levels of dopant incorporation into the $Sr_3(Sc_{2-x}Y_x)O_5Cu_2Se_2$ MALMs. Values were derived from the wt % of the yttrium-containing impurities of each sample. The pristine material $Sr_3Sc_2O_5Cu_2Se_2$ is included as a reference at x = 0 mol and is represented by a star. The red dashed line represents 100 % dopant incorporation into the MALM, statistically no values may surpass this line. The black data points are the estimated upper bound of dopant incorporation for each sample.

The cell parameter variations in Figure 126 support the tolerance of a small yttrium incorporation, specifically the immediate increase in the *a* lattice parameter followed by a plateau after x = 0.050, leading to an overall volume increase. These changes, while not within error, are still too small for meaningful conclusions. As expected from a rejected dopant, the optical band gap did not increase, showing no trend, therefore the primary objective of this doping study was unsuccessful. There is no optimum sample in this study, as all had an yttrium impurity and none yielded an increase in band gap.

Interestingly, the one property that does show improvement by yttrium doping is the one neither expected nor intended to: conductivity. Yttrium doping has been shown in literature to improve conductivity, but when aliovalently doped *n*-type such as $(Sr_{1-x}Y_x)TiO_3$[269] or $(Li_{1-x}Y_x)NiPO_4$,[270] or *p*-type such as $Ba(Zr_{1-x}Y_x)O_3$[271], but not through isovalent doping. Here a 2 orders of magnitude improvement is observed, Figure 127, suggesting either that very small amounts of isovalent yttrium incorporation cause drastic conductivity increases, or, more likely, that its rejection leaves scandium vacancies which enhance the charge carrying ability through the unintentional introduction of holes.

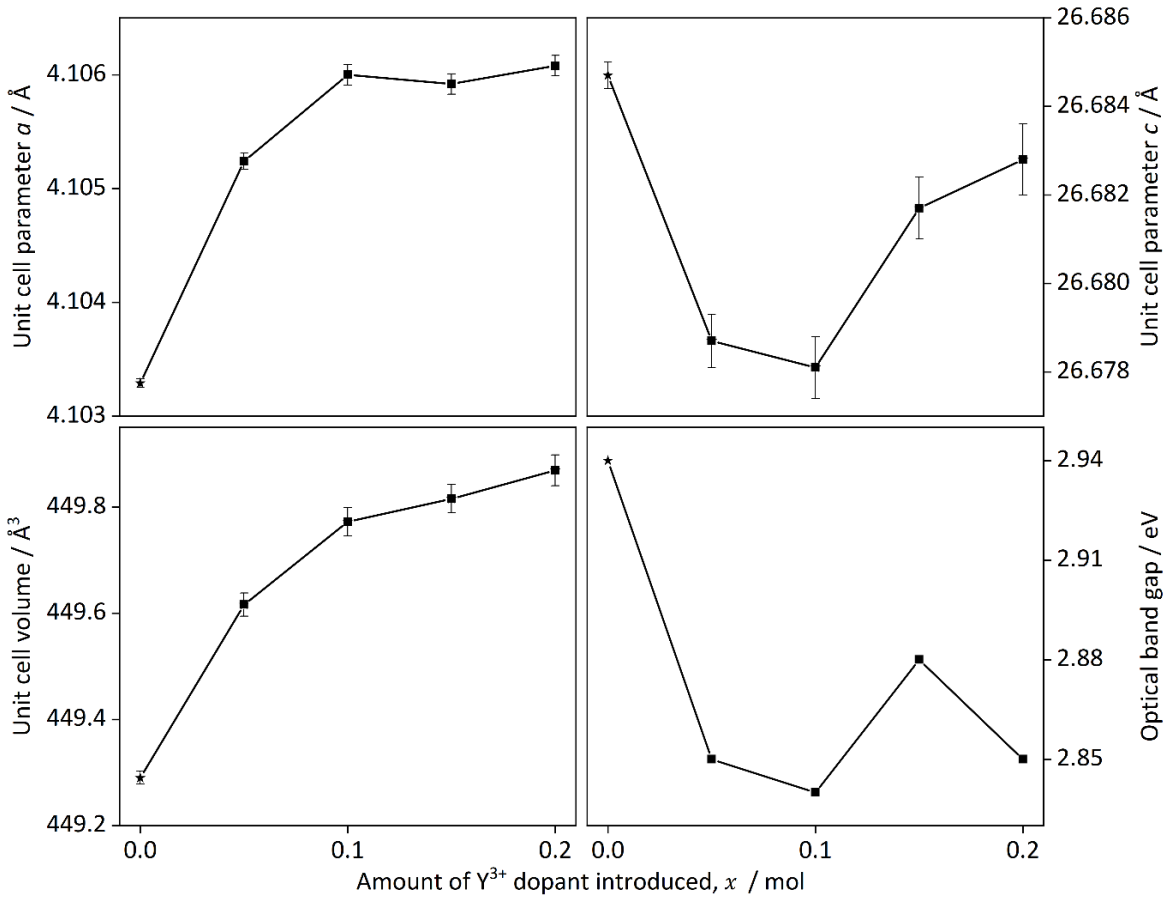

Figure 126 *Comparisons of a) the α unit cell parameter, b) the c unit cell parameter, c) unit cell volume, and d) the optical band gap, of the yttrium doped 325 selenide MALMs with general formula $Sr_3(Sc_{2-x}Y_x)O_5Cu_2Se_2$. The pristine material $Sr_3Sc_2O_5Cu_2Se_2$ is included as a reference at $x = 0$ mol and is represented by a star.*

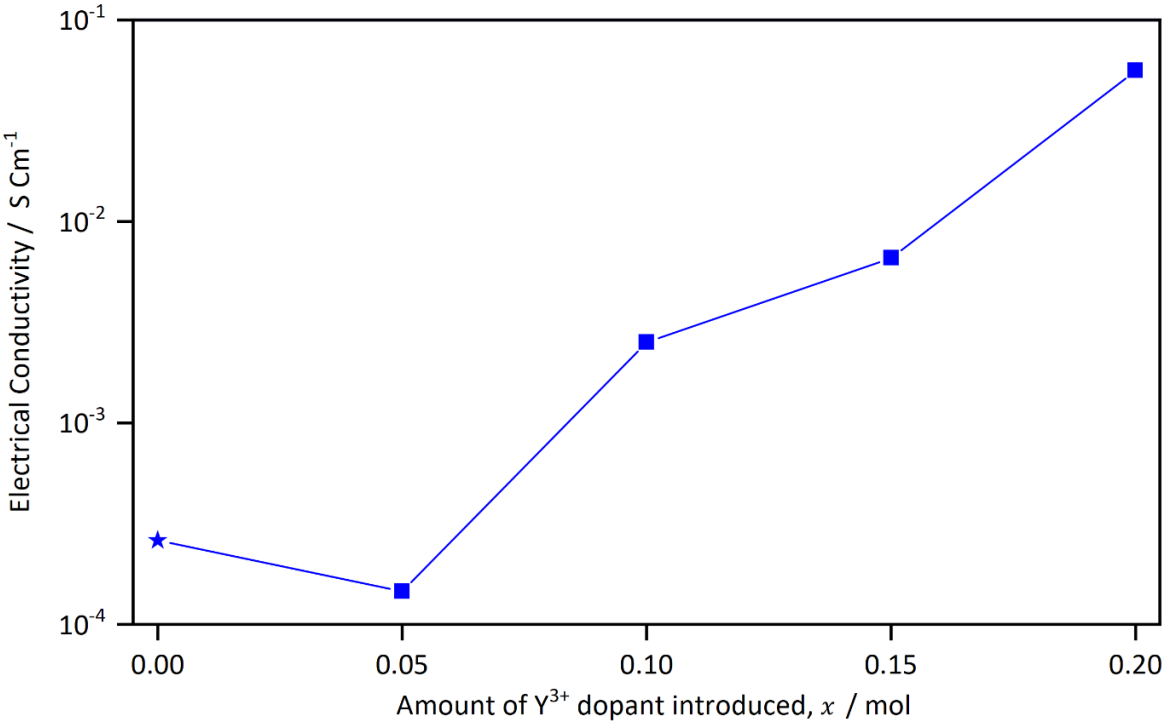

Figure 127 *The electrical conductivities of the four yttrium doped MALMs in the $Sr_3(Sc_{2-x}Y_x)O_5Cu_2Se_2$ series, represented on a log_{10} scale. The pristine material $Sr_3Sc_2O_5Cu_2Se_2$ is included as a reference at $x = 0$ mol and is represented by a star. All values are derived from van der Pauw 4 probe resistivity measurements of 8mm annealed pellet samples.*

3.4.7 Lanthanum Doping, $Sr_3(Sc_{2-x}La_x)O_5Cu_2Se_2$

In a third and final attempt to increase the *a* lattice parameter and the optical band gap by isovalent doping with a larger cation, lanthanum doping of the $Sr_3Sc_2O_5Cu_2Se_2$ scandium site was attempted. The La^{3+} ion (1.032 Å) is larger than Y^{3+} (0.90 Å), versus 0.745 Å for the host ion Sc^{3+}. So, if the rejection of yttrium as a dopant was due to its size, lanthanum is expected to be tolerated even less by the host MALM. Doping with La^{3+} has been performed in literature to improve conductivity aliovalently,[272, 273] but has not been used in isovalent doping to improve transparency.

Lanthanum was introduced as an isovalent dopant onto the scandium site of $Sr_3Sc_2O_5Cu_2Se_2$ such that the target material takes the form $Sr_3(Sc_{2-x}La_x)O_5Cu_2Se_2$. This was achieved by reducing Sc_2O_3 content and supplementing with La_2O_3, according to Equation 54 below:

Equation 54
$$2\,SrO + (1 - \tfrac{x}{2})\,Sc_2O_3 + Cu_2Se + SrSe + \tfrac{x}{2}\,La_2O_3 \rightarrow Sr_3(Sc_{2-x}La_x)O_5Cu_2Se_2$$

The ground powder precursors (1 gram scale) were heated within an ampoule for 12 hours at 800 °C. They were then reground, pelletised, and heated again for 24 hours at 800 °C. Four samples were synthesised, with a dopant level ranging from x = 0.050 mol to x = 0.200 mol at equal increments of 0.050 mol, all synthesised in one self-consistent sample set. The complete compositional, analytical and graphical data for each sample in this section can be found in *Appendix B.1.9.*

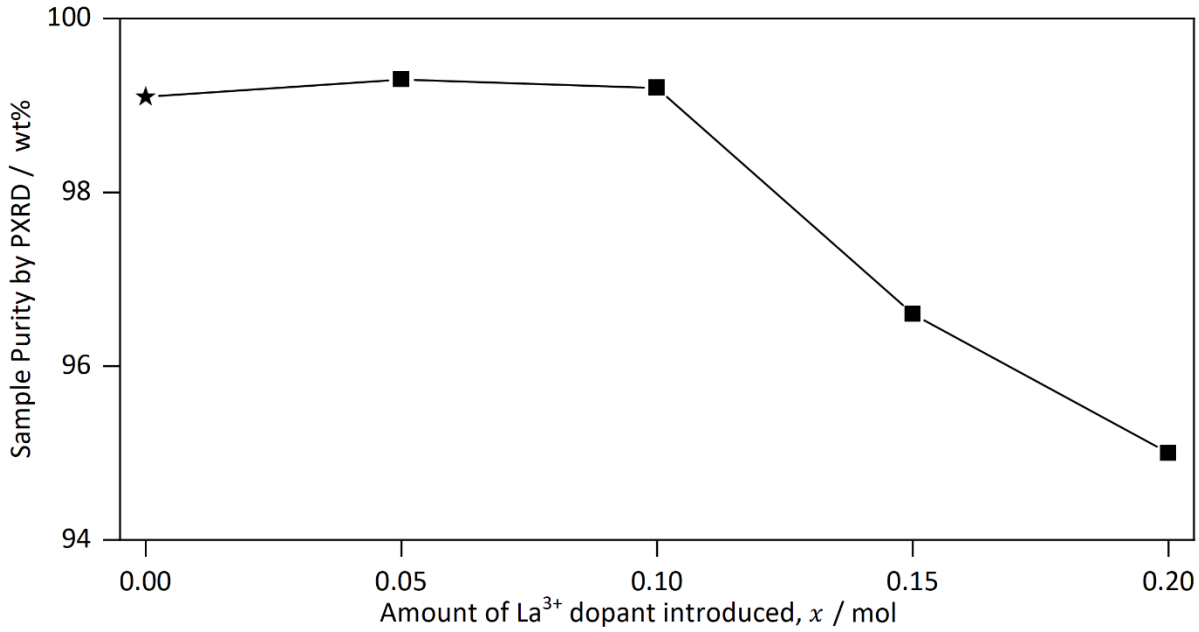

Figure 128 Purities of the four lanthanum doped MALMs in the $Sr_3(Sc_{2-x}La_x)O_5Cu_2Se_2$ series. The pristine material $Sr_3Sc_2O_5Cu_2Se_2$ is included as a reference at x = 0 mol and is represented by a star. All values are derived from the Rietveld refinements of PXRD data using GSAS-II, and reported as weight percentages.

The first two samples at x = 0.050 and x = 0.100 mol have purities on par with that of the undoped pristine, but beyond this, purity begins to drop away linearly. Similar to the yttrium series, there is a small amount of SrSe and $SrCO_3$ in each sample which remain at low levels, but crucially a lanthanum-containing impurity appears from x = 0.150 mol onwards. This impurity is not the supplied precursor La_2O_3 but a copper-containing material $La_2CuO_{3.98}$.[274]

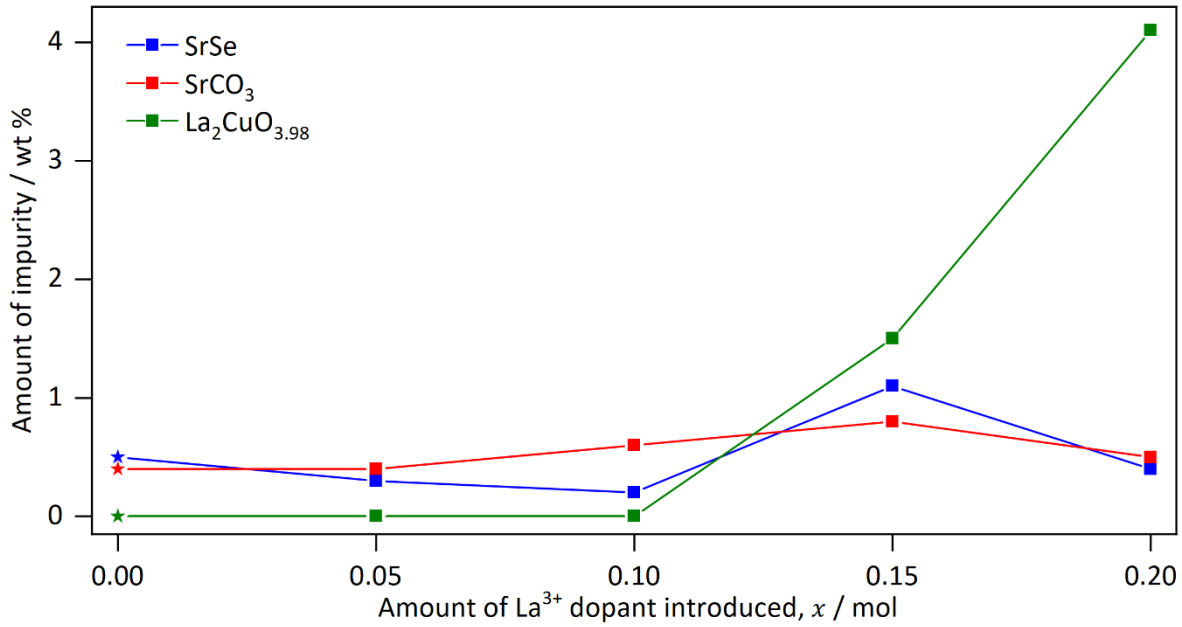

Figure 129 The weight percentages of three impurity phases present in the $Sr_3(Sc_{2-x}La_x)O_5Cu_2Se_2$ series. The pristine material $Sr_3Sc_2O_5Cu_2S_2$ is included as a reference at x = 0 mol and is represented by stars.

This unusual impurity was identified by the Rigaku PDXL-2 software, employed occasionally within this work to scan CIF databases when an unknown or uncommon material such as this needs to be identified within a diffraction pattern. The impurity is likely La_2CuO_4, however the slightly oxygen deficient analogue $La_2CuO_{3.98}$ yielded the better fit in the Rietveld refined model. The exact stoichiometry is not important here, especially given the negligible difference in relative lanthanum content by weight between $La_2CuO_{3.98}$ and La_2CuO_4, instead its presence dictates a saturation point for lanthanum doping somewhere between x = 0.100 and x = 0.150 mol. $La_2CuO_{3.98}$ does not appear (or rather is not measurable) in the first two samples, hence their high purity, but increases linearly in phase fraction therein. The largest peak of the diffraction pattern of $La_2CuO_{3.98}$ can be observed in the comparative PXRD plot Figure 130, at 2θ = 31.1 ° between the two major MALM phase peaks in that area.

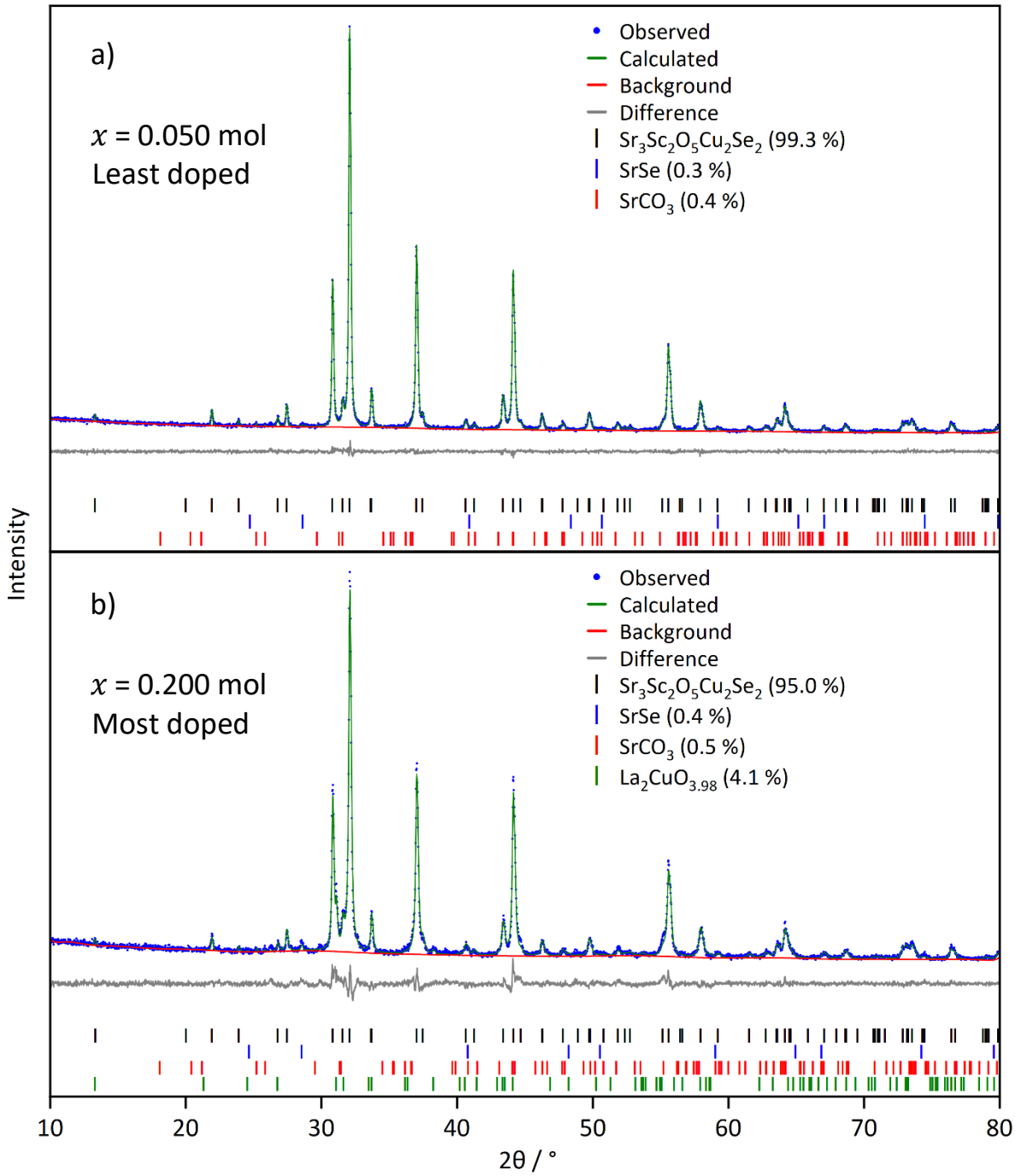

Figure 130 *Powder X-ray diffractograms of a) the least doped sample of the series with target composition $Sr_3(Sc_{1.95}La_{0.05})O_5Cu_2Se_2$, and b) the most doped sample of the series with target composition $Sr_3(Sc_{1.80}La_{0.20})O_5Cu_2Se_2$ (both space group I4/mmm) after 36 hours of heating at 800 °C. The small blue circles represent the observed diffracted intensities, the green lines represent the Rietveld-refined calculated models, the red lines represent the backgrounds, and the grey lines represent the differences between observed and calculated intensities. The black tick marks show the reflections of the refined model of $Sr_3Sc_2O_5Cu_2Se_2$, whilst the blue, red and green tick marks represent refined impurity phases SrSe, $SrCO_3$ and $La_2CuO_{3.98}$ respectively. Weight fractions for each phase are cited in the figure legends.*

a) Duration: 45 minutes. Data points: 3457. Interval: 0.02 °. GOF: 1.11. R_{wp}: 4.497 %.

b) Duration: 45 minutes. Data points: 3457. Interval: 0.02 °. GOF: 1.49. R_{wp}: 6.606 %.

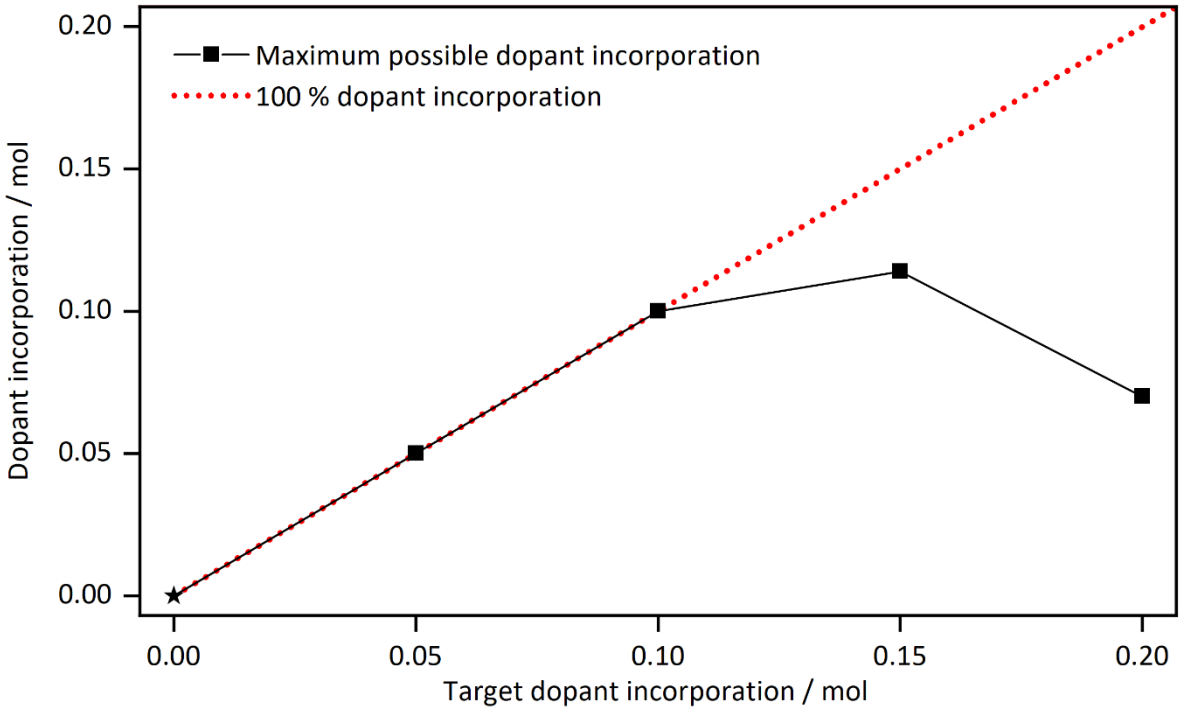

Figure 131 *The calculated maximum possible levels of dopant incorporation into the $Sr_3(Sc_{2-x}La_x)O_5Cu_2Se_2$ MALMs. Values were derived from the wt % of the lanthanum-containing impurities of each sample. The pristine material $Sr_3Sc_2O_5Cu_2Se_2$ is included as a reference at x = 0 mol and is represented by a star. The red dashed line represents 100 % dopant incorporation into the MALM, statistically no values may surpass this line. The black data points are the estimated upper bound of dopant incorporation for each sample.*

Table 8 *The target and maximum possible dopant content within the MALMs of the $Sr_3(Sc_{2-x}La_x)O_5Cu_2Se_2$ series. The pristine material $Sr_3Sc_2O_5Cu_2S_2$ is included as a reference.*

Target x / mol	**Maximum La in product / %**	**Maximum x / mol**
0 (pristine)	100	0
0.05	100	0.050
0.10	100	0.100
0.15	76.196	0.114
0.20	34.934	0.070

The phase fractions of the lanthanum impurity are large enough that the samples in which it appears deviate significantly from the target values of dopant incorporation, see Figure 131 and Table 8. This suggests that the scandium site is not tolerant of isovalent doping by large cations such as lanthanum or yttrium, unlike that of the strontium site when barium doping. While some lanthanum appears to have been incorporated into the MALM based on weight percentages, incorporation slows significantly beyond x = 0.100 mol.

Like the yttrium series before it, lanthanum doping produced an unexpected increase in conductivity, Figure 132. The by-product La_2CuO_4 is often the study of superconductivity research,[275] and has an undoped room temperature conductivity of 40 S cm^{-1} rendering it significantly more conductive than the MALMs being measured.[276]

The rise in conductivity observed here, which is too large to be deemed within an experimental error range so must have an underlying cause in the chemistry of the material, may be attributed to the rise in quantity of this by-product, as were the group 1 metal aliovalent doping series where the ACu_3Ch_2 impurity was believed to have artificially increased sample purity. It may also be the product of scandium vacancies that arise from the removal of scandium from the reaction mixture to accommodate the lanthanum ions whose incorporation was eventually unsuccessful, producing holes.

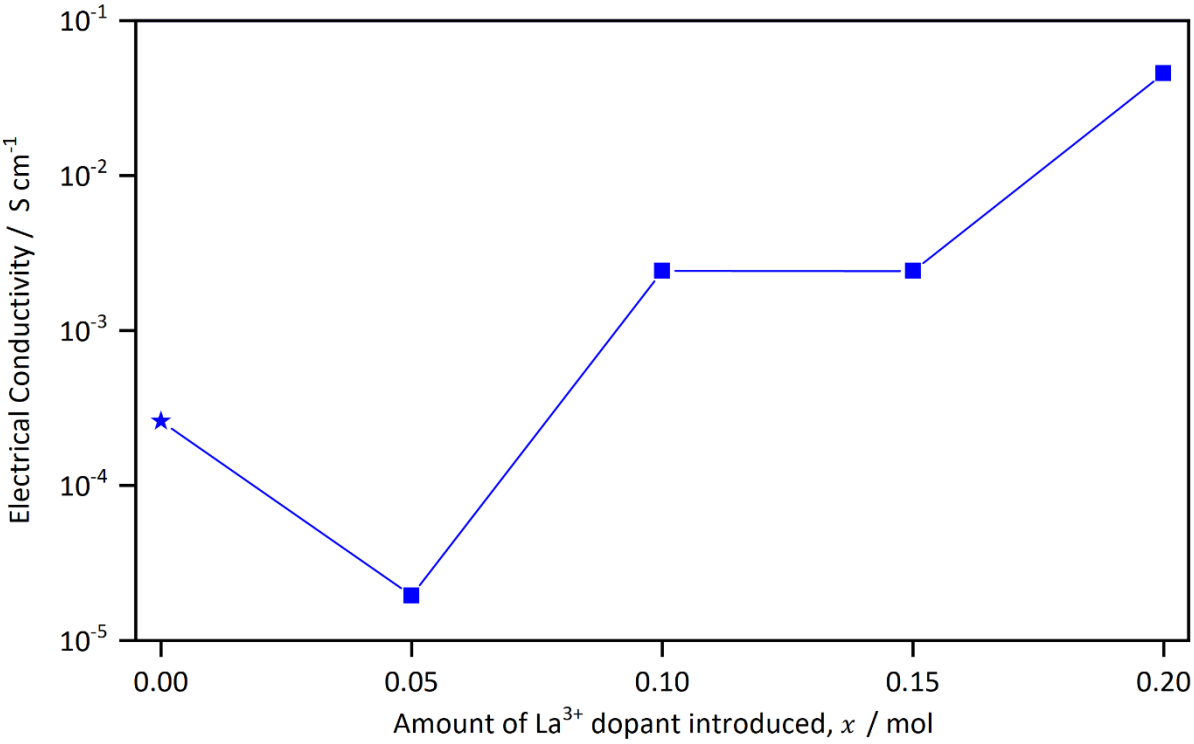

Figure 132 The electrical conductivities of the four lanthanum doped MALMs in the $Sr_3(Sc_{2-x}La_x)O_5Cu_2Se_2$ series, represented on a log_{10} scale. The pristine material $Sr_3Sc_2O_5Cu_2Se_2$ is included as a reference at x = 0 mol and is represented by a star. All values are derived from van der Pauw 4 probe resistivity measurements of 8mm annealed pellet samples.

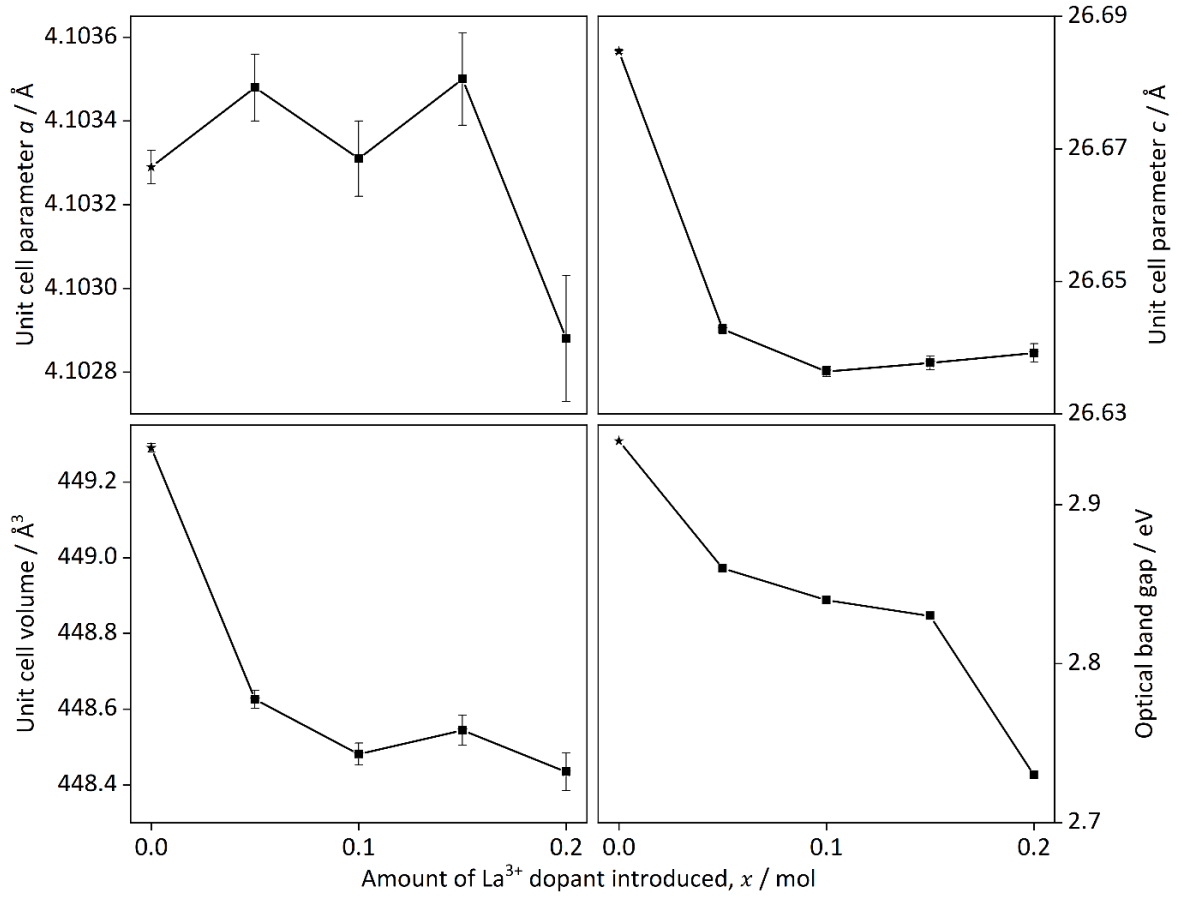

Figure 133 Comparisons of a) the α unit cell parameter, b) the c unit cell parameter, c) unit cell volume, and d) the optical band gap, of the lanthanum doped 325 selenide MALMs with general formula $Sr_3(Sc_{2-x}La_x)O_5Cu_2Se_2$. The pristine material $Sr_3Sc_2O_5Cu_2Se_2$ is included as a reference at $x = 0$ mol and is represented by a star.

Despite evidence of some incorporation of lanthanum as a dopant here, the resulting *a* parameter shows no trend, whilst the volume and the optical band gap trend down, illustrated in Figure 133.

Isovalent doping in this work has yielded a range of incorporation levels: barium doping on the strontium site appeared to be tolerated entirely, lanthanum doping on the scandium site led to moderate incorporation, akin to that of potassium or sodium on the strontium site, and finally yttrium yielded very little to no incorporation at all. None of the three investigated isovalent dopants resulted in the intended improvement in optical band gap. No optimum sample is again possible here, because the aim of transparency improvement by lanthanum doping was not met.

3.4.8 Strontium Deficiencies, $Sr_{3-x}Sc_2O_5Cu_2Se_2$

The final two investigations in this broad analysis of $Sr_3Sc_2O_5Cu_2Se_2$ and its propensity for doping, are deficiencies on the strontium and the copper sites. The aim of the strontium vacancy investigation is to support the doping effects observed in the K^+ and Na^+ doping series, and to possibly explain the observed increases in electrical conductivity once doping had reached saturation or significantly slowed. The copper deficiency series in the next section targets the atomic site responsible for conductivity in materials of this type.[151] It is known that these materials can tolerate a copper deficiency and even 'pristine' materials inherently may have a small deficiency, but by intentionally targeting one, the deficiency limit can be explored, and its effect on transparency and conductivity.

A vacancy on the strontium site of $Sr_3Sc_2O_5Cu_2Se_2$ was introduced to simulate the effect of a dopant, such that the target material takes the form $Sr_{3-x}Sc_2O_5Cu_2Se_2$. This was achieved by reducing SrSe content and supplementing with Se, according to Equation 55 below:

Equation 55 $$2\ SrO + Sc_2O_3 + Cu_2Se + 1\text{-}x\ SrSe + x\ Se \rightarrow Sr_{3-x}Sc_2O_5Cu_2Se_2$$

The ground powder precursors (1 gram scale) were heated within an ampoule for 12 hours at 180 °C, then raised to 800 °C for a further 12 hours in the same ampoule. They were then reground, pelletised, and heated again for 24 hours at 800 °C. Seven samples were synthesised, four with a dopant level ranging from x = 0.050 mol to x = 0.200 mol at equal increments of 0.050 mol, plus x = 0.500, 0.750 and 1.000 mol, all synthesised in one self-consistent sample set. The complete compositional, analytical and graphical data for each sample in this section can be found in *Appendix B.1.10.*

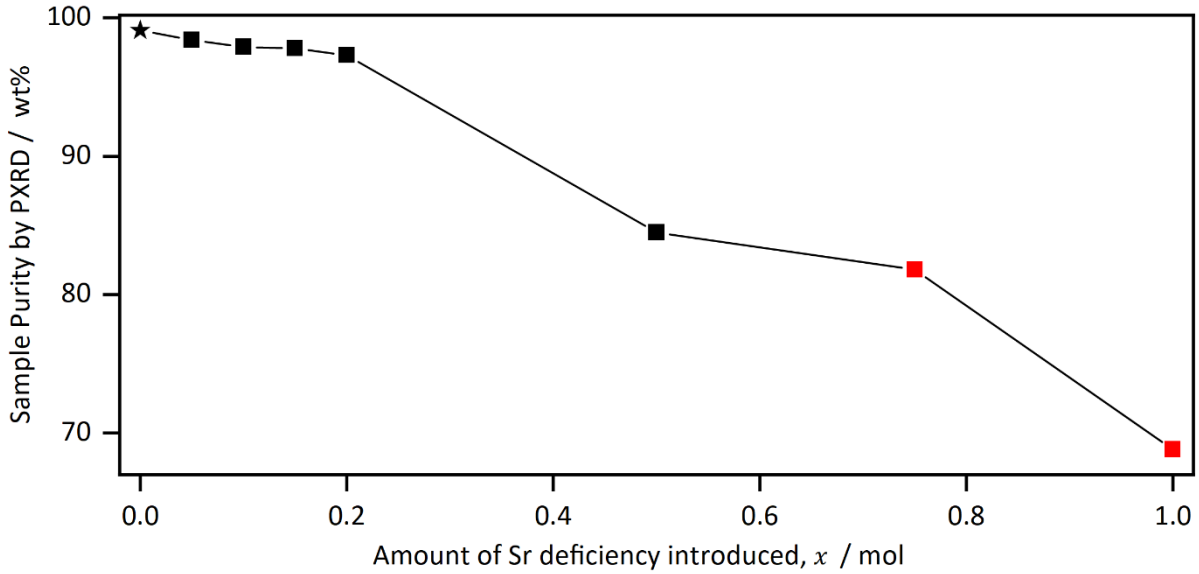

Figure 134 Purities of the seven strontium deficient MALMs in the $Sr_{3-x}Sc_2O_5Cu_2Se_2$ series. The pristine material $Sr_3Sc_2O_5Cu_2Se_2$ is included as a reference at x = 0 mol and is represented by a star. The two data points at x = 0.750 mol and x = 0.100 mol are coloured red to indicate the presence of unknown impurities in these samples, and as a result the cited purity values are likely to be slight overestimates. All values are derived from the Rietveld refinements of PXRD data using GSAS-II, and reported as weight percentages.

In *Section 3.3.4* it was tenuously concluded that a very small deficiency may be tolerable on the strontium site of $Sr_3Sc_2O_5Cu_2S_2$, as evidenced by a conductivity improvement, but that a large or even moderate deficiency was not stable. Attempts to introduce one were met with a rapid purity drop off after x = 0.150 mol, and even the least doped sample had a modest purity of only 91 wt %. Exact behaviour was uncertain, but purities were poor and conductivity improvement was weak.

In this analogous study of $Sr_3Sc_2O_5Cu_2Se_2$ one can observe a strong maintenance of purity across the first four doped samples which all measure 97 wt % or greater (Figure 134) which would be impressive purities even for the pristine. Across this large range of target deficiencies, a drop off is inevitable, $Sr_3Sc_2O_5Cu_2Se_2$ is not expected to accommodate a deficiency even close to x = 1.000 mol, instead this range is designed to elucidate the drop off where the increasing strontium deficiency suddenly ceases to be tolerable, which appears here to be a point between x = 0.200 and 0.500 mol.

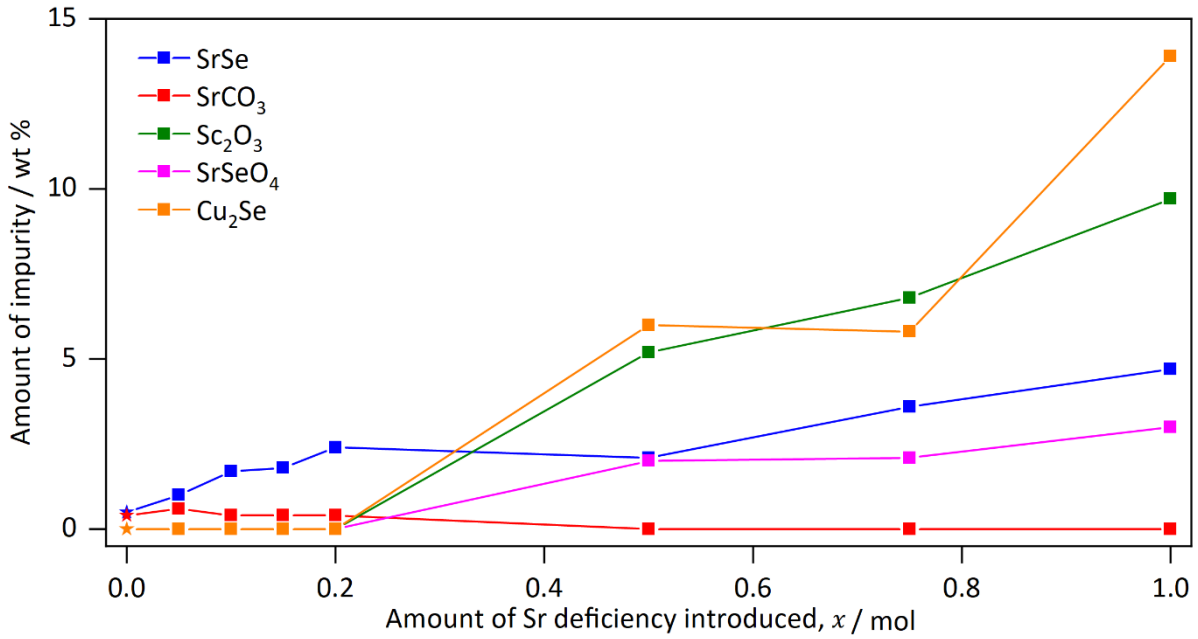

Figure 135 *The weight percentages of five impurity phases present in strontium deficient 325 selenide MALMs with general formula $Sr_{3-x}Sc_2O_5Cu_2Se_2$. The pristine material $Sr_3Sc_2O_5Cu_2Se_2$ is included as a reference at x = 0 mol and is represented by stars.*

The limiting atom in these samples should be strontium, thus it would be expected that the impurities would be comprised of all atoms but strontium. However this is not the case, strontium still appears as it does in every sample of this chapter, Figure 135, leading to the unusual situation where in later samples all component atoms appear as impurities because the target deficiency is so unattainable. It is predicted that this is due to the prevalence of strontium as a component atom across the usual impurity phases, so that when atoms like selenium or copper are not incorporated within the MALM, surplus strontium is extracted from the mixture to accompany these atoms in impurity materials, further reducing the capacity for MALM formation. The red squares in Figure 134 represent samples with some small unknown material, as can be observed in comparative PXRD plot Figure 136 on the next page, comparing x = 0.050 and 1.000 mol.

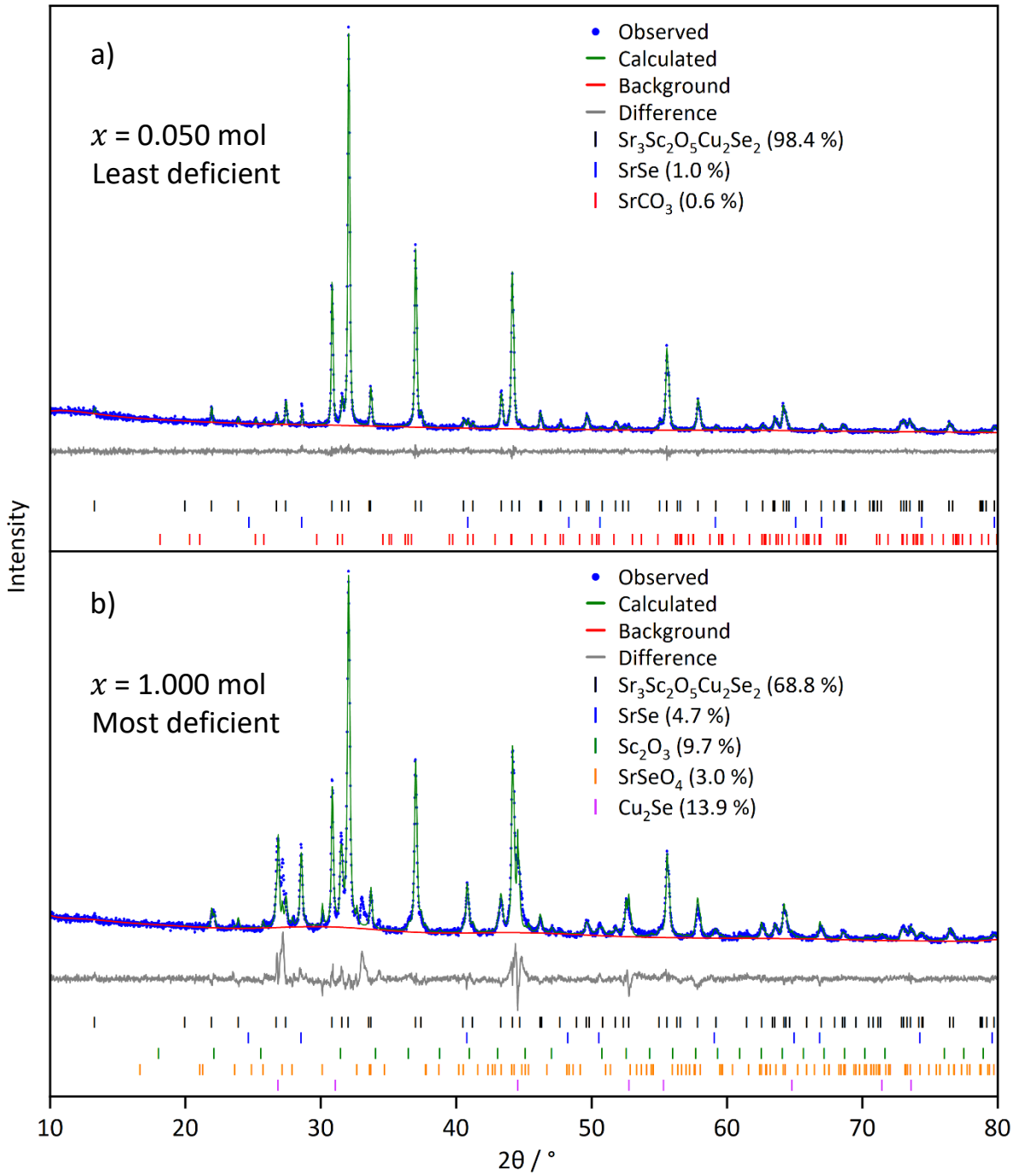

Figure 136 *Powder X-ray diffractograms of a) the least deficient sample of the series with target composition $Sr_{2.95}Sc_2O_5Cu_2Se_2$, and b) the most deficient sample of the series with target composition $Sr_{2.00}Sc_2O_5Cu_2Se_2$ (both space group I4/mmm) after 36 hours of heating at 800 °C. The small blue circles represent the observed diffracted intensities, the green lines represent the Rietveld-refined calculated models, the red lines represent the backgrounds, and the grey lines represent the differences between observed and calculated intensities. The black tick marks show the reflections of the refined model of $Sr_3Sc_2O_5Cu_2Se_2$, whilst the blue, red, green, orange and pink tick marks represent refined impurity phases SrSe, $SrCO_3$, Sc_2O_3, $SrSeO_4$ and Cu_2Se respectively. Weight fractions for each phase are cited in the figure legends.*
a) Duration: 45 minutes. Data points: 3457. Interval: 0.02 °. GOF: 1.05. R_{wp}: 6.288 %.
b) Duration: 45 minutes. Data points: 3457. Interval: 0.02 °. GOF: 2.18. R_{wp}: 8.641 %.

Impurity formation increases moderately across the series, as is expected, but the identified drop off in purity is the result of the significant emergence of Cu_2Se. This material has not been observed thus far as an impurity, and is very conductive (reports cite this value between 160 to 1400 S cm^{-1})[277-279] Only in the most ambitious target deficiency samples, x = 0.500 onwards, does this material appear, but it is expected to yield unintended conductivity improvements coinciding with exceeding the saturation point of strontium deficiency.

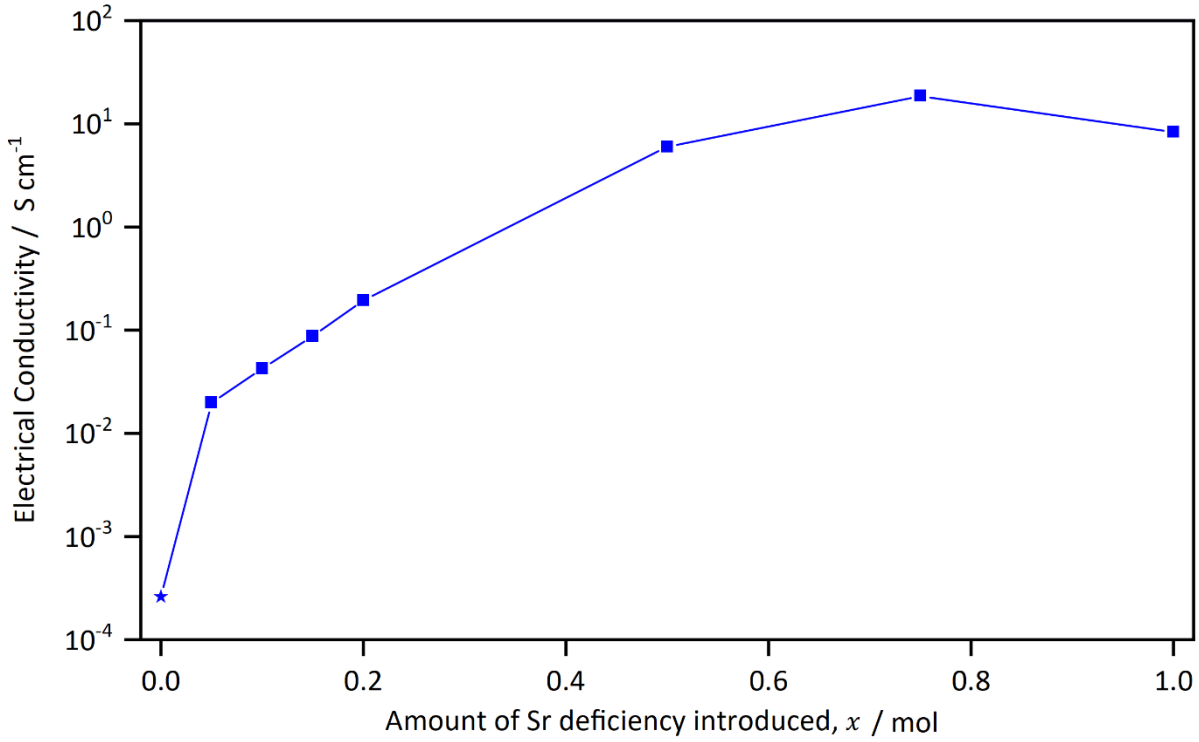

Figure 137 The electrical conductivities of the strontium deficient 325 selenide MALMs with general formula $Sr_{3-x}Sc_2O_5Cu_2Se_2$, represented on a log_{10} scale. The pristine material $Sr_3Sc_2O_5Cu_2Se_2$ is included as a reference at x = 0 mol and is represented by a star. All values are derived from van der Pauw 4 probe resistivity measurements of 8mm diameter annealed pellet samples.

The initial increase in conductivity, Figure 137, when purity is high and Cu_2Se is not present, is strongly suggestive of a genuine strontium deficiency. The conductivity improvement between the pristine sample at 6.21 × 10^{-4} S cm^{-1} and the x = 0.200 sample at 1.95 × 10^{-1} S cm^{-1} is almost 750 times, with all evidence indicating this is the result of a strontium deficiency. Beyond this, as was the case with many doping series previously, the conductivity still increases beyond this point at a significantly reduced rate, reaching a maximum conductivity measurement of 1.85 S cm^{-1} in the x = 0.750 sample, over 70,000 times more conductive than pristine $Sr_3Sc_2O_5Cu_2Se_2$.

This maximum coincides with (and is almost certainly the result of) a large purity decrease from the emergence of Cu_2Se, indicating concurrently both that the targeted strontium deficiency is no longer tolerable and that the conductivity increase is the product of the high concentrations of undesirable copper selenide impurities.

There is no tangible method with which to estimate x values in a deficiency study, as there is in a doping study, with which to produce a dopant incorporation plot. The non-incorporation of dopant can be measured by the presence of dopant-containing impurities, but the absence of a vacancy cannot be quantified, only inferred from other data. The effect of dopants and deficiencies on unit cell size are also too insufficient as to be used as a genuine indicator of success.

Another detrimental effect arises as a result of the Cu_2Se impurity emergence, that of sample colour. Figure 138 illustrates the gradient from light brown to dark brown across this series, primarily over the three most deficient samples, those with a measured and increasing presence of Cu_2Se. The consequence of this is that optical band gaps could not be obtained for these three samples, a combination of the sample being too absorbing due to its darkened colour, and a severe purity drop contributing to a weaker UV-Vis drop off. Transparency is not the focus of this series and is recorded only for data set completion, so the absent data does not impair this data set, but it does indicate that too severe a deficiency (or impurity) will harm the ability to measure a band gap if this were the focus.

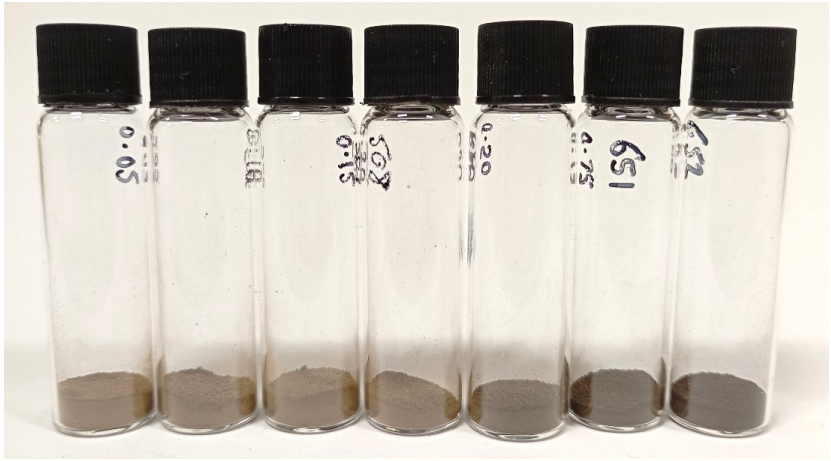

Figure 138 A photographic comparison of the colour of the strontium deficient $Sr_{3-x}Sc_2O_5Cu_2Se_2$ series. Dopant concentration increases from left to right.

Strontium deficiencies on $Sr_3Sc_2O_5Cu_2Se_2$ appear to be surprisingly stable, to a level of approximately x = 0.200 mol and therefore on par with the saturation points of dopants such as K^+ and Na^+. It is likely from the combinations of these data sets that when a strontium site dopant reaches saturation, the site is able to, and may, tolerate a further site deficiency up to a value of x = 0.200 to 0.500 mol. The two effects cannot be summative (i.e. the MALM cannot accept 0.150 mol of dopant and then 0.200 to 0.500 mol of deficiency) else one would expect to observe up to ten orders of magnitude of combined conductivity increase. Instead, it is more likely that the dopant is incorporated up until the point where full incorporation ends, at which point either incorporation continues at a slower rate or a small strontium deficiency is accommodated, likely a combination of both. This contributes to a continuous overall increase in charge carriers, regardless of the source, evidenced by the sharp doping conductivity improvement of those series, followed by a steady further improvement by strontium deficiency. This suitably supports the conductivity data of the K (page 179) and Na (page 185) series.

3.4.9 Copper Deficiencies, $Sr_3Sc_2O_5Cu_{2-x}Se_2$

A vacancy on the copper site of $Sr_3Sc_2O_5Cu_2Se_2$ was introduced to simulate the effect of a dopant, such that the target material takes the form $Sr_3Sc_2O_5Cu_{2-x}Se_2$. This was achieved by reducing Cu_2Se content and supplementing with Se, according to Equation 56 below:

Equation 56 $$2\ SrO + Sc_2O_3 + (1 - \tfrac{x}{2})\ Cu_2Se + SrSe + \tfrac{x}{2}\ Se \rightarrow Sr_3Sc_2O_5Cu_{2-x}Se_2$$

The ground powder precursors (1 gram scale) were heated within an ampoule for 12 hours at 180 °C, then raised to 800 °C for a further 12 hours in the same ampoule. They were then reground, pelletised, and heated again for 24 hours at 800 °C. Seven samples were synthesised, four with a dopant level ranging from x = 0.050 mol to x = 0.200 mol at equal increments of 0.050 mol, plus x = 0.500, 0.750 and 1.000 mol, all synthesised in one self-consistent sample set. The complete compositional, analytical and graphical data for each sample in this section can be found in *Appendix B.1.11.*

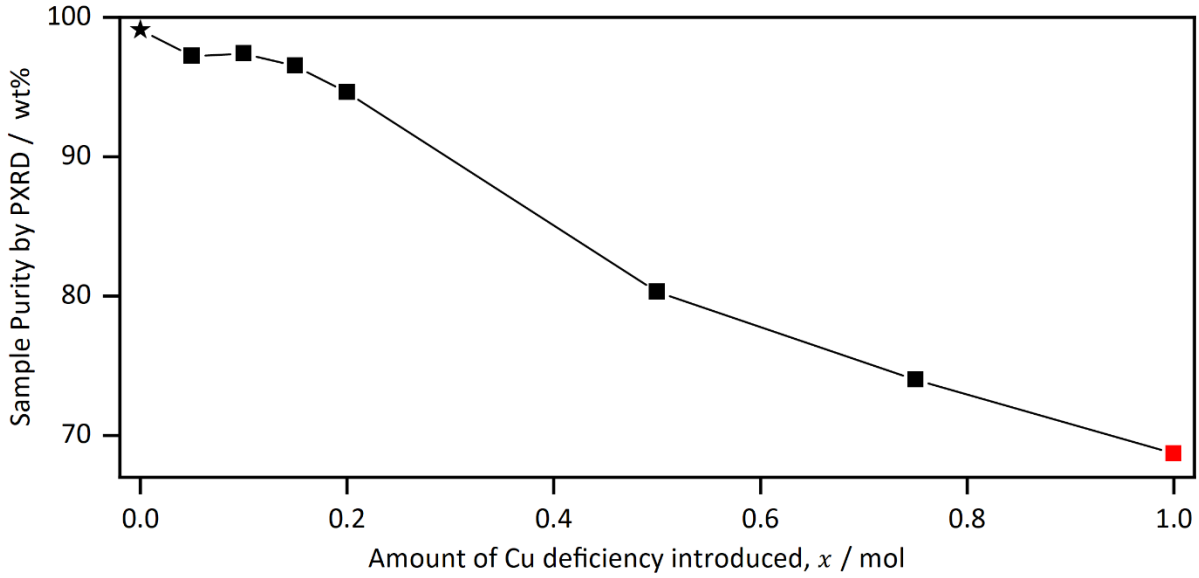

Figure 139 *Purities of the seven copper deficient MALMs in the $Sr_3Sc_2O_5Cu_{2-x}Se_2$ series. The pristine material $Sr_3Sc_2O_5Cu_2Se_2$ is included as a reference at x = 0 mol and is represented by a star. The data points at x = 0.100 mol is coloured red to indicate the presence of unknown impurities in this sample, and as a result the cited purity value is likely to be a slight overestimate. All values are derived from the Rietveld refinements of PXRD data using GSAS-II, and reported as weight percentages.*

In this series there is a significant drop-off in purity, Figure 139, on par with that which was observed in the strontium deficient series previous to this, but without the early region of maintained high purity which was indicative of a supposed successful vacancy introduction. Purity linearly decreases across the entire series, from 97.2 wt % in the first sample, x = 0.050 mol, down to 68.7 wt % in the highest targeted deficiency of x = 1.000 mol. The next page, Figure 140, is a comparison of the diffractograms of these two materials, where the latter suffers significant purity reduction and an unusually large quantity of SrSe. It also contains a small amount of unknown material and is represented therefore by a red data point in Figure 139 above.

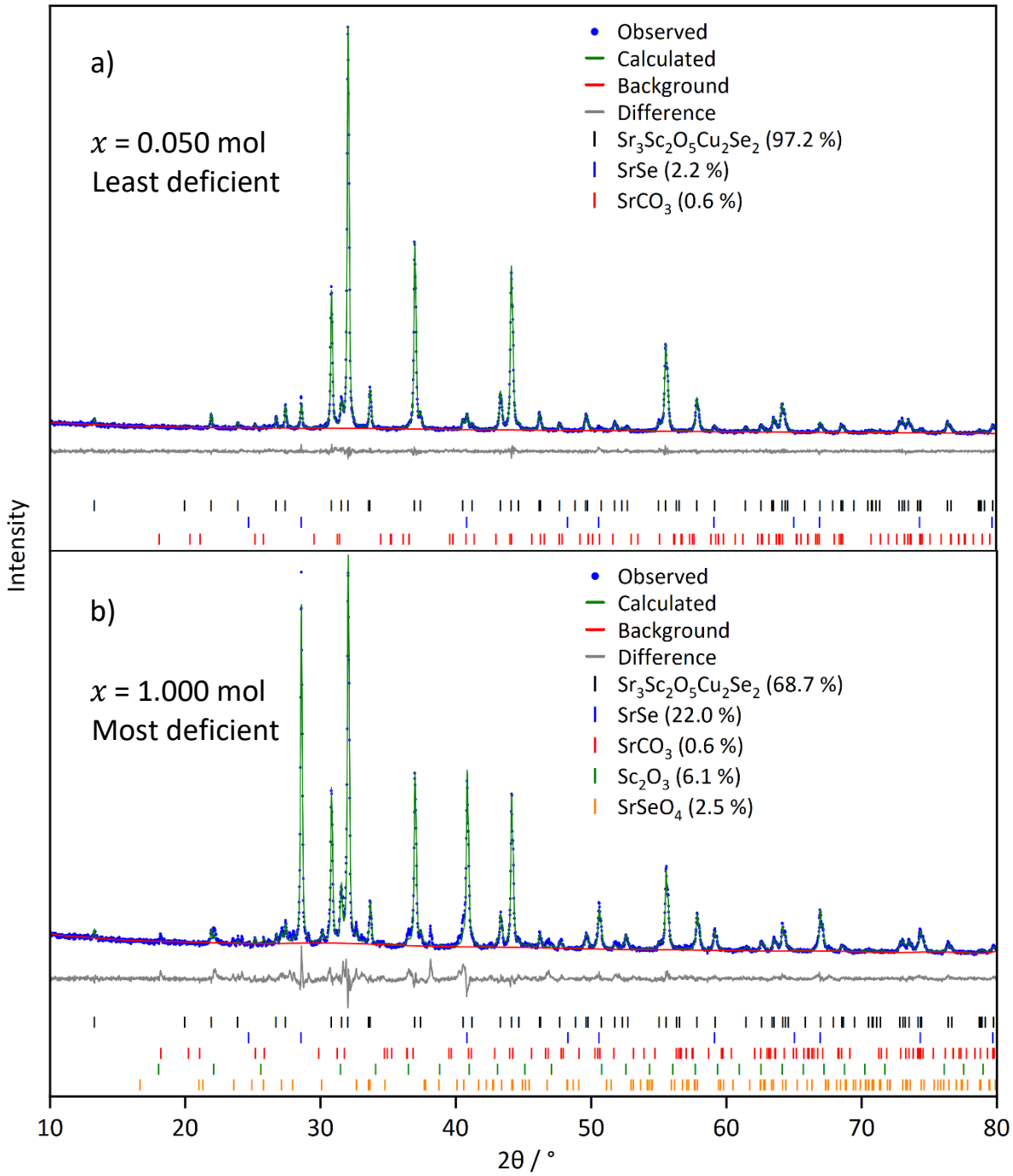

Figure 140 *Powder X-ray diffractograms of a) the least deficient sample of the series with target composition $Sr_3Sc_2O_5Cu_{1.95}Se_2$, and b) the most deficient sample of the series with target composition $Sr_3Sc_2O_5Cu_{1.00}Se_2$ (both space group I4/mmm) after 36 hours of heating at 800 °C. The small blue circles represent the observed diffracted intensities, the green lines represent the Rietveld-refined calculated models, the red lines represent the backgrounds, and the grey lines represent the differences between observed and calculated intensities. The black tick marks show the reflections of the refined model of $Sr_3Sc_2O_5Cu_2Se_2$, whilst the blue, red, green and orange tick marks represent refined impurity phases SrSe, $SrCO_3$, Sc_2O_3, and $SrSeO_4$ respectively. Weight fractions for each phase are cited in the figure legends.*

a) Duration: 45 minutes. Data points: 3457. Interval: 0.02 °. GOF: 1.07. R_{wp}: 4.998 %.

b) Duration: 45 minutes. Data points: 3457. Interval: 0.02 °. GOF: 1.92. R_{wp}: 8.116 %.

The impurities present across this series are SrSe, Sc_2O_3, $SrCO_3$, and $SrSeO_4$, which increase steadily across the seven samples. SrSe, which is present in almost every selenide material in this chapter, appears in uncharacteristically large quantities here, increasing linearly with x. Crucially no conductive impurities are present here, which eliminates the variable of any conductivity improvements being attributable to extraneous conductive materials that are not the target MALM. The absence of conductive impurities is very likely a direct result of the deficiencies of copper, the atom usually responsible for the conductive impurities.

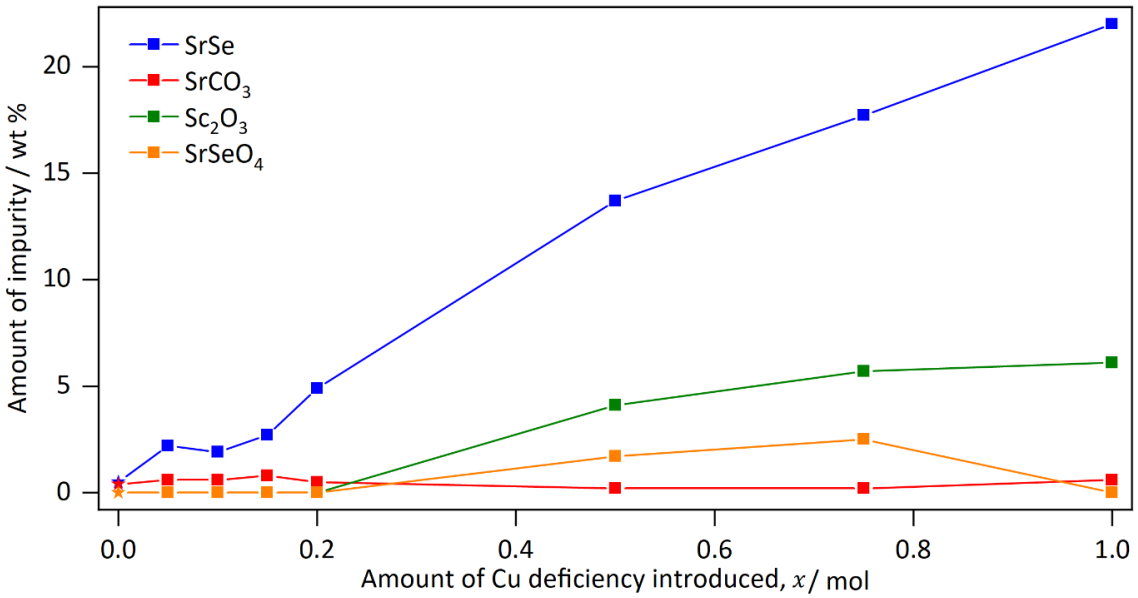

Figure 141 The weight percentages of five impurity phases present in the copper deficient 325 selenide MALMs with general formula $Sr_3Sc_2O_5Cu_{2-x}Se_2$. The pristine material $Sr_3Sc_2O_5Cu_2Se_2$ is included as a reference at x = 0 mol and is represented by stars.

The omission of conductive by-products (which are usually dark in colour) eliminates the sample colour gradient from this series, an artifact which rendered the band gaps of the strontium deficient samples impossible to measure by UV-Vis spectroscopy. All seven samples here are identical in colour, and resemble the pristine material.

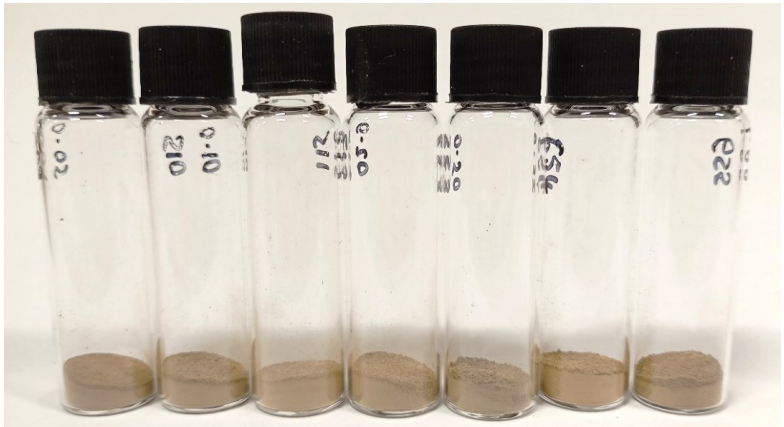

Figure 142 A photographic comparison of the colour of the copper deficient 325 selenide MALMs with general formula $Sr_3Sc_2O_5Cu_{2-x}Se_2$. Deficiency increases from left to right.

Optical band gaps, now measurable due to high purities and an absence of black by-products, decrease across the $Sr_3Sc_2O_5Cu_{2-x}Se_2$ series, Figure 143. Whilst this is the undesirable direction for applications of these materials such as *p*-type TCOs, this is one of the most convincing trends in band gap observed in this work. This trend is an expected result of copper vacancies in MALMs, because a vacancy on the copper site, the site central to optical and electrical properties, may catalyse the oxidation of some Cu^+ (d^{10}) to Cu^{2+} (d^9) to maintain charge balance which effects the hybridisation of the Cu-S, creating localised defect states in the Cu_2Ch_2 band structure. These localised defect microstates allow transport of charge carriers across the band gap, thus reducing the effective distance between the valence and conduction bands, shortening the optical band gap.[151, 280] To properly investigate this effect, X-ray photoelectron spectroscopy is recommended to probe the oxidation states of copper.[281]

As with many trends in conductivity within this chapter, the band gaps of this series present an initial sharper decline followed by a plateau. The obvious inference from this data is a 'saturation point' of copper vacancies in the structure. The observed band gap reduction from 2.94 eV (x = 0) to 2.86 eV (x = 0.200 mol) is indicative of successful copper vacancies, after which the reduction abruptly stops and further vacancy introduction has no effect.

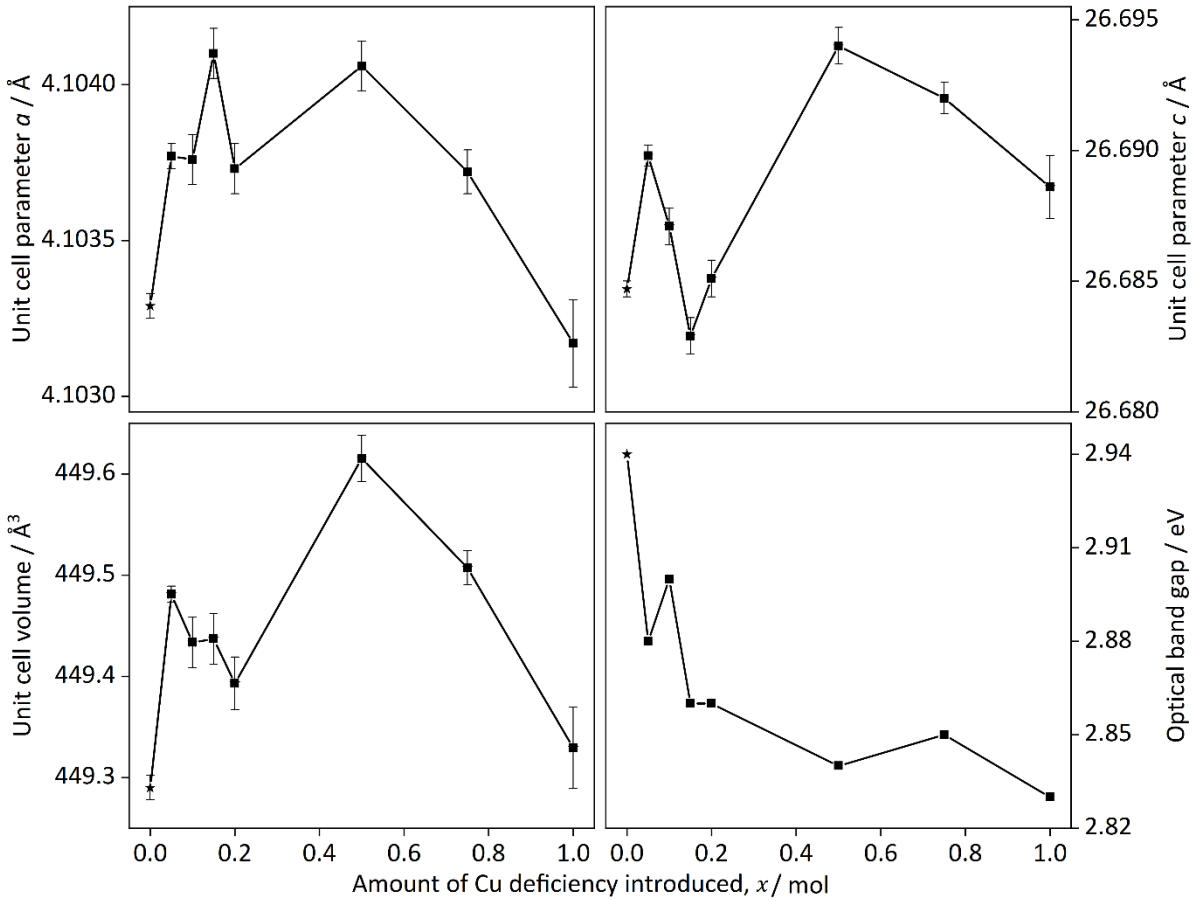

Figure 143 Comparisons of a) the a unit cell parameter, b) the c unit cell parameter, c) unit cell volume, and d) the optical band gap, of the copper deficient 325 selenide MALMs with general formula $Sr_3Sc_2O_5Cu_{2-x}Se_2$. The pristine material $Sr_3Sc_2O_5Cu_2Se_2$ is included as a reference at x = 0 mol and is represented by a star.

Correlating inversely with the band gap reduction, a promising initial increase in conductivity is observed. This trend is commonplace in the majority of series in this work due to the very poor conductivity of the pristine and relative ease of improvement on this value by charge carrier increase, regardless of method. It does appear that a small copper vacancy is achievable, indicated by the two orders of magnitude increase across the pristine and the first four doped samples. It is acknowledged that while this increase appears unimpressive here in comparison to far superior improvements in other discussed doping permutations, it is still larger than any of the improvements observed across the sulfide $Sr_3Sc_2O_5Cu_2S_2$ doping series.

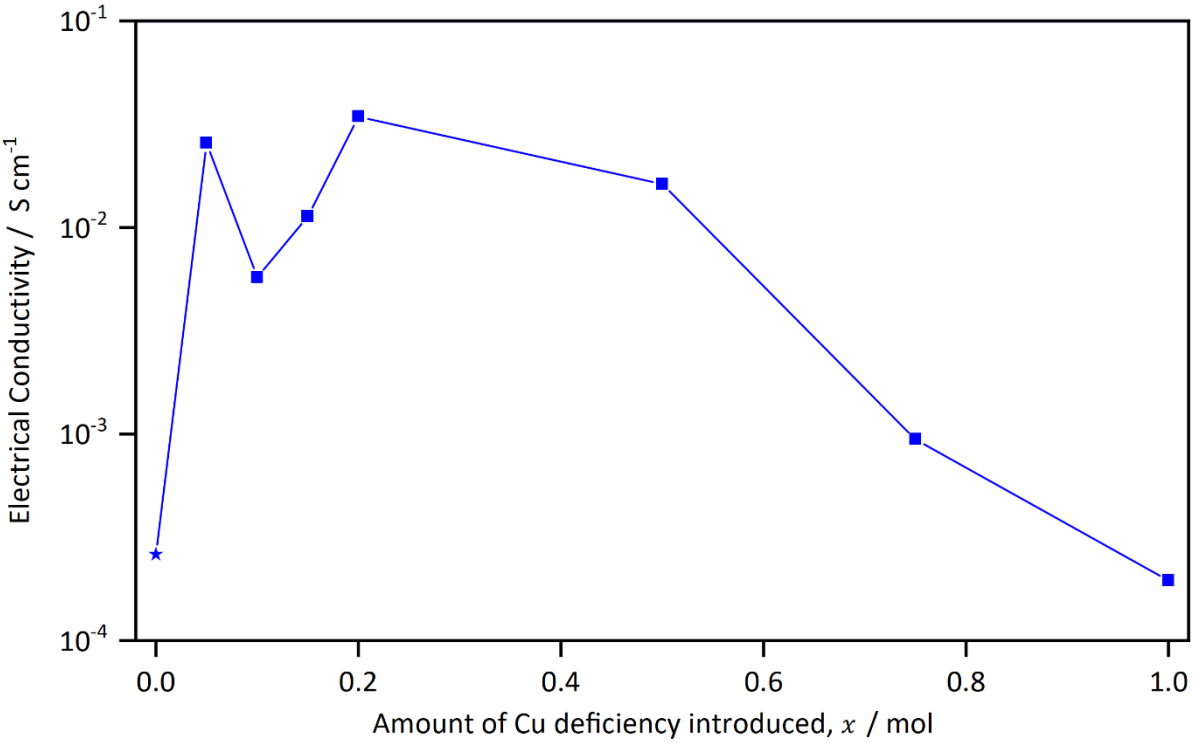

Figure 144 The electrical conductivities of the copper deficient 325 selenide MALMs with general formula $Sr_3Sc_2O_5Cu_{2-x}Se_2$, represented on a log_{10} scale. The pristine material $Sr_3Sc_2O_5Cu_2Se_2$ is included as a reference at x = 0 mol and is represented by a star. All values are derived from van der Pauw 4 probe resistivity measurements of 8mm diameter annealed pellet samples.

The initial increase is quickly followed by a decline after x = 0.200 mol, a decline which becomes visible in the rare scenario here where it can be confidently assumed that no copper-based impurities are present in the samples, the presence of which often mask a plateau or decline in sample quality by supplementing the conductivities. Here that is not the case. This decline is attributed to poor sample purity in this region of the series, where mobility-damaging impurities are abundant.

Copper vacancies and defects are a widely researched phenomenon in materials chemsitry, and this series highlights the effect of these on MALM conductivities and band gaps. While admittedly serving as an interesting investigaiton on key mechanisms of the copper-chalcogen system, the undesirable band gap reduction and only modest conductivity improvement means that the introduction of copper vacancies in $Sr_3Sc_2O_5Cu_2Se_2$ is a poor method for increasing charge carriers and conductivity.

3.4.10 $Sr_3Sc_2O_5Cu_2Se_2$ Doping Conclusions

In this section, $Sr_3Sc_2O_5Cu_2Se_2$ was systematically modified with a range of dopants and deficiencies to tune its electrical and optical properties. The aim was to enhance desirable characteristics for *p*-type conductors such as improved electrical conductivity through enhanced charge carrying capacity, and improved transparency to visible light through widening of the optical band gap.

Aliovalent doping with group 1 metal ions K^+ and Na^+ on the Sr^{2+} site of $Sr_3Sc_2O_5Cu_2Se_2$ demonstrated a generous accommodation of dopant onto the site (whilst maintaining the band gap), up to x = 0.200, yielding a three orders of magnitude conductivity improvement in both cases, which behaved very similarly, see Figure 145 on the next page. Beyond this, excess dopant segregates into a secondary conductive phase which compromises purity. A further 1.5 order of magnitude increase is observed beyond the points where dopant no longer fully incorporates, due either to a strontium deficiency, further but reduced doping, or the conductive impurities.

Magnesium doping on the scandium site, an approach rarely employed in MALMs of this type, proved particularly effective. It afforded exceptional purity, apparent full dopant concentration up to a x = 0.200 mol, and a 2000 fold conductivity improvement across the series. These samples, as illustrated in Figure 145, showed the highest conductivities of any samples in the range of x = 0 to x = 0.200 mol. An extension of this series, and the application of Mg^{2+} doping to other materials, is strongly recommended. It did come at the extent of a modest band gap reduction, however if applied to a material that can tolerate this loss without the band gap dropping below the visible light threshold, it may offer outstanding charge carrier enhancement with a minimal loss in transparency.

In contrast, isovalent doping with yttrium and lanthanum proved unsuccessful. Both dopants, particularly yttrium, exhibited near full complete rejection attributed to a size mismatch. Unincorporated yttrium manifested as the stable oxide precursor, whilst lanthanum as a conductive impurity phase after saturating at around x = 0.100. Both actually yielded a modest conductivity improvement, predicted to be the result of a scandium deficiency, but both failed in the primary objective of widening the optical band gap. A combination of purity, secondary phases and poor incorporation means that neither Y^{3+} nor La^{3+} are recommended for the pursuit of transparent conductivity.

Barium was fully incorporated as an isovalent dopant on the strontium site, producing high yields and a desired lattice expansion. This expansion did not however improve the transparency, which is predominantly governed by the hybridisation of the Cu-Se layers which appeared not to be manipulated as intended. A conductivity improvement was neither targeted nor achieved, rendering barium a poor choice of dopant.

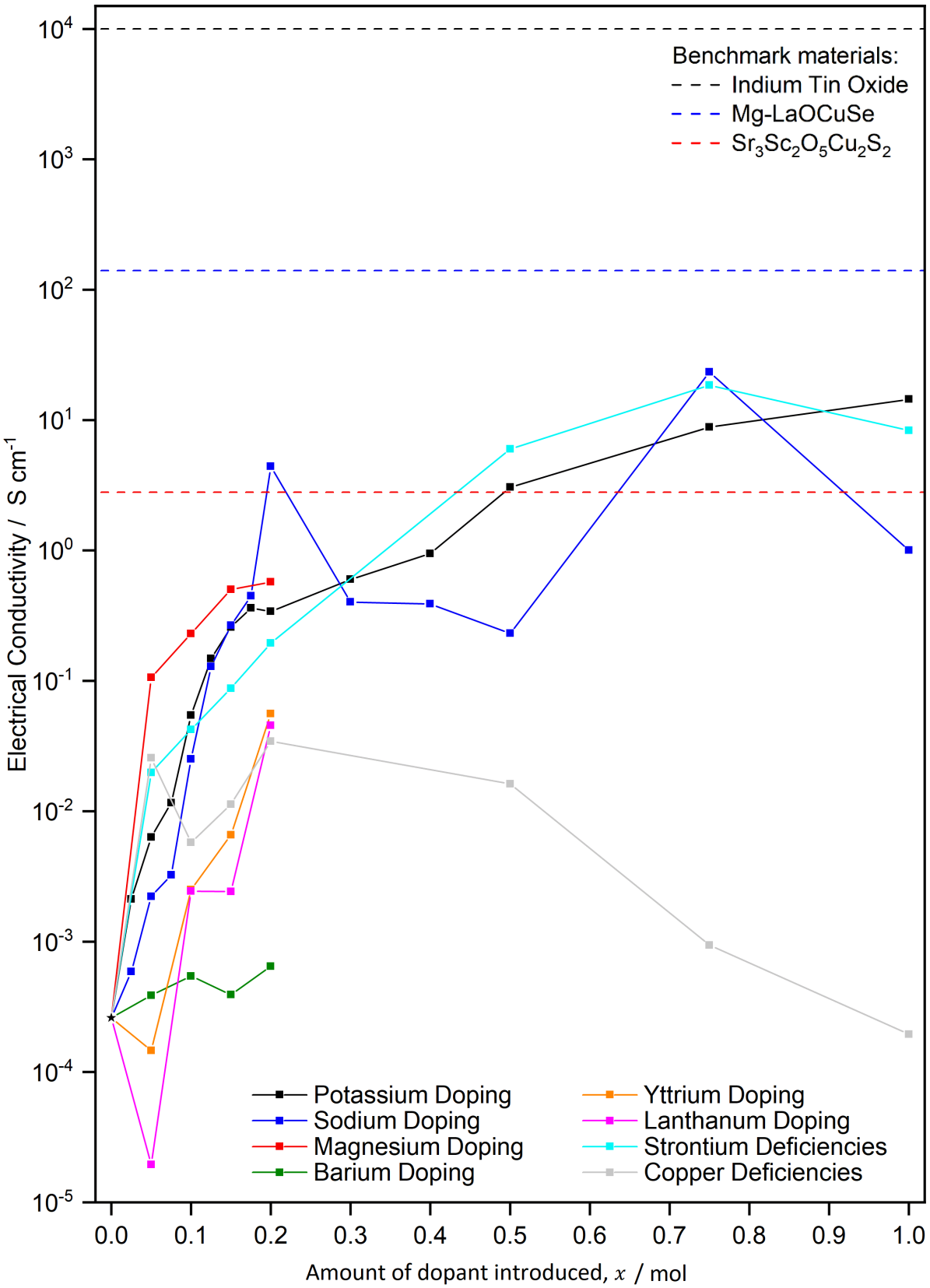

Figure 145 *The electrical conductivities of the potassium (black), sodium (blue), magnesium (red), barium (green), yttrium (orange), and lanthanum (pink) doped, and strontium (cyan) and copper (grey) deficient $Sr_3Sc_2O_5Cu_2Se_2$ series, presented on a log_{10} scale. The pristine material $Sr_3Sc_2O_5Cu_2Se_2$ is included as a reference at $x = 0$ mol and is represented by a star. The horizontal dashed lines represent the electrical conductivities of three 'champion' benchmark materials: Indium Tin Oxide (black), Magnesium doped LaOCuSe (blue), and the pristine $Sr_3Sc_2O_5Cu_2S_2$ reported by Liu et al (red).*

Deficiency studies revealed that $Sr_3Sc_2O_5Cu_2Se_2$ can support a moderate strontium vacancy which strongly enhances its charge carrying ability through the introduction of holes. At high deficiency levels, further vacancy accommodation fails but conductivity improvement continues through the undesirable synthesis of conductive by-products. Copper deficiencies yielded mixed results, a small conductivity improvement followed by a rapid drop-off and a band gap detraction. Scandium deficiencies should be considered fruitful future work, the accommodation of which may explain the surprising conductivity improvements yielded by the rejection of yttrium and lanthanum dopants.

Also included in the comparative Figure 145 are the electrical conductivities of three 'champion' benchmark materials with which the materials synthesised in this work may be compared. The black line represents Indium Tin Oxide, the industry standard and current state-of-the-art TCO, at 10^4 S cm^{-1}. The blue lines represents magnesium doped LaOCuSe, the greatest reported *p*-type conductivity of a Mixed Anion Layered Material (140 S cm^{-1}),[260] reported by Hiramatsu et al 2003, and the red line represents the benchmark quinternary MALM conductivity of $Sr_3Sc_2O_5Cu_2S_2$ (2.8 S cm^{-1}) reported by Liu et al 2007, against which many materials in this work have been compared. It can be seen that while the doped materials do not rival ITO, they do surpass the conductivity recorded by Liu which as amply discussed previously was considered a breakthrough material, as yet unmatched by any pristine MALM. The most conductive samples in this investigation are within an order of magnitude of the most conductive *p*-type MALM ever reported, magnesium doped LaOCuSe, which supports the contribution of this study to the field of *p*-type MALM TCO research. Future work should further investigate improvements to the transparency of these materials, and methods of deposition for use in applications, which could culminate in a genuine competitive transparent conductive oxide material rivalling the current champion materials of literature.

Collectively, these eight studies into $Sr_3Sc_2O_5Cu_2Se_2$ display a convincing improvement of its properties, and highlight that optimal performance is a compromise between maximising incorporation and minimising deleterious impurity phases. Potassium, sodium and magnesium are recommended dopants to improve sample conductivity, and none may be recommended for enhancement of transparency.

3.5 Conclusions and Future Work

A comprehensive doping investigation into $Sr_3Sc_2O_5Cu_2S_2$ and $Sr_3Sc_2O_5Cu_2Se_2$ has yielded a rich assortment of results that probe the electrical, optical, compositional and structural properties of the MALMs. Desirable improvements to properties such as the electrical conductivity and the optical band gap have been demonstrated by various means. Further to this, multiple instances of doping until failure have revealed not only the behaviour of the material under such conditions but the level of dopant or deficiency at which the decline occurs.

The sulfides exhibit superior optical band gaps, which were maintained when doping with K^+ and Na^+, but with only modest improvements to the sample conductivities. Conversely, whilst the selenides inherently have a lower optical band gap, attempts to improve this were largely unsuccessful, but improvements to the electrical conductivity by aliovalent doping proved very effective. The best conductive performance was observed from $Sr_3Sc_2O_5Cu_2Se_2$ doped with sodium, potassium and magnesium. The most conductive sample in both this chapter and the entirety of this work is sodium doped $Sr_3Sc_2O_5Cu_2Se_2$ where x = 0.750, $(Sr_{2.250}Na_{0.750})Sc_2O_5Cu_2Se_2$, which measured a very impressive 23.4 S cm^{-1} whilst maintaining a wide optical band gap of 2.91 eV.

Future work in this field should explore the combination of dopants, attempting both to widen the band gap alongside increasing charge carrier concentration. If one considers $Sr_3Sc_2O_5Cu_2S_2$ as the parent material, on which the original recommendations were based, then this was technically performed here with Se^{2-} doping on the S^{2-} site and aliovalent doping to attempt transparency improvements, but further exploration could prove enlightening.

In conclusion, the 325 materials of the Sr-Sc-O-Cu-*Ch* system are excellent candidates for the application of transparent conductivity. If in an application transparency is the most important metric, the sulfide series should be favoured. For applications where a higher conductivity is the key property, the electrically tuneable and versatile selenides should be employed.

Since writing, publication of this chapter is in progress, in: *Optical and electronic properties of alkali metal doped layered oxychalcogenides $Sr_3Sc_2O_5Cu_2S_2$ and $Sr_3Sc_2O_5Cu_2Se_2$ - L. Kemp, Z. Malik, G. Limburn and G. Hyett.*

Chapter 4 The Synthesis and Conductivity Investigation of Doped $Sr_4B_2O_6Cu_2Ch_2$ '426' Oxychalcogenides

4.1 Introduction

A thorough investigation of the scandium 325 MALMs in the previous chapter demonstrated their potential application as *p*-type transparent conductors, as materials with wide band gaps and conductivities which, while low when undoped, may be greatly enhanced by doping. Group 1 metal ion doping proved particularly effective at doing so.

The discussed scandium system Sr-Sc-O-Cu-*Ch* forms not only the 325 $Sr_3Sc_2O_5Cu_2Ch_2$ structure, but the 426 $Sr_4Sc_2O_6Cu_2Ch_2$ structure also, the differentiating factors between these being the inclusion or exclusion of one molar unit of SrO, and a variation in synthesis conditions. The 426 material was not observed as a competing phase or impurity in any of the 325 samples in *Chapter 3* because it forms at a lower temperature in this system,[57, 89] and the precursor ratios of those reactions targeted specifically the 325. As will be observed throughout this chapter as a perpetual quandary, the 325 material appears frequently within syntheses of the 426.

This chapter describes the synthesis and analysis of the 426 members of the Sr-Sc-O-Cu-*Ch* system, both pristine, and doped with group 1 metal ions Na^+ and K^+. This formed part of a larger collaborative work, contributing towards a publication investigating the 426 materials $Sr_4B_2O_6Cu_2Ch_2$ where *B* = Sc, Ga or In, and *Ch* = S or Se, which was published in November 2024.[64] It was found that the conductivities of these six materials, one of which is reported for the first time, may be improved by *p*-type doping to increase the hole carrier concentration. This was admittedly less effective than doping of the 325 materials, but yielded a conductivity increase in almost every case.

Doping of the gallium MALM $Sr_4Ga_2O_6Cu_2S_2$ with Na^+ has been previously reported,[67] yielding an enhancement from 10^{-4} S cm^{-1} to 10^{-2} S cm^{-1} at x = 0.1. Here this is expanded to include the scandium and indium systems of sulfide and selenide, and potassium as a dopant, for a total of 6 undoped and 12 doped materials.

4.2 Experimental

The syntheses of 426 materials within this chapter are analogous to those of the 325 materials described in *Chapter 3*, but with different heating conditions. Intimate powder mixtures of precursors were ground to homogeneity in a nitrogen glovebox with a pestle and mortar, then added to an alumina crucible and sealed within a silica ampoule. Ampoules were heated in a box furnace, cooled naturally, and then reground within the glovebox. The initial heat cycle of any material herein was done so as a powder to avoid any the exposure to air of sensitive precursors during pelletisation, but subsequent heats often employed a pelletisation step, outlined where relevant. Samples were analysed by powder X-ray diffraction and modelled by Rietveld refinement to assess composition, purity and structural features, and then by UV-Vis spectroscopy to estimate an optical band gap. Finally, a small 8mm pellet of approximately 0.15 grams of completed sample was subjected to a third heating cycle to anneal it ahead of 4 probe van der Pauw resistivity testing to measure the conductivity. Precise diameter and thickness values were also obtained from the annealed pellet in order to calculate an estimation of density, as a percentage of the density of the bulk crystal.

In the syntheses of doped materials, the same precautions were taken as in the previous chapter. An initial lower temperature heat cycle allowed the incorporation of elemental sulfur and selenium into the reaction mixture, minimising sublimation. The unreacted precursor mixtures of [A_2Ch + Ch] (A = Na or K, Ch = S or Se) were again used, to reduce weighing error associated with the miniscule amounts of A_2Ch or Ch otherwise required in a doped sample synthesis. The developed technique for normalising the modelling of doped samples during Rietveld refinement described in *Section 3.2.4*, is employed once more, whereby doped MALMs are modelled as if pristine.

Specific reaction equations for each dopant, along with any deviations from this general procedure, are outlined within each respective section.

4.2.1 Precursors

Materials within this chapter were synthesised using the following precursors:

SrO (made in-house by the decomposition of $SrCO_3$, Merck, 99.9 %), Sc_2O_3 (Thermo Scientific, 99.999 %), Ga_2O_3 (Alfa Aesar, 99.99 %), In_2O_3 (Alfa Aesar, 99.9 %) Cu_2S (made in-house by the reaction of Cu, Alfa Aesar, 99.9 %, and S, Thermo Fisher Scientific, 99.9995 %), Cu_2Se (Thermo Fisher Scientific, 99.5 %), SrS (made in-house by the reaction of $SrCO_3$, Merck, 99.9 %, and CS_2, Honeywell, 99.9 %), SrSe (made in-house by reduction of $SrSeO_4$, also made in-house), Na_2Se (made in-house by the reaction of Na, Aldrich, 99.9 %, and Se, Strem, 99.99 %), Na_2S (Thermo Scientific, 95 %), K_2S (Strem, 95 %), K_2Se (Thermo Scientific, 95 %), S (Thermo Fisher Scientific, 99.9995 %), and Se (Strem, 99.99 %).

4.3 $Sr_4Sc_2O_6Cu_2S_2$

4.3.1 Pristine Synthesis

Of the six materials synthesised for inclusion in our publication "*Transport Properties of Doped Wide Band Gap Layered Oxychalcogenide Semiconductors Sr_2GaO_3CuCh, Sr_2ScO_3CuCh, and Sr_2InO_3CuCh (Ch = S or Se)*",[64] this work was responsible for and herein describes the pristine and doped variants of the two scandium 426 MALMs $Sr_4Sc_2O_6Cu_2S_2$ and $Sr_4Sc_2O_6Cu_2Se_2$. The gallium and indium analogues were produced by colleague and first author of the publication, Dr. Zahida Malik.

Unknowingly, it transpired that the scandium materials were the most difficult to produce to a high purity due to competition from the higher stability $Sr_3Sc_2O_5Cu_2Ch_2$ phases. In general, it was observed that the more aggressive a given condition (such as a higher temperature, a greater number of heat cycles, or a longer duration heat cycle), the more likely the emergence and at times complete domination of the 325 phase. Reduce these conditions too low however, and conditions are insufficient to synthesise either phase. There exists, therefore, a delicate thermodynamic balance between maximising target product synthesis and minimising undesirable further reactions.

After investigating variables such as sintering temperature, sintering duration, and number of heat cycles, the optimal synthesis procedure for $Sr_4Sc_2O_6Cu_2S_2$ was found through trial and error to be an initial 500 °C heat cycle of the unpelletised powder mixture for 24 hours, followed by a second pelletised heat at 600 °C for 24 hours, with an intermediate regrind in a glovebox. Every heating cycle within in this chapter took place within an inert ampoule. $Sr_4Sc_2O_6Cu_2S_2$ was synthesised on a 1 gram scale using conventional solid-state chemistry, according to Equation 57:

Equation 57 $3\ SrO + Sc_2O_3 + Cu_2S + SrS \rightarrow Sr_4Sc_2O_6Cu_2S_2$

The highest quality example of $Sr_4Sc_2O_6Cu_2S_2$, Figure 146, had a purity of 98 wt %, alongside traces of SrS and Cu; it is hypothesised that the elemental copper is observed resulting from the decomposition of Cu_2S. The sole report of this material in literature, a 2012 publication by Ogino et al, cites a reaction temperature range of 700 - 1000 °C,[57] but notes that "*$Sr_3Sc_2O_5Cu_2S_2$ appeared as the main phase upon sintering above 900 °C.*" Whilst true, $Sr_3Sc_2O_5Cu_2S_2$ was also observed here at temperatures as low at 600 °C, and was found to depend on more variables than simply the reaction temperature.

A van der Pauw resistivity measurement on this sample revealed a conductivity of 8.48×10^{-5} S cm^{-1}. This is low, but there is potential for improvement by doping. The resistivity measurements were performed on a pellet that had been annealed at 450 °C for 24 hours; the rationale for such mild conditions is explained in the upcoming sections. The optical band gap of this material was measured to be 3.17 eV, Figure 147. Whilst below the visible threshold of 3.3 eV, this material is still transparent to most visible light and is therefore considered a promising candidate for transparent conductivity.

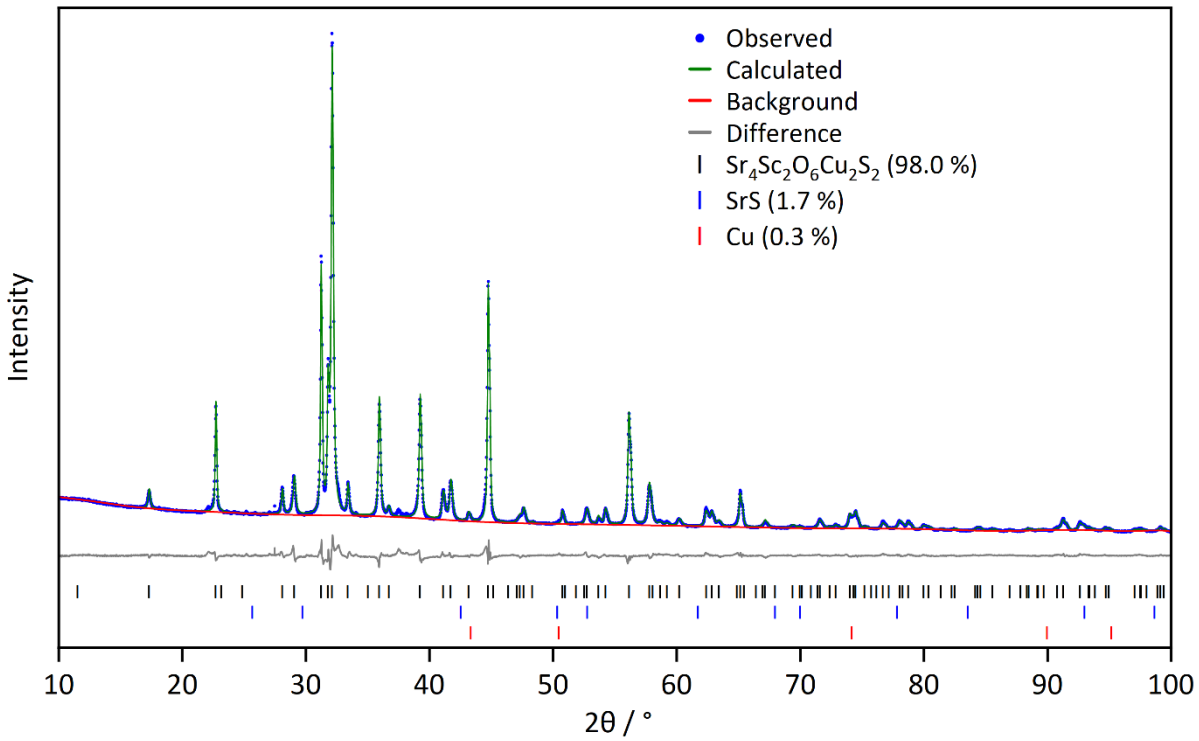

Figure 146 *Powder X-ray diffractogram of material with target composition $Sr_4Sc_2O_6Cu_2S_2$ (space group P4/nmm) after 48 hours of heating at 500 - 600 °C. The small blue circles represent the observed diffracted intensity, the green line represents the Rietveld-refined calculated model, the red line represents the background, and the grey line represents the difference between observed and calculated intensities. The black tick marks show the reflections of the refined model of $Sr_4Sc_2O_6Cu_2S_2$ (98.0 %), whilst the blue and red tick marks represent refined impurity phases SrS (1.7 %), and Cu (0.3 %) respectively.*
Duration: 16 hours. Data points: 8985. Interval: 0.01 °. GOF: 1.61. R_{wp}: 2.617 %.

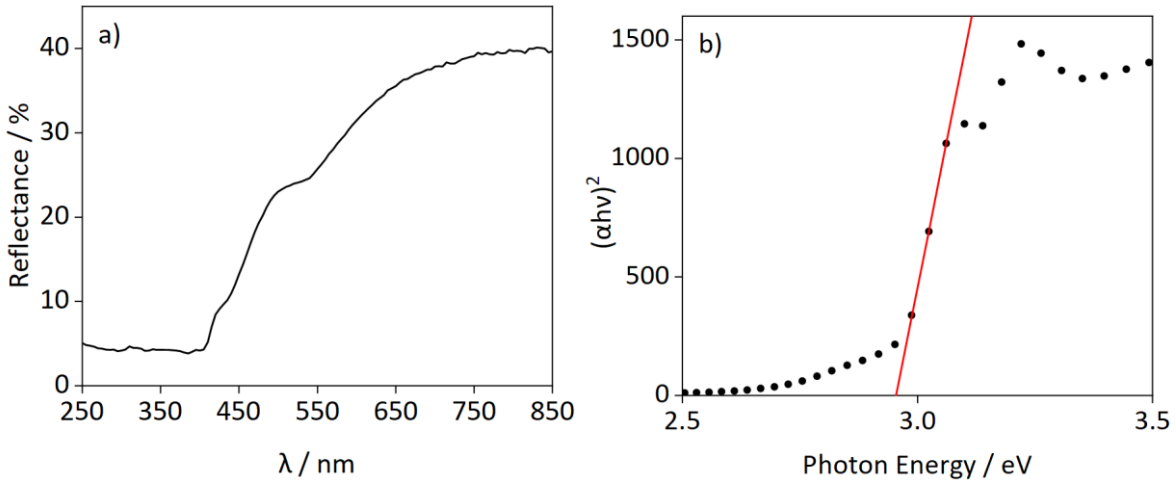

Figure 147 *UV-Vis spectrometry data for material with target composition $Sr_4Sc_2O_6Cu_2S_2$ after 48 hours of heating at 500-600 °C. Plot a) is the raw diffuse reflectance data, and plot b) is the associated magnified Tauc plot for this region, where the intercept between the red extrapolated tangent line and the x-axis is used to estimate an optical band gap of 3.17 eV, which corresponds to 391 nm.*

4.3.2 The Annealing Impasse

The conversion of $Sr_4Sc_2O_6Cu_2S_2$ to $Sr_3Sc_2O_5Cu_2S_2$ is irreversible; supplementary heating will only advance the conversion further toward the 325. Throughout the entirety of this work a scandium 325 phase has never been observed to convert to the 426, therefore one may infer that the 325 is the more thermodynamically stable phase and that the 426 is a metastable kinetic phase. Note that this relationship is asserted only for the scandium MALMs for which this work primarily investigates, and is not meant as a generalised to other systems where both the 325 and 426 phases are known, such as the Ba-In-O-Cu-S or Sr-Fe-O-Cu-S systems,[20, 41, 65] which may behave differently. In the latter for example, $Sr_3Fe_2O_5Cu_2S_2$ and $Sr_4Fe_2O_6Cu_2S_2$ form at very similar temperatures and are selected for by the inclusion or exclusion of the mole of SrO precursor that differentiates their structures.[41]

It is when annealing the synthesised material for a van der Pauw resistivity measurement that one encounters the greatest instability of the 426 phase relative to its 325 counterpart. $Sr_4Sc_2O_6Cu_2S_2$ is extremely susceptible to degradation when the optimum conditions are exceeded, and the annealing step of a synthesis is essentially a further synthetic heat cycle, pushing the already complete reaction further and encouraging the undesirable conversion. The annealing step is crucial to achieve improvements in conductivity, for increasing charge carriers alone is not enough, the mobility-enhancing densification step is important and has been shown widely in literature to result in conductivity enhancements.[39, 134, 282-285]

In this work so far, annealing is usually performed at 800 °C for 12 hours, which is sufficient to densify a material for improved charge carrying capability. In most cases, such as all 325 materials in *Chapter 3*, this supplementary 800 °C heat cycle does not degrade the sample or decrease purity in any way, due to the thermodynamic stability of those phases. The stability is so ubiquitous that until this point post-anneal purities are not stated or discussed as they have never been observed to change. In theory, the longer the annealing process and the greater the temperature, the greater the densification will be and the fewer the conductivity-inhibiting grain boundaries. The standard conditions of 12 hours at 800 °C employed throughout this work are therefore a compromise of optimal annealing, time, practicality, and green chemistry.

Here, no such luxury is afforded. Annealing drastically increases the 426 to 325 conversion. Figure 148 depicts a sample of $Sr_4Sc_2O_6Cu_2S_2$ annealed at 800 °C, with approximately one third conversion to 325. This is but one example, the degree of degradation was found to vary widely under seemingly identical conditions, anywhere from 0 to 100 % and unpredictably. Full conversion of the entire 426 phase to 325 was not uncommon, irreparably damaging the sample. Conversion was observed as low as 500 °C during annealing, at which point the conditions are likely too mild to even sufficiently densify the pelletised material, an assumption tested later. Note that exposure to air was tested and eliminated as a source of the degradation. It is with high confidence that annealing is stated as the instigator.

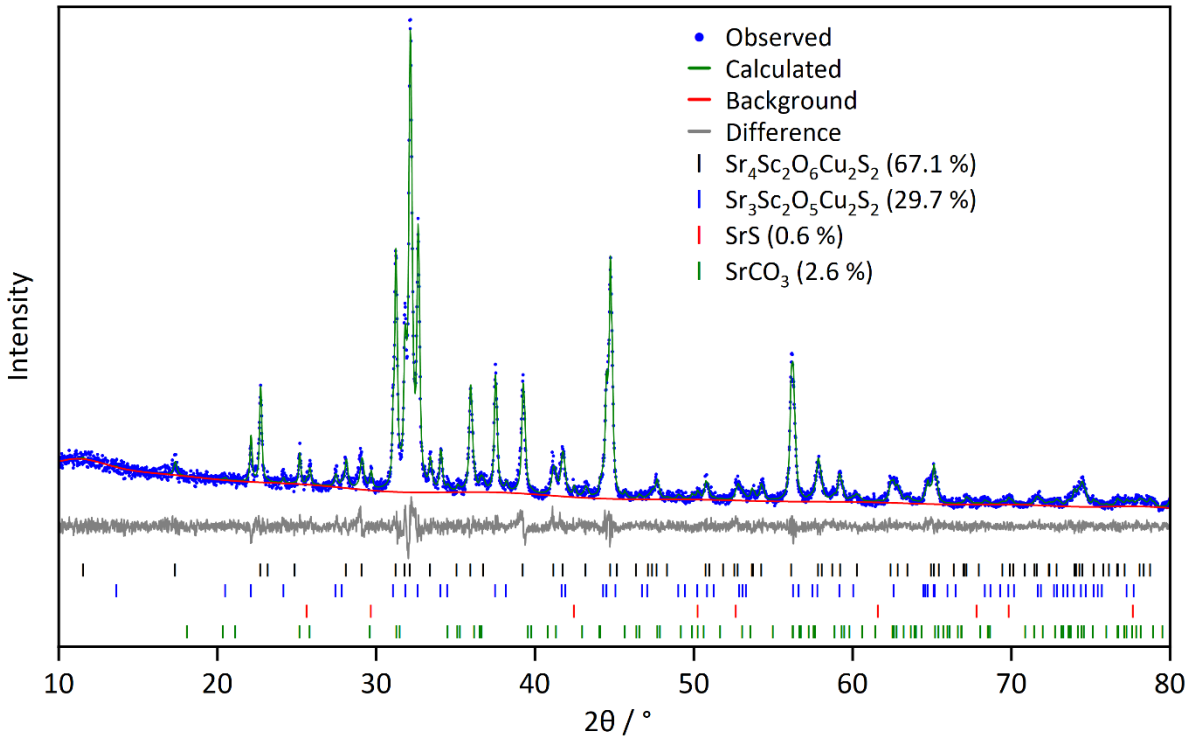

Figure 148 *Powder X-ray diffractogram of material with target composition $Sr_4Sc_2O_6Cu_2S_2$ (space group P4/nmm) after annealing for 12 hours at 800 °C. The small blue circles represent the observed diffracted intensity, the green line represents the Rietveld-refined calculated model, the red line represents the background, and the grey line represents the difference between observed and calculated intensities. The black tick marks show the reflections of the refined model of $Sr_4Sc_2O_6Cu_2S_2$ (67.1 %), whilst the blue, red and green tick marks represent refined impurity phases $Sr_3Sc_2O_5Cu_2S_2$ (29.7 %), SrS (0.6 %) and $SrCO_3$ (2.6 %) respectively.*
Duration: 45 minutes. Data points: 4444. Interval: 0.02 °. GOF: 1.14. R_{wp}: 7.141 %.

In summary, high temperature annealing is not viable in this case. There are, fortunately, alternative methods by which this risk of degradation may be circumvented. The first is a simple one: do not heat the pellet before a resistivity measurement, measuring instead the resistivity of the unannealed and high purity pellet. The act of pelletisation greatly densifies a powder sample and permits a four probe measurement, the heating step is merely a further densification,* and without it conductivity measurements are severely hindered but not impossible. The second method to minimise degradation is a low temperature anneal, at a temperature such as 400 - 500 °C where densification may still occur but 426 to 325 conversion is low or negligible.

Fortunately, both of these methods could be tested within the same experiment. A supply of pristine $Sr_3Sc_2O_5Cu_2Se_2$ (synthesised for experiments described in *Chapter 3*) was subjected to different annealing conditions, presented in Figure 149, with the conductivities measured before and after annealing. This material was chosen for its proven exceptional thermal stability and therefore the assurance of uniform sample composition at all times, a surety not afforded by the 426 materials.

* In some fields such as battery electrode research, the is instead described as a decrease in porosity.

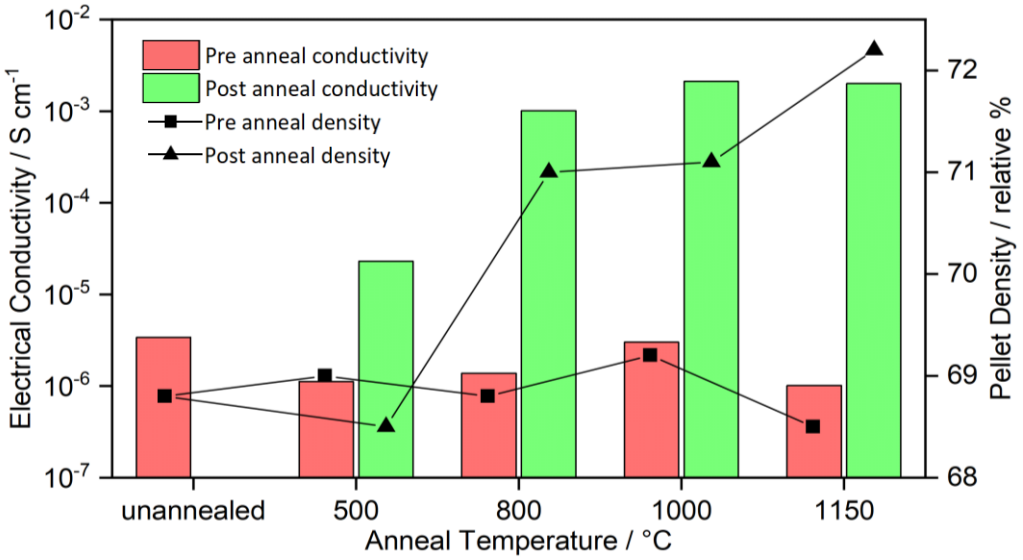

Figure 149 *The effect of increasing annealing temperature on the electrical conductivity (left y-axis, bar chart) and pellet density (right y-axis, line graph). All anneal experiments were performed for 24 hours.*

Various conclusions can be drawn from the anneal temperature analysis shown above. Firstly and simply, as one would expect, conductivity correlates with pellet density. The variation in pellet density is not large, spanning only 4 % between unannealed and annealed pellets. The consistent densities measured across the undoped samples suggest that the pelletisation itself is responsible for increasing the density of a pellet (relative to the bulk crystal) to around 69 ± 0.5 %. The further 3 - 4 % gained from annealing is responsible for an increase of 2 - 3 orders of magnitude in conductivity. Another reassuring observation is that 800 °C is sufficient, above which one observes diminishing returns for unnecessarily high temperature and high energy reactions.

These results rule out the possibility of conductivity measurements performed without annealing. Purity may be maintained, but conductivities are so low as to be insulating and far below their potential, even in the case of the 325 materials presented above which have greater conductivities than the 426 analogues. A low temperature anneal however, is an option. Some 426 to 325 conversion was observed at 500 °C but never below it. For this reason, 450 °C was selected as the anneal temperature for the maiden doping study of the $Sr_4Sc_2O_6Cu_2Ch_2$ family in the next section.

It should be noted that a third alternative to conventional annealing was considered: using the final step of the sample synthesis, for which a sample is pelletised, as both the synthesis and the annealing step combined. This step should yield a dense pellet which has been heated enough to reach completion but not enough to begin any undesirable conversion to 325. There are flaws to this notion. Firstly, the pellet cannot be assumed to be uniform, a thorough regrind is necessary for sample homogeneity. Secondly, a pellet often emerges from synthesis sunken, bent or misshapen rendering it ineligible for van der Pauw measurements. Finally, PXRD analysis of a completed sample would require destruction of the pellet, which not only risks impurity from the silver paint, but eliminates any possibility of retesting the conductivity. For these various reasons, this technique was not pursued.

4.3.3 Sodium Doping, $(Sr_{4-x}Na_x)Sc_2O_6Cu_2S_2$

Sodium was introduced as an aliovalent dopant onto the strontium site of $Sr_4Sc_2O_6Cu_2S_2$ such that the target material takes the form $(Sr_{4-x}Na_x)Sc_2O_6Cu_2S_2$. This was achieved by reducing SrS content and supplementing with $[Na_2S + S]$, according to Equation 58 below. This is identical to the process by which $Sr_3Sc_2O_5Cu_2S_2$ was sodium doped in *Section 3.3*, but with the inclusion of one extra molar unit of SrO.

Equation 58 $$3\ SrO + Sc_2O_3 + Cu_2S + 1\text{-}x\ SrS + \frac{x}{2}[Na_2S + S] \rightarrow (Sr_{4-x}Na_x)Sc_2O_6Cu_2S_2$$

The ground powder precursors (1 gram scale) were heated within an ampoule for 12 hours at 100 °C, then raised to 500 °C for a further 12 hours in the same ampoule. They were then reground, pelletised, and heated again for 24 hours at 550 °C. Note that this is slightly lower than the synthesis temperature for pristine $Sr_4Sc_2O_6Cu_2S_2$, for preliminary testing found doped versions of this material to be even more susceptible to 325 conversion than the undoped counterparts, necessitating even milder reaction conditions and forecasting greater difficulties for the annealing stage. Ten samples were synthesised in one self-consistent sample set: eight with a dopant level ranging from $x = 0.025$ to 0.200 mol at equal increments of 0.025 mol, and a further two samples at $x = 0.500$ and 1.000. The complete compositional, analytical and graphical data for each sample in this section can be found in *Appendix B.2.1.*

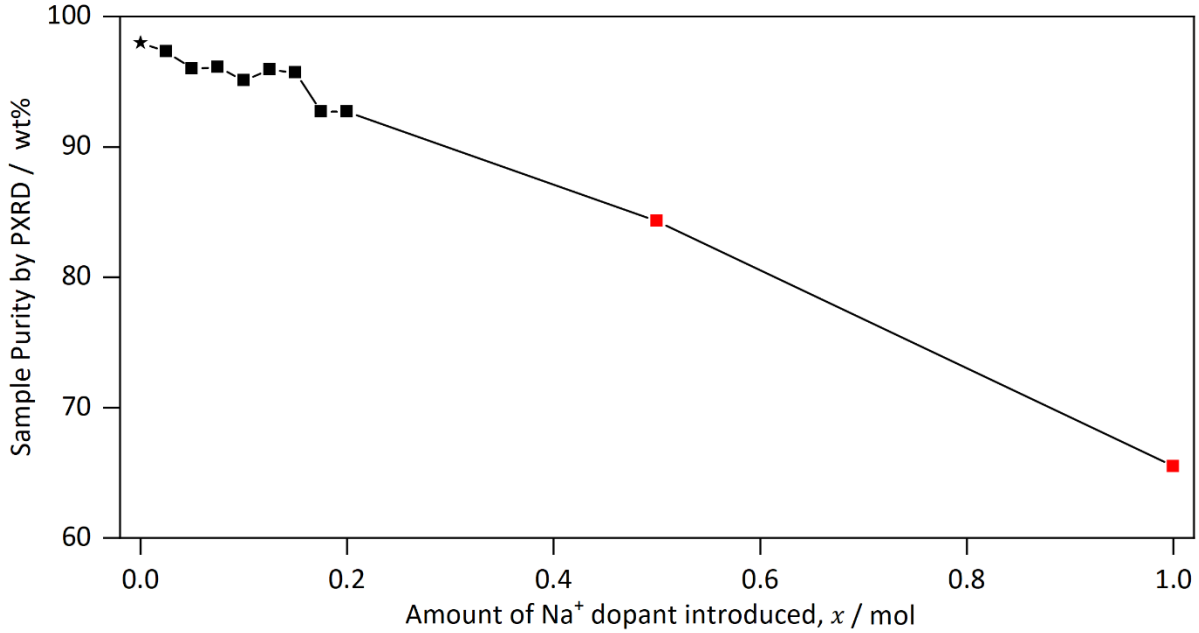

Figure 150 Purities of the ten sodium doped MALMs in the $(Sr_{4-x}Na_x)Sc_2O_6Cu_2S_2$ series. The pristine material $Sr_3Sc_2O_5Cu_2Se_2$ is included as a reference at $x = 0$ mol and is represented by a star. The two data points at $x = 0.500$mol and $x = 0.100$ mol are coloured red to indicate the presence of unknown impurities in these samples, and as a result the cited purity values are likely to be very slight overestimates. All values are derived from the Rietveld refinements of PXRD data using GSAS-II, and reported as weight percentages.

The purities (assessed by Rietveld refinement) of the ten doped samples are shown in Figure 150 in comparison to the highest quality pristine example. There is a very convincing linear decrease in purity across the series, a trend common in doped series, usually indicating an intolerance to dopant incorporation especially if the lightly doped samples display a decrease.

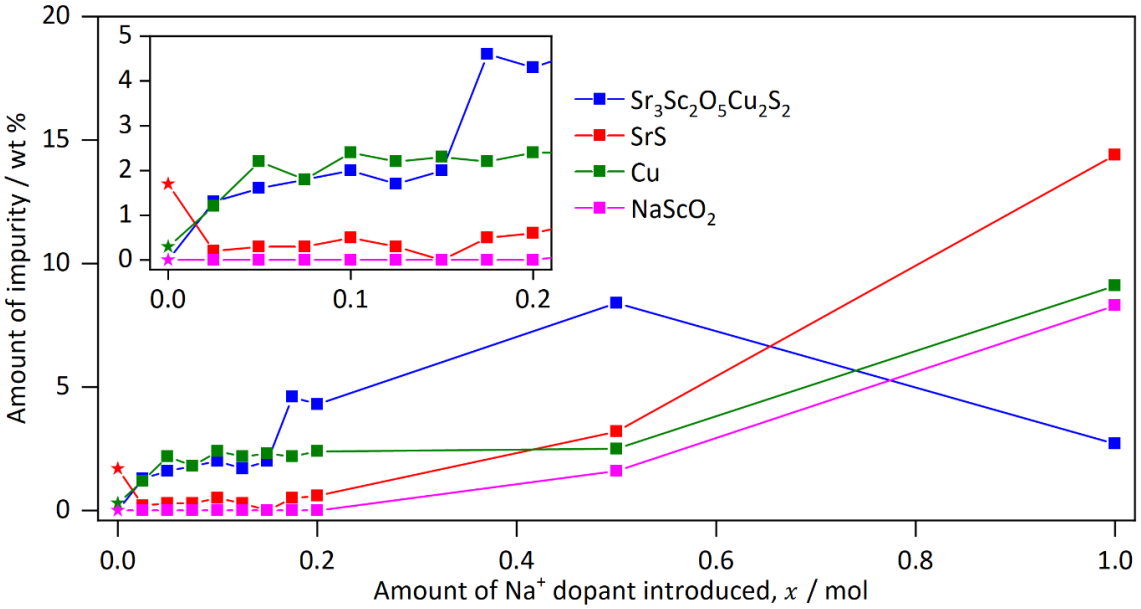

Figure 151 The weight percentages of four impurity phases present in the sodium doped 426 sulfide MALMs with general formula $(Sr_{4-x}Na_x)Sc_2O_6Cu_2S_2$. The pristine material $Sr_4Sc_2O_6Cu_2S_2$ is included as a reference at x = 0 mol and is represented by a star.

Figure 151 shows the four observed impurities and their increase in concentration across the series. $Sr_3Sc_2O_5Cu_2S_2$ was observed in every sample, which were synthesised not only at a lower temperature than the pristine but for a shorter reaction time, further illustrating the extreme difficulty in eliminating this pervasive by-product. SrS and Cu were widespread, but our work has shown no increase in overall sample conductivity from small impurities of elemental copper, despite its high conductivity.[64]

Interestingly, unincorporated sodium appears not as $NaCu_3S_2$ as might be predicted based on the study of $(Sr_{3-x}Na_x)Sc_2O_5Cu_2S_2$ in *Section 3.3.3*, but instead as $NaScO_2$,[286] a hexagonal ternary compound which crystallises in the structure of *Caswellsilverite* $NaCrO_2$,[287] was and identified using Rigaku PDXL-2 phase identification software. Sodium impurities only appear in the final two samples, which based on previous series is extremely promising evidence of high sodium incorporation. Only those final two samples, where x = 0.500 and 0.100 mol, contained any unknown or unrefined material, thus the likelihood of sodium impurities existing within earlier fully refined samples is low.

Figure 152 on the next page is a comparison of the least and most doped samples of the series where x = 0.025 and 1.000. Despite steadily increasing across all other samples in the series, the concentration of $Sr_3Sc_2O_5Cu_2S_2$ in the most doped sample is lower (see the blue data series in Figure 151 above). Therefore, despite very different target stoichiometries, the amount of 325 impurity in the two compared samples is, coincidentally, similar and small.

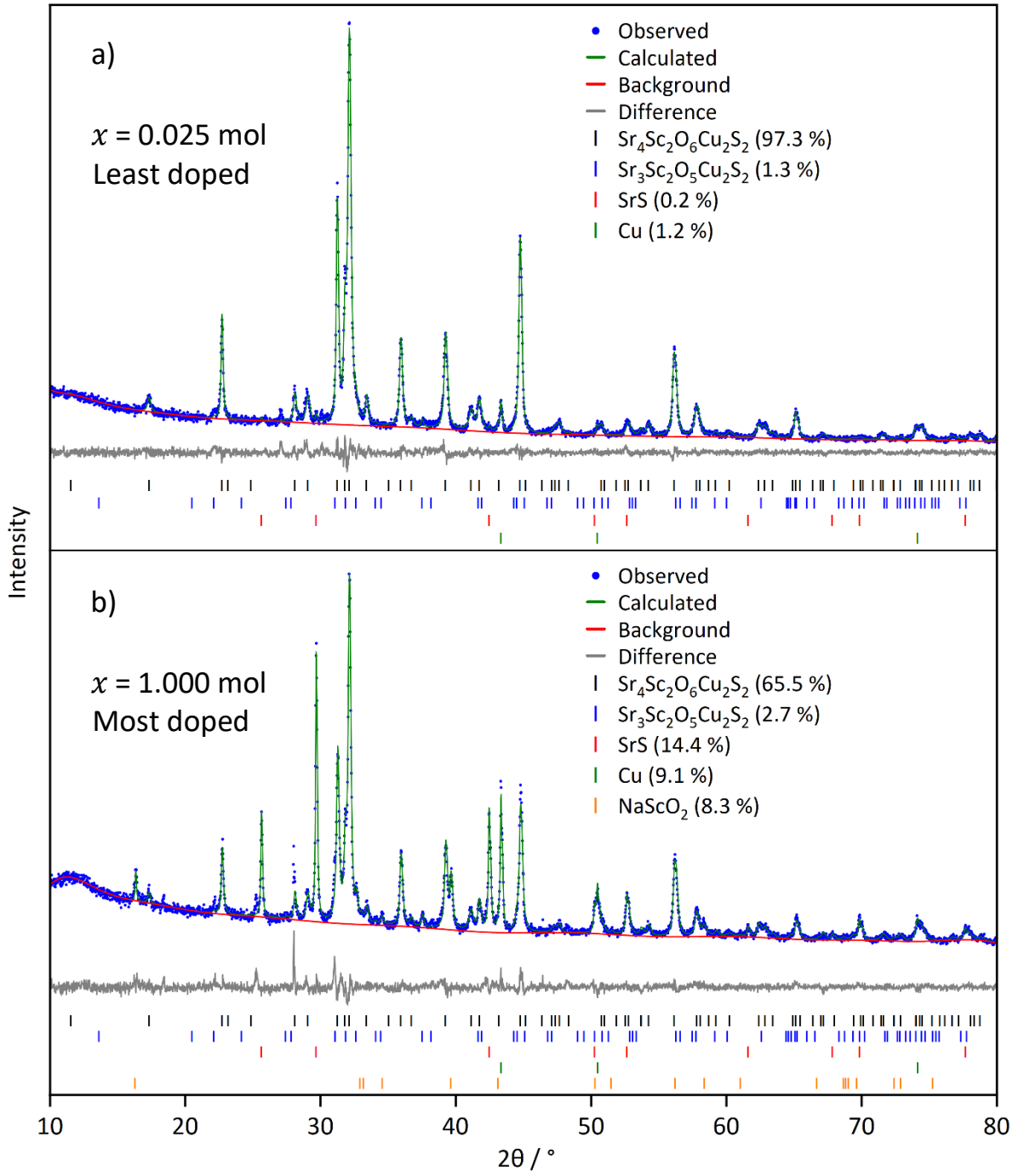

Figure 152 *Powder X-ray diffractograms of a) the least doped sample of the series with target composition $(Sr_{3.975}Na_{0.025})Sc_2O_6Cu_2S_2$, and b) the most doped sample of the series with target composition $(Sr_{3.000}Na_{1.000})Sc_2O_6Cu_2S_2$ (both space group P4/nmm) after 36 hours of heating at 500 - 550 °C. The small blue circles represent the observed diffracted intensities, the green lines represent the Rietveld refined calculated models, the red lines represent the backgrounds, and the grey lines represent the differences between observed and calculated intensities. The black tick marks show the reflections of the refined model of $Sr_4Sc_2O_6Cu_2S_2$, whilst the blue, red, green and orange tick marks represent refined impurity phases $Sr_3Sc_2O_5Cu_2S_2$, SrS, Cu and $NaScO_2$ respectively. Weight fractions for each phase are cited in the figure legends.*
a) Duration: 45 minutes. Data points: 3457. Interval: 0.02 °. GOF: 1.29. R_{wp}: 5.892 %.
b) Duration: 45 minutes. Data points: 3457. Interval: 0.02 °. GOF: 1.35. R_{wp}: 6.016 %.

Counter to the declining purities, the lack of any impurity phases containing sodium in any sample from x = 0 through to x = 0.200 mol suggests strong incorporation of sodium into $Sr_4Sc_2O_6Cu_2S_2$ in this range. That said, the perpetual presence of $Sr_3Sc_2O_5Cu_2S_2$ in every sample should not be dismissed as a competing source of dopant incorporation, as it has been shown in *Section 3.3.3*, that sodium is readily incorporated into this phase. A dopant incorporation plot created using this data shows full incorporation until x = 0.200 mol followed by a plateau, with little difference in maximum possible dopant content between x = 0.500 mol and 1.000 mol. These two samples have maximum actual x values of 0.389 mol and 0.449 mol. Incorporation data is tabulated in Table 56 of *Appendix B.2.1*.

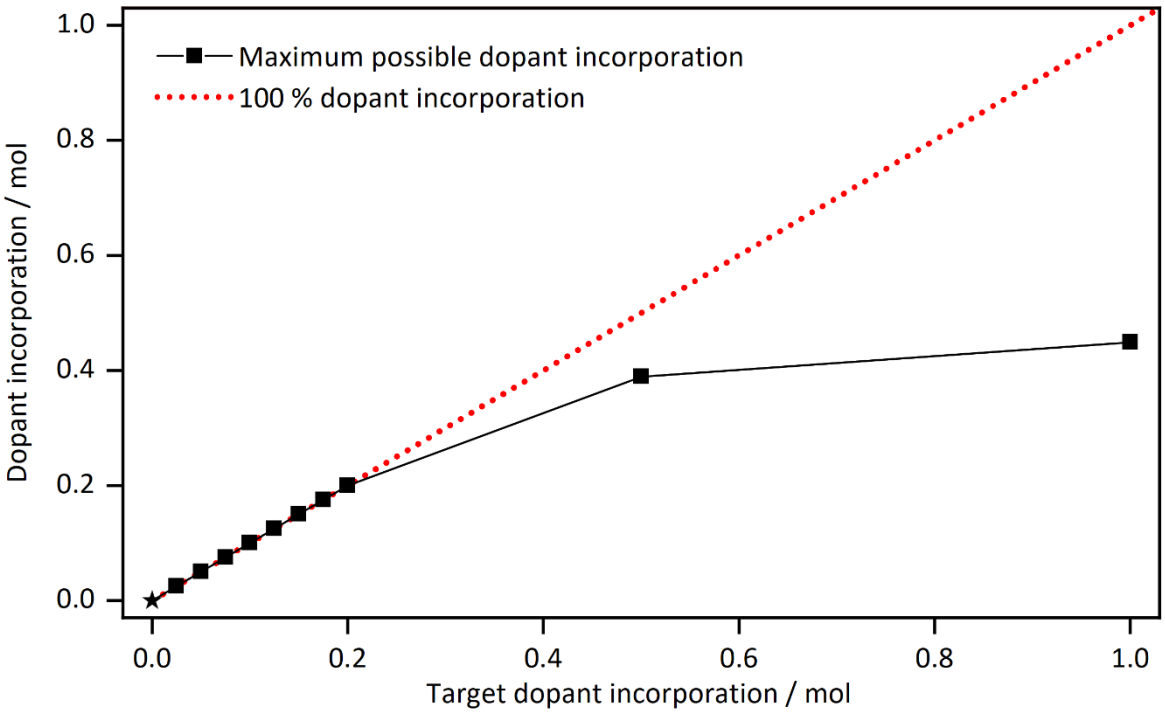

Figure 153 The calculated maximum possible levels of dopant incorporation into the $(Sr_{4-x}Na_x)Sc_2O_6Cu_2S_2$ MALMs. Values were derived from the wt % of the sodium-containing impurities of each sample. The pristine material $Sr_4Sc_2O_6Cu_2S_2$ is included as a reference at x = 0 mol and is represented by a star. The red dashed line represents 100 % dopant incorporation into the MALM, statistically no values may surpass this line. The black data points are the estimated upper bound of dopant incorporation for each sample.

Despite promising evidence of sodium incorporation into $Sr_4Sc_2O_6Cu_2S_2$, the measured electrical conductivities, shown in Figure 154 on the next page, are very poor. Each of the ten samples measured approximately 10^{-5} S cm^{-1}, with no discernible trend across the series and an unusual level of consistency. It is believed that these are not the true values of conductivity, but rather suppressed by poor sample density due to an inability to sufficiently anneal these samples at high temperatures. The incorporation of sodium suggests an increase in charge carriers, but conductivity remains limited by poor mobility due to porous materials with small particles and therefore many grain boundaries to obstruct the transport of holes.

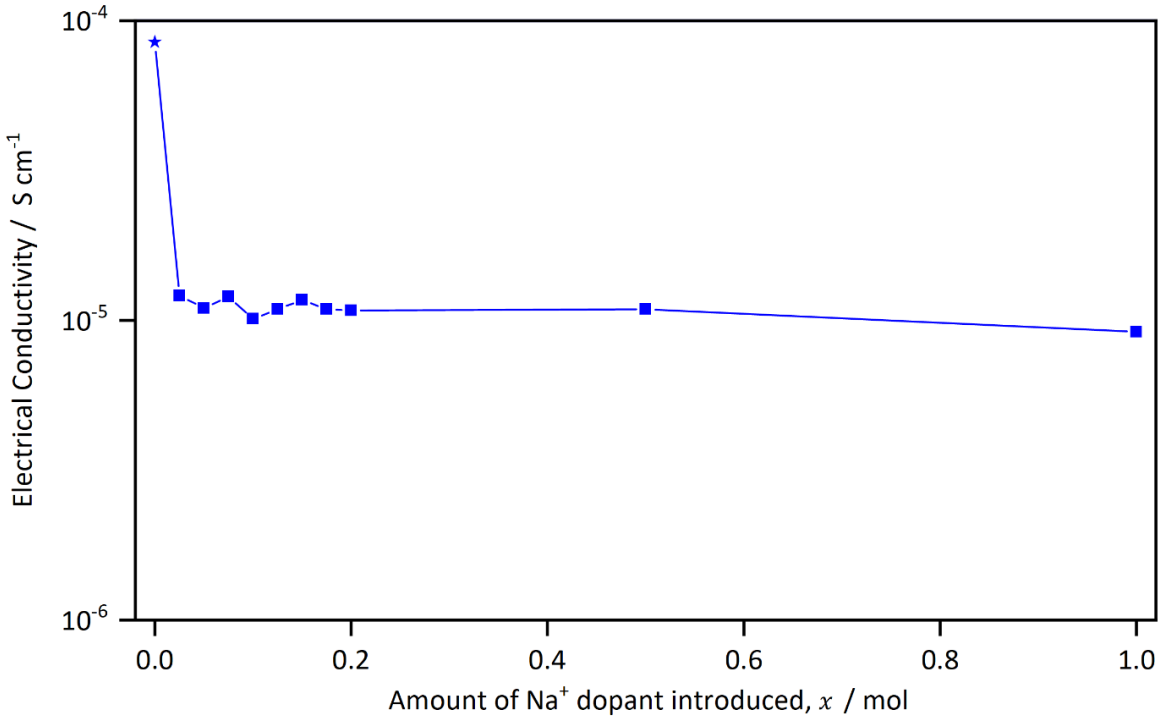

Figure 154 *The electrical conductivities of the ten sodium doped MALMs in the $(Sr_{4-x}Na_x)Sc_2O_5Cu_2S_2$ series, represented on a log_{10} scale. The pristine material $Sr_4Sc_2O_6Cu_2S_2$ is included as a reference at x = 0 mol and is represented by a star. All values are derived from van der Pauw 4 probe resistivity measurements of 8mm diameter annealed pellet samples.*

PXRD analysis post annealing revealed some, but only very small, degradation of the 426 samples to the 325 phase. It is clear that these annealing conditions are insufficient: too mild to anneal the samples adequately, with potentially multiple orders of magnitude of electrical conductivity improvement unable to be realised, but conditions any harsher will produce sample degradation.

With no valid method by which to anneal these materials, this line of research was postponed in lieu of the more promising and compliant 325 MALMs. That was until a novel method of annealing, termed the 'flash anneal technique', was discovered by accident.

4.3.4 The Flash Anneal Technique

A pelletised sample of pristine $Sr_4Sc_2O_6Cu_2S_2$ was synthesised in a 12 hour 550 °C reaction whilst attempting to optimise the synthesis conditions. This was the second of two identical heat cycles, which would see the reaction to completion. The box furnace which facilitated this reaction was then used for another short experiment at 1000 °C with the pristine $Sr_4Sc_2O_6Cu_2S_2$ ampoule left unknowingly within it. After a temperature ramp comprising multiple hours, the material had been held at 1000 °C for 20 minutes before cooling naturally to room temperature. When discovered, it was assumed that this sample would be significantly if not fully degraded, but was explored by PXRD as a curiosity. The sample was found to be 93.6 % pure from Reitveld refinement, as shown in Figure 155, surviving the accidental anneal with minimal, if any, degradation.

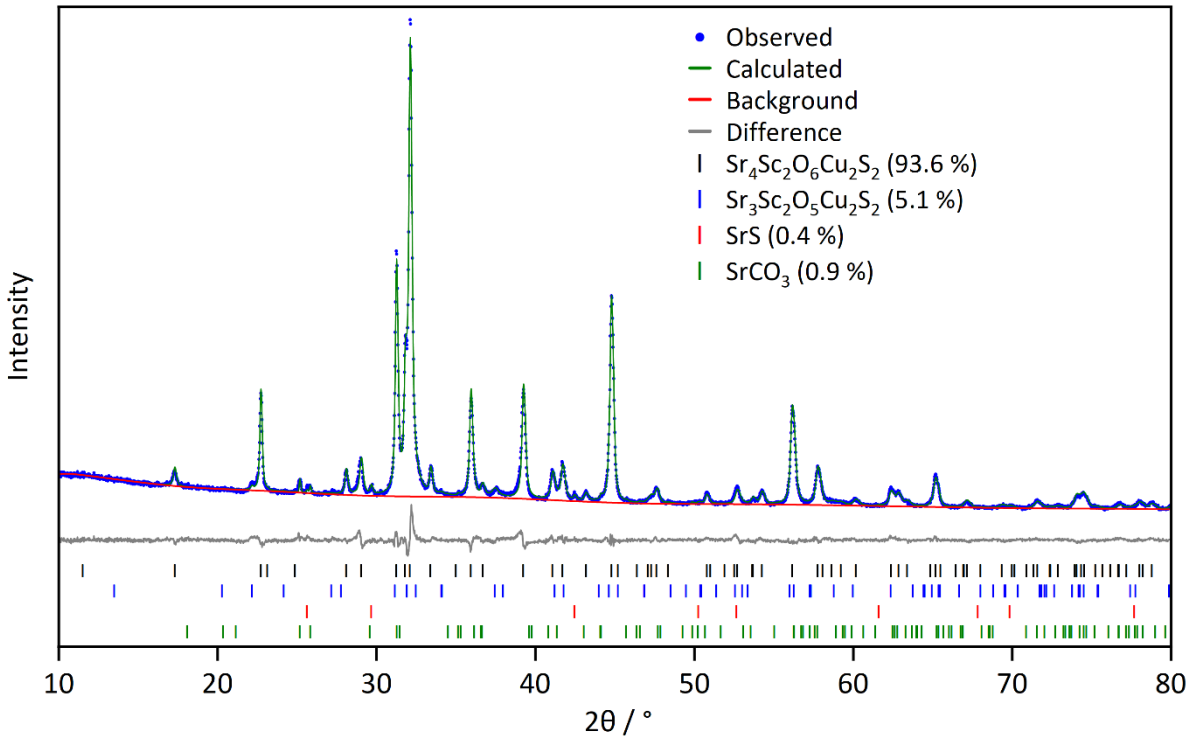

Figure 155 *Powder X-ray diffractogram of material with target composition $Sr_4Sc_2O_6Cu_2S_2$ (space group P4/nmm) after annealing for 10 - 30 minutes at 1000 °C. The small blue circles represent the observed diffracted intensity, the green line represents the Rietveld-refined calculated model, the red line represents the background, and the grey line represents the difference between observed and calculated intensities. The black tick marks show the reflections of the refined model of $Sr_4Sc_2O_6Cu_2S_2$ (93.6 %), whilst the blue, red and green tick marks represent refined impurity phases $Sr_3Sc_2O_5Cu_2S_2$ (5.1 %), SrS (0.4 %) and $SrCO_3$ (0.9 %) respectively.*
Duration: 3 hours. Data points: 4444. Interval: 0.02 °. GOF: 1.67. R_{wp}: 4.158 %.

This inadvertent high temperature reaction revealed a gap in the conditions explored for sample annealing. Short annealing times had been trialled, those on the scale of 2 to 6 hours, short compared to the usual 12 or 24 hour heat cycles. An anneal on the scale of *minutes* had not been considered. It is impossible to know the product purity before the 1000 °C heating, but the 426 to 325 irreversibility dictates it can only be equal to or greater than 93.6 %, therefore any degradation was small. This suggests that the scandium 426 materials may be invulnerable from 325 conversion over this very short time scale, permitting a small window to densify the pellet before the onset of conversion. These are by no means ideal annealing conditions, but may allow for a truer realisation of electrical conductivity.

Preliminary testing on pristine MALMs supported the initial test, showing reduced degradation compared to regular 'slow and hot' annealing, but greater densification than a low temperature anneal (or no anneal). This process, which was termed the 'flash anneal' due to its short and intense nature, appears to be a sweet-spot in conditions to optimise the trade-off between purity and pellet density.

Reattempting the large doping range was deemed an inefficient use of time especially with an unproven novel technique, so samples of composition $(Sr_{3.9}Na_{0.1})Sc_2O_6Cu_2S_2$ and $(Sr_{3.9}K_{0.1})Sc_2O_6Cu_2S_2$ were targeted instead, in line with the accompanying gallium and indium materials in our publication.

The value of x = 0.1 (which when expressed in the empirical '213' notation is x = 0.05) was selected based upon previous work investigating the 212 MALM class, wherein this value was found to be the optimum.[39] The work of *Chapter 3* which suggests, at least in the case of the 325 class, that higher dopant levels are likely more optimal, was performed after the fact. Exploration of higher dopant levels to explore saturation levels is reserved as future work in this field, but will inevitably be fraught with significant 426 to 325 conversion unless a more stable method of annealing is established.

4.3.5 Flash Annealed Sodium and Potassium Doped $Sr_4Sc_2O_6Cu_2S_2$

Akin to the previously described series, $(Sr_{3.9}Na_{0.1})Sc_2O_6Cu_2S_2$ was synthesised according to Equation 59. A short 6 hour heat at 180 °C initiated the reaction to incorporate the elemental sulfur, followed by two 12 hour reactions at 550 °C. This produced a high purity (95.4 wt %) material with no competing $Sr_3Sc_2O_5Cu_2S_2$ phase present and no impurities containing the dopant. At this dopant level full incorporation of sodium is expected, in agreement with the observed experimental data.

Equation 59 $3\ SrO + Sc_2O_3 + Cu_2S + 0.9\ SrS + 0.05\ [Na_2S + S] \rightarrow (Sr_{3.9}Na_{0.1})Sc_2O_6Cu_2S_2$

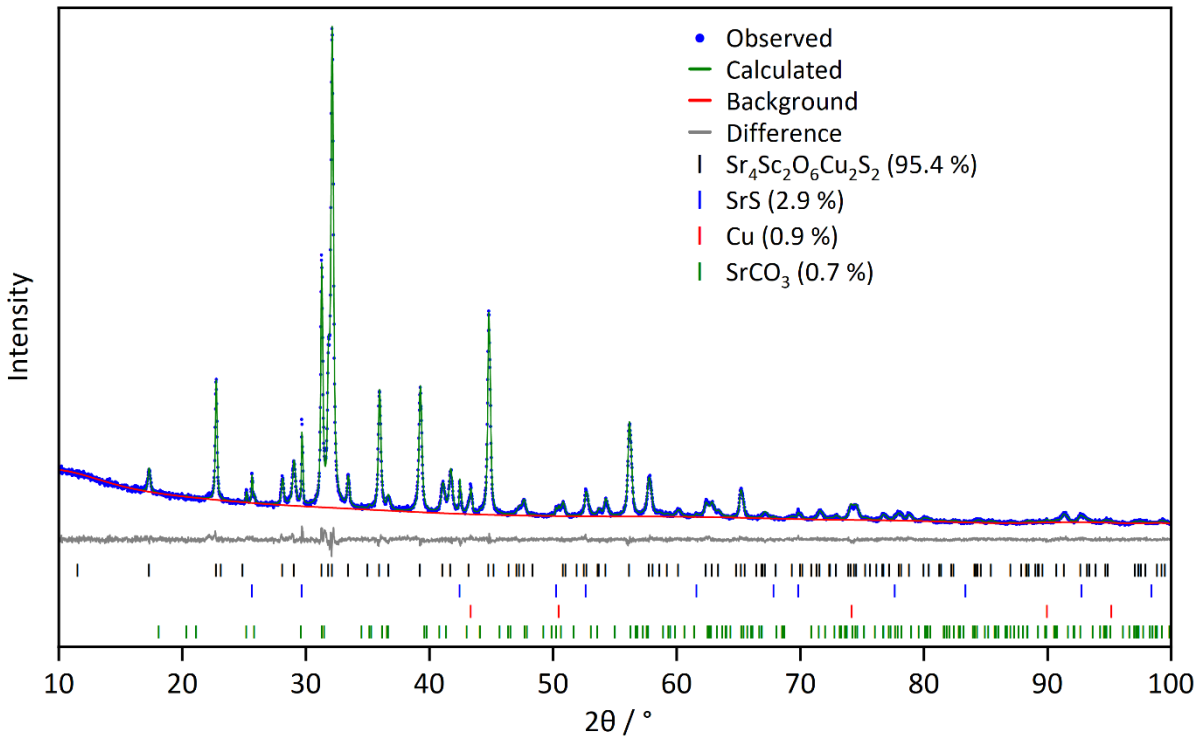

Figure 156 Powder X-ray diffractogram of material with target composition $(Sr_{3.9}Na_{0.1})Sc_2O_6Cu_2S_2$ (space group P4/nmm) after 24 hours of heating at 550 °C. The small blue circles represent the observed diffracted intensity, the green line represents the Rietveld-refined calculated model, the red line represents the background, and the grey line represents the difference between observed and calculated intensities. The black tick marks show the reflections of the refined model of $Sr_4Sc_2O_6Cu_2S_2$ (95.4 %), whilst the blue, red and green tick marks represent refined impurity phases SrS (2.9 %), Cu (0.9 %) and $SrCO_3$ (0.7 %) respectively. Duration: 3 hours. Data points: 4444. Interval: 0.02 °. GOF: 1.22. R_{wp}: 3.523 %.

The potassium doped analogue $(Sr_{3.9}K_{0.1})Sc_2O_6Cu_2S_2$ was synthesised in parallel, Equation 60, with the resulting Rietveld refined PXRD presented in Figure 157 below. This material was extremely similar to the sodium phase in its composition and purity, and neither had dopant-containing impurities.

Equation 60 $3\ SrO + Sc_2O_3 + Cu_2S + 0.9\ SrS + 0.05\ [K_2S + S] \rightarrow (Sr_{3.9}K_{0.1})Sc_2O_6Cu_2S_2$

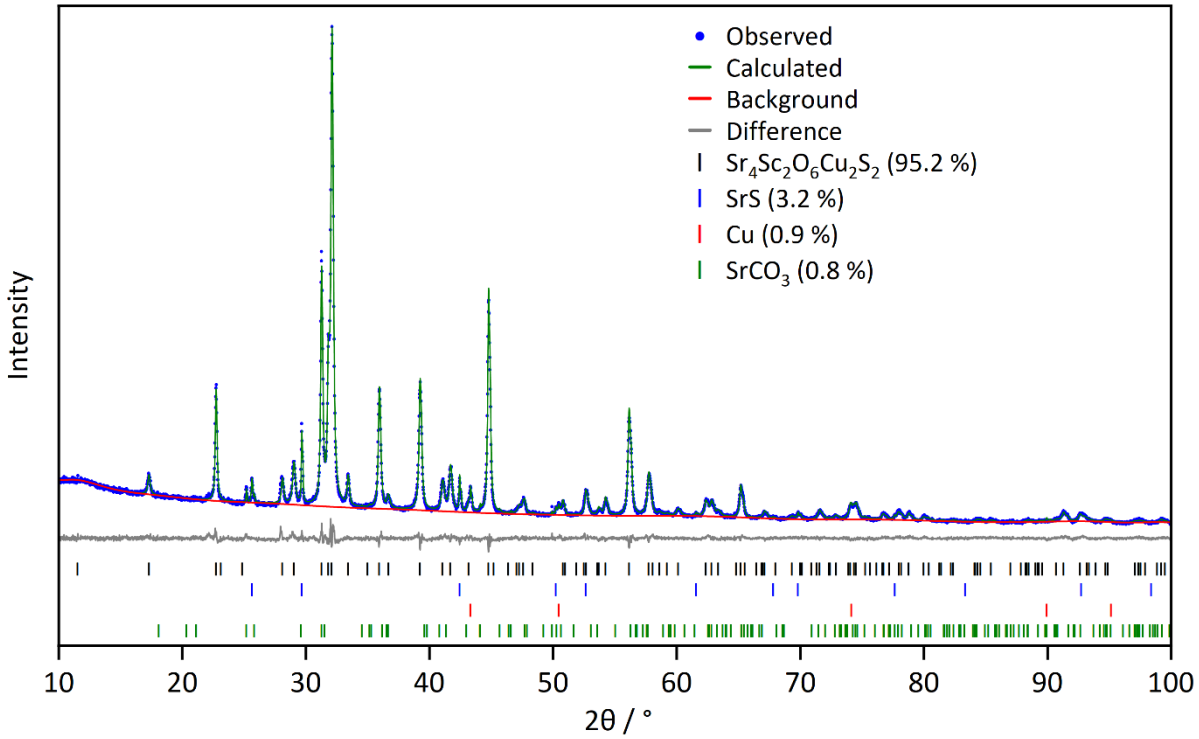

Figure 157 *Powder X-ray diffractogram of material with target composition $(Sr_{3.9}K_{0.1})Sc_2O_6Cu_2S_2$ (space group P4/nmm) after 24 hours of heating at 550 °C. The small blue circles represent the observed diffracted intensity, the green line represents the Rietveld-refined calculated model, the red line represents the background, and the grey line represents the difference between observed and calculated intensities. The black tick marks show the reflections of the refined model of $Sr_4Sc_2O_6Cu_2S_2$ (95.2 %), whilst the blue, red and green tick marks represent refined impurity phases SrS (3.2 %), Cu (0.9 %) and $SrCO_3$ (0.8 %) respectively. Duration: 3 hours. Data points: 4444. Interval: 0.02 °. GOF: 1.39. R_{wp}: 3.631 %.*

8 mm pellets of each sample (approximately 0.15 grams) were pressed, sealed within ampoules, and densified by the flash anneal technique to 800 °C for 30 minutes. The conductivity of each was then determined by the van der Pauw method, after which an unpainted part of each pellet was reground for PXRD to assess for a drop in purity during annealing.

The sodium sample $(Sr_{3.9}Na_{0.1})Sc_2O_6Cu_2S_2$ recorded an electrical conductivity of 2.22×10^{-4} S cm^{-1}, an improvement over the pristine (8.48×10^{-5} S cm^{-1}) and the larger series in *Section 4.3.3*. The flash annealing technique yielded a modest pellet density of only 66 %, but crucially a negligible purity drop from 95.4 % to 93.6 %, remaining a compromise between the two competing variables. The potassium sample recorded a slight conductivity drop to 2.05×10^{-5} S cm^{-1}, but retained a purity of 91.6 % after annealing. All pre and post anneal PXRD data as well as optical data is listed in *Appendix B.2.*

4.4 $Sr_4Sc_2O_6Cu_2Se_2$

4.4.1 Pristine Synthesis

The synthesis of the selenide MALM $Sr_4Sc_2O_6Cu_2Se_2$ was very similar to that of the sulfide. Though the sulfide has stood as the focus of discussions thus far, both $Sr_4Sc_2O_6Cu_2S_2$ and $Sr_4Sc_2O_6Cu_2Se_2$ were hindered similarly by the thermodynamic competition of their 325 phases, and all previous descriptions of this delicate balance for $Sr_4Sc_2O_6Cu_2S_2$ apply also to $Sr_4Sc_2O_6Cu_2Se_2$. This material was targeted on a 1 gram scale by conventional solid-state chemistry according to Equation 61:

Equation 61 $3\ SrO + Sc_2O_3 + Cu_2Se + SrSe \rightarrow Sr_4Sc_2O_6Cu_2Se_2$

A slightly higher temperature of 650 °C for 24 hours was found to be the optimum reaction conditions for this pristine sample, again with a 24 hour powder pre-heat at 500 °C and an intermediate regrind. These conditions produced a purity of 98.5 %, with a small 1.2 % $Sr_3Sc_2O_5Cu_2Se_2$ impurity, and a trace of unreacted SrSe precursor, see Figure 158. There is one report of this material in literature, a 2018 luminescence study by Iwasa et al, who also cite a reaction temperature of 650 °C but for a singular 40 hour heat cycle.[89]

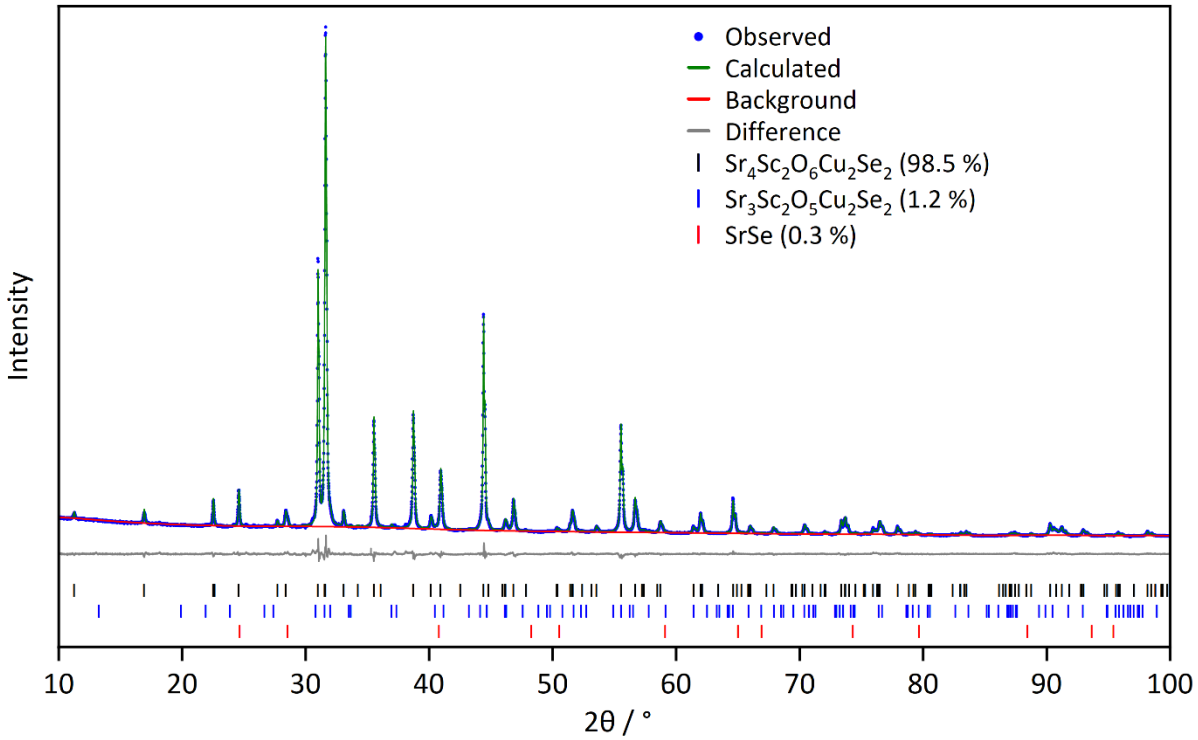

Figure 158 *Powder X-ray diffractogram of material with target composition $Sr_4Sc_2O_6Cu_2Se_2$ (space group P4/nmm) after 48 hours of heating at 500 - 650 °C. The small blue circles represent the observed diffracted intensity, the green line represents the Rietveld-refined calculated model, the red line represents the background, and the grey line represents the difference between observed and calculated intensities. The black tick marks show the reflections of the refined model of $Sr_4Sc_2O_6Cu_2Se_2$ (98.5 %), whilst the blue and red tick marks represent refined impurity phases $Sr_3Sc_2O_5Cu_2Se_2$ (1.2 %), and SrSe (0.3 %) respectively.*
Duration: 16 hours. Data points: 8887. Interval: 0.01 °. GOF: 3.72. R_{wp}: 3.107 %.

$Sr_4Sc_2O_6Cu_2Se_2$ is expected to exhibit both a smaller band gap but a greater conductivity versus the sulfide, in line with the trend observed of more diffuse orbitals across the series S to Se to Te, producing a better overlap with copper as described in *Section 1.2.3.3*. This was found to be the case. $Sr_4Sc_2O_6Cu_2Se_2$ has a band gap of 2.95 eV, Figure 159, and an electrical conductivity of 6.29×10^{-4} S cm^{-1}, which is still relatively low but approximately 7 times greater than the sulfide.

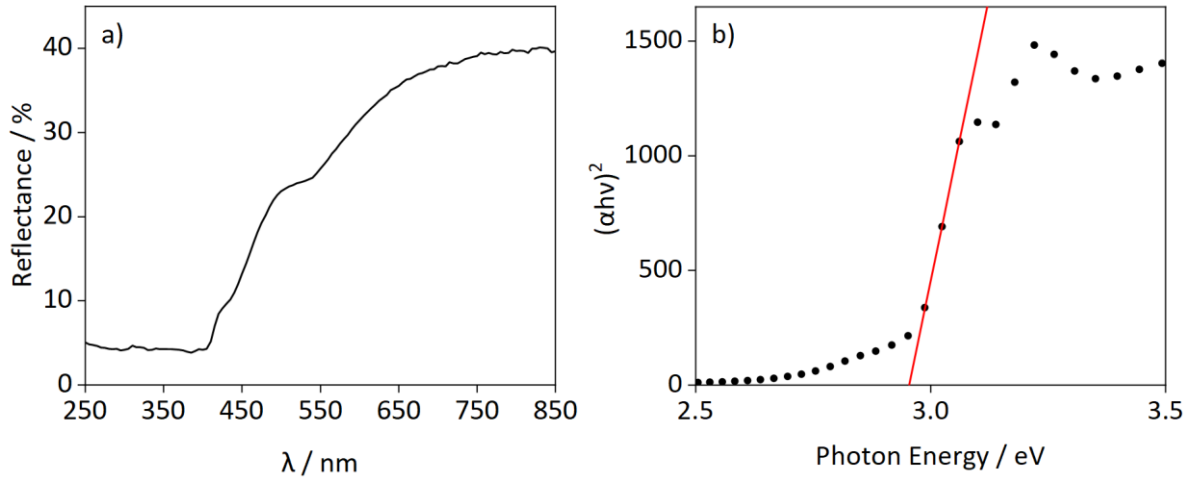

Figure 159 *UV-Vis spectrometry data for material with target composition $Sr_4Sc_2O_6Cu_2Se_2$ after 48 hours of heating at 500 - 650 °C. Plot a) is the raw diffuse reflectance data, and plot b) is the associated magnified Tauc plot for this region, where the intercept between the red extrapolated tangent line and the x-axis is used to estimate an optical band gap of 2.95 eV, which corresponds to 420 nm.*

4.4.2 Flash Annealed Sodium and Potassium Doped $Sr_4Sc_2O_6Cu_2Se_2$

An x = 0.1 sodium doped sample of $Sr_4Sc_2O_6Cu_2Se_2$ with composition $(Sr_{3.9}Na_{0.1})Sc_2O_6Cu_2Se_2$ was synthesised according to Equation 62 below. A purity of 95.2 % was achieved after an initial heat cycle at 180 °C and two 12 hour heat cycles at 550 °C, analogous conditions to the sulfide doped samples. No 325 nor dopant-containing impurities were detected, as shown in Figure 160.

Equation 62 $3\ SrO + Sc_2O_3 + Cu_2Se + 0.9\ SrSe + 0.05\ [Na_2Se + Se] \rightarrow (Sr_{3.9}Na_{0.1})Sc_2O_6Cu_2Se_2$

A pellet of this material was flash annealed at 800 °C for 30 minutes, which caused a small purity drop of approximately 3 %. The pellet density was measured to be 68 %, a value which would usually be poor for an annealed sample, but is respectable given the relatively tame conditions of the flash anneal technique. This yielded an electrical conductivity of 2.14×10^{-3} S cm^{-1}, an impressive three-fold increase over the pristine.

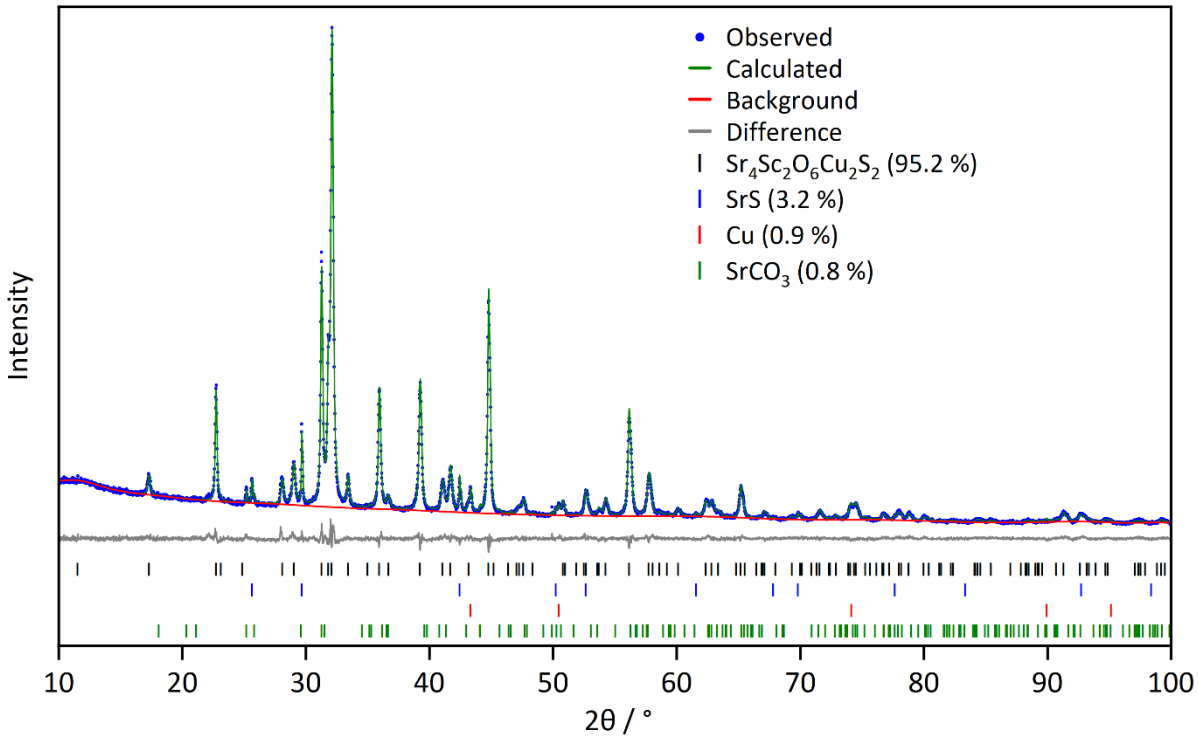

Figure 160 *Powder X-ray diffractogram of material with target composition $(Sr_{3.900}K_{0.100})Sc_2O_6Cu_2S_2$ (space group P4/nmm) after 24 hours of heating at 550 °C and before flash annealing. The small blue circles represent the observed diffracted intensity, the green line represents the Rietveld-refined calculated model, the red line represents the background, and the grey line represents the difference between observed and calculated intensities. The black tick marks show the reflections of the refined model of $Sr_4Sc_2O_6Cu_2S_2$ (95.2 %), whilst the blue, red and green tick marks represent refined impurity phases SrS (3.2 %), Cu (0.9 %) and $SrCO_3$ (0.8 %) respectively.*
Duration: 3 hours. Data points: 4444. Interval: 0.02 °. GOF: 1.39. R_{wp}: 3.631 %.

Finally, the potassium doped $(Sr_{3.9}K_{0.1})Sc_2O_6Cu_2Se_2$ was synthesised according to Equation 63. This material had a good purity of 95.1 %, but contained a 1.3 % trace of potassium impurity KCu_3Se_2. This accounts for approximately one quarter of the supplied potassium, which at x = 1 was a quantity usually fully incorporated by a MALM, indicating poor tolerance of $Sr_4Sc_2O_6Cu_2Se_2$ to K^+ doping. The calculated maximum possible x is 0.073. No 325 was detected in the pre-annealed material.

Equation 63 $$3\ SrO + Sc_2O_3 + Cu_2Se + 0.9\ SrSe + 0.05\ [K_2Se + Se] \rightarrow (Sr_{3.9}K_{0.1})Sc_2O_6Cu_2Se_2$$

A 30 minute flash anneal yielded a pellet with a density of 66 % of the theoretical crystal density, and a good conductivity of 2.30×10^{-2} S cm^{-1}.

Figure 161 on the next page shows the Rietveld refined diffractogram of the powder sample pre-anneal. The associated post-anneal diffractograms of all four published samples in this section are omitted here for conciseness but can be found can be found in *Appendix B.2*.

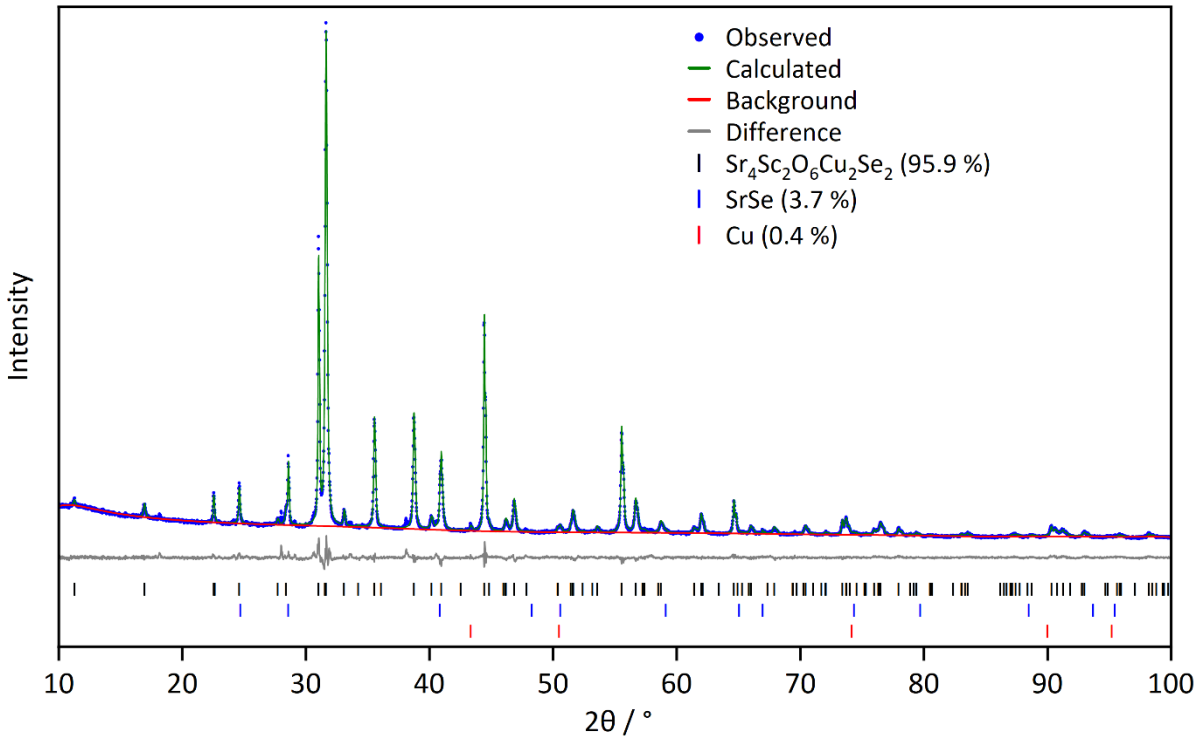

Figure 161 *Powder X-ray diffractogram of material with target composition $(Sr_{3.900}Na_{0.100})Sc_2O_6Cu_2Se_2$ (space group P4/nmm) after 24 hours of heating at 550 °C and before flash annealing. The small blue circles represent the observed diffracted intensity, the green line represents the Rietveld-refined calculated model, the red line represents the background, and the grey line represents the difference between observed and calculated intensities. The black tick marks show the reflections of the refined model of $Sr_4Sc_2O_6Cu_2Se_2$ (95.9 %), whilst the blue and red tick marks represent refined impurity phases SrSe (3.7 %) and Cu (0.4 %) respectively.*
Duration: 3 hours. Data points: 4444. Interval: 0.02 °. GOF: 1.59. R_{wp}: 4.412 %.

The properties of the four doped 426 MALMs described throughout this section are tabulated below in Table 9 for comparison, particularly those properties which pertain to the novel flash anneal process. It can be observed that the flash anneal maintains sample purity with only a 2 - 4 % reduction in each case, which is usually attributed to a conversion from $Sr_4Sc_2O_6Cu_2Ch_2$ to $Sr_3Sc_2O_5Cu_2Ch_2$. Pellet densities are unfortunately poor, likely still severely limiting the conductivities.

Table 9 *A comparison of the four doped samples of $Sr_4Sc_2O_6Cu_2Ch_2$ densified by flash anneal.*

Sample	Purity / wt %		Conductivity / S cm^{-1}	Density / %
	Pre anneal	Post anneal		
$(Sr_{3.9}Na_{0.1})Sc_2O_6Cu_2S_2$	95.4	93.6	2.22×10^{-4}	64.99
$(Sr_{3.9}K_{0.1})Sc_2O_6Cu_2S_2$	95.2	91.6	2.05×10^{-5}	67.29
$(Sr_{3.9}Na_{0.1})Sc_2O_6Cu_2Se_2$	95.6	92.7	2.14×10^{-3}	68.40
$(Sr_{3.9}K_{0.1})Sc_2O_6Cu_2Se_2$	95.1	91.5	2.30×10^{-2}	66.47

4.5 Comparison to the Gallium and Indium Analogues

In pursuit of promising candidates exhibiting *p*-type conductivity, the scandium MALMs are compared to the gallium and indium analogues of $Sr_4B_2O_6Cu_2Ch_2$. The syntheses of these four materials, which were produced by a colleague, are briefly outlined here. In the Rietveld refinement of novel materials or those with unpublished structures, the structural model of $Sr_4Ga_2O_6Cu_2S_2$ was used as a reference,[63] obtained as a CIF from the ICSD, with atom site substitutions to model the target structure. The Rietveld refined diffractograms of $Sr_4Ga_2O_6Cu_2S_2$ and $Sr_4Ga_2O_6Cu_2Se_2$ are compared in Figure 162 on the next page, whilst $Sr_4In_2O_6Cu_2S_2$ and $Sr_4In_2O_6Cu_2Se_2$ are compared in Figure 163.

The synthesis of $Sr_4Ga_2O_6Cu_2S_2$ was performed at 700 °C according to Equation 64, producing a purity of 99.1 wt % alongside $Sr_3Ga_2O_6$ and SrS impurities. In literature this synthesis has only been reported at higher temperatures of 800 - 950 °C,[59, 63, 67] including an example where sodium doping improves the electrical conductivity of $Sr_4Ga_2O_6Cu_2S_2$ from 2.2×10^{-4} to 2.4×10^{-2} S cm^{-1}.[67] There are no known gallium 325 phases,[59] so the syntheses of $Sr_4Ga_2O_6Cu_2Ch_2$ were not hampered by the 426 - 325 thermodynamic balance described in the scandium case.

Equation 64 $3\ SrO + Ga_2O_3 + Cu_2S + SrS \rightarrow Sr_4Ga_2O_6Cu_2S_2$

$Sr_4Ga_2O_6Cu_2Se_2$ is a novel MALM reported in our publication for the first time and synthesised according to Equation 65. A maximum purity of 97 wt % was achieved following synthesis at 830 °C. The remaining sample content is $Sr_3Ga_2O_6$.

Equation 65 $3\ SrO + Ga_2O_3 + Cu_2Se + SrSe \rightarrow Sr_4Ga_2O_6Cu_2Se_2$

$Sr_4In_2O_6Cu_2S_2$ has been reported previously at 750 - 920 °C.[41, 65, 67] Synthesis was achieved here at 800 °C according to Equation 66, with a sample purity of 95.2 wt % and traces of $SrIn_2O_4$ and SrS. Like the gallium MALMs above there is also no known competing 325 phase for this material.

Equation 66 $3\ SrO + In_2O_3 + Cu_2S + SrS \rightarrow Sr_4In_2O_6Cu_2S_2$

Finally, $Sr_4In_2O_6Cu_2Se_2$was synthesised at 700 °C with 96.5 % purity according to Equation 67, in agreement with literature,[65] and with impurities of $SrIn_2O_4$ and SrSe. At the time of writing, and stated within our publication,[64] it was believed that there is no known 325 phase for this system. This assertion later proved incorrect, $Sr_3In_2O_5Cu_2Se_2$ was discovered for the first time during the final phase of the writing of this work, reported in *Chapter 6*.

Equation 67 $3\ SrO + In_2O_3 + Cu_2Se + SrSe \rightarrow Sr_4In_2O_6Cu_2Se_2$

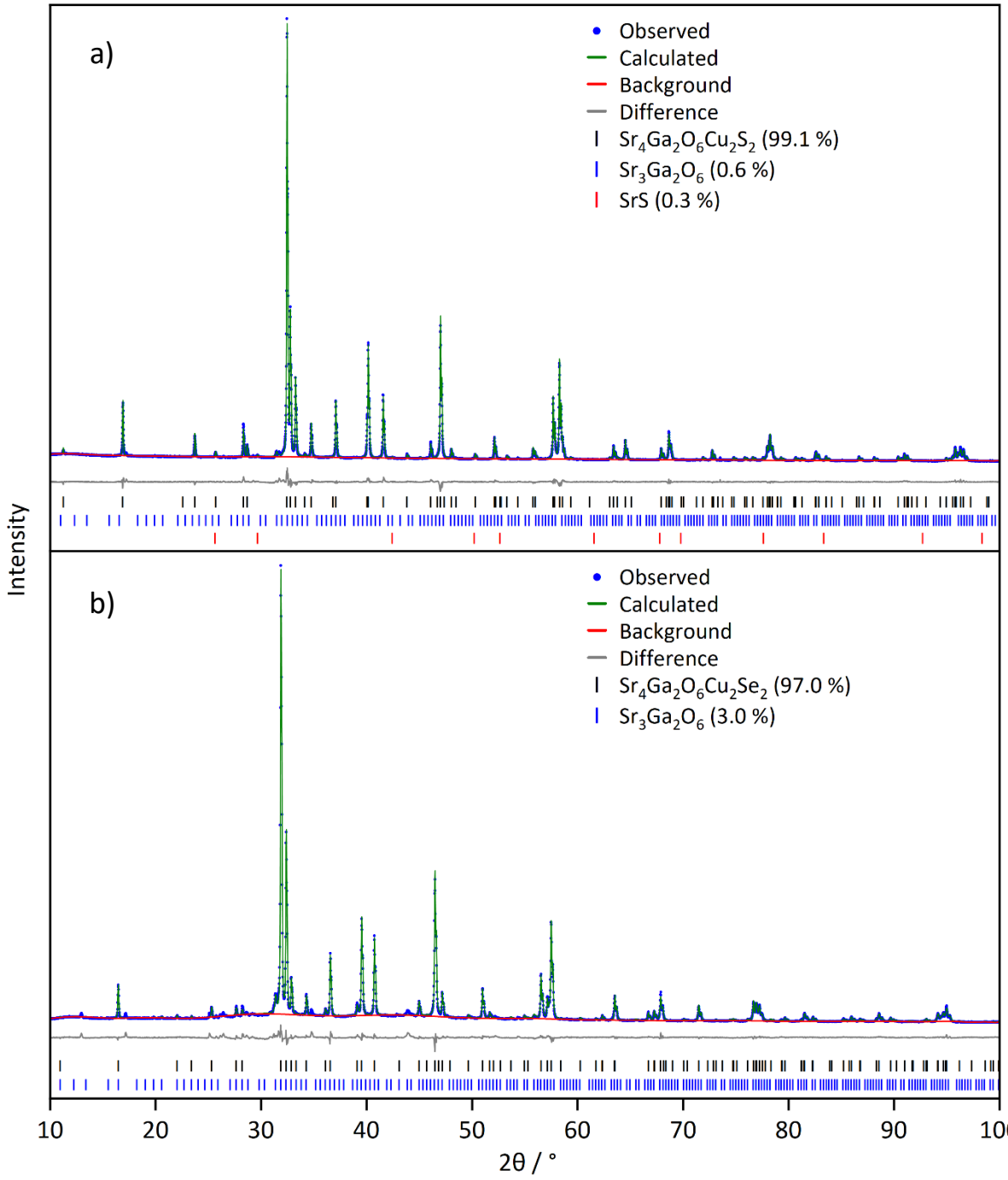

Figure 162 *Powder X-ray diffractogram of materials with target composition a) $Sr_4Ga_2O_6Cu_2S_2$ after synthesis at 700 °C, and b) $Sr_4Ga_2O_6Cu_2Se_2$ after synthesis at 830 °C (both space group P4/nmm). The small blue circles represent the observed diffracted intensity, the green line represents the Rietveld-refined calculated model, the red line represents the background, and the grey line represents the difference between observed and calculated intensities. The black, blue, and red tick marks show the reflections of the refined models of $Sr_4Ga_2O_6Cu_2Ch_2$, $Sr_3Ga_2O_6$, and SrS respectively. Weight fractions for each phase are cited in the figure legends.*
a) Duration: 12 hours. Data points: 8887. Interval: 0.01 °. GOF: 2.28. R_{wp}: 3.16 %.
b) Duration: 12 hours. Data points: 8887. Interval: 0.01 °. GOF: 3.72. R_{wp}: 3.30 %.

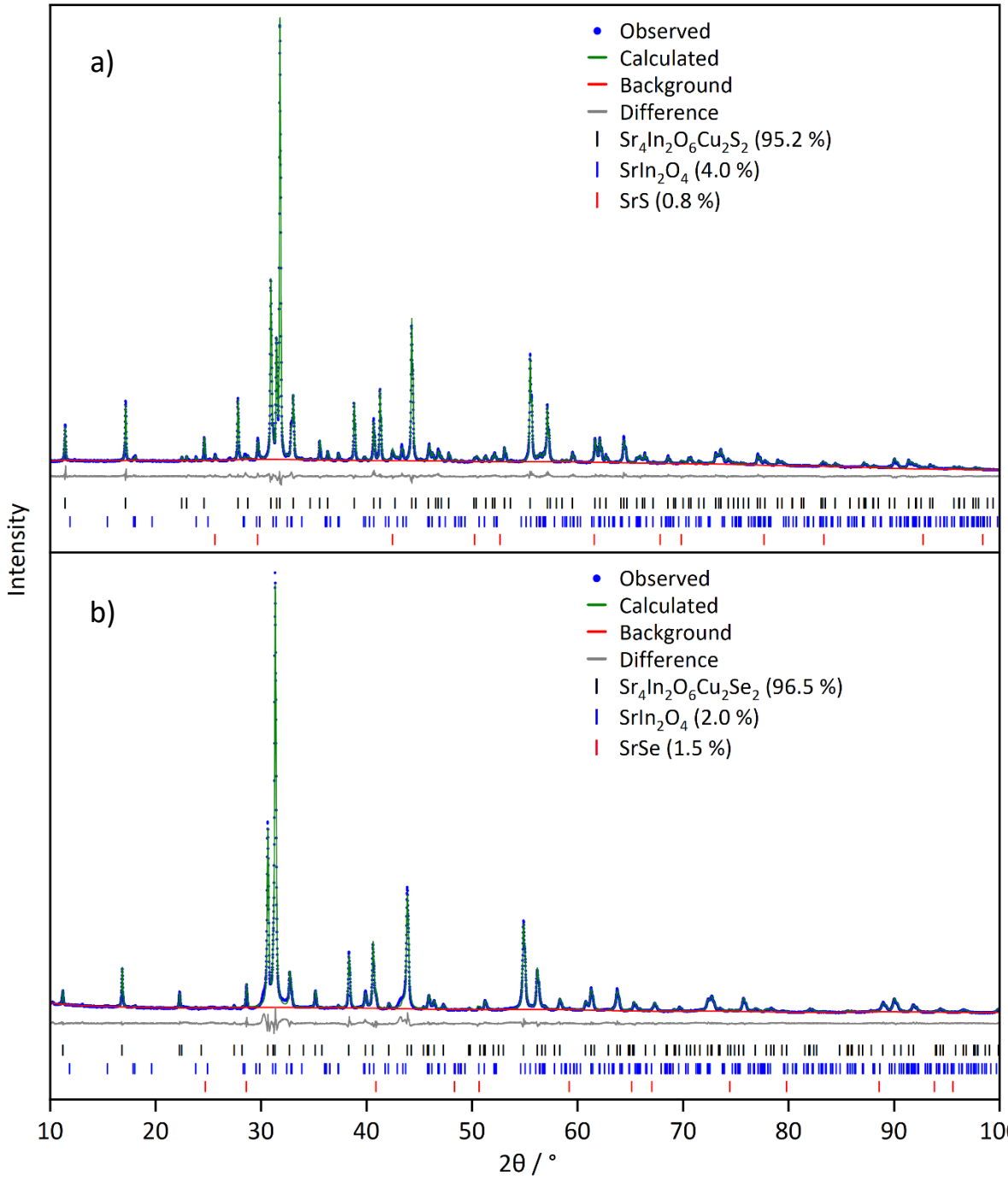

Figure 163 *Powder X-ray diffractogram of materials with target composition a) $Sr_4In_2O_6Cu_2S_2$ after synthesis at 800 °C, and b) $Sr_4In_2O_6Cu_2Se_2$ after synthesis at 700 °C (both space group P4/nmm). The small blue circles represent the observed diffracted intensity, the green line represents the Rietveld-refined calculated model, the red line represents the background, and the grey line represents the difference between observed and calculated intensities. The black, blue, and red tick marks show the reflections of the refined models of $Sr_4In_2O_6Cu_2Ch_2$, $SrIn_2O_4$, and SrCh respectively. Weight fractions for each phase are cited in the figure legends.*
a) Duration: 12 hours. Data points: 8887. Interval: 0.01 °. GOF: 2.09. R_{wp}: 2.81 %.
b) Duration: 12 hours. Data points: 8887. Interval: 0.01 °. GOF: 3.07. R_{wp}: 4.01 %.

Figure 164 below compares the lattice parameter values of the six pristine MALM structures $Sr_4B_2O_6Cu_2Ch_2$ where *B* = Ga, Sc or In, and *Ch* = S or Se, plotted as a function of the *B* ion radius. Ga^{3+} is the smallest at 0.62 Å, then Sc^{3+} at 0.745 Å, and In^{3+} the largest at 0.80 Å. This data supports site substitution at both the *B* and *Ch* sites in this structural family. The trend in *Ch* ion is, in every case, an expansion in unit cell size upon substitution of the smaller (1.84 Å) S^{2-} ion for the larger (1.98 Å) Se^{2-} ion, as would be expected.

A similar trend is observed across increasing *B* ion size from Ga^{3+} to Sc^{3+} to In^{3+}. The scandium MALMs present an unusual case where despite a significantly larger *B* ion, they are smaller in the *c* unit cell parameter than the gallium MALMs. That means substitution of Ga^{3+} for the larger Sc^{3+} actually reduces the unit cell height. This is compensated for by expansion in the *a* direction leading to, as would be expected, an increase in overall cell volume. This is rationalised by the bond angles and lengths, reported in the supplementary information of the publication and graphically illustrated in the main text,[64] which show a reduction in *c* in both the *rock salt* $[Sr_2O_2]$ and geometrically flexible $[Cu_2Ch_2]^{2-}$ units as they expand in *a*, in order to maintain bond length upon the substitution of Ga for Sc. Only the square pyramidal $[BO_5]$ units, of which the *B* atom resides at the centre, increase in *c*.

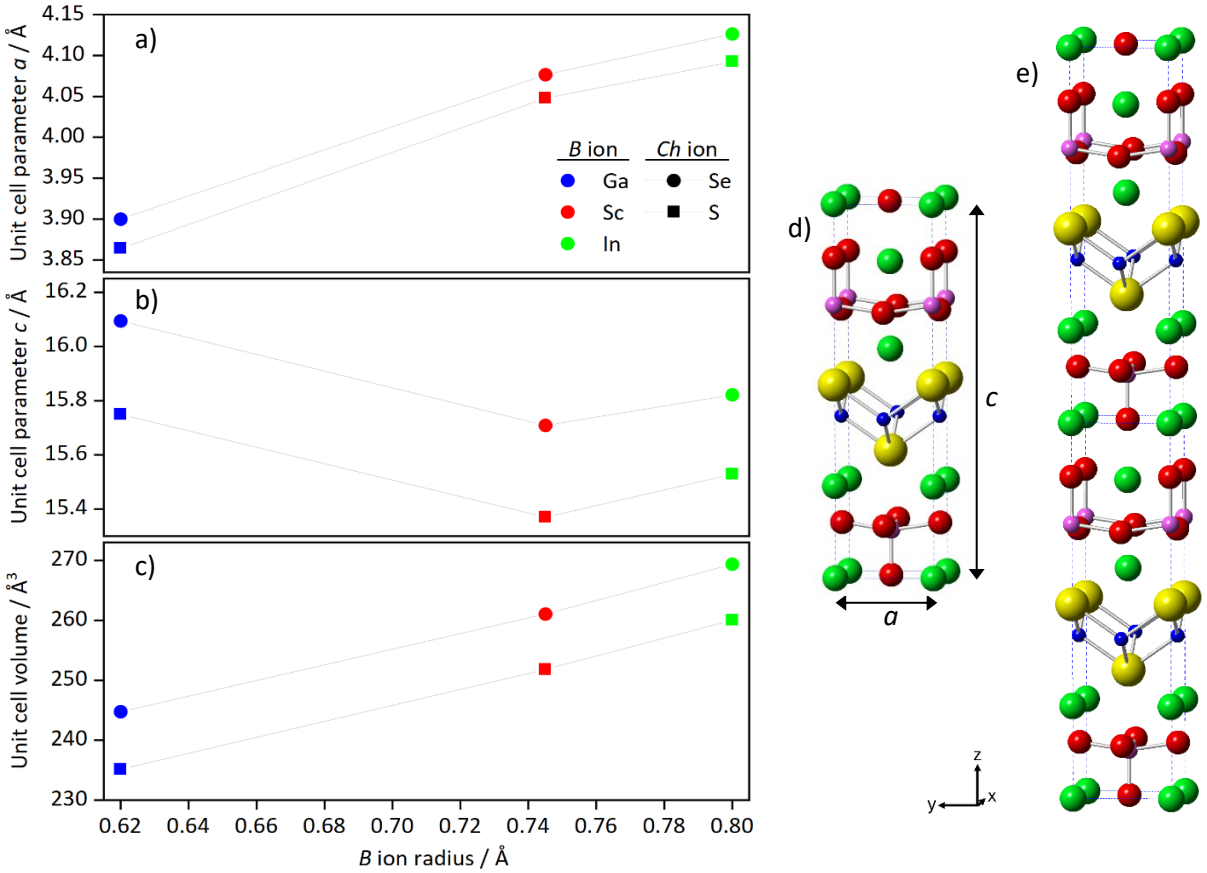

Figure 164 A comparison of the six synthesised pristine $Sr_4B_2O_6Cu_2Ch_2$ materials (B = Ga, Sc, or In. Ch = S or Se), comparing the B ion radii against a) the unit cell a parameter, b) the unit cell c parameter, and c) the unit cell volume. Circles represent selenide materials and squares represent sulfides. Blue, red and green data points represent gallium, scandium and indium MALMs respectively. Part d) depicts a generic unit cell of the 426 structure highlighting the a and c parameters, and e) depicts the 'doubled' unit cell convention used throughout this work.

The optical band gaps of the six materials range from 1.88 eV to 3.17 eV, and are published in Table 10 below. A DFT analysis, details of which can be found within the publication, showed indirect band gaps for each of the six studied MALM systems. Each sulfide MALM exhibited a larger band gap than its selenide analogue because the more electronegative sulfide ion reduces the VBM, which is primarily composed of chalcogenide ions, widening the band gap. The pair of scandium materials synthesised within this work showed the largest band gaps, which the computational analysis rationalised by the composition of the CBM in these MALMs, which is primarily Cu 4*s* and Sc 5*d*. Replacement of Sc^{3+} for Ga^{3+} or In^{3+} lowers the CBM due to the greater electronegativity of Ga and In and hence the lower energy of their VBM contributing orbitals. The electronegativities of Sc, Ga and In are 1.36, 1.81 and 1.71 respectively.[19] There is little difference between Ga and In, hence the similar band gaps.

Table 10 A comparison of the synthesis conditions and physical properties of the six synthesised pristine $Sr_4B_2O_6Cu_2Ch_2$ materials (B = Ga, Sc, or In. Ch = S or Se).

Sample	Reaction Temperature / °C	Purity / wt %	Band gap / eV	Electrical conductivity / S cm^{-1}		
				Pristine	Na doped	K doped
$Sr_4Ga_2O_6Cu_2S_2$	700	99.1	2.43	2.38×10^{-4}	1.61×10^{-2}	2.84×10^{-4}
$Sr_4Ga_2O_6Cu_2Se_2$	830	97.0	1.86	1.54×10^{-1}	1.00×10^{-1}	4.59×10^{-1}
$Sr_4Sc_2O_6Cu_2S_2$	600	99.4	3.17	8.48×10^{-5}	2.22×10^{-4}	2.05×10^{-5}
$Sr_4Sc_2O_6Cu_2Se_2$	650	98.5	2.95	6.29×10^{-4}	2.14×10^{-3}	2.30×10^{-2}
$Sr_4In_2O_6Cu_2S_2$	800	95.2	2.29	1.40×10^{-5}	2.09×10^{-6}	7.52×10^{-6}
$Sr_4In_2O_6Cu_2Se_2$	700	96.5	1.88	1.45×10^{-3}	1.24×10^{-2}	4.35×10^{-3}

Also shown in Table 10 are the measured electrical conductivities. Without the competing phases experienced in the scandium systems, the indium and gallium MALMs could be conventionally annealed at high temperatures (700 - 800 °C) to produce dense pellets.

$Sr_4Ga_2O_6Cu_2S_2$ showed negligible improvement upon doping with K^+, showing an intolerance to full incorporation by the measurement of a KCu_7S_4 impurity which accounts for 13 % of the supplied potassium. In contract, sodium doping produced the largest improvement observed within this data set, of approximately two orders of magnitude.

The most conductive pristine sample was found to be the novel $Sr_4Ga_2O_6Cu_2Se_2$ phase at an impressive 1.54×10^{-1} S cm^{-1}. Doping was not very effective in this case, leaving unidentified impurities in the final samples. Sodium doping resulted in a conductivity decrease and potassium only a small increase up to 4.59×10^{-1} S cm^{-1}. Despite only a small improvement, $(Sr_{3.9}K_{0.1})Ga_2O_6Cu_2Se_2$ was the most conductive sample of the study.

The conductive properties of the indium MALMs were underwhelming. The intolerance of $Sr_4In_2O_6Cu_2S_2$ to Na^+ doping has been reported by Ueda et al,[67] and was confirmed in this work by the purity decrease and inability to improve the conductivity of this material. Each of the Na and K doped $Sr_4In_2O_6Cu_2S_2$ samples exhibited reduced conductivities, on the order of 10^{-6} S cm^{-1}. The selenide analogue $Sr_4In_2O_6Cu_2Se_2$ showed a significantly greater pristine conductivity, more than 100 times that of the sulfide, and demonstrated promising improvement upon incorporation of dopant.

Generally, the selenide materials showed greater conductivities than the sulfides, rationalised by the greater size, dispersion and therefore overlap (with copper) of the selenide orbitals compared to sulfide. A 2024 study concerning the telluride indium MALM $Sr_4In_2O_6Cu_2Te_2$ continues this trend with a superior conductivity of 1.7 S cm^{-1} but a band gap of only 1.2 eV, far too small for commercial transparent conducting applications.[65]

4.6 Conclusions and Future Work

There is an unfortunate inability to realise the true potential of the scandium 426 MALMs. Dopant incorporation appeared promising and sample purities remained very high (often higher than the gallium and indium versions) despite the greatest threat from competing phases. Pellet density was the inhibiting factor, which could not be sufficiently improved by the flash anneal technique in order to measure the true effects of the hole concentration increase.

The flash anneal technique did however prove successful in yielding a compromise between density and purity for the scandium MALMs. To the best of the author's knowledge such a technique has not been reported in literature previously. There is vast room for optimisation, but this technique successfully maintained the purities of these delicate metastable materials, with enough improvement in density to allow some, albeit severely hampered, measurement of their conductive potentials.

Despite their difficult synthetic propensities, only the scandium MALMs possess band gaps large enough to be classified as candidates for *p*-type transparent conductors. $Sr_4Ga_2O_6Cu_2S_2$ has potential, with a band gap of 2.43 eV and therefore semi-transparency to visible light. The indium materials are not only poorly receptive to doping but exhibit band gaps too small for transparent applications.

It is the potassium doped scandium MALM $(Sr_{3.9}K_{0.1})Sc_2O_6Cu_2Se_2$ which presents the best compromise of optical transparency and electrical conductivity, with a large band gap of 2.95 eV and a conductivity of 2.30×10^{-2} S cm^{-1}. This conductivity is too low for commercial applications currently, but the poor density leaves great potential for improvement if a method can be developed which maintains sample purity whilst significantly improving the density, for example spark plasma sintering. There is promising future work in this material if the sample density may be sufficiently improved.

Chapter 5 Solid-State Metathesis: A Viable Pathway to Combinatorial MALM Synthesis?

5.1 Introduction

5.1.1 Solid-State Metathesis

In a conventional ceramic synthesis, all powder precursors are directly combined and subjected to multiple cycles of grinding and heating at high temperatures until the reaction is complete, usually monitored by powder X-ray diffraction. This is the method of synthesis employed for all materials thus far in this work. The synthesis of $Sr_3Fe_2O_5Cu_2Se_2$,[61] a material explored thoroughly throughout this chapter, is given in Equation 68 below to demonstrate this process.

Equation 68 $2\ SrO + SrSe + Fe_2O_3 + Cu_2Se \rightarrow Sr_3Fe_2O_5Cu_2Se_2$

Almost all reports of MALMs and similar solid-state materials in the literature employ the conventional ceramic synthesis. In some cases, one heat cycle is sufficient to yield the thermodynamic, homogenous, phase pure material.

There exists, however, a lesser explored alternate method to synthesise layered materials: solid-state metathesis. Metathesis reactions are a branch of solid-state reactions that involve the exchange of elemental or ionic components between materials, driven by a difference in Gibbs free energy between the precursors and the products.

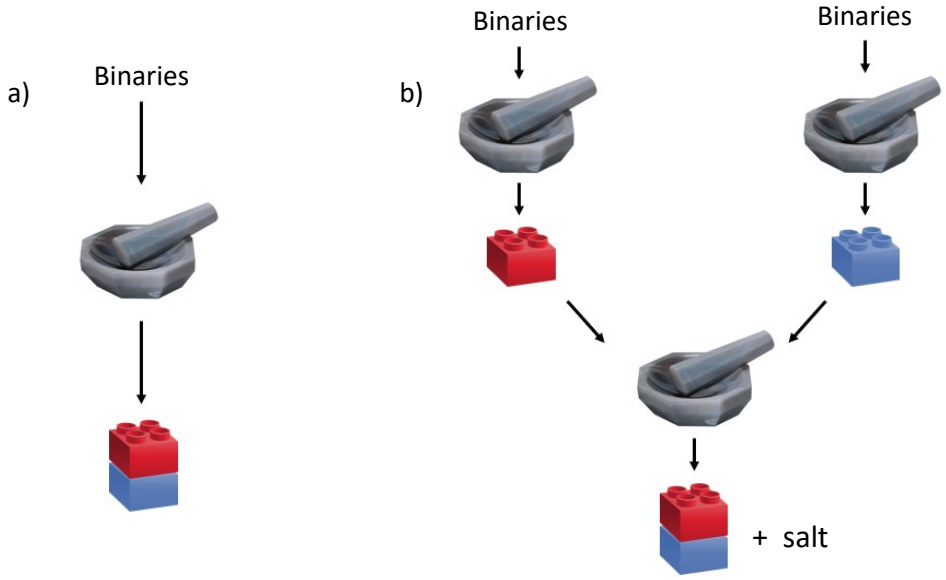

Figure 165 A comparative illustration of the synthesis of a material via a) the conventional ceramic method, and b) solid-state metathesis. Samples are depicted as building blocks to highlight the pre-formed ionic blocks employed in the metathetic pathway.

Solid-State Metathesis (SSM) reactions involve the double displacement of ionic 'building block' subunits, each with counterions, to assemble the layered product alongside a salt by-product, illustrated in Figure 165. The driving force for SSM is both the thermodynamic stability of the product (relative to the instability of the precursors), and the formation of the simple salt by-product from the recombination of the counterions.[288]

This driving force usually permits a lower reaction temperature or shorter reaction times, as the input energy must no longer overcome the conventional slow diffusion of ions in the solid state. Often in SSM, covalent bonds are not broken nor formed, with reactions proceeding only via ionic displacements. If successful, the salt may be washed away with water.

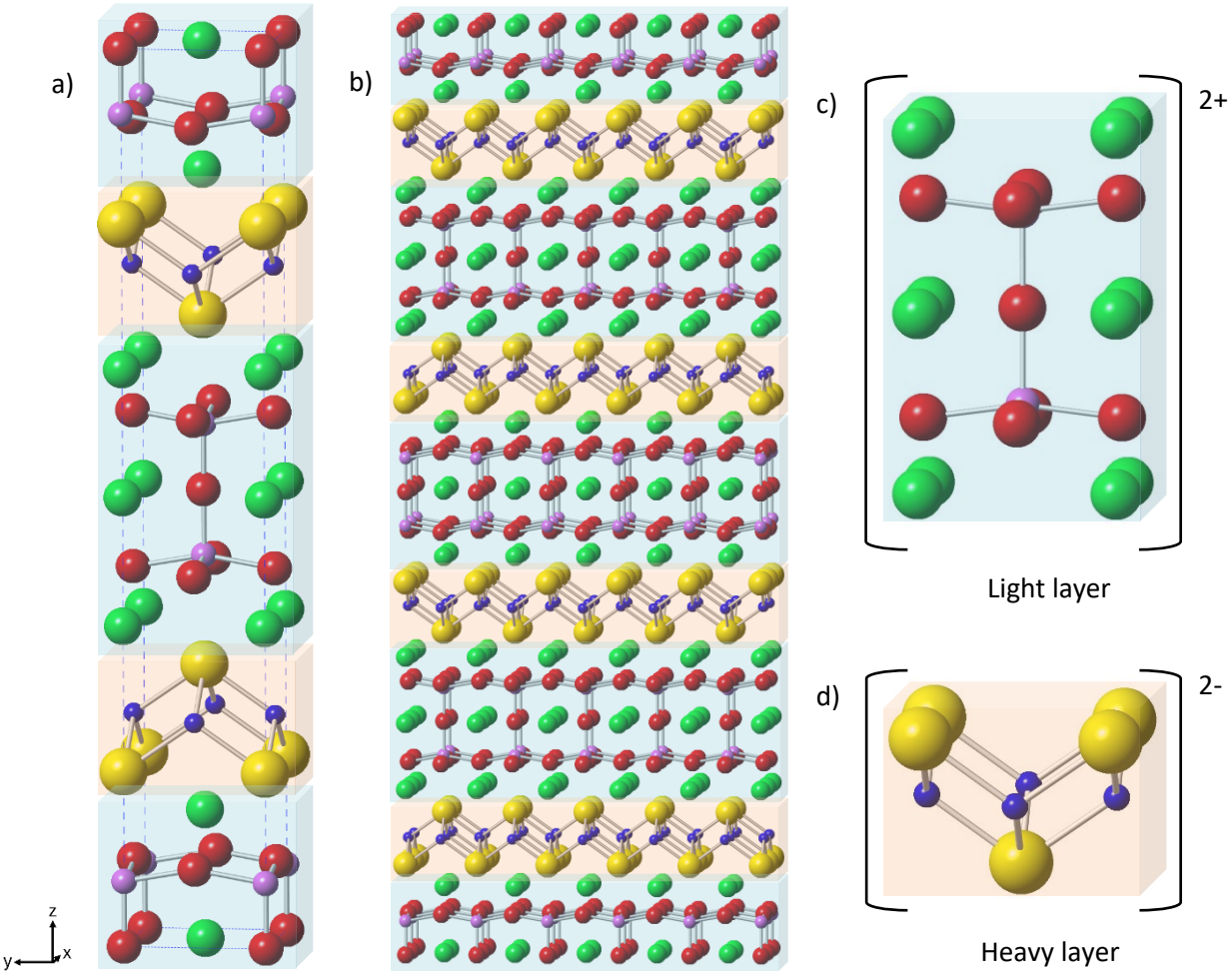

Figure 166 *Isometric projections of the $A_3B_2O_5M_2Q_2$ '325' structure type MALM, showing a) one unit cell, b) a 2×5×2 expanded unit cell, c) the $[A_3B_2O_5]^{2+}$ light layer subunit, and d) the $[M_2Q_2]^{2-}$ heavy layer subunit. Projections are viewed primarily along the x-axis, and are not to scale with each other. The blue dashed lines denote the unit cell. The coloured regions represent the light (pastel blue) and heavy (pastel pink) layer subunits, which are the ionic building blocks in a metathesis synthesis.*
Colour key: green - A, pink - B, red - O, blue - M, and yellow - Q.

The first report of solid-state metathesis applied to the synthesis of mixed anion layered materials was Cario et al, who in 2005 synthesised the quaternary MALM BaFZnP by metathesis at 600 °C (Equation 69) and a conventional synthesis at 900 °C.[289]

Equation 69 $NaZnP + BaFCl \rightarrow BaFZnP + NaCl$

Since then, the authors have extrapolated this technique to over a dozen layered materials,[290] notably to the synthesis of a quinternary MALM with the 325 structure type: $Sr_3Fe_2O_5Cu_2Se_2$.[61] As before, the combined driving forces of the layering and NaCl formation allows the reaction to proceed as low as 600 °C, compared to the conventional synthesis at 900 °C.[61]

Concerning MALM synthesis, SSM is the reaction of 'light' and 'heavy' layer subunits, the metathetic combination of which takes advantage of the natural layering of MALMs. Metathesis requires the individual pre-syntheses of the desired light layer $[A_aB_bO_c]^{2+}$ subunit with a counter-anion such as a halide, and the desired heavy layer $[M_2Q_2]^{2-}$ subunit with a counter-cation such as an alkaline earth metal. This is illustrated in Figure 166 by the pastel blue and pink regions using the 325 MALM structure as an example. When reacted in a 1 : 1 molar ratio the subunits combine to form the layered structure. MALMs are insoluble in water, so the salt may be easily washed from the sample.

Each of the quinternary MALM structures described within this work (notably the 212, 325 and 426 classes) have the potential to be synthesised by metathesis, provided the appropriate precursors exist. In each, the light and heavy layers possess equal and opposite charges of +2 and -2 respectively, thus react in a 1 : 1 ratio and stack alternately in the *c* direction.

An example metathetic synthesis for $Sr_3Fe_2O_5Cu_2Se_2$ is outlined below. As discussed, the precursors must be synthesised individually before a metathesis reaction can take place which is a significant disadvantage versus the conventional ceramic method. Later in this chapter, this apparent disadvantage becomes a key underpinning feature of a novel synthetic concept based on SSM. For precursor syntheses, purities must be exceptionally high, ideally approaching 100 %, as any impurities may be magnified through subsequent reactions.

Equation 70 outlines the pre-synthesis of $Sr_3Fe_2O_5Br_2$, containing a light layer $[A_aB_bO_c]^{2+}$ subunit, while Equation 71 outlines the pre-synthesis of $Na_2Cu_2Se_2$, a precursor with the heavy layer subunit $[M_2Q_2]^{2-}$, and finally Equation 72 is the metathesis reaction of the two. The metathesis reaction is illustrated in Figure 167. Herein, materials of this type are referred to within this context as 'light layer precursors' and 'heavy layer precursors' respectively.

Equation 70 $2\ SrO + Fe_2O_3 + SrBr_2 \rightarrow Sr_3Fe_2O_5Br_2$

Equation 71 $Cu_2Se + Na_2Se \rightarrow Na_2Cu_2Se_2$

Equation 72 $Sr_3Fe_2O_5Br_2 + 2\ Na_2Cu_2Se_2 \rightarrow Sr_3Fe_2O_5Cu_2Se_2 + 2\ NaBr$

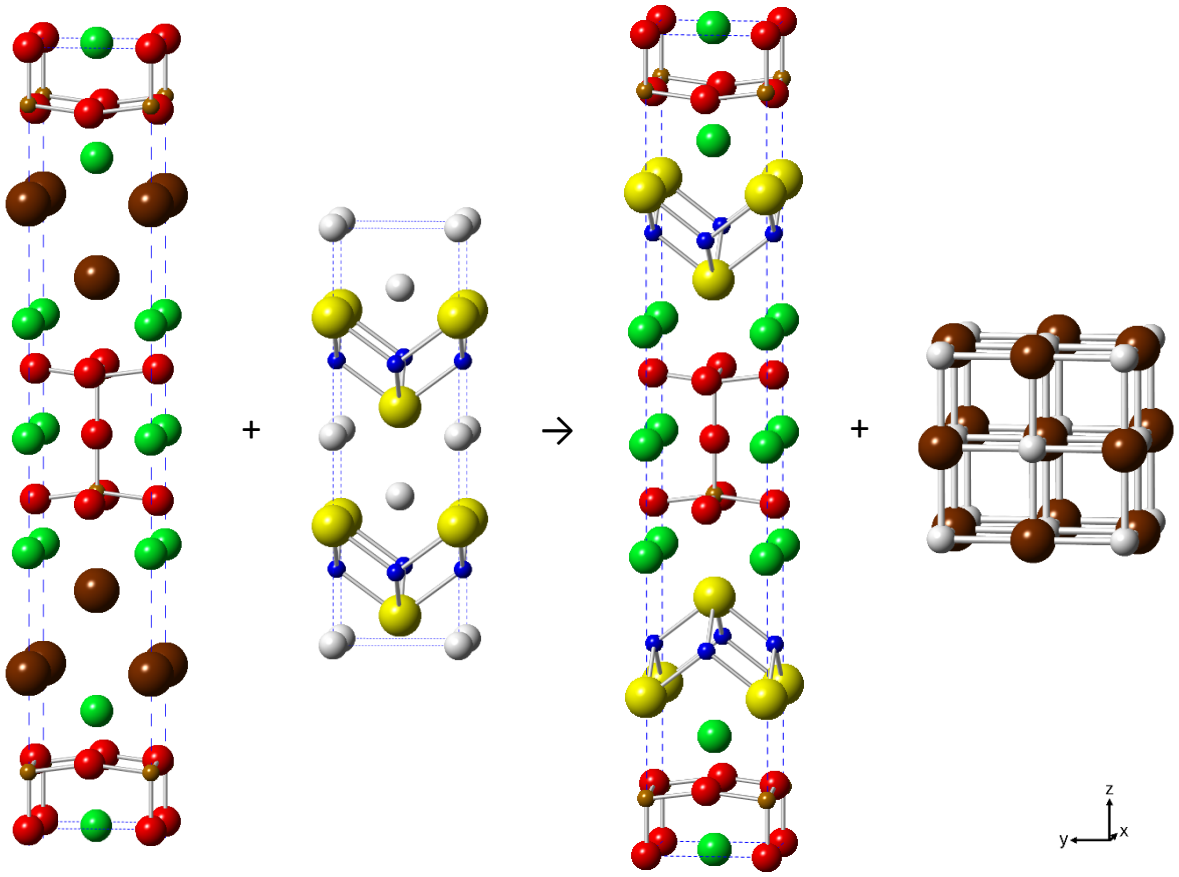

Figure 167 *Isometric projections of the precursors and products in the synthesis of $Sr_3Fe_2O_5Cu_2Se_2$ via a metathesis pathway. Projections are viewed primarily along the x-axis, and are to scale with each other. The blue dashed lines denote the unit cell.*
Colour key: green - Sr, light brown - Fe, red - O, blue - Cu, yellow - Se, white - Na, and dark brown - Br.

5.1.2 Parallel Synthesis: A Novel Route to Rapid Materials Discovery?

Solid-State Metathesis is a largely unexplored process usually rendered redundant by the versatility and speed of the conventional ceramic synthesis, yet there are functions and potential applications of the metathesis route which may render it an exciting candidate method for MALM discovery research.

In isolation, the metathetic pathway appears inferior, as the pre-synthesis of the heavy and light layer precursors greatly increases the time and energy cost versus the conventional route. The reaction also generates a salt by-product which must be washed away post-reaction to purify the product. Further to this, the washing step must be performed in air requiring the product to be both air and water stable. For these reasons, the conventional method is far more prevalent in literature. When targeting a single material or a small number of materials, it is simply more economical to synthesise them directly.

Despite these downsides, this work will utilise the metathesis pathway in an exciting novel concept for rapid materials discovery, a possible method to ascertain the existence of multiple unknown MALMs in a single combinatorial experiment: parallel synthesis. This proposed process takes advantage of the previously discussed metathesis disadvantages, particularly the pre-syntheses of the building block precursors, a hindrance which now becomes a valuable tool. In a parallel synthesis (a technique which has, to the best of the author's knowledge, never been applied to solid-state chemistry), multiple pre-synthesised light and heavy precursors may be reacted together to form a number of products all at once, allowing for batch-testing of multiple known and novel materials in one reaction and permitting a faster investigation of the unexplored MALM phase space.

Table 11 *An illustration of the parallel synthesis technique using the building block analogy discussed previously. Three light layers represented by white, red and green blocks react with three (grey, yellow and blue block) heavy layers, to produce nine potential products.*

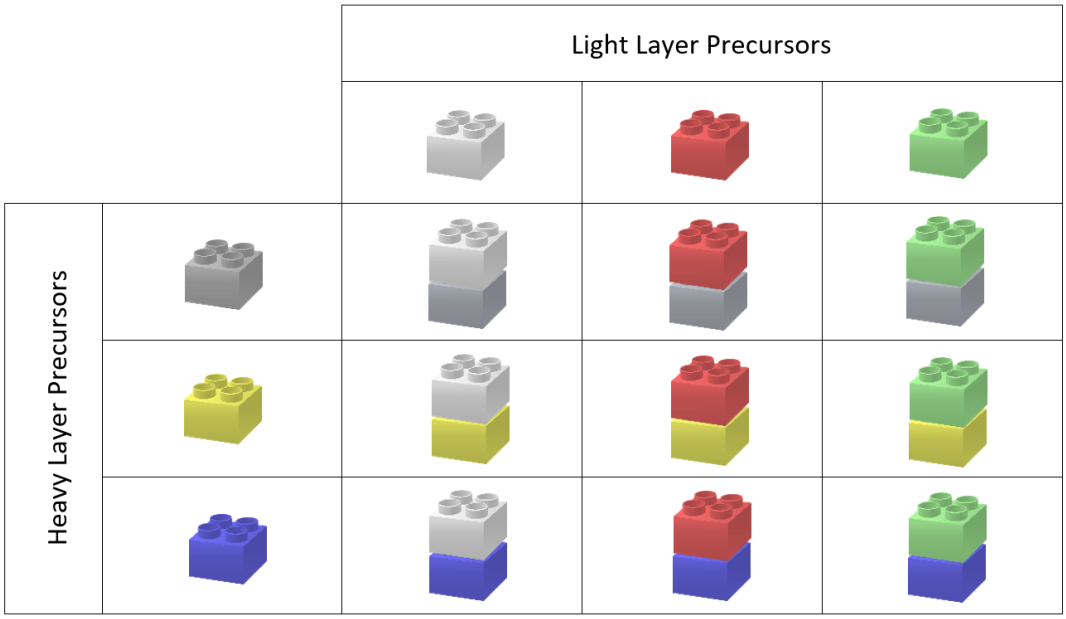

This method is illustrated in Table 11 which uses the building block analogy discussed previously, and used within literature.[61, 288, 289] If scaled appropriately, parallel synthesis has the potential to greatly reduce synthesis time, compared to synthesising each material individually.

The salt by-product, which originally posed a small disadvantage to the metathesis method, is again utilised as a positive in this process. The presence of a simple salt by-product such as $BaCl_2$ or LiBr indicates the successful combination of the associated light and heavy layer precursors by metathesis. The resulting XRD diffractograms will be extremely complicated regardless of the level of success of the component reactions, as most MALMs exhibit very similar XRD patterns to their light layer precursors. Therefore, the salts (whose symmetrical crystalline structures produce large, sharp and readily detectable XRD reflections) may be used as a screening tool to either support or replace a difficult Rietveld refinement of the convoluted pattern.

In theory, if a successful product can be identified by tell-tale salt reflections in the X-ray diffractogram, a full analysis of the pattern may not be explicitly required. It will be far easier to spot the presence of a small salt impurity than to interpret a very congested pattern for the identities of MALMs, so the expected salts can provide a qualitative 'hit or miss' outcome for each individual permutation within the batch, from which successful materials can be individually synthesised for further study. Note that for this screening method to be viable, each possible salt by-product *must* be different.

Table 12 *A hypothetical 3 × 2 parallel synthesis reaction between light layer precursors $Sr_2CoO_2Cl_2$, $Sr_3Fe_2O_5Br_2$, and $Ba_4In_2O_6F_2$, with heavy layer precursors $Na_2Cu_2Se_2$ and $Li_2Fe_2As_2$. Green boxes indicate known published MALM products and red boxes indicate unknown potential new MALM products. Salt by-products are omitted for brevity.*

		Light Layer Precursors		
		$Sr_2CoO_2Cl_2$	$Sr_3Fe_2O_5Br_2$	$Ba_4In_2O_6F_2$
Heavy Layer Precursors	$Na_2Cu_2Se_2$	$Sr_2CoO_2Cu_2Se_2$ *[Reported]* [291] **+ 2 NaCl**	$Sr_3Fe_2O_5Cu_2Se_2$ *[Reported]* [61] **+ 2 NaBr**	$Ba_4In_2O_6Cu_2Se_2$ *[Not reported]* **+ 2 NaF**
	$Li_2Fe_2As_2$	$Sr_2CoO_2Fe_2As_2$ *[Not reported]* **+ 2 LiCl**	$Sr_3Fe_2O_5Fe_2As_2$ *[Reported]* [50] **+ 2 LiBr**	$Ba_4In_2O_6Fe_2As_2$ *[Not reported]* **+ 2 LiF**

The greater the available bank of precursors, the faster new materials can be screened. This permits a looser attitude towards risk, where no longer must only those materials most likely to exist be targeted due to time and cost. Now, multiple new materials including those which are not expected to be stable may be attempted, parallel synthesis may yield rich information on previously unexplored materials. The disadvantage of precursor pre-synthesis is amplified in earlier stages, where time must be devoted to precursor synthesis, but once a large precursor bank has been amassed multiple novel MALMs may be targeted in quick succession. Table 12 above depicts a hypothetical 3 × 2 parallel synthesis where three of the six possible products are unknown, and may be discoverable novel MALMs.

A parallel approach to MALM synthesis would save time, energy and money compared to performing reactions individually (by either the conventional or metathesis methods alone). There is also another, arguably more important, advantage. Individually reacting one heavy layer with one light layer affords one product, but scaling this method will yield exponentially more products. As discussed, reacting m light layers with n heavy layers gives $m \times n$ potential products, meaning any combination greater than 2 × 2 will yield more possible MALMs than there are precursors. The synthesis in Table 12 for example, combines 5 total precursors to produce 6 total theoretical products. By running metathesis reactions in parallel the possible products are greater than the sum of their parts.

5.1.3 The Phase Space of Light and Heavy Layer Precursors

A comprehensive literature search of more than 450 research publications was carried out by searching by structure type in the International Crystal Structure Database (ICSD), to identify all materials that could potentially be used as light or heavy layer precursors in metathetic syntheses of MALMs.

For quinternary MALM synthesis there are a variety of potential light layer precursors. Any oxyhalide material with formula $A_{n+1}B_nO_{3n-1}X_2$ can impart the $[A_{n+1}B_nO_{3n-1}]^{2+}$ subunit necessary to form a 212, 325 or 438 MALM, and $A_4B_2O_6X_2$ for the 426 structure. *X* can be F, Cl or Br, but is most commonly Cl. These materials crystallise in the *I*4/*mmm* space group, akin to that of the MALMs they may be used to form. These oxyhalides are themselves quaternary MALMs by definition, but within this work they are treated as precursors for the higher order quinternary MALMs. Examples of light layer precursors with 212, 325, 438 and 426 structures respectively are $Sr_2CoO_2Br_2$,[292] $Sr_3Fe_2O_5Cl_2$,[293, 294] $Sr_4Mn_3O_{8-y}Cl_2$,[295-297] and $Ba_4In_2O_6F_2$.[298] The systematic literature review found 4, 18, 2 and 14 examples respectively of 212, 325, 438 and 426 oxyhalide materials, for a total of 38 potential light layer precursors. Omitting repeat materials where the same light layer subunit appears with more than one halide such as $Ba_3In_2O_5Cl_2$[299] and $Ba_3In_2O_5Br_2$,[300] leaves 27 unique light layer structures which may be incorporated into a MALM.

Pertaining to the heavy layer precursors, there are three structure types which exhibit the distinct *anti-litharge* $[M_2Q_2]^{2-}$ motif of these types of MALMs, with formulae $A_2M_2Q_2$ or AM_2Q_2. These are: the *PbClF* structure type such as $Na_2Cu_2Se_2$,[301] the *BaZn₂P₂* structure type such as $CsMn_2P_2$,[302] or the *ThCr₂Sr₂* structure type such as $EuNi_2As_2$.[303] The *BaZn₂P₂* and *ThCr₂Sr₂* structure types appear very similar and both crystallise in the *I*4/*mmm* space group like the light layer precursors and MALMs.[304] Reviewing materials in literature that possess these structure types, the key difference appears to be the size and oxidation state of the counter-cation. *BaZn₂P₂* favours larger group 1 or 2 *A* cations such as K^+, Cs^+, and Ba^{2+} (in the cases of the +1 metals, the *M* site metal exhibits a I/II mixed oxidation state, thus the layers have charges of ±1), whilst the *ThCr₂Sr₂* structure types favours small late transition or lanthanide cations such as Eu^{2+}, Ho^{2+}, and Tb^{2+}, in oxidation state +2. *ThCr₂Sr₂* therefore has a shorter *c* lattice parameter. The *PbClF* structure type, which differs from the others in terms of stoichiometry and always accommodates +1 oxidation state cations, crystallises in the *P*4/*nmm* space group.

The literature review found 141, 47, and 555 materials sporting the *PbClF*, *BaZn₂P₂*, and *ThCr₂Sr₂* structure types respectively. Many of these contain toxic metals such as cadmium or iridium, or expensive metals such as rhodium and osmium. Excluding these, and also those of the *BaZn₂P₂* type with group 1 metal counter-cations and ±1, incompatible for use in a MALM, leaves 283 heavy layer precursors across the three structure types. Omitting repeat materials where the same heavy layer subunit appears with multiple metal cations such as $Na_2Zn_2P_2$[305] and $K_2Zn_2P_2$[301] leaves 45 unique $[M_2Q_2]^{2-}$ permutations for possible metathesis reactions. Figure 168 depicts the four light and three heavy layer precursor structures discussed in this section.

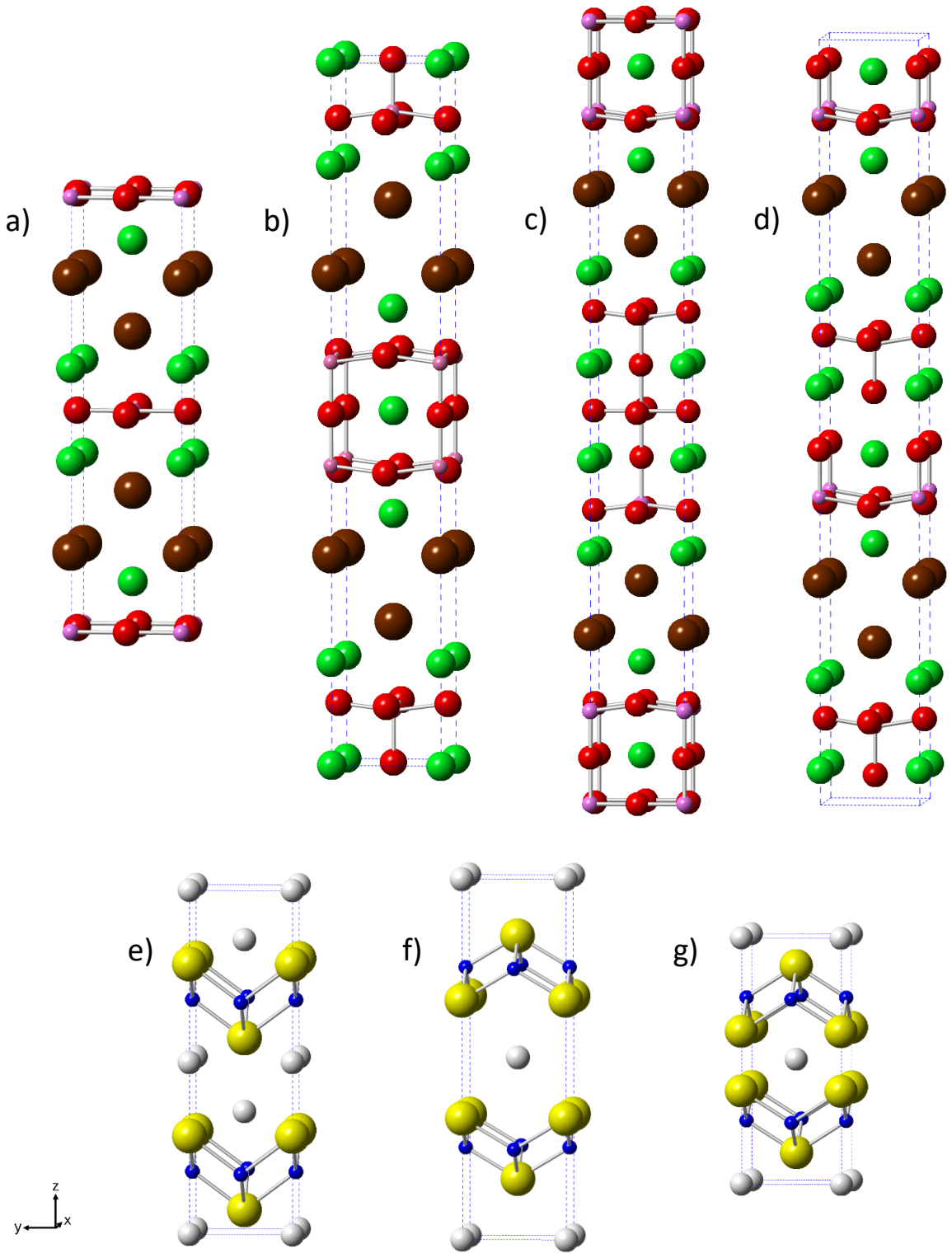

Figure 168 *Isometric projections of generic depictions of the possible light layer and heavy layer precursors utilised in a MALM metathetic synthesis. The light layer precursors with structure types a) 212, b) 325, c) 438 and d) 426, contain halide counter-anions. The heavy layer precursors with structure types e) PbClF, f) $BaZn_2P_2$ and g) $ThCr_2Sr_2$ contain group 1 or 2 metal counter-cations. Projections are viewed primarily along the x-axis, and are not to scale with each other. The blue dashed lines denote the unit cell.*
Colour key: green - A, pink - B, red - O, blue - M, yellow - Q, brown - halide counter anion, and white - metal counter cation.

5.1.4 Potential Flaws of Metathesis in a Parallel Synthesis Application

Before beginning investigation into the novel parallel technique, it is sensible to consider possible flaws that may be discovered. There are, understandably, multiple potential issues with a parallel synthesis method for materials discovery. In this section three primary disadvantages are discussed which may realistically limit the usefulness of a parallel metathesis model. These are: the predicted complexity of PXRD patterns resulting from multiple reactions occurring at once, the lack of diversity in the phase space of potential light layer precursors, and a hypothesis that the low melting point salt by-products may react with each other to form the most thermodynamically stable permutation rather than those dictated by the reacting subunits, or worse melt the whole sample which facilitates ceramic synthesis instead of exclusively metathetic.

5.1.4.1 X-ray Diffractogram Convolution

It is predicted that the size of a parallel synthesis grid will correlate highly with its usefulness in practice. Too small (specifically, too few precursors being combined at any one time), and individual syntheses become the faster option, and the time-saving benefits of parallel synthesis become redundant. Too many, and the XRD pattern may become so crowded as to be completely unintelligible.

Considering the example parallel synthesis described in Table 12 on page 258, 3 light layers and 2 heavy layers comprised a 3×2 grid of potential new materials. If a batch of this size is completely successful, yielding 6 new materials and subsequently 6 salt by-products, the XRD pattern would contain 12 total materials assuming 100 % yields and no impurities or side-reactions. Even in this 'best-case scenario', the pattern is going to be very complicated, and the screening of salt by-products will be key to interpreting the results. If one assumes the 'worst case scenario' where all possible products and salts form but yields are low so low that all precursors are still present in the mixture, still conservatively assuming no other impurities, the total number of materials becomes 17 and the resulting pattern is likely to become so convoluted as to be completely unintelligible.

Figure 169 is a simulated powder pattern resulting from the 'worst case scenario' of the example parallel synthesis, assuming all possible products, their salts, and all precursors are present. The simulation assumes equal weight contributions of all phases, for simplicity. One can immediately see the impossibility of an accurate refinement of this pattern, even in this case where peaks are clearly resolved and all phases are highly crystalline (a property unlikely in practice). For this reason, batch sizes should be kept small initially, especially within this work when investigating a proof of concept for this novel and unproven synthesis method.

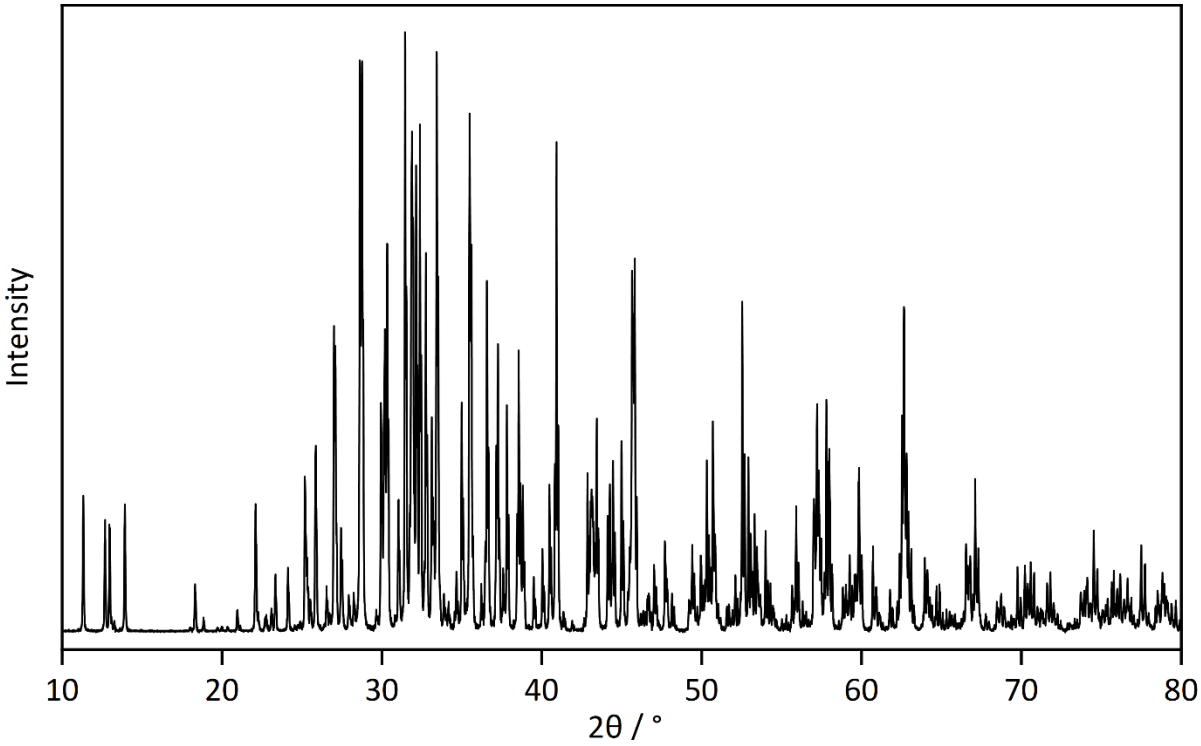

Figure 169 A simulated Powder X-ray diffractogram of the example 3×2 parallel synthesis described in Table 12 on page 258. This simulation assumes the 'worst case scenario' for diffractogram convolution, where all precursors are present, as well as three reported MALMs and their associated salt by-products. All included phases are at equal weight ratios.

5.1.4.2 Precursor Diversity

Another drawback of the metathesis pathway is the availability of light layer subunits which could be used in metathesis reactions. At the time of writing there are at least 105 different MALMs reported in literature, of various structures and compositions, but the pool of known light layer structures contains just 38, as explained in the phase space review previously. There are therefore many MALM structures which, at present, could not be synthesised through the metathesis pathway as the light layer precursor is not reported or synthesisable. That said, the phase space of potential MALMs even with just 38 light layer subunit structures, is vast.

Of those 38 light layers, 50 % are 325 structures, and 70 % have chlorine on the *X* site. When employing multiple light layer precursors in a parallel synthesis, if one desires to use the salt by-products as a screening method, every component metathesis reaction must have a unique salt by-product, so the light layer halogens must be different in order to identify the successful MALM from a salt. With most containing chlorine (and only three containing fluoride) the possible permutations are significantly diminished before any experimentation has even taken place.

5.1.4.3 The Salt By-Product Hypothesis

Alongside the conceptualisation of the parallel synthesis approach explored herein, an immediate potential flaw was recognised in the proposal to use the salt by-products as markers of a successful pairing between a light and heavy layer precursor. These salts are relatively stable – in fact their stability is in part the driving force of these reactions, but their melting points are low compared to MALMs, 700 – 1000 °C.

If these salts melt, they may act as a flux and melt the whole sample. This would invalidate the effect of metathesis by permitting the reaction of all atoms in a liquid-state synthesis, including the salt atoms. Group 1 metals may incorporate into the other materials akin to that of doping, which is not only undesirable here but largely undetectable. A melt also renders the MALMs free to form the most stable permutations, such as targeted 426 materials forming their more stable 325 counterparts, an undesirable side-reaction that often plagues conventional syntheses (see *Chapter 4*) but should not be possible if metathesis is the sole mechanism within a reaction.

Even if the salts do not melt the sample, and the component metatheses proceed as planned and in the solid state, the salts may still react amongst themselves at the elevated reaction temperature (in the solid state) to form either one homogenous salt material containing all present salt atoms, or undergo displacement to form the most stable permutations. If NaCl and KBr were the by-products of a MALM synthesis, and reacted to form for example, NaKClBr, or NaBr and KCl, or a mixture of all four binary salt permutations, one could not use the salts as screening markers for the associated MALM syntheses, or worse be misled by the erroneous salts.

This hypothesis presents a valid flaw not in the proposed parallel synthetic approach as a whole (whose validity as a process remains, if the products can be identified without resorting to screening by the salts), but it does threaten the screening technique. The salt by-product hypothesis is explored in depth later in *Section 5.5*, where multiple pairs of simple salts are reacted at elevated temperatures to probe their behaviour and uncover any tendencies to melt or to crystallise ambiguously. The removal of the salt by-product by washing with deionised water is also explored later, in *Section 5.4.2*, resulting in the highest purity MALM produced in this entire work.

5.1.5 Research motivation

The research in this chapter aims to investigate metathesis reactions which, even without the parallel approach, have received little research attention in materials chemistry to date. Parallel techniques have found exciting application in fields such as in fields such as combinatorial chemistry,[306] drug discovery,[307] and antimicrobial screening.[308] Its use here would be completely novel. The most notable work is that previously discussed of Cario who demonstrated parallel synthesis in its singular synthesis of a quinternary MALM to date, $Sr_3Fe_2O_5Cu_2Se_2$.[61] Even within this publication, the conventional method appeared superior, able to further synthesise $Sr_3Fe_2O_5Ag_2S_2$ and $Sr_3Fe_2O_5Ag_2Se_2$ where metathesis could not. In this singular example of quinternary MALM synthesis, there is no discussion of phase purity of $Sr_3Fe_2O_5Cu_2Se_2$, only its successful synthesis. Therefore, in this work, this material is explored in a comparative study between conventional and metathetic syntheses across multiple reaction temperatures, seeking evidence for the successful application of metathesis and at which temperature conventional solid-state chemistry overtakes metathesis as the dominant mechanism. To the best of the author's knowledge, a side-by-side experiment of this type, with details of purities rather than a qualitative answer, has not been undertaken in literature. A similar investigation was first performed on $Sr_3Sc_2O_5Cu_2Se_2$, the material at the centre of the doping study in *Chapter 3*, whose synthesis by metathesis has also not been reported to date in literature, so is reported here for the first time.

In this chapter, a small bank of precursors is first created, and individual metathesis experiments carried out at temperatures lower than that which would be expected to sustain a conventional ceramic synthesis. Following the in-depth investigations into $Sr_3Sc_2O_5Cu_2Se_2$ and $Sr_3Fe_2O_5Cu_2Se_2$, the hypothesis of salt flux mixtures is investigated and found to be a significant flaw in the screening method proposed of these salt materials in a hypothetical parallel synthesis. Finally, four small scale proof-of-concept parallel syntheses are performed, before an evaluation of the scalability and applicability of the parallel method to further materials research.

If successful, one of the most promising applications of metathetic parallel synthesis is the rapid exploration of many unusual or unexplored heavy layer pairs, such as Pd_2Ge_2,[309] Cu_2P_2[310] or Ru_2Si_2.[311]

The PXRD diffractograms for all precursors syntheses, trial metatheses, salt flux experiments and proof of concept parallel syntheses discussed herein can be found in *Appendix B.3*.

5.2 Experimental

All conventional[18] ceramic syntheses in this work were performed by the same procedures discussed at large previously throughout this work: heating in vacuum sealed ampoules within a box furnace, and manipulated within a glovebox. Many light layer syntheses took place in air using air-stable precursors, specific details of these syntheses are described in each section.

Metathesis syntheses are approached largely the same as conventional syntheses in practice, where the primary differences are the precursors employed and the lower reaction temperature. Metathesis samples in this work were never pelletised, in order to protect the unstable heavy layer precursors from air. Powder materials were ground to homogeneity within a nitrogen glovebox, placed into alumina crucibles, sealed within silica tubes under vacuum and heated within a box furnace akin to the conventional process. Bar some exceptions, metathesis products were analysed with air-sensitive PXRD, a technique outlined in *Section 2.2.1.7,* and used widely within this chapter.

The light layer precursors are air stable, allowing both synthesis and storage in air. This usually permits facile syntheses. The heavy layers were found to be the opposite, the most unstable materials explored within this entire work, degrading within seconds and requiring strict air exclusion at all times.

5.2.1 Precursors

Materials within this chapter were synthesised using the following precursors:

SrO (made in-house by the decomposition of $SrCO_3$, Merck, 99.9 %), Co_3O_4 (Alfa Aesar, 99.7 %), $SrCl_2$ (Alfa Aesar, 99.5 %), $SrCl_2{\cdot}6H_2O$ (Alfa Aesar, 99 %), $SrCO_3$ (Merck, 99.9 %), SrO_2 (Aldrich, 98 %), Fe_2O_3 (Acros, 99.999 %), $SrBr_2$ (Alfa Aesar, 99 %), $SrBr_2{\cdot}6H_2O$ (Alfa Aesar, 99 %), Sc_2O_3 (Thermo Scientific, 99.999 %), BaO (Sigma Aldrich, 99.5 %), Y_2O_3 (Alfa Aesar, 99.999 %), $BaCl_2$ (Alfa Aesar, 99 %), Na_2Se (made in-house by the reaction of Na, Aldrich, 99.9 %, and Se, Strem, 99.99 %), Cu_2Se (Thermo Fisher Scientific, 99.5 %), SrSe (made in-house by reduction of $SrSeO_4$, also made in-house), NaF (Thermo Scientific, 99 %), NaCl (Sigma, 99.5 %), NaBr (Sigma Aldrich, 99.5 %), KF (Sigma, 99.5 %), KCl (Fischer, 99.5 %), and KBr (Alfa Aesar, 99 %).

[18] Herein, the term 'conventional' will refer to the standard solid-state chemistry syntheses utilised in all previous experiments within this work, where precursors (usually binary) are combined and reacted to very high temperatures in order to synthesise the target MALM by decomposing all precursors and encouraging the diffusion of ions in the solid state. Alternatively, 'metathesis' or 'metathetic' reactions refer specifically to the double displacement solid-state reactions between the pre-synthesised light and heavy layered precursors, forming a salt by-product. These typically occur at lower temperatures to ideally maintain the structural integrity of the building blocks and not break down all precursors as in the conventional approach, instead merely facilitating the rearrangement and assembly of the layered building block components.

5.3 Precursor Syntheses

5.3.1 Light Layer Precursors

A precursor bank of nine light layer precursors was created, of which eight were considered of sufficient purity to take forward into metathesis investigations. Anything less than very high purity at this stage was deemed unacceptable, as any impurities will be carried into the later metathesis reactions using these precursors. All precursors in this section were prepared on a 1 gram scale initially, and then when successful were reproduced on a 5 gram scale for inclusion in the precursor bank. They were all observed to be air-stable on the order of (at least) multiple years.

In general, the syntheses here proceed by the general reaction formula outlined in Equation 73 for 325 structures and Equation 74 for 426 structures. In both, the metal ion *B* has a +3 oxidation state, so the B_2O_3 metal oxide structure is the ideal precursor because it introduces the *B* metal in the correct stoichiometry and oxidation state for the light layer and MALM. All metals investigated here have a stable available oxide in this formula, except cobalt. In some cases, air stable and more affordable precursors were used, ACO_3 for AO, and $AX_2{\cdot}xH_2O$ for AX_2; substitutions which permit in-air syntheses.

Equation 73 $2\,AO + B_2O_3 + AX_2 \rightarrow A_3B_2O_5X_2$

Equation 74 $3\,AO + B_2O_3 + AX_2 \rightarrow A_4B_2O_6X_2$

Where *A* = Sr or Ba, *B* = Sc, Fe, or Y, *X* = Cl or Br

5.3.1.1 $Sr_3Co_2O_5Cl_2$

The first light layer precursor, $Sr_3Co_2O_5Cl_2$, was selected specifically because it has no $Sr_3Co_2O_5M_2Q_2$ MALM analogues. Therefore, it could be used within a metathesis or parallel synthesis to intentionally simulate a failed experiment. In terms of synthesis this precursor was the most difficult, due to the available oxides of cobalt. Despite some speculative claims,[312] Co_2O_3 does not exist as a stable oxide of cobalt, so the general formula described above is not applicable. Instead, cobalt forms only CoO or Co_3O_4, where Co is in an average oxidation state of +2 and $+2.\dot{6}$ respectively. The oxidation state of $+2.\dot{6}$ in Co_3O_4 (which is, more specifically a 1 : 2 ratio of Co^{2+} and Co^{3+}) is closer to the desired +3 so was selected. This still necessitates cobalt oxidation however, and adjustment of the above formula to:

Equation 75 $2\,SrO + {}^{2}/_{3}\,Co_3O_4 + SrCl_2 + {}^{1}/_{6}\,O_2 \rightarrow Sr_3Co_2O_5Cl_2$

An amendment to this formula was made so that $SrCO_3$ and $SrCl_2{\cdot}6H_2O$ were used instead of SrO and $SrCl_2$, in order to use less expensive and more widely available precursors. This relies on the evolution of CO_2 and H_2O to create SrO and $SrCl_2$ respectively in situ.

Equation 76 $2\ SrCO_3 + {}^{2}/_{3}\ Co_3O_4 + SrCl_2{\cdot}6H_2O + {}^{1}/_{6}\ O_2 \rightarrow Sr_3Co_2O_5Cl_2 + 2\ CO_2 + 6\ H_2O$

$Sr_3Co_2O_5Cl_2$ was synthesised on a 5 gram scale using conventional solid-state chemistry, according to Equation 76 above. Powder samples were heated to three 12 hour cycles in air at 800 °C. This process must take place in air not only because gases are evolved, but because an oxygen rich atmosphere was required to balance stoichiometry and oxidise the cobalt from $Co^{2.6+}$ to Co^{3+}. The use of carbonate and hexahydrate precursors meant that all precursors were air-stable, rendering the use of a glovebox unnecessary.

This approach yielded no positive results, with only very small traces of product detected via XRD. Multiple attempts at this synthesis with more aggressive temperatures and more intermediate regrinds all proved unsuccessful in forcing the reaction to completion. Using SrO and $SrCl_2$ instead of $SrCO_3$ and $SrCl_2{\cdot}6H_2O$ also yielded no success, both in air and within an ampoule. It was hypothesised that the mere availability of oxygen in the air was not a strong enough driving force to oxidise cobalt, therefore stronger conditions were required. The use of strontium peroxide as an oxidising agent has been reported for this synthesis,[313, 314] but with a maximum yield of only 84 % due to the formation of $Sr_6Co_5O_{15}$ as a by-product.[313] Another synthetic route was found in literature which proceeded via a *Brownmillerite* $A_2B_2O_5$ intermediate,[315, 316] Equation 77, which then reacts with $SrCl_2$ to synthesise the oxychloride product, Equation 78. The overall reaction is the same as the initial route, but split into two component parts to complete the oxidation of cobalt from $Co^{2.6+}$ to Co^{3+} before the addition of $SrCl_2$ to form the oxychloride. In literature syntheses of $Sr_2Co_2O_5$, the use of carbonates and hydrates is again reported.[317-319]

Equation 77 $2\ SrCO_3 + {}^{2}/_{3}\ Co_3O_4 + {}^{1}/_{6}\ O_2 \rightarrow Sr_2Co_2O_5 + 2\ CO_2$

Equation 78 $Sr_2Co_2O_5 + SrCl_2{\cdot}6H_2O \rightarrow Sr_3Co_2O_5Cl_2 + 6\ H_2O$

The synthesis of $Sr_2Co_2O_5$ was attempted from $SrCO_3$ and Co_3O_4 at 1000 °C in three 12 hour heat cycles. This formed a dark black solid which was determined by PXRD to be not $Sr_2Co_2O_5$, but $Sr_6Co_5O_{15}$, a similar material with a cobalt deficiency (empirically $Sr_2Co_{1.667}O_5$). Interestingly, this material is the frequently reported impurity of the strontium peroxide synthesis. Its synthesis here is believed to be due to an omitted quenching step in liquid nitrogen after the final heat cycle, often reported in literature. When $Sr_2Co_2O_5$ cools naturally, $Sr_6Co_5O_{15}$ prevails following a phase change at 750 °C where Co_3O_4 separates upon absorption of oxygen.[320, 321] PXRD of this material confirmed that this had occurred, showing the material consisted of 98.5 % $Sr_6Co_5O_{15}$ and 1.5 % Co_3O_4.

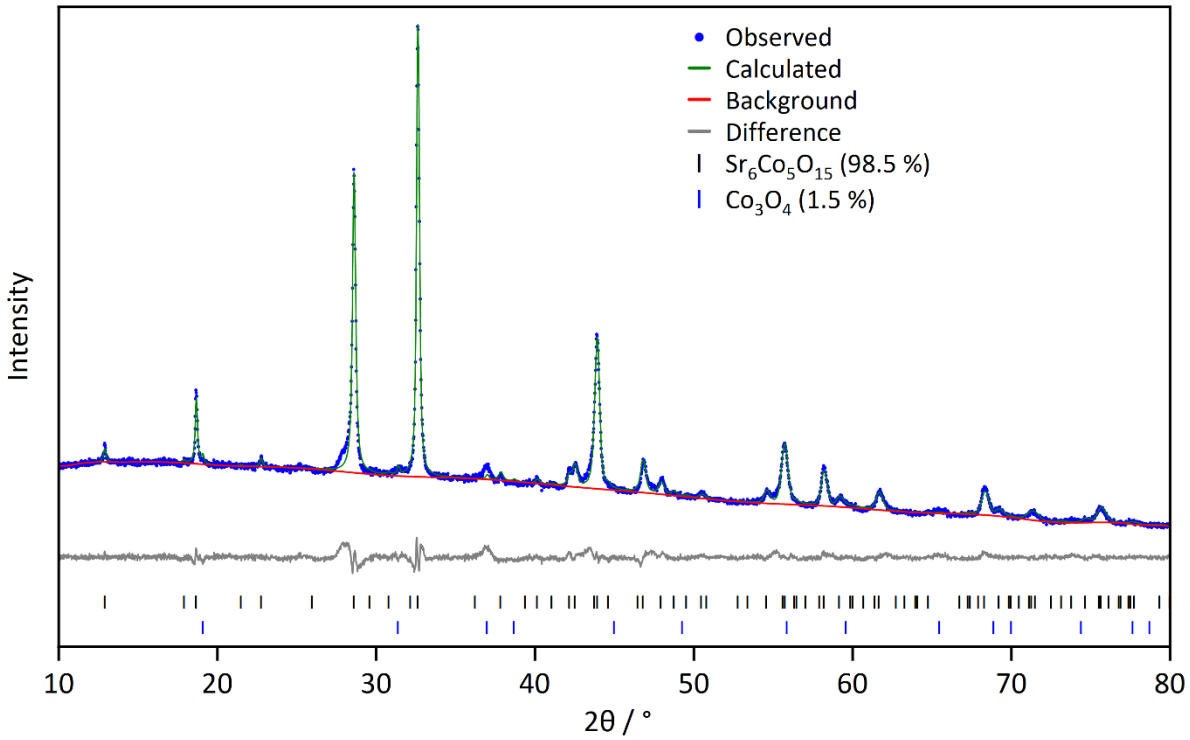

Figure 170 *Powder X-ray diffractogram of material with target composition $Sr_2Co_2O_5$ (space group I4/mmm) after 36 hours of heating at 1000 °C. The small blue circles represent the observed diffracted intensity, the green line represents the Rietveld-refined calculated model, the red line represents the background, and the grey line represents the difference between observed and calculated intensities. The black and blue tick marks show the reflections of the refined models of $Sr_6Co_5O_{15}$ (98.5 %) and Co_3O_4 (1.5 %).*
Duration: 5 hours. Data points: 3457. Interval: 0.02 °. GOF: 2.03. R_{wp}: 1.468 %.

The average oxidation state of cobalt in $Sr_6Co_5O_{15}$ is +3.6, with four Co^{4+} ions and one Co^{2+} ions,[322] effectively $Sr_6Co^{4+}{}_4Co^{2+}O_{15}$. Given this phase itself was not of direct interest here, but rather the pre-oxidation of cobalt ready for further reaction, $Sr_6Co_5O_{15}$ was pursued as a precursor. All desired atoms were present irrelevant of structure, and the cobalt oxidation was successful. The cobalt now actually requires a slight reduction; however this should be achieved simply through heating in the next reaction step.

$Sr_6Co_5O_{15}$ was reacted with $SrCl_2$ as planned and successfully produced the black oxychloride product $Sr_3Co_2O_5Cl_2$ phase pure, see Figure 171. This reaction was deemed successful following three 24 hour cycles in air at 800 °C, followed by 24 hours at 900 °C. The accomplishment of correct stoichiometry is further evidence for the presence of Co_3O_4 in the $Sr_6Co_5O_{15}$ mixture, thus the reaction was hypothesised to have proceeded according to Equation 79:

Equation 79 $$Sr_6Co_5O_{15} + {}^1/_3\, Co_3O_4 + 3\, SrCl_2{\cdot}6H_2O \rightarrow 3\, Sr_3Co_2O_5Cl_2 + {}^2/_3\, O_2 + 18\, H_2O$$

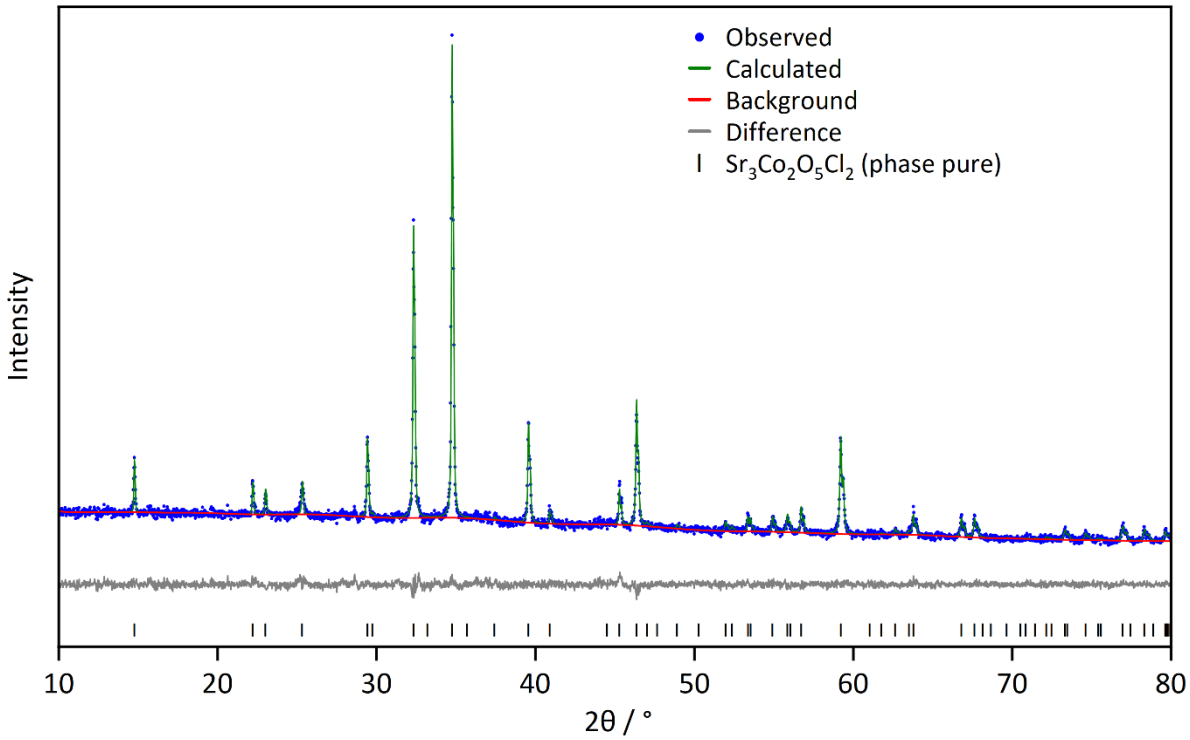

Figure 171 *Powder X-ray diffractogram of material with target composition $Sr_3Co_2O_5Cl_2$ (space group I4/mmm) after 96 hours of heating at 800 to 900 °C. The small blue circles represent the observed diffracted intensity, the green line represents the Rietveld-refined calculated model, the red line represents the background, and the grey line represents the difference between observed and calculated intensities. The black tick marks show the reflections of the refined model of $Sr_3Co_2O_5Cl_2$, no impurity phases are observed.*
Duration: 45 minutes. Data points: 3457. Interval: 0.02 °. GOF: 1.20. R_{wp}: 2.849 %.

Following the successful synthesis of $Sr_3Co_2O_5Cl_2$ via the $Sr_6Co_5O_{15}$ intermediate, the synthesis method using strontium peroxide was explored as an interesting alternative, and for completeness. This method, which as discussed previously is not reported in literature with a yield higher than 84 % due to the formation of $Sr_6Co_5O_{15}$ as a by-product, was attempted according to Equation 80:

Equation 80 $$2\ SrO_2 + {}^{2}/_{3}\ Co_3O_4 + SrCl_2 \rightarrow Sr_3Co_2O_5Cl_2 + {}^{5}/_{3}\ O_2$$

Three 24 hour heat cycles at 580, 800 and 850 °C yielded phase pure $Sr_3Co_2O_5Cl_2$. The peroxide was of sufficient oxidising ability to produce Co^{3+} as required for the target material, and further supports that oxidation (or lack thereof) was the inhibitor of the initial synthesis attempt. The PXRD of this product was analogous to that shown above, and can be seen in *Appendix Figure 242*. To the best of the author's knowledge this is a greater purity than any literature reports of this method.

5.3.1.2 $Sr_3Fe_2O_5Br_2$

$Sr_3Fe_2O_5Br_2$ was synthesised on a 5 gram scale using conventional solid-state chemistry, according to Equation 81 below:

Equation 81 $2\ SrCO_3 + Fe_2O_3 + SrBr_2{\cdot}6H_2O \rightarrow Sr_3Fe_2O_5Br_2 + 2\ CO_2 + 6\ H_2O$

Carbonate and hydrate air-stable precursors were again employed here, in an attempt to use more widely available and cheaper materials, and eliminate the use of a glovebox. Due to the availability of the B_2O_3 oxide form of iron in the +3 oxidation state, thus the subsequent nonrequirement of metal oxidation, this synthesis was far simpler than that of the cobalt material previously.

The powder mixture was heated in air to 580 °C for two 24 hour heat cycles with an intermediate regrind. A final 24 hour heat at 850 °C, conditions in agreement to those reported in literature,[323, 324] yielded the red oxybromide material phase pure. The XRD pattern obtained following this synthesis is shown in Figure 172.

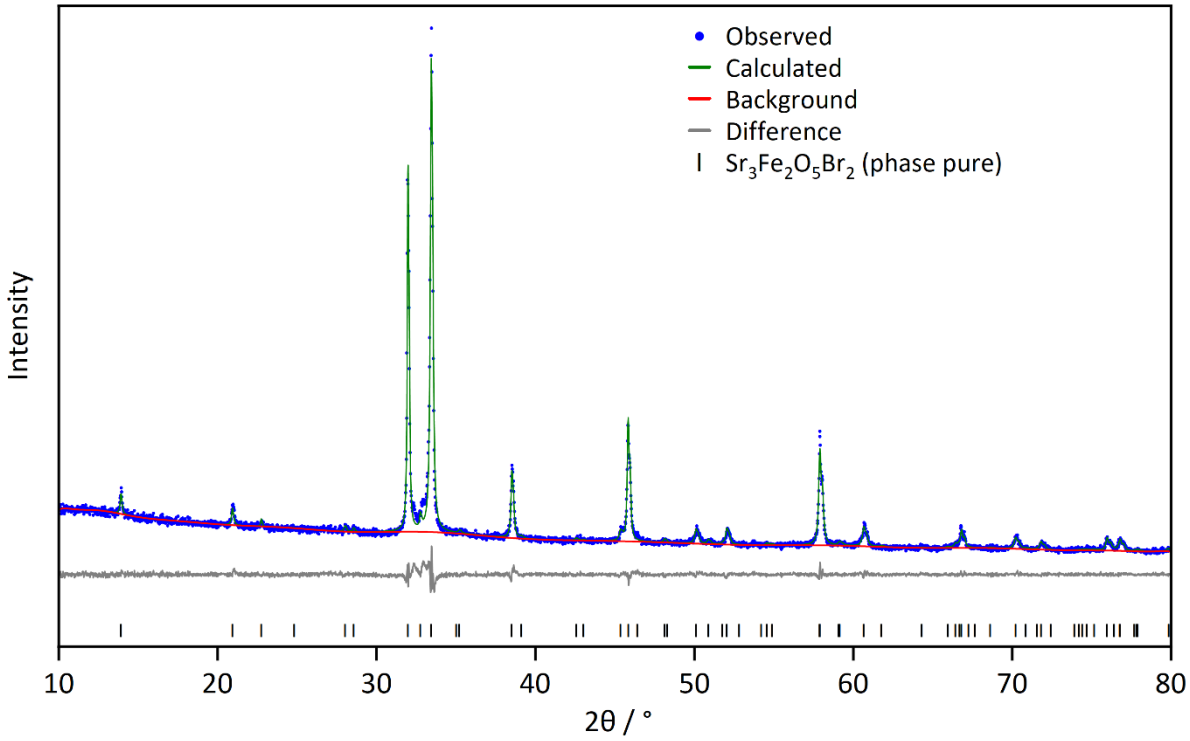

Figure 172 *Powder X-ray diffractogram of material with target composition $Sr_3Fe_2O_5Br_2$ (space group I4/mmm) after 72 hours of heating at 580 to 850 °C. The small blue circles represent the observed diffracted intensity, the green line represents the Rietveld-refined calculated model, the red line represents the background, and the grey line represents the difference between observed and calculated intensities. The black tick marks show the reflections of the refined model of $Sr_3Fe_2O_5Br_2$, no impurity phases are observed.*
Duration: 45 minutes. Data points: 3457. Interval: 0.02 °. GOF: 1.43. R_{wp}: 5.344 %.

5.3.1.3 $Sr_4Co_2O_6Cl_2$

As detailed in *Section 5.3.1.1*, the synthesis of $Sr_3Co_2O_5Cl_2$ was performed successfully by two pathways, one via a '$Sr_2Co_2O_5$' intermediate and another using SrO_2 as an oxidising agent. $Sr_2Co_2O_5$ absorbed oxygen upon cooling and changed phase to form $Sr_6Co_5O_{15}$ and Co_3O_4, but the exact composition of the intermediate was not important, only the oxidation of cobalt which was successful. Reaction of this mixture with $SrCl_2$ produced the 325 oxychloride phase pure.

It was theorised that the same $Sr_6Co_5O_{15}$ / Co_3O_4 mixture may be used to synthesise the 426 analogue $Sr_4Co_2O_6Cl_2$, in which the oxidation state of cobalt is also +3, therefore requiring only the addition of a further SrO or $SrCO_3$ unit, according to Equation 82. Like $Sr_3Co_2O_5Cl_2$, the synthesis of $Sr_4Co_2O_6Cl_2$ in literature is achieved by the peroxide route[313, 314, 319] or the *Brownmillerite* route.[315]

Equation 82 $$Sr_6Co_5O_{15} + {}^1/_3\, Co_3O_4 + 3\, SrCO_3 + 3\, SrCl_2 \rightarrow 3\, Sr_4Co_2O_6Cl_2 + {}^2/_3\, O_2 + 3\, CO_2$$

Three heat cycles at 500, 800 and 900 °C with intermediate regrinds in air produced phase pure $Sr_4Co_2O_6Cl_2$, a black powder, the XRD data of which is shown in Figure 173 below.

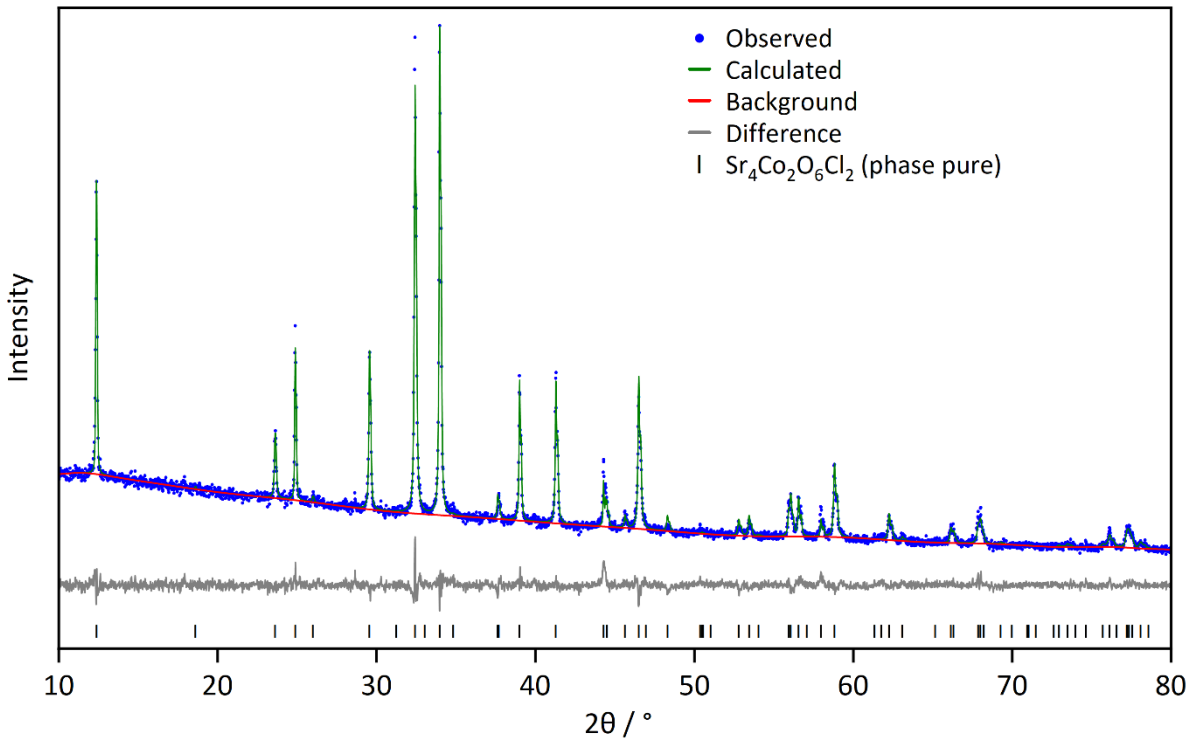

Figure 173 *Powder X-ray diffractogram of material with target composition $Sr_4Co_2O_6Cl_2$ (space group I4/mmm) after 72 hours of heating at 800 to 900 °C. The small blue circles represent the observed diffracted intensity, the green line represents the Rietveld-refined calculated model, the red line represents the background, and the grey line represents the difference between observed and calculated intensities. The black tick marks show the reflections of the refined model of $Sr_4Co_2O_6Cl_2$, no impurity phases are observed.*
Duration: 45 minutes. Data points: 3457. Interval: 0.02 °. GOF: 1.34. R_{wp}: 3.617 %.

5.3.1.4 $Sr_4Sc_2O_6Cl_2$

The fourth material produced for the light layer precursor bank was $Sr_4Sc_2O_6Cl_2$. This is the light layer precursor that would, if reacted with a $[Cu_2Ch_2]^{2-}$ subunit in a metathesis reaction, produce the MALM materials $Sr_4Sc_2O_6Cu_2Ch_2$ studied in *Chapter 4*. $Sr_4Sc_2O_6Cl_2$ was synthesised on a 5 gram scale according to Equation 83.

Equation 83 $3\ SrO + Sc_2O_3 + SrCl_2 \rightarrow Sr_4Sc_2O_6Cl_2$

Powder samples were prepared in a glovebox for accuracy of measurement, but heated in air, as any gas absorption by the precursors would be completely reversible upon heating. Four 24 hour heat cycles at 500, 700, 900 and 1050 °C produced a white powder product that was phase pure by PXRD, Figure 174. These conditions are analogous to those used in literature,[325] and it has been shown that air stable precursors can also be applied to this synthesis.[326]

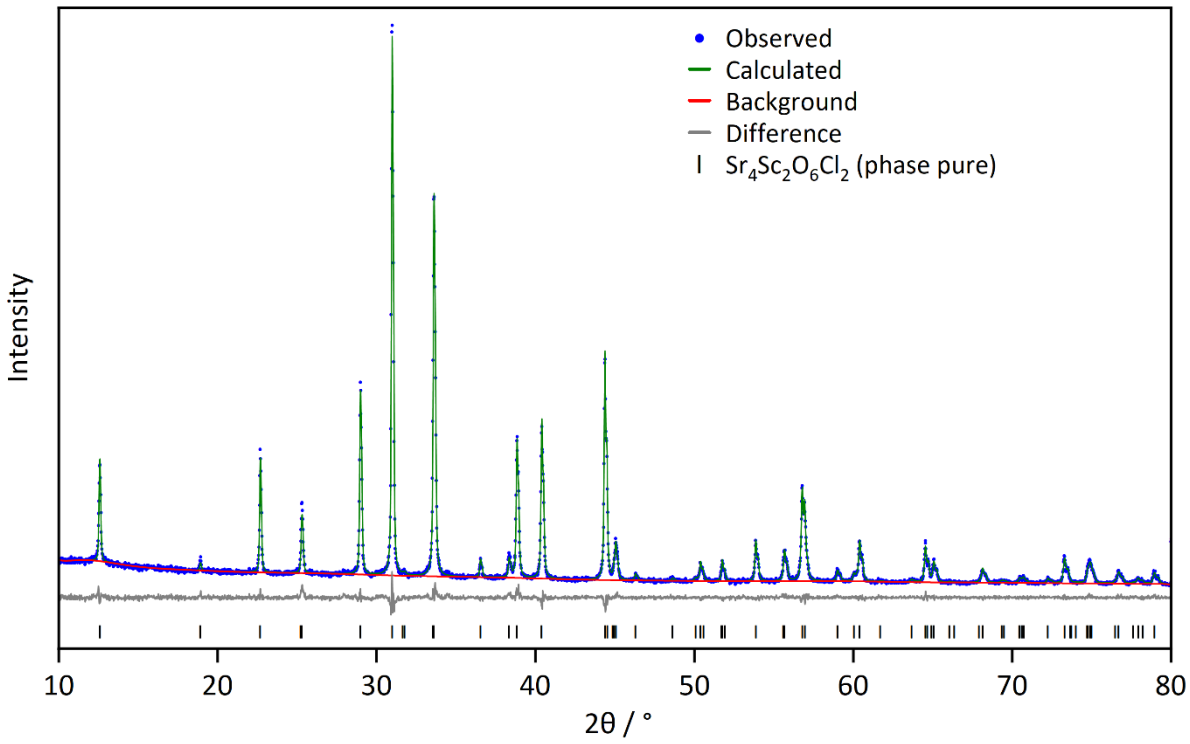

Figure 174 *Powder X-ray diffractogram of material with target composition $Sr_4Sc_2O_6Cl_2$ (space group I4/mmm) after 96 hours of heating at 500 to 1050 °C. The small blue circles represent the observed diffracted intensity, the green line represents the Rietveld-refined calculated model, the red line represents the background, and the grey line represents the difference between observed and calculated intensities. The black tick marks show the reflections of the refined model of $Sr_4Sc_2O_6Cl_2$, no impurity phases are observed.*
Duration: 45 minutes. Data points: 3457. Interval: 0.02 °. GOF: 1.16. R_{wp}: 6.118 %.

5.3.1.5 $Sr_3Sc_2O_5Cl_2$

$Sr_3Sc_2O_5Cl_2$, the fifth targeted light layer precursor, was synthesised alongside the previous $Sr_4Sc_2O_6Cl_2$ under identical conditions, using one less molar equivalent of SrO.[325, 326] The reaction, which comprised four 24 hour heat cycles between 500 and 1050 °C in air with intermediate regrinds, therefore proceeded according to Equation 84:

Equation 84 $2\ SrO + Sc_2O_3 + SrCl_2 \rightarrow Sr_3Sc_2O_5Cl_2$

The white powder product was deemed phase pure by XRD, Figure 175. Later, in *Section 5.4.1*, this material is used as a light layer precursor in a detailed comparison between metathesis and conventional reactions, producing the same 325 MALMs that were explored in great detail in the doping studies of *Chapter 3*.

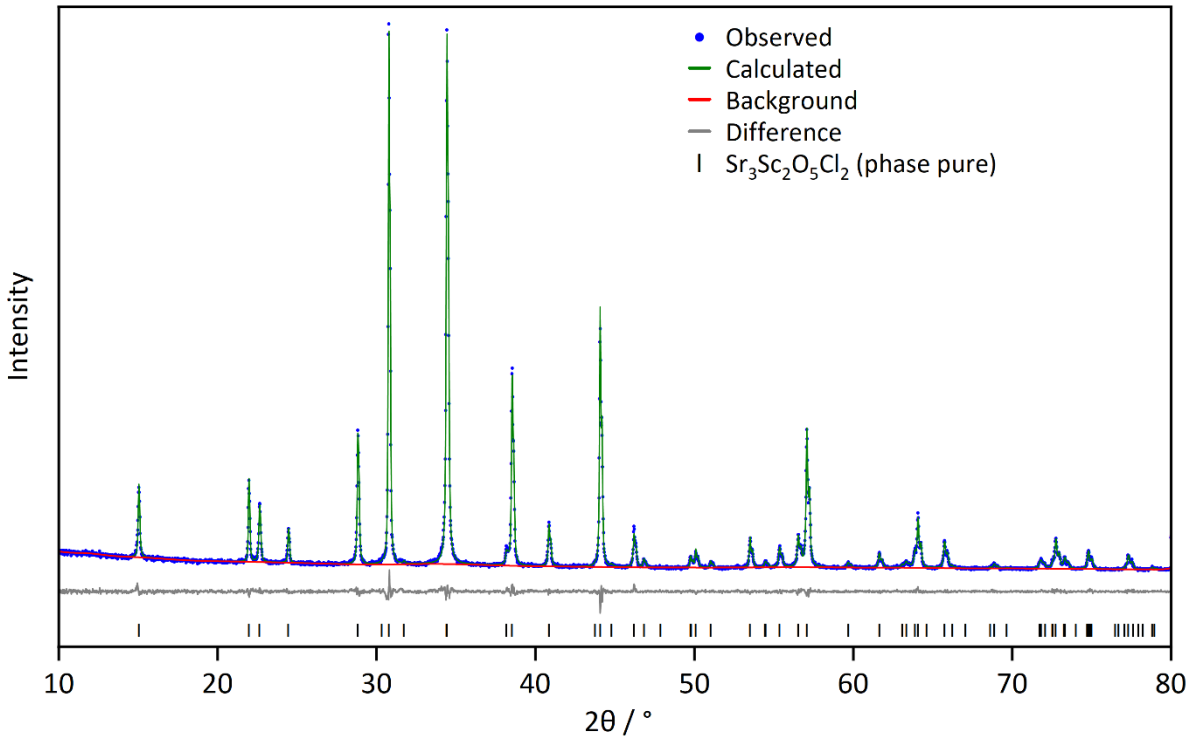

Figure 175 *Powder X-ray diffractogram of material with target composition $Sr_3Sc_2O_5Cl_2$ (space group I4/mmm) after 96 hours of heating at 500 to 1050 °C. The small blue circles represent the observed diffracted intensity, the green line represents the Rietveld-refined calculated model, the red line represents the background, and the grey line represents the difference between observed and calculated intensities. The black tick marks show the reflections of the refined model of $Sr_3Sc_2O_5Cl_2$, no impurity phases are observed.*
Duration: 45 minutes. Data points: 3457. Interval: 0.02 °. GOF: 1.17. R_{wp}: 6.082 %.

5.3.1.6 $Sr_3Fe_2O_5Cl_2$

$Sr_3Fe_2O_5Cl_2$ is one of the light layer precursors used in the sole MALM metathesis study published in literature, used to synthesise $Sr_3Fe_2O_5Cu_2Se_2$.[61] In this work, like the previous material $Sr_3Sc_2O_5Cl_2$, $Sr_3Fe_2O_5Cl_2$ is also explored in a comparison of metathetic and conventional syntheses later in this work.

Equation 85 $2\ SrO + Fe_2O_3 + SrCl_2 \rightarrow Sr_3Fe_2O_5Cl_2$

$Sr_3Fe_2O_5Cl_2$ was synthesised in air according to Equation 85 above. Three heat cycles at 600, 750 and 850 °C, 24 hours each, produced the phase pure red powder, which are conditions in line with those published in literature.[294, 324] Some publications report the synthesis of this material sealed within an ampoule,[61, 293] as is the case with many published syntheses of these oxyhalide materials, but this work has shown this step is not necessary as the end product is air stable and the degradation of any air sensitive precursors is completely reversible.

The phase pure XRD of $Sr_3Fe_2O_5Cl_2$ is seen in Figure 176 below.

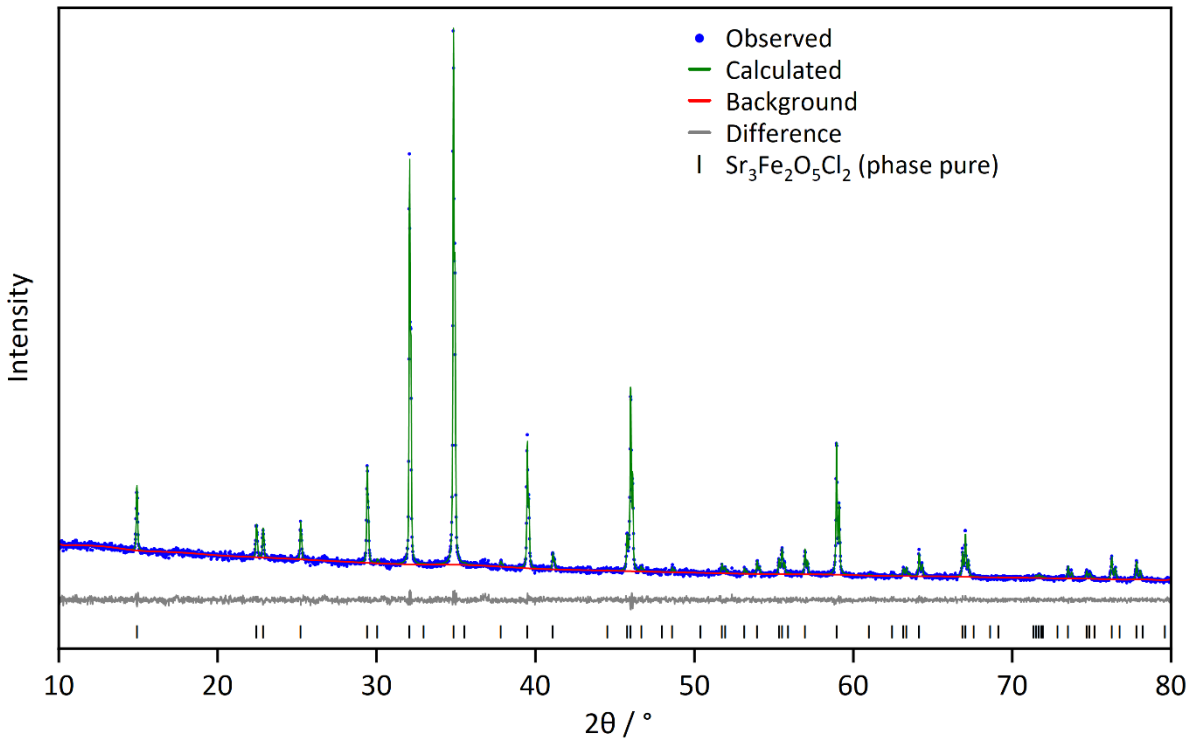

Figure 176 *Powder X-ray diffractogram of material with target composition $Sr_3Fe_2O_5Cl_2$ (space group I4/mmm) after 72 hours of heating at 600-850 °C. The small blue circles represent the observed diffracted intensity, the green line represents the Rietveld-refined calculated model, the red line represents the background, and the grey line represents the difference between observed and calculated intensities. The black tick marks show the reflections of the refined model of $Sr_3Fe_2O_5Cl_2$, no impurity phases are observed.*
Duration: 45 minutes. Data points: 3457. Interval: 0.02 °. GOF: 1.07. R_{wp}: 3.972 %.

5.3.1.7 $Sr_4Fe_2O_6Cl_2$

The synthesis of $Sr_4Fe_2O_6Cl_2$ was performed alongside the previously described $Sr_3Fe_2O_5Cl_2$ under identical conditions,[323, 324] with an extra molar unit of SrO, according to Equation 86:

Equation 86 $3\ SrO + Fe_2O_3 + SrCl_2 \rightarrow Sr_4Fe_2O_6Cl_2$

This light brown powder product actually exhibits a small impurity (Figure 177), and therefore unlike the other light layer precursors is not phase pure. The impurity could not be identified thus has not been refined into the diffractogram. However, the purity was deemed high enough for this light layer precursor to be used within the precursor bank in metathesis reactions.

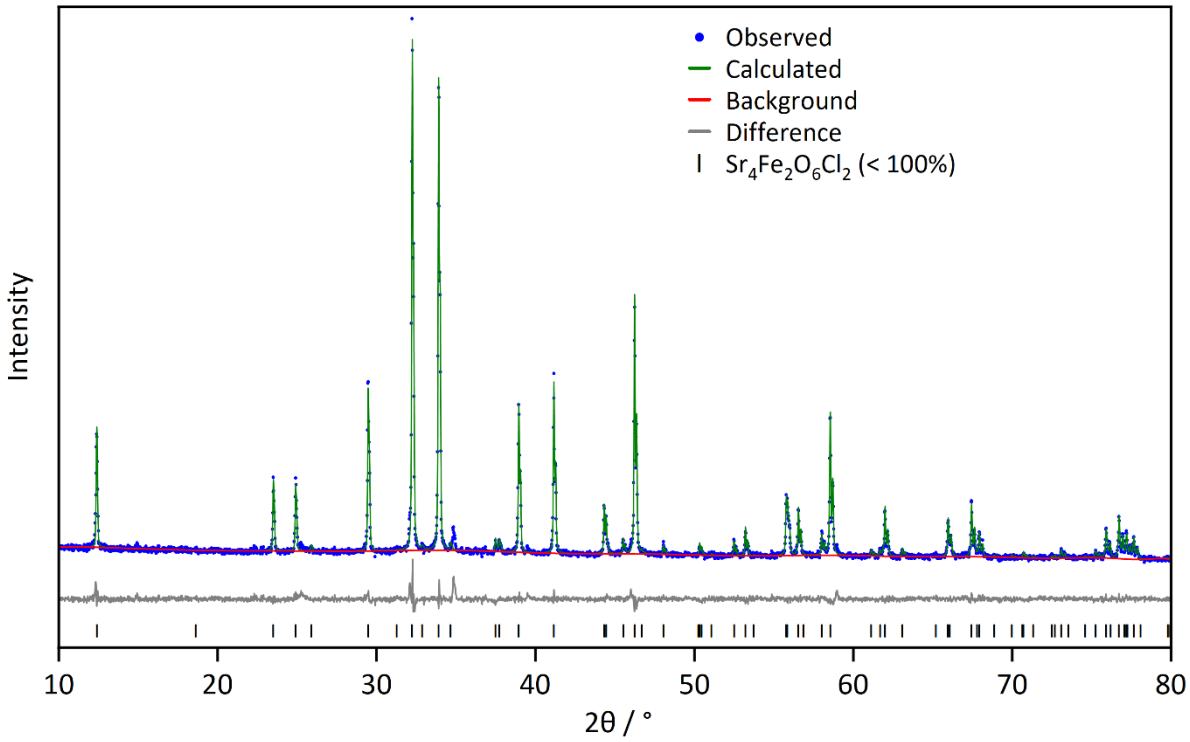

Figure 177 *Powder X-ray diffractogram of material with target composition $Sr_4Fe_2O_6Cl_2$ (space group I4/mmm) after 72 hours of heating at 600-850 °C. The small blue circles represent the observed diffracted intensity, the green line represents the Rietveld-refined calculated model, the red line represents the background, and the grey line represents the difference between observed and calculated intensities. The black tick marks show the reflections of the refined model of $Sr_4Fe_2O_6Cl_2$. A small unknown impurity is present in the material. Duration: 45 minutes. Data points: 3457. Interval: 0.02 °. GOF: 1.35. R_{wp}: 4.381 %.*

5.3.1.8 $Sr_4Fe_2O_6Br_2$

The eighth and final light layer precursor synthesised for the bank was $Sr_4Fe_2O_6Br_2$. This is the bromide equivalent of the previous material $Sr_4Fe_2O_6Cl_2$. In a metathesis reaction with a given heavy layer precursor, these two materials would produce the same MALM, $Sr_4Fe_2O_6M_2Q_2$, but would produce different by-product salts.

This material was synthesised according to Equation 87. It was produced alongside and under identical conditions to the previous two materials: three 24 hour heating cycles at 600, 750 and 850 °C, in agreement with literature conditions.[323, 324]

Equation 87 $3\ SrO + Fe_2O_3 + SrBr_2 \rightarrow Sr_4Fe_2O_6Br_2$

The resulting brown powder contained a small 2 % $SrCO_3$ impurity resulting from unreacted SrO which has absorbed CO_2 in air, Figure 178. Despite this, it was considered of sufficient purity to be taken forward in this investigation.

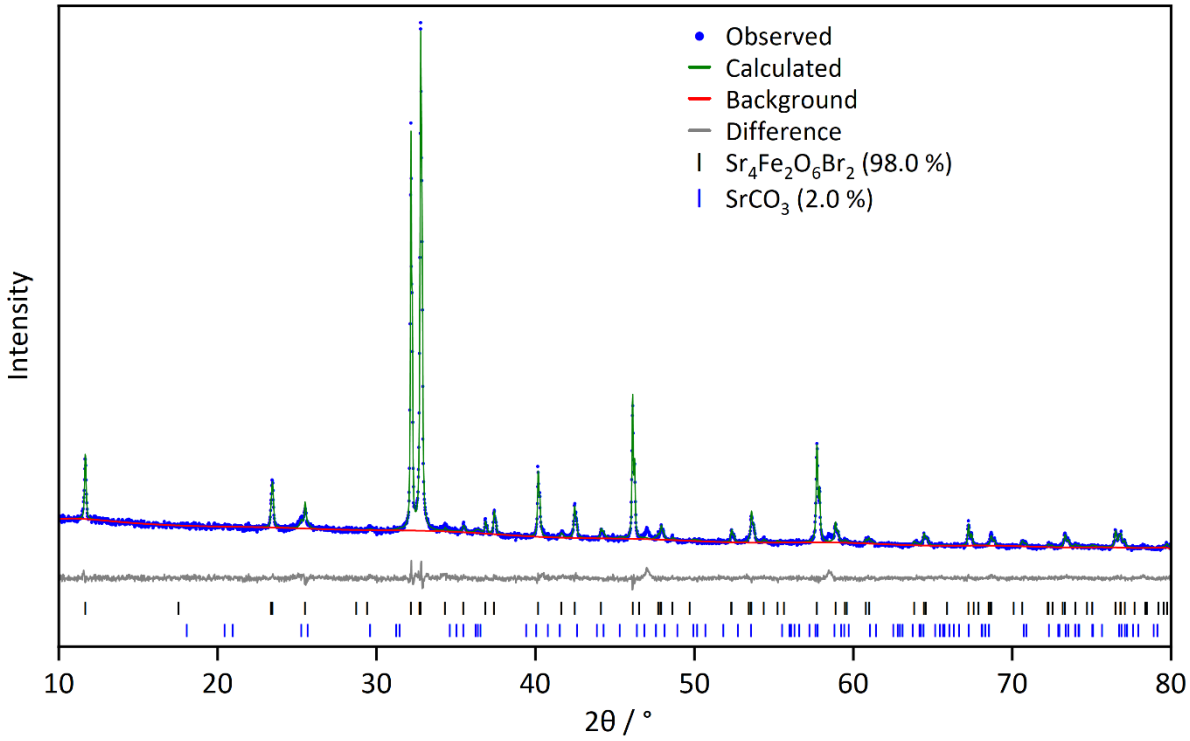

Figure 178 *Powder X-ray diffractogram of material with target composition $Sr_4Fe_2O_6Br_2$ (space group I4/mmm) after 72 hours of heating at 600-850 °C. The small blue circles represent the observed diffracted intensity, the green line represents the Rietveld-refined calculated model, the red line represents the background, and the grey line represents the difference between observed and calculated intensities. The black tick marks show the reflections of the refined model of $Sr_4Fe_2O_6Br_2$ (98.0 %), whilst the blue marks represent refined impurity phase $SrCO_3$ (2.0 %).*
Duration: 45 minutes. Data points: 3457. Interval: 0.02 °. GOF: 1.28. R_{wp}: 4.142 %.

5.3.1.9 Other Attempted Light Layer Synthesis

$Ba_3Y_2O_5Cl_2$ was targeted in order to introduce a barium analogue into the bank of light layer precursors. This material is reported in literature synthesised by the same method used in the previous light layer precursors,[326, 327] shown in Equation 88:

Equation 88 $2\ BaO + Y_2O_3 + BaCl_2 \rightarrow Ba_3Y_2O_5Cl_2$

A replica of this literature synthesis was attempted, using four 24 hour heat cycles between 900 and 1050 °C within an ampoule, which produced the target material but incomplete and with significant impurities. Further heat treatments were unable to increase the product purity above 81 %. Interestingly, all constituent elements are present in the impurity phases in appreciable quantity, so it is unlikely that there was a deficiency of any one element, nor was any oxidation or reduction required. It is unknown therefore why this synthesis was not successful, and successive attempts yielded no improvements. $Ba_3Y_2O_5Cl_2$ was deemed too impure to be used in future metatheses and was retired.

The XRD data for the chalky white powder product is shown in Figure 179, where the impurities Y_2O_3 and Ba_4OCl_6 can be observed alongside the main phase $Ba_3Y_2O_5Cl_2$. An unknown phase is also present within the material which was not recognised nor refined.

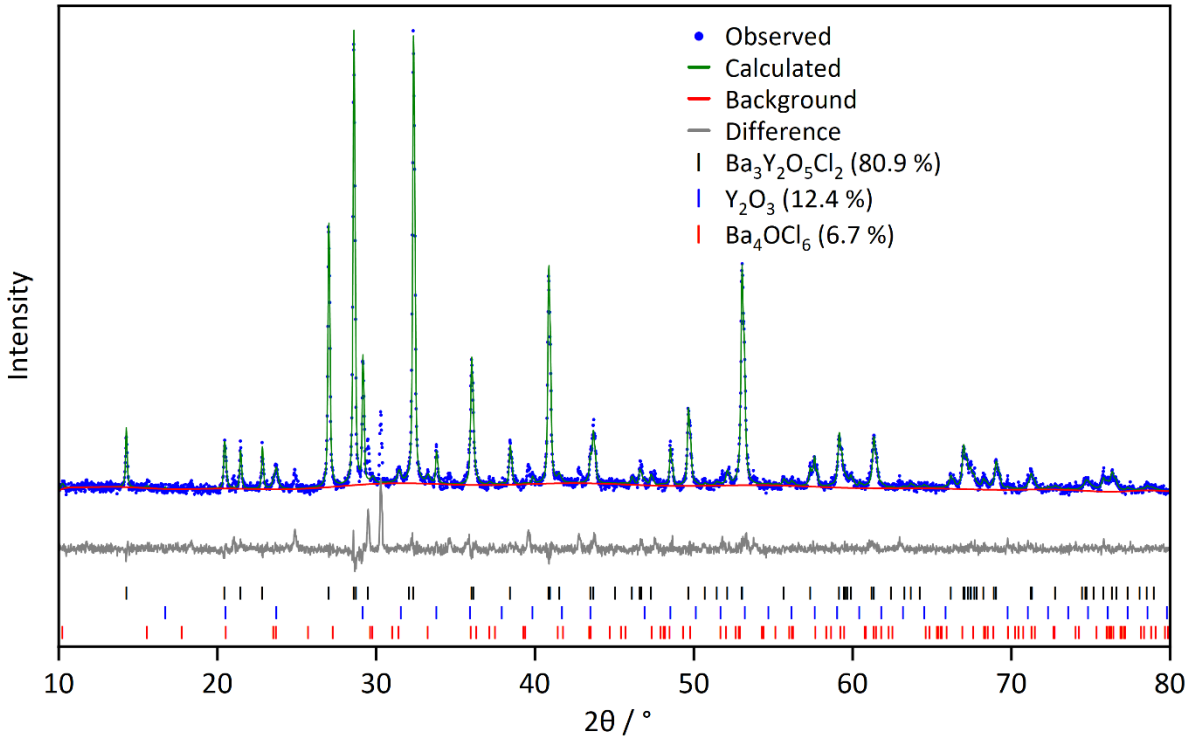

Figure 179 *Powder X-ray diffractogram of material with target composition $Ba_3Y_2O_5Cl_2$ (space group I4/mmm) after 96 hours of heating at 900 to 1050 °C. The small blue circles represent the observed diffracted intensity, the green line represents the Rietveld-refined calculated model, the red line represents the background, and the grey line represents the difference between observed and calculated intensities. The black tick marks show the reflections of the refined model of $Ba_3Y_2O_5Cl_2$ (80.9 %), whilst the blue and red marks represent refined impurity phases Y_2O_3 (12.4 %) and Ba_4OCl_6 (6.7 %) respectively.*
Duration: 45 minutes. Data points: 3457. Interval: 0.02 °. GOF: 1.55. R_{wp}: 8.979 %.

5.3.2 Heavy Layer Precursors

The vast majority of reports of heavy layer precursors found in the comprehensive literature search involved a synthesis either from the elements (a process which is preferentially avoided in this work due to risks of oxidation or volatility harming the sample purity) or with equipment unavailable during this research such as spark plasma sintering or induction melt furnaces, usually also as elements.[328-330] This limits the pool of available materials, reducing it only to those which may be synthesised from the combination of, ideally, two binary precursors.

For this reason and the difficulty of synthesis, purity and storage, only one heavy layer was targeted. As discussed previously, the grid size of a parallel metathesis will correlate highly with the complexity or perhaps impossibility of PXRD analysis, thus for this proof of concept investigation, a $1 \times x$ grid where x is a number of high purity light layers, is more than sufficient to investigate the process.

A sensible choice of heavy layer with a $[M_2Q_2]^{2-}$ motif that appears abundantly in literature such as $[Cu_2Se_2]^{2-}$ will increase the number of light layers with which it is compatible, furthering its usefulness in testing a parallel synthesis proof-of-concept.

5.3.2.1 $Na_2Cu_2Se_2$

The heavy layer precursor selected was $Na_2Cu_2Se_2$, whose synthesis is reported twice in literature, first by Savelsberg in 1978,[301] then by Cario et al in 2005.[61] In both, $Na_2Cu_2Se_2$ was synthesised through direct elemental combination of Na, Cu and Se, Equation 89:

Equation 89 $2\ Na + 2\ Cu + 2\ Se \rightarrow Na_2Cu_2Se_2$

As this route was not possible, a 1 : 1 combination of Na_2Se and Cu_2Se binaries was deemed a logical alternative. Given the novelty of the chosen method, conditions such as duration, temperature, and number of heating cycles were unknown and must be optimised. Before the synthesis of $Na_2Cu_2Se_2$ could proceed, the complex air-sensitive synthesis of the binary precursor Na_2Se from elemental Na and Se in liquid ammonia was first carried out, a process described in *Section 2.3.5.*

$Na_2Cu_2Se_2$, like most heavy layer precursors in literature, is very unstable. Savelsberg reported in their synthesis of $Na_2Cu_2Se_2$:

> *"The crystals are extremely sensitive to moist air and completely disintegrate within a few hours to a black powder. Even under dry paraffin oil the decomposition proceeds so rapidly, that the chemical and analytical characterisation is fraught with great preparative difficulties."*
>
> Savelsberg, 1978.[301] Translated from German.

The synthesis of $Na_2Cu_2Se_2$ was attempted on a 1 gram scale using conventional solid-state chemistry, according to Equation 90 below:

Equation 90 $Na_2Se + Cu_2Se \rightarrow Na_2Cu_2Se_2$

The ground powder material was subjected to one heat cycle in a sealed silica ampoule for 24 hours at 900 °C, the same heating conditions employed by Savelsberg in their synthesis from the elements. This yielded an extremely tough black charred product which had melted and was not retrievable in any useful quantity. The melting points of Na_2Se and Cu_2Se are 875 °C and 1113 °C respectively, therefore the reaction temperature was too high and had surpassed the melting point of Na_2Se. Whilst melting is often desirable in elemental reactions, it is not in conventional solid-state chemistry.

A similar 5 gram experiment was performed, this time consisting of 12 hour heating cycles at 500 °C, 650 °C and 800 °C with intermediate regrinds. Similar to the protocol employed in previous chapters when using elemental sulfur or selenium in doping studies, the lower initial temperature was employed initially to begin the reaction, which was increased following a regrind, but remaining sufficiently below the melting point of Na_2Se to avoid melting. The resulting dark black crystalline material was found to be phase pure by air-sensitive XRD, but completely degraded to an amorphous by-product if analysed in air. The lower initial temperature had proven promising in preventing melting or degradation of the precursors during synthesis, with no signs of melting.

In a later re-stock synthesis of $Na_2Cu_2Se_2$, a very low initial temperature of 250 °C for 24 hours was investigated, followed by a 12 hour heat at 800 °C. It was found that the product was phase pure and identical to that produced above, indicating firstly that two heating cycles is sufficient (the material after one cycle at either 250 °C or 500 °C showed some unknown intermediates) and also that 500 - 800 °C is a suitable temperature range for the synthesis. No synthesis attempts described here employed pelletisation due to the extremely unstable nature of both Na_2Se and $Na_2Cu_2Se_2$.

The diffractogram of the resulting product is shown in Figure 180, where a short scan within the air-sensitive dome revealed what is, to the best of the authors knowledge, the highest quality PXRD data of this very unstable material published to date. 10 minutes was the longest scan possible before the material significantly decomposes, even within the inert atmosphere dome. This is also the first reported successful synthesis of this material using binary precursors rather than from the elements.

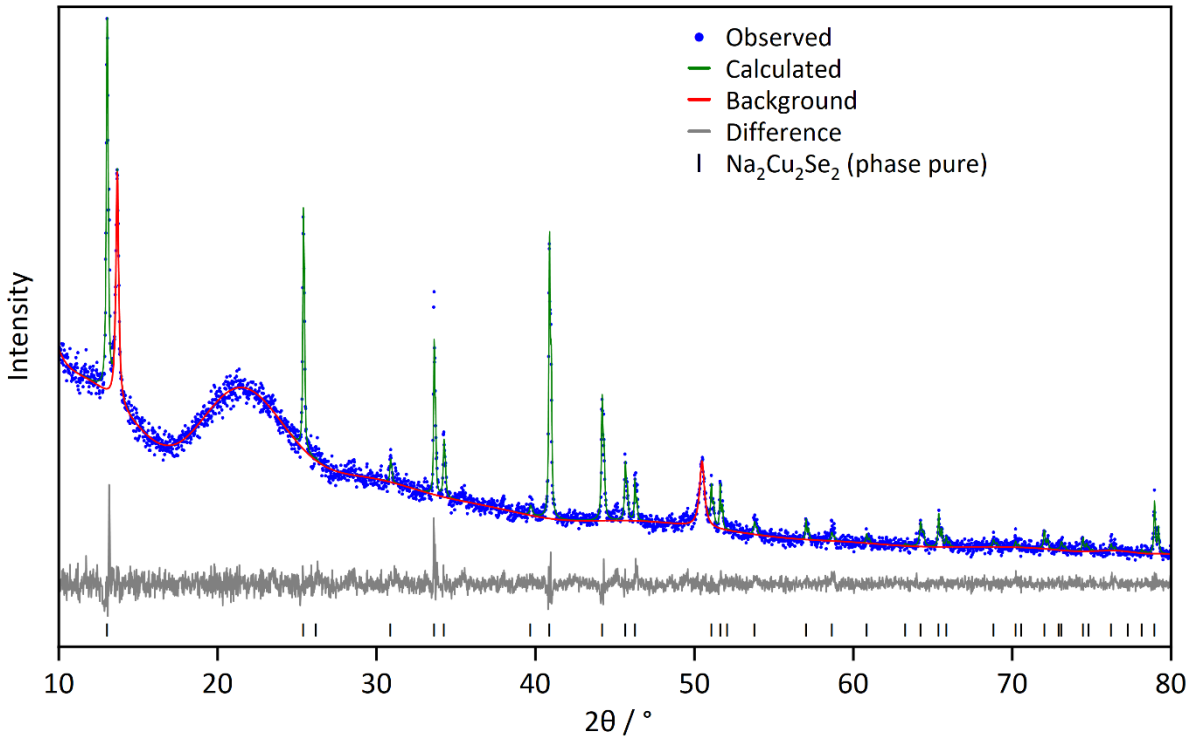

Figure 180 *Powder X-ray diffractogram of material with target composition $Na_2Cu_2Se_2$ (space group I4/mmm) after 24 hours of heating at 800 °C. The small blue circles represent the observed diffracted intensity, the green line represents the Rietveld-refined calculated model, the red line represents the background, and the grey line represents the difference between observed and calculated intensities. The black tick marks show the reflections of the refined model of $Na_2Cu_2Se_2$, no impurity phases are observed. Data was collected with the domed air-tight holder, responsible for the background-refined peaks at 13.3 and 50.5 °. Duration: 10 minutes. Data points: 3457. Interval: 0.02 °. GOF: 1.15. R_{wp}: 5.847 %.*

$Na_2Cu_2Se_2$ completes a bank of nine total pre-formed subunit precursors, eight light and one heavy, to be taken forward into metathetic reactions. A comparison of the colours of the nine materials can be seen in Figure 181 below.

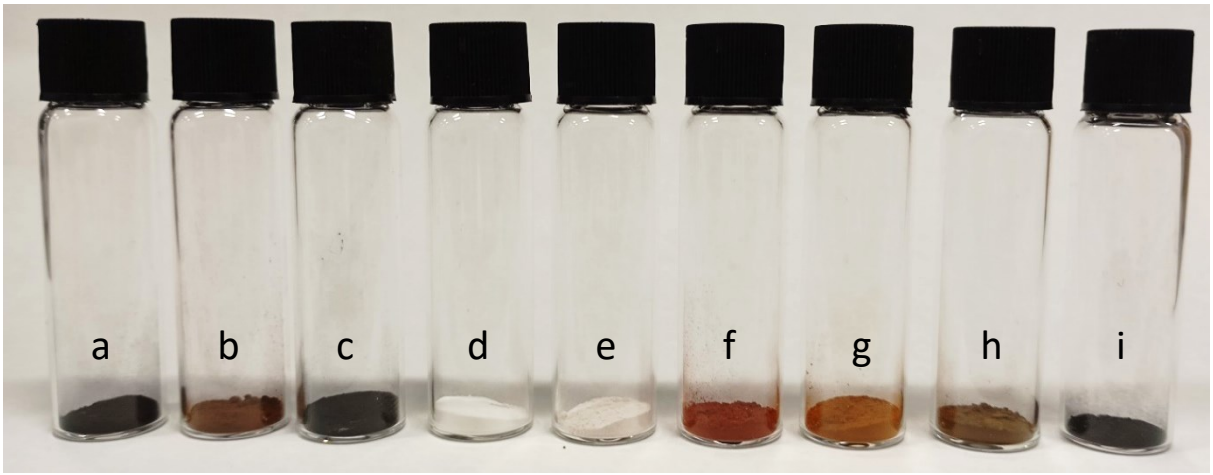

Figure 181 *A comparison of the colours of the bank of metathesis precursors: a) $Sr_3Co_2O_5Cl_2$, b) $Sr_3Fe_2O_5Br_2$, c) $Sr_4Co_2O_6Cl_2$, d) $Sr_4Sc_2O_6Cl_2$, e) $Sr_3Sc_2O_5Cl_2$, f) $Sr_3Fe_2O_5Cl_2$, g) $Sr_4Fe_2O_6Cl_2$, h) $Sr_4Fe_2O_6Br_2$, and i) $Na_2Cu_2Se_2$.*

5.4 Metathesis Investigations

The creation of a bank of metathesis precursors resulted in the syntheses of eight oxyhalide light layer precursors and one heavy layer precursor, all of high purity and in 5 g quantities to serve as a feedstock for multiple future reactions.

Before any extrapolation of the metathesis method to a parallel synthesis process, the metathetic pathway itself warrants attention. Publications of metathesis are sparse in literature, and those relating to MALMs even sparser. No claims about sample purity have been reported, and no publications report any phase purity[19] or high yields resulting from this method of MALM synthesis.

Two light layer precursors were selected to react with $Na_2Cu_2Se_2$ in an investigation of metathesis: $Sr_3Sc_2O_5Cl_2$ and $Sr_3Fe_2O_5Cl_2$. In a preliminary investigation such as this where novel materials are not the aim, but rather an exploration of the synthetic process, target materials with high probabilities of success should be selected. As such, it was decided that $Sr_3Sc_2O_5Cu_2Se_2$, a stable MALM widely explored in this work and found to have no competing MALM phases (and found to be significantly more stable than the 426 analogue), would be a good choice of material for this preliminary test. The second selected light layer $Sr_3Fe_2O_5Cl_2$ produces $Sr_3Fe_2O_5Cu_2Se_2$ on reaction with $Na_2Cu_2Se_2$. This is the reaction reported by Cario in his MALM metathesis study, thus the only quinternary MALM shown thus far to be synthesisable by metathesis. These two materials presented the greatest probability for successful metathesis.

In each of the $Sr_3Sc_2O_5Cu_2Se_2$ and $Sr_3Fe_2O_5Cu_2Se_2$ investigations, metathesis experiments are compared directly to analogous conventional experiments at 500, 600, 700, 800 and 900 °C. It was hypothesised that if the metathesis pathway is possible, it would proceed at a lower temperature, and that at regular synthesis temperatures of ≥ 800 °C the mixture would react by conventional solid-state chemistry and all atoms would be free to react to form the most thermodynamically stable materials, not just those dictated by metathesis.

The presence of NaCl in the metathesis mixture, especially at low temperatures, implies successful metathesis. It was assumed that standard MALM impurities like SrSe and $SrCO_3$ would be absent or at very low quantities due to the limited capacity for conventional solid-state ion diffusion at low temperatures.

[19] A successful metathesis reaction cannot of course be phase pure in the conventional sense, due to the salt by-product which comprises a significant amount of the resulting sample. Within this chapter only, 'phase pure' in a metathetic context refers to the presence only of the target MALM, and its salt by-product, with no evidence of non-negligible impurities or unreacted precursor.

5.4.1 $Sr_3Sc_2O_5Cu_2Se_2$ Investigation

Two 5 gram batches of precursors targeting the MALM $Sr_3Sc_2O_5Cu_2Se_2$ were prepared. The first comprised the binary precursors of a conventional synthesis, according to Equation 91, and the second comprised the light and heavy layer precursors for a metathesis reaction according to Equation 92.

Equation 91 $2\ SrO + Sc_2O_3 + SrSe + Cu_2Se \rightarrow Sr_3Sc_2O_5Cu_2Se_2$

Equation 92 $Sr_3Sc_2O_5Cl_2 + Na_2Cu_2Se_2 \rightarrow Sr_3Sc_2O_5Cu_2Se_2 + 2\ NaCl$

These batches were ground to homogeneity in a nitrogen glovebox and then split into five samples of approximately 1 gram each. Placed into alumina crucibles and sealed within silica tubes under vacuum, these samples were reacted individually, as powders. Pelletising was omitted in both batches as a control measure given the air instability of heavy layer precursor $Na_2Cu_2Se_2$. The five samples of each batch were heated to 500, 600, 700, 800 and 900 °C respectively, for one 12 hour heat cycle. Following this, reground samples were analysed by air sensitive XRD within a Bruker air-tight domed specimen holder.

The results of the five samples in the metathesis batch are presented in Table 13, and the bar chart of Figure 182 on the following page. There are some immediate observations. Firstly, the synthesis of $Sr_3Sc_2O_5Cu_2Se_2$ was observed in every sample, the phase fraction of which correlates with increasing temperature. This is normal; however it resembles a trend expected more from a conventional synthesis than a metathesis synthesis and gives the impression that (at least some) conventional ceramic synthesis may be responsible for some $Sr_3Sc_2O_5Cu_2Se_2$ formation.

Table 13 *Tabulated phase fractions of the five component samples in the series of experiments targeting $Sr_3Sc_2O_5Cu_2Se_2$ by metathesis. The phases are colour coded to match the accompanying bar chart, and the tick marks on all constituent diffractograms.*

		Synthesis Temperature / °C				
		500	**600**	**700**	**800**	**900**
Phase Fraction / wt %	$Sr_3Sc_2O_5Cu_2Se_2$	2.2	34.4	54.4	59.6	66.1
	$Sr_3Sc_2O_5Cl_2$	65.6	28.1	23.4	12.9	2.8
	$Na_2Cu_2Se_2$	28.9	-	-	-	-
	SrSe	-	10.1	0.3	11.3	17.5
	$NaCu_3Se_2$	-	21.5	10.7	2.1	-
	NaCl	3.2	5.9	11.2	14.0	13.5

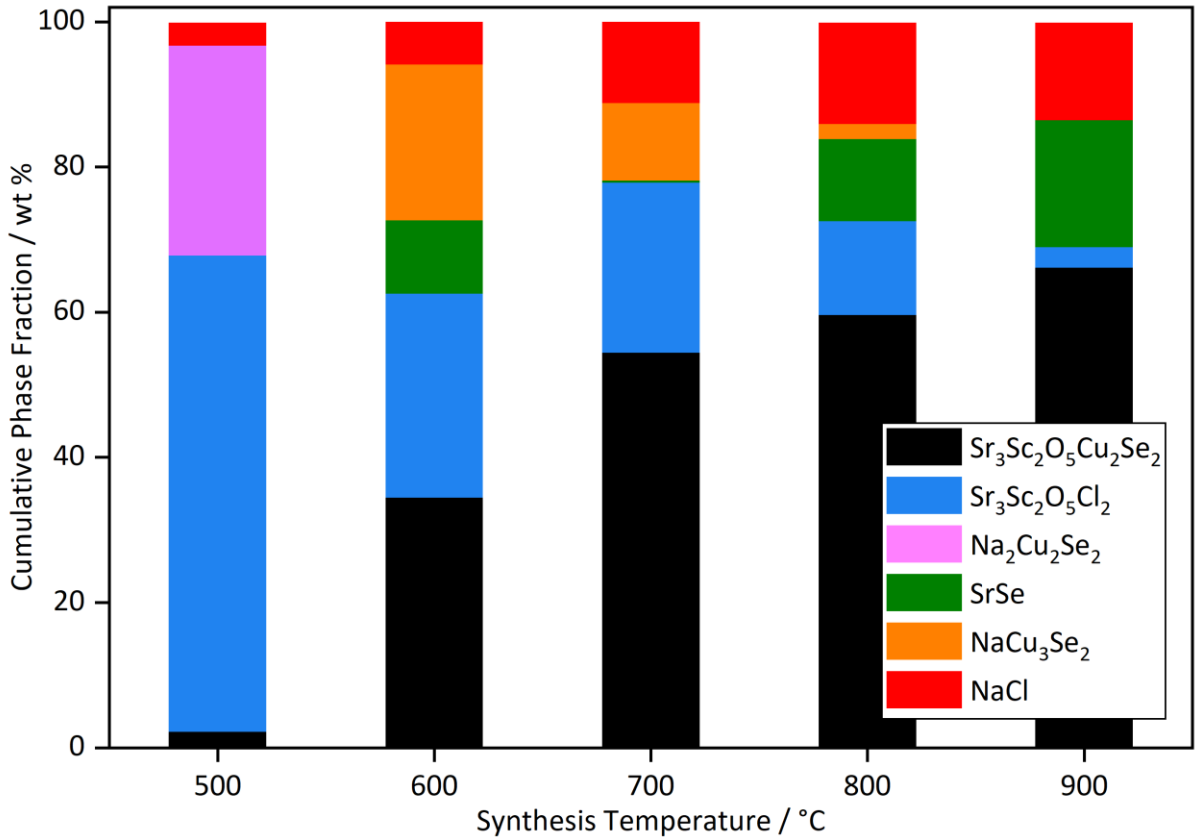

Figure 182 A bar chart illustrating the phase fractions of $Sr_3Sc_2O_5Cu_2Se_2$ (black), $Sr_3Sc_2O_5Cl_2$ (blue), $Na_2Cu_2Se_2$ (pink), SrSe (green), $NaCu_3Se_2$ (orange) and NaCl (red) from the five component samples in the series of experiments targeting $Sr_3Sc_2O_5Cu_2Se_2$ by metathesis.

The presence of NaCl, and its growth in phase fraction with increasing temperature, is a good indicator that metathesis is taking place here. While NaCl is a stable salt whose driving force could facilitate its formation in a conventional ceramic reaction as well as a metathesis reaction, the presence of other Na and Cl containing phases suggests the NaCl is not forming from a ceramic reaction else more NaCl would be formed, assisting the decomposition of the less stable layered precursors.

The light layer decreases in phase fraction across the temperature range, which is a good indicator of its consumption in a metathesis reaction. The heavy layer appears to decompose fully above 500 °C to a more stable form, $NaCu_3Se_2$, the ACu_3Ch_2 impurity observed frequently in the doping studies of *Chapter 3*. This structure appears to still contribute to metathesis and contains the necessary heavy layer component, so may be considered a more stable and partially decomposed form of $Na_2Cu_2Se_2$ in a chlorine rich environment where some Na has been removed to form NaCl.

A comparison of the 500 °C and 800 °C samples is shown on the following page, visualising an increase in the target 325 MALM phase. The 900 °C sample is largely a control sample, because given 800 °C is sufficient for conventional synthesis, it will surely be the primary reaction type at any point above 800 °C. Eliminating conventional reactions is impossible, therefore the lower temperature reactions at 500 and 600 °C are very interesting because they present $Sr_3Sc_2O_5Cu_2Se_2$ where it would not usually be expected.

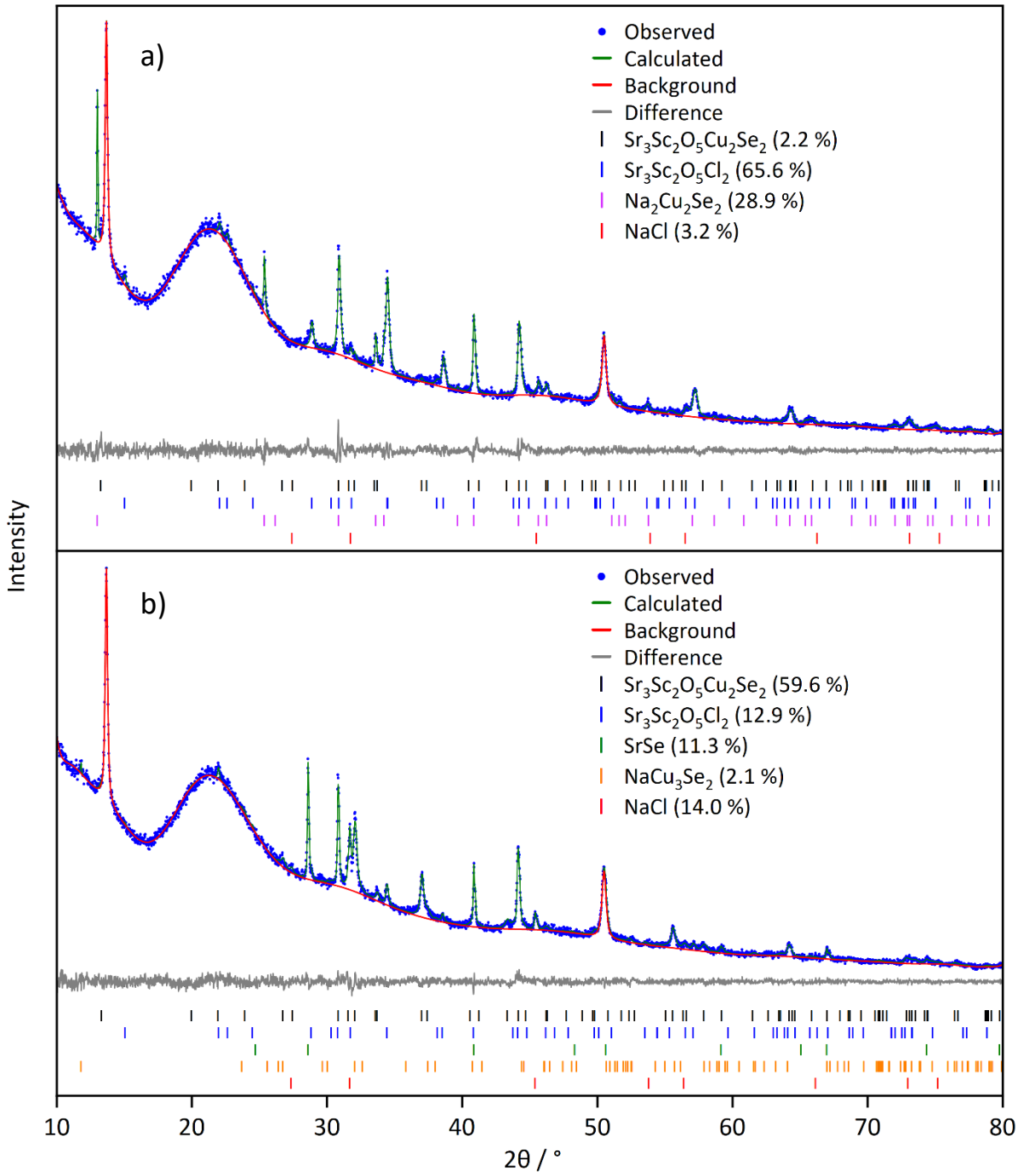

Figure 183 *Powder X-ray diffractograms of materials resulting from attempted metathesis synthesis of $Sr_3Sc_2O_5Cu_2Se_2$ after 12 hours of heating at a) 500 °C and b) 800 °C. The small blue circles represent the observed diffracted intensity, the green line represents the Rietveld-refined calculated model, the red line represents the background, and the grey line represents the difference between observed and calculated intensities. The black, blue, pink, green, orange and red tick marks show the reflections of the refined models of $Sr_3Sc_2O_5Cu_2Se_2$, $Sr_3Sc_2O_5Cl_2$, $Na_2Cu_2Se_2$, SrSe, $NaCu_3Se_2$ and NaCl respectively. Weight fractions for each phase are cited in the figure legends. Data was collected with the domed air-tight holder, responsible for the background-refined peaks at 13.3 and 50.5 °.*
a) Duration: 45 minutes. Data points: 3457. Interval: 0.02 °. GOF: 1.28. R_{wp}: 2.945 %.
b) Duration: 45 minutes. Data points: 3457. Interval: 0.02 °. GOF: 1.17. R_{wp}: 2.779 %.

(Rietveld refined diffractograms for all samples in this investigation can be found in *Appendix B.3.3*)

Whilst the results of the metathesis series provide some evidence for metathesis such as the increase in NaCl across the series, the consumption of the layered precursors and the synthesis of $Sr_3Sc_2O_5Cu_2Se_2$ at temperatures lower than would be typically expected for a reaction usually performed at 800 °C, they do not present clear evidence of metathesis in isolation.

However, when combined with the results of the temperature series targeting a conventional ceramic synthesis of $Sr_3Sc_2O_5Cu_2Se_2$, Figure 184 and Table 14, the two series together present very strong evidence in favour of metathesis. The most striking result in the series targeting a conventional synthesis is the formation of the 426 phase $Sr_4Sc_2O_6Cu_2Se_2$ at 500 to 700 °C. This should be expected, given the complex 325 / 426 stability balance described in *Section 4.3.2*, but the 426 MALM was not observed at any point in the metathesis series. This suggests that while one may view the metathesis series as actually a combination of both metathetic and conventional ceramic syntheses, this series consists solely of conventional ceramic and presents significantly different results.

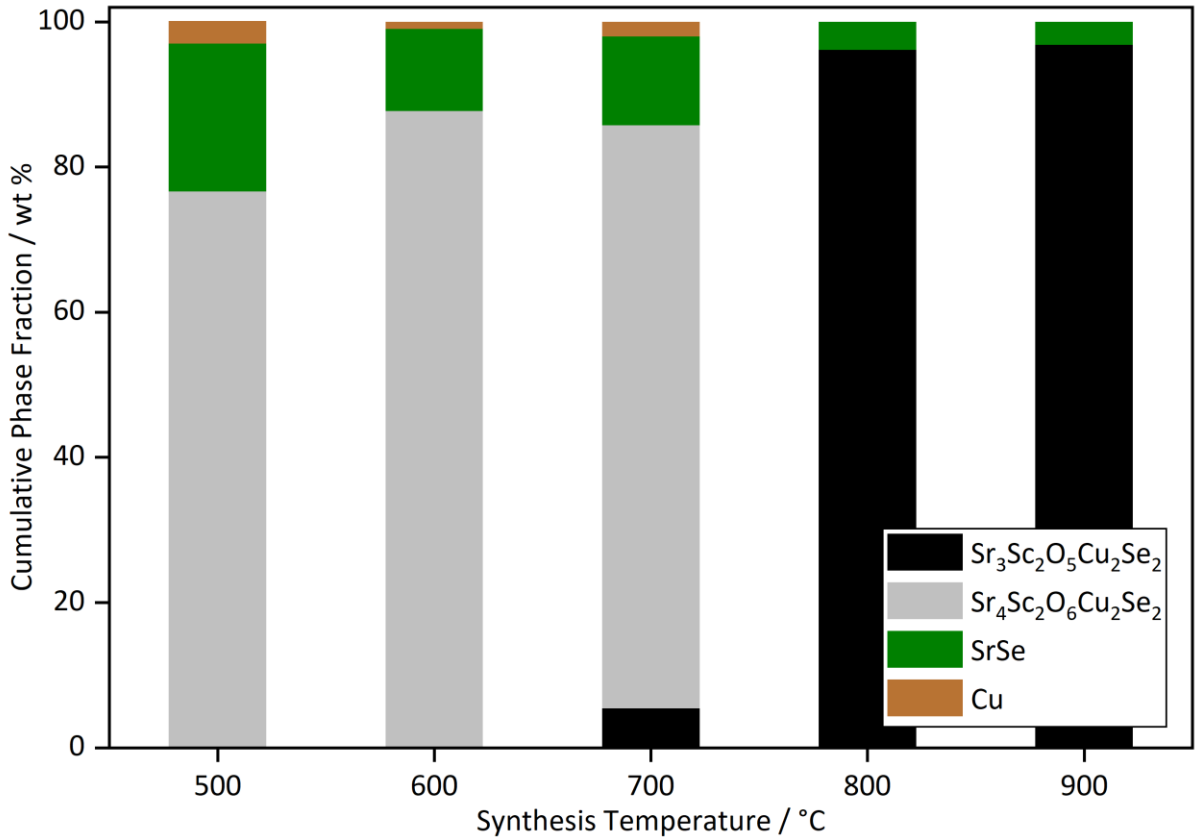

Figure 184 A bar chart illustrating the phase fractions of $Sr_3Sc_2O_5Cu_2Se_2$ (black), $Sr_4Sc_2O_6Cu_2Se_2$ (grey), SrSe (green), and Cu (copper) from the five component samples in the series of experiments targeting $Sr_3Sc_2O_5Cu_2Se_2$ by conventional ceramic syntheses.

This series is a benchmark against which to compare the metathesis series and to validate its results. It shows that at 800 °C and above, the 325 phase dominates as the thermodynamic product and no 426 remains. At 700 °C both phases are observed, and below 700 °C the 426 phase dominates. The complete omission of the 426 phase in the metathesis series strongly suggests that the 325 formation there (which, if conventional ceramic, would favour the 426) is the result of solid-state metathesis.

Table 14 Tabulated phase fractions of the five component samples in the series of experiments targeting $Sr_3Sc_2O_5Cu_2Se_2$ by conventional ceramic syntheses. The phases are colour coded to match the accompanying bar chart, and the tick marks on all constituent diffractograms.

		Synthesis Temperature / °C				
		500	**600**	**700**	**800**	**900**
Phase Fraction / wt %	$Sr_3Sc_2O_5Cu_2Se_2$	-	-	5.4	96.1	96.8
	$Sr_4Sc_2O_6Cu_2Se_2$	76.6	87.7	80.3	-	-
	SrSe	20.4	11.3	12.3	3.9	3.2
	Cu	3.1	1.0	2.0	-	-

The conventional synthesis series gives an interesting insight into the temperature dependence of the thermodynamic competition between $Sr_3Sc_2O_5Cu_2Se_2$ and $Sr_4Sc_2O_6Cu_2Se_2$, but also the extent to which a 325 MALM may be synthesised pure under less aggressive conditions than have previously been employed in this work. This series presents $Sr_3Sc_2O_5Cu_2Se_2$ with excellent purity, on par with the samples in the doping studies prior, showing that such purity is achievable with just one heat cycle and without pelletisation, likely due to the high thermodynamic stability of this phase. The complete emergence of $Sr_3Sc_2O_5Cu_2Se_2$ across the series from 0 % to almost phase purity is visualised in the comparative diffractogram in Figure 185.

In conclusion, this experiment targeted metathetic and ceramic syntheses of the same material and produced surprisingly different results, which together strongly support the occurrence of metathesis in the former. $Sr_3Sc_2O_5Cu_2Se_2$ has been shown here to be synthesisable by conventional synthesis at 700 °C and above, therefore one must assume some conventional synthesis is likely occurring at those temperatures in the metathesis series. The presence of $Sr_3Sc_2O_5Cu_2Se_2$ at those temperatures cannot therefore be attributed, at least solely, to metathesis. However, the synthesis of $Sr_3Sc_2O_5Cu_2Se_2$ below 700 °C cannot be explained by the conventional ceramic pathway, thus can be assumed to be the result of successful metathesis.

To the best of the author's knowledge this is the first synthesis of $Sr_3Sc_2O_5Cu_2Se_2$ at temperatures as low as 500 or 600 °C, a feat that may only be realised by a metathesis reaction. This is also the first reported synthesis of this material by metathesis.

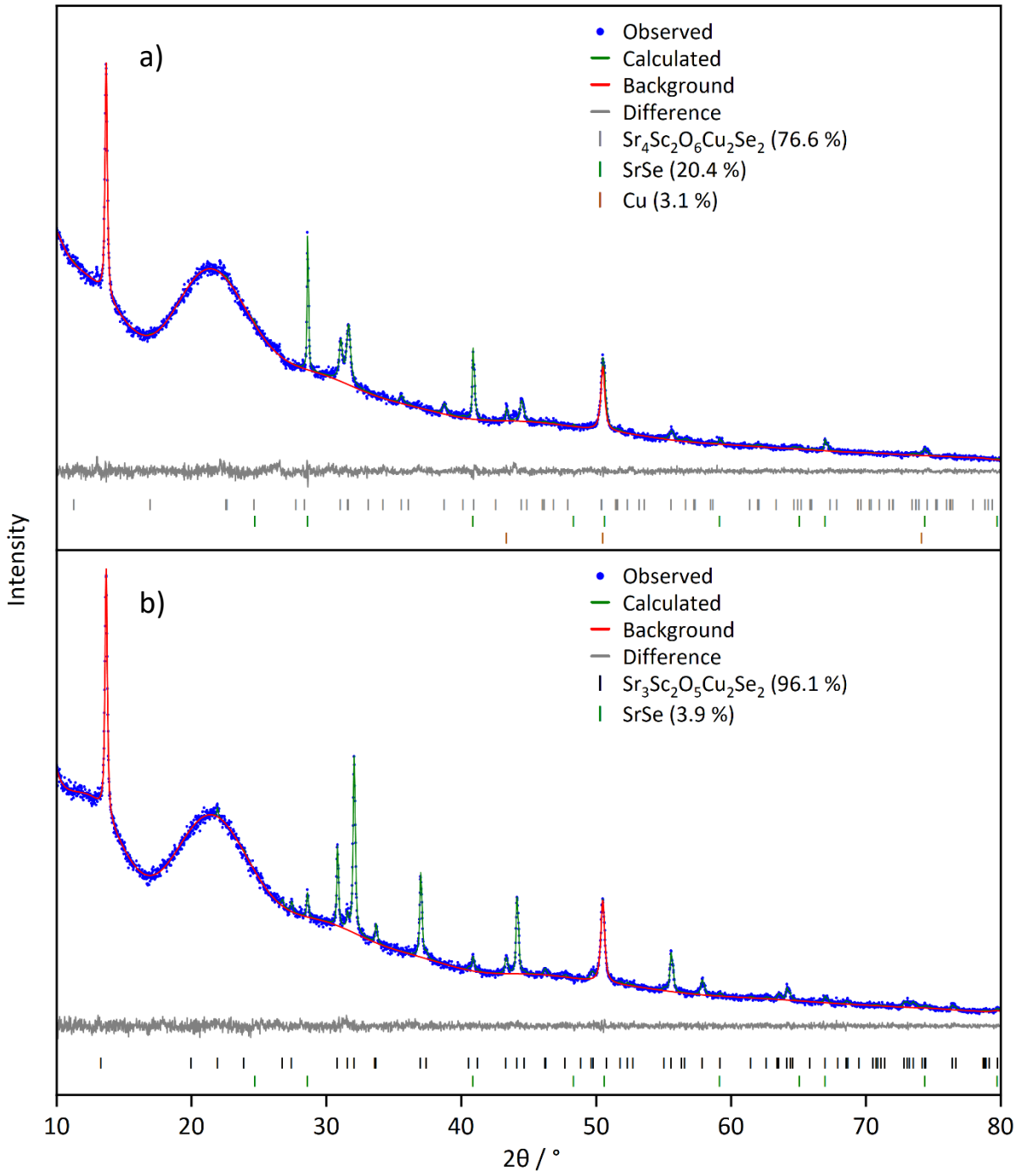

Figure 185 *Powder X-ray diffractograms of materials resulting from attempted conventional synthesis of $Sr_3Sc_2O_5Cu_2Se_2$ after 12 hours of heating at a) 500 °C and b) 800 °C. The small blue circles represent the observed diffracted intensity, the green line represents the Rietveld-refined calculated model, the red line represents the background, and the grey line represents the difference between observed and calculated intensities. The black, grey, green, and copper tick marks show the reflections of the refined models of $Sr_3Sc_2O_5Cu_2Se_2$, $S_4Sc_2O_6Cu_2Se_2$, SrSe and Cu respectively. Weight fractions for each phase are cited in the figure legends. Data was collected with the domed air-tight holder, responsible for the background-refined peaks at 13.3 and 50.5 °.*
a) Duration: 45 minutes. Data points: 3457. Interval: 0.02 °. GOF: 1.15. R_{wp}: 2.750 %.
b) Duration: 45 minutes. Data points: 3457. Interval: 0.02 °. GOF: 1.04. R_{wp}: 2.543 %.

5.4.2 $Sr_3Fe_2O_5Cu_2Se_2$ Investigation

Following the interesting outcome of the $Sr_3Sc_2O_5Cu_2Se_2$ syntheses by both metathesis and ceramic routes, an exact replica of the experiment was carried out but instead targeting $Sr_3Fe_2O_5Cu_2Se_2$. A batch of binary precursors in the form of a conventional synthesis was composed according to Equation 93, and a second comprised the precursors for a metathesis reaction according to Equation 94.

Equation 93 $2\ SrO + Fe_2O_3 + SrSe + Cu_2Se \rightarrow Sr_3Fe_2O_5Cu_2Se_2$

Equation 94 $Sr_3Fe_2O_5Cl_2 + Na_2Cu_2Se_2 \rightarrow Sr_3Fe_2O_5Cu_2Se_2 + 2\ NaCl$

This time, the series targeting a metathesis pathway was immediately more convincing, as shown in Figure 186 and Table 15. $Sr_3Fe_2O_5Cu_2Se_2$ was synthesised in appreciable quantity in every sample, including a 40 wt % phase fraction in the lowest temperature sample at 500 °C. This is very unusual for a MALM and is strong evidence for a metathesis reaction having taken place.

Remarkably, the 700 and 800 °C samples were 'phase pure' in the metathesis sense, in that they contained only the target products of $Sr_3Fe_2O_5Cu_2Se_2$ and NaCl with no impurities or unreacted precursor. A 6.6 wt % impurity of SrSe was observed in the 900 °C sample but at this temperature ceramic synthesis surely dominates, thus this sample serves more as a control to test the upper limit.

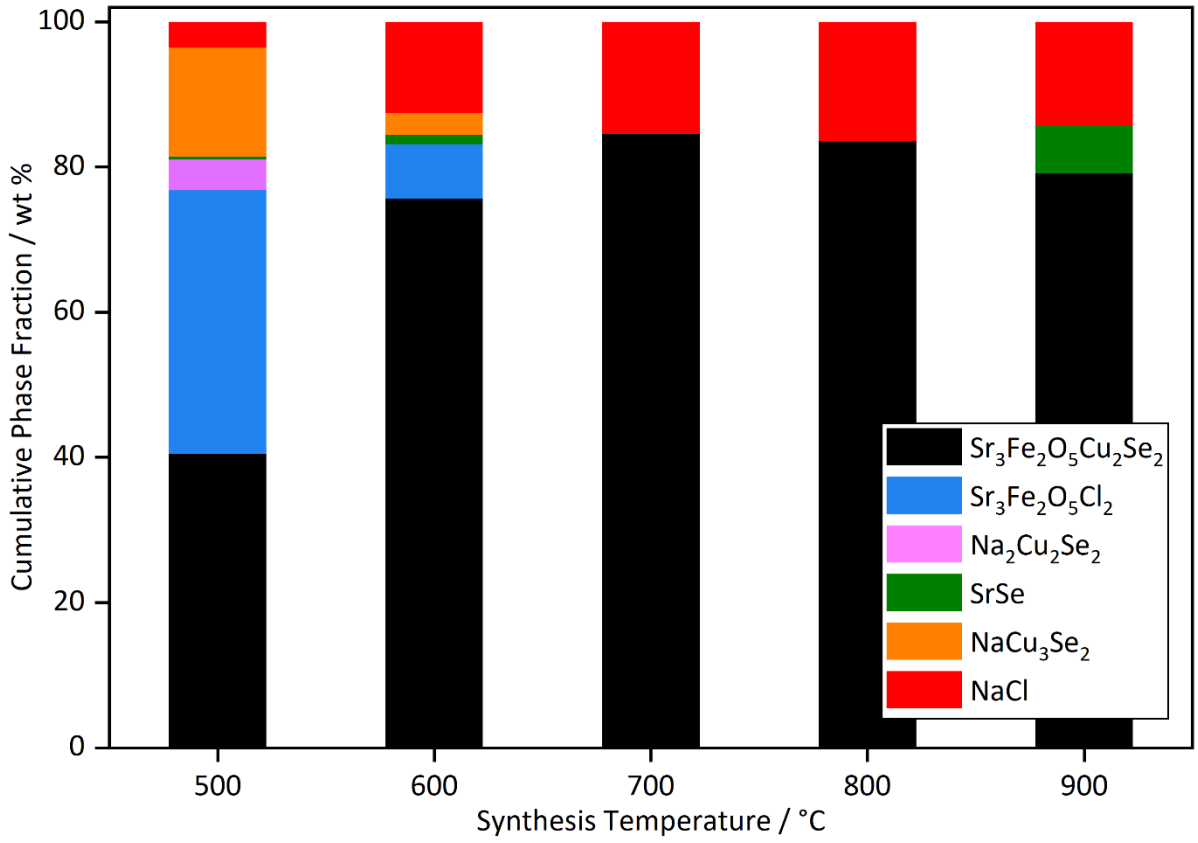

Figure 186 A bar chart illustrating the phase fractions of $Sr_3Fe_2O_5Cu_2Se_2$ (black), $Sr_3Fe_2O_5Cl_2$ (blue), $Na_2Cu_2Se_2$ (pink), SrSe (green), $NaCu_3Se_2$ (orange) and NaCl (red) from the five component samples in the series of experiments targeting $Sr_3Fe_2O_5Cu_2Se_2$ by metathesis.

Table 15 Tabulated phase fractions of the five component samples in the series of experiments targeting $Sr_3Fe_2O_5Cu_2Se_2$ by metathesis. The phases are colour coded to match the accompanying bar chart, and the tick marks on all constituent diffractograms.

		Synthesis Temperature / °C				
		500	**600**	**700**	**800**	**900**
Phase Fraction / wt %	$Sr_3Fe_2O_5Cu_2Se_2$	40.5	75.6	84.5	83.5	79.1
	$Sr_3Fe_2O_5Cl_2$	36.3	7.5	-	-	-
	$Na_2Cu_2Se_2$	4.2	-	-	-	-
	SrSe	0.4	1.3	-	-	6.6
	$NaCu_3Se_2$	15.0	3.0	-	-	-
	NaCl	3.6	12.6	15.5	16.5	14.3

It was observed in the scandium series previously that the light and heavy layers would depreciate in phase fraction with increasing temperature, so neither was fully removed from the system even at temperatures where conventional ceramic conditions are expected to have dominated. In this series, the light layer oxychloride $Sr_3Fe_2O_5Cl_2$ is rapidly consumed alongside the heavy layer $Na_2Cu_2Se_2$ and its degradation product $NaCu_3Se_2$. By 700 °C these precursors have reacted completely and no trace is observed beyond. This difference may be due to the relative stability of the $Sr_3Sc_2O_5Cl_2$ phase vs the $Sr_3Fe_2O_5Cl_2$ phase thus a tendency not to undergo metathesis as readily. By the same logic, the MALM $Sr_3Sc_2O_5Cu_2Se_2$ may not be as thermodynamically stable compared to the iron analogue, which would yield the same observation.

The weight percentages measured in the lowest temperature sample of this series should be considered slightly imprecise due to relatively non-crystalline material in the diffraction pattern, Figure 187a. This is expected at this temperature, and amplified by the inclusion of multiple phases. It also contained a small amount of unknown impurity, which was not refined. More importantly however, the samples beyond this temperature exhibited very clear patterns with highly crystalline MALM and salt, and were the most convincing evidence for the metathetic synthesis of a MALM thus far.

The salt by-product NaCl, prevalent and consistent in the metathesis reactions of both $Sr_3Sc_2O_5Cu_2Se_2$ and $Sr_3Fe_2O_5Cu_2Se_2$, did not (or appeared not to) melt in this study. Given its melting point of 801 °C, this is promising, as the melting of metathesis salts may facilitate undesirable reactions between multiple salt materials of a parallel syntheses reaction, potentially recrystallising as new salts and producing false positive 'hits' for MALMs that were not successfully synthesised.

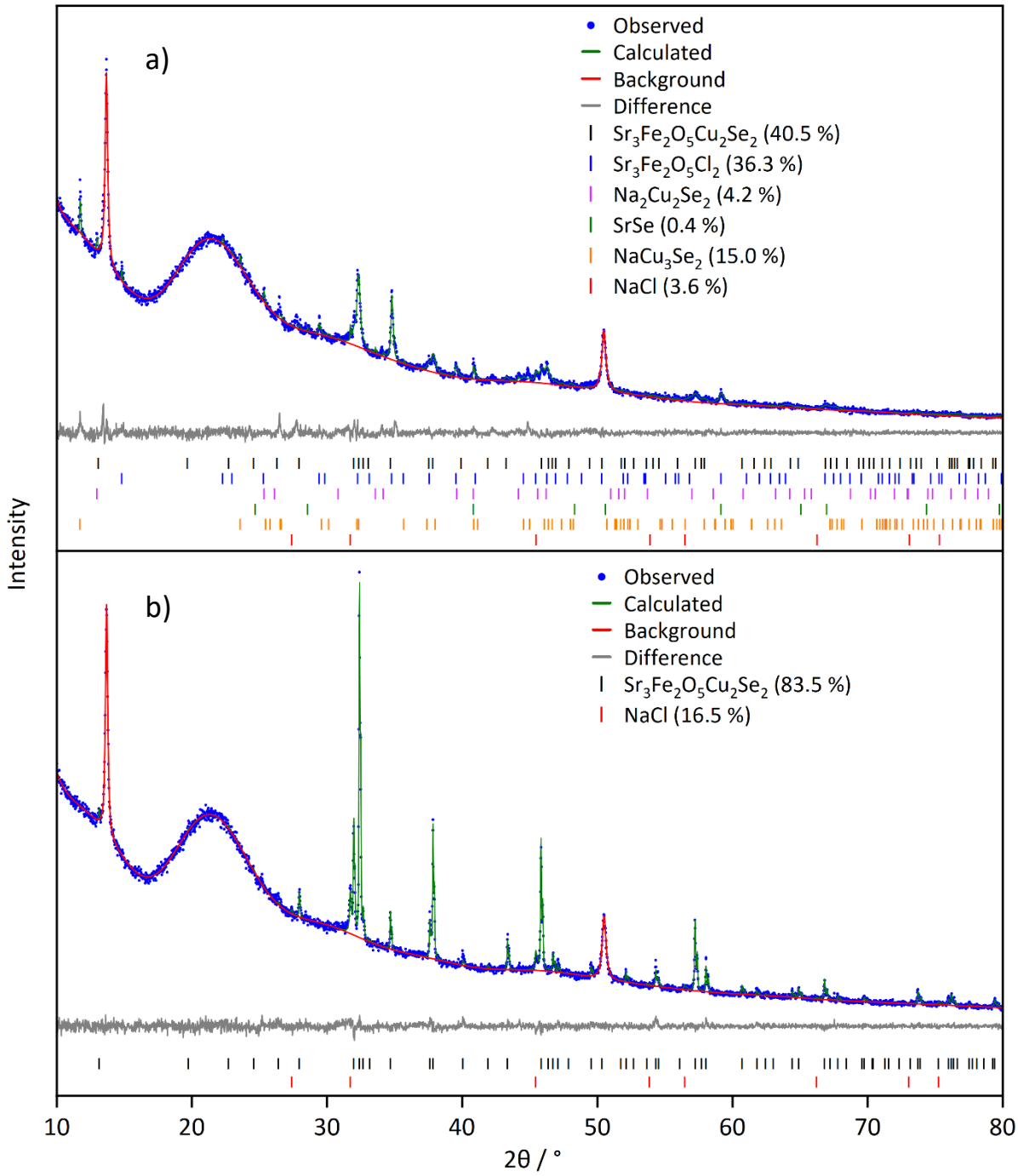

Figure 187 *Powder X-ray diffractograms of materials resulting from attempted metathesis synthesis of $Sr_3Fe_2O_5Cu_2Se_2$ after 12 hours of heating at a) 500 °C and b) 800 °C. The small blue circles represent the observed diffracted intensity, the green line represents the Rietveld-refined calculated model, the red line represents the background, and the grey line represents the difference between observed and calculated intensities. The black, blue, pink, green, orange and red tick marks show the reflections of the refined models of $Sr_3Fe_2O_5Cu_2Se_2$, $Sr_3Fe_2O_5Cl_2$, $Na_2Cu_2Se_2$, SrSe, $NaCu_3Se_2$ and NaCl respectively. Weight fractions for each phase are cited in the figure legends. Data was collected with the domed air-tight holder, responsible for the background-refined peaks at 13.3 and 50.5 °.*
a) Duration: 45 minutes. Data points: 3457. Interval: 0.02 °. GOF: 1.27. R_{wp}: 2.920 %.
b) Duration: 45 minutes. Data points: 3457. Interval: 0.02 °. GOF: 1.13. R_{wp}: 2.557 %.

The successful metathesis samples described here, which presented only $Sr_3Fe_2O_5Cu_2Se_2$ and NaCl as constituent phases, present an opportunity to test the removal of NaCl (or any salt by-product) by washing. This should yield, in theory, a phase pure MALM. The 700 °C sample was washed with distilled water and dried under vacuum in air before a 16 hour PXRD measurement on the usual in air low-background sample holder. The associated diffraction pattern, Figure 188, reveals an exquisitely pure material, the highest quality within this work, with no trace of impurity.

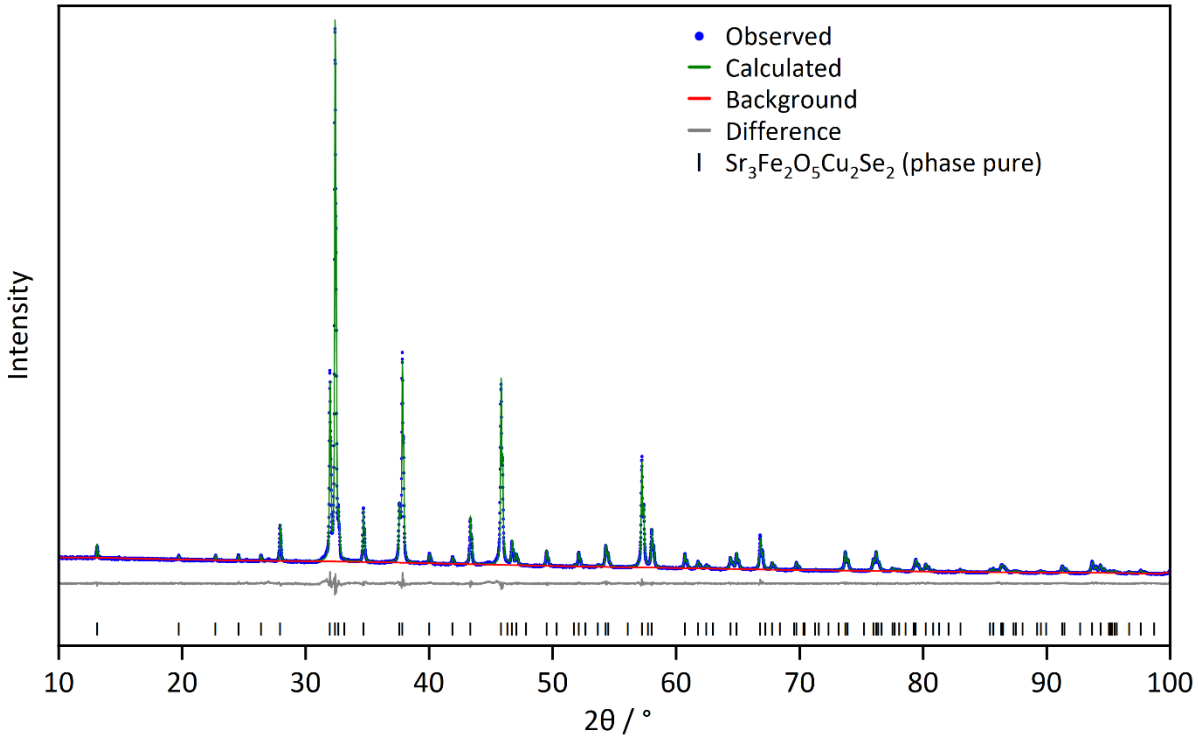

Figure 188 *Powder X-ray diffractogram of material resulting from attempted metathesis synthesis of $Sr_3Fe_2O_5Cu_2Se_2$ (space group I4/mmm) after 12 hours of heating at 700 °C, then washed in distilled H_2O to remove the NaCl by-product. The small blue circles represent the observed diffracted intensity, the green line represents the Rietveld-refined calculated model, the red line represents the background, and the grey line represents the difference between observed and calculated intensities. The black tick marks show the reflections of the refined model of $Sr_3Fe_2O_5Cu_2Se_2$, no NaCl or impurity phases were observed.*
Duration: 16 hours. Data points: 8887. Interval: 0.01 °. GOF: 1.70. R_{wp}: 1.642 %.

The synthesis of $Sr_3Fe_2O_5Cu_2Se_2$ is not novel, nor is its synthesis specifically by metathesis, but the Cario publication lacked details on phase purity for this route, stating only that the material was made, comparing it to the conventional route which was described as 'pure'. In the current work it can be unambiguously stated, whether it be for the first time or not, that $Sr_3Fe_2O_5Cu_2Se_2$ has been synthesised successfully by metathesis, and washed to remove NaCl yielding the MALM material phase pure.

The refined structure of the Rietveld refined model of $Sr_3Fe_2O_5Cu_2Se_2$ is published in *Appendix A.5,* along with all other pristine MALMs synthesised within this work.

Table 16 below and Figure 189 on the following page display the results of the final series in this detailed metathesis proof of concept; that of the synthesis of $Sr_3Fe_2O_5Cu_2Se_2$ by a conventional ceramic method. Like the scandium analogues, these experiments serve the purpose of supporting the metathesis investigations, by establishing the synthetic behaviour of the studied MALM across the investigated temperature range, therefore supporting or opposing the occurrence of metathesis. As before, the conventional syntheses support the results of the previous series being the result of metathesis.

Table 16 *Tabulated phase fractions of the five component samples in the series of experiments targeting $Sr_3Fe_2O_5Cu_2Se_2$ by conventional ceramic syntheses. The phases are colour coded to match the accompanying bar chart, and the tick marks on all constituent diffractograms.*

		Synthesis Temperature / °C				
		500	**600**	**700**	**800**	**900**
Phase Fraction / wt %	$Sr_3Fe_2O_5Cu_2Se_2$	-	62.4	97.7	100	100
	$Sr_4Fe_2O_6Cu_2Se_2$	76.7	29.3	-	-	-
	SrSe	18.2	8.3	2.3	-	-
	Fe_2O_3	5.1	-	-	-	-

The 426 material dominates once again at low temperatures, a behaviour typical of conventional ceramic syntheses but absent in the metathesis samples. This is evidence for metathesis because the 426 structure can only form by a ceramic route, and its presence in a metathesis sample would invalidate claims that any 325 MALM present was made by metathesis.

The preference for $Sr_3Fe_2O_5Cu_2Se_2$ formation over $Sr_4Fe_2O_6Cu_2Se_2$ occurs at a lower temperature here compared to the scandium MALMs. The crossover temperature where both phases are present is 600 °C, approximately 100 °C lower than in the scandium samples. Above 600 °C only the 325 phase is present, suggesting that the delicate phase equilibrium explored in *Section 4.3.2* is not unique only to the scandium MALMs.

The 700 °C sample in this series has a phase fraction of 97.7 wt %, very close to phase purity bar a small SrSe impurity, standard in MALM synthesis and observed throughout this work. However, the two samples at higher temperatures both demonstrate complete phase purity, a behaviour uncommon in many MALM syntheses and especially in those subjected to just one 12 hour heat cycle with no intermediate regrind and no pelletisation. The driving force of $Sr_3Fe_2O_5Cu_2Se_2$ formation is impressive and this series shows that the driving force cannot be attributed solely to metathesis and the instability of the precursors utilised within it, as conventional syntheses yield equally high purities.

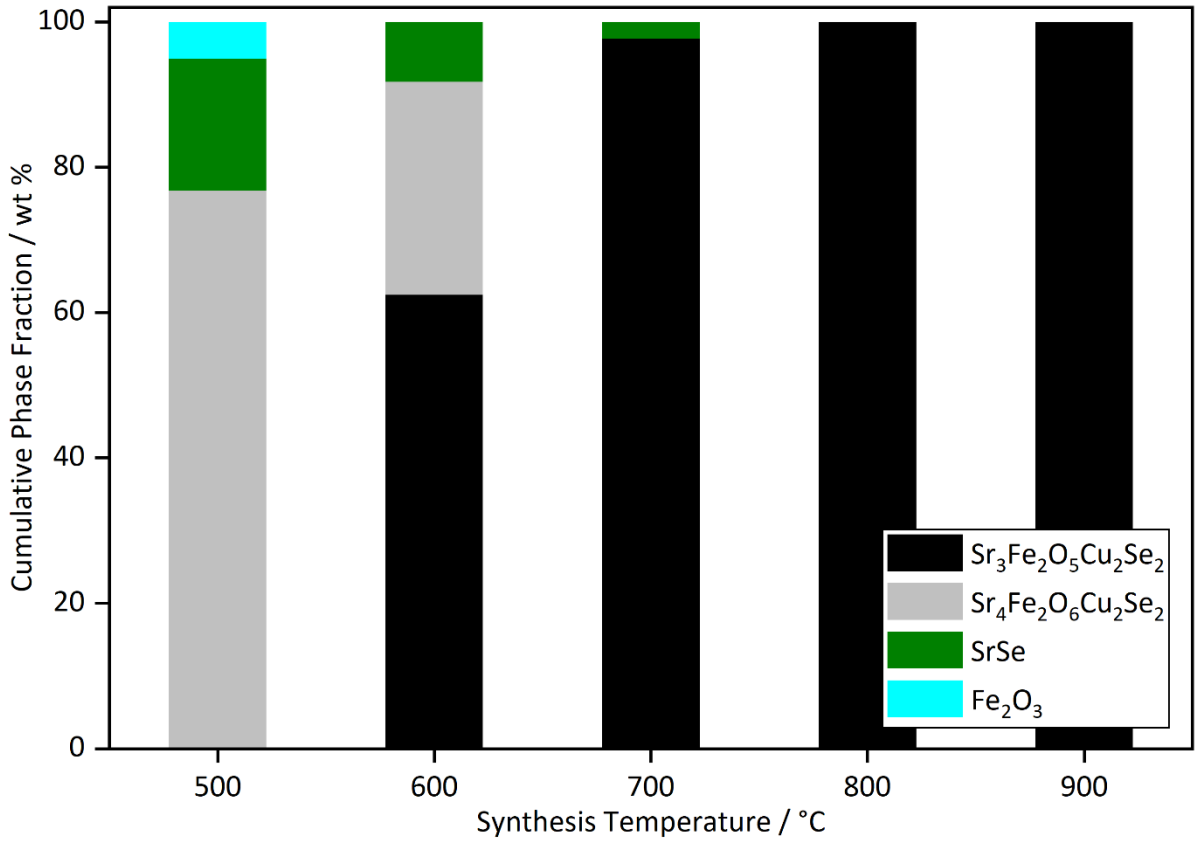

Figure 189 A bar chart illustrating the phase fractions of $Sr_3Fe_2O_5Cu_2Se_2$ (black), $Sr_4Fe_2O_6Cu_2Se_2$ (grey), SrSe (green), and Fe_2O_3 (cyan) from the five component samples in the series of experiments targeting $Sr_3Fe_2O_5Cu_2Se_2$ by conventional ceramic syntheses.

The difference in formation temperatures between the scandium and iron MALMs by metathesis is interesting but raises another unforeseen problem in the application of these reactions to parallel synthesis: selection of a reaction temperature. The optimum metathesis temperature for $Sr_3Fe_2O_5Cu_2Se_2$ is 700 °C, the lowest temperature at which maximum conversion was achieved, but the Sc sample metathesis was weaker here. To optimise the Sc sample, a higher temperature is required, which risks enabling conventional synthesis in both materials.

Metatheses targeting 426 materials, which are not investigated here but are attempted in the next section, would likely proceed at the same temperatures as 325 MALM metathesis, but risks the emergence of 325 MALMs as a by-product by the competing conventional pathway which is difficult or impossible to negate.

Selecting a reaction temperature at which to carry out a metathesis reaction will therefore always be a compromise, and should ideally be an underestimate. Aiming lower than the optimum will prioritise the qualitative presence of the metathesis product, even if the yield is compromised, whilst ensuring that little to no competing conventional by-products are present. A qualitative observation is after all the aim of parallel synthesis, not yield, as a full Rietveld refinement may not be necessary or possible, therefore an underestimate of reaction temperature is suggested, but it is acknowledged that all component systems will behave differently and that no single reaction temperature is perfect.

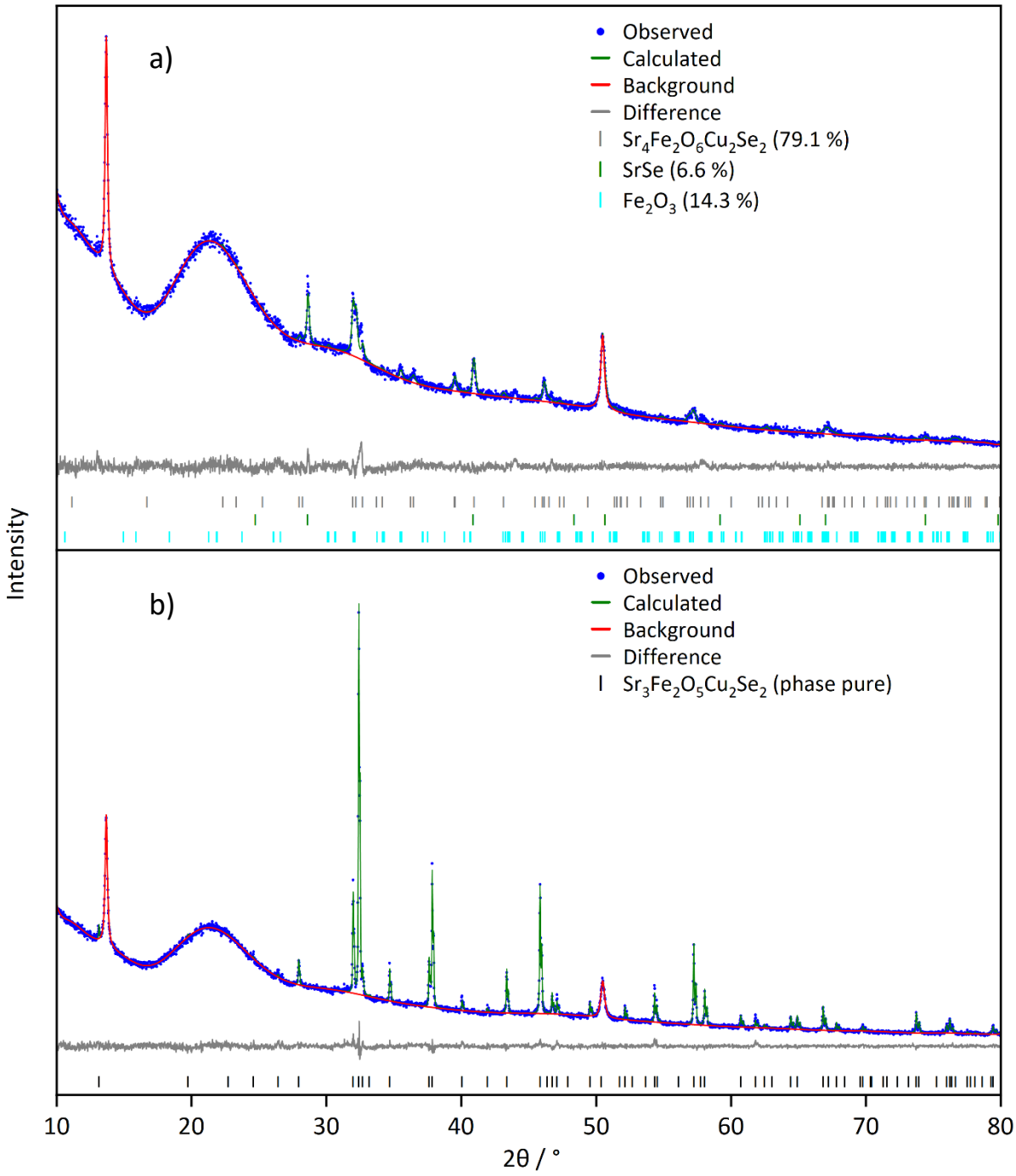

Figure 190 *Powder X-ray diffractograms of materials resulting from attempted conventional synthesis of $Sr_3Fe_2O_5Cu_2Se_2$ after 12 hours of heating at a) 500 °C and b) 800 °C. The small blue circles represent the observed diffracted intensity, the green line represents the Rietveld-refined calculated model, the red line represents the background, and the grey line represents the difference between observed and calculated intensities. The black, grey, green, and cyan tick marks show the reflections of the refined models of $Sr_3Fe_2O_5Cu_2Se_2$, $S_4Fe_2O_6Cu_2Se_2$, SrSe and Fe_2O_3 respectively. Weight fractions for each phase are cited in the figure legends. Data was collected with the domed air-tight holder, responsible for the background-refined peaks at 13.3 and 50.5 °.*
a) Duration: 45 minutes. Data points: 3457. Interval: 0.02 °. GOF: 1.24. R_{wp}: 2.839 %.
b) Duration: 45 minutes. Data points: 3457. Interval: 0.02 °. GOF: 1.15. R_{wp}: 2.574 %.

A small iron oxide Fe_2O_3 impurity is observed in the 500 °C sample, which is not seen again throughout the series and is likely an intermediate phase resulting from the preferential formation of $Sr_4Fe_2O_6Cu_2Se_2$ over the more iron-rich $Sr_3Fe_2O_5Cu_2Se_2$ phase. Analysis of this sample once again produced low intensity poorly crystalline reflections, which resulted in difficult and erroneous refinements, but were expected given the experimental conditions. The 500 °C sample can be seen in Figure 190 on the previous page, a comparative PXRD plot between this and the 800 °C sample; an example of phase pure $Sr_3Fe_2O_5Cu_2Se_2$.

In conclusion this series has, like the previous scandium investigation but to a greater extent, supported the observation of metathesis in the double displacement synthesis of $Sr_3Fe_2O_5Cu_2Se_2$ between $Sr_3Fe_2O_5Cl_2$ and $Na_2Cu_2Se_2$. It has demonstrated the formation of the 325 MALM using metathesis precursors, which could not be explained or replicated by a conventional ceramic synthesis under analogous conditions. The conventional pathway favours the 426 analogue at lower temperatures, a behaviour not observed by metathesis due to the pre-formed nature of the building block precursors. The MALMs studied here have been synthesised at temperatures significantly lower (on the order of approximately 25 - 30 %) than cited in publications employing conventional syntheses.

5.4.3 Metathesis Experiments with Remaining Light Layer Precursors

Metathetic reactions of $Sr_3Sc_2O_5Cu_2Se_2$ and $Sr_3Fe_2O_5Cu_2Se_2$ have been demonstrated, and produced convincing evidence that attributes the syntheses to metathesis. These materials were selected for their high likelihood of success compared to the remainder of the light layer pool, and warranted a detailed analysis. Next, the other six light layer precursors, those which are predicted to be less successful or not successful at all, are reacted with $Na_2Cu_2Se_2$ in a metathesis reaction to gauge the behaviour of each under these conditions. A reaction temperature of 600 °C was selected; deemed a valid compromise between observing the target MALM in good yield and minimising conventional solid-state reactions. This was also judged to be a temperature that 426 materials may remain stable at, where any higher would risk undesirable conversion to the 325 phase. All materials were heated as homogenous powders to 600 °C for one 12 hour heat cycle, before air-sensitive XRD analysis.

5.4.3.1 Cobalt MALMs

The first light layer $Sr_3Co_2O_5Cl_2$ presents the interesting scenario where the target MALM $Sr_3Co_2O_5Cu_2Se_2$ does not exist. Under reaction temperatures the metathesis precursors are expected to decompose, but not to form $Sr_3Co_2O_5Cu_2Se_2$, so this experiment simulates how an unsuccessful permutation in a parallel synthesis combination may behave. The target reaction was as follows:

Equation 95 $Sr_3Co_2O_5Cl_2 + Na_2Cu_2Se_2 \rightarrow Sr_3Co_2O_5Cu_2Se_2 + 2\ NaCl$

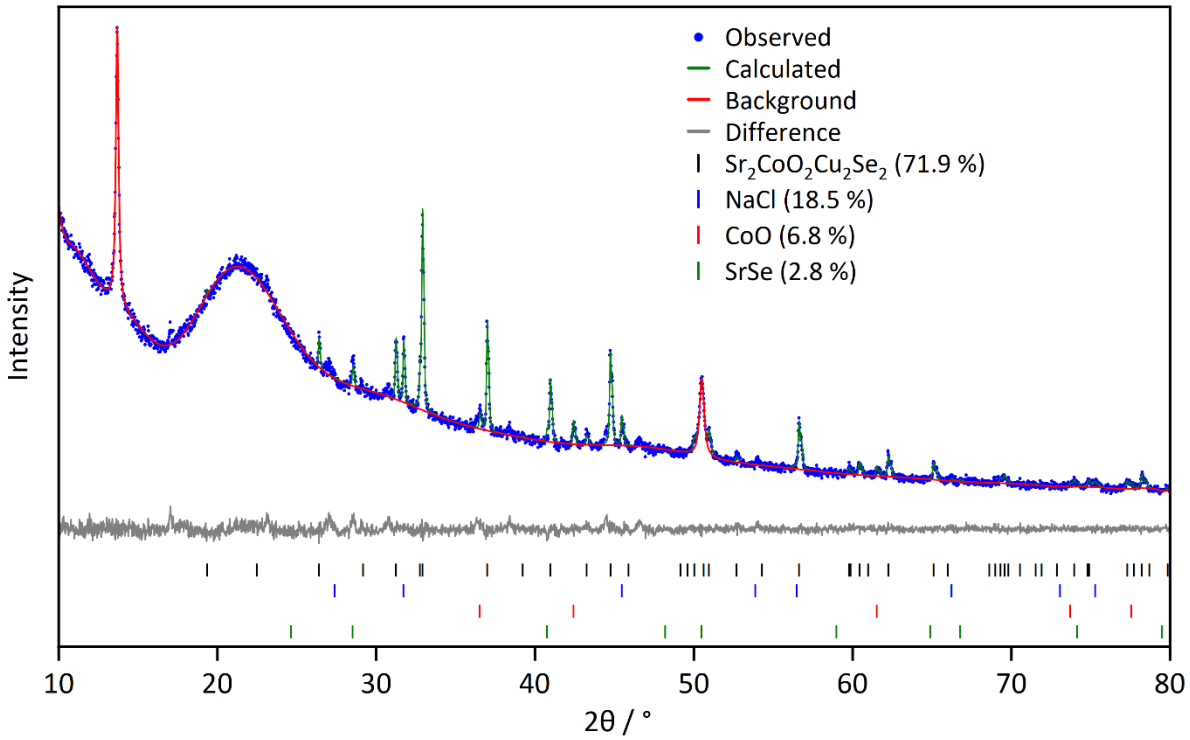

Figure 191 *Powder X-ray diffractogram of material resulting from attempted metathesis synthesis of $Sr_3Co_2O_5Cu_2Se_2$ after 12 hours of heating at 600 °C. The small blue circles represent the observed diffracted intensity, the green line represents the Rietveld-refined calculated model, the red line represents the background, and the grey line represents the difference between observed and calculated intensities. The black, blue, red, and green tick marks show the reflections of the refined models of $Sr_2CoO_2Cu_2Se_2$ (71.9 %), NaCl (18.5 %), CoO (6.8 %), and SrSe (2.8 %) respectively. Data was collected with the domed air-tight holder, responsible for the background-refined peaks at 13.3 and 50.5 °.*
Duration: 45 minutes. Data points: 3457. Interval: 0.02 °. GOF: 1.24. R_{wp}: 2.692 %.

As can be observed in Figure 191 above, the metathesis reaction of $Sr_3Co_2O_5Cu_2Se_2$ was not successful, as predicted. Cobalt 325 or 426 oxychalcogenides are not known, only the 212 analogue $Sr_2CoO_2Cu_2Se_2$ which was observed here. This material is widely reported, by conventional syntheses at 800 to 1000 °C,[38, 263, 331, 332] by hydroxide flux,[333] or from the elements at 1300 °C.[334]

It was unlikely due to relative stabilities that the metathesis precursors would remain unreacted if the target material was not possible, thus the synthesis of $Sr_2CoO_2Cu_2Se_2$ by a conventional pathway is a logical alternative. However, this reaction inherently still produces NaCl. In isolation this is not a negative as it can be removed by washing, but it challenges the validity of the proposed screening method using the salt by-products of a metathetic parallel synthesis reaction, as the presence of NaCl would imply the successful formation of $Sr_3Co_2O_5Cu_2Se_2$, which is incorrect.

The formation of $Sr_2CoO_2Cu_2Se_2$ is achieved at a temperature significantly lower than literature examples. This suggests that a hybrid of metathesis and conventional processes might be occurring in tandem, where the pre-formed $[Sr_3Co_2O_5]^{2+}$ light layer subunit decomposes to $[Sr_2CoO_2]^{2+}$ in order to metathesise with the heavy layer subunit $[Cu_2Se_2]^{2-}$, and produce NaCl.

Given the behaviour of light layer precursor $Sr_3Co_2O_5Cl_2$ in a metathesis reaction, $Sr_4Co_2O_6Cl_2$ is therefore expected to behave similarly, as the 426 phase target material $Sr_4Co_2O_6Cu_2Se_2$ also does not exist in literature. The target reaction, both expected and intended to be unsuccessful, was attempted according to Equation 96:

Equation 96 $Sr_4Co_2O_6Cl_2 + Na_2Cu_2Se_2 \rightarrow Sr_4Co_2O_6Cu_2Se_2 + 2\ NaCl$

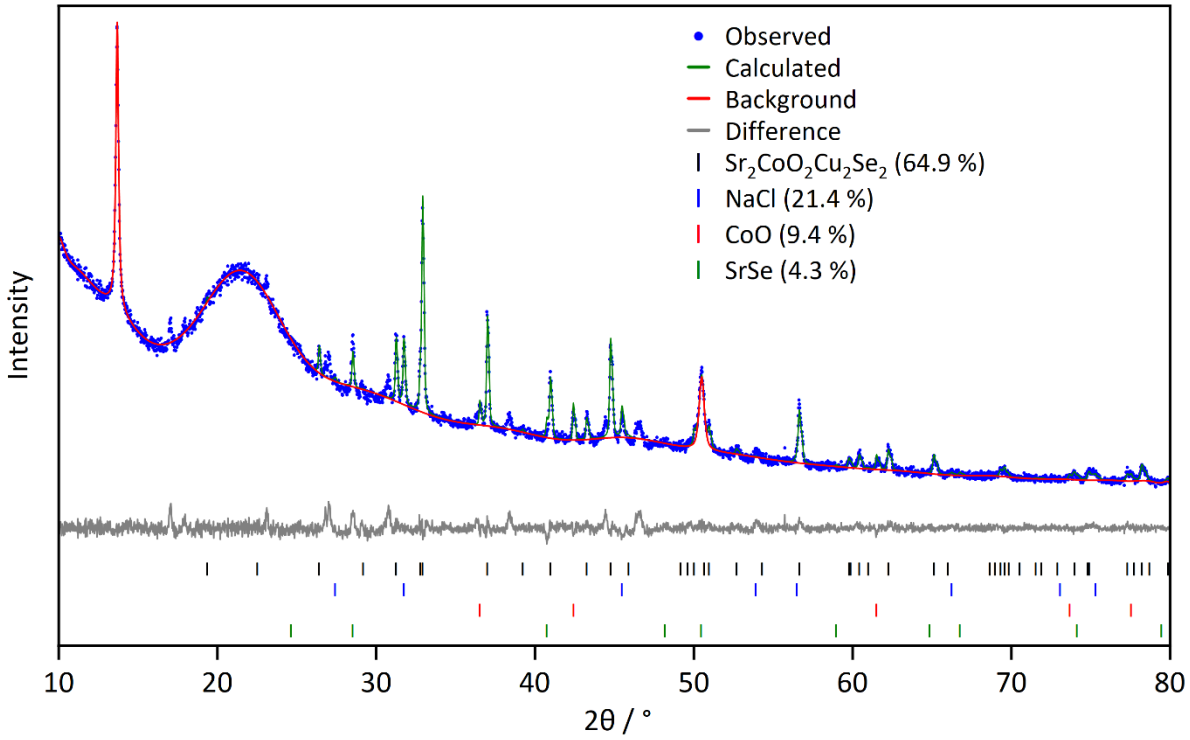

Figure 192 *Powder X-ray diffractogram of material resulting from attempted metathesis synthesis of $Sr_4Co_2O_6Cu_2Se_2$ after 12 hours of heating at 600 °C. The small blue circles represent the observed diffracted intensity, the green line represents the Rietveld-refined calculated model, the red line represents the background, and the grey line represents the difference between observed and calculated intensities. The black, blue, red, and green tick marks show the reflections of the refined models of $Sr_2CoO_2Cu_2Se_2$ (64.9 %), NaCl (21.4 %), CoO (9.4 %), and SrSe (4.3 %) respectively. Data was collected with the domed air-tight holder, responsible for the background-refined peaks at 13.3 and 50.5 °.*
Duration: 45 minutes. Data points: 3457. Interval: 0.02 °. GOF: 1.47. R_{wp}: 3.156 %.

In a very similar result to the 325 analogue, $Sr_4Co_2O_6Cu_2Se_2$ was not observed, and the 212 material $Sr_2CoO_2Cu_2Se_2$ was synthesised instead. NaCl is once again present, an expected by-product even without the synthesis of the target material, as a result of decomposition and full consumption of the light and heavy layer precursors.

CoO and SrSe are observed in both samples, resulting from the phase change between the 325/426 phase to the 212 phase. Some unrecognised material is also present, against which simulated models of $Sr_3Co_2O_5Cu_2Se_2$ and $Sr_4Co_2O_6Cu_2Se_2$ were refined. Neither resembled any of the unrecognised material.

5.4.3.2 Iron MALMs

Next, the bromide analogue of the previously investigated $Sr_3Fe_2O_5Cl_2$ light layer precursor, $Sr_3Fe_2O_5Br_2$, was investigated. The resulting MALM on reaction with $Na_2Cu_2Se_2$ is $Sr_3Fe_2O_5Cu_2Se_2$.

Equation 97 $Sr_3Fe_2O_5Br_2 + Na_2Cu_2Se_2 \rightarrow Sr_3Fe_2O_5Cu_2Se_2 + 2\ NaBr$

Given previous experiments, and the tendency for this material to form phase pure alongside sodium chloride, it was expected that the result would be identical to that $Sr_3Fe_2O_5Cl_2$, according to Equation 97. This hypothesis proved correct, as shown in Figure 193, a clean and crystalline 3:1 weight ratio between target material $Sr_3Fe_2O_5Cu_2Se_2$ and NaBr.

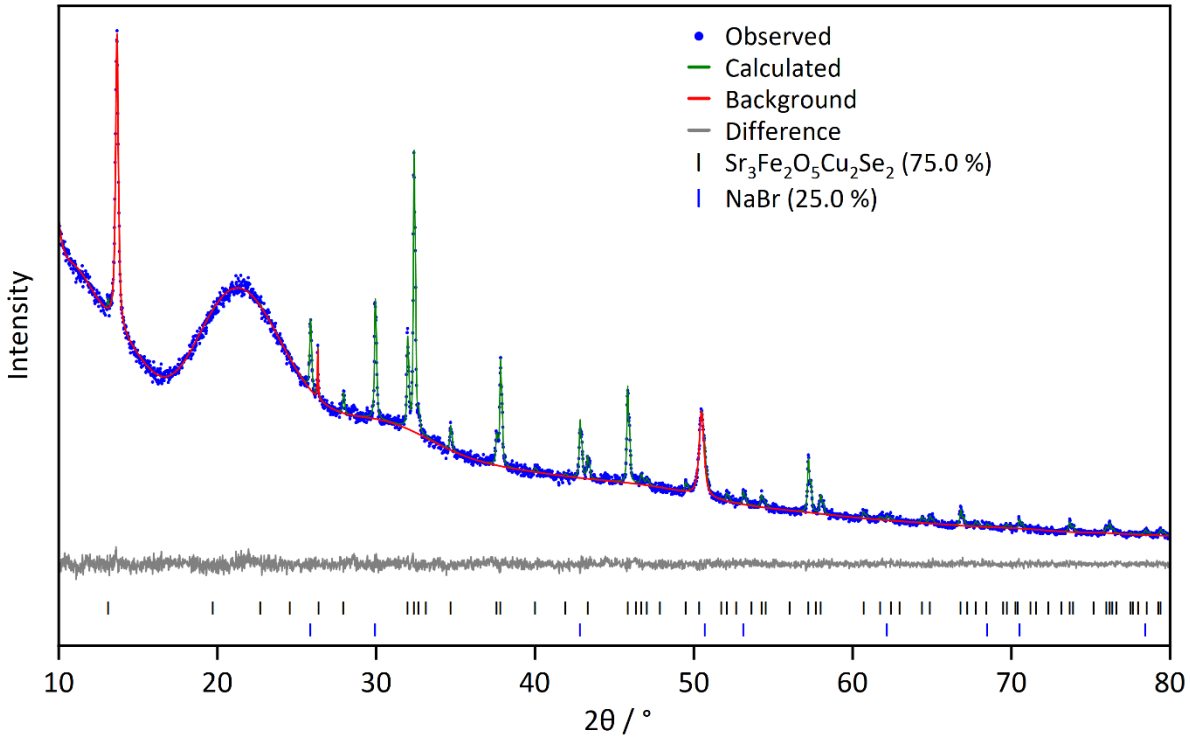

Figure 193 *Powder X-ray diffractogram of material resulting from attempted metathesis synthesis of $Sr_3Fe_2O_5Cu_2Se_2$ after 12 hours of heating at 600 °C. The small blue circles represent the observed diffracted intensity, the green line represents the Rietveld-refined calculated model, the red line represents the background, and the grey line represents the difference between observed and calculated intensities. The black and blue tick marks show the reflections of the refined models of $Sr_3Fe_2O_5Cu_2Se_2$ (75.0 %) and NaBr (25.0 %) respectively. Data was collected with the domed air-tight holder, responsible for the background-refined peaks at 13.3 and 50.5 °.*
Duration: 45 minutes. Data points: 3457. Interval: 0.02 °. GOF: 1.06. R_{wp}: 2.369 %.

The chloride and bromide light layer precursors $Sr_4Fe_2O_6Cl_2$ and $Sr_4Fe_2O_6Br_2$ were reacted with the heavy layer precursor $Na_2Cu_2Se_2$, according to Equation 98 and Equation 99. Both target the same iron MALM product $Sr_4Fe_2O_6Cu_2Se_2$, but should produce different identifying salt by-products.

Equation 98 $Sr_4Fe_2O_6Cl_2 + Na_2Cu_2Se_2 \rightarrow Sr_4Fe_2O_6Cu_2Se_2 + 2\ NaCl$

Equation 99 $Sr_4Fe_2O_6Br_2 + Na_2Cu_2Se_2 \rightarrow Sr_4Fe_2O_6Cu_2Se_2 + 2\ NaBr$

Both experiments successfully produced the target phase $Sr_4Fe_2O_6Cu_2Se_2$ and the corresponding salt by-product. However, both also contained the competing phase $Sr_3Fe_2O_5Cu_2Se_2$, 28.9 % for the oxychloride and 47.6 % for the oxybromide. There difference between these conversion rates is not known. It appears that the phase balance between the two structures is delicate, akin to that explored in the scandium materials in *Chapter 4* where 426 to 325 conversion was unpredictable. The powder diffractograms in Figure 194 on the next page compare the results of these experiments.

The $Sr_4Fe_2O_6Cu_2Se_2$ MALM targeted here was previously observed unintentionally in the conventional synthesis of $Sr_3Fe_2O_5Cu_2Se_2$ at 600 °C, in a phase mixture with the target product. Above 600 °C the 325 dominates and below it the 426 dominates, suggesting this temperature is within the crossover where both phases coexist, which may explain the phase mixture observed here. Like in the earlier case of $Sr_3Co_2O_5Cl_2$ producing $Sr_2CoO_2Cu_2Se_2$ instead of $Sr_3Co_2O_5Cu_2Se_2$, it is very likely that a conventional ceramic synthesis, or a combination of both conventional and metathesis, is responsible for this, because without some ceramic degradation of the light layer phase the metathesis precursors should not be able to form products other than that which they are pre-formed to synthesise. This is the first example where a MALM which does exist is targeted by metathesis and still forms a competing phase.

In literature $Sr_4Fe_2O_6Cu_2Se_2$ is synthesised phase pure at temperatures of 850 to 900 °C with no competing 325 phase,[38, 87] and the 325 phase itself also forms pure at similar temperatures when targeted by the precursor stoichiometry.[61] This is in contrast with the results observed here and in the $Sr_3Fe_2O_5Cu_2Se_2$ conventional syntheses in the previous section, where temperature was indicated to be the determining variable rather than stoichiometry. However, stoichiometry in the previous section targeted the 325 phase conventionally, and this section used metathesis precursors, so should not be directly compared or extrapolated to the conventional synthesis of the 426 phase, which may behave differently.

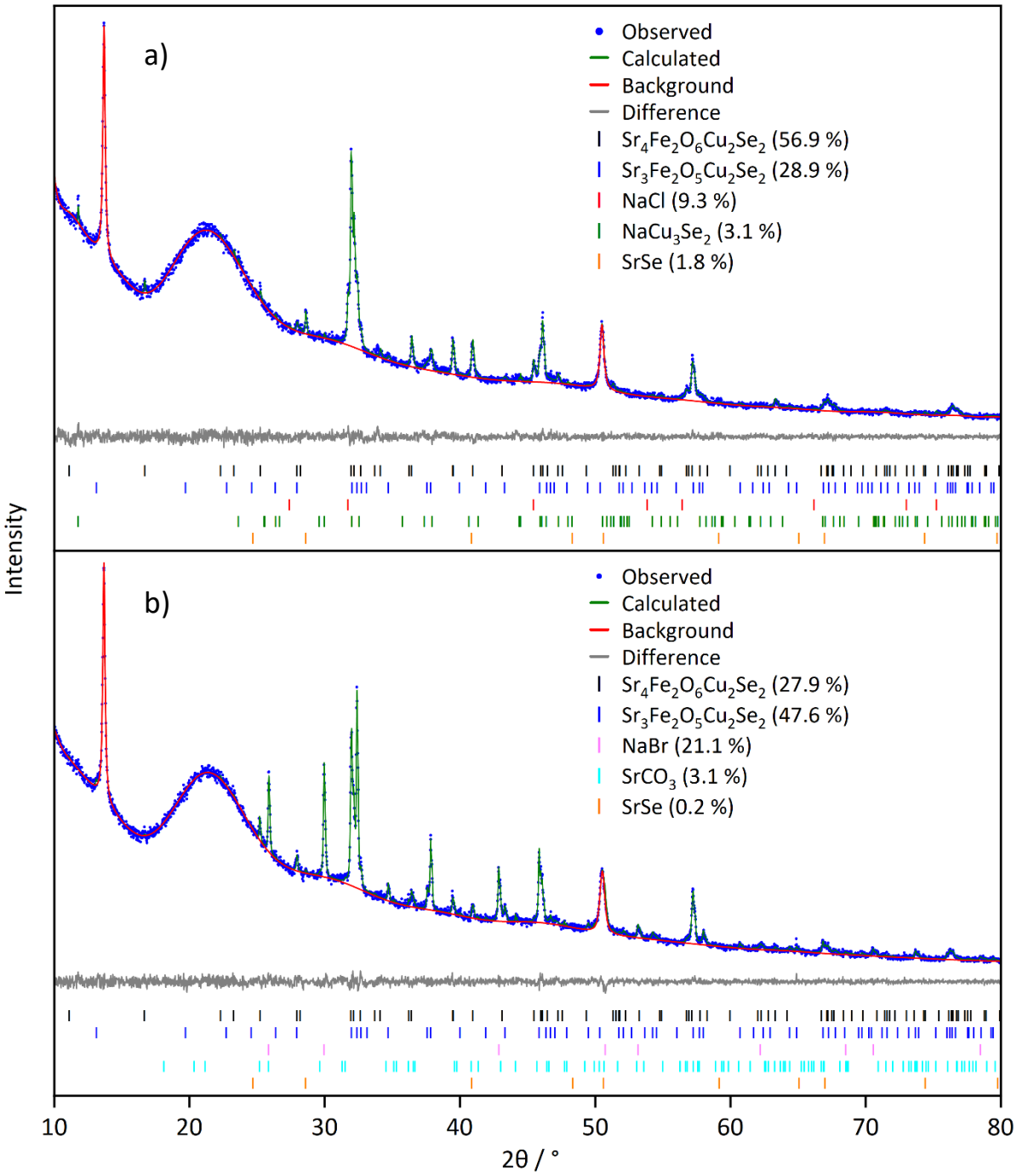

Figure 194 *Powder X-ray diffractograms of materials resulting from the attempted metathesis syntheses of $Sr_4Fe_2O_6Cu_2Se_2$ with a) $Sr_4Fe_2O_6Cl_2$ and b) $Sr_4Fe_2O_6Br_2$, after 12 hours of heating at 600 °C. The small blue circles represent the observed diffracted intensity, the green lines represent the Rietveld-refined calculated model, the red lines represent the background, and the grey lines represent the difference between observed and calculated intensities. The black, blue, red, green, orange, pink and cyan tick marks show the reflections of the refined models of $Sr_4Fe_2O_6Cu_2Se_2$, $Sr_3Fe_2O_5Cu_2Se_2$, NaCl, $NaCu_3Se_2$, SrSe, NaBr and $SrCO_3$ respectively. Weight fractions for each phase are cited in the figure legends. Data was collected with the domed air-tight holder, responsible for the background-refined peaks at 13.3 and 50.5 °.*
a) Duration: 45 minutes. Data points: 3457. Interval: 0.02 °. GOF: 1.13. R_{wp}: 2.597 %.
b) Duration: 45 minutes. Data points: 3457. Interval: 0.02 °. GOF: 1.13. R_{wp}: 2.500 %.

5.4.3.3 Scandium MALMs

The final light layer precursor to be combined with $Na_2Cu_2Se_2$ in a trial metathesis reaction is $Sr_4Sc_2O_6Cl_2$. A metathesis synthesis according to Equation 100 was carried out, of which the results are shown below in Figure 195.

Equation 100 $Sr_4Sc_2O_6Cl_2 + Na_2Cu_2Se_2 \rightarrow Sr_4Sc_2O_6Cu_2Se_2 + 2\ NaCl$

As has been described in *Chapter 4* to often be the case during the conventional ceramic synthesis of $Sr_4Sc_2O_6Cu_2Se_2$, the 325 phase exists in competition and may often dominate (*Section 4.3.2*), as it has here. Interestingly, this is a very low temperature for the 325 phase to dominate in this way. This experiment is the single instance of a material whose synthesis should be successful, and that has been reported in literature,[64, 89] not forming at all. This presents another flaw in the deteriorating allure of parallel synthesis, in that one cannot assume a material will be formed metathetically based on its synthesisability elsewhere. $Sr_4Sc_2O_6Cu_2Se_2$ is meta stable but should be observed even if the yield is poor, yet it was not observed here due to the overpowering stability of the 325 phase.

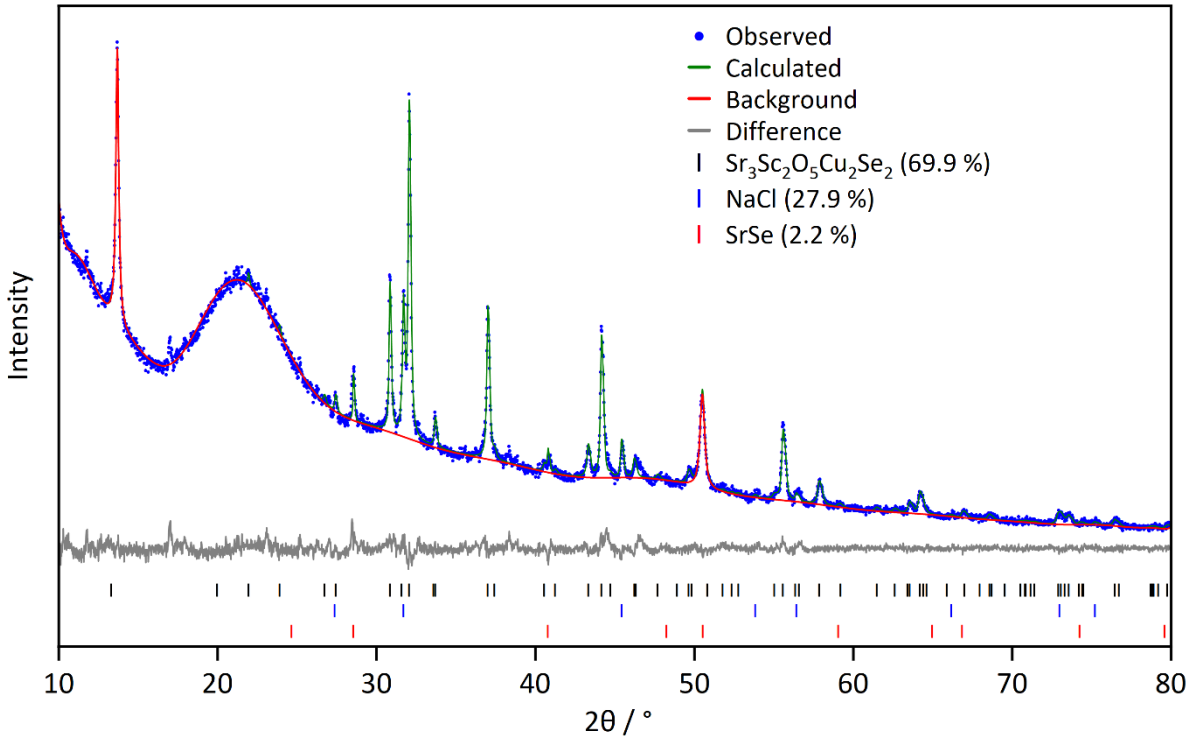

Figure 195 *Powder X-ray diffractogram of material resulting from attempted metathesis synthesis of $Sr_4Sc_2O_6Cu_2Se_2$ after 12 hours of heating at 600 °C. The small blue circles represent the observed diffracted intensity, the green line represents the Rietveld-refined calculated model, the red line represents the background, and the grey line represents the difference between observed and calculated intensities. The black, blue, and red tick marks show the reflections of the refined models of $Sr_3Sc_2O_5Cu_2Se_2$ (69.9 %), NaCl (27.9 %), and SrSe (2.2 %) respectively. Data was collected with the domed air-tight holder, responsible for the background-refined peaks at 13.3 and 50.5 °.*
Duration: 45 minutes. Data points: 3457. Interval: 0.02 °. GOF: 1.43. R_{wp}: 3.417 %.

5.4.3.4 Comparison

The eight individual metathesis reactions assessed at the selected 'compromise' reaction temperature of 600 °C produced mixed results. Table 17 at the bottom of this page summarises the outcomes.

The two cobalt precursors were specifically chosen to simulate a failed metathesis reaction. They are an example of an uncommon permutation where the quaternary oxychloride is stable but the quinternary oxyselenide is not. As expected, these reactions failed, but rather than re-emerging as the unreacted precursor (with degradation of the heavy layer very likely) the precursors instead, in both cases, formed the 212 structure presumably through a conventional route.

The iron experiments were the best performing, with the two 325 precursors both forming the expected product $Sr_3Fe_2O_5Cu_2Se_2$ phase pure, and the two 426 precursors forming a mixed phase of the target material $Sr_4Fe_2O_6Cu_2Se_2$ and competing by-product $Sr_3Fe_2O_5Cu_2Se_2$.

Similarly, the scandium 325 precursor $Sr_3Sc_2O_5Cl_2$ formed target material $Sr_3Sc_2O_5Cu_2Se_2$ with good purity but with some competing non-MALM phases, whilst its 426 analogue $Sr_4Sc_2O_6Cl_2$ did not form its target product $Sr_4Sc_2O_6Cu_2Se_2$, instead manifesting only as the more stable 325 MALM $Sr_3Sc_2O_5Cu_2Se_2$.

These experiments do provide some convincing evidence of metathesis reactions applied to MALMs, especially those of $Sr_3Fe_2O_5Br_2$ and $Sr_3Sc_2O_5Cl_2$ whose mechanisms were analysed across a temperature range in comparison to the conventional route. However, the indication of a conventional solid-state mechanism occurring in five of eight experiments is not a promising endorsement for the applicability of metathesis in larger scale experiments. For a parallel synthesis to be valid it is essential that conventional solid-state does not occur, but these initial results suggest such an assumption cannot be made with certainty.

Table 17 Tabulated results of the eight individual metathesis reactions.

Metathesis Reaction	Target MALM	Prediction	Outcome	Comments
$Sr_3Co_2O_5Cl_2 + Na_2Cu_2Se_2$	$Sr_3Co_2O_5Cu_2Se_2$	Unsuccessful	Unsuccessful	Forms 212
$Sr_4Co_2O_6Cl_2 + Na_2Cu_2Se_2$	$Sr_4Co_2O_6Cu_2Se_2$	Unsuccessful	Unsuccessful	Forms 212
$Sr_3Fe_2O_5Cl_2 + Na_2Cu_2Se_2$	$Sr_3Fe_2O_5Cu_2Se_2$	Successful	Successful	Phase Pure
$Sr_3Fe_2O_5Br_2 + Na_2Cu_2Se_2$	$Sr_3Fe_2O_5Cu_2Se_2$	Successful	Successful	Phase Pure
$Sr_4Fe_2O_6Cl_2 + Na_2Cu_2Se_2$	$Sr_4Fe_2O_6Cu_2Se_2$	Successful	Successful	Forms 426 + 325
$Sr_4Fe_2O_6Br_2 + Na_2Cu_2Se_2$	$Sr_4Fe_2O_6Cu_2Se_2$	Successful	Successful	Forms 426 + 325
$Sr_3Sc_2O_5Cl_2 + Na_2Cu_2Se_2$	$Sr_3Sc_2O_5Cu_2Se_2$	Successful	Successful	Good yield
$Sr_4Sc_2O_6Cl_2 + Na_2Cu_2Se_2$	$Sr_4Sc_2O_6Cu_2Se_2$	Successful	Unsuccessful	Forms 325

5.5 The Salt Hypothesis

In *Section 5.1.4.3* previously, a potential flaw in the metathetic parallel synthesis technique was discussed which relates to the salt by-products. The flaw concerns the low melting points of the salts, which may result not only in the melting of samples at reaction temperatures by the salts acting as a flux, but more concerningly may allow for ionic displacement of multiple salts, settling in the most thermodynamically stable permutations regardless of which of the component metathesis reactions were successful. Melting is unlikely as it this did not occur in any of the individual metathesis of the previous sections, but the displacement of salt ions remains a possibility that should be explored.

This potential flaw does not threaten the validity of the parallel process as a whole, (in fact if one were to refine the entire PXRD pattern it would make very little difference to the process) but it does threaten the ability to screen for reaction success using only the salts as markers of a successful reaction. The upcoming proof of concept reactions cannot sufficiently test this hypothesis because only sodium chloride and sodium bromide are available as potential salt products. Therefore, in a final investigation of parallel synthesis validity before the proof of concept reactions were performed, this hypothesis was investigated by gauging the reactions of six simple salts reacted in pairs to test for ionic displacement or combination under simulated metathesis conditions.

The salts of sodium and potassium with either fluorine, chlorine or bromine were investigated, a representative sample of the simple salts that may result from metathesis reactions. Their melting points, listed in Table 18, range from 700 to 1000 °C. Melting points decrease down Group 1 from sodium to potassium, and also decrease down Group 17 from fluorine to chlorine to bromine, such that sodium fluoride and potassium bromide have the highest and lowest melting points respectively.

Table 18 The melting points of six salts with formula AX where A = Na or K, and X = F, Cl or Br.

Salt	**Melting point / °C**
NaF	993
NaCl	801
NaBr	747
KF	858
KCl	770
KBr	734

The six salts were reacted in pairs, which gives 36 possible combinations. Omitting duplicate tests gives the 21 combinations shown in Table 19 below. Combinations where either the cation or the anion is present in both salts were also eliminated, shown in grey, which includes pairings where a salt reacts with itself. This leaves six unique permutations, coloured in gold and listed in Permutations 1 - 6, which were pursued.

Table 19 *The permutations of the combination of two salts with a cation of either sodium or potassium, and an anion of either fluorine, chlorine or bromine. Grey permutations represent pairings where either the cation or anion repeat, gold permutations represent the six unique permutations where the ions do not repeat.*

		K			Na		
		F	Cl	Br	F	Cl	Br
Na	F						
	Cl						
	Br						
K	F						
	Cl						
	Br						

Permutation 1 NaF + KCl

Permutation 2 NaF + KBr

Permutation 3 NaCl + KF

Permutation 4 NaCl + KBr

Permutation 5 NaBr + KF

Permutation 6 NaBr + KCl

1 gram 1 : 1 molar combinations of the six pairings were combined, ground, and heated in air at 700 °C for 12 hours. The samples were analysed by PXRD both before and after heating to assess any difference from the simulated metathesis reaction conditions. The PXRD pre-heating confirmed that all samples were the intended composition with no extraneous phases present. All Rietveld refined PXRD scans pre and post heating can be found in *Appendix B.3.6*.

Owing to the high crystallinity of these salts, PXRD scans were kept extremely short, on the order of minutes. This was deemed appropriate here not only for experimental convenience but because merely a qualitative result is sufficient. Exact ratios of products are not the primary concern, rather the sample compositions and any changes resulting from heating.

The identity of constituent phases within the diffractograms were ascertained using primarily the *200* reflection, which is the largest peak in each of the constituent phases, appearing between 2θ = 28 to 38 °. Simulated patterns of the phases are compared in Figure 196 below using CIF files from the International Crystal Structure Database (ICSD). Each of the six phases is highly ionic and crystallises in the *NaCl* structure type with space group *Fm*-3*m*.

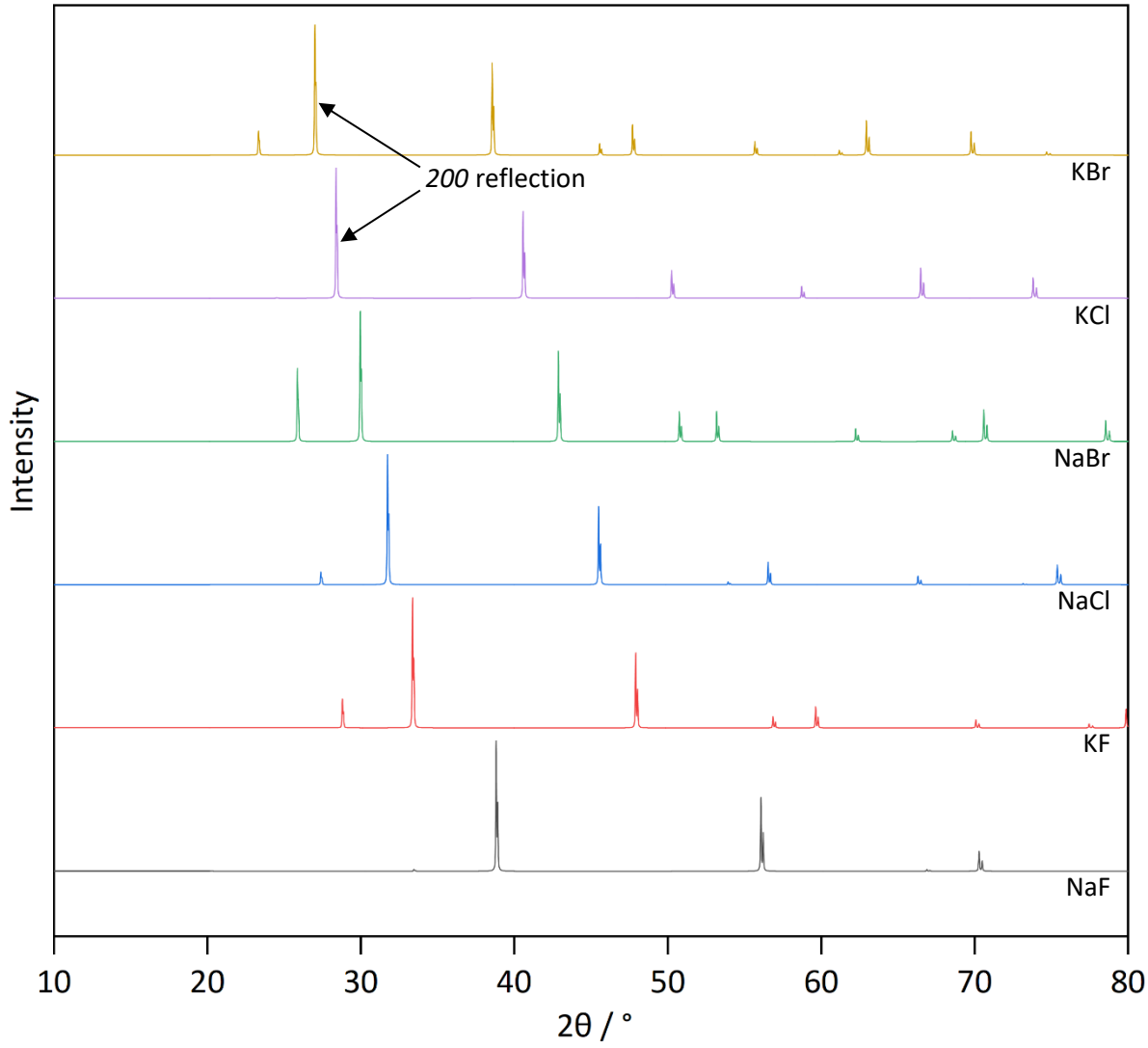

Figure 196 The simulated powder X-ray diffractograms of KBr (orange), KCl (pink), NaBr (green), NaCl (blue), KF (red), and NaF (black). Plots are labelled, and listed in ascending order of the 2θ value of the 200 reflection.

Three of the pairings, Permutations 1, 2 and 4, showed no change in composition, Figure 197. This is the intended and desirable outcome whereby one may assume that if those pairings appeared as metathesis products, they would not partake in anomalous side reactions. Note that the reaction of KCl with KBr unexpectedly produced a significant unknown impurity which could not be identified.

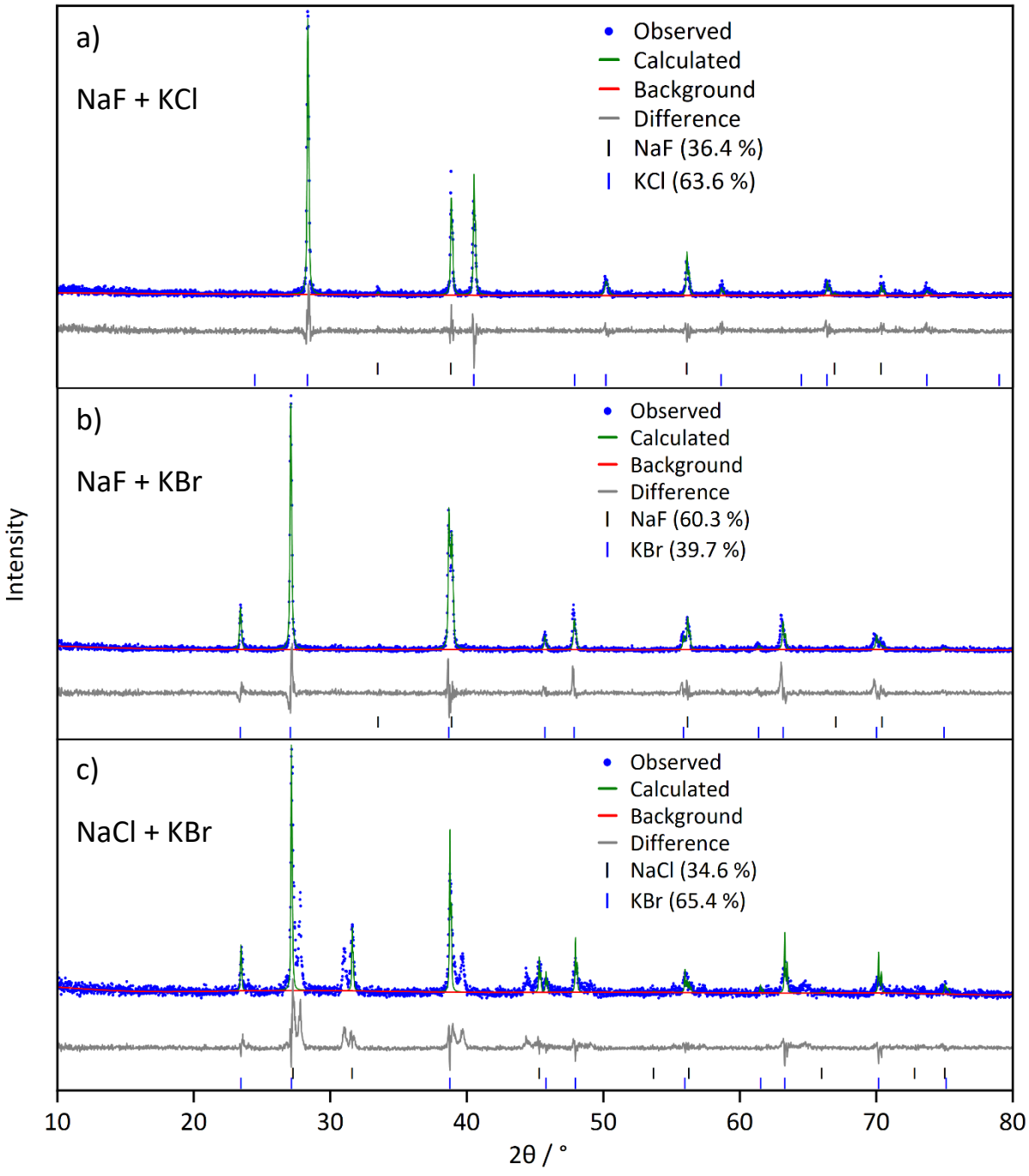

Figure 197 *Powder X-ray diffractograms of materials resulting from the reactions of a) NaF and KCl, b) NaF and KBr, and c) NaCl and KBr, after 12 hours of heating at 700 °C. The small blue circles represent the observed diffracted intensities, the green lines represent the Rietveld-refined calculated models, the red lines represent the backgrounds, and the grey lines represent the differences between observed and calculated intensities. Weight fractions for each phase are cited in the figure legends but should be approached qualitatively.*
a) Duration: 2 minutes. Data points: 3457. Interval: 0.02 °. GOF: 1.19. R_{wp}: 39.476 %.
b) Duration: 2 minutes. Data points: 3457. Interval: 0.02 °. GOF: 1.33. R_{wp}: 34.434 %.
c) Duration: 2 minutes. Data points: 3457. Interval: 0.02 °. GOF: 1.80. R_{wp}: 47.499 %.

The results of the reactions of Permutations 3 and 6, presented below in Figure 198, show that the hypothesis of salt side reactions is valid. In these experiments, the ions displaced during heating, forming two salt products opposite to those which were supplied. The same unknown impurity found in Permutation 4 is present in 6, which could not be refined to match any of the salt phases and returned no match to any other possible by-products such as carbonates, oxides, or hydroxides.

Permutation 3 proceeded in a displacement reaction according to Equation 101. It formed therefore the same products (KCl and NaF) in similar ratios to Permutation 1; the reaction of KCl and NaF.

Equation 101 $NaCl + KF \rightarrow KCl + NaF$

Similarly, Permutation 6 proceeded in a displacement reaction according to Equation 102, presenting near identically to Permutation 4.

Equation 102 $NaBr + KCl \rightarrow KBr + NaCl$

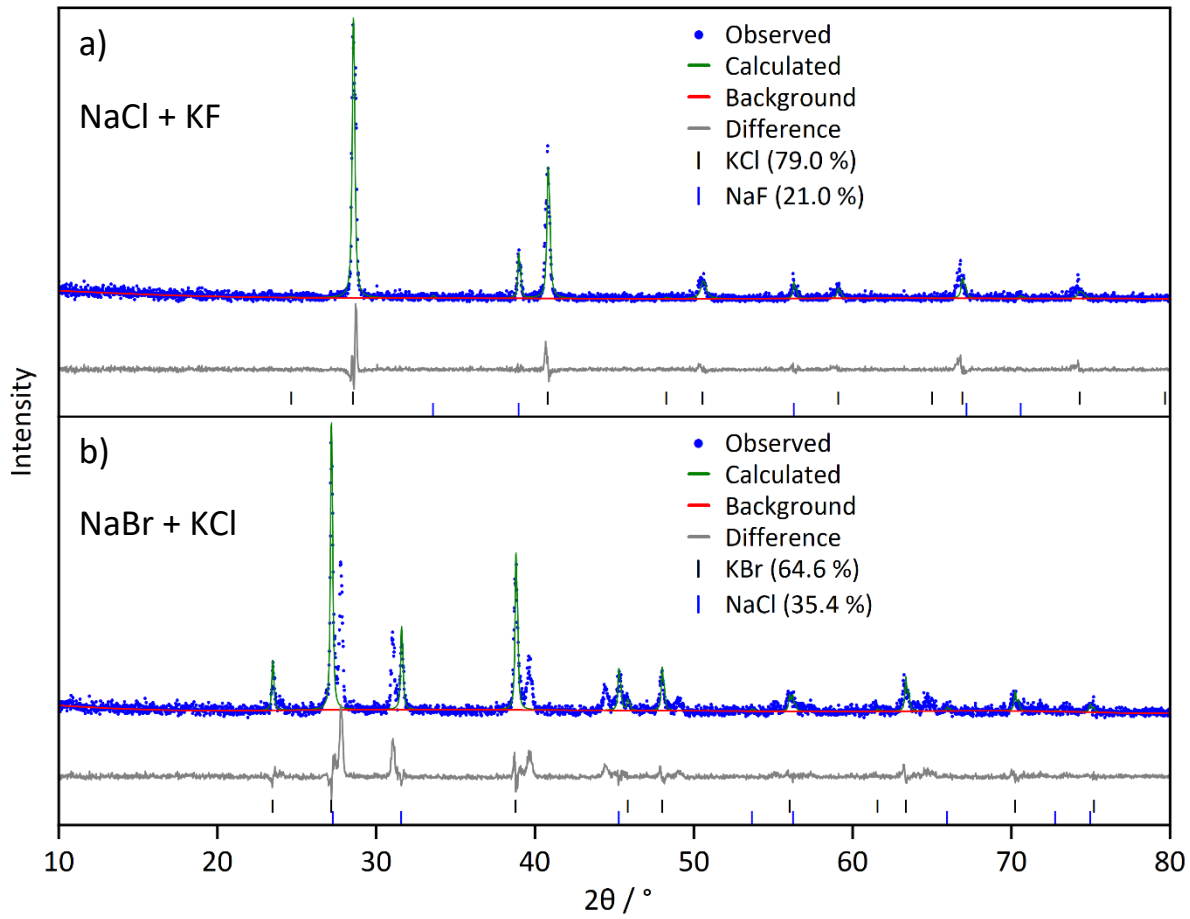

Figure 198 Powder X-ray diffractograms of materials resulting from the reactions of a) NaCl and KF, and b) NaBr and KCl, after 12 hours of heating at 700 °C. The small blue circles represent the observed diffracted intensities, the green lines represent the Rietveld-refined calculated models, the red lines represent the backgrounds, and the grey lines represent the differences between observed and calculated intensities. Weight fractions for each phase are cited in the figure legends but should be approached qualitatively.
a) Duration: 2 minutes. Data points: 3457. Interval: 0.02 °. GOF: 1.21. R_{wp}: 44.674 %.
b) Duration: 2 minutes. Data points: 3457. Interval: 0.02 °. GOF: 1.66. R_{wp}: 42.694 %.

Permutation 5, the last to be discussed, presented the most unusual and unexpected outcome. The two salts neither remained unreacted nor underwent displacement, they instead combined into one phase: NaKBrF. Figure 199 below is by far the cleanest and most crystalline of the six reactions in this section because bar a small 'impurity' of the NaBr precursor the sample is effectively phase pure NaKBrF. The structure of this phase was solved by modelling NaBr with half of its Na^+ sites replaced with K^+, and half of its Br^- sites replaced with F^-, relaxing the unit cell size as expected until a good match with the main observed phase was achieved. Permutation 5 proceeded according to Equation 103:

Equation 103 NaBr + KF → NaKBrF

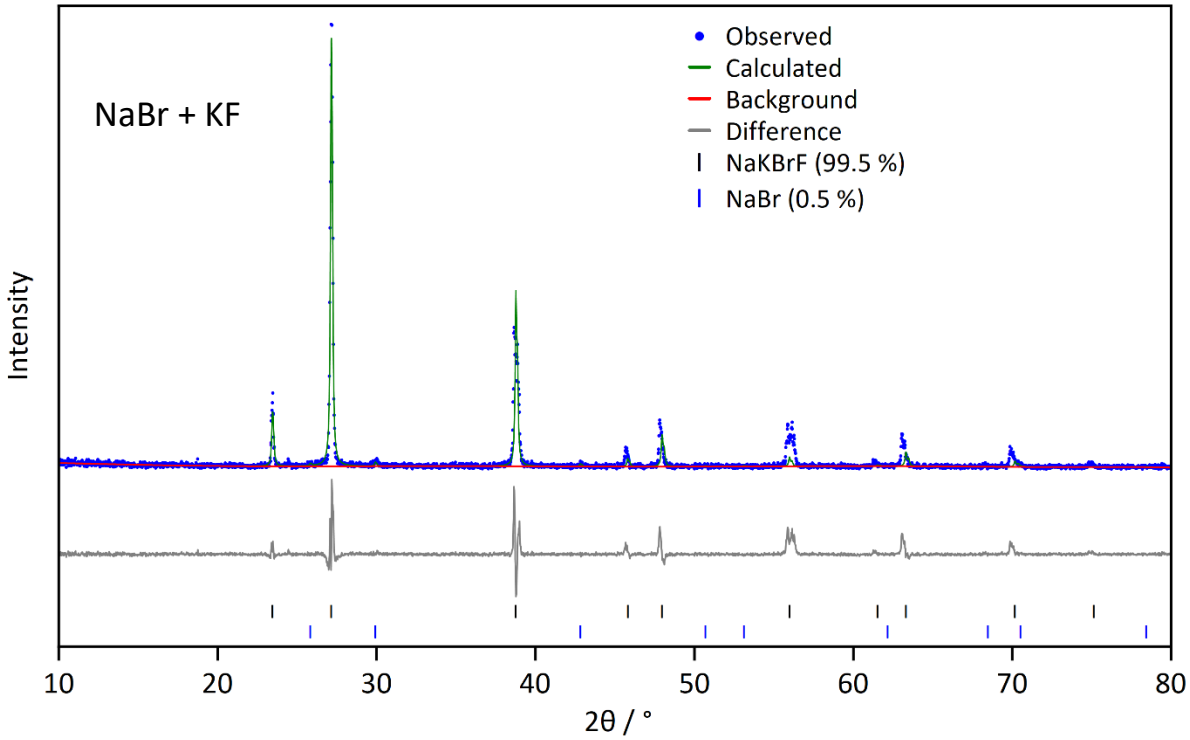

Figure 199 *Powder X-ray diffractogram of material resulting from the reaction of NaBr and KF, after 12 hours of heating at 700 °C. The small blue circles represent the observed diffracted intensity, the green line represents the Rietveld-refined calculated model, the red line represents the background, and the grey line represents the difference between observed and calculated intensities. The black and blue tick marks show the reflections of the refined models of NaBr (0.5 %) and NaKBrF (99.5 %) respectively.*
Duration: 2 minutes. Data points: 3457. Interval: 0.02 °. GOF: 1.76. R_{wp}: 42.060 %.

It is interesting to note that Permutation 2, which was the opposite combination of these precursors, NaF + KBr, does not show any salt combination of this kind, instead containing the original precursors unchanged.

Table 20 Tabulated qualitative results of the reactions of the six salt permutations.

Permutation	Main Products	Outcome	Comments
1) NaF + KCl	NaF + KCl	Salts unchanged	-
2) NaF + KBr	NaF + KBr	Salts unchanged	-
3) NaCl + KF	KCl + NaF	Salts displaced	-
4) NaCl + KBr	NaCl + KBr	Salts unchanged	+ unknown phase
5) NaBr + KF	NaKBrF	Salts combined	+ small trace of NaBr
6) NaBr + KCl	KBr + NaCl	Salts displaced	+ unknown phase

The results of this short side-investigation are presented in Table 20 above. It is interesting to note that neither NaBr nor KF were present in any the outcomes, omitting the trace NaBr remaining after the salt combination of Permutation 6. Whilst KF is considered relatively reactive due to the highly electronegative and nucleophilic fluoride ion, NaBr is instead rather unreactive so there appears to be no trend nor prediction for which salts are expected to be stable as metathesis products.

The strong evidence of salt combination in Permutation 5, even if just one example, is enough that one cannot assume that salt combination or mixing will not occur within a given parallel synthesis. It is possible therefore that mixing is occurring on some small scale within each of the permutations, a theory which could be assessed with higher quality PXRD data and variations in the unit cell size. In very small, symmetrical and cubic unit cells such as these, where $a = b = c$, small deviations in the lattice parameter can have a significant effect on observed peak positions, so site mixing or full combination, whilst not measured here besides the formation of NaKBrF, should be noticeable in higher quality data.

As noted previously, the PXRD scans were performed over very short time scales given that qualitative results were sufficient for this experiment, and as such the weight fractions are expected to be imprecise. After all, if salts are used to screen a parallel synthesis for a successful reaction, the exact quantities are of little use, instead merely the presence or absence of the salt should be indicative of a metathesis outcome.

The results of this investigation are not promising for the screening of parallel synthesis reactions using the salt by-products. That said, this should not be considered damaging for the validity of the parallel concept as a whole. The behaviour of the salts does not impact the primary concern of either a metathesis or a parallel synthesis test, which is the synthesis of the MALMs. It does however impact the screening process, which if successful would be a very significant selling point for the novel procedure. These experiments suggest that screening using salts should not be the exclusive method through which to ascertain the outcome of a metathesis reaction.

5.6 Proof of Concept Parallel Synthesis Trials

Four experiments were devised to test the proposed parallel technique for the solid-state metathetic syntheses of MALM. The precursors of each were decided based on the results of the individual metatheses to target specific outcomes. Given the mixed results of the individual reactions, it is not predicted that these trials will be high purity, fully successful, nor free from impurities or conventional solid-state chemistry. Potential weaknesses and flaws of the approach are intentionally probed by these trials, which target both positive and negative reaction outcomes.

Trial 1 targets two viable products. Trial 2 targets the same viable product twice, using different precursors. Trials 3 and 4 both target two successful and one unsuccessful products, targeting 325 and 426 materials respectively. All trials were performed simultaneously on a 1 gram scale and, like each of the individual metathesis tests, consist of a single 12 hour heat cycle at 600 °C. The rationale for each trial is explained in greater detail in the upcoming sections, and summarised in Table 21 below.

Table 21 *The targeted constituent metathesis reactions of the four parallel synthesis proof of concept trials. Based on the individual metathesis experiments previously: green boxes indicate a predicted successful outcome, red indicates a predicted unsuccessful outcome (due to target product instability) and orange indicates uncertainty.*

		Light Layers		
Trial #1		$Sr_3Sc_2O_5Cl_2$	$Sr_3Fe_2O_5Br_2$	
Heavy Layer	$Na_2Cu_2Se_2$	$Sr_3Sc_2O_5Cu_2Se_2$ + 2 NaCl	$Sr_3Fe_2O_5Cu_2Se_2$ + 2 NaBr	
Trial #2		$Sr_3Fe_2O_5Cl_2$	$Sr_3Fe_2O_5Br_2$	
Heavy Layer	$Na_2Cu_2Se_2$	$Sr_3Fe_2O_5Cu_2Se_2$ + 2 NaCl	$Sr_3Fe_2O_5Cu_2Se_2$ + 2 NaBr	
Trial #3		$Sr_3Sc_2O_5Cl_2$	$Sr_3Fe_2O_5Br_2$	$Sr_3Co_2O_5Cl_2$
Heavy Layer	$Na_2Cu_2Se_2$	$Sr_3Sc_2O_5Cu_2Se_2$ + 2 NaCl	$Sr_3Fe_2O_5Cu_2Se_2$ + 2 NaBr	$Sr_3Co_2O_5Cu_2Se_2$ + 2 NaCl
Trial #4		$Sr_4Sc_2O_6Cl_2$	$Sr_4Fe_2O_6Br_2$	$Sr_4Co_2O_6Cl_2$
Heavy Layer	$Na_2Cu_2Se_2$	$Sr_4Sc_2O_6Cu_2Se_2$ + 2 NaCl	$Sr_4Fe_2O_6Cu_2Se_2$ + 2 NaBr	$Sr_4Co_2O_6Cu_2Se_2$ + 2 NaCl

5.6.1 Trial 1

The first trial targets the two MALMs which were explored in detail in the temperature dependence studies of *Section 5.4*: $Sr_3Sc_2O_5Cu_2Se_2$ and $Sr_3Fe_2O_5Cu_2Se_2$. This is a 2×1 parallel synthesis experiment, described by Table 22 and with a targeted total reaction according to Equation 104.

Both metatheses are expected to be successful, as it has been shown that each of the constituent products can be synthesised successfully by metathesis, with little to no contribution by conventional solid-state chemistry. In both systems, the 426 phases dominate at 600 °C under conventional conditions, but were not observed at all under metathetic conditions.

Table 22 *The two constituent metathesis reactions of Parallel Synthesis Trial 1. Green boxes indicate predicted successful reactions.*

		Light Layers	
Trial #1		$Sr_3Sc_2O_5Cl_2$	$Sr_3Fe_2O_5Br_2$
Heavy Layer	$Na_2Cu_2Se_2$	$Sr_3Sc_2O_5Cu_2Se_2$ + 2 NaCl	$Sr_3Fe_2O_5Cu_2Se_2$ + 2 NaBr

Equation 104 $Sr_3Sc_2O_5Cl_2 + Sr_3Fe_2O_5Br_2 + 2\ Na_2Cu_2Se_2 \rightarrow Sr_3Sc_2O_5Cu_2Se_2 + Sr_3Fe_2O_5Cu_2Se_2 + 2\ NaCl + 2\ NaBr$

XRD analysis of the product of this trial,[20] shown on the next page in Figure 200, immediately presents not only a failed metathesis experiment, but exposes a flaw in the procedure which was not foreseen thus far. The potential site mixing or combination of the salt by-products was discussed in the previous section and found to be a valid concern, but one which does not detract from the parallel process if treated as merely an impurity to be washed away and not a telltale marker of successful metatheses. What was not considered was the mixing of the metathesis products themselves.

The two targeted products $Sr_3Fe_2O_5Cu_2Se_2$ and $Sr_3Sc_2O_5Cu_2Se_2$, which have been shown to be stable both within this work and within literature,[61, 89] and synthesisable by metathesis, were not formed here at all. Instead, the primary product is a 426 phase with mixed occupancy of Fe and Sc on the *B* site. A refinement of the exact stoichiometry would require higher quality XRD or NPD analysis, so is assumed to be approximately 1:1, and is described in Figure 200 as "$Sr_4(FeSc)O_6Cu_2Se_2$".

The dominant formation of the 426 phase is underwhelming yet very interesting. This trial was constructed to present two positive parallel metatheses, using two proven component reactions. *B* site mixing was not anticipated; and is assumed to arise from the thermodynamic stability of one mixed MALM vs two single occupancy MALMs.

[20] The four PXRD analyses in this section were performed in air, owing to a combination of the expected complexity of patterns, and the lack of unstable products in the individual metatheses previously.

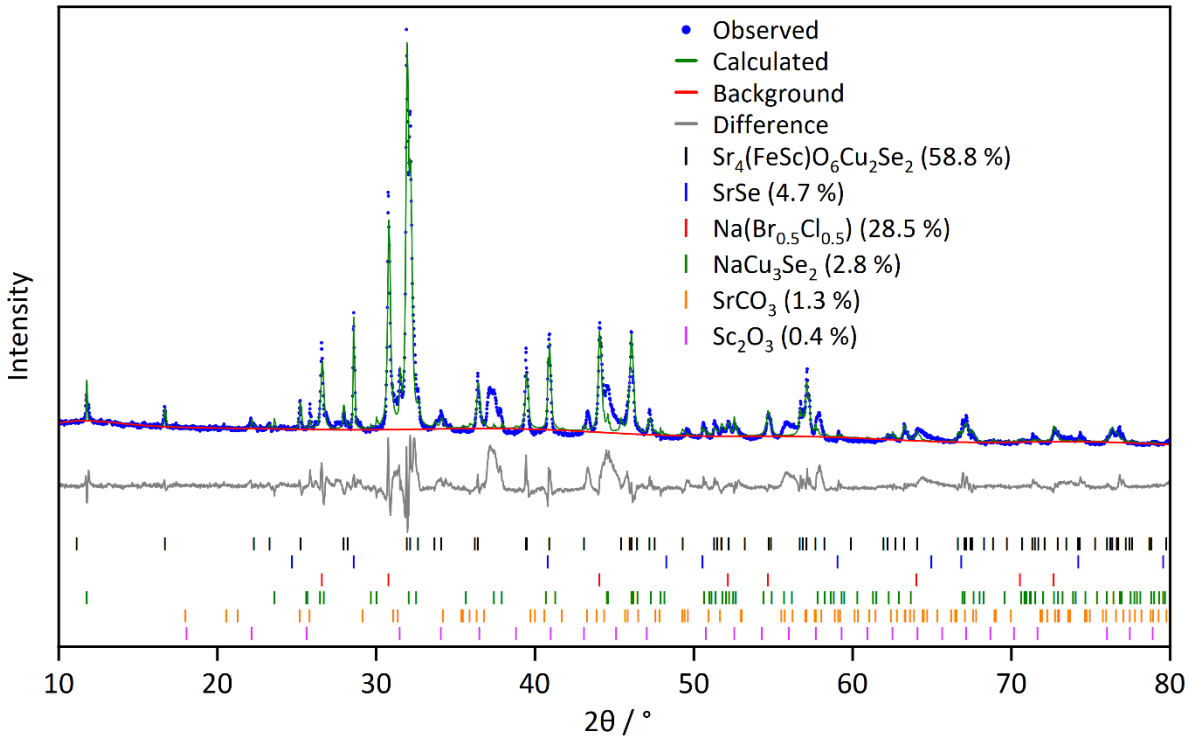

Figure 200 *Powder X-ray diffractogram of material resulting from attempted parallel metathetic syntheses of $Sr_3Fe_2O_5Cu_2Se_2$ and $Sr_3Sc_2O_5Cu_2Se_2$ after 12 hours of heating at 600 °C. The small blue circles represent the observed diffracted intensity, the green line represents the Rietveld-refined calculated model, the red line represents the background, and the grey line represents the difference between observed and calculated intensities. The black, blue, red, green, orange, and pink tick marks show the reflections of the refined models of $Sr_4(FeSc)O_6Cu_2Se_2$ (58.8 %), SrSe (4.7 %), $Na(Br_{0.5}Cl_{0.5})$ (28.5 %), $NaCu_3Se_2$ (2.8 %), $SrCO_3$ (1.3 %), and Sc_2O_3 (0.4 %) respectively.*
Duration: 3 hours. Data points: 4444. Interval: 0.02 °. GOF: 5.28. R_{wp}: 10.021 %.

The refined unit cell parameters of the mixed occupancy phase $Sr_4(FeSc)O_6Cu_2Se_2$ are presented in Table 23 below in comparison to the pristine phases $Sr_4Fe_2O_6Cu_2Se_2$ and $Sr_4Sc_2O_6Cu_2Se_2$. Whilst clearly closer to the iron analogue, the unit cell geometry of $Sr_4(FeSc)O_6Cu_2Se_2$ is in agreement with the assertion that it is a mixed occupancy phase in between that of the Fe and Sc pristine phases. The presence of Sc_2O_3 in the sample supports a larger iron component in $Sr_4(FeSc)O_6Cu_2Se_2$ than scandium.

Table 23 *Refined unit cell parameters of $Sr_4Fe_2O_6Cu_2Se_2$ and $Sr_4Sc_2O_6Cu_2Se_2$, alongside the mixed occupancy MALM product $Sr_4(FeSc)O_6Cu_2Se_2$ of Trial 1. Pristine data obtained from literature.*[87, 89]

	***a* / Å**	***c* / Å**	**Volume / Å³**
$Sr_4Fe_2O_6Cu_2Se_2$	3.937	15.970	247.498
$Sr_4(FeSc)O_6Cu_2Se_2$	3.943	15.988	248.569
$Sr_4Sc_2O_6Cu_2Se_2$	4.076	15.709	260.986

Alluded to in *Section 5.5 - The Salt Hypothesis*, the salt by-products also combined to form one mixed phase, denoted $Na(Br_{0.5}Cl_{0.5})$ because NaBr and NaCl were expected to form in a 1 : 1 ratio. Table 24 presents a unit cell parameter analysis for $Na(Br_{0.5}Cl_{0.5})$ similar to that of $Sr_4(FeSc)O_6Cu_2Se_2$ above, which again supports the site mixing.

Table 24 Refined unit cell parameters of NaCl and NaBr, alongside the mixed occupancy phase $Na(Br_{0.5}Cl_{0.5})$ of Trial 1. Pristine data obtained from literature.[335, 336]

	***a* / Å**	**Volume / Å^3**
NaCl	5.634	178.834
$Na(Br_{0.5}Cl_{0.5})$	5.818	196.934
NaBr	5.962	211.922

This salt combination is likely made more probable by the fact that both salts contain sodium, deriving from the same heavy layer precursor. This is an unavoidable outcome in a parallel synthesis if a given precursor is involved in two successful reaction (or, in this case, unsuccessful but forming the displacement salt anyway).

Salt mixing, as forecast, detracts slightly but negligibly from the validity of the parallel synthesis concept as a whole. Product mixing however, is incredibly damaging to the validity of the concept. The preliminary tests showed that $Sr_3Fe_2O_5Cu_2Se_2$ and $Sr_3Sc_2O_5Cu_2Se_2$ can be formed as stable high quality metathesis products, and crucially it also showed that $Sr_4Fe_2O_6Cu_2Se_2$ and $Sr_4Sc_2O_6Cu_2Se_2$ cannot. If performed as a real parallel synthesis, this test would provide no valuable information about the stability or existence of the target $Sr_3Fe_2O_5Cu_2Se_2$ and $Sr_3Sc_2O_5Cu_2Se_2$ phases, instead suggesting that the $Sr_4B_2O_6Cu_2Se_2$ phase is the more stable which has been shown amply within this work to be untrue. Further to this, in the individual tests, 600 °C was sufficient to limit conventional solid-state chemistry, but when combined the conventional route now prevails, demonstrated by the 325 to 426 transition, the mixed phases, and the presence of common impurities of the conventional route such as SrSe and $SrCO_3$.

It should be noted that there is an unknown phase within the PXRD pattern in Figure 200. Models of neither the iron nor the scandium pristine 325 or 426 phases could be refined to fit this phase, nor any phase mixture of the two *B* metals. Unknown phases are not uncommon in solid-state chemistry, but here serve to further contribute to a crowded diffraction pattern which already contains six known phases and is very complex.

5.6.2 Trial 2

Similar to the first, Trial 2 is comprised of two metathesis reactions that were shown to be successful at 600 °C in the individual tests. The difference here is that the two reactions target the same material, $Sr_3Fe_2O_5Cu_2Se_2$, by the parallel reaction of an oxychloride and an oxybromide, described in Table 25 and Equation 105.

Table 25 *The two constituent metathesis reactions of Parallel Synthesis Trial 2. Green boxes indicate predicted successful reactions.*

		Light Layers	
Trial #2		$Sr_3Fe_2O_5Cl_2$	$Sr_3Fe_2O_5Br_2$
Heavy Layer	$Na_2Cu_2Se_2$	$Sr_3Fe_2O_5Cu_2Se_2$ + 2 NaCl	$Sr_3Fe_2O_5Cu_2Se_2$ + 2 NaBr

Equation 105 $Sr_3Fe_2O_5Cl_2 + Sr_3Fe_2O_5Br_2 + 2\ Na_2Cu_2Se_2 \rightarrow 2\ Sr_3Fe_2O_5Cu_2Se_2 + 2\ NaCl + 2\ NaBr$

This trial was successful. The target MALM $Sr_3Fe_2O_5Cu_2Se_2$ was synthesised phase pure, Figure 201, in a reaction that is assumed to be wholly metathetic in nature because a conventional reaction at the same temperature was earlier found to yield approximately 62 % purity, in *Section 5.4.2*.

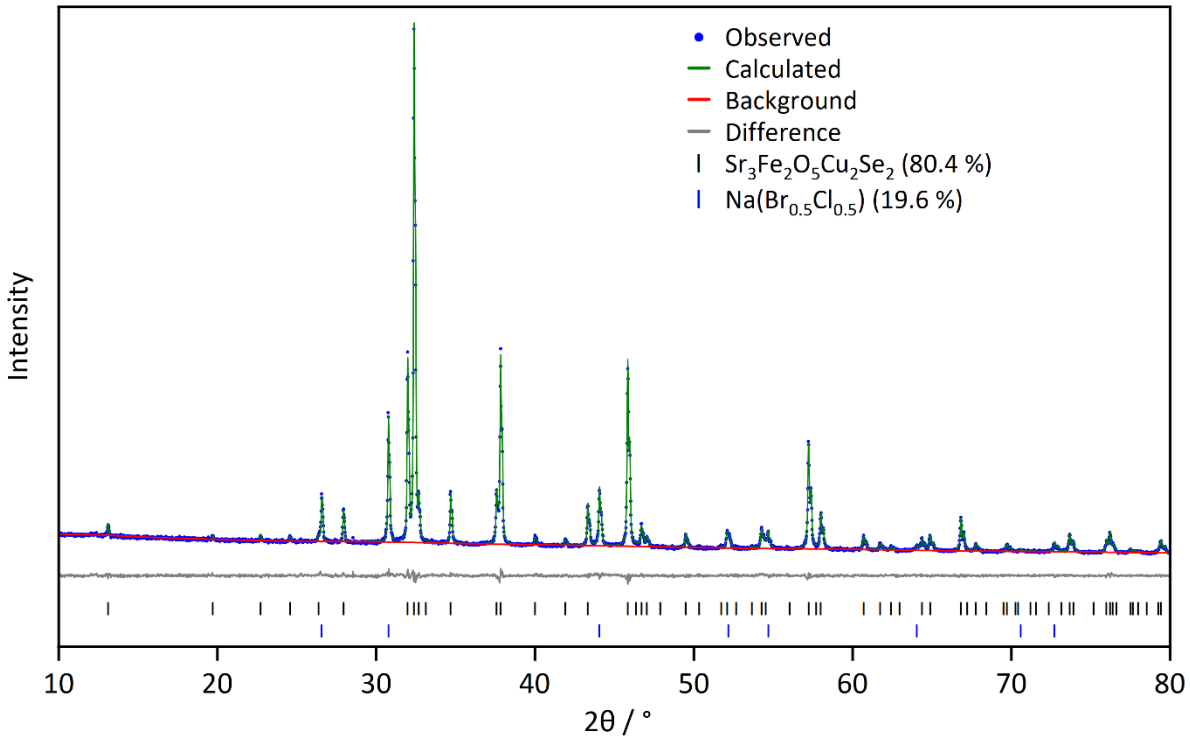

Figure 201 *Powder X-ray diffractogram of material resulting from attempted parallel metathetic synthesis of $Sr_3Fe_2O_5Cu_2Se_2$ after 12 hours of heating at 600 °C. The small blue circles represent the observed diffracted intensity, the green line represents the Rietveld-refined calculated model, the red line represents the background, and the grey line represents the difference between observed and calculated intensities. The black and blue tick marks show the reflections of the refined models of $Sr_3Fe_2O_5Cu_2Se_2$ (80.4 %), and $Na(Br_{0.5}Cl_{0.5})$ (19.6 %) respectively.*
Duration: 3 hours. Data points: 4444. Interval: 0.02 °. GOF: 1.20. R_{wp}: 2.326 %.

The 325 product is the only MALM product phase, as intended, forming the salt by-products NaBr and NaCl in equal proportions which again have undergone phase combination to form $Na(Br_{0.5}Cl_{0.5})$. Phase fractions are on par with the analogous phase pure $Sr_3Fe_2O_5Cu_2Se_2$ metathesis reactions in *Section 5.4.2*, and the unit cell parameters of $Sr_3Fe_2O_5Cu_2Se_2$ (a = 3.958 Å, c = 27.034 Å) are in close agreement with literature values of a = 3.958 Å and c = 27.004 Å reported in literature.[61]

The exclusive synthesis of the 426 phase in Trial 1 and its complete omission in Trial 2 suggests that its formation previously was a result of the parallel presence of the scandium and iron phases, and that the combination of the two *B* ions is accommodated with greater stability in the 426 structure than the 325.

5.6.3 Trial 3

The third trial contained three component reactions, see Table 26 and Equation 106. The two metatheses explored in Trial 1 are present, those of $Sr_3Sc_2O_5Cu_2Se_2$ and $Sr_3Fe_2O_5Cu_2Se_2$, alongside a third reaction targeting the cobalt analogue $Sr_3Co_2O_5Cu_2Se_2$ which is predicted to be unsuccessful. Therefore, in this trial one of the three component reactions is expected, and intended, to fail. Hypothetically, in a larger scale parallel synthesis designed to rapidly screen for the existence of new potential MALMs, a large quantity of the component reactions will be unsuccessful if not all, so simulating such scenarios is important.

On initial discussion and conception of the parallel method in the introduction to this chapter, this simulated failure might have been expected to yield unreacted light and heavy layer precursors and therefore no MALM nor salt. However, the preliminary individual metathesis testing and the known instability of the heavy layer render this assumption extremely unlikely. Instead, the facile degradation of the unreacted heavy layer (more specifically the component of it that does not react with $Sr_3Sc_2O_5Cl_2$ or $Sr_3Fe_2O_5Br_2$) is expected, facilitating a reaction with the cobalt light layer $Sr_3Co_2O_5Cl_2$ to yield a 212 MALM and a salt by-product.

Table 26 *The three constituent metathesis reactions of Parallel Synthesis Trial 3. Green boxes indicate predicted successful reactions, and red unsuccessful reactions.*

		Light Layers		
Trial #3		$Sr_3Sc_2O_5Cl_2$	$Sr_3Fe_2O_5Br_2$	$Sr_3Co_2O_5Cl_2$
Heavy Layer	$Na_2Cu_2Se_2$	$Sr_3Sc_2O_5Cu_2Se_2$ + 2 NaCl	$Sr_3Fe_2O_5Cu_2Se_2$ + 2 NaBr	$Sr_3Co_2O_5Cu_2Se_2$ + 2 NaCl

Equation 106 $Sr_3Sc_2O_5Cl_2 + Sr_3Fe_2O_5Br_2 + Sr_3Co_2O_5Cl_2 + 3\ Na_2Cu_2Se_2 \rightarrow Sr_3Sc_2O_5Cu_2Se_2 + Sr_3Fe_2O_5Cu_2Se_2 + Sr_3Co_2O_5Cu_2Se_2 + 4\ NaCl + 2\ NaBr$

As expected, the cobalt reaction did not form the 325 MALM $Sr_3Co_2O_5Cu_2Se_2$ because this product is not stable and has never been reported. As in all previous tests, the 212 MALM $Sr_2CoO_2Cu_2Se_2$ formed instead, the only stable cobalt material of this type.[332] The scandium and iron precursors again combined into a single phase as seen in Trial 1, exhibiting once more the 426 structure rather than the intended (and usually more stable) 325 structure, see Figure 202.

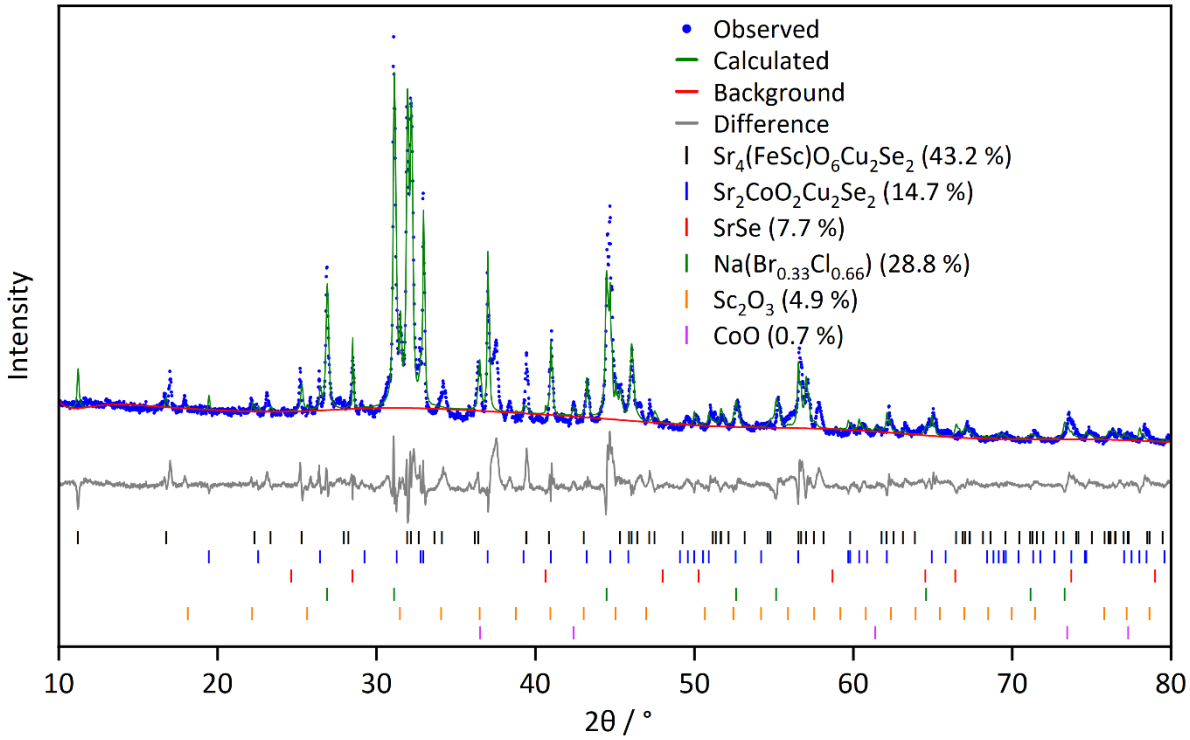

Figure 202 *Powder X-ray diffractogram of material resulting from attempted parallel metathetic syntheses of $Sr_3Fe_2O_5Cu_2Se_2$, $Sr_3Sc_2O_5Cu_2Se_2$ and $Sr_3Co_2O_5Cu_2Se_2$ after 12 hours of heating at 600 °C. The small blue circles represent the observed diffracted intensity, the green line represents the Rietveld-refined calculated model, the red line represents the background, and the grey line represents the difference between observed and calculated intensities. The black, blue, red, green, orange, and pink tick marks show the reflections of the refined models of $Sr_4(FeSc)O_6Cu_2Se_2$ (43.2 %), $Sr_2CoO_2Cu_2Se_2$ (14.7 %), SrSe (7.7 %), $Na(Br_{0.33}Cl_{0.66})$ (28.8 %), Sc_2O_3 (4.9 %), and CoO (0.7 %) respectively.*
Duration: 3 hours. Data points: 4444. Interval: 0.02 °. GOF: 4.33. R_{wp}: 7.638 %.

Table 27 *Refined unit cell parameters of NaCl and NaBr, alongside the mixed occupancy phase $Na(Br_{0.033}Cl_{0.66})$ of Trial 3. Pristine data obtained from literature.[335, 336]*

	***a* / Å**	**Volume / Å³**
NaCl	5.634	178.834
$Na(Br_{0.033}Cl_{0.66})$	5.782	193.255
NaBr	5.962	211.922

The unit cell parameters of $Sr_4(FeSc)O_6Cu_2Se_2$ (a = 3.954 and c = 16.055) are once again between and in agreement with the pristine $Sr_4B_2O_6Cu_2Se_2$ MALMs tabulated in the discussion of Trial 1. The salt by-product unit cell parameters are also in agreement with the data discussed prior, see Table 27. There is likely a greater chlorine component in the salt compared to previous trials due to the supplementary chlorine counterion of the Co light layer, and as expected this results in a smaller unit cell. For this reason, the salt is described as $Na(Br_{0.033}Cl_{0.66})$ to represent the 1 : 2 ratio of Br : Cl.

Like Trial 1, this test provided an underwhelming testimonial for the novel parallel synthesis method, where two of three target products were expected to form, yet all three were unsuccessful.

5.6.4 Trial 4

The final experiment in this parallel synthesis investigation, Trial 4, was devised to stress the combinatorial method to the greatest extent thus far by employing two metathesis reactions whose target 426 products formed mixed phase or not at all during the individual metathesis tests, alongside a target synthesis of the cobalt 426 which is again expected and intended to fail. This 3×1 trial, outlined in Table 28 and Equation 107, may be considered the 426 equivalent of the previous Trial 3. In that case, the 426 structure prevailed, and it was expected to do so again in this trial.

Table 28 *The three constituent metathesis reactions of Parallel Synthesis Trial 4. Red boxes indicate predicted unsuccessful reactions, orange indicates uncertainty.*

		Light Layers		
Trial #4		$Sr_4Sc_2O_6Cl_2$	$Sr_4Fe_2O_6Br_2$	$Sr_4Co_2O_6Cl_2$
Heavy Layer	$Na_2Cu_2Se_2$	$Sr_4Sc_2O_6Cu_2Se_2$ + 2 NaCl	$Sr_4Fe_2O_6Cu_2Se_2$ + 2 NaBr	$Sr_4Co_2O_6Cu_2Se_2$ + 2 NaCl

Equation 107

$$Sr_4Sc_2O_6Cl_2 + Sr_4Fe_2O_6Br_2 + Sr_4Co_2O_6Cl_2 + 3\ Na_2Cu_2Se_2 \rightarrow Sr_4Sc_2O_6Cu_2Se_2 + Sr_4Fe_2O_6Cu_2Se_2 + Sr_4Co_2O_6Cu_2Se_2 + 4\ NaCl + 2\ NaBr$$

The outcome of this trial is near identical to that of the previous. The iron and scandium precursors combine to form the usual mixed *B* site 426 MALM $Sr_4(FeSc)O_6Cu_2Se_2$, and the cobalt metathesis fails, defaulting to the 212. The diffractogram, Figure 203, is therefore extremely similar to that of Trial 3.

This time, the 426 MALM was the target product. In the individual metathesis experiments of *Section 5.4.3*, $Sr_4Fe_2O_6Cu_2Se_2$ formed as a metastable phase mixture with its more stable 325 analogue $Sr_3Fe_2O_5Cu_2Se_2$, and $Sr_4Sc_2O_6Cu_2Se_2$ did not form at all, converting entirely to the 325 analogue $Sr_3Sc_2O_5Cu_2Se_2$. Given this, the complete formation of a 426 phase here, even if suggested by the previous trials, is very surprising.

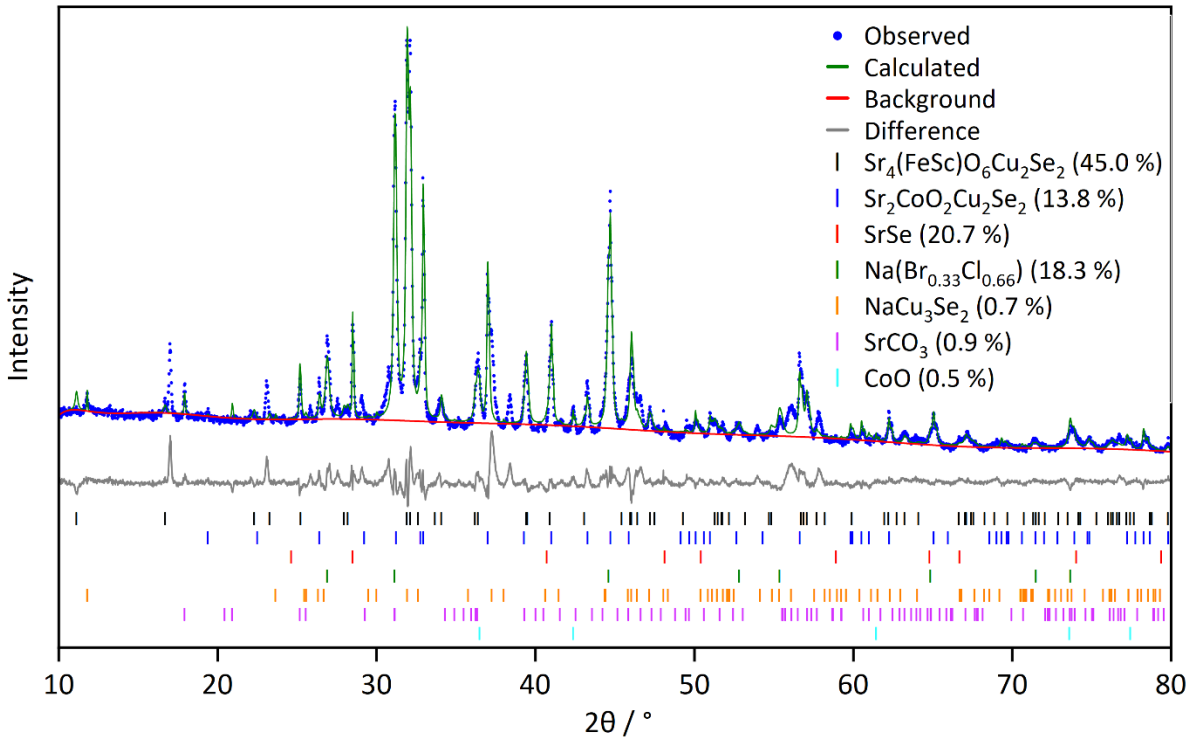

Figure 203 *Powder X-ray diffractogram of material resulting from attempted parallel metathetic syntheses of $Sr_4Fe_2O_6Cu_2Se_2$, $Sr_4Sc_2O_6Cu_2Se_2$ and $Sr_4Co_2O_6Cu_2Se_2$ after 12 hours of heating at 600 °C. The small blue circles represent the observed diffracted intensity, the green line represents the Rietveld-refined calculated model, the red line represents the background, and the grey line represents the difference between observed and calculated intensities. The black, blue, red, green, orange, pink and cyan tick marks show the reflections of the refined models of $Sr_4(FeSc)O_6Cu_2Se_2$ (45.0 %), $Sr_2CoO_2Cu_2Se_2$ (13.8 %), SrSe (20.7 %), $Na(Br_{0.33}Cl_{0.66})$ (18.3 %), $NaCu_3Se_2$ (0.7 %), $SrCO_3$ (0.9 %) and CoO (0.5 %) respectively. Duration: 3 hours. Data points: 4444. Interval: 0.02 °. GOF: 3.79. R_{wp}: 6.647 %.*

5.7 An Evaluation of Solid-State Metathesis and Parallel Synthesis

The concept of solid-state metathesis has been widely researched as a whole, but only once has it been applied to syntheses of quinternary Mixed Anion Layered Materials, until this current work. In this chapter, the concept of solid-state metathesis for MALM synthesis has been explored in great detail, from the synthesis of relevant building block precursors in *Section 5.3*, the individual metathesis reactions of *Section 5.4*, and the application of SSM in *Section 5.6* to the concept of parallel synthesis, a novel synthetic method hitherto uncharted in literature.

This work presents strong evidence for the metathesis mechanism and expands upon Cario's work,[289] showcasing the phase pure synthesis of $Sr_3Fe_2O_5Cu_2Se_2$ by metathesis within an investigation of its formation between 500 - 900 °C. The metathesis pathway was supported by a conventional solid-state reaction performed concurrently, revealing that the 426 phase $Sr_4Fe_2O_6Cu_2Se_2$ forms as a lower temperature kinetic intermediate product during conventional synthesis, and was never observed in the metathesis study.

Conventional and metathetic syntheses of the scandium analogue $Sr_3Sc_2O_5Cu_2Se_2$ behaved similarly, where the 426 intermediate was not present in the metathesis batch implying it did not proceed via a conventional pathway. Applying the metathesis method to other light layer precursors yielded mixed results, with some clearly proceeding via a conventional pathway and forming differently structured MALMs, which should not be possible if metathesis is the only contributing mechanism. This was particularly relevant in the cases where 426 MALMs were targeted which appear to be the least stable structural permutation and even at 600 °C favour the 325 phase via a conventional route. While clearly not an ideal method of MALM synthesis in isolation, and potentially not possible for all known MALMs, this work provides strong evidence for the progression of MALM synthesis via the metathetic route.

The novel concept of parallel synthesis was proposed, which utilises the pre-syntheses of layered building blocks, a feature of the metathesis route which in isolation is a significant disadvantage, to facilitate a larger scale reaction of multiple precursors. This was explored in four proof of concept trials in the previous section. These four trials, realistically, are a poor endorsement for parallel synthesis. It is clear that whilst metatheses are a valid synthesis method for MALMs individually, when combined there is very little control over the reaction outcome, and the products are often not reflective either of the target material nor the relative stabilities in the phase space of the target system.

Part of the parallel synthesis proposition was a screening method for identifying positive metatheses using distinctive reflections of the highly crystalline metathesis salt by-products. The parallel approach at large does not depend on this screening technique but would be complimented by it. Unfortunately, a hypothesised flaw, that of salt mixing or displacement at elevated temperatures, proved true both in the salt investigations of *Section 5.5* and all four proof of concept trials in *Section 5.6*.

This chapter has shown that solid-state metathesis can successfully be applied to MALM syntheses. This proof of concept for the metathesis process suggests that other MALMs and MALM types may also be accessible by metathesis, but the ideal conditions of each system will vary. Despite succeeding and often excelling as an isolated approach, metathesis fails in a combinatorial application. For example, 426 MALMs generally form at lower temperatures than 325 MALMs in systems where both exist, such as the scandium and iron analogues explored throughout this chapter. Any temperature selected for a parallel synthesis will invariably favour one phase over the other, so exploring multiple material classes within the same sample is not recommended in applications of the parallel technique.

Other MALMs such as the 212 and 438 families were not explored here, but light layer precursors for these families have been reported, such as $Ca_2CuO_2Cl_2$,[337, 338] and $Sr_4Co_3O_{7.5}Cl_2$.[313, 339] There exist, more interestingly, numerous other structural permutations of layered oxyhalide light layers which do not exist as quinternary MALMs. These include $Ca_2Fe_2O_4Cl_2$,[324, 340] $Ca_3Cu_2O_4Cl_2$,[341] and $Pb_8Fe_6O_{16}Cl_2$,[342-344] the metathetic exploration of which presents fruitful future work in this field, and grants the potential for the discovery of new MALM structures, some of which may be accessible only by metathesis.

If the parallel process can be optimised such that it can be appropriately applied to materials discovery, uncovering new MALMs and new structure types is just one benefit. A parallel approach (if optimised to maximise reaction consistency and predictability whilst minimising any conventional solid-state chemistry) may be faster in terms of materials discovery than individual syntheses. Simultaneously eliminating multiple negative tests from a batch at once will, in time, prove faster than if each of those materials were produced individually. A parallel approach also allows exploration of 'higher risk' materials (where risk refers to likelihood of success, not safety), of which MALM analogues of the '224', '324' and '8616' oxychlorides above are a perfect example. Parallel synthesis and metathesis in general are also lower temperature processes than conventional syntheses, increasing the green credentials of MALM syntheses which often run at extremely high temperatures. Finally, if optimised, a metathesis or parallel reaction should yield less impurities than a conventional reaction provided the precursors are high purity, because only the displacement of the pre-formed building blocks should be occurring.

Alongside this promising list of positive aspects to metathesis and parallel synthesis, there are a significant number of negatives: Firstly, as demonstrated even in the small-scale parallel synthesis trials which were either 2×1 or 3×1, the XRD diffractograms can become rapidly complex. Figure 169 on page 262 depicts an (albeit extreme) simulation of the diffraction pattern of a low yield but fully successful 3×2 parallel synthesis diffractogram, far beyond the point of credible translation. The risk of self-ignition reported in many instances of solid-state metathesis is very low but cannot be entirely discounted. The lack of diversity in the halides of the light layer precursors is another issue, which would quickly diminish the efficiency of an optimised parallel technique through unnecessary sample repetition because chlorides dominate the phase space. The heavy layers are incredibly diverse with hundreds of examples, but are very difficult to synthesise and store especially without specialist equipment or techniques such as platinum crucibles or spark plasma sintering.

Other drawbacks of parallel synthesis include a confinement to air-sensitive XRD if one believes the heavy layer precursor may remain unreacted in a given sample, the high probability for false negatives such as was observed in Trials 1 and 3, the difficulty of controlling product mixing as observed in all trials, and the inevitable disruptive contributions of conventional solid-state chemistry.

There are, unfortunately, many more negatives to a parallel approach than there are positives. Metathesis is a proven, valid, and useful technique that warrants more research attention within this field; however the combinatorial chemistry parallel approach cannot be recommended for use in materials discovery at this time. The complexity, unpredictability, and most pressingly the tendency for product combination associated with this technique render it inferior to the conventional pathway at this time.

Since writing, this chapter was published in: *Metathesis and the building block approach to novel layered mixed anion materials - useful tool or synthetic dead-end? - Materials Horizons, 2025. L. Kemp and G. Hyett.*

Chapter 6 $Sr_3In_2O_5Cu_2Se_2$: A Novel Oxychalcogenide

6.1 $Sr_3In_2O_5Cu_2Se_2$

During this project, the syntheses of many MALMs were attempted outside of the primarily scandium-based materials described thus far, in an attempt to discover new materials and TCO candidates. Most were unsuccessful, such as attempted syntheses of materials which were deemed unlikely to exist or had been previously reported to not exist, either in the literature or by colleagues. One material however, which had been assumed to be too unstable based on prior work by colleagues, yielded a surprising result.

One investigation into novel materials discovery concerned the 325 MALMs with formula $Sr_3In_2O_5Cu_2Ch_2$ (*Ch* = S or Se). The rationale for this attempt was the stability and publication of the 426 materials $Sr_4In_2O_6Cu_2Se_2$[64, 65] and $Sr_4In_2O_6Cu_2S_2$.[41, 67] These were investigated in *Chapter 4* in comparison to the gallium analogues $Sr_4Ga_2O_6Cu_2Ch_2$, which have been definitively shown to have no stable 325 equivalents, and the scandium analogues $Sr_4Sc_2O_6Cu_2Ch_2$, which have known stable 426 analogues. The indium materials were, like $Sr_4Ga_2O_6Cu_2Ch_2$, believed to have no stable 325 analogues. Attempts by colleagues proved unsuccessful, and our 2024 publication "*Transport Properties of Doped Wide Band Gap Layered Oxychalcogenide Semiconductors Sr_2GaO_3CuCh, Sr_2ScO_3CuCh, and Sr_2InO_3CuCh (Ch = S or Se)*",[64] from which *Chapter 4* was created, asserted that no such $Sr_3In_2O_5Cu_2Ch_2$ materials are stable. This current work now renders this assertion incorrect - $Sr_3In_2O_5Cu_2Se_2$ was found to be a stable material unreported in the literature at the time of writing.

Synthesis of the MALM $Sr_3In_2O_5Cu_2Se_2$ was attempted on a 1-gram scale using conventional solid-state chemistry at 900 °C for three 12 hour heat cycles with intermediate regrinds, according to Equation 108:

Equation 108 $2\ SrO + In_2O_3 + Cu_2Se + SrSe \rightarrow Sr_3In_2O_5Cu_2Se_2$

The resulting product was a crystalline black powder, the XRD for which is shown in Figure 204 on the next page. A maximum purity of 80.2 wt % was achieved after multiple attempts, alongside impurity phases $SrIn_2O_4$ and SrSe. Increased temperatures, reaction time and number of heat cycles were insufficient to progress the reaction completion further than 80.2 %. Quenching was also employed in an attempt to 'lock in' a potentially metastable high temperature phase pure material, but this produced lower purities than a conventional synthesis.

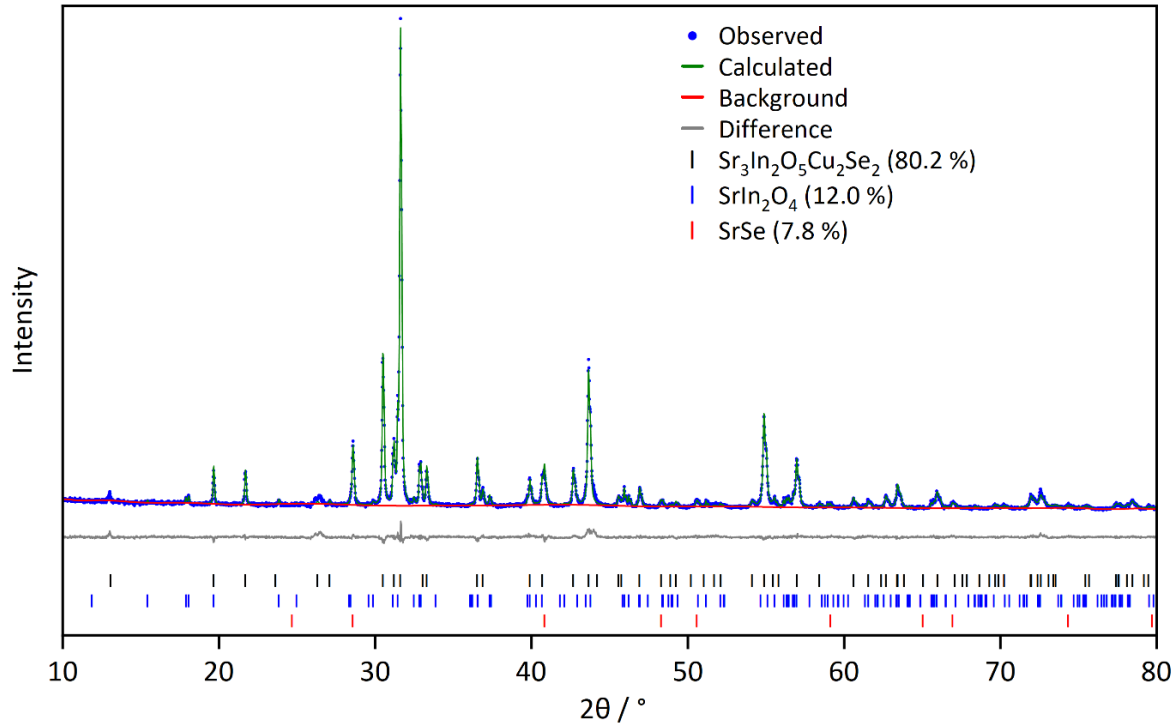

Figure 204 *Powder X-ray diffractogram of material with target composition $Sr_3In_2O_5Cu_2Se_2$ (space group I4/mmm) after 36 hours of heating at 900 °C. The small blue circles represent the observed diffracted intensity, the green line represents the Rietveld-refined calculated model, the red line represents the background, and the grey line represents the difference between observed and calculated intensities. The black tick marks show the reflections of the refined model of $Sr_3In_2O_5Cu_2Se_2$ (80.2 %), whilst the blue and red tick marks represent refined impurity phases $SrIn_2O_4$ (12.0 %), and SrSe (7.8 %) respectively.*
Duration: 12 hours. Data points: 3457. Interval: 0.01 °. GOF: 1.52. R_{wp}: 7.227 %.

The refined structural parameters of $Sr_3In_2O_5Cu_2Se_2$ can be found in Table 29 below. Full details of the refinement, structure and analysis can be found in *Appendix A.6*. The unit cell parameters *a* and *c* were found to be 4.14553 Å and 27.1013 Å respectively, for a cell volume of 465.747 Å^3.

Table 29 *Structural parameters of the refined model of pristine $Sr_3In_2O_5Cu_2Se_2$ in the I4/mmm space group at room temperature, where a = 4.14553(9) Å and c = 27.1013(7) Å.*

Atom	Fractional coordinates			Fractional Occupancy	Isotropic Thermal Parameter / Å^2
	x	*y*	*z*		
Sr1	0.5	0.5	0	1	0.0534(21)
Sr2	0.5	0.5	0.14275(15)	1	0.0205(24)
In	0	0	0.07419(11)	1	0.0174(14)
O1	0.5	0	0.0774(5)	1	0.022(8)
O2	0	0	0	1	0.093(25)
Cu	0.5	0	0.25	1	0.030(3)
Se	0	0	0.19594(13)	1	0.043(3)

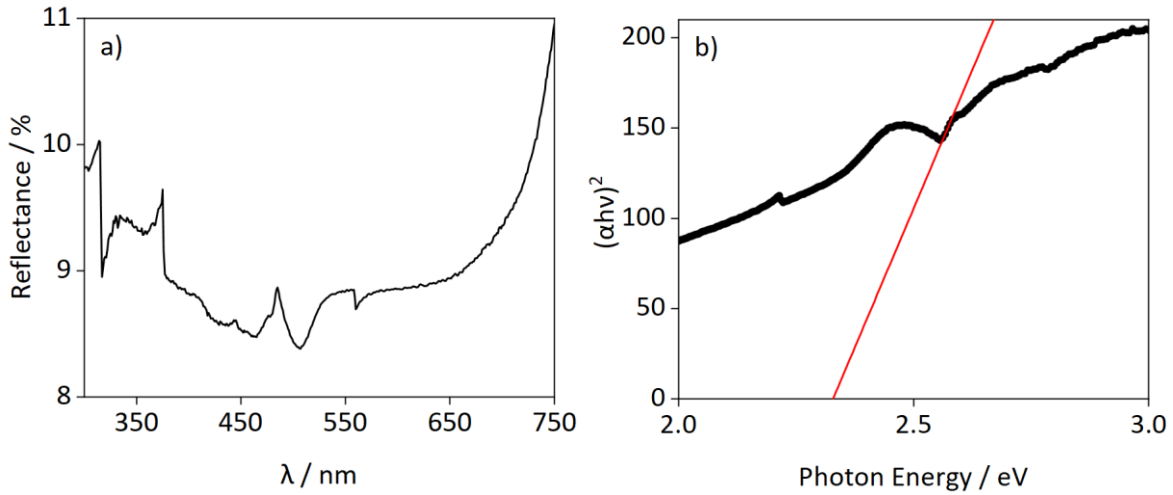

Figure 205 UV-Vis spectrometry data for material with target composition $Sr_3In_2O_5Cu_2Se_2$ after 48 hours of heating at 500 - 900 °C. Plot a) is the raw diffuse reflectance data, and plot b) is the associated magnified Tauc plot for this region, where the intercept between the red extrapolated tangent line and the x-axis is used to estimate an optical band gap of 2.33 eV, which corresponds to 532 nm.

Like most black-coloured materials encountered in this work, obtaining a band gap value was very difficult due to the strong absorbance of both UV and visible light. A small drop-off in diffuse reflectance was observed, which corresponds to an (albeit untrustworthy) estimate of a 2.33 eV band gap, Figure 205. This value is too small to warrant further investigation into transparent conductivity.

This is the first report of the synthesis or existence of $Sr_3In_2O_5Cu_2Se_2$. It was decided that the purity of this material, whilst more than sufficient to convincingly argue the existence and successful formation of this novel compound, was insufficient to warrant further investigation into pellet conductivity. Future work, if able to drive this reaction to completion, should explore the conductivity of $Sr_3In_2O_5Cu_2Se_2$ and its applicability to conductive applications.

6.2 $Sr_3In_2O_5Cu_2S_2$

It should be noted that the sulfide 325 material $Sr_3In_2O_5Cu_2S_2$ was also attempted numerous times under various conditions, but on no occasion did the target product form. Synthesis of the MALM $Sr_3In_2O_5Cu_2S_2$ was attempted on a 1-gram scale using conventional solid-state chemistry at 900 °C for three 12 hour heat cycles with intermediate regrinds, according to Equation 109 below:

Equation 109 $2\ SrO + In_2O_3 + Cu_2S + SrS \rightarrow Sr_3In_2O_5Cu_2S_2$

All attempts to synthesise $Sr_3In_2O_5Cu_2S_2$ were unsuccessful, resulting in a mix of $SrIn_2O_4$, SrS, and some unknown crystalline material which could not be fit to any known possible material, such as $Sr_4In_2O_6Cu_2S_2$ or a simulated pattern of target material $Sr_3In_2O_5Cu_2S_2$. An example Reitveld fit from one of these synthesis attempts can be seen below in Figure 206.

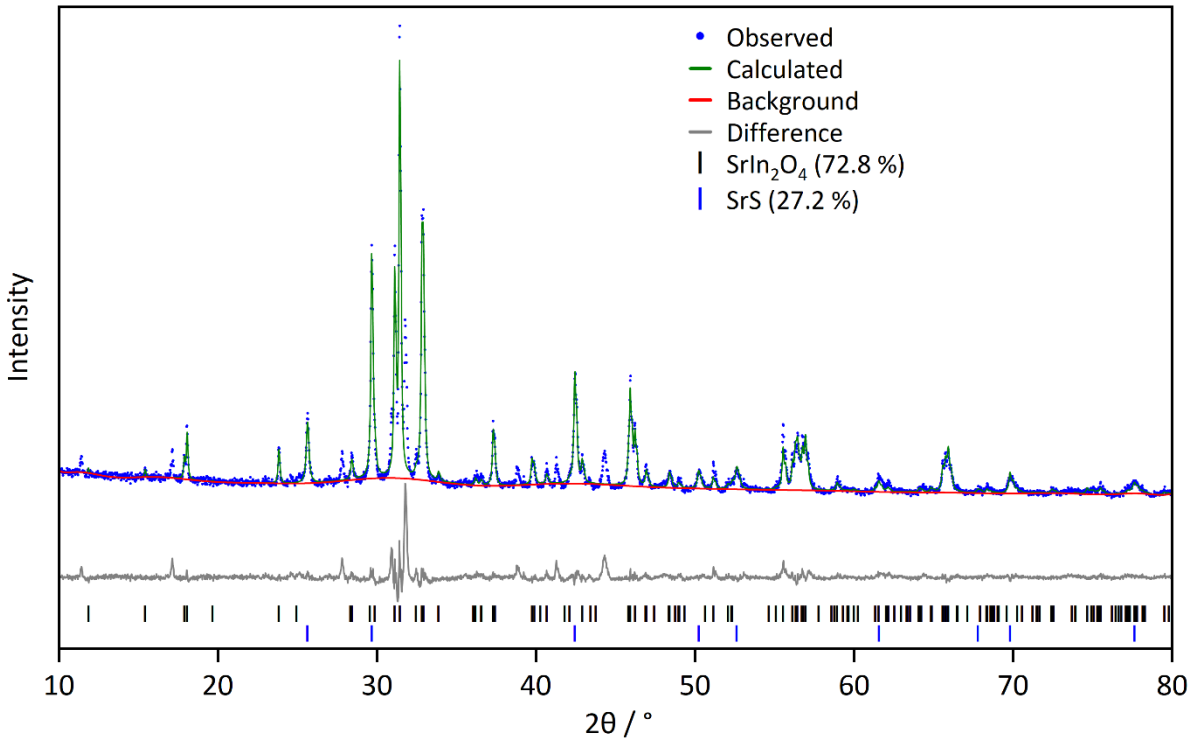

Figure 206 *Powder X-ray diffractogram of material with target composition $Sr_3In_2O_5Cu_2S_2$ after 48 hours of heating at 500 - 900 °C. The small blue circles represent the observed diffracted intensity, the green line represents the Rietveld-refined calculated model, the red line represents the background, and the grey line represents the difference between observed and calculated intensities. The black and blue tick marks show the reflections of the refined models of $SrIn_2O_4$ (72.8 %) and SrS (27.2 %) respectively.*
Duration: 1 hour. Data points: 3457. Interval: 0.02 °. GOF: 2.54. R_{wp}: 13.422 %.

6.3 $Sr_3In_2O_5Cl_2$

Following the new evidence for the existence of the novel 325 phase $Sr_3In_2O_5Cu_2Se_2$, the oxychloride 'light layer precursor' $Sr_3In_2O_5Cl_2$ was attempted, akin to those investigated in the metathesis exploration in *Chapter 5.* If successful, this material could in theory be utilised in a metathesis reaction with $Na_2Cu_2Se_2$ that would form the 325 MALM $Sr_3In_2O_5Cu_2Se_2$ discussed previously.

Synthesis of $Sr_3In_2O_5Cl_2$ was attempted on a 1-gram scale with three heat cycles at 700 °C, 850 °C and 1000 °C using conventional solid-state chemistry, according to Equation 110 below.

Equation 110 $2\ SrO + In_2O_3 + SrCl_2 \rightarrow Sr_3In_2O_5Cl_2$

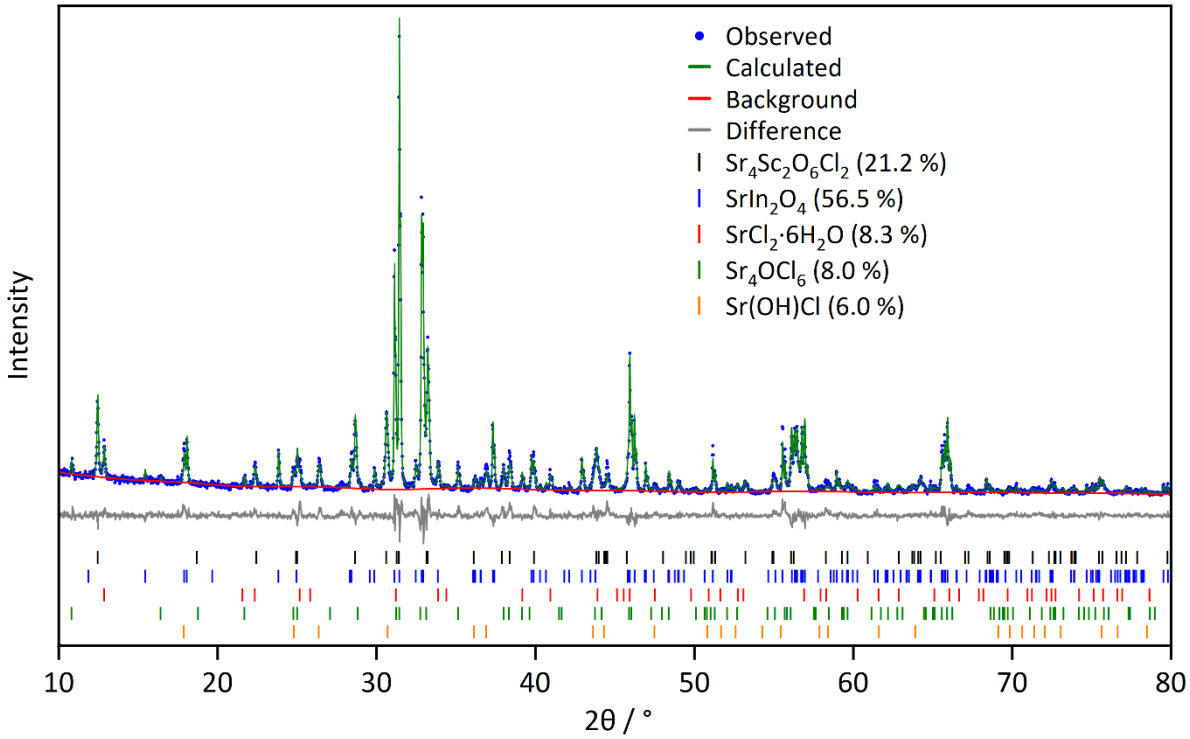

Figure 207 Powder X-ray diffractogram of material with target composition $Sr_3In_2O_5Cl_2$ after 36 hours of heating at 700 - 1000 °C. The small blue circles represent the observed diffracted intensity, the green line represents the Rietveld-refined calculated model, the red line represents the background, and the grey line represents the difference between observed and calculated intensities. The black, blue, red, green and orange tick marks show the reflections of the refined models of $Sr_4In_2O_6Cl_2$ (21.2 %), $SrIn_2O_4$ (56.5 %), $SrCl_2{\cdot}6H_2O$ (8.3 %), Sr_4OCl_6 (8.0 %) and Sr(OH)Cl (6.0 %) respectively.
Duration: 1 hour. Data points: 4691. Interval: 0.02 °. GOF: 1.48. R_{wp}: 10.350 %.

The PXRD diffractogram of the resulting black powder product is shown in Figure 207 above. Interestingly, there is no sign of the target material, but a significant quantity (21.1 %) of a phase which could be fit to the (unreported) 426 analogue $Sr_4In_2O_6Cl_2$, alongside a range of impurities and by-products. Further attempts to synthesise the target material $Sr_3In_2O_5Cl_2$ were all also unsuccessful, so the novel 426 oxychloride, consistently observed here, was directly targeted instead.

6.4 $Sr_4In_2O_6Cl_2$

The unintentionally synthesised material $Sr_4In_2O_6Cl_2$ was targeted on a 1-gram scale using conventional solid-state chemistry, according to Equation 111 below:

Equation 111 $3\ SrO + In_2O_3 + SrCl_2 \rightarrow Sr_4In_2O_6Cl_2$

Now, when targeted directly with the correct stoichiometry for a 426 material, $Sr_4In_2O_6Cl_2$ formed in far greater quantity. The maximum purity attainable after multiple synthesis attempts was 88 % (Figure 208). This is a good yield for a new material unreported in the literature, however it remains too low to be considered as a light layer precursor for a metathesis synthesis of the 325 $Sr_3In_2O_5Cu_2Se_2$, and like the other novel material $Sr_3In_2O_5Cu_2Se_2$ remains as yet too impure to warrant application.

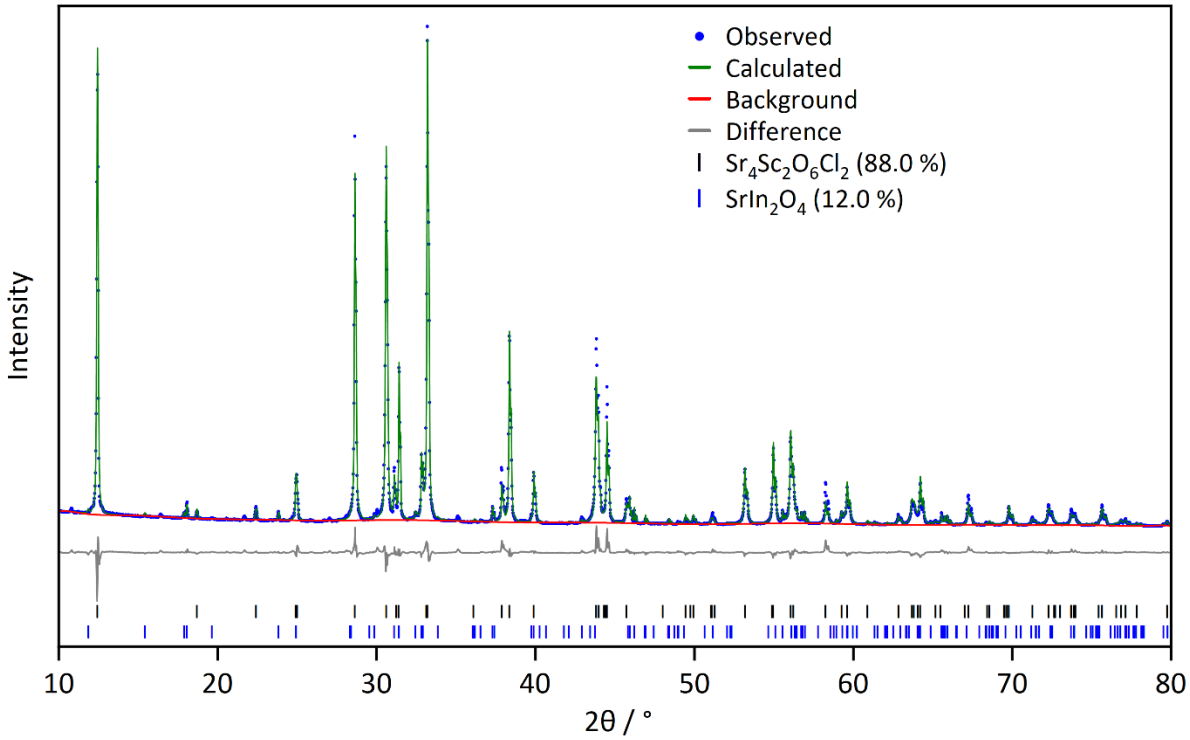

Figure 208 *Powder X-ray diffractogram of material with target composition $Sr_4In_2O_6Cl_2$ (space group P4/nmm) after 72 hours of heating at 1000 °C. The small blue circles represent the observed diffracted intensity, the green line represents the Rietveld-refined calculated model, the red line represents the background, and the grey line represents the difference between observed and calculated intensities. The black tick marks show the reflections of the refined model of $Sr_4In_2O_6Cl_2$ (88.0 %), whilst the blue tick marks represent refined impurity phase $SrIn_2O_4$ (12.0 %).*
Duration: 13 hours. Data points: 3457. Interval: 0.02 °. GOF: 7.88. R_{wp}: 8.992 %.

$Sr_4In_2O_6Cl_2$ is a white product with a wide band gap, measuring 4.35 eV across a strong UV-Vis diffuse reflectance drop off (Figure 209). The unit cell parameters *a* and *c* were found to be 4.12995 Å and 14.24373 Å respectively, for a cell volume of 242.948 $Å^3$ (Table 30). Full details of the refinement, structure and analysis can be found in *Appendix A.7*. It is interesting that the 426 oxychloride exists, as do the $Sr_3In_2O_5Cu_2Se_2$ and $Sr_4In_2O_6Cu_2Ch_2$ MALMs, but not the 325 oxychloride. Future research attention should be devoted to investigation into this material to expand the phase space.

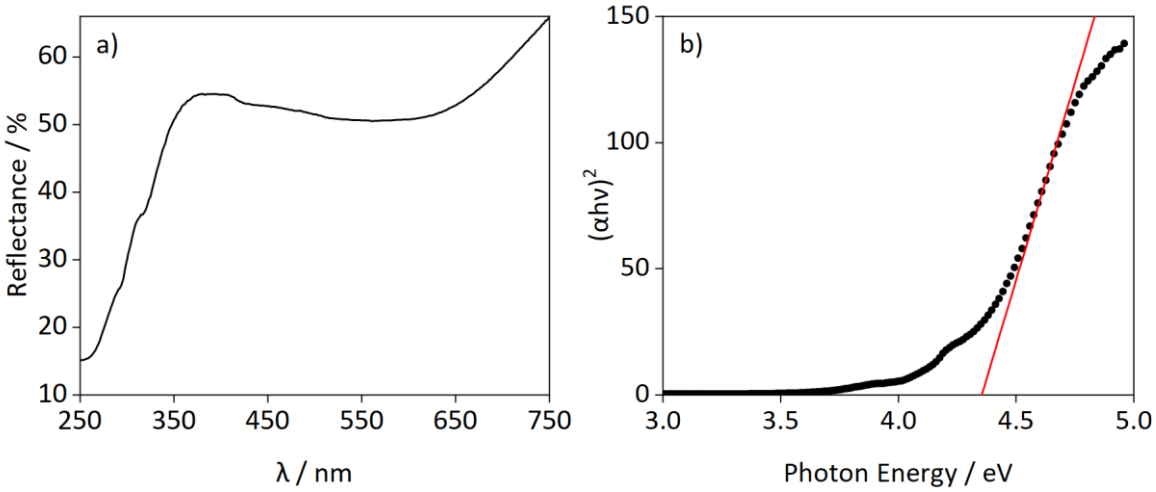

Figure 209 *UV-Vis spectrometry data for material with target composition $Sr_4In_2O_6Cl_2$ after 84 hours of heating at 750 - 1000 °C. Plot a) is the raw diffuse reflectance data, and plot b) is the associated magnified Tauc plot for this region, where the intercept between the red extrapolated tangent line and the x-axis is used to estimate an optical band gap of 4.35 eV, which corresponds to 285 nm.*

Table 30 *Structural parameters of the refined model of pristine $Sr_4In_2O_6Cl_2$ in the P4/nmm space group at room temperature, where a = 4.12995(6) Å and c = 14.24373(19) Å.*

Atom	Fractional coordinates			Fractional Occupancy	Isotropic Thermal Parameter / Å²
	x	y	z		
Sr1	0.25	0.25	0.09249(17)	1	0.0330(13)
Sr2	0.25	0.25	0.35340(16)	1	0.0246(12)
In	0.75	0.75	0.21467(11)	1	0.0223(10)
O1	0.75	0.25	0.2333(6)	1	0.0074(31)
O2	0.75	0.75	0.0672(10)	1	0.040(5)
Cl	0.75	0.75	0.4296(5)	1	0.0179(20)

6.5 Conclusions and Future Work

Two novel Mixed Anion Layered Materials are described in this chapter, expanding the MALM phase space. Firstly, the quinternary oxychalcogenide $Sr_3In_2O_5Cu_2Se_2$ which was not only hitherto unreported but actively believed to be unstable. Attempts to synthesise the sulfide analogue $Sr_3In_2O_5Cu_2S_2$ were not successful.

Secondly, the novel quaternary oxychloride $Sr_4In_2O_6Cl_2$ is reported, also for the first time. This is analogous to the 'light layer' precursors synthesised for and explored in metathesis reactions in *Chapter 5* of this work, but was deemed insufficiently pure for investigations of that type. The 325 analogue $Sr_3In_2O_5Cl_2$ could not be realised.

Chapter 7 Conclusions and Outlook

This work presents the successful doping investigation of $Sr_3Sc_2O_5Cu_2S_2$, a material praised for its remarkable undoped hole mobility and potential for use as a *p*-type transparent conductor. Potassium and sodium doping on the strontium site yielded improvements of approximately one order of magnitude, each without compromising sample transparency. Conductive enhancement continues beyond the point where $Sr_3Sc_2O_5Cu_2S_2$ no longer tolerates full incorporation of the dopant, for which it was hypothesised that strontium vacancies may be the cause. These were investigated, and produced similar improvements to the dopants, suggesting an interplay between the two effects.

This is the first doping study of $Sr_3Sc_2O_5Cu_2S_2$, a material cited as a benchmark *p*-type TCO for which a list of doping recommendations speculated to improve electrical properties has been published, yet for 15 years has remained explored until now. The listed recommendations include K and Na doping, and the substitution of sulfur for selenium. The fully substituted end member of this $Sr_3Sc_2O_5Cu_2(S_{2-y}Se_y)$ solid solution is $Sr_3Sc_2O_5Cu_2Se_2$, a MALM even lesser explored but sporting a greater conductivity than $Sr_3Sc_2O_5Cu_2S_2$ at the expense of a narrower optical band gap, 3.10 eV vs 2.94 eV respectively.

Owing to its better tolerance to doping, $Sr_3Sc_2O_5Cu_2Se_2$ was subjected to a far greater range of the doping recommendations in efforts to enhance its electrical properties. This enhancement was a success, and it was found that potassium and sodium doping on the strontium site can increase the modest undoped conductivity from 2.61×10^{-4} S cm^{-1}, to 14.4 and 23.4 S cm^{-1} respectively at the highest recorded points. Strontium deficiencies again proved an effective method to increase the hole carrier concentration of this material, yielding a maximum recorded conductivity of 1.85 S cm^{-1} when x = 0.750, a 70,000 times increase over the pristine conductivity without any dopant ions present.

Magnesium doping, the mechanism behind the highest reported conductivity of any *p*-type TCO: 140 S cm^{-1} in Mg doped LaOCuSe,[179] proved surprisingly effective in enhancing the electrical properties of $Sr_3Sc_2O_5Cu_2Se_2$, yielding a conductivity of 0.572 S cm^{-1} when x = 0.200 mol, a more than 2000 fold improvement over the pristine. It showed full incorporation up to this point, the exploration beyond which should be considered promising future work.

Attempts to improve the transparency of $Sr_3Sc_2O_5Cu_2Se_2$ were not successful. Barium showed full isovalent incorporation onto the strontium site, a well-established substitutional relationship,[263, 264, 266] but at the low quantities attempted showed no widening of the band gap by increase of the *a* lattice parameter. Isovalent doping with yttrium and lanthanum was also attempted, but incorporation was low and performance enhancement was negligible, likely due to an ionic radii mismatch.

In *Chapter 4*, the 426 analogues $Sr_4Sc_2O_6Cu_2Ch_2$ were explored. A study as broad as that of $Sr_3Sc_2O_5Cu_2Se_2$ would make for a rigorous and enlightening investigation of the entire Sr-Sc-O-Cu-*Ch* system. However, this was not to be the case due to the delicacy of these 426 phases upon heating. These samples suffered significant conversion to the stable 325 competing phase, which presented a constant and often unpredictable presence in almost every sample. The conversion was irreversible and severely limited the reach of doping by rendering any attempt to anneal a trade-off between purity and density. The scandium 426 MALMs $Sr_4Sc_2O_6Cu_2Ch_2$ have impressive band gaps: 3.17 eV where *Ch* = S and 2.95 eV where *Ch* = Se, indicating that they may be model TCO candidates if not for the competing phase. A sodium doping study of $Sr_4Sc_2O_6Cu_2S_2$ was carried out but all resulting conductivities, despite good dopant uptake, were less than that of the pristine due to poor pellet densities. A singular sodium and potassium doped sample for each of $Sr_4Sc_2O_6Cu_2S_2$ and $Sr_4Sc_2O_6Cu_2Se_2$ was produced, for comparison with gallium and indium analogues produced by a colleague. In each of the scandium MALMs, a small conductivity increase was observed, but the true performance could not be realised without greater densification. Optimisation of the densification of the $Sr_4Sc_2O_6Cu_2Ch_2$ MALMs whilst avoiding the irreparable conversion to the 325 phase is fruitful future work that may reveal a tolerance to doping similar to that of the $Sr_3Sc_2O_5Cu_2Ch_2$ class.

In *Chapter 5*, the application of solid-state metathesis to MALMs was explored for only the second time. The Sr-Sc-O-Cu-Se system was investigated, and whilst the 426 MALM could not be formed, the 325 was produced convincingly by metathesis in a comparative experiment alongside a conventional synthesis, which provided strong evidence for the metathetic nature of the $Sr_3Sc_2O_5Cu_2Se_2$ synthesis mechanism. A reproduction of the other published metathetic MALM synthesis, that of Cario et al,[61] yielded phase pure $Sr_3Fe_2O_5Cu_2Se_2$ and the highest quality diffraction pattern of this entire work, Figure 188. The metathesis technique was applied to a novel combinatorial approach to rapid materials discovery. Preliminary tests were not successful and it is clear that this technique is not suitable nor practical for material discovery, nor should it be scaled beyond that which was investigated in *Section 5.6.* In isolation, the metathesis method is a valid if not convoluted synthesis technique which proved successful in individual MALM syntheses. It may shine in applications where MALMs cannot be otherwise be produced by conventional methods, and warrants future exploration beyond its limited coverage in the literature to date.

Finally, in *Chapter 6*, the novel oxychalcogenide MALM $Sr_3In_2O_5Cu_2Se_2$ is reported for the first time. This novel material does not possess a sufficiently wide band gap for transparent conductivity, but future work should be devoted firstly to improving reaction completion beyond 80 %, and then further investigation into its properties, such as pellet or thin film conductivity.

Appendix A Refined Crystal Structure Parameters

A.1 $Sr_3Sc_2O_5Cu_2S_2$

Table 1 Structural parameters of the refined model of pristine $Sr_3Sc_2O_5Cu_2S_2$ in the I4/mmm space group at room temperature, where a = 4.07463(4) Å and c = 25.9578(3) Å.

Atom	Fractional coordinates			Fractional Occupancy	Isotropic Thermal Parameter / Å^2
	x	y	z		
Sr1	0.5	0.5	0	1	0.0479(7)
Sr2	0.5	0.5	0.14455(5)	1	0.0410(5)
Sc	0	0	0.07650(10)	1	0.0358(6)
O1	0.5	0	0.08642(16)	1	0.0666(15)
O2	0	0	0	1	0.0541(30)
Cu	0.5	0	0.25	1	0.0577(7)
S	0	0	0.19790(12)	1	0.0390(11)

Table 2 Details of the Rietveld refinement of pristine material $Sr_3Sc_2O_5Cu_2S_2$.

	$Sr_3Sc_2O_5Cu_2S_2$
Space Group	*I*4/*mmm* (139)
***a* / Å**	4.07463(4)
***b* / Å**	4.07463(4)
***c* / Å**	25.9578(3)
Volume / Å^3	430.967(12)
Data points	4444
Reflections	96
Parameters	48
Purity / %	96.5
R_{wp} / %	2.49
GOF	1.92

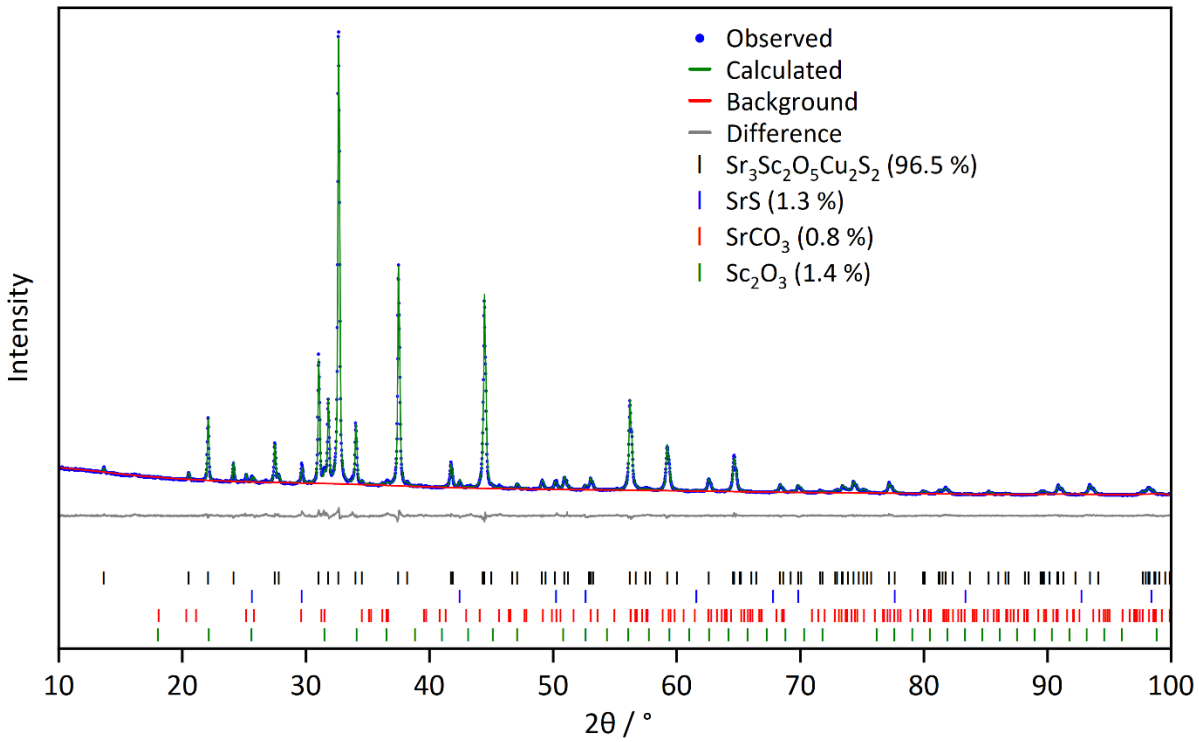

Figure 1 *Powder X-ray diffractogram of material with target composition $Sr_3Sc_2O_5Cu_2S_2$ (space group I4/mmm) after 36 hours of heating at 800 °C. The small blue circles represent the observed diffracted intensity, the green line represents the Rietveld-refined calculated model, the red line represents the background, and the grey line represents the difference between observed and calculated intensities. The black tick marks show the reflections of the refined model of $Sr_3Sc_2O_5Cu_2S_2$ (96.5 %), whilst the blue, red and green tick marks represent impurity phases SrS (1.3 %), $SrCO_3$ (0.8 %) and Sc_2O_3 (1.4 %) respectively. Duration: 12.5 hours. Data points: 4444. Interval: 0.02 °. GOF: 1.92. R_{wp}: 2.49 %.*

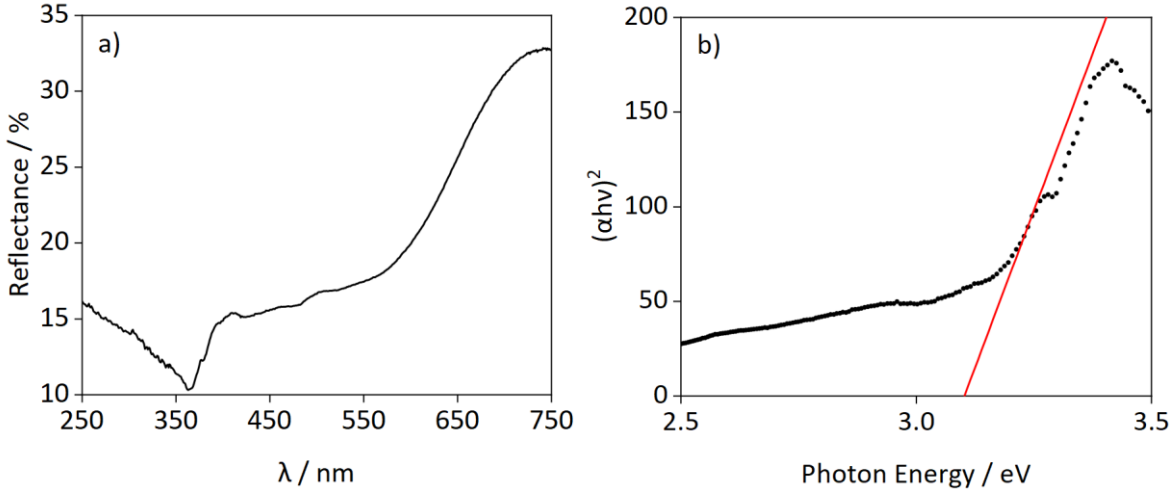

Figure 2 *UV-Vis spectrometry data for material with target composition $Sr_3Sc_2O_5Cu_2S_2$ after 36 hours of heating at 800 °C. Plot a) is the raw diffuse reflectance data, and plot b) is the associated magnified Tauc plot for this region, where the intercept between the red extrapolated tangent line and the x-axis is used to estimate an optical band gap of 3.10 eV, which corresponds to 400 nm.*

A.2 $Sr_3Sc_2O_5Cu_2Se_2$

Table 3 Structural parameters of the refined model of pristine $Sr_3Sc_2O_5Cu_2Se_2$ in the I4/mmm space group at room temperature, where a = 4.10329(4) Å and c = 26.6847(3) Å.

Atom	Fractional coordinates			Fractional Occupancy	Isotropic Thermal Parameter / Å^2
	x	y	z		
Sr1	0.5	0.5	0	1	0.0407(3)
Sr2	0.5	0.5	0.139926(23)	1	0.03136(26)
Sc	0	0	0.07407(4)	1	0.0270(4)
O1	0.5	0	0.08404(8)	1	0.0483(8)
O2	0	0	0	1	0.0422(15)
Cu	0.5	0	0.25	1	0.0436(3)
Se	0	0	0.194700(22)	1	0.03483(29)

Table 4 Details of the Rietveld refinement of pristine material $Sr_3Sc_2O_5Cu_2Se_2$.

	$Sr_3Sc_2O_5Cu_2Se_2$
Space Group	*I*4/*mmm* (139)
***a* / Å**	4.10329(4)
***b* / Å**	4.10329(4)
***c* / Å**	26.6847(3)
Volume / Å^3	449.290(12)
Data points	8887
Reflections	97
Parameters	53
Purity / %	99.1
R_{wp} / %	2.483
GOF	1.50

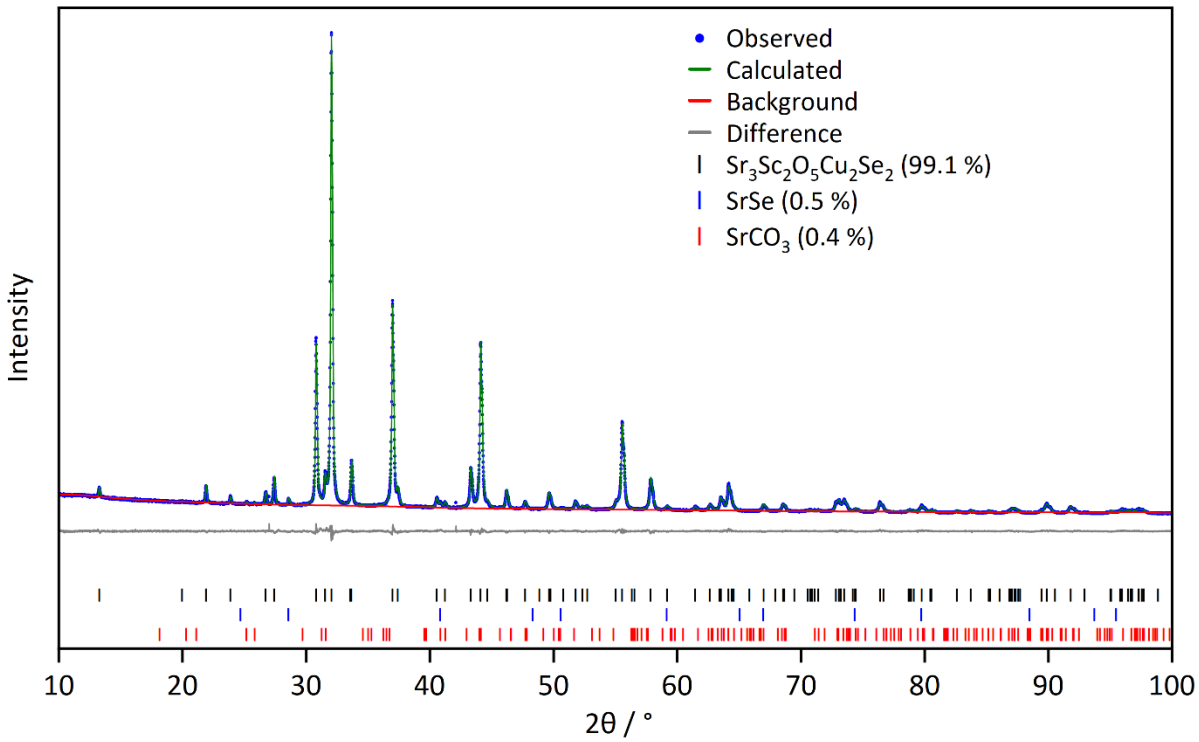

Figure 3 *Powder X-ray diffractogram of material with target composition $Sr_3Sc_2O_5Cu_2Se_2$ (space group I4/mmm) after 36 hours of heating at 800 °C. The small blue circles represent the observed diffracted intensity, the green line represents the Rietveld-refined calculated model, the red line represents the background, and the grey line represents the difference between observed and calculated intensities. The black tick marks show the reflections of the refined model of $Sr_3Sc_2O_5Cu_2Se_2$ (99.1 %), whilst the blue and red tick marks represent refined impurity phases SrSe (0.5 %), and $SrCO_3$ (0.4 %) respectively.*
Duration: 12 hours. Data points: 8887. Interval: 0.01 °. GOF: 1.50. R_{wp}: 2.483 %.

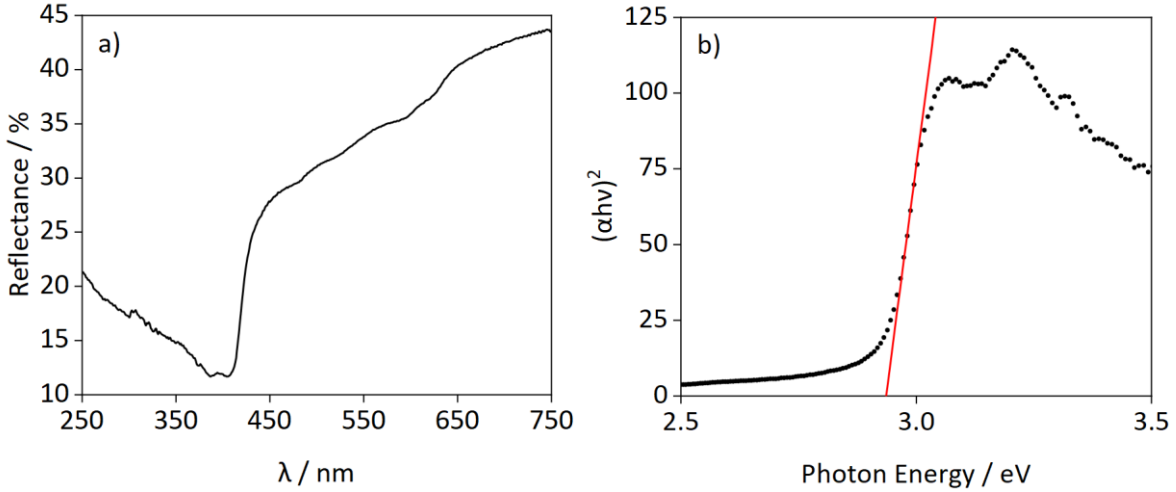

Figure 4 *UV-Vis spectrometry data for material with target composition $Sr_3Sc_2O_5Cu_2Se_2$ after 36 hours of heating at 800 °C. Plot a) is the raw diffuse reflectance data, and plot b) is the associated magnified Tauc plot for this region, where the intercept between the red extrapolated tangent line and the x-axis is used to estimate an optical band gap of 2.94 eV, which corresponds to 422 nm.*

A.3 $Sr_4Sc_2O_6Cu_2S_2$

Table 5 Structural parameters of the refined model of pristine $Sr_4Sc_2O_6Cu_2S_2$ in the P4/nmm space group at room temperature, where a = 4.04780(4) Å and c = 15.37012(20) Å.

Atom	Fractional coordinates			Fractional Occupancy	Isotropic Thermal Parameter / Å²
	x	y	z		
Sr1	0.75	0.75	0.17947(5)	1	0.0563(5)
Sr2	0.75	0.75	0.41286(5)	1	0.0553(5)
Sc	0.25	0.25	0.30250(14)	1	0.0430(5)
O1	0.25	0.75	0.28218(22)	1	0.0919(14)
O2	0.25	0.25	0.43048(27)	1	0.0430(14)
Cu	0.25	0.75	0	1	0.0785(6)
S	0.25	0.25	0.08830(13)	1	0.0593(9)

Table 6 Details of the Rietveld refinement of pristine material $Sr_4Sc_2O_6Cu_2S_2$.

	$Sr_4Sc_2O_6Cu_2S_2$
Space Group	*P*4/*nmm* (129)
***a* / Å**	4.04780(4)
***b* / Å**	4.04780(4)
***c* / Å**	15.37012(20)
Volume / Å³	251.835(6)
Data points	8985
Reflections	111
Parameters	44
Purity / %	98.0
R_{wp} / %	2.617
GOF	1.61

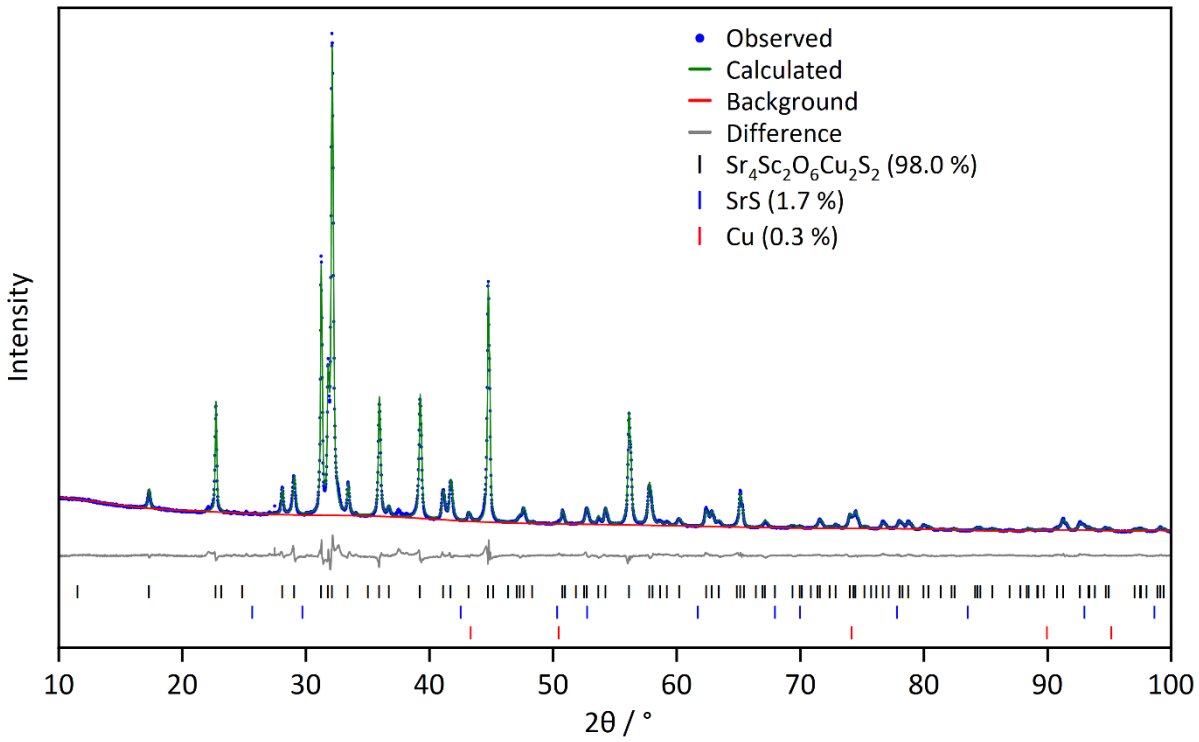

Figure 5 *Powder X-ray diffractogram of material with target composition $Sr_4Sc_2O_6Cu_2S_2$ (space group P4/mmm) after 48 hours of heating at 500-600 °C. The small blue circles represent the observed diffracted intensity, the green line represents the Rietveld-refined calculated model, the red line represents the background, and the grey line represents the difference between observed and calculated intensities. The black tick marks show the reflections of the refined model of $Sr_4Sc_2O_6Cu_2S_2$ (98.0 %), whilst the blue and red tick marks represent refined impurity phases SrS (1.7 %), and $SrCO_3$ (0.3 %) respectively.*
Duration: 16 hours. Data points: 8985. Interval: 0.01 °. GOF: 1.61. R_{wp}: 2.617 %.

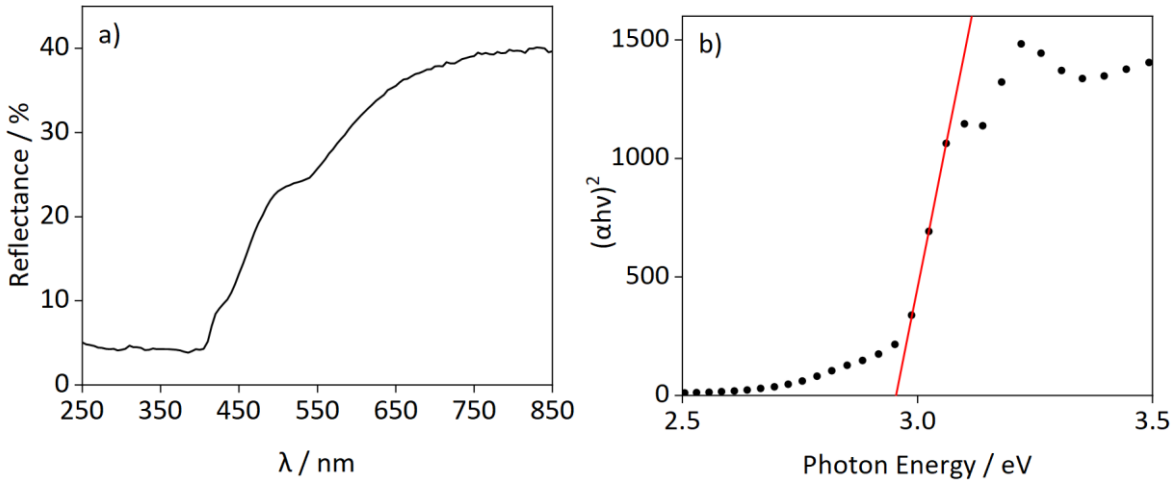

Figure 6 *UV-Vis spectrometry data for material with target composition $Sr_4Sc_2O_6Cu_2S_2$ after 48 hours of heating at 500-600 °C. Plot a) is the raw diffuse reflectance data, and plot b) is the associated magnified Tauc plot for this region, where the intercept between the red extrapolated tangent line and the x-axis is used to estimate an optical band gap of 3.17 eV, which corresponds to 391 nm.*

A.4 $Sr_4Sc_2O_6Cu_2Se_2$

Table 7 Structural parameters of the refined model of pristine $Sr_4Sc_2O_6Cu_2Se_2$ in the P4/nmm space group at room temperature, where a = 3.89988(4) Å and c = 16.09379(17) Å.

Atom	Fractional coordinates			Fractional Occupancy	Isotropic Thermal Parameter / Å^2
	x	y	z		
Sr1	0.75	0.75	0.18840(9)	1	0.0449(4)
Sr2	0.75	0.75	0.41500(7)	1	0.0431(4)
Sc	0.25	0.25	0.30730(18)	1	0.0344(6)
O1	0.25	0.75	0.28796(23)	1	0.0731(16)
O2	0.25	0.25	0.43136(28)	1	0.0636(19)
Cu	0.25	0.75	0	1	0.0567(5)
Se	0.25	0.25	0.09413(9)	1	0.0465(5)

Table 8 Details of the Rietveld refinement of pristine material $Sr_4Sc_2O_6Cu_2Se_2$.

	$Sr_4Sc_2O_6Cu_2Se_2$
Space Group	*P*4/*nmm* (129)
***a* / Å**	3.89988(4)
***b* / Å**	3.89988(4)
***c* / Å**	16.09379(17)
Volume / Å^3	244.771(6)
Data points	8887
Reflections	113
Parameters	48
Purity / %	98.5
R_{wp} / %	3.107
GOF	3.72

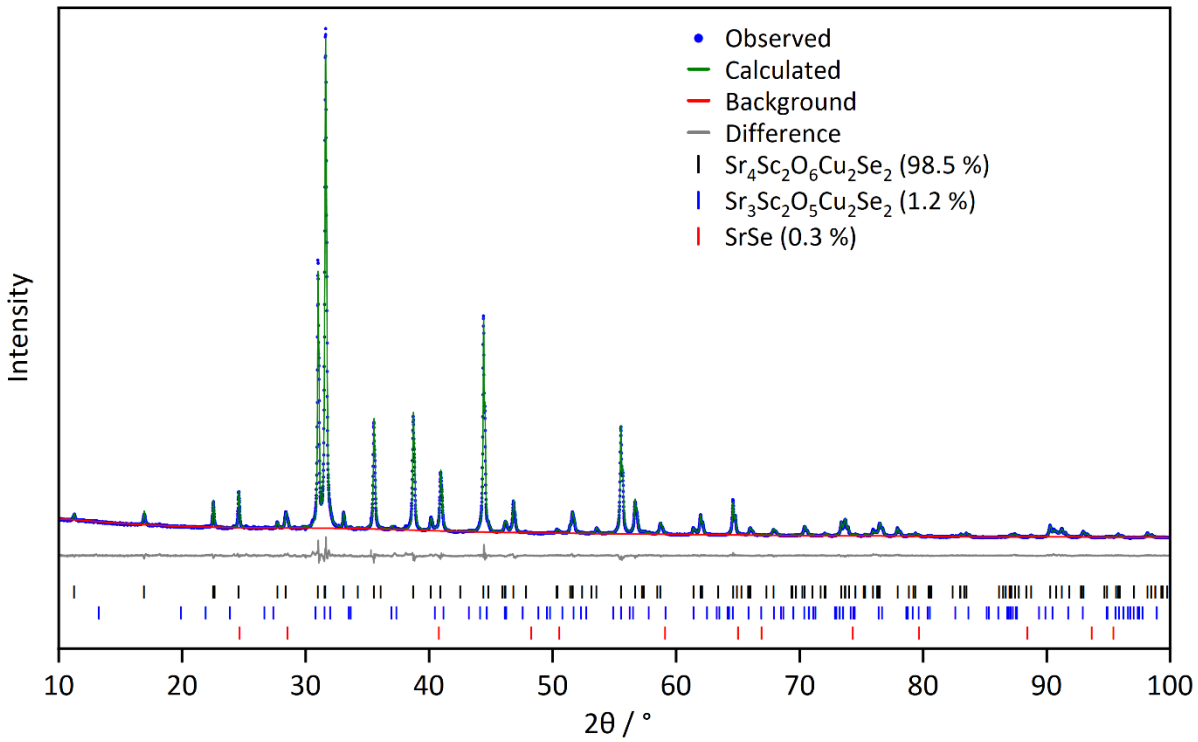

Figure 7 *Powder X-ray diffractogram of material with target composition $Sr_4Sc_2O_6Cu_2Se_2$ (space group P4/nmm) after 48 hours of heating at 500 - 650 °C. The small blue circles represent the observed diffracted intensity, the green line represents the Rietveld-refined calculated model, the red line represents the background, and the grey line represents the difference between observed and calculated intensities. The black tick marks show the reflections of the refined model of $Sr_4Sc_2O_6Cu_2Se_2$ (98.5 %), whilst the blue and red tick marks represent refined impurity phases $Sr_3Sc_2O_5Cu_2Se_2$ (1.2 %), and SrSe (0.3 %) respectively.*
Duration: 16 hours. Data points: 8887. Interval: 0.01 °. GOF: 3.72. R_{wp}: 3.107 %.

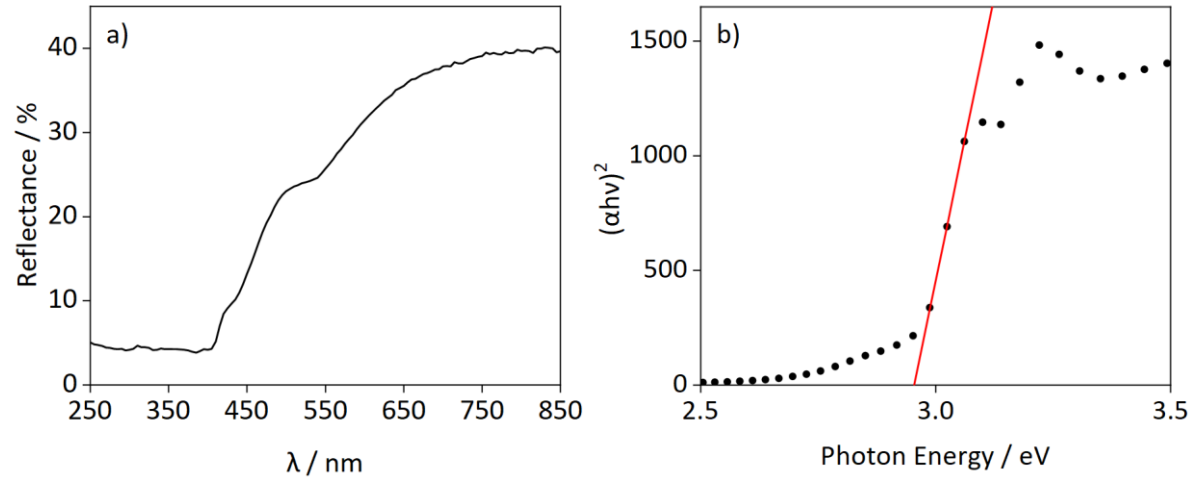

Figure 8 *UV-Vis spectrometry data for material with target composition $Sr_4Sc_2O_6Cu_2Se_2$ after 48 hours of heating at 500 - 650 °C. Plot a) is the raw diffuse reflectance data, and plot b) is the associated magnified Tauc plot for this region, where the intercept between the red extrapolated tangent line and the x-axis is used to estimate an optical band gap of 2.95 eV, which corresponds to 420 nm.*

A.5 $Sr_3Fe_2O_5Cu_2Se_2$

Table 9 Structural parameters of the refined model of pristine $Sr_3Fe_2O_5Cu_2Se_2$ in the I4/mmm space group at room temperature, where a = 3.957895(17) Å and c = 27.01393(15) Å.

Atom	Fractional coordinates			Fractional Occupancy	Isotropic Thermal Parameter / Å^2
	x	y	z		
Sr1	0	0	0.5	1	0.0282(4)
Sr2	0	0	0.637083(24)	1	0.02415(31)
Fe	0	0	0.06932(4)	1	0.0258(5)
O1	0	0.5	0.07810(9)	1	0.0392(9)
O2	0	0	0	1	0.0266(17)
Cu	0	0.5	0.25	1	0.0359(4)
Se	0	0	0.192663(23)	1	0.0269(3)

Table 10 Details of the Rietveld refinement of novel pristine material $Sr_3Fe_2O_5Cu_2Se_2$.

	$Sr_3Fe_2O_5Cu_2Se_2$
Space Group	*I*4/*mmm* (139)
***a* / Å**	3.957895(17)
***b* / Å**	3.957895(17)
***c* / Å**	27.01393(15)
Volume / Å^3	423.171(5)
Data points	8887
Reflections	92
Parameters	41
Purity / %	Phase pure
R_{wp} / %	1.642
GOF	1.70

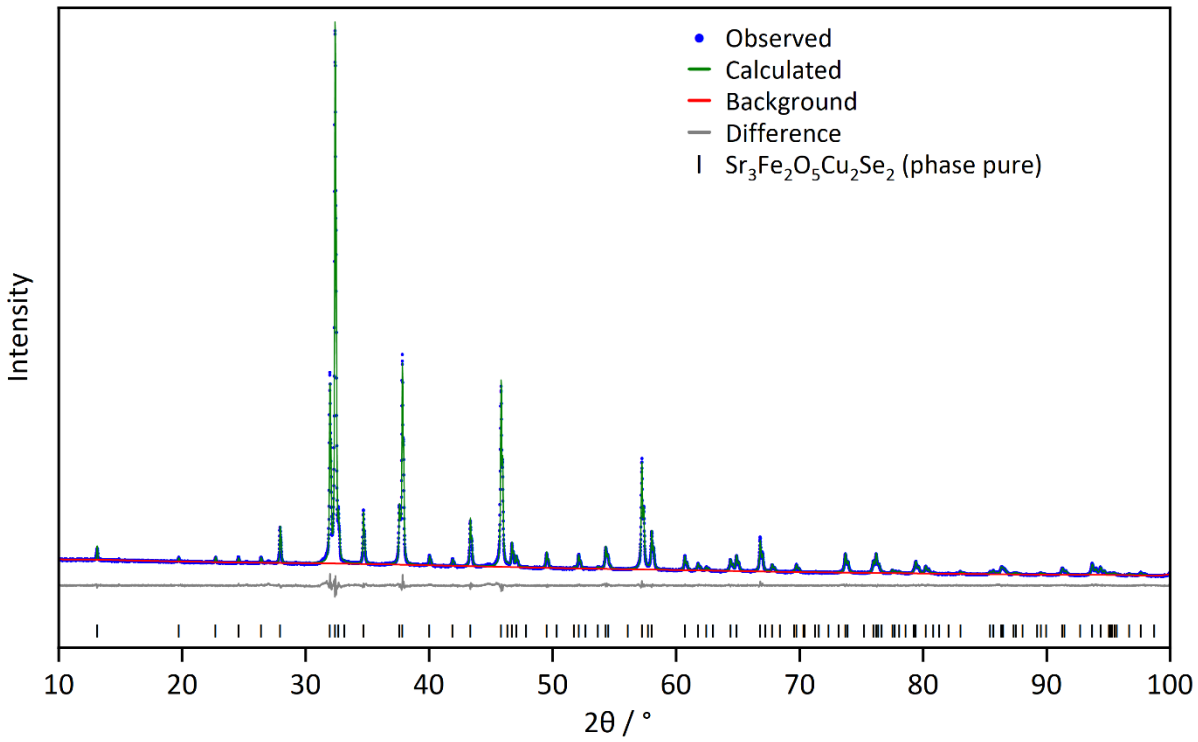

Figure 9 *Powder X-ray diffractogram of material resulting from attempted metathesis synthesis of $Sr_3Fe_2O_5Cu_2Se_2$ (space group I4/mmm) after 12 hours of heating at 700 °C, then washed in distilled H_2O to remove the NaCl metathesis by-product. The small blue circles represent the observed diffracted intensity, the green line represents the Rietveld-refined calculated model, the red line represents the background, and the grey line represents the difference between observed and calculated intensities. The black tick marks show the reflections of the refined model of $Sr_3Fe_2O_5Cu_2Se_2$, no NaCl or impurity phases were observed. Duration: 16 hours. Data points: 8887. Interval: 0.01 °. GOF: 1.70. R_{wp}: 1.642 %.*

A.6 $Sr_3In_2O_5Cu_2Se_2$

Table 11 Structural parameters of the refined model of pristine $Sr_3In_2O_5Cu_2Se_2$ in the I4/mmm space group at room temperature, where a = 4.14553(9) Å and c = 27.1013(7) Å.

Atom	Fractional coordinates			Fractional Occupancy	Isotropic Thermal Parameter / Å²
	x	y	z		
Sr1	0.5	0.5	0	1	0.0534(21)
Sr2	0.5	0.5	0.14275(15)	1	0.0205(24)
In	0	0	0.07419(11)	1	0.0174(14)
O1	0.5	0	0.0774(5)	1	0.022(8)
O2	0	0	0	1	0.093(25)
Cu	0.5	0	0.25	1	0.030(3)
Se	0	0	0.19594(13)	1	0.043(3)

Table 12 Details of the Rietveld refinement of novel pristine material $Sr_3In_2O_5Cu_2Se_2$.

	$Sr_3In_2O_5Cu_2Se_2$
Space Group	*I*4/*mmm* (139)
***a* / Å**	4.14553(9)
***b* / Å**	4.14553(9)
***c* / Å**	27.1013(7)
Volume / Å³	465.747(23)
Data points	3457
Reflections	68
Parameters	35
Purity / %	80.2
R_{wp} / %	7.227
GOF	1.52

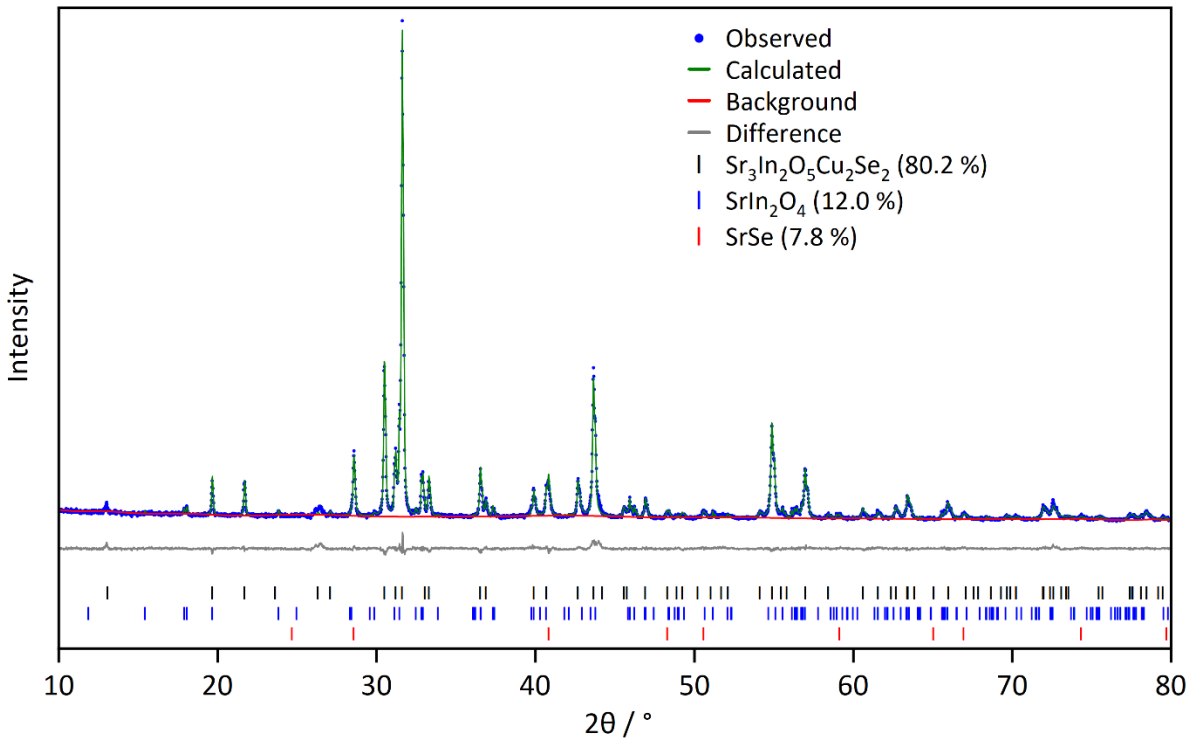

Figure 10 *Powder X-ray diffractogram of material with target composition $Sr_3In_2O_5Cu_2Se_2$ (space group I4/mmm) after 36 hours of heating at 900 °C. The small blue circles represent the observed diffracted intensity, the green line represents the Rietveld-refined calculated model, the red line represents the background, and the grey line represents the difference between observed and calculated intensities. The black tick marks show the reflections of the refined model of $Sr_3In_2O_5Cu_2Se_2$ (80.2 %), whilst the blue and red tick marks represent refined impurity phases $SrIn_2O_4$ (12.0 %), and SrSe (7.8 %) respectively.*
Duration: 12 hours. Data points: 3457. Interval: 0.01 °. GOF: 1.52. R_{wp}: 7.227 %.

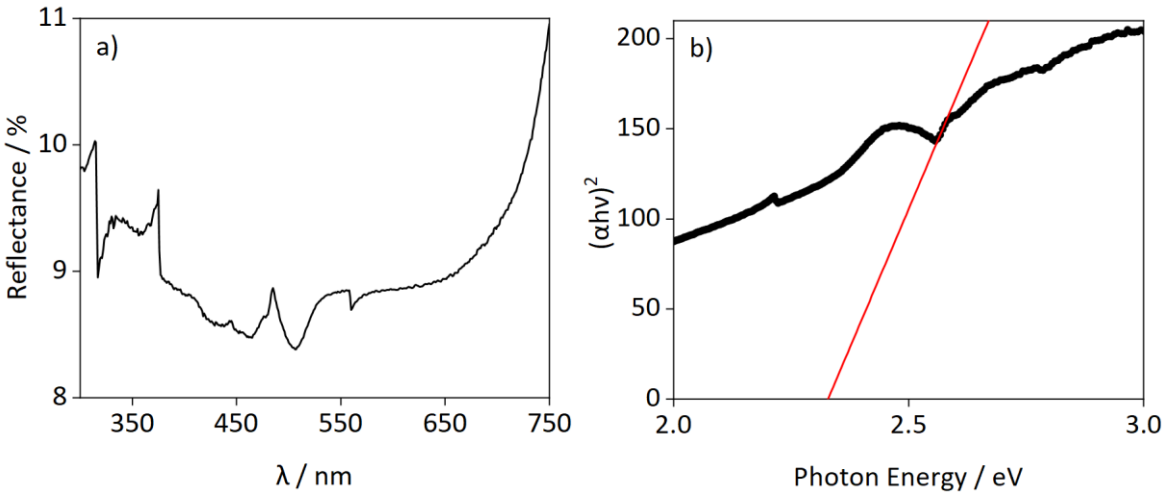

Figure 11 *UV-Vis spectrometry data for material with target composition $Sr_3In_2O_5Cu_2Se_2$ after 36 hours of heating at 900 °C. Plot a) is the raw diffuse reflectance data, and plot b) is the associated magnified Tauc plot for this region, where the intercept between the red extrapolated tangent line and the x-axis is used to estimate an optical band gap of 2.33 eV, which corresponds to 532 nm.*

A.7 $Sr_4In_2O_6Cl_2$

Table 13 Structural parameters of the refined model of pristine $Sr_4In_2O_6Cl_2$ in the P4/nmm space group at room temperature, where a = 4.12995(6) Å and c = 14.24373(19) Å.

Atom	Fractional coordinates			Fractional Occupancy	Isotropic Thermal Parameter / Å²
	x	y	z		
Sr1	0.25	0.25	0.09249(17)	1	0.0330(13)
Sr2	0.25	0.25	0.35340(16)	1	0.0246(12)
In	0.75	0.75	0.21467(11)	1	0.0223(10)
O1	0.75	0.25	0.2333(6)	1	0.0074(31)
O2	0.75	0.75	0.0672(10)	1	0.040(5)
Cl	0.75	0.75	0.4296(5)	1	0.0179(20)

Table 14 Details of the Rietveld refinement of novel pristine material $Sr_4In_2O_6Cl_2$.

	$Sr_4In_2O_6Cl_2$
Space Group	*P*4/*nmm* (129)
***a* / Å**	4.12995(6)
***b* / Å**	4.12995(6)
***c* / Å**	14.24373(19)
Volume / Å³	242.948(8)
Data points	3457
Reflections	67
Parameters	28
Purity / %	88.0
R_{wp} / %	8.992
GOF	7.88

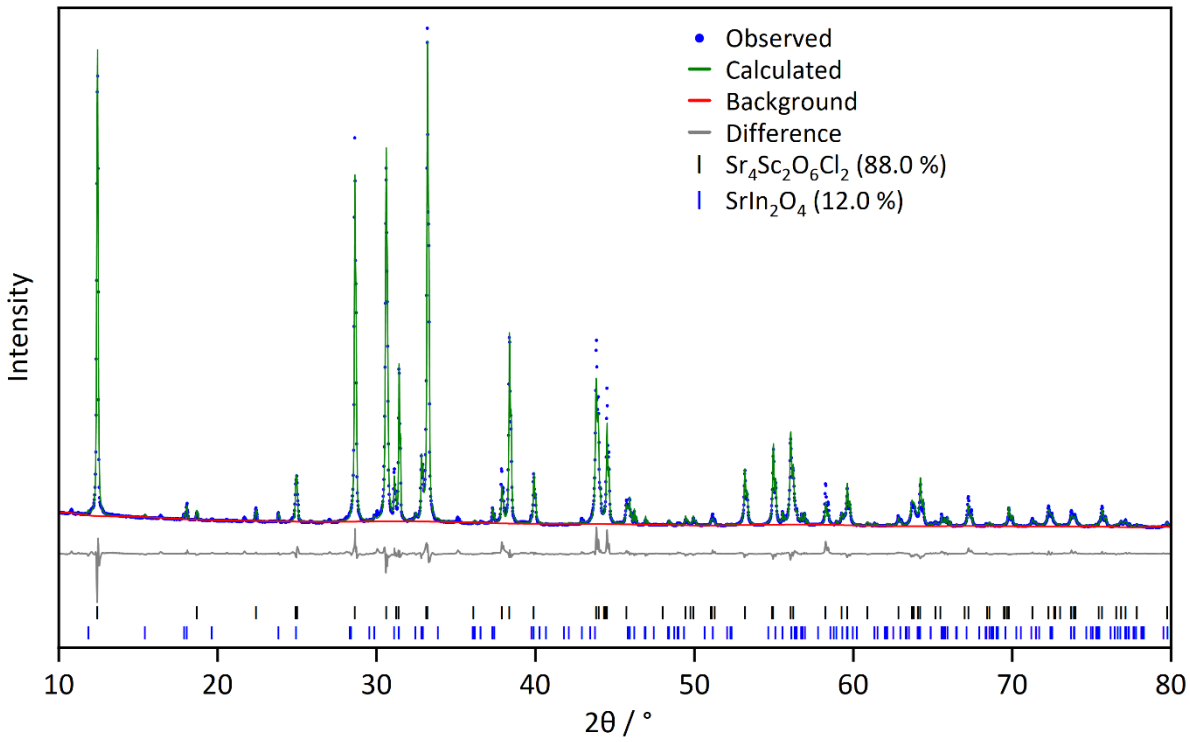

Figure 12 *Powder X-ray diffractogram of material with target composition $Sr_4In_2O_6Cl_2$ (space group P4/nmm) after 72 hours of heating at 1000 °C. The small blue circles represent the observed diffracted intensity, the green line represents the Rietveld-refined calculated model, the red line represents the background, and the grey line represents the difference between observed and calculated intensities. The black tick marks show the reflections of the refined model of $Sr_4In_2O_6Cl_2$ (88.0 %), whilst the blue tick marks represent refined impurity phase $SrIn_2O_4$ (12.0 %).*
Duration: 13 hours. Data points: 3457. Interval: 0.02 °. GOF: 7.88. R_{wp}: 8.992 %.

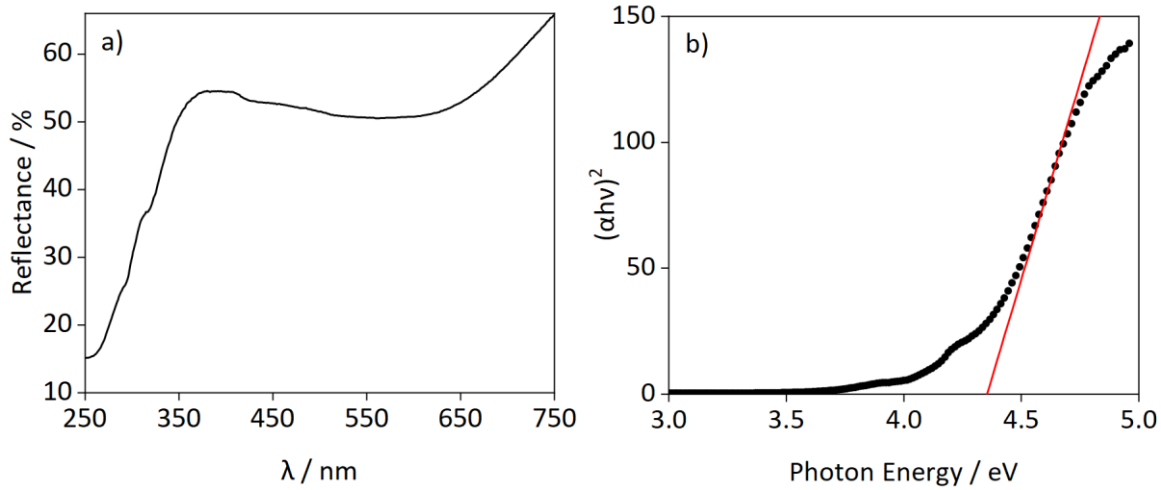

Figure 13 *UV-Vis spectrometry data for material with target composition $Sr_4In_2O_6Cl_2$ after 72 hours of heating at 1000 °C. Plot a) is the raw diffuse reflectance data, and plot b) is the associated magnified Tauc plot for this region, where the intercept between the red extrapolated tangent line and the x-axis is used to estimate an optical band gap of 4.35 eV, which corresponds to 285 nm.*

Appendix B Structural, Compositional, Analytical and Graphical Data for Synthesised Materials

B.1 Materials from Chapter 3

B.1.1 Potassium doped 325 sulfide MALMs, $(Sr_{3-x}K_x)Sc_2O_5Cu_2S_2$

Table 15 Tabulated structural data of the potassium doped 325 sulfide MALMs with general formula $(Sr_{3-x}K_x)Sc_2O_5Cu_2S_2$. The pristine material $Sr_3Sc_2O_5Cu_2S_2$ is included as a reference. All values are derived from the Rietveld refinement of PXRD data using GSAS-II. Note that because all materials listed are tetragonal (space group I4/mmm), the b parameter is identical to a, and thus omitted.

x / mol	Target Composition	a / Å	c / Å	Volume / Å^3
0 (pristine)	$Sr_3Sc_2O_5Cu_2S_2$	4.07463(4)	25.9578(3)	430.967(12)
0.025	$(Sr_{2.975}K_{0.025})Sc_2O_5Cu_2S_2$	4.07504(9)	25.9745(7)	431.332(26)
0.050	$(Sr_{2.950}K_{0.050})Sc_2O_5Cu_2S_2$	4.07449(8)	25.9821(6)	431.340(23)
0.075	$(Sr_{2.925}K_{0.075})Sc_2O_5Cu_2S_2$	4.07438(8)	25.9796(6)	431.276(24)
0.100	$(Sr_{2.900}K_{0.100})Sc_2O_5Cu_2S_2$	4.07445(8)	25.9778(6)	431.261(23)
0.125	$(Sr_{2.875}K_{0.125})Sc_2O_5Cu_2S_2$	4.07444(7)	25.9740(6)	431.196(21)
0.150	$(Sr_{2.850}K_{0.150})Sc_2O_5Cu_2S_2$	4.07415(8)	25.9744(7)	431.143(25)

Table 16 Tabulated compositional data of the potassium doped 325 sulfide MALMs with general formula $(Sr_{3-x}K_x)Sc_2O_5Cu_2S_2$. The pristine material $Sr_3Sc_2O_5Cu_2S_2$ is included as a reference. All values are cited as a weight percent (wt %) of the total weight, and are derived from the Rietveld refinement of PXRD data using GSAS-II.

x / mol	Target phase / wt %	SrS / wt %	$SrCO_3$ / wt %	Sc_2O_3 / wt %	KCu_3S_2 / wt %
0 (pristine)	96.5	1.3	0.8	1.4	-
0.025	96.9	1.1	0.6	1.6	-
0.050	97.4	0.5	0.9	1.2	-
0.075	96.7	0.9	1.1	1.3	-
0.100	97.2	0.6	0.9	1.2	-
0.125	94.8	0.6	1.5	1.7	1.4
0.150	93.7	1.0	1.9	1.9	1.5

Table 17 *Tabulated data on both the target and maximum actual dopant content of the potassium doped 325 sulfide MALMs with general formula $(Sr_{3-x}K_x)Sc_2O_5Cu_2S_2$. The pristine material $Sr_3Sc_2O_5Cu_2S_2$ is included as a reference. The minimum possible amount of total K contained within impurities was extracted from the refined wt % of KCu_3S_2 from GSAS-II. The remaining K content is the maximum possible K within the MALM.*

Target x / mol	**Target x / wt %**	**Minimum K in impurities / %**	**Maximum K in product / %**	**Maximum x / mol**
0 (pristine)	0.000	0.000	100.000	0.000
0.025	0.157	0.000	100.000	0.025
0.050	0.315	0.000	100.000	0.050
0.075	0.473	0.000	100.000	0.075
0.100	0.632	0.000	100.000	0.100
0.125	0.791	23.551	76.449	0.096
0.150	0.951	20.986	79.014	0.119

Table 18 Tabulated analytical data of to the measured properties of the potassium doped 325 sulfide MALMs with general formula $(Sr_{3-x}K_x)Sc_2O_5Cu_2S_2$. The pristine material $Sr_3Sc_2O_5Cu_2S_2$ is included as a reference. Optical band gaps were estimated from UV-Vis data. Pellet densities were estimated from the mass and volume of annealed pellet samples, and are cited as a relative percentage of the bulk crystal. Resistivities and conductivities were estimated from 4 probe van der Pauw analysis of the pellet samples.

x / mol	Band Gap / eV	Pellet Density / %	Raw Resistivities from 4-Probe measurement, for each probe permutation / kΩ								Resistivity / Ω cm	Conductivity / S cm^{-1}
			1	2	3	4	5	6	7	8		
0 (pristine)	3.10	70.67	1.90 E+00	1.41 E+00	1.48 E-01	1.64 E+00	1.20 E-01	1.15 E+00	9.00 E-01	1.61 E+00	4.39 E+02	2.28 E-03
0.025	3.09	68.49	5.51 E-01	5.60 E-01	5.55 E-01	5.56 E-01	5.46 E-01	5.45 E-01	5.49 E-01	5.45 E-01	2.22 E+02	4.50 E-03
0.050	3.06	69.55	5.60 E-01	1.49 E-01	4.62 E-01	5.13 E-01	8.65 E-01	8.61 E-01	9.31 E-01	9.90 E-01	2.53 E+02	3.96 E-03
0.075	3.12	71.08	2.54 E-01	2.56 E-01	1.99 E-01	1.78 E-01	3.22 E-01	4.14 E-01	3.53 E-01	4.15 E-01	1.14 E+02	8.79 E-03
0.100	3.09	71.41	3.52 E-01	3.17 E-01	3.47 E-01	5.30 E-01	1.50 E-01	2.41 E-01	2.72 E-01	2.91 E-01	1.19 E+02	8.37 E-03
0.125	3.15	70.25	8.80 E-02	9.90 E-02	5.70 E-02	7.90 E-02	8.80 E-02	9.90 E-02	7.30 E-02	1.21 E-01	3.42 E+01	2.92 E-02
0.150	3.15	70.68	5.80 E-02	7.20 E-02	4.90 E-02	7.00 E-02	6.20 E-02	7.60 E-02	3.60 E-02	1.05 E-01	2.57 E+01	3.89 E-02

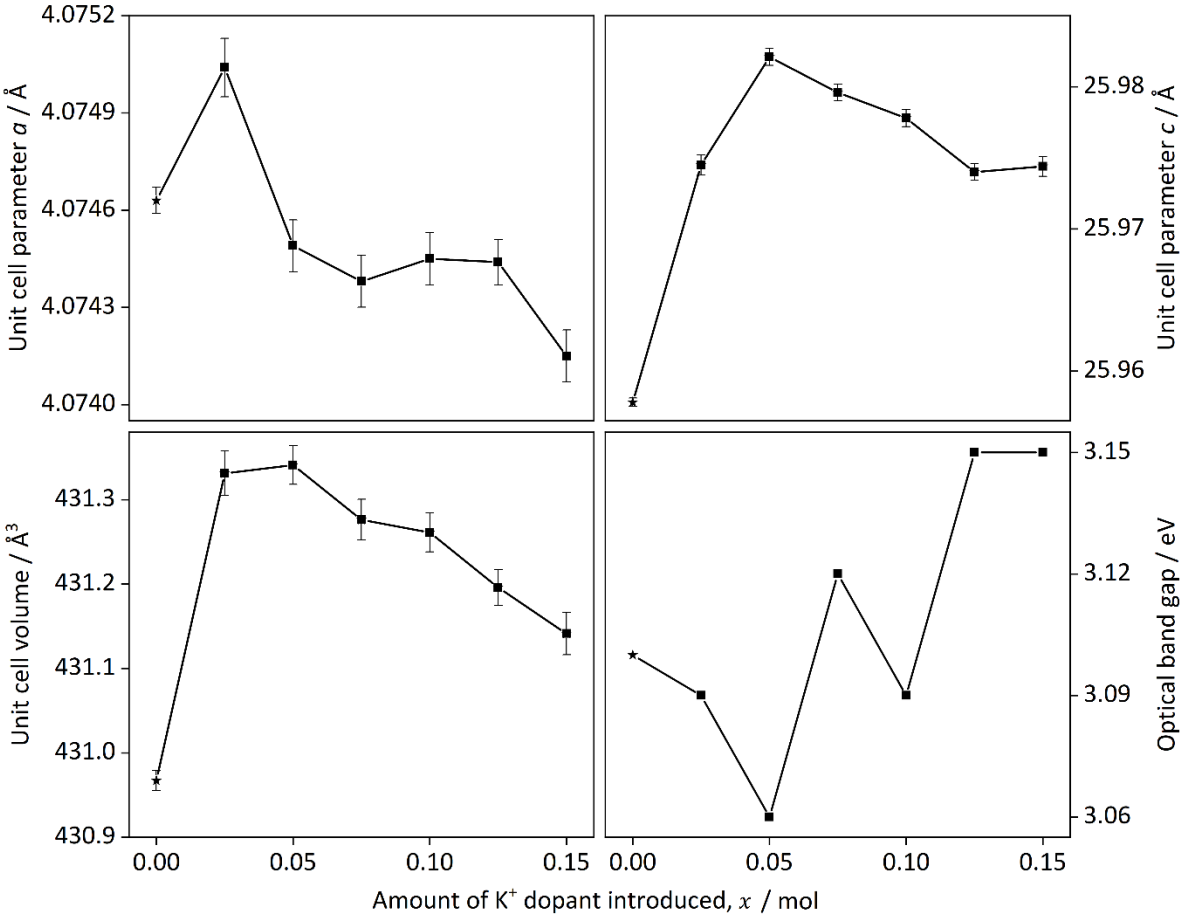

Figure 14 *Comparisons of a) the a unit cell parameter, b) the c unit cell parameter, c) unit cell volume, and d) the optical band gap, of the potassium doped 325 sulfide MALMs with general formula $(Sr_{3-x}K_x)Sc_2O_5Cu_2S_2$. The pristine material $Sr_3Sc_2O_5Cu_2S_2$ is included as a reference at $x = 0$ mol and is represented by a star.*

Figure 15 *A photographic comparison of the colour of the potassium doped 325 sulfide MALMs with general formula $(Sr_{3-x}K_x)Sc_2O_5Cu_2S_2$. Dopant concentration increases from left to right.*

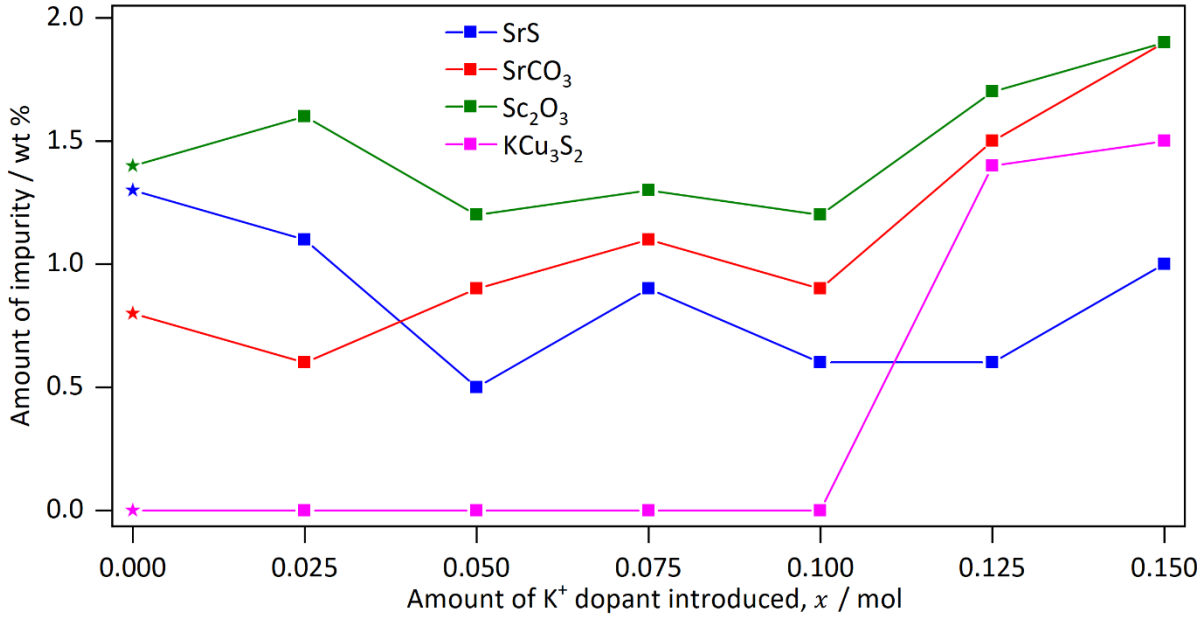

Figure 16 *The weight percentages of four impurity phases present in the potassium doped 325 sulfide MALMs with general formula $(Sr_{3-x}K_x)Sc_2O_5Cu_2S_2$. The pristine material $Sr_3Sc_2O_5Cu_2S_2$ is included as a reference at $x = 0$ mol and is represented by a star.*

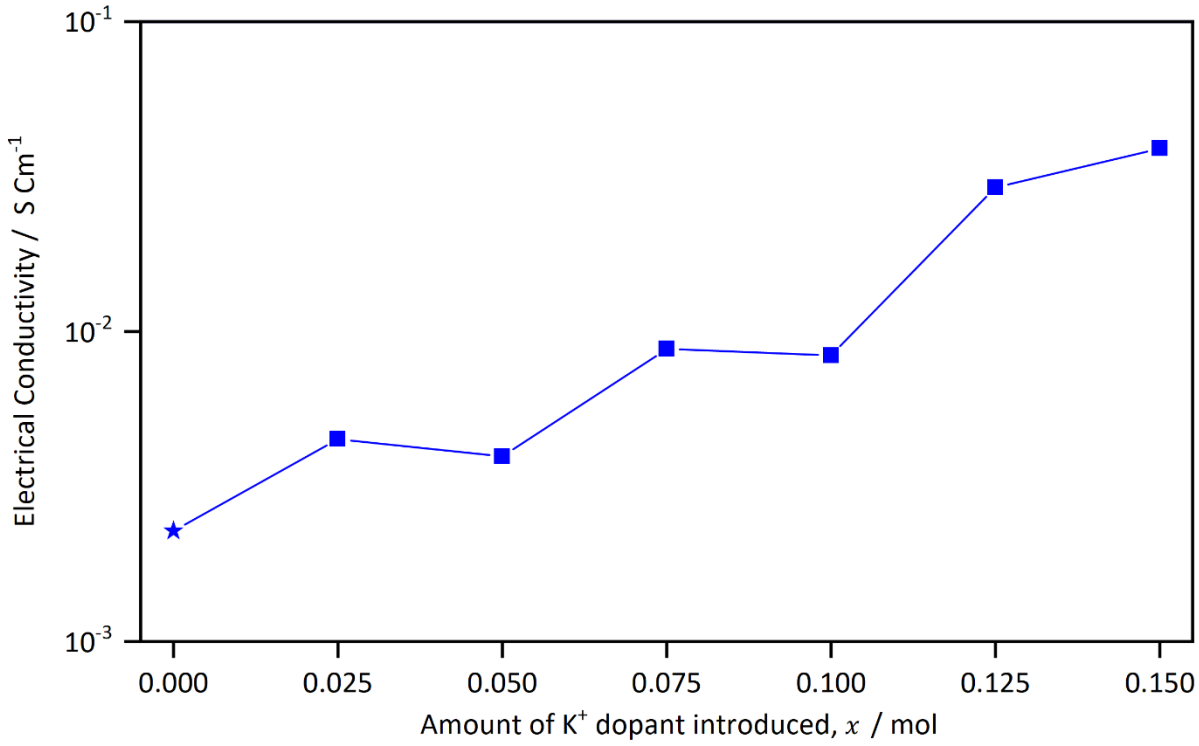

Figure 17 *The electrical conductivities of the potassium doped 325 sulfide MALMs with general formula $(Sr_{3-x}K_x)Sc_2O_5Cu_2S_2$, represented on a log_{10} scale. The pristine material $Sr_3Sc_2O_5Cu_2S_2$ is included as a reference at $x = 0$ mol and is represented by a star. All values are derived from van der Pauw 4 probe resistivity measurements of 8mm diameter annealed pellet samples.*

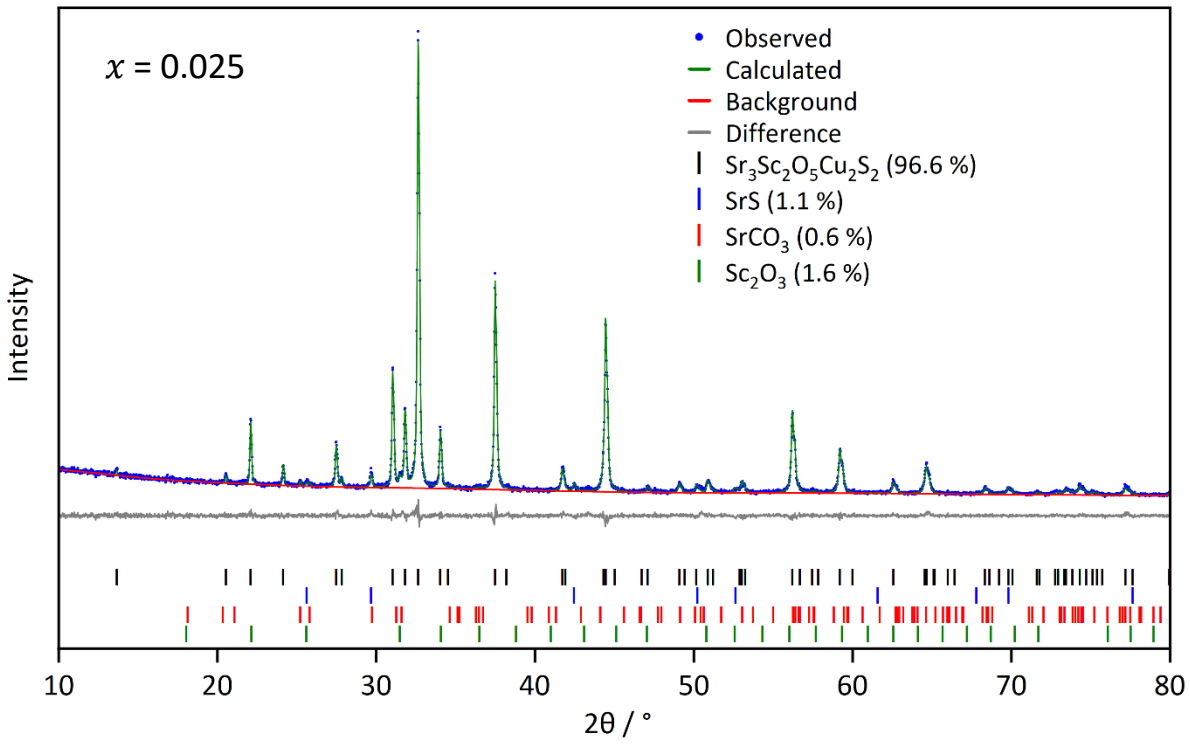

Figure 18 *Powder X-ray diffractogram of material with target composition $(Sr_{2.975}K_{0.025})Sc_2O_5Cu_2S_2$ (space group I4/mmm) after 36 hours of heating at 800 °C. The small blue circles represent the observed diffracted intensity, the green line represents the Rietveld-refined calculated model, the red line represents the background, and the grey line represents the difference between observed and calculated intensities. The black tick marks show the reflections of the refined model of $Sr_3Sc_2O_5Cu_2S_2$ (96.6 %), whilst the blue, red and green tick marks represent refined impurity phases SrS (1.1 %), $SrCO_3$ (0.6 %) and Sc_2O_3 (1.6 %) respectively. Duration: 45 minutes. Data points: 3457. Interval: 0.02 °. GOF: 1.16. R_{wp}: 5.282 %.*

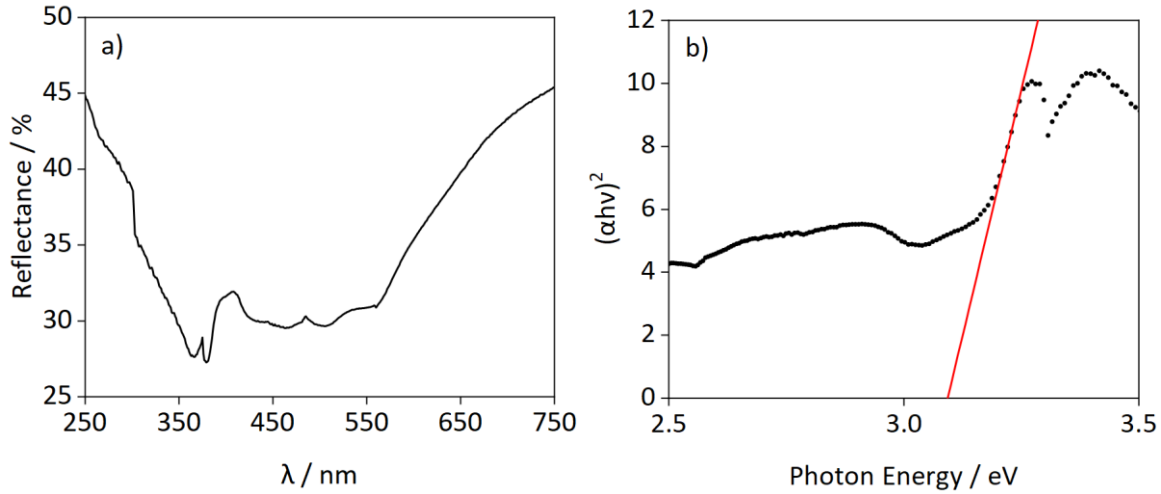

Figure 19 *UV-Vis spectrometry data for material with target composition $(Sr_{2.975}K_{0.025})Sc_2O_5Cu_2S_2$ after 36 hours of heating at 800 °C. Plot a) is the raw diffuse reflectance data, and plot b) is the associated magnified Tauc plot for this region, where the intercept between the red extrapolated tangent line and the x-axis is used to estimate an optical band gap of 3.09 eV, which corresponds to 401 nm.*

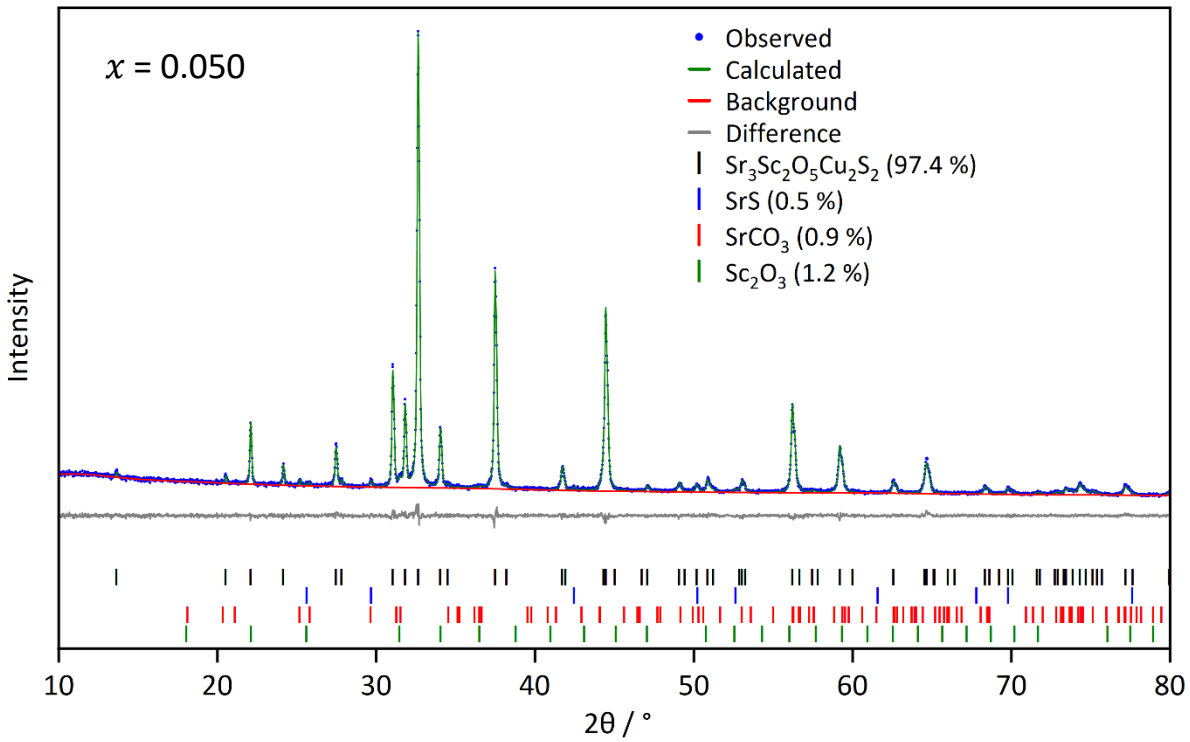

Figure 20 *Powder X-ray diffractogram of material with target composition $(Sr_{2.950}K_{0.050})Sc_2O_5Cu_2S_2$ (space group I4/mmm) after 36 hours of heating at 800 °C. The small blue circles represent the observed diffracted intensity, the green line represents the Rietveld-refined calculated model, the red line represents the background, and the grey line represents the difference between observed and calculated intensities. The black tick marks show the reflections of the refined model of $Sr_3Sc_2O_5Cu_2S_2$ (97.4 %), whilst the blue, red and green tick marks represent refined impurity phases SrS (0.5 %), $SrCO_3$ (0.9 %) and Sc_2O_3 (1.2 %) respectively. Duration: 45 minutes. Data points: 3457. Interval: 0.02 °. GOF: 1.10. R_{wp}: 4.499 %.*

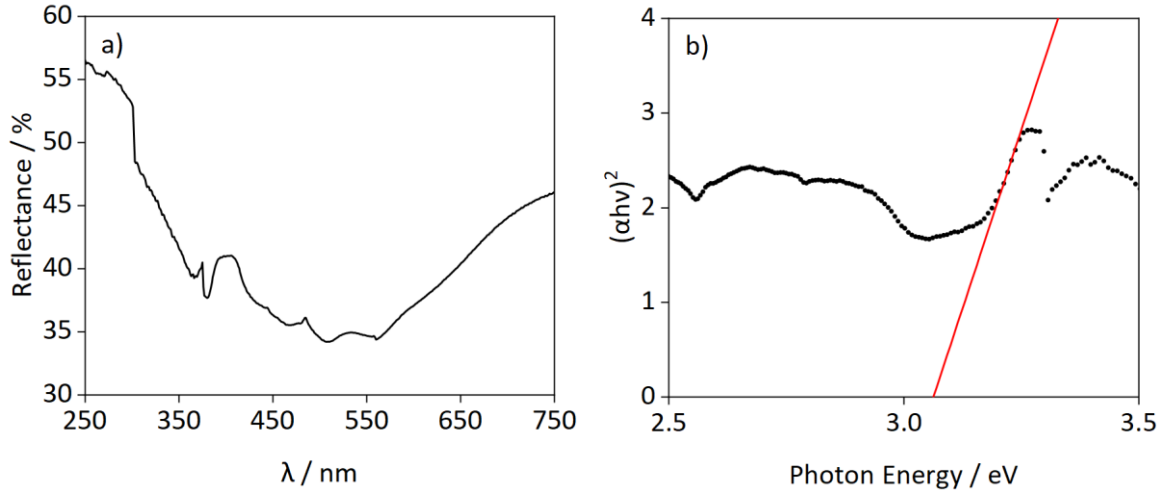

Figure 21 *UV-Vis spectrometry data for material with target composition $(Sr_{2.950}K_{0.050})Sc_2O_5Cu_2S_2$ after 36 hours of heating at 800 °C. Plot a) is the raw diffuse reflectance data, and plot b) is the associated magnified Tauc plot for this region, where the intercept between the red extrapolated tangent line and the x-axis is used to estimate an optical band gap of 3.06 eV, which corresponds to 405 nm.*

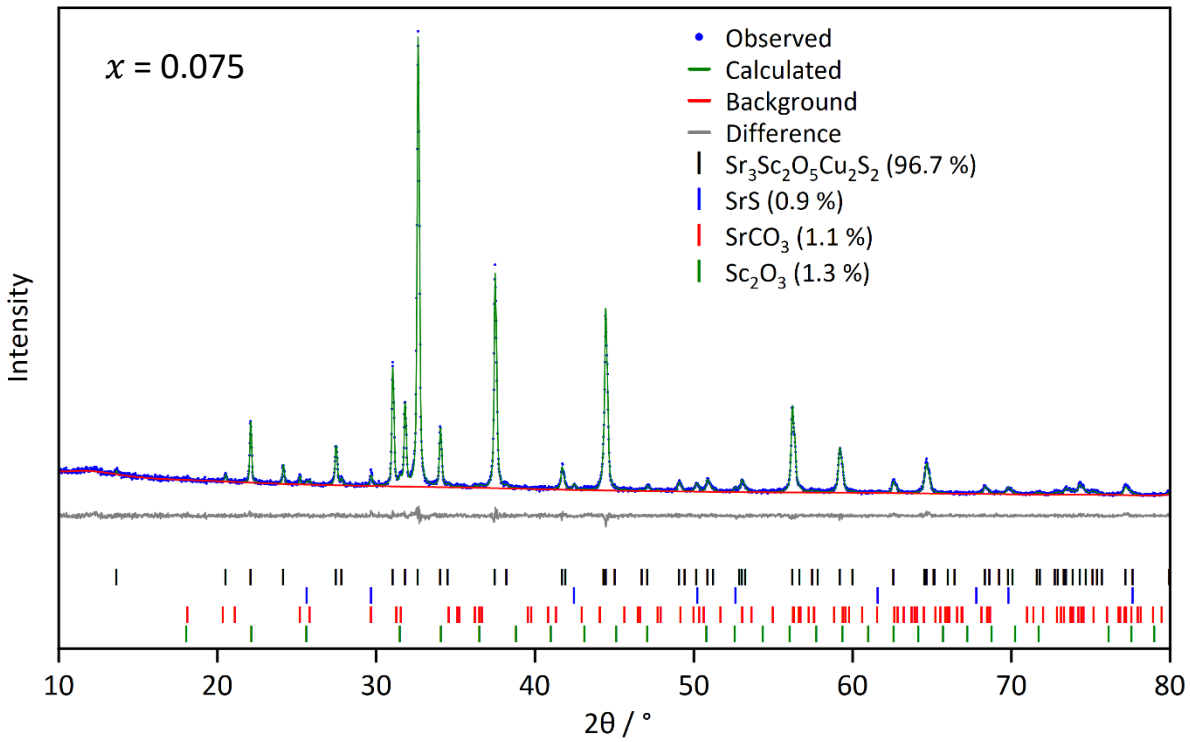

Figure 22 *Powder X-ray diffractogram of material with target composition $(Sr_{2.925}K_{0.075})Sc_2O_5Cu_2S_2$ (space group I4/mmm) after 36 hours of heating at 800 °C. The small blue circles represent the observed diffracted intensity, the green line represents the Rietveld-refined calculated model, the red line represents the background, and the grey line represents the difference between observed and calculated intensities. The black tick marks show the reflections of the refined model of $Sr_3Sc_2O_5Cu_2S_2$ (96.7 %), whilst the blue, red and green tick marks represent refined impurity phases SrS (0.9 %), $SrCO_3$ (1.1 %) and Sc_2O_3 (1.3 %) respectively. Duration: 45 minutes. Data points: 3457. Interval: 0.02 °. GOF: 1.12. R_{wp}: 4.563 %.*

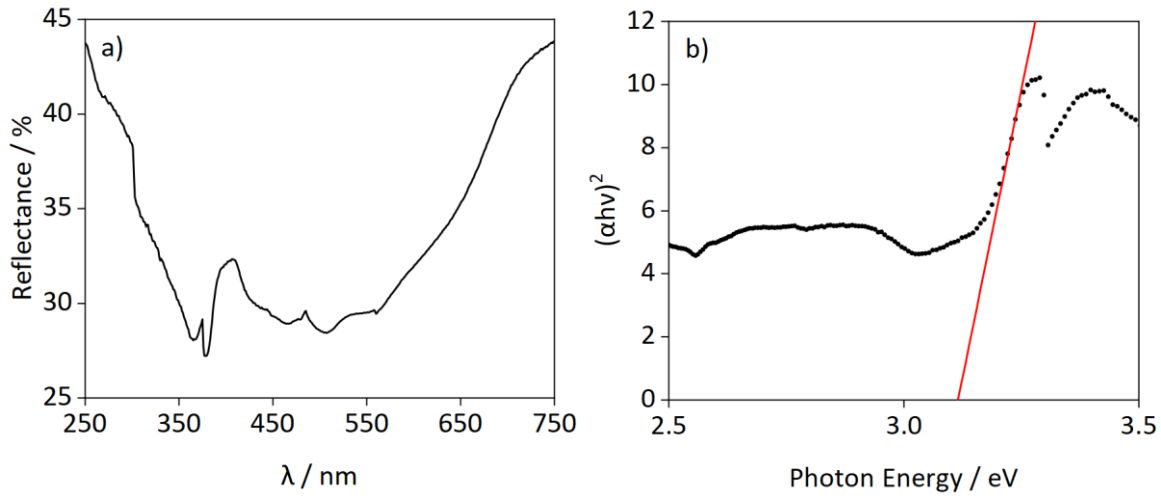

Figure 23 *UV-Vis spectrometry data for material with target composition $(Sr_{2.925}K_{0.075})Sc_2O_5Cu_2S_2$ after 36 hours of heating at 800 °C. Plot a) is the raw diffuse reflectance data, and plot b) is the associated magnified Tauc plot for this region, where the intercept between the red extrapolated tangent line and the x-axis is used to estimate an optical band gap of 3.12 eV, which corresponds to 397 nm.*

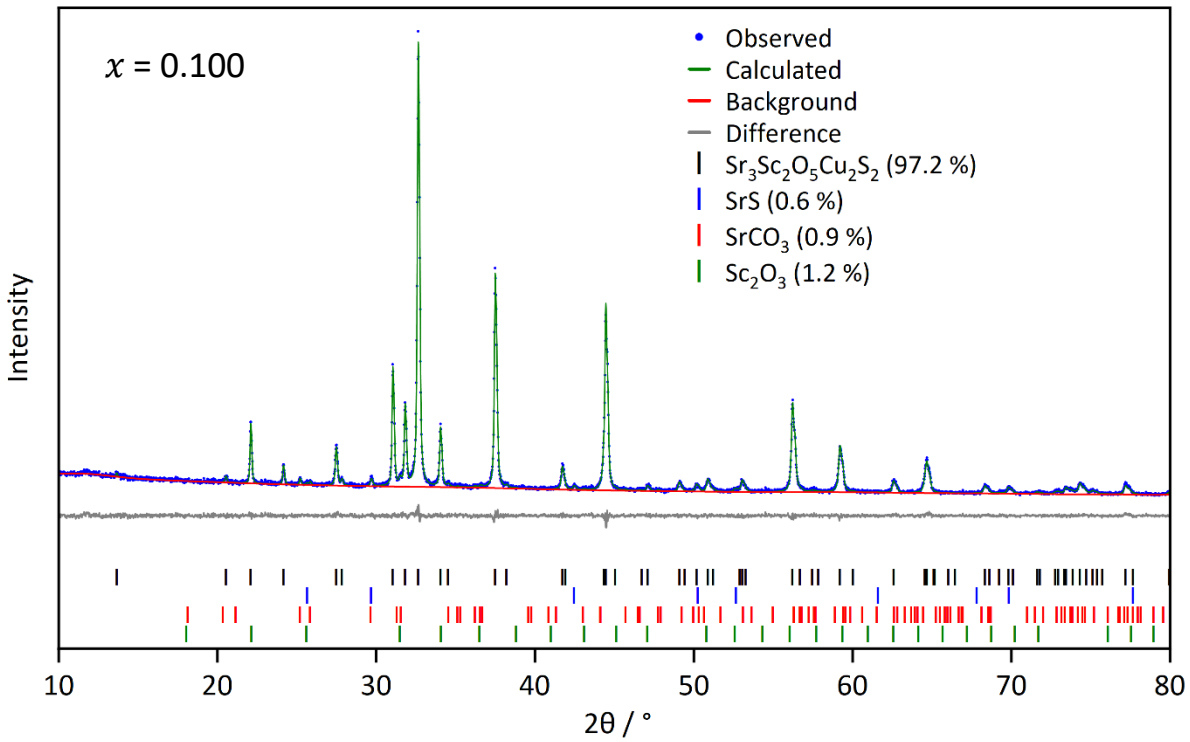

Figure 24 *Powder X-ray diffractogram of material with target composition $(Sr_{2.900}K_{0.100})Sc_2O_5Cu_2S_2$ (space group I4/mmm) after 36 hours of heating at 800 °C. The small blue circles represent the observed diffracted intensity, the green line represents the Rietveld-refined calculated model, the red line represents the background, and the grey line represents the difference between observed and calculated intensities. The black tick marks show the reflections of the refined model of $Sr_3Sc_2O_5Cu_2S_2$ (97.2 %), whilst the blue, red and green tick marks represent refined impurity phases SrS (0.6 %), $SrCO_3$ (0.9 %) and Sc_2O_3 (1.2 %) respectively. Duration: 45 minutes. Data points: 3457. Interval: 0.02 °. GOF: 1.09. R_{wp}: 4.533 %.*

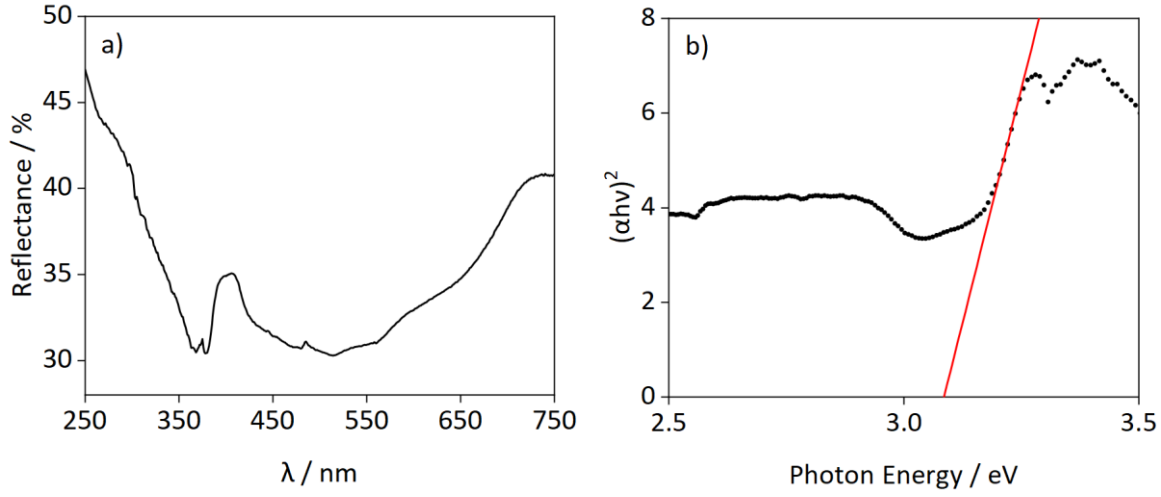

Figure 25 *UV-Vis spectrometry data for material with target composition $(Sr_{2.900}K_{0.100})Sc_2O_5Cu_2S_2$ after 36 hours of heating at 800 °C. Plot a) is the raw diffuse reflectance data, and plot b) is the associated magnified Tauc plot for this region, where the intercept between the red extrapolated tangent line and the x-axis is used to estimate an optical band gap of 3.09 eV, which corresponds to 401 nm.*

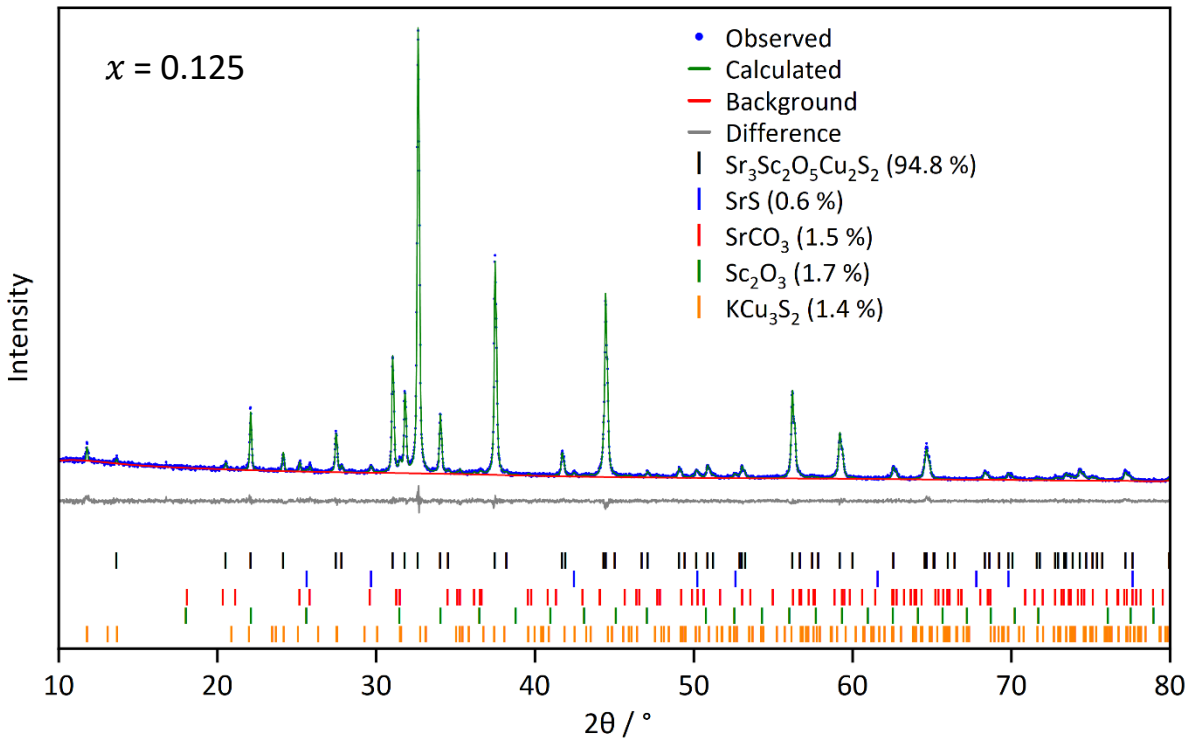

Figure 26 *Powder X-ray diffractogram of material with target composition $(Sr_{2.875}K_{0.125})Sc_2O_5Cu_2S_2$ (space group I4/mmm) after 36 hours of heating at 800 °C. The small blue circles represent the observed diffracted intensity, the green line represents the Rietveld-refined calculated model, the red line represents the background, and the grey line represents the difference between observed and calculated intensities. The black tick marks show the reflections of the refined model of $Sr_3Sc_2O_5Cu_2S_2$ (94.8 %), whilst the blue, red, green and orange tick marks represent refined impurity phases SrS (0.6 %), $SrCO_3$ (1.5 %), Sc_2O_3 (1.7 %) and KCu_3S_2 (1.4 %) respectively.*
Duration: 45 minutes. Data points: 3457. Interval: 0.02 °. GOF: 1.10. R_{wp}: 4.473 %.

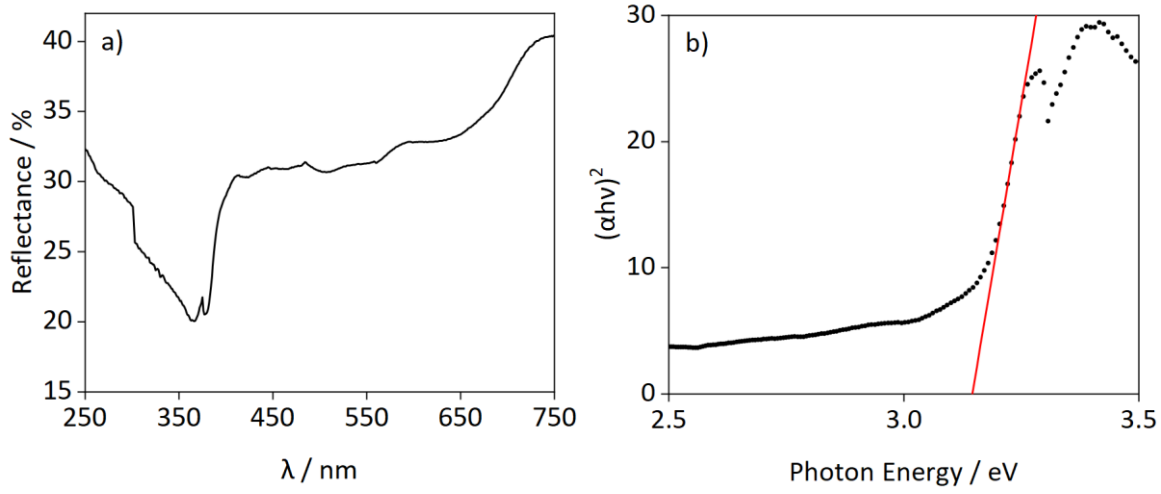

Figure 27 *UV-Vis spectrometry data for material with target composition $(Sr_{2.875}K_{0.125})Sc_2O_5Cu_2S_2$ after 36 hours of heating at 800 °C. Plot a) is the raw diffuse reflectance data, and plot b) is the associated magnified Tauc plot for this region, where the intercept between the red extrapolated tangent line and the x-axis is used to estimate an optical band gap of 3.15 eV, which corresponds to 394 nm.*

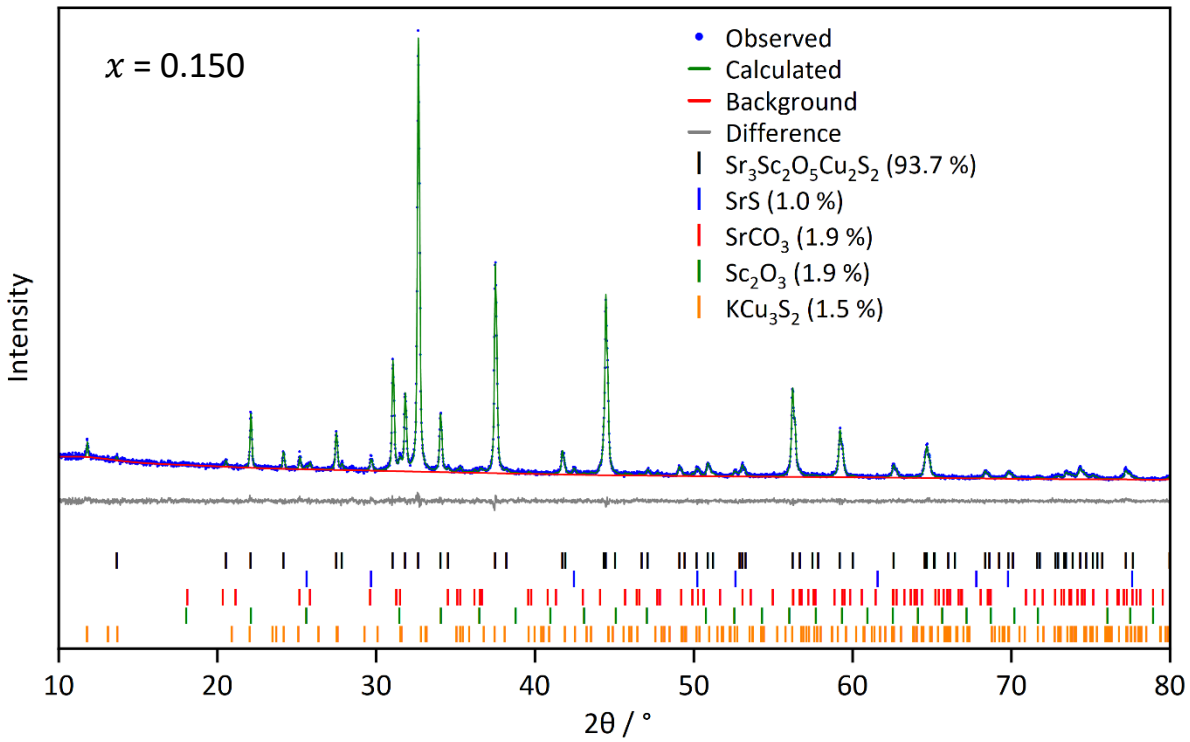

Figure 28 *Powder X-ray diffractogram of material with target composition $(Sr_{2.850}K_{0.150})Sc_2O_5Cu_2S_2$ (space group I4/mmm) after 36 hours of heating at 800 °C. The small blue circles represent the observed diffracted intensity, the green line represents the Rietveld-refined calculated model, the red line represents the background, and the grey line represents the difference between observed and calculated intensities. The black tick marks show the reflections of the refined model of $Sr_3Sc_2O_5Cu_2S_2$ (93.7 %), whilst the blue, red, green and orange tick marks represent refined impurity phases SrS (1.0 %), $SrCO_3$ (1.9 %), Sc_2O_3 (1.9 %) and KCu_3S_2 (1.5 %) respectively.*
Duration: 45 minutes. Data points: 3457. Interval: 0.02 °. GOF: 1.09. R_{wp}: 4.756 %.

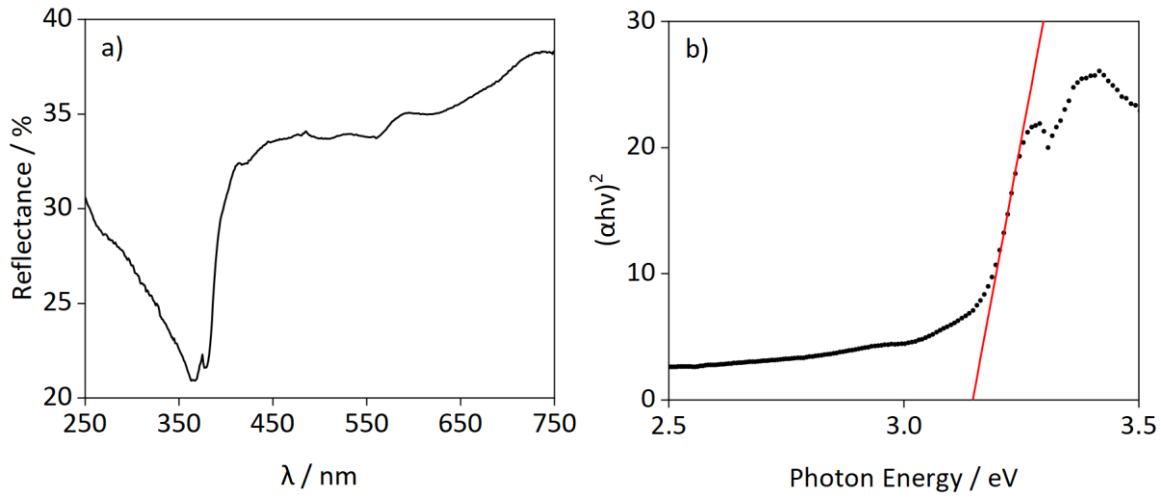

Figure 29 *UV-Vis spectrometry data for material with target composition $(Sr_{2.850}K_{0.150})Sc_2O_5Cu_2S_2$ after 36 hours of heating at 800 °C. Plot a) is the raw diffuse reflectance data, and plot b) is the associated magnified Tauc plot for this region, where the intercept between the red extrapolated tangent line and the x-axis is used to estimate an optical band gap of 3.15 eV, which corresponds to 394 nm.*

B.1.2 Sodium doped 325 sulfide MALMs, $(Sr_{3-x}Na_x)Sc_2O_5Cu_2S_2$

Table 19 Tabulated structural data of the sodium doped 325 sulfide MALMs with general formula $(Sr_{3-x}Na_x)Sc_2O_5Cu_2S_2$. The pristine material $Sr_3Sc_2O_5Cu_2S_2$ is included as a reference. All values are derived from the Rietveld refinement of PXRD data using GSAS-II. Note that because all materials listed are tetragonal (space group I4/mmm), the b parameter is identical to a, and thus omitted.

x **/ mol**	**Target Composition**	***a*** **/ Å**	***c*** **/ Å**	**Volume / Å^3**
0 (pristine)	$Sr_3Sc_2O_5Cu_2S_2$	4.07463(4)	25.9578(3)	430.967(12)
0.025	$(Sr_{2.975}Na_{0.025})Sc_2O_5Cu_2S_2$	4.07471(9)	25.9688(7)	431.166(25)
0.050	$(Sr_{2.950}Na_{0.050})Sc_2O_5Cu_2S_2$	4.07463(9)	25.9762(7)	431.272(25)
0.075	$(Sr_{2.925}Na_{0.075})Sc_2O_5Cu_2S_2$	4.07453(8)	25.9803(7)	431.319(25)
0.100	$(Sr_{2.900}Na_{0.100})Sc_2O_5Cu_2S_2$	4.07440(8)	25.9753(7)	431.209(25)
0.125	$(Sr_{2.875}Na_{0.125})Sc_2O_5Cu_2S_2$	4.07461(8)	25.9752(7)	431.251(24)
0.150	$(Sr_{2.850}Na_{0.150})Sc_2O_5Cu_2S_2$	4.07436(7)	25.9720(6)	431.145(22)
0.175	$(Sr_{2.825}Na_{0.175})Sc_2O_5Cu_2S_2$	4.07455(8)	25.9676(7)	431.114(24)
0.200	$(Sr_{2.800}Na_{0.200})Sc_2O_5Cu_2S_2$	4.07455(9)	25.9677(7)	431.113(26)

Table 20 Tabulated compositional data of the sodium doped 325 sulfide MALMs with general formula $(Sr_{3-x}Na_x)Sc_2O_5Cu_2S_2$. The pristine material $Sr_3Sc_2O_5Cu_2S_2$ is included as a reference. All values are cited as a weight percent (wt %) of the total weight, and are derived from the Rietveld refinement of PXRD data using GSAS-II.

x / mol	Target phase / wt %	SrS / wt %	$SrCO_3$ / wt %	Sc_2O_3 / wt %	$NaCu_3S_2$ / wt %
0 (pristine)	96.5	1.3	0.8	1.4	-
0.025	96.8	1.5	0.4	1.3	-
0.050	98.3	0.5	0.4	0.8	-
0.075	97.5	0.1	1.2	1.2	-
0.100	97.7	1.0	0.4	1.0	-
0.125	97.0	1.0	0.4	1.4	0.2
0.150	96.8	1.2	0.5	1.2	0.4
0.175	95.8	1.1	0.7	1.9	0.5
0.200	94.3	1.4	1.0	2.6	0.7

Table 21 Tabulated data on both the target and maximum actual dopant content of the sodium doped 325 sulfide MALMs with general formula $(Sr_{3-x}Na_x)Sc_2O_5Cu_2S_2$. The pristine material $Sr_3Sc_2O_5Cu_2S_2$ is included as a reference. The minimum possible amount of total Na contained within impurities was extracted from the refined wt % of $NaCu_3S_2$ from GSAS-II. The remaining Na content is the maximum possible Na within the MALM.

Target x / mol	**Target x / wt %**	**Minimum Na in impurities / %**	**Maximum Na in product / %**	**Maximum x / mol**
0 (pristine)	0.000	0.000	100.000	0.000
0.025	0.092	0.000	100.000	0.025
0.050	0.185	0.000	100.000	0.050
0.075	0.278	0.000	100.000	0.075
0.100	0.372	0.000	100.000	0.100
0.125	0.467	3.548	96.452	0.121
0.150	0.561	5.898	94.102	0.141
0.175	0.657	6.302	93.698	0.164
0.200	0.752	7.700	92.300	0.185

Table 22 Tabulated analytical data of to the measured properties of the sodium doped 325 sulfide MALMs with general formula $(Sr_{3-x}Na_x)Sc_2O_5Cu_2S_2$. The pristine material $Sr_3Sc_2O_5Cu_2S_2$ is included as a reference. Optical band gaps were estimated from UV-Vis data. Pellet densities were estimated from the mass and volume of annealed pellet samples, and are cited as a relative percentage of the bulk crystal. Resistivities and conductivities were estimated from 4 probe van der Pauw analysis of the pellet samples.

x / mol	Band Gap / eV	Pellet Density / %	Raw Resistivities from 4-Probe measurement, for each probe permutation / kΩ								Resistivity / Ω cm	Conductivity / S cm^{-1}
			1	2	3	4	5	6	7	8		
0 (pristine)	3.10	70.67	1.90 E+00	1.41 E+00	1.48 E-01	1.64 E+00	1.20 E-01	1.15 E+00	9.00 E-01	1.61 E+00	4.39 E+02	2.28 E-03
0.025	3.04	67.55	2.05 E-01	2.15 E-01	2.16 E-01	2.25 E-01	1.55 E-01	1.79 E-01	1.78 E-01	2.04 E-01	7.93 E+01	1.26 E-02
0.050	3.03	69.64	4.99 E-01	6.50 E-01	4.09 E-01	2.50 E-01	6.02 E-01	6.00 E-01	6.00 E-01	5.78 E-01	2.06 E+02	4.85 E-03
0.075	3.00	65.87	1.62 E-01	2.60 E-01	1.26 E-01	1.86 E-01	1.82 E-01	1.75 E-01	1.54 E-01	1.83 E-01	7.42 E+01	1.35 E-02
0.100	3.03	71.77	7.00 E-02	3.00 E-02	8.00 E-02	4.00 E-02	2.00 E-01	1.38 E-01	1.48 E-01	2.00 E-01	3.93 E+01	2.54 E-02
0.125	3.07	73.13	2.00 E-01	2.90 E-01	1.90 E-01	1.51 E-01	8.00 E-02	3.00 E-02	1.00 E-01	2.60 E-01	5.92 E+01	1.69 E-02
0.150	3.03	72.41	2.50 E-01	2.07 E-01	2.36 E-01	2.10 E-01	2.00 E-01	2.00 E-01	9.00 E-02	4.00 E-01	8.63 E+01	1.16 E-02
0.175	3.06	67.50	1.09 E-01	1.39 E-01	3.30 E-02	1.23 E-01	1.10 E-01	6.80 E-02	1.20 E-01	1.18 E-01	4.20 E+01	2.38 E-02
0.200	2.96	68.22	4.10 E-02	2.89 E-02	2.72 E-02	2.74 E-02	2.22 E-02	2.30 E-02	2.15 E-02	1.50 E-02	1.05 E+01	9.55 E-02

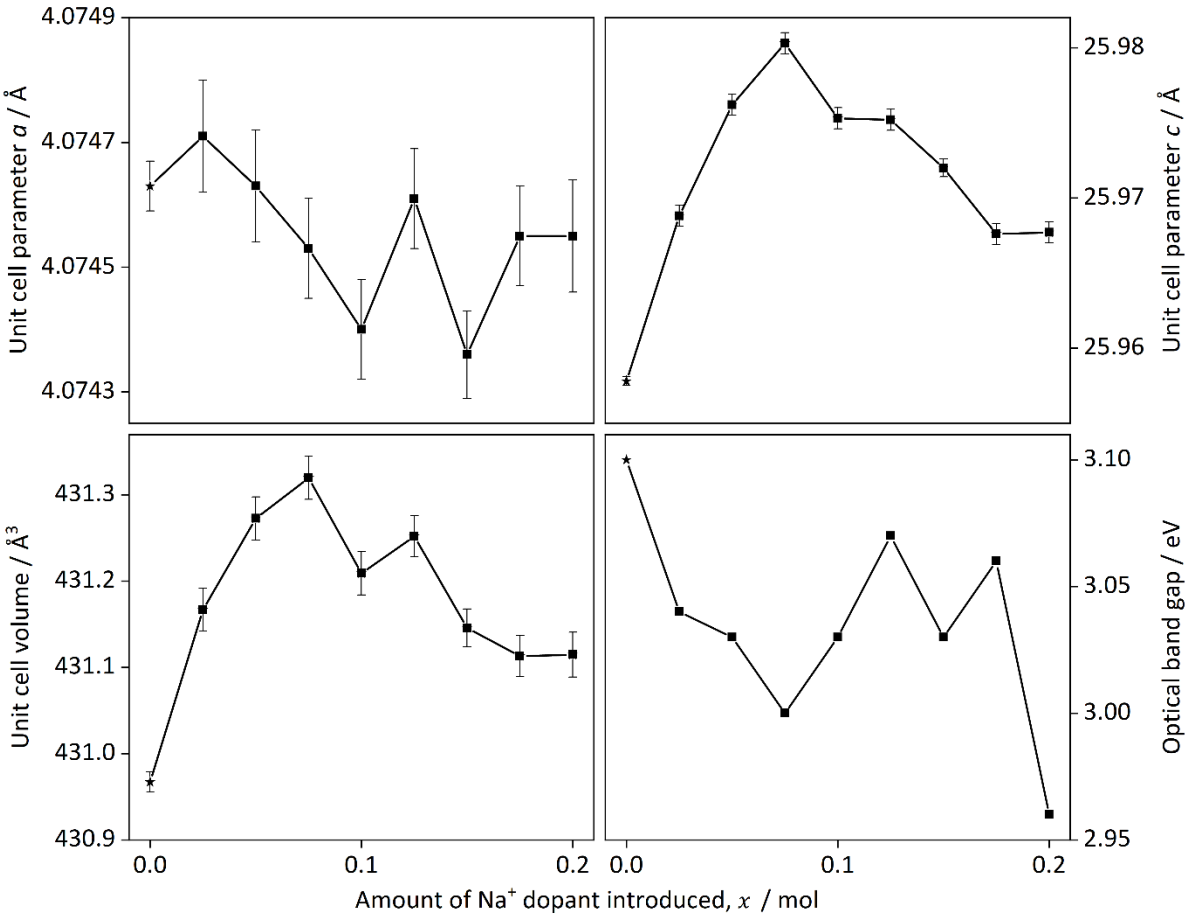

Figure 30 *Comparisons of a) the a unit cell parameter, b) the c unit cell parameter, c) unit cell volume, and d) the optical band gap, of the sodium doped 325 sulfide MALMs with general formula $(Sr_{3-x}Na_x)Sc_2O_5Cu_2S_2$. The pristine material $Sr_3Sc_2O_5Cu_2S_2$ is included as a reference at $x = 0$ mol and is represented by a star.*

Figure 31 *A photographic comparison of the colour of the sodium doped 325 sulfide MALMs with general formula $(Sr_{3-x}Na_x)Sc_2O_5Cu_2S_2$. Dopant concentration increases from left to right.*

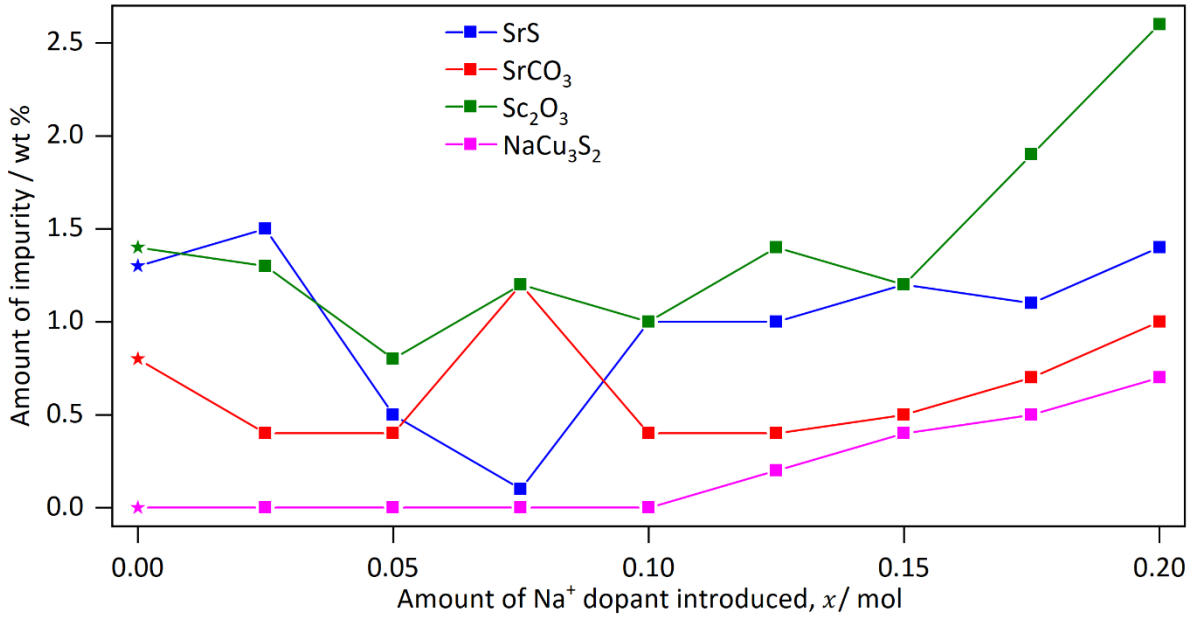

Figure 32 *The weight percentages of four impurity phases present in the sodium doped 325 sulfide MALMs with general formula $(Sr_{3-x}Na_x)Sc_2O_5Cu_2S_2$. The pristine material $Sr_3Sc_2O_5Cu_2S_2$ is included as a reference at x = 0 mol and is represented by a star.*

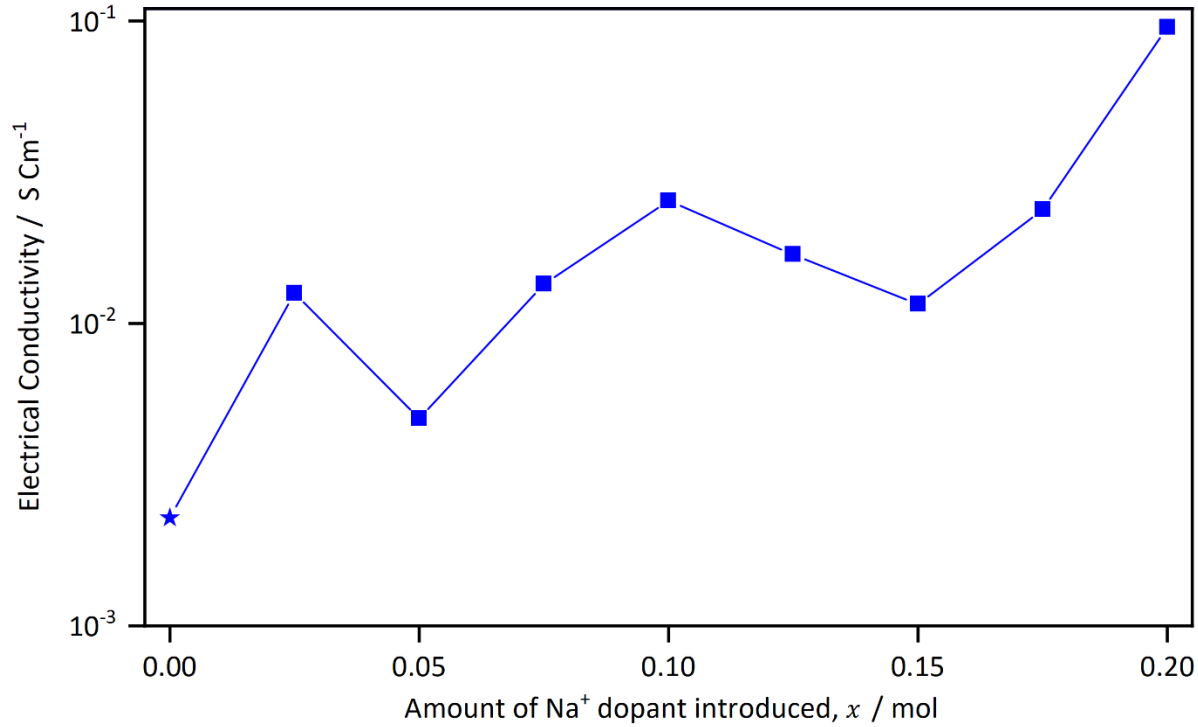

Figure 33 *The electrical conductivities of the sodium doped 325 sulfide MALMs with general formula $(Sr_{3-x}Na_x)Sc_2O_5Cu_2S_2$, represented on a log_{10} scale. The pristine material $Sr_3Sc_2O_5Cu_2S_2$ is included as a reference at x = 0 mol and is represented by a star. All values are derived from van der Pauw 4 probe resistivity measurements of 8mm diameter annealed pellet samples.*

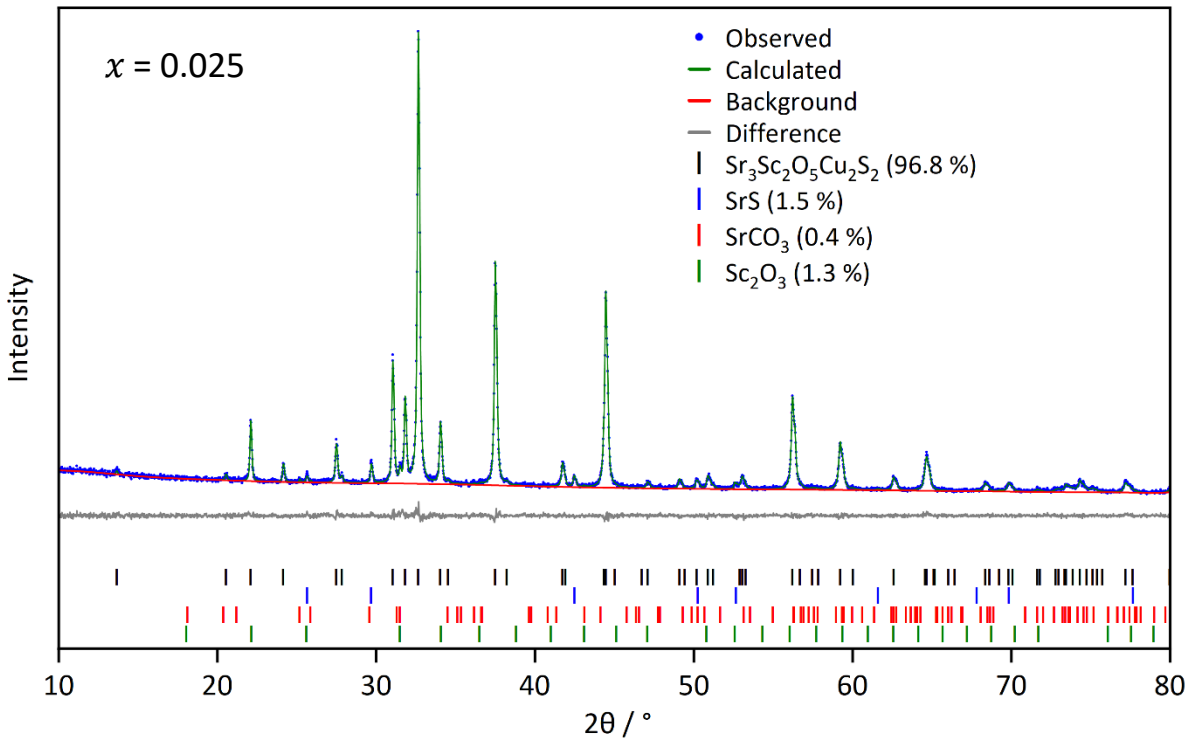

Figure 34 *Powder X-ray diffractogram of material with target composition $(Sr_{2.975}Na_{0.025})Sc_2O_5Cu_2S_2$ (space group I4/mmm) after 36 hours of heating at 800 °C. The small blue circles represent the observed diffracted intensity, the green line represents the Rietveld-refined calculated model, the red line represents the background, and the grey line represents the difference between observed and calculated intensities. The black tick marks show the reflections of the refined model of $Sr_3Sc_2O_5Cu_2S_2$ (96.8 %), whilst the blue, red and green tick marks represent refined impurity phases SrS (1.5 %), $SrCO_3$ (0.4 %) and Sc_2O_3 (1.3 %) respectively. Duration: 45 minutes. Data points: 3457. Interval: 0.02 °. GOF: 1.08. R_{wp}: 4.456 %.*

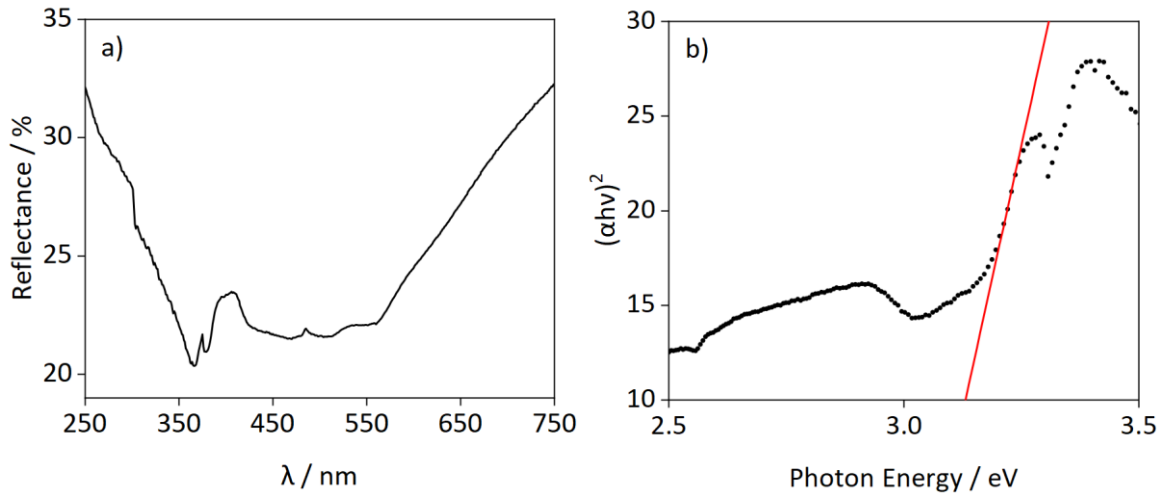

Figure 35 *UV-Vis spectrometry data for material with target composition $(Sr_{2.975}Na_{0.025})Sc_2O_5Cu_2S_2$ after 36 hours of heating at 800 °C. Plot a) is the raw diffuse reflectance data, and plot b) is the associated magnified Tauc plot for this region, where the intercept between the red extrapolated tangent line and the x-axis is used to estimate an optical band gap of 3.04 eV, which corresponds to 408 nm.*

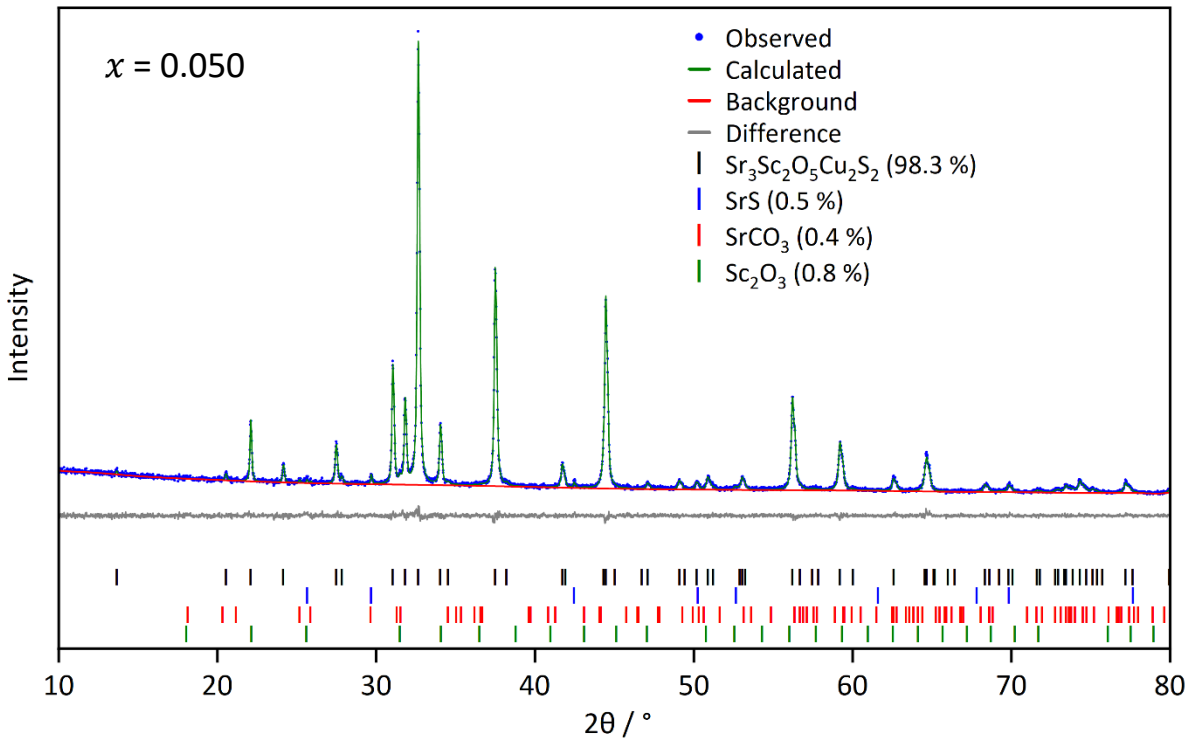

Figure 36 *Powder X-ray diffractogram of material with target composition $(Sr_{2.950}Na_{0.050})Sc_2O_5Cu_2S_2$ (space group I4/mmm) after 36 hours of heating at 800 °C. The small blue circles represent the observed diffracted intensity, the green line represents the Rietveld-refined calculated model, the red line represents the background, and the grey line represents the difference between observed and calculated intensities. The black tick marks show the reflections of the refined model of $Sr_3Sc_2O_5Cu_2S_2$ (98.3 %), whilst the blue, red and green tick marks represent refined impurity phases SrS (0.5 %), $SrCO_3$ (0.4 %) and Sc_2O_3 (0.8 %) respectively. Duration: 45 minutes. Data points: 3457. Interval: 0.02 °. GOF: 1.09. R_{wp}: 4.559 %.*

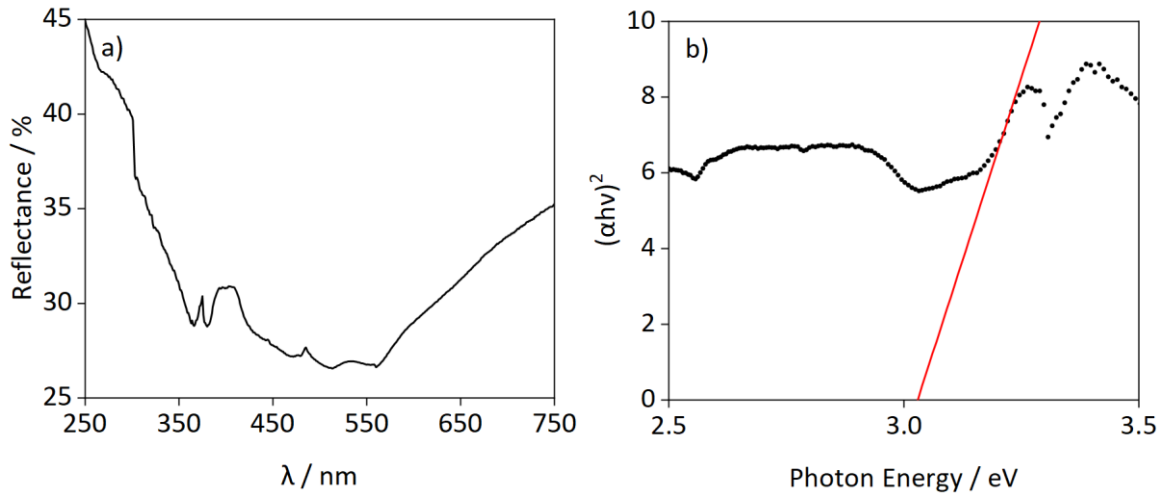

Figure 37 *UV-Vis spectrometry data for material with target composition $(Sr_{2.950}Na_{0.050})Sc_2O_5Cu_2S_2$ after 36 hours of heating at 800 °C. Plot a) is the raw diffuse reflectance data, and plot b) is the associated magnified Tauc plot for this region, where the intercept between the red extrapolated tangent line and the x-axis is used to estimate an optical band gap of 3.03 eV, which corresponds to 409 nm.*

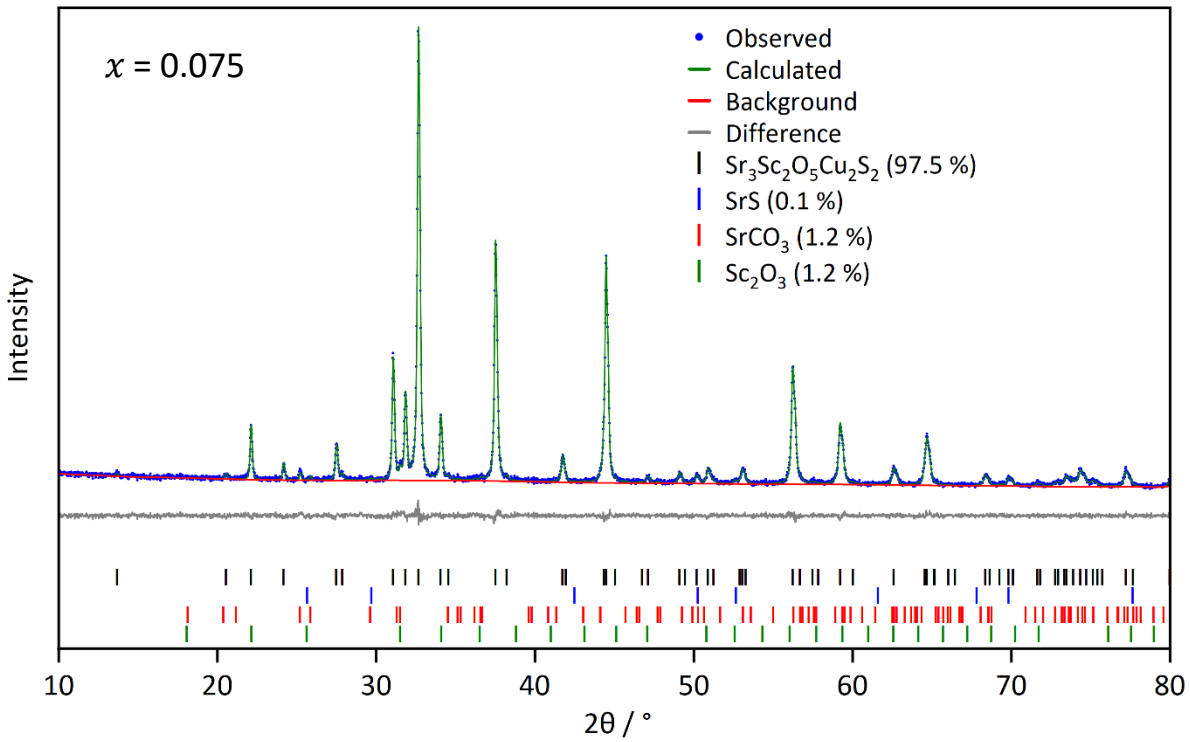

Figure 38 *Powder X-ray diffractogram of material with target composition $(Sr_{2.925}Na_{0.075})Sc_2O_5Cu_2S_2$ (space group I4/mmm) after 36 hours of heating at 800 °C. The small blue circles represent the observed diffracted intensity, the green line represents the Rietveld-refined calculated model, the red line represents the background, and the grey line represents the difference between observed and calculated intensities. The black tick marks show the reflections of the refined model of $Sr_3Sc_2O_5Cu_2S_2$ (97.5 %), whilst the blue, red and green tick marks represent refined impurity phases SrS (0.1 %), $SrCO_3$ (1.2 %) and Sc_2O_3 (1.2 %) respectively. Duration: 45 minutes. Data points: 3457. Interval: 0.02 °. GOF: 1.06. R_{wp}: 4.147 %.*

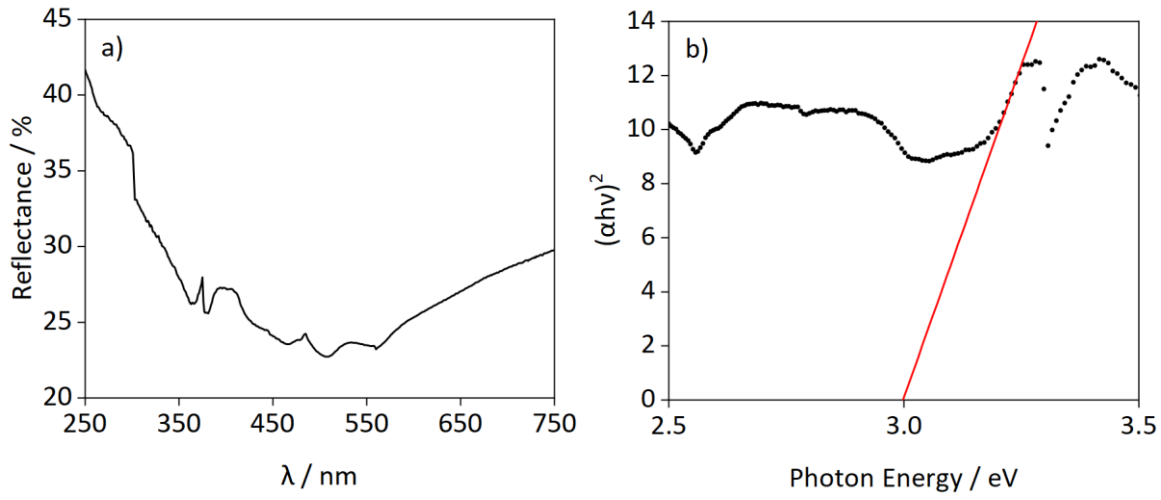

Figure 39 *UV-Vis spectrometry data for material with target composition $(Sr_{2.925}Na_{0.075})Sc_2O_5Cu_2S_2$ after 36 hours of heating at 800 °C. Plot a) is the raw diffuse reflectance data, and plot b) is the associated magnified Tauc plot for this region, where the intercept between the red extrapolated tangent line and the x-axis is used to estimate an optical band gap of 3.00 eV, which corresponds to 413 nm.*

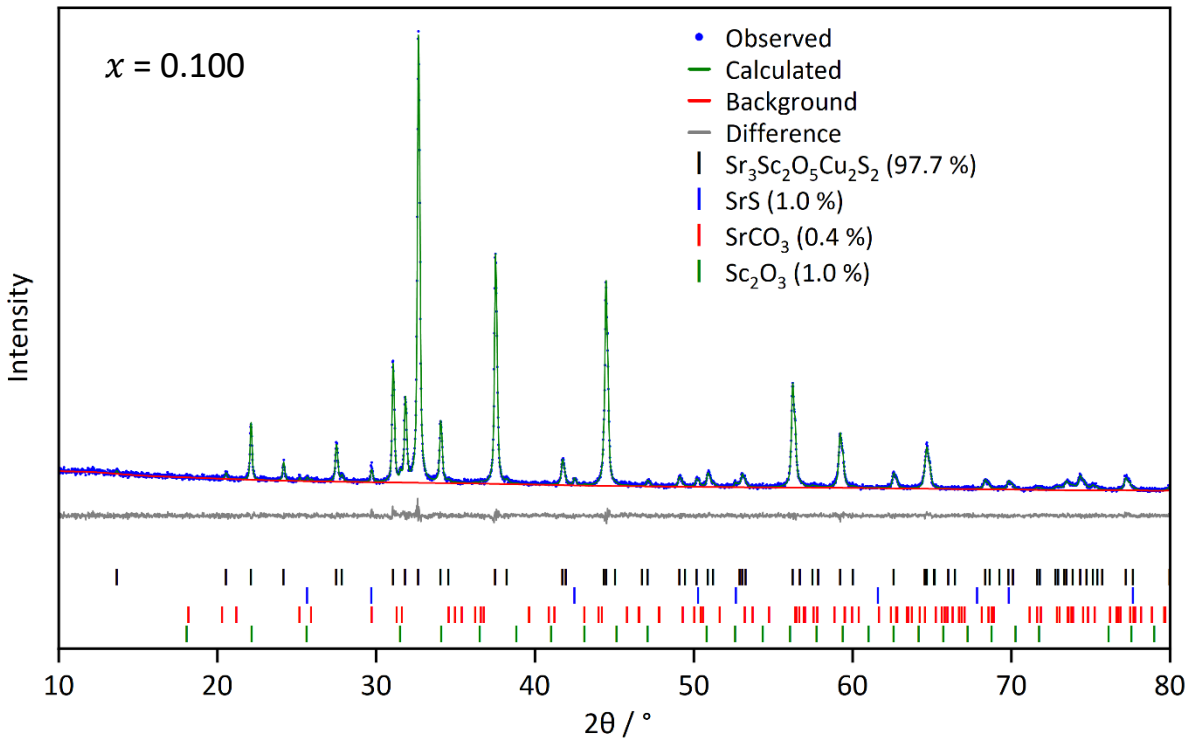

Figure 40 *Powder X-ray diffractogram of material with target composition $(Sr_{2.900}Na_{0.100})Sc_2O_5Cu_2S_2$ (space group I4/mmm) after 36 hours of heating at 800 °C. The small blue circles represent the observed diffracted intensity, the green line represents the Rietveld-refined calculated model, the red line represents the background, and the grey line represents the difference between observed and calculated intensities. The black tick marks show the reflections of the refined model of $Sr_3Sc_2O_5Cu_2S_2$ (97.7 %), whilst the blue, red and green tick marks represent refined impurity phases SrS (1.0 %), $SrCO_3$ (0.4 %) and Sc_2O_3 (1.0 %) respectively. Duration: 45 minutes. Data points: 3457. Interval: 0.02 °. GOF: 1.05. R_{wp}: 4.415 %.*

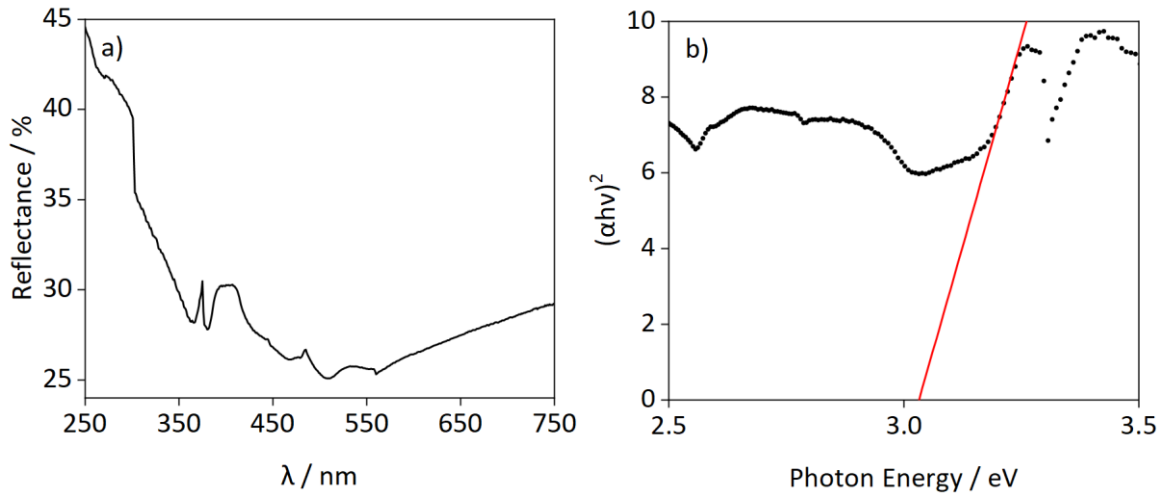

Figure 41 *UV-Vis spectrometry data for material with target composition $(Sr_{2.900}Na_{0.100})Sc_2O_5Cu_2S_2$ after 36 hours of heating at 800 °C. Plot a) is the raw diffuse reflectance data, and plot b) is the associated magnified Tauc plot for this region, where the intercept between the red extrapolated tangent line and the x-axis is used to estimate an optical band gap of 3.03 eV, which corresponds to 409 nm.*

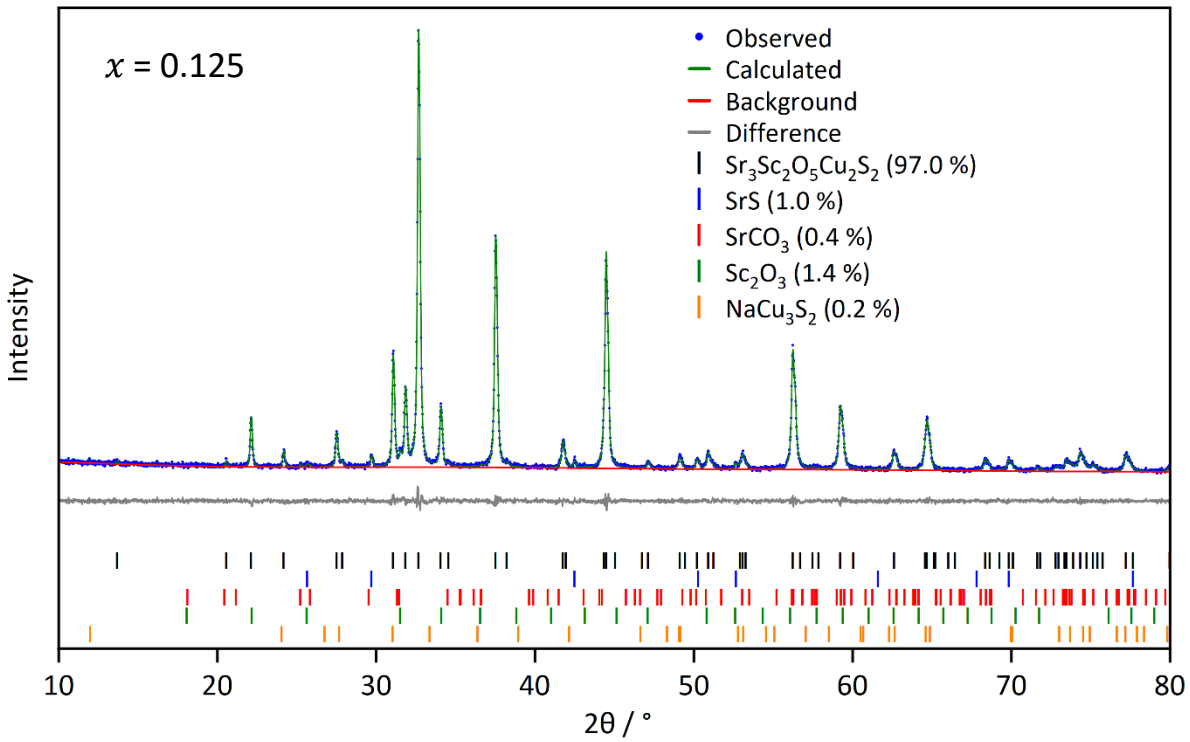

Figure 42 *Powder X-ray diffractogram of material with target composition $(Sr_{2.875}Na_{0.125})Sc_2O_5Cu_2S_2$ (space group I4/mmm) after 36 hours of heating at 800 °C. The small blue circles represent the observed diffracted intensity, the green line represents the Rietveld-refined calculated model, the red line represents the background, and the grey line represents the difference between observed and calculated intensities. The black tick marks show the reflections of the refined model of $Sr_3Sc_2O_5Cu_2S_2$ (97.0 %), whilst the blue, red, green and orange tick marks represent refined impurity phases SrS (1.0 %), $SrCO_3$ (0.4 %), Sc_2O_3 (1.4 %) and $NaCu_3S_2$ (0.2 %) respectively.*
Duration: 45 minutes. Data points: 3457. Interval: 0.02 °. GOF: 1.04. R_{wp}: 3.984 %.

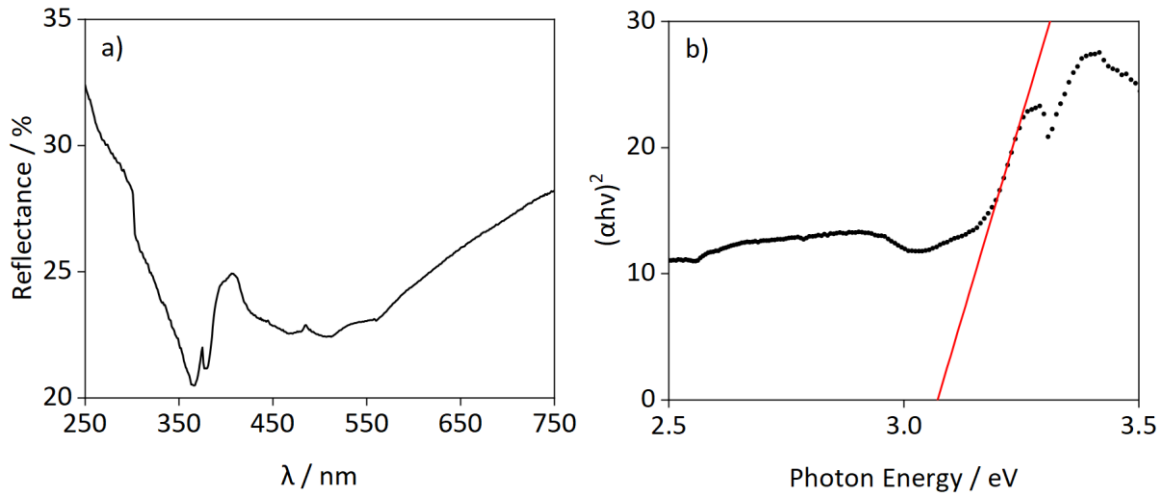

Figure 43 *UV-Vis spectrometry data for material with target composition $(Sr_{2.875}Na_{0.125})Sc_2O_5Cu_2S_2$ after 36 hours of heating at 800 °C. Plot a) is the raw diffuse reflectance data, and plot b) is the associated magnified Tauc plot for this region, where the intercept between the red extrapolated tangent line and the x-axis is used to estimate an optical band gap of 3.07 eV, which corresponds to 404 nm.*

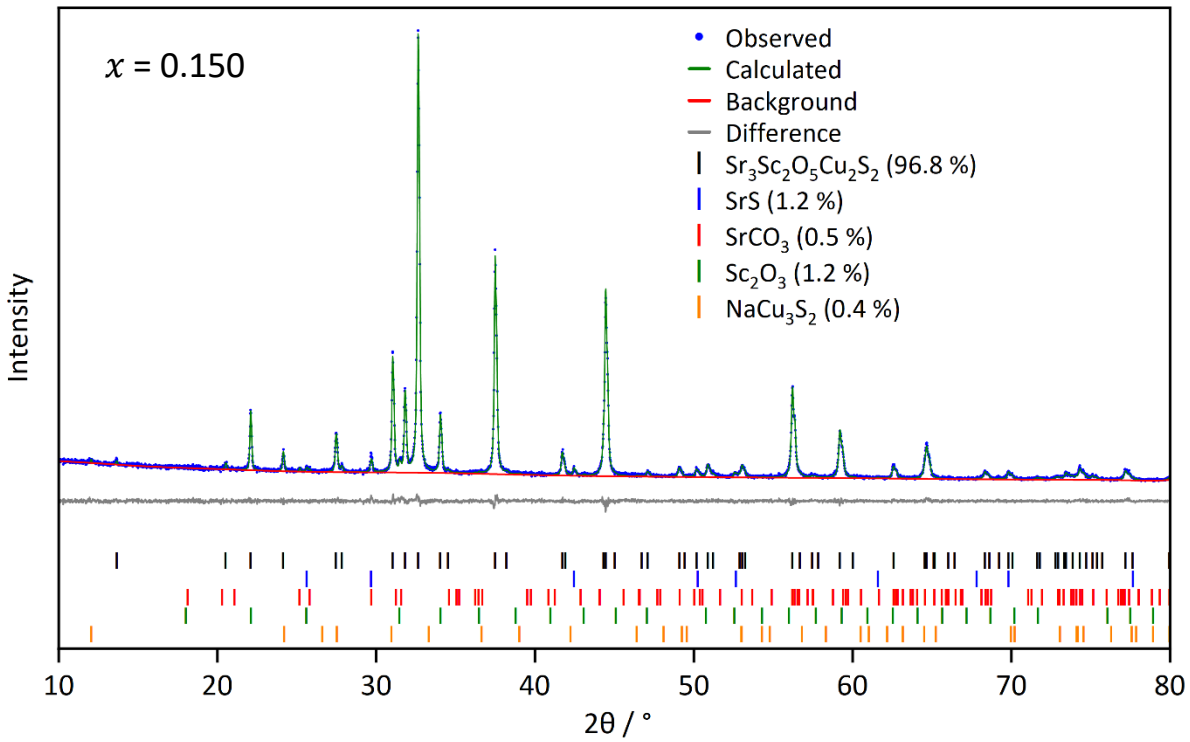

Figure 44 *Powder X-ray diffractogram of material with target composition $(Sr_{2.850}Na_{0.150})Sc_2O_5Cu_2S_2$ (space group I4/mmm) after 36 hours of heating at 800 °C. The small blue circles represent the observed diffracted intensity, the green line represents the Rietveld-refined calculated model, the red line represents the background, and the grey line represents the difference between observed and calculated intensities. The black tick marks show the reflections of the refined model of $Sr_3Sc_2O_5Cu_2S_2$ (96.8 %), whilst the blue, red, green and orange tick marks represent refined impurity phases SrS (1.2 %), $SrCO_3$ (0.5 %), Sc_2O_3 (1.2 %) and $NaCu_3S_2$ (0.4 %) respectively.*
Duration: 45 minutes. Data points: 3457. Interval: 0.02 °. GOF: 1.10. R_{wp}: 4.448 %.

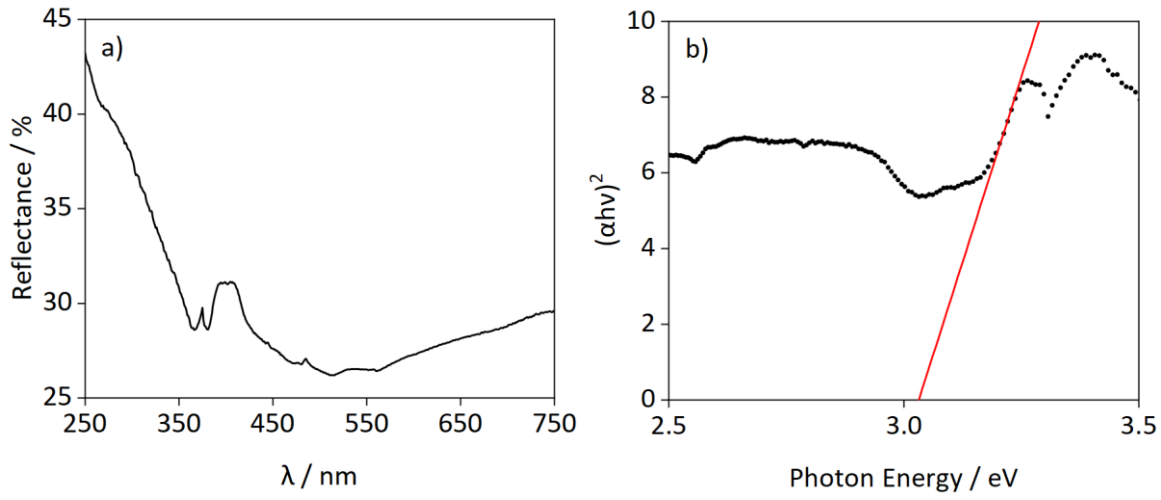

Figure 45 *UV-Vis spectrometry data for material with target composition $(Sr_{2.850}Na_{0.150})Sc_2O_5Cu_2S_2$ after 36 hours of heating at 800 °C. Plot a) is the raw diffuse reflectance data, and plot b) is the associated magnified Tauc plot for this region, where the intercept between the red extrapolated tangent line and the x-axis is used to estimate an optical band gap of 3.03 eV, which corresponds to 409 nm.*

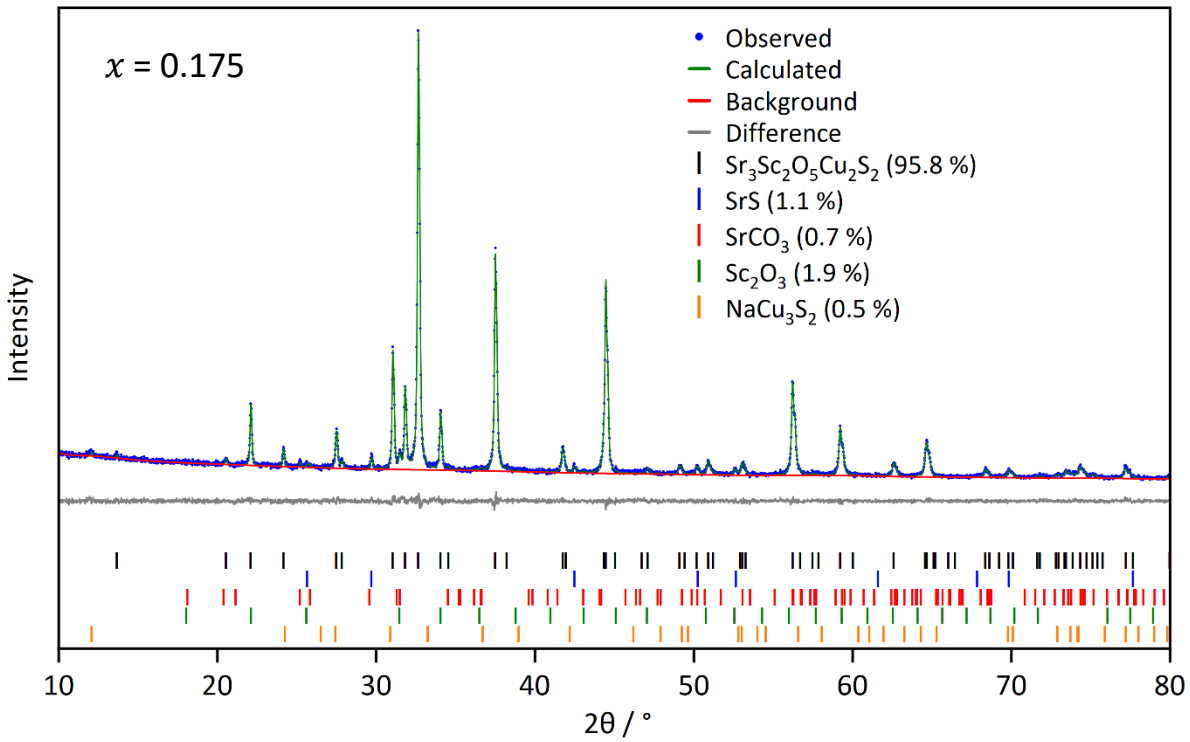

Figure 46 *Powder X-ray diffractogram of material with target composition $(Sr_{2.825}Na_{0.175})Sc_2O_5Cu_2S_2$ (space group I4/mmm) after 36 hours of heating at 800 °C. The small blue circles represent the observed diffracted intensity, the green line represents the Rietveld-refined calculated model, the red line represents the background, and the grey line represents the difference between observed and calculated intensities. The black tick marks show the reflections of the refined model of $Sr_3Sc_2O_5Cu_2S_2$ (95.8 %), whilst the blue, red, green and orange tick marks represent refined impurity phases SrS (1.1 %), $SrCO_3$ (0.7 %), Sc_2O_3 (1.9 %) and $NaCu_3S_2$ (0.5 %) respectively.*
Duration: 45 minutes. Data points: 3457. Interval: 0.02 °. GOF: 1.07. R_{wp}: 4.662 %.

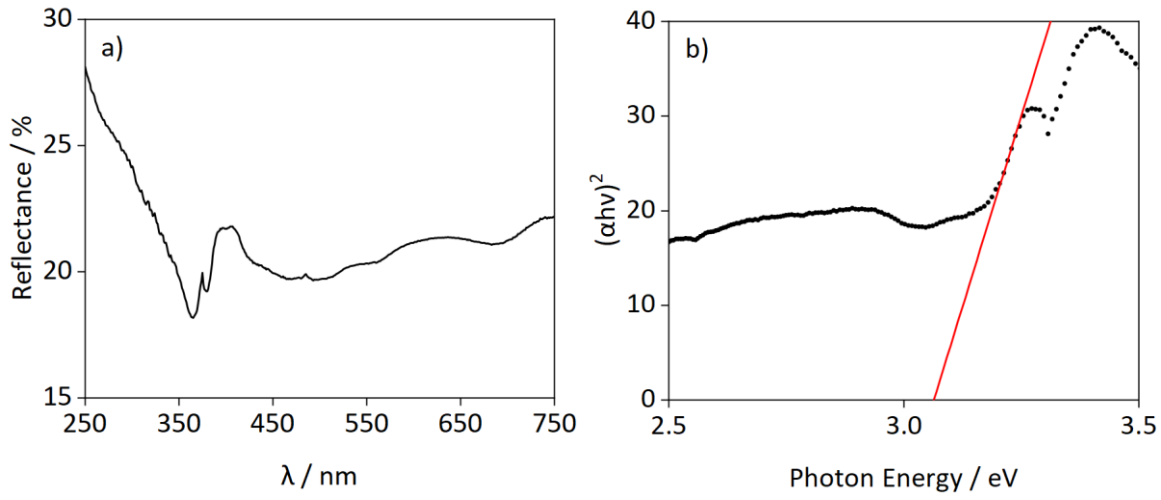

Figure 47 *UV-Vis spectrometry data for material with target composition $(Sr_{2.825}Na_{0.175})Sc_2O_5Cu_2S_2$ after 36 hours of heating at 800 °C. Plot a) is the raw diffuse reflectance data, and plot b) is the associated magnified Tauc plot for this region, where the intercept between the red extrapolated tangent line and the x-axis is used to estimate an optical band gap of 3.06 eV, which corresponds to 405 nm.*

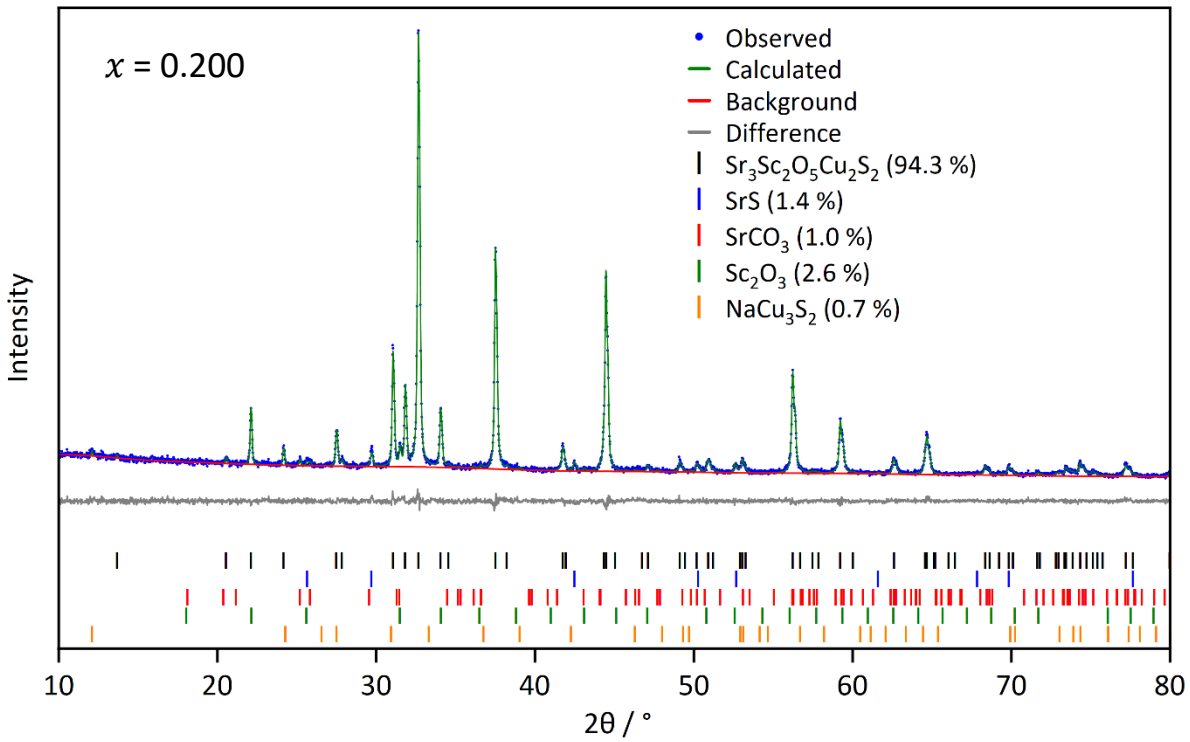

Figure 48 *Powder X-ray diffractogram of material with target composition $(Sr_{2.800}Na_{0.200})Sc_2O_5Cu_2S_2$ (space group I4/mmm) after 36 hours of heating at 800 °C. The small blue circles represent the observed diffracted intensity, the green line represents the Rietveld-refined calculated model, the red line represents the background, and the grey line represents the difference between observed and calculated intensities. The black tick marks show the reflections of the refined model of $Sr_3Sc_2O_5Cu_2S_2$ (94.3 %), whilst the blue, red, green and orange tick marks represent refined impurity phases SrS (1.4 %), $SrCO_3$ (1.0 %), Sc_2O_3 (2.6 %) and $NaCu_3S_2$ (0.7 %) respectively.*
Duration: 45 minutes. Data points: 3457. Interval: 0.02 °. GOF: 1.12. R_{wp}: 4.844 %.

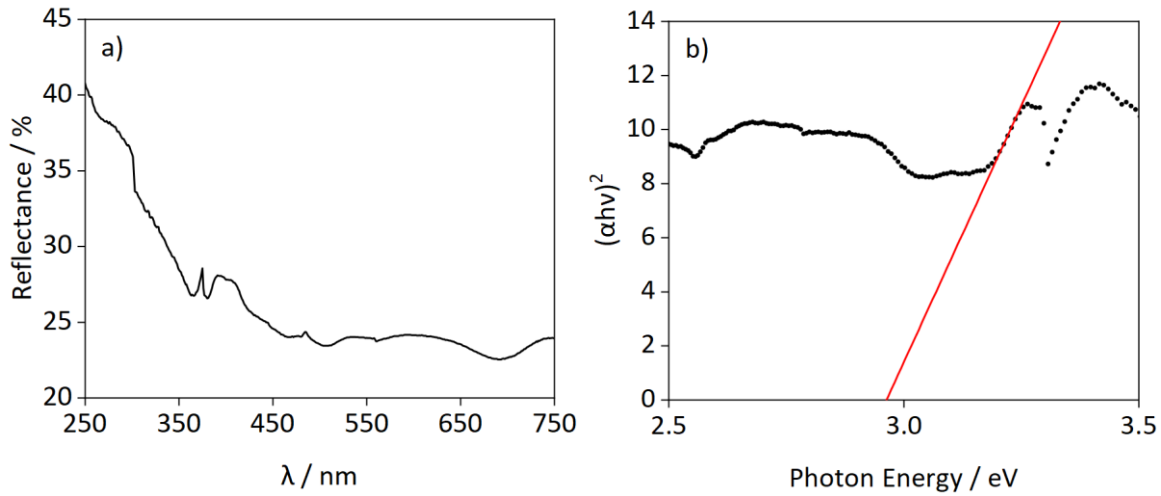

Figure 49 *UV-Vis spectrometry data for material with target composition $(Sr_{2.800}Na_{0.200})Sc_2O_5Cu_2S_2$ after 36 hours of heating at 800 °C. Plot a) is the raw diffuse reflectance data, and plot b) is the associated magnified Tauc plot for this region, where the intercept between the red extrapolated tangent line and the x-axis is used to estimate an optical band gap of 2.96 eV, which corresponds to 419 nm.*

B.1.3 Strontium deficient 325 sulfide MALMs, $Sr_{3-x}Sc_2O_5Cu_2S_2$

Table 23 Tabulated structural data of the strontium deficient 325 sulfide MALMs with general formula $Sr_{3-x}Sc_2O_5Cu_2S_2$. The pristine material $Sr_3Sc_2O_5Cu_2S_2$ is included as a reference. All values are derived from the Rietveld refinement of PXRD data using GSAS-II. Note that because all materials listed are tetragonal (space group I4/mmm), the b parameter is identical to a, and thus omitted.

x **/ mol**	**Target Composition**	***a*** **/ Å**	***c*** **/ Å**	**Volume / Å^3**
0 (pristine)	$Sr_3Sc_2O_5Cu_2S_2$	4.07463(4)	25.9578(3)	430.967(12)
0.05	$Sr_{2.95}Sc_2O_5Cu_2S_2$	4.07432(9)	25.9718(7)	431.134(26)
0.10	$Sr_{2.90}Sc_2O_5Cu_2S_2$	4.07406(9)	25.9735(7)	431.108(26)
0.15	$Sr_{2.85}Sc_2O_5Cu_2S_2$	4.07413(10)	25.9771(8)	431.183(29)
0.20	$Sr_{2.80}Sc_2O_5Cu_2S_2$	4.07344(11)	25.9772(10)	431.040(30)
0.50	$Sr_{2.50}Sc_2O_5Cu_2S_2$	4.07242(18)	25.9923(19)	431.070(50)
0.75	$Sr_{2.25}Sc_2O_5Cu_2S_2$	4.07220(23)	26.0080(30)	431.280(70)
1.00	$Sr_{2.00}Sc_2O_5Cu_2S_2$	4.07176(21)	26.0010(24)	431.080(70)

Table 24 Tabulated compositional data of the strontium deficient 325 sulfide MALMs with general formula $Sr_{3-x}Sc_2O_5Cu_2S_2$. The pristine material $Sr_3Sc_2O_5Cu_2S_2$ is included as a reference. All values are cited as a weight percent (wt %) of the total weight, and are derived from the Rietveld refinement of PXRD data using GSAS-II.

x / mol	Target phase / wt %	SrS / wt %	$SrCO_3$ / wt %	Sc_2O_3 / wt %	$SrSO_4$ / wt %
0 (pristine)	96.5	1.3	0.8	1.4	-
0.05	91.0	2.6	1.2	3.8	1.4
0.10	89.1	4.0	1.0	4.1	1.7
0.15	88.3	4.5	0.7	4.6	1.9
0.20	81.5	8.1	0.7	6.8	3.0
0.50	67.0	11.1	1.1	14.7	6.2
0.75	62.6	10.2	0.9	18.6	7.7
1.00	62.5	1.8	0.5	28.9	6.4

Table 25 Tabulated analytical data of to the measured properties of the strontium deficient 325 sulfide MALMs with general formula $Sr_{3-x}Sc_2O_5Cu_2S_2$. The pristine material $Sr_3Sc_2O_5Cu_2S_2$ is included as a reference. Optical band gaps were estimated from UV-Vis data. Pellet densities were estimated from the mass and volume of annealed pellet samples, and are cited as a relative percentage of the bulk crystal. Resistivities and conductivities were estimated from 4 probe van der Pauw analysis of the pellet samples.

x / mol	Band Gap / eV	Pellet Density / %	Raw Resistivities from 4-Probe measurement, for each probe permutation / kΩ								Resistivity / Ω cm	Conductivity / S cm^{-1}
			1	2	3	4	5	6	7	8		
0 (pristine)	3.10	70.67	1.90 E+00	1.41 E+00	1.48 E-01	1.64 E+00	1.20 E-01	1.15 E+00	9.00 E-01	1.61 E+00	4.39 E+02	2.28 E-03
0.05	*n/a* †	69.87	1.22 E-01	9.40 E-02	1.17 E-01	8.45 E-02	8.50 E-02	1.06 E-01	1.30 E-01	1.37 E-01	4.31 E+01	2.32 E-02
0.10	*n/a* †	69.61	4.90 E-02	8.20 E-02	8.90 E-02	5.50 E-02	6.30 E-02	9.50 E-02	1.03 E-01	5.20 E-02	2.94 E+01	3.40 E-02
0.15	*n/a* †	70.38	6.30 E-02	9.90 E-02	6.40 E-02	7.80 E-02	1.13 E-01	1.35 E-01	1.20 E-01	1.30 E-01	3.92 E+01	2.55 E-02
0.20	*n/a* †	71.09	4.20 E-02	8.30 E-02	4.70 E-02	3.50 E-02	3.10 E-02	1.10 E-01	4.50 E-02	4.20 E-02	2.17 E+01	4.61 E-02
0.50	*n/a* †	74.49	8.93 E-03	7.30 E-03	7.61 E-03	7.91 E-03	6.24 E-03	6.00 E-03	6.30 E-03	7.62 E-03	2.86 E+00	3.49 E-01
0.75	*n/a* †	78.18	3.12 E-03	5.16 E-03	5.13 E-03	5.26 E-03	6.27 E-03	6.16 E-03	6.18 E-03	2.90 E-03	2.00 E+00	5.00 E-01
1.00	*n/a* †	79.30	4.30 E-05	1.06 E-02	3.00 E-05	9.80 E-03	5.29 E-03	6.05 E-03	5.63 E-02	5.66 E-02	5.81 E+00	1.72 E-01

† A band gap estimation for these samples was not possible due to a lack of drop-off in reflectance between the UV and visible regions. The samples were either too impure or too dark in colour for any difference to be justified, and the Tauc plots were deemed too subjective for the usual tangent approximation.

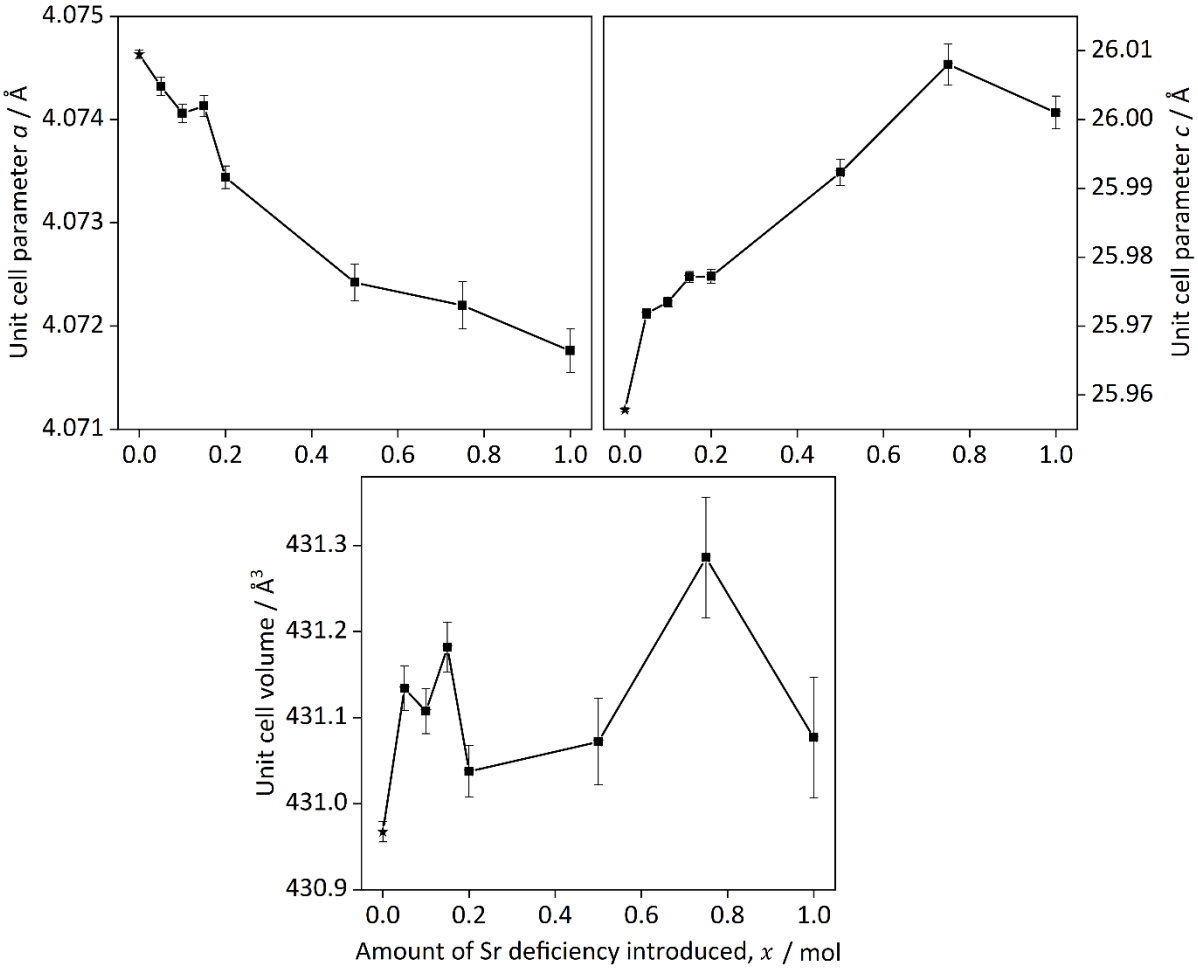

Figure 50 *Comparisons of a) the a unit cell parameter, b) the c unit cell parameter, and c) the unit cell volume, of the strontium deficient 325 sulfide MALMs with general formula $Sr_{3-x}Sc_2O_5Cu_2S_2$. The pristine material $Sr_3Sc_2O_5Cu_2S_2$ is included as a reference at $x = 0$ mol and is represented by a star. Sample band gaps are missing due to lack of drop-off in diffuse reflectance, see Table 25.*

Figure 51 *A photographic comparison of the colour of the strontium deficient 325 sulfide MALMs with general formula $Sr_{3-x}Sc_2O_5Cu_2S_2$. Deficiency increases from left to right.*

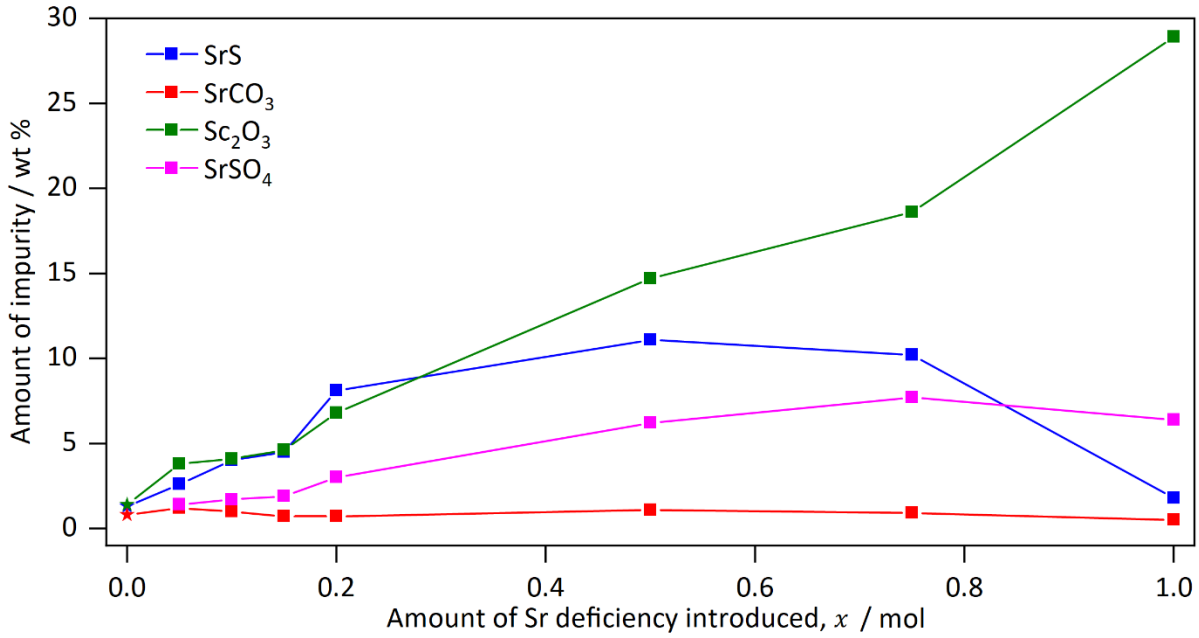

Figure 52 *The weight percentages of four impurity phases present in the strontium deficient 325 sulfide MALMs with general formula $Sr_{3-x}Sc_2O_5Cu_2S_2$. The pristine material $Sr_3Sc_2O_5Cu_2S_2$ is included as a reference at x = 0 mol and is represented by a star.*

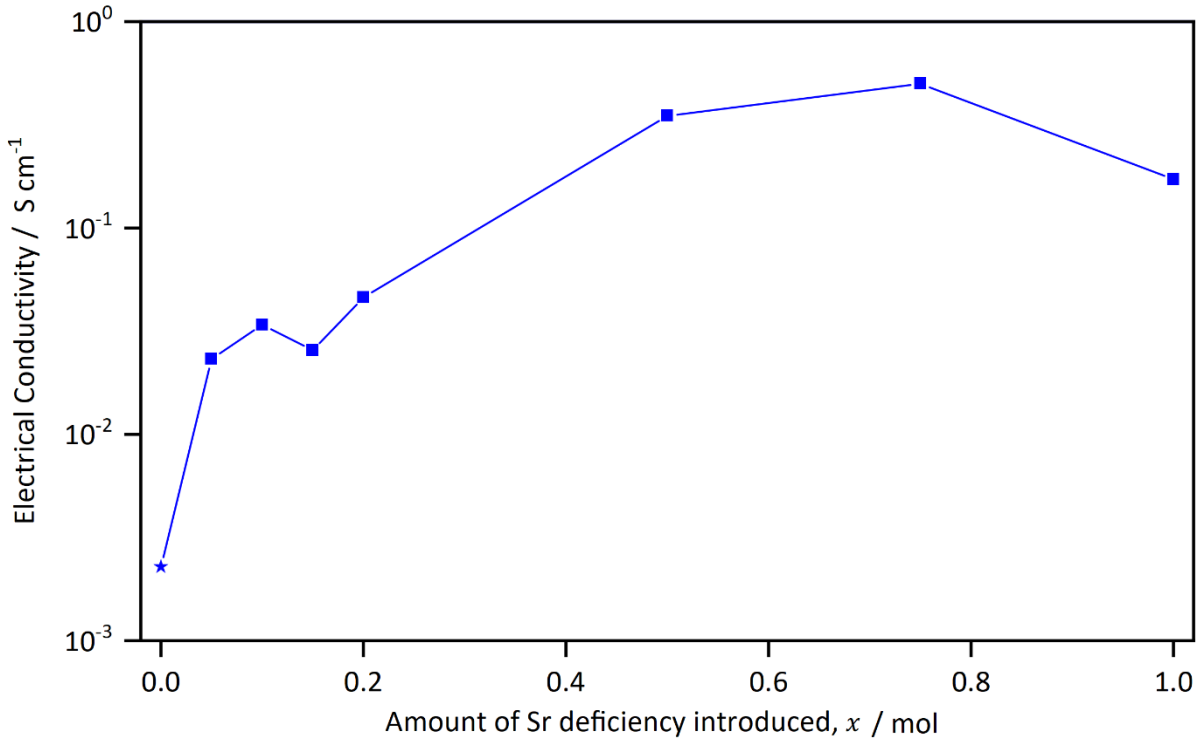

Figure 53 *The electrical conductivities of the strontium deficient 325 sulfide MALMs with general formula $Sr_{3-x}Sc_2O_5Cu_2S_2$, represented on a log_{10} scale. The pristine material $Sr_3Sc_2O_5Cu_2S_2$ is included as a reference at x = 0 mol and is represented by a star. All values are derived from van der Pauw 4 probe resistivity measurements of 8mm diameter annealed pellet samples.*

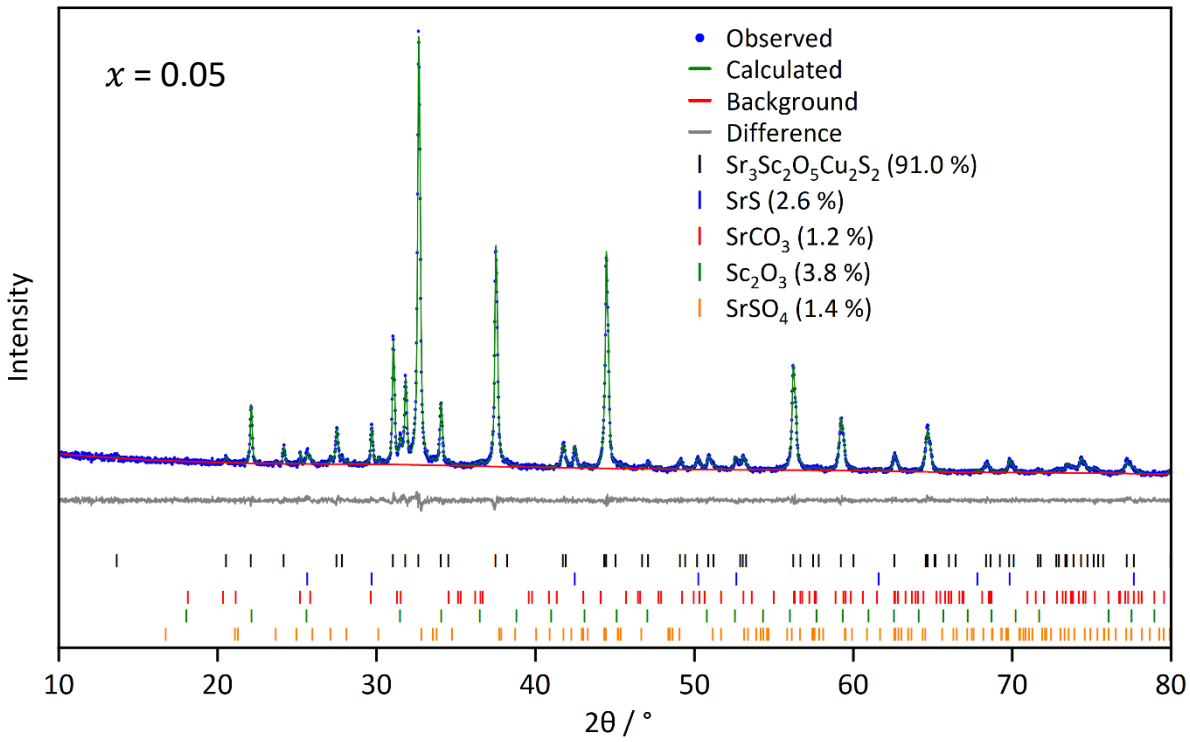

Figure 54 *Powder X-ray diffractogram of material with target composition $Sr_{2.95}Sc_2O_5Cu_2S_2$ (space group I4/mmm) after 36 hours of heating at 800 °C. The small blue circles represent the observed diffracted intensity, the green line represents the Rietveld-refined calculated model, the red line represents the background, and the grey line represents the difference between observed and calculated intensities. The black tick marks show the reflections of the refined model of $Sr_3Sc_2O_5Cu_2S_2$ (91.0 %), whilst the blue, red, green and orange tick marks represent refined impurity phases SrS (2.6 %), $SrCO_3$ (1.2 %), Sc_2O_3 (3.8 %), and $SrSO_4$ (1.4 %) respectively.*
Duration: 45 minutes. Data points: 3457. Interval: 0.02 °. GOF: 1.10. R_{wp}: 4.416 %.

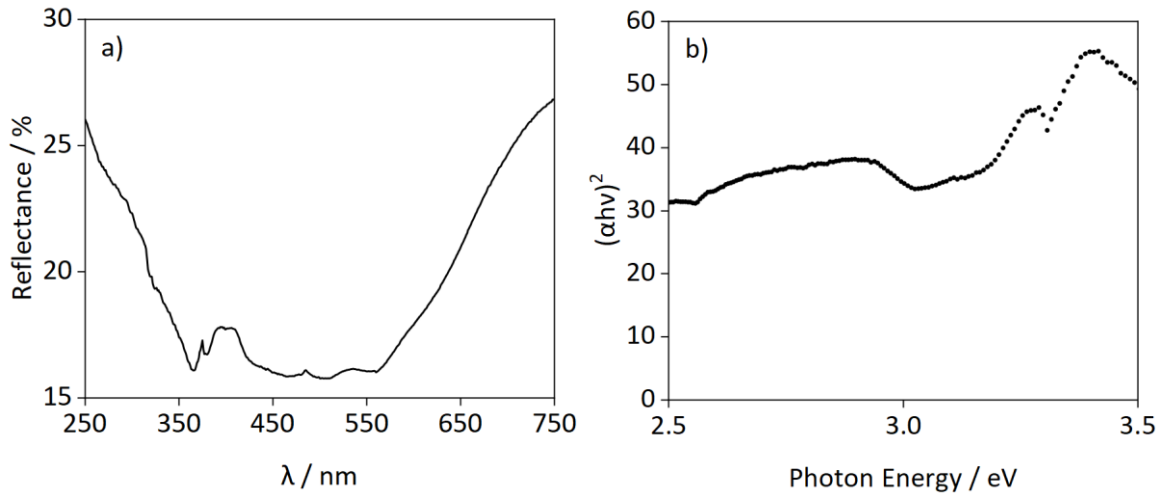

Figure 55 *UV-Vis spectrometry data for material with target composition $Sr_{2.95}Sc_2O_5Cu_2S_2$ after 36 hours of heating at 800 °C. Plot a) is the raw diffuse reflectance data, and plot b) is the associated magnified Tauc plot for this region where this material would be expected to show a drop-off in reflectance indicating an optical band gap, but does not. The lack of such drop-off makes estimating an optical band gap with this method impossible. This anomalous data point is therefore excluded from analyses in Chapter 3.*

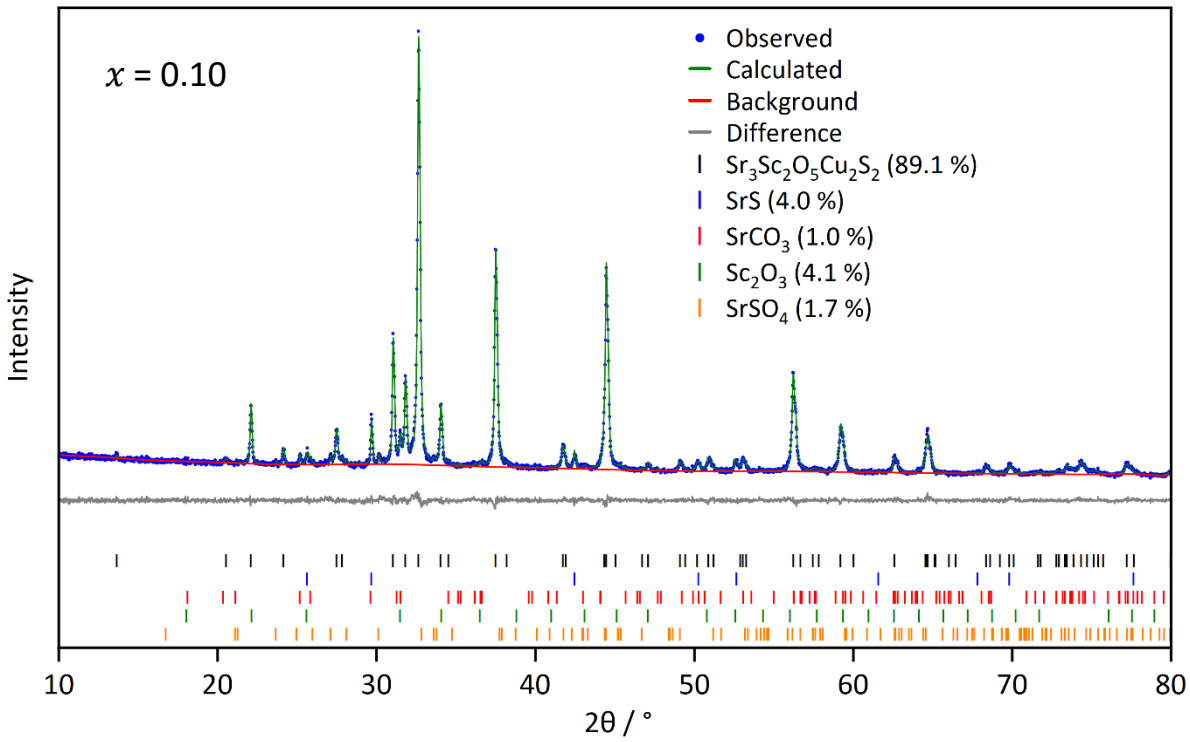

Figure 56 *Powder X-ray diffractogram of material with target composition $Sr_{2.90}Sc_2O_5Cu_2S_2$ (space group I4/mmm) after 36 hours of heating at 800 °C. The small blue circles represent the observed diffracted intensity, the green line represents the Rietveld-refined calculated model, the red line represents the background, and the grey line represents the difference between observed and calculated intensities. The black tick marks show the reflections of the refined model of $Sr_3Sc_2O_5Cu_2S_2$ (89.1 %), whilst the blue, red, green and orange tick marks represent refined impurity phases SrS (4.0 %), $SrCO_3$ (1.0 %), Sc_2O_3 (4.1 %) and $SrSO_4$ (1.7 %) respectively.*
Duration: 45 minutes. Data points: 3457. Interval: 0.02 °. GOF: 1.12. R_{wp}: 4.363 %.

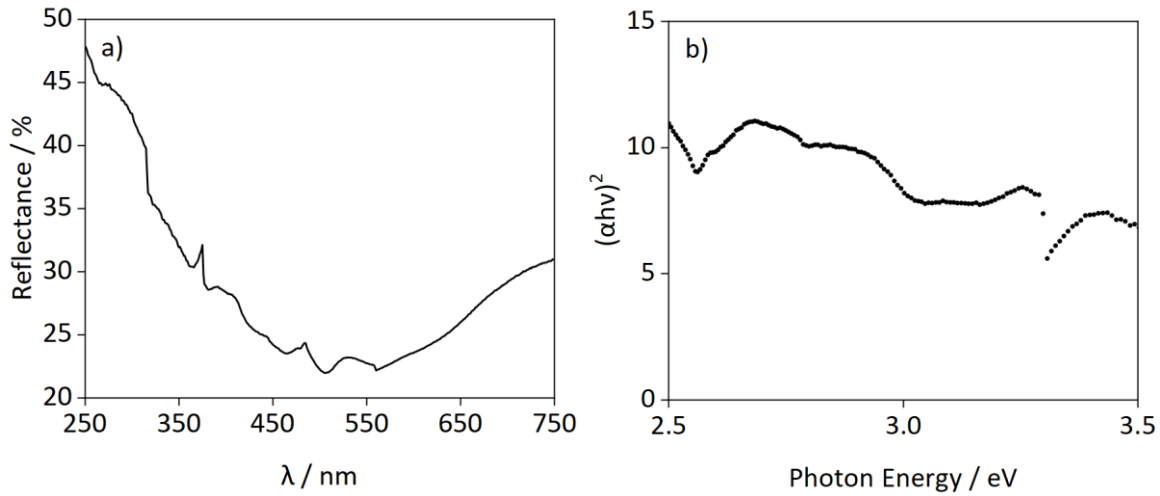

Figure 57 *UV-Vis spectrometry data for material with target composition $Sr_{2.90}Sc_2O_5Cu_2S_2$ after 36 hours of heating at 800 °C. Plot a) is the raw diffuse reflectance data, and plot b) is the associated magnified Tauc plot for this region where this material would be expected to show a drop-off in reflectance indicating an optical band gap, but does not. The lack of such drop-off makes estimating an optical band gap with this method impossible. This anomalous data point is therefore excluded from analyses in Chapter 3.*

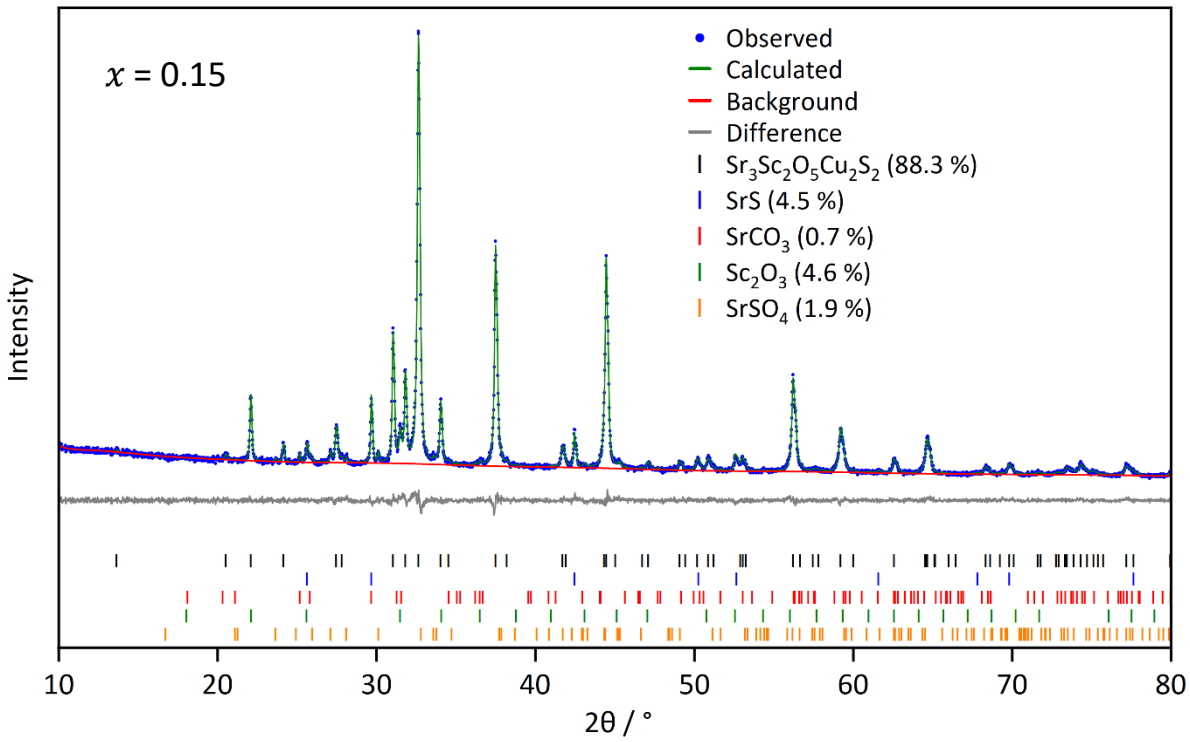

Figure 58 *Powder X-ray diffractogram of material with target composition $Sr_{2.85}Sc_2O_5Cu_2S_2$ (space group I4/mmm) after 36 hours of heating at 800 °C. The small blue circles represent the observed diffracted intensity, the green line represents the Rietveld-refined calculated model, the red line represents the background, and the grey line represents the difference between observed and calculated intensities. The black tick marks show the reflections of the refined model of $Sr_3Sc_2O_5Cu_2S_2$ (88.3 %), whilst the blue, red, green and orange tick marks represent refined impurity phases SrS (4.5 %), $SrCO_3$ (0.7 %), Sc_2O_3 (4.6 %) and $SrSO_4$ (1.9 %) respectively.*
Duration: 45 minutes. Data points: 3457. Interval: 0.02 °. GOF: 1.13. R_{wp}: 4.591 %.

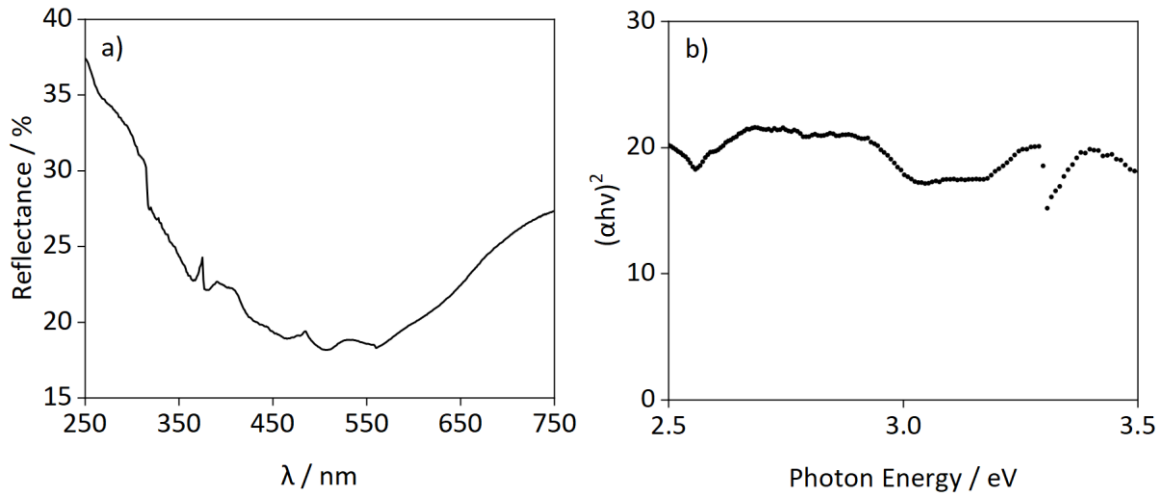

Figure 59 *UV-Vis spectrometry data for material with target composition $Sr_{2.85}Sc_2O_5Cu_2S_2$ after 36 hours of heating at 800 °C. Plot a) is the raw diffuse reflectance data, and plot b) is the associated magnified Tauc plot for this region where this material would be expected to show a drop-off in reflectance indicating an optical band gap, but does not. The lack of such drop-off makes estimating an optical band gap with this method impossible. This anomalous data point is therefore excluded from analyses in Chapter 3.*

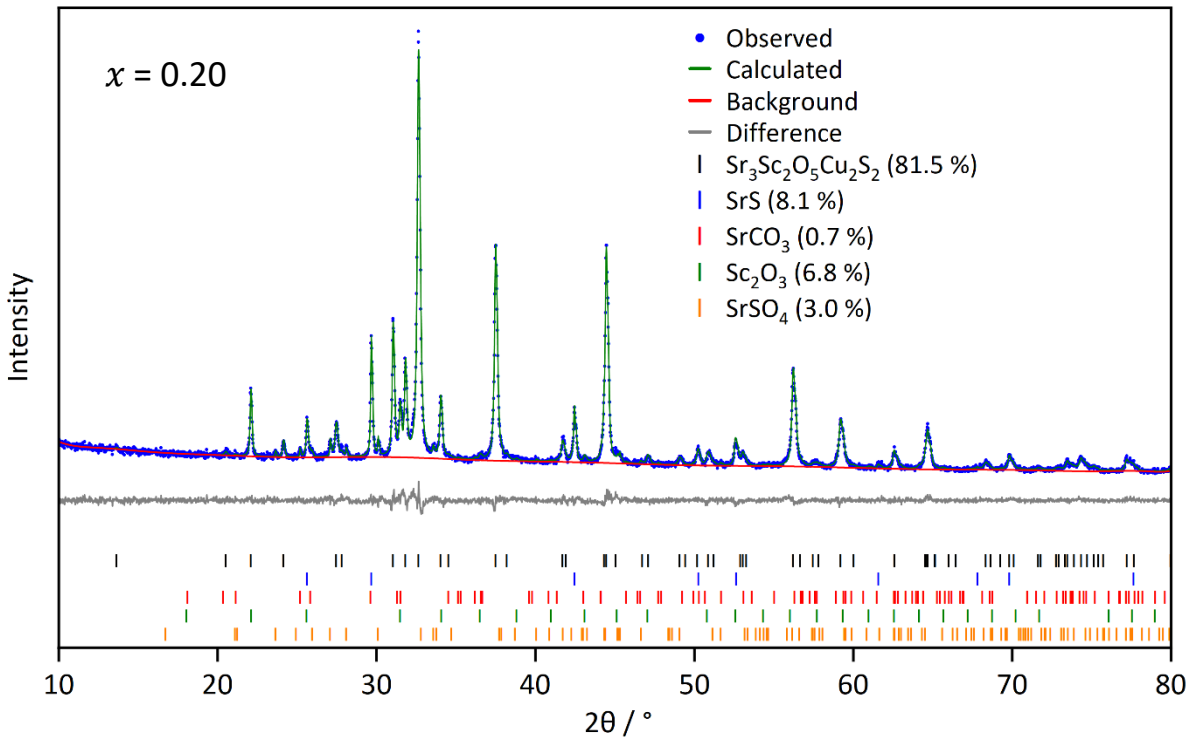

Figure 60 *Powder X-ray diffractogram of material with target composition $Sr_{2.80}Sc_2O_5Cu_2S_2$ (space group I4/mmm) after 36 hours of heating at 800 °C. The small blue circles represent the observed diffracted intensity, the green line represents the Rietveld-refined calculated model, the red line represents the background, and the grey line represents the difference between observed and calculated intensities. The black tick marks show the reflections of the refined model of $Sr_3Sc_2O_5Cu_2S_2$ (81.5 %), whilst the blue, red, green and orange tick marks represent refined impurity phases SrS (8.1 %), $SrCO_3$ (0.7 %), Sc_2O_3 (6.8 %) and $SrSO_4$ (3.0 %) respectively.*
Duration: 45 minutes. Data points: 3457. Interval: 0.02 °. GOF: 1.23. R_{wp}: 4.817 %.

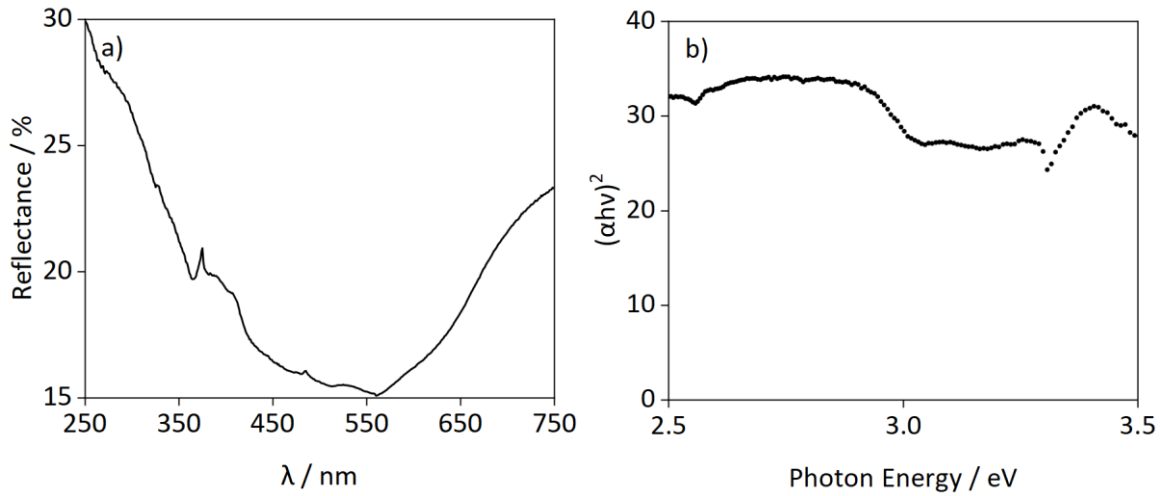

Figure 61 *UV-Vis spectrometry data for material with target composition $Sr_{2.80}Sc_2O_5Cu_2S_2$ after 36 hours of heating at 800 °C. Plot a) is the raw diffuse reflectance data, and plot b) is the associated magnified Tauc plot for this region where this material would be expected to show a drop-off in reflectance indicating an optical band gap, but does not. The lack of such drop-off makes estimating an optical band gap with this method impossible. This anomalous data point is therefore excluded from analyses in Chapter 3.*

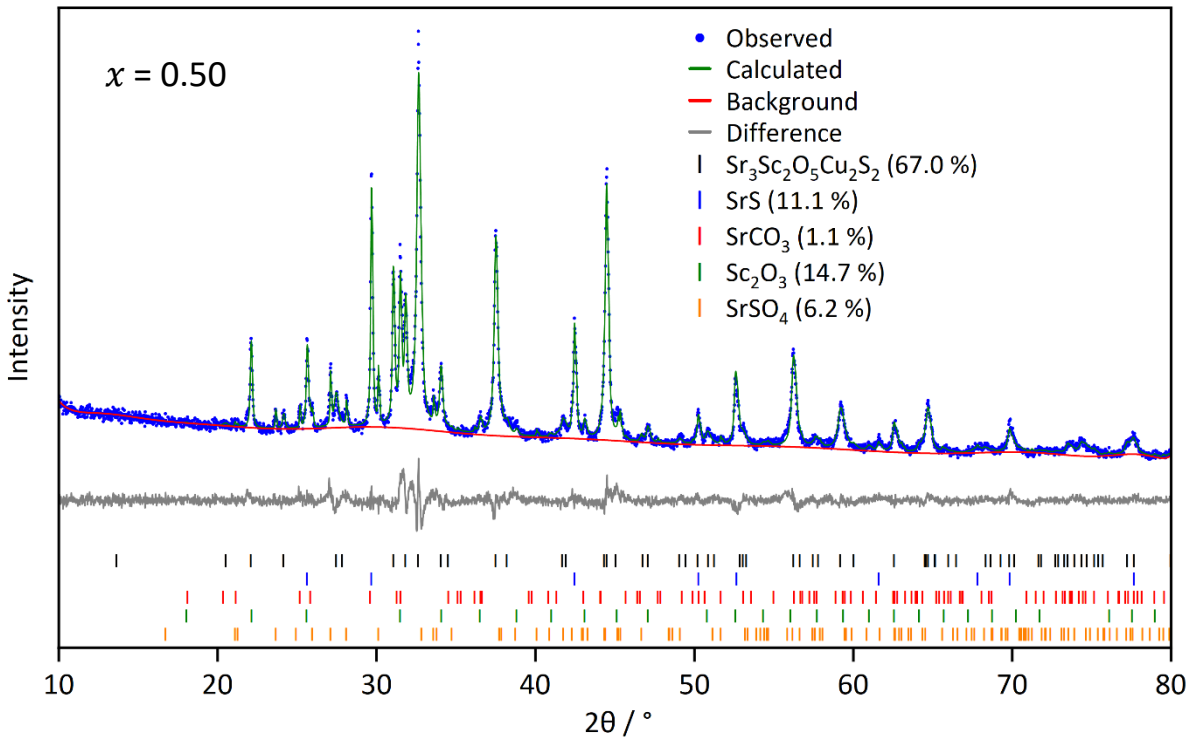

Figure 62 *Powder X-ray diffractogram of material with target composition $Sr_{2.50}Sc_2O_5Cu_2S_2$ (space group I4/mmm) after 36 hours of heating at 800 °C. The small blue circles represent the observed diffracted intensity, the green line represents the Rietveld-refined calculated model, the red line represents the background, and the grey line represents the difference between observed and calculated intensities. The black tick marks show the reflections of the refined model of $Sr_3Sc_2O_5Cu_2S_2$ (67.0 %), whilst the blue, red, green and orange tick marks represent refined impurity phases SrS (11.1 %), $SrCO_3$ (1.1 %), Sc_2O_3 (14.7 %) and $SrSO_4$ (6.2 %) respectively.*
Duration: 45 minutes. Data points: 3457. Interval: 0.02 °. GOF: 1.48. R_{wp}: 5.699 %.

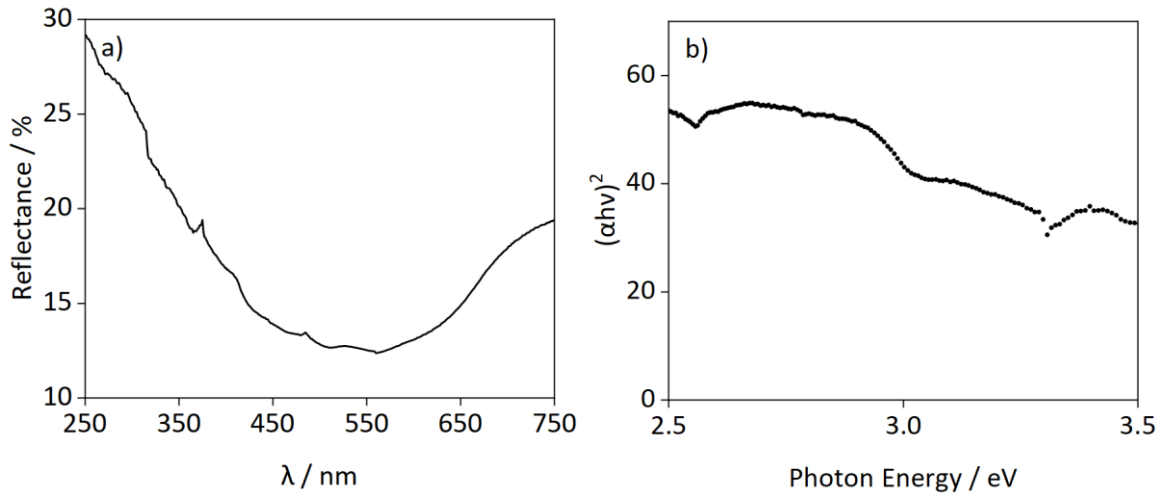

Figure 63 *UV-Vis spectrometry data for material with target composition $Sr_{2.50}Sc_2O_5Cu_2S_2$ after 36 hours of heating at 800 °C. Plot a) is the raw diffuse reflectance data, and plot b) is the associated magnified Tauc plot for this region where this material would be expected to show a drop-off in reflectance indicating an optical band gap, but does not. The lack of such drop-off makes estimating an optical band gap with this method impossible. This anomalous data point is therefore excluded from analyses in Chapter 3.*

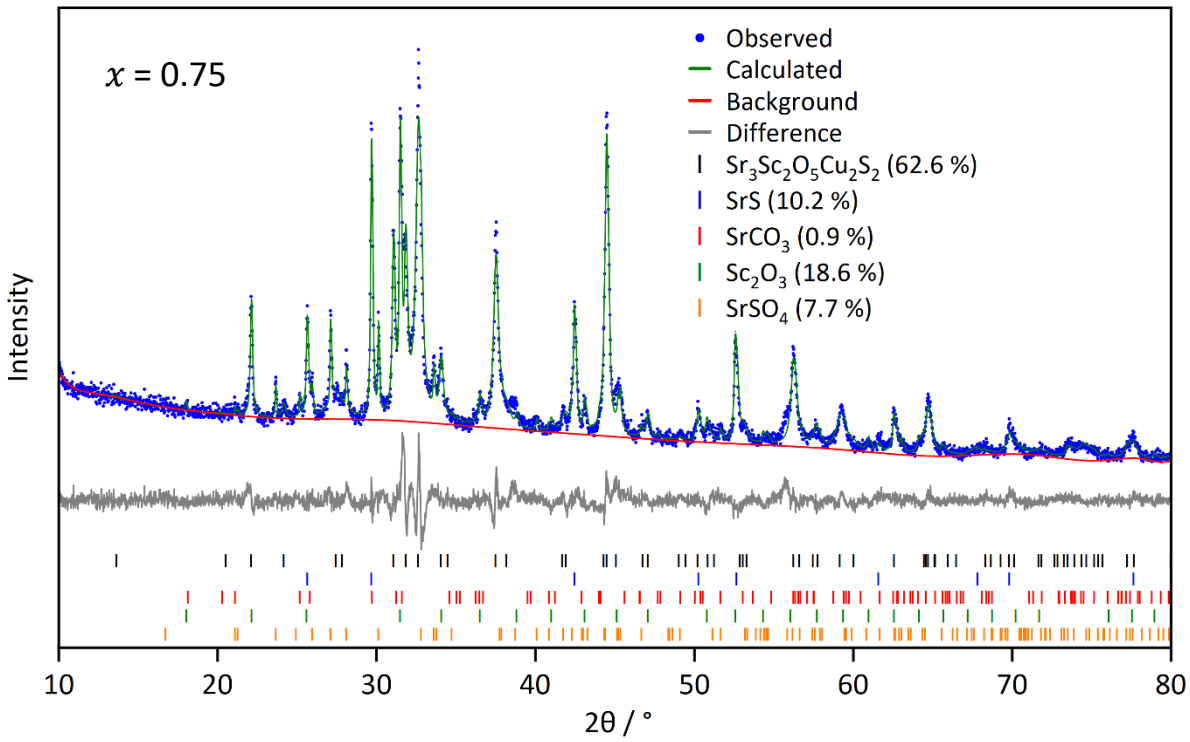

Figure 64 *Powder X-ray diffractogram of material with target composition $Sr_{2.25}Sc_2O_5Cu_2S_2$ (space group I4/mmm) after 36 hours of heating at 800 °C. The small blue circles represent the observed diffracted intensity, the green line represents the Rietveld-refined calculated model, the red line represents the background, and the grey line represents the difference between observed and calculated intensities. The black tick marks show the reflections of the refined model of $Sr_3Sc_2O_5Cu_2S_2$ (62.6 %), whilst the blue, red, green and orange tick marks represent refined impurity phases SrS (10.2 %), $SrCO_3$ (0.9 %), Sc_2O_3 (18.6 %) and $SrSO_4$ (7.7 %) respectively.*
Duration: 45 minutes. Data points: 3457. Interval: 0.02 °. GOF: 1.57. R_{wp}: 6.167 %.

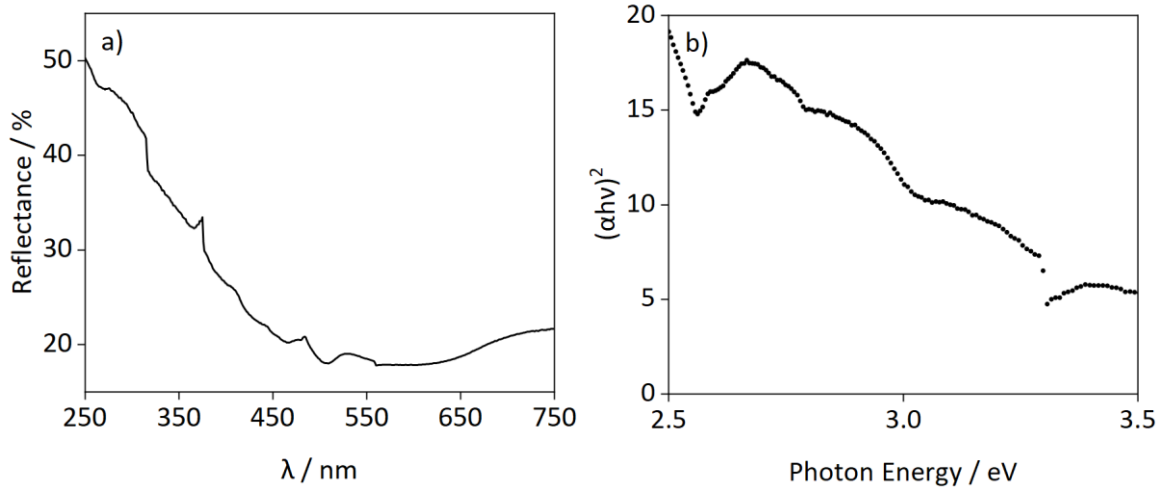

Figure 65 *UV-Vis spectrometry data for material with target composition $Sr_{2.25}Sc_2O_5Cu_2S_2$ after 36 hours of heating at 800 °C. Plot a) is the raw diffuse reflectance data, and plot b) is the associated magnified Tauc plot for this region where this material would be expected to show a drop-off in reflectance indicating an optical band gap, but does not. The lack of such drop-off makes estimating an optical band gap with this method impossible. This anomalous data point is therefore excluded from analyses in Chapter 3.*

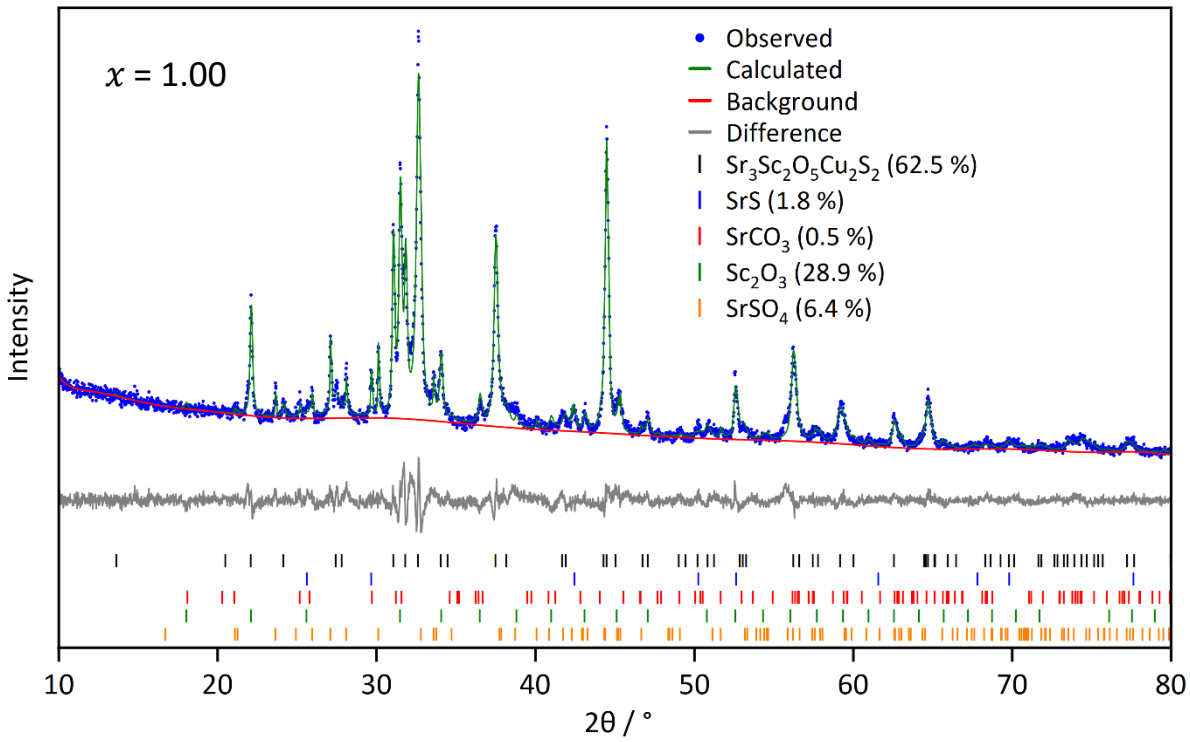

Figure 66 *Powder X-ray diffractogram of material with target composition $Sr_{2.00}Sc_2O_5Cu_2S_2$ (space group I4/mmm) after 36 hours of heating at 800 °C. The small blue circles represent the observed diffracted intensity, the green line represents the Rietveld-refined calculated model, the red line represents the background, and the grey line represents the difference between observed and calculated intensities. The black tick marks show the reflections of the refined model of $Sr_3Sc_2O_5Cu_2S_2$ (62.5 %), whilst the blue, red, green and orange tick marks represent refined impurity phases SrS (1.8 %), $SrCO_3$ (0.5 %), Sc_2O_3 (28.9 %) and $SrSO_4$ (6.4 %) respectively.*
Duration: 45 minutes. Data points: 3457. Interval: 0.02 °. GOF: 1.54. R_{wp}: 6.080 %.

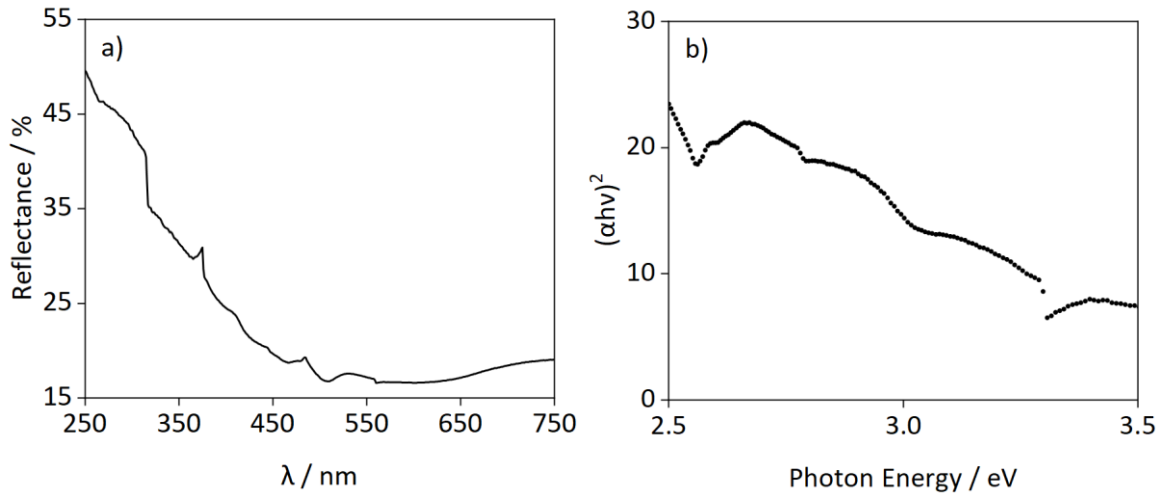

Figure 67 *UV-Vis spectrometry data for material with target composition $Sr_{2.00}Sc_2O_5Cu_2S_2$ after 36 hours of heating at 800 °C. Plot a) is the raw diffuse reflectance data, and plot b) is the associated magnified Tauc plot for this region where this material would be expected to show a drop-off in reflectance indicating an optical band gap, but does not. The lack of such drop-off makes estimating an optical band gap with this method impossible. This anomalous data point is therefore excluded from analyses in Chapter 3.*

B.1.4 Potassium doped 325 selenide MALMs, $(Sr_{3-x}K_x)Sc_2O_5Cu_2Se_2$

Table 26 Tabulated structural data of the potassium doped 325 selenide MALMs with general formula $(Sr_{3-x}K_x)Sc_2O_5Cu_2Se_2$. The pristine material $Sr_3Sc_2O_5Cu_2Se_2$ is included as a reference. All values are derived from the Rietveld refinement of PXRD data using GSAS-II. Note that because all materials listed are tetragonal (space group I4/mmm), the b parameter is identical to a, and thus omitted.

x / mol	Target Composition	a / Å	c / Å	Volume / Å^3
0 (pristine)	$Sr_3Sc_2O_5Cu_2Se_2$	4.10329(4)	26.6847(3)	449.290(12)
0.025	$(Sr_{2.975}K_{0.025})Sc_2O_5Cu_2Se_2$	4.10322(5)	26.6844(5)	449.271(9)
0.050	$(Sr_{2.950}K_{0.050})Sc_2O_5Cu_2Se_2$	4.10305(8)	26.6930(7)	449.376(25)
0.075	$(Sr_{2.925}K_{0.075})Sc_2O_5Cu_2Se_2$	4.10263(8)	26.6910(7)	449.252(24)
0.100	$(Sr_{2.900}K_{0.100})Sc_2O_5Cu_2Se_2$	4.10287(8)	26.6927(7)	449.333(25)
0.125	$(Sr_{2.875}K_{0.125})Sc_2O_5Cu_2Se_2$	4.10283(9)	26.6951(8)	449.364(27)
0.150	$(Sr_{2.850}K_{0.150})Sc_2O_5Cu_2Se_2$	4.10331(8)	26.6851(7)	449.301(24)
0.175	$(Sr_{2.825}K_{0.175})Sc_2O_5Cu_2Se_2$	4.10308(5)	26.6901(5)	449.334(9)
0.200	$(Sr_{2.800}K_{0.200})Sc_2O_5Cu_2Se_2$	4.10378(6)	26.6926(6)	449.531(20)
0.300	$(Sr_{2.700}K_{0.300})Sc_2O_5Cu_2Se_2$	4.10394(6)	26.6912(5)	449.542(19)
0.400	$(Sr_{2.600}K_{0.400})Sc_2O_5Cu_2Se_2$	4.10404(8)	26.6901(8)	449.545(26)
0.500	$(Sr_{2.500}K_{0.500})Sc_2O_5Cu_2Se_2$	4.10414(8)	26.6878(7)	449.527(26)
0.750	$(Sr_{2.250}K_{0.750})Sc_2O_5Cu_2Se_2$	4.10412(12)	26.6866(11)	449.500(40)
1.000	$(Sr_{2.000}K_{1.000})Sc_2O_5Cu_2Se_2$	4.10474(16)	26.6856(16)	449.620(50)

Table 27 Tabulated compositional data of the potassium doped 325 selenide MALMs with general formula $(Sr_{3-x}K_x)Sc_2O_5Cu_2Se_2$. The pristine material $Sr_3Sc_2O_5Cu_2Se_2$ is included as a reference. All values are cited as a weight percent (wt %) of the total weight, and are derived from the Rietveld refinement of PXRD data using GSAS-II.

x / mol	Target phase / wt %	SrSe / wt %	$SrCO_3$ / wt %	KCu_3Se_2 / wt %	$SrSc_2O_4$ / wt %	$K_3Cu_8Se_6$ / wt %
0 (pristine)	99.1	0.5	0.4	-	-	-
0.025	99.4	0.6	-	-	-	-
0.050	99.3	0.7	-	-	-	-
0.075	98.4	1.0	0.6	-	-	-
0.100	98.2	1.1	0.6	-	-	-
0.125	97.4	0.9	0.5	1.2	-	-
0.150	96.7	1.5	0.9	0.9	-	-
0.175	96.6	2.0	0.8	0.6	-	-
0.200	99.2	0.8	-	-	-	-
0.300	96.9	0.3	1.2	1.6	-	-
0.400	94.8	1.2	1.0	3.0	-	-
0.500	86.6	0.9	0.4	2.5	9.7	-
0.750 *	60.4	1.3	4.4	14.8	19.1	-
1.000 *	39.0	0.2	3.7	13.3	35.0	8.9

* Indicates that the sample also contained traces of an unknown impurity phase(s) distinct from those detailed above

Table 28 Tabulated data on both the target and maximum actual dopant content of the potassium doped 325 selenide MALMs with general formula $(Sr_{3-x}K_x)Sc_2O_5Cu_2Se_2$. The pristine material $Sr_3Sc_2O_5Cu_2Se_2$ is included as a reference. The minimum possible amount of total K contained within impurities was extracted from the refined wt % of KCu_3Se_2 and $K_3Cu_8Se_6$ from GSAS-II. The remaining K content is the maximum possible K within the MALM.

Target x / mol	Target x / wt %	Minimum K in impurities / %	Maximum K in product / %	Maximum x / mol
0 (pristine)	0.000	0.000	100.000	0.000
0.025	0.136	0.000	100.000	0.025
0.050	0.273	0.000	100.000	0.050
0.075	0.411	0.000	100.000	0.075
0.100	0.548	0.000	100.000	0.100
0.125	0.687	17.625	82.375	0.103
0.150	0.825	10.997	89.003	0.134
0.175	0.965	6.273	93.727	0.164
0.200	1.104	0.000	100.000	0.200
0.300	1.668	9.675	90.325	0.271
0.400	2.239	13.511	86.489	0.346
0.500	2.819	8.945	91.055	0.455
0.750	4.304	34.686	65.314	0.490
1.000	5.842	39.215	60.785	0.608

Table 29 Tabulated analytical data of to the measured properties of the potassium doped 325 selenide MALMs with general formula $(Sr_{3-x}K_x)Sc_2O_5Cu_2Se_2$. The pristine material $Sr_3Sc_2O_5Cu_2Se_2$ is included as a reference. Optical band gaps were estimated from UV-Vis data. Pellet densities were estimated from the mass and volume of annealed pellet samples, and are cited as a relative percentage of the bulk crystal. Resistivities and conductivities were estimated from 4 probe van der Pauw analysis of the pellet samples.

x / mol	Band Gap / eV	Pellet Density / %	Raw Resistivities from 4-Probe measurement, for each probe permutation / kΩ								Resistivity / Ω cm	Conductivity / S cm^{-1}
			1	2	3	4	5	6	7	8		
0 (pristine)	2.94	71.72	1.20 E+01	1.21 E+01	1.22 E+01	1.22 E+01	1.03 E+01	1.02 E+01	1.02 E+01	1.01 E+01	3.83 E+03	2.61 E-04
0.025	2.89	68.49	1.00 E+00	9.80 E-01	9.80 E-01	9.80 E-01	1.69 E+00	1.68 E+00	1.68 E+00	1.69 E+00	4.72 E+02	2.12 E-03
0.050	2.91	68.62	4.10 E-01	4.20 E-01	4.20 E-01	3.90 E-01	4.40 E-01	4.55 E-01	4.55 E-01	4.50 E-01	1.58 E+02	6.34 E-03
0.075	2.90	69.52	2.70 E-01	2.80 E-01	2.70 E-01	2.81 E-01	2.20 E-01	2.20 E-01	2.00 E-01	2.00 E-01	8.63 E+01	1.16 E-02
0.100	2.91	70.72	4.80 E-02	4.70 E-02	4.60 E-02	4.50 E-02	5.70 E-02	5.80 E-02	5.80 E-02	5.90 E-02	1.84 E+01	5.44 E-02
0.125	2.90	68.82	1.10 E-02	1.30 E-02	1.30 E-02	1.40 E-02	2.80 E-02	2.70 E-02	2.70 E-02	2.50 E-02	6.75 E+00	1.48 E-01
0.150	2.89	69.43	1.25 E-02	1.27 E-02	1.27 E-02	1.26 E-02	9.20 E-03	9.27 E-03	9.25 E-03	9.23 E-03	3.88 E+00	2.58 E-01
0.175	2.87 ‡	66.64	1.52 E-02	1.51 E-02	1.53 E-02	1.53 E-02	3.35 E-03	2.71 E-03	3.35 E-03	3.26 E-03	2.76 E+00	3.62 E-01
0.200	2.91	72.14	8.90 E-03	8.90 E-03	8.90 E-03	8.90 E-03	6.20 E-03	6.20 E-03	6.20 E-03	6.20 E-03	8.90 E-03	3.40E-01
0.300	2.90	68.77	3.60 E-03	1.60 E-03	3.10 E-03	1.03 E-02	5.00 E-03	8.50 E-03	1.60 E-03	2.20 E-03	1.67 E+00	6.00 E-01
0.400	2.90	72.11	1.66 E-03	8.60 E-03	1.32 E-03	9.50 E-04	1.00 E-03	7.90 E-03	1.13 E-03	1.40 E-03	1.06 E+00	9.45 E-01
0.500	2.88	67.53	2.70 E-04	2.70 E-04	2.68 E-04	2.68 E-04	3.30 E-04	3.28 E-04	3.26 E-04	3.25 E-04	1.13 E-01	3.05 E+00
0.750	2.83	71.98	8.33 E-04	8.40 E-04	8.45 E-04	8.53 E-04	8.97 E-04	8.80 E-04	8.86 E-04	8.57 E-04	3.28 E-01	8.84 E+00
1.000	*n/a* †	62.67	1.87 E-04	1.86 E-04	1.85 E-04	1.89 E-04	1.62 E-04	1.61 E-04	1.58 E-04	1.63 E-04	6.92 E-02	1.44 E+01

† A band gap estimation for this sample was not possible due to a lack of drop-off in reflectance between the UV and visible regions. The sample was either too impure or too dark in colour for any difference to be justified, and the Tauc plot was deemed too subjective for the usual tangent approximation.

‡ Data for this sample was collected at a lower data resolution than all others (5nm vs 1nm) as the sample was submitted to the ISIS Neutron and Muon Source and therefore unavailable for later data recollection. This data point is not considered accurate and was excluded from analyses in the corresponding work in *Chapter 3*.

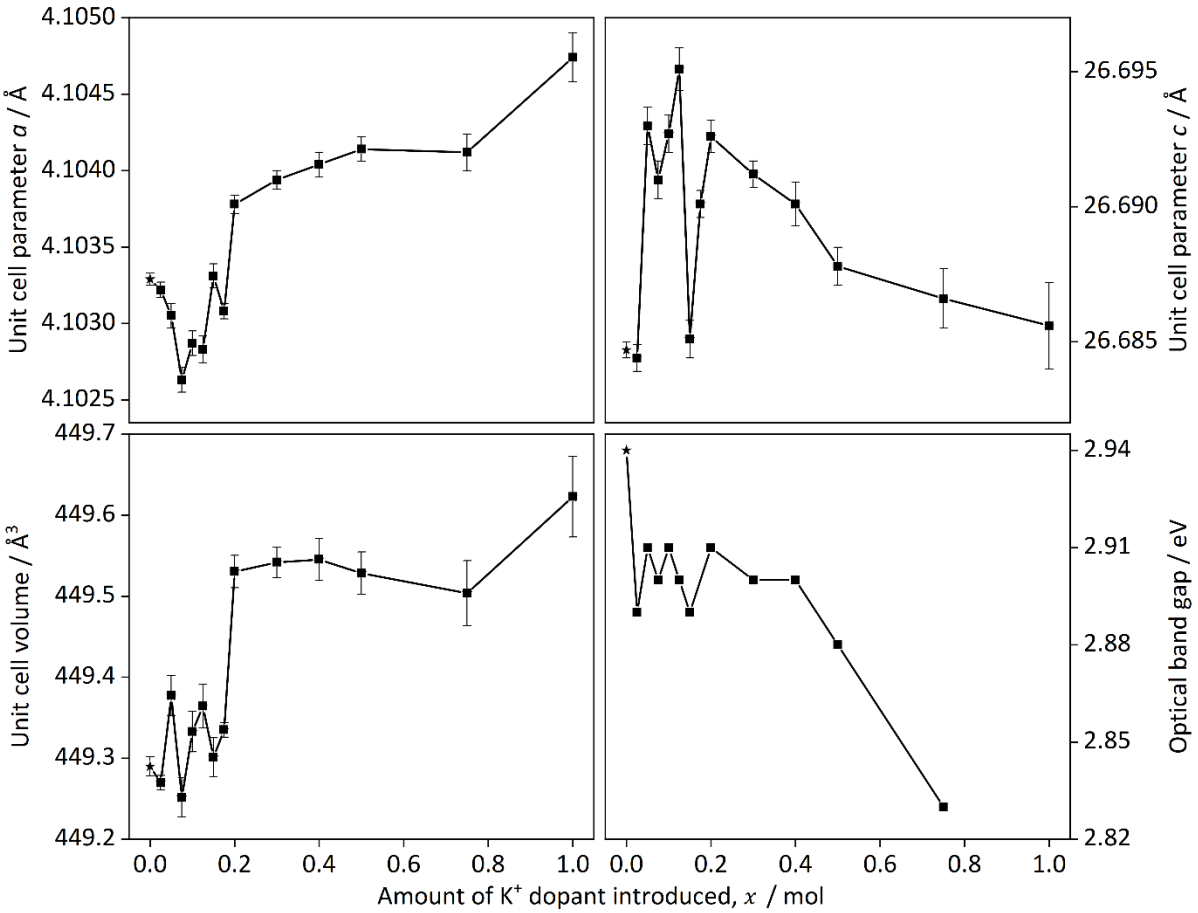

Figure 68 *Comparisons of a) the α unit cell parameter, b) the c unit cell parameter, c) unit cell volume, and d) the optical band gap, of the potassium doped 325 selenide MALMs with general formula $(Sr_{3-x}K_x)Sc_2O_5Cu_2Se_2$. The pristine material $Sr_3Sc_2O_5Cu_2Se_2$ is included as a reference at $x = 0$ mol and is represented by a star. The $x = 0.175$ mol sample band gap was omitted for consistency as it was recorded at a different resolution, and the $x = 1.000$ mol sample band gap is missing due to lack of drop-off in diffuse reflectance, see Table 29.*

Figure 69 *A photographic comparison of the colour of the potassium doped 325 selenide MALMs with general formula $(Sr_{3-x}K_x)Sc_2O_5Cu_2Se_2$. Dopant concentration increases from left to right. The sample where $x = 0.175$ mol is absent from this photograph as it was sent to the ISIS Neutron and Muon Source for Neutron Powder Diffraction at the time of writing.*

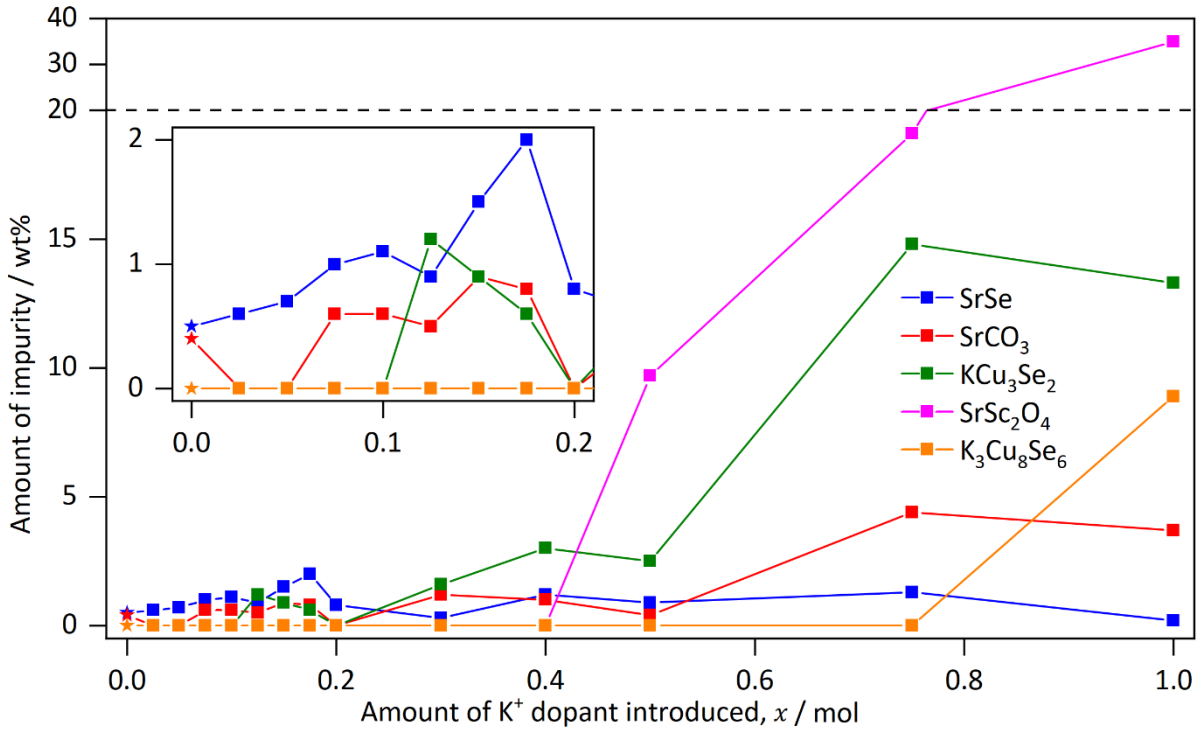

Figure 70 *The weight percentages of five impurity phases present in the potassium doped 325 selenide MALMs with general formula $(Sr_{3-x}K_x)Sc_2O_5Cu_2Se_2$. The inset plot is a magnification of the x = 0 to 0.200 mol region where doping and impurity quantities are low. The pristine material $Sr_3Sc_2O_5Cu_2Se_2$ is included as a reference at x = 0 mol and is represented by a star. Note the change in y-axis scaling at 20 wt %.*

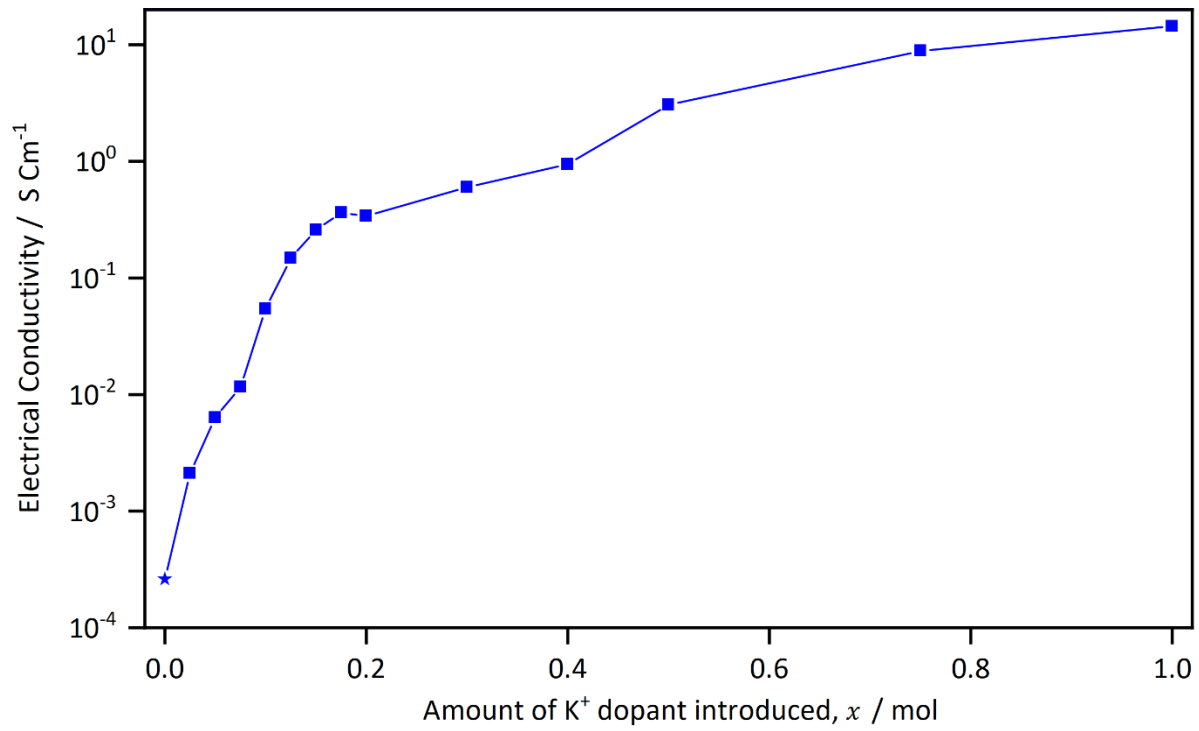

Figure 71 *The electrical conductivities of the potassium doped 325 selenide MALMs with general formula $(Sr_{3-x}K_x)Sc_2O_5Cu_2Se_2$. represented on a log_{10} scale. The pristine material $Sr_3Sc_2O_5Cu_2Se_2$ is included as a reference at x = 0 mol and is represented by a star. All values are derived from van der Pauw 4 probe resistivity measurements of 8mm diameter annealed pellet samples.*

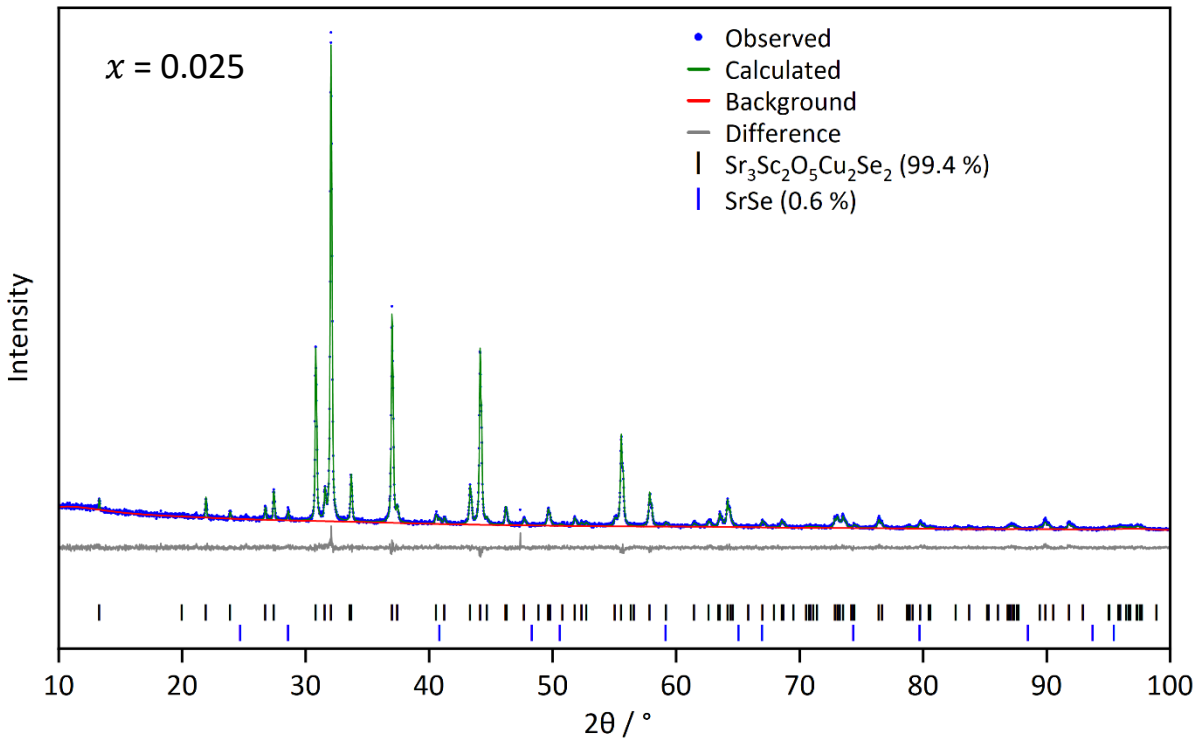

Figure 72 *Powder X-ray diffractogram of material with target composition $(Sr_{2.975}K_{0.025})Sc_2O_5Cu_2Se_2$ (space group I4/mmm) after 36 hours of heating at 800 °C. The small blue circles represent the observed diffracted intensity, the green line represents the Rietveld-refined calculated model, the red line represents the background, and the grey line represents the difference between observed and calculated intensities. The black tick marks show the reflections of the refined model of $Sr_3Sc_2O_5Cu_2Se_2$ (99.4 %), whilst the blue tick marks represent refined impurity phase SrSe (0.6 %).*
Duration: 45 minutes. Data points: 4444. Interval: 0.02 °. GOF: 1.11. R_{wp}: 6.050 %.

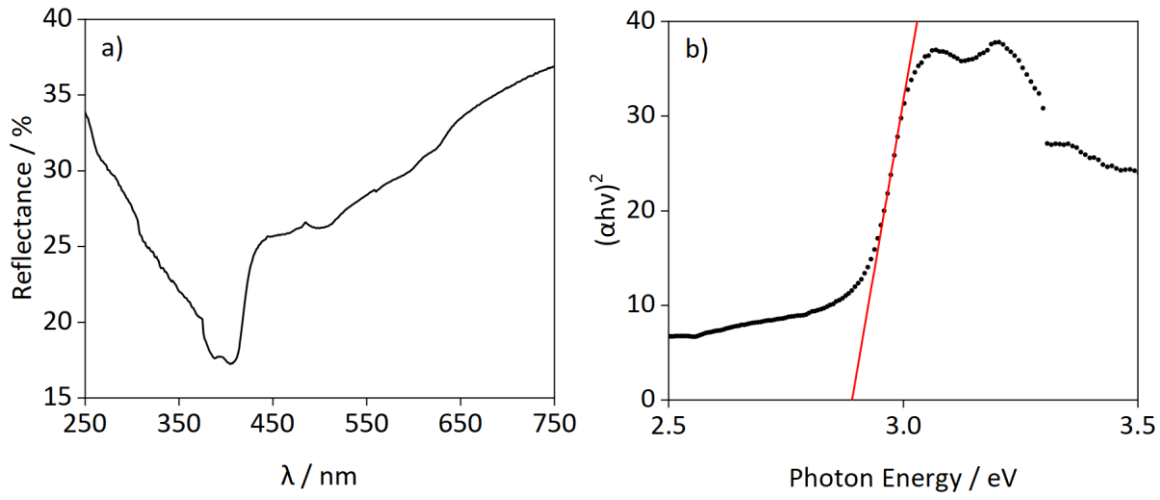

Figure 73 *UV-Vis spectrometry data for material with target composition $(Sr_{2.975}K_{0.025})Sc_2O_5Cu_2Se_2$ after 36 hours of heating at 800 °C. Plot a) is the raw diffuse reflectance data, and plot b) is the associated magnified Tauc plot for this region, where the intercept between the red extrapolated tangent line and the x-axis is used to estimate an optical band gap of 2.89 eV, which corresponds to 429 nm.*

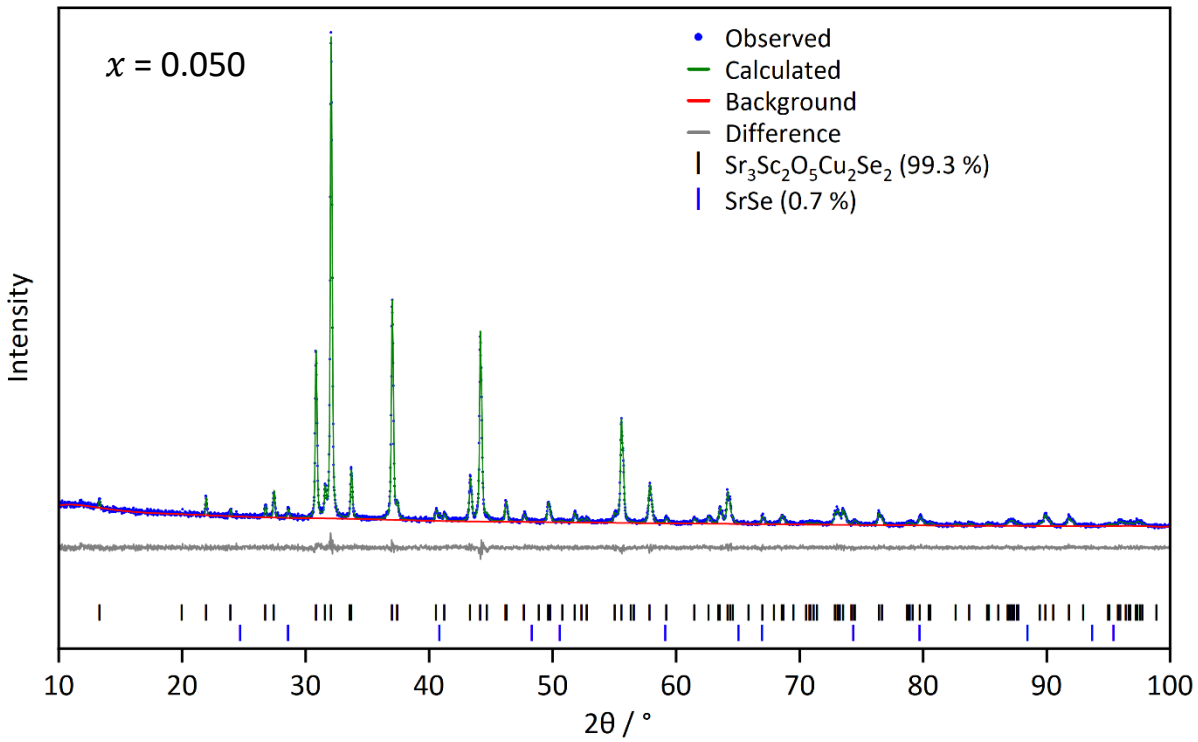

Figure 74 *Powder X-ray diffractogram of material with target composition $(Sr_{2.950}K_{0.050})Sc_2O_5Cu_2Se_2$ (space group I4/mmm) after 36 hours of heating at 800 °C. The small blue circles represent the observed diffracted intensity, the green line represents the Rietveld-refined calculated model, the red line represents the background, and the grey line represents the difference between observed and calculated intensities. The black tick marks show the reflections of the refined model of $Sr_3Sc_2O_5Cu_2Se_2$ (99.3 %), whilst the blue tick marks represent refined impurity phase SrSe (0.7 %).*
Duration: 45 minutes. Data points: 4444. Interval: 0.02 °. GOF: 1.05. R_{wp}: 5.505 %.

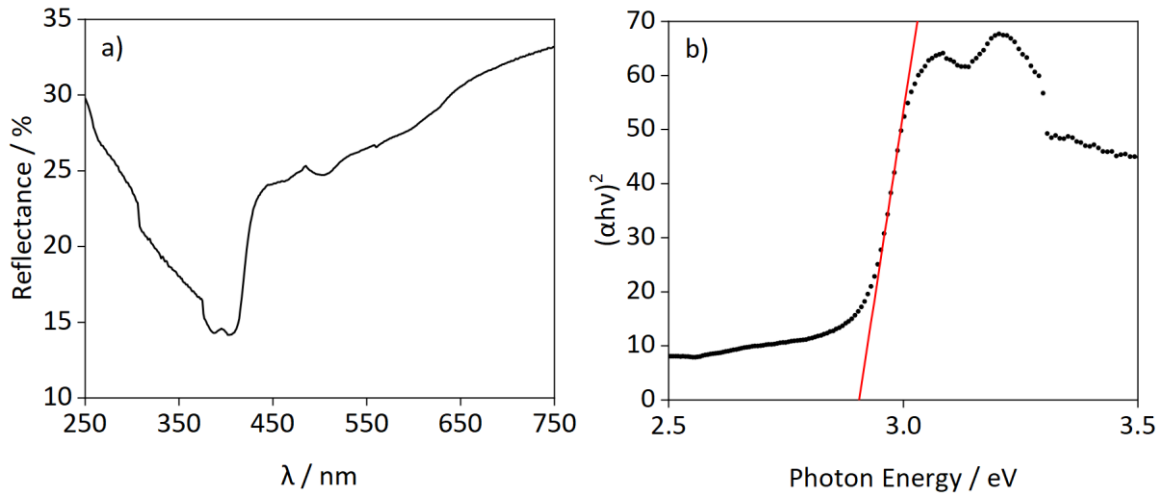

Figure 75 *UV-Vis spectrometry data for material with target composition $(Sr_{2.950}K_{0.050})Sc_2O_5Cu_2Se_2$ after 36 hours of heating at 800 °C. Plot a) is the raw diffuse reflectance data, and plot b) is the associated magnified Tauc plot for this region, where the intercept between the red extrapolated tangent line and the x-axis is used to estimate an optical band gap of 2.91 eV, which corresponds to 426 nm.*

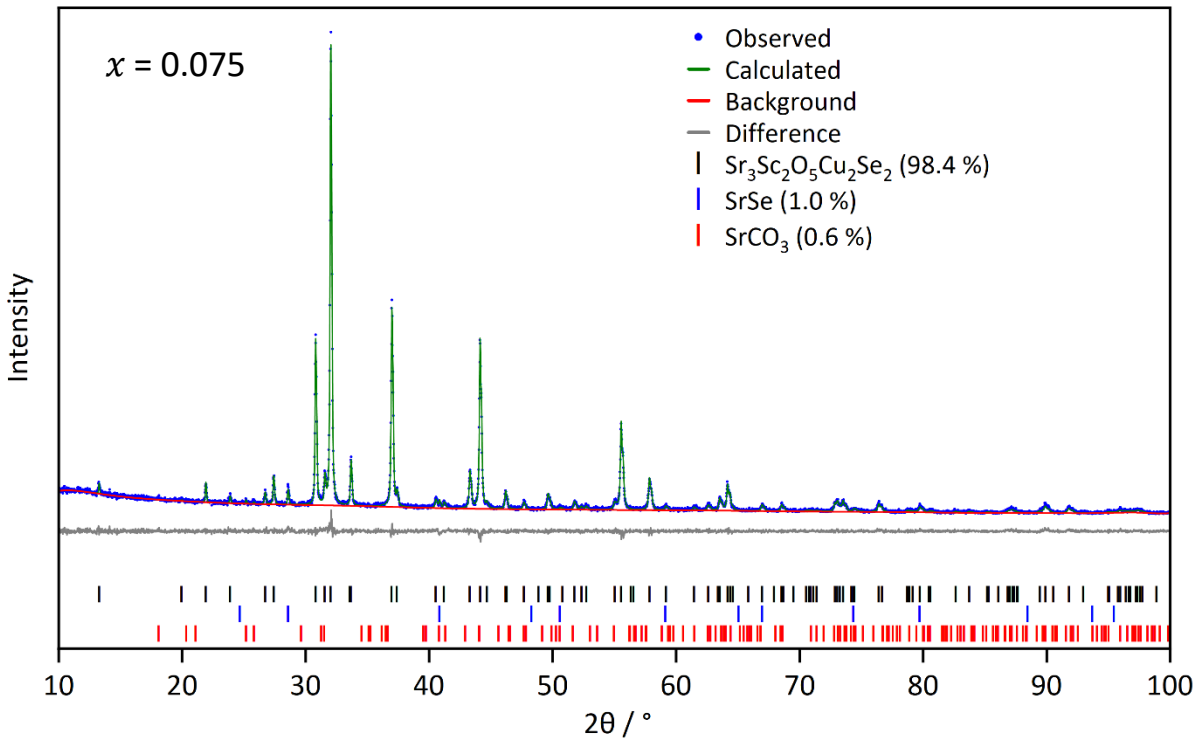

Figure 76 *Powder X-ray diffractogram of material with target composition $(Sr_{2.925}K_{0.075})Sc_2O_5Cu_2Se_2$ (space group I4/mmm) after 36 hours of heating at 800 °C. The small blue circles represent the observed diffracted intensity, the green line represents the Rietveld-refined calculated model, the red line represents the background, and the grey line represents the difference between observed and calculated intensities. The black tick marks show the reflections of the refined model of $Sr_3Sc_2O_5Cu_2Se_2$ (98.4 %), whilst the blue and red tick marks represent refined impurity phases SrSe (1.0 %), and $SrCO_3$ (0.6 %) respectively.*
Duration: 45 minutes. Data points: 4444. Interval: 0.02 °. GOF: 1.08. R_{wp}: 5.893 %.

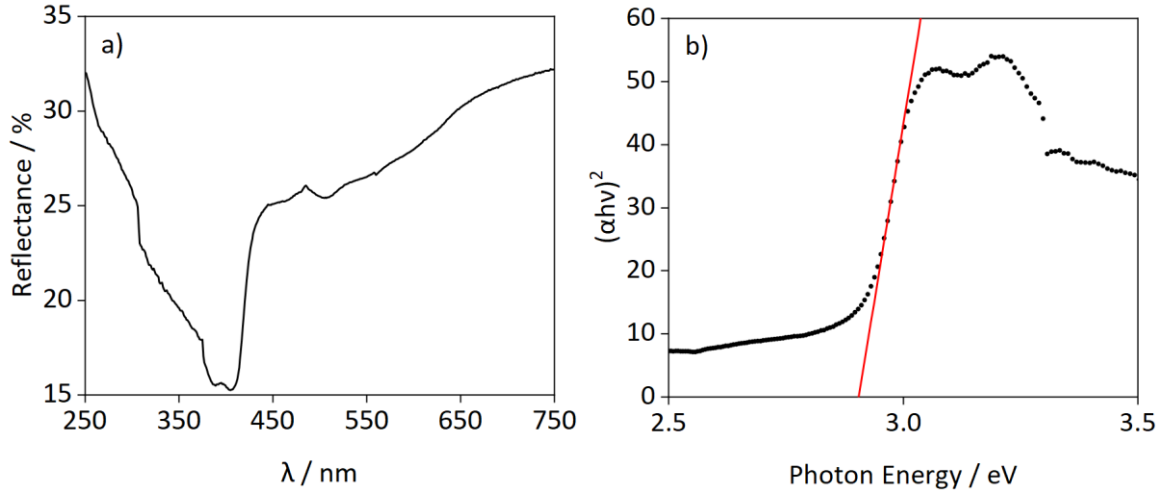

Figure 77 *UV-Vis spectrometry data for material with target composition $(Sr_{2.925}K_{0.075})Sc_2O_5Cu_2Se_2$ after 36 hours of heating at 800 °C. Plot a) is the raw diffuse reflectance data, and plot b) is the associated magnified Tauc plot for this region, where the intercept between the red extrapolated tangent line and the x-axis is used to estimate an optical band gap of 2.90 eV, which corresponds to 428 nm.*

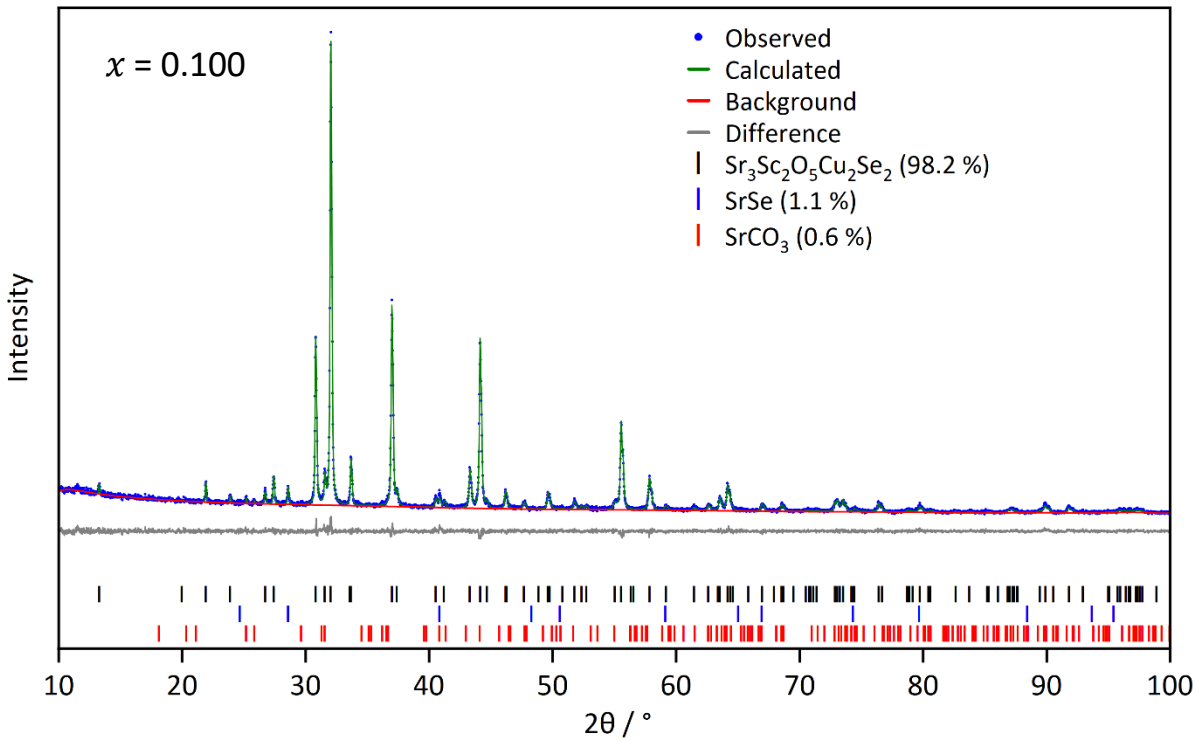

Figure 78 *Powder X-ray diffractogram of material with target composition $(Sr_{2.900}K_{0.100})Sc_2O_5Cu_2Se_2$ (space group I4/mmm) after 36 hours of heating at 800 °C. The small blue circles represent the observed diffracted intensity, the green line represents the Rietveld-refined calculated model, the red line represents the background, and the grey line represents the difference between observed and calculated intensities. The black tick marks show the reflections of the refined model of $Sr_3Sc_2O_5Cu_2Se_2$ (98.2 %), whilst the blue and red tick marks represent refined impurity phases SrSe (1.1 %), and $SrCO_3$ (0.6 %) respectively.*
Duration: 45 minutes. Data points: 4444. Interval: 0.02 °. GOF: 1.10. R_{wp}: 6.053 %.

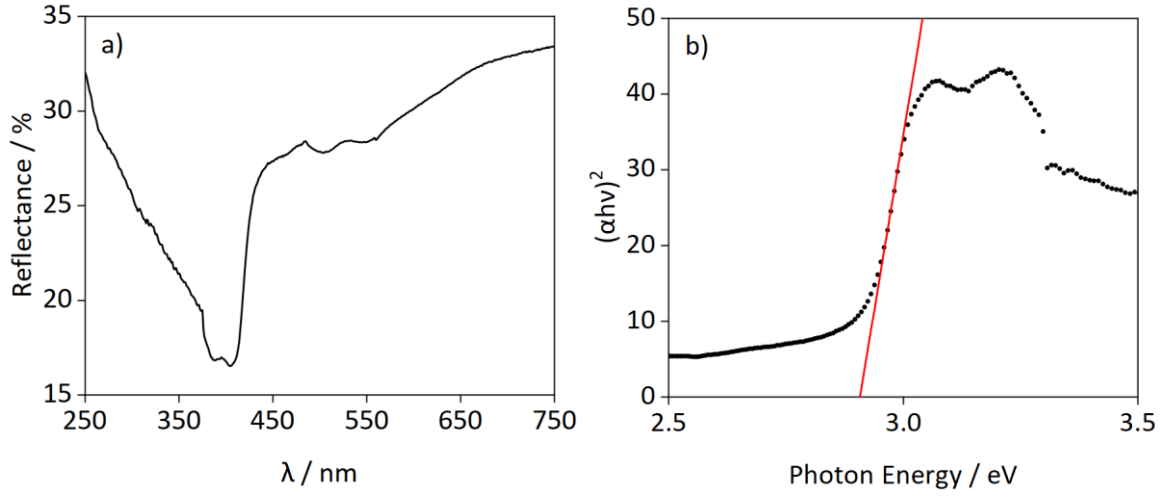

Figure 79 *UV-Vis spectrometry data for material with target composition $(Sr_{2.900}K_{0.100})Sc_2O_5Cu_2Se_2$ after 36 hours of heating at 800 °C. Plot a) is the raw diffuse reflectance data, and plot b) is the associated magnified Tauc plot for this region, where the intercept between the red extrapolated tangent line and the x-axis is used to estimate an optical band gap of 2.91 eV, which corresponds to 426 nm.*

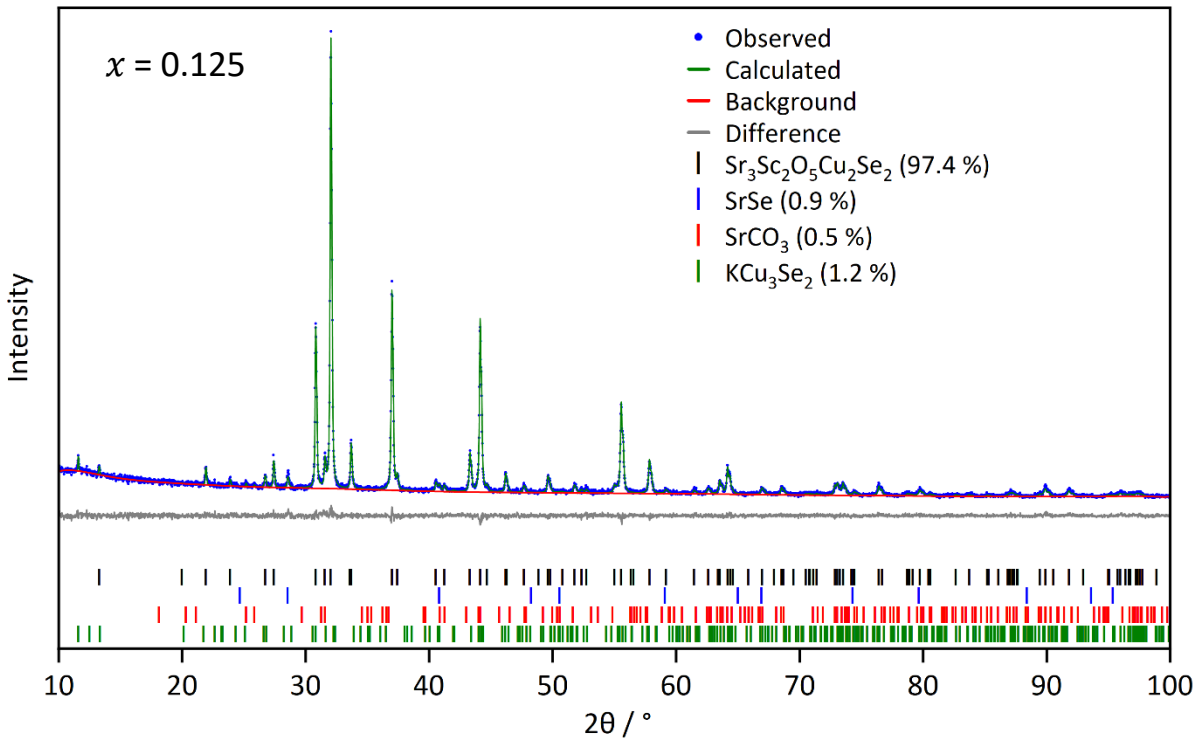

Figure 80 *Powder X-ray diffractogram of material with target composition $(Sr_{2.875}K_{0.125})Sc_2O_5Cu_2Se_2$ (space group I4/mmm) after 36 hours of heating at 800 °C. The small blue circles represent the observed diffracted intensity, the green line represents the Rietveld-refined calculated model, the red line represents the background, and the grey line represents the difference between observed and calculated intensities. The black tick marks show the reflections of the refined model of $Sr_3Sc_2O_5Cu_2Se_2$ (97.4 %), whilst the blue, red and green tick marks represent refined impurity phases SrSe (0.9 %), $SrCO_3$ (0.5 %), and KCu_3Se_2 (1.2 %) respectively.*
Duration: 45 minutes. Data points: 4444. Interval: 0.02 °. GOF: 1.07. R_{wp}: 6.303 %.

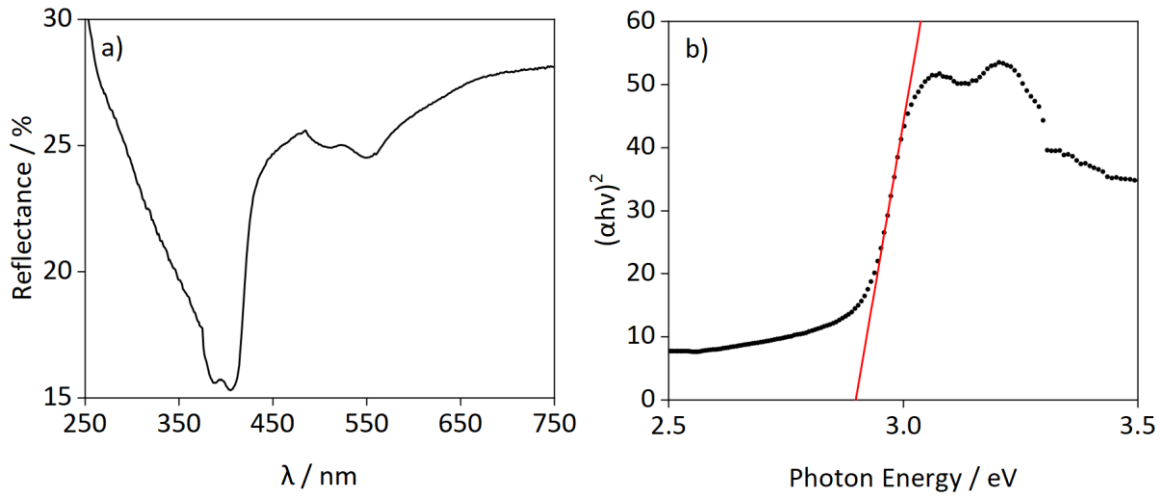

Figure 81 *UV-Vis spectrometry data for material with target composition $(Sr_{2.875}K_{0.125})Sc_2O_5Cu_2Se_2$ after 36 hours of heating at 800 °C. Plot a) is the raw diffuse reflectance data, and plot b) is the associated magnified Tauc plot for this region, where the intercept between the red extrapolated tangent line and the x-axis is used to estimate an optical band gap of 2.90 eV, which corresponds to 428 nm.*

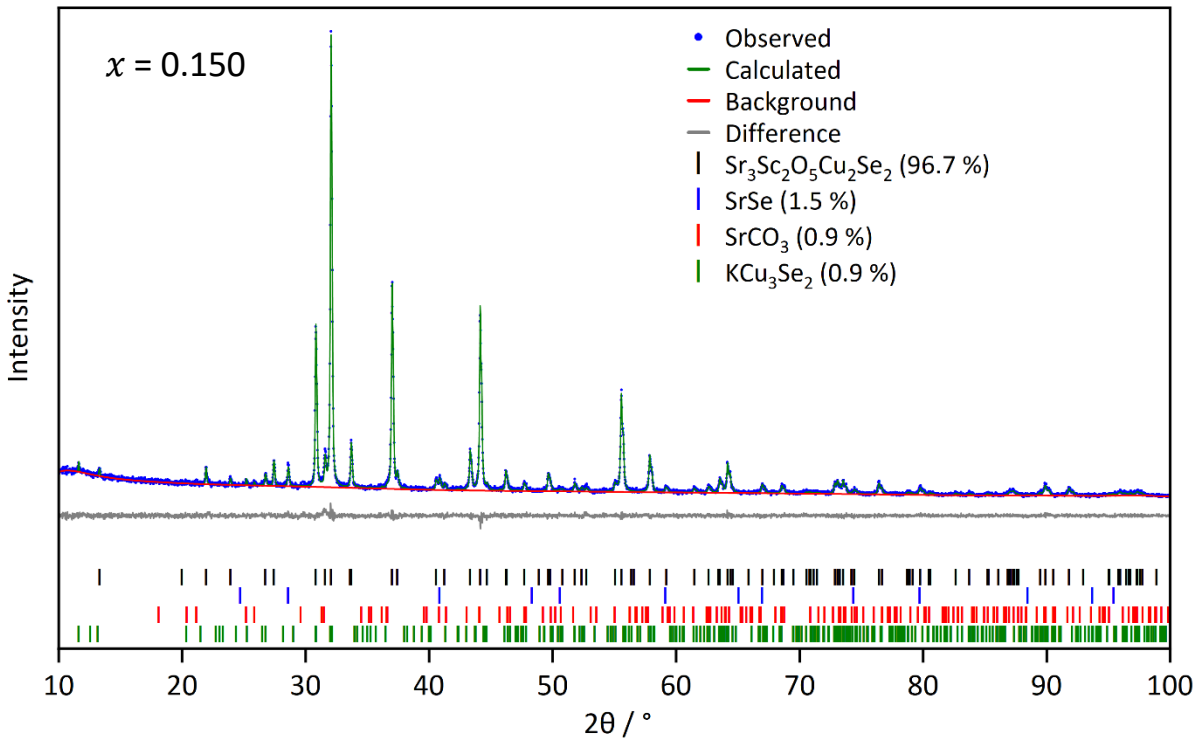

Figure 82 *Powder X-ray diffractogram of material with target composition $(Sr_{2.850}K_{0.150})Sc_2O_5Cu_2Se_2$ (space group I4/mmm) after 36 hours of heating at 800 °C. The small blue circles represent the observed diffracted intensity, the green line represents the Rietveld-refined calculated model, the red line represents the background, and the grey line represents the difference between observed and calculated intensities. The black tick marks show the reflections of the refined model of $Sr_3Sc_2O_5Cu_2Se_2$ (96.7 %), whilst the blue, red and green tick marks represent refined impurity phases SrSe (1.5 %), $SrCO_3$ (0.9 %), and KCu_3Se_2 (0.9 %) respectively.*
Duration: 45 minutes. Data points: 4444. Interval: 0.02 °. GOF: 1.05. R_{wp}: 5.674 %.

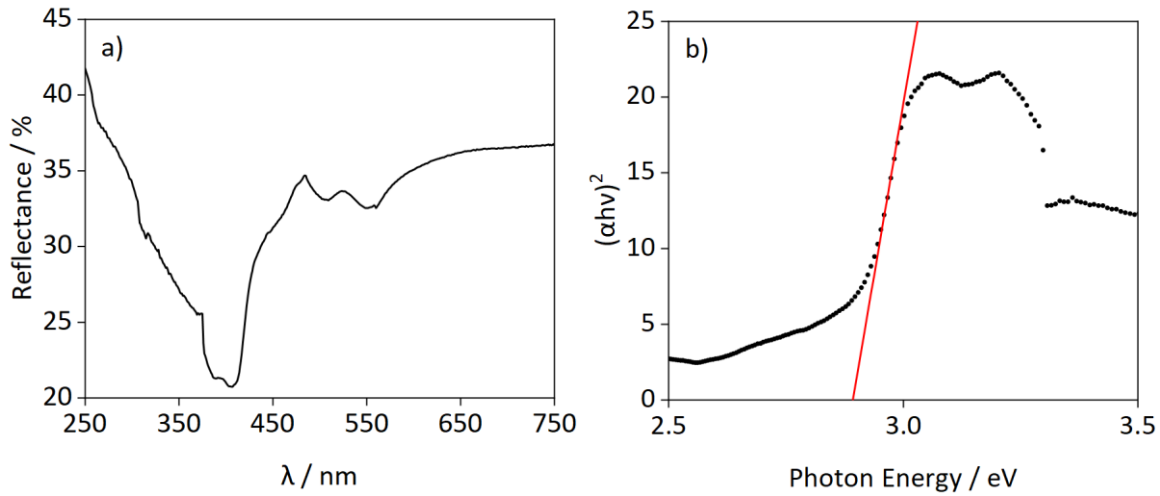

Figure 83 *UV-Vis spectrometry data for material with target composition $(Sr_{2.850}K_{0.150})Sc_2O_5Cu_2Se_2$ after 36 hours of heating at 800 °C. Plot a) is the raw diffuse reflectance data, and plot b) is the associated magnified Tauc plot for this region, where the intercept between the red extrapolated tangent line and the x-axis is used to estimate an optical band gap of 2.89 eV, which corresponds to 429 nm.*

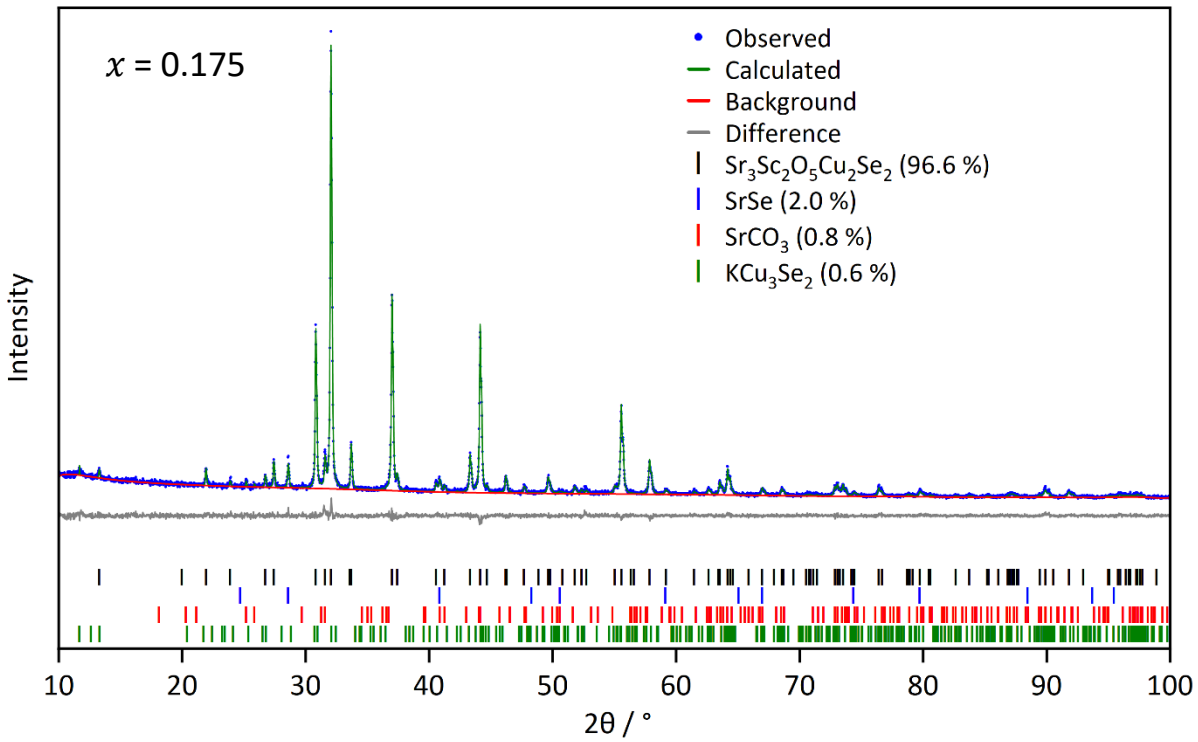

Figure 84 *Powder X-ray diffractogram of material with target composition $(Sr_{2.825}K_{0.175})Sc_2O_5Cu_2Se_2$ (space group I4/mmm) after 36 hours of heating at 800 °C. The small blue circles represent the observed diffracted intensity, the green line represents the Rietveld-refined calculated model, the red line represents the background, and the grey line represents the difference between observed and calculated intensities. The black tick marks show the reflections of the refined model of $Sr_3Sc_2O_5Cu_2Se_2$ (96.6 %), whilst the blue, red and green tick marks represent refined impurity phases SrSe (2.0 %), $SrCO_3$ (0.8 %), and KCu_3Se_2 (0.6 %) respectively.*
Duration: 45 minutes. Data points: 4444. Interval: 0.02 °. GOF: 1.10. R_{wp}: 6.085 %.

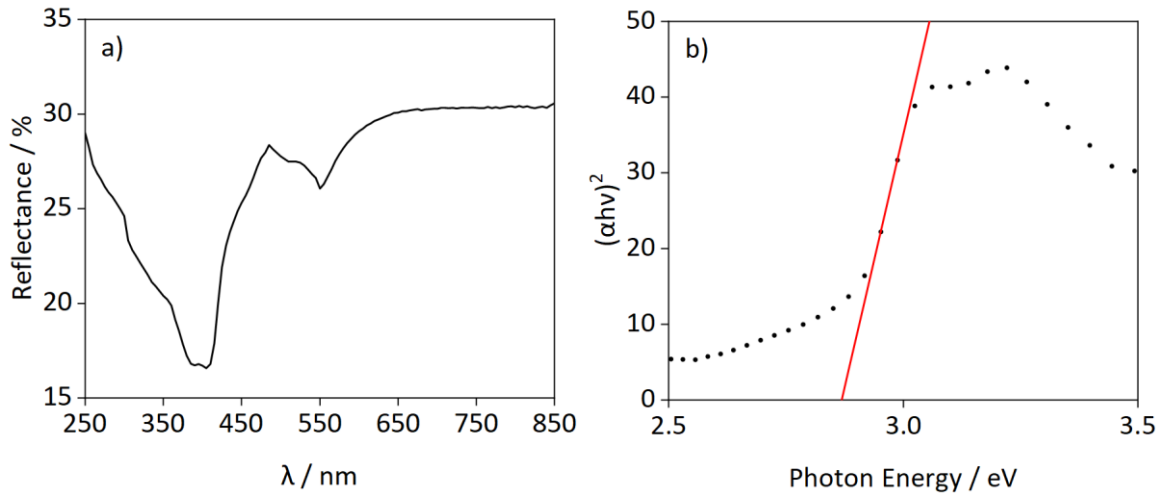

Figure 85 *UV-Vis spectrometry data for material with target composition $(Sr_{2.825}K_{0.175})Sc_2O_5Cu_2Se_2$ after 36 hours of heating at 800 °C. Plot a) is the raw diffuse reflectance data, and plot b) is the associated magnified Tauc plot for this region, where the intercept between the red extrapolated tangent line and the x-axis is used to estimate an optical band gap of 2.87 eV, which corresponds to 432 nm.*

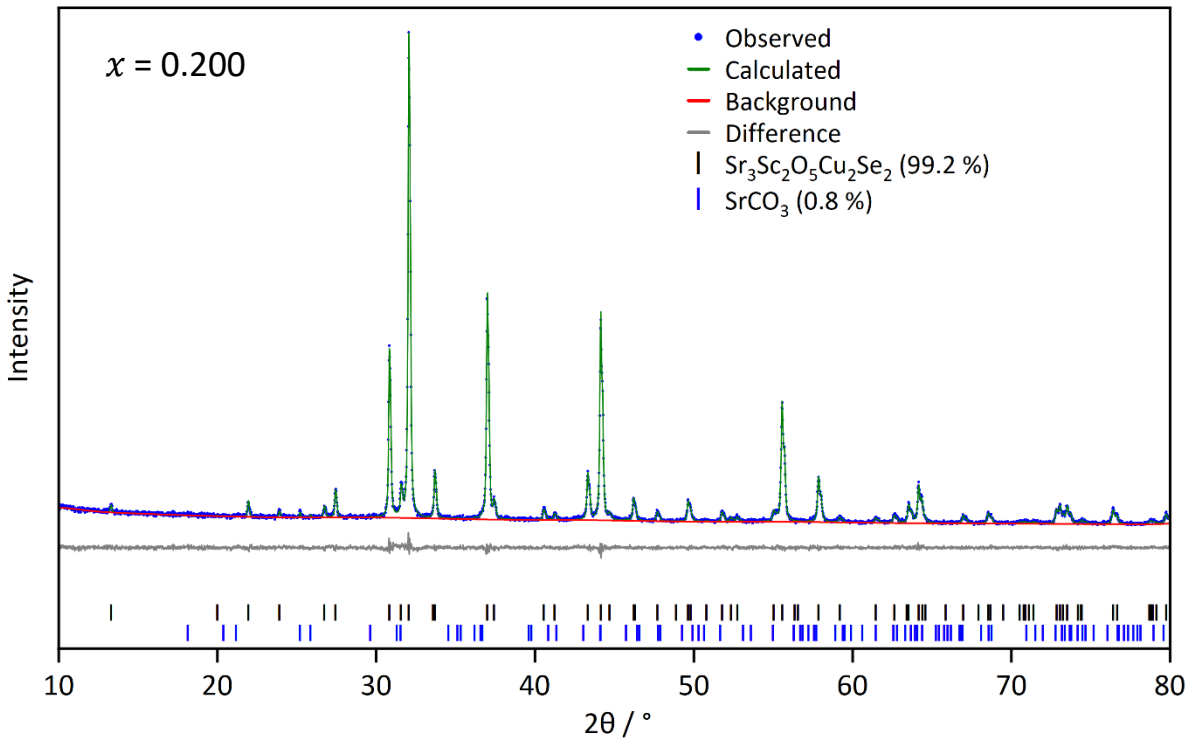

Figure 86 *Powder X-ray diffractogram of material with target composition $(Sr_{2.800}K_{0.200})Sc_2O_5Cu_2Se_2$ (space group I4/mmm) after 36 hours of heating at 800 °C. The small blue circles represent the observed diffracted intensity, the green line represents the Rietveld-refined calculated model, the red line represents the background, and the grey line represents the difference between observed and calculated intensities. The black tick marks show the reflections of the refined model of $Sr_3Sc_2O_5Cu_2Se_2$ (99.2 %), whilst the blue marks represent refined impurity phase $SrCO_3$ (0.8 %).*
Duration: 45 minutes. Data points: 3457. Interval: 0.02 °. GOF: 1.08. R_{wp}: 4.549 %.

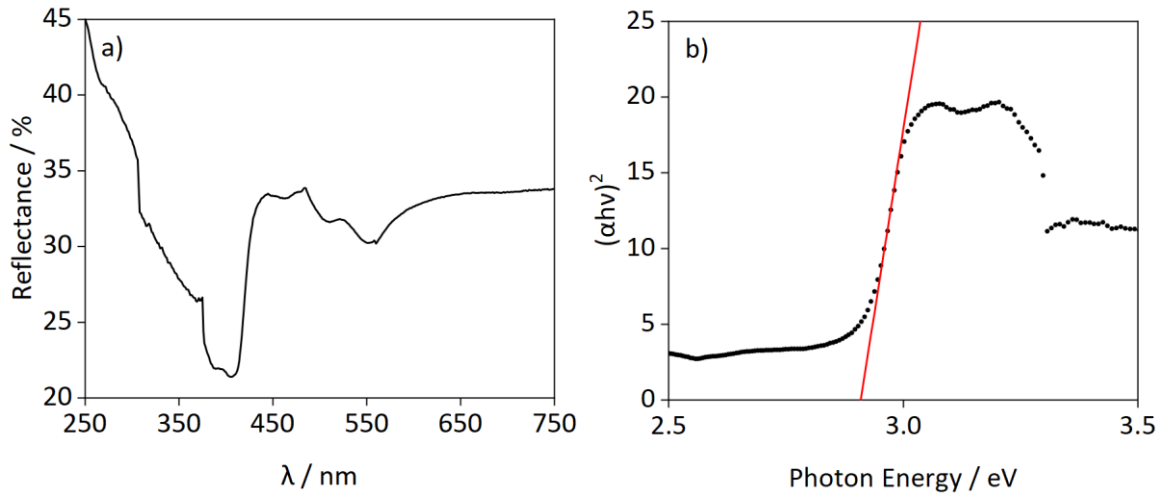

Figure 87 *UV-Vis spectrometry data for material with target composition $(Sr_{2.800}K_{0.200})Sc_2O_5Cu_2Se_2$ after 36 hours of heating at 800 °C. Plot a) is the raw diffuse reflectance data, and plot b) is the associated magnified Tauc plot for this region, where the intercept between the red extrapolated tangent line and the x-axis is used to estimate an optical band gap of 2.91 eV, which corresponds to 426 nm.*

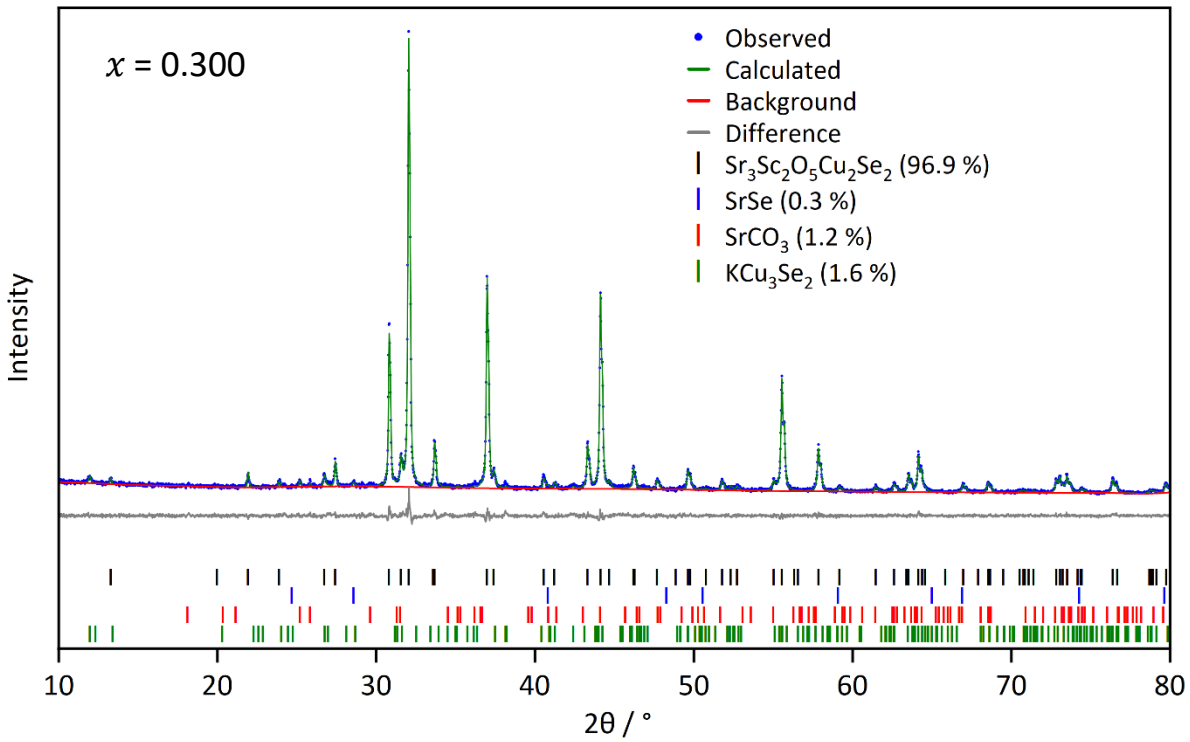

Figure 88 *Powder X-ray diffractogram of material with target composition $(Sr_{2.700}K_{0.300})Sc_2O_5Cu_2Se_2$ (space group I4/mmm) after 36 hours of heating at 800 °C. The small blue circles represent the observed diffracted intensity, the green line represents the Rietveld-refined calculated model, the red line represents the background, and the grey line represents the difference between observed and calculated intensities. The black tick marks show the reflections of the refined model of $Sr_3Sc_2O_5Cu_2Se_2$ (96.9 %), whilst the blue, red and green tick marks represent refined impurity phases SrSe (0.3 %), $SrCO_3$ (1.2 %), and KCu_3Se_2 (1.6 %) respectively.*
Duration: 45 minutes. Data points: 3457. Interval: 0.02 °. GOF: 1.20. R_{wp}: 4.761 %.

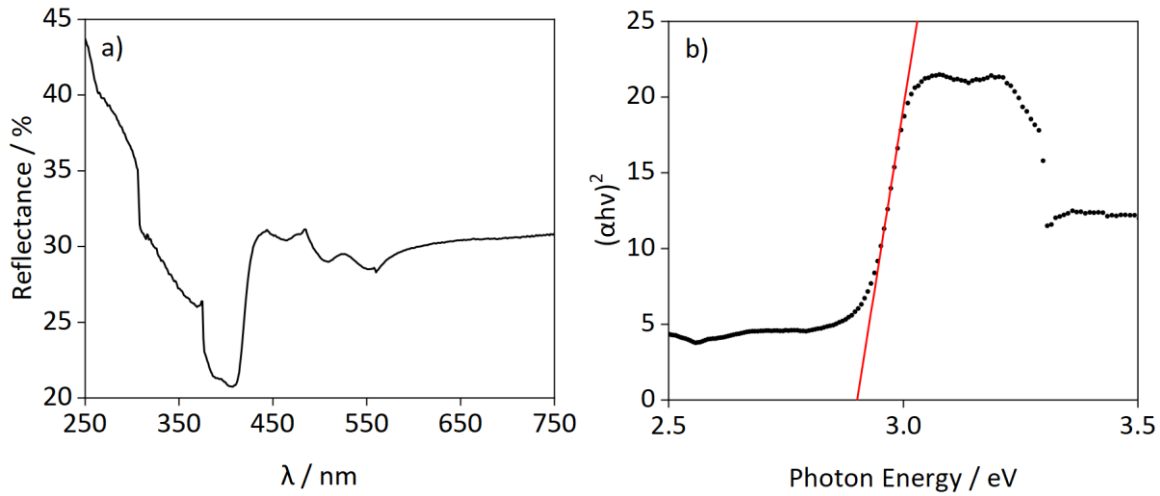

Figure 89 *UV-Vis spectrometry data for material with target composition $(Sr_{2.700}K_{0.300})Sc_2O_5Cu_2Se_2$ after 36 hours of heating at 800 °C. Plot a) is the raw diffuse reflectance data, and plot b) is the associated magnified Tauc plot for this region, where the intercept between the red extrapolated tangent line and the x-axis is used to estimate an optical band gap of 2.90 eV, which corresponds to 428 nm.*

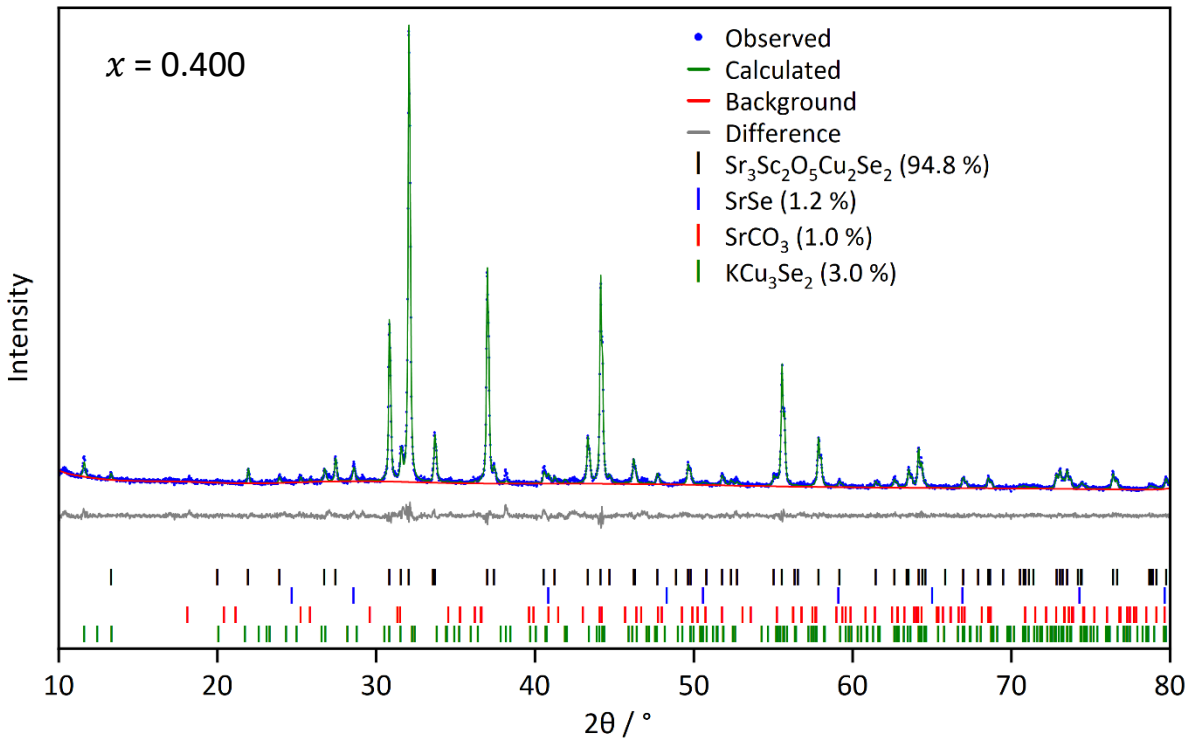

Figure 90 *Powder X-ray diffractogram of material with target composition $(Sr_{2.600}K_{0.400})Sc_2O_5Cu_2Se_2$ (space group I4/mmm) after 36 hours of heating at 800 °C. The small blue circles represent the observed diffracted intensity, the green line represents the Rietveld-refined calculated model, the red line represents the background, and the grey line represents the difference between observed and calculated intensities. The black tick marks show the reflections of the refined model of $Sr_3Sc_2O_5Cu_2Se_2$ (94.8 %), whilst the blue, red and green tick marks represent refined impurity phases SrSe (1.2 %), $SrCO_3$ (1.0 %), and KCu_3Se_2 (3.0 %) respectively.*
Duration: 45 minutes. Data points: 3457. Interval: 0.02 °. GOF: 1.34. R_{wp}: 5.430 %.

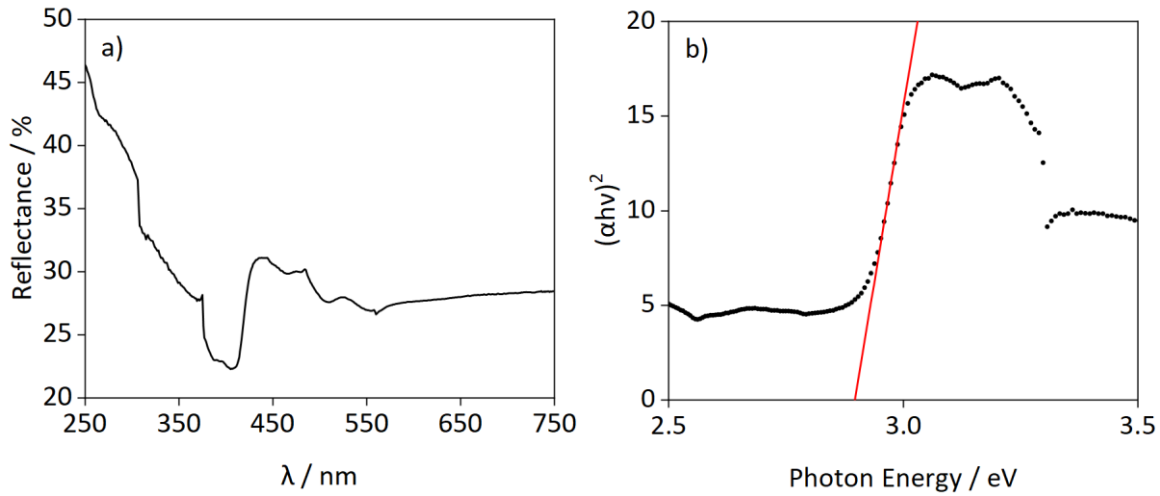

Figure 91 *UV-Vis spectrometry data for material with target composition $(Sr_{2.600}K_{0.400})Sc_2O_5Cu_2Se_2$ after 36 hours of heating at 800 °C. Plot a) is the raw diffuse reflectance data, and plot b) is the associated magnified Tauc plot for this region, where the intercept between the red extrapolated tangent line and the x-axis is used to estimate an optical band gap of 2.90 eV, which corresponds to 428 nm.*

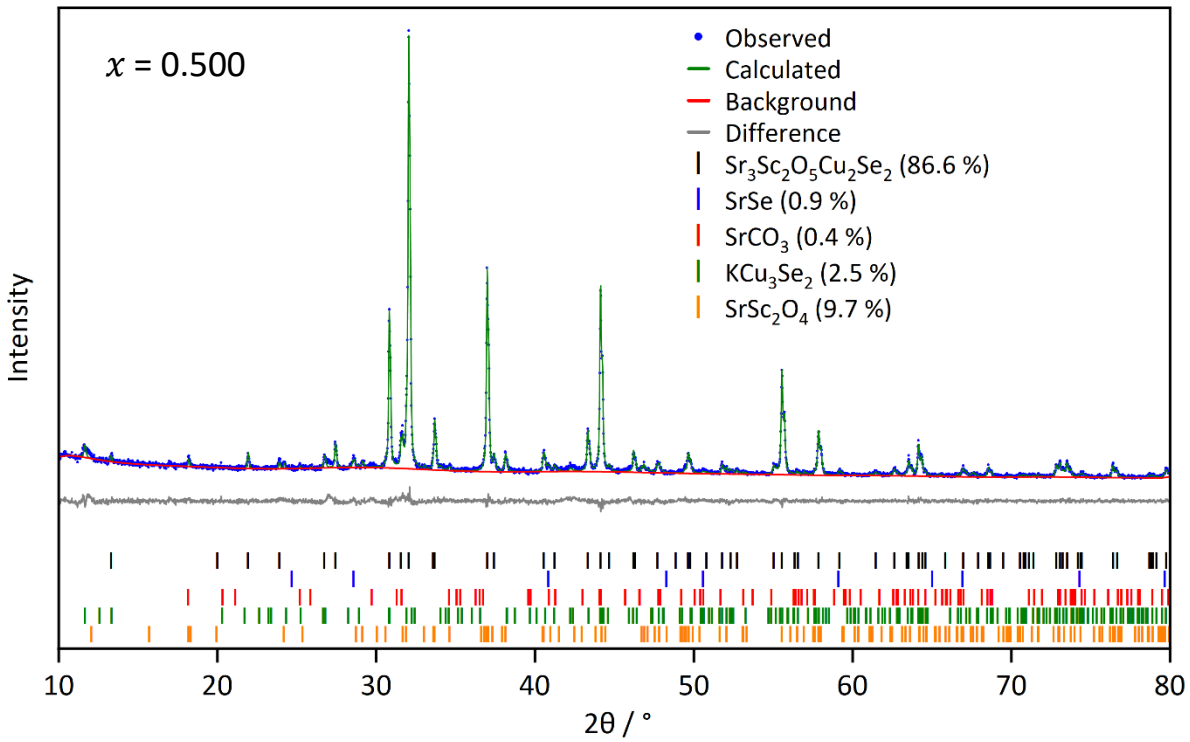

Figure 92 *Powder X-ray diffractogram of material with target composition $(Sr_{2.500}K_{0.500})Sc_2O_5Cu_2Se_2$ (space group I4/mmm) after 36 hours of heating at 800 °C. The small blue circles represent the observed diffracted intensity, the green line represents the Rietveld-refined calculated model, the red line represents the background, and the grey line represents the difference between observed and calculated intensities. The black tick marks show the reflections of the refined model of $Sr_3Sc_2O_5Cu_2Se_2$ (86.6 %), whilst the blue, red, green and orange tick marks represent refined impurity phases SrSe (0.9 %), $SrCO_3$ (0.4 %), KCu_3Se_2 (2.5 %) and $SrSc_2O_4$ (9.7 %) respectively.*
Duration: 45 minutes. Data points: 3457. Interval: 0.02 °. GOF: 1.28. R_{wp}: 5.432 %.

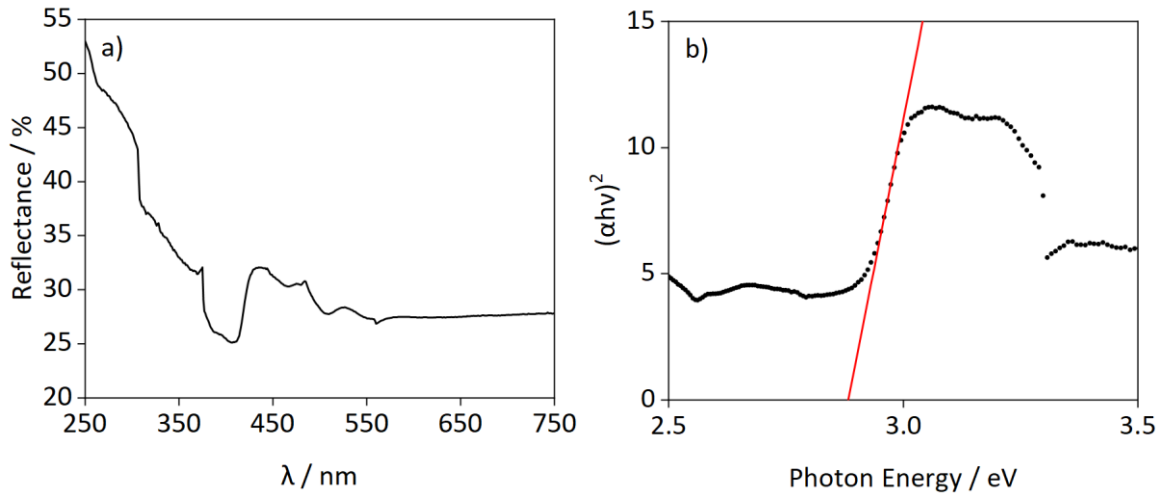

Figure 93 *UV-Vis spectrometry data for material with target composition $(Sr_{2.500}K_{0.500})Sc_2O_5Cu_2Se_2$ after 36 hours of heating at 800 °C. Plot a) is the raw diffuse reflectance data, and plot b) is the associated magnified Tauc plot for this region, where the intercept between the red extrapolated tangent line and the x-axis is used to estimate an optical band gap of 2.88 eV, which corresponds to 430 nm.*

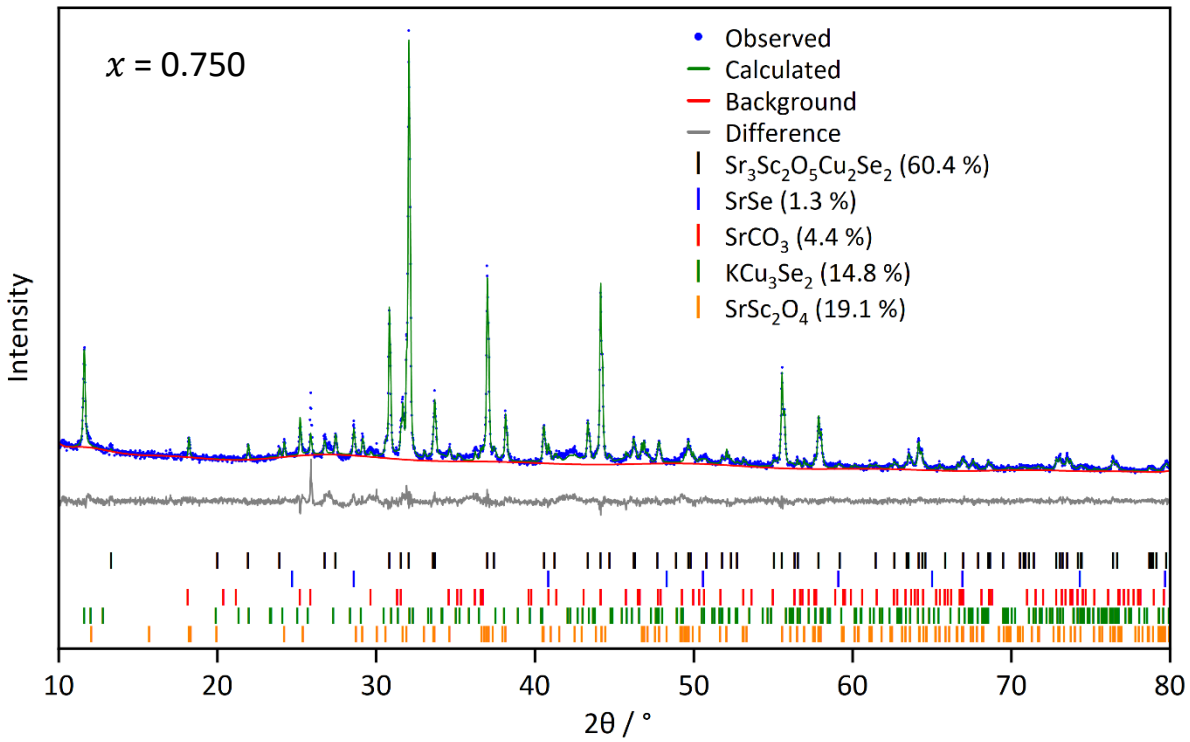

Figure 94 *Powder X-ray diffractogram of material with target composition $(Sr_{2.250}K_{0.750})Sc_2O_5Cu_2Se_2$ (space group I4/mmm) after 36 hours of heating at 800 °C. The small blue circles represent the observed diffracted intensity, the green line represents the Rietveld-refined calculated model, the red line represents the background, and the grey line represents the difference between observed and calculated intensities. The black tick marks show the reflections of the refined model of $Sr_3Sc_2O_5Cu_2Se_2$ (60.4 %), whilst the blue, red, green and orange tick marks represent refined impurity phases SrSe (1.3 %), $SrCO_3$ (4.4 %), KCu_3Se_2 (14.8 %) and $SrSc_2O_4$ (19.1 %) respectively.*
Duration: 45 minutes. Data points: 3457. Interval: 0.02 °. GOF: 1.46. R_{wp}: 6.183 %.

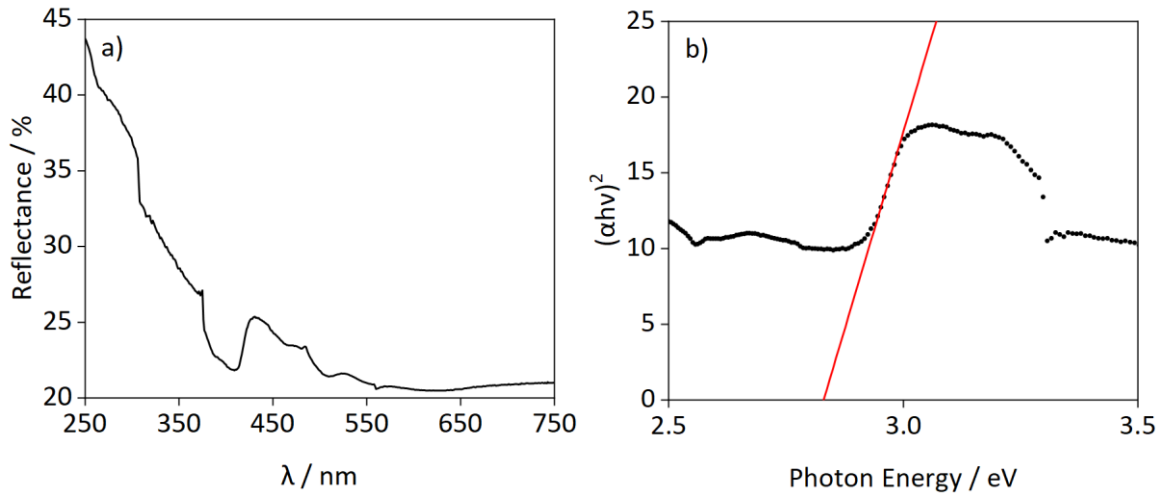

Figure 95 *UV-Vis spectrometry data for material with target composition $(Sr_{2.250}K_{0.750})Sc_2O_5Cu_2Se_2$ after 36 hours of heating at 800 °C. Plot a) is the raw diffuse reflectance data, and plot b) is the associated magnified Tauc plot for this region, where the intercept between the red extrapolated tangent line and the x-axis is used to estimate an optical band gap of 2.83 eV, which corresponds to 438 nm.*

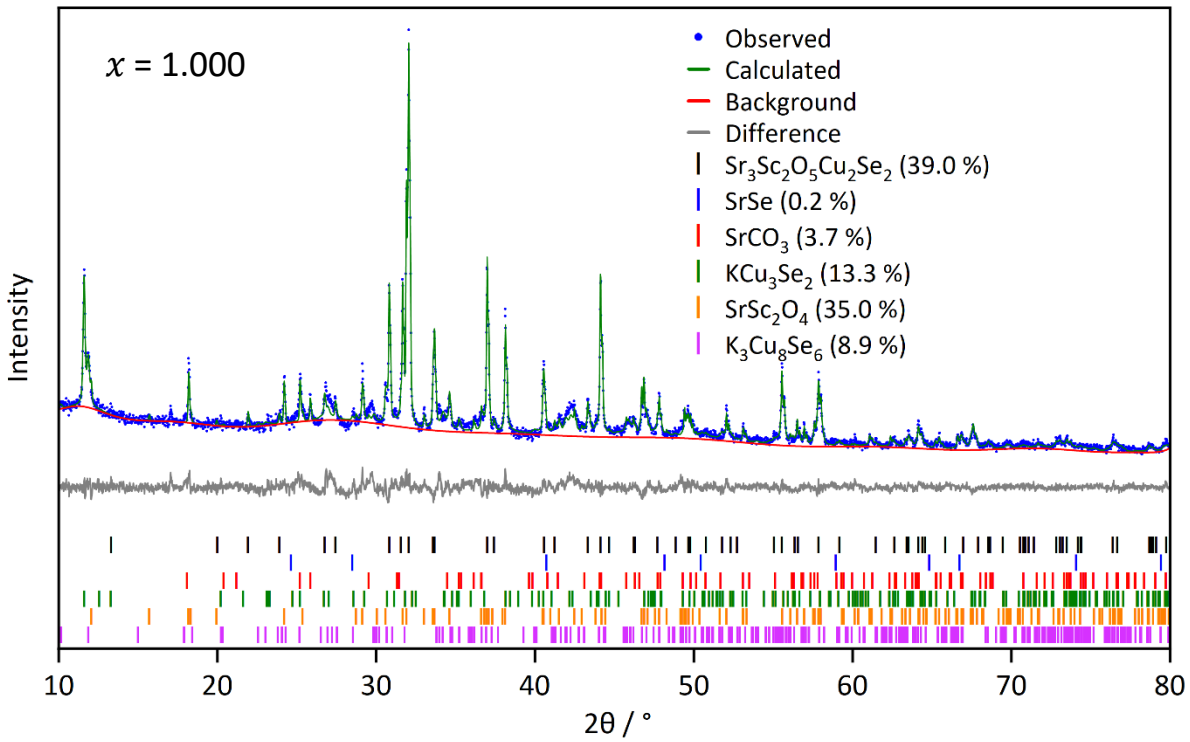

Figure 96 *Powder X-ray diffractogram of material with target composition $(Sr_{2.000}K_{1.000})Sc_2O_5Cu_2Se_2$ (space group I4/mmm) after 36 hours of heating at 800 °C. The small blue circles represent the observed diffracted intensity, the green line represents the Rietveld-refined calculated model, the red line represents the background, and the grey line represents the difference between observed and calculated intensities. The black tick marks show the reflections of the refined model of $Sr_3Sc_2O_5Cu_2Se_2$ (39.0 %), whilst the blue, red, green, orange and pink tick marks represent refined impurity phases SrSe (0.2 %), $SrCO_3$ (3.7 %), KCu_3Se_2 (13.3 %), $SrSc_2O_4$ (35.0 %) and $K_3Cu_8Se_6$ (8.9 %) respectively.*
Duration: 45 minutes. Data points: 3457. Interval: 0.02 °. GOF: 1.53. R_{wp}: 6.628 %.

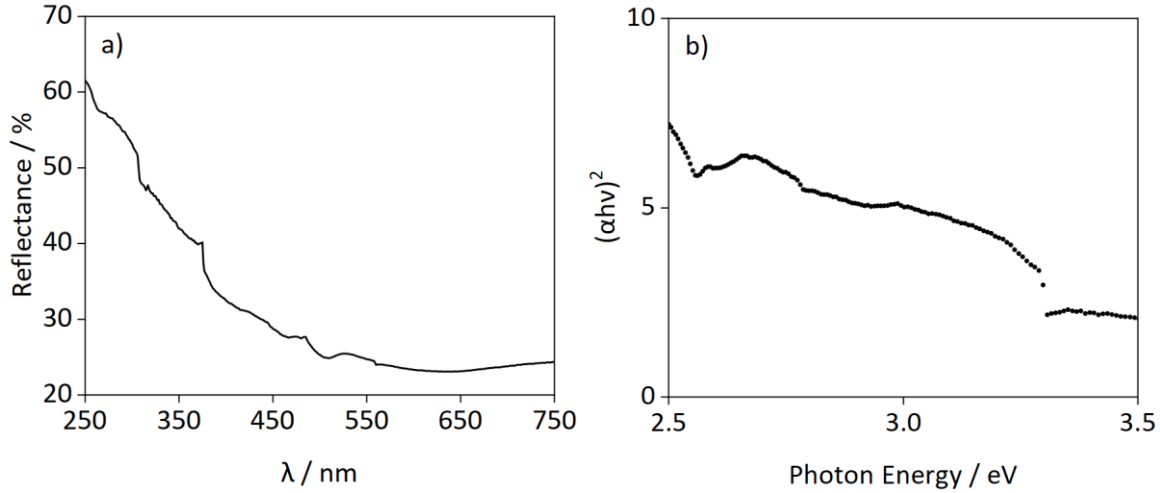

Figure 97 *UV-Vis spectrometry data for material with target composition $(Sr_{2.000}K_{1.000})Sc_2O_5Cu_2Se_2$ after 36 hours of heating at 800 °C. Plot a) is the raw diffuse reflectance data and plot b) is the associated magnified Tauc plot for this region where this material would be expected to show a drop-off in reflectance indicating an optical band gap, but does not. The lack of such drop-off makes estimating an optical band gap with this method impossible. This anomalous data point is therefore excluded from analyses in Chapter 3.*

B.1.5 Sodium doped 325 selenide MALMs, $(Sr_{3-x}Na_x)Sc_2O_5Cu_2Se_2$

Table 30 Tabulated structural data of the sodium doped 325 selenide MALMs with general formula $(Sr_{3-x}Na_x)Sc_2O_5Cu_2Se_2$. The pristine material $Sr_3Sc_2O_5Cu_2Se_2$ is included as a reference. All values are derived from the Rietveld refinement of PXRD data using GSAS-II. Note that because all materials listed are tetragonal (space group I4/mmm), the b parameter is identical to a, and thus omitted.

x / mol	Target Composition	a / Å	c / Å	Volume / Å^3
0 (pristine)	$Sr_3Sc_2O_5Cu_2Se_2$	4.10329(4)	26.6847(3)	449.290(12)
0.025	$(Sr_{2.975}Na_{0.025})Sc_2O_5Cu_2Se_2$	4.10349(9)	26.6804(7)	449.260(28)
0.050	$(Sr_{2.950}Na_{0.050})Sc_2O_5Cu_2Se_2$	4.10344(7)	26.6868(6)	449.358(22)
0.075	$(Sr_{2.925}Na_{0.075})Sc_2O_5Cu_2Se_2$	4.10328(7)	26.6852(6)	449.297(21)
0.100	$(Sr_{2.900}Na_{0.100})Sc_2O_5Cu_2Se_2$	4.10326(6)	26.6862(5)	449.308(19)
0.125	$(Sr_{2.875}Na_{0.125})Sc_2O_5Cu_2Se_2$	4.10326(10)	26.6871(9)	449.323(31)
0.150	$(Sr_{2.850}Na_{0.150})Sc_2O_5Cu_2Se_2$	4.10284(8)	26.6860(6)	449.214(23)
0.175	$(Sr_{2.825}Na_{0.175})Sc_2O_5Cu_2Se_2$	4.10332(8)	26.6858(7)	449.315(25)
0.200	$(Sr_{2.800}Na_{0.200})Sc_2O_5Cu_2Se_2$	4.10320(11)	26.6826(9)	449.240(30)
0.300	$(Sr_{2.700}Na_{0.300})Sc_2O_5Cu_2Se_2$	4.10332(8)	26.6957(8)	449.483(27)
0.400	$(Sr_{2.600}Na_{0.400})Sc_2O_5Cu_2Se_2$	4.10403(8)	26.6988(7)	449.689(25)
0.500	$(Sr_{2.500}Na_{0.500})Sc_2O_5Cu_2Se_2$	4.10384(8)	26.6998(7)	449.663(25)
0.750	$(Sr_{2.250}Na_{0.750})Sc_2O_5Cu_2Se_2$	4.10364(12)	26.6974(10)	449.580(40)
1.000	$(Sr_{2.000}Na_{1.000})Sc_2O_5Cu_2Se_2$	4.10374(18)	26.6894(16)	449.470(60)

Table 31 Tabulated compositional data of the sodium doped 325 selenide MALMs with general formula $(Sr_{3-x}Na_x)Sc_2O_5Cu_2Se_2$. The pristine material $Sr_3Sc_2O_5Cu_2Se_2$ is included as a reference. All values are cited as a weight percent (wt %) of the total weight, and are derived from the Rietveld refinement of PXRD data using GSAS-II.

x / mol	Target phase / wt %	SrSe / wt %	$SrCO_3$ / wt %	Sc_2O_3 / wt %	$NaCu_3Se_2$ / wt %	$SrSc_2O_4$ / wt %
0 (pristine)	99.1	0.5	0.4	-	-	-
0.025	99.5	-	0.5	-	-	-
0.050	99.9	-	0.1	-	-	-
0.075	99.5	-	0.5	-	-	-
0.100	99.5	-	0.5	-	-	-
0.125	99.1	0.4	0.5	-	-	-
0.150	98.3	0.7	1.0	-	-	-
0.175	98.3	0.6	1.1	-	-	-
0.200	96.4	1.3	2.3	-	-	-
0.300	99.0	-	-	-	1.0	-
0.400	96.0	-	-	2.1	1.9	-
0.500	95.3	-	2.8	-	1.9	-
0.750 *	85.0	0.2	0.3	3.3	4.8	6.4
1.000 *	87.3	0.6	0.3	5.1	5.1	1.6

* Sample also contained traces of an unknown impurity phases distinct from those detailed above

Table 32 Tabulated data on both the target and maximum actual dopant content of the sodium doped 325 selenide MALMs with general formula $(Sr_{3-x}Na_x)Sc_2O_5Cu_2Se_2$. The pristine material $Sr_3Sc_2O_5Cu_2Se_2$ is included as a reference. The minimum possible amount of total Na contained within impurities was extracted from the refined wt % of $NaCu_3Se_2$ from GSAS-II. The remaining Na content is the maximum possible Na within the MALM.

Target x / mol	**Target x / wt %**	**Minimum Na in impurities / %**	**Maximum Na in product / %**	**Maximum x / mol**
0 (pristine)	0.000	0.000	100.000	0.000
0.025	0.080	0.000	100.000	0.025
0.050	0.161	0.000	100.000	0.050
0.075	0.242	0.000	100.000	0.075
0.100	0.323	0.000	100.000	0.100
0.125	0.405	0.000	100.000	0.125
0.150	0.487	0.000	100.000	0.150
0.175	0.569	0.000	100.000	0.175
0.200	0.652	0.000	100.000	0.200
0.300	0.988	6.266	93.734	0.281
0.400	1.329	8.846	91.154	0.365
0.500	1.677	7.011	92.989	0.465
0.750	2.576	11.529	88.471	0.664
1.000	3.520	8.965	91.035	0.910

Table 33 Tabulated analytical data of to the measured properties of the sodium doped 325 selenide MALMs with general formula $(Sr_{3-x}Na_x)Sc_2O_5Cu_2Se_2$. The pristine material $Sr_3Sc_2O_5Cu_2Se_2$ is included as a reference. Optical band gaps were estimated from UV-Vis data. Pellet densities were estimated from the mass and volume of annealed pellet samples, and are cited as a relative percentage of the bulk crystal. Resistivities and conductivities were estimated from 4 probe van der Pauw analysis of the pellet samples.

x / mol	Band Gap / eV	Pellet Density / %	Raw Resistivities from 4-Probe measurement, for each probe permutation / kΩ								Resistivity / Ω cm	Conductivity / S cm^{-1}
			1	2	3	4	5	6	7	8		
0 (pristine)	2.94	71.72	1.20 E+01	1.21 E+01	1.22 E+01	1.22 E+01	1.03 E+01	1.02 E+01	1.02 E+01	1.01 E+01	3.83 E+03	2.61 E-04
0.025	2.91	64.40	2.90 E+00	2.00 E+00	7.29 E+00	2.18 E+00	3.00 E-01	4.00 E+00	1.15 E+01	7.70 E+00	1.70 E+03	5.88 E-04
0.050	2.92	67.80	2.87 E+00	2.90 E+00	2.92 E+00	2.94 E+00	4.70 E-01	2.00 E-01	4.00 E-01	4.60 E-01	4.51 E+02	2.22 E-03
0.075	2.93	70.85	1.21 E+00	1.11 E+00	1.24 E+00	1.20 E+00	5.60 E-01	6.20 E-01	6.60 E-01	6.40 E-01	3.09 E+02	3.24 E-03
0.100	2.89	71.67	1.10 E-01	1.03 E-01	1.10 E-01	1.08 E-01	1.17 E-01	1.10 E-01	1.24 E-01	1.27 E-01	3.96 E+01	2.52 E-02
0.125	2.91	70.02	1.69 E-02	1.69 E-02	1.68 E-02	1.68 E-02	2.70 E-02	2.76 E-02	2.74 E-02	2.75 E-02	7.76 E+00	1.29 E-01
0.150	2.92	72.97	1.42 E-02	1.42 E-02	1.42 E-02	1.42 E-02	8.22 E-03	8.25 E-03	8.25 E-03	8.25 E-03	3.77 E+00	2.66 E-01
0.175	2.93	73.07	7.30 E-03	7.29 E-03	7.46 E-03	7.39 E-03	5.77 E-03	5.70 E-03	5.80 E-03	5.59 E-03	2.24 E+00	4.47 E-01
0.200	2.74 ‡	70.99	8.30 E-04	9.20 E-04	8.30 E-04	8.40 E-04	4.40 E-04	5.06 E-04	4.30 E-04	4.31 E-04	2.26 E-01	4.42 E+00
0.300	2.91	77.65	4.52 E-03	1.52 E-02	5.70 E-03	4.90 E-03	4.30 E-03	1.48 E-02	5.20 E-03	3.90 E-03	2.49 E+00	4.02 E-01
0.400	2.93	75.78	4.52 E-03	1.52 E-02	5.70 E-03	4.90 E-03	4.30 E-03	1.48 E-02	5.20 E-03	3.90 E-03	2.57 E+00	3.89 E-01
0.500	2.91	77.88	2.20 E-03	3.30 E-03	1.91 E-03	1.09 E-01	1.01 E-02	4.20 E-03	1.00 E-03	1.00 E-03	4.33 E+00	2.31 E-01
0.750	2.91	78.49	1.90 E-04	1.90 E-04	1.30 E-04	3.00 E-05	7.00 E-05	1.60 E-04	6.00 E-05	1.40 E-04	4.27 E-02	2.34 E+01
1.000	2.91	72.72	2.00 E-05	5.00 E-04	1.00 E-02	1.00 E-03	2.10 E-03	2.50 E-03	4.90 E-03	1.80 E-04	1.00 E+00	1.00 E+00

‡ Data for this sample was collected at a lower data resolution than all others (5nm vs 1nm) as the sample was submitted to the ISIS Neutron and Muon Source and therefore unavailable for later data recollection. This data point is not considered accurate and was excluded from analyses in the corresponding work in *Chapter 3*.

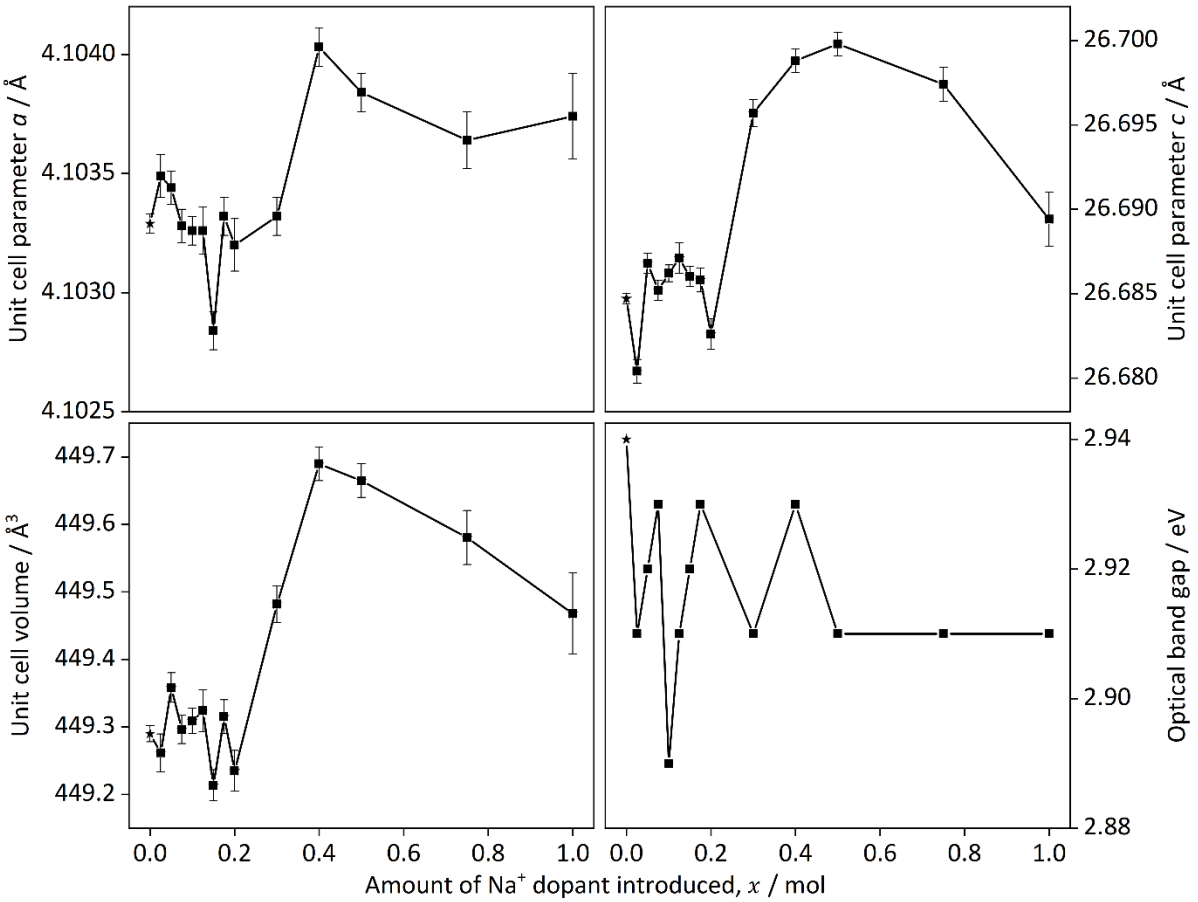

Figure 98 *Comparisons of a) the α unit cell parameter, b) the c unit cell parameter, c) unit cell volume, and d) the optical band gap, of the sodium doped 325 selenide MALMs with general formula $(Sr_{3-x}Na_x)Sc_2O_5Cu_2Se_2$. The pristine material $Sr_3Sc_2O_5Cu_2Se_2$ is included as a reference at $x = 0$ mol and is represented by a star. The $x = 0.200$ mol sample band gap was omitted for consistency as it was recorded at a different resolution, see Table 33.*

Figure 99 *A photographic comparison of the colour of the sodium doped 325 selenide MALMs with general formula $(Sr_{3-x}Na_x)Sc_2O_5Cu_2Se_2$. Dopant concentration increases from left to right. The sample where $x = 0.200$ mol is absent from this photograph as it was sent to the ISIS Neutron and Muon Source for Neutron Powder Diffraction at the time of writing.*

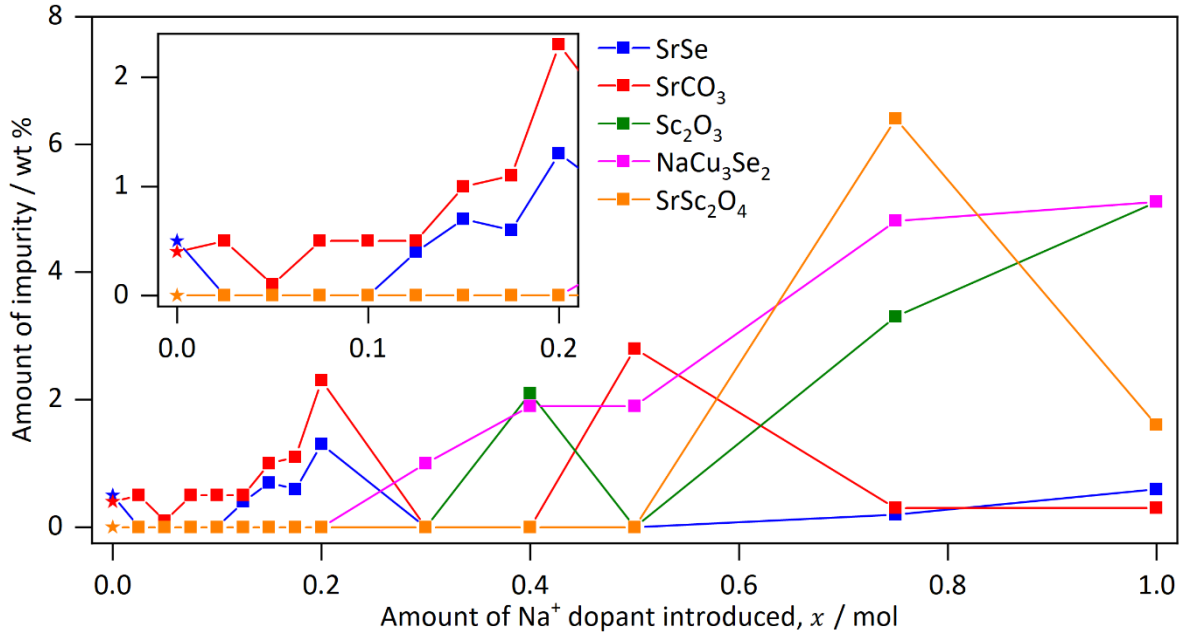

Figure 100 *The weight percentages of five impurity phases present in the sodium doped 325 selenide MALMs with general formula $(Sr_{3-x}Na_x)Sc_2O_5Cu_2Se_2$. The inset plot is a magnification of the $x = 0$ to 0.200 mol region where doping and impurity quantities are low. The pristine material $Sr_3Sc_2O_5Cu_2Se_2$ is included as a reference at $x = 0$ mol and is represented by a star.*

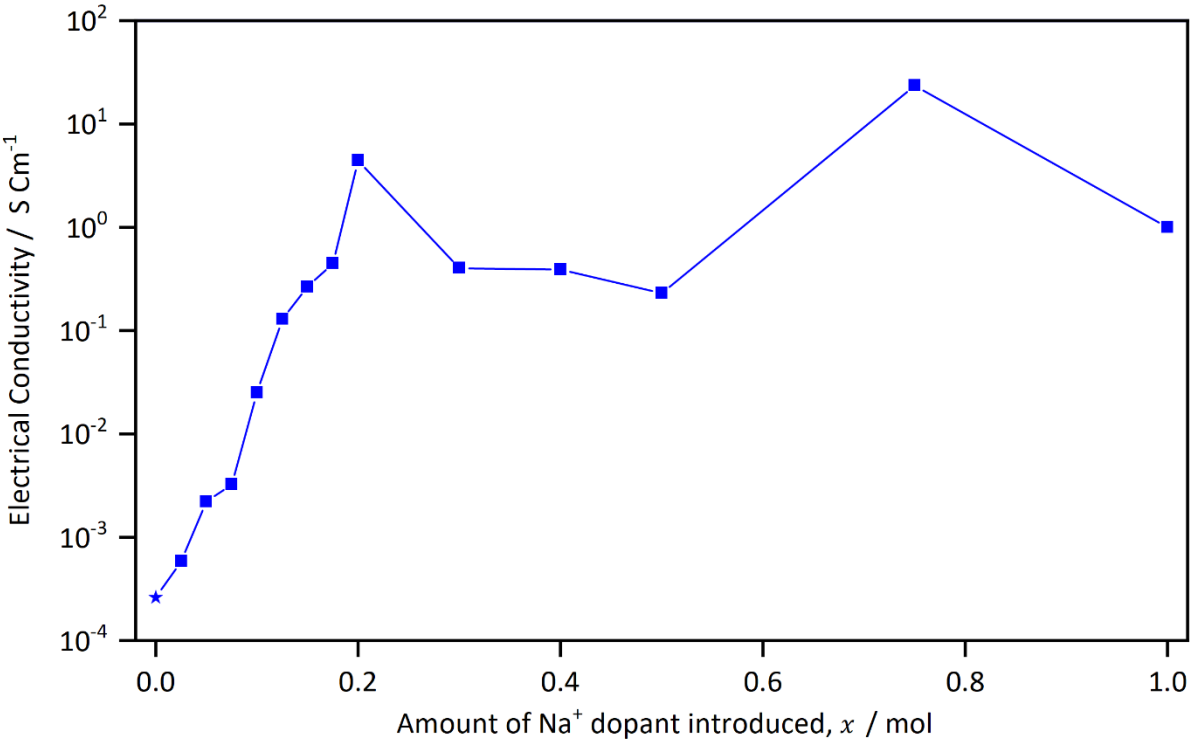

Figure 101 *The electrical conductivities of sodium doped 325 selenide MALMs with general formula $(Sr_{3-x}Na_x)Sc_2O_5Cu_2Se_2$, represented on a log_{10} scale. The pristine material $Sr_3Sc_2O_5Cu_2Se_2$ is included as a reference at $x = 0$ mol and is represented by a star. All values are derived from van der Pauw 4 probe resistivity measurements of 8mm diameter annealed pellet samples.*

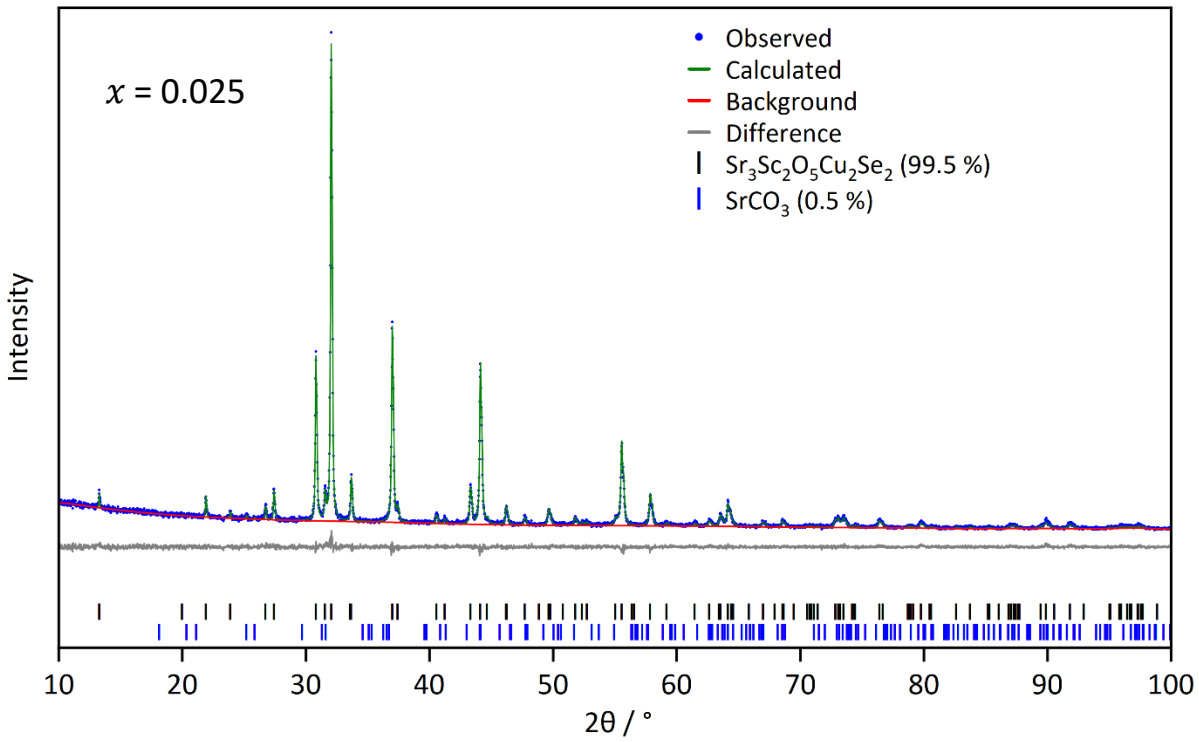

Figure 102 *Powder X-ray diffractogram of material with target composition $(Sr_{2.975}Na_{0.025})Sc_2O_5Cu_2Se_2$ (space group I4/mmm) after 36 hours of heating at 800 °C. The small blue circles represent the observed diffracted intensity, the green line represents the Rietveld-refined calculated model, the red line represents the background, and the grey line represents the difference between observed and calculated intensities. The black tick marks show the reflections of the refined model of $Sr_3Sc_2O_5Cu_2Se_2$ (99.5 %), whilst the blue marks represent refined impurity phase $SrCO_3$ (0.5 %).*
Duration: 45 minutes. Data points: 4444. Interval: 0.02 °. GOF: 1.07. R_{wp}: 6.269 %.

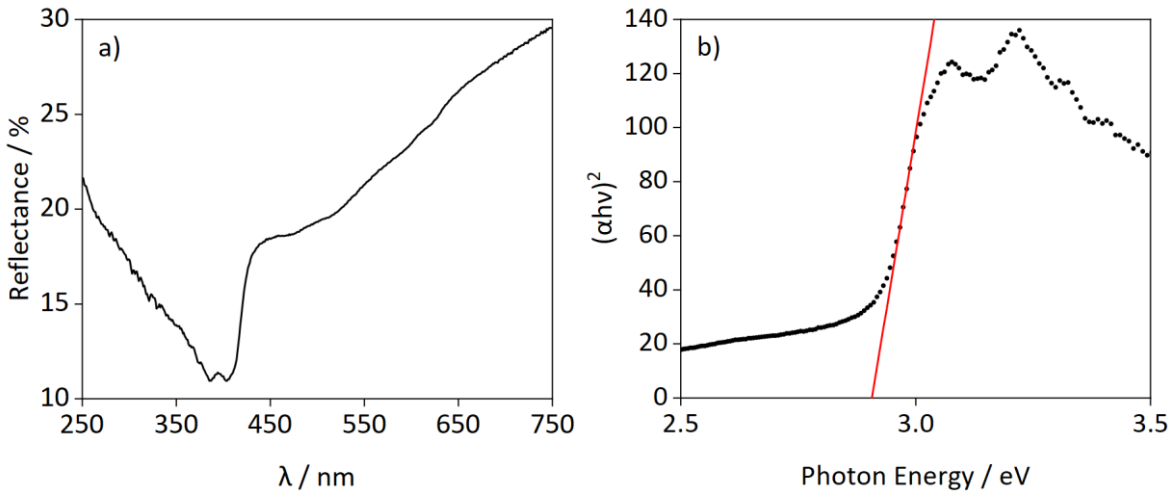

Figure 103 *UV-Vis spectrometry data for material with target composition $(Sr_{2.975}Na_{0.025})Sc_2O_5Cu_2Se_2$ after 36 hours of heating at 800 °C. Plot a) is the raw diffuse reflectance data, and plot b) is the associated magnified Tauc plot for this region, where the intercept between the red extrapolated tangent line and the x-axis is used to estimate an optical band gap of 2.91 eV, which corresponds to 426 nm.*

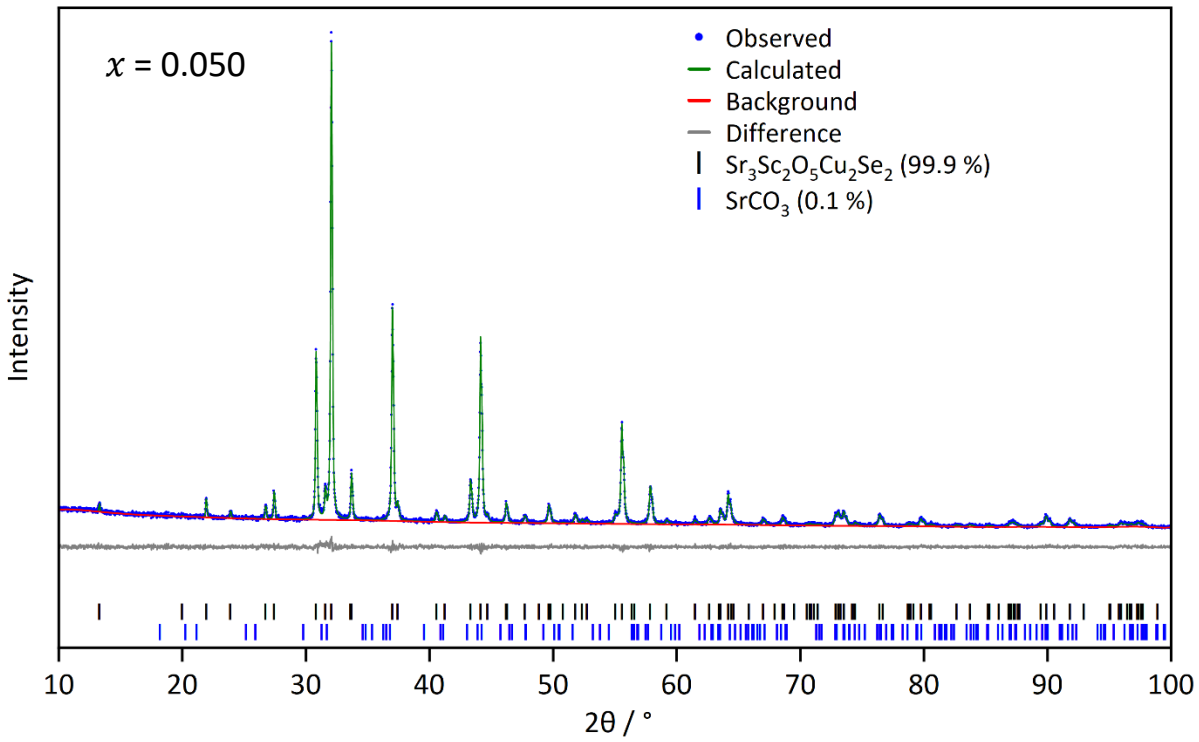

Figure 104 *Powder X-ray diffractogram of material with target composition $(Sr_{2.950}Na_{0.050})Sc_2O_5Cu_2Se_2$ (space group I4/mmm) after 36 hours of heating at 800 °C. The small blue circles represent the observed diffracted intensity, the green line represents the Rietveld-refined calculated model, the red line represents the background, and the grey line represents the difference between observed and calculated intensities. The black tick marks show the reflections of the refined model of $Sr_3Sc_2O_5Cu_2Se_2$ (99.9 %), whilst the blue marks represent refined impurity phase $SrCO_3$ (0.1 %).*
Duration: 45 minutes. Data points: 4444. Interval: 0.02 °. GOF: 1.06. R_{wp}: 5.240 %.

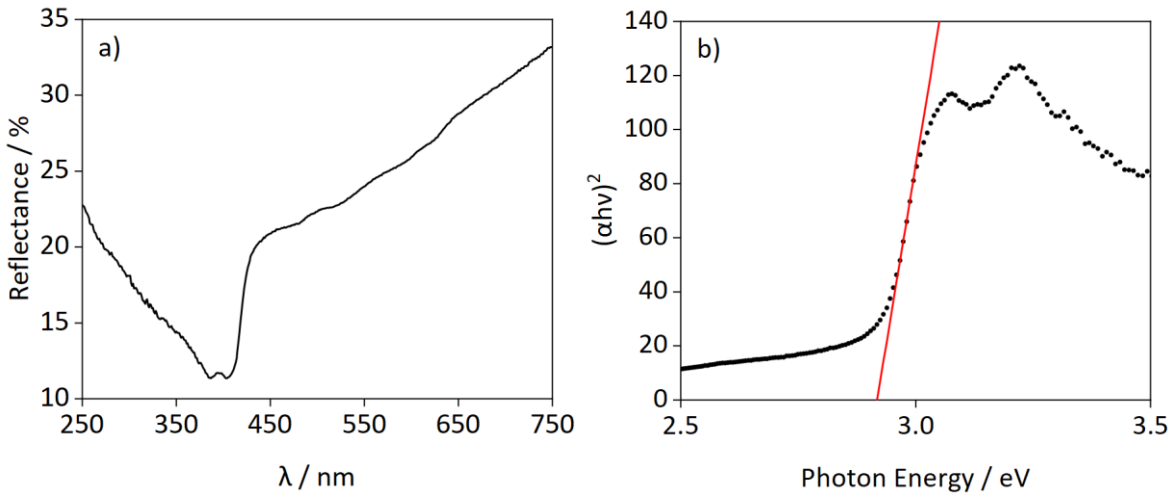

Figure 105 *UV-Vis spectrometry data for material with target composition $(Sr_{2.950}Na_{0.050})Sc_2O_5Cu_2Se_2$ after 36 hours of heating at 800 °C. Plot a) is the raw diffuse reflectance data, and plot b) is the associated magnified Tauc plot for this region, where the intercept between the red extrapolated tangent line and the x-axis is used to estimate an optical band gap of 2.92 eV, which corresponds to 425 nm.*

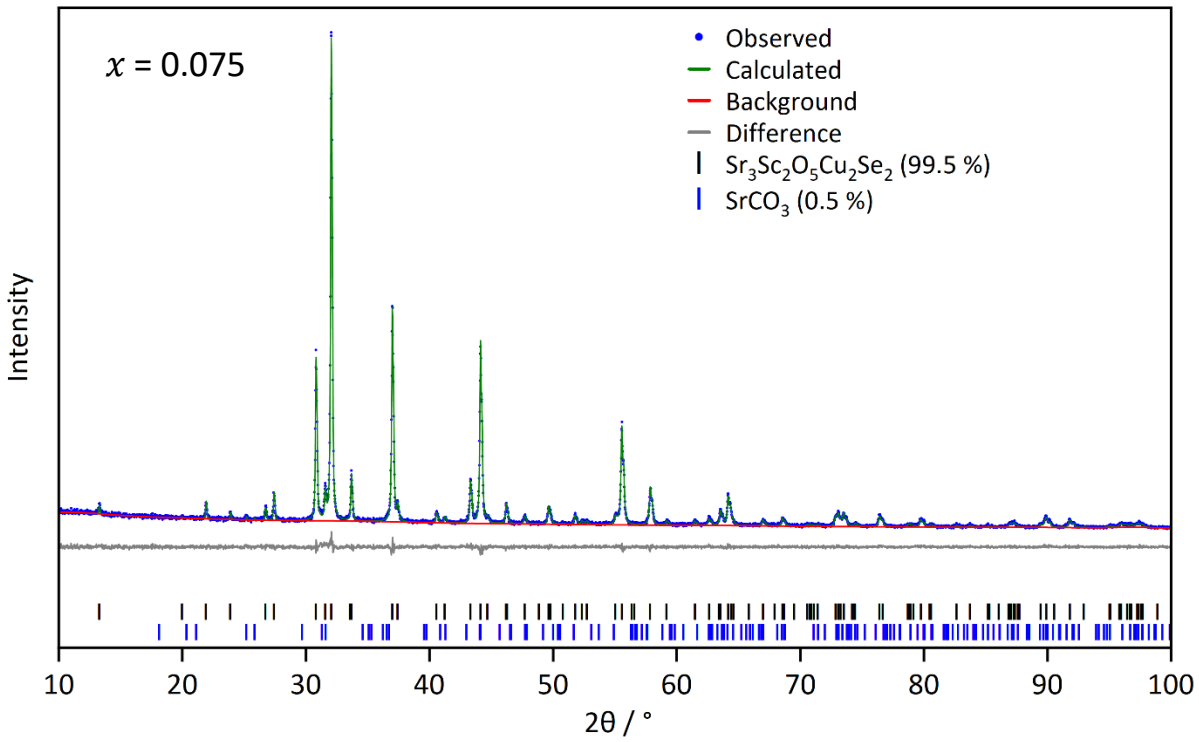

Figure 106 *Powder X-ray diffractogram of material with target composition $(Sr_{2.925}Na_{0.075})Sc_2O_5Cu_2Se_2$ (space group I4/mmm) after 36 hours of heating at 800 °C. The small blue circles represent the observed diffracted intensity, the green line represents the Rietveld-refined calculated model, the red line represents the background, and the grey line represents the difference between observed and calculated intensities. The black tick marks show the reflections of the refined model of $Sr_3Sc_2O_5Cu_2Se_2$ (99.5 %), whilst the blue marks represent refined impurity phase $SrCO_3$ (0.5 %).*
Duration: 45 minutes. Data points: 4444. Interval: 0.02 °. GOF: 1.06. R_{wp}: 5.166 %.

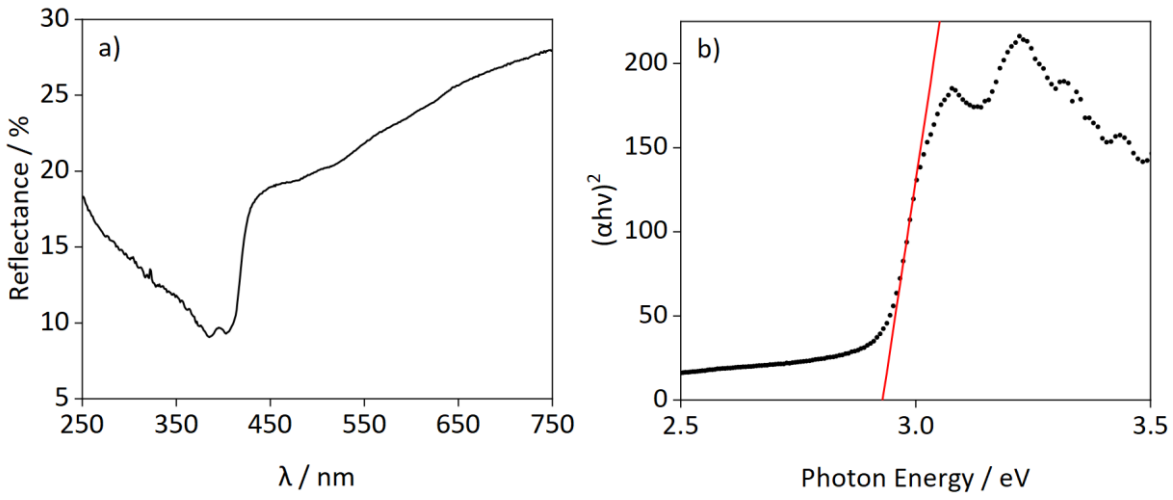

Figure 107 *UV-Vis spectrometry data for material with target composition $(Sr_{2.925}Na_{0.075})Sc_2O_5Cu_2Se_2$ after 36 hours of heating at 800 °C. Plot a) is the raw diffuse reflectance data, and plot b) is the associated magnified Tauc plot for this region, where the intercept between the red extrapolated tangent line and the x-axis is used to estimate an optical band gap of 2.93 eV, which corresponds to 423 nm.*

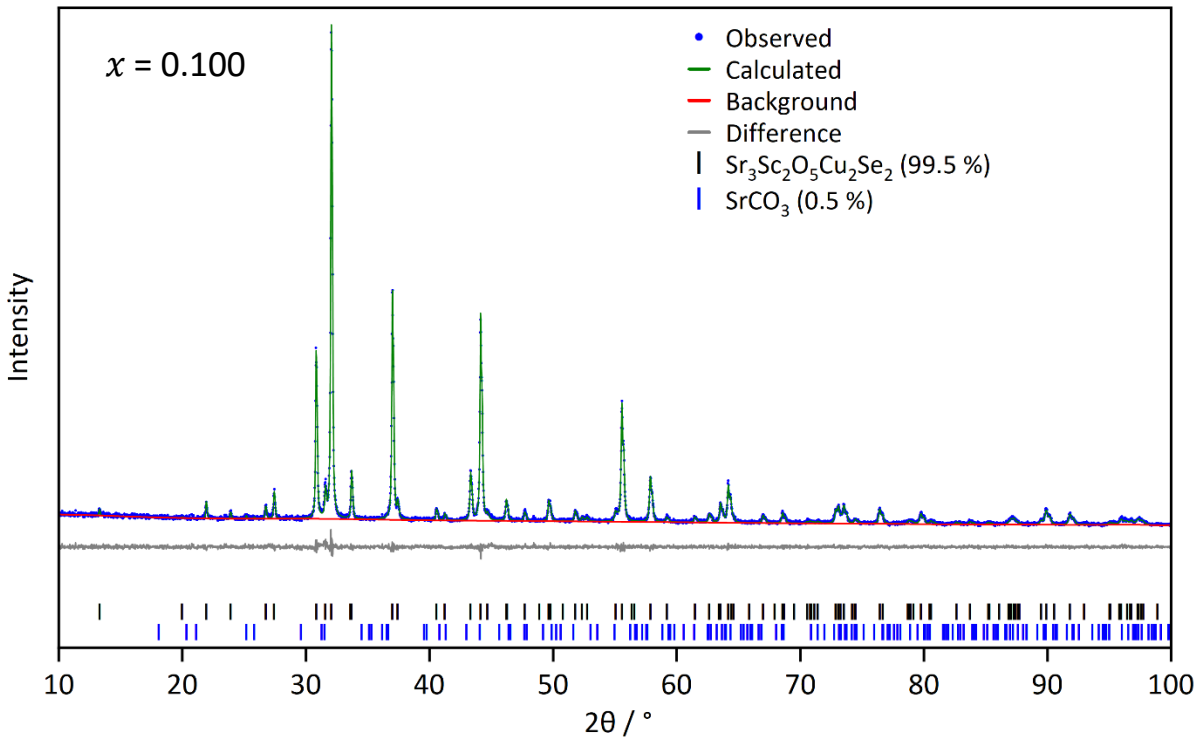

Figure 108 *Powder X-ray diffractogram of material with target composition $(Sr_{2.900}Na_{0.100})Sc_2O_5Cu_2Se_2$ (space group I4/mmm) after 36 hours of heating at 800 °C. The small blue circles represent the observed diffracted intensity, the green line represents the Rietveld-refined calculated model, the red line represents the background, and the grey line represents the difference between observed and calculated intensities. The black tick marks show the reflections of the refined model of $Sr_3Sc_2O_5Cu_2Se_2$ (99.5 %), whilst the blue marks represent refined impurity phase $SrCO_3$ (0.5 %).*
Duration: 45 minutes. Data points: 4444. Interval: 0.02 °. GOF: 1.06. R_{wp}: 4.972 %.

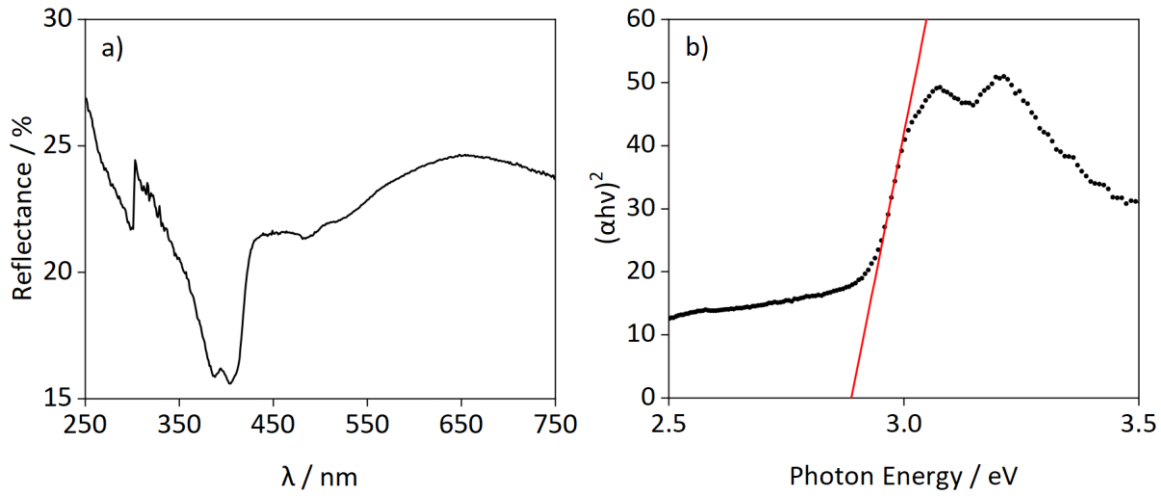

Figure 109 *UV-Vis spectrometry data for material with target composition $(Sr_{2.900}Na_{0.100})Sc_2O_5Cu_2Se_2$ after 36 hours of heating at 800 °C. Plot a) is the raw diffuse reflectance data, and plot b) is the associated magnified Tauc plot for this region, where the intercept between the red extrapolated tangent line and the x-axis is used to estimate an optical band gap of 2.89 eV, which corresponds to 429 nm.*

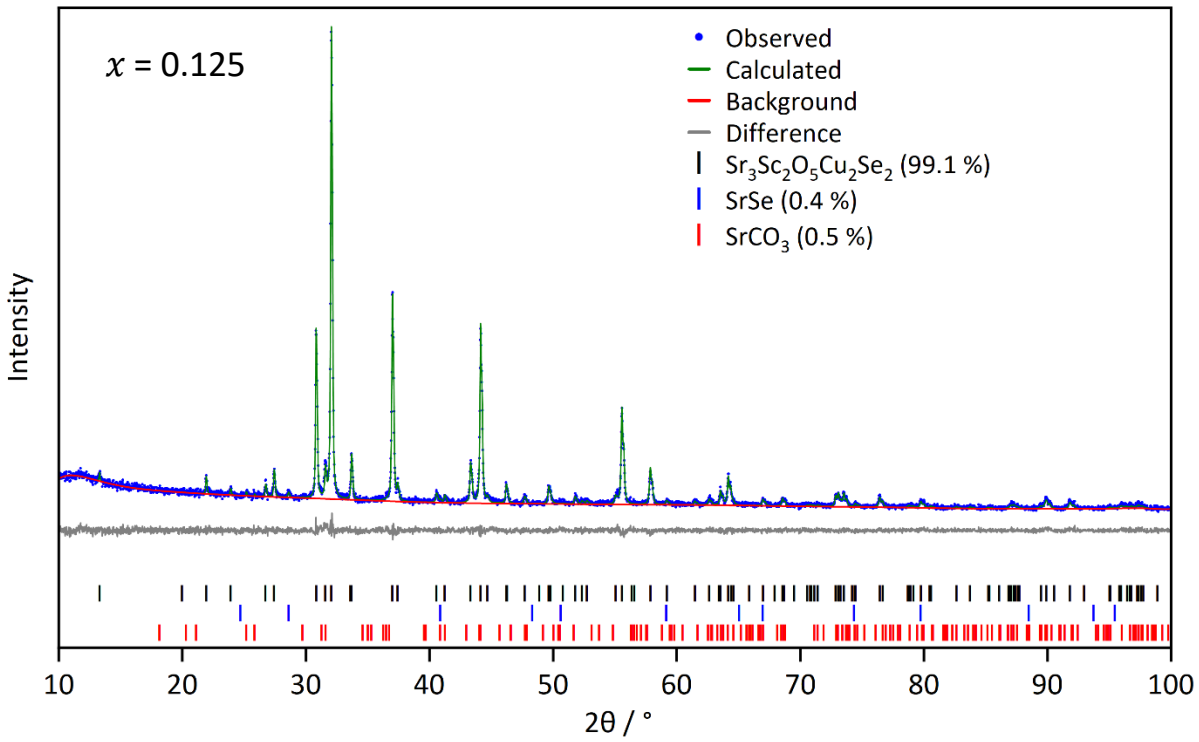

Figure 110 *Powder X-ray diffractogram of material with target composition $(Sr_{2.875}Na_{0.125})Sc_2O_5Cu_2Se_2$ (space group I4/mmm) after 36 hours of heating at 800 °C. The small blue circles represent the observed diffracted intensity, the green line represents the Rietveld-refined calculated model, the red line represents the background, and the grey line represents the difference between observed and calculated intensities. The black tick marks show the reflections of the refined model of $Sr_3Sc_2O_5Cu_2Se_2$ (99.1 %), whilst the blue and red marks represent refined impurity phases SrSe (0.4 %) and $SrCO_3$ (0.5 %) respectively.*
Duration: 45 minutes. Data points: 4444. Interval: 0.02 °. GOF: 1.07. R_{wp}: 6.660 %.

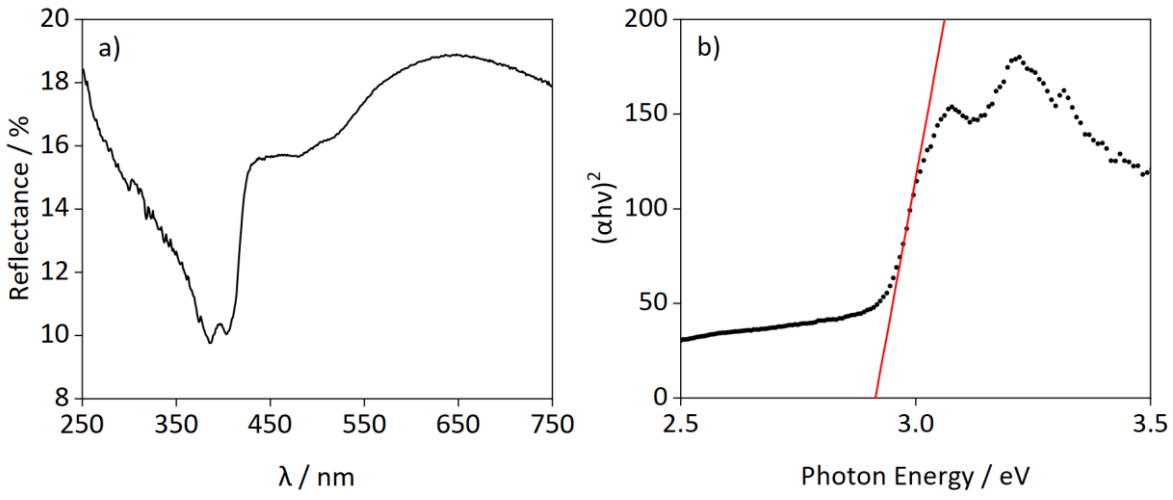

Figure 111 *UV-Vis spectrometry data for material with target composition $(Sr_{2.875}Na_{0.125})Sc_2O_5Cu_2Se_2$ after 36 hours of heating at 800 °C. Plot a) is the raw diffuse reflectance data, and plot b) is the associated magnified Tauc plot for this region, where the intercept between the red extrapolated tangent line and the x-axis is used to estimate an optical band gap of 2.91 eV, which corresponds to 426 nm.*

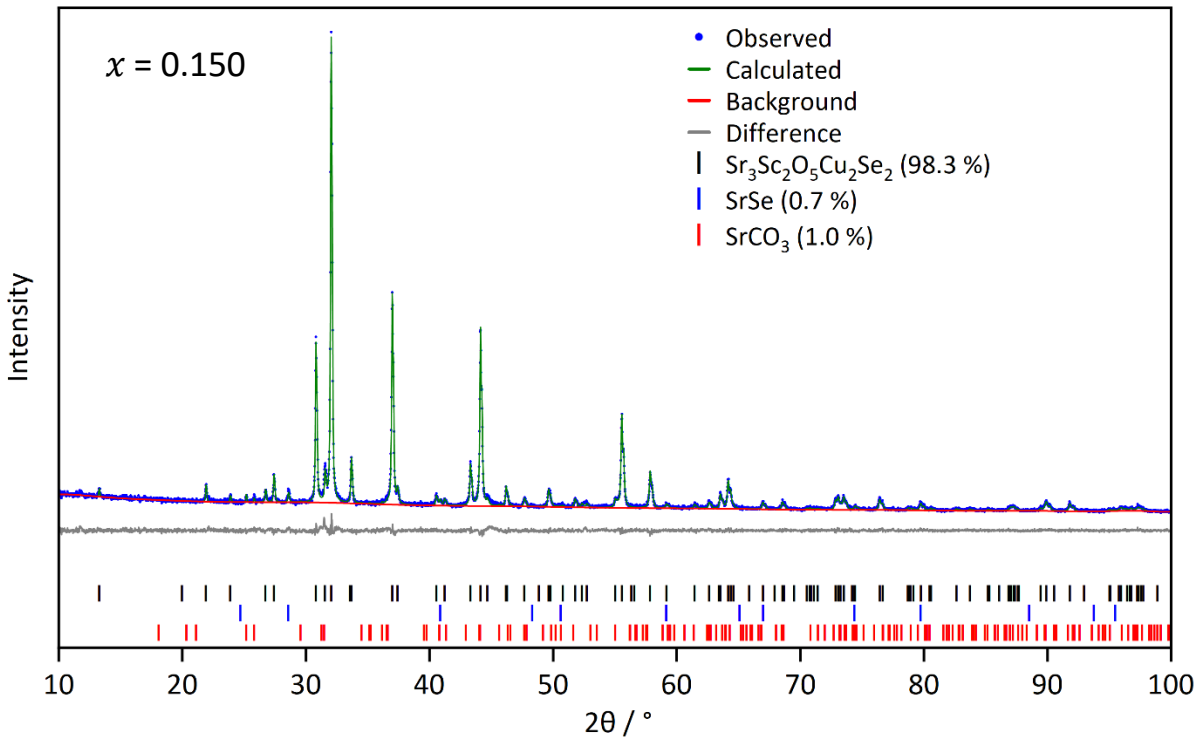

Figure 112 *Powder X-ray diffractogram of material with target composition $(Sr_{2.850}Na_{0.150})Sc_2O_5Cu_2Se_2$ (space group I4/mmm) after 36 hours of heating at 800 °C. The small blue circles represent the observed diffracted intensity, the green line represents the Rietveld-refined calculated model, the red line represents the background, and the grey line represents the difference between observed and calculated intensities. The black tick marks show the reflections of the refined model of $Sr_3Sc_2O_5Cu_2Se_2$ (98.3 %), whilst the blue and red marks represent refined impurity phases SrSe (0.7 %) and $SrCO_3$ (1.0 %) respectively.*
Duration: 45 minutes. Data points: 4444. Interval: 0.02 °. GOF: 1.19. R_{wp}: 5.801 %.

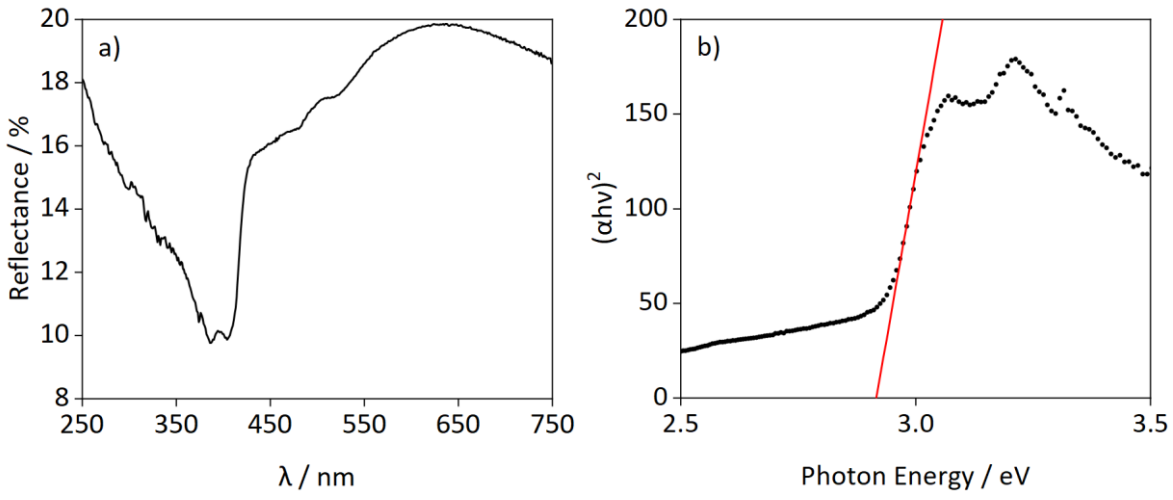

Figure 113 *UV-Vis spectrometry data for material with target composition $(Sr_{2.850}Na_{0.150})Sc_2O_5Cu_2Se_2$ after 36 hours of heating at 800 °C. Plot a) is the raw diffuse reflectance data, and plot b) is the associated magnified Tauc plot for this region, where the intercept between the red extrapolated tangent line and the x-axis is used to estimate an optical band gap of 2.92 eV, which corresponds to 425 nm.*

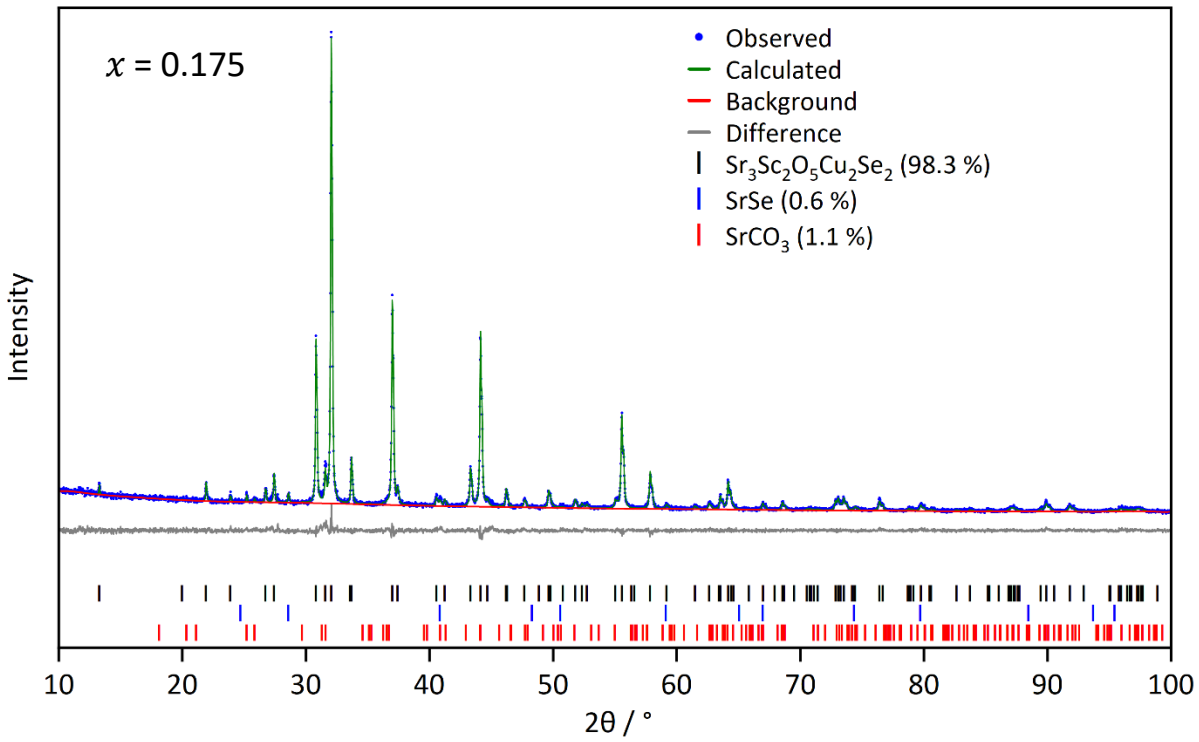

Figure 114 *Powder X-ray diffractogram of material with target composition $(Sr_{2.825}Na_{0.175})Sc_2O_5Cu_2Se_2$ (space group I4/mmm) after 36 hours of heating at 800 °C. The small blue circles represent the observed diffracted intensity, the green line represents the Rietveld-refined calculated model, the red line represents the background, and the grey line represents the difference between observed and calculated intensities. The black tick marks show the reflections of the refined model of $Sr_3Sc_2O_5Cu_2Se_2$ (98.3 %), whilst the blue and red marks represent refined impurity phases SrSe (0.6 %) and $SrCO_3$ (1.1 %) respectively.*
Duration: 45 minutes. Data points: 4444. Interval: 0.02 °. GOF: 1.14. R_{wp}: 6.173 %.

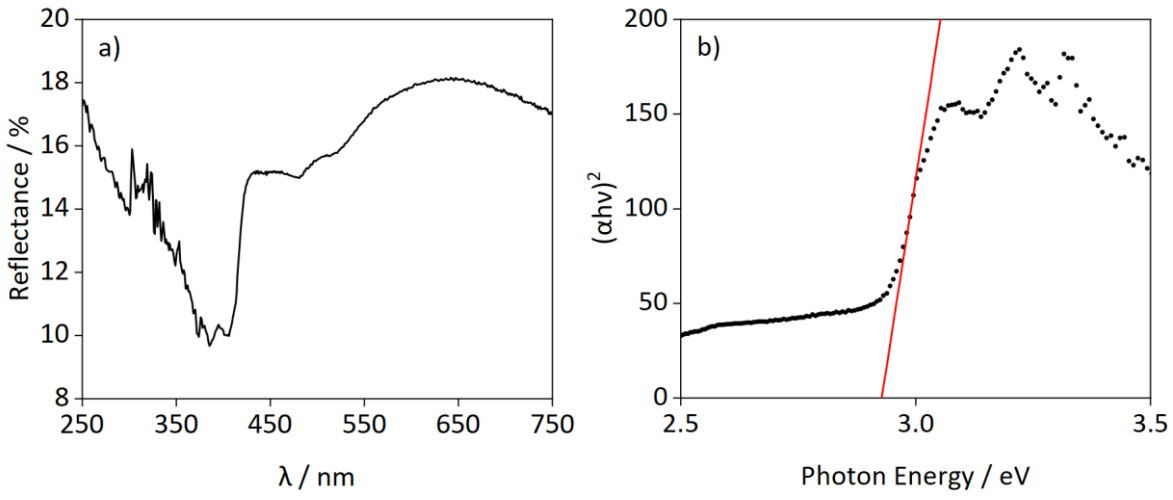

Figure 115 *UV-Vis spectrometry data for material with target composition $(Sr_{2.825}Na_{0.175})Sc_2O_5Cu_2Se_2$ after 36 hours of heating at 800 °C. Plot a) is the raw diffuse reflectance data, and plot b) is the associated magnified Tauc plot for this region, where the intercept between the red extrapolated tangent line and the x-axis is used to estimate an optical band gap of 2.93 eV, which corresponds to 423 nm.*

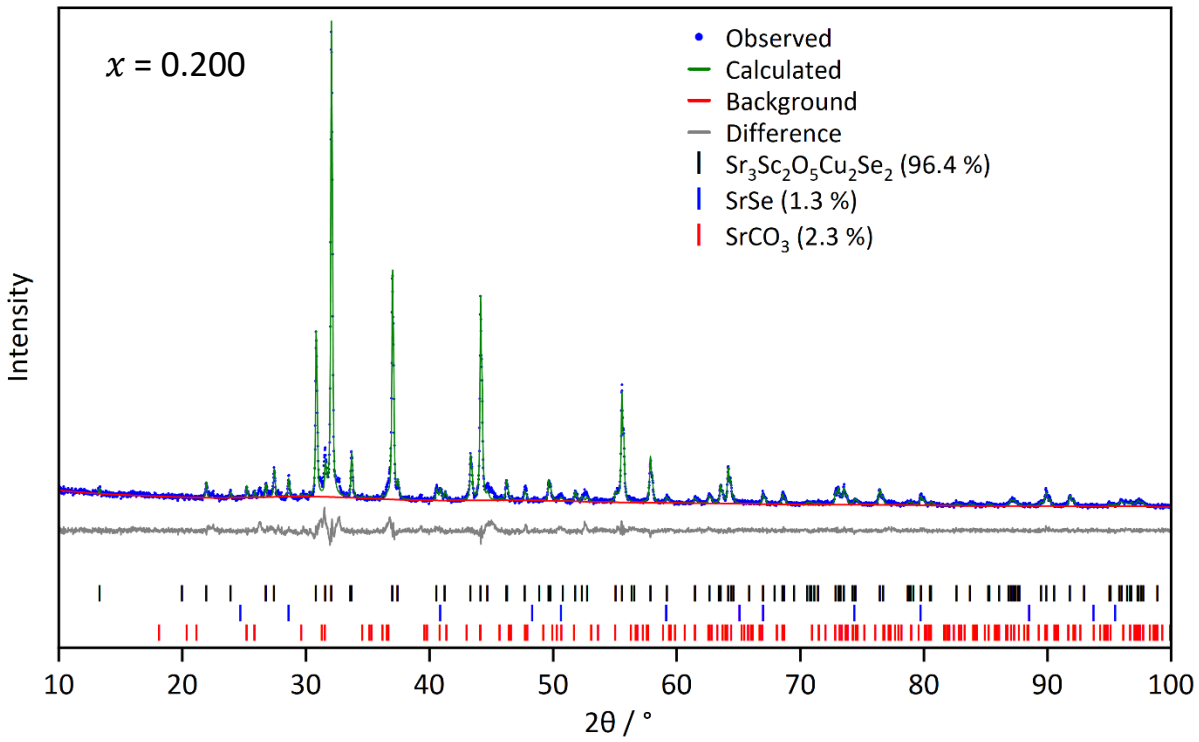

Figure 116 *Powder X-ray diffractogram of material with target composition $(Sr_{2.800}Na_{0.200})Sc_2O_5Cu_2Se_2$ (space group I4/mmm) after 36 hours of heating at 800 °C. The small blue circles represent the observed diffracted intensity, the green line represents the Rietveld-refined calculated model, the red line represents the background, and the grey line represents the difference between observed and calculated intensities. The black tick marks show the reflections of the refined model of $Sr_3Sc_2O_5Cu_2Se_2$ (96.4 %), whilst the blue and red marks represent refined impurity phases SrSe (1.3 %) and $SrCO_3$ (2.3 %) respectively.*
Duration: 45 minutes. Data points: 4444. Interval: 0.02 °. GOF: 1.55. R_{wp}: 7.584 %.

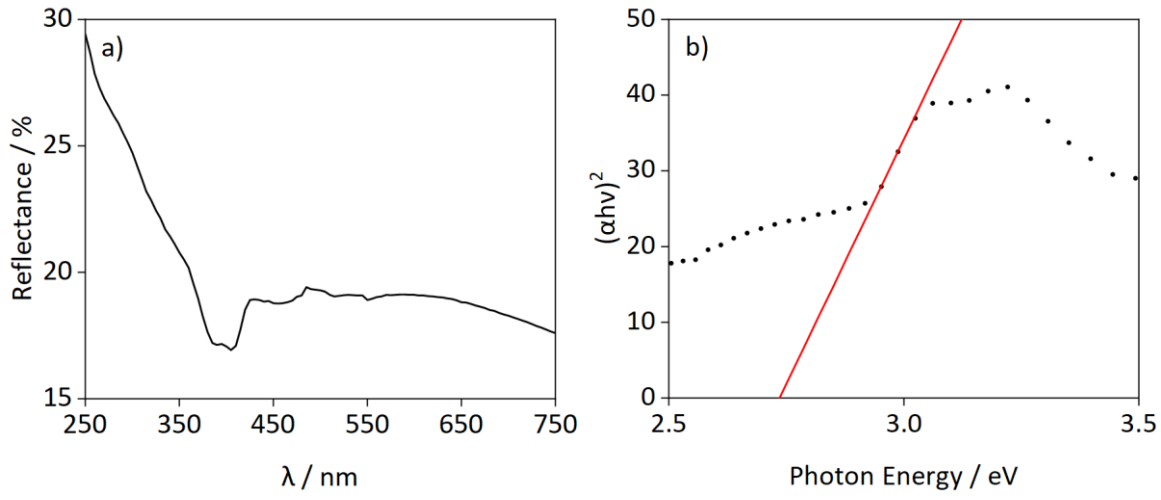

Figure 117 *UV-Vis spectrometry data for material with target composition $(Sr_{2.800}Na_{0.200})Sc_2O_5Cu_2Se_2$ after 36 hours of heating at 800 °C. Plot a) is the raw diffuse reflectance data, and plot b) is the associated magnified Tauc plot for this region, where the intercept between the red extrapolated tangent line and the x-axis is used to estimate an optical band gap of 2.74 eV, which corresponds to 452 nm.*

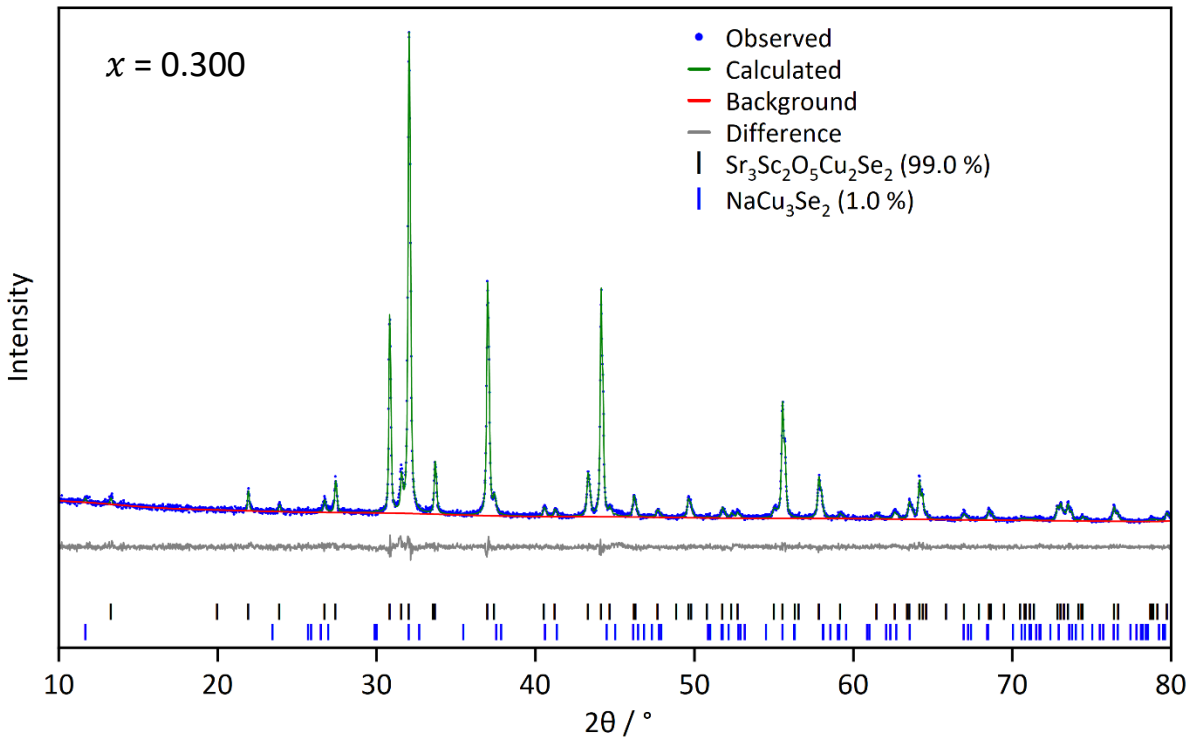

Figure 118 *Powder X-ray diffractogram of material with target composition $(Sr_{2.700}Na_{0.300})Sc_2O_5Cu_2Se_2$ (space group I4/mmm) after 36 hours of heating at 800 °C. The small blue circles represent the observed diffracted intensity, the green line represents the Rietveld-refined calculated model, the red line represents the background, and the grey line represents the difference between observed and calculated intensities. The black tick marks show the reflections of the refined model of $Sr_3Sc_2O_5Cu_2Se_2$ (99.0 %), whilst the blue marks represent refined impurity phase $NaCu_3Se_2$ (1.0 %).*
Duration: 45 minutes. Data points: 3457. Interval: 0.02 °. GOF: 1.12. R_{wp}: 5.380 %.

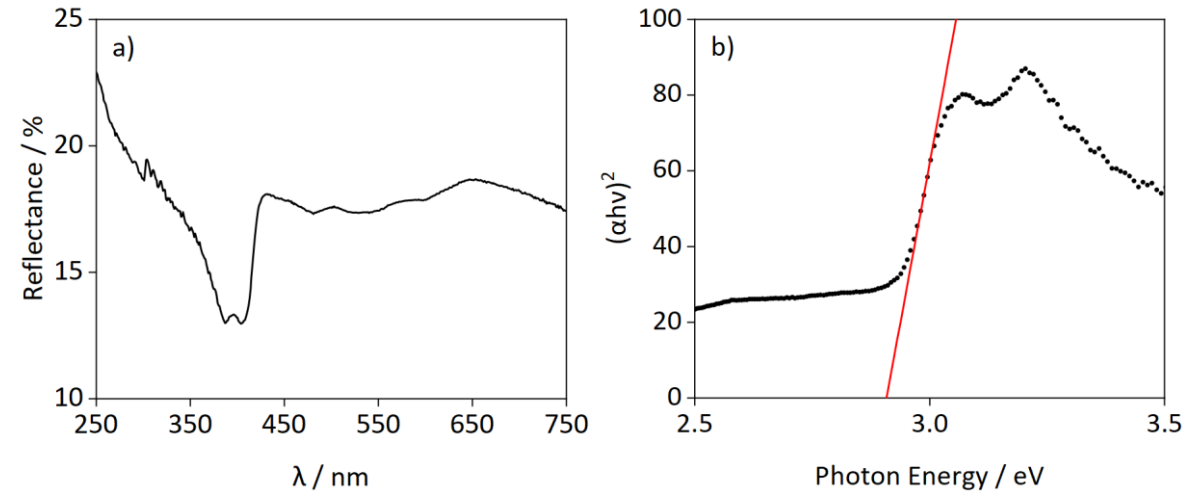

Figure 119 *UV-Vis spectrometry data for material with target composition $(Sr_{2.700}Na_{0.300})Sc_2O_5Cu_2Se_2$ after 36 hours of heating at 800 °C. Plot a) is the raw diffuse reflectance data, and plot b) is the associated magnified Tauc plot for this region, where the intercept between the red extrapolated tangent line and the x-axis is used to estimate an optical band gap of 2.91 eV, which corresponds to 426 nm.*

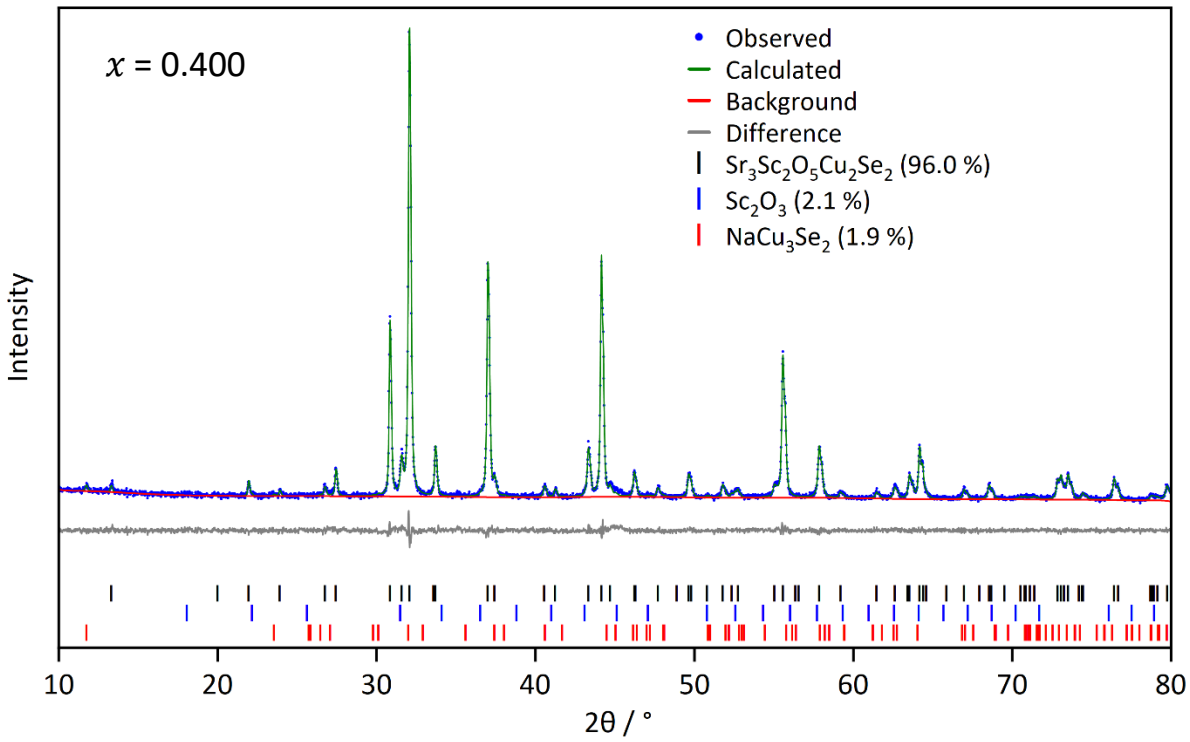

Figure 120 *Powder X-ray diffractogram of material with target composition $(Sr_{2.600}Na_{0.400})Sc_2O_5Cu_2Se_2$ (space group I4/mmm) after 36 hours of heating at 800 °C. The small blue circles represent the observed diffracted intensity, the green line represents the Rietveld-refined calculated model, the red line represents the background, and the grey line represents the difference between observed and calculated intensities. The black tick marks show the reflections of the refined model of $Sr_3Sc_2O_5Cu_2Se_2$ (96.0 %), whilst the blue and red marks represent refined impurity phases Sc_2O_3 (2.1 %) and $NaCu_3Se_2$ (1.9 %) respectively.*
Duration: 45 minutes. Data points: 3457. Interval: 0.02 °. GOF: 1.13. R_{wp}: 4.714 %.

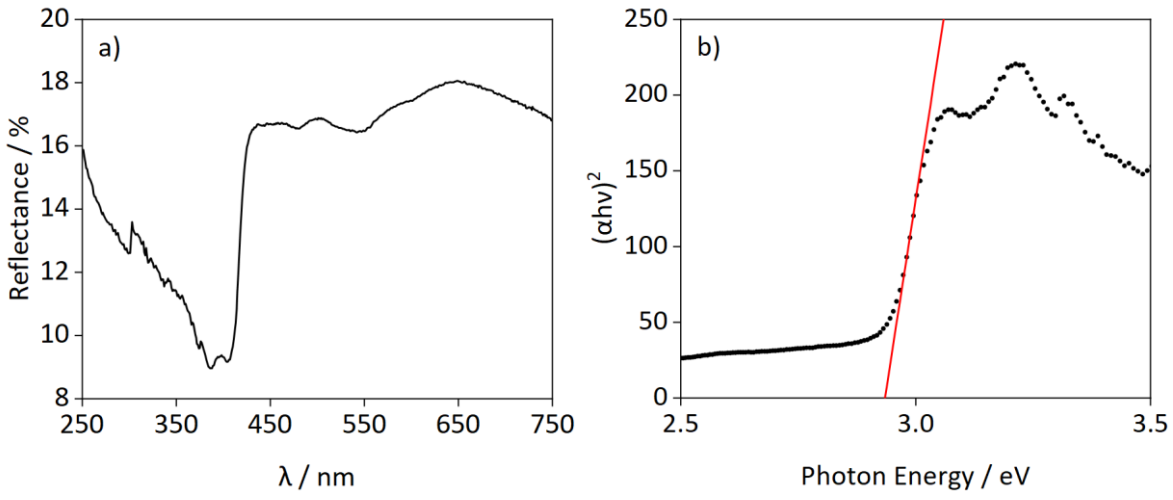

Figure 121 *UV-Vis spectrometry data for material with target composition $(Sr_{2.600}Na_{0.400})Sc_2O_5Cu_2Se_2$ after 36 hours of heating at 800 °C. Plot a) is the raw diffuse reflectance data, and plot b) is the associated magnified Tauc plot for this region, where the intercept between the red extrapolated tangent line and the x-axis is used to estimate an optical band gap of 2.93 eV, which corresponds to 423 nm.*

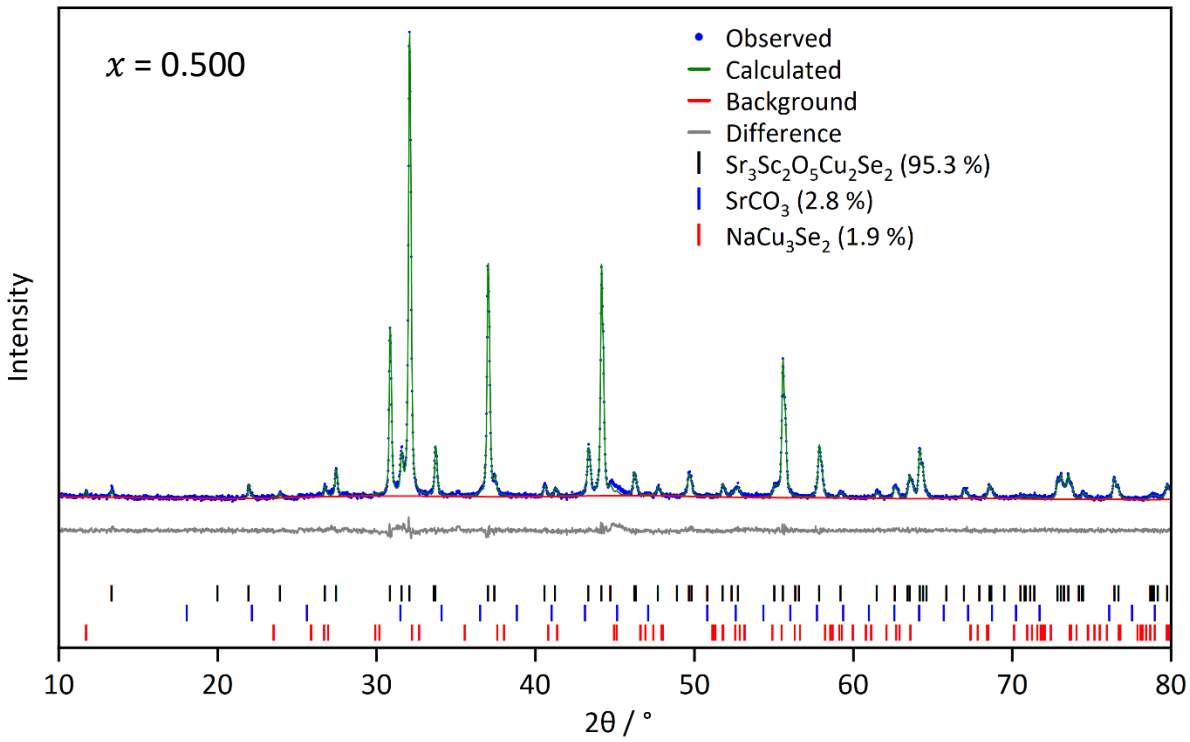

Figure 122 *Powder X-ray diffractogram of material with target composition $(Sr_{2.500}Na_{0.500})Sc_2O_5Cu_2Se_2$ (space group I4/mmm) after 36 hours of heating at 800 °C. The small blue circles represent the observed diffracted intensity, the green line represents the Rietveld-refined calculated model, the red line represents the background, and the grey line represents the difference between observed and calculated intensities. The black tick marks show the reflections of the refined model of $Sr_3Sc_2O_5Cu_2Se_2$ (95.3 %), whilst the blue and red marks represent refined impurity phases $SrCO_3$ (2.8 %) and $NaCu_3Se_2$ (1.9 %) respectively.*
Duration: 45 minutes. Data points: 3457. Interval: 0.02 °. GOF: 1.24. R_{wp}: 4.657 %.

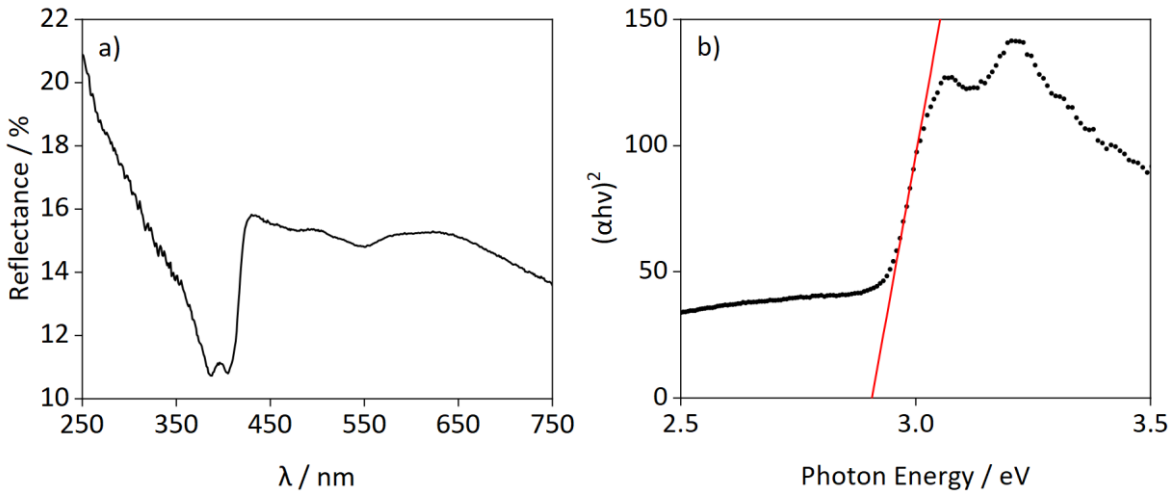

Figure 123 *UV-Vis spectrometry data for material with target composition $(Sr_{2.500}Na_{0.500})Sc_2O_5Cu_2Se_2$ after 36 hours of heating at 800 °C. Plot a) is the raw diffuse reflectance data, and plot b) is the associated magnified Tauc plot for this region, where the intercept between the red extrapolated tangent line and the x-axis is used to estimate an optical band gap of 2.91 eV, which corresponds to 426 nm.*

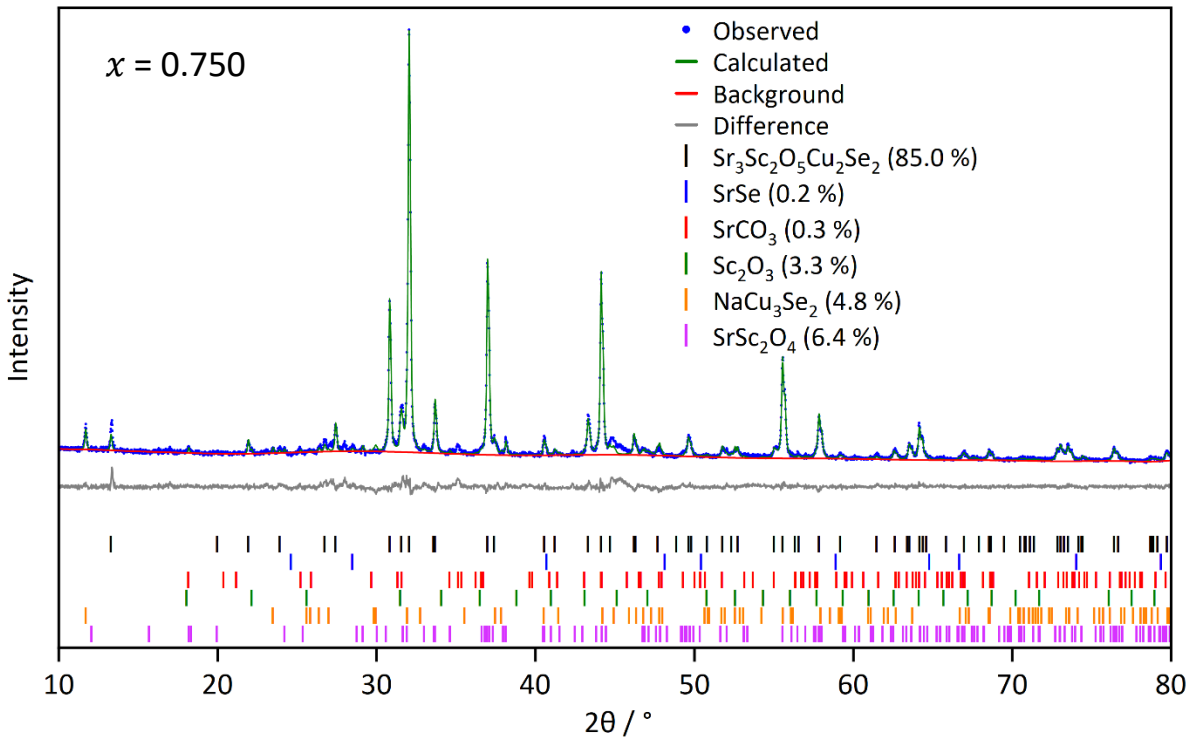

Figure 124 *Powder X-ray diffractogram of material with target composition $(Sr_{2.250}Na_{0.750})Sc_2O_5Cu_2Se_2$ (space group I4/mmm) after 36 hours of heating at 800 °C. The small blue circles represent the observed diffracted intensity, the green line represents the Rietveld-refined calculated model, the red line represents the background, and the grey line represents the difference between observed and calculated intensities. The black tick marks show the reflections of the refined model of $Sr_3Sc_2O_5Cu_2Se_2$ (85.0 %), whilst the blue, red, green, orange and pink marks represent refined impurity phases SrSe (0.2 %), $SrCO_3$ (0.3 %), Sc_2O_3 (3.3 %), $NaCu_3Se_2$ (4.8 %) and $SrSc_2O_4$ (6.4 %) respectively.*
Duration: 45 minutes. Data points: 3457. Interval: 0.02 °. GOF: 1.70. R_{wp}: 6.490 %.

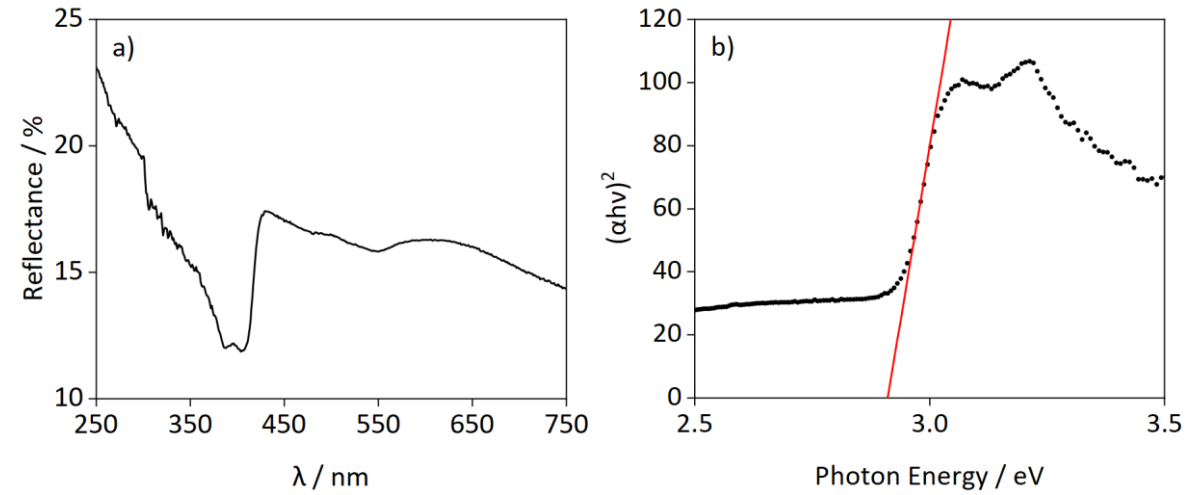

Figure 125 *UV-Vis spectrometry data for material with target composition $(Sr_{2.250}Na_{0.750})Sc_2O_5Cu_2Se_2$ after 36 hours of heating at 800 °C. Plot a) is the raw diffuse reflectance data, and plot b) is the associated magnified Tauc plot for this region, where the intercept between the red extrapolated tangent line and the x-axis is used to estimate an optical band gap of 2.91 eV, which corresponds to 426 nm.*

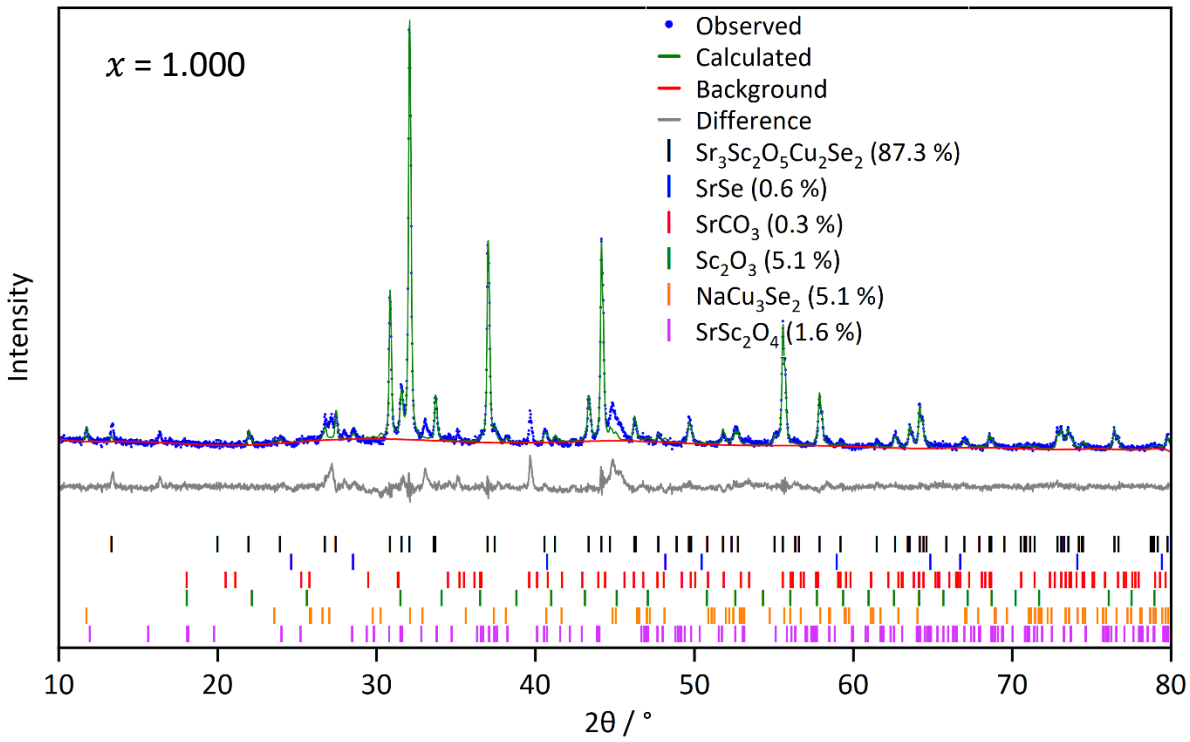

Figure 126 *Powder X-ray diffractogram of material with target composition $(Sr_{2.000}Na_{1.000})Sc_2O_5Cu_2Se_2$ (space group I4/mmm) after 36 hours of heating at 800 °C. The small blue circles represent the observed diffracted intensity, the green line represents the Rietveld-refined calculated model, the red line represents the background, and the grey line represents the difference between observed and calculated intensities. The black tick marks show the reflections of the refined model of $Sr_3Sc_2O_5Cu_2Se_2$ (87.3 %), whilst the blue, red, green, orange and pink marks represent refined impurity phases SrSe (0.6 %), $SrCO_3$ (0.3 %), Sc_2O_3 (5.1 %), $NaCu_3Se_2$ (5.1 %) and $SrSc_2O_4$ (1.6 %) respectively.*
Duration: 45 minutes. Data points: 3457. Interval: 0.02 °. GOF: 2.05. R_{wp}: 8.228 %.

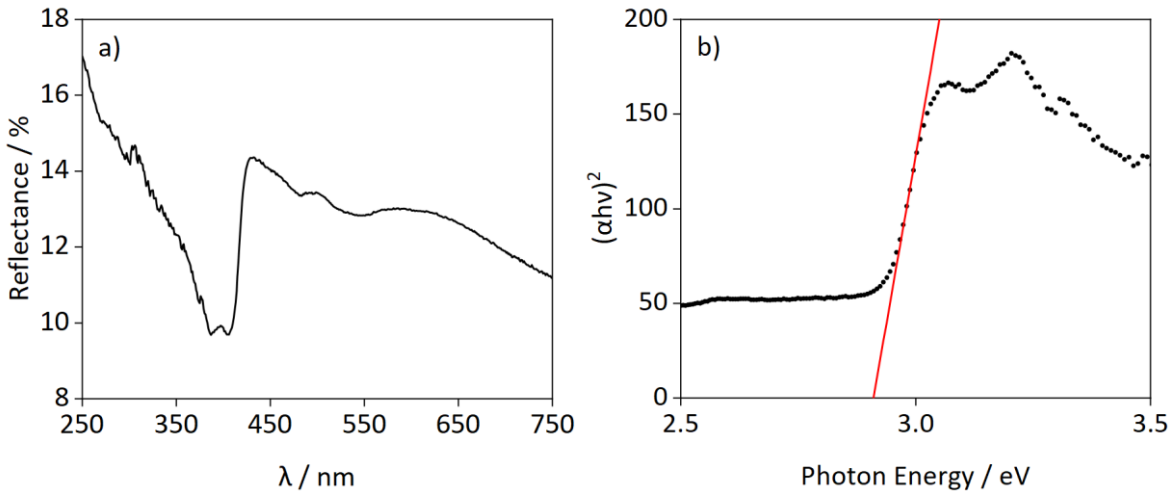

Figure 127 *UV-Vis spectrometry data for material with target composition $(Sr_{2.000}Na_{1.000})Sc_2O_5Cu_2Se_2$ after 36 hours of heating at 800 °C. Plot a) is the raw diffuse reflectance data, and plot b) is the associated magnified Tauc plot for this region, where the intercept between the red extrapolated tangent line and the x-axis is used to estimate an optical band gap of 2.91 eV, which corresponds to 426 nm.*

B.1.6 Magnesium doped 325 selenide MALMs, $Sr_3(Sc_{2-x}Mg_x)O_5Cu_2Se_2$

Table 34 Tabulated structural data of the magnesium doped 325 selenide MALMs with general formula $Sr_3(Sc_{2-x}Mg_x)O_5Cu_2Se_2$. The pristine material $Sr_3Sc_2O_5Cu_2Se_2$ is included as a reference. All values are derived from the Rietveld refinement of PXRD data using GSAS-II. Note that because all materials listed are tetragonal (space group I4/mmm), the b parameter is identical to a, and thus omitted.

x / mol	Target Composition	a / Å	c / Å	Volume / Å^3
0 (pristine)	$Sr_3Sc_2O_5Cu_2Se_2$	4.10329(4)	26.6847(3)	449.290(12)
0.05	$Sr_3(Sc_{1.95}Mg_{0.05})O_5Cu_2Se_2$	4.10303(7)	26.6910(6)	449.339(20)
0.10	$Sr_3(Sc_{1.90}Mg_{0.10})O_5Cu_2Se_2$	4.10271(8)	26.6883(7)	449.223(24)
0.15	$Sr_3(Sc_{1.85}Mg_{0.15})O_5Cu_2Se_2$	4.10243(8)	26.6955(7)	449.283(25)
0.20	$Sr_3(Sc_{1.80}Mg_{0.20})O_5Cu_2Se_2$	4.10235(9)	26.6902(7)	449.179(27)

Table 35 Tabulated compositional data of the magnesium doped 325 selenide MALMs with general formula $Sr_3(Sc_{2-x}Mg_x)O_5Cu_2Se_2$. The pristine material $Sr_3Sc_2O_5Cu_2Se_2$ is included as a reference. All values are cited as a weight percent (wt %) of the total weight, and are derived from the Rietveld refinement of PXRD data using GSAS-II.

x / mol	Target phase / wt %	SrSe / wt %	$SrCO_3$ / wt %
0 (pristine)	99.1	0.5	0.4
0.05	99.5	0.5	-
0.10	99.4	0.6	-
0.15	98.5	0.7	0.8
0.20	98.1	1.1	0.8

Table 36 Tabulated analytical data of to the measured properties of the magnesium doped 325 selenide MALMs with general formula $Sr_3(Sc_{2-x}Mg_x)O_5Cu_2Se_2$. The pristine material $Sr_3Sc_2O_5Cu_2Se_2$ is included as a reference. Optical band gaps were estimated from UV-Vis data. Pellet densities were estimated from the mass and volume of annealed pellet samples, and are cited as a relative percentage of the bulk crystal. Resistivities and conductivities were estimated from 4 probe van der Pauw analysis of the pellet samples.

x / mol	Band Gap / eV	Pellet Density / %	Raw Resistivities from 4-Probe measurement, for each probe permutation / kΩ								Resistivity / Ω cm	Conductivity / S cm^{-1}
			1	2	3	4	5	6	7	8		
0 (pristine)	2.94	71.72	1.20 E+01	1.21 E+01	1.22 E+01	1.22 E+01	1.03 E+01	1.02 E+01	1.02 E+01	1.01 E+01	3.83 E+03	2.61 E-04
0.05	2.90	68.21	2.50 E-02	2.50 E-02	2.46 E-02	2.31 E-02	2.59 E-02	2.58 E-02	2.78 E-02	2.86 E-02	9.44 E+00	1.06 E-01
0.10	2.89	69.16	1.64 E-02	1.62 E-02	1.67 E-02	1.67 E-02	8.95 E-03	8.90 E-03	8.99 E-03	8.94 E-03	4.36 E+00	2.30 E-01
0.15	2.84	71.89	4.47 E-03	4.55 E-03	4.53 E-03	4.57 E-03	6.97 E-03	6.97 E-03	6.97 E-03	6.93 E-03	1.99 E+00	5.03 E-01
0.20	2.82	72.03	3.81 E-03	3.83 E-03	3.82 E-03	3.95 E-03	6.46 E-03	6.48 E-03	6.46 E-03	6.47 E-03	1.75 E+00	5.72 E-01

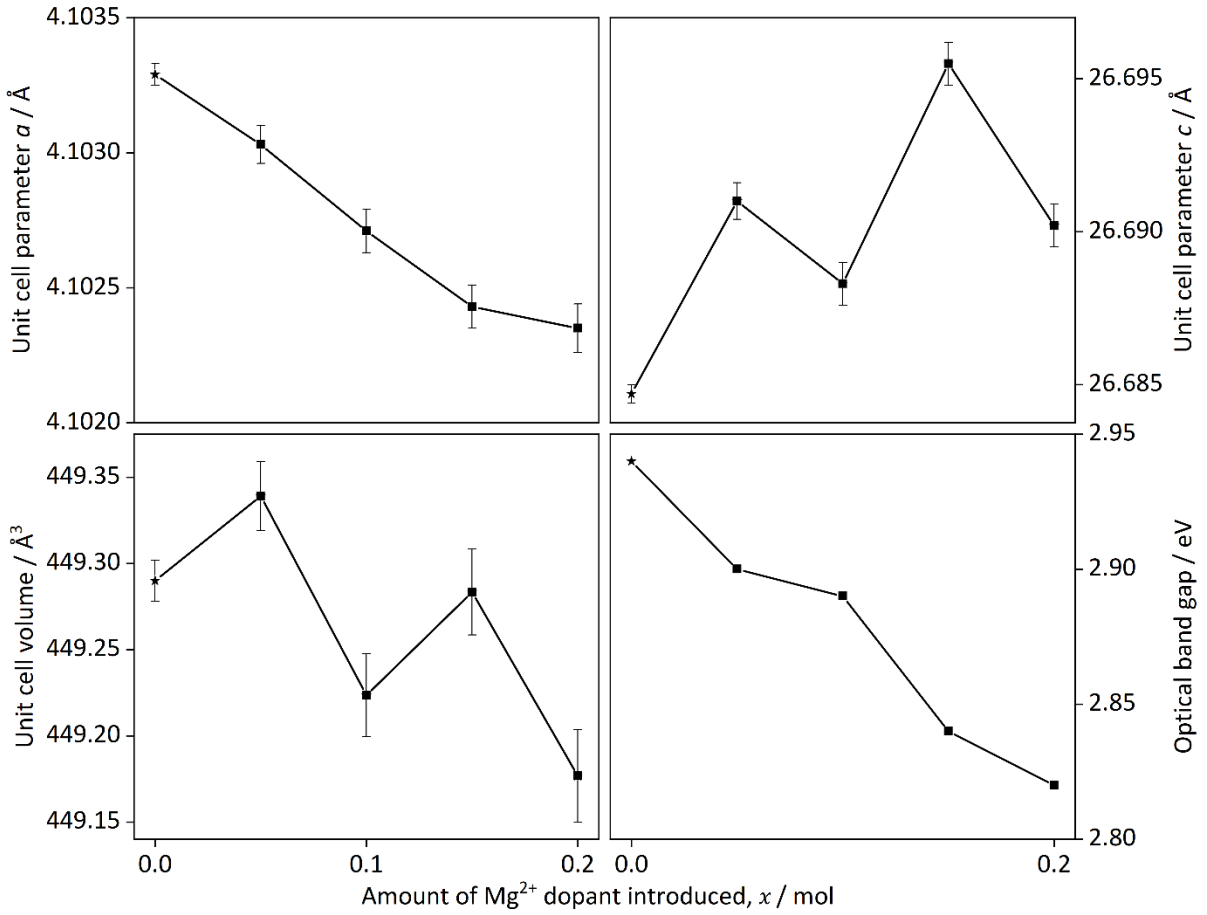

Figure 128 *Comparisons of a) the α unit cell parameter, b) the c unit cell parameter, c) unit cell volume, and d) the optical band gap, of the magnesium doped 325 selenide MALMs with general formula $Sr_3(Sc_{2-x}Mg_x)O_5Cu_2Se_2$. The pristine material $Sr_3Sc_2O_5Cu_2Se_2$ is included as a reference at x = 0 mol and is represented by a star.*

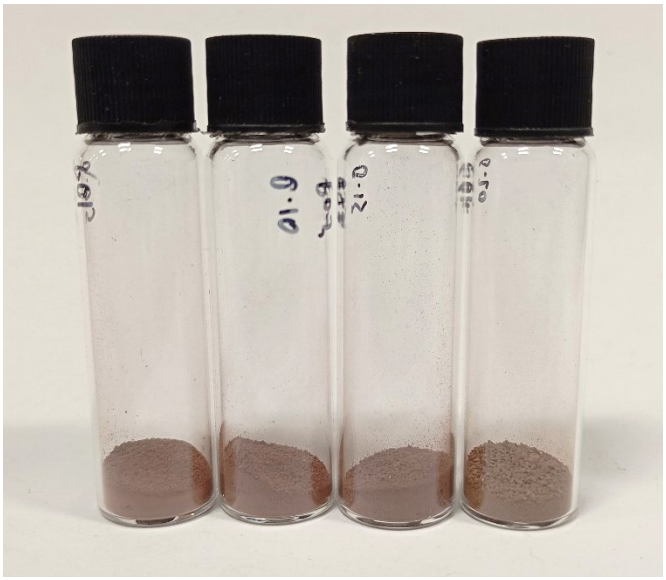

Figure 129 *A photographic comparison of the colour of the magnesium doped 325 selenide MALMs with general formula $Sr_3(Sc_{2-x}Mg_x)O_5Cu_2Se_2$. Dopant concentration increases from left to right.*

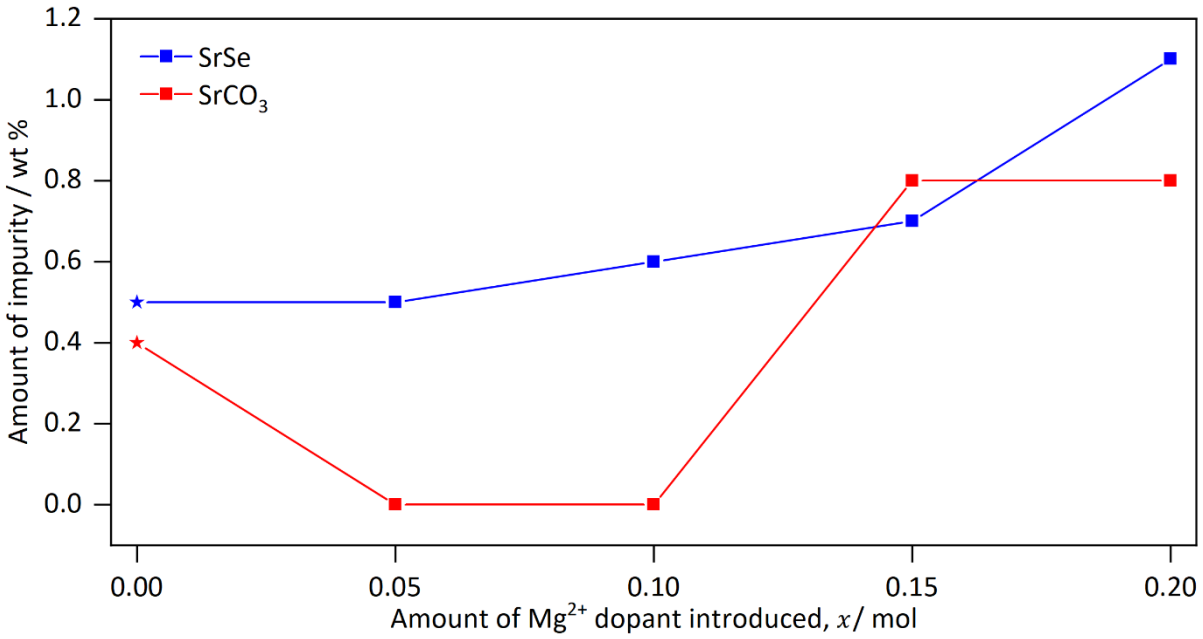

Figure 130 *The weight percentages of two impurity phases present in the magnesium doped 325 selenide MALMs with general formula $Sr_3(Sc_{2-x}Mg_x)O_5Cu_2Se_2$. The pristine material $Sr_3Sc_2O_5Cu_2Se_2$ is included as a reference at $x = 0$ mol and is represented by a star.*

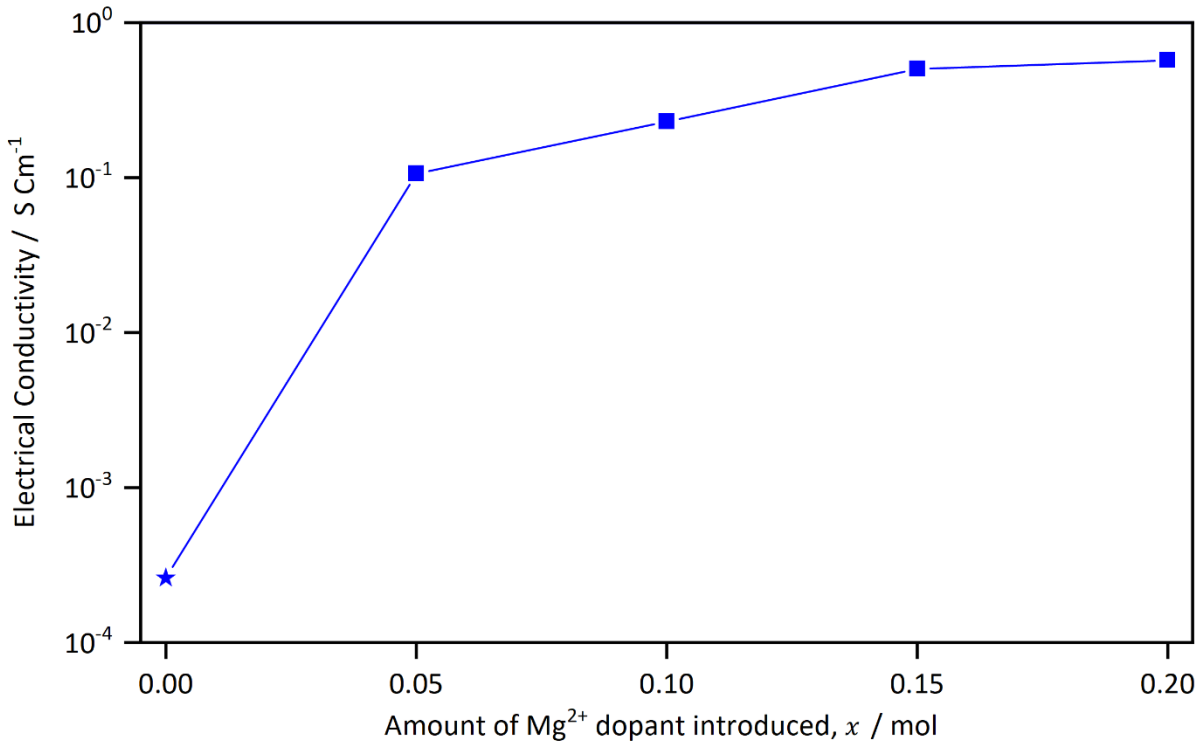

Figure 131 *The electrical conductivities of the magnesium doped 325 selenide MALMs with general formula $Sr_3(Sc_{2-x}Mg_x)O_5Cu_2Se_2$, represented on a log_{10} scale. The pristine material $Sr_3Sc_2O_5Cu_2Se_2$ is included as a reference at $x = 0$ mol and is represented by a star. All values are derived from van der Pauw 4 probe resistivity measurements of 8mm diameter annealed pellet samples.*

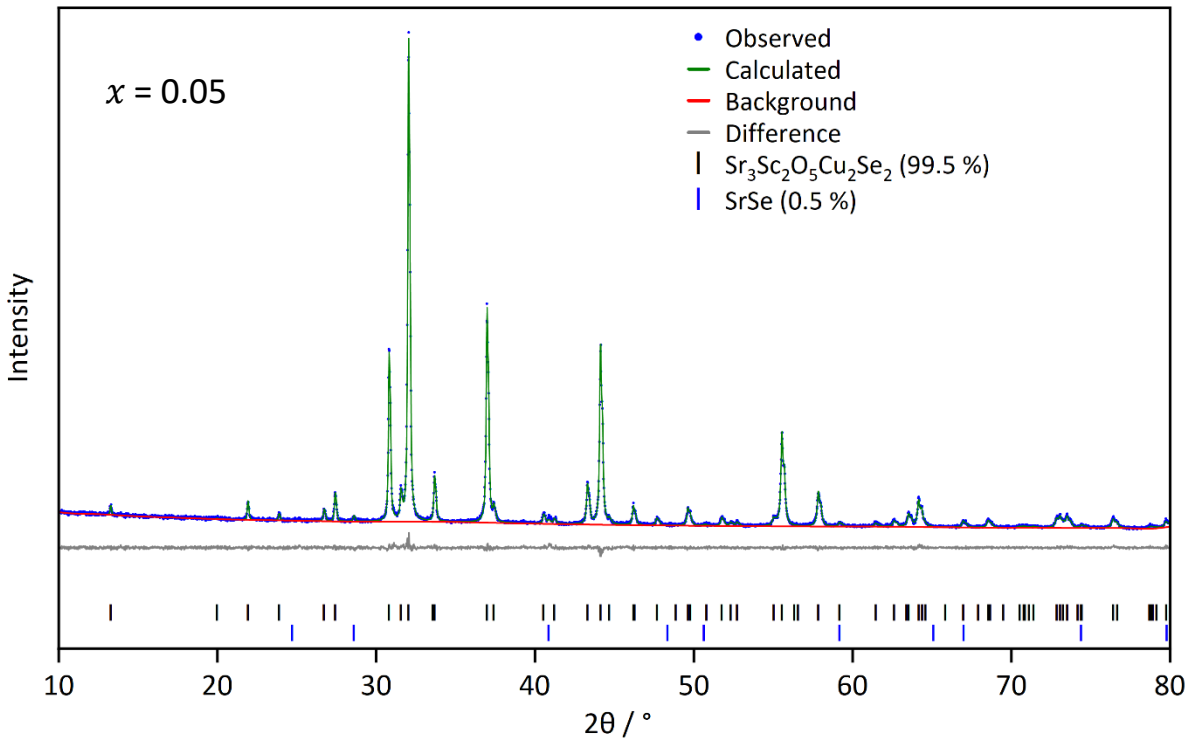

Figure 132 *Powder X-ray diffractogram of material with target composition $Sr_3(Sc_{1.95}Mg_{0.05})O_5Cu_2Se_2$ (space group I4/mmm) after 36 hours of heating at 800 °C. The small blue circles represent the observed diffracted intensity, the green line represents the Rietveld-refined calculated model, the red line represents the background, and the grey line represents the difference between observed and calculated intensities. The black tick marks show the reflections of the refined model of $Sr_3Sc_2O_5Cu_2Se_2$ (99.5 %), whilst the blue marks represent refined impurity phase SrSe (0.5 %).*
Duration: 45 minutes. Data points: 3457. Interval: 0.02 °. GOF: 1.13. R_{wp}: 4.460 %.

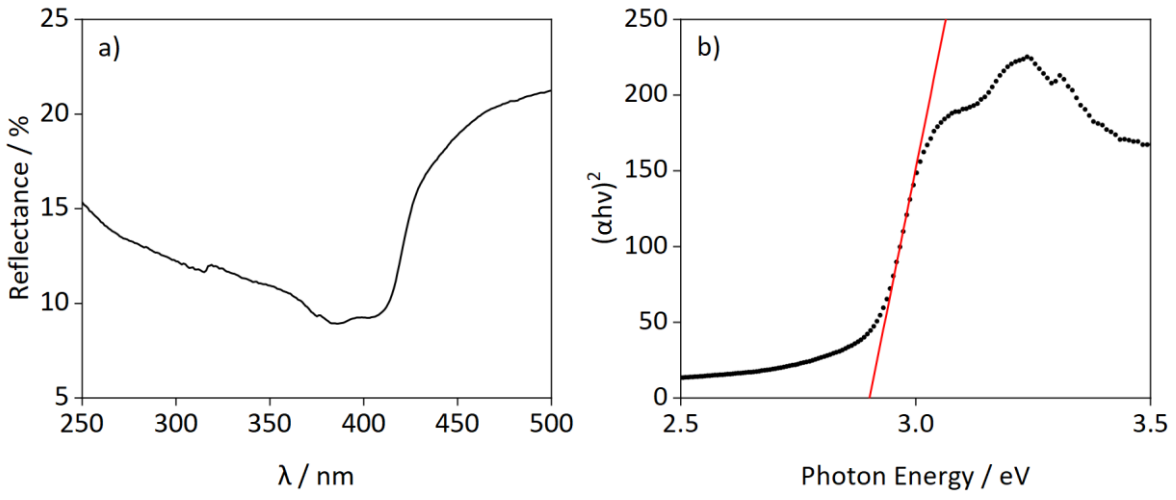

Figure 133 *UV-Vis spectrometry data for material with target composition $Sr_3(Sc_{1.95}Mg_{0.05})O_5Cu_2Se_2$ after 36 hours of heating at 800 °C. Plot a) is the raw diffuse reflectance data, and plot b) is the associated magnified Tauc plot for this region, where the intercept between the red extrapolated tangent line and the x-axis is used to estimate an optical band gap of 2.90 eV, which corresponds to 428 nm.*

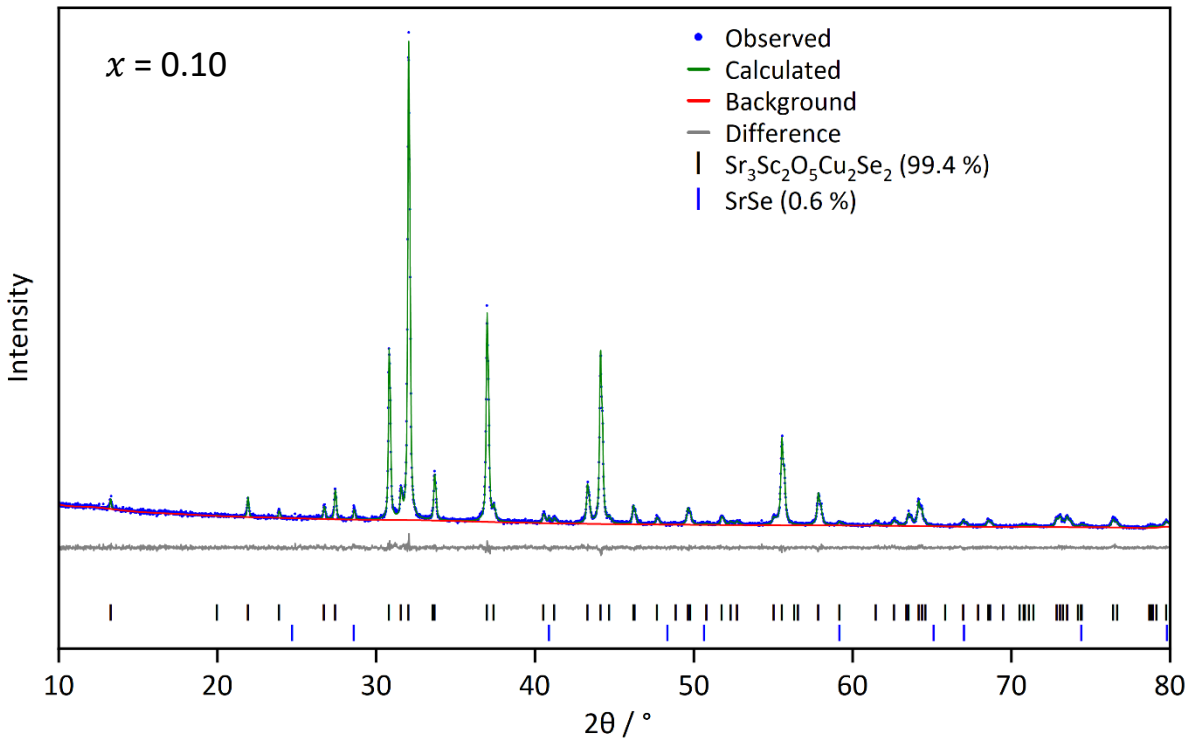

Figure 134 *Powder X-ray diffractogram of material with target composition $Sr_3(Sc_{1.90}Mg_{0.10})O_5Cu_2Se_2$ (space group I4/mmm) after 36 hours of heating at 800 °C. The small blue circles represent the observed diffracted intensity, the green line represents the Rietveld-refined calculated model, the red line represents the background, and the grey line represents the difference between observed and calculated intensities. The black tick marks show the reflections of the refined model of $Sr_3Sc_2O_5Cu_2Se_2$ (99.4 %), whilst the blue marks represent refined impurity phase SrSe (0.6 %).*
Duration: 45 minutes. Data points: 3457. Interval: 0.02 °. GOF: 1.09. R_{wp}: 4.851 %.

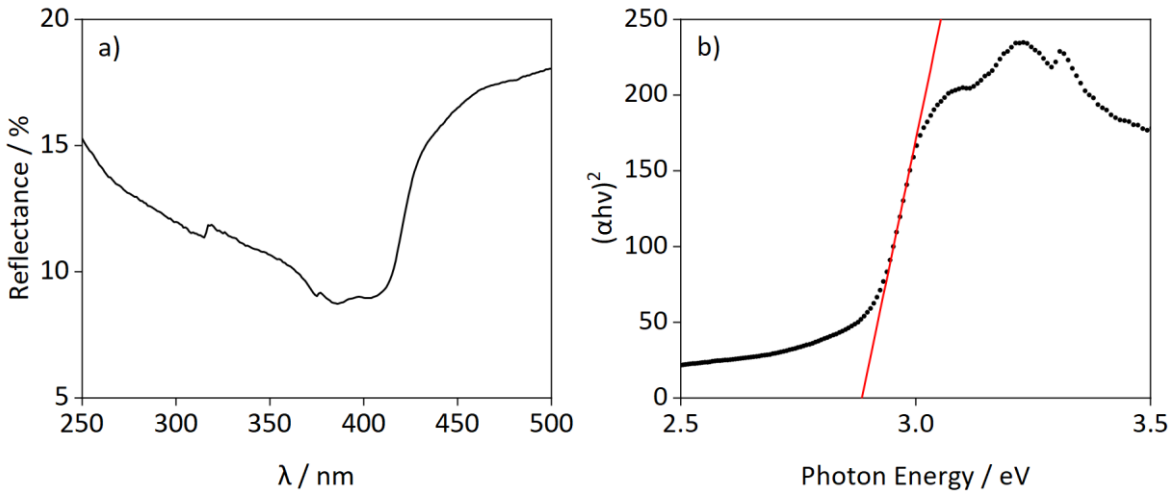

Figure 135 *UV-Vis spectrometry data for material with target composition $Sr_3(Sc_{1.90}Mg_{0.10})O_5Cu_2Se_2$ after 36 hours of heating at 800 °C. Plot a) is the raw diffuse reflectance data, and plot b) is the associated magnified Tauc plot for this region, where the intercept between the red extrapolated tangent line and the x-axis is used to estimate an optical band gap of 2.89 eV, which corresponds to 429 nm.*

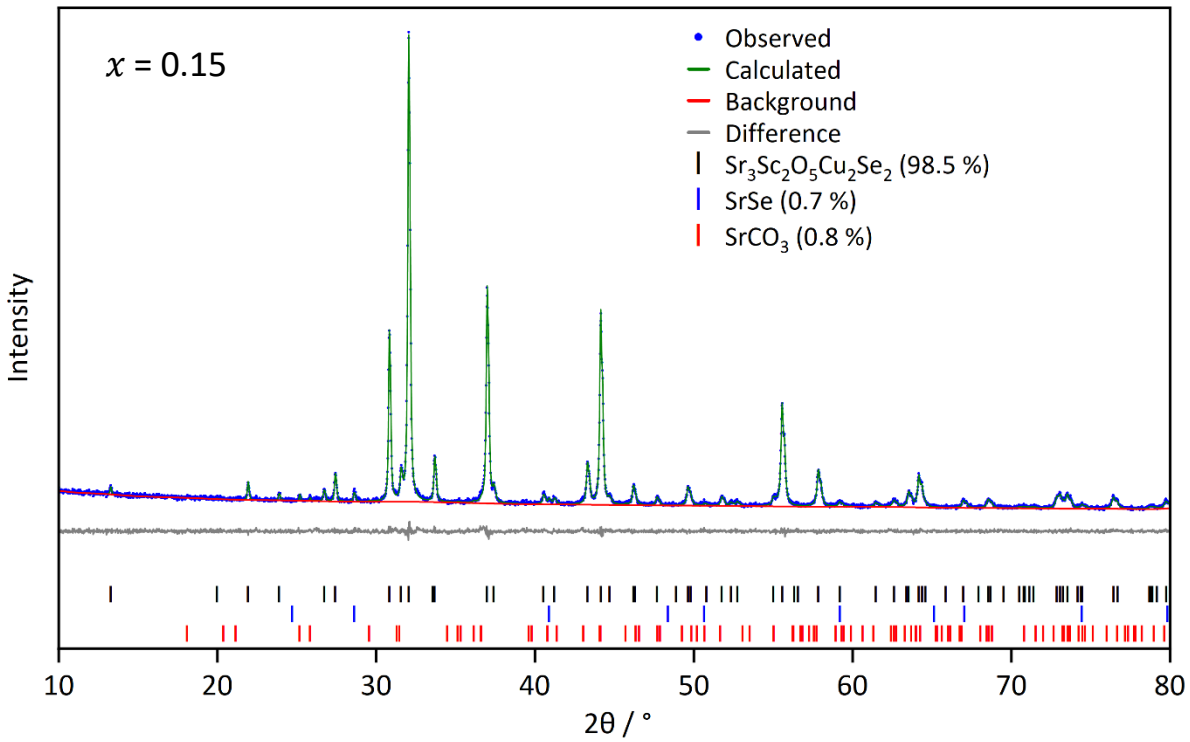

Figure 136 *Powder X-ray diffractogram of material with target composition $Sr_3(Sc_{1.85}Mg_{0.15})O_5Cu_2Se_2$ (space group I4/mmm) after 36 hours of heating at 800 °C. The small blue circles represent the observed diffracted intensity, the green line represents the Rietveld-refined calculated model, the red line represents the background, and the grey line represents the difference between observed and calculated intensities. The black tick marks show the reflections of the refined model of $Sr_3Sc_2O_5Cu_2Se_2$ (98.5 %), whilst the blue and red marks represent refined impurity phases SrSe (0.7 %) and $SrCO_3$ (0.8 %) respectively.*
Duration: 45 minutes. Data points: 3457. Interval: 0.02 °. GOF: 1.09. R_{wp}: 4.683 %.

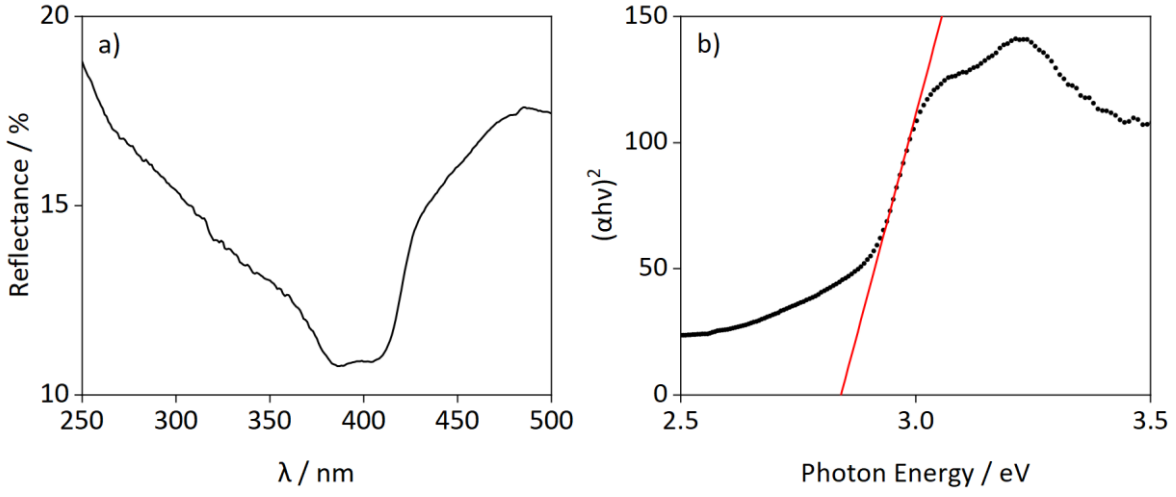

Figure 137 *UV-Vis spectrometry data for material with target composition $Sr_3(Sc_{1.85}Mg_{0.15})O_5Cu_2Se_2$ after 36 hours of heating at 800 °C. Plot a) is the raw diffuse reflectance data, and plot b) is the associated magnified Tauc plot for this region, where the intercept between the red extrapolated tangent line and the x-axis is used to estimate an optical band gap of 2.84 eV, which corresponds to 437 nm.*

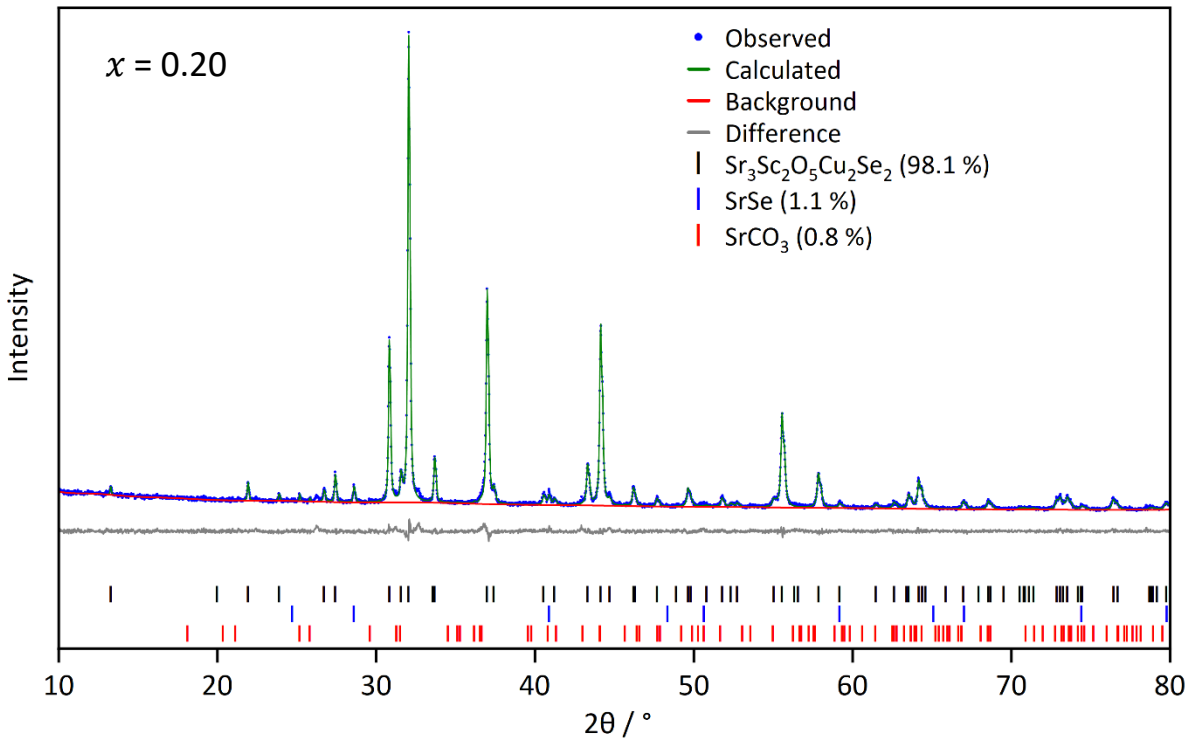

Figure 138 *Powder X-ray diffractogram of material with target composition $Sr_3(Sc_{1.80}Mg_{0.20})O_5Cu_2Se_2$ (space group I4/mmm) after 36 hours of heating at 800 °C. The small blue circles represent the observed diffracted intensity, the green line represents the Rietveld-refined calculated model, the red line represents the background, and the grey line represents the difference between observed and calculated intensities. The black tick marks show the reflections of the refined model of $Sr_3Sc_2O_5Cu_2Se_2$ (98.1 %), whilst the blue and red marks represent refined impurity phases SrSe (1.1 %) and $SrCO_3$ (0.8 %) respectively.*
Duration: 45 minutes. Data points: 3457. Interval: 0.02 °. GOF: 1.24. R_{wp}: 5.274 %.

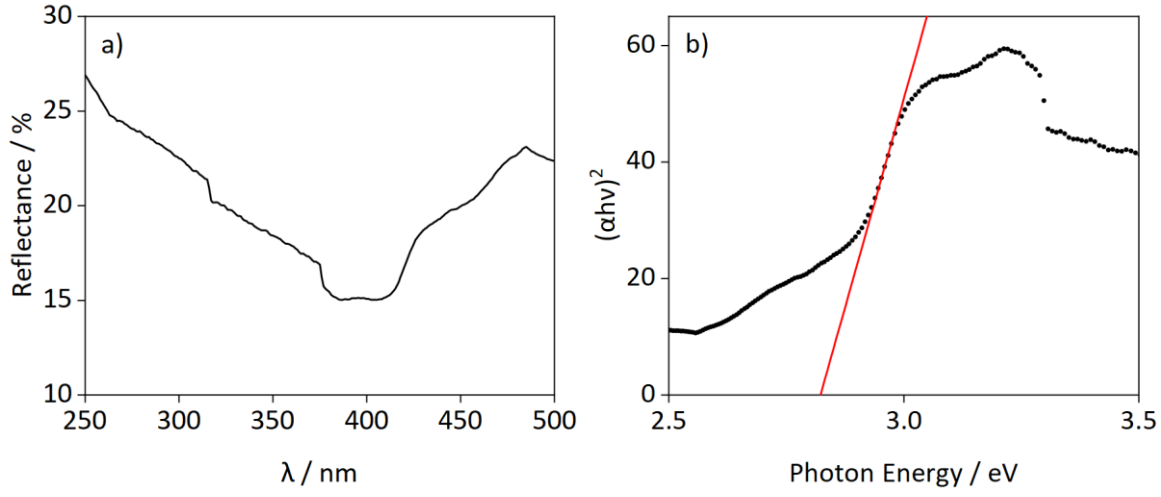

Figure 139 *UV-Vis spectrometry data for material with target composition $Sr_3(Sc_{1.80}Mg_{0.20})O_5Cu_2Se_2$ after 36 hours of heating at 800 °C. Plot a) is the raw diffuse reflectance data, and plot b) is the associated magnified Tauc plot for this region, where the intercept between the red extrapolated tangent line and the x-axis is used to estimate an optical band gap of 2.82 eV, which corresponds to 440 nm.*

B.1.7 Barium doped 325 selenide MALMs, $(Sr_{3-x}Ba_x)Sc_2O_5Cu_2Se_2$

Table 37 Tabulated structural data of the barium doped 325 selenide MALMs with general formula $(Sr_{3-x}Ba_x)Sc_2O_5Cu_2Se_2$. The pristine material $Sr_3Sc_2O_5Cu_2Se_2$ is included as a reference. All values are derived from the Rietveld refinement of PXRD data using GSAS-II. Note that because all materials listed are tetragonal (space group I4/mmm), the b parameter is identical to a, and thus omitted.

x / mol	Target Composition	a / Å	c / Å	Volume / Å^3
0 (pristine)	$Sr_3Sc_2O_5Cu_2Se_2$	4.10329(4)	26.6847(3)	449.290(12)
0.05	$(Sr_{2.95}Ba_{0.05})Sc_2O_5Cu_2Se_2$	4.10474(7)	26.6842(6)	449.599(23)
0.10	$(Sr_{2.90}Ba_{0.10})Sc_2O_5Cu_2Se_2$	4.10566(7)	26.6913(6)	449.920(21)
0.15	$(Sr_{2.85}Ba_{0.15})Sc_2O_5Cu_2Se_2$	4.10628(8)	26.6997(7)	450.197(24)
0.20	$(Sr_{2.80}Ba_{0.20})Sc_2O_5Cu_2Se_2$	4.10729(7)	26.7105(6)	450.601(23)

Table 38 Tabulated compositional data of the barium doped 325 selenide MALMs with general formula $(Sr_{3-x}Ba_x)Sc_2O_5Cu_2Se_2$. The pristine material $Sr_3Sc_2O_5Cu_2Se_2$ is included as a reference. All values are cited as a weight percent (wt %) of the total weight, and are derived from the Rietveld refinement of PXRD data using GSAS-II.

x / mol	Target phase / wt %	SrSe / wt %	$SrCO_3$ / wt %
0 (pristine)	99.1	0.5	0.4
0.05	98.3	1.3	0.4
0.10	98.9	0.8	0.3
0.15	99.4	0.4	0.2
0.20	99.2	0.4	0.4

Table 39 Tabulated analytical data of to the measured properties of the barium doped 325 selenide MALMs with general formula $(Sr_{3-x}Ba_x)Sc_2O_5Cu_2Se_2$. The pristine material $Sr_3Sc_2O_5Cu_2Se_2$ is included as a reference. Optical band gaps were estimated from UV-Vis data. Pellet densities were estimated from the mass and volume of annealed pellet samples, and are cited as a relative percentage of the bulk crystal. Resistivities and conductivities were estimated from 4 probe Van der Pauw analysis of the pellet samples.

x / mol	Band Gap / eV	Pellet Density / %	Raw Resistivities from 4-Probe measurement, for each probe permutation / kΩ								Resistivity / Ω cm	Conductivity / S cm^{-1}
			1	2	3	4	5	6	7	8		
0 (pristine)	2.94	71.72	1.20 E+01	1.21 E+01	1.22 E+01	1.22 E+01	1.03 E+01	1.02 E+01	1.02 E+01	1.01 E+01	3.83 E+03	2.61 E-04
0.05	2.86	67.58	6.84 E+00	6.83 E+00	6.99 E+00	6.86 E+00	7.67 E+00	7.64 E+00	7.80 E+00	7.69 E+00	2.57 E+03	3.88 E-04
0.10	2.83	70.87	6.76 E+00	6.81 E+00	6.83 E+00	6.86 E+00	4.10 E+00	4.10 E+00	4.10 E+00	4.11 E+00	1.84 E+03	5.44 E-04
0.15	2.89	69.96	8.29 E+00	8.31 E+00	8.34 E+00	8.44 E+00	6.55 E+00	6.49 E+00	6.54 E+00	6.53 E+00	2.55 E+03	3.92 E-04
0.20	2.90	71.08	3.14 E+00	3.13 E+00	3.15 E+00	3.14 E+00	6.15 E+00	6.18 E+00	6.22 E+00	6.21 E+00	1.55 E+03	6.47 E-04

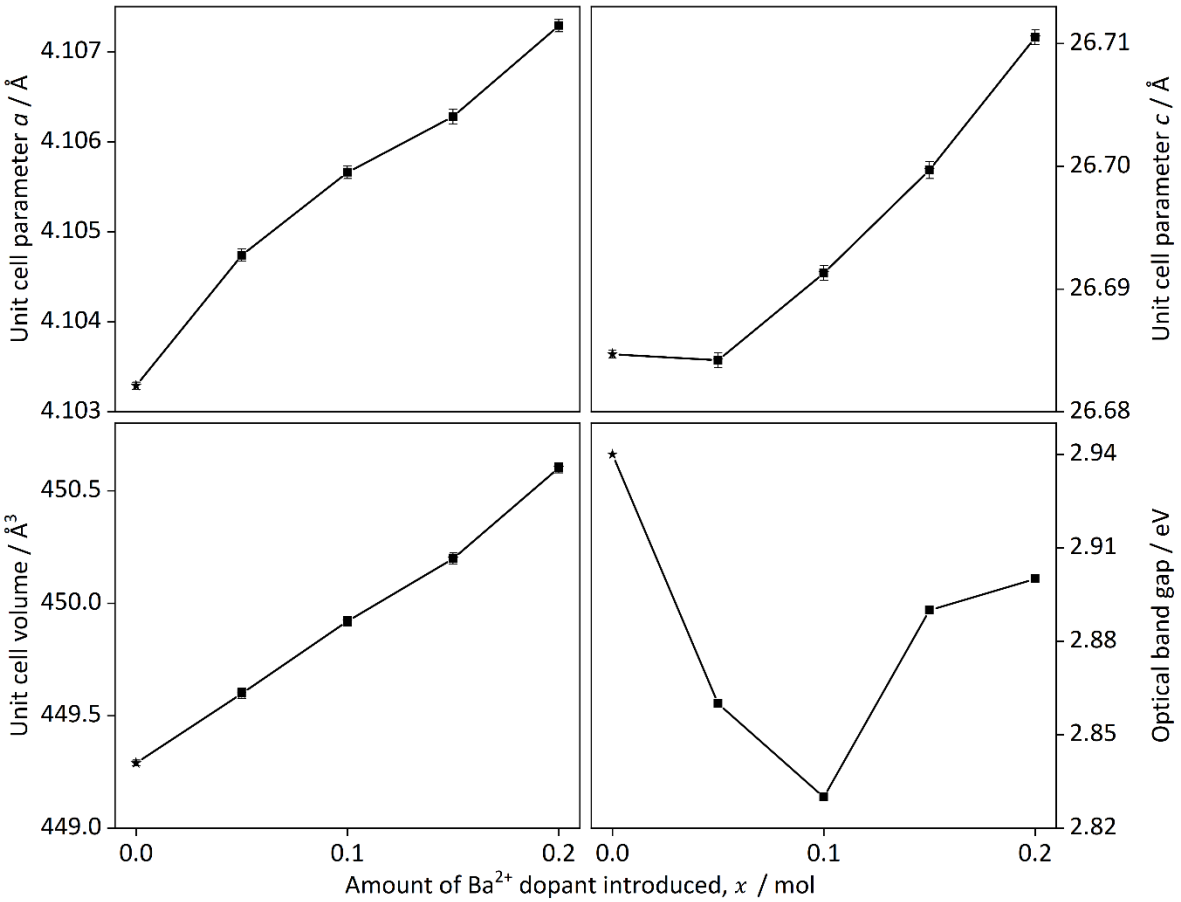

Figure 140 Comparisons of a) the α unit cell parameter, b) the c unit cell parameter, c) unit cell volume, and d) the optical band gap, of the barium doped 325 selenide MALMs with general formula $(Sr_{3-x}Ba_x)Sc_2O_5Cu_2Se_2$. The pristine material $Sr_3Sc_2O_5Cu_2Se_2$ is included as a reference at x = 0 mol and is represented by a star.

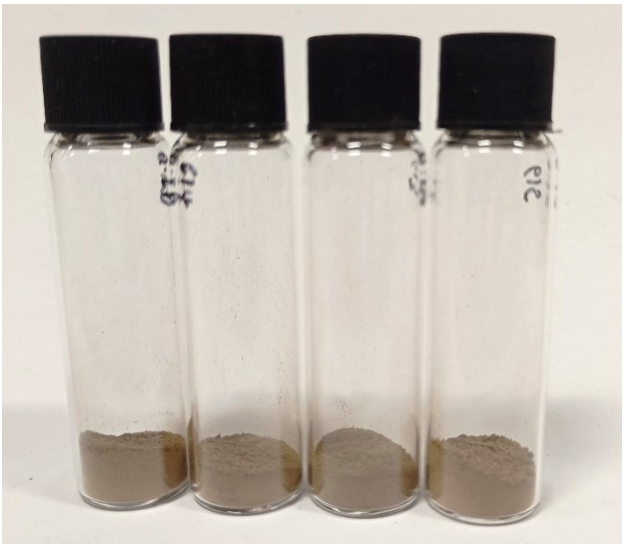

Figure 141 A photographic comparison of the colour of the barium doped 325 selenide MALMs with general formula $(Sr_{3-x}Ba_x)Sc_2O_5Cu_2Se_2$. Dopant concentration increases from left to right.

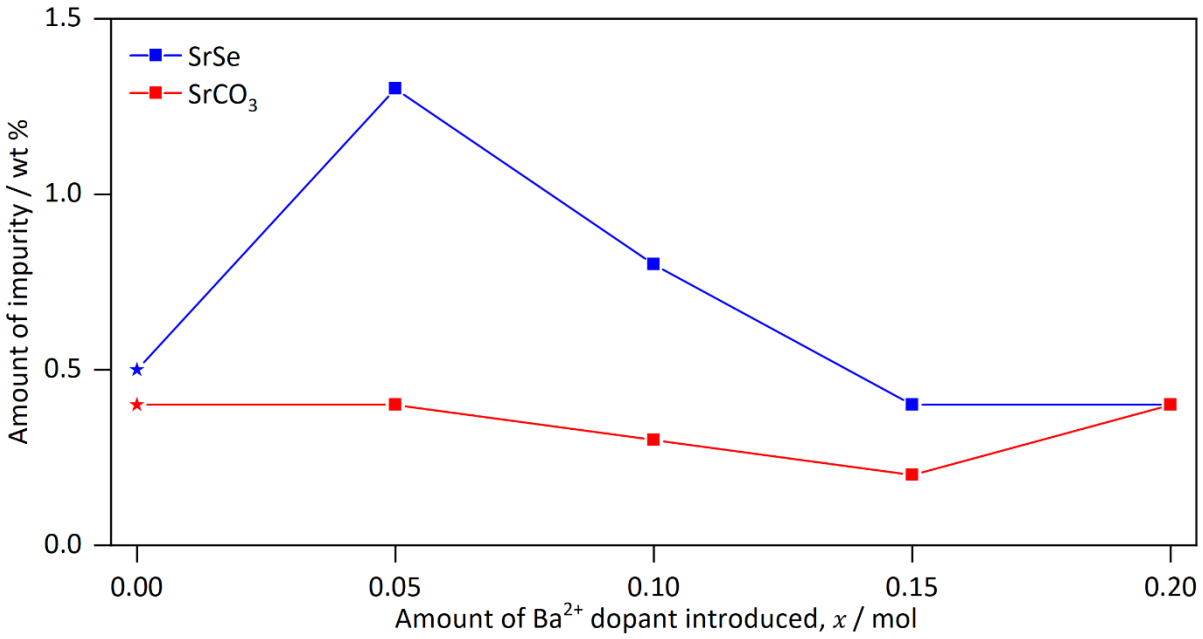

Figure 142 *The weight percentages of two impurity phases present in the barium doped 325 selenide MALMs with general formula $(Sr_{3-x}Ba_x)Sc_2O_5Cu_2Se_2$. The pristine material $Sr_3Sc_2O_5Cu_2Se_2$ is included as a reference at $x = 0$ mol and is represented by a star.*

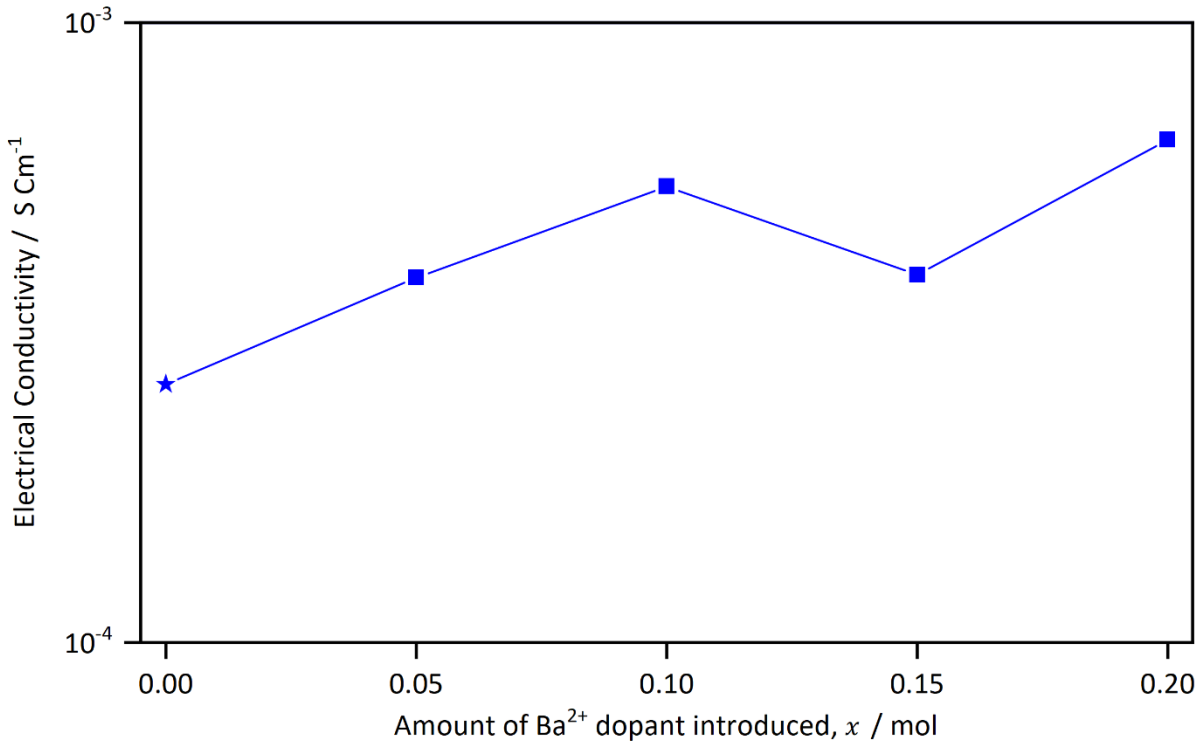

Figure 143 *The electrical conductivities of the barium doped 325 selenide MALMs with general formula $(Sr_{3-x}Ba_x)Sc_2O_5Cu_2Se_2$, represented on a log_{10} scale. The pristine material $Sr_3Sc_2O_5Cu_2Se_2$ is included as a reference at $x = 0$ mol and is represented by a star. All values are derived from van der Pauw 4 probe resistivity measurements of 8mm diameter annealed pellet samples.*

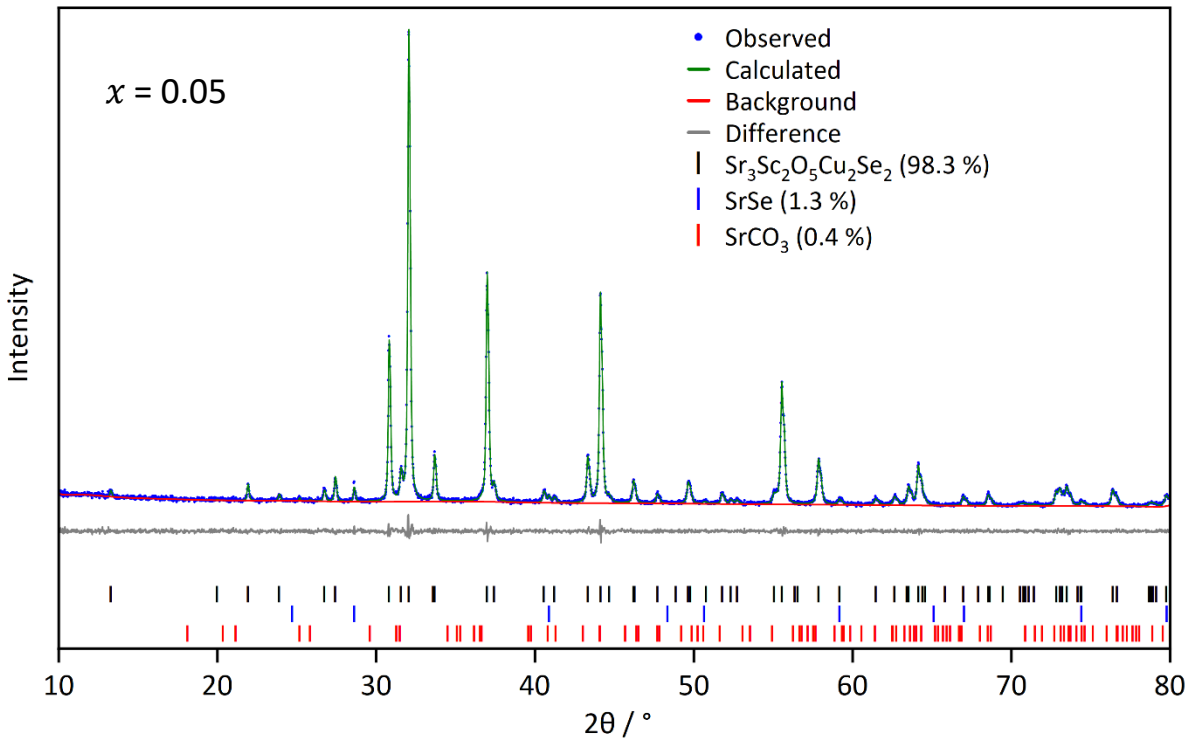

Figure 144 *Powder X-ray diffractogram of material with target composition $(Sr_{2.95}Ba_{0.05})Sc_2O_5Cu_2Se_2$ (space group I4/mmm) after 36 hours of heating at 800 °C. The small blue circles represent the observed diffracted intensity, the green line represents the Rietveld-refined calculated model, the red line represents the background, and the grey line represents the difference between observed and calculated intensities. The black tick marks show the reflections of the refined model of $Sr_3Sc_2O_5Cu_2Se_2$ (98.3 %), whilst the blue and red marks represent refined impurity phases SrSe (1.3 %) and $SrCO_3$ (0.4 %) respectively.*
Duration: 45 minutes. Data points: 3457. Interval: 0.02 °. GOF: 1.04. R_{wp}: 4.430 %.

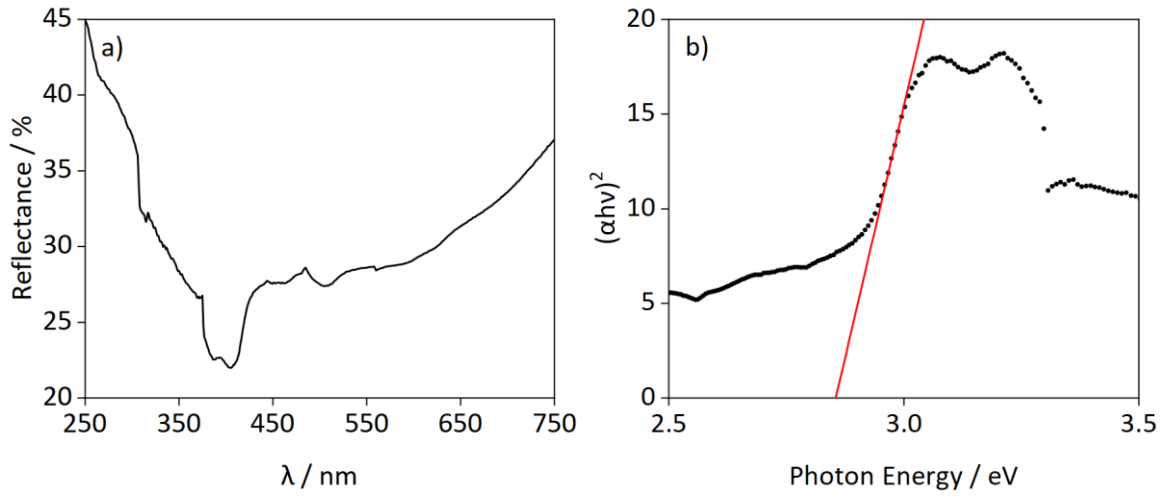

Figure 145 *UV-Vis spectrometry data for material with target composition $(Sr_{2.95}Ba_{0.05})Sc_2O_5Cu_2Se_2$ after 36 hours of heating at 800 °C. Plot a) is the raw diffuse reflectance data, and plot b) is the associated magnified Tauc plot for this region, where the intercept between the red extrapolated tangent line and the x-axis is used to estimate an optical band gap of 2.86 eV, which corresponds to 433 nm.*

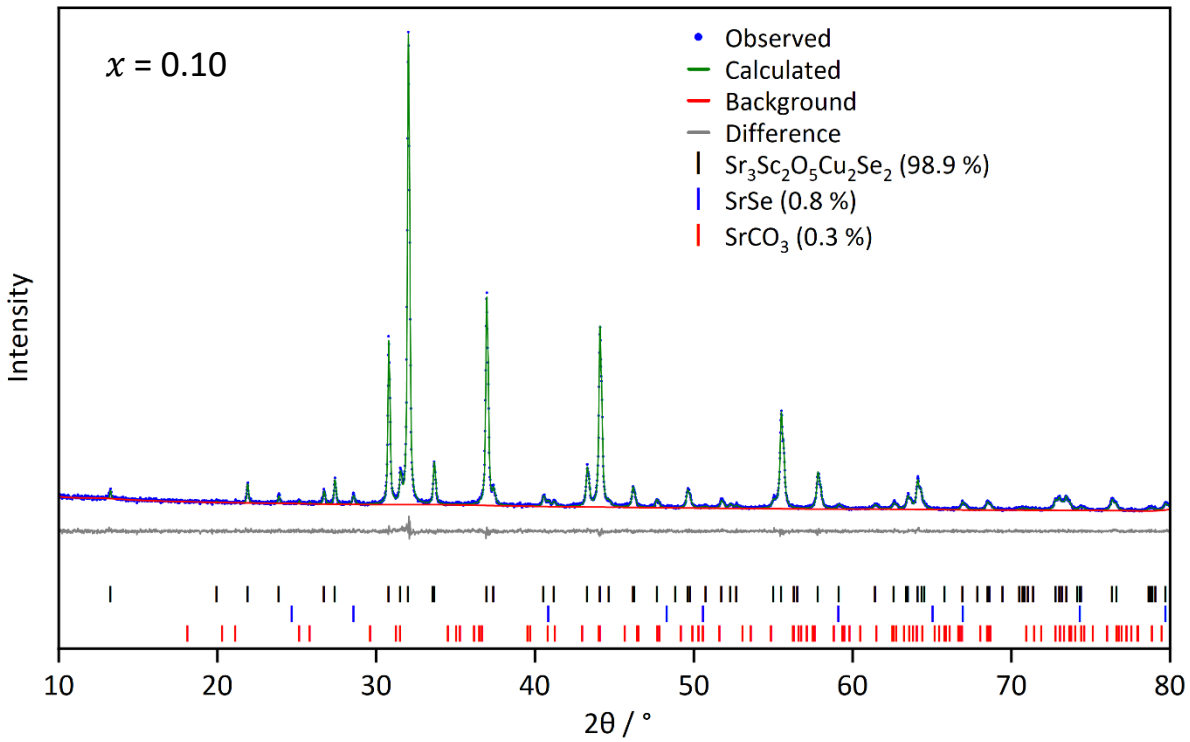

Figure 146 *Powder X-ray diffractogram of material with target composition $(Sr_{2.90}Ba_{0.10})Sc_2O_5Cu_2Se_2$ (space group I4/mmm) after 36 hours of heating at 800 °C. The small blue circles represent the observed diffracted intensity, the green line represents the Rietveld-refined calculated model, the red line represents the background, and the grey line represents the difference between observed and calculated intensities. The black tick marks show the reflections of the refined model of $Sr_3Sc_2O_5Cu_2Se_2$ (98.9 %), whilst the blue and red marks represent refined impurity phases SrSe (0.8 %) and $SrCO_3$ (0.3 %) respectively.*
Duration: 45 minutes. Data points: 3457. Interval: 0.02 °. GOF: 1.09. R_{wp}: 4.300 %.

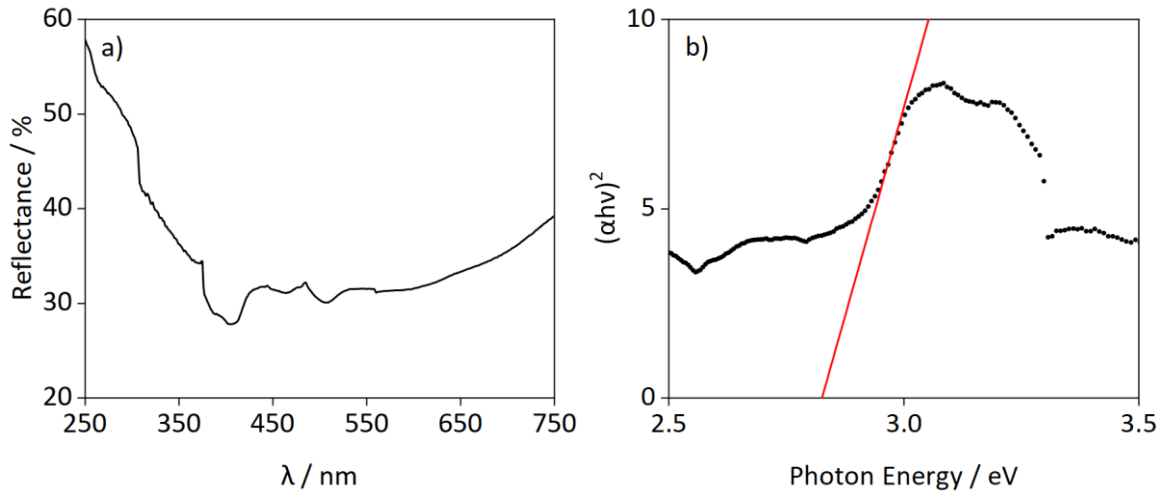

Figure 147 *UV-Vis spectrometry data for material with target composition $(Sr_{2.90}Ba_{0.10})Sc_2O_5Cu_2Se_2$ after 36 hours of heating at 800 °C. Plot a) is the raw diffuse reflectance data, and plot b) is the associated magnified Tauc plot for this region, where the intercept between the red extrapolated tangent line and the x-axis is used to estimate an optical band gap of 2.83 eV, which corresponds to 438 nm.*

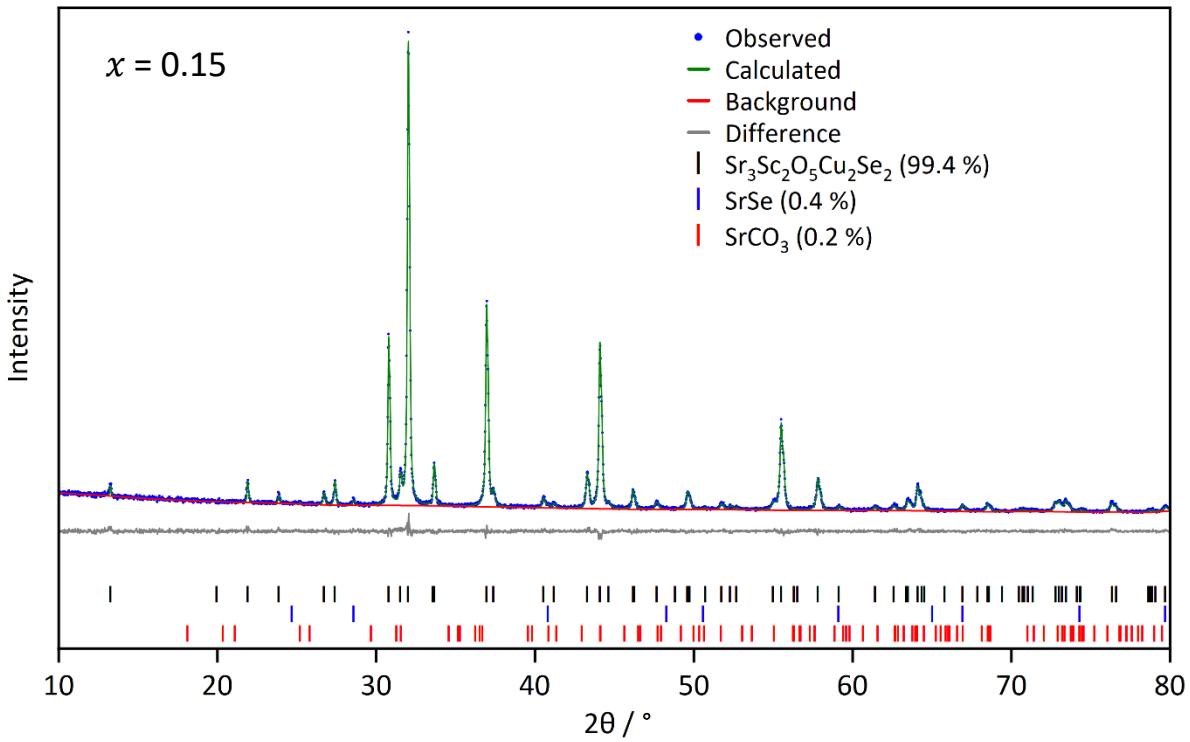

Figure 148 *Powder X-ray diffractogram of material with target composition $(Sr_{2.85}Ba_{0.15})Sc_2O_5Cu_2Se_2$ (space group I4/mmm) after 36 hours of heating at 800 °C. The small blue circles represent the observed diffracted intensity, the green line represents the Rietveld-refined calculated model, the red line represents the background, and the grey line represents the difference between observed and calculated intensities. The black tick marks show the reflections of the refined model of $Sr_3Sc_2O_5Cu_2Se_2$ (99.4 %), whilst the blue and red marks represent refined impurity phases SrSe (0.4 %) and $SrCO_3$ (0.2 %) respectively.*
Duration: 45 minutes. Data points: 3457. Interval: 0.02 °. GOF: 1.11. R_{wp}: 4.920 %.

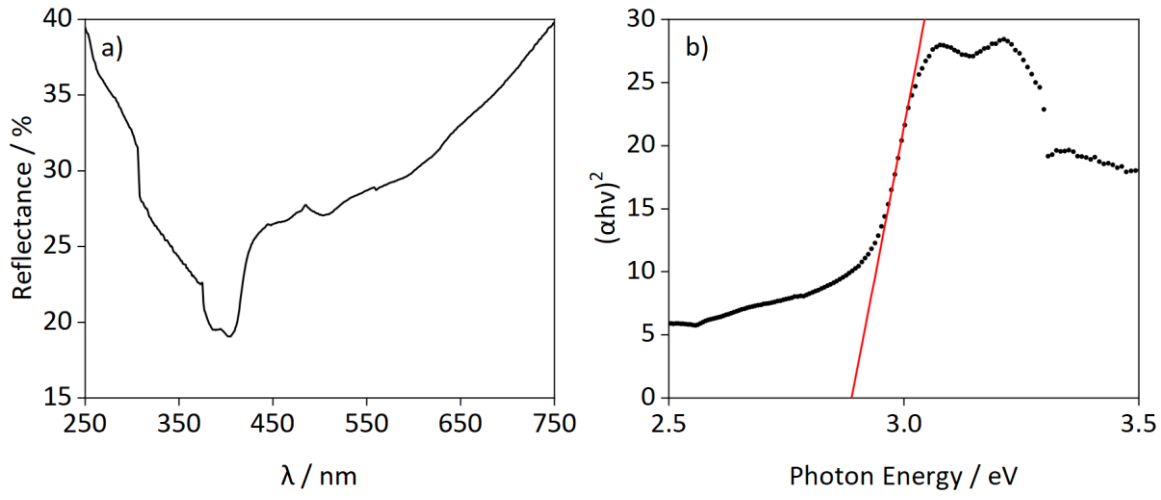

Figure 149 *UV-Vis spectrometry data for material with target composition $(Sr_{2.85}Ba_{0.15})Sc_2O_5Cu_2Se_2$ after 36 hours of heating at 800 °C. Plot a) is the raw diffuse reflectance data, and plot b) is the associated magnified Tauc plot for this region, where the intercept between the red extrapolated tangent line and the x-axis is used to estimate an optical band gap of 2.89 eV, which corresponds to 429 nm.*

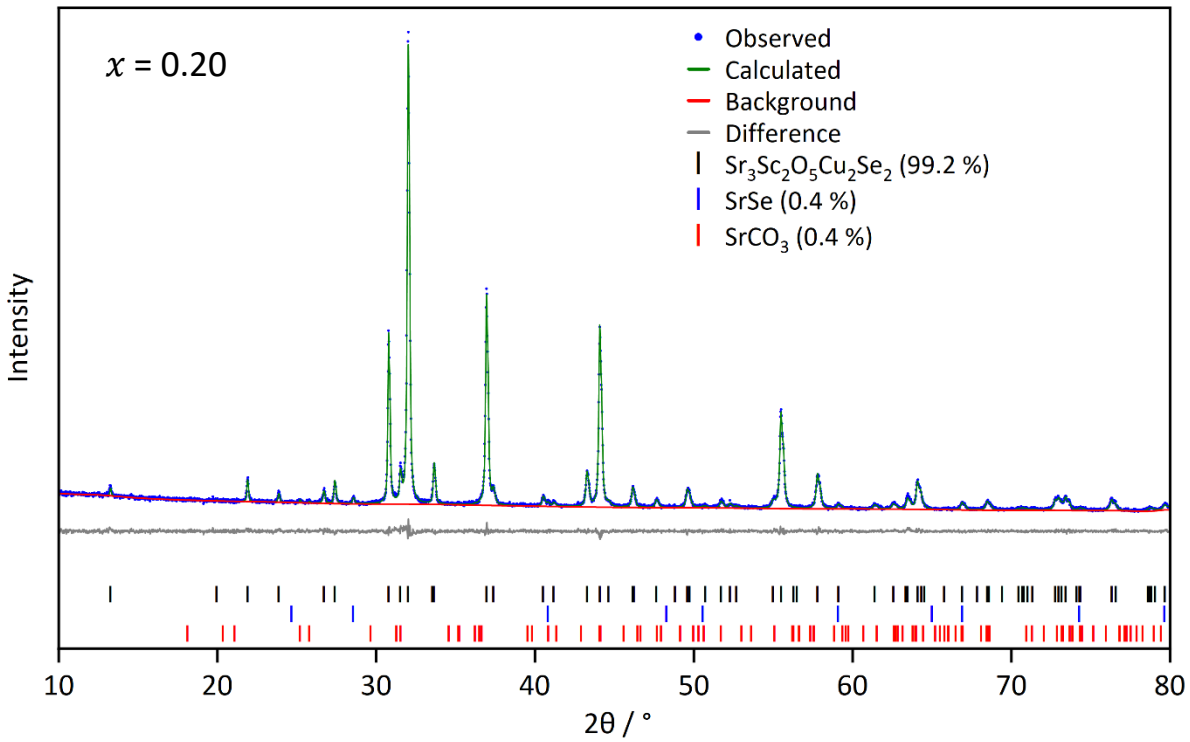

Figure 150 *Powder X-ray diffractogram of material with target composition $(Sr_{2.80}Ba_{0.20})Sc_2O_5Cu_2Se_2$ (space group I4/mmm) after 36 hours of heating at 800 °C. The small blue circles represent the observed diffracted intensity, the green line represents the Rietveld-refined calculated model, the red line represents the background, and the grey line represents the difference between observed and calculated intensities. The black tick marks show the reflections of the refined model of $Sr_3Sc_2O_5Cu_2Se_2$ (99.2 %), whilst the blue and red marks represent refined impurity phases SrSe (0.4 %) and $SrCO_3$ (0.4 %) respectively.*
Duration: 45 minutes. Data points: 3457. Interval: 0.02 °. GOF: 1.05. R_{wp}: 4.496 %.

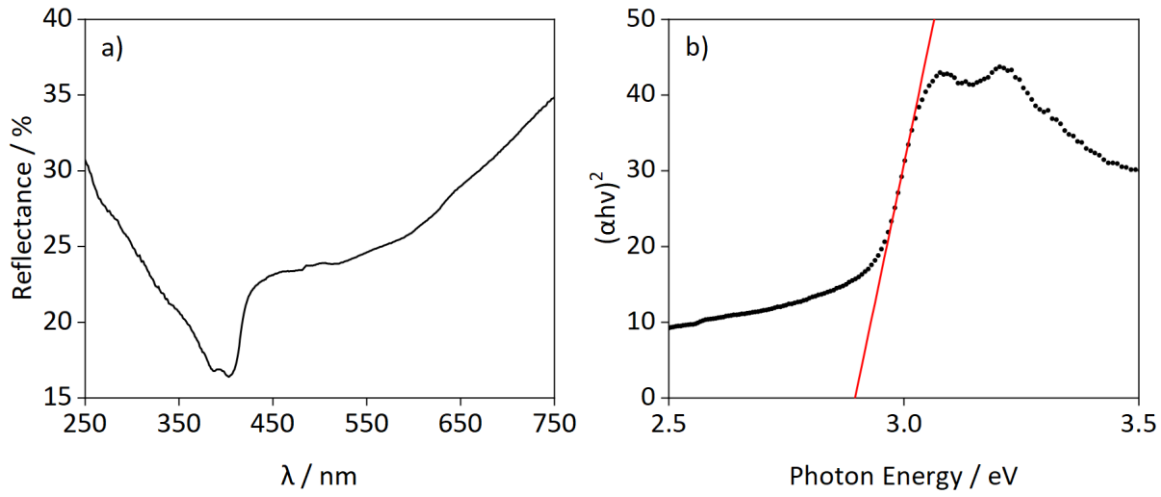

Figure 151 *UV-Vis spectrometry data for material with target composition $(Sr_{2.80}Ba_{0.20})Sc_2O_5Cu_2Se_2$ after 36 hours of heating at 800 °C. Plot a) is the raw diffuse reflectance data, and plot b) is the associated magnified Tauc plot for this region, where the intercept between the red extrapolated tangent line and the x-axis is used to estimate an optical band gap of 2.90 eV, which corresponds to 428 nm.*

B.1.8 Yttrium doped 325 selenide MALMs, $Sr_3(Sc_{2-x}Y_x)O_5Cu_2Se_2$

Table 40 Tabulated structural data of the yttrium doped 325 selenide MALMs with general formula $Sr_3(Sc_{2-x}Y_x)O_5Cu_2Se_2$. The pristine material $Sr_3Sc_2O_5Cu_2Se_2$ is included as a reference. All values are derived from the Rietveld refinement of PXRD data using GSAS-II. Note that because all materials listed are tetragonal (space group I4/mmm), the b parameter is identical to a, and thus omitted.

x / mol	Target Composition	a / Å	c / Å	Volume / Å^3
0 (pristine)	$Sr_3Sc_2O_5Cu_2Se_2$	4.10329(4)	26.6847(3)	449.290(12)
0.05	$Sr_3(Sc_{1.95}Y_{0.05})O_5Cu_2Se_2$	4.10524(7)	26.6787(6)	449.616(22)
0.10	$Sr_3(Sc_{1.90}Y_{0.10})O_5Cu_2Se_2$	4.10600(9)	26.6781(7)	449.772(27)
0.15	$Sr_3(Sc_{1.85}Y_{0.15})O_5Cu_2Se_2$	4.10592(9)	26.6817(7)	449.815(27)
0.20	$Sr_3(Sc_{1.80}Y_{0.20})O_5Cu_2Se_2$	4.10608(9)	26.6828(8)	449.869(29)

Table 41 Tabulated compositional data of the yttrium doped 325 selenide MALMs with general formula $Sr_3(Sc_{2-x}Y_x)O_5Cu_2Se_2$. The pristine material $Sr_3Sc_2O_5Cu_2Se_2$ is included as a reference. All values are cited as a weight percent (wt %) of the total weight, and are derived from the Rietveld refinement of PXRD data using GSAS-II.

x / mol	Target phase / wt %	SrSe / wt %	$SrCO_3$ / wt %	Y_2O_3 / wt %
0 (pristine)	99.1	0.5	0.4	-
0.05	98.9	0.7	-	0.4
0.10	97.8	0.5	0.5	1.1
0.15	96.6	0.9	0.5	1.9
0.20	95.7	0.9	0.7	2.7

Table 42 *Tabulated data on both the target and maximum actual dopant content of the yttrium doped 325 selenide MALMs with general formula $Sr_3(Sc_{2-x}Y_x)O_5Cu_2Se_2$. The pristine material $Sr_3Sc_2O_5Cu_2S_2$ is included as a reference. The minimum possible amount of total Y contained within impurities was extracted from the refined wt % of Y_2O_3 from GSAS-II. The remaining Y content is the maximum possible Y within the MALM.*

Target x / mol	**Target x / wt %**	**Minimum Y in impurities / %**	**Maximum Y in product / %**	**Maximum x / mol**
0 (pristine)	0.000	0.000	100.000	0.000
0.05	0.710	44.369	55.631	0.028
0.10	1.415	61.221	38.779	0.039
0.15	2.115	70.744	29.256	0.044
0.20	2.810	75.661	24.339	0.049

Table 43 Tabulated analytical data of to the measured properties of the yttrium doped 325 selenide MALMs with general formula $Sr_3(Sc_{2-x}Y_x)O_5Cu_2Se_2$. The pristine material $Sr_3Sc_2O_5Cu_2Se_2$ is included as a reference. Optical band gaps were estimated from UV-Vis data. Pellet densities were estimated from the mass and volume of annealed pellet samples, and are cited as a relative percentage of the bulk crystal. Resistivities and conductivities were estimated from 4 probe van der Pauw analysis of the pellet samples.

x / mol	Band Gap / eV	Pellet Density / %	Raw Resistivities from 4-Probe measurement, for each probe permutation / kΩ								Resistivity / Ω cm	Conductivity / S cm^{-1}
			1	2	3	4	5	6	7	8		
0 (pristine)	2.94	71.72	1.20 E+01	1.21 E+01	1.22 E+01	1.22 E+01	1.03 E+01	1.02 E+01	1.02 E+01	1.01 E+01	3.83 E+03	2.61 E-04
0.05	2.85	69.17	1.40 E+01	2.91 E+01	1.49 E+01	1.72 E+01	1.93 E+01	1.93 E+01	1.94 E+01	1.95 E+01	6.83 E+03	1.46 E-04
0.10	2.84	68.03	1.11 E+00	1.12 E+00	1.12 E+00	1.12 E+00	1.07 E+00	1.07 E+00	1.07 E+00	1.07 E+00	3.99 E+02	2.51 E-03
0.15	2.88	71.80	1.05 E-01	1.12 E-01	1.05 E-01	1.08 E-01	1.18 E+00	1.19 E+00	1.18 E+00	1.19 E+00	1.52 E+02	6.58 E-03
0.20	2.85	65.34	2.80 E-02	3.96 E-02	3.13 E-02	3.18 E-02	7.17 E-02	7.20 E-02	7.17 E-02	6.88 E-02	1.79 E+01	5.59 E-02

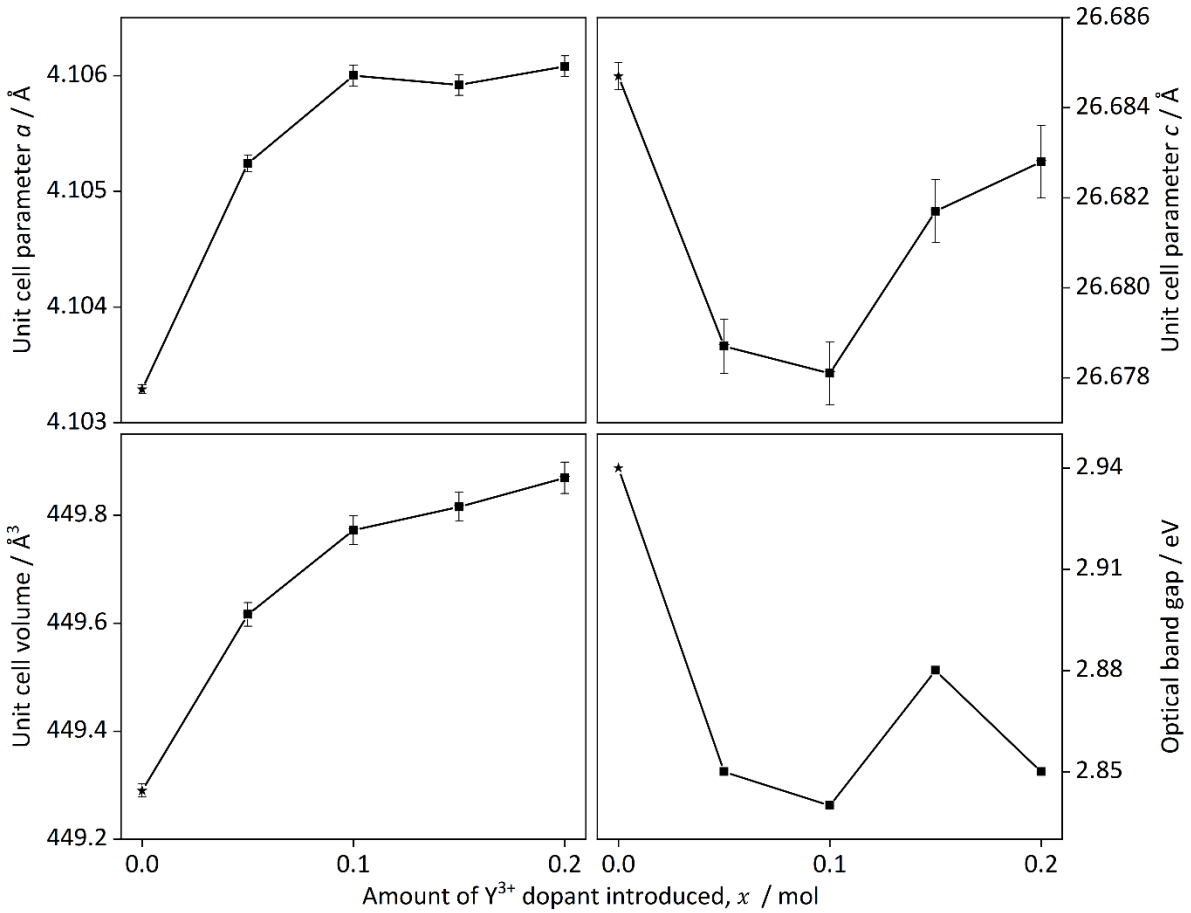

Figure 152 Comparisons of a) the α unit cell parameter, b) the c unit cell parameter, c) unit cell volume, and d) the optical band gap, of the yttrium doped 325 selenide MALMs with general formula $Sr_3(Sc_{2-x}Y_x)O_5Cu_2Se_2$. The pristine material $Sr_3Sc_2O_5Cu_2Se_2$ is included as a reference at x = 0 mol and is represented by a star.

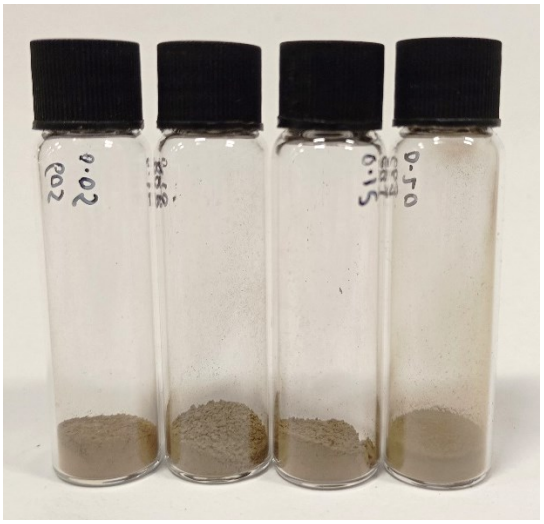

Figure 153 A photographic comparison of the colour of the yttrium doped 325 selenide MALMs with general formula $Sr_3(Sc_{2-x}Y_x)O_5Cu_2Se_2$. Dopant concentration increases from left to right.

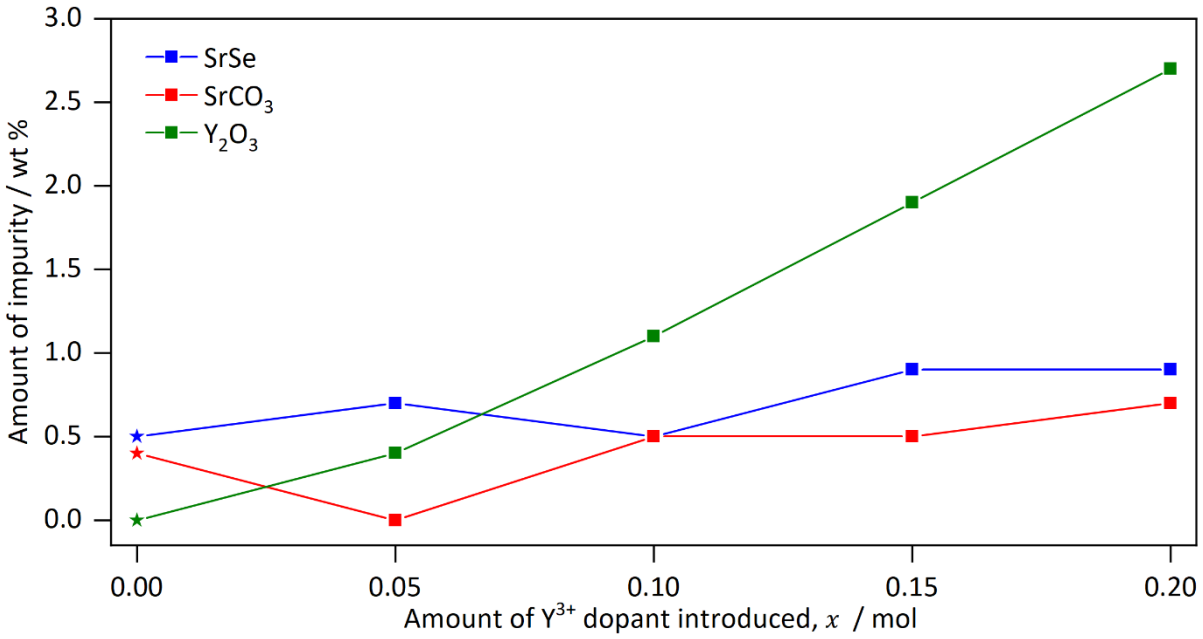

Figure 154 *The weight percentages of three impurity phases present in the yttrium doped 325 selenide MALMs with general formula $Sr_3(Sc_{2-x}Y_x)O_5Cu_2Se_2$. The pristine material $Sr_3Sc_2O_5Cu_2Se_2$ is included as a reference at $x = 0$ mol and is represented by a star.*

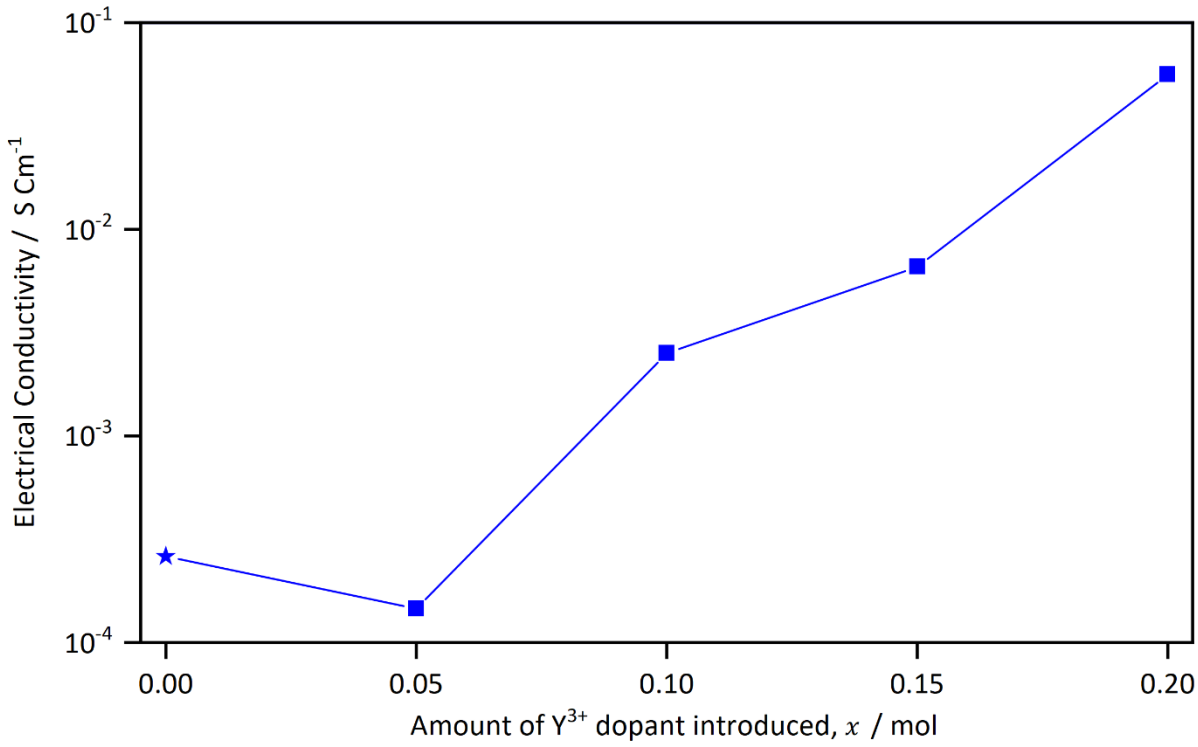

Figure 155 *The electrical conductivities of the yttrium doped 325 selenide MALMs with general formula $Sr_3(Sc_{2-x}Y_x)O_5Cu_2Se_2$, represented on a log_{10} scale. The pristine material $Sr_3Sc_2O_5Cu_2Se_2$ is included as a reference at $x = 0$ mol and is represented by a star. All values are derived from van der Pauw 4 probe resistivity measurements of 8mm diameter annealed pellet samples.*

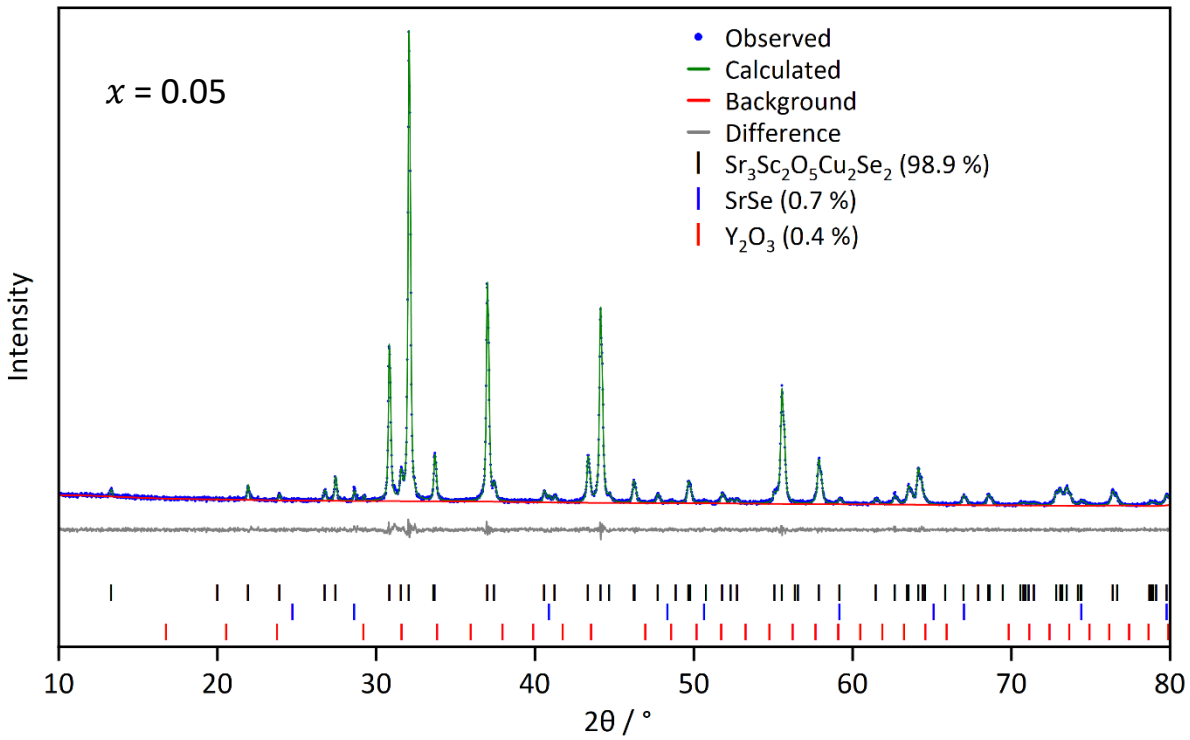

Figure 156 *Powder X-ray diffractogram of material with target composition $Sr_3(Sc_{1.95}Y_{0.05})O_5Cu_2Se_2$ (space group I4/mmm) after 36 hours of heating at 800 °C. The small blue circles represent the observed diffracted intensity, the green line represents the Rietveld-refined calculated model, the red line represents the background, and the grey line represents the difference between observed and calculated intensities. The black tick marks show the reflections of the refined model of $Sr_3Sc_2O_5Cu_2Se_2$ (98.9 %), whilst the blue and red marks represent refined impurity phases SrSe (0.7 %) and Y_2O_3 (0.4 %) respectively.*
Duration: 45 minutes. Data points: 3457. Interval: 0.02 °. GOF: 1.09. R_{wp}: 4.244 %.

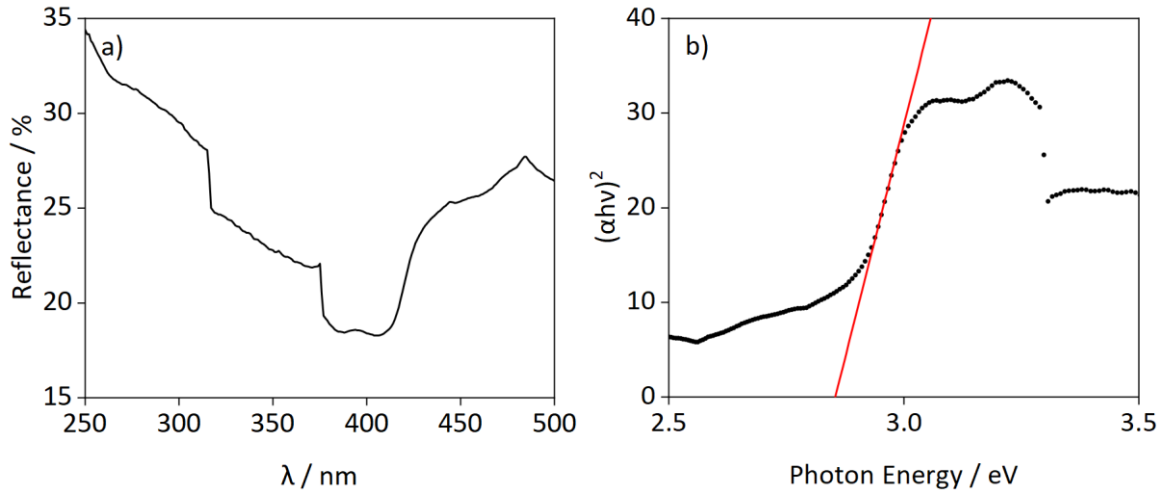

Figure 157 *UV-Vis spectrometry data for material with target composition $Sr_3(Sc_{1.95}Y_{0.05})O_5Cu_2Se_2$ after 36 hours of heating at 800 °C. Plot a) is the raw diffuse reflectance data, and plot b) is the associated magnified Tauc plot for this region, where the intercept between the red extrapolated tangent line and the x-axis is used to estimate an optical band gap of 2.85 eV, which corresponds to 435 nm.*

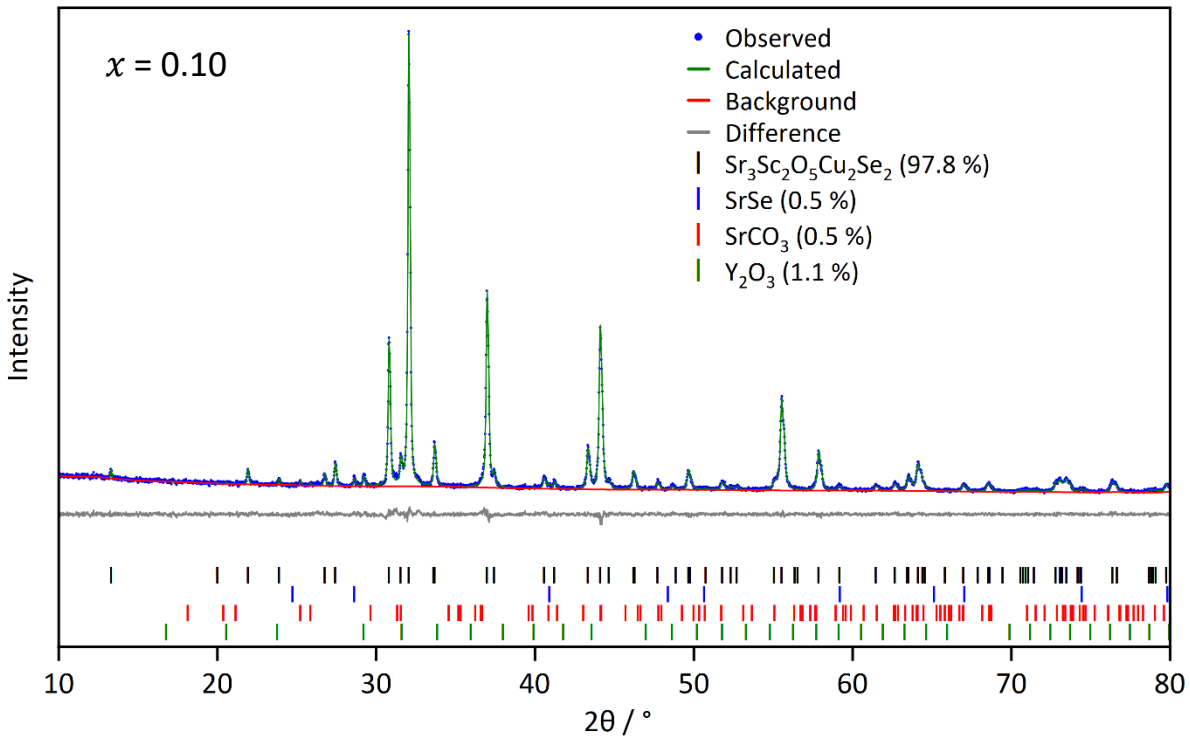

Figure 158 *Powder X-ray diffractogram of material with target composition $Sr_3(Sc_{1.90}Y_{0.10})O_5Cu_2Se_2$ (space group I4/mmm) after 36 hours of heating at 800 °C. The small blue circles represent the observed diffracted intensity, the green line represents the Rietveld-refined calculated model, the red line represents the background, and the grey line represents the difference between observed and calculated intensities. The black tick marks show the reflections of the refined model of $Sr_3Sc_2O_5Cu_2Se_2$ (97.8 %), whilst the blue, red and green marks represent refined impurity phases SrSe (0.5 %), $SrCO_3$ (0.5 %) and Y_2O_3 (1.1 %) respectively. Duration: 45 minutes. Data points: 3457. Interval: 0.02 °. GOF: 1.10. R_{wp}: 5.154 %.*

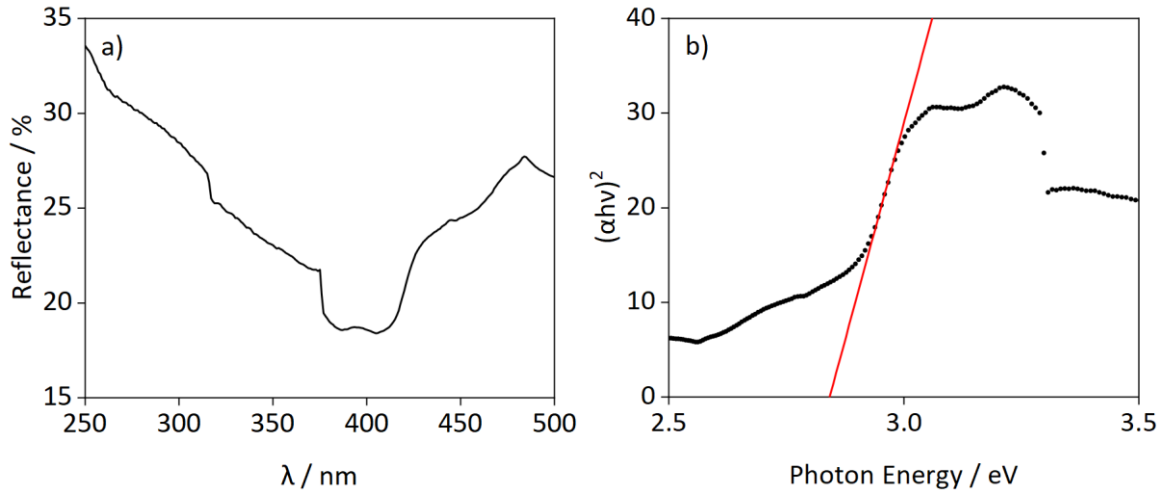

Figure 159 *UV-Vis spectrometry data for material with target composition $Sr_3(Sc_{1.90}Y_{0.10})O_5Cu_2Se_2$ after 36 hours of heating at 800 °C. Plot a) is the raw diffuse reflectance data, and plot b) is the associated magnified Tauc plot for this region, where the intercept between the red extrapolated tangent line and the x-axis is used to estimate an optical band gap of 2.84 eV, which corresponds to 437 nm.*

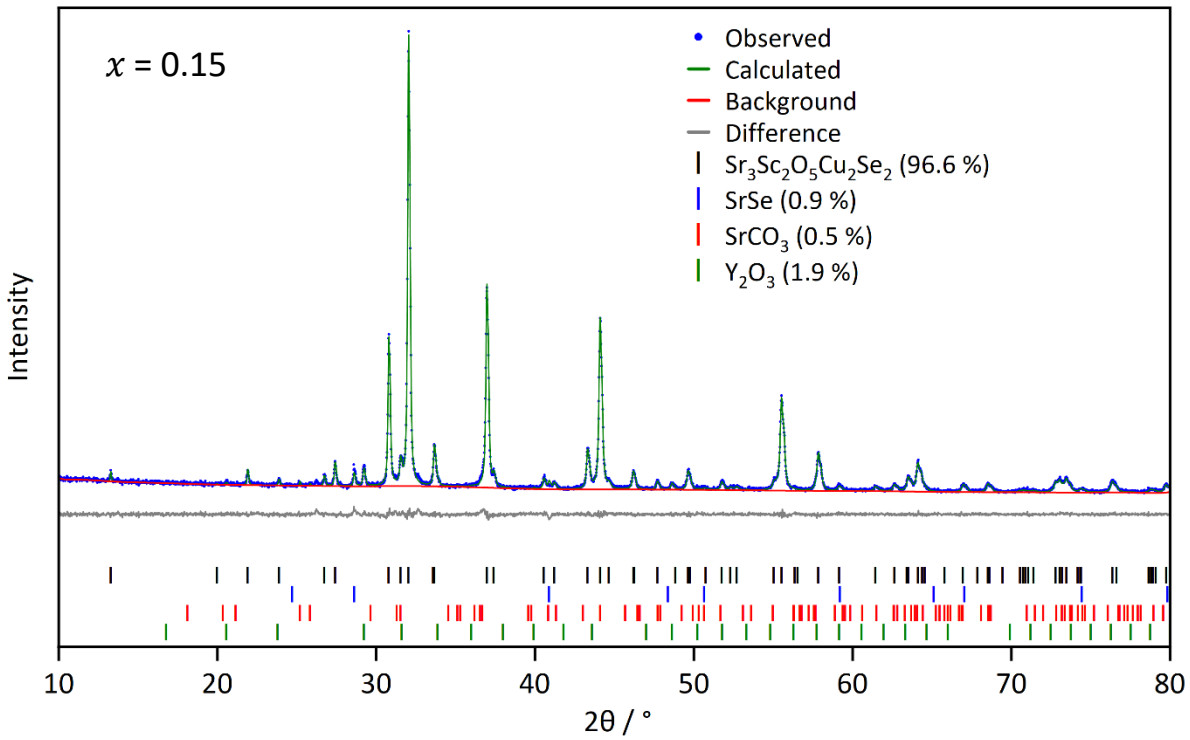

Figure 160 *Powder X-ray diffractogram of material with target composition $Sr_3(Sc_{1.85}Y_{0.15})O_5Cu_2Se_2$ (space group I4/mmm) after 36 hours of heating at 800 °C. The small blue circles represent the observed diffracted intensity, the green line represents the Rietveld-refined calculated model, the red line represents the background, and the grey line represents the difference between observed and calculated intensities. The black tick marks show the reflections of the refined model of $Sr_3Sc_2O_5Cu_2Se_2$ (96.6 %), whilst the blue, red and green marks represent refined impurity phases SrSe (0.9 %), $SrCO_3$ (0.5 %) and Y_2O_3 (1.9 %) respectively. Duration: 45 minutes. Data points: 3457. Interval: 0.02 °. GOF: 1.22. R_{wp}: 4.762 %.*

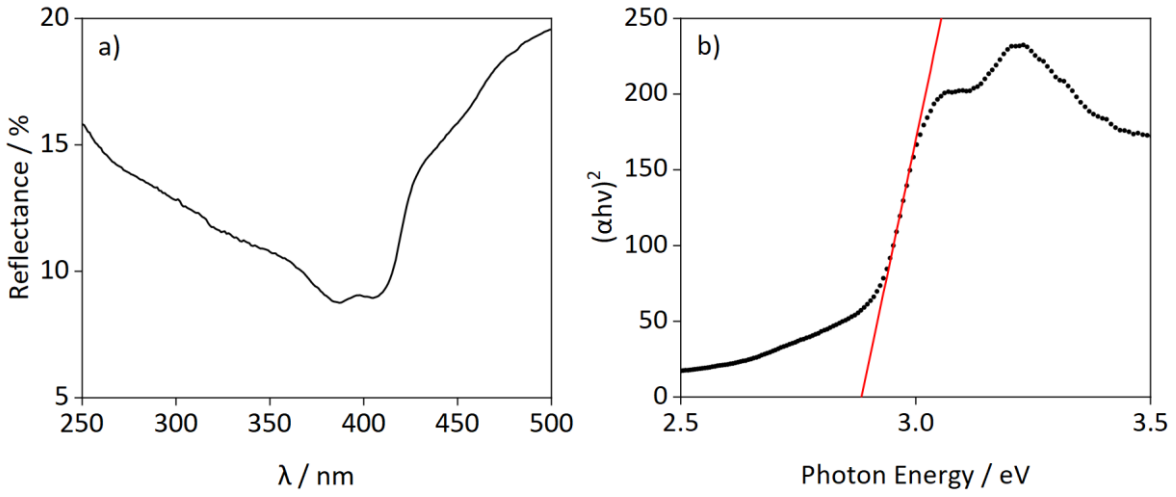

Figure 161 *UV-Vis spectrometry data for material with target composition $Sr_3(Sc_{1.85}Y_{0.15})O_5Cu_2Se_2$ after 36 hours of heating at 800 °C. Plot a) is the raw diffuse reflectance data, and plot b) is the associated magnified Tauc plot for this region, where the intercept between the red extrapolated tangent line and the x-axis is used to estimate an optical band gap of 2.88 eV, which corresponds to 430 nm.*

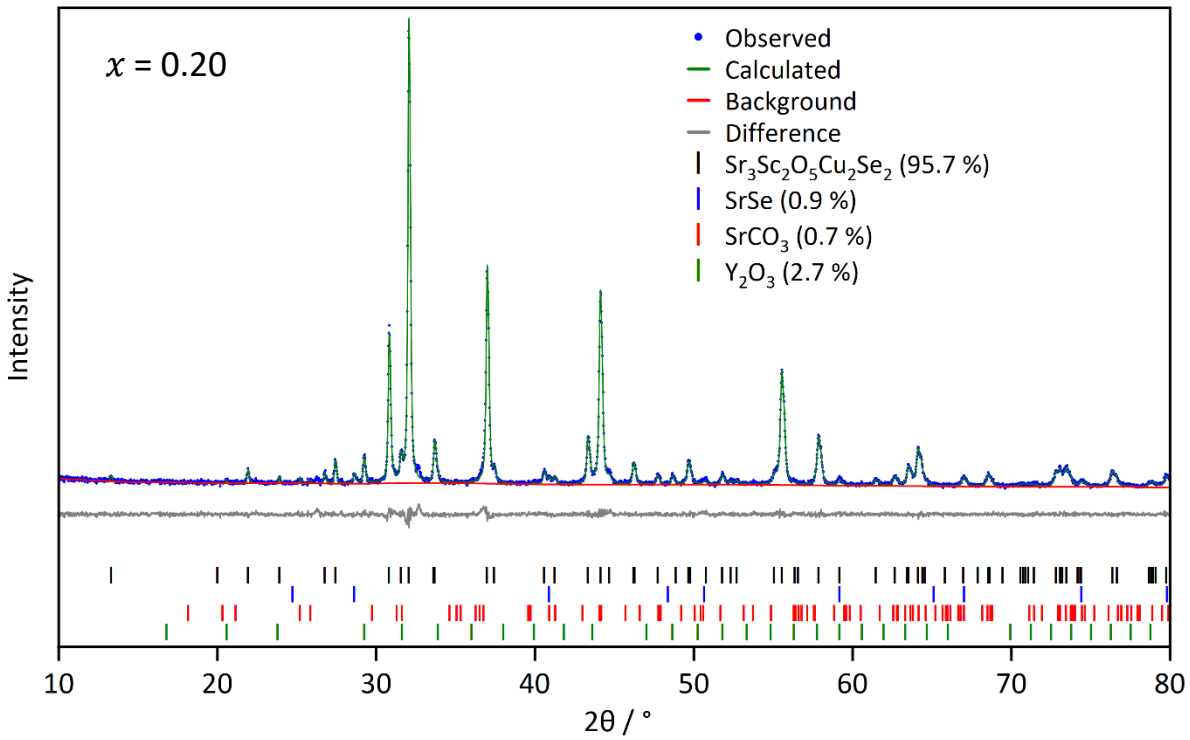

Figure 162 *Powder X-ray diffractogram of material with target composition $Sr_3(Sc_{1.80}Y_{0.20})O_5Cu_2Se_2$ (space group I4/mmm) after 36 hours of heating at 800 °C. The small blue circles represent the observed diffracted intensity, the green line represents the Rietveld-refined calculated model, the red line represents the background, and the grey line represents the difference between observed and calculated intensities. The black tick marks show the reflections of the refined model of $Sr_3Sc_2O_5Cu_2Se_2$ (95.7 %), whilst the blue, red and green marks represent refined impurity phases SrSe (0.9 %), $SrCO_3$ (0.7 %) and Y_2O_3 (2.7 %) respectively. Duration: 45 minutes. Data points: 3457. Interval: 0.02 °. GOF: 1.21. R_{wp}: 4.777 %.*

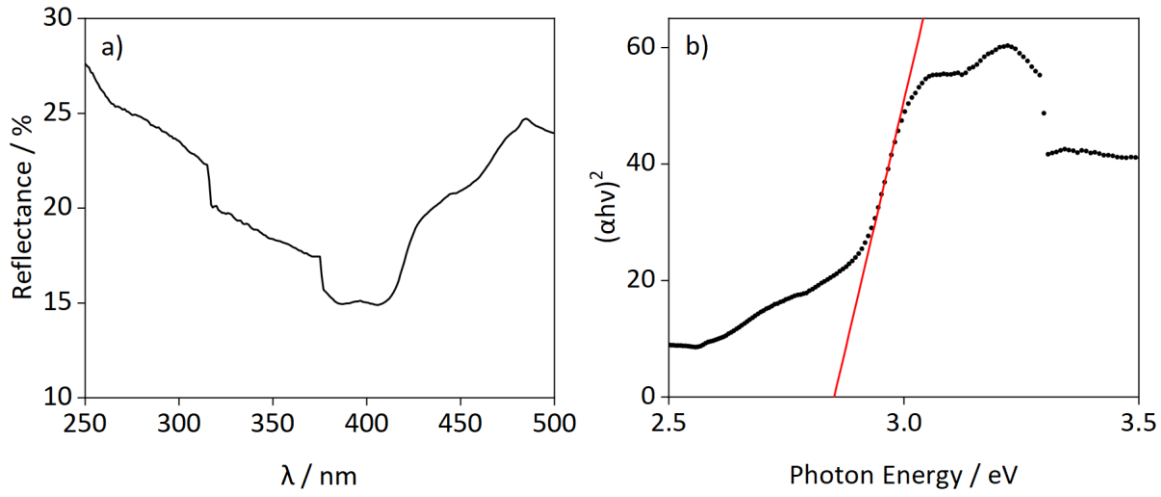

Figure 163 *UV-Vis spectrometry data for material with target composition $Sr_3(Sc_{1.80}Y_{0.20})O_5Cu_2Se_2$ after 36 hours of heating at 800 °C. Plot a) is the raw diffuse reflectance data, and plot b) is the associated magnified Tauc plot for this region, where the intercept between the red extrapolated tangent line and the x-axis is used to estimate an optical band gap of 2.85 eV, which corresponds to 435 nm.*

B.1.9 Lanthanum doped 325 selenide MALMs, $Sr_3(Sc_{2-x}La_x)O_5Cu_2Se_2$

Table 44 Tabulated structural data of the lanthanum doped 325 selenide MALMs with general formula $Sr_3(Sc_{2-x}La_x)O_5Cu_2Se_2$. The pristine material $Sr_3Sc_2O_5Cu_2Se_2$ is included as a reference. All values are derived from the Rietveld refinement of PXRD data using GSAS-II. Note that because all materials listed are tetragonal (space group I4/mmm), the b parameter is identical to a, and thus omitted.

x / mol	Target Composition	a / Å	c / Å	Volume / Å^3
0 (pristine)	$Sr_3Sc_2O_5Cu_2Se_2$	4.10329(4)	26.6847(3)	449.290(12)
0.05	$Sr_3(Sc_{1.95}La_{0.05})O_5Cu_2Se_2$	4.10348(8)	26.6428(7)	448.625(24)
0.10	$Sr_3(Sc_{1.90}La_{0.10})O_5Cu_2Se_2$	4.10331(9)	26.6364(8)	448.481(29)
0.15	$Sr_3(Sc_{1.85}La_{0.15})O_5Cu_2Se_2$	4.10350(11)	26.6377(10)	448.540(40)
0.20	$Sr_3(Sc_{1.80}La_{0.20})O_5Cu_2Se_2$	4.10288(15)	26.6392(14)	448.430(50)

Table 45 Tabulated compositional data of the lanthanum doped 325 selenide MALMs with general formula $Sr_3(Sc_{2-x}La_x)O_5Cu_2Se_2$. The pristine material $Sr_3Sc_2O_5Cu_2Se_2$ is included as a reference. All values are cited as a weight percent (wt %) of the total weight, and are derived from the Rietveld refinement of PXRD data using GSAS-II.

x / mol	Target phase / wt %	SrSe / wt %	$SrCO_3$ / wt %	$La_2CuO_{3.98}$ / wt %
0 (pristine)	99.1	0.5	0.4	-
0.05	99.3	0.3	0.4	-
0.10	99.2	0.2	0.6	-
0.15	96.6	1.1	0.8	1.5
0.20	95.0	0.4	0.5	4.1

Table 46 Tabulated data on both the target and maximum actual dopant content of the lanthanum doped 325 selenide MALMs with general formula $Sr_3(Sc_{2-x}La_x)O_5Cu_2Se_2$. The pristine material $Sr_3Sc_2O_5Cu_2S_2$ is included as a reference. The minimum possible amount of total La contained within impurities was extracted from the refined wt % of $La_2CuO_{3.98}$ from GSAS-II. The remaining La content is the maximum possible La within the MALM.

Target x / mol	**Target x / wt %**	**Minimum La in impurities / %**	**Maximum La in product / %**	**Maximum x / mol**
0 (pristine)	0.000	0.000	100.000	0.000
0.05	1.105	0.000	100.000	0.050
0.10	2.193	0.000	100.000	0.100
0.15	3.265	23.804	76.196	0.114
0.20	4.322	65.066	34.934	0.070

Table 47 Tabulated analytical data of to the measured properties of the lanthanum doped 325 selenide MALMs with general formula $Sr_3(Sc_{2-x}La_x)O_5Cu_2Se_2$. The pristine material $Sr_3Sc_2O_5Cu_2Se_2$ is included as a reference. Optical band gaps were estimated from UV-Vis data. Pellet densities were estimated from the mass and volume of annealed pellet samples, and are cited as a relative percentage of the bulk crystal. Resistivities and conductivities were estimated from 4 probe van der Pauw analysis of the pellet samples.

x / mol	Band Gap / eV	Pellet Density / %	Raw Resistivities from 4-Probe measurement, for each probe permutation / kΩ								Resistivity / Ω cm	Conductivity / S cm^{-1}
			1	2	3	4	5	6	7	8		
0 (pristine)	2.94	71.72	1.20 E+01	1.21 E+01	1.22 E+01	1.22 E+01	1.03 E+01	1.02 E+01	1.02 E+01	1.01 E+01	3.83 E+03	2.61 E-04
0.05	2.86	71.27	1.69 E+02	1.70 E+02	1.71 E+02	1.71 E+02	1.26 E+02	1.26 E+02	1.26 E+02	1.27 E+02	5.13 E+04	1.95 E-05
0.10	2.84	65.77	1.29 E+00	1.30 E+00	1.30 E+00	1.31 E+00	9.35 E-01	9.37 E-01	9.38 E-01	9.40 E-01	4.12 E+02	2.43 E-03
0.15	2.83	67.82	1.05 E+00	1.06 E+00	1.06 E+00	1.06 E+00	1.21 E+00	1.22 E+00	1.21 E+00	1.21 E+00	4.13 E+02	2.42 E-03
0.20	2.73	60.62	7.60 E-02	7.60 E-02	7.70 E-02	7.70 E-02	3.80 E-02	3.70 E-02	3.90 E-02	3.80 E-02	2.19 E+01	4.56 E-02

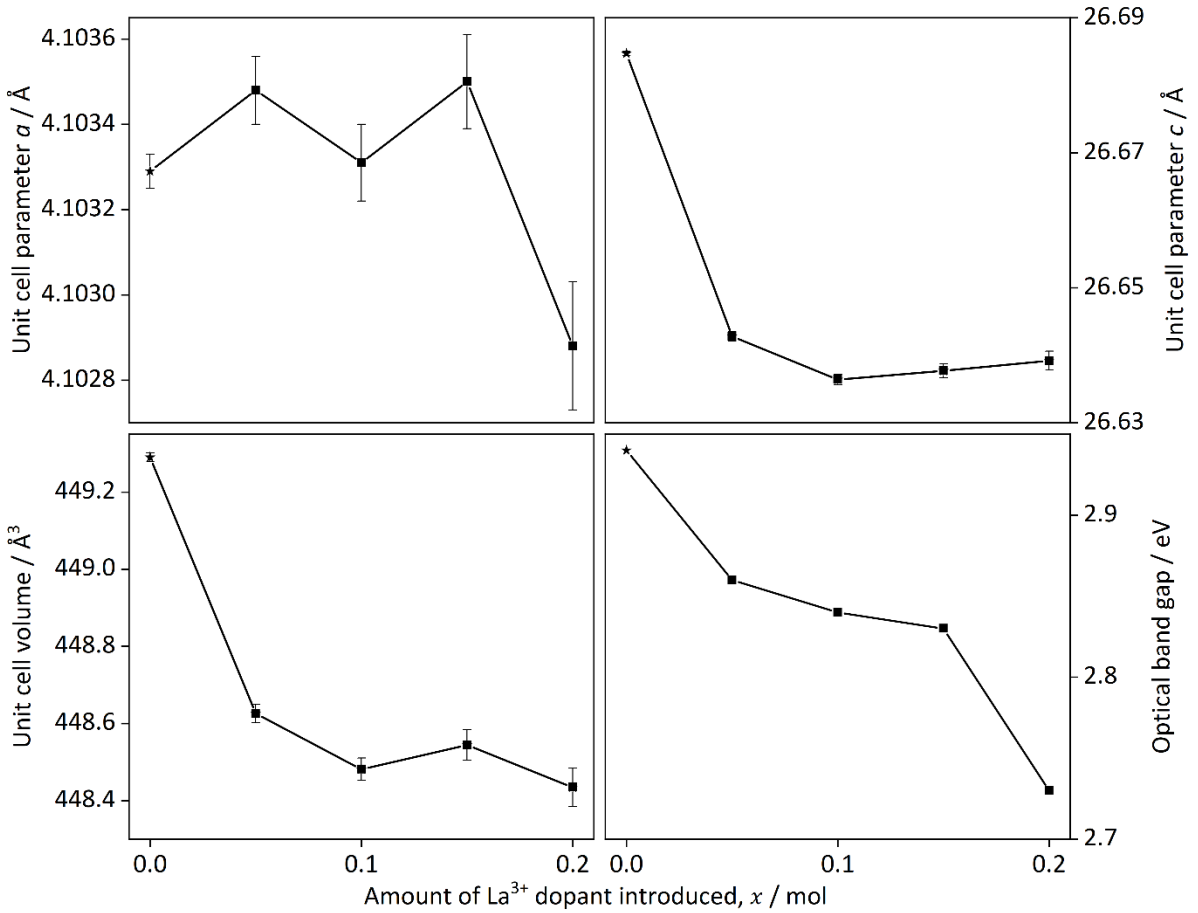

Figure 164 *Comparisons of a) the α unit cell parameter, b) the c unit cell parameter, c) unit cell volume, and d) the optical band gap, of the lanthanum doped 325 selenide MALMs with general formula $Sr_3(Sc_{2-x}La_x)O_5Cu_2Se_2$. The pristine material $Sr_3Sc_2O_5Cu_2Se_2$ is included as a reference at x = 0 mol and is represented by a star.*

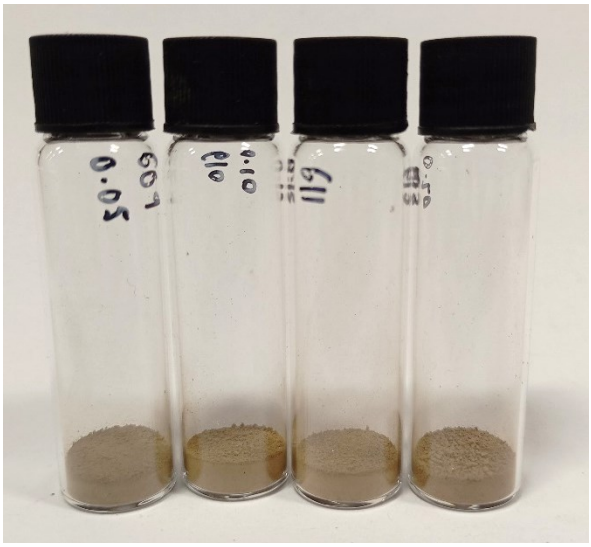

Figure 165 *A photographic comparison of the colour of the lanthanum doped 325 selenide MALMs with general formula $Sr_3(Sc_{2-x}La_x)O_5Cu_2Se_2$. Dopant concentration increases from left to right.*

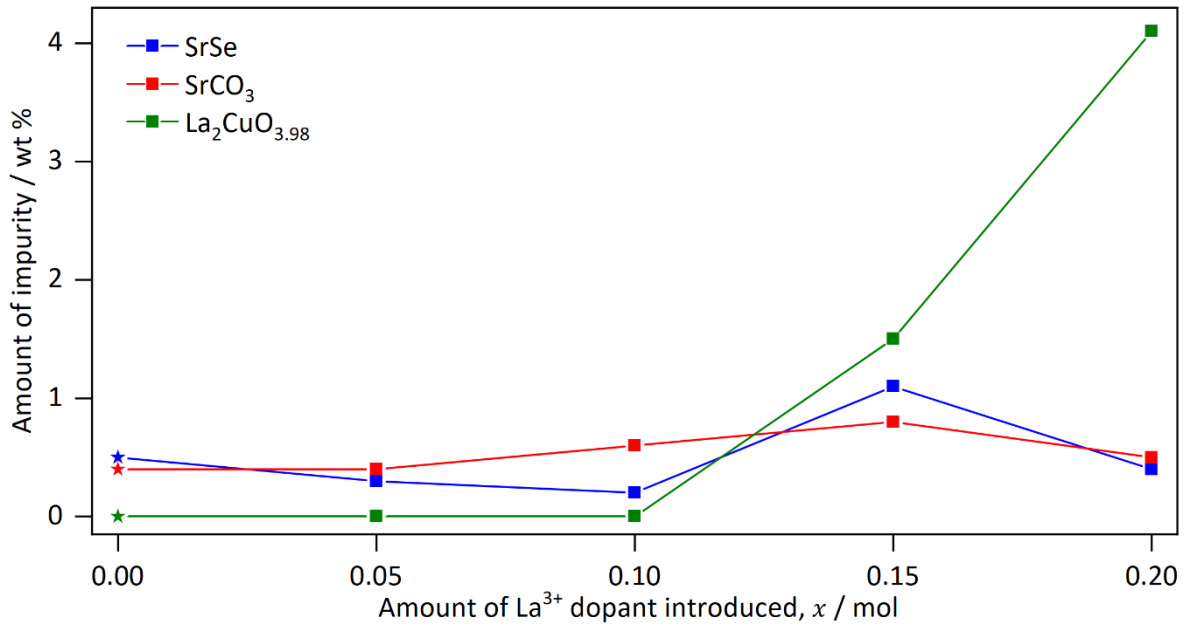

Figure 166 *The weight percentages of three impurity phases present in the lanthanum doped 325 selenide MALMs with general formula $Sr_3(Sc_{2-x}La_x)O_5Cu_2Se_2$. The pristine material $Sr_3Sc_2O_5Cu_2Se_2$ is included as a reference at $x = 0$ mol and is represented by a star.*

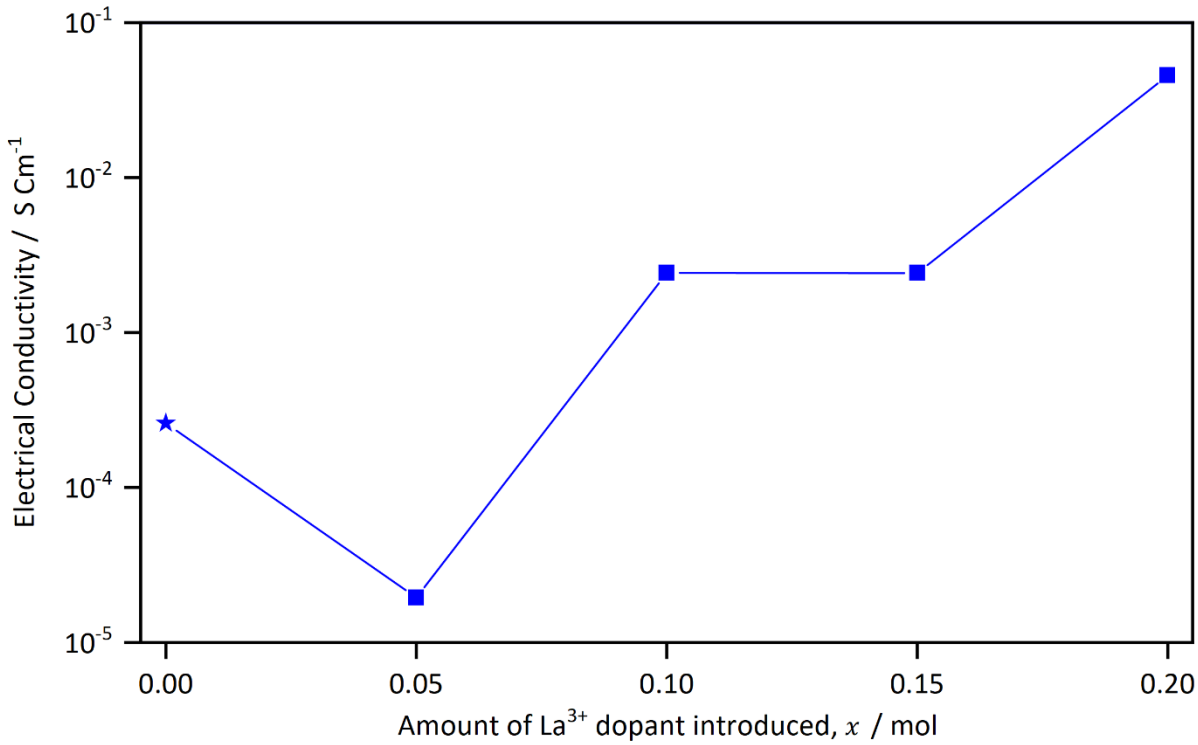

Figure 167 *The electrical conductivities of the lanthanum doped 325 selenide MALMs with general formula $Sr_3(Sc_{2-x}La_x)O_5Cu_2Se_2$, represented on a log_{10} scale. The pristine material $Sr_3Sc_2O_5Cu_2Se_2$ is included as a reference at $x = 0$ mol and is represented by a star. All values are derived from van der Pauw 4 probe resistivity measurements of 8mm diameter annealed pellet samples.*

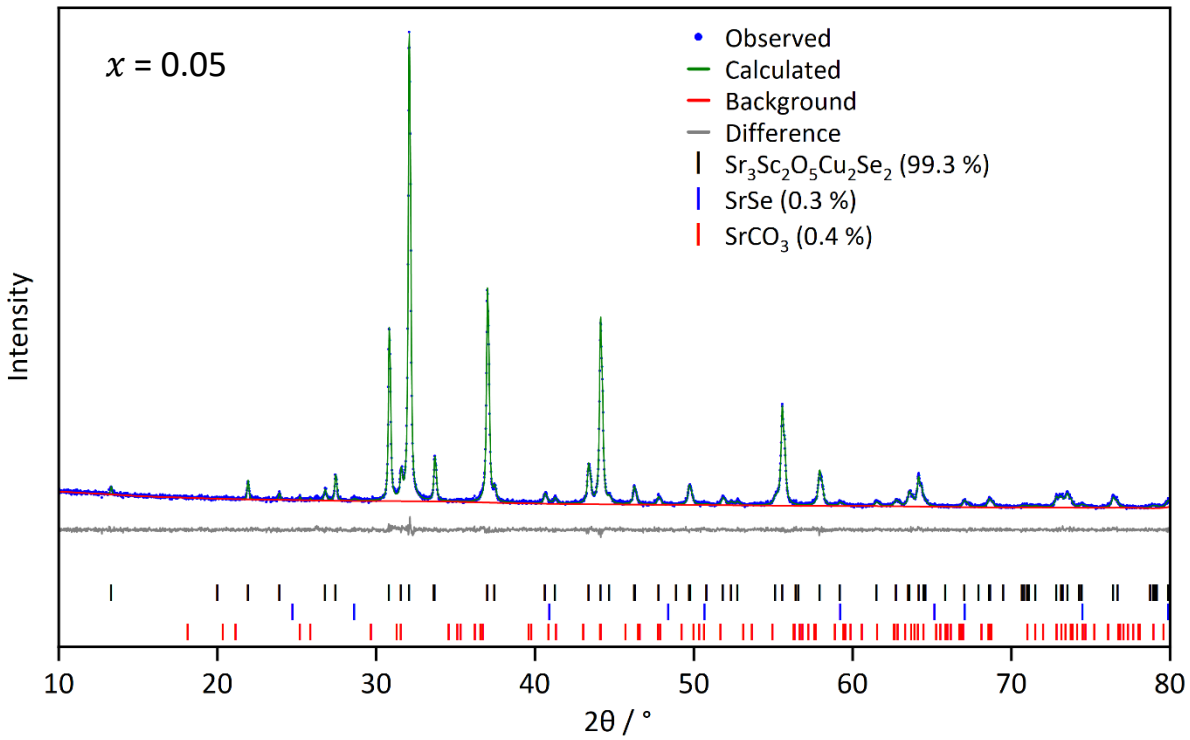

Figure 168 *Powder X-ray diffractogram of material with target composition $Sr_3(Sc_{1.95}La_{0.05})O_5Cu_2Se_2$ (space group I4/mmm) after 36 hours of heating at 800 °C. The small blue circles represent the observed diffracted intensity, the green line represents the Rietveld-refined calculated model, the red line represents the background, and the grey line represents the difference between observed and calculated intensities. The black tick marks show the reflections of the refined model of $Sr_3Sc_2O_5Cu_2Se_2$ (99.3 %), whilst the blue and red marks represent refined impurity phases SrSe (0.3 %) and $SrCO_3$ (0.4 %) respectively.*
Duration: 45 minutes. Data points: 3457. Interval: 0.02 °. GOF: 1.11. R_{wp}: 4.497 %.

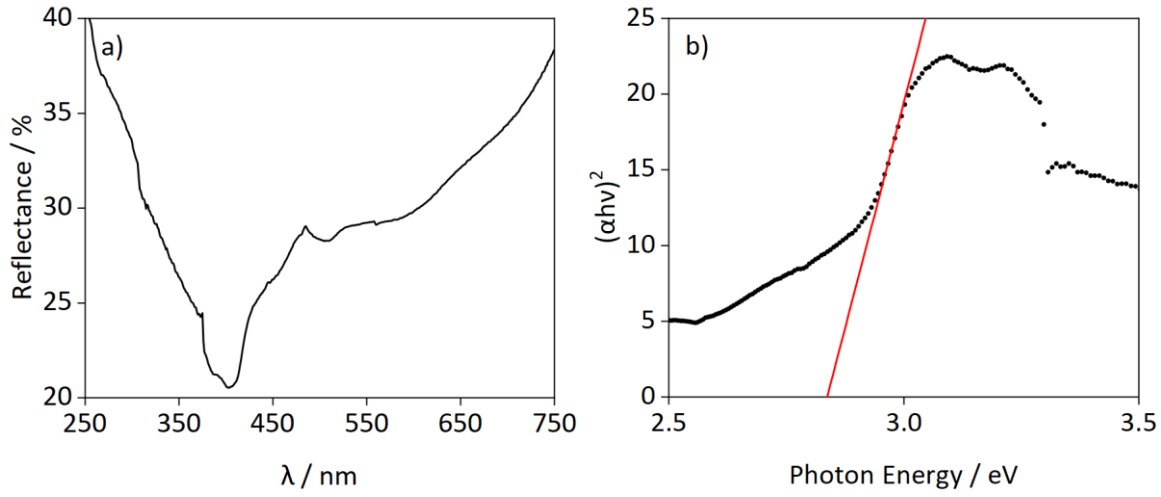

Figure 169 *UV-Vis spectrometry data for material with target composition $Sr_3(Sc_{1.95}La_{0.05})O_5Cu_2Se_2$ after 36 hours of heating at 800 °C. Plot a) is the raw diffuse reflectance data, and plot b) is the associated magnified Tauc plot for this region, where the intercept between the red extrapolated tangent line and the x-axis is used to estimate an optical band gap of 2.86 eV, which corresponds to 433 nm.*

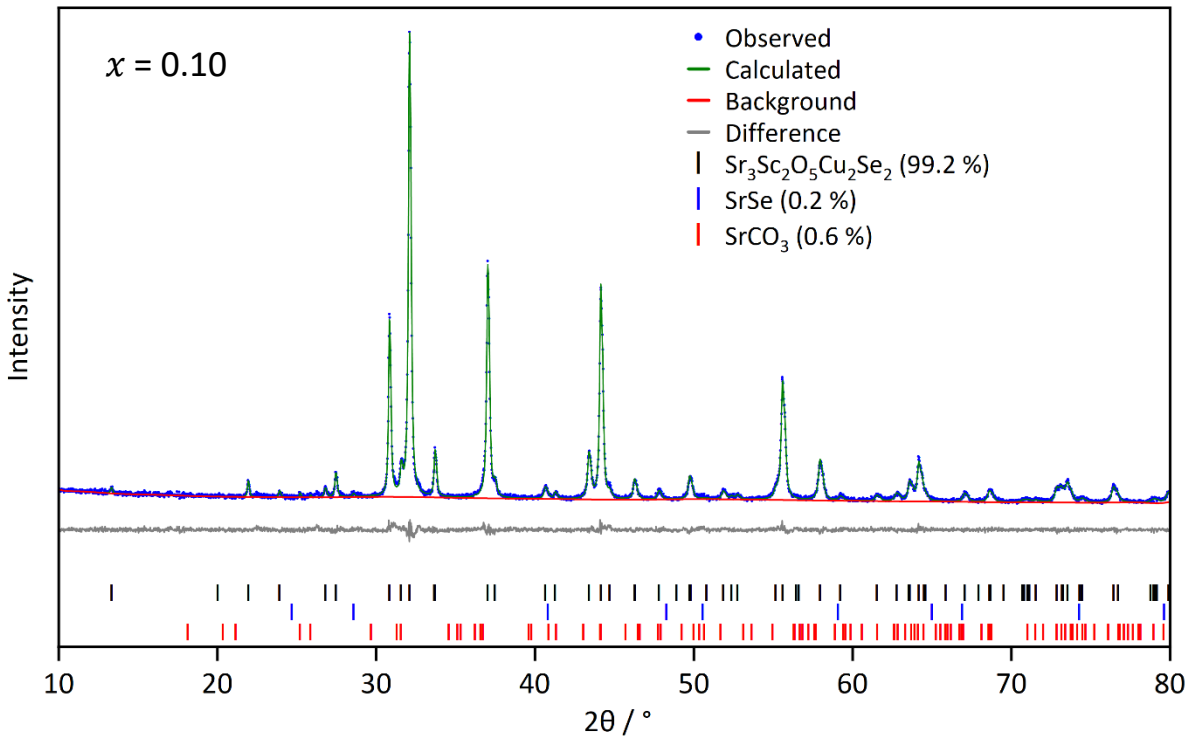

Figure 170 *Powder X-ray diffractogram of material with target composition $Sr_3(Sc_{1.90}La_{0.10})O_5Cu_2Se_2$ (space group I4/mmm) after 36 hours of heating at 800 °C. The small blue circles represent the observed diffracted intensity, the green line represents the Rietveld-refined calculated model, the red line represents the background, and the grey line represents the difference between observed and calculated intensities. The black tick marks show the reflections of the refined model of $Sr_3Sc_2O_5Cu_2Se_2$ (99.2 %), whilst the blue and red marks represent refined impurity phases SrSe (0.2 %) and $SrCO_3$ (0.6 %) respectively.*
Duration: 45 minutes. Data points: 3457. Interval: 0.02 °. GOF: 1.14. R_{wp}: 4.610 %.

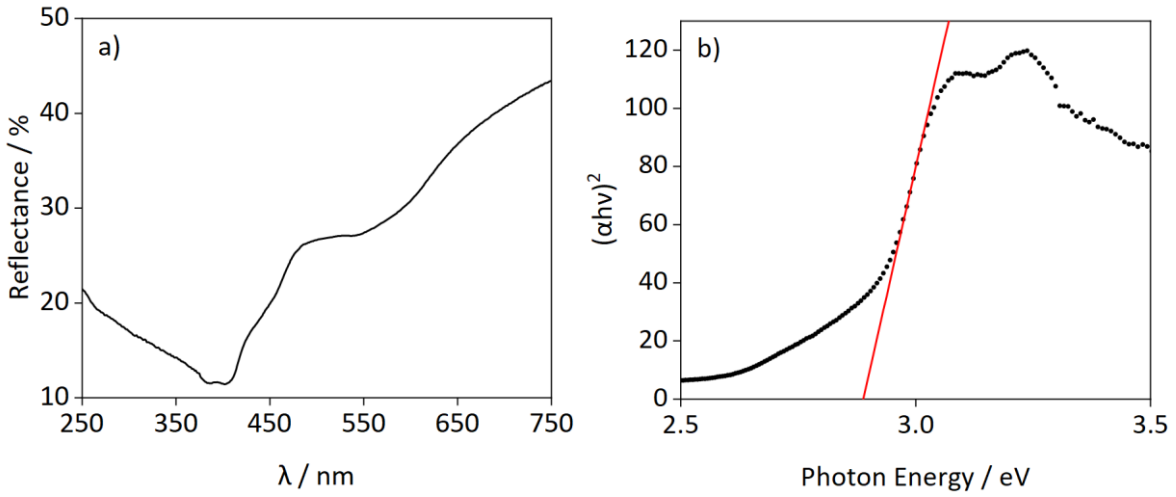

Figure 171 *UV-Vis spectrometry data for material with target composition $Sr_3(Sc_{1.90}La_{0.10})O_5Cu_2Se_2$ after 36 hours of heating at 800 °C. Plot a) is the raw diffuse reflectance data, and plot b) is the associated magnified Tauc plot for this region, where the intercept between the red extrapolated tangent line and the x-axis is used to estimate an optical band gap of 2.84 eV, which corresponds to 437 nm.*

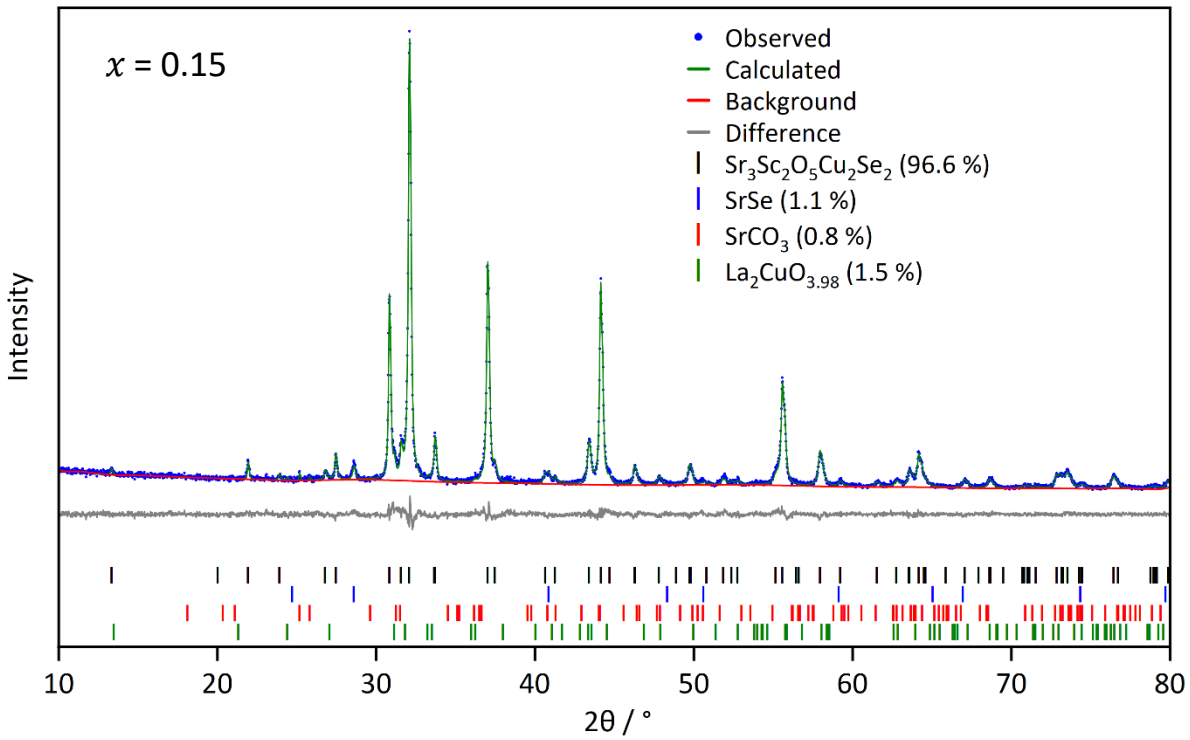

Figure 172 *Powder X-ray diffractogram of material with target composition $Sr_3(Sc_{1.85}La_{0.15})O_5Cu_2Se_2$ (space group I4/mmm) after 36 hours of heating at 800 °C. The small blue circles represent the observed diffracted intensity, the green line represents the Rietveld-refined calculated model, the red line represents the background, and the grey line represents the difference between observed and calculated intensities. The black tick marks show the reflections of the refined model of $Sr_3Sc_2O_5Cu_2Se_2$ (96.6 %), whilst the blue, red and green marks represent refined impurity phases SrSe (1.1 %), $SrCO_3$ (0.8 %) and $La_2CuO_{3.98}$ (1.5 %) respectively.*
Duration: 45 minutes. Data points: 3457. Interval: 0.02 °. GOF: 1.24. R_{wp}: 5.464 %.

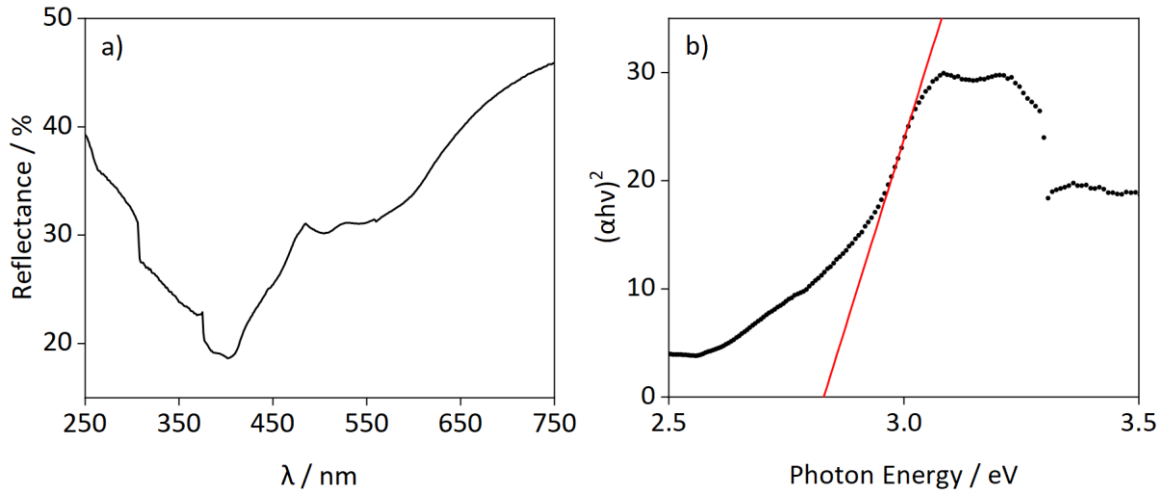

Figure 173 *UV-Vis spectrometry data for material with target composition $Sr_3(Sc_{1.85}La_{0.15})O_5Cu_2Se_2$ after 36 hours of heating at 800 °C. Plot a) is the raw diffuse reflectance data, and plot b) is the associated magnified Tauc plot for this region, where the intercept between the red extrapolated tangent line and the x-axis is used to estimate an optical band gap of 2.83 eV, which corresponds to 438 nm.*

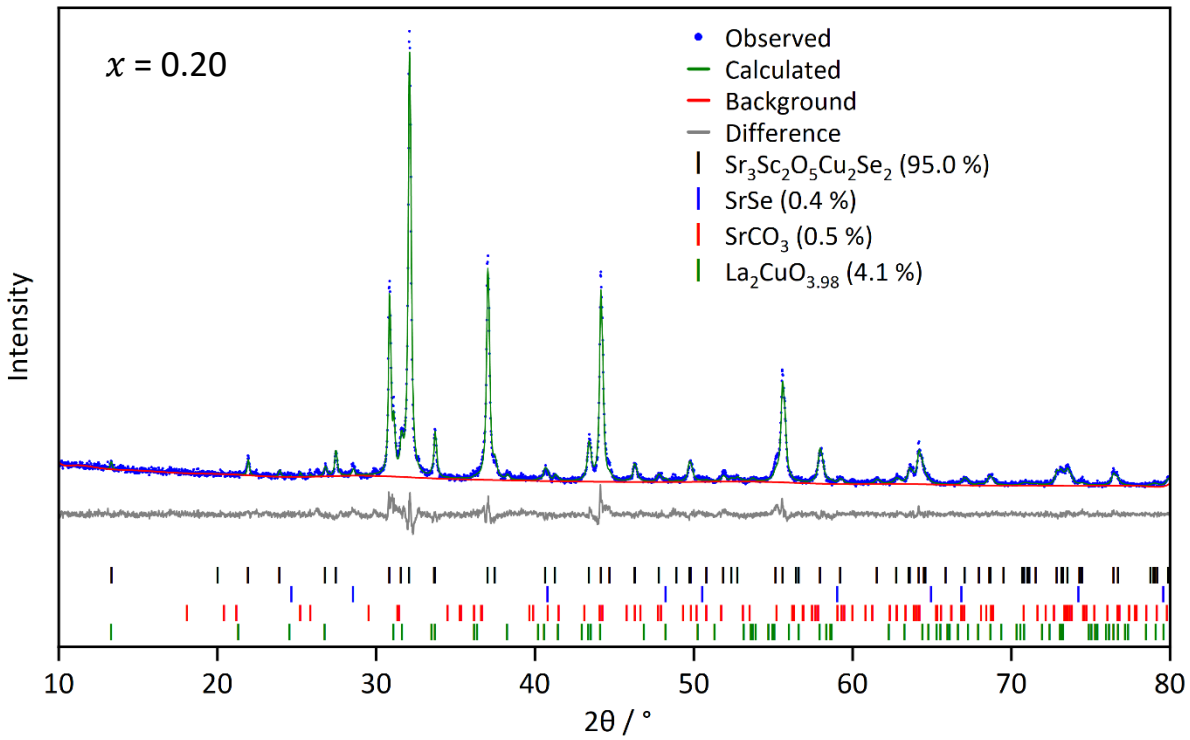

Figure 174 *Powder X-ray diffractogram of material with target composition $Sr_3(Sc_{1.80}La_{0.20})O_5Cu_2Se_2$ (space group I4/mmm) after 36 hours of heating at 800 °C. The small blue circles represent the observed diffracted intensity, the green line represents the Rietveld-refined calculated model, the red line represents the background, and the grey line represents the difference between observed and calculated intensities. The black tick marks show the reflections of the refined model of $Sr_3Sc_2O_5Cu_2Se_2$ (95.0 %), whilst the blue, red and green marks represent refined impurity phases SrSe (0.4 %), $SrCO_3$ (0.5 %) and $La_2CuO_{3.98}$ (4.1 %) respectively.*
Duration: 45 minutes. Data points: 3457. Interval: 0.02 °. GOF: 1.49. R_{wp}: 6.606 %.

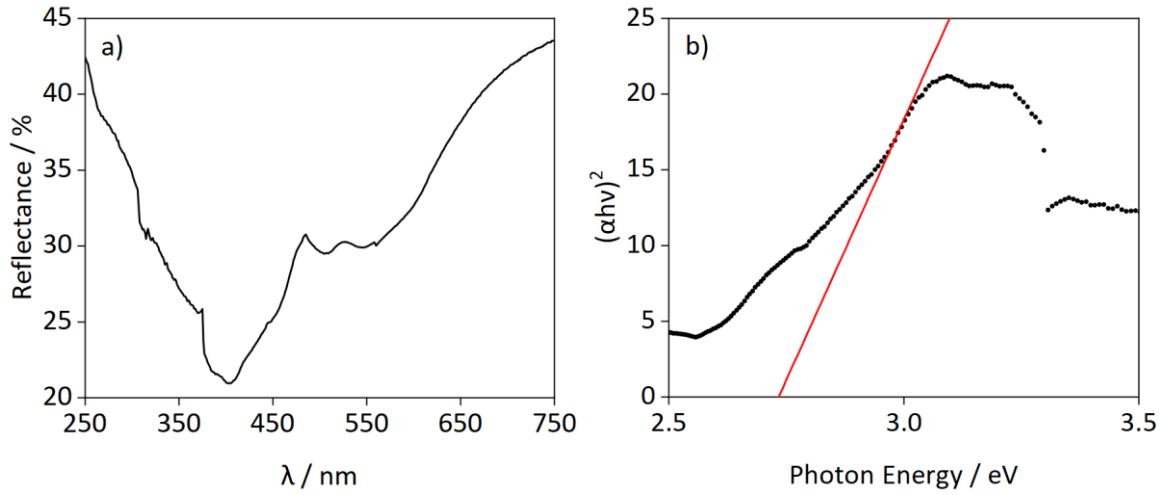

Figure 175 *UV-Vis spectrometry data for material with target composition $Sr_3(Sc_{1.80}La_{0.20})O_5Cu_2Se_2$ after 36 hours of heating at 800 °C. Plot a) is the raw diffuse reflectance data, and plot b) is the associated magnified Tauc plot for this region, where the intercept between the red extrapolated tangent line and the x-axis is used to estimate an optical band gap of 2.73 eV, which corresponds to 454 nm.*

B.1.10 Strontium deficient 325 selenide MALMs, $Sr_{3-x}Sc_2O_5Cu_2Se_2$

Table 48 Tabulated structural data of the strontium deficient 325 selenide MALMs with general formula $Sr_{3-x}Sc_2O_5Cu_2Se_2$. The pristine material $Sr_3Sc_2O_5Cu_2Se_2$ is included as a reference. All values are derived from the Rietveld refinement of PXRD data using GSAS-II. Note that because all materials listed are tetragonal (space group I4/mmm), the b parameter is identical to a, and thus omitted.

x **/ mol**	**Target Composition**	***a*** **/ Å**	***c*** **/ Å**	**Volume / Å^3**
0 (pristine)	$Sr_3Sc_2O_5Cu_2Se_2$	4.10329(4)	26.6847(3)	449.290(12)
0.05	$Sr_{2.95}Sc_2O_5Cu_2Se_2$	4.10353(10)	26.6873(9)	449.386(30)
0.10	$Sr_{2.90}Sc_2O_5Cu_2Se_2$	4.10360(8)	26.6903(7)	449.453(25)
0.15	$Sr_{2.85}Sc_2O_5Cu_2Se_2$	4.10339(8)	26.6953(7)	449.491(25)
0.20	$Sr_{2.80}Sc_2O_5Cu_2Se_2$	4.10333(11)	26.6953(10)	449.480(30)
0.50	$Sr_{2.50}Sc_2O_5Cu_2Se_2$	4.10212(11)	26.7058(10)	449.390(40)
0.75	$Sr_{2.25}Sc_2O_5Cu_2Se_2$	4.10143(18)	26.7056(15)	449.230(50)
1.00	$Sr_{2.00}Sc_2O_5Cu_2Se_2$	4.10053(21)	26.7078(20)	449.070(60)

Table 49 Tabulated compositional data of the strontium deficient 325 selenide MALMs with general formula $Sr_{3-x}Sc_2O_5Cu_2Se_2$. The pristine material $Sr_3Sc_2O_5Cu_2Se_2$ is included as a reference. All values are cited as a weight percent (wt %) of the total weight, and are derived from the Rietveld refinement of PXRD data using GSAS-II.

x / mol	Target phase / wt %	SrSe / wt %	$SrCO_3$ / wt %	Sc_2O_3 / wt %	$SrSeO_4$ / wt %	Cu_2Se / wt %
0 (pristine)	99.1	0.5	0.4	-	-	-
0.05	98.4	1.0	0.6	-	-	-
0.10	97.9	1.7	0.4	-	-	-
0.15	97.8	1.8	0.4	-	-	-
0.20	97.3	2.4	0.4	-	-	-
0.50	84.5	2.1	-	5.2	2.0	6.0
0.75	81.8	3.6	-	6.8	2.1	5.8
1.00	68.8	4.7	-	9.7	3.0	13.9

Table 50 Tabulated analytical data of to the measured properties of the strontium deficient 325 selenide MALMs with general formula $Sr_{3-x}Sc_2O_5Cu_2Se_2$. The pristine material $Sr_3Sc_2O_5Cu_2Se_2$ is included as a reference. Optical band gaps were estimated from UV-Vis data. Pellet densities were estimated from the mass and volume of annealed pellet samples, and are cited as a relative percentage of the bulk crystal. Resistivities and conductivities were estimated from 4 probe van der Pauw analysis of the pellet samples.

x / mol	Band Gap / eV	Pellet Density / %	Raw Resistivities from 4-Probe measurement, for each probe permutation / kΩ								Resistivity / Ω cm	Conductivity / S cm^{-1}
			1	2	3	4	5	6	7	8		
0 (pristine)	2.94	71.72	1.20 E+01	1.21 E+01	1.22 E+01	1.22 E+01	1.03 E+01	1.02 E+01	1.02 E+01	1.01 E+01	3.83 E+03	2.61 E-04
0.05	2.87	70.24	1.75 E-01	1.49 E-01	1.49 E-01	1.46 E-01	1.27 E-01	1.26 E-01	1.28 E-01	1.48 E-01	5.06 E+01	1.98 E-02
0.10	2.89	71.05	6.80 E-02	6.80 E-02	6.70 E-02	6.60 E-02	6.50 E-02	6.50 E-02	6.40 E-02	6.40 E-02	2.36 E+01	4.24 E-02
0.15	2.87	71.16	3.40 E-02	3.40 E-02	3.36 E-02	3.34 E-02	3.01 E-02	3.06 E-02	2.99 E-02	2.99 E-02	1.14 E+01	8.75 E-02
0.20	2.82	73.11	1.86 E-02	1.85 E-02	1.84 E-02	1.83 E-02	1.12 E-02	1.12 E-02	1.12 E-02	1.12 E-02	5.13 E+00	1.95 E-01
0.50	*n/a* †	77.07	6.41 E-04	6.43 E-04	6.41 E-04	6.38 E-04	3.45 E-04	3.48 E-04	3.44 E-04	3.48 E-04	1.67 E-01	6.00 E+00
0.75	*n/a* †	78.10	1.16 E-04	1.14 E-04	1.14 E-04	1.14 E-04	2.19 E-04	2.19 E-04	2.19 E-04	2.19 E-04	5.40 E-02	1.85 E+01
1.00	*n/a* †	75.09	2.27 E-04	2.29 E-04	2.26 E-04	2.25 E-04	4.88 E-04	4.88 E-04	4.87 E-04	4.87 E-04	1.20 E-01	8.32 E+00

† A band gap estimation for these samples was not possible due to a lack of drop-off in reflectance between the UV and visible regions. The samples were either too impure or too dark in colour for any difference to be justified, and the Tauc plots were deemed too subjective for the usual tangent approximation.

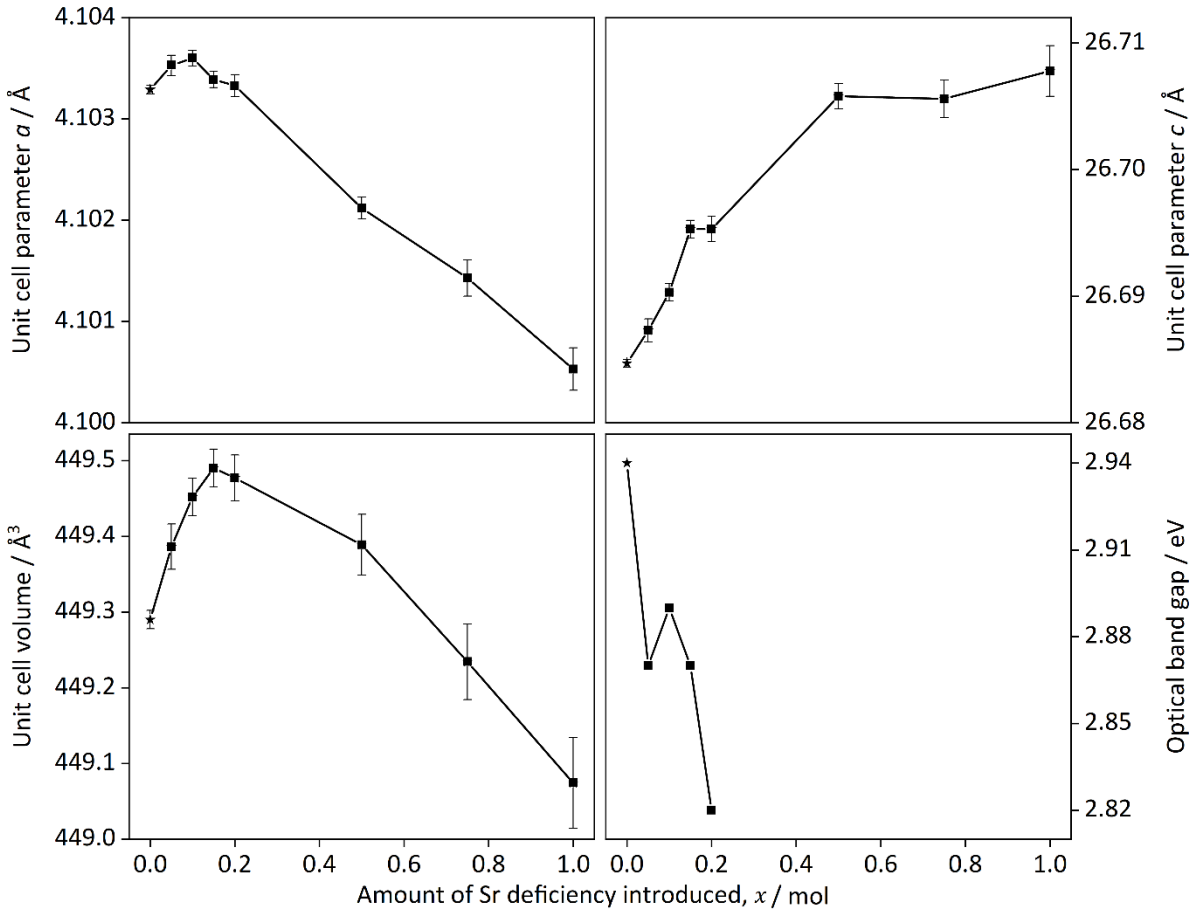

Figure 176 Comparisons of a) the a unit cell parameter, b) the c unit cell parameter, c) unit cell volume, and d) the optical band gap, of the strontium deficient 325 selenide MALMs with general formula $Sr_{3-x}Sc_2O_5Cu_2Se_2$. The pristine material $Sr_3Sc_2O_5Cu_2Se_2$ is included as a reference at $x = 0$ mol and is represented by a star. The three $x = 0.500$ to 1.000 mol sample band gaps are missing due to lack of drop-off in diffuse reflectance, see Table 50.

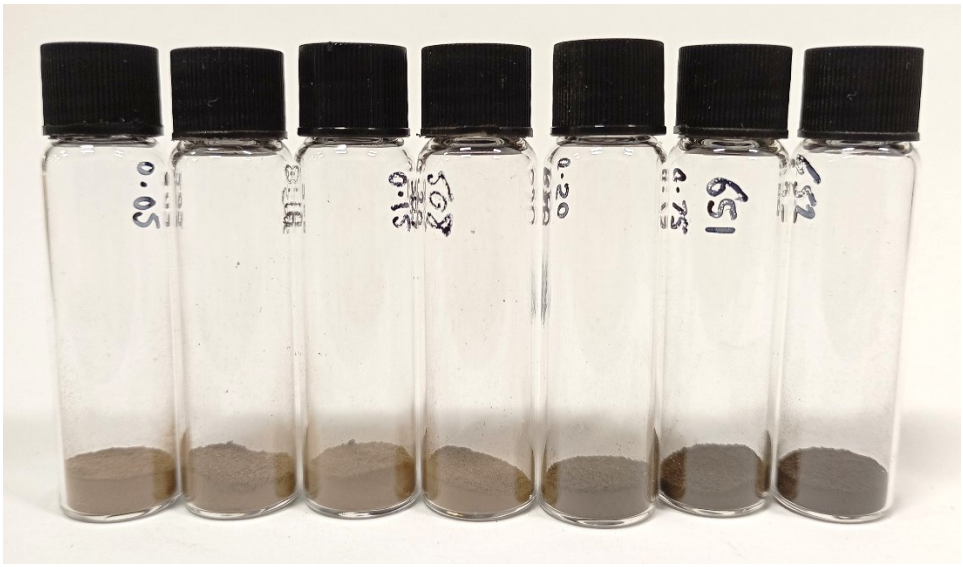

Figure 177 A photographic comparison of the colour of the strontium deficient 325 selenide MALMs with general formula $Sr_{3-x}Sc_2O_5Cu_2Se_2$. Deficiency increases from left to right.

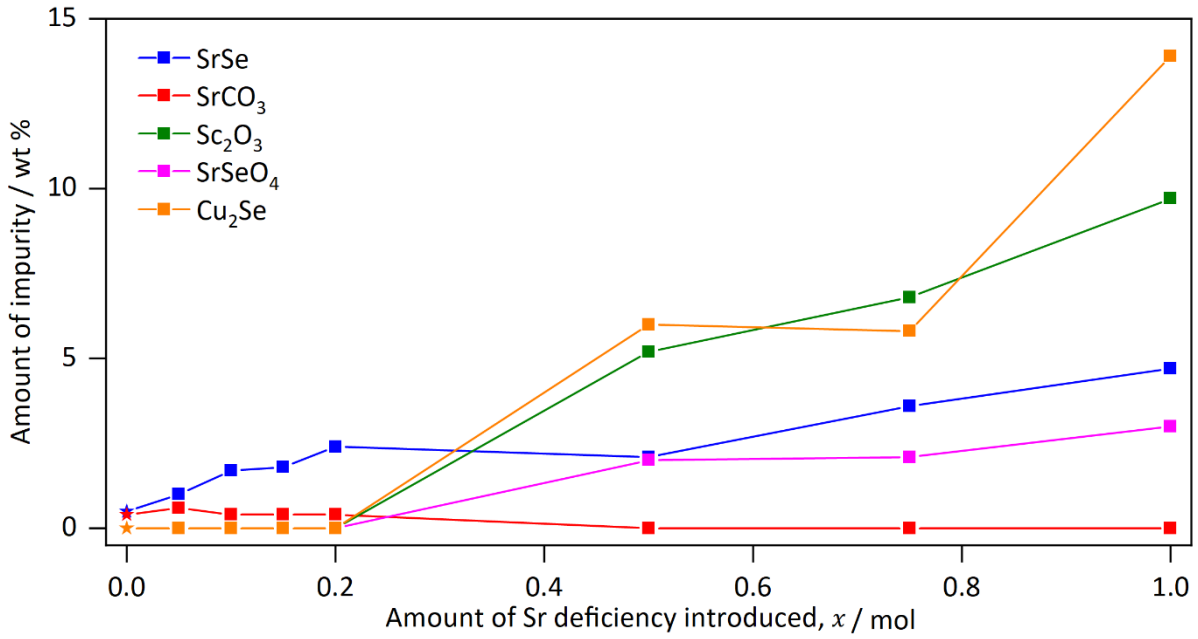

Figure 178 *The weight percentages of five impurity phases present in strontium deficient 325 selenide MALMs with general formula $Sr_{3-x}Sc_2O_5Cu_2Se_2$. The pristine material $Sr_3Sc_2O_5Cu_2Se_2$ is included as a reference at $x = 0$ mol and is represented by a star.*

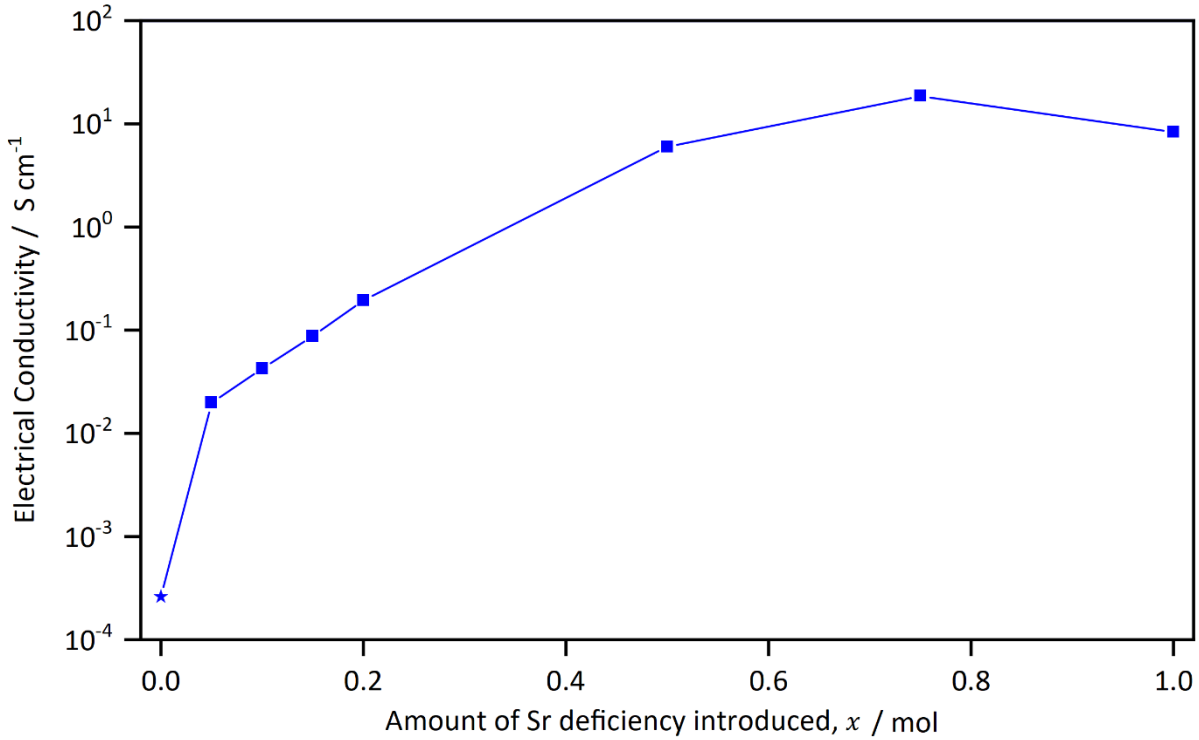

Figure 179 *The electrical conductivities of the strontium deficient 325 selenide MALMs with general formula $Sr_{3-x}Sc_2O_5Cu_2Se_2$, represented on a $\log_{10}$ scale. The pristine material $Sr_3Sc_2O_5Cu_2Se_2$ is included as a reference at $x = 0$ mol and is represented by a star. All values are derived from van der Pauw 4 probe resistivity measurements of 8mm diameter annealed pellet samples.*

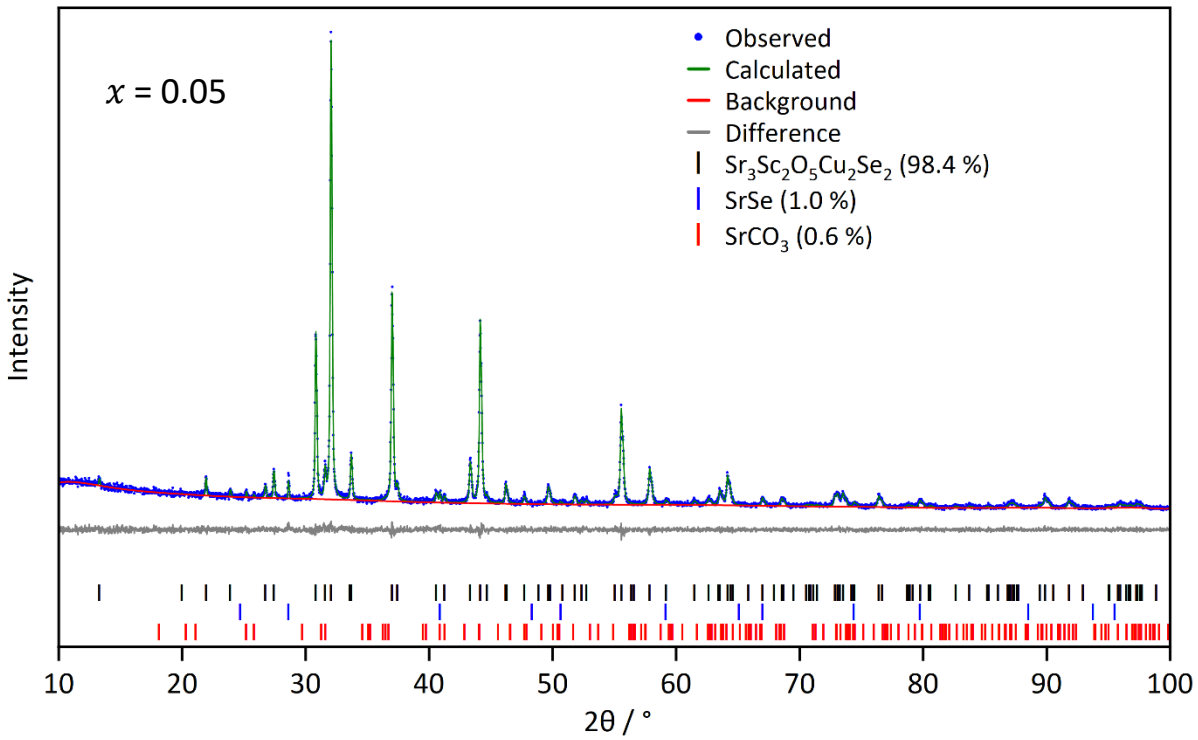

Figure 180 *Powder X-ray diffractogram of material with target composition $Sr_{2.95}Sc_2O_5Cu_2Se_2$ (space group I4/mmm) after 36 hours of heating at 800 °C. The small blue circles represent the observed diffracted intensity, the green line represents the Rietveld-refined calculated model, the red line represents the background, and the grey line represents the difference between observed and calculated intensities. The black tick marks show the reflections of the refined model of $Sr_3Sc_2O_5Cu_2Se_2$ (98.4 %), whilst the blue and red marks represent refined impurity phases SrSe (1.0 %) and $SrCO_3$ (0.6 %) respectively.*
Duration: 45 minutes. Data points: 4444. Interval: 0.02 °. GOF: 1.05. R_{wp}: 6.288 %.

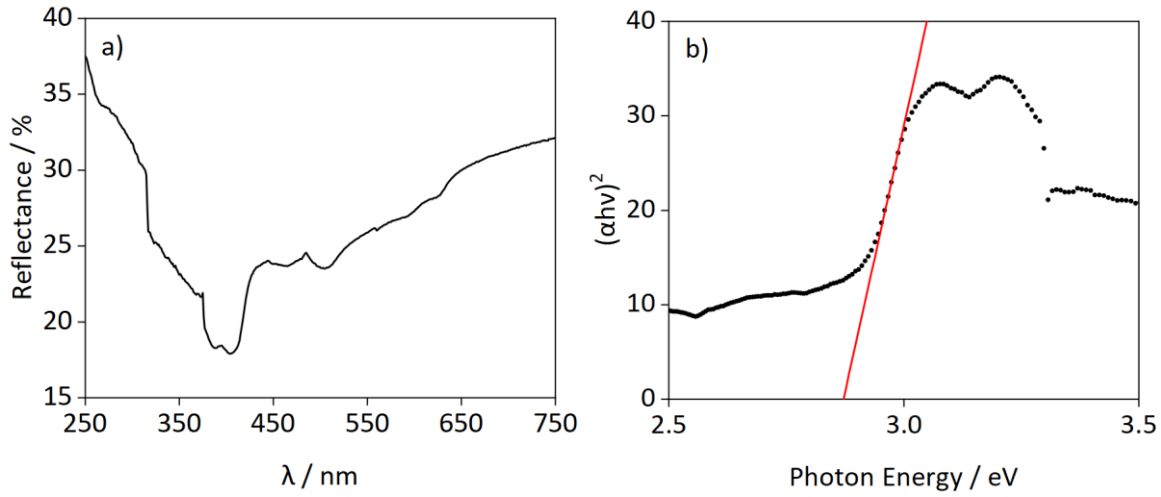

Figure 181 *UV-Vis spectrometry data for material with target composition $Sr_{2.95}Sc_2O_5Cu_2Se_2$ after 36 hours of heating at 800 °C. Plot a) is the raw diffuse reflectance data, and plot b) is the associated magnified Tauc plot for this region, where the intercept between the red extrapolated tangent line and the x-axis is used to estimate an optical band gap of 2.87 eV, which corresponds to 432 nm.*

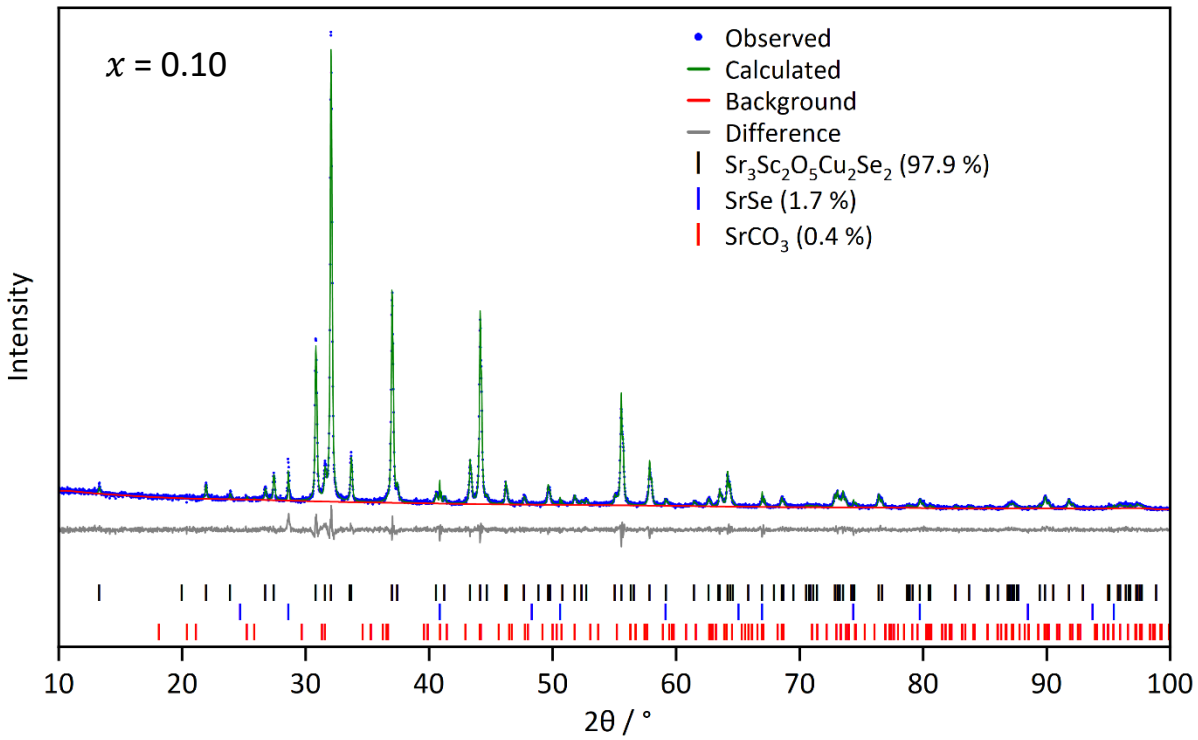

Figure 182 *Powder X-ray diffractogram of material with target composition $Sr_{2.90}Sc_2O_5Cu_2Se_2$ (space group I4/mmm) after 36 hours of heating at 800 °C. The small blue circles represent the observed diffracted intensity, the green line represents the Rietveld-refined calculated model, the red line represents the background, and the grey line represents the difference between observed and calculated intensities. The black tick marks show the reflections of the refined model of $Sr_3Sc_2O_5Cu_2Se_2$ (97.9 %), whilst the blue and red marks represent refined impurity phases SrSe (1.7 %) and $SrCO_3$ (0.4 %) respectively.*
Duration: 45 minutes. Data points: 4444. Interval: 0.02 °. GOF: 1.26. R_{wp}: 6.580 %.

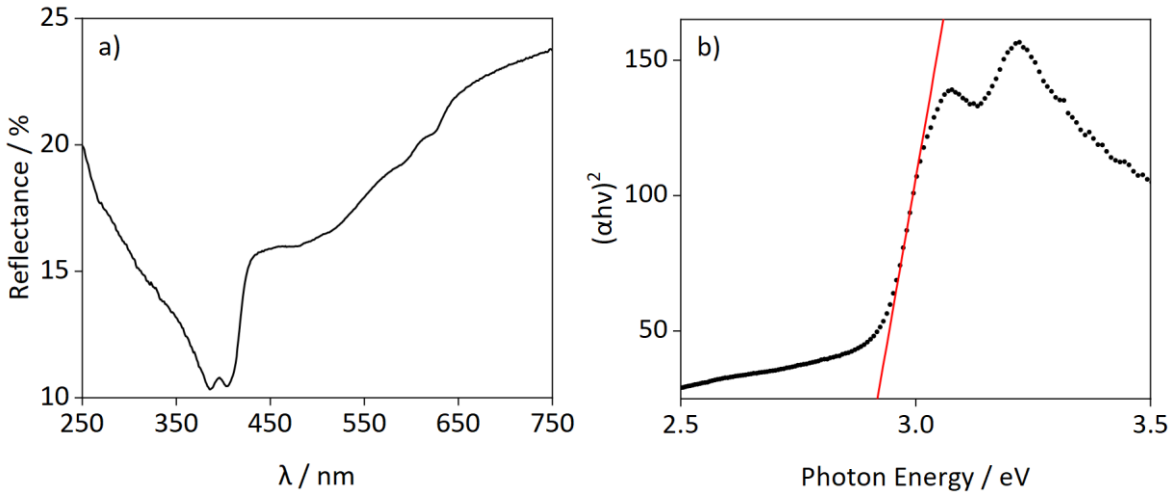

Figure 183 *UV-Vis spectrometry data for material with target composition $Sr_{2.90}Sc_2O_5Cu_2Se_2$ after 36 hours of heating at 800 °C. Plot a) is the raw diffuse reflectance data, and plot b) is the associated magnified Tauc plot for this region, where the intercept between the red extrapolated tangent line and the x-axis is used to estimate an optical band gap of 2.89 eV, which corresponds to 429 nm.*

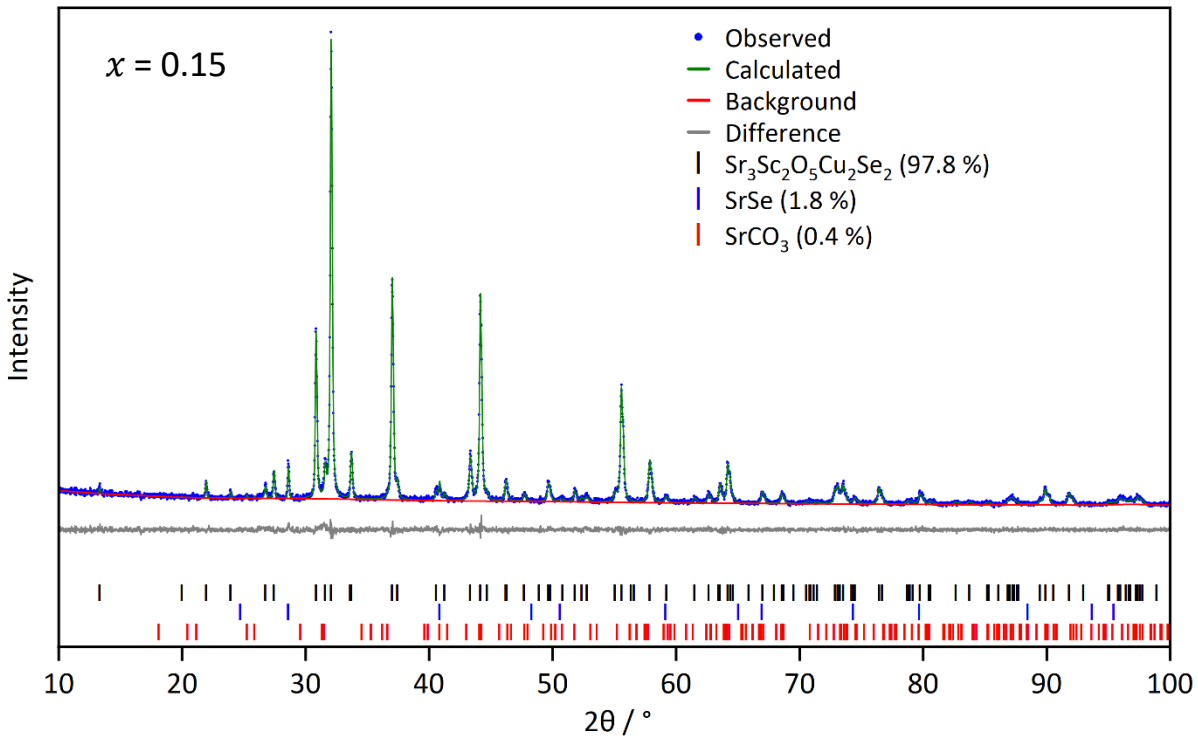

Figure 184 *Powder X-ray diffractogram of material with target composition $Sr_{2.85}Sc_2O_5Cu_2Se_2$ (space group I4/mmm) after 36 hours of heating at 800 °C. The small blue circles represent the observed diffracted intensity, the green line represents the Rietveld-refined calculated model, the red line represents the background, and the grey line represents the difference between observed and calculated intensities. The black tick marks show the reflections of the refined model of $Sr_3Sc_2O_5Cu_2Se_2$ (97.8 %), whilst the blue and red marks represent refined impurity phases SrSe (1.8 %) and $SrCO_3$ (0.4 %) respectively.*
Duration: 45 minutes. Data points: 4444. Interval: 0.02 °. GOF: 1.07. R_{wp}: 5.358 %.

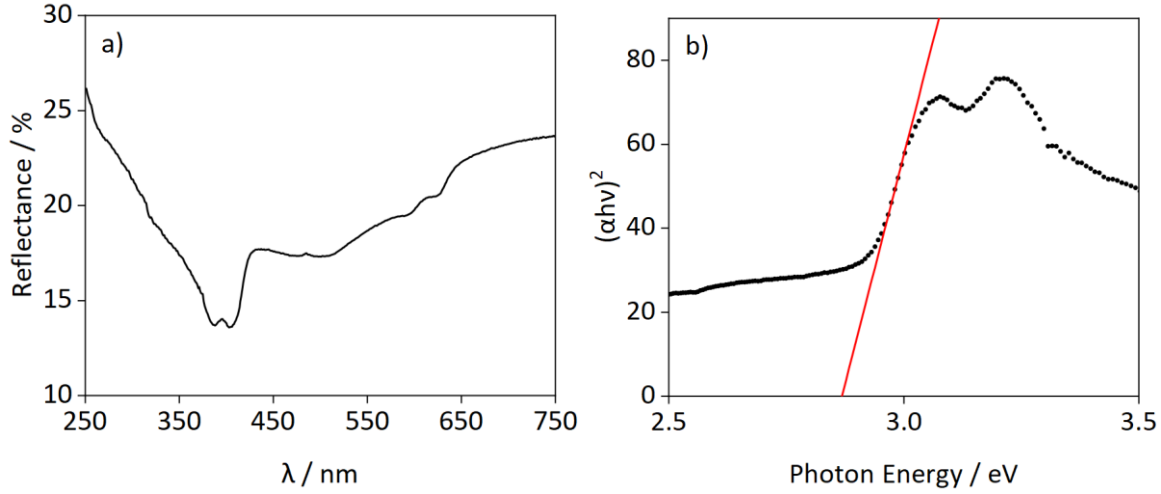

Figure 185 *UV-Vis spectrometry data for material with target composition $Sr_{2.85}Sc_2O_5Cu_2Se_2$ after 36 hours of heating at 800 °C. Plot a) is the raw diffuse reflectance data, and plot b) is the associated magnified Tauc plot for this region, where the intercept between the red extrapolated tangent line and the x-axis is used to estimate an optical band gap of 2.87 eV, which corresponds to 432 nm.*

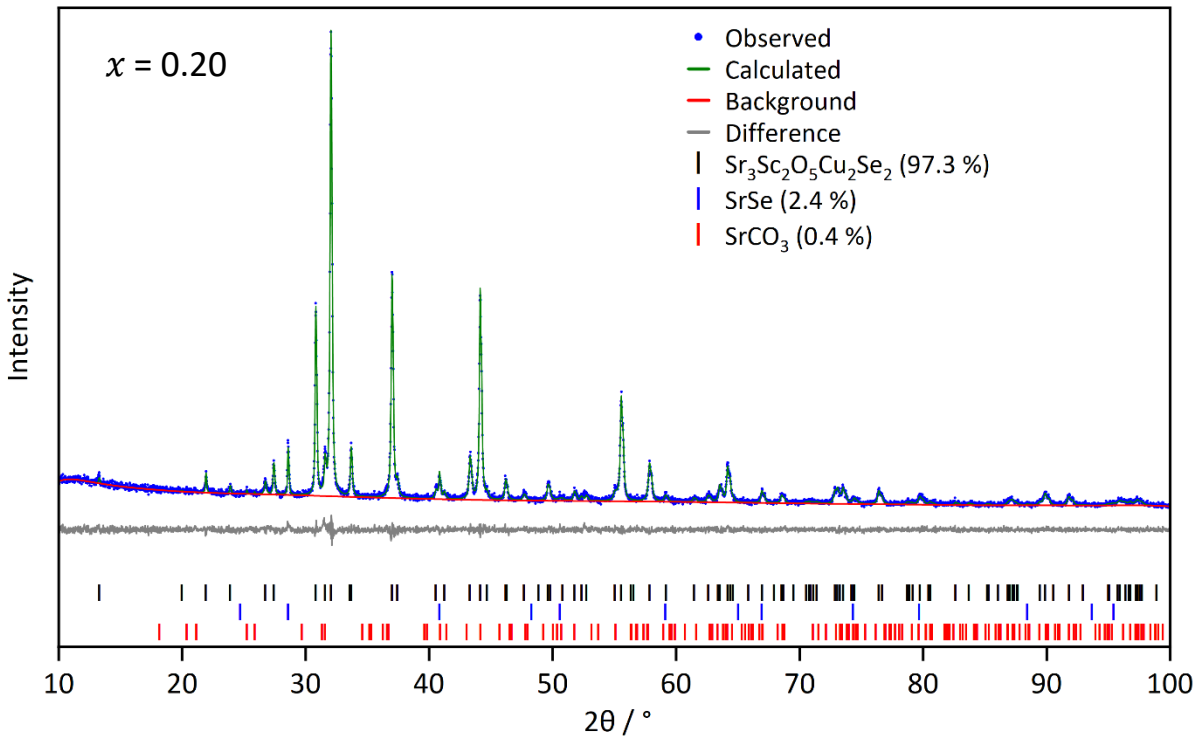

Figure 186 *Powder X-ray diffractogram of material with target composition $Sr_{2.80}Sc_2O_5Cu_2Se_2$ (space group I4/mmm) after 36 hours of heating at 800 °C. The small blue circles represent the observed diffracted intensity, the green line represents the Rietveld-refined calculated model, the red line represents the background, and the grey line represents the difference between observed and calculated intensities. The black tick marks show the reflections of the refined model of $Sr_3Sc_2O_5Cu_2Se_2$ (97.3 %), whilst the blue and red marks represent refined impurity phases SrSe (2.4 %) and $SrCO_3$ (0.4 %) respectively.*
Duration: 45 minutes. Data points: 4444. Interval: 0.02 °. GOF: 1.07. R_{wp}: 6.268 %.

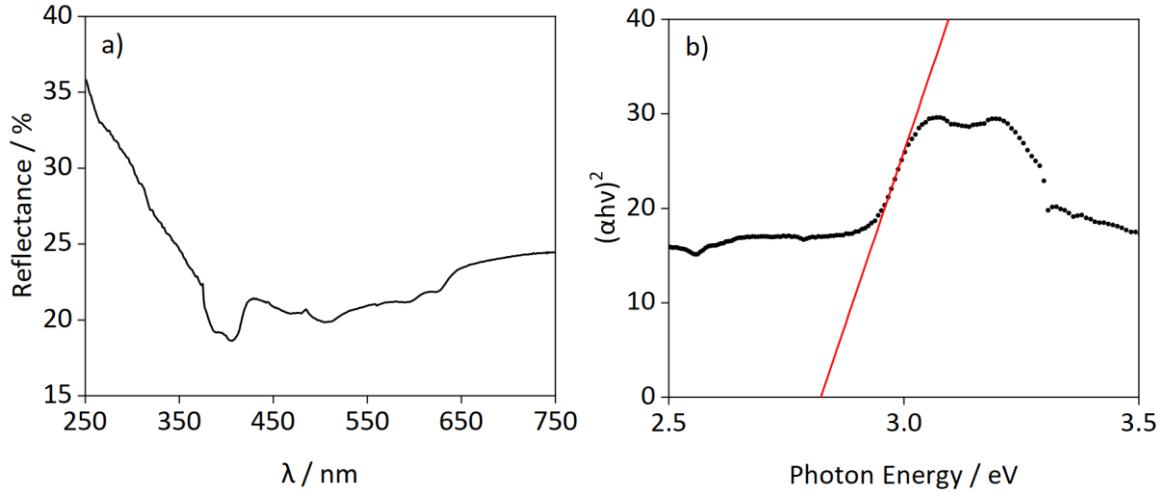

Figure 187 *UV-Vis spectrometry data for material with target composition $Sr_{2.80}Sc_2O_5Cu_2Se_2$ after 36 hours of heating at 800 °C. Plot a) is the raw diffuse reflectance data, and plot b) is the associated magnified Tauc plot for this region, where the intercept between the red extrapolated tangent line and the x-axis is used to estimate an optical band gap of 2.82 eV, which corresponds to 440 nm.*

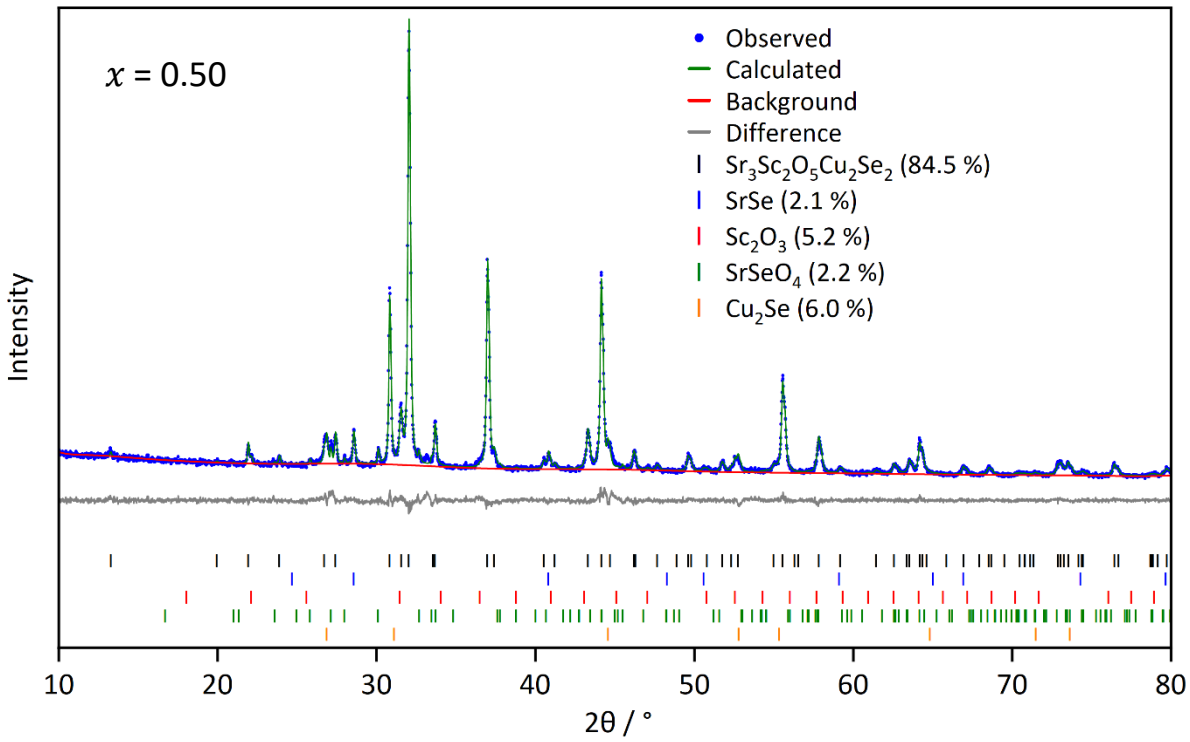

Figure 188 *Powder X-ray diffractogram of material with target composition $Sr_{2.50}Sc_2O_5Cu_2Se_2$ (space group I4/mmm) after 36 hours of heating at 800 °C. The small blue circles represent the observed diffracted intensity, the green line represents the Rietveld-refined calculated model, the red line represents the background, and the grey line represents the difference between observed and calculated intensities. The black tick marks show the reflections of the refined model of $Sr_3Sc_2O_5Cu_2Se_2$ (84.5 %), whilst the blue, red, green and orange tick marks represent refined impurity phases SrSe (2.1 %), Sc_2O_3 (5.2 %), $SrSeO_4$ (2.2 %) and Cu_2Se (6.0 %) respectively.*
Duration: 45 minutes. Data points: 3457. Interval: 0.02 °. GOF: 1.37. R_{wp}: 5.578 %.

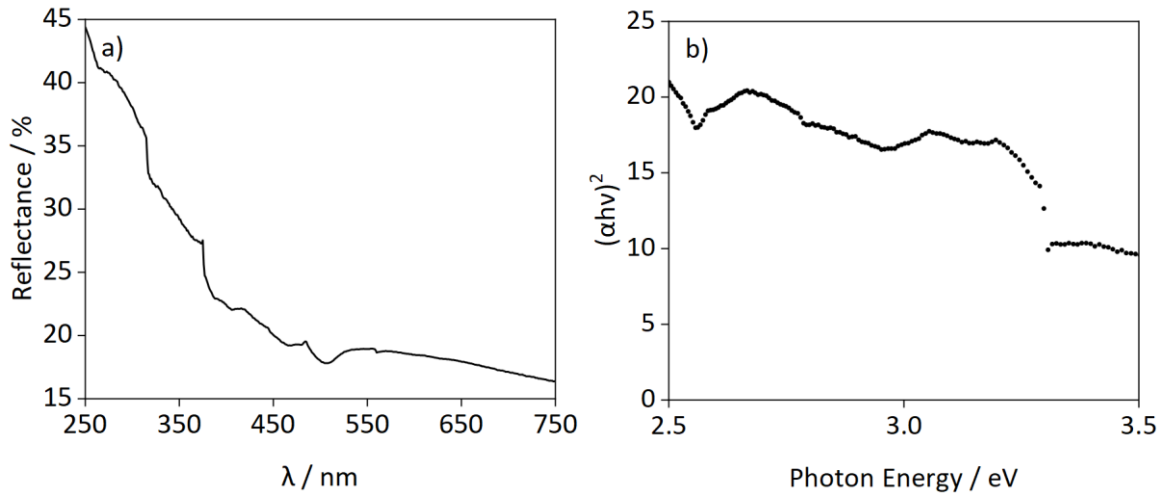

Figure 189 *UV-Vis spectrometry data for material with target composition $Sr_{2.50}Sc_2O_5Cu_2Se_2$ after 36 hours of heating at 800 °C. Plot a) is the raw diffuse reflectance data, and plot b) is the associated magnified Tauc plot for this region where this material would be expected to show a drop-off in reflectance indicating an optical band gap, but does not. The lack of such drop-off makes estimating an optical band gap with this method impossible. This anomalous data point is therefore excluded from analyses in Chapter 3.*

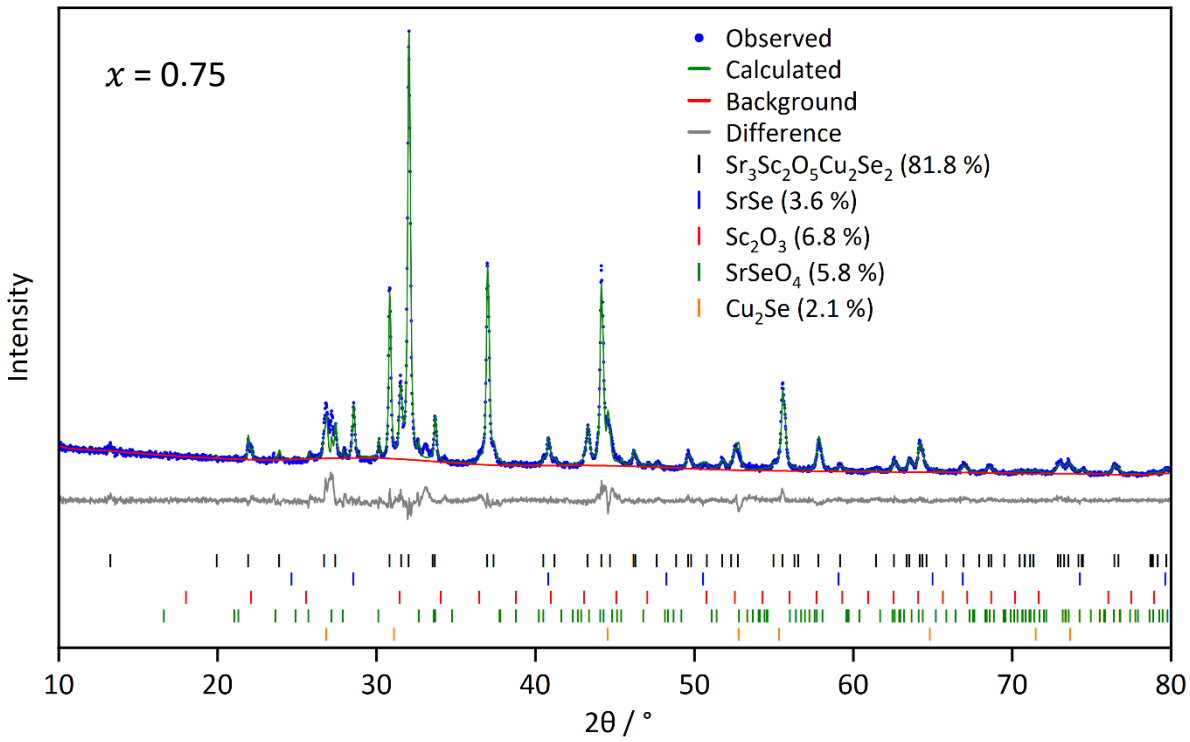

Figure 190 *Powder X-ray diffractogram of material with target composition $Sr_{2.25}Sc_2O_5Cu_2Se_2$ (space group I4/mmm) after 36 hours of heating at 800 °C. The small blue circles represent the observed diffracted intensity, the green line represents the Rietveld-refined calculated model, the red line represents the background, and the grey line represents the difference between observed and calculated intensities. The black tick marks show the reflections of the refined model of $Sr_3Sc_2O_5Cu_2Se_2$ (81.8 %), whilst the blue, red, green and orange tick marks represent refined impurity phases SrSe (3.6 %), Sc_2O_3 (6.8 %), $SrSeO_4$ (5.8 %) and Cu_2Se (2.1 %) respectively.*
Duration: 45 minutes. Data points: 3457. Interval: 0.02 °. GOF: 1.87. R_{wp}: 7.339 %.

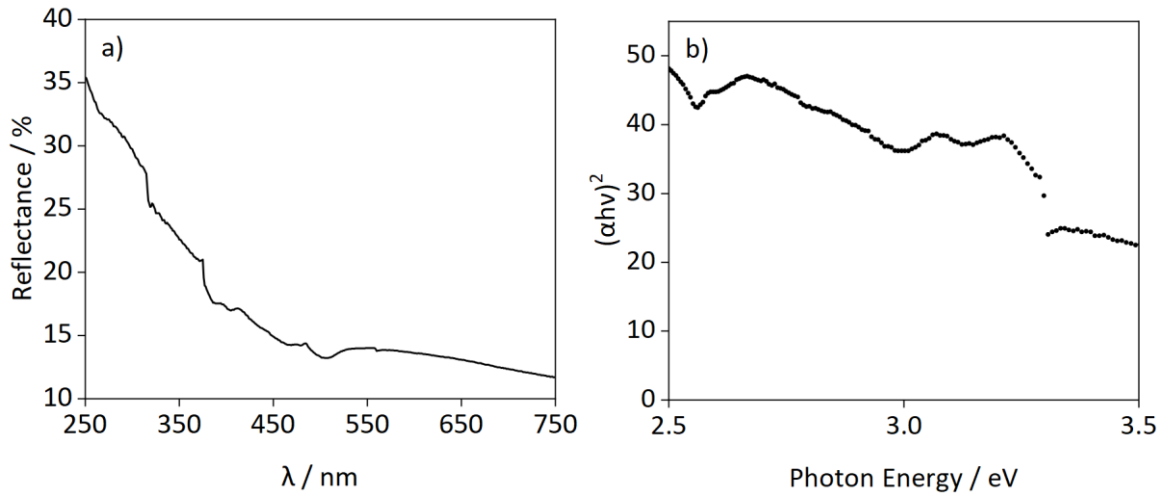

Figure 191 *UV-Vis spectrometry data for material with target composition $Sr_{2.25}Sc_2O_5Cu_2Se_2$ after 36 hours of heating at 800 °C. Plot a) is the raw diffuse reflectance data, and plot b) is the associated magnified Tauc plot for this region where this material would be expected to show a drop-off in reflectance indicating an optical band gap, but does not. The lack of such drop-off makes estimating an optical band gap with this method impossible. This anomalous data point is therefore excluded from analyses in Chapter 3.*

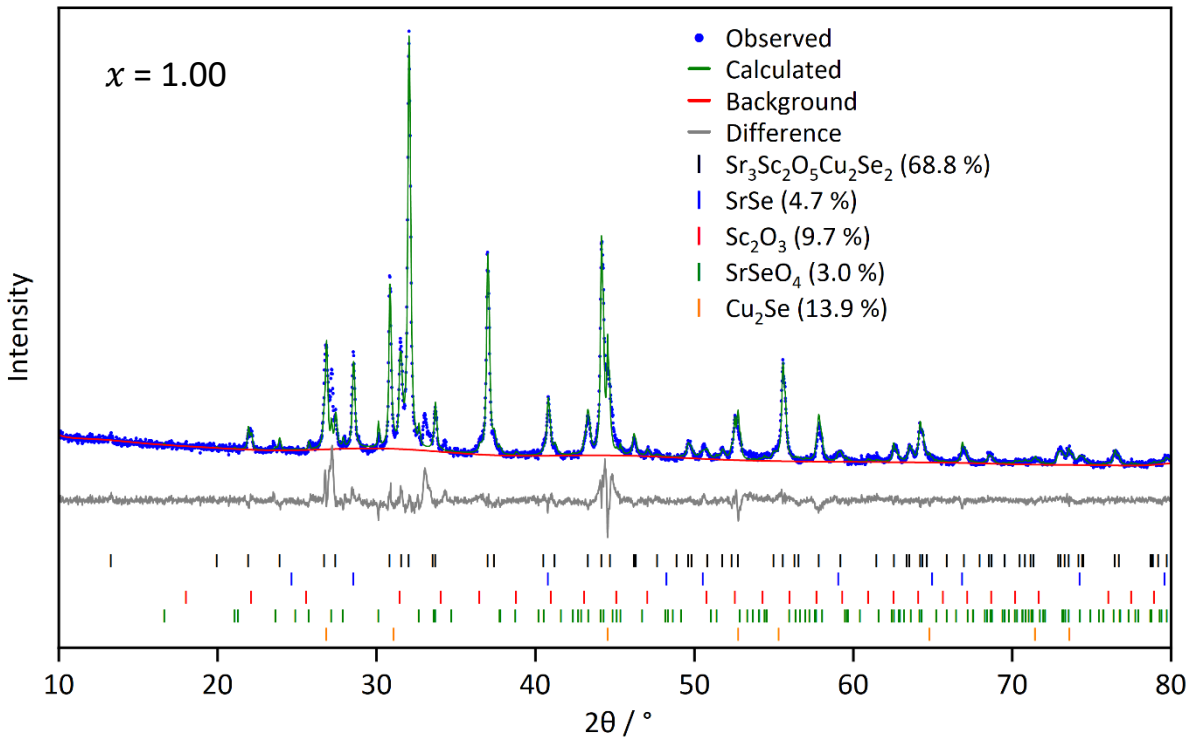

Figure 192 *Powder X-ray diffractogram of material with target composition $Sr_{2.00}Sc_2O_5Cu_2Se_2$ (space group I4/mmm) after 36 hours of heating at 800 °C. The small blue circles represent the observed diffracted intensity, the green line represents the Rietveld-refined calculated model, the red line represents the background, and the grey line represents the difference between observed and calculated intensities. The black tick marks show the reflections of the refined model of $Sr_3Sc_2O_5Cu_2Se_2$ (68.8 %), whilst the blue, red, green and orange tick marks represent refined impurity phases SrSe (4.7 %), Sc_2O_3 (9.7 %), $SrSeO_4$ (3.0 %) and Cu_2Se (13.9 %) respectively.*
Duration: 45 minutes. Data points: 3457. Interval: 0.02 °. GOF: 2.18. R_{wp}: 8.641 %.

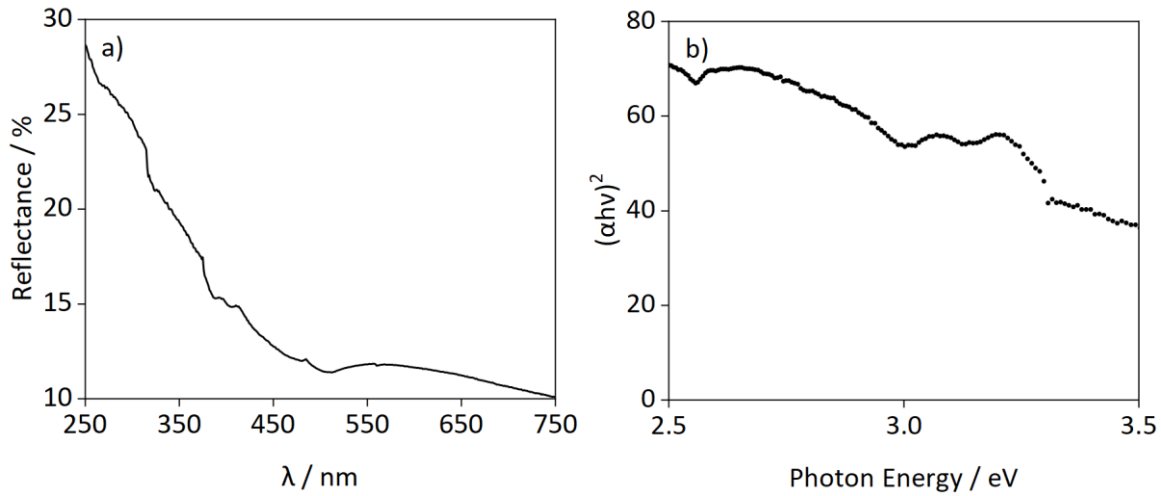

Figure 193 *UV-Vis spectrometry data for material with target composition $Sr_{2.00}Sc_2O_5Cu_2Se_2$ after 36 hours of heating at 800 °C. Plot a) is the raw diffuse reflectance data, and plot b) is the associated magnified Tauc plot for this region where this material would be expected to show a drop-off in reflectance indicating an optical band gap, but does not. The lack of such drop-off makes estimating an optical band gap with this method impossible. This anomalous data point is therefore excluded from analyses in Chapter 3.*

B.1.11 Copper deficient 325 selenide MALMs, $Sr_3Sc_2O_5Cu_{2-x}Se_2$

Table 51 Tabulated structural data of the copper deficient 325 selenide MALMs with general formula $Sr_3Sc_2O_5Cu_{2-x}Se_2$. The pristine material $Sr_3Sc_2O_5Cu_2Se_2$ is included as a reference. All values are derived from the Rietveld refinement of PXRD data using GSAS-II. Note that because all materials listed are tetragonal (space group I4/mmm), the b parameter is identical to a, and thus omitted.

x / mol	Target Composition	a / Å	c / Å	Volume / Å^3
0 (pristine)	$Sr_3Sc_2O_5Cu_2Se_2$	4.10329(4)	26.6847(3)	449.290(12)
0.05	$Sr_3Sc_2O_5Cu_{1.95}Se_2$	4.10377(4)	26.6898(4)	449.482(8)
0.10	$Sr_3Sc_2O_5Cu_{1.90}Se_2$	4.10376(8)	26.6871(7)	449.433(25)
0.15	$Sr_3Sc_2O_5Cu_{1.85}Se_2$	4.10410(8)	26.6829(7)	449.436(25)
0.20	$Sr_3Sc_2O_5Cu_{1.80}Se_2$	4.10373(8)	26.6851(7)	449.393(26)
0.50	$Sr_3Sc_2O_5Cu_{1.50}Se_2$	4.10406(8)	26.6940(7)	449.615(23)
0.75	$Sr_3Sc_2O_5Cu_{1.25}Se_2$	4.10372(7)	26.6920(6)	449.508(17)
1.00	$Sr_3Sc_2O_5Cu_{1.00}Se_2$	4.10317(14)	26.6886(12)	449.330(40)

Table 52 Tabulated compositional data of the copper deficient 325 selenide MALMs with general formula $Sr_3Sc_2O_5Cu_{2-x}Se_2$. The pristine material $Sr_3Sc_2O_5Cu_2Se_2$ is included as a reference. All values are cited as a weight percent (wt %) of the total weight, and are derived from the Rietveld refinement of PXRD data using GSAS-II.

x / mol	Target phase / wt %	SrSe / wt %	$SrCO_3$ / wt %	Sc_2O_3 / wt %	$SrSeO_4$ / wt %
0 (pristine)	99.1	0.5	0.4	-	-
0.05	97.2	2.2	0.6	-	-
0.10	97.4	1.9	0.6	-	-
0.15	96.5	2.7	0.8	-	-
0.20	94.6	4.9	0.5	-	-
0.50	80.3	13.7	0.2	4.1	1.7
0.75	74.0	17.7	0.2	5.7	2.5
1.00	68.7	22.0	0.6	6.1	-

Table 53 Tabulated analytical data of to the measured properties of the copper deficient 325 selenide MALMs with general formula $Sr_3Sc_2O_5Cu_{2-x}Se_2$. The pristine material $Sr_3Sc_2O_5Cu_2Se_2$ is included as a reference. Optical band gaps were estimated from UV-Vis data. Pellet densities were estimated from the mass and volume of annealed pellet samples, and are cited as a relative percentage of the bulk crystal. Resistivities and conductivities were estimated from 4 probe van der Pauw analysis of the pellet samples.

x / mol	Band Gap / eV	Pellet Density / %	Raw Resistivities from 4-Probe measurement, for each probe permutation / kΩ								Resistivity / Ω cm	Conductivity / S cm^{-1}
			1	2	3	4	5	6	7	8		
0 (pristine)	2.94	71.72	1.20 E+01	1.21 E+01	1.22 E+01	1.22 E+01	1.03 E+01	1.02 E+01	1.02 E+01	1.01 E+01	3.83 E+03	2.61 E-04
0.05	2.88	71.62	1.93 E-01	1.95 E-01	1.97 E-01	1.96 E-01	5.50 E-02	5.50 E-02	5.50 E-02	5.40 E-02	3.89 E+01	2.57 E-02
0.10	2.90	68.95	5.83 E-01	5.90 E-01	5.95 E-01	5.97 E-01	3.81 E-01	3.83 E-01	3.84 E-01	3.85 E-01	1.74 E+02	5.75 E-03
0.15	2.86	68.30	2.22 E-01	2.23 E-01	2.23 E-01	2.23 E-01	2.56 E-01	2.56 E-01	2.56 E-01	2.57 E-01	8.89 E+01	1.13 E-02
0.20	2.86	67.84	1.05 E-01	1.06 E-01	1.06 E-01	1.06 E-01	5.31 E-02	5.30 E-02	5.30 E-02	5.30 E-02	2.90 E+01	3.44 E-02
0.50	2.84	73.21	1.75 E-01	1.77 E-01	1.76 E-01	1.79 E-01	1.69 E-01	1.61 E-01	1.59 E-01	1.61 E-01	6.19 E+01	1.62 E-02
0.75	2.85	63.54	7.80 E-01	7.87 E-01	7.85 E-01	7.93 E-01	6.46 E+00	6.49 E+00	6.51 E+00	6.53 E+00	1.06 E+03	9.40 E-04
1.00	2.83	71.90	1.20 E+01	1.13 E+01	1.11 E+01	1.12 E+01	1.52 E+01	1.54 E+01	1.55 E+01	1.56 E+01	5.13 E+03	1.95 E-04

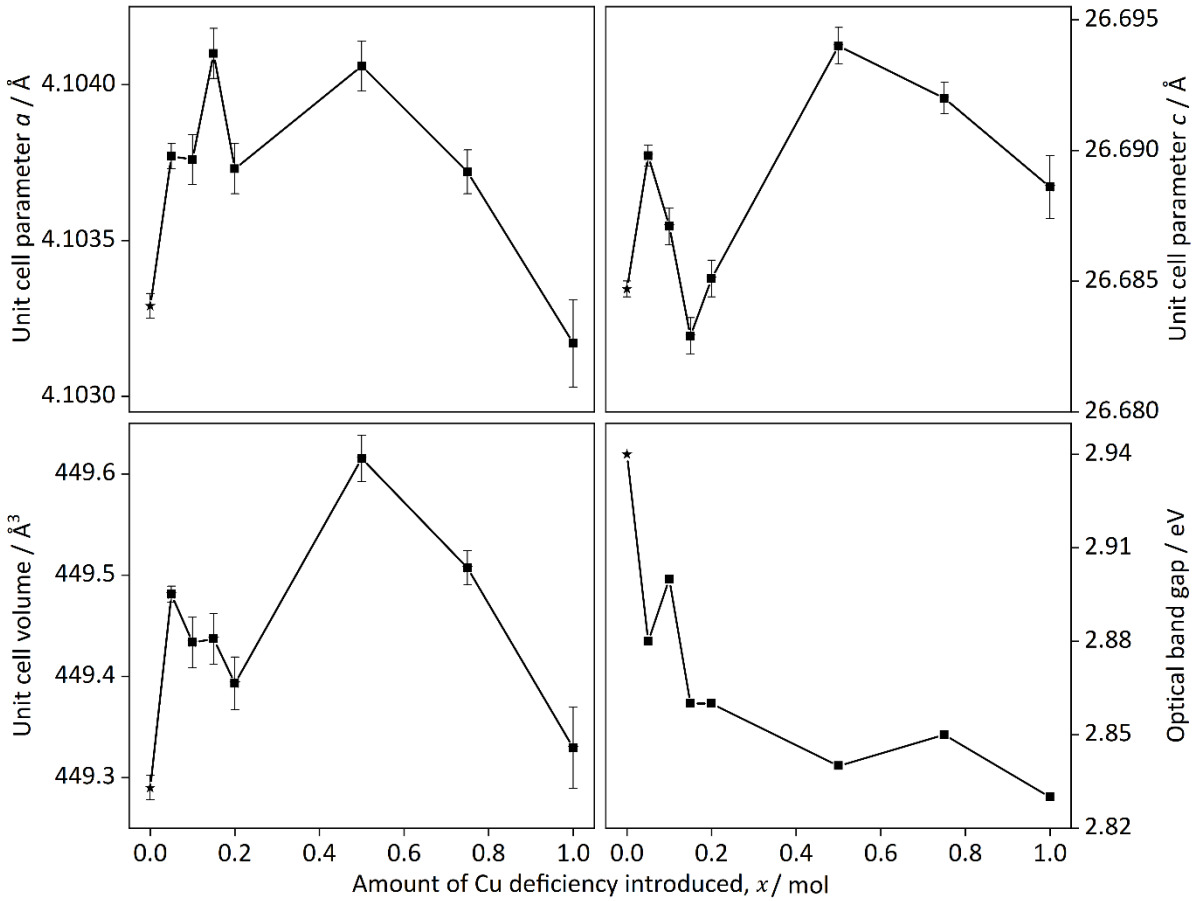

Figure 194 *Comparisons of a) the a unit cell parameter, b) the c unit cell parameter, c) unit cell volume, and d) the optical band gap, of the copper deficient 325 selenide MALMs with general formula $Sr_3Sc_2O_5Cu_{2-x}Se_2$. The pristine material $Sr_3Sc_2O_5Cu_2Se_2$ is included as a reference at $x = 0$ mol and is represented by a star.*

Figure 195 *A photographic comparison of the colour of the copper deficient 325 selenide MALMs with general formula $Sr_3Sc_2O_5Cu_{2-x}Se_2$. Deficiency increases from left to right.*

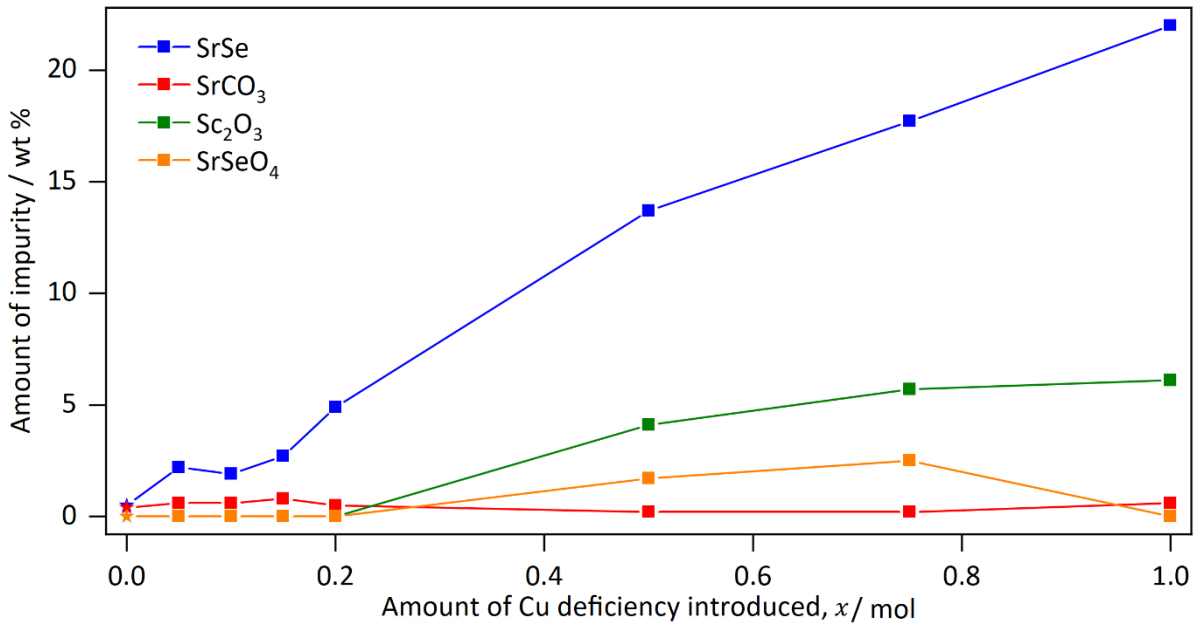

Figure 196 *The weight percentages of five impurity phases present in the copper deficient 325 selenide MALMs with general formula $Sr_3Sc_2O_5Cu_{2-x}Se_2$. The pristine material $Sr_3Sc_2O_5Cu_2Se_2$ is included as a reference at $x = 0$ mol and is represented by a star.*

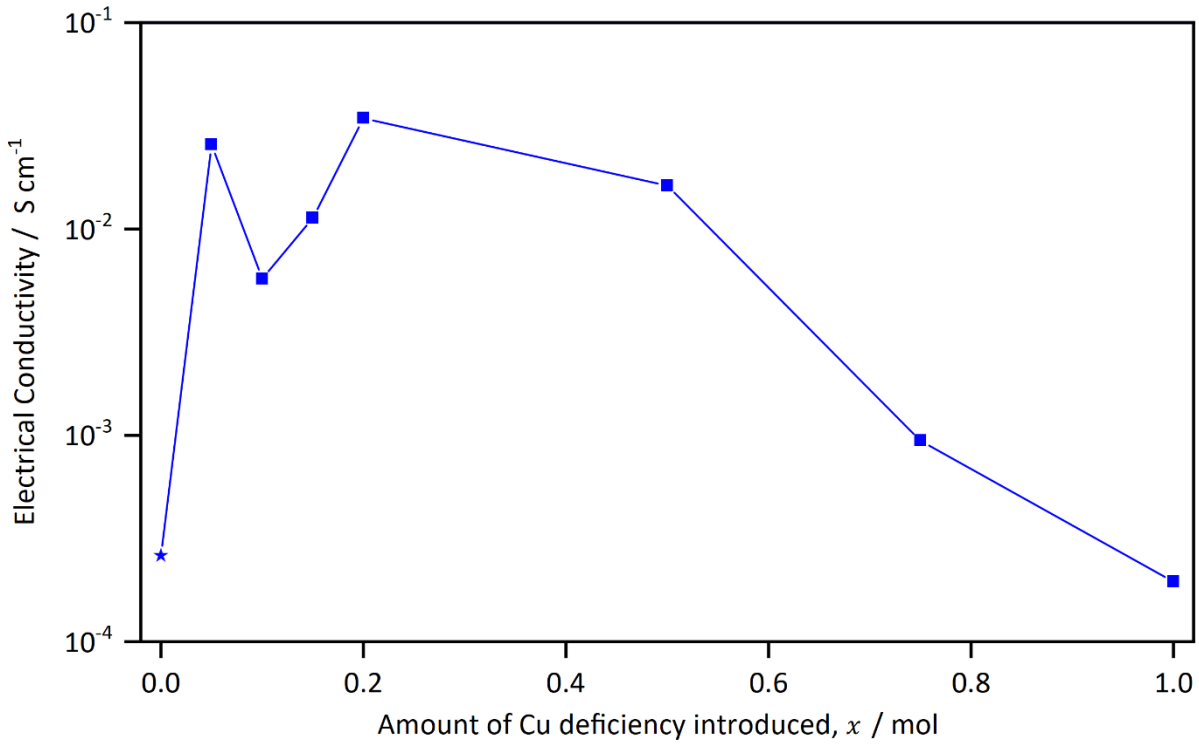

Figure 197 *The electrical conductivities of the copper deficient 325 selenide MALMs with general formula $Sr_3Sc_2O_5Cu_{2-x}Se_2$, represented on a $\log_{10}$ scale. The pristine material $Sr_3Sc_2O_5Cu_2Se_2$ is included as a reference at $x = 0$ mol and is represented by a star. All values are derived from van der Pauw 4 probe resistivity measurements of 8mm diameter annealed pellet samples.*

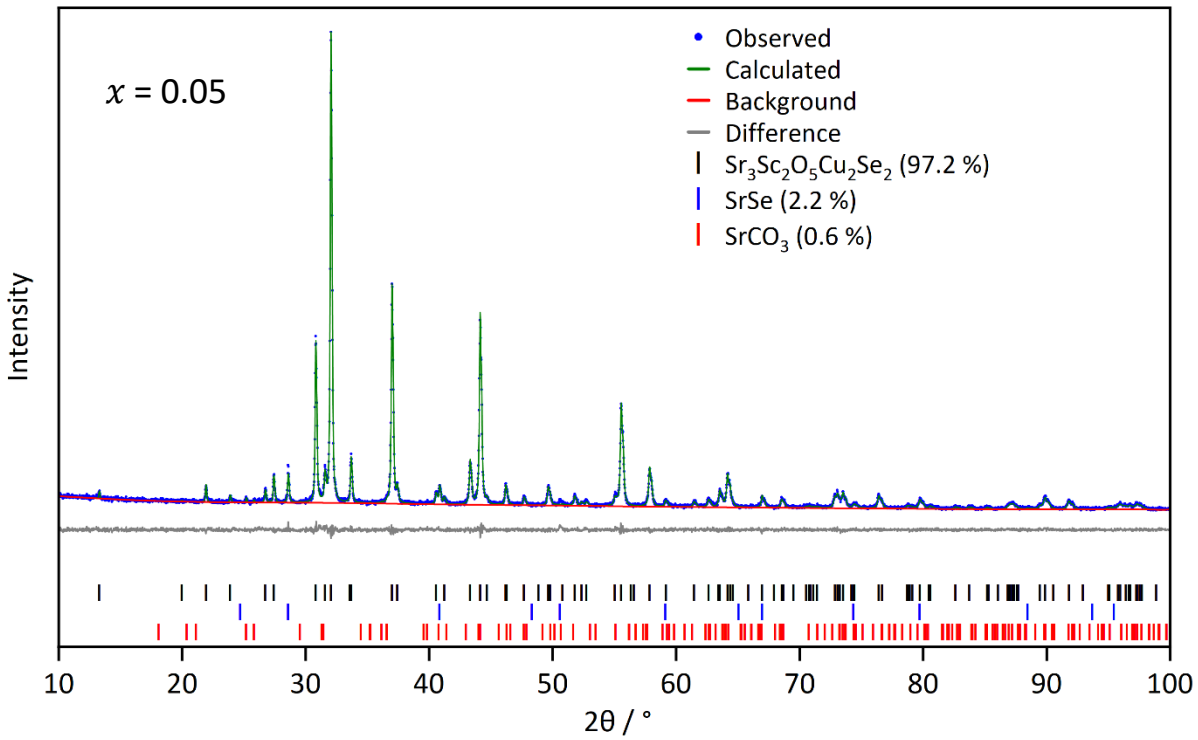

Figure 198 *Powder X-ray diffractogram of material with target composition $Sr_3Sc_2O_5Cu_{1.95}Se_2$ (space group I4/mmm) after 36 hours of heating at 800 °C. The small blue circles represent the observed diffracted intensity, the green line represents the Rietveld-refined calculated model, the red line represents the background, and the grey line represents the difference between observed and calculated intensities. The black tick marks show the reflections of the refined model of $Sr_3Sc_2O_5Cu_2Se_2$ (97.2 %), whilst the blue and red marks represent refined impurity phases SrSe (2.2 %) and $SrCO_3$ (0.6 %) respectively.*
Duration: 45 minutes. Data points: 4444. Interval: 0.02 °. GOF: 1.07. R_{wp}: 4.998 %.

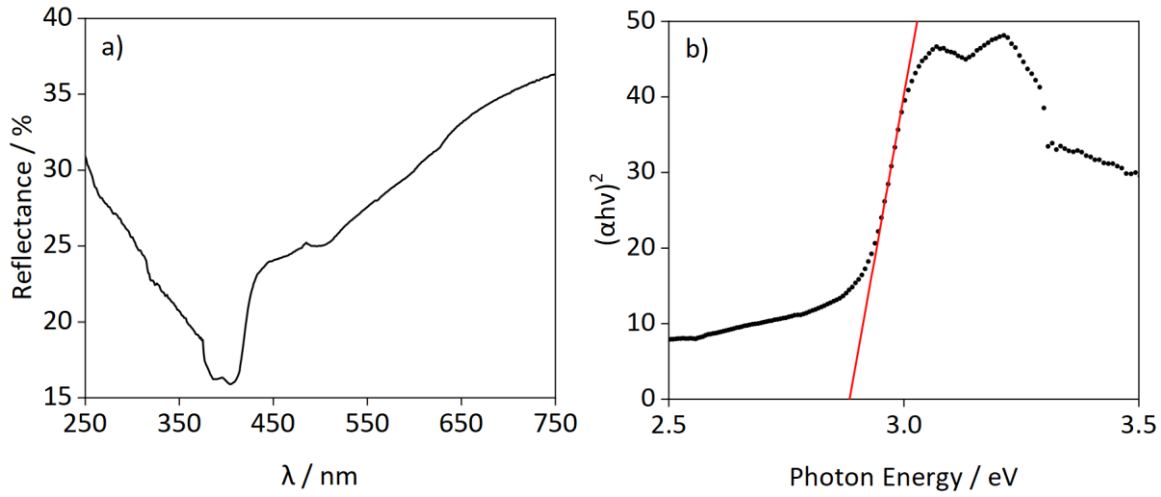

Figure 199 *UV-Vis spectrometry data for material with target composition $Sr_3Sc_2O_5Cu_{1.95}Se_2$ after 36 hours of heating at 800 °C. Plot a) is the raw diffuse reflectance data, and plot b) is the associated magnified Tauc plot for this region, where the intercept between the red extrapolated tangent line and the x-axis is used to estimate an optical band gap of 2.88 eV, which corresponds to 430 nm.*

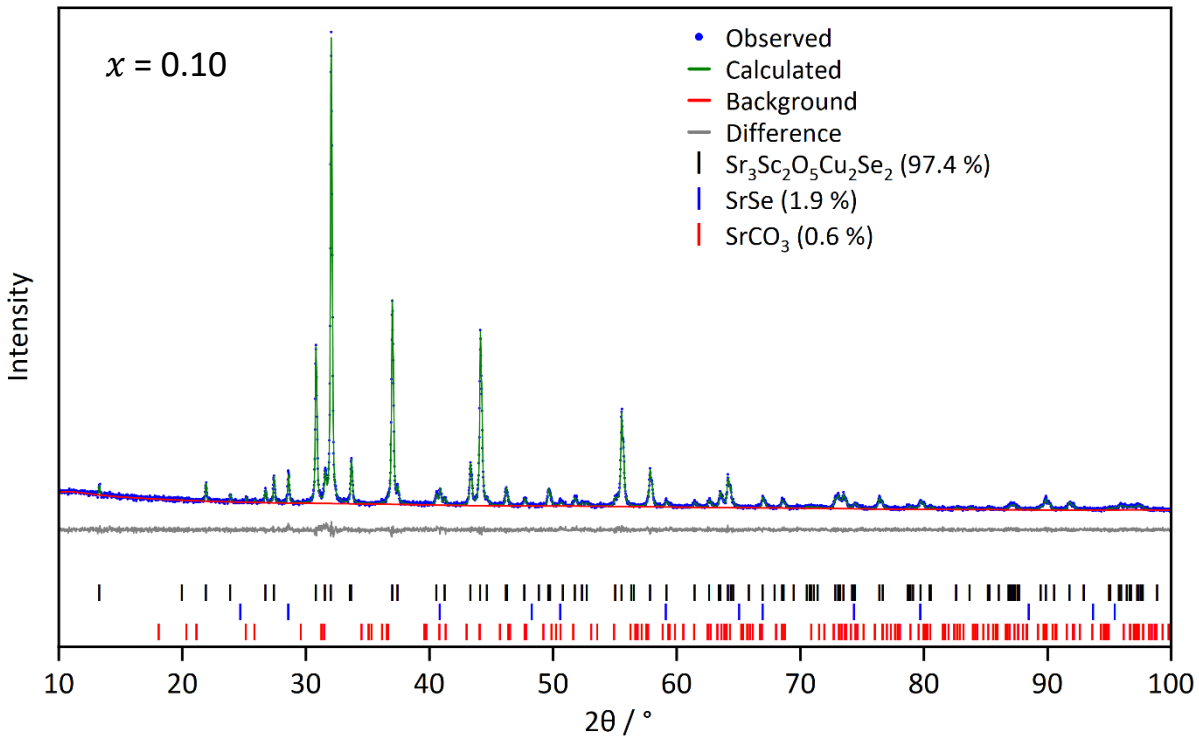

Figure 200 *Powder X-ray diffractogram of material with target composition $Sr_3Sc_2O_5Cu_{1.90}Se_2$ (space group I4/mmm) after 36 hours of heating at 800 °C. The small blue circles represent the observed diffracted intensity, the green line represents the Rietveld-refined calculated model, the red line represents the background, and the grey line represents the difference between observed and calculated intensities. The black tick marks show the reflections of the refined model of $Sr_3Sc_2O_5Cu_2Se_2$ (97.4 %), whilst the blue and red marks represent refined impurity phases SrSe (1.9 %) and $SrCO_3$ (0.6 %) respectively.*
Duration: 45 minutes. Data points: 4444. Interval: 0.02 °. GOF: 1.07. R_{wp}: 5.802 %.

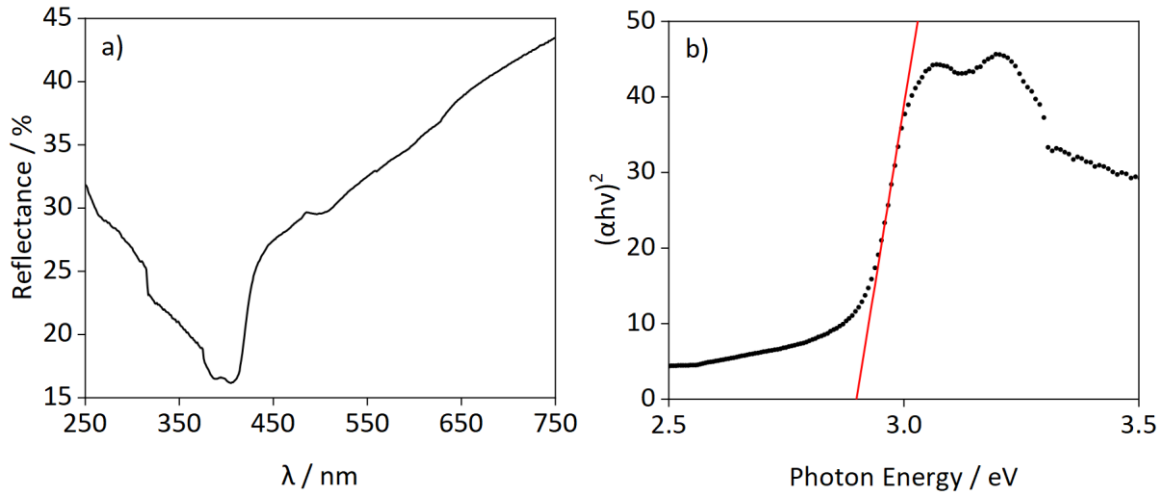

Figure 201 *UV-Vis spectrometry data for material with target composition $Sr_3Sc_2O_5Cu_{1.90}Se_2$ after 36 hours of heating at 800 °C. Plot a) is the raw diffuse reflectance data, and plot b) is the associated magnified Tauc plot for this region, where the intercept between the red extrapolated tangent line and the x-axis is used to estimate an optical band gap of 2.90 eV, which corresponds to 428 nm.*

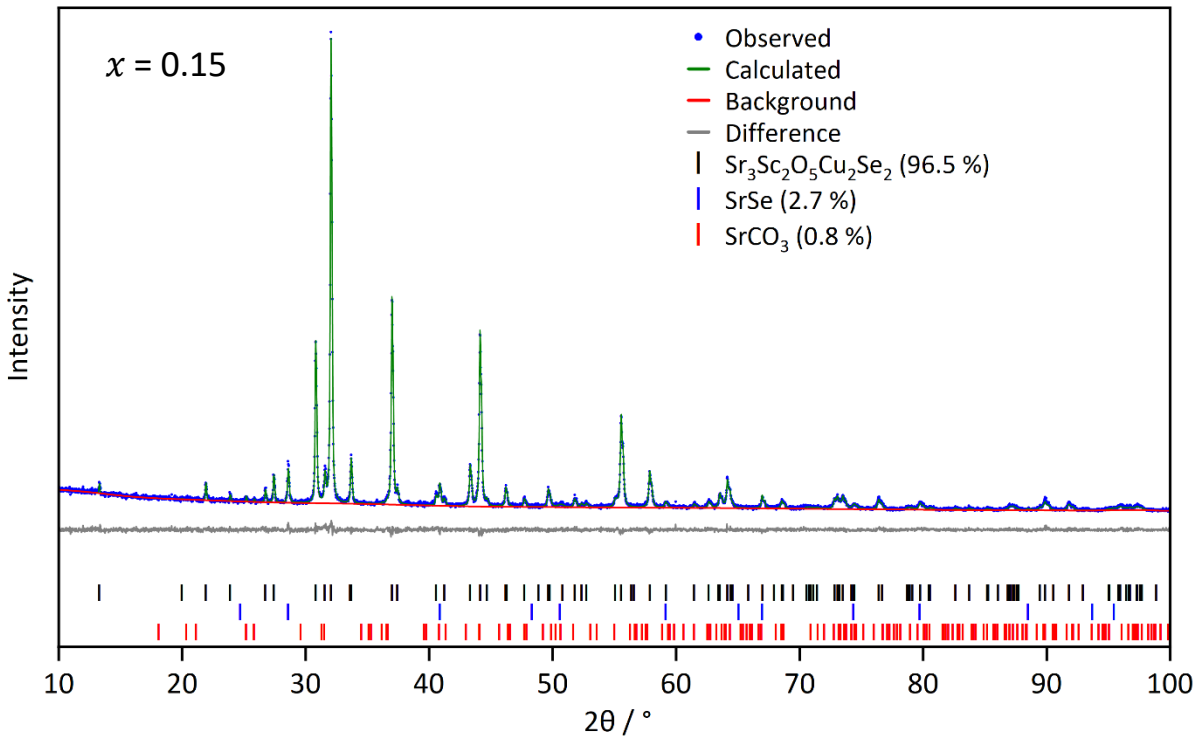

Figure 202 *Powder X-ray diffractogram of material with target composition $Sr_3Sc_2O_5Cu_{1.85}Se_2$ (space group I4/mmm) after 36 hours of heating at 800 °C. The small blue circles represent the observed diffracted intensity, the green line represents the Rietveld-refined calculated model, the red line represents the background, and the grey line represents the difference between observed and calculated intensities. The black tick marks show the reflections of the refined model of $Sr_3Sc_2O_5Cu_2Se_2$ (96.5 %), whilst the blue and red marks represent refined impurity phases SrSe (2.7 %) and $SrCO_3$ (0.8 %) respectively.*
Duration: 45 minutes. Data points: 4444. Interval: 0.02 °. GOF: 1.09. R_{wp}: 5.813 %.

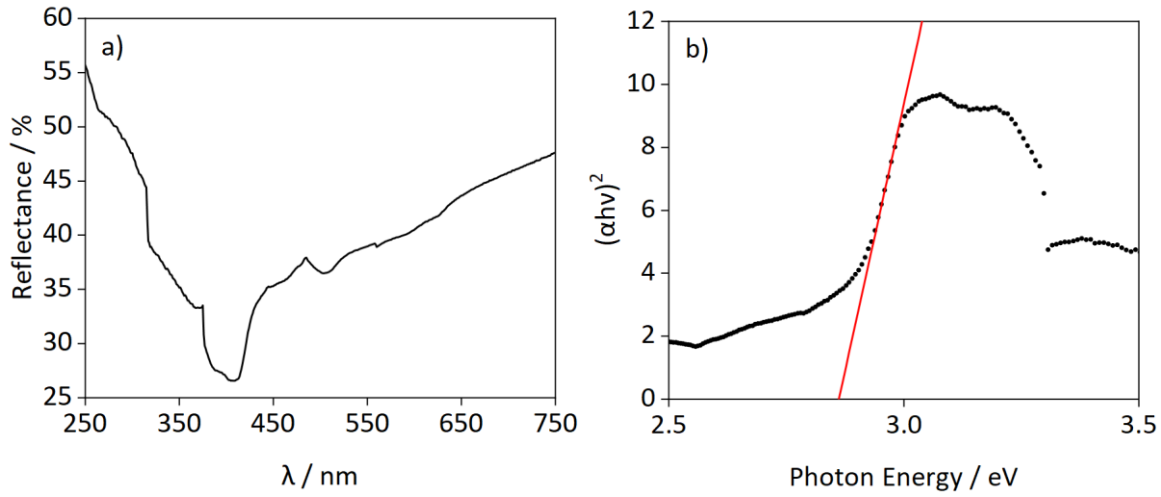

Figure 203 *UV-Vis spectrometry data for material with target composition $Sr_3Sc_2O_5Cu_{1.85}Se_2$ after 36 hours of heating at 800 °C. Plot a) is the raw diffuse reflectance data, and plot b) is the associated magnified Tauc plot for this region, where the intercept between the red extrapolated tangent line and the x-axis is used to estimate an optical band gap of 2.86 eV, which corresponds to 433 nm.*

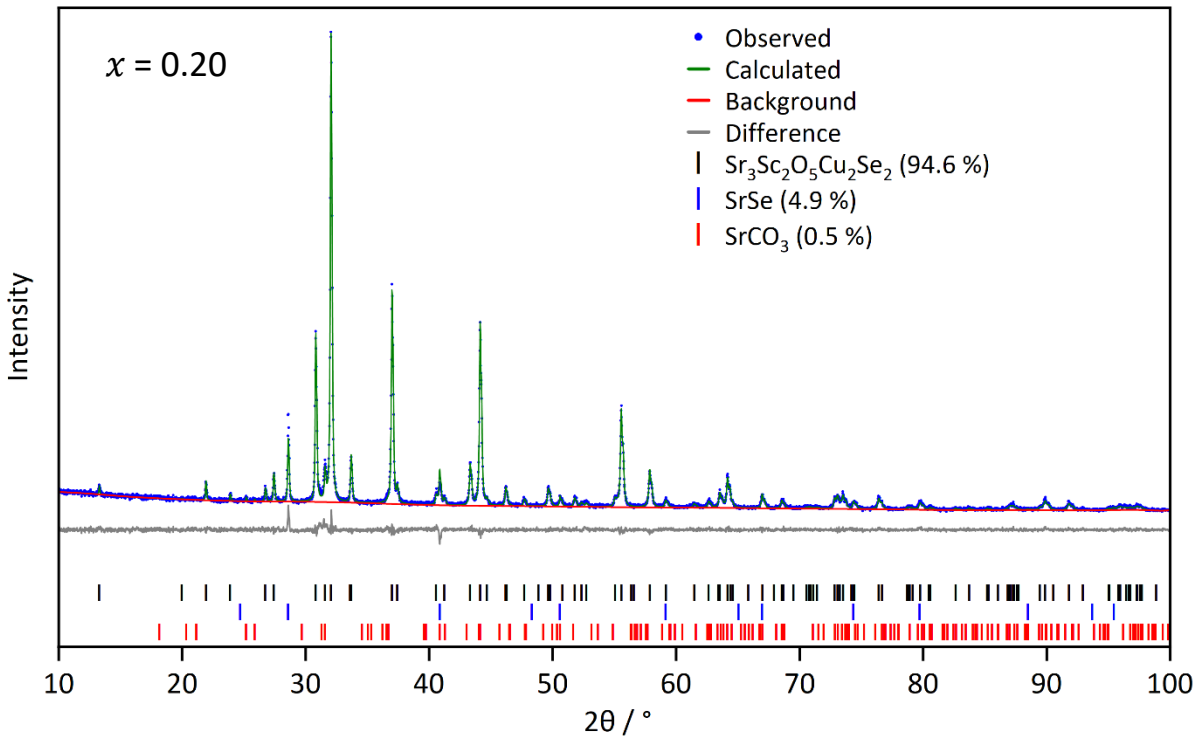

Figure 204 *Powder X-ray diffractogram of material with target composition $Sr_3Sc_2O_5Cu_{1.80}Se_2$ (space group I4/mmm) after 36 hours of heating at 800 °C. The small blue circles represent the observed diffracted intensity, the green line represents the Rietveld-refined calculated model, the red line represents the background, and the grey line represents the difference between observed and calculated intensities. The black tick marks show the reflections of the refined model of $Sr_3Sc_2O_5Cu_2Se_2$ (94.6 %), whilst the blue and red marks represent refined impurity phases SrSe (4.9 %) and $SrCO_3$ (0.5 %) respectively.*
Duration: 45 minutes. Data points: 4444. Interval: 0.02 °. GOF: 1.23. R_{wp}: 6.221 %.

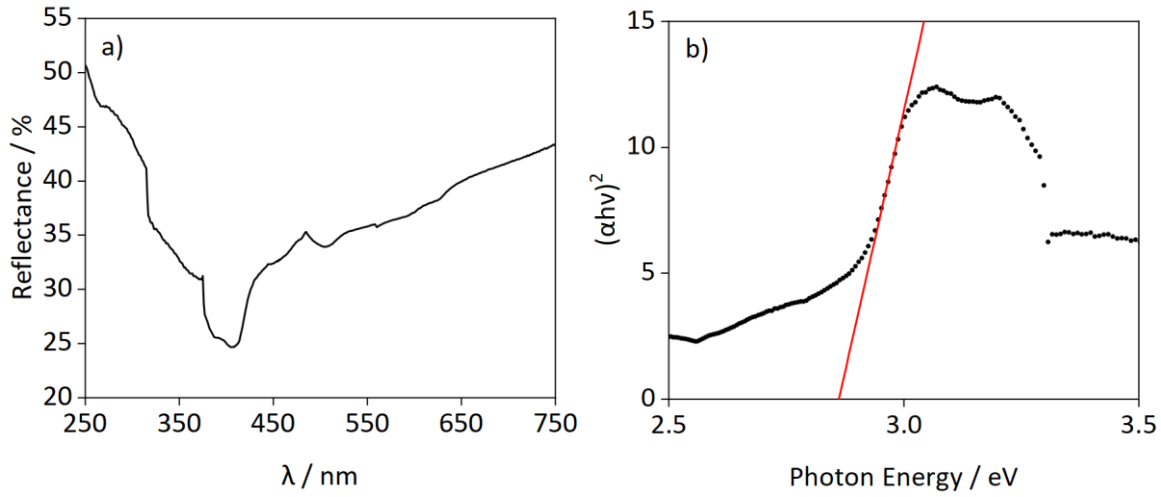

Figure 205 *UV-Vis spectrometry data for material with target composition $Sr_3Sc_2O_5Cu_{1.80}Se_2$ after 36 hours of heating at 800 °C. Plot a) is the raw diffuse reflectance data, and plot b) is the associated magnified Tauc plot for this region, where the intercept between the red extrapolated tangent line and the x-axis is used to estimate an optical band gap of 2.86 eV, which corresponds to 433 nm.*

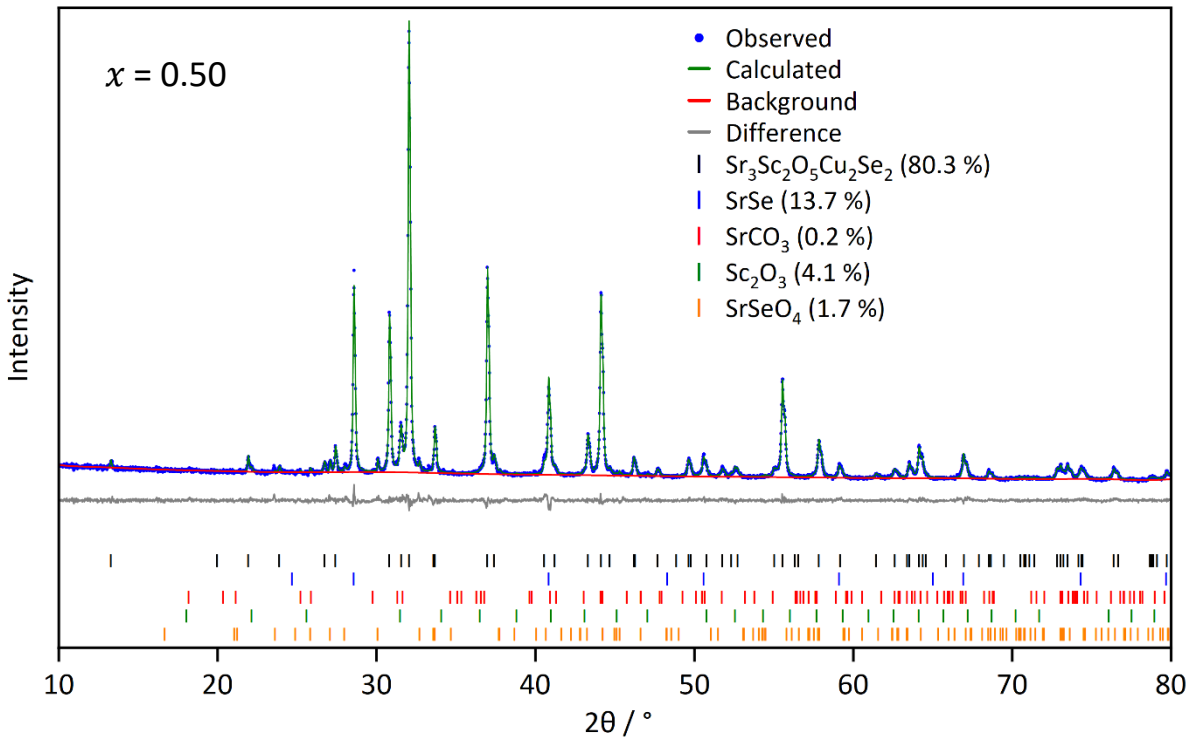

Figure 206 *Powder X-ray diffractogram of material with target composition $Sr_3Sc_2O_5Cu_{1.50}Se_2$ (space group I4/mmm) after 36 hours of heating at 800 °C. The small blue circles represent the observed diffracted intensity, the green line represents the Rietveld-refined calculated model, the red line represents the background, and the grey line represents the difference between observed and calculated intensities. The black tick marks show the reflections of the refined model of $Sr_3Sc_2O_5Cu_2Se_2$ (80.3 %), whilst the blue, red, green and orange tick marks represent refined impurity phases SrSe (13.7 %), $SrCO_3$ (0.2 %), Sc_2O_3 (4.1 %) and $SrSeO_4$ (1.7 %) respectively.*
Duration: 45 minutes. Data points: 3457. Interval: 0.02 °. GOF: 1.28. R_{wp}: 5.025 %.

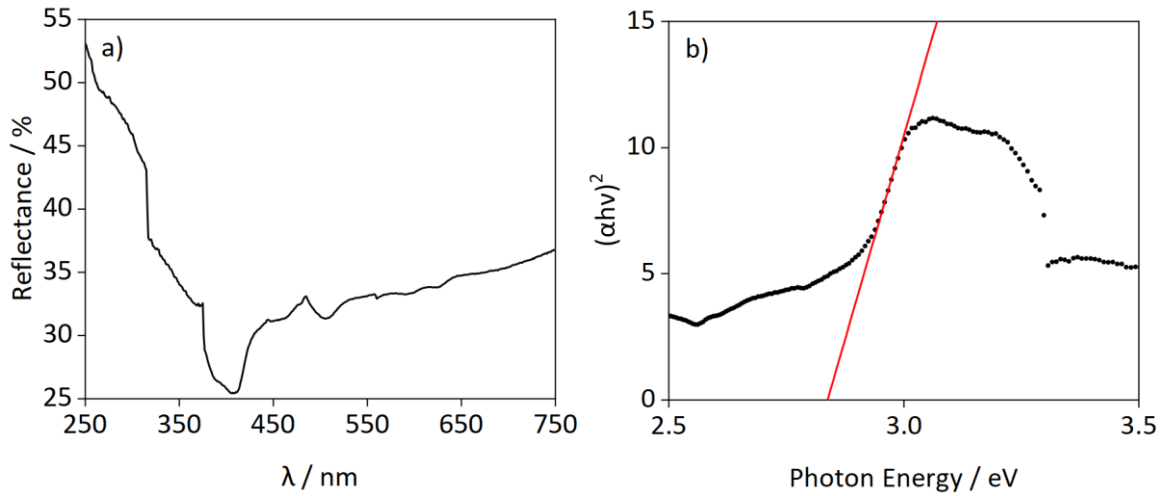

Figure 207 *UV-Vis spectrometry data for material with target composition $Sr_3Sc_2O_5Cu_{1.50}Se_2$ after 36 hours of heating at 800 °C. Plot a) is the raw diffuse reflectance data, and plot b) is the associated magnified Tauc plot for this region, where the intercept between the red extrapolated tangent line and the x-axis is used to estimate an optical band gap of 2.84 eV, which corresponds to 437 nm.*

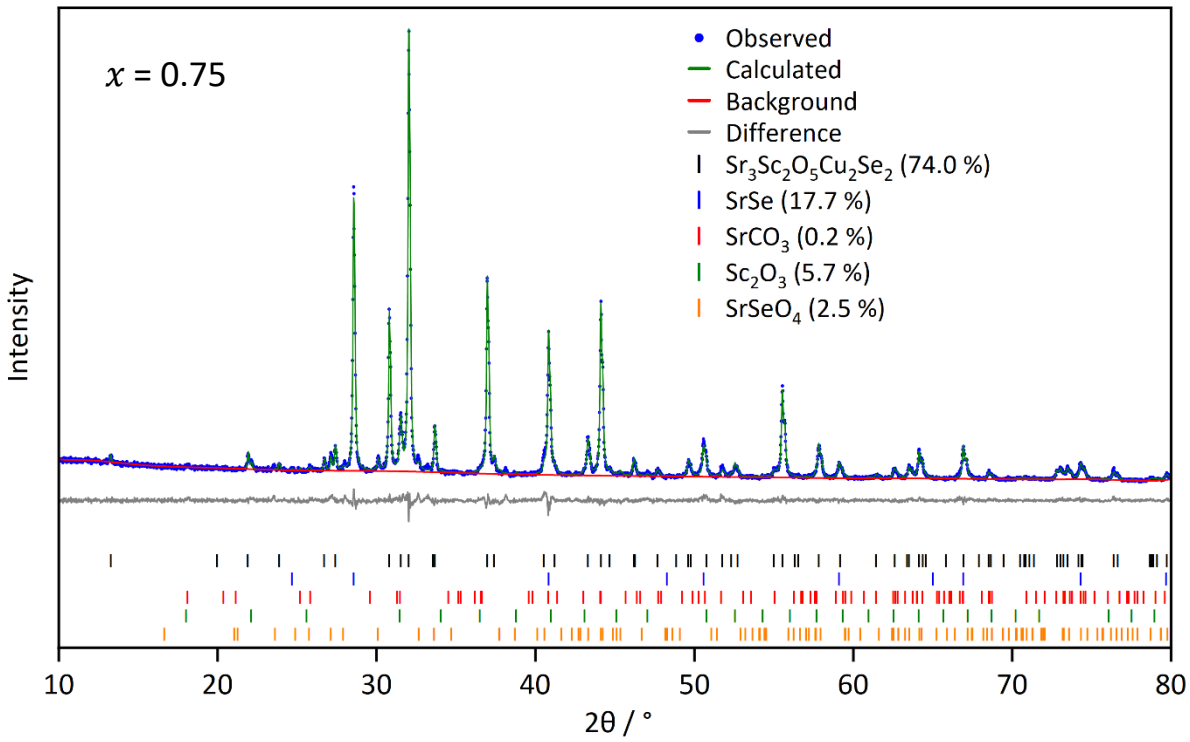

Figure 208 *Powder X-ray diffractogram of material with target composition $Sr_3Sc_2O_5Cu_{1.25}Se_2$ (space group I4/mmm) after 36 hours of heating at 800 °C. The small blue circles represent the observed diffracted intensity, the green line represents the Rietveld-refined calculated model, the red line represents the background, and the grey line represents the difference between observed and calculated intensities. The black tick marks show the reflections of the refined model of $Sr_3Sc_2O_5Cu_2Se_2$ (74.0 %), whilst the blue, red, green and orange tick marks represent refined impurity phases SrSe (17.7 %), $SrCO_3$ (0.2 %), Sc_2O_3 (5.7 %) and $SrSeO_4$ (2.5 %) respectively.*
Duration: 45 minutes. Data points: 3457. Interval: 0.02 °. GOF: 1.36. R_{wp}: 5.717 %.

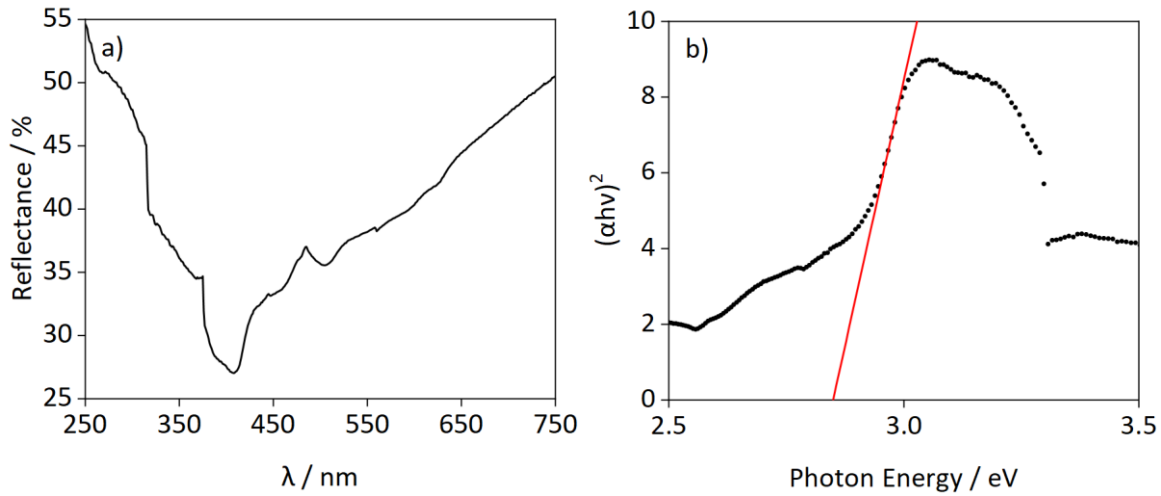

Figure 209 *UV-Vis spectrometry data for material with target composition $Sr_3Sc_2O_5Cu_{1.25}Se_2$ after 36 hours of heating at 800 °C. Plot a) is the raw diffuse reflectance data, and plot b) is the associated magnified Tauc plot for this region, where the intercept between the red extrapolated tangent line and the x-axis is used to estimate an optical band gap of 2.85 eV, which corresponds to 435 nm.*

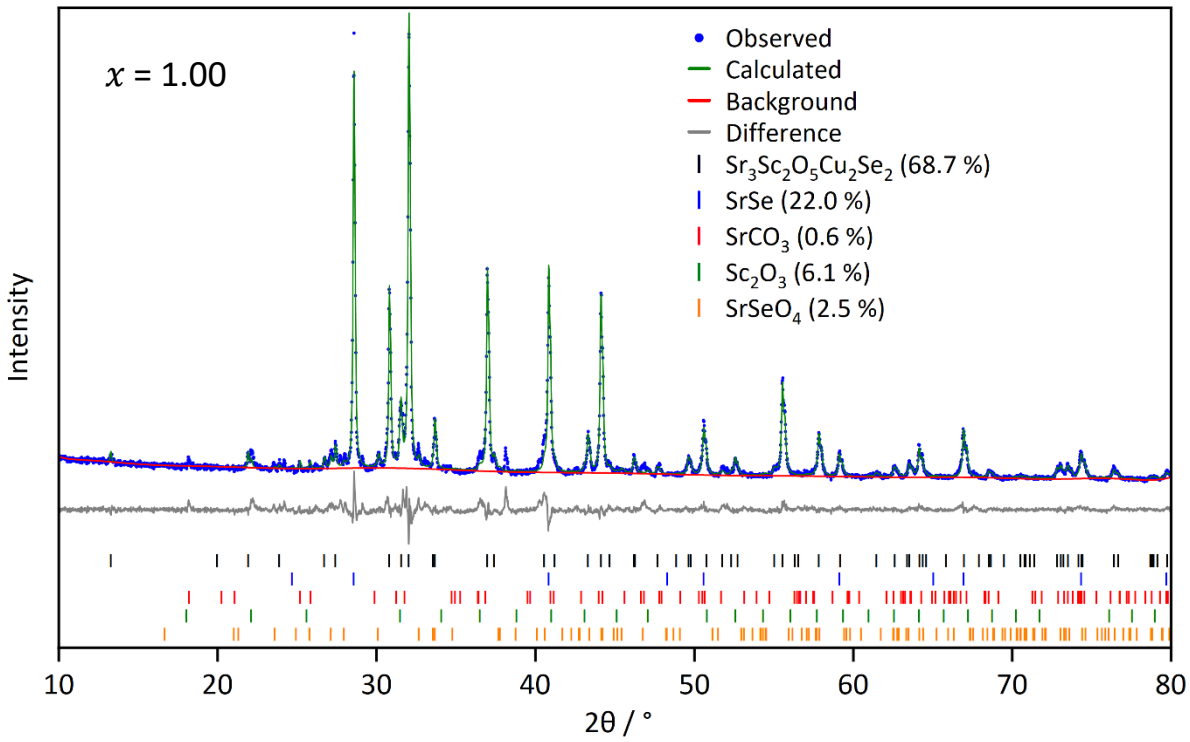

Figure 210 *Powder X-ray diffractogram of material with target composition $Sr_3Sc_2O_5Cu_{1.00}Se_2$ (space group I4/mmm) after 36 hours of heating at 800 °C. The small blue circles represent the observed diffracted intensity, the green line represents the Rietveld-refined calculated model, the red line represents the background, and the grey line represents the difference between observed and calculated intensities. The black tick marks show the reflections of the refined model of $Sr_3Sc_2O_5Cu_2Se_2$ (68.7 %), whilst the blue, red, green and orange tick marks represent refined impurity phases SrSe (22.0 %), $SrCO_3$ (0.6 %), Sc_2O_3 (6.1 %) and $SrSeO_4$ (2.5 %) respectively.*
Duration: 45 minutes. Data points: 3457. Interval: 0.02 °. GOF: 1.92. R_{wp}: 8.116 %.

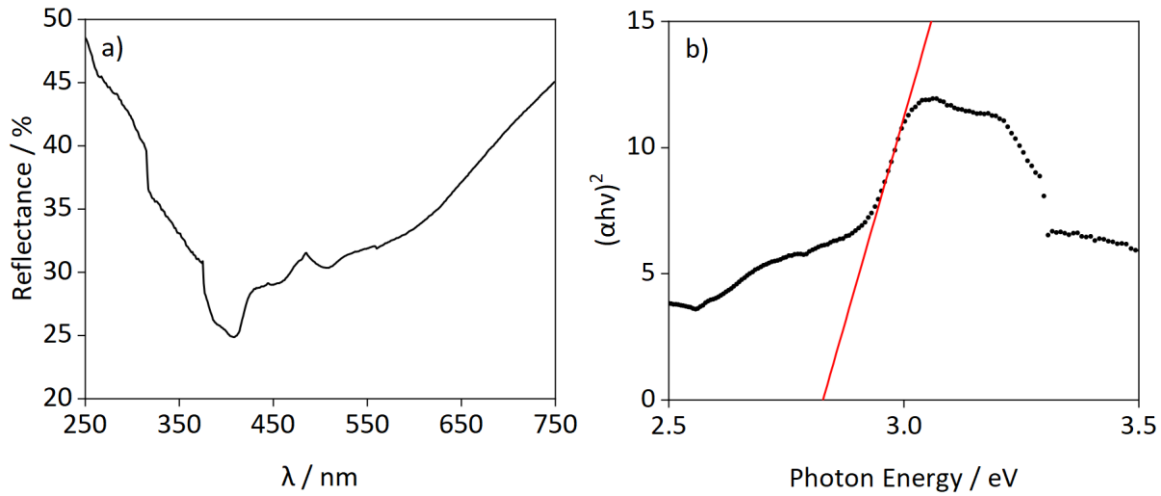

Figure 211 *UV-Vis spectrometry data for material with target composition $Sr_3Sc_2O_5Cu_{1.00}Se_2$ after 36 hours of heating at 800 °C. Plot a) is the raw diffuse reflectance data, and plot b) is the associated magnified Tauc plot for this region, where the intercept between the red extrapolated tangent line and the x-axis is used to estimate an optical band gap of 2.83 eV, which corresponds to 438 nm.*

B.2 Materials from Chapter 4

B.2.1 Sodium doped 426 sulfide MALMs, $(Sr_{4-x}Na_x)Sc_2O_6Cu_2S_2$

Table 54 Tabulated structural data of the sodium doped 426 sulfide MALMs with general formula $(Sr_{4-x}Na_x)Sc_2O_6Cu_2S_2$. The pristine material $Sr_4Sc_2O_6Cu_2S_2$ is included as a reference. All values are derived from the Rietveld refinement of PXRD data using GSAS-II. Note that because all materials listed are tetragonal (space group P4/nmm), the b parameter is identical to a, and thus omitted.

x / mol	Target Composition	a / Å	c / Å	Volume / Å^3
0 (pristine)	$Sr_4Sc_2O_6Cu_2S_2$	4.04786(3)	15.36089(26)	251.691(5)
0.025	$(Sr_{3.975}Na_{0.025})Sc_2O_6Cu_2S_2$	4.04843(8)	15.3587(6)	251.726(11)
0.050	$(Sr_{3.950}Na_{0.050})Sc_2O_6Cu_2S_2$	4.04846(8)	15.3592(7)	251.738(12)
0.075	$(Sr_{3.925}Na_{0.075})Sc_2O_6Cu_2S_2$	4.04845(16)	15.3571(9)	251.702(28)
0.100	$(Sr_{3.900}Na_{0.100})Sc_2O_6Cu_2S_2$	4.04786(19)	15.3553(11)	251.600(30)
0.125	$(Sr_{3.875}Na_{0.125})Sc_2O_6Cu_2S_2$	4.04812(16)	15.3563(9)	251.649(28)
0.150	$(Sr_{3.850}Na_{0.150})Sc_2O_6Cu_2S_2$	4.04783(16)	15.3530(9)	251.558(29)
0.175	$(Sr_{3.825}Na_{0.175})Sc_2O_6Cu_2S_2$	4.04754(16)	15.3516(9)	251.499(29)
0.200	$(Sr_{3.800}Na_{0.200})Sc_2O_6Cu_2S_2$	4.04751(14)	15.3535(8)	251.526(25)
0.500	$(Sr_{3.500}Na_{0.500})Sc_2O_6Cu_2S_2$	4.04740(15)	15.3564(9)	251.561(25)
1.000	$(Sr_{3.000}Na_{1.000})Sc_2O_6Cu_2S_2$	4.04528(15)	15.3651(9)	251.440(19)

Table 55 Tabulated compositional data of the sodium doped 426 sulfide MALMs with general formula $(Sr_{4-x}Na_x)Sc_2O_6Cu_2S_2$. The pristine material $Sr_4Sc_2O_6Cu_2S_2$ is included as a reference. All values are cited as a weight percent (wt %) of the total weight, and are derived from the Rietveld refinement of PXRD data using GSAS-II.

x / mol	Target phase / wt %	$Sr_3Sc_2O_5Cu_2S_2$ / wt %	SrS / wt %	Cu / wt %	$NaScO_2$ / wt %
0 (pristine)	98.0	-	1.7	0.3	-
0.025	97.3	1.3	0.2	1.2	-
0.050	96.0	1.6	0.3	2.2	-
0.075	96.1	1.8	0.3	1.8	-
0.100	95.1	2.0	0.5	2.4	-
0.125	95.9	1.7	0.3	2.2	-
0.150	95.7	2.0	-	2.3	-
0.175	92.7	4.6	0.5	2.2	-
0.200	92.7	4.3	0.6	2.4	-
0.500	84.3	8.4	3.2	2.5	1.6
1.000	65.5	2.7	14.4	9.1	8.3

Table 56 Tabulated data on both the target and maximum actual dopant content of the sodium doped 325 sulfide MALMs with general formula $(Sr_{3-x}Na_x)Sc_2O_5Cu_2S_2$. The pristine material $Sr_3Sc_2O_5Cu_2S_2$ is included as a reference. The minimum possible amount of total Na contained within impurities was extracted from the refined wt % of $NaCu_3S_2$ from GSAS-II. The remaining Na content is the maximum possible Na within the MALM.

Target x / mol	Target x / wt %	Minimum Na in impurities / %	Maximum Na in product / %	Maximum x / mol
0 (pristine)	0.000	0.000	100.000	0.000
0.025	0.079	0.000	100.000	0.025
0.050	0.159	0.000	100.000	0.050
0.075	0.239	0.000	100.000	0.075
0.100	0.319	0.000	100.000	0.100
0.125	0.399	0.000	100.000	0.125
0.150	0.480	0.000	100.000	0.150
0.175	0.562	0.000	100.000	0.175
0.200	0.643	0.000	100.000	0.200
0.500	1.653	22.262	77.738	0.389
1.000	3.468	55.058	44.942	0.449

Table 57 Tabulated analytical data of to the measured properties of the sodium doped 426 sulfide MALMs with general formula $(Sr_{4-x}Na_x)Sc_2O_6Cu_2S_2$. The pristine material $Sr_4Sc_2O_6Cu_2S_2$ is included as a reference. Pellet densities were estimated from the mass and volume of annealed pellet samples, and are cited as a relative percentage of the bulk crystal. Resistivities and conductivities were estimated from 4 probe van der Pauw analysis of the pellet samples.

x / mol	Pellet Density / %	Raw Resistivities from 4-Probe measurement, for each probe permutation / kΩ								Resistivity / Ω cm	Conductivity / S cm^{-1}
		1	2	3	4	5	6	7	8		
0 (pristine)	64.95	1.37 E+01	1.38 E+01	1.40 E+01	1.41 E+01	1.33 E+01	1.33 E+01	1.34 E+01	1.34 E+01	1.18 E+04	8.48 E-05
0.025	70.53	1.47 E+02	1.48 E+02	1.61 E+02	1.67 E+02	1.54 E+02	1.58 E+02	1.36 E+02	1.50 E+02	8.23 E+04	1.21 E-05
0.050	69.49	1.66 E+02	1.73 E+02	1.60 E+02	1.69 E+02	1.54 E+02	1.52 E+02	1.71 E+02	1.72 E+02	9.10 E+04	1.10 E-05
0.075	68.86	1.45 E+02	1.54 E+02	1.80 E+02	1.98 E+02	1.20 E+02	1.40 E+02	1.34 E+02	1.39 E+02	8.32 E+04	1.20 E-05
0.100	68.82	1.55 E+02	1.60 E+02	1.39 E+02	1.51 E+02	1.97 E+02	1.95 E+02	2.15 E+02	2.28 E+02	9.86 E+04	1.01 E-05
0.125	68.89	1.13 E+02	1.11 E+02	1.26 E+02	1.24 E+02	2.35 E+02	2.49 E+02	2.13 E+02	2.16 E+02	9.17 E+04	1.09 E-05
0.150	69.62	1.63 E+02	1.71 E+02	1.91 E+02	2.01 E+02	1.55 E+02	1.59 E+02	1.11 E+02	1.17 E+02	8.56 E+04	1.17 E-05
0.175	68.04	1.26 E+02	1.30 E+02	1.50 E+02	1.51 E+02	1.73 E+02	1.73 E+02	2.15 E+02	2.15 E+02	9.20 E+04	1.09 E-05
0.200	73.35	1.79 E+02	1.85 E+02	1.37 E+02	1.42 E+02	1.89 E+02	1.97 E+02	1.97 E+02	2.08 E+02	9.23 E+04	1.08 E-05
0.500	68.91	1.67 E+02	1.72 E+02	1.61 E+02	1.64 E+02	1.61 E+02	1.62 E+02	1.73 E+02	1.73 E+02	9.14 E+04	1.09 E-05
1.000	68.16	1.42 E+02	1.43 E+02	1.51 E+02	1.59 E+02	2.33 E+02	2.28 E+02	2.73 E+02	2.76 E+02	1.09 E+05	9.16 E-06

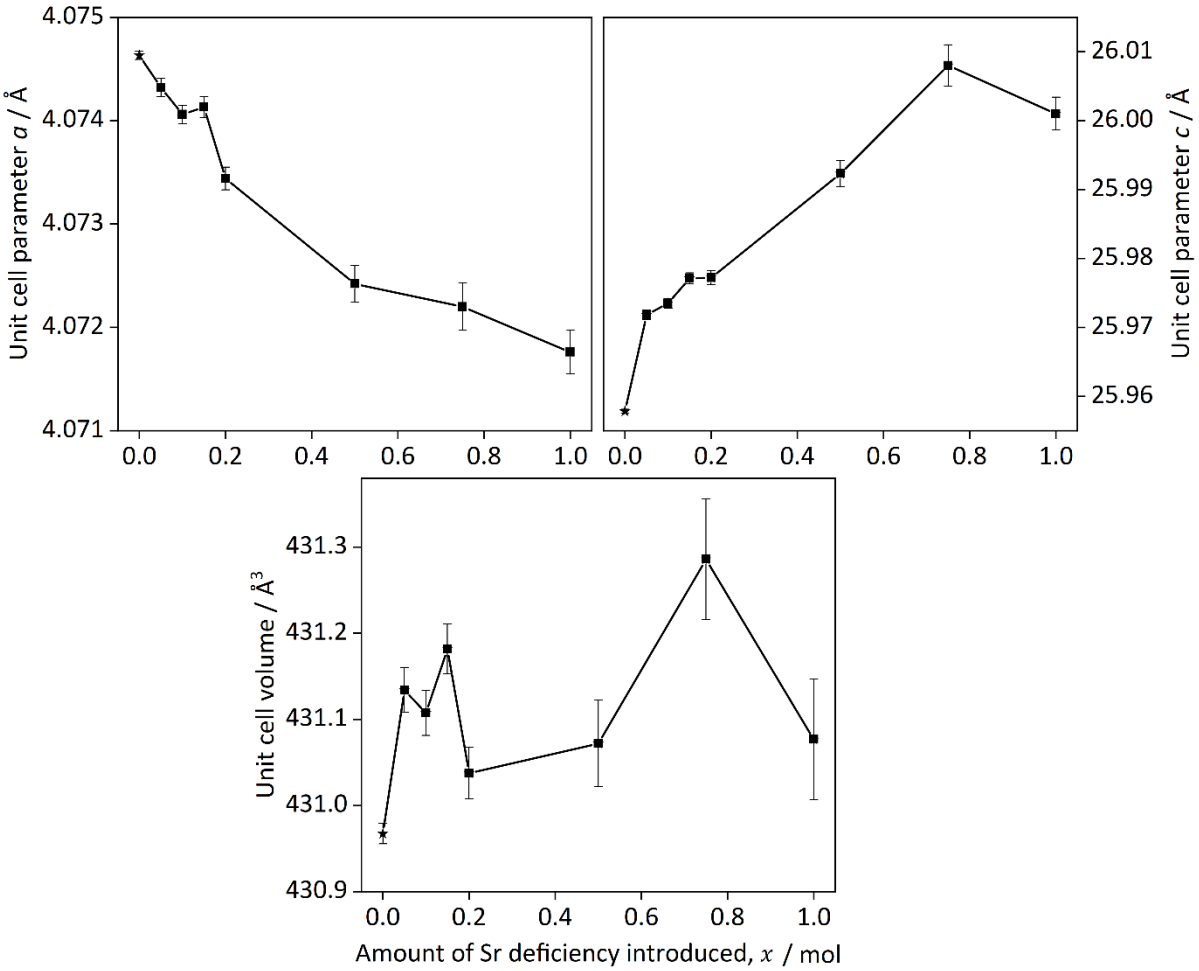

Figure 212 Comparisons of a) the a unit cell parameter, b) the c unit cell parameter, and c) the unit cell volume, of the sodium doped 426 sulfide MALMs with general formula $(Sr_{4-x}Na_x)Sc_2O_6Cu_2S_2$. The pristine material $Sr_4Sc_2O_6Cu_2S_2$ is included as a reference at $x = 0$ mol and is represented by a star. Sample band gaps are missing due to lack of drop-off in diffuse reflectance.

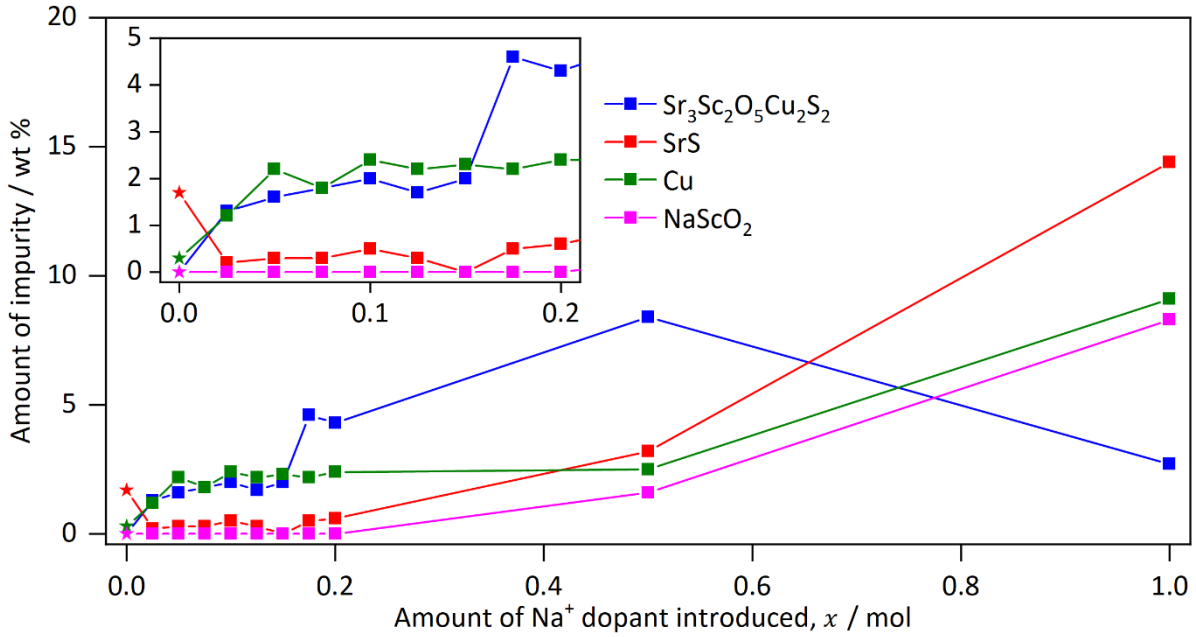

Figure 213 *The weight percentages of four impurity phases present in the sodium doped 426 sulfide MALMs with general formula $(Sr_{4-x}Na_x)Sc_2O_6Cu_2S_2$. The pristine material $Sr_4Sc_2O_6Cu_2S_2$ is included as a reference at $x = 0$ mol and is represented by a star.*

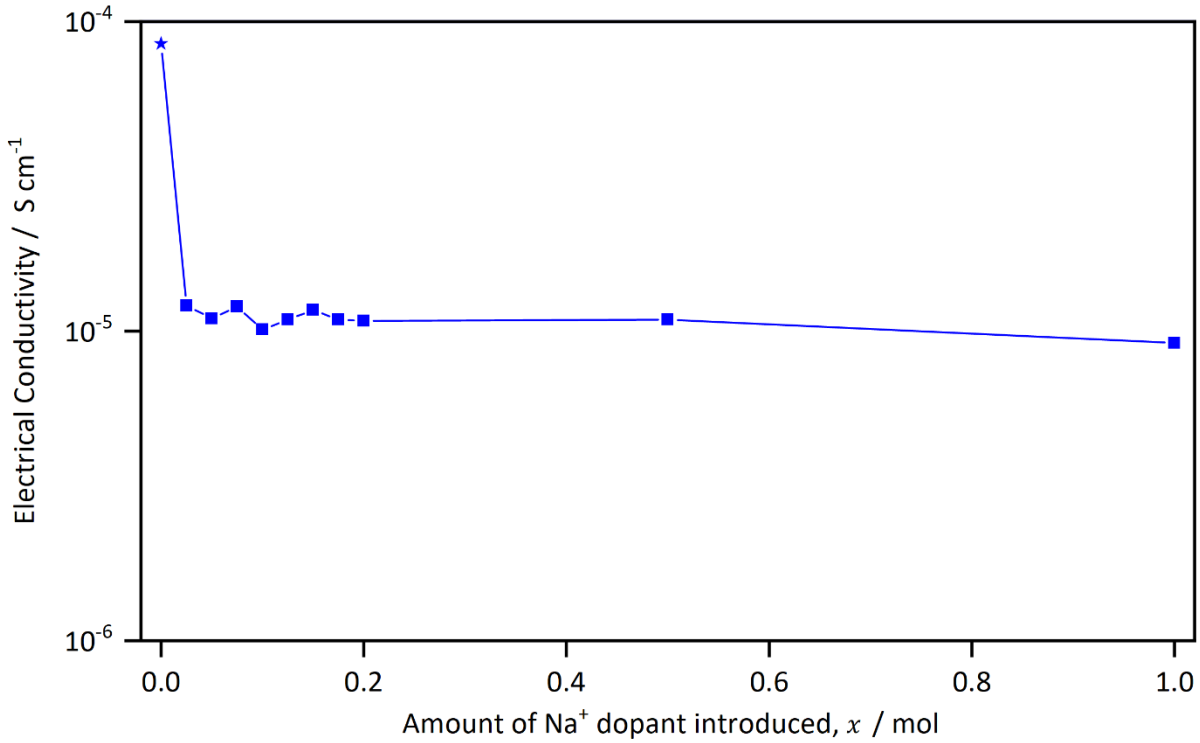

Figure 214 *The electrical conductivities of the sodium doped 426 sulfide MALMs with general formula $(Sr_{4-x}Na_x)Sc_2O_6Cu_2S_2$, represented on a log_{10} scale. The pristine material $Sr_4Sc_2O_6Cu_2S_2$ is included as a reference at $x = 0$ mol and is represented by a star. All values are derived from van der Pauw 4 probe resistivity measurements of 8mm diameter annealed pellet samples.*

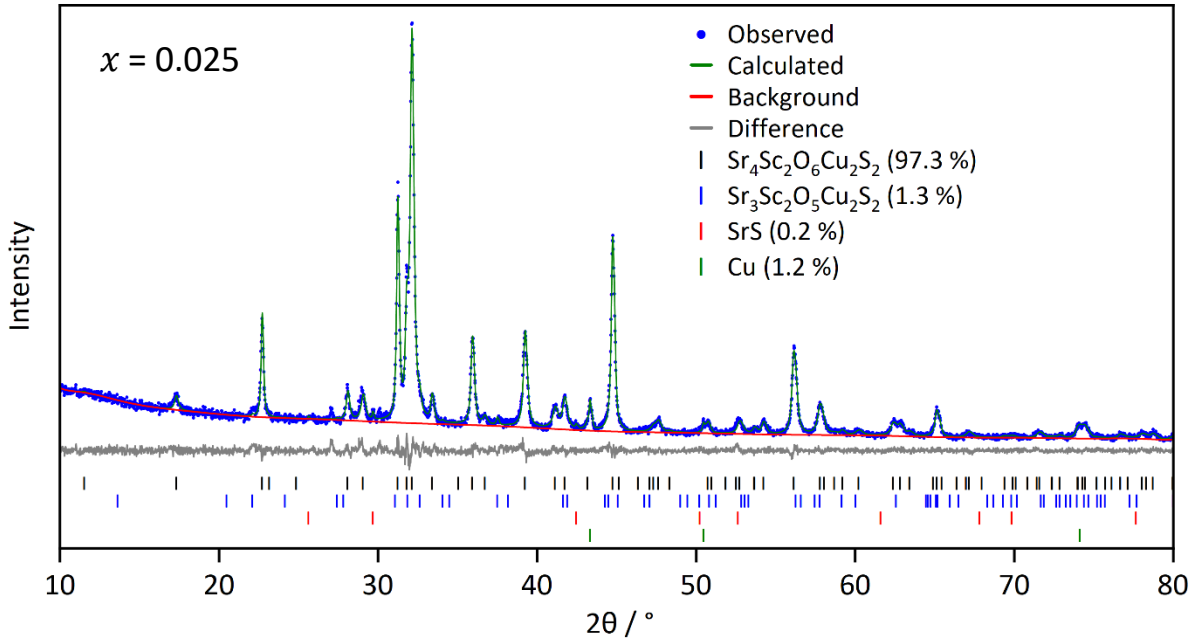

Figure 215 *Powder X-ray diffractogram of material with target composition $(Sr_{3.975}Na_{0.025})Sc_2O_6Cu_2S_2$ (space group P4/nmm) after 24 hours of heating at 550 °C. The small blue circles represent the observed diffracted intensity, the green line represents the Rietveld-refined calculated model, the red line represents the background, and the grey line represents the difference between observed and calculated intensities. The black tick marks show the reflections of the refined model of $Sr_4Sc_2O_6Cu_2S_2$ (97.3 %), whilst the blue, red and green tick marks represent refined impurity phases $Sr_3Sc_2O_5Cu_2S_2$ (1.3 %), SrS (0.2 %) and Cu (1.2 %) respectively.*
Duration: 45 minutes. Data points: 3457. Interval: 0.02 °. GOF: 1.29. R_{wp}: 5.892 %.

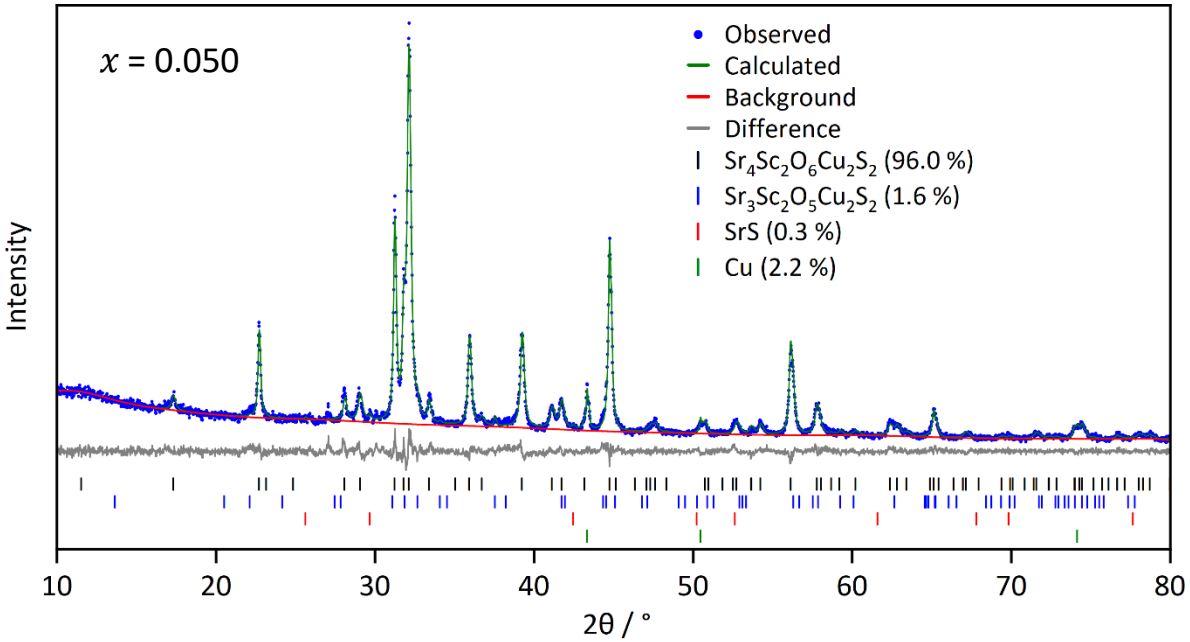

Figure 216 *Powder X-ray diffractogram of material with target composition $(Sr_{3.950}Na_{0.050})Sc_2O_6Cu_2S_2$ (space group P4/nmm) after 24 hours of heating at 550 °C. The small blue circles represent the observed diffracted intensity, the green line represents the Rietveld-refined calculated model, the red line represents the background, and the grey line represents the difference between observed and calculated intensities. The black tick marks show the reflections of the refined model of $Sr_4Sc_2O_6Cu_2S_2$ (96.0 %), whilst the blue, red and green tick marks represent refined impurity phases $Sr_3Sc_2O_5Cu_2S_2$ (1.6 %), SrS (0.3 %) and Cu (2.2 %) respectively.*
Duration: 45 minutes. Data points: 3457. Interval: 0.02 °. GOF: 1.31. R_{wp}: 5.964 %.

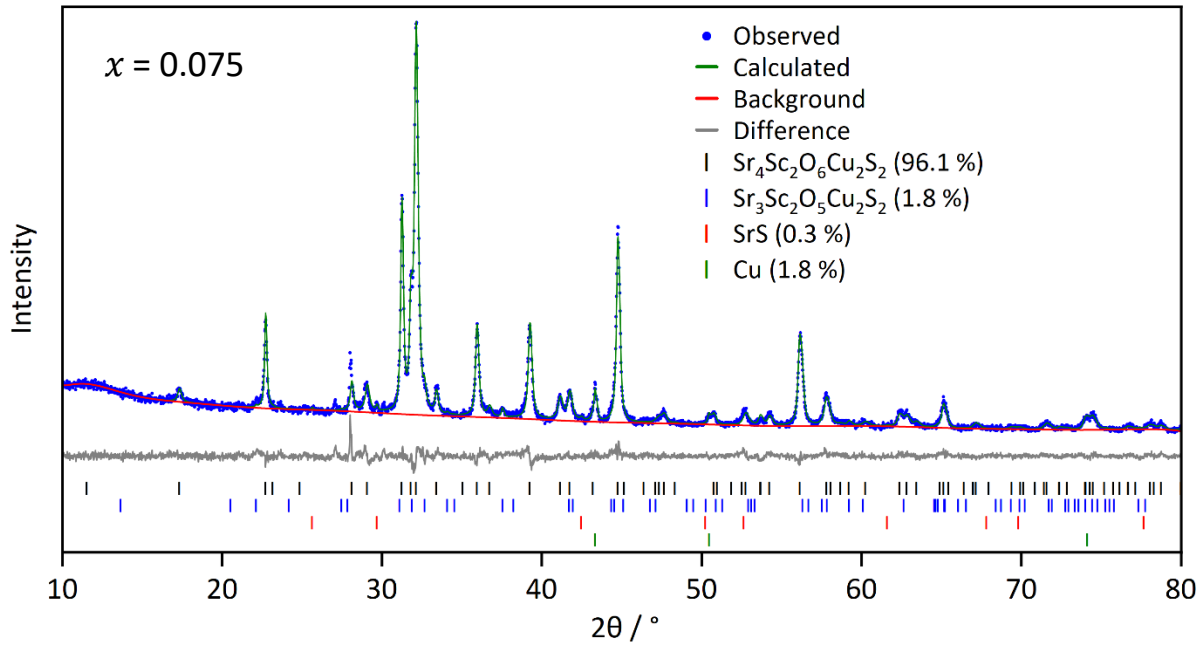

Figure 217 *Powder X-ray diffractogram of material with target composition $(Sr_{3.925}Na_{0.075})Sc_2O_6Cu_2S_2$ (space group P4/nmm) after 24 hours of heating at 550 °C. The small blue circles represent the observed diffracted intensity, the green line represents the Rietveld-refined calculated model, the red line represents the background, and the grey line represents the difference between observed and calculated intensities. The black tick marks show the reflections of the refined model of $Sr_4Sc_2O_6Cu_2S_2$ (96.1 %), whilst the blue, red and green tick marks represent refined impurity phases $Sr_3Sc_2O_5Cu_2S_2$ (1.8 %), SrS (0.3 %) and Cu (1.8 %) respectively.*
Duration: 45 minutes. Data points: 3457. Interval: 0.02 °. GOF: 1.40. R_{wp}: 5.888 %.

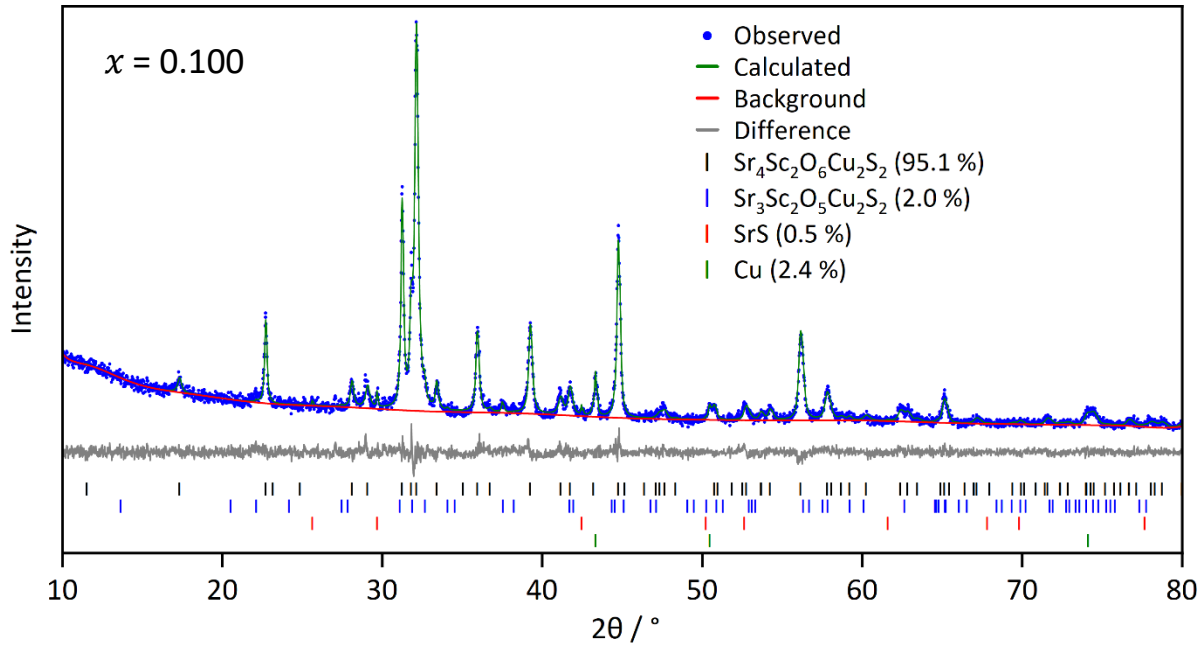

Figure 218 *Powder X-ray diffractogram of material with target composition $(Sr_{3.900}Na_{0.100})Sc_2O_6Cu_2S_2$ (space group P4/nmm) after 24 hours of heating at 550 °C. The small blue circles represent the observed diffracted intensity, the green line represents the Rietveld-refined calculated model, the red line represents the background, and the grey line represents the difference between observed and calculated intensities. The black tick marks show the reflections of the refined model of $Sr_4Sc_2O_6Cu_2S_2$ (95.1 %), whilst the blue, red and green tick marks represent refined impurity phases $Sr_3Sc_2O_5Cu_2S_2$ (2.0 %), SrS (0.5 %) and Cu (2.4 %) respectively.*
Duration: 45 minutes. Data points: 3457. Interval: 0.02 °. GOF: 1.13. R_{wp}: 6.645 %.

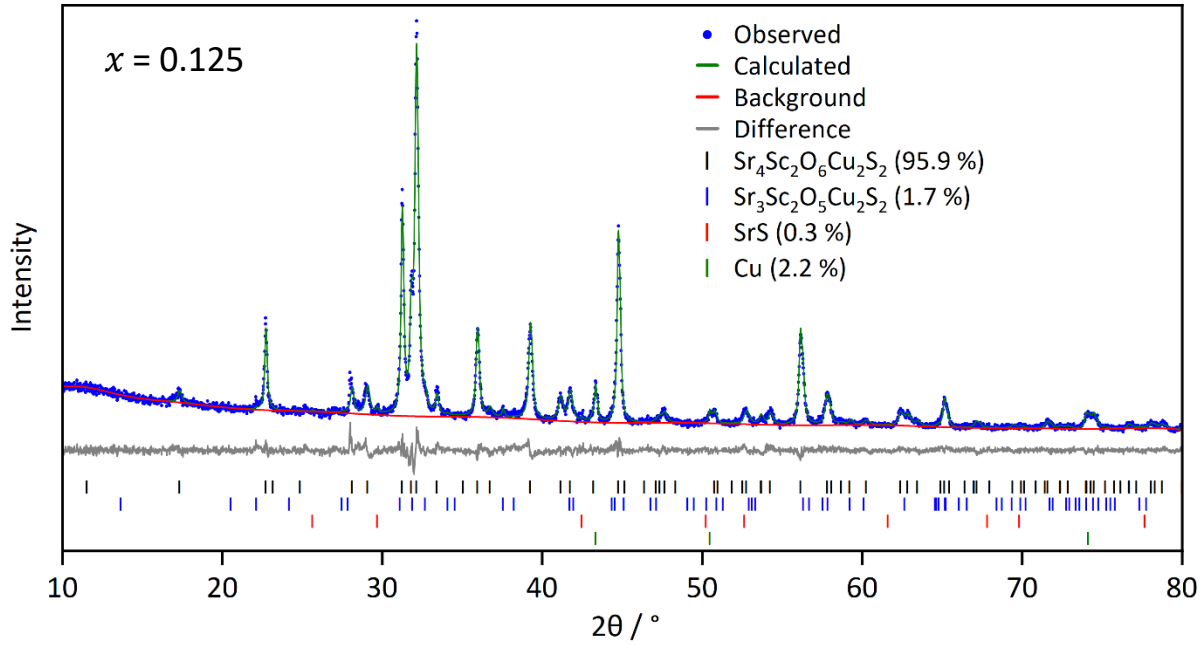

Figure 219 *Powder X-ray diffractogram of material with target composition $(Sr_{3.875}Na_{0.125})Sc_2O_6Cu_2S_2$ (space group P4/nmm) after 24 hours of heating at 550 °C. The small blue circles represent the observed diffracted intensity, the green line represents the Rietveld-refined calculated model, the red line represents the background, and the grey line represents the difference between observed and calculated intensities. The black tick marks show the reflections of the refined model of $Sr_4Sc_2O_6Cu_2S_2$ (95.9 %), whilst the blue, red and green tick marks represent refined impurity phases $Sr_3Sc_2O_5Cu_2S_2$ (1.7 %), SrS (0.3 %) and Cu (2.2 %) respectively.*
Duration: 45 minutes. Data points: 3457. Interval: 0.02 °. GOF: 1.32. R_{wp}: 6.141 %.

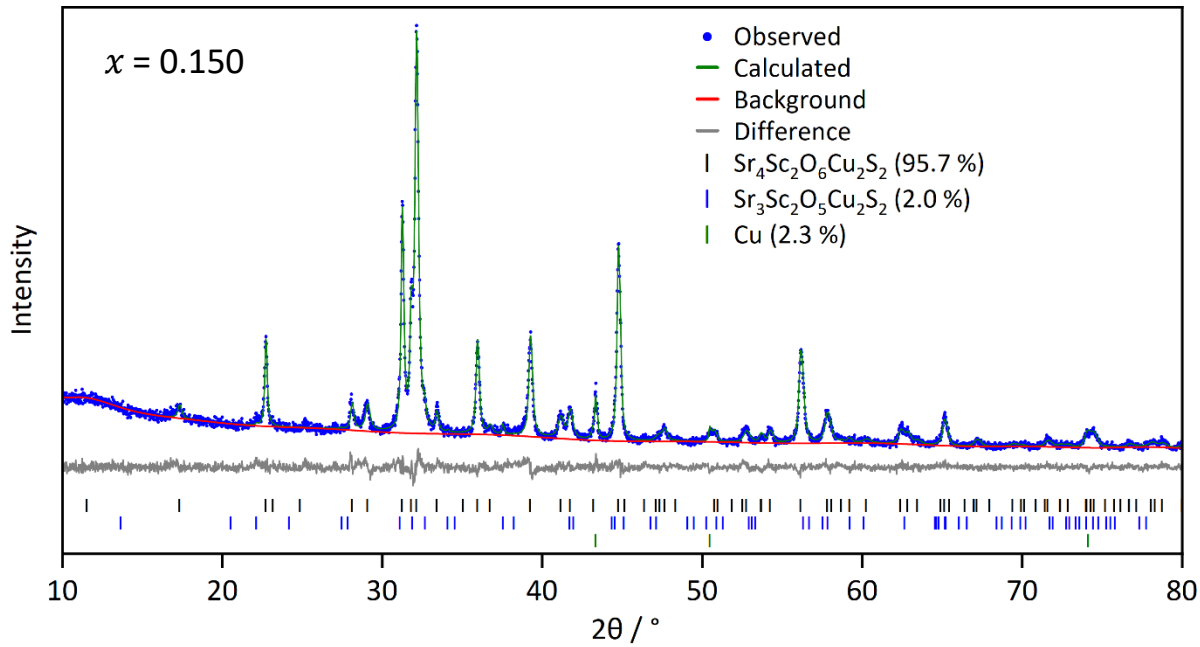

Figure 220 *Powder X-ray diffractogram of material with target composition $(Sr_{3.850}Na_{0.150})Sc_2O_6Cu_2S_2$ (space group P4/nmm) after 24 hours of heating at 550 °C. The small blue circles represent the observed diffracted intensity, the green line represents the Rietveld-refined calculated model, the red line represents the background, and the grey line represents the difference between observed and calculated intensities. The black tick marks show the reflections of the refined model of $Sr_4Sc_2O_6Cu_2S_2$ (95.7 %), whilst the blue and green tick marks represent refined impurity phases $Sr_3Sc_2O_5Cu_2S_2$ (2.0 %), and Cu (2.3 %) respectively.*
Duration: 45 minutes. Data points: 3457. Interval: 0.02 °. GOF: 1.26. R_{wp}: 6.150 %.

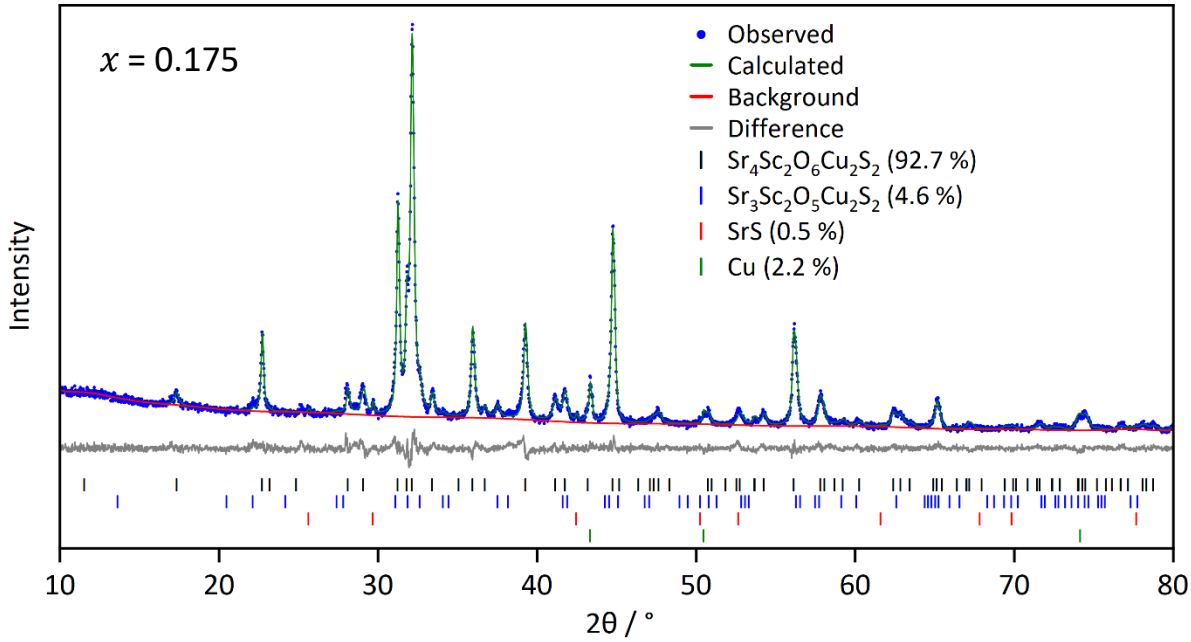

Figure 221 *Powder X-ray diffractogram of material with target composition $(Sr_{3.825}Na_{0.175})Sc_2O_6Cu_2S_2$ (space group P4/nmm) after 24 hours of heating at 550 °C. The small blue circles represent the observed diffracted intensity, the green line represents the Rietveld-refined calculated model, the red line represents the background, and the grey line represents the difference between observed and calculated intensities. The black tick marks show the reflections of the refined model of $Sr_4Sc_2O_6Cu_2S_2$ (92.7 %), whilst the blue, red and green tick marks represent refined impurity phases $Sr_3Sc_2O_5Cu_2S_2$ (4.6 %), SrS (0.5 %) and Cu (2.2 %) respectively.*
Duration: 45 minutes. Data points: 3457. Interval: 0.02 °. GOF: 1.36. R_{wp}: 5.801 %.

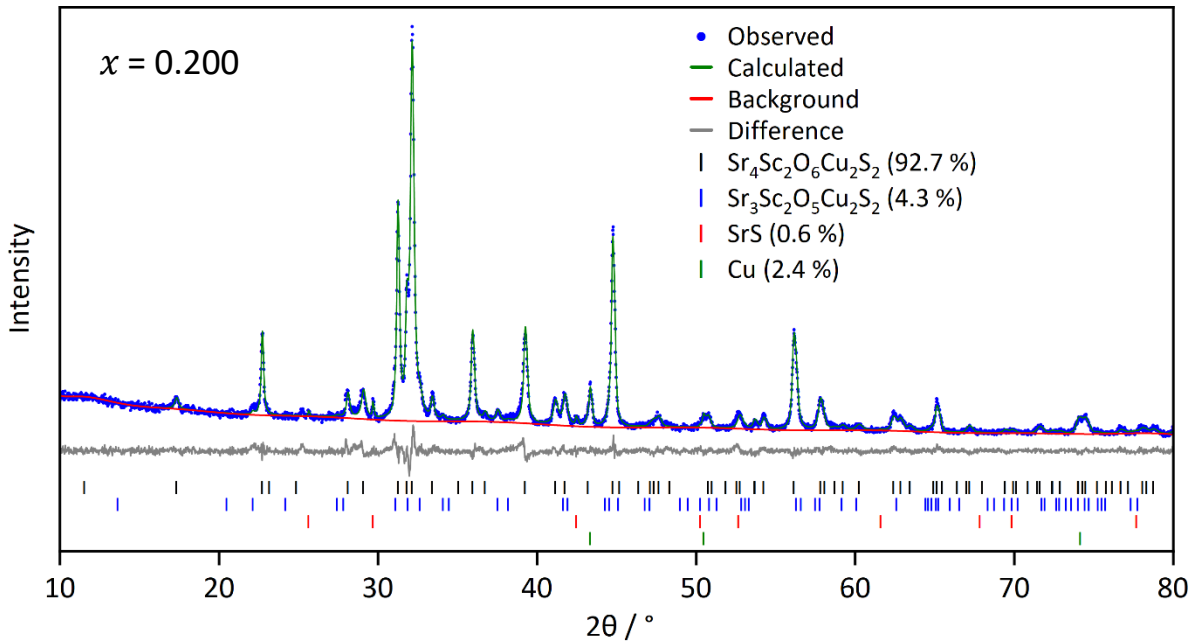

Figure 222 *Powder X-ray diffractogram of material with target composition $(Sr_{3.800}Na_{0.200})Sc_2O_6Cu_2S_2$ (space group P4/nmm) after 24 hours of heating at 550 °C. The small blue circles represent the observed diffracted intensity, the green line represents the Rietveld-refined calculated model, the red line represents the background, and the grey line represents the difference between observed and calculated intensities. The black tick marks show the reflections of the refined model of $Sr_4Sc_2O_6Cu_2S_2$ (92.7 %), whilst the blue, red and green tick marks represent refined impurity phases $Sr_3Sc_2O_5Cu_2S_2$ (4.3 %), SrS (0.6 %) and Cu (2.4 %) respectively.*
Duration: 45 minutes. Data points: 3457. Interval: 0.02 °. GOF: 1.40. R_{wp}: 5.788 %.

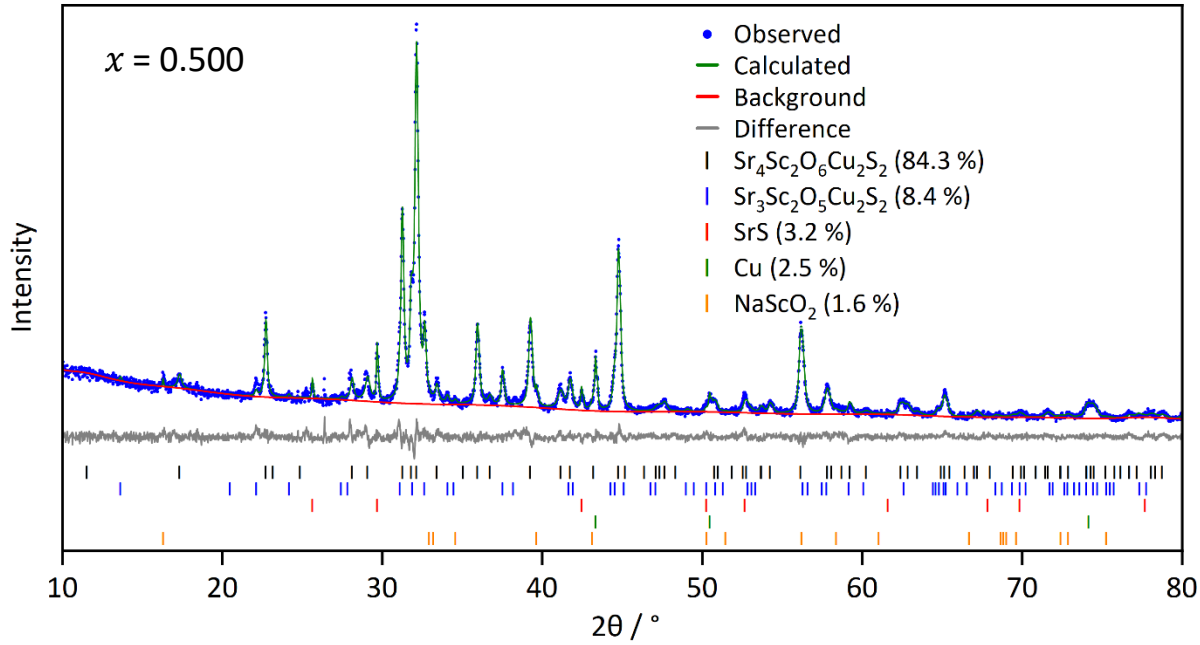

Figure 223 *Powder X-ray diffractogram of material with target composition $(Sr_{3.500}Na_{0.500})Sc_2O_6Cu_2S_2$ (space group P4/nmm) after 24 hours of heating at 550 °C. The small blue circles represent the observed diffracted intensity, the green line represents the Rietveld-refined calculated model, the red line represents the background, and the grey line represents the difference between observed and calculated intensities. The black tick marks show the reflections of the refined model of $Sr_4Sc_2O_6Cu_2S_2$ (84.3 %), whilst the blue, red, green and orange tick marks represent refined impurity phases $Sr_3Sc_2O_5Cu_2S_2$ (8.4 %), SrS (3.2 %), Cu (2.5 %) and $NaScO_2$ (1.6 %) respectively.*
Duration: 45 minutes. Data points: 3457. Interval: 0.02 °. GOF: 1.36. R_{wp}: 6.448 %.

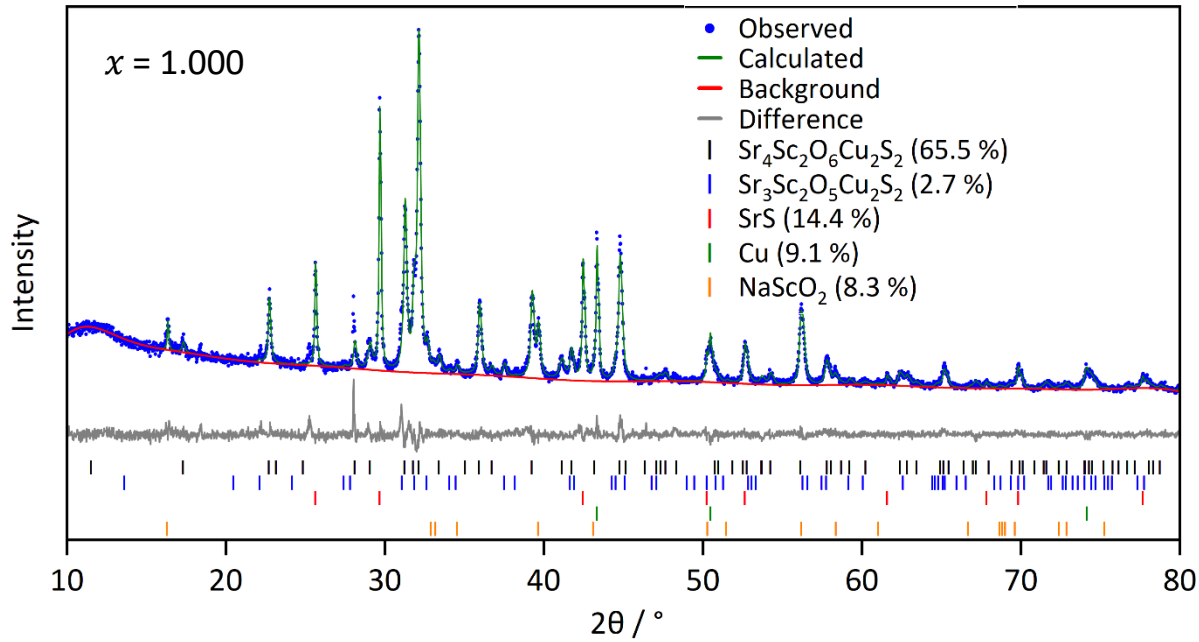

Figure 224 *Powder X-ray diffractogram of material with target composition $(Sr_{3.000}Na_{1.000})Sc_2O_6Cu_2S_2$ (space group P4/nmm) after 24 hours of heating at 550 °C. The small blue circles represent the observed diffracted intensity, the green line represents the Rietveld-refined calculated model, the red line represents the background, and the grey line represents the difference between observed and calculated intensities. The black tick marks show the reflections of the refined model of $Sr_4Sc_2O_6Cu_2S_2$ (65.5 %), whilst the blue, red, green and orange tick marks represent refined impurity phases $Sr_3Sc_2O_5Cu_2S_2$ (2.7 %), SrS (14.4 %), Cu (9.1 %) and $NaScO_2$ (8.3 %) respectively.*
Duration: 45 minutes. Data points: 3457. Interval: 0.02 °. GOF: 1.35. R_{wp}: 6.016 %.

B.2.2 Flash Annealed $(Sr_{3.9}Na_{0.1})Sc_2O_6Cu_2S_2$

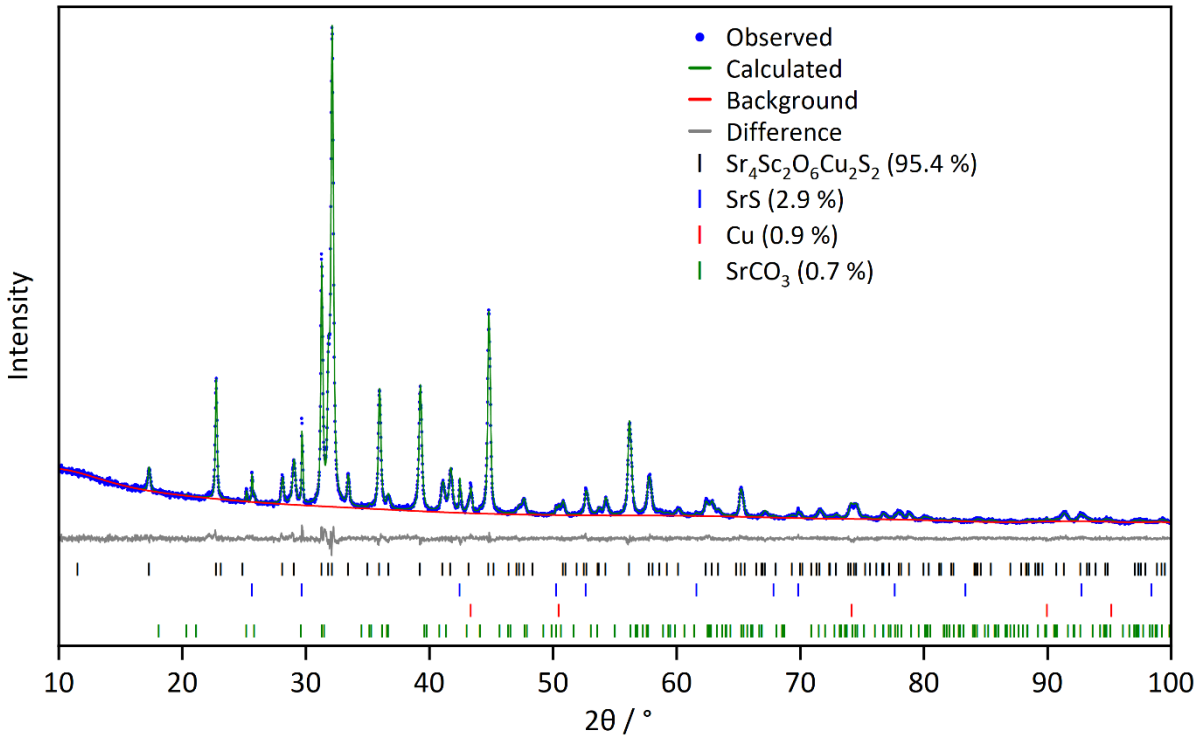

Figure 225 *Powder X-ray diffractogram of material with target composition $(Sr_{3.900}Na_{0.100})Sc_2O_6Cu_2S_2$ (space group P4/nmm) after 24 hours of heating at 550 °C and before flash annealing. The small blue circles represent the observed diffracted intensity, the green line represents the Rietveld-refined calculated model, the red line represents the background, and the grey line represents the difference between observed and calculated intensities. The black tick marks show the reflections of the refined model of $Sr_4Sc_2O_6Cu_2S_2$ (95.4 %), whilst the blue, red and green tick marks represent refined impurity phases SrS (2.9 %), Cu (0.9 %) and $SrCO_3$ (0.7 %) respectively.*
Duration: 3 hours. Data points: 4444. Interval: 0.02 °. GOF: 1.22. R_{wp}: 3.523 %.

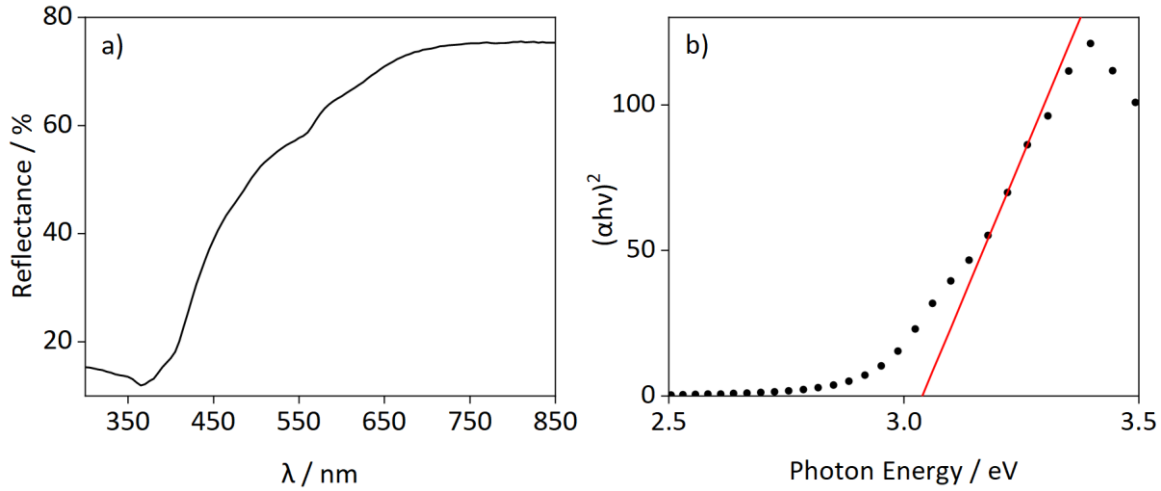

Figure 226 *UV-Vis spectrometry data for material with target composition $(Sr_{3.900}Na_{0.100})Sc_2O_6Cu_2S_2$ after 24 hours of heating at 550 °C. Plot a) is the raw diffuse reflectance data, and plot b) is the associated magnified Tauc plot for this region, where the intercept between the red extrapolated tangent line and the x-axis is used to estimate an optical band gap of 3.04 eV, which corresponds to 408 nm.*

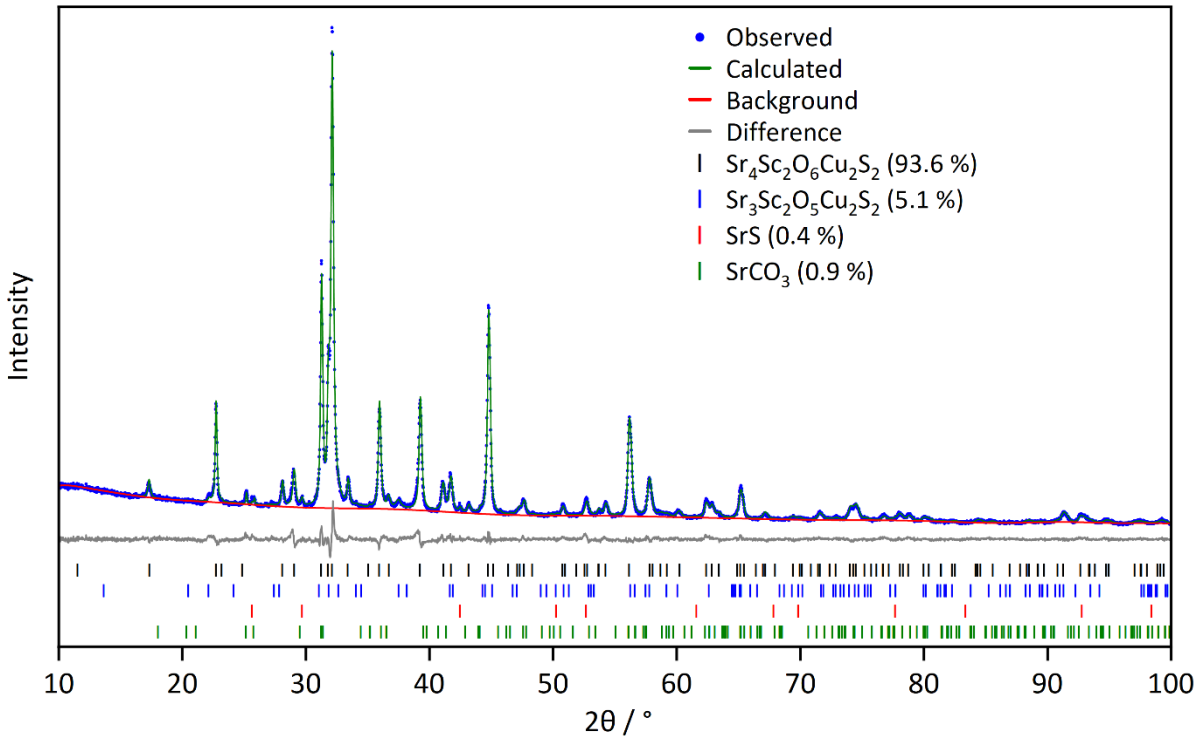

Figure 227 *Powder X-ray diffractogram of material with target composition $(Sr_{3.900}Na_{0.100})Sc_2O_6Cu_2S_2$ (space group P4/nmm) after 24 hours of heating at 550 °C after flash annealing for 30 minutes at 800 °C. The small blue circles represent the observed diffracted intensity, the green line represents the Rietveld-refined calculated model, the red line represents the background, and the grey line represents the difference between observed and calculated intensities. The black tick marks show the reflections of the refined model of $Sr_4Sc_2O_6Cu_2S_2$ (93.6 %), whilst the blue, red and green tick marks represent refined impurity phases $Sr_3Sc_2O_5Cu_2S_2$ (5.1 %), SrS (0.4 %) and $SrCO_3$ (0.9 %) respectively.*
Duration: 3 hours. Data points: 4444. Interval: 0.02 °. GOF: 1.67. R_{wp}: 4.158 %.

B.2.3 Flash Annealed $(Sr_{3.9}K_{0.1})Sc_2O_6Cu_2S_2$

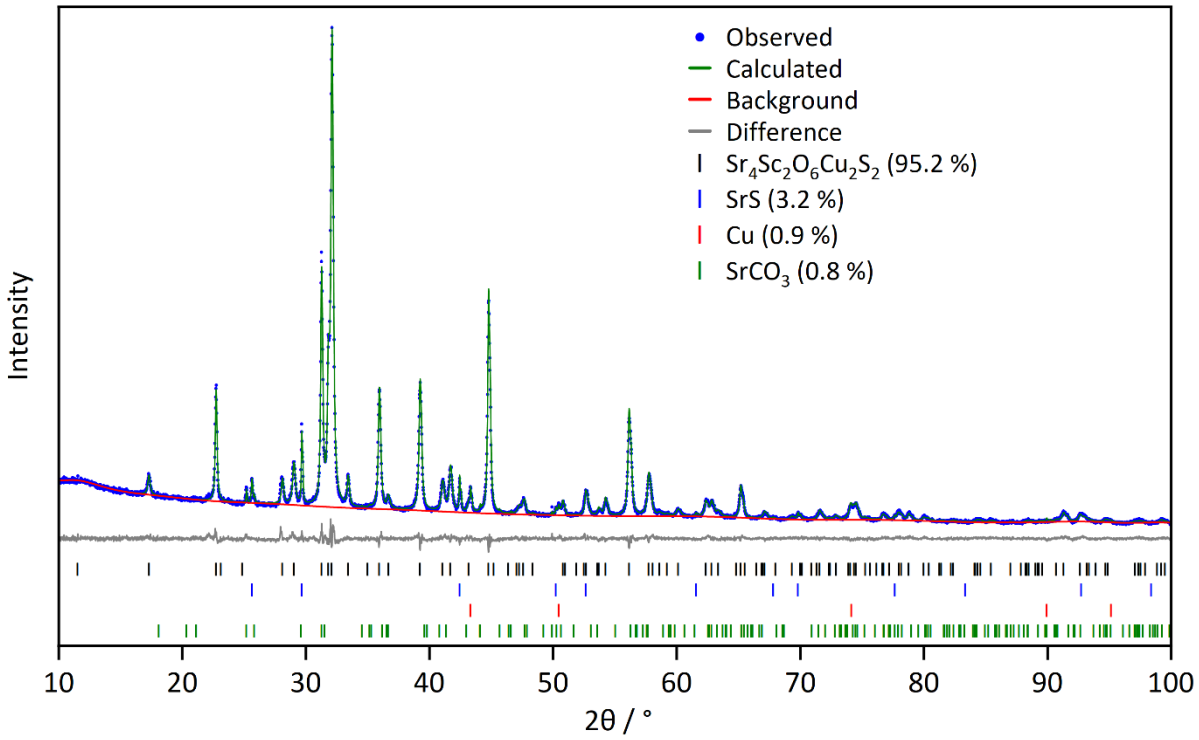

Figure 228 *Powder X-ray diffractogram of material with target composition $(Sr_{3.900}K_{0.100})Sc_2O_6Cu_2S_2$ (space group P4/nmm) after 24 hours of heating at 550 °C and before flash annealing. The small blue circles represent the observed diffracted intensity, the green line represents the Rietveld-refined calculated model, the red line represents the background, and the grey line represents the difference between observed and calculated intensities. The black tick marks show the reflections of the refined model of $Sr_4Sc_2O_6Cu_2S_2$ (95.2 %), whilst the blue, red and green tick marks represent refined impurity phases SrS (3.2 %), Cu (0.9 %) and $SrCO_3$ (0.8 %) respectively.*
Duration: 3 hours. Data points: 4444. Interval: 0.02 °. GOF: 1.39. R_{wp}: 3.631 %.

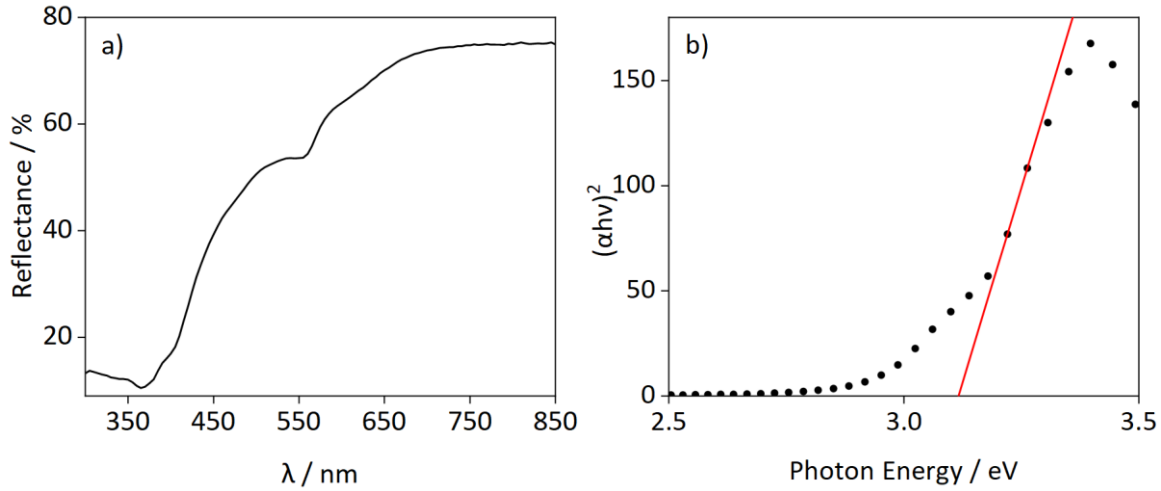

Figure 229 *UV-Vis spectrometry data for material with target composition $(Sr_{3.900}K_{0.100})Sc_2O_6Cu_2S_2$ after 24 hours of heating at 550 °C. Plot a) is the raw diffuse reflectance data, and plot b) is the associated magnified Tauc plot for this region, where the intercept between the red extrapolated tangent line and the x-axis is used to estimate an optical band gap of 3.12 eV, which corresponds to 397 nm.*

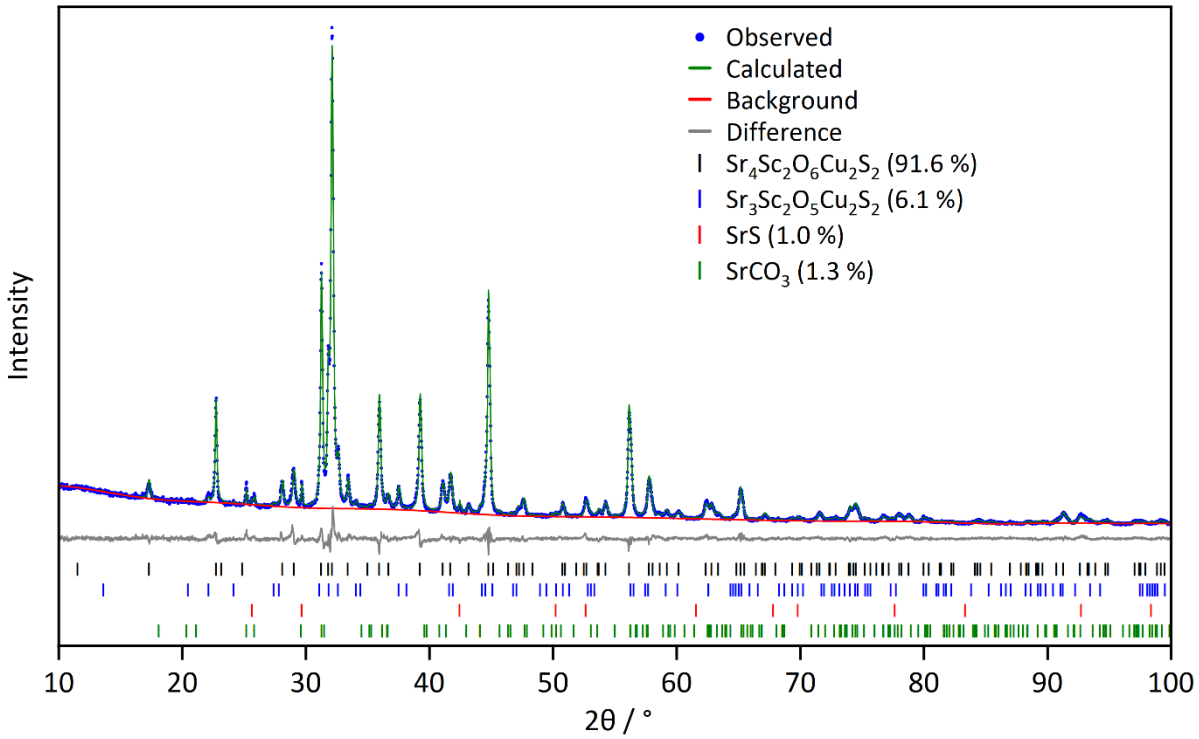

Figure 230 *Powder X-ray diffractogram of material with target composition $(Sr_{3.900}K_{0.100})Sc_2O_6Cu_2S_2$ (space group P4/nmm) after 24 hours of heating at 550 °C after flash annealing for 30 minutes at 800 °C. The small blue circles represent the observed diffracted intensity, the green line represents the Rietveld-refined calculated model, the red line represents the background, and the grey line represents the difference between observed and calculated intensities. The black tick marks show the reflections of the refined model of $Sr_4Sc_2O_6Cu_2S_2$ (91.6 %), whilst the blue, red and green tick marks represent refined impurity phases $Sr_3Sc_2O_5Cu_2S_2$ (6.1 %), SrS (1.0 %) and $SrCO_3$ (1.3 %) respectively.*
Duration: 3 hours. Data points: 4444. Interval: 0.02 °. GOF: 1.78. R_{wp}: 4.354 %.

B.2.4 Flash Annealed $(Sr_{3.9}Na_{0.1})Sc_2O_6Cu_2Se_2$

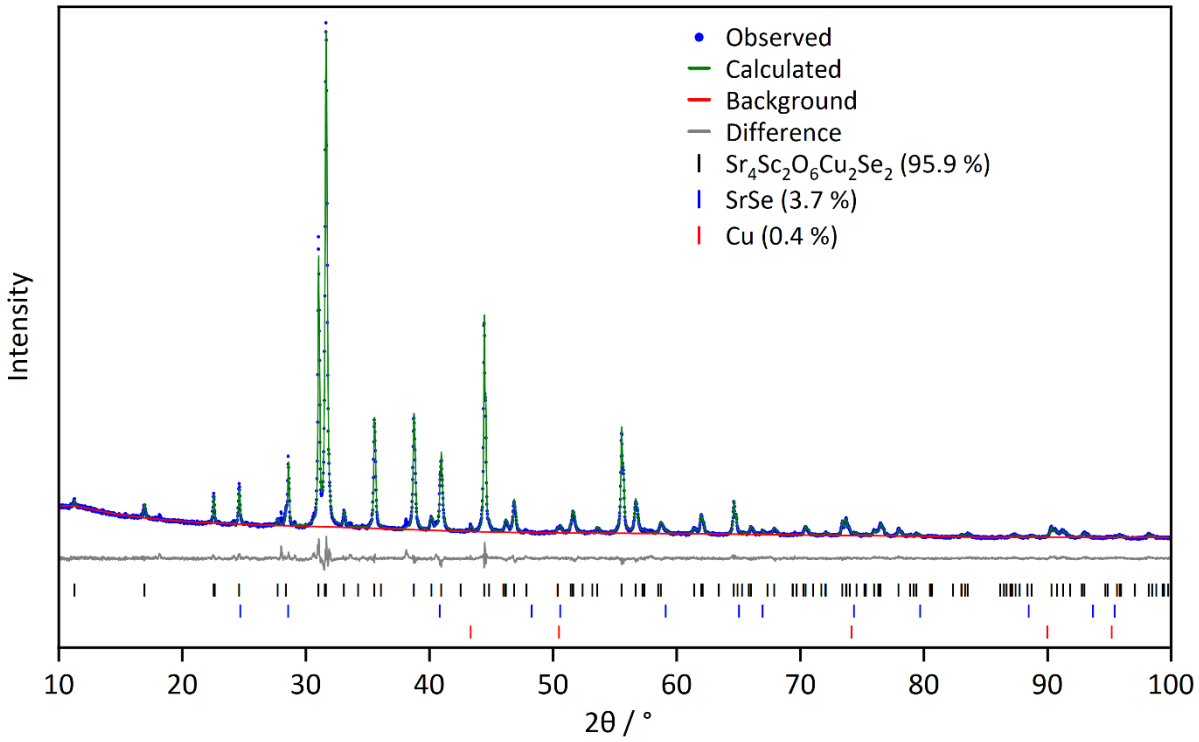

Figure 231 *Powder X-ray diffractogram of material with target composition $(Sr_{3.900}Na_{0.100})Sc_2O_6Cu_2Se_2$ (space group P4/nmm) after 24 hours of heating at 550 °C and before flash annealing. The small blue circles represent the observed diffracted intensity, the green line represents the Rietveld-refined calculated model, the red line represents the background, and the grey line represents the difference between observed and calculated intensities. The black tick marks show the reflections of the refined model of $Sr_4Sc_2O_6Cu_2Se_2$ (95.9 %), whilst the blue and red tick marks represent refined impurity phases SrSe (3.7 %) and Cu (0.4 %) respectively.*
Duration: 3 hours. Data points: 4444. Interval: 0.02 °. GOF: 1.59. R_{wp}: 4.412 %.

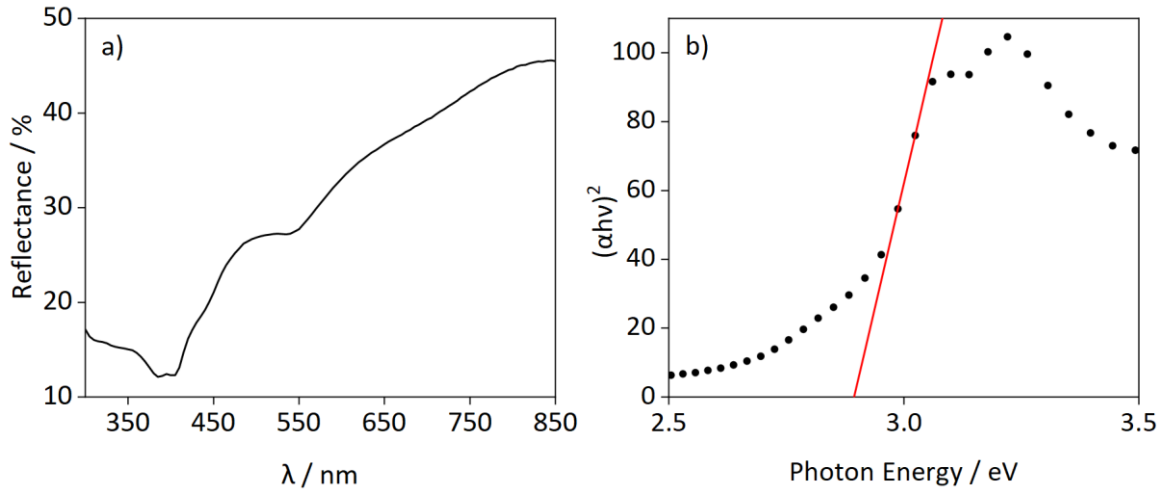

Figure 232 *UV-Vis spectrometry data for material with target composition $(Sr_{3.900}Na_{0.100})Sc_2O_6Cu_2Se_2$ after 24 hours of heating at 550 °C. Plot a) is the raw diffuse reflectance data, and plot b) is the associated magnified Tauc plot for this region, where the intercept between the red extrapolated tangent line and the x-axis is used to estimate an optical band gap of 2.89 eV, which corresponds to 429 nm.*

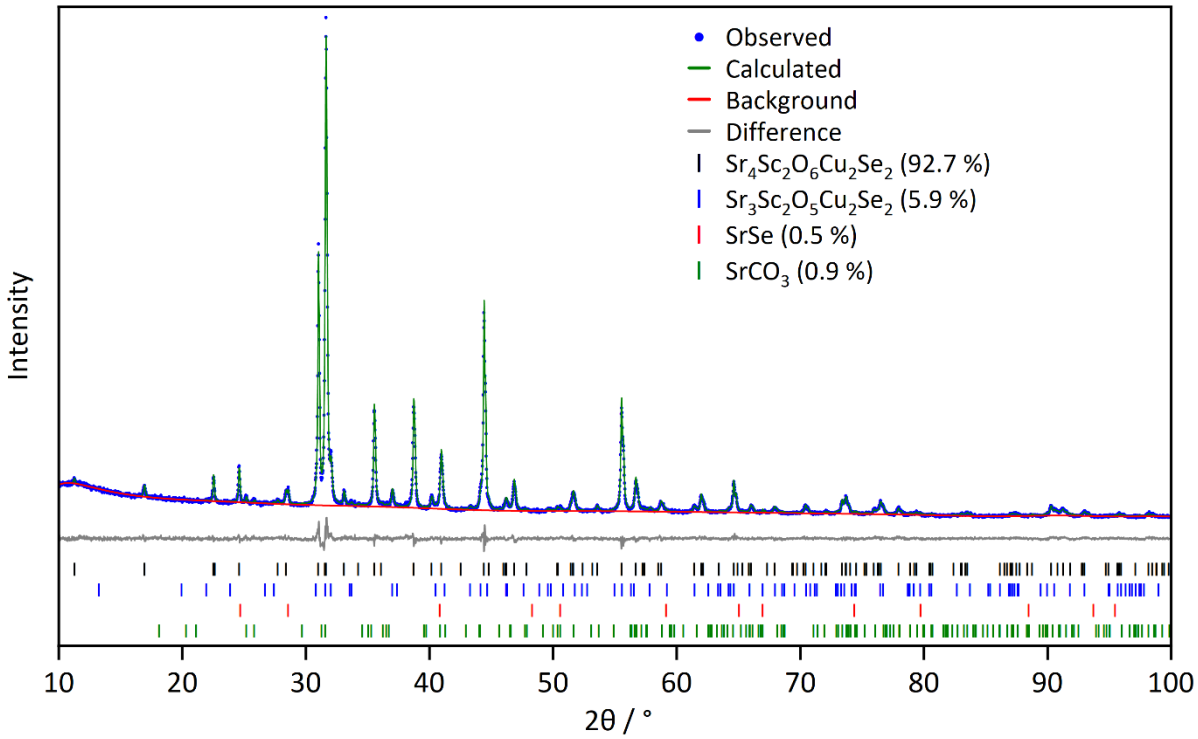

Figure 233 *Powder X-ray diffractogram of material with target composition $(Sr_{3.900}Na_{0.100})Sc_2O_6Cu_2Se_2$ (space group P4/nmm) after 24 hours of heating at 550 °C after flash annealing for 30 minutes at 800 °C. The small blue circles represent the observed diffracted intensity, the green line represents the Rietveld-refined calculated model, the red line represents the background, and the grey line represents the difference between observed and calculated intensities. The black tick marks show the reflections of the refined model of $Sr_4Sc_2O_6Cu_2Se_2$ (92.7 %), whilst the blue, red and green tick marks represent refined impurity phases $Sr_3Sc_2O_5Cu_2Se_2$ (5.9 %), SrSe (0.5 %) and $SrCO_3$ (0.9 %) respectively.*
Duration: 3 hours. Data points: 4444. Interval: 0.02 °. GOF: 1.37. R_{wp}: 4.191 %.

B.2.5 Flash Annealed $(Sr_{3.9}Na_{0.1})Sc_2O_6Cu_2Se_2$

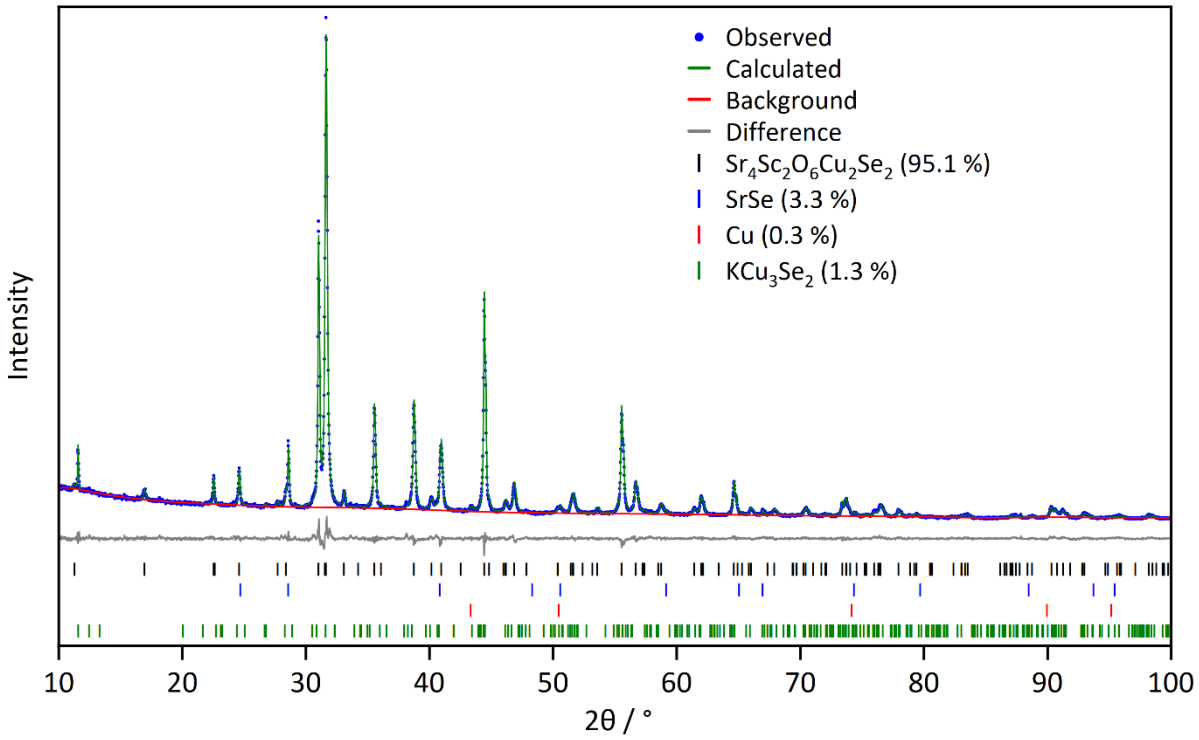

Figure 234 *Powder X-ray diffractogram of material with target composition $(Sr_{3.900}K_{0.100})Sc_2O_6Cu_2Se_2$ (space group P4/nmm) after 24 hours of heating at 550 °C and before flash annealing. The small blue circles represent the observed diffracted intensity, the green line represents the Rietveld-refined calculated model, the red line represents the background, and the grey line represents the difference between observed and calculated intensities. The black tick marks show the reflections of the refined model of $Sr_4Sc_2O_6Cu_2Se_2$ (95.1 %), whilst the blue, red and green tick marks represent refined impurity phases SrSe (3.3 %), Cu (0.3 %) and KCu_3Se_2 (1.3 %) respectively.*
Duration: 3 hours. Data points: 4444. Interval: 0.02 °. GOF: 1.60. R_{wp}: 4.126 %.

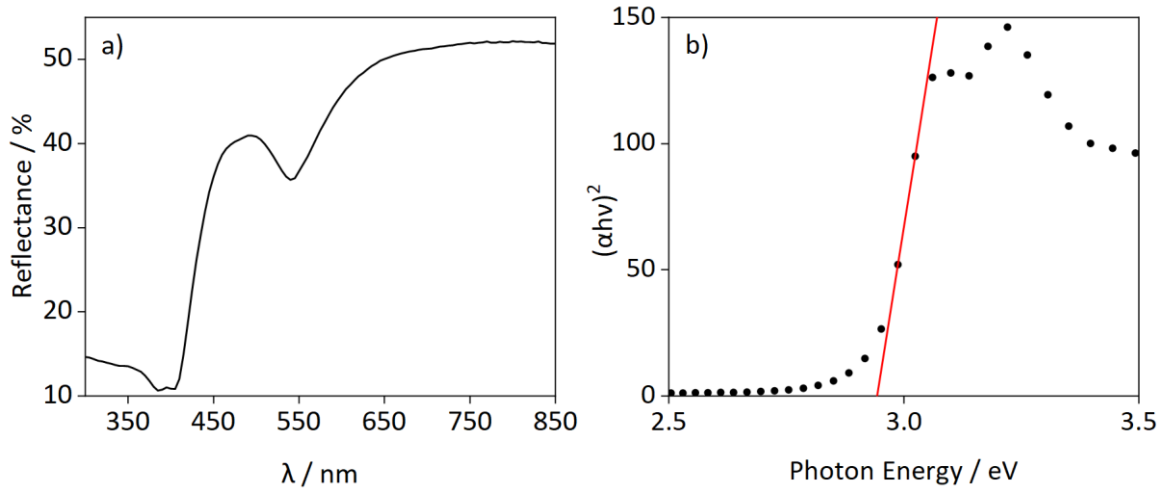

Figure 235 *UV-Vis spectrometry data for material with target composition $(Sr_{3.900}K_{0.100})Sc_2O_6Cu_2Se_2$ after 24 hours of heating at 550 °C. Plot a) is the raw diffuse reflectance data, and plot b) is the associated magnified Tauc plot for this region, where the intercept between the red extrapolated tangent line and the x-axis is used to estimate an optical band gap of 2.94 eV, which corresponds to 422 nm.*

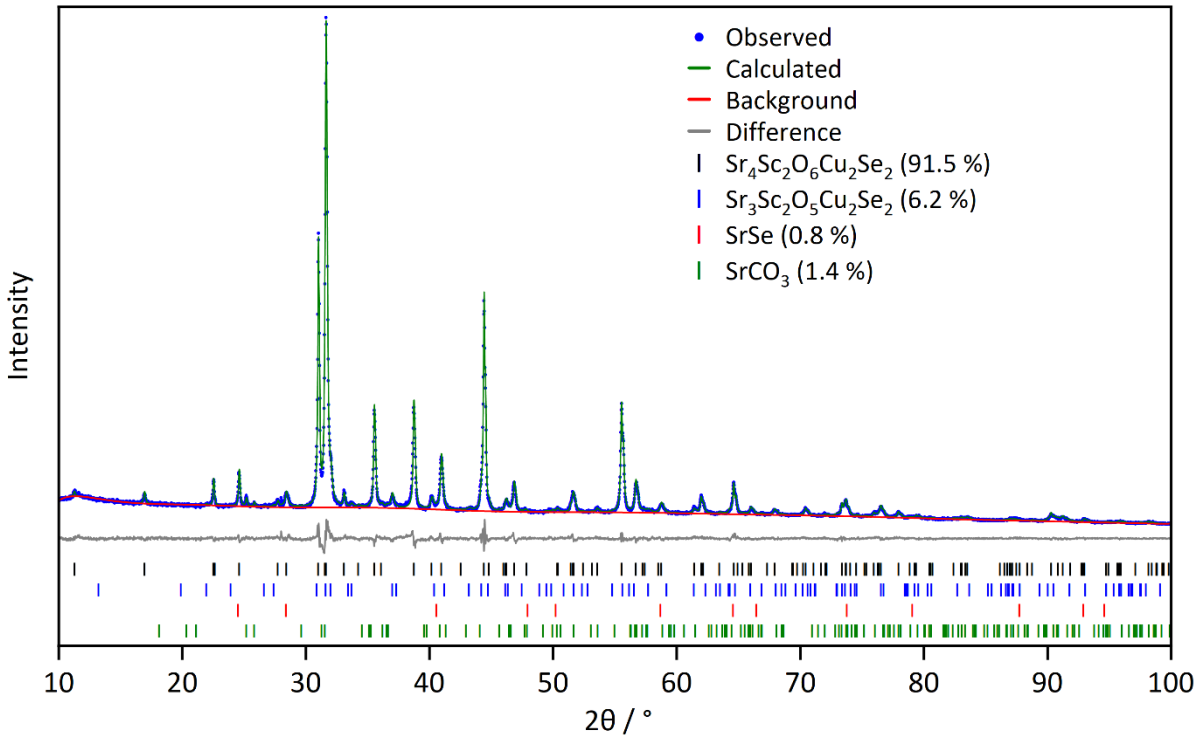

Figure 236 *Powder X-ray diffractogram of material with target composition $(Sr_{3.900}K_{0.100})Sc_2O_6Cu_2Se_2$ (space group P4/nmm) after 24 hours of heating at 550 °C after flash annealing for 30 minutes at 800 °C. The small blue circles represent the observed diffracted intensity, the green line represents the Rietveld-refined calculated model, the red line represents the background, and the grey line represents the difference between observed and calculated intensities. The black tick marks show the reflections of the refined model of $Sr_4Sc_2O_6Cu_2Se_2$ (91.5 %), whilst the blue, red and green tick marks represent refined impurity phases $Sr_3Sc_2O_5Cu_2Se_2$ (6.2 %), SrSe (0.8 %) and $SrCO_3$ (1.4 %) respectively.*
Duration: 3 hours. Data points: 4444. Interval: 0.02 °. GOF: 1.71. R_{wp}: 4.732 %.

B.2.6 Gallium Pristines

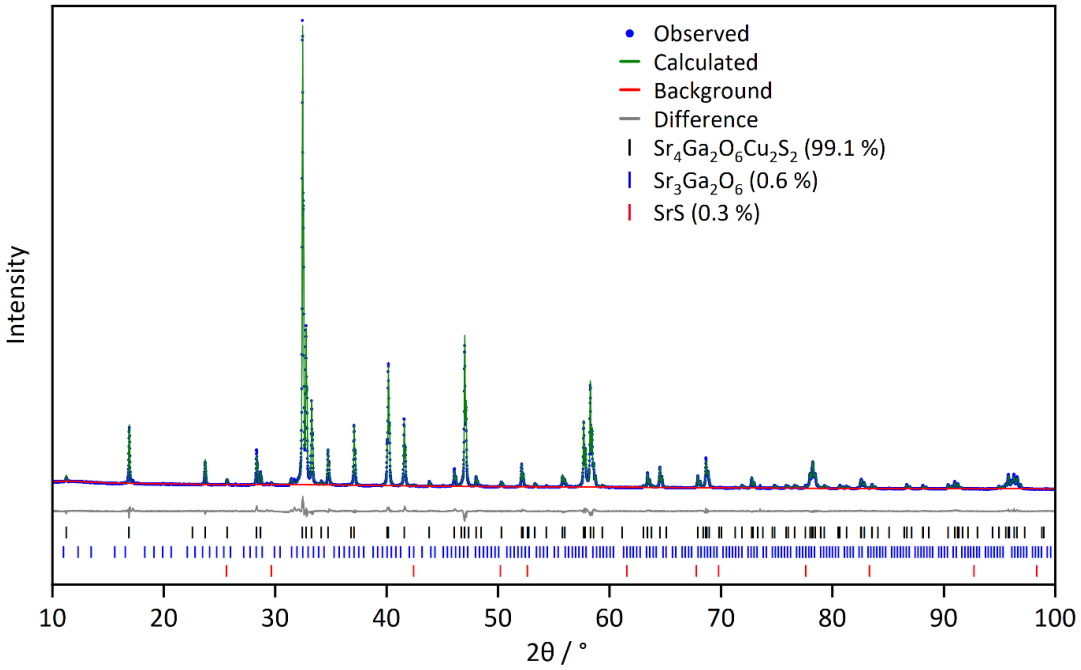

Figure 237 Powder X-ray diffractogram of material with target composition $Sr_4Ga_2O_6Cu_2S_2$ (space group P4/nmm) after 48 hours of heating at 700 °C. The small blue circles represent the observed diffracted intensity, the green line represents the Rietveld-refined calculated model, the red line represents the background, and the grey line represents the difference between observed and calculated intensities. The black tick marks show the reflections of the refined model of $Sr_4Ga_2O_6Cu_2S_2$ (99.1 %), whilst the blue and red tick marks represent refined impurity phases $Sr_3Ga_2O_6$ (0.6 %) and SrS (0.3 %) respectively.
Duration: 45 minutes. Data points: 3457. Interval: 0.02 °. GOF: 2.28. R_{wp}: 3.16 %.

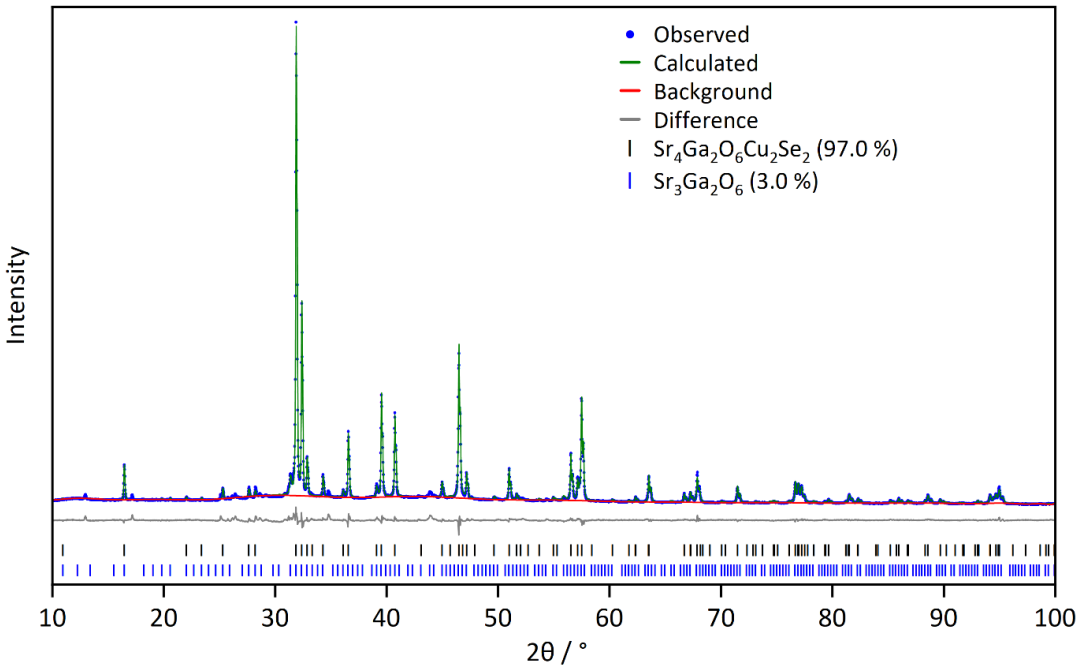

Figure 238 Powder X-ray diffractogram of material with target composition $Sr_4Ga_2O_6Cu_2Se_2$ (space group P4/nmm) after 48 hours of heating at 830 °C. The small blue circles represent the observed diffracted intensity, the green line represents the Rietveld-refined calculated model, the red line represents the background, and the grey line represents the difference between observed and calculated intensities. The black tick marks show the reflections of the refined model of $Sr_4Ga_2O_6Cu_2Se_2$ (97.0 %), whilst the blue tick marks represent refined impurity phase $Sr_3Ga_2O_6$ (3.0 %).
Duration: 45 minutes. Data points: 3457. Interval: 0.02 °. GOF: 3.72. R_{wp}: 3.30 %.

B.2.7 Indium Pristines

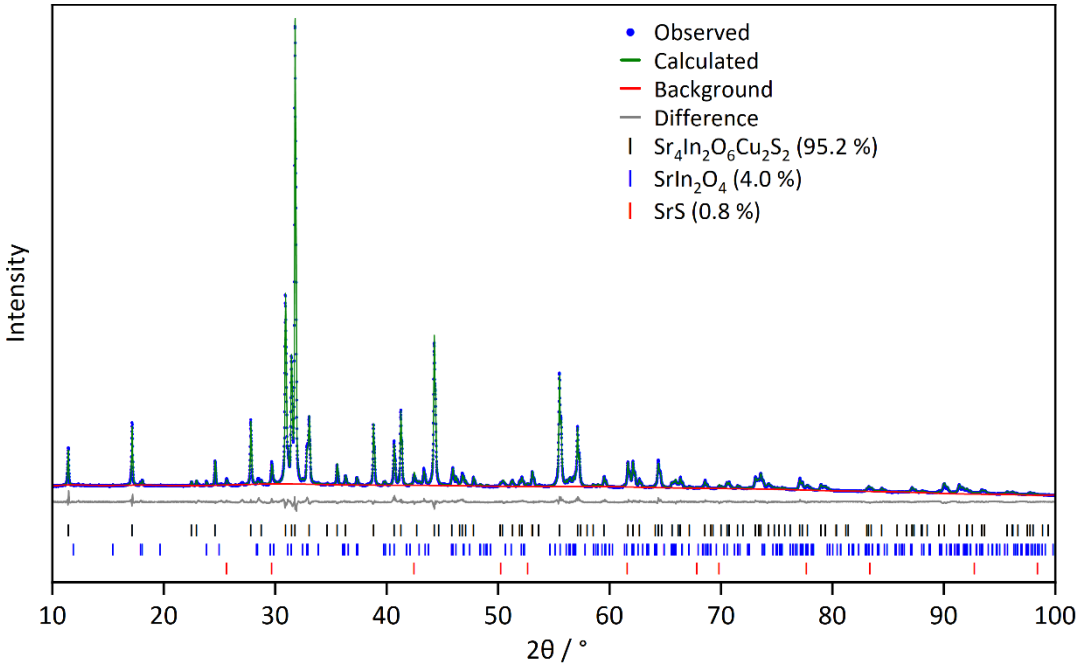

Figure 239 *Powder X-ray diffractogram of material with target composition $Sr_4In_2O_6Cu_2S_2$ (space group P4/nmm) after 48 hours of heating at 800 °C. The small blue circles represent the observed diffracted intensity, the green line represents the Rietveld-refined calculated model, the red line represents the background, and the grey line represents the difference between observed and calculated intensities. The black tick marks show the reflections of the refined model of $Sr_4In_2O_6Cu_2S_2$ (95.2 %), whilst the blue and red tick marks represent refined impurity phases $SrIn_2O_4$ (4.0 %) and SrS (0.8 %) respectively.*
Duration: 45 minutes. Data points: 3457. Interval: 0.02 °. GOF: 2.09. R_{wp}: 2.811 %.

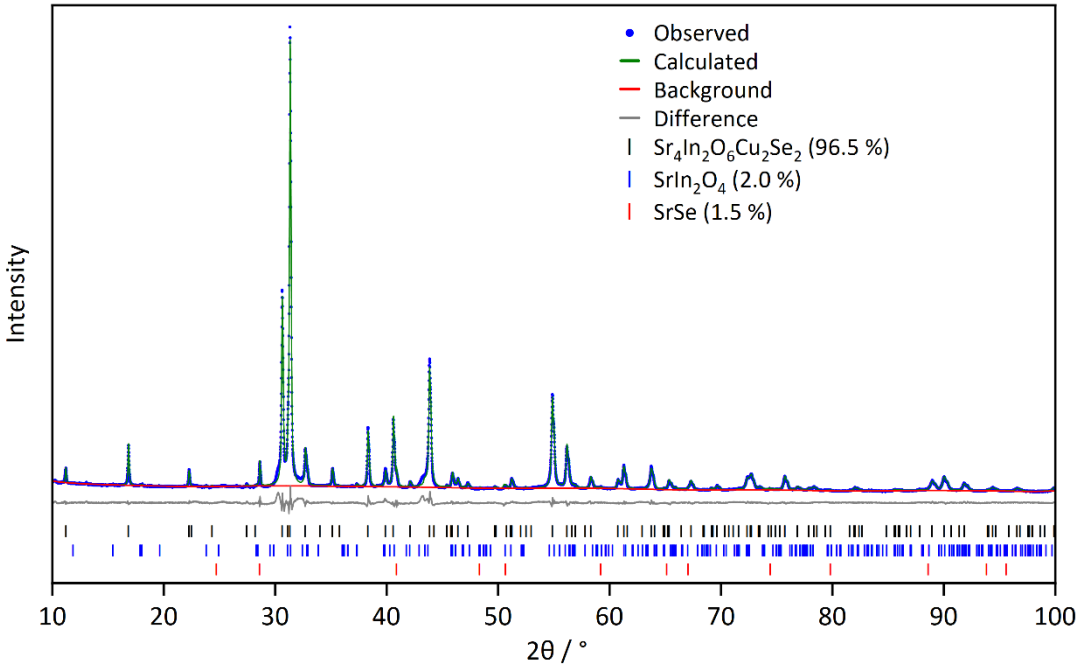

Figure 240 *Powder X-ray diffractogram of material with target composition $Sr_4In_2O_6Cu_2Se_2$ (space group P4/nmm) after 48 hours of heating at 700 °C. The small blue circles represent the observed diffracted intensity, the green line represents the Rietveld-refined calculated model, the red line represents the background, and the grey line represents the difference between observed and calculated intensities. The black tick marks show the reflections of the refined model of $Sr_4In_2O_6Cu_2Se_2$ (96.5 %), whilst the blue and red tick marks represent refined impurity phases $SrIn_2O_4$ (2.0 %) and SrSe (1.5 %) respectively.*
Duration: 45 minutes. Data points: 3457. Interval: 0.02 °. GOF: 3.07. R_{wp}: 4.01 %.

B.3 Materials from Chapter 5

B.3.1 Light Layer Precursors

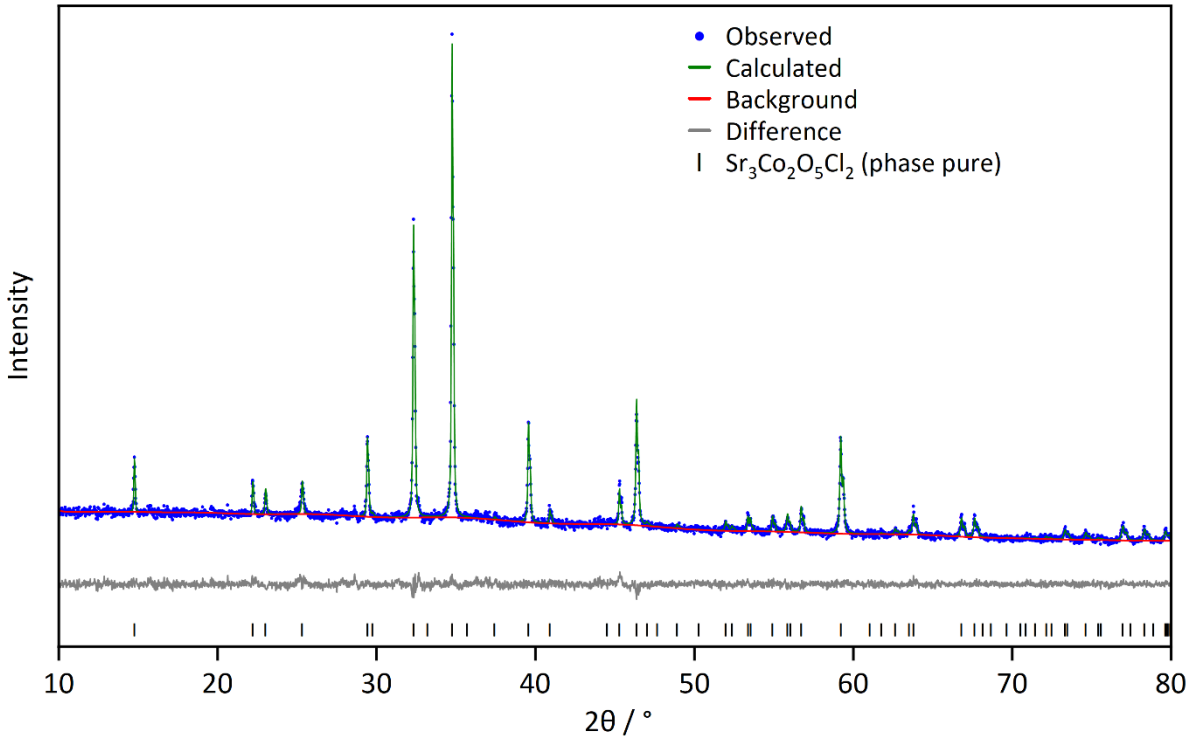

Figure 241 Powder X-ray diffractogram of material with target composition $Sr_3Co_2O_5Cl_2$ (space group I4/mmm) after 96 hours of heating at 800 to 900 °C. The small blue circles represent the observed diffracted intensity, the green line represents the Rietveld-refined calculated model, the red line represents the background, and the grey line represents the difference between observed and calculated intensities. The black tick marks show the reflections of the refined model of $Sr_3Co_2O_5Cl_2$, no impurity phases are observed.
Duration: 45 minutes. Data points: 3457. Interval: 0.02 °. GOF: 1.20. R_{wp}: 2.849 %.

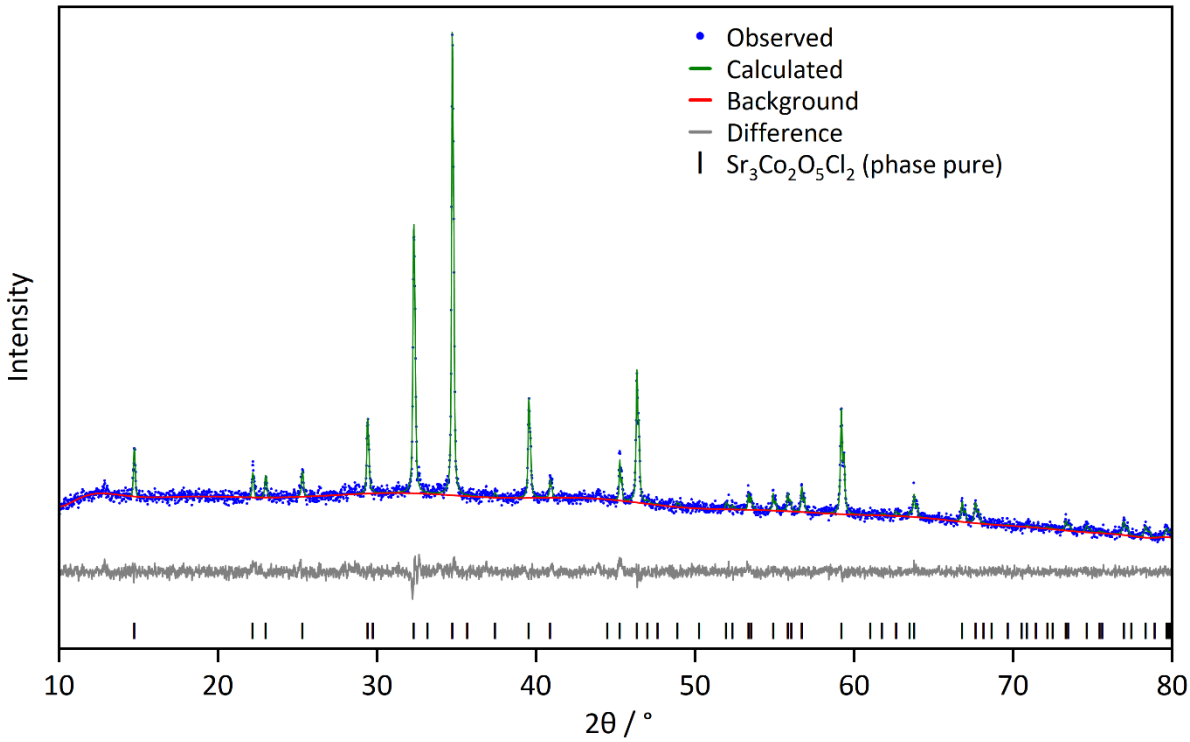

Figure 242 *Powder X-ray diffractogram of material with target composition $Sr_3Co_2O_5Cl_2$ (space group I4/mmm) after 96 hours of heating at 500 to 850 °C using the alternative peroxide method. The small blue circles represent the observed diffracted intensity, the green line represents the Rietveld-refined calculated model, the red line represents the background, and the grey line represents the difference between observed and calculated intensities. The black tick marks show the reflections of the refined model of $Sr_3Co_2O_5Cl_2$, no impurity phases are observed.*
Duration: 45 minutes. Data points: 3456. Interval: 0.02 °. GOF: 1.10. R_{wp}: 3.265 %.

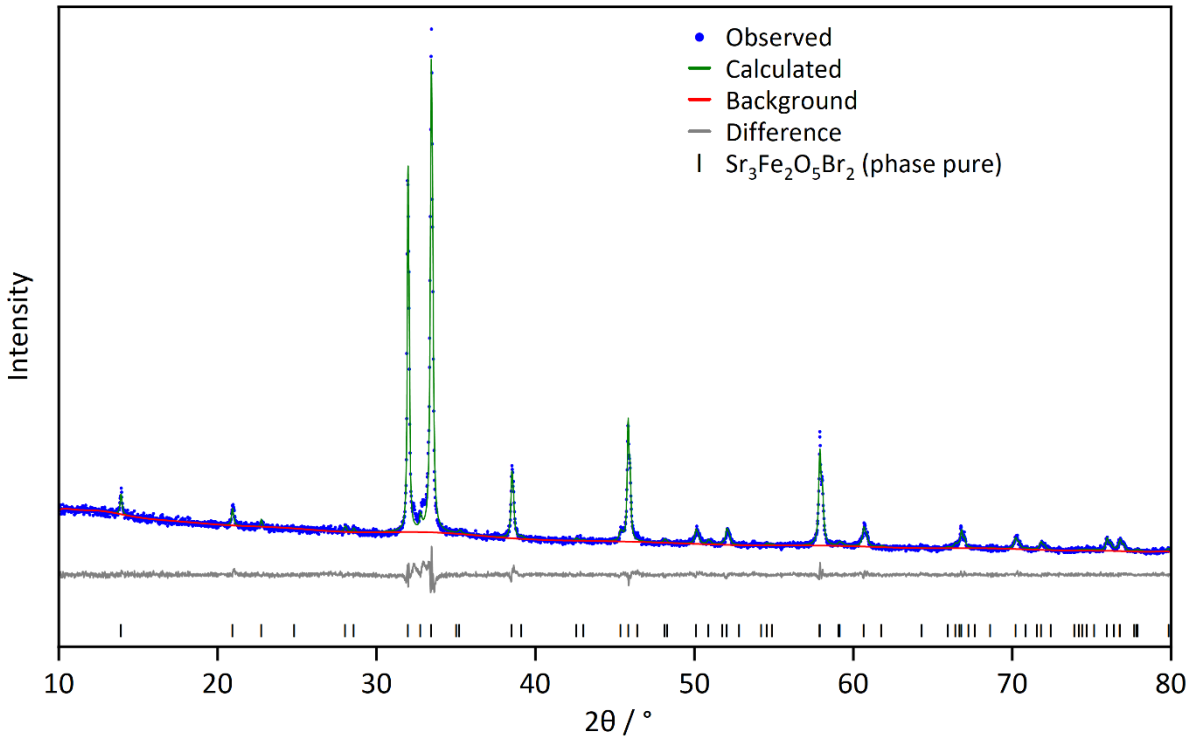

Figure 243 *Powder X-ray diffractogram of material with target composition $Sr_3Fe_2O_5Br_2$ (space group I4/mmm) after 72 hours of heating at 850 °C. The small blue circles represent the observed diffracted intensity, the green line represents the Rietveld-refined calculated model, the red line represents the background, and the grey line represents the difference between observed and calculated intensities. The black tick marks show the reflections of the refined model of $Sr_3Fe_2O_5Br_2$, no impurity phases are observed.*
Duration: 45 minutes. Data points: 3457. Interval: 0.02 °. GOF: 1.43. R_{wp}: 5.344 %.

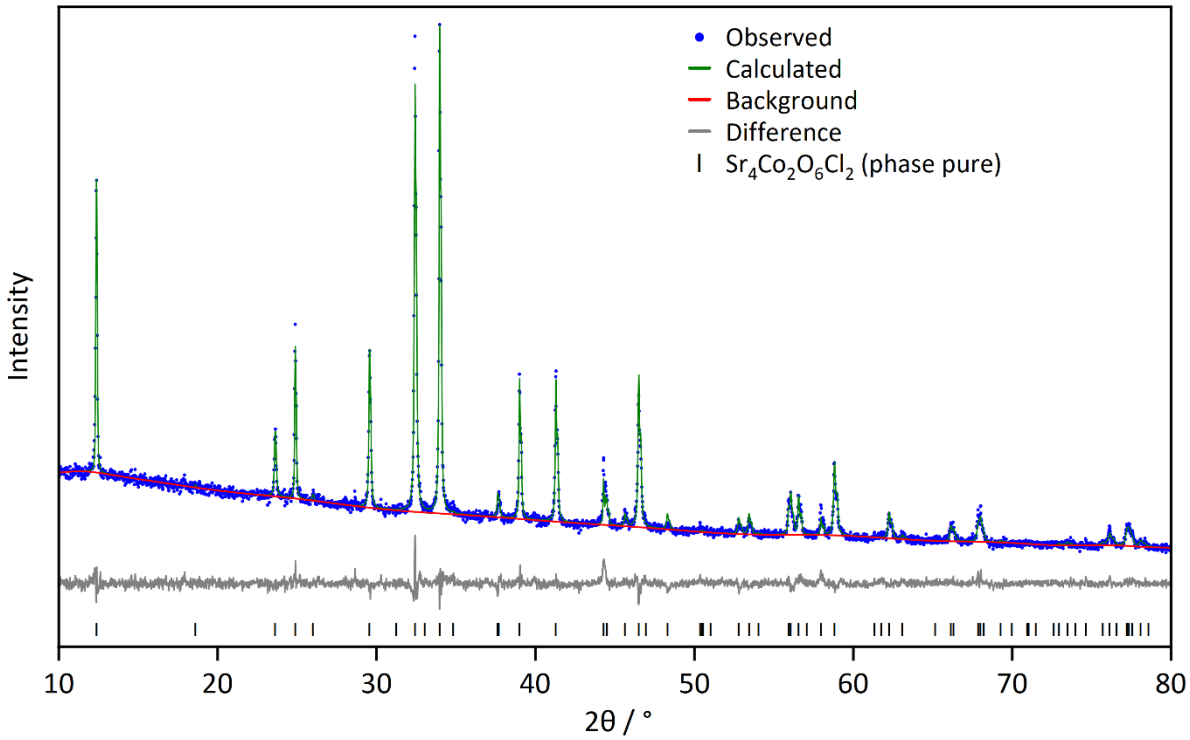

Figure 244 *Powder X-ray diffractogram of material with target composition $Sr_4Co_2O_6Cl_2$ (space group I4/mmm) after 72 hours of heating at 800 to 900 °C. The small blue circles represent the observed diffracted intensity, the green line represents the Rietveld-refined calculated model, the red line represents the background, and the grey line represents the difference between observed and calculated intensities. The black tick marks show the reflections of the refined model of $Sr_4Co_2O_6Cl_2$, no impurity phases are observed.*
Duration: 45 minutes. Data points: 3457. Interval: 0.02 °. GOF: 1.34. R_{wp}: 3.617 %.

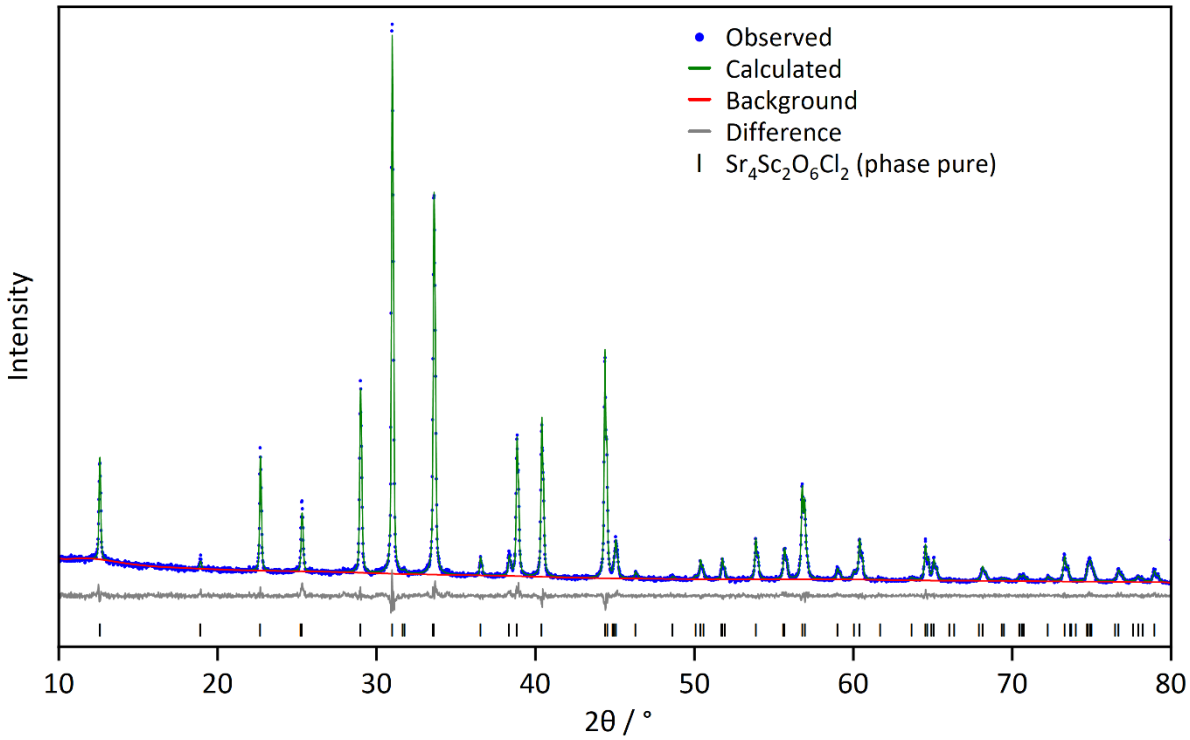

Figure 245 *Powder X-ray diffractogram of material with target composition $Sr_4Sc_2O_6Cl_2$ (space group I4/mmm) after 96 hours of heating at 500 to 1050 °C. The small blue circles represent the observed diffracted intensity, the green line represents the Rietveld-refined calculated model, the red line represents the background, and the grey line represents the difference between observed and calculated intensities. The black tick marks show the reflections of the refined model of $Sr_4Sc_2O_6Cl_2$, no impurity phases are observed.*
Duration: 45 minutes. Data points: 3457. Interval: 0.02 °. GOF: 1.16. R_{wp}: 6.118 %.

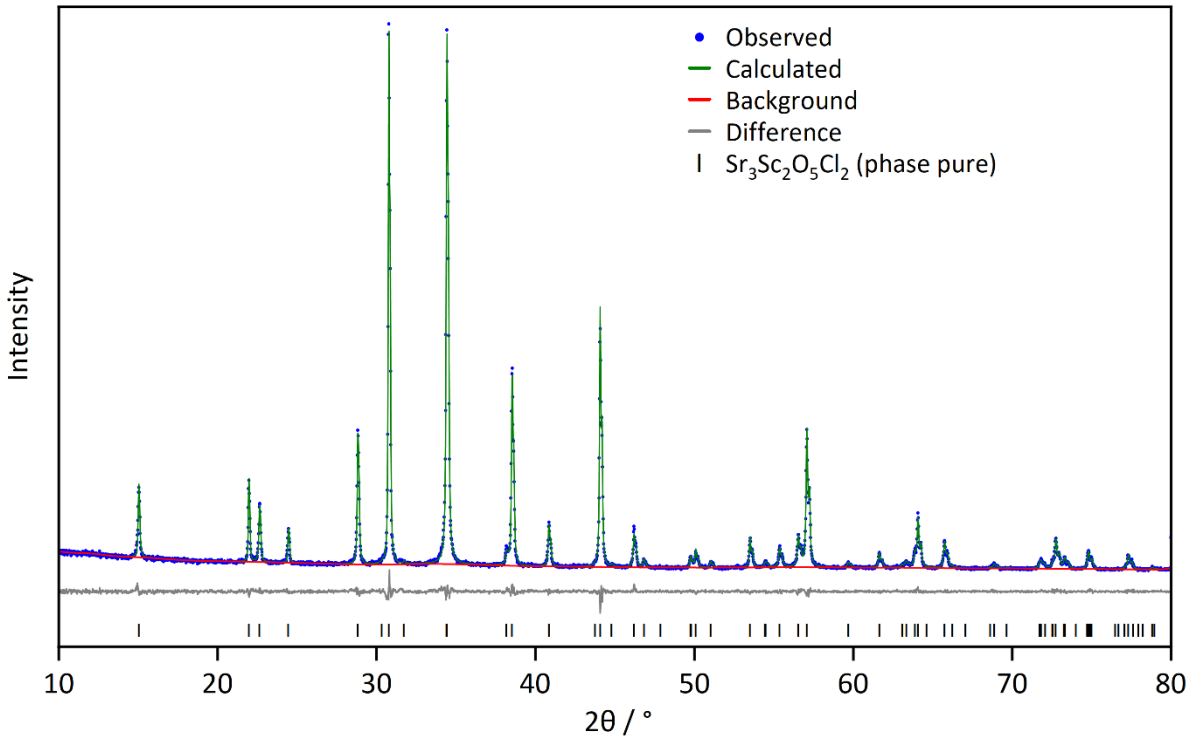

Figure 246 *Powder X-ray diffractogram of material with target composition $Sr_3Sc_2O_5Cl_2$ (space group I4/mmm) after 96 hours of heating at 500 to 1050 °C. The small blue circles represent the observed diffracted intensity, the green line represents the Rietveld-refined calculated model, the red line represents the background, and the grey line represents the difference between observed and calculated intensities. The black tick marks show the reflections of the refined model of $Sr_3Sc_2O_5Cl_2$, no impurity phases are observed.*
Duration: 45 minutes. Data points: 3457. Interval: 0.02 °. GOF: 1.17. R_{wp}: 6.082 %.

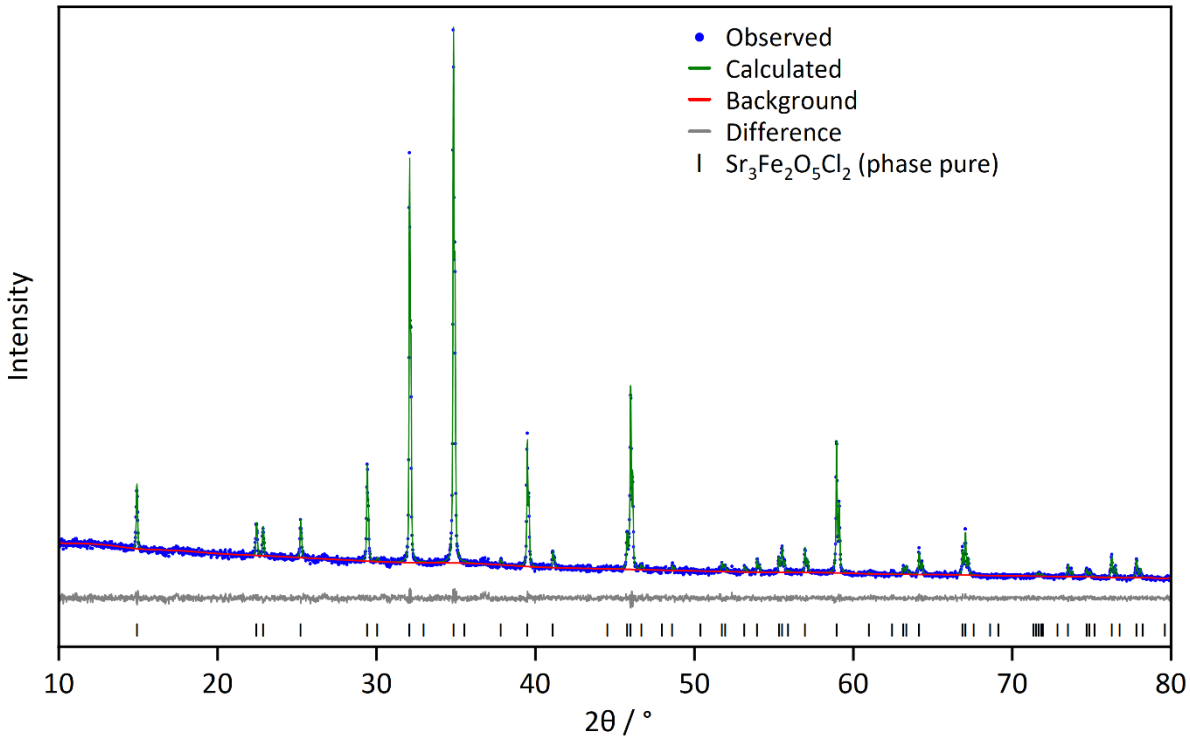

Figure 247 *Powder X-ray diffractogram of material with target composition $Sr_3Fe_2O_5Cl_2$ (space group I4/mmm) after 72 hours of heating at 600-850 °C. The small blue circles represent the observed diffracted intensity, the green line represents the Rietveld-refined calculated model, the red line represents the background, and the grey line represents the difference between observed and calculated intensities. The black tick marks show the reflections of the refined model of $Sr_3Fe_2O_5Cl_2$, no impurity phases are observed.*
Duration: 45 minutes. Data points: 3457. Interval: 0.02 °. GOF: 1.07. R_{wp}: 3.972 %.

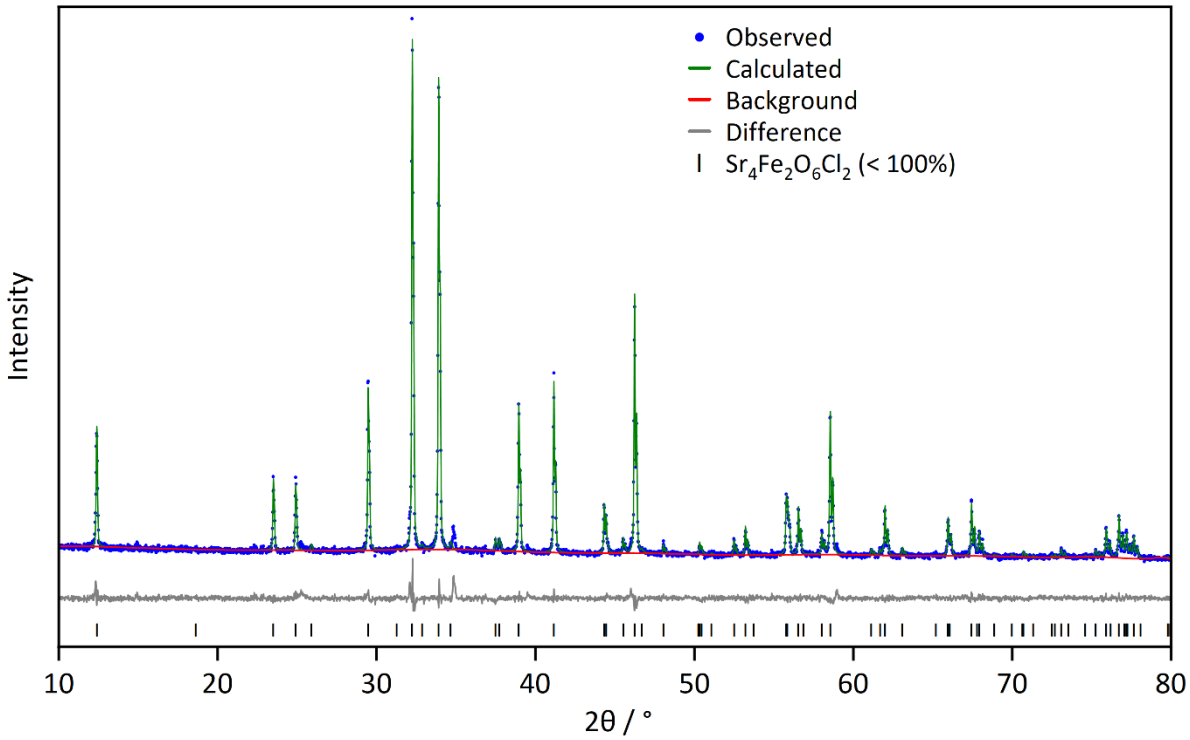

Figure 248 *Powder X-ray diffractogram of material with target composition $Sr_4Fe_2O_6Cl_2$ (space group I4/mmm) after 72 hours of heating at 600-850 °C. The small blue circles represent the observed diffracted intensity, the green line represents the Rietveld-refined calculated model, the red line represents the background, and the grey line represents the difference between observed and calculated intensities. The black tick marks show the reflections of the refined model of $Sr_4Fe_2O_6Cl_2$. A small unknown impurity is present in the material. Duration: 45 minutes. Data points: 3457. Interval: 0.02 °. GOF: 1.35. R_{wp}: 4.381 %.*

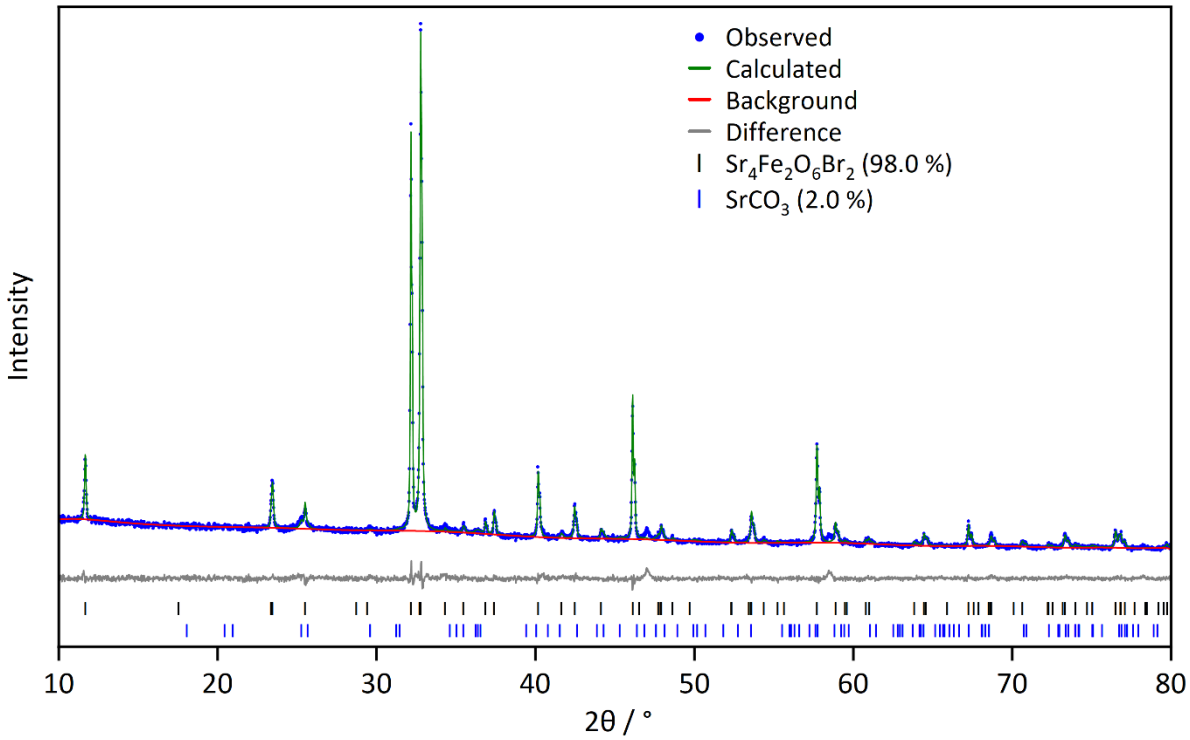

Figure 249 *Powder X-ray diffractogram of material with target composition $Sr_4Fe_2O_6Br_2$ (space group I4/mmm) after 72 hours of heating at 600-850 °C. The small blue circles represent the observed diffracted intensity, the green line represents the Rietveld-refined calculated model, the red line represents the background, and the grey line represents the difference between observed and calculated intensities. The black tick marks show the reflections of the refined model of $Sr_4Fe_2O_6Br_2$ (98.0 %), whilst the blue marks represent refined impurity phase $SrCO_3$ (2.0 %).*
Duration: 45 minutes. Data points: 3457. Interval: 0.02 °. GOF: 1.28. R_{wp}: 4.142 %.

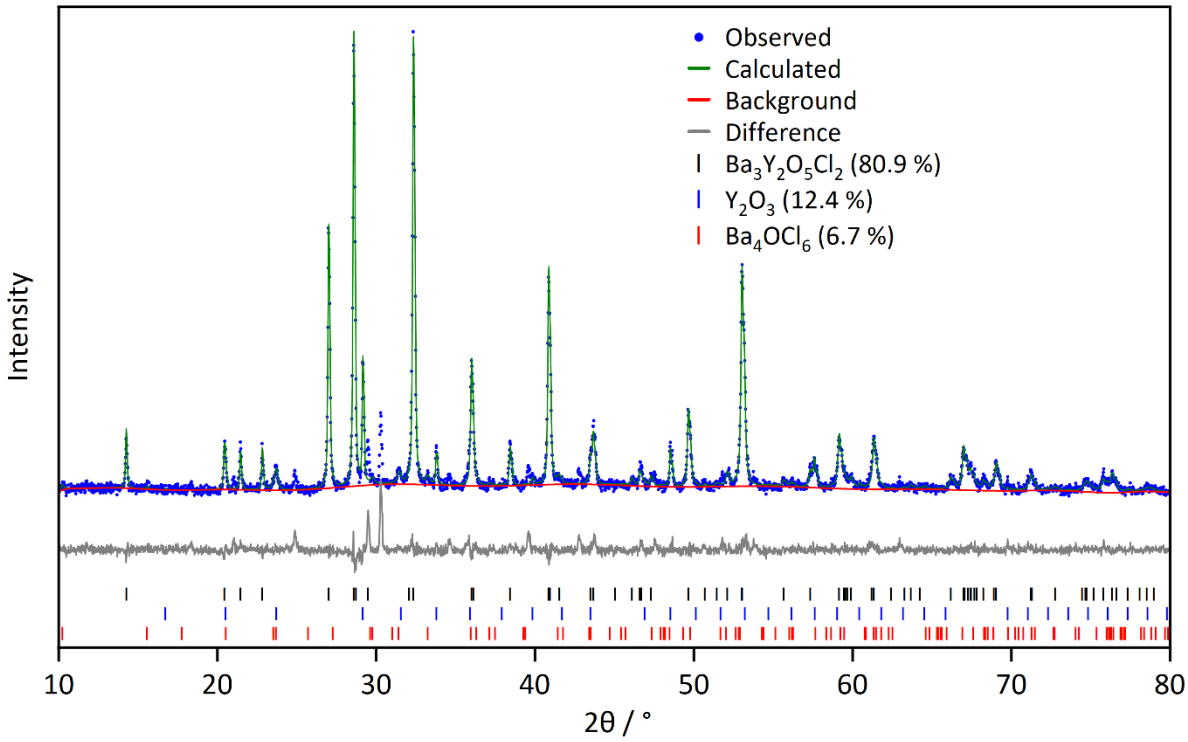

Figure 250 *Powder X-ray diffractogram of material with target composition $Ba_3Y_2O_5Cl_2$ (space group I4/mmm) after 96 hours of heating at 900 to 1050 °C. The small blue circles represent the observed diffracted intensity, the green line represents the Rietveld-refined calculated model, the red line represents the background, and the grey line represents the difference between observed and calculated intensities. The black tick marks show the reflections of the refined model of $Ba_3Y_2O_5Cl_2$ (80.9 %), whilst the blue and red marks represent refined impurity phases Y_2O_3 (12.4 %) and Ba_4OCl_6 (6.7 %) respectively.*
Duration: 45 minutes. Data points: 3457. Interval: 0.02 °. GOF: 1.55. R_{wp}: 8.979 %.

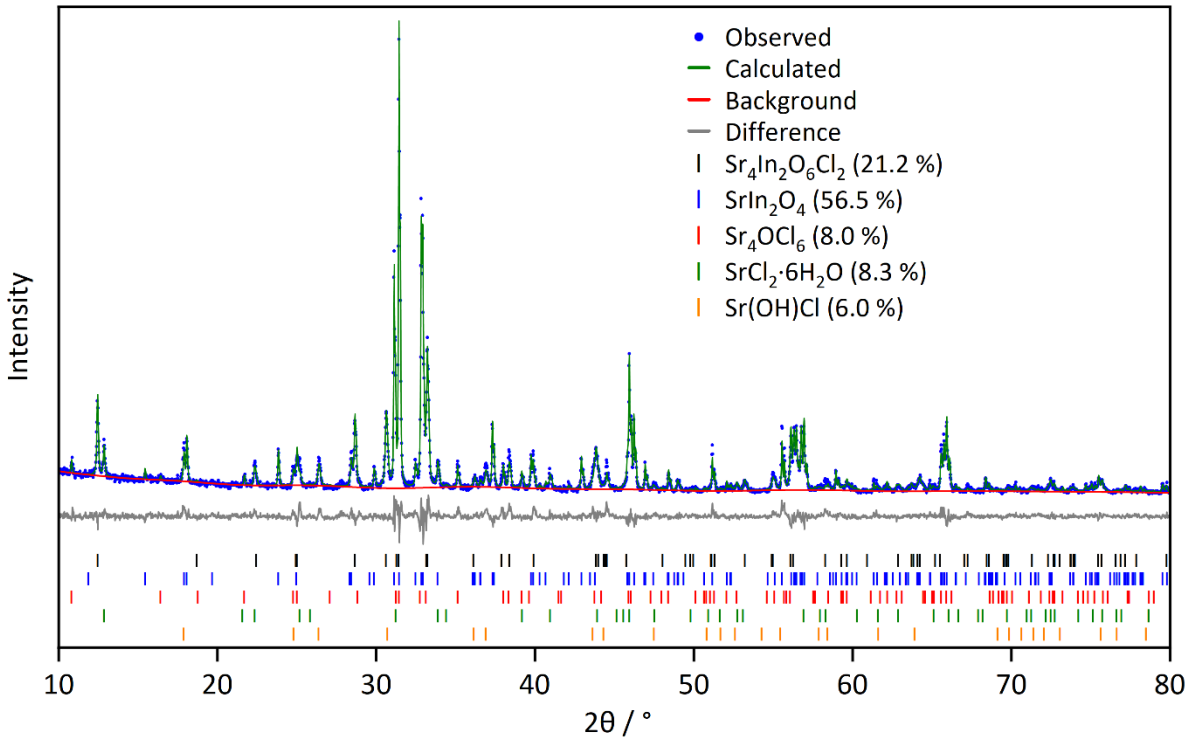

Figure 251 *Powder X-ray diffractogram of material with target composition $Sr_3In_2O_5Cl_2$ (space group I4/mmm) after 36 hours of heating at 700 to 1000 °C. The small blue circles represent the observed diffracted intensity, the green line represents the Rietveld-refined calculated model, the red line represents the background, and the grey line represents the difference between observed and calculated intensities. The black, blue, red, green and orange tick marks show the reflections of the refined models of $Sr_4In_2O_6Cl_2$ (21.2 %), $SrIn_2O_4$ (56.5 %), Sr_4OCl_6 (8.0 %), $SrCl_2{\cdot}6H_2O$ (8.3 %) and Sr(OH)Cl (6.0 %) respectively.*
Duration: 45 minutes. Data points: 3457. Interval: 0.02 °. GOF: 1.48. R_{wp}: 10.350 %.

B.3.2 Heavy Layer Precursors

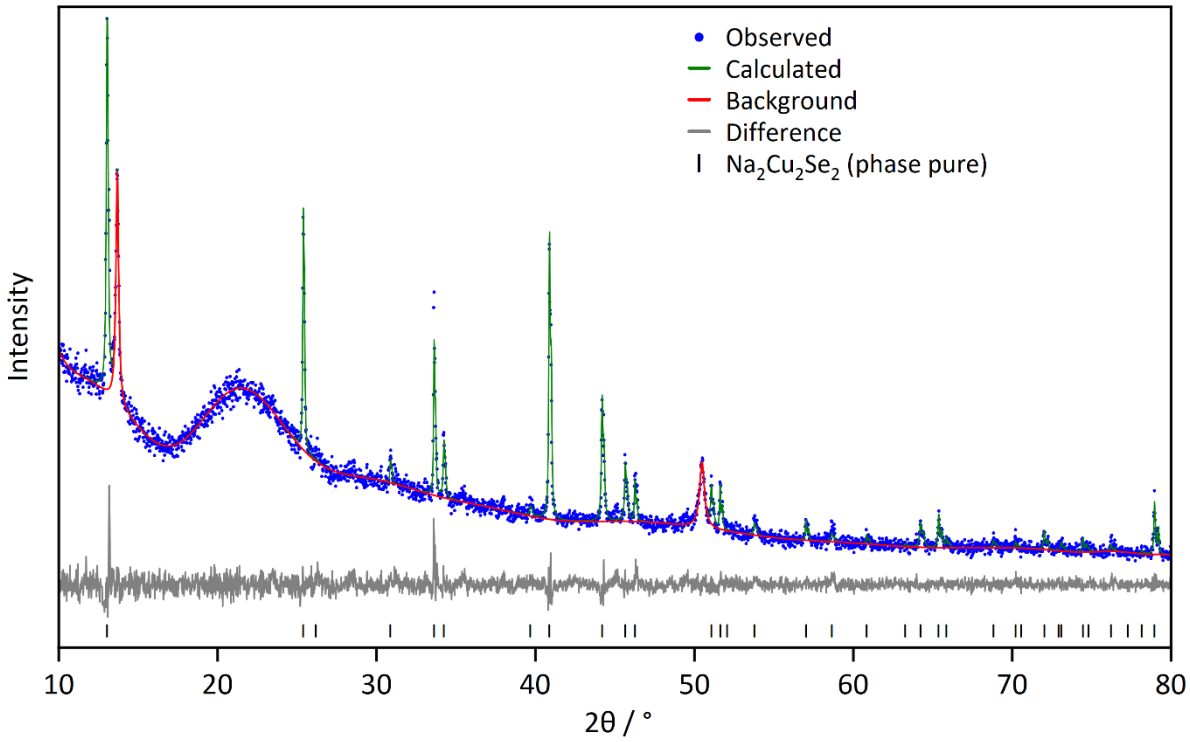

Figure 252 Powder X-ray diffractogram of material with target composition $Na_2Cu_2Se_2$ (space group I4/mmmZ) after 24 hours of heating at 800 °C. The small blue circles represent the observed diffracted intensity, the green line represents the Rietveld-refined calculated model, the red line represents the background, and the grey line represents the difference between observed and calculated intensities. The black tick marks show the reflections of the refined model of $Na_2Cu_2Se_2$, no impurity phases are observed. Data was collected with the domed air-tight holder, responsible for the background-refined peaks at 13.3 and 50.5 °.
Duration: 10 minutes. Data points: 3457. Interval: 0.02 °. GOF: 1.15. R_{wp}: 5.847 %.

B.3.3 $Sr_3Sc_2O_5Cu_2Se_2$ Metathesis Investigation

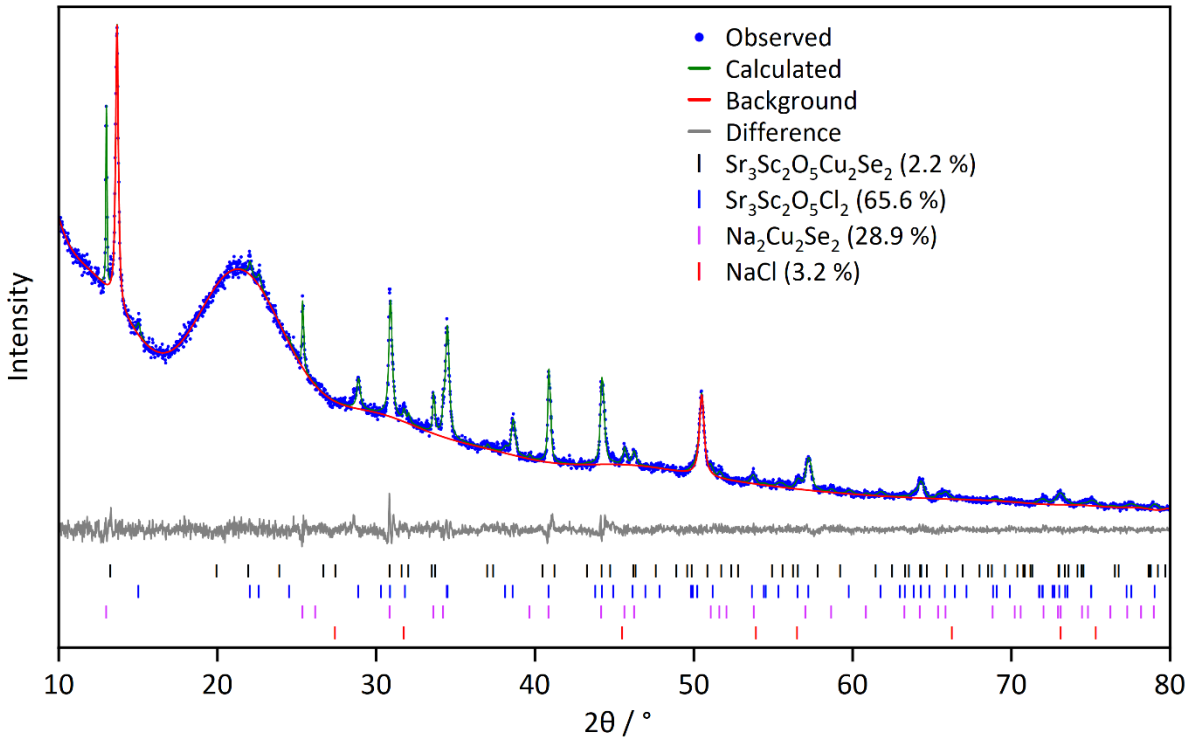

Figure 253 *Powder X-ray diffractograms of materials resulting from attempted metathesis synthesis of $Sr_3Sc_2O_5Cu_2Se_2$ after 12 hours of heating at a) 500 °C and b) 800 °C. The small blue circles represent the observed diffracted intensity, the green line represents the Rietveld-refined calculated model, the red line represents the background, and the grey line represents the difference between observed and calculated intensities. The black, blue, pink, green, orange and red tick marks show the reflections of the refined models of $Sr_3Sc_2O_5Cu_2Se_2$, $Sr_3Sc_2O_5Cl_2$, $Na_2Cu_2Se_2$, SrSe, $NaCu_3Se_2$ and NaCl respectively. Weight fractions for each phase are cited in the figure legends. Data was collected with the domed air-tight holder, responsible for the background-refined peaks at 13.3 and 50.5 °.*
Duration: 45 minutes. Data points: 3457. Interval: 0.02 °. GOF: 1.28. R_{wp}: 2.945 %.

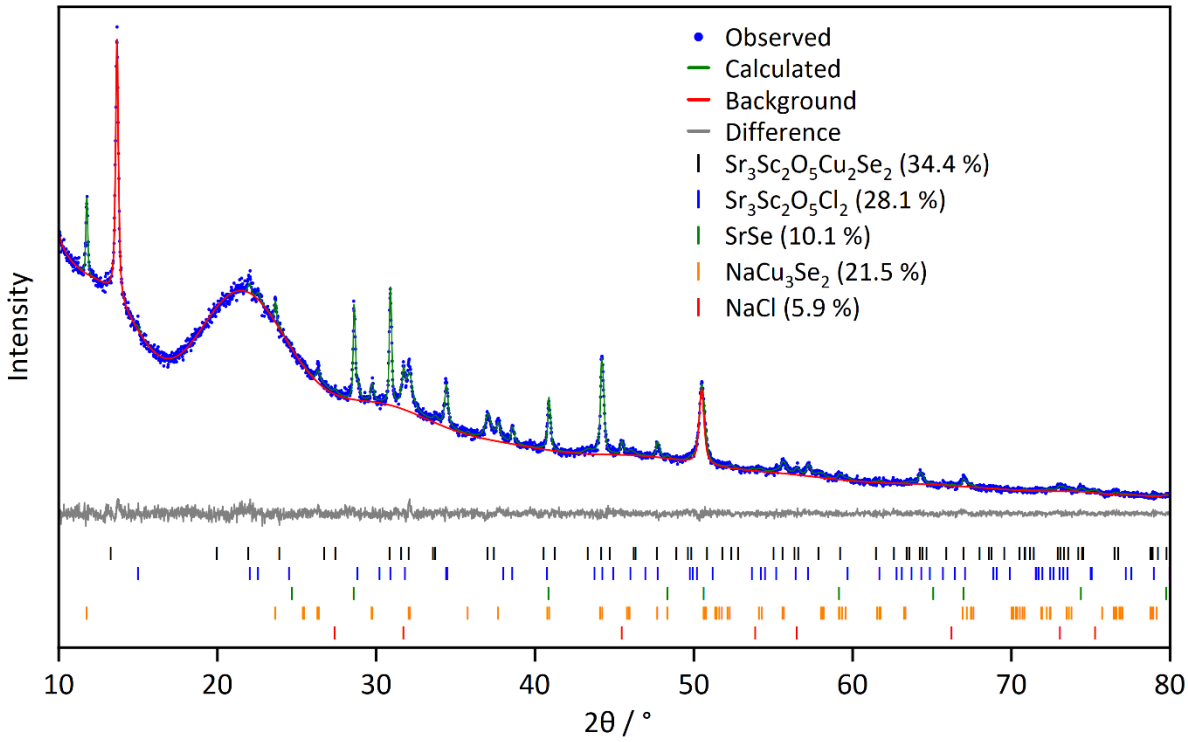

Figure 254 *Powder X-ray diffractogram of material resulting from attempted metathesis synthesis of $Sr_3Sc_2O_5Cu_2Se_2$ (space group I4/mmm) after 12 hours of heating at 600 °C. The small blue circles represent the observed diffracted intensity, the green line represents the Rietveld-refined calculated model, the red line represents the background, and the grey line represents the difference between observed and calculated intensities. The black, blue, green, orange and red tick marks show the reflections of the refined models of $Sr_3Sc_2O_5Cu_2Se_2$ (34.4 %), $Sr_3Sc_2O_5Cl_2$ (28.1 %), SrSe (10.1 %), $NaCu_3Se_2$ (21.5 %) and NaCl (5.9 %) respectively. Data was collected with the domed air-tight holder, responsible for the background-refined peaks at 13.3 and 50.5 °.*
Duration: 45 minutes. Data points: 3457. Interval: 0.02 °. GOF: 1.09. R_{wp}: 2.546 %.

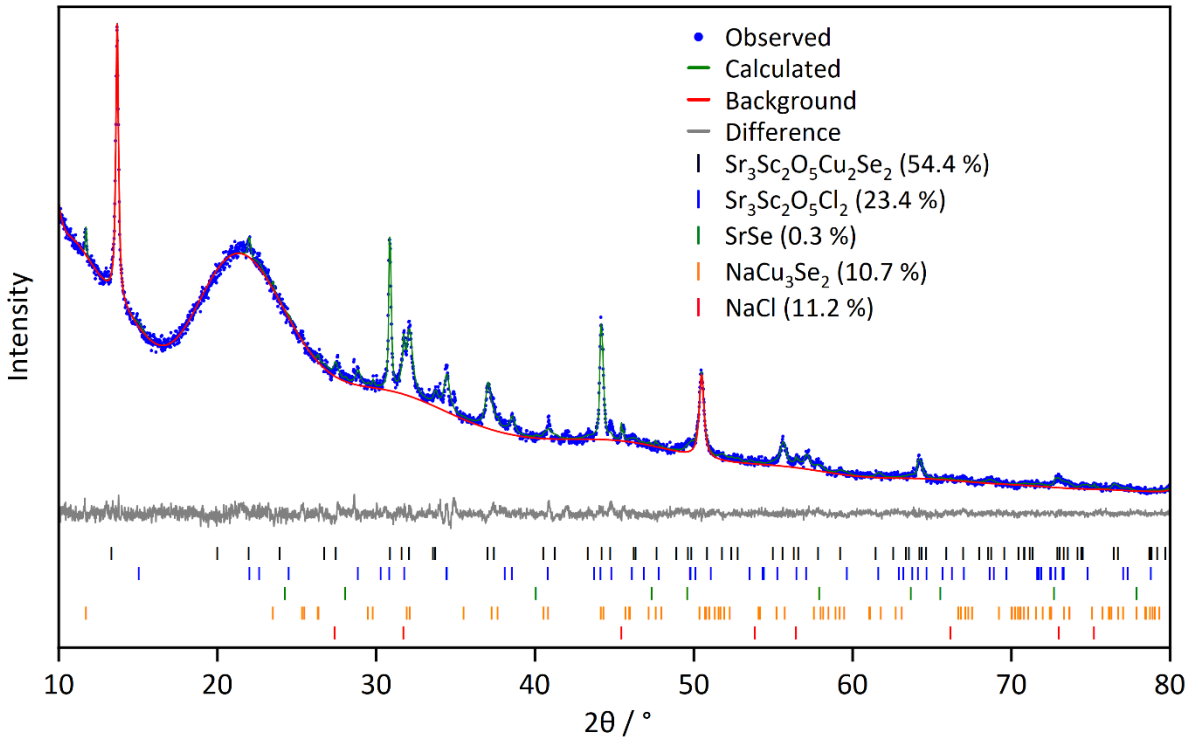

Figure 255 *Powder X-ray diffractogram of material resulting from attempted metathesis synthesis of $Sr_3Sc_2O_5Cu_2Se_2$ (space group I4/mmm) after 12 hours of heating at 700 °C. The small blue circles represent the observed diffracted intensity, the green line represents the Rietveld-refined calculated model, the red line represents the background, and the grey line represents the difference between observed and calculated intensities. The black, blue, green, orange and red tick marks show the reflections of the refined models of $Sr_3Sc_2O_5Cu_2Se_2$ (54.4 %), $Sr_3Sc_2O_5Cl_2$ (23.4 %), SrSe (0.3 %), $NaCu_3Se_2$ (10.7 %) and NaCl (11.2 %) respectively. Data was collected with the domed air-tight holder, responsible for the background-refined peaks at 13.3 and 50.5 °.*
Duration: 45 minutes. Data points: 3457. Interval: 0.02 °. GOF: 1.26. R_{wp}: 2.894 %.

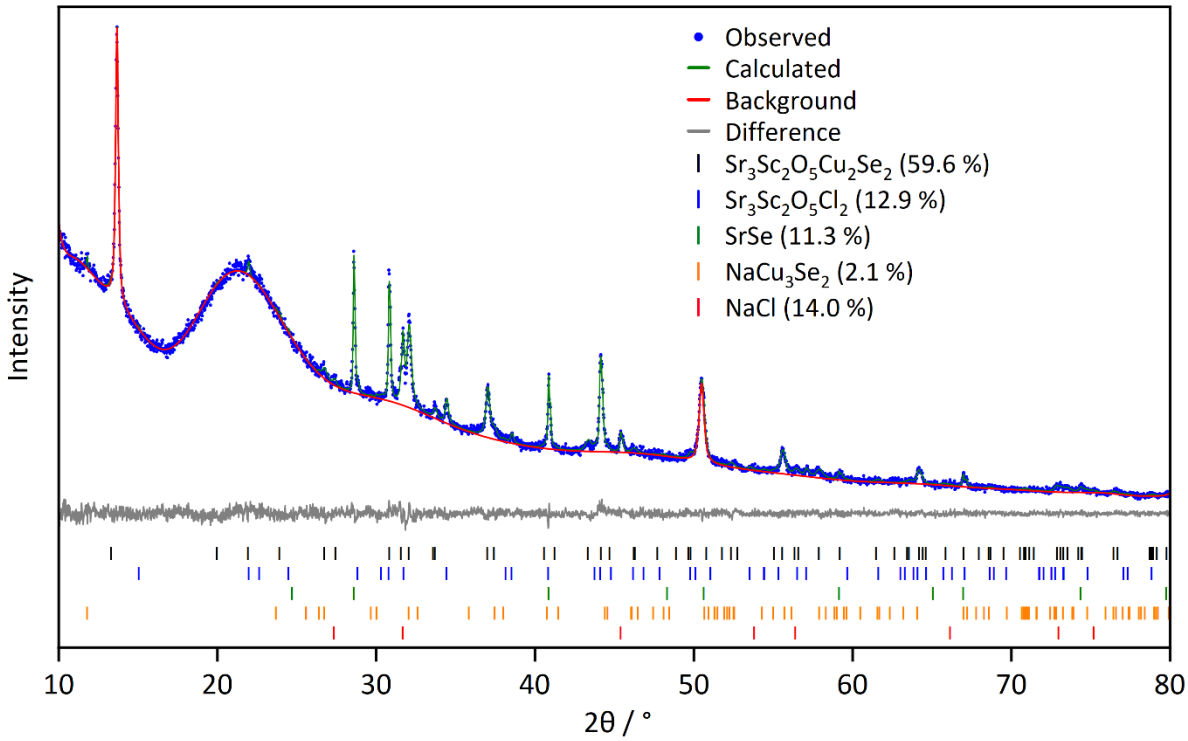

Figure 256 *Powder X-ray diffractogram of material resulting from attempted metathesis synthesis of $Sr_3Sc_2O_5Cu_2Se_2$ (space group I4/mmm) after 12 hours of heating at 800 °C. The small blue circles represent the observed diffracted intensity, the green line represents the Rietveld-refined calculated model, the red line represents the background, and the grey line represents the difference between observed and calculated intensities. The black, blue, green, orange and red tick marks show the reflections of the refined models of $Sr_3Sc_2O_5Cu_2Se_2$ (59.6 %), $Sr_3Sc_2O_5Cl_2$ (12.9 %), SrSe (11.3 %), $NaCu_3Se_2$ (2.1 %) and NaCl (14.0 %) respectively. Data was collected with the domed air-tight holder, responsible for the background-refined peaks at 13.3 and 50.5 °.*
Duration: 45 minutes. Data points: 3457. Interval: 0.02 °. GOF: 1.17. R_{wp}: 2.779 %.

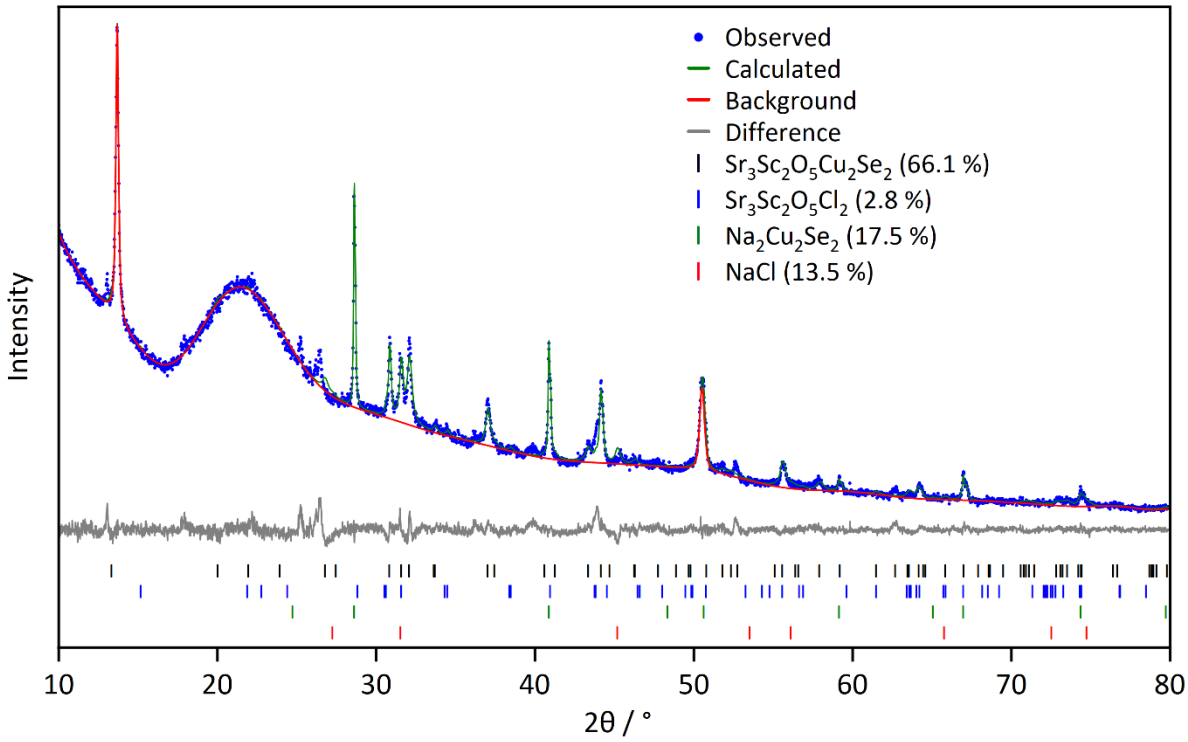

Figure 257 *Powder X-ray diffractogram of material resulting from attempted metathesis synthesis of $Sr_3Sc_2O_5Cu_2Se_2$ (space group I4/mmm) after 12 hours of heating at 900 °C. The small blue circles represent the observed diffracted intensity, the green line represents the Rietveld-refined calculated model, the red line represents the background, and the grey line represents the difference between observed and calculated intensities. The black, blue, green and red tick marks show the reflections of the refined models of $Sr_3Sc_2O_5Cu_2Se_2$ (66.1 %), $Sr_3Sc_2O_5Cl_2$ (2.8 %), SrSe (17.5 %) and NaCl (13.5 %) respectively. Data was collected with the domed air-tight holder, responsible for the background-refined peaks at 13.3 and 50.5 °*

Duration: 45 minutes. Data points: 3457. Interval: 0.02 °. GOF: 1.57. R_{wp}: 3.765 %.

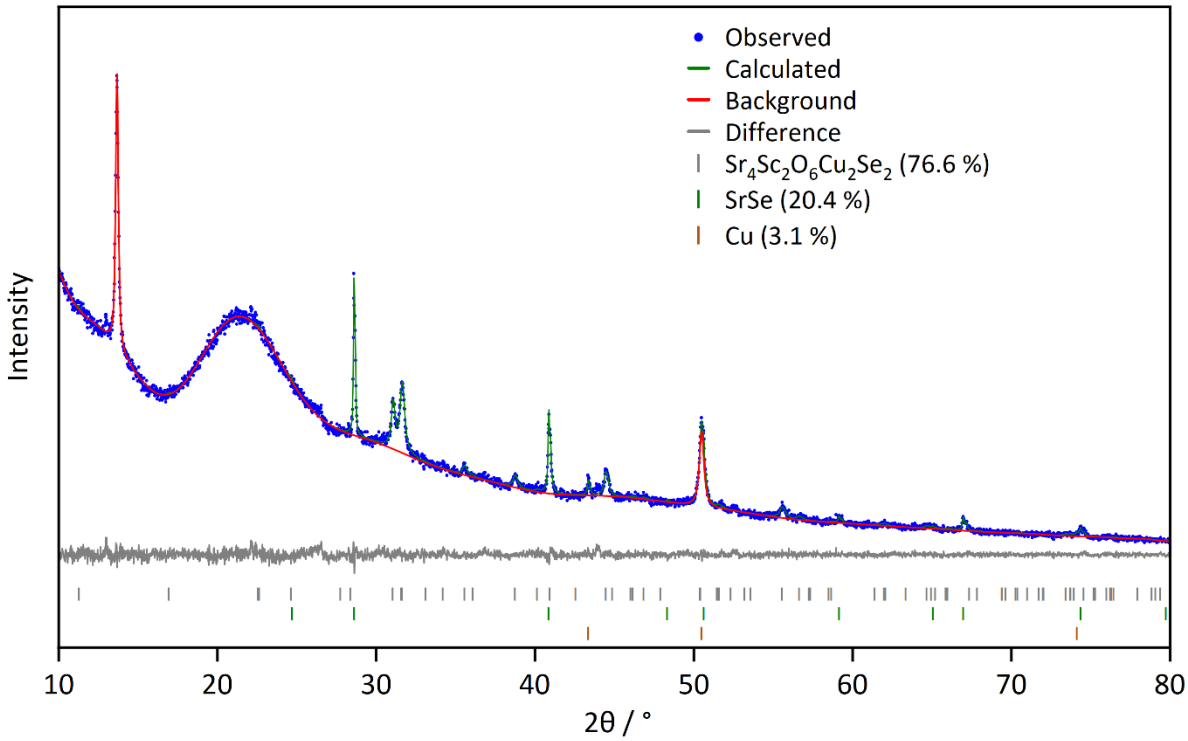

Figure 258 *Powder X-ray diffractogram of material resulting from attempted conventional synthesis of $Sr_3Sc_2O_5Cu_2Se_2$ (space group I4/mmm) after 12 hours of heating at 500 °C. The small blue circles represent the observed diffracted intensity, the green line represents the Rietveld-refined calculated model, the red line represents the background, and the grey line represents the difference between observed and calculated intensities. The grey, green, and copper tick marks show the reflections of the refined models of $S_4Sc_2O_6Cu_2Se_2$ (76.6 %), SrSe (20.4 %) and Cu (3.1 %) respectively. Data was collected with the domed air-tight holder, responsible for the background-refined peaks at 13.3 and 50.5 °.*
Duration: 45 minutes. Data points: 3457. Interval: 0.02 °. GOF: 1.15. R_{wp}: 2.750 %.

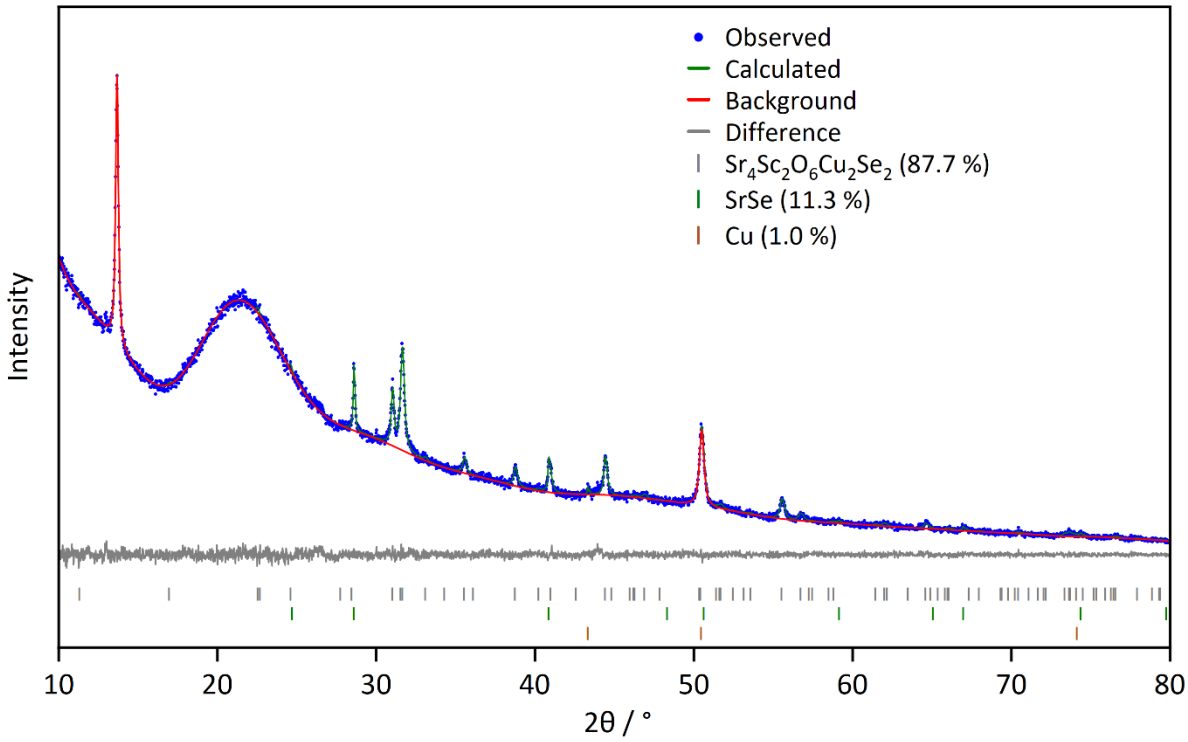

Figure 259 *Powder X-ray diffractogram of material resulting from attempted conventional synthesis of $Sr_3Sc_2O_5Cu_2Se_2$ (space group I4/mmm) after 12 hours of heating at 600 °C. The small blue circles represent the observed diffracted intensity, the green line represents the Rietveld-refined calculated model, the red line represents the background, and the grey line represents the difference between observed and calculated intensities. The grey, green, and copper tick marks show the reflections of the refined models of $S_4Sc_2O_6Cu_2Se_2$ (87.7 %), SrSe (11.3 %) and Cu (1.0 %) respectively. Data was collected with the domed air-tight holder, responsible for the background-refined peaks at 13.3 and 50.5 °.*
Duration: 45 minutes. Data points: 3457. Interval: 0.02 °. GOF: 1.04. R_{wp}: 2.436 %.

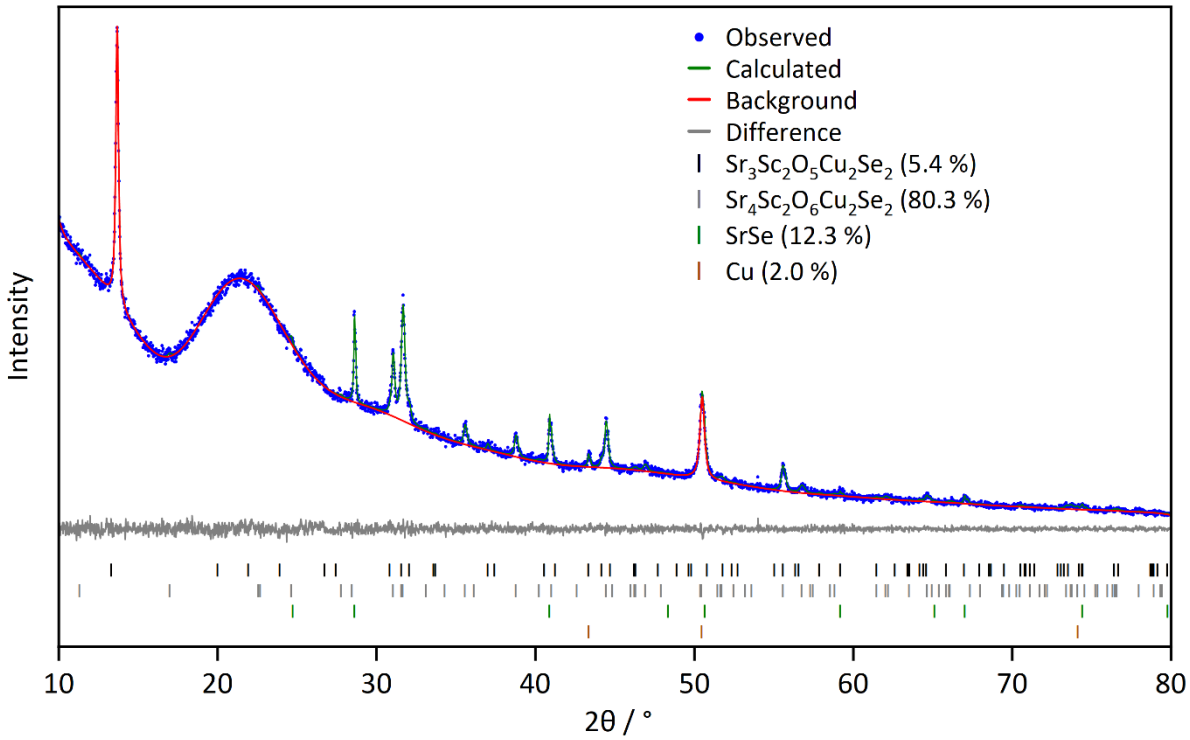

Figure 260 *Powder X-ray diffractogram of material resulting from attempted conventional synthesis of $Sr_3Sc_2O_5Cu_2Se_2$ (space group I4/mmm) after 12 hours of heating at 700 °C. The small blue circles represent the observed diffracted intensity, the green line represents the Rietveld-refined calculated model, the red line represents the background, and the grey line represents the difference between observed and calculated intensities. The black, grey, green, and copper tick marks show the reflections of the refined models of $Sr_3Sc_2O_5Cu_2Se_2$ (5.4 %), $S_4Sc_2O_6Cu_2Se_2$ (80.3 %), SrSe (12.3 %) and Cu (2.0 %) respectively. Data was collected with the domed air-tight holder, responsible for the background-refined peaks at 13.3 and 50.5 °.*
Duration: 45 minutes. Data points: 3457. Interval: 0.02 °. GOF: 1.05. R_{wp}: 2.465 %.

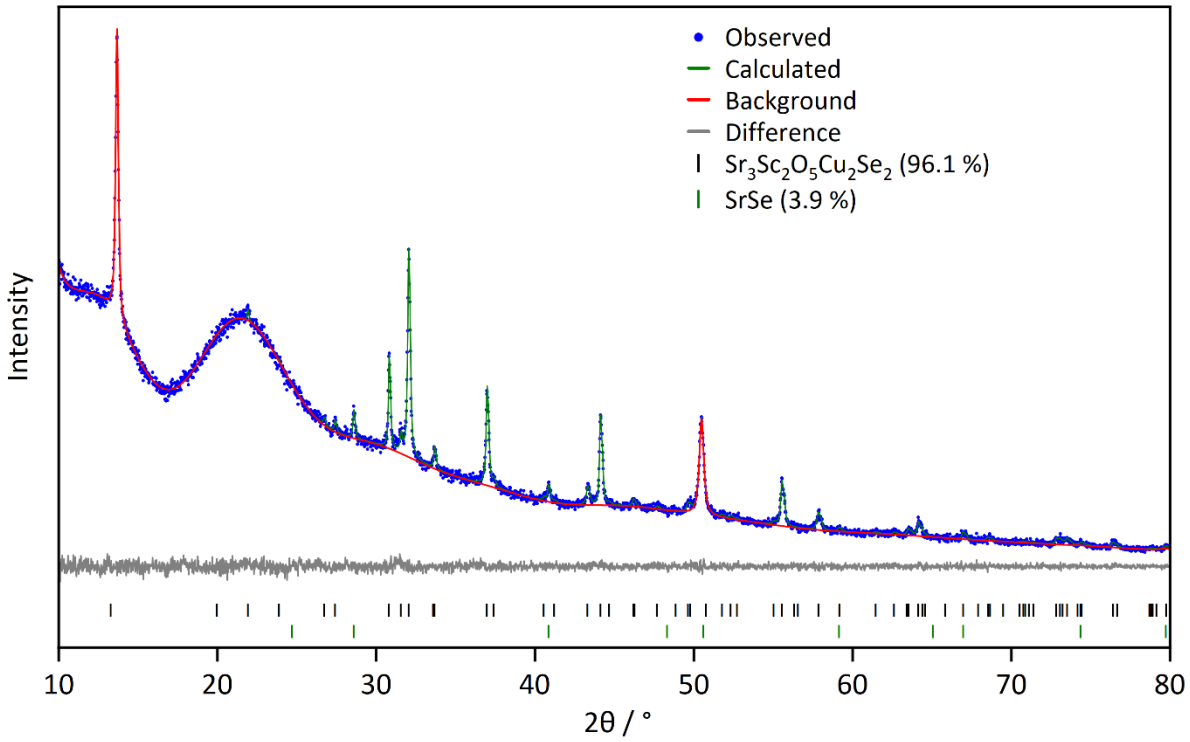

Figure 261 *Powder X-ray diffractogram of material resulting from attempted conventional synthesis of $Sr_3Sc_2O_5Cu_2Se_2$ (space group I4/mmm) after 12 hours of heating at 800 °C. The small blue circles represent the observed diffracted intensity, the green line represents the Rietveld-refined calculated model, the red line represents the background, and the grey line represents the difference between observed and calculated intensities. The black and green tick marks show the reflections of the refined models of $Sr_3Sc_2O_5Cu_2Se_2$ (96.1 %) and SrSe (3.9 %) respectively. Data was collected with the domed air-tight holder, responsible for the background-refined peaks at 13.3 and 50.5 °.*
Duration: 45 minutes. Data points: 3457. Interval: 0.02 °. GOF: 1.04. R_{wp}: 2.543 %.

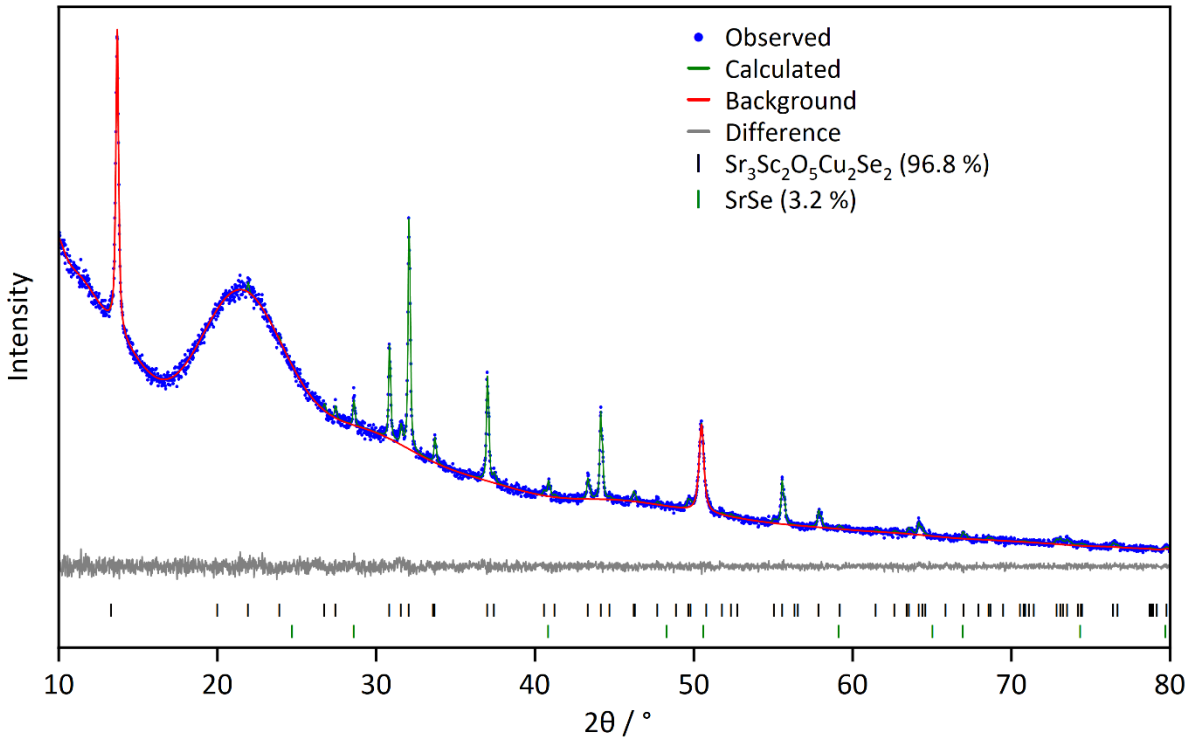

Figure 262 *Powder X-ray diffractogram of material resulting from attempted conventional synthesis of $Sr_3Sc_2O_5Cu_2Se_2$ (space group I4/mmm) after 12 hours of heating at 900 °C. The small blue circles represent the observed diffracted intensity, the green line represents the Rietveld-refined calculated model, the red line represents the background, and the grey line represents the difference between observed and calculated intensities. The black and green tick marks show the reflections of the refined models of $Sr_3Sc_2O_5Cu_2Se_2$ (96.8 %) and SrSe (3.2 %) respectively. Data was collected with the domed air-tight holder, responsible for the background-refined peaks at 13.3 and 50.5 °.*
Duration: 45 minutes. Data points: 3457. Interval: 0.02 °. GOF: 1.04. R_{wp}: 2.515 %.

B.3.4 $Sr_3Fe_2O_5Cu_2Se_2$ Metathesis Investigation

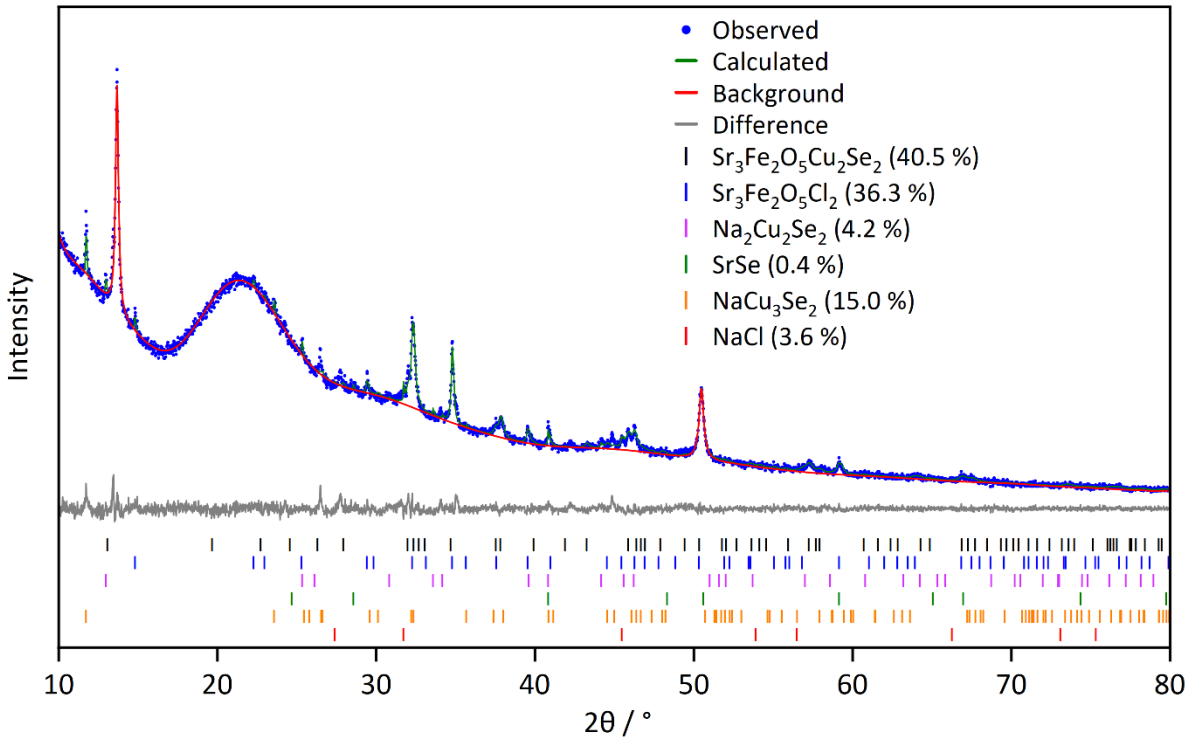

Figure 263 *Powder X-ray diffractogram of material resulting from attempted metathesis synthesis of $Sr_3Fe_2O_5Cu_2Se_2$ (space group I4/mmm) after 12 hours of heating at 500 °C. The small blue circles represent the observed diffracted intensity, the green line represents the Rietveld-refined calculated model, the red line represents the background, and the grey line represents the difference between observed and calculated intensities. The black, blue, pink, green, orange and red tick marks show the reflections of the refined models of $Sr_3Fe_2O_5Cu_2Se_2$ (40.5 %), $Sr_3Fe_2O_5Cl_2$ (36.3 %), $Na_2Cu_2Se_2$ (4.2 %), SrSe (0.4 %), $NaCu_3Se_2$ (15.0 %) and NaCl (3.6 %) respectively. Data was collected with the domed air-tight holder, responsible for the background-refined peaks at 13.3 and 50.5 °.*
Duration: 45 minutes. Data points: 3457. Interval: 0.02 °. GOF: 1.27. R_{wp}: 2.920 %.

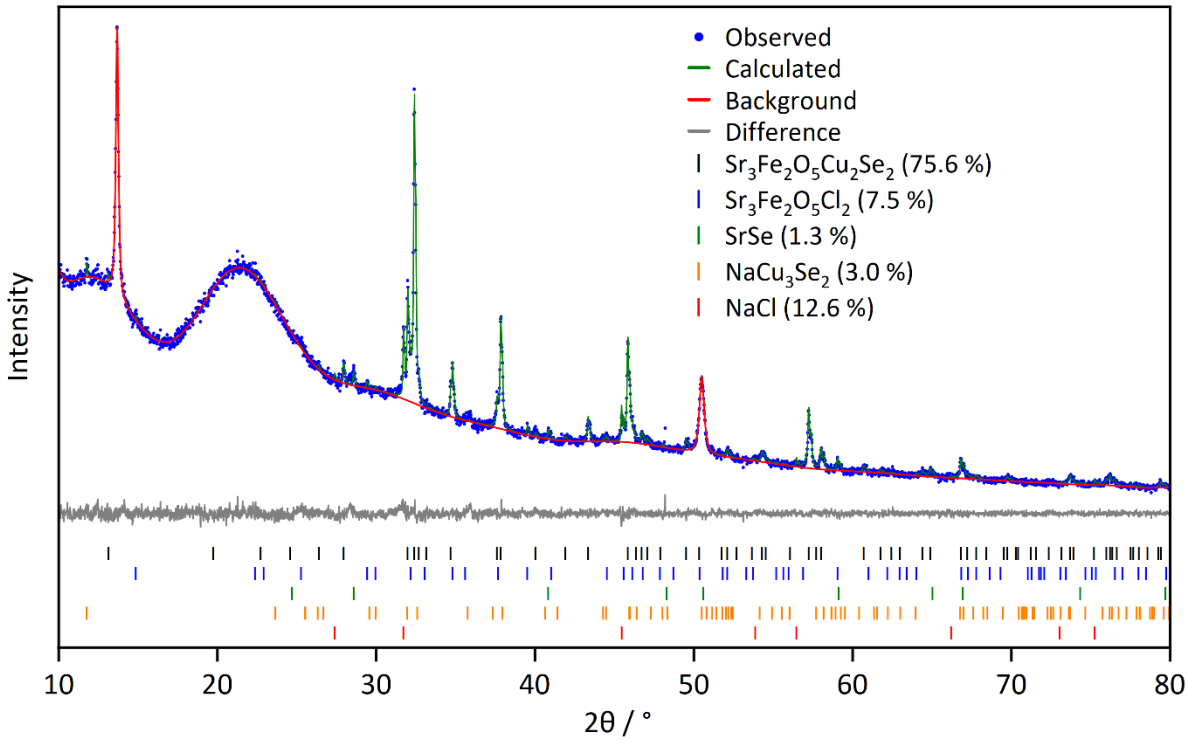

Figure 264 *Powder X-ray diffractogram of material resulting from attempted metathesis synthesis of $Sr_3Fe_2O_5Cu_2Se_2$ (space group I4/mmm) after 12 hours of heating at 600 °C. The small blue circles represent the observed diffracted intensity, the green line represents the Rietveld-refined calculated model, the red line represents the background, and the grey line represents the difference between observed and calculated intensities. The black, blue, green, orange and red tick marks show the reflections of the refined models of $Sr_3Fe_2O_5Cu_2Se_2$ (75.6 %), $Sr_3Fe_2O_5Cl_2$ (7.5 %), SrSe (1.3 %), $NaCu_3Se_2$ (3.0 %) and NaCl (12.6 %) respectively. Data was collected with the domed air-tight holder, responsible for the background-refined peaks at 13.3 and 50.5 °.*
Duration: 45 minutes. Data points: 3457. Interval: 0.02 °. GOF: 1.14. R_{wp}: 2.575 %.

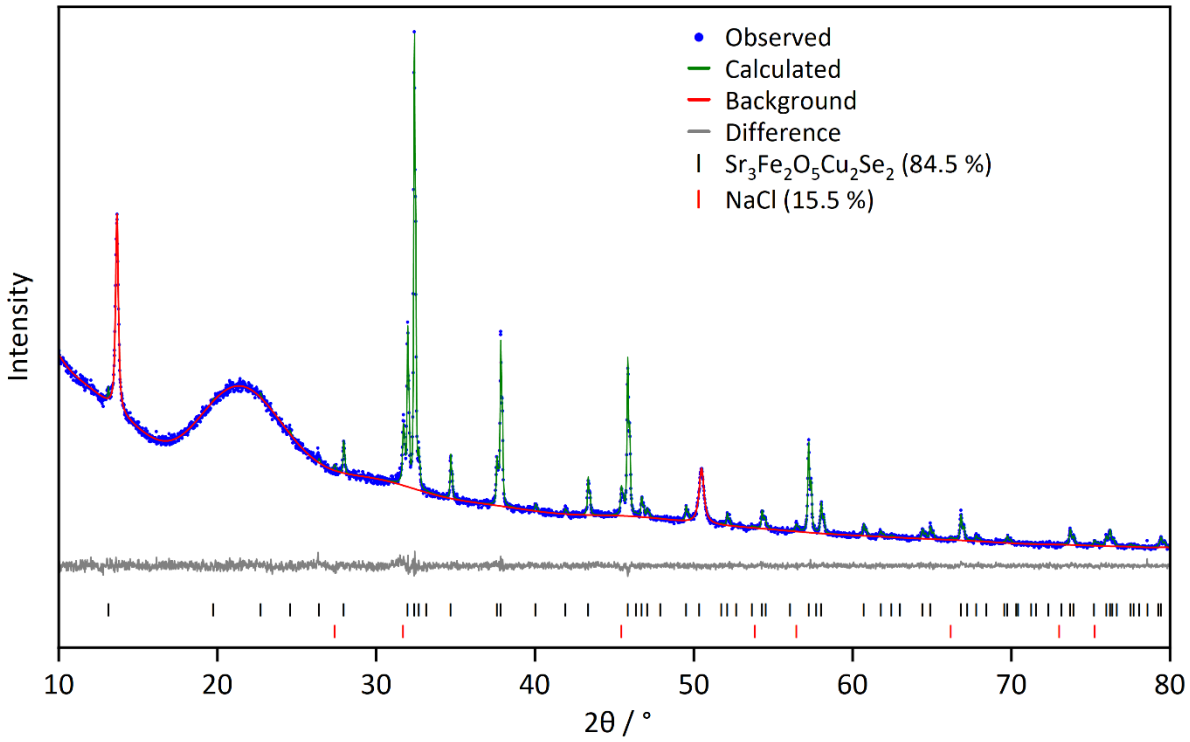

Figure 265 *Powder X-ray diffractogram of material resulting from attempted metathesis synthesis of $Sr_3Fe_2O_5Cu_2Se_2$ (space group I4/mmm) after 12 hours of heating at 700 °C. The small blue circles represent the observed diffracted intensity, the green line represents the Rietveld-refined calculated model, the red line represents the background, and the grey line represents the difference between observed and calculated intensities. The black and red tick marks show the reflections of the refined models of $Sr_3Fe_2O_5Cu_2Se_2$ (84.5 %) and NaCl (15.5 %) respectively. Data was collected with the domed air-tight holder, responsible for the background-refined peaks at 13.3 and 50.5 °.*
Duration: 45 minutes. Data points: 3457. Interval: 0.02 °. GOF: 1.10. R_{wp}: 2.367 %.

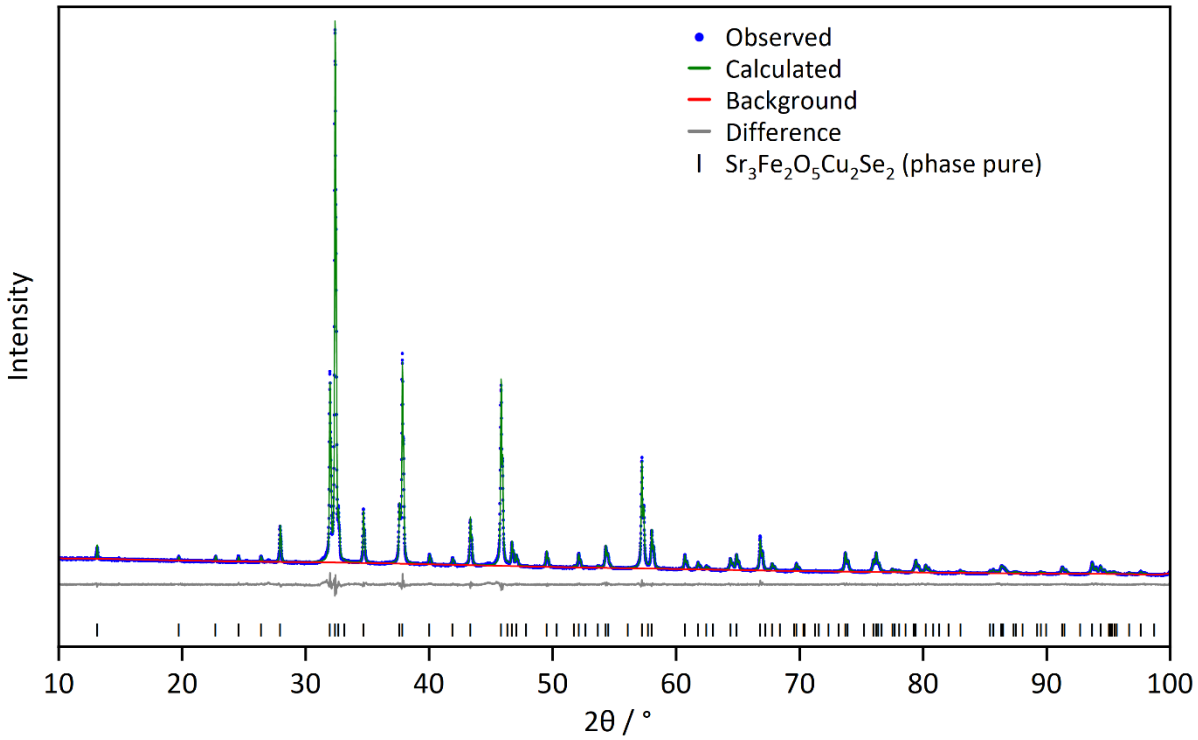

Figure 266 *Powder X-ray diffractogram of material resulting from attempted metathesis synthesis of $Sr_3Fe_2O_5Cu_2Se_2$ (space group I4/mmm) after 12 hours of heating at 700 °C, then washed in distilled H_2O to remove the NaCl by-product. The small blue circles represent the observed diffracted intensity, the green line represents the Rietveld-refined calculated model, the red line represents the background, and the grey line represents the difference between observed and calculated intensities. The black tick marks show the reflections of the refined model of $Sr_3Fe_2O_5Cu_2Se_2$, no NaCl or impurity phases were observed.*
Duration: 16 hours. Data points: 8887. Interval: 0.01 °. GOF: 1.70. R_{wp}: 1.642 %.

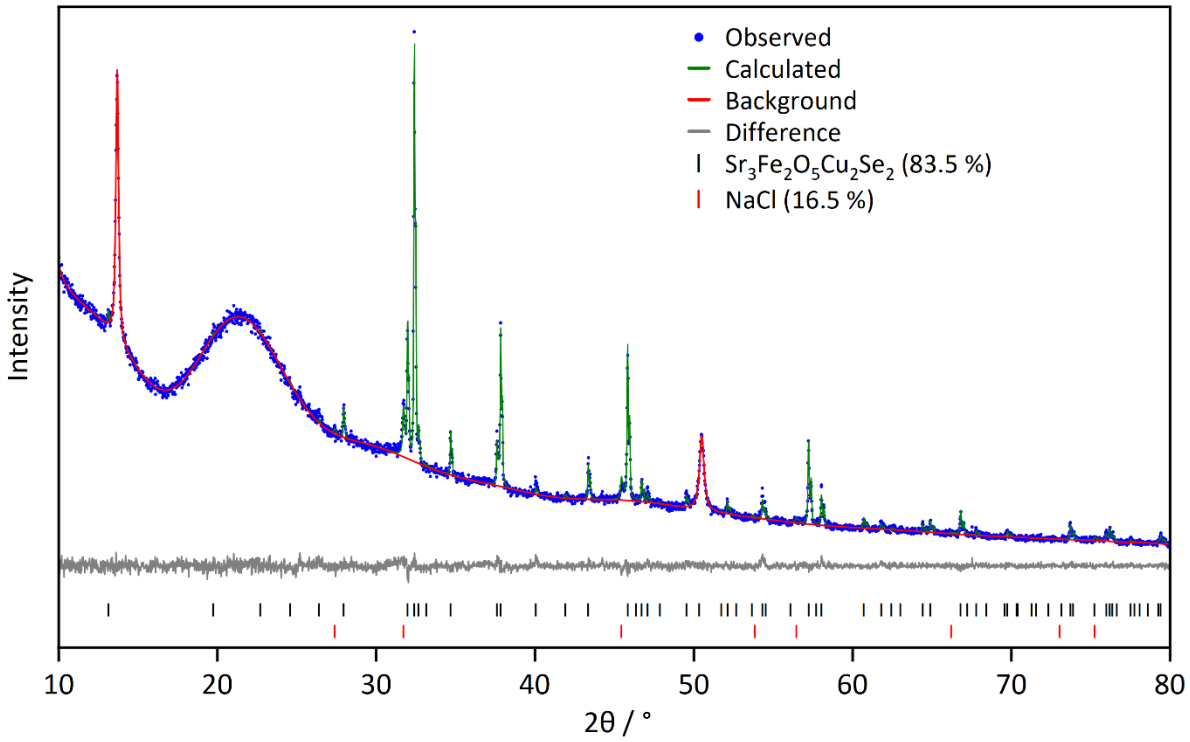

Figure 267 *Powder X-ray diffractogram of material resulting from attempted metathesis synthesis of $Sr_3Fe_2O_5Cu_2Se_2$ (space group I4/mmm) after 12 hours of heating at 800 °C. The small blue circles represent the observed diffracted intensity, the green line represents the Rietveld-refined calculated model, the red line represents the background, and the grey line represents the difference between observed and calculated intensities. The black and red tick marks show the reflections of the refined models of $Sr_3Fe_2O_5Cu_2Se_2$ (83.5 %) and NaCl (16.5 %) respectively. Data was collected with the domed air-tight holder, responsible for the background-refined peaks at 13.3 and 50.5 °.*
Duration: 45 minutes. Data points: 3457. Interval: 0.02 °. GOF: 1.13. R_{wp}: 2.557 %.

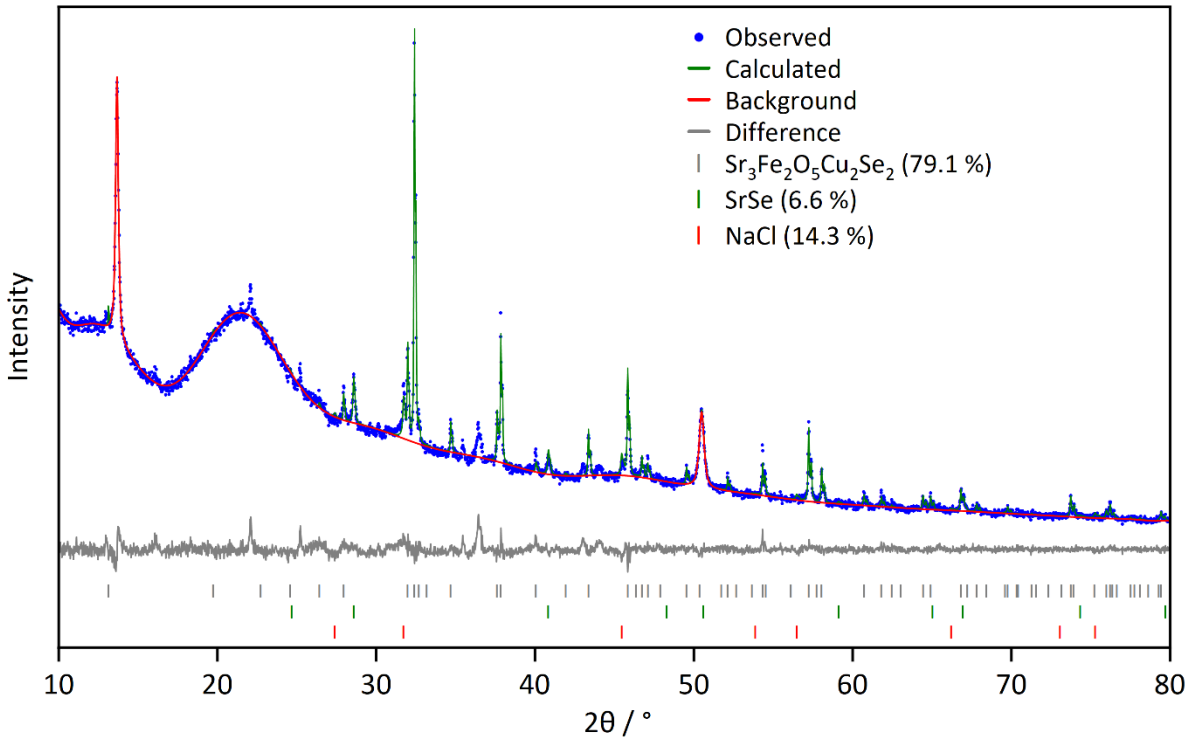

Figure 268 *Powder X-ray diffractogram of material resulting from attempted metathesis synthesis of $Sr_3Fe_2O_5Cu_2Se_2$ (space group I4/mmm) after 12 hours of heating at 900 °C. The small blue circles represent the observed diffracted intensity, the green line represents the Rietveld-refined calculated model, the red line represents the background, and the grey line represents the difference between observed and calculated intensities. The black, green and red tick marks show the reflections of the refined models of $Sr_3Fe_2O_5Cu_2Se_2$ (79.1 %), SrSe (6.6 %), and NaCl (14.3 %) respectively. Data was collected with the domed air-tight holder, responsible for the background-refined peaks at 13.3 and 50.5 °.*
Duration: 45 minutes. Data points: 3457. Interval: 0.02 °. GOF: 1.51. R_{wp}: 3.399 %.

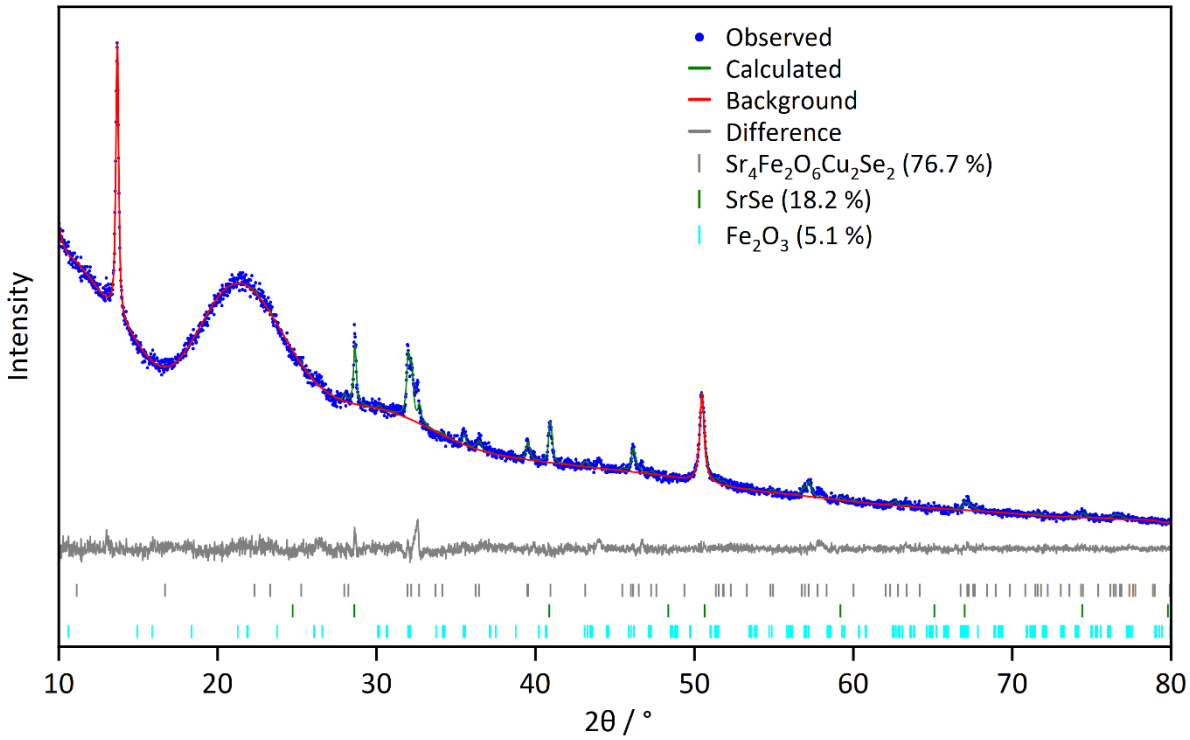

Figure 269 *Powder X-ray diffractogram of material resulting from attempted conventional synthesis of $Sr_3Fe_2O_5Cu_2Se_2$ (space group I4/mmm) after 12 hours of heating at 500 °C. The small blue circles represent the observed diffracted intensity, the green line represents the Rietveld-refined calculated model, the red line represents the background, and the grey line represents the difference between observed and calculated intensities. The grey, green, and cyan tick marks show the reflections of the refined models of $S_4Fe_2O_6Cu_2Se_2$ (76.7 %), SrSe (18.2 %) and Fe_2O_3 (5.1 %) respectively. Data was collected with the domed air-tight holder, responsible for the background-refined peaks at 13.3 and 50.5 °. Duration: 45 minutes. Data points: 3457. Interval: 0.02 °. GOF: 1.24. R_{wp}: 2.839 %.*

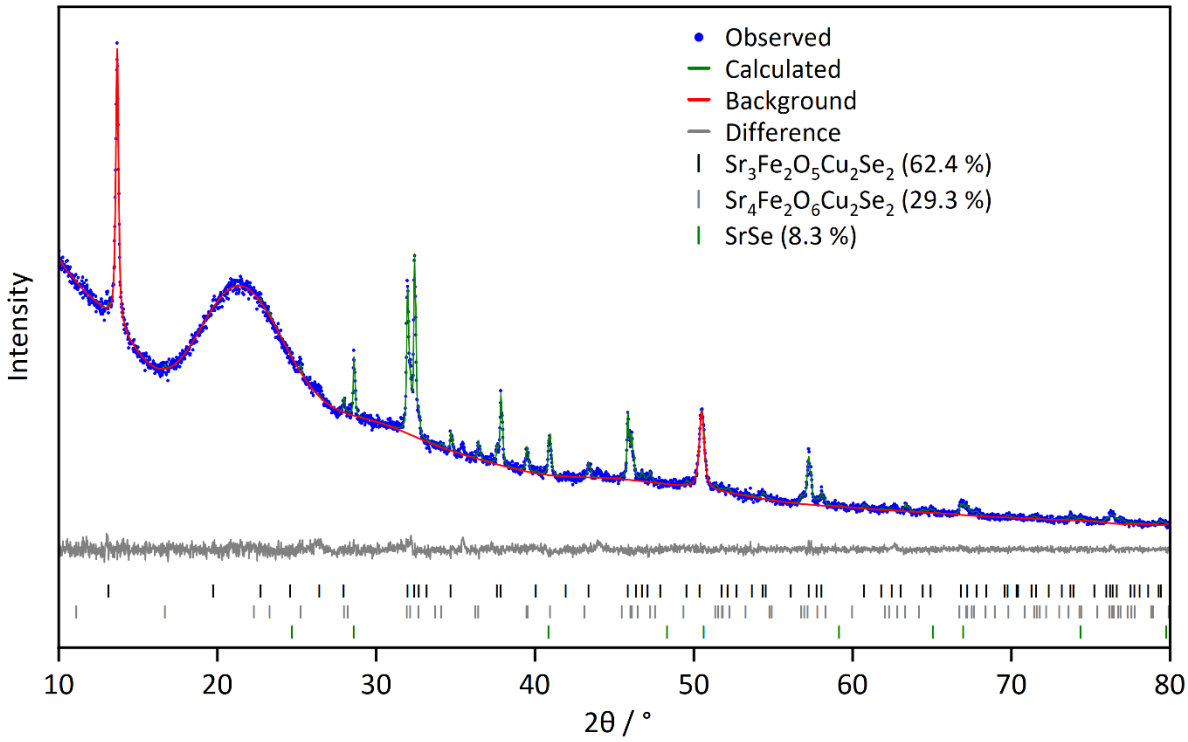

Figure 270 *Powder X-ray diffractogram of material resulting from attempted conventional synthesis of $Sr_3Fe_2O_5Cu_2Se_2$ (space group I4/mmm) after 12 hours of heating at 600 °C. The small blue circles represent the observed diffracted intensity, the green line represents the Rietveld-refined calculated model, the red line represents the background, and the grey line represents the difference between observed and calculated intensities. The black, grey and green tick marks show the reflections of the refined models of $S_3Fe_2O_5Cu_2Se_2$ (62.4 %), $S_4Fe_2O_6Cu_2Se_2$ (29.3 %) and SrSe (8.3 %) respectively. Data was collected with the domed air-tight holder, responsible for the background-refined peaks at 13.3 and 50.5 °. Duration: 45 minutes. Data points: 3457. Interval: 0.02 °. GOF: 1.13. R_{wp}: 2.569 %.*

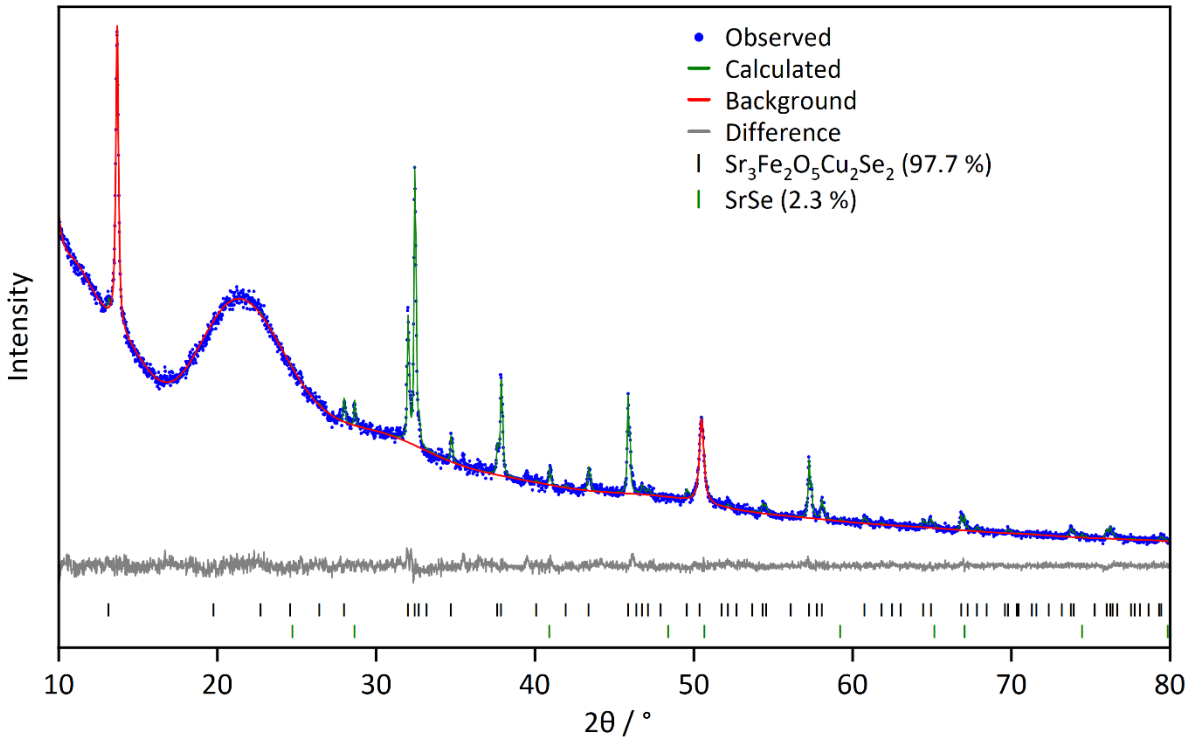

Figure 271 *Powder X-ray diffractogram of material resulting from attempted conventional synthesis of $Sr_3Fe_2O_5Cu_2Se_2$ (space group I4/mmm) after 12 hours of heating at 700 °C. The small blue circles represent the observed diffracted intensity, the green line represents the Rietveld-refined calculated model, the red line represents the background, and the grey line represents the difference between observed and calculated intensities. The black and green tick marks show the reflections of the refined models of $S_3Fe_2O_5Cu_2Se_2$ (97.7 %) and SrSe (2.3 %) respectively. Data was collected with the domed air-tight holder, responsible for the background-refined peaks at 13.3 and 50.5 °.*
Duration: 45 minutes. Data points: 3457. Interval: 0.02 °. GOF: 1.19. R_{wp}: 2.745 %.

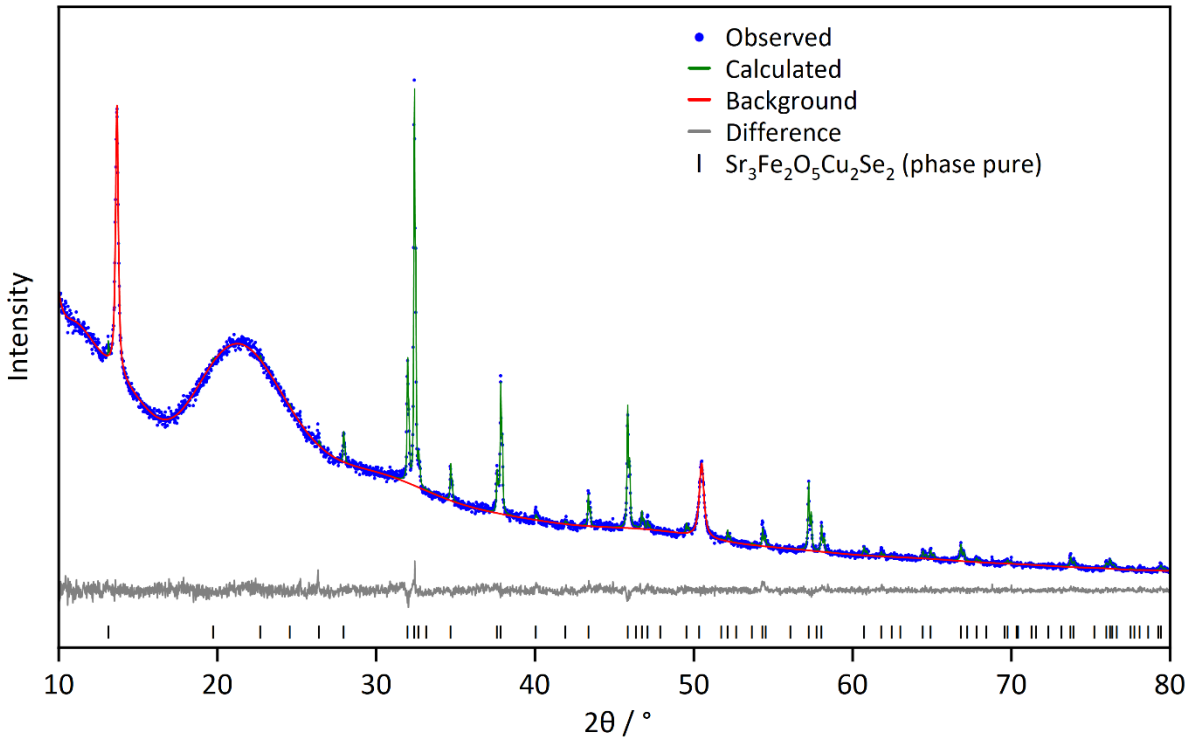

Figure 272 *Powder X-ray diffractogram of material resulting from attempted conventional synthesis of $Sr_3Fe_2O_5Cu_2Se_2$ (space group I4/mmm) after 12 hours of heating at 800 °C. The small blue circles represent the observed diffracted intensity, the green line represents the Rietveld-refined calculated model, the red line represents the background, and the grey line represents the difference between observed and calculated intensities. The black tick marks show the reflections of the refined models of $S_3Fe_2O_5Cu_2Se_2$, no impurity phases are observed. Data was collected with the domed air-tight holder, responsible for the background-refined peaks at 13.3 and 50.5 °.*
Duration: 45 minutes. Data points: 3457. Interval: 0.02 °. GOF: 1.15. R_{wp}: 2.574 %.

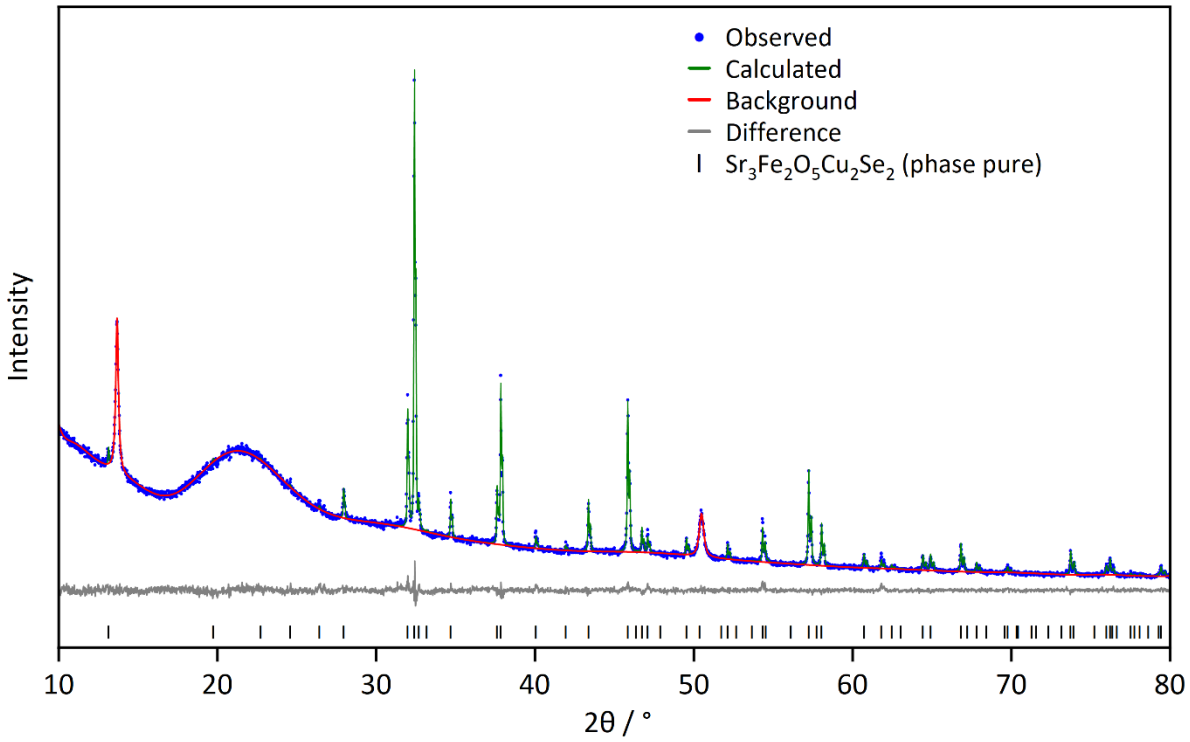

Figure 273 *Powder X-ray diffractogram of material resulting from attempted conventional synthesis of $Sr_3Fe_2O_5Cu_2Se_2$ (space group I4/mmm) after 12 hours of heating at 900 °C. The small blue circles represent the observed diffracted intensity, the green line represents the Rietveld-refined calculated model, the red line represents the background, and the grey line represents the difference between observed and calculated intensities. The black tick marks show the reflections of the refined models of $S_3Fe_2O_5Cu_2Se_2$, no impurity phases are observed. Data was collected with the domed air-tight holder, responsible for the background-refined peaks at 13.3 and 50.5 °.*
Duration: 45 minutes. Data points: 3457. Interval: 0.02 °. GOF: 1.22. R_{wp}: 2.656 %.

B.3.5 Metathesis Tests with Remaining Light Layers

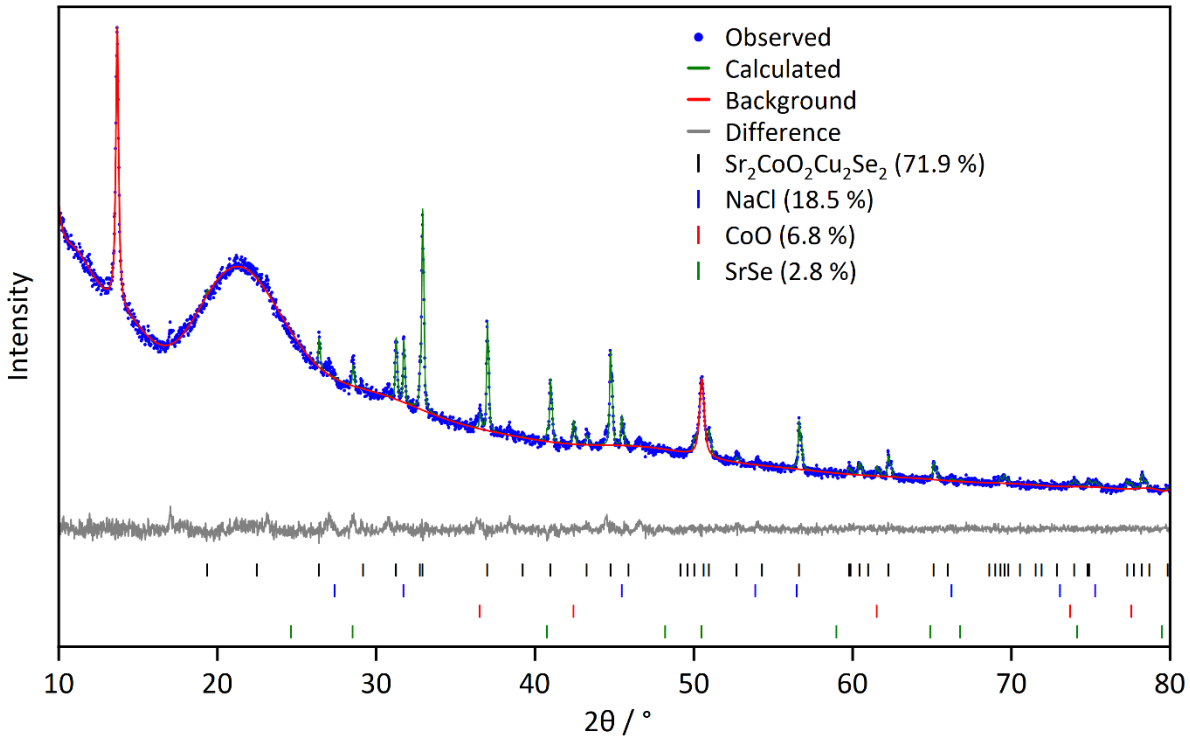

Figure 274 *Powder X-ray diffractogram of material resulting from attempted metathesis synthesis of $Sr_3Co_2O_5Cu_2Se_2$ after 12 hours of heating at 600 °C. The small blue circles represent the observed diffracted intensity, the green line represents the Rietveld-refined calculated model, the red line represents the background, and the grey line represents the difference between observed and calculated intensities. The black, blue, red, and green tick marks show the reflections of the refined models of $Sr_2CoO_2Cu_2Se_2$ (71.9 %), NaCl (18.5 %), CoO (6.8 %), and SrSe (2.8 %) respectively. Data was collected with the domed air-tight holder, responsible for the background-refined peaks at 13.3 and 50.5 °.*
Duration: 45 minutes. Data points: 3457. Interval: 0.02 °. GOF: 1.24. R_{wp}: 2.692 %.

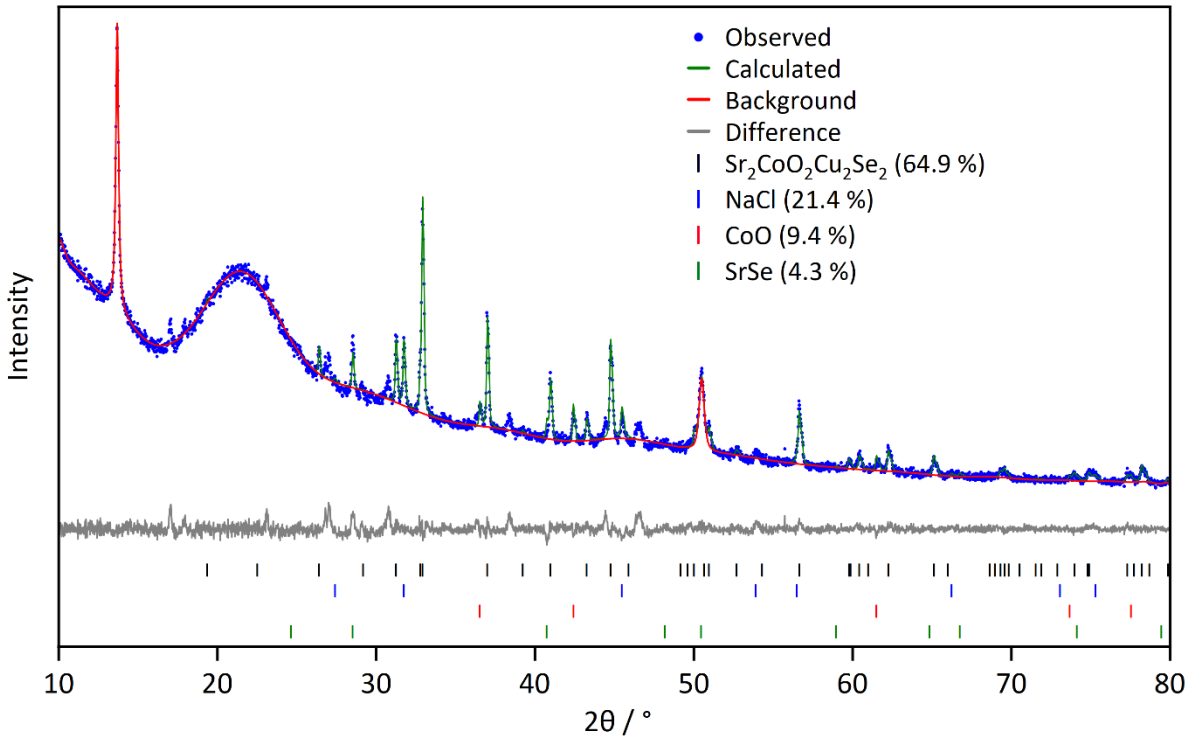

Figure 275 *Powder X-ray diffractogram of material resulting from attempted metathesis synthesis of $Sr_4Co_2O_6Cu_2Se_2$ after 12 hours of heating at 600 °C. The small blue circles represent the observed diffracted intensity, the green line represents the Rietveld-refined calculated model, the red line represents the background, and the grey line represents the difference between observed and calculated intensities. The black, blue, red, and green tick marks show the reflections of the refined models of $Sr_2CoO_2Cu_2Se_2$ (64.9 %), NaCl (21.4 %), CoO (9.4 %), and SrSe (4.3 %) respectively. Data was collected with the domed air-tight holder, responsible for the background-refined peaks at 13.3 and 50.5 °.*
Duration: 45 minutes. Data points: 3457. Interval: 0.02 °. GOF: 1.47. R_{wp}: 3.156 %.

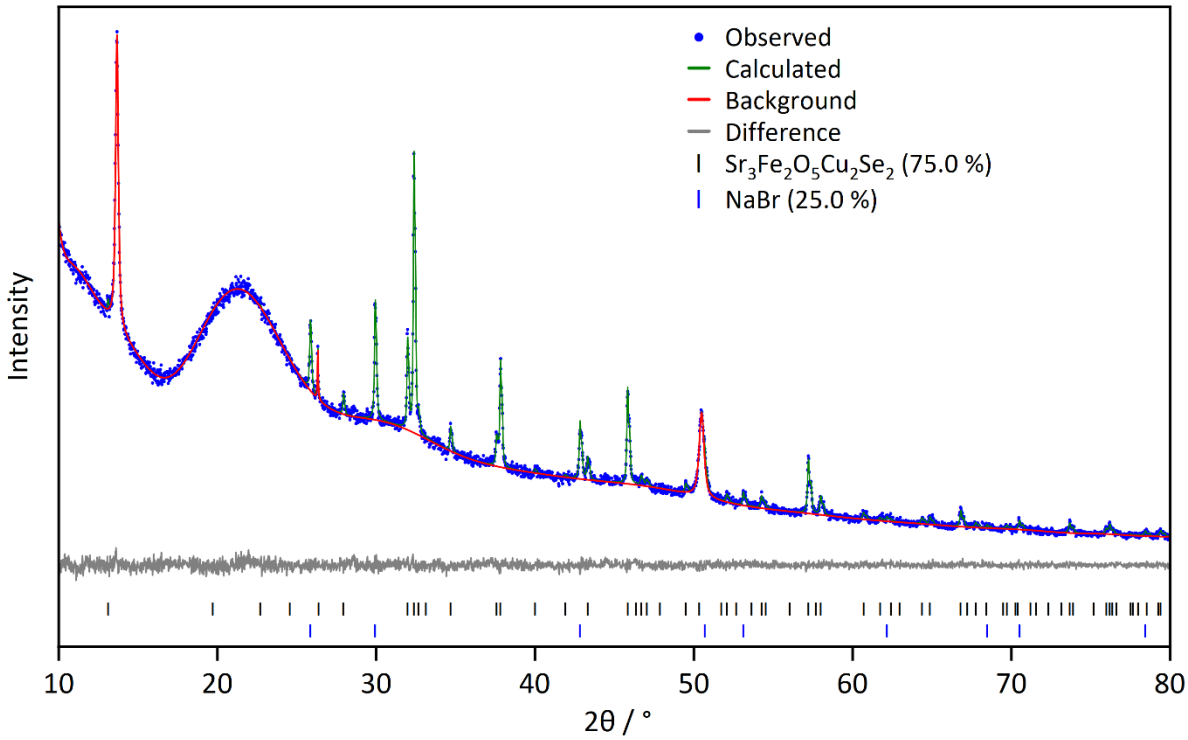

Figure 276 *Powder X-ray diffractogram of material resulting from attempted metathesis synthesis of $Sr_3Fe_2O_5Cu_2Se_2$ after 12 hours of heating at 600 °C. The small blue circles represent the observed diffracted intensity, the green line represents the Rietveld-refined calculated model, the red line represents the background, and the grey line represents the difference between observed and calculated intensities. The black and blue tick marks show the reflections of the refined models of $Sr_3Fe_2O_5Cu_2Se_2$ (75.0 %) and NaBr (25.0 %) respectively. Data was collected with the domed air-tight holder, responsible for the background-refined peaks at 13.3 and 50.5 °.*
Duration: 45 minutes. Data points: 3457. Interval: 0.02 °. GOF: 1.06. R_{wp}: 2.369 %.

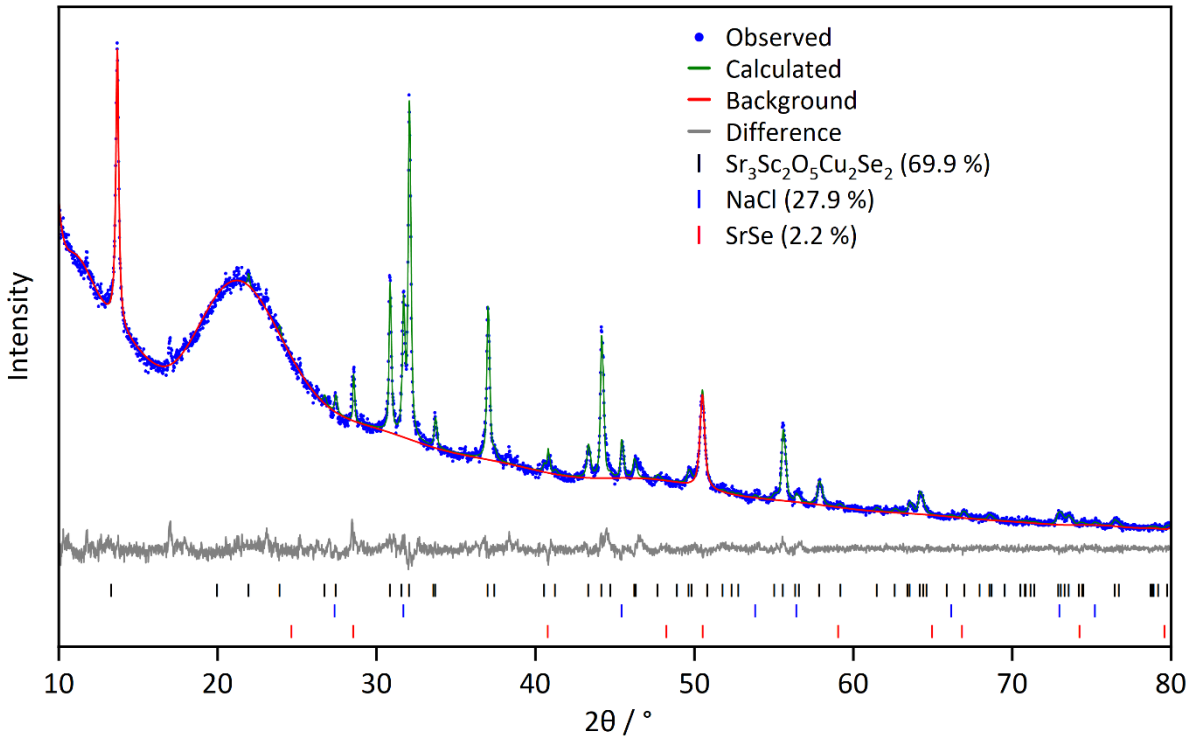

Figure 277 *Powder X-ray diffractogram of material resulting from attempted metathesis synthesis of $Sr_4Sc_2O_6Cu_2Se_2$ after 12 hours of heating at 600 °C. The small blue circles represent the observed diffracted intensity, the green line represents the Rietveld-refined calculated model, the red line represents the background, and the grey line represents the difference between observed and calculated intensities. The black, blue, and red tick marks show the reflections of the refined models of $Sr_3Sc_2O_5Cu_2Se_2$ (69.9 %), NaCl (27.9 %), and SrSe (2.2 %) respectively. Data was collected with the domed air-tight holder, responsible for the background-refined peaks at 13.3 and 50.5 °.*
Duration: 45 minutes. Data points: 3457. Interval: 0.02 °. GOF: 1.43. R_{wp}: 3.417 %.

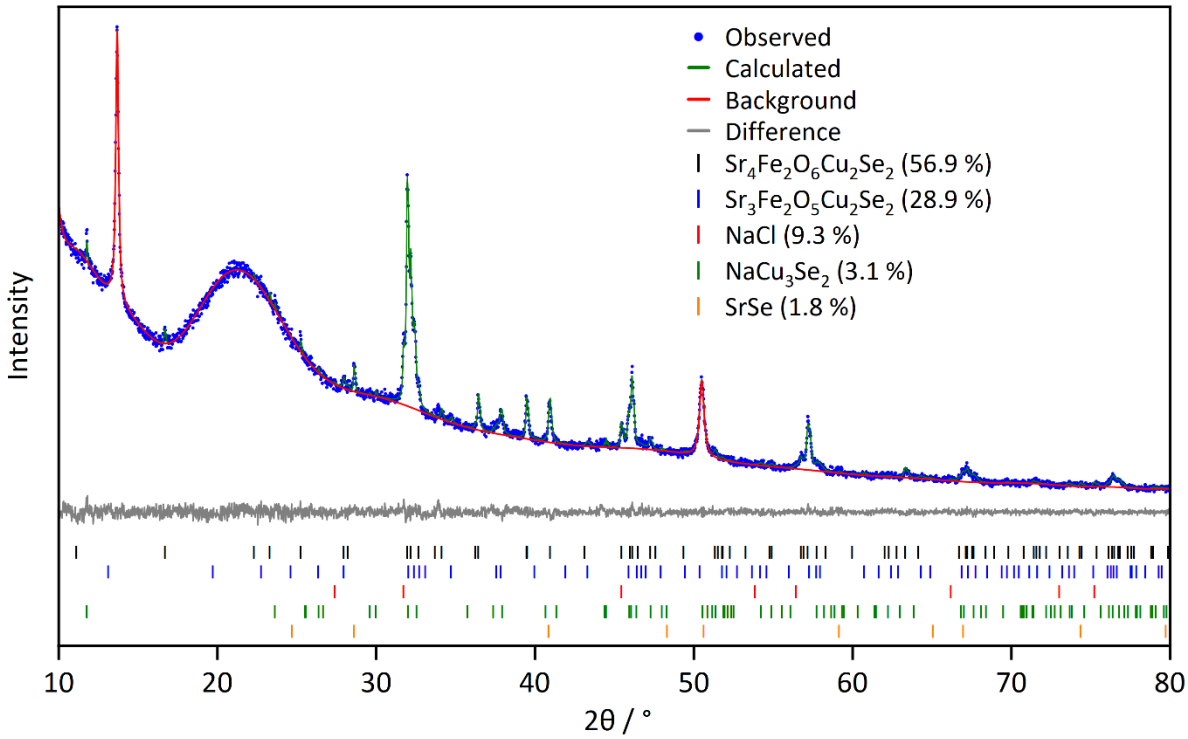

Figure 278 *Powder X-ray diffractogram of material resulting from attempted metathesis synthesis of $Sr_4Fe_2O_6Cu_2Se_2$ after 12 hours of heating at 600 °C. The small blue circles represent the observed diffracted intensity, the green line represents the Rietveld-refined calculated model, the red line represents the background, and the grey line represents the difference between observed and calculated intensities. The black, blue, red, green and orange tick marks show the reflections of the refined models of $Sr_4Fe_2O_6Cu_2Se_2$ (56.9 %), $Sr_3Fe_2O_5Cu_2Se_2$ (28.9 %), NaCl (9.3 %), $NaCu_3Se_2$ (3.1 %), and SrSe (1.8 %) respectively. Data was collected with the domed air-tight holder, responsible for the background-refined peaks at 13.3 and 50.5 °.*
Duration: 45 minutes. Data points: 3457. Interval: 0.02 °. GOF: 1.13. R_{wp}: 2.597 %.

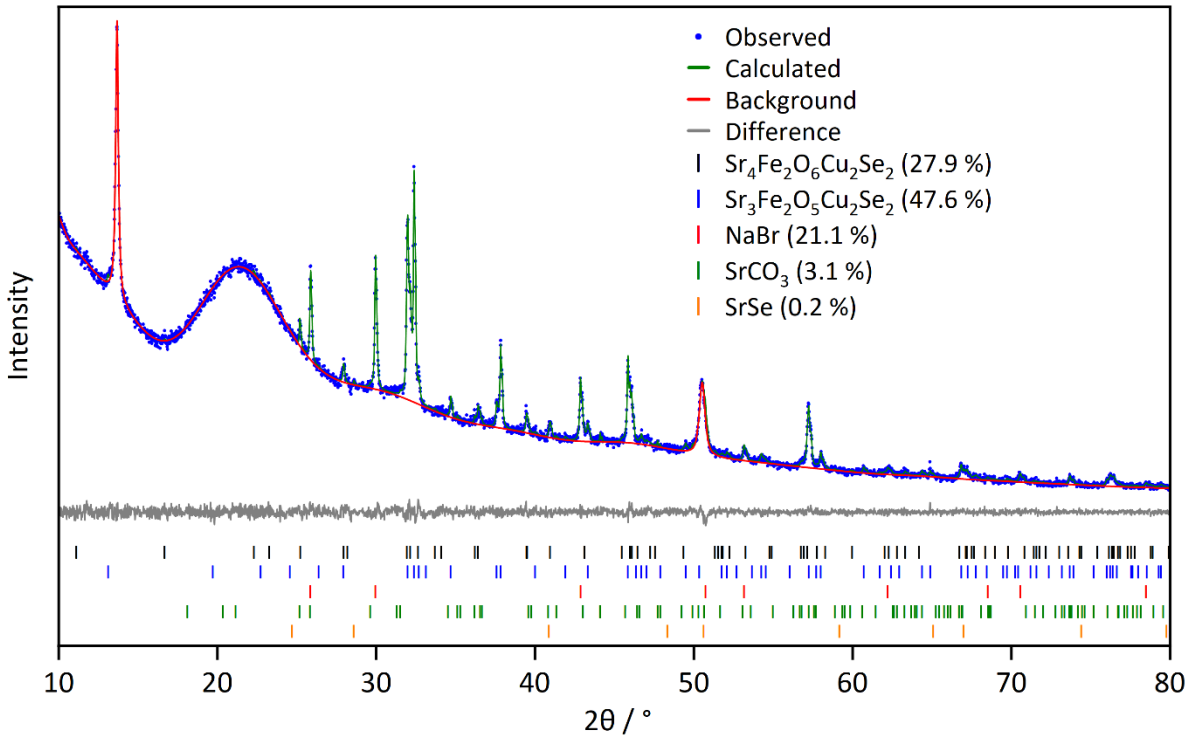

Figure 279 *Powder X-ray diffractogram of material resulting from attempted metathesis synthesis of $Sr_4Fe_2O_6Cu_2Se_2$ after 12 hours of heating at 600 °C. The small blue circles represent the observed diffracted intensity, the green line represents the Rietveld-refined calculated model, the red line represents the background, and the grey line represents the difference between observed and calculated intensities. The black, blue, red, green and orange tick marks show the reflections of the refined models of $Sr_4Fe_2O_6Cu_2Se_2$ (27.9 %), $Sr_3Fe_2O_5Cu_2Se_2$ (47.6 %), NaBr (21.1 %), $SrCO_3$ (3.1 %), and SrSe (0.2 %) respectively. Data was collected with the domed air-tight holder, responsible for the background-refined peaks at 13.3 and 50.5 °.*
Duration: 45 minutes. Data points: 3457. Interval: 0.02 °. GOF: 1.13. R_{wp}: 2.500 %.

B.3.6 Salt Flux Investigation

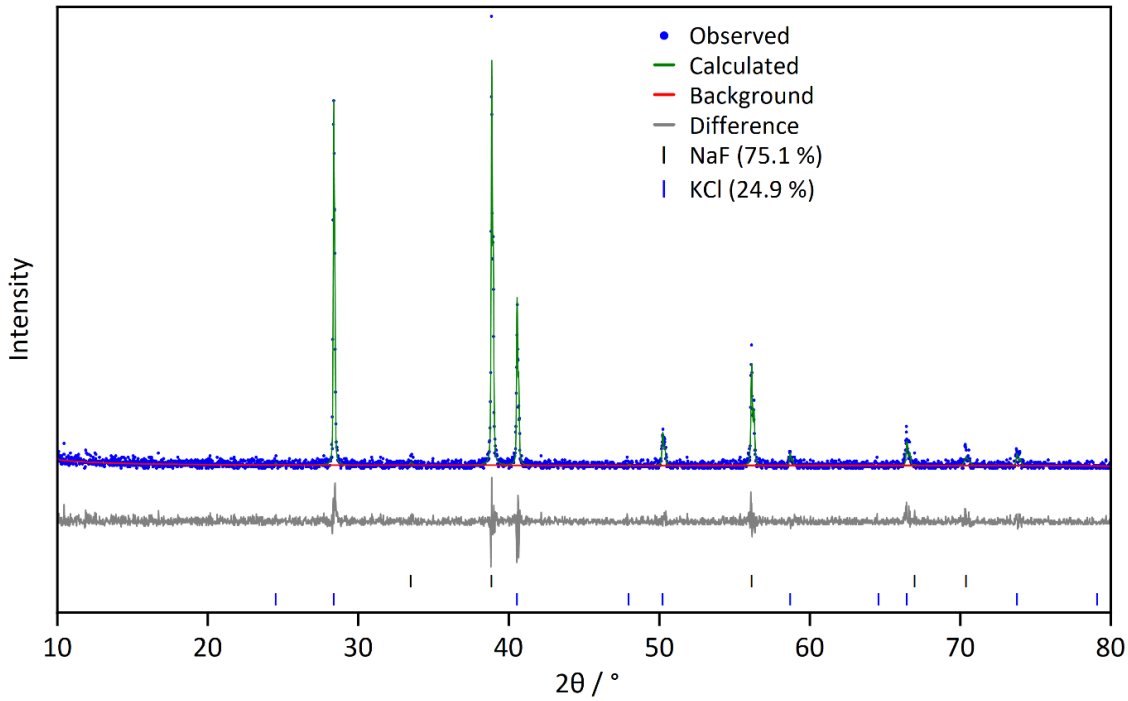

Figure 280 *Powder X-ray diffractogram of the unreacted precursors of the reaction of NaF and KCl. The small blue circles represent the observed diffracted intensity, the green line represents the Rietveld-refined calculated model, the red line represents the background, and the grey line represents the difference between observed and calculated intensities. The black and blue tick marks show the reflections of the refined models of NaF (75.1 %) and KCl (24.9 %) respectively.*
Duration: 1 minute. Data points: 3457. Interval: 0.02 °. GOF: 0.87. R_{wp}: 40.386 %.

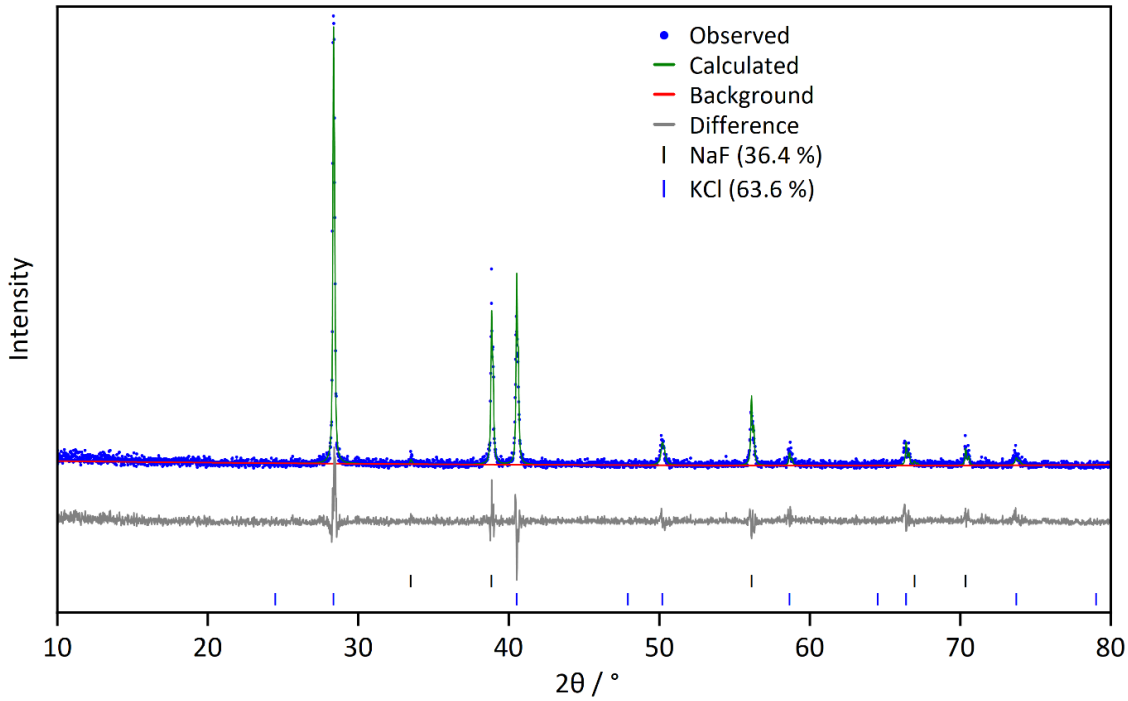

Figure 281 *Powder X-ray diffractogram of material resulting from the reaction of NaF and KCl, after 12 hours of heating at 700 °C. The small blue circles represent the observed diffracted intensity, the green line represents the Rietveld-refined calculated model, the red line represents the background, and the grey line represents the difference between observed and calculated intensities. The black and blue tick marks show the reflections of the refined models of NaF (36.4 %) and KCl (63.6 %) respectively.*
Duration: 2 minutes. Data points: 3457. Interval: 0.02 °. GOF: 1.19. R_{wp}: 39.476 %.

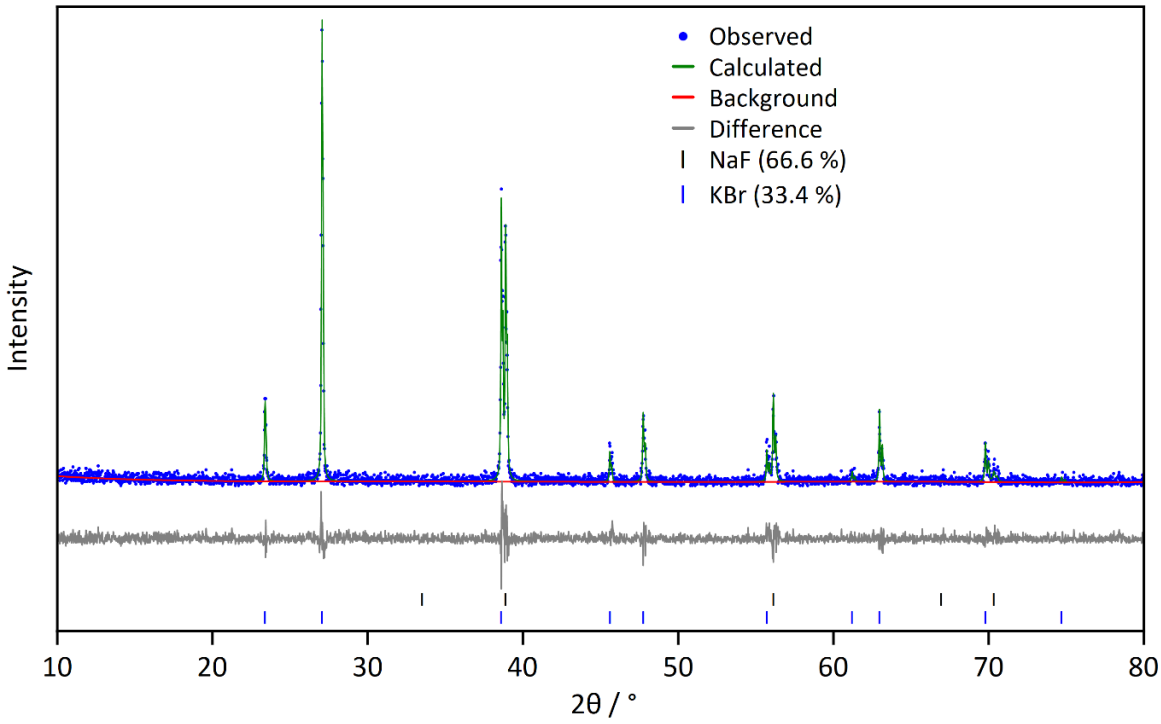

Figure 282 *Powder X-ray diffractogram of the unreacted precursors of the reaction of NaF and KBr. The small blue circles represent the observed diffracted intensity, the green line represents the Rietveld-refined calculated model, the red line represents the background, and the grey line represents the difference between observed and calculated intensities. The black and blue tick marks show the reflections of the refined models of NaF (66.6 %) and KBr (33.4 %) respectively.*
Duration: 1 minute. Data points: 3457. Interval: 0.02 °. GOF: 1.04. R_{wp}: 40.750 %.

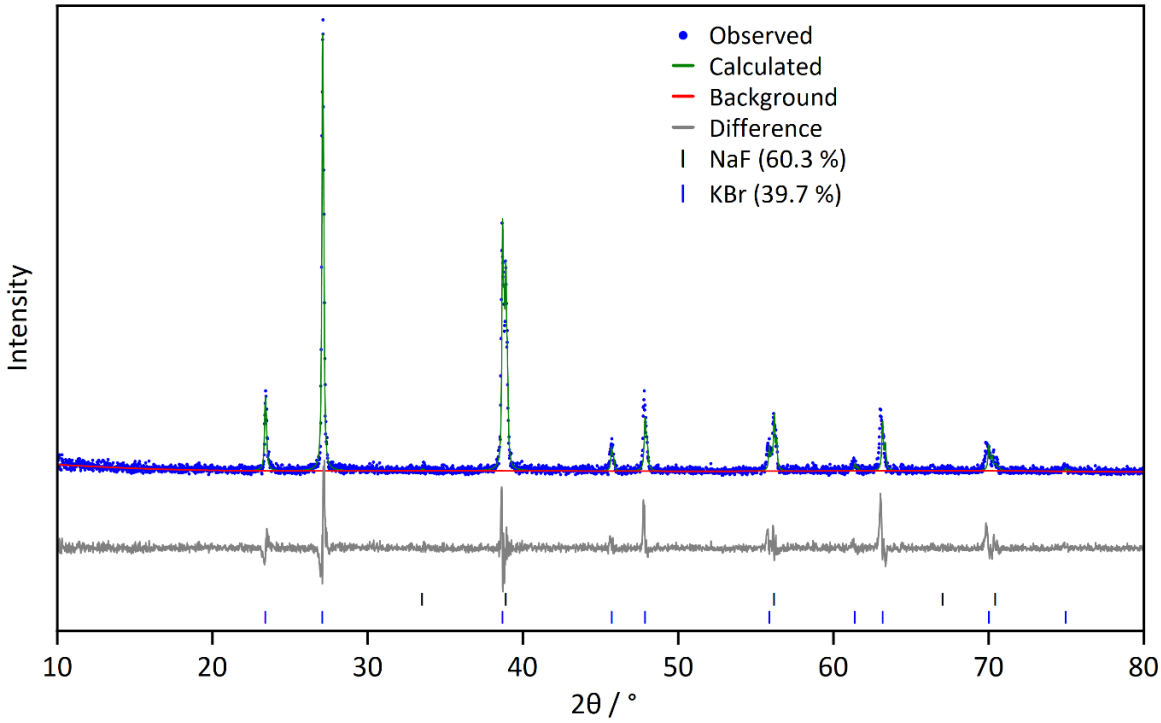

Figure 283 *Powder X-ray diffractogram of material resulting from the reaction of NaF and KBr, after 12 hours of heating at 700 °C. The small blue circles represent the observed diffracted intensity, the green line represents the Rietveld-refined calculated model, the red line represents the background, and the grey line represents the difference between observed and calculated intensities. The black and blue tick marks show the reflections of the refined models of NaF (60.3 %) and KBr (39.7 %) respectively.*
Duration: 2 minutes. Data points: 3457. Interval: 0.02 °. GOF: 1.33. R_{wp}: 34.434 %.

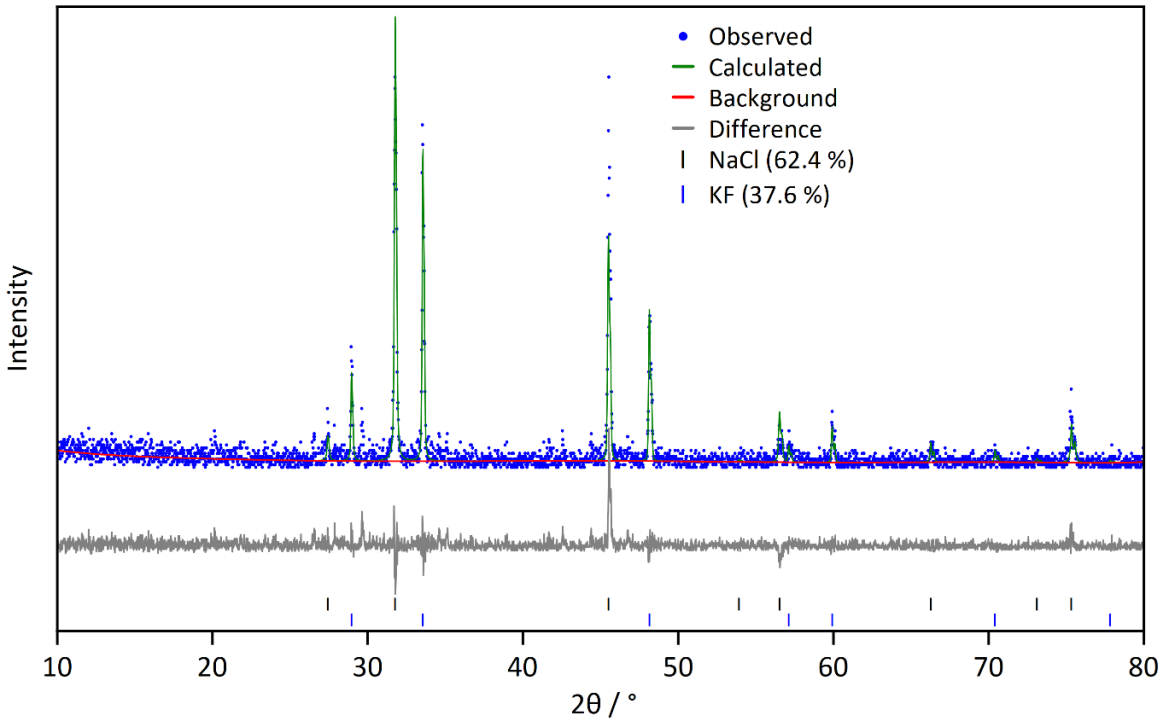

Figure 284 *Powder X-ray diffractogram of the unreacted precursors of the reaction of NaCl and KF. The small blue circles represent the observed diffracted intensity, the green line represents the Rietveld-refined calculated model, the red line represents the background, and the grey line represents the difference between observed and calculated intensities. The black and blue tick marks show the reflections of the refined models of NaCl (62.4 %) and KF (37.6 %) respectively.*
Duration: 1 minute. Data points: 3457. Interval: 0.02 °. GOF: 0.99. R_{wp}: 46.205 %.

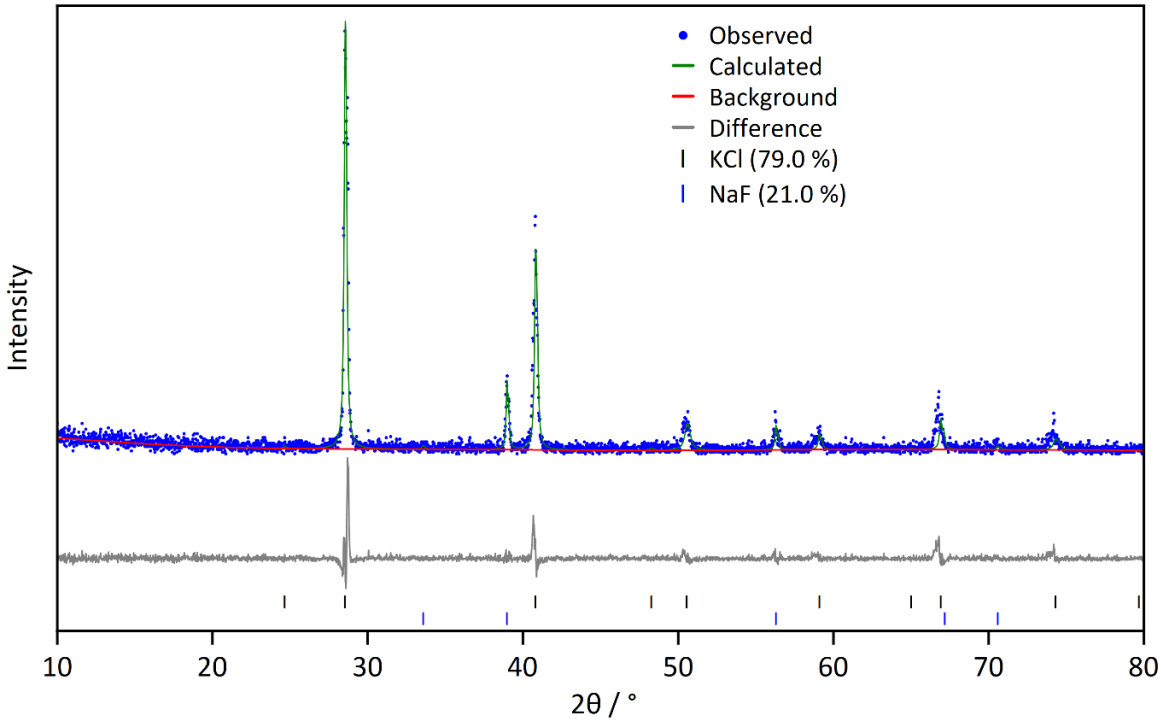

Figure 285 *Powder X-ray diffractogram of material resulting from the reaction of NaCl and KF, after 12 hours of heating at 700 °C. The small blue circles represent the observed diffracted intensity, the green line represents the Rietveld-refined calculated model, the red line represents the background, and the grey line represents the difference between observed and calculated intensities. The black and blue tick marks show the reflections of the refined models of KCl (79.0 %) and NaF (21.0 %) respectively.*
Duration: 2 minutes. Data points: 3457. Interval: 0.02 °. GOF: 1.21. R_{wp}: 44.674 %.

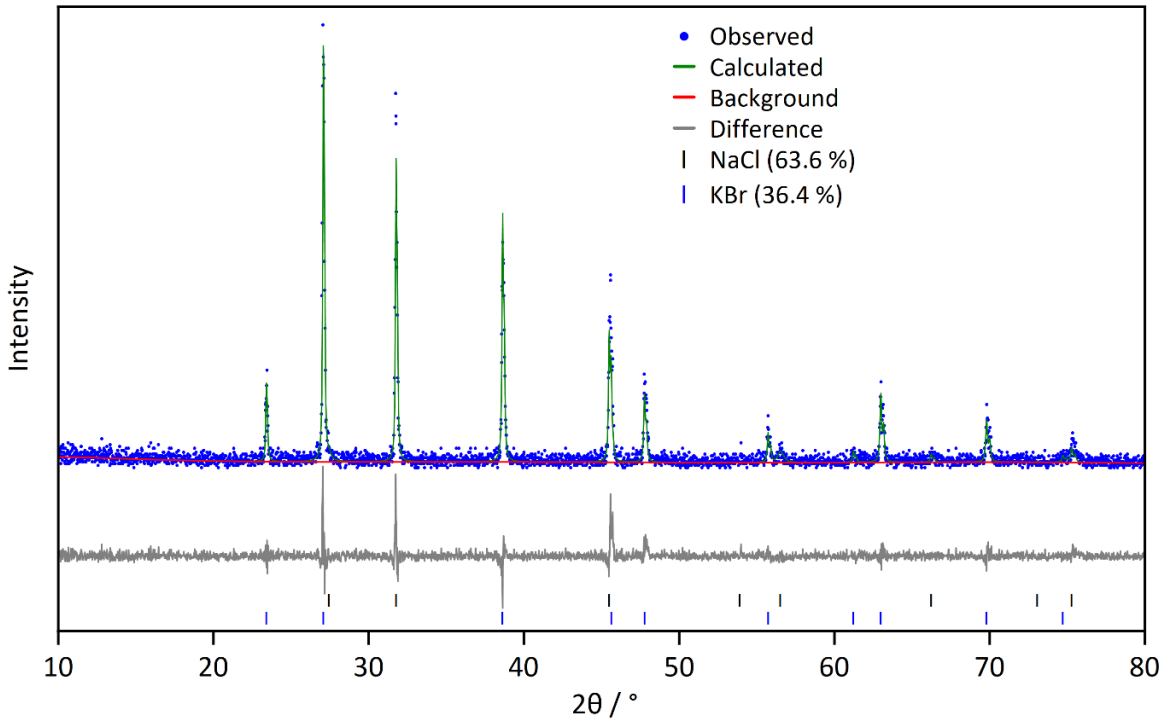

Figure 286 *Powder X-ray diffractogram of the unreacted precursors of the reaction of NaCl and KBr. The small blue circles represent the observed diffracted intensity, the green line represents the Rietveld-refined calculated model, the red line represents the background, and the grey line represents the difference between observed and calculated intensities. The black and blue tick marks show the reflections of the refined models of NaCl (63.6 %) and KBr (36.4 %) respectively.*
Duration: 1 minute. Data points: 3457. Interval: 0.02 °. GOF: 1.08. R_{wp}: 42.863 %.

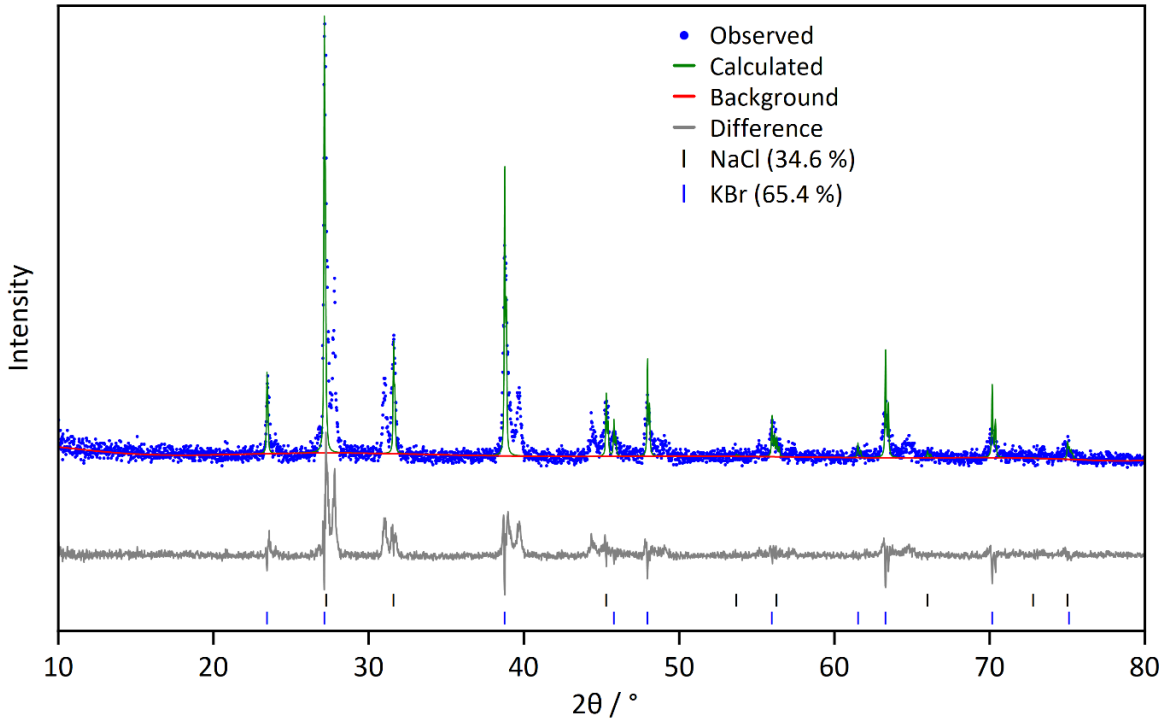

Figure 287 *Powder X-ray diffractogram of material resulting from the reaction of NaCl and KBr, after 12 hours of heating at 700 °C. The small blue circles represent the observed diffracted intensity, the green line represents the Rietveld-refined calculated model, the red line represents the background, and the grey line represents the difference between observed and calculated intensities. The black and blue tick marks show the reflections of the refined models of NaCl (34.6 %) and KBr (65.4 %) respectively.*
Duration: 2 minutes. Data points: 3457. Interval: 0.02 °. GOF: 1.80. R_{wp}: 47.499 %.

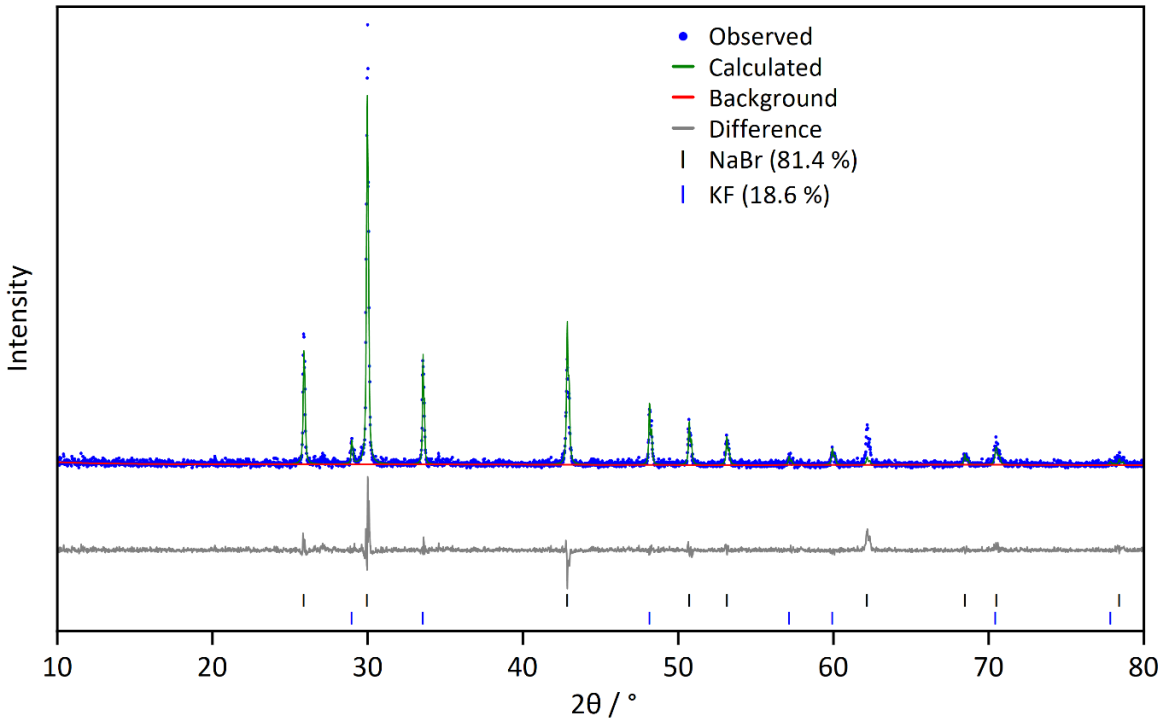

Figure 288 *Powder X-ray diffractogram of the unreacted precursors of the reaction of NaBr and KF. The small blue circles represent the observed diffracted intensity, the green line represents the Rietveld-refined calculated model, the red line represents the background, and the grey line represents the difference between observed and calculated intensities. The black and blue tick marks show the reflections of the refined models of NaBr (81.4 %) and KF (18.6 %) respectively.*
Duration: 1 minute. Data points: 3457. Interval: 0.02 °. GOF: 1.19. R_{wp}: 40.802 %.

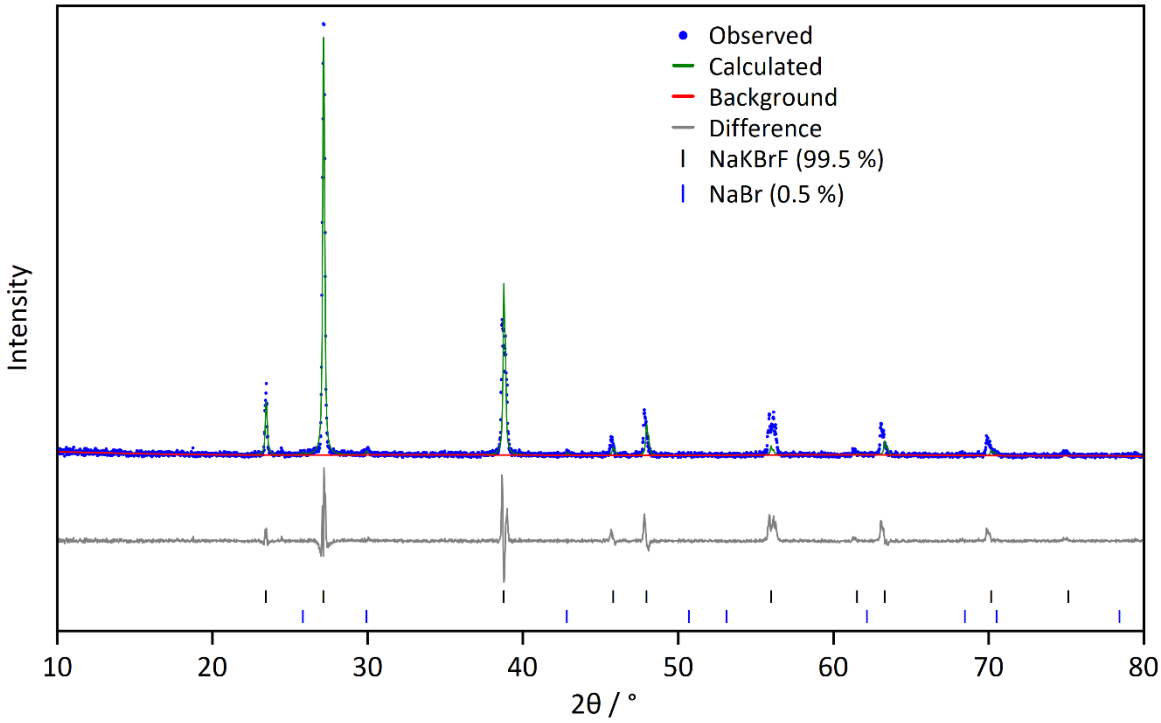

Figure 289 *Powder X-ray diffractogram of material resulting from the reaction of NaBr and KF, after 12 hours of heating at 700 °C. The small blue circles represent the observed diffracted intensity, the green line represents the Rietveld-refined calculated model, the red line represents the background, and the grey line represents the difference between observed and calculated intensities. The black and blue tick marks show the reflections of the refined models of NaKBrF (99.5 %) and NaBr (0.5 %) respectively.*
Duration: 2 minutes. Data points: 3457. Interval: 0.02 °. GOF: 1.76. R_{wp}: 42.060 %.

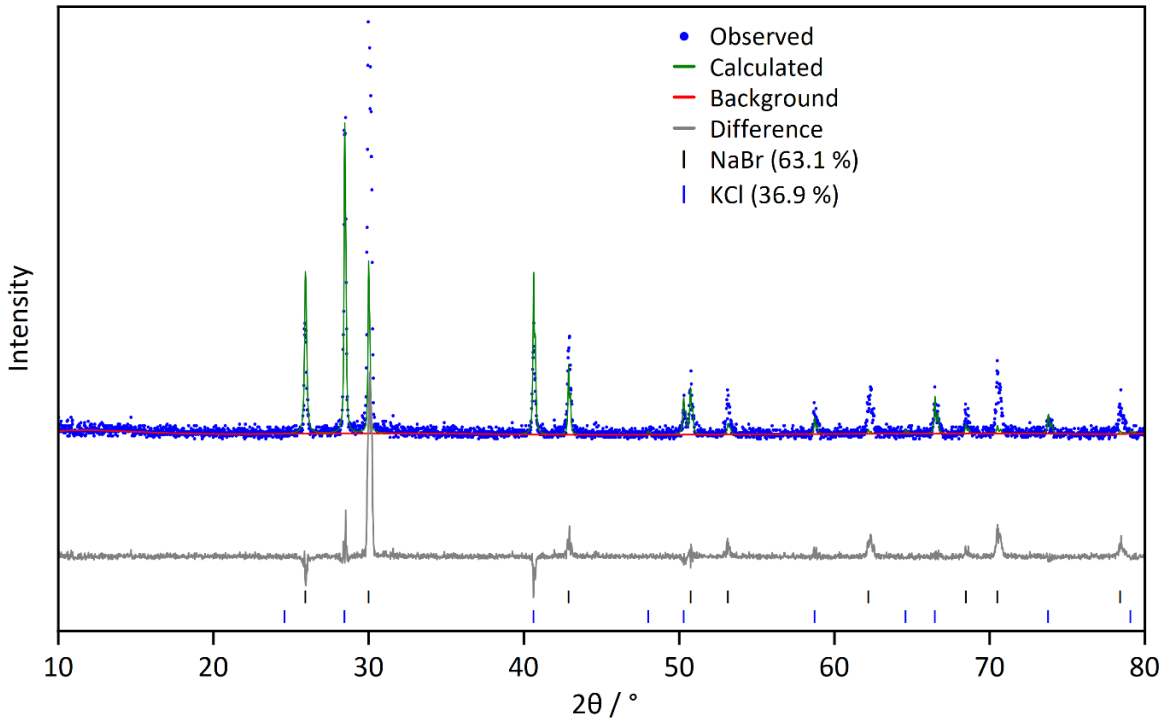

Figure 290 *Powder X-ray diffractogram of the unreacted precursors of the reaction of NaBr and KCl. The small blue circles represent the observed diffracted intensity, the green line represents the Rietveld-refined calculated model, the red line represents the background, and the grey line represents the difference between observed and calculated intensities. The black and blue tick marks show the reflections of the refined models of NaBr (63.1 %) and KCl (36.9 %) respectively.*
Duration: 1 minute. Data points: 3457. Interval: 0.02 °. GOF: 1.56. R_{wp}: 55.260 %.

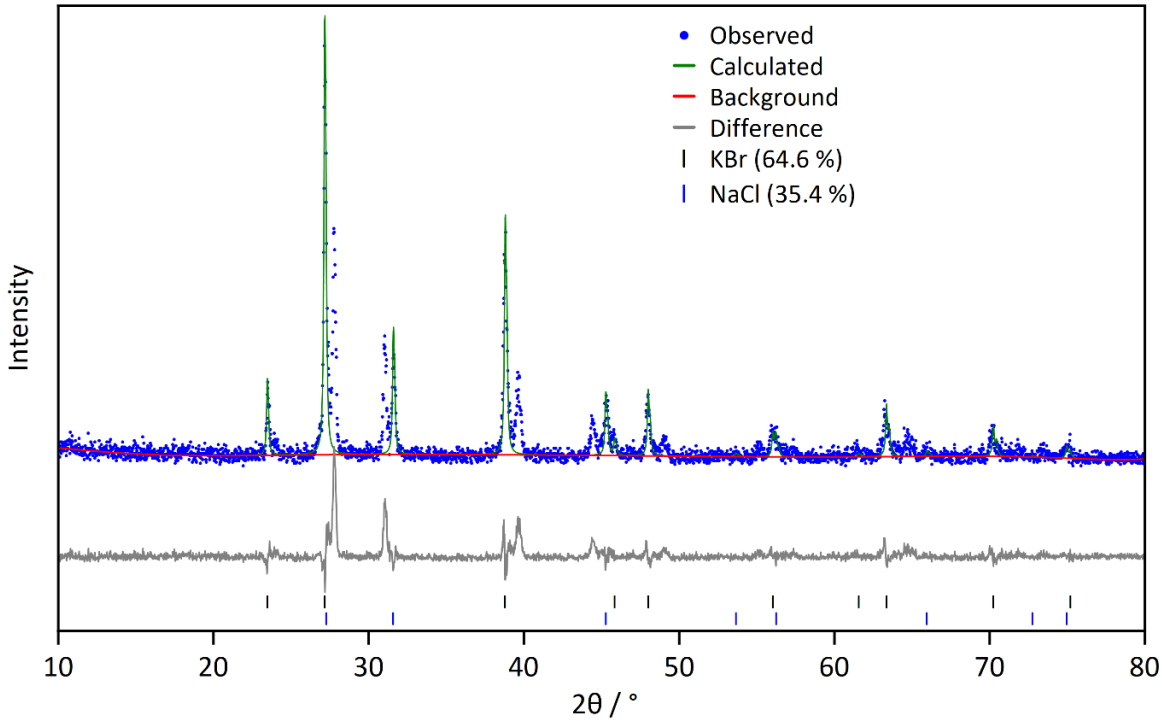

Figure 291 *Powder X-ray diffractogram of material resulting from the reaction of NaBr and KCl, after 12 hours of heating at 700 °C. The small blue circles represent the observed diffracted intensity, the green line represents the Rietveld-refined calculated model, the red line represents the background, and the grey line represents the difference between observed and calculated intensities. The black and blue tick marks show the reflections of the refined models of KBr (64.6 %), and NaCl (35.4 %) respectively.*
Duration: 2 minutes. Data points: 3457. Interval: 0.02 °. GOF: 1.66. R_{wp}: 42.694 %.

B.3.7 Parallel Synthesis Attempts

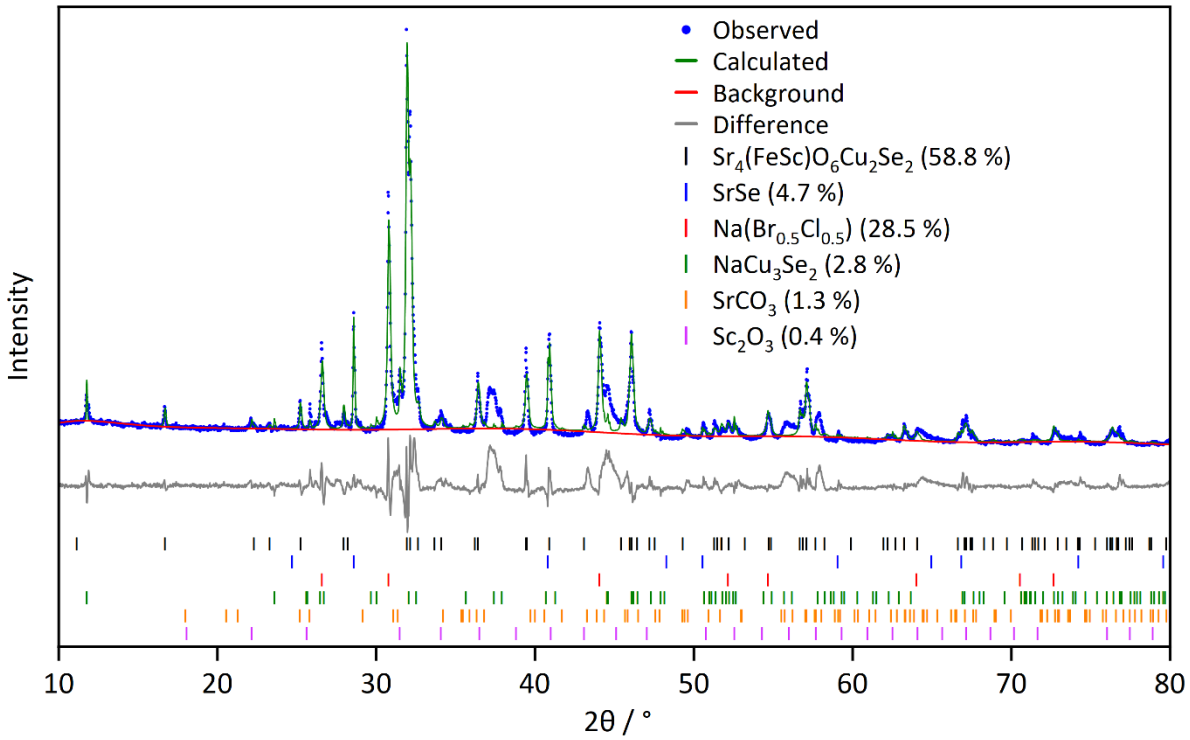

Figure 292 *Powder X-ray diffractogram of material resulting from attempted parallel metathetic syntheses of $Sr_3Fe_2O_5Cu_2Se_2$ and $Sr_3Sc_2O_5Cu_2Se_2$ after 12 hours of heating at 600 °C. The small blue circles represent the observed diffracted intensity, the green line represents the Rietveld-refined calculated model, the red line represents the background, and the grey line represents the difference between observed and calculated intensities. The black, blue, red, green, orange, and pink tick marks show the reflections of the refined models of $Sr_4(FeSc)O_6Cu_2Se_2$ (58.8 %), SrSe (4.7 %), $Na(Br_{0.5}Cl_{0.5})$ (28.5 %), $NaCu_3Se_2$ (2.8 %), $SrCO_3$ (1.3 %), and Sc_2O_3 (0.4 %) respectively.*
Duration: 3 hours. Data points: 4444. Interval: 0.02 °. GOF: 5.28. R_{wp}: 10.021 %.

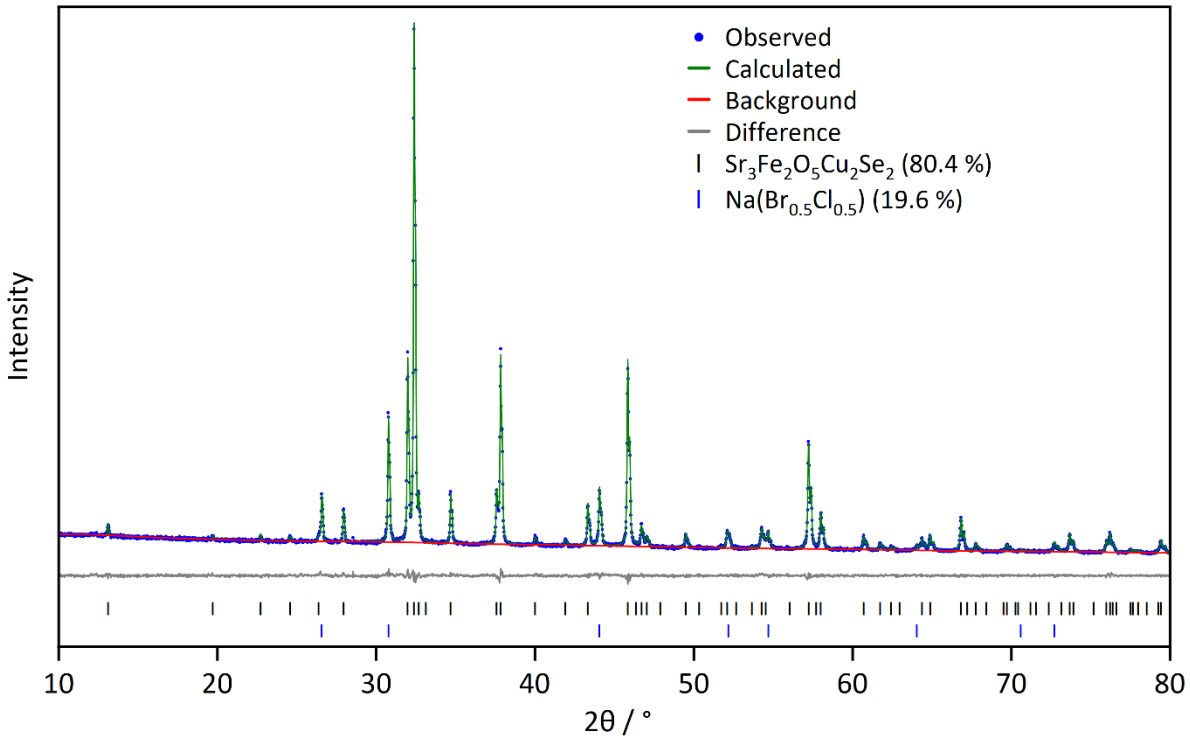

Figure 293 *Powder X-ray diffractogram of material resulting from attempted parallel metathetic synthesis of $Sr_3Fe_2O_5Cu_2Se_2$ after 12 hours of heating at 600 °C. The small blue circles represent the observed diffracted intensity, the green line represents the Rietveld-refined calculated model, the red line represents the background, and the grey line represents the difference between observed and calculated intensities. The black and blue tick marks show the reflections of the refined models of $Sr_3Fe_2O_5Cu_2Se_2$ (80.4 %), and $Na(Br_{0.5}Cl_{0.5})$ (19.6 %) respectively.*
Duration: 3 hours. Data points: 4444. Interval: 0.02 °. GOF: 1.20. R_{wp}: 2.326 %.

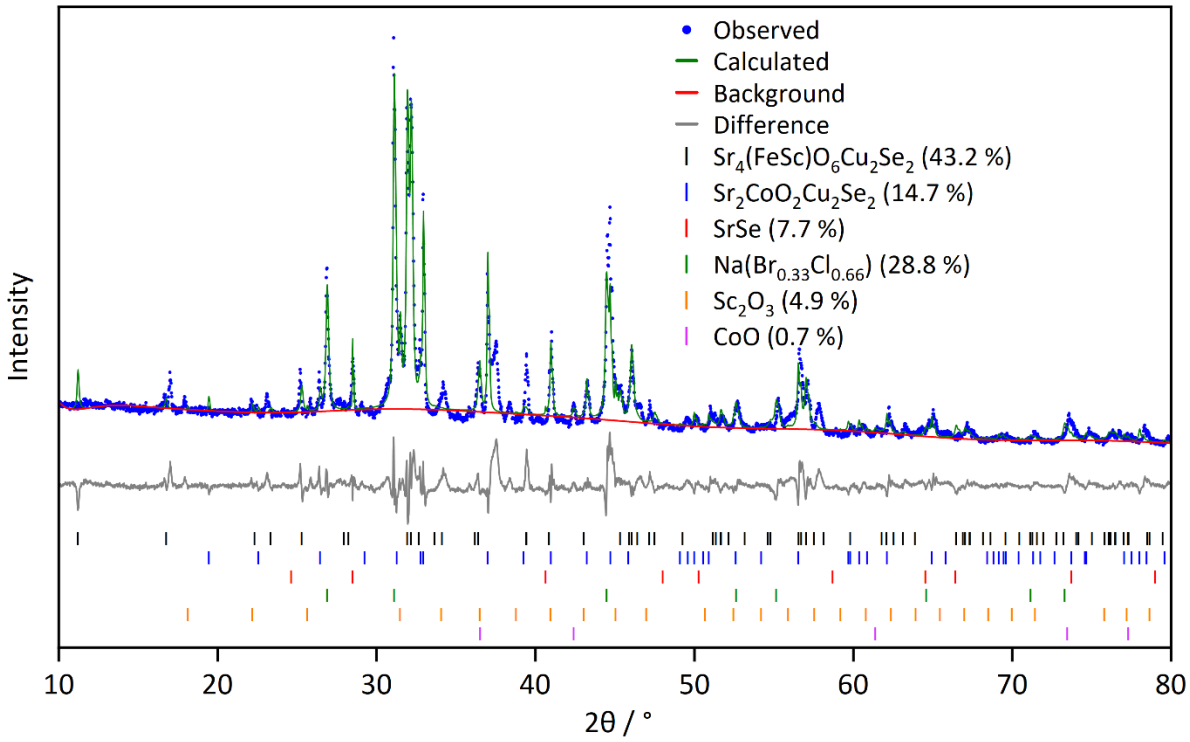

Figure 294 *Powder X-ray diffractogram of material resulting from attempted parallel metathetic syntheses of $Sr_3Fe_2O_5Cu_2Se_2$, $Sr_3Sc_2O_5Cu_2Se_2$ and $Sr_3Co_2O_5Cu_2Se_2$ after 12 hours of heating at 600 °C. The small blue circles represent the observed diffracted intensity, the green line represents the Rietveld-refined calculated model, the red line represents the background, and the grey line represents the difference between observed and calculated intensities. The black, blue, red, green, orange, and pink tick marks show the reflections of the refined models of $Sr_4(FeSc)O_6Cu_2Se_2$ (43.2 %), $Sr_2CoO_2Cu_2Se_2$ (14.7 %), SrSe (7.7 %), $Na(Br_{0.33}Cl_{0.66})$ (28.8 %), Sc_2O_3 (4.9 %), and CoO (0.7 %) respectively.*
Duration: 3 hours. Data points: 4444. Interval: 0.02 °. GOF: 4.33. R_{wp}: 7.638 %.

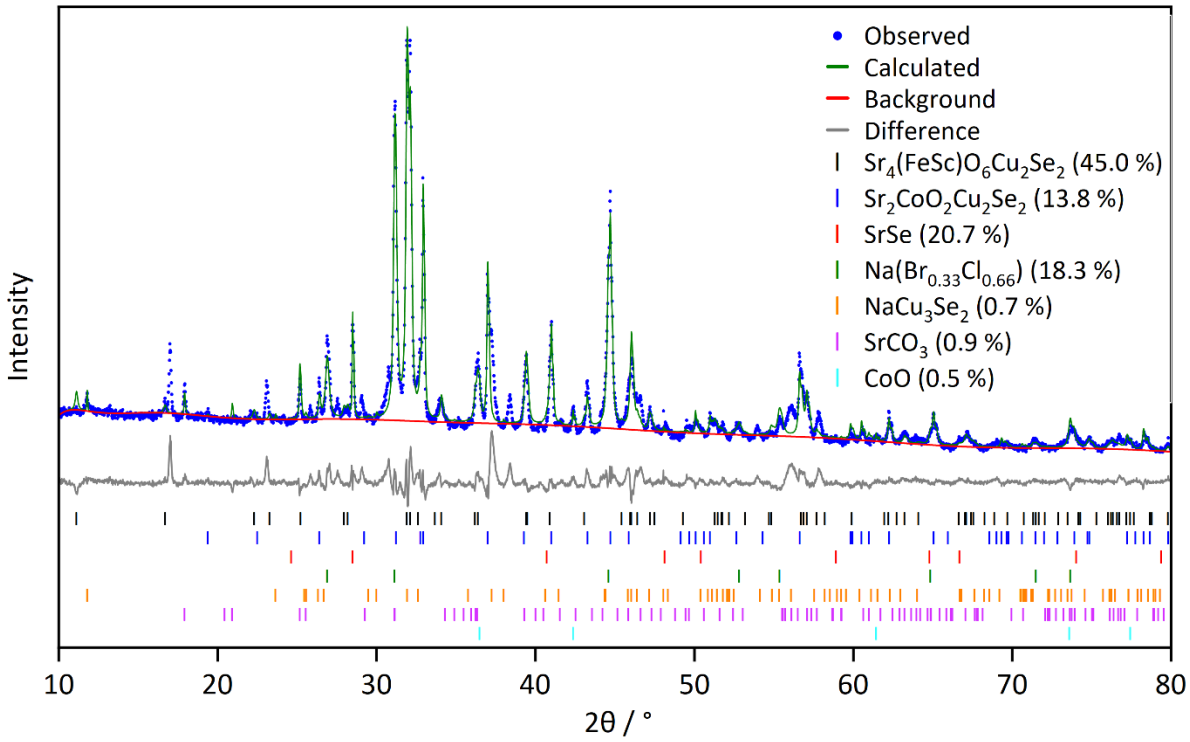

Figure 295 *Powder X-ray diffractogram of material resulting from attempted parallel metathetic syntheses of $Sr_4Fe_2O_6Cu_2Se_2$, $Sr_4Sc_2O_6Cu_2Se_2$ and $Sr_4Co_2O_6Cu_2Se_2$ after 12 hours of heating at 600 °C. The small blue circles represent the observed diffracted intensity, the green line represents the Rietveld-refined calculated model, the red line represents the background, and the grey line represents the difference between observed and calculated intensities. The black, blue, red, green, orange, pink and cyan tick marks show the reflections of the refined models of $Sr_4(FeSc)O_6Cu_2Se_2$ (45.0 %), $Sr_2CoO_2Cu_2Se_2$ (13.8 %), SrSe (20.7 %), $Na(Br_{0.33}Cl_{0.66})$ (18.3 %), $NaCu_3Se_2$ (0.7 %), $SrCO_3$ (0.9 %) and CoO (0.5 %) respectively. Duration: 3 hours. Data points: 4444. Interval: 0.02 °. GOF: 3.79. R_{wp}: 6.647 %.*

Bibliography

1. H. Hiramatsu, H. Kamioka, K. Ueda, H. Ohta, T. Kamiya, M. Hirano and H. Hosono, *physica status solidi (a)*, 2006, **203**, 2800–2811.
2. Y. Mizuguchi and Y. Takano, *arXiv: Superconductivity*, 2010.
3. A. Chaupatnaik, A. M. Abakumov, G. Rousse and J.-M. Tarascon, *Energy Storage Materials*, 2023, **63**, 103042.
4. A. L. S. Bacha, Doctor of Philosophy (PhD), University of Kent, 2023.
5. J. F. Wager, M. M. Valencia, J. P. Bender, B. J. Norris, H. Q. Chiang, D. Hong, B. J. Norris, T. V. Harman, C. H. Park, J. Anderson, C. H. Park, D. A. Keszler, J. Tate, H. Yanagi, M. Price and R. Hoffman, *Transparent electronics and prospects for transparent displays*, SPIE, 2003.
6. S. J. Clarke, P. Adamson, S. J. C. Herkelrath, O. J. Rutt, D. R. Parker, M. J. Pitcher and C. F. Smura, *Inorganic Chemistry*, 2008, **47**, 8473–8486.
7. K. Ueda and H. Hosono, *Thin Solid Films*, 2002, **411**, 115–118.
8. K. Otzschi, H. Ogino, J. Shimoyama and K. Kishio, *Journal of Low Temperature Physics*, 1999, **117**, 729–733.
9. W. J. Zhu and P. H. Hor, *Journal of Solid State Chemistry*, 1997, **130**, 319–321.
10. D. C. Palmer and S. E. Palmer, CrystalMaker®: a crystal and molecular structures program for Mac and Windows, (www.crystalmaker.com, 2020).
11. R. G. Pearson, *Journal of Chemical Education*, 1968, **45**, 581.
12. B. Morosin, *Acta Crystallographica Section B*, 1973, **29**, 2647–2648.
13. F. A. Bannister, *Journal of the Mineralogical Society*, 1935, **24**, 49–58.
14. W. Zachariasen, *Zeitschrift für Physikalische Chemie*, 1926, **123U**, 134–150.
15. F. A. Bannister, *Mineralogical magazine and journal of the Mineralogical Society*, 1934, **23**, 587–597.
16. V. Johnson and W. Jeitschko, *Journal of Solid State Chemistry*, 1974, **11**, 161–166.
17. J. M. Mayer, L. F. Schneemeyer, T. Siegrist, J. V. Waszczak and B. Van Dover, *Angewandte Chemie International Edition in English*, 1992, **31**, 1645–1647.
18. N. G. Connelly, T. Damhus, R. M. Hartshorn and A. T. Hutton, *The IUPAC Red Book - Nomenclature of Inorganic Chemistry*, RSC Publishing, RSC Publishing, 2005.
19. L. Pauling, *Nature of the Chemical Bond*, Cornell University Press, Cornell University Press, 1932.
20. G. J. Limburn, M. J. P. Stephens, B. A. D. Williamson, A. Iborra-Torres, D. O. Scanlon and G. Hyett, *Journal of Materials Chemistry A*, 2020, **8**, 19887–19897.
21. B. C. Sheath, S. J. Cassidy and S. J. Clarke, *Journal of Solid State Chemistry*, 2021, **293**, 121761.

22. W. Li, Z. Fu, X. Wang, J. Zhang, M. Liu, J. Zhao, M. Jin, G. Zhao, G. Dai, Z. Deng, S. Zhang, S. Feng, Z. Hu, Q. Huang, H. Lin, C. T. Chen, Y. Yang and C. Jin, *Inorganic Chemistry*, 2018, **57**, 5108–5113.

23. R. Nath, V. O. Garlea, A. I. Goldman and D. C. Johnston, *Physical Review B*, 2010, **81**, 224513.

24. D. O. Charkin, A. V. Urmanov, I. V. Plokhikh, A. D. Korshunov, A. N. Kuznetsov and S. M. Kazakov, *Journal of Alloys and Compounds*, 2014, **585**, 644–649.

25. H. Mao, C. Wang, H. E. Maynard-Casely, Q. Huang, Z. Wang, G. Cao, S. Li and H. Luo, *Europhysics Letters*, 2017, **117**, 57005.

26. F. Pors, R. Marchand and Y. Laurent, *Journal of Solid State Chemistry*, 1993, **107**, 39–42.

27. E. Günther, R. Hagenmayer and M. Jansen, *Zeitschrift für anorganische und allgemeine Chemie*, 2000, **626**, 1519–1525.

28. N. Diot, R. Marchand, J. Haines, J. M. Léger, P. Macaudière and S. Hull, *Journal of Solid State Chemistry*, 1999, **146**, 390–393.

29. D. Balz and K. Plieth, *Zeitschrift für Elektrochemie, Berichte der Bunsengesellschaft für physikalische Chemie*, 1955, **59**, 545–551.

30. S. N. Ruddlesden and P. Popper, *Acta Crystallographica*, 1958, **11**, 54–55.

31. S. N. Ruddlesden and P. Popper, *Acta Crystallographica*, 1957, **10**, 538–539.

32. W. Bensch, H. W. Schmalle and A. Reller, *Solid State Ionics*, 1990, **43**, 171–177.

33. Y. Matsumoto, T. Yamamoto, K. Nakano, H. Takatsu, T. Murakami, K. Hongo, R. Maezono, H. Ogino, D. Song, C. M. Brown, C. Tassel and H. Kageyama, *Angewandte Chemie International Edition*, 2019, **58**, 756–759.

34. H. Ogino, Y. Katagi, J. Shimoyama, K. Yamanoi, M. Tsuboi, T. Shimizu, N. Sarukura and K. Kishio, *Optical Materials*, 2014, **36**, 1978–1981.

35. E. Brechtel, G. Cordier and H. Schäfer, *Zeitschrift für Naturforschung B*, 1979, **34**, 777–780.

36. S. L. Brock and S. M. Kauzlarich, *Inorganic Chemistry*, 1994, **33**, 2491–2492.

37. W. J. Zhu, P. H. Hor, A. J. Jacobson, G. Crisci, T. A. Albright, S. H. Wang and T. Vogt, *Journal of the American Chemical Society*, 1997, **119**, 12398–12399.

38. Y. Yang, Z. Zhou, B. Wei, J. Liu, J.-L. Lan, M. Zou, Y. Xu, Y. Zheng, C.-W. Nan and Y.-H. Lin, *Journal of the American Ceramic Society*, 2023, **106**, 2918–2929.

39. Z. Malik, S. Broadley, S. J. C. Herkelrath, D. W. Newbrook, L. Kemp, G. Rutt, Z. A. Gál, J. N. Blandy, J. Hadermann, D. W. Davies, R. D. Smyth, D. O. Scanlon, R. Huang, S. J. Clarke and G. Hyett, *Journal of Materials Chemistry C*, 2024, **12**, 17574–17586.

40. O. Y. Mruz, V. K. Pecharskij, A. N. Sobolev and O. I. Bodak, *Kristallografiya*, 1990, **35**, 202–204.

41. W. J. Zhu and P. H. Hor, *Journal of Solid State Chemistry*, 1997, **134**, 128–131.

42. M.-L. Liu, L.-B. Wu, F.-Q. Huang, L.-D. Chen and I. W. Chen, *Journal of Applied Physics*, 2007, **102**, 116108.

43. S. Park, D. A. Keszler, M. M. Valencia, R. L. Hoffman, J. P. Bender and J. F. Wager, *Applied Physics Letters*, 2002, **80**, 4393–4394.

44. K. Ueda, S. Inoue, S. Hirose, H. Kawazoe and H. Hosono, *Applied Physics Letters*, 2000, **77**, 2701–2703.

45. H. Hiramatsu, M. Orita, M. Hirano, K. Ueda and H. Hosono, *Journal of Applied Physics*, 2002, **91**, 9177–9181.

46. D. O. Scanlon and G. W. Watson, *Chemistry of Materials*, 2009, **21**, 5435–5442.

47. D. Johrendt and R. Pöttgen, *Physica C: Superconductivity*, 2009, **469**, 332–339.

48. J. H. Tapp, Z. Tang, B. Lv, K. Sasmal, B. Lorenz, P. C. W. Chu and A. M. Guloy, *Physical Review B*, 2008, **78**, 060505.

49. M. Tegel, I. Schellenberg, F. Hummel, R. Pöttgen and D. Jorendt, *Zeitschrift für Naturforschung B*, 2009, **64**, 815–820.

50. X. Zhu, F. Han, G. Mu, B. Zeng, P. Cheng, B. Shen and H.-H. Wen, *Physical Review B*, 2009, **79**, 024516.

51. P. M. Shirage, K. Kihou, C.-H. Lee, H. Kito, H. Eisaki and A. Iyo, *Journal of the American Chemical Society*, 2011, **133**, 9630–9633.

52. K. Machida, H. Ogino, A. Yamamoto, K. Kishio and J. Shimoyama, *Physics Procedia*, 2012, **36**, 727–730.

53. W. Kohn and L. J. Sham, *Physical Review*, 1965, **140**, A1133–A1138.

54. R. Haunschild, A. Barth and B. French, *Journal of Cheminformatics*, 2019, **11**, 72.

55. J. P. Perdew, K. Burke and M. Ernzerhof, *Physical Review Letters*, 1996, **77**, 3865–3868.

56. D. S. Sholl and J. A. Steckel, in *Density Functional Theory: A Practical Introduction*, 2009, DOI: 10.1002/9780470447710.ch1, pp. 1–33.

57. H. Ogino, J. Shimoyama, K. Kishio, Y. Katsura, M. Tsuboi, K. Yamanoi, M. Cadatal-Raduban, T. Nakazato, T. Shimizu and N. Sarukura, *Applied Physics Letters*, 2012, **101**.

58. Y. Iwasa, H. Ogino, D. Song, V. C. Agulto, K. Yamanoi, T. Shimizu, J. Ueda, K. Hongo, R. Maezono, S. Tanabe and N. Sarukura, *Journal of Materials Science: Materials in Electronics*, 2019, **30**, 16827–16832.

59. G. J. Limburn, Doctor of Philosophy, University of Southampton, 2020.

60. L. Vegard, *Zeitschrift für Physik*, 1921, **5**, 17–26.

61. L. Cario, A. Lafond, T. Morvan, H. Kabbour, G. André and P. Palvadeau, *Solid State Sciences*, 2005, **7**, 936–944.

62. B. A. D. Williamson, G. J. Limburn, G. W. Watson, G. Hyett and D. O. Scanlon, *Matter*, 2020, **3**, 759–781.

63. W. J. Zhu and P. H. Hor, *Inorganic Chemistry*, 1997, **36**, 3576–3577.

64. Z. Malik, L. Kemp, B. F. Grosso, D. W. Davies, D. O. Scanlon and G. Hyett, *Chemistry of Materials*, 2024, **36**, 11326–11337.

65. X. He, T. Cho, T. Katase, K. Hanzawa, S. Kitani, H. Hiramatsu, H. Hosono and T. Kamiya, *Chemistry of Materials*, 2024, DOI: 10.1021/acs.chemmater.4c00724.

66. W. J. Zhu and P. H. Hor, *Journal of Solid State Chemistry*, 2000, **153**, 26–29.

67. K. Ueda, S. Hirose, H. Kawazoe and H. Hosono, *Chemistry of Materials*, 2001, **13**, 1880–1883.

68. H. Ogino, Y. Matsumura, Y. Katsura, K. Ushiyama, S. Horii, K. Kishio and J.-i. Shimoyama, *Superconductor Science and Technology*, 2009, **22**, 075008.

69. I. R. Shein and A. L. Ivanovskii, *arXiv: Superconductivity*, 2009.

70. K. Yates, I. Usman, K. Morrison, J. Moore, A. Gilbertson, A. Caplin, L. Cohen, H. Ogino and J. Shimoyama, *Superconductor Science and Technology*, 2009, DOI: 10.1088/0953-2048/23/2/022001.

71. H. Nakamura and M. Machida, *Journal of the Physical Society of Japan*, 2010, **79**, 013705.

72. H. Ogino, Y. Katsura, S. Horii, K. Kishio and J. Shimoyama, *arXiv: Superconductivity*, 2009, **22**, 085001.

73. I. Shein and A. Ivanovskii, *Open Physics*, 2010, **8**, 432–437.

74. I. R. Shein and A. L. Ivanovskii, *Journal of Superconductivity and Novel Magnetism*, 2009, **22**, 613–617.

75. J. Zhao, Q. Huang, C. de la Cruz, S. Li, J. W. Lynn, Y. Chen, M. A. Green, G. F. Chen, G. Li, Z. Li, J. L. Luo, N. L. Wang and P. Dai, *Nature Materials*, 2008, **7**, 953–959.

76. H. Ogino, S. Sato, Y. Matsumura, N. Kawaguchi, K. Ushiyama, Y. Katsura, S. Horii, K. Kishio and J. Shimoyama, *Physica C-superconductivity and Its Applications*, 2010, **470**, 280–281.

77. M. Tegel, F. Hummel, S. Lackner, I. Schellenberg, R. Pöttgen and D. Johrendt, *Zeitschrift für anorganische und allgemeine Chemie*, 2009, **635**, 2242–2248.

78. M. Tegel, F. Hummel, Y. Su, T. Chatterji, M. Brunelli and D. Johrendt, *Europhysics Letters*, 2010, **89**, 37006.

79. F. Han, X. Zhu, G. Mu, P. Cheng, B. Shen, B. Zeng and H. Wan, *Science China Physics, Mechanics and Astronomy*, 2010, **53**, 1202–1206.

80. I. I. Mazin, *Physical Review B*, 2010, **81**, 020507.

81. A. Sefat, D. Singh, V. O. Garlea, Y. Zuev, M. McGuire and B. Sales, *Physica C-superconductivity and Its Applications*, 2011, **471**, 143–149.

82. X. Zhu, F. Han, G. Mu, P. Cheng, B. Shen, B. Zeng and H.-H. Wen, *Physical Review B*, 2009, **79**, 220512.

83. H. Kotegawa, T. Kawazoe, H. Tou, K. Murata, H. Ogino, K. Kishio and J. Shimoyama, *arXiv: Superconductivity*, 2009.

84. H. Kotegawa, Y. Tao, H. Tou, H. Ogino, S. Horii, K. Kishio and J. Shimoyama, *Journal of the Physical Society of Japan*, 2011, **80**, 014712–014712.

85. D. O. Charkin, A. Sadakov, O. E. Omel'yanovskii and S. Kazakov, *Materials Research Bulletin*, 2010, **45**, 2012–2016.

86. D. V. Suetin and A. L. Ivanovskii, *Journal of Solid State Chemistry*, 2012, **194**, 100–105.

87. D. Berthebaud, O. Lebedev, D. Pelloquin and A. Maignan, *Solid State Sciences*, 2014, **36**, 94–100.

88. S. Okada, Y. Kamihara, N. Ohkubo, S. Ban and M. Matoba, 2014.

89. Y. Iwasa, H. Ogino, D. Song, K. Yamanoi, T. Shimizu, J. Ueda, S. Tanabe and N. Sarukura, *Optical Materials*, 2018, **84**, 205–208.

90. G. Hyett, N. Barrier, S. J. Clarke and J. Hadermann, *Journal of the American Chemical Society*, 2007, **129**, 11192–11201.

91. S. Horii, H. Ogino, M. Yamaki, M. Haruta, T. Maeda and J.-i. Shimoyama, *Applied Superconductivity, IEEE Transactions on*, 2011, **21**, 2741–2744.

92. N. Kawaguchi, H. Ogino, Y. Shimizu, K. Kishio and J.-i. Shimoyama, *Applied Physics Express*, 2010, **3**, 063102.

93. H. Ogino, K. Machida, A. Yamamoto, K. Kishio, J.-i. Shimoyama, T. Tohei and Y. Ikuhara, *Superconductor Science and Technology*, 2010, **23**, 115005.

94. H. Ogino, S. Sato, K. Kishio, J. Shimoyama, T. Tohei and Y. Ikuhara, *Applied Physics Letters*, 2010, **97**, 072506.

95. H. Ogino, S. Sato, K. Kishio and J.-i. Shimoyama, *Physics Procedia*, 2012, **36**, 722–726.

96. S. J. Singh, H. Ogino, J.-i. Shimoyama and K. Kishio, *Superconductor Science and Technology*, 2013, **26**, 105020.

97. S. J. Singh, J. Shimoyama, H. Ogino and K. Kishio, *Physica C: Superconductivity and its Applications*, 2015, **518**, 18–22.

98. H. Ogino, Y. Shimizu, N. Kawaguchi, K. Kishio, J. Shimoyama, T. Tohei and Y. Ikuhara, *Superconductor Science and Technology*, 2011, **24**, 085020.

99. J.-i. Shimoyama, H. Ogino, A. Yamamoto and K. Kishio, *Solid State Communications*, 2012, **152**, 640–643.

100. G. Hyett, Z. A. Gál, C. F. Smura and S. J. Clarke, *Chemistry of Materials*, 2008, **20**, 559–566.

101. Z. A. Gál, O. J. Rutt, C. F. Smura, T. P. Overton, N. Barrier, S. J. Clarke and J. Hadermann, *Journal of the American Chemical Society*, 2006, **128**, 8530–8540.

102. O. J. Rutt, G. R. Williams and S. J. Clarke, *Chemical Communications*, 2006, DOI: 10.1039/B605105G, 2869–2871.

103. S. Indris, J. Cabana, O. J. Rutt, S. J. Clarke and C. P. Grey, *Journal of the American Chemical Society*, 2006, **128**, 13354–13355.

104. K. H. Zhang, K. Xi, M. G. Blamire and R. G. Egdell, *Journal of Physics: Condensed Matter*, 2016, **28**, 383002.

105. C. G. Granqvist and A. Hultåker, *Thin Solid Films*, 2002, **411**, 1–5.

106. Z. Chen, W. Li, R. Li, Y. Zhang, G. Xu and H. Cheng, *Langmuir*, 2013, **29**, 13836–13842.

107. A. M. Alfantazi and R. R. Moskalyk, *Minerals Engineering*, 2003, **16**, 687–694.

108. G.-h. Wang, P.-p. Du, L.-j. Zhang, Y. Long and J.-s. Zhang, *Scientific Reports*, 2024, **14**, 30153.

109. S. Wang, Y. Tian, C. Hang and C. Wang, *Scientific Reports*, 2018, **8**, 5260.

110. A. Thomas, G. Fribourg, J.-J. Blandin, P. Lhuissier, R. Dendievel and G. Martin, *Additive Manufacturing*, 2021, **48**, 102393.

111. M. Pozzo, C. Davies, D. Gubbins and D. Alfè, *Earth and Planetary Science Letters*, 2014, **393**, 159–164.

112. S. Fan, G. Plascencia and T. Utigard, *Canadian Metallurgical Quarterly*, 2008, **47**, 509–512.

113. M. Suzuki, Y. Maeda and Y. Sawada, *Japanese Journal of Applied Physics*, 1998, **37**, 34.

114. H. B. Saim and D. S. Campbell, *Solar Energy Materials*, 1987, **15**, 249–260.

115. W.-H. Baek, M. Choi, T.-S. Yoon, H. H. Lee and Y.-S. Kim, *Applied Physics Letters*, 2010, **96**.

116. T. Kawashima, T. Ezure, K. Okada, H. Matsui, K. Goto and N. Tanabe, *Journal of Photochemistry and Photobiology A: Chemistry*, 2004, **164**, 199–202.

117. A. A. F. Husain, W. Z. W. Hasan, S. Shafie, M. N. Hamidon and S. S. Pandey, *Renewable and Sustainable Energy Reviews*, 2018, **94**, 779–791.

118. F. Bloch, *Zeitschrift für Physik*, 1929, **52**, 555–600.

119. E. Fermi, *Rendiconti Lincei*, 1926, **3**, 145–149.

120. X. Pi, *Journal of Nanomaterials*, 2012, **2012**, 912903.

121. U. Schwingenschlögl, A. Chroneos, C. Schuster and R. Grimes, *Applied Physics Letters*, 2010, **96**, 242107–242107.

122. W. H. Strehlow and E. L. Cook, *Journal of Physical and Chemical Reference Data*, 1973, **2**, 163–200.

123. E. O. Kane, *Journal of Physics and Chemistry of Solids*, 1957, **1**, 249–261.

124. D. Wang, S. Kamezawa, K. Yamamoto and H. Nakashima, 2014.

125. J. Low, *American Journal of Undergraduate Research*, 2009, **8**, 29–34.

126. J. A. Owolabi, M. Y. Onimisi, S. G. Abdu and G. O. Olowomofe, *Computational Chemistry*, 2016, **4**.

127. M. Heinemann, B. Eifert and C. Heiliger, *Physical Review B*, 2013, **87**, 115111.

128. V. N. Jafarova and G. S. Orudzhev, *Solid State Communications*, 2021, **325**, 114166.

129. C. J. H. Wort and R. S. Balmer, *Materials Today*, 2008, **11**, 22–28.

130. L. Garvie, P. Rez, J. Alvarez, P. Buseck, A. Craven and R. Brydson, *American Mineralogist*, 2000, **85**.

131. W. Seiler, M. Nistor, C. Hebert and J. Perrière, *Solar Energy Materials and Solar Cells*, 2013, **116**, 34–42.

132. P. Song, H. Akao, M. Kamei, Y. Shigesato and I. Yasui, *Japanese Journal of Applied Physics*, 1999, **38**, 5224–5226.

133. W. S. Lau and S. J. Fonash, *Journal of Electronic Materials*, 1986, **15**, 117–123.

134. M. A. Flores-Mendoza, R. Castanedo-Perez, G. Torres-Delgado, J. Márquez Marín and O. Zelaya-Angel, *Thin Solid Films*, 2008, **517**, 681–685.

135. T. S. Moss, *Proceedings of the Physical Society. Section B*, 1954, **67**, 775.

136. E. Burstein, *Physical Review*, 1954, **93**, 632–633.

137. S. Gahlawat, J. Singh, A. K. Yadav and P. P. Ingole, *Physical Chemistry Chemical Physics*, 2019, **21**, 20463–20477.

138. L. Zhang, J. Zhang, H. Yu and J. Yu, *Advanced Materials*, 2022, **34**, 2107668.

139. V. Rajendran, A. Prathuru, C. Fernandez, D. Sujatha, S. K. Panda and N. H. Faisal, *Engineering Reports*, 2024, **6**, e12836.

140. H. Li, L. Guo, X. Liu, T. Sun, Q. Li, F. Zhang, G. Xiao, T. Fu and Y. Chen, *Frontiers in Materials*, 2020, **7**.

141. S. Geiger, O. Kasian, A. M. Mingers, K. J. J. Mayrhofer and S. Cherevko, *Scientific Reports*, 2017, **7**, 4595.

142. M. Senthilkumar, J. Mathiyarasu, J. Joseph, K. L. N. Phani and V. Yegnaraman, *Materials Chemistry and Physics*, 2008, **108**, 403–407.

143. Z. Yu, I. R. Perera, T. Daeneke, S. Makuta, Y. Tachibana, J. J. Jasieniak, A. Mishra, P. Bäuerle, L. Spiccia and U. Bach, *NPG Asia Materials*, 2016, **8**, e305–e305.

144. H. Kim, C. M. Gilmore, A. Piqué, J. S. Horwitz, H. Mattoussi, H. Murata, Z. H. Kafafi and D. B. Chrisey, *Journal of Applied Physics*, 1999, **86**, 6451–6461.

145. T. Maruyama and K. Tabata, *Japanese Journal of Applied Physics*, 1990, **29**, L355.

146. P. Semenza, *Information Display*, 2013, **29**, 40–42.

147. M. Frenzel, C. Mikolajczak, M. A. Reuter and J. Gutzmer, *Resources Policy*, 2017, **52**, 327–335.

148. M. Redlinger, R. Eggert and M. Woodhouse, *Solar Energy Materials and Solar Cells*, 2015, **138**, 58–71.

149. H. Ritchie, M. Roser and P. Rosado, Renewable Energy, https://ourworldindata.org/renewable-energy, (accessed Nov 20, 2024).

150. D. Ginley, *Handbook of Transparent Conductors*, Springer, 2011.

151. N. Zhang, J. Sun and H. Gong, *Coatings*, 2019, **9**, 137.

152. A. J. Freeman, K. R. Poeppelmeier, T. O. Mason, R. P. H. Chang and T. J. Marks, *MRS Bulletin*, 2000, **25**, 45–51.

153. K. Bädeker, *Annalen der Physik*, 1907, **327**, 749–766.

154. M. Grundmann, *physica status solidi (a)*, 2015, **212**.

155. E. Przezdziecka, A. Wierzbicka, P. Dłuzewski, I. Sankowska, P. Sybilski, K. Morawiec, M. A. Pietrzyk and A. Kozanecki, *Crystal Growth & Design*, 2020, **20**, 5466–5472.

156. *USA Pat.,* US2429420A, 1947.

157. D.-C. Woo, C.-Y. Koo, H.-C. Ma and H. Lee, *Transactions on Electrical and Electronic Materials*, 2012, **13**, 241–244.

158. J. Kim, B. J. Murdoch, J. G. Partridge, K. Xing, D.-C. Qi, J. Lipton-Duffin, C. F. McConville, J. van Embden and E. D. Gaspera, *Advanced Materials Interfaces*, 2020, **7**, 2000655.

159. E. P. Zironi, J. Rickards, A. Maldonado and R. Asomoza, *Nuclear Instruments and Methods in Physics Research Section B: Beam Interactions with Materials and Atoms*, 1990, **45**, 115–118.

160. E. Ching-Prado, A. Watson and H. Miranda, *Journal of Materials Science: Materials in Electronics*, 2018, **29**, 15299–15306.

161. J. M. Kim, Y. J. Lee, S.-h. Kim, K.-H. Chae, K. R. Yoon, K. A. Lee, A. Byeon, Y. S. Kang, H.-Y. Park, M. K. Cho, H. C. Ham and J. Y. Kim, *Nano Energy*, 2019, **65**, 104008.

162. B. K. Sarma and P. Rajkumar, *Materials Today Communications*, 2020, **23**, 100870.

163. Y. L. Zhang, X. P. Zhang, R. Q. Tan, Y. Yang, J. H. Zhao, W. Y. Wang, P. Cui and W. J. Song, *Materials Science Forum*, 2011, **685**, 6–12.

164. M. M. Hamasha, S. d. Hamasha, K. Alzoubi, M. S. Obeidat and R. Massadeh, *Coatings*, 2024, **14**.

165. D. Z. Dimitrov, Z. F. Chen, V. Marinova, D. Petrova, C. Y. Ho, B. Napoleonov, B. Blagoev, V. Strijkova, K. Y. Hsu, S. H. Lin and J. Y. Juang, *Nanomaterials (Basel)*, 2021, **11**.

166. K. Ellmer, *Nature Photonics*, 2012, **6**, 809–817.

167. H. Kawazoe, H. Yanagi, K. Ueda and H. Hosono, *MRS Bulletin*, 2000, **25**, 28–36.

168. A. N. Banerjee and K. K. Chattopadhyay, *Progress in Crystal Growth and Characterization of Materials*, 2005, **50**, 52–105.

169. H. Kawazoe, M. Yasukawa, H. Hyodo, M. Kurita, H. Yanagi and H. Hosono, *Nature*, 1997, **389**, 939–942.

170. H. Yanagi, T. Hase, S. Ibuki, K. Ueda and H. Hosono, *Applied Physics Letters*, 2001, **78**, 1583–1585.

171. H. Gao, X. Zeng, Q. Guo, Z. Yang, Y. Deng, H. Li and D. Xiong, *Dalton Transactions*, 2021, **50**, 5262–5268.

172. N. Duan, A. W. Sleight, M. K. Jayaraj and J. Tate, *Applied Physics Letters*, 2000, **77**, 1325–1326.

173. K. Ueda, T. Hase, H. Yanagi, H. Kawazoe, H. Hosono, H. Ohta, M. Orita and M. Hirano, *Journal of Applied Physics*, 2001, **89**, 1790–1793.

174. O. T. Tambunan, H. Tukiman, K. J. Parwanta, D. W. Jeong, C. U. Jung, S. J. Rhee and C. Liu, *Superlattices and Microstructures*, 2012, **52**, 774–781.

175. H. Ohta, K.-i. Kawamura, M. Orita, M. Hirano, N. Sarukura and H. Hosono, *Applied Physics Letters*, 2000, **77**, 475–477.

176. H. Hiramatsu, K. Ueda, H. Ohta, M. Hirano, T. Kamiya and H. Hosono, *Applied Physics Letters*, 2003, **82**, 1048–1050.

177. S.-i. Inoue, K. Ueda, H. Hosono and N. Hamada, *Physical Review B*, 2001, **64**, 245211.

178. M. L. Liu, L. B. Wu, F. Q. Huang, L. D. Chen and J. A. Ibers, *Journal of Solid State Chemistry*, 2007, **180**, 62–69.

179. H. Hiramatsu, K. Ueda, H. Ohta, M. Hirano, M. Kikuchi, H. Yanagi, T. Kamiya and H. Hosono, *Applied Physics Letters*, 2007, **91**.

180. Y. B. Smida, ed. M. Riadh, IntechOpen, Rijeka, 2020, DOI: 10.5772/intechopen.93337.

181. C. N. R. Rao and K. Biswas, *Essentials of Inorganic Materials Synthesis*, 2015.

182. M. Eckert, *Annalen der Physik*, 2012, **524**, A83–A85.

183. W. Friedrich, P. Knipping and M. Laue, in *Mathematisch-Physikalische Klasse*, Verlag der Königlich Bayerischen Akademie der Wissenschaften, 1912.

184. W. H. Bragg and W. L. Bragg, *Proceedings of the Royal Society of London. Series A, Containing Papers of a Mathematical and Physical Character*, 1913, **88**, 428–438.

185. Nobelprize.org, The Nobel Prize in Physics 1915, https://www.nobelprize.org/prizes/physics/1915/summary/, (accessed May 9, 2022).

186. Nobelprize.org, The Nobel Prize in Physics 1901, https://www.nobelprize.org/prizes/physics/1901/summary/, (accessed May 9, 2022).

187. Nobelprize.org, The Nobel Prize in Physics 1914, https://www.nobelprize.org/prizes/physics/1914/summary/, (accessed May 9, 2022).

188. C. Humphreys, *Acta crystallographica. Section A, Foundations of crystallography*, 2013, **69**, 45–50.

189. D. L. Bish and J. E. Post, *Modern Powder Diffraction*, Mineralogical Society of America, 1989.

190. D. Kriegner, Z. Matěj, R. Kužel and V. Holy, *Journal of Applied Crystallography*, 2015, **48**, 613–618.

191. B. Toby and R. Dreele, *Journal of Applied Crystallography*, 2013, **46**, 544–549.

192. The International Crystal Structure Database, https://icsd.products.fiz-karlsruhe.de/en, (accessed September, 2020).

193. H. M. Rietveld, *Journal of Applied Crystallography*, 1969, **2**, 65–71.

194. H. M. Rietveld, *Physica Scripta*, 2014, **89**, 098002.

195. J. Tauc, *Materials Research Bulletin*, 1968, **3**, 37–46.

196. V. M. Huxter, Doctor of Philosphy, University of Toronto, 2009.

197. S. Chalk and L. McEwen, *Chemistry International*, 2017, **39**.

198. P. Kubelka and F. Munk, *Zeitschrift für Technische Physik*, 1931, **12**, 593–601.

199. D. W. Koon and C. J. Knickerbocker, *Review of Scientific Instruments*, 1992, **63**, 207–210.

200. L. J. van der Pauw, in *Semiconductor Devices: Pioneering Papers*, 1958, DOI: 10.1142/9789814503464_0017, pp. 174–182.

201. J. G. Webster, *The Measurement, Instrumentation, and Sensors Handbook*, CRC Press, CRC Press, 1999.

202. K. Szymański, J. L. Cieśliński and K. Łapiński, *Physics Letters A*, 2013, **377**, 651–654.

203. K. Szymański, K. Łapiński and J. L. Cieśliński, *Measurement Science and Technology*, 2015, **26**, 055003.

204. R. Chwang, B. J. Smith and C. R. Crowell, *Solid-State Electronics*, 1974, **17**, 1217–1227.

205. J. Wallis, *A Treatise of Algebra both Historical and Practical*, 1685.

206. J. Raphson, *Analysis aequationum universalis*, 1690.

207. T. Petzel and J. Kohle, *Zeitschrift für anorganische und allgemeine Chemie*, 1977, **437**, 193–196.

208. A. Henglein, *Zeitschrift für anorganische und allgemeine Chemie*, 1923, **126**, 227–236.

209. D. Errandonea, A. Muñoz, P. Rodríguez-Hernández, J. E. Proctor, F. Sapiña and M. Bettinelli, *Inorganic Chemistry*, 2015, **54**, 7524–7535.

210. D. R. Lide, *CRC Handbook of Chemistry and Physics*, CRC Press, 85 edn., 2005.

211. C. W. F. T. Pistorius and M. C. Pistorius, *Zeitschrift für Kristallographie*, 1962, **117**, 259–272.

212. N. M. Selivanova and G. A. Zubova, *Zhur. Fiz. Khim.*, 1958, **33**.

213. T. A. Hoang, H. M. Ang and A. L. Rohl, *Powder Technology*, 2007, **179**, 31–37.

214. A. Apelblat, *The Journal of Chemical Thermodynamics*, 1985, **17**, 769–773.

215. R. S. Treptow, *Journal of Chemical Education*, 1984, **61**, 499.

216. F. Feher, *Handbook of Preparative Inorganic Chemistry*, Academic Press Inc, 1963.

217. G. J. Limburn, D. W. Davies, N. Langridge, Z. Malik, B. A. D. Williamson, D. O. Scanlon and G. Hyett, *Journal of Materials Chemistry C*, 2022, **10**, 3784–3795.

218. L. Tschugaeff and W. Chlopin, *Berichte der deutschen chemischen Gesellschaft*, 1914, **47**, 1269–1275.

219. L. Syper and J. Młochowski, 1984, **1984**, 439–442.

220. W. Klemm, H. Sodomann and P. Langmesser, *Zeitschrift für anorganische und allgemeine Chemie*, 1939, **241**, 281–304.

221. K. W. Sharp and W. H. Koehler, *Inorganic Chemistry*, 1977, **16**, 2258–2265.

222. J. Młochowski and L. Syper, in *Encyclopedia of Reagents for Organic Synthesis*, John Wiley & Sons, Ltd, 2001, DOI: 10.1002/047084289X.rs101.

223. L. Brandsma and H. E. Wijers, *Recueil des Travaux Chimiques des Pays-Bas*, 1963, **82**, 68–74.

224. S. Patai, *The Chemistry of Organic Selenium and Tellurium Compounds*, 2010.

225. *China Pat.,* CN103818885A, 2014.

226. K. Brace, C. Combellas, M. Delamar, A. Fritsch, F. Kanoufi, M. E. R. Shanahan and A. Thiébault, *Chemical Communications*, 1996, **134**, 403–404.

227. V. V. Chaban and O. V. Prezhdo, *The Journal of Physical Chemistry B*, 2016, **120**, 2500–2506.

228. M. C. R. Symons, *Chemical Society Reviews*, 1976, **5**, 337–358.

229. T. Havlík, in *Hydrometallurgy*, ed. T. Havlík, Woodhead Publishing, 2008, DOI: 10.1533/9781845694616.29, pp. 29–59.

230. D. J. Chakrabarti and D. E. Laughlin, *Bulletin of Alloy Phase Diagrams*, 1983, **4**, 254–271.

231. H. T. Evans, *Zeitschrift für Kristallographie - Crystalline Materials*, 1979, **150**, 299–320.

232. S. Djurle, S. P., S. E., H. K., V. S. and D. E., *Acta Chemica Scandinavica*, 1958, **12**, 1415–1426.

233. K. Szopa, T. Krzykawski, K. Banasik, P. Król, S. Skreczko, S. Mounteanou and M. Koziarska, *Minerals*, 2021, **11**, 454.

234. J. E. Dutrizac and R. J. C. MacDonald, *Materials Research Bulletin*, 1973, **8**, 961–971.

235. R. Mulla and M. K. Rabinal, *Ultrasonics Sonochemistry*, 2017, **39**, 528–533.

236. C. Song, H. Yin, N. Zhang, S. Li, B. C. Zhao and K. Yu, *Materials Letters*, 2014, **137**, 56–58.

237. D. Li, J. Ma, L. Zhou, Y. Li and C. Zou, *Optik*, 2015, **126**, 4971–4973.

238. D. Santamaria-Perez, G. Garbarino, R. Chulia-Jordan, M. A. Dobrowolski, C. Mühle and M. Jansen, *Journal of Alloys and Compounds*, 2014, **610**, 645–650.

239. R. Blachnik and A. Müller, *Thermochimica Acta*, 2000, **361**, 31–52.

240. J. C. W. Folmer and F. Jellinek, *Journal of the Less Common Metals*, 1980, **76**, 153–162.

241. J. Y. Kim, J. A. Rodriguez, J. C. Hanson, A. I. Frenkel and P. L. Lee, *Journal of the American Chemical Society*, 2003, **125**, 10684–10692.

242. A. G. M. Ferreira and L. Q. Lobo, *The Journal of Chemical Thermodynamics*, 2011, **43**, 95–104.

243. C. Burschka and W. Bronger, 1977, **32**, 11–14.

244. A. J. E. Rettie, M. Sturza, C. D. Malliakas, A. S. Botana, D. Y. Chung and M. G. Kanatzidis, *Chemistry of Materials*, 2017, **29**, 6114–6121.

245. X. Zhou, V. S. C. Kolluru, W. Xu, L. Wang, T. Chang, Y.-S. Chen, L. Yu, J. Wen, M. K. Y. Chan, D. Y. Chung and M. G. Kanatzidis, *Nature*, 2022, **612**, 72–77.

246. C. Näther, D. Röhnert and W. Bensch, *European Journal of Solid State and Inorganic Chemistry*, 1998, **35**, 565–577.

247. L. W. ter Haar, F. J. Di Salvo, H. E. Bair, R. M. Fleming, Waszczak, V. J and W. E. Hatfield, *Physical Review B*, 1987, **35**, 1932–1938.

248. M. G. Kanatzidis, *Inorganic Chemistry*, 2017, **56**, 3158–3173.

249. V. V. Brazhkin, S. V. Popova and R. N. Voloshin, *Physica B: Condensed Matter*, 1999, **265**, 64–71.

250. K. Jiang, Z. Chen and X. Meng, *ChemElectroChem*, 2019, **6**, 2825–2840.

251. G. B. Abdullaev, Z. A. Aliyarova, E. H. Zamanova and G. A. Asadov, *physica status solidi (b)*, 1968, **26**, 65–68.

252. A. Novitskii, G. Guélou, A. Voronin, T. Mori and V. Khovaylo, *Direct synthesis of p-type bulk BiCuSeO oxyselenides by reactive spark plasma sintering and related thermoelectric properties*, 2020.

253. Z. Shen, M. Johnsson, Z. Zhao and M. Nygren, *Journal of the American Ceramic Society*, 2002, **85**, 1921–1927.

254. H. Zhu, A. Prasad, S. Doja, L. Bichler and J. Liu, *Nanomaterials (Basel)*, 2019, **9**.

255. J. Zou, S. Xu, J. Chen, P. Wang, C. Yan, C. Cao, Y. You, J. Lu, L. Zhu, Z. Zhu and J. Lin, *Journal of Nuclear Materials*, 2023, **585**, 154649.

256. N. Kanas, B. A. D. Williamson, F. Steinbach, R. Hinterding, M.-A. Einarsrud, S. M. Selbach, A. Feldhoff and K. Wiik, *ACS Applied Energy Materials*, 2022, **5**, 12396–12407.

257. Z. Wang, Q. Yang, W. Liu, H. Ran, C. Zhang, X. Han, X. He, X. Wang and C. Hu, *Nano Energy*, 2019, **59**, 129–137.

258. A. N. Papathanassiou, *Physical Review B*, 1998, **58**, 4432–4437.

259. J. G. Smith, J. Naruse, H. Hiramatsu and D. J. Siegel, *Chemistry of Materials*, 2017, **29**, 3152–3163.

260. H. Hiramatsu, K. Ueda, H. Ohta, M. Hirano, T. Kamiya and H. Hosono, *Thin Solid Films*, 2003, **445**, 304–308.

261. B. Saha, M. Garbrecht, J. A. Perez-Taborda, M. H. Fawey, Y. R. Koh, A. Shakouri, M. Martin-Gonzalez, L. Hultman and T. D. Sands, *Applied Physics Letters*, 2017, **110**.

262. S. S. A. Gillani, R. Ahmad, M. Rizwan, M. Rafique, G. Ullah, C. B. Cao and H. B. Jin, *Optik*, 2019, **191**, 132–138.

263. T. L. Chou, O. Mustonen, T. S. Tripathi and M. Karppinen, *J Phys Condens Matter*, 2016, **28**, 035802.

264. R. D. Smyth, J. A. D. Wilson, P. Manuel and S. J. Clarke, *Journal of Solid State Chemistry*, 2022, **307**, 122841.

265. M. H. Miah, M. U. Khandaker, M. B. Rahman, M. Nur-E-Alam and M. A. Islam, *RSC Advances*, 2024, **14**, 15876–15906.

266. A. J. Corkett, D. G. Free, S. J. Cassidy, S. Ramos and S. J. Clarke, *Journal of Solid State Chemistry*, 2014, **216**, 91–98.

267. P. Shirage, K. Kihou, C. Lee, H. Kitô, H. Eisaki and A. Iyo, *Physica C-superconductivity and Its Applications*, 2013, **484**, 12–15.

268. Y. Zhang, X. Tao and M. Tan, *Solid State Communications*, 2013, **172**, 41–48.

269. S. Hui and A. Petric, *Materials Research Bulletin*, 2002, **37**, 1215–1231.

270. M. Prabu, S. Selvasekarapandian, A. R. Kulkarni, S. Karthikeyan, G. Hirankumar and C. Sanjeeviraja, *Ionics*, 2011, **17**, 201–207.

271. S. Tao and J. T. S. Irvine, *Journal of Solid State Chemistry*, 2007, **180**, 3493–3503.

272. P. Kumar, P. Jena, P. K. Patro, R. K. Lenka, A. S. K. Sinha, P. Singh and R. K. Singh, *ACS Appl Mater Interfaces*, 2019, **11**, 24659–24667.

273. U. Balachandran and N. G. Eror, *Journal of The Electrochemical Society*, 1982, **129**, 1021.

274. K. Yamada, E. Kudo, Y. Endoh, K. Tsuda, M. Tanaka, K. Kokusho, H. Asano, F. Izumi, M. Oda, Y. Hidaka, M. Suzuki and T. Murakami, *Japanese Journal of Applied Physics*, 1988, **27**, 1132.

275. P. G. Radaelli, J. D. Jorgensen, A. J. Schultz, B. A. Hunter, J. L. Wagner, F. C. Chou and D. C. Johnston, *Physical Review B*, 1993, **48**, 499–510.

276. W. Xu, Y. Liu, D. Chen, Y.-H. Lin, Z. Wu, Y. Xie, B.-P. Zhang, B. Cheng, C.-W. Nan and Z. Wu, *Journal of the American Ceramic Society*, 2011, **94**, 1471–1476.

277. J. Yu, X. Liu, H. Hu, Y. Jiang, H.-L. Zhuang, H. Li, B. Su, J.-W. Li, Z. Han, Z. Wang, L. Chen, K. Hayashi, Y. Miyazaki, B. L. Mehdi and J.-F. Li, *Joule*, 2024, **8**, 2652–2666.

278. C. Rudradawong, S. Khammuang, K. Kotmool, T. Bovornratanaraks, P. Limsuwan, N. Somdock, R. Sakdanuphab and A. Sakulkalavek, *Journal of the European Ceramic Society*, 2023, **43**, 401–406.

279. Y.-X. Zhang, Y.-Q. Tang, Z. Ma, M.-Y. Hu, J. Feng and Z.-H. Ge, *Inorganic Chemistry*, 2021, **60**, 13269–13277.

280. P. Lunca Popa, J. Crêpellière, P. Nukala, R. Leturcq and D. Lenoble, *Applied Materials Today*, 2017, **9**, 184–191.

281. L. Farrell, E. Norton, B. J. O'Dowd, D. Caffrey, I. V. Shvets and K. Fleischer, *Applied Physics Letters*, 2015, **107**.

282. M. S. Diallo, T. Shi, Y. Zhang, X. Peng, I. Shozib, Y. Wang, L. J. Miara, M. C. Scott, Q. H. Tu and G. Ceder, *Nature Communications*, 2024, **15**, 858.

283. V. S. Gangoli, C. J. Barnett, J. D. McGettrick, A. Orbaek White and A. R. Barron, *C - Journal of Carbon Research*, 2022, **8**, 1.

284. K. Bindra, N. Suri and R. Thangaraj, *Chalcogenide Letters*, 2007, **3**, 133–138.

285. P. Baranowski, S. Starzonek, A. Drozd-Rzoska, S. J. Rzoska, M. Bockowski, P. Keblinski, T. K. Pietrzak and J. E. Garbarczyk, *Sci Rep*, 2019, **9**, 16607.

286. R. Hoppe, B. Schepers, H.-J. Rohrborn and E. Vielhaber, *Zeitschrift für anorganische und allgemeine Chemie*, 1965, **339**, 130–143.

287. I. Galuskina, *Minerals*, 2023, **13**.

288. R. E. Schaak and T. E. Mallouk, *Chemistry of Materials*, 2002, **14**, 1455–1471.

289. L. Cario, H. Kabbour and A. Meerschaut, *Chemistry of Materials*, 2005, **17**, 234–236.

290. H. Kabbour and L. Cario, *physica status solidi c*, 2006, **3**, 2867–2870.

291. J. N. Blandy, S. Liu, C. F. Smura, S. J. Cassidy, D. N. Woodruff, J. E. McGrady and S. J. Clarke, *Inorganic Chemistry*, 2018, **57**, 15379–15388.

292. C. S. Knee and M. T. Weller, *Journal of Solid State Chemistry*, 2002, **168**, 1–4.

293. C. S. Knee, M. A. L. Field and M. T. Weller, *Solid State Sciences*, 2004, **6**, 443–450.

294. W. Leib and H. Müller-Buschbaum, *Zeitschrift für anorganische und allgemeine Chemie*, 1984, **518**, 115–119.

295. C. S. Knee, A. A. Zhukov and M. T. Weller, *Chemistry of Materials*, 2002, **14**, 4249–4255.

296. C. S. Knee and M. T. Weller, *MRS Proceedings*, 2002, **718**, D7.33.

297. C. S. Knee and M. T. Weller, *Chem Commun (Camb)*, 2002, DOI: 10.1039/b110122f, 256–257.

298. R. L. Needs and M. T. Weller, *Journal of the Chemical Society, Chemical Communications*, 1995, DOI: 10.1039/C39950000353, 353–354.

299. W. Gutau and H. Müller-Buschbaum, *Zeitschrift für anorganische und allgemeine Chemie*, 1990, **584**, 125–128.

300. M. Abed and H. Müller-Buschbaum, *Journal of Alloys and Compounds*, 1992, **183**, 24–29.

301. G. Savelsberg, *Zeitschrift für Naturforschung B*, 1978, **33**, 370–373.

302. H. G. von Schnering, R. Türck, W. Hönle, K. Peters, E. M. Peters, R. Kremer and J. H. Chang, *Zeitschrift für anorganische und allgemeine Chemie*, 2002, **628**, 2772–2777.

303. W. T. Jin, N. Qureshi, Z. Bukowski, Y. Xiao, S. Nandi, M. Babij, Z. Fu, Y. Su and T. Brückel, *Physical Review B*, 2019, **99**, 014425.

304. A. Balvanz, S. Baranets, M. O. Ogunbunmi and S. Bobev, *Inorganic Chemistry*, 2021, **60**, 14426–14435.

305. B. Eisenmann and M. Somer, *Zeitschrift für Naturforschung B*, 1985, **40**, 1419–1423.

306. O. W. Gooding, *Current Opinion in Chemical Biology*, 2004, **8**, 297–304.

307. A. W. Dombrowski, A. L. Aguirre, A. Shrestha, K. A. Sarris and Y. Wang, *The Journal of Organic Chemistry*, 2022, **87**, 1880–1897.

308. S. K. Vooturi and S. M. Firestine, *Journal of Combinatorial Chemistry*, 2010, **12**, 151–160.

309. H. Fujii and A. Sato, *Journal of Alloys and Compounds*, 2009, **487**, 198–201.

310. J.-T. Han, J.-S. Zhou, J.-G. Cheng and J. B. Goodenough, *Journal of the American Chemical Society*, 2010, **132**, 908–909.

311. C. Godart, C. Ammarguellat, M. F. Ravet, N. Wetta, C. Levy-Clement, H. Noel and G. Krill, *Solid State Communications*, 1986, **59**, 241–244.

312. P. N. Shanbhag, R. K. Biswas, S. K. Pati, A. Sundaresan and C. N. R. Rao, *ACS Omega*, 2020, **5**, 29009–29016.

313. S. M. Loureiro, C. Felser, Q. Huang and R. J. Cava, *Chemistry of Materials*, 2000, **12**, 3181–3185.

314. N. McGlothlin, D. Ho and R. J. Cava, *Materials Research Bulletin*, 2000, **35**, 1035–1043.

315. Y. Miyahara, K. Miyazaki, T. Fukutsuka and T. Abe, *Chemical Communications*, 2017, **53**, 2713–2716.

316. F. D. Romero, L. Coyle and M. A. Hayward, *Journal of the American Chemical Society*, 2012, **134**, 15946–15952.

317. E. Sullivan, J. Hadermann and C. Greaves, *Journal of Solid State Chemistry*, 2011, **184**, 649–654.

318. J.-C. Grenier, S. Ghodbane, G. Demazeau, M. Pouchard and P. Hagenmuller, *Materials Research Bulletin*, 1979, **14**, 831–839.

319. C. S. Knee, D. J. Price, M. R. Lees and M. T. Weller, *Physical Review B*, 2003, **68**, 174407.

320. W. T. A. Harrison, S. L. Hegwood and A. J. Jacobson, *Journal of the Chemical Society, Chemical Communications*, 1995, DOI: 10.1039/C39950001953, 1953–1954.

321. T. Takeda, Y. Yamaguchi and H. Watanabe, *Journal of the Physical Society of Japan*, 1972, **33**, 970–972.

322. W. Wong-Ng, J. A. Kaduk and G. Liu, *Powder Diffraction*, 2011, **26**, 22–30.

323. A. L. Hector, J. A. Hutchings, R. L. Needs, M. F. Thomas and M. T. Weller, *Journal of Materials Chemistry*, 2001, **11**, 527–532.

324. J. F. Ackerman, *Journal of Solid State Chemistry*, 1991, **92**, 496–513.

325. Y. Su, Y. Tsujimoto, K. Fujii, M. Tatsuta, K. Oka, M. Yashima, H. Ogino and K. Yamaura, *Inorganic Chemistry*, 2018, **57**, 5615–5623.

326. H. Yaguchi, K. Fujii, Y. Tsuchiya, H. Ogino, Y. Tsujimoto and M. Yashima, *ACS Applied Energy Materials*, 2022, **5**, 295–304.

327. Y. Iwasa, Y. Su, Y. Tsuchiya, M. Tatsuda, K. Kishio, T. Yanagida, F. Takada, T. Nishio, Y. Tsujimoto, K. Fujii, M. Yashima and H. Ogino, *Journal of Materials Chemistry C*, 2020, **8**, 17162–17168.

328. R. Welter, G. Venturini, B. Malaman and E. Ressouche, *Journal of Alloys and Compounds*, 1993, **202**, 165–172.

329. S. Ganesanpotti, T. Yajima, K. Nakano, Y. Nozaki, T. Yamamoto, C. Tassel, Y. Kobayashi and H. Kageyama, *Journal of Alloys and Compounds*, 2014, **613**, 370–374.

330. D. T. Adroja and B. D. Rainford, *Journal of Magnetism and Magnetic Materials*, 1994, **135**, 333–342.

331. S. Jin, X. Chen, J. Guo, M. Lei, J. Lin, J. Xi, W. Wang and W. Wang, *Inorganic Chemistry*, 2012, **51**, 10185–10192.

332. T. Kato, Y. Iwasa, Y. Yokota, S. Ishida, J. Kato, Y. Mino, S. P. K. Naik, T. Horiai, A. Yoshikawa, T. Nishio, H. Eisaki and H. Ogino, *Journal of the Korean Ceramic Society*, 2025, DOI: 10.1007/s43207-024-00473-y.

333. X. Zhou, C. D. Malliakas, A. A. Yakovenko, B. Wilfong, S. G. Wang, Y.-S. Chen, L. Yu, J. Wen, M. Balasubramanian, H.-H. Wang, D. Y. Chung and M. G. Kanatzidis, *Nature Synthesis*, 2022, **1**, 729–737.

334. S. G. Tan, H. C. Lei, W. J. Lu, P. Tong, L. J. Li, S. Lin, Y. N. Huang, Z. H. Huang, Y. Liu, B. C. Zhao and Y. P. Sun, *Journal of Alloys and Compounds*, 2014, **598**, 171–176.

335. S. Lee, H. Xu, H. Xu and J. Neuefeind, *Minerals*, 2021, **11**, 272.

336. H. Ott, *Zeitschrift für Kristallographie - Crystalline Materials*, 1926, **63**, 222–230.

337. B. Baptiste, M. Azuma, R. Yu, P. Giura and M. d'Astuto, *IUCrData*, 2018, **3**, x181645.

338. Z. Hiroi, N. Kobayashi and M. Takano, *Physica C: Superconductivity*, 1996, **266**, 191–202.

339. H. Müller-Buschbaum and J. Boje, *Zeitschrift für anorganische und allgemeine Chemie*, 1991, **592**, 73–78.

340. B. Rendenbach, S. Klenner, R. Pöttgen and D. Johrendt, *Zeitschrift für Naturforschung B*, 2019, **75**, 105–110.

341. J. G. Lee, K. V. Ramanujachary and M. Greenblatt, *Materials Research Bulletin*, 1991, **26**, 1027–1034.

342. C. S. Knee and M. T. Weller, *Journal of Materials Chemistry*, 2001, **11**, 2350–2357.

343. J. Pannetier and P. Batail, *Journal of Solid State Chemistry*, 1981, **39**, 15–21.

344. R. C. Rouse, *Mineralogical Magazine*, 1973, **39**, 49–53.